ICCC 2023 - Guidelines for citation and reuse



Please cite the conference proceedings as following:
Thailand Concrete Association, Ed. *Further Reduction of CO2 -Emissions and Circularity in the Cement and Concrete Industry, 16th International Congress on the Chemistry of Cement 2023 - ICCC2023* (Bangkok 18.-22.09.2023). Bangkok, 2023. Available at: https://www.iccc-online.org/archive/

Please cite individual papers as following:
Author. Title. In: Thailand Concrete Association, Ed. *Further Reduction of CO2 -Emissions and Circularity in the Cement and Concrete Industry, 16th International Congress on the Chemistry of Cement 2023 - ICCC2023* (Bangkok 18.-22.09.2023). Bangkok, 2023. Available at: https://www.iccc-online.org/archive/

All papers in the 2023 conference proceedings are published under the license CC-BY-ND 4.0.
(https://creativecommons.org/licenses/by-nd/4.0/legalcode)

Organized by

TCA
สมาคมคอนกรีตแห่งประเทศไทย
Thailand Concrete Association

THE 16TH INTERNATIONAL CONGRESS ON THE CHEMISTRY OF CEMENT
ICCC 2023
BANGKOK THAILAND



ICCC 16th 2023

INTERNATIONAL CONGRESS ON THE CHEMISTRY OF CEMENT

CONGRESS PROCEEDING VOLUME I

Further reduction of CO_2-emission and circularity in the cement and concrete industry

SEPTEMBER 18-22, 2023

CENTARA GRAND & BANGKOK CONVENTION CENTRE @CENTRALWORLD

Co-Sponsor by

aci American Concrete Institute

SEADMA

gcca

ASTM INTERNATIONAL

Contact infomation :
Email: iccc2023.tca@gmail.com
Website : https://www.iccc2023.org/

PREFACE

The International Congress on the Chemistry of Cement (ICCC) is the renowned global platform that summarizes the state of the art of cement chemistry as well as major trends in cement application. Since the first International Congress on the Chemistry of Cement started in London in 1918, it has provided a strong and fruitful link between the academic world and the cement industry. It has always stimulated scientific exchanges and discussions between researchers, students, and those who have already gained working experience in many fields of chemistry relevant to cement production and its use in concrete and mortar. The ICCC is the venue to present cement and environmental development together with meeting worldwide and renowned experts from all over the world who come to present their works at the congress.

This proceeding collects the papers submitted to the 16th International Congress on the Chemistry of Cement (ICCC 2023), which was held in Bangkok, Thailand between September 18-22, 2023, and organized by Thailand Concrete Association on the theme of "further reduction of CO2-emission and circularity in the cement and concrete industry". The ICCC 2023 attracted more than 565 papers and more than 800 delegates and students from 49 countries.

The scientific program covers the topics of the newest and the most important research and development describing the new dimensions in clinker production, advances in hydration chemistry, enhancing clinker substitution and supplementary cementitious materials, advances in characterization methods and modelling, new low carbon cement and carbonatable binders, new findings in admixture & rheology, new technology for quality concrete, durability & reactive transport, sustainability, circular economy, waste processing and recycling, and standardization of cement and concrete.

The Organizing Committee and the Scientific Committee believe that our participants will be most satisfied with the congress and will gain the knowledge to improve their professional works in the future.



Prof.Thanakorn Pheeraphan
Chairman of the Organizing Committee



Prof.Somnuk Tangtermsirikul
Chairman of the Scientific Committee

Steering Committee Members

The Steering Committee is comprised of 26 members.

1. Prof. Dr. Mark G. Alexander, University of Cape Town, South Africa
2. Prof. Dr. Alexandra Bertron, INSA Toulouse, France
3. Prof. Dr. Shashank Bishnoi; Indian Institute of Technology Delhi, India
4. Prof. Dr. Leon Black, University of Leeds, United Kingdom
5. Dr. Cesar Constantino; Titan America LLC, USA
6. Jesper Sand Damtoft, Aalborg Portland A/S, Denmark
7. Prof. Dr. Jan Deja; Stowarzyszenie Producentów Cementu – PCA, Poland
8. Dr. Wolfgang Dienemann, HeidelbergCement AG, Germany
9. Daniel Duque, Cementos Argos S.A., Columbia
10. Ing. Jan Gemrich, Czech Cement Association, Czech Republic
11. Prof. Dr. Frederik Paul Glasser, University of Aberdeen, Scotland
12. Prof. Dr. R. Doug Hooton, University of Toronto, Canada
13. Prof. Dr. Vanderley M. John, Escola Politécnica da USP, Brasil
14. Prof. Dr. Kimberly Kurtis, Georgia Institute of Technology, USA
15. Christophe Levy, Lafarge Holcim Innovation Center (Chairman), France
16. Prof. Dr. Ippei Maruyama, Nagoya University Furocho, Japan
17. Dr. Bibekananda Mohapatra, Director General of the National Council for Cement and Building Materials, India
18. Dr. Marta Palacios, Instituto Eduardo Torroja, Spain
19. Prof. Dr. Angel Palomo, Instituto Eduardo Torroja, Spain
20. Prof. Dr. Thanakorn Pheeraphan, Thailand Concrete Association (Deputy-Chairman), Thailand
21. Prof. Dr. Martin Schneider, VDZ e.V., Research Institute, Germany
22. Prof. Dr. Karen Scrivener, École Polytechnique Fédérale de Lausanne – EPFL, Switzerland
23. Prof. Dr. Caijun Shi, Hunan University, China
24. Prof. Dr. Sui Tongbo, Sinoma International Engineering Co., Ltd., China
25. Prof. Dr. Jannie S. J. Van Deventer, Zeobond Pty Ltd, Australia
26. Dr. Kazuo Yamada, National Institute for Environmental Studies, Japan

Dr. Joerg Rickert, VDZ (Permanent Secretariat of ICCC), Germany - (Without the right to vote)

Organizing Committee Members

Advisory committee members

1. Dr. Wonchalerm Chalodhorn, Siam City Cement Co. Ltd.
2. Prof.Dr. Chai Jaturapitakkul, King Mongkut's University of Technology Thonburi
3. Prof.Dr. Parinya Jindaprasert, KhonKaen University
4. Mr. Ferdinand Leopolder, The South East Asia Drymix Mortar Association SEADMA,
5. Assoc.Prof.Dr. Pichai Nimityongskul , 1st President of Thailand Concrete Association
6. Mr. Chakporn Oonjitt, Construction Institute of Thailand
7. Mr. Wanchai Phanomchai, Thai Industrial Standards Institute
8. Mr. Chana Poomee, Thai Cement Manufacturers Association
9. Dr. Phirun Saiyasitpanich, Office of Natural Resources and Environmental Policy and Planning
10. Mr. Manasit Sarigaphuti, The Siam Cement Group Public Company Limited
11. Assoc.Prof. Anek Siripanichgorn, Engineering Institute of Thailand
12. Prof.Dr. Boonchai Stitmannaithum, Chulalongkorn University
13. Prof.Dr. Piti Sukontasukkul, King Mongkut's University of Technology North Bangkok
14. Mr. Sumate Surabotsopon, Italian-Thai Development Public Company Limited
15. Prof.Dr. Somnuk Tantermsirikul, Sirindhorn International Institute of Technology
16. Dr. Saranyu Viriyavejakul, Neighboring Countries Economic Development Cooperation Agencies
17. Prof.Dr. Pennung Warnitchai, Asian Institute of Technology
18. Mr. Boonyanit Wongrukmit, Electricity Generating Authority of Thailand

Organizing Committee members

1. Prof.Dr. Thanakorn Pheeraphan, Thailand Concrete Association and NavamindaKasatriyadhiraj Royal Air Force Academy (Chairman)
2. Asst.Prof. Dr. Chuchai Sujivorakul, King Mongkut's University of Technology Thonburi (Deputy Chairman)
3. Mr. Boonrawd Kuptitanhi, The Concrete Products and Aggregate Co., Ltd. (Treasurer)
4. Asst.Prof.Dr. Nattapong Magaratat , King Mongkut's University of Technology North Bangkok (Secretariat)
5. Dr. Praveen Chompreda, K.C.S. & ASSOCIATES. Co., Ltd.
6. Assoc.Prof.Dr. Phongthorn Julphunthong, Naresuan University
7. Miss Sunkamol Khongsawatvorakul, Saint-Gobain Thailand.
8. Mr. Sumet Kiatmetha, Hilti (Thailand) Ltd.
9. Gp.Capt. Nuth Limsuwan, Office of Civil Engineering Royal Thai Armed Forces.
10. Dr. Nontapat Nimityongskul, Asia Cement Public Company Limited.
11. Assoc.Prof. Panuwat Joykad, Srinakharinwirote University
12. Dr. Yut Panitanwong, Concrete Product and Aggregate Co.,Ltd.
13. Mr. Suwatchai Puwapattanachat, SIKA (Thailand) Ltd.
14. Mr. Narin Sayanwisuttikam, KAO Industrial (Thailand) Co., Ltd.
15. Dr. Kritsada Sisomphon, The Siam Cement Group Public Company Limited.
16. Mr. Chalermwut Snguanyat, The Siam Cement Group Public Company Limited.
17. Mr. Pakorn Sutthiwaree, Siam City Cement Public Company Limited.
18. Assoc.Prof.Dr. Weerachart Tangchirapat, King Mongkut's University of Technology Thonburi
19. Asst. Prof. Dr. WarangkanaSaengsoy, Construction and Maintenance Technology Research Center, SIIT
20. Prof.Dr. Wanchai Yodsudjai, Kasetsart University

Scientific Committee Members

1. Prof.Mark Alexander, South Africa
2. Prof.Carmen Andrade, Spain
3. Prof.Sergio Angulo, Brazil
4. Dr.Mohsen Ben Haha, Germany
5. Prof.Susan Bernal Lopez, UK
6. Prof.Alexandra Bertron, France
7. Prof.Shashank Bishnoi, India
8. Prof.Maria Blanco, Spain
9. Prof.Jeff Bullard, USA
10. Prof.Maria Alba Cincotto, Brazil
11. Prof.Jan Deja, Poland
12. Prof.Donguk Choi, South Korea
13. Prof.Josee Duchesne, Canada
14. Mr.Wilmar Echeverri, Colombia
15. Prof.Ivan Escalante, Mexico
16. Dr.Duncan Herfort, Denmark
17. Prof.Bruno Huet, France
18. Prof.Jason Ideker, USA
19. Prof.Edgardo Irassar, Argentinia
20. Prof.Zhengwu Jiang, China
21. Prof.Maria Juenger, USA
22. Dr.Marios Katsiotis, Greece
23. Prof.Shiho Kawashima, USA
24. Prof.Paula Kirchheim, Brazil
25. Prof.Jiaping Liu, China
26. Mr.Federico Lopez, Mexico
27. Prof.Barbara Lothenbach, Switzerland
28. Prof.Horst Ludwig, Germany
29. Prof.Ippei Maruyama, Japan
30. Prof.Thomas Matschei, Germany
31. Mr.Mike McDonald, South Africa
32. Dr.Sean Monkman, Canada
33. Prof.Paulo Monteiro, USA
34. Mr.Carlos Orozco, Colombia
35. Dr.Marta Palacios, Spain
36. Prof.Martin Palou, Slovakia
37. Dr.César Pedrajas, Spain
38. Prof.Rafael Pileggi, Brazil
39. Prof.Kedsarin Pimraksa, Thailand
40. Prof.John Provis, UK
41. Prof.Francisca Puertas, Spain

Scientific Committee Members

42.Prof.Jueshi Qian, China
43.Prof.Aleksandra Radlinska, USA
44.Dr.Nailia Rakhimova, Russia
45.Prof.Matteo Romano, Italy
46.Prof.Nicolas Roussel, France
47.Dr.Kwesi Sagoe-Crentsil, Australia
48.Prof.Manu Sanathanam, India
49.Prof.Miguel Sanjuán, Spain
50.Prof.Caijun Shi, China
51.Dr.Denise Silva, USA
52.Prof.Somnuk Tangtermsirikul, Thailand (Chairman)
53.Dr.Theodor Staněk, CZ
54.Prof.Arezki Tagnit-Hamou, Canada
55.Mr.Antonio Telesca, Italy
56.Dr.Paul Tennis, USA
57.Prof.Michael Thomas, Canada
58.Prof.Jorge Tobon, Canada
59.Prof.Sandro Torres, Brazil
60.Prof.Matthieu Vandamme, France
61.Dr.Yury Villagrán Zaccardi, Argentina
62.Prof.Fazhou Wang, China
63.Prof.Zhang Wensheng, China
64.Prof.Claire White, USA
65.Dr.Frank Winnefeld, Switzerland
66.Dr.Hong Wong, UK
67.Dr.Kazuo Yamada, Japan
68.Prof.Cheng Yu, China
69.Prof.Doug Hooton, Canada
70.Peter Kruspan, Switzerland

Contents

	Topics	Page
	Preface	i
	Committees	
	- Steering Committee Members	ii
	- Organizing Committee Members	iii
	- Scientific Committee Members	v
	Papers	
PA0001	Effect on Graphene Oxide and Silica Fume on the Performance of Concrete under Standard Curing Conditions	1
PA0008	Comparison of the mode of action of a shotcrete accelerator in a slag cement and an OPC cement	5
PA0009	3D-printable magnesium-silicate-hydrate cement composites: A feasibility study	9
PA0010	Evaluation of Internal Cracks and Three-Dimensional Deformation due to Different Nozzle Paths in a Material Extrusion 3D Printer	13
PA0012	Use of volcanic ash in an ECC material for 3D printing	18
PA0013	Future projection of carbon dioxide emission in calcium carbonate concrete (CCC) production	22
PA0015	Novel Soluble Boron Compounds to Improve Shielding of Cement Systems	26
PA0016	Constructing solutions using cement-based materials for energy harvesting and storage	30
PA0020	Use of biomass ash in the fabrication of Self-healing engineered cementitious composites (ECC)	34
PA0021	Assessment of early-age drying induced microstructural changes in 3D printed cement mortar	38
PA0025	3D Printing Mortar and Concrete: Advancement and Application of Laboratory Test Protocol to Evaluate Properties physicochemical and mechanical.	42
PA0028	The Role of Belitic Calcium Sulfoaluminate Cement in Achieving Net-zero	46
PA0035	Carbon neutral concrete based on a sea snail shell: a green solution for the urban heat island	50
PB0001	Prediction of Total Bond Order Density of Cement Crystals using Fermionic Hubbard Model and Bloch and Fermi Surface	54

Contents

	Topics	Page
	PAPERS	
PB0002	Digitalization in cement production: prediction of free lime content in clinker production	58
PB0003	Method of Intensifying Cement Clinker Production	62
PB0004	Piezoresistive performance of GNP-modified highly deformable cementitious materials	66
PB0007	Research on the preparation of low-calcium Portland cement	70
PB0008	Determination of Clinker Performance with Chemical Additives by use of XRF, QXRD and Microscopy Analysis.	74
PB0009	Preparation and Characterization of Portland cement Clinker by High Magnesium Limestone and Iron Tailings	78
PB0010	Production and Analysis of BYF Clinker Produced via the Combustion of Elemental Sulfur	82
PB0015	Effect of cooling rates on the properties of Portland cement clinkers in the presence of Mg	86
PB0016	Effect of chlorides on the clinkering and reactivity of ye'elimite	90
PB0017	Effect of Synthesis Conditions, Zn Doping and Al/Fe Ratio on Calcium [Alumino] Ferrite Structure	94
PC0002	Recent advances in understanding the hydration of limestone calcined clay cements (LC^3)	98
PC0003	Microstructural mechanism involved in the expansion generated in cementitious materials with expansive agent type K	105
PC0011	The influence of free water removal approaches on the composition and morphologies of CAC hydrates cured at different temperatures	109
PC0016	Effect of temperature rise inhibitor on heat evolution of cement-quartz system	113
PC0020	Influence of ferronickel slag on early hydration and microstructure of alkali-activated ground granulated blast furnace slag	117
PC0022	Synthesis and characterization of iron and aluminium-containing AFm phases	122
PC0024	Effect of titanium dioxide nanoparticles on hydration and mechanical properties of mortar based on a ternary binder system	126

Contents

	Topics	Page
	PAPERS	
PC0025	Role of Gypsum on Early Age Hydration of Alite Polymorphs (TI and TIII): A Temporal X-ray PDF Analysis	130
PC0026	Adsorption of Ca^{2+} at Micro Aggregate Surface and Its Effect on Particle Interaction, C-S-H Formation and Adhesion	134
PC0027	In Situ X-ray Total Scattering Study on the Impact of Gypsum in C3S-Metakaolin-Limestone Systems	138
PC0029	Hydration of CAC pastes at high temperature	142
PC0031	A Combined Calorimetry and XRD Study of The First 15 Minutes of Portland Cement Hydration	146
PC0037	Comparative study of the hydration kinetics of oil well cement and model cement retarded by tartaric acid at elevated temperatures	150
PC0039	Hydration of tricalcium aluminate-sulphate systems in presence of alkanolamines	154
PC0040	Thermogravimetric analysis on the effect of SAP addition on the microstructure of cement based materials	158
PC0042	Sodium sites and hydration state in C-S-H phases synthesized under alkaline conditions from ^{1}H and ^{23}Na MAS NMR experiments	162
PC0043	Effect of irradiation on Portland cement pastes: impact on mineralogy, mechanical properties, and microstructure	166
PC0044	Influence of TiO_2 on the kinetic reaction of white Portland cement suspensions	170
PC0046	Early hydration and rheological behavior of the calcium aluminates mixtures in the presence of gypsum	171
PC0048	Elucidation of hydration reaction of blended OPC by the utilization of alkanolamine-base grinding agent	176
PC0049	An insight on the effect of $KAlO_2$ on hydration kinetics and mechanical properties of ternesite	179
PC0050	Synthesis of sodium iron silicate hydrate (N-F-S-H)	183
PC0052	Nucleation of C-S-H from Molecular Dynamics	187
PC0053	Study of early age hydration behavior of sulfate-rich belite sulfoaluminate cements with anhydrite and gypsum	191
PC0054	Identification of Phases in Cementitious Materials at Critical Elevated Temperatures	196

Contents

	Topics	Page
	PAPERS	
PC0055	Time resolved synchrotron X-ray diffraction investigations of LC3 hydration in the presence of hydroxyethyl methyl cellulose ethers	200
PC0056	Mineral dissolution mechanism of different polymorphs of alite from ReaxFF molecular dynamics simulation	204
PC0058	Hydration of Calcium [Alumino] Ferrite with Limestone	209
PC0059	Deciphering the defects of alite particles at the single-atom level	213
PC0077	The Influence of Aluminum Uptake on the Mechanical Properties of Calcium Silicate Hydrate	217
PD0001	New steel production processes and their consequences for slag utilization in cement	221
PD0003	The effect of iron phases on the performance of calcined clays in calcined clay-limestone cement	225
PD0005	Dilution Effects in Cementitious Matrices by Using Calcined Clay and Limestone for Reduced Clinker Factors	229
PD0006	Study on Calcined Clay-Recycled Concrete Powder Composite as Supplementary Cementitious Material	233
PD0007	Study of filler effect of VGP on cement hydration	238
PD0008	Reactivity of alternative supplementary cementitious materials assessed by the R^3 method	243
PD0009	Activation of LC^3 low-carbon cements by C-S-H seeding	247
PD0012	Nucleation Effects of Biologically Architected Calcium Carbonate in Portland Limestone Cements	251
PD0014	Dune sand powders characterization for their use in cement-based materials	258
PD0019	Pore structure refinement of calcium-sulfate-aluminate--Portland cement mortars by early-age CO_2 curing	262
PD0021	Simulation of sulfate attack on carbonated Portland cement-blast furnace slag binary cement	266
PD0022	A Study on Hydration Properties of Cement Matrix according to Limestone Content for Portland Cement	270
PD0023	Mineralogical analysis of BOF slag with different grinding characteristics	274
PD0026	Cement Hydration Kinetics of LC3 Paste Synthesized with Biologically Architected $CaCO_3$	278

Contents

	Topics	Page
	PAPERS	
PD0029	Effect of silica fume on long-term hydration and compressive strength of UHPC under different curing regimes	282
PD0033	Variation of Fluidity of Calcined Clay Limestone Cements by Power Ultrasound and Gypsum Addition	286
PD0034	Effect of solid wastes with different activities on the rheological properties of 3D printing low carbon concrete	291
PD0035	Assessing the activity of potential SCM's using the R3 test method	295
PD0036	The effect of ionic environment of cement pore solution on the PCE's molecular conformation, adsorption and performance	299
PD0040	Performance of calcined anthill clay as a supplementary cementitious material	304
PD0042	Reactivity of alternative SCMs from Nordic Countries – Input for the R^3 test	309
PD0043	New Insights on the Use of Sewage Sludge Ashes as Supplementary Cementitious Materials	313
PD0044	Impact of Ca/Si and Al/Si ratio on the alumina-silica gel formed by wet carbonation of synthesized C-S-H phases	317
PD0045	About The Effect Of Portland Cement Activation On Supersulfated Cements Properties	321
PD0046	Determining the reaction kinetics of supplementary cementitious materials for input into thermodynamic-kinetic models	325
PD0048	Characterization of (A/F) H_3 Phase Microstructure with Different Al/(Fe+Al) Ratios based on Calcium Sulfoaluminate Cement	329
PD0052	Restraining strength retrogression of silica-cement at high temperature above 200 ℃ using flint clay and graphite	333
PD0054	Influence of mineralogical composition on the calcinability of shales	338
PD0055	A New Soluble Alkali Test to Predict the Alkali Contribution of SCMs to Concrete Pore Solution	343
PD0056	Sensitivity of the Modified Chapelle test for measuring the reactivity of different types of clays calcined under different conditions	347

Contents

	Topics	Page
	PAPERS	
PD0057	Use of alkaline salts to improve the reactivity of cements with high fly ash content: hybrid alkaline cements	351
PD0059	Reduced OPC content in limestone calcined clay cement (LC^3) with C-S-H seeding	356
PD0061	Novel strength enhancing cement additives to enable production of low-clinker cements	360
PD0062	How siderite ($FeCO_3$) might be a future low-CO_2 reactive binder component for composite cements	365
PD0063	A Particle Packing Approach for Eco-efficient Ultra High-Performance Concrete (E-UHPC)	369
PD0065	Production of Low-Heat Cement from Industrial Waste	373
PD0067	Hydration of ternary blended cements comprising co-calcined bauxite residue and kaolinitic clay	377
PD0068	Effect of chloride salts on cement hydration: influence of the cation - part II	381
PD0070	Correlating initial chemistry, reaction degree and phase assemblage in alkali-activated systems	385
PD0071	Preliminary Selection Criteria of Clays for Limestone Calcined Clay Cement	389
PD0078	Scientific dosage of self-compacting concretes containing ternary cement mixtures	393
PD0079	Impact of curing time on carbonation of low-clinker binders	397
PD0080	Effect of Admixture for Slag on the Strength Development of Cement blend containing Cement, Slag, and Calcium Carbonate	401
PD0081	Refinement of activation methods for increased reactivity of kaolinitic and illitic clays	405
PD0082	Effect of temperature on the heat of hydration and compressive strength of ternary blends	409
PD0090	Alkali-carbonate activated waste glass-based cements	413
PD0091	Alkali-activation and chemical stabilization of incineration fly ash using slag for dangerous waste storage	417
PD0095	Impact of calcination technology on the properties of a low kaolinite calcined clay	421
PD0096	Fresh and hardened state properties of ternary slag cement concrete with high filler content	425

Contents

	Topics	Page
	PAPERS	
PD0097	LC^3 application in Non-structural Concrete	429
PD0099	Functionalization of Metakaolin with Non-Ionic Surfactants: Swelling and Pozzolanic Reactivity	433
PD0101	Reactivity (R^3) and hydration products of Fe(II)-rich slags: from $CaO\text{-}FeO_x\text{-}SiO_2$ to $CaO\text{-}Al_2O_3\text{-}Na_2O\text{-}FeO_x\text{-}SiO_2$	437
PD0104	Bauxite residue as a new source of SCM: its impact on cement hydration and interaction with fly ash	441
PD0108	Development of supplementary cementitious materials using weathered volcanic eject	445
PD0110	Beyond kaolinite content: untangling the influence of other clay properties on the reactivity of calcined clays	449
PD0111	Use Of Supplementary Cementitious Materials For Composite Cements: An Overview	453
PD0113	Application of Interparticle Spacing Model to Maximize Filler Content in Cementitious Pastes	457
PD0115	Effects of Blast Furnace Slag Fineness on Cement Physical, Mechanical and Chemical Properties	461
PD0118	Improving early-age strength of limestone-calcined clay cement by using finer cement and cement kiln dust	465
PD0122	Alkali-activated fly ash synthetized with pre-polymerized suspension combined with ultrafine fly ash at ambient temperature	469
PD0123	A unified method for efficient and reliable determination of pozzolanic reaction degree of SCMs in blended cement pastes	473
PD0124	Power ultrasound assisted production of sustainable concrete	477
PD0125	Feasibility of using volcanic debris from the island of La Palma as building materials	481
PD0127	Blended systems with OPC-Pozzolan-High limestone filler	485
PD0131	Relationship between reactive alumina content of Calcined Clays and fresh cement pastes behaviour.	489
PD0133	Quantitative microstructure analysis of SCM-blended cementitious materials through deep learning-based computer vision methods	494
PD0134	Effect of steam curing on the hydration of limestone calcined clay cements (LC^3) with low kaolinite content	498

Contents

	Topics	Page
	PAPERS	
PE0002	Relationship between rate of hydration and physical and chemical characteristics of Portland cement	502
PE0003	Combined use of laboratory X-ray diffraction and microtomography in early age cement hydration	512
PE0004	Characterization of siliceous hydrogarnet ($Ca_3Al_2(SiO_4)x(OH)_{12-4x}$) by solid-state NMR spectroscopy	516
PE0006	Influence of MgO on formation of clinker with different alumina modulus based on big data	520
PE0007	Multiscale investigation on the thermal stability of synthetic C-S-H pastes according to Ca/Si ratios	524
PE0008	Molecular dynamics on the pressure exerted by water molecules confined in microporous C-S-H	528
PE0009	Investigation of Selective Dissolution Method for Separation of Ferrite Phase in Cement and Characterization	532
PE0010	A comparative study of tribometer rotor configurations and analytical methods for concrete pumping pressure prediction	536
PE0011	Microstructural analysis of the effect of clinker phase distribution on cement hydration using computer-based approaches	540
PE0012	Application of artificial intelligence on the reconstruction of multi-phase cement paste microstructures	543
PE0013	Numerical Model for Growth and Porosity of C-S-H Structures in Cement Hydration	547
PE0014	Micromechanical properties of C-A-S-H and C-A-S-H/CH mixtures based on nanoindentation	551
PE0015	Methods for measuring internal stress and expansion deformation of fresh concrete during steam curing	555
PE0019	Mineralogical Investigation of Coal Fly Ash using Combined SEM-EDS and Raman Spectroscopy	559
PE0020	Study of alite and belite dissolution by kinetic Monte Carlo simulations and its effect in cement hydration.	563
PE0022	Machine learning atomic potential for C-S-H	567
PE0023	Assessment of Radiation-Induced Degradation in a Siliceous Rock via Correlative Characterization	571

Contents

	Topics	Page
	PAPERS	
PE0024	Solid state NMR study of the hydration of a fast-setting ternary binder added with lithium carbonate or trisodium-citrate	575
PE0025	Exploring C-S-H clusters with evolutionary algorithms	579
PE0027	Structure and mechanical properties of calcium silicate hydrate and calcium carbonate nano composites resolved by reactive molecular dynamics simulations	583
PE0029	MD study of radiocesium immobilization in the geopolymer matrix	587
PE0031	Modelling of the Flocculated Polydisperse Microstructure of Fresh Cement Paste	591
PE0037	Simulation of heat transport in extruded concrete structure	595
PE0042	In situ monitoring of microstructure evolution of C3A – gypsum system by low field NMR	599
PE0045	Thermodynamic modelling of Portland cement clinkers.	603
PE0048	Calcium Silicate Hydrate Surface	607
PE0050	Experimental thermodynamic study of selected cement clinker phases	611
PE0052	Atomic Scale Insight of Hydration Temperature Rise Inhibitors (TRI) Affecting Calcium Activity via AIMD	615
PE0053	Impact of autoclaving on the phase assemblage of Portland cement: Experiment and thermodynamic modelling	619
PE0054	A Multi-scale Model of Reinforcement Bars Corrosion Based on the Concentrated Electrolyte Theory and Three Dimensional Hierarchical Structure of Concrete	623
PE0057	Multi-scale model for characterizing thermal conductivity of cement-based materials with nano inclusions	628

The 16th International Congress on the Chemistry of Cement 2023 (ICCC2023)
"Further Reduction of CO_2 -Emissions and Circularity in the Cement and Concrete Industry"
September 18–22, 2023, Bangkok, Thailand

Effect on Graphene Oxide and Silica Fume on the Performance of Concrete under Standard Curing Conditions

G.Y. Ma, C.J. Liu*, S.T. Fang, W.C. Su, W.H. Ye, Y.J. Deng

School of Civil Engineering, Guangzhou university, Guangzhou 510006, China

** Corresponding author email: cjliu@gzhu.edu.cn*

ABSTRACT

The prefabricated buildings have been receiving much attention with the development of new green building technology. Compared with traditional cast-in-place buildings, prefabricated buildings are widely used in industrial, public and residential buildings due to their advantages of high speed, beauty, high quality and low price. However, the current concrete has a long demoulding time because of its insufficient early strength, which is difficult to meet the needs of efficient production of prefabricated buildings. To optimize the performance of concrete, graphene oxide (GO) and silica fume (SF) were compounded with concrete to improve its mechanical properties in this study. The results showed that the excellent properties of GO and SF have a significant improvement effect on the mechanical of concrete. Among them, the compressive, splitting tensile, flexural strength of B-1 group(GO, 0.01wt% and SF, 2.5wt%) were increased by 11.04%, 12.23%, 20.11% compared with the reference group after 3 days of curing. Moreover, concretes' composition, and microstructure were investigated, using XRD and SEM to explore its modification mechanism. The results showed that the main role of GO and SF is to promote the early hydration reaction, improve the internal structure of the matrix, and enhance the compactness of the matrix. The research results of this paper provide a good reference for improving the early strength of prefabricated building concrete, and have positive significance for improving the production efficiency and product quality of prefabricated concrete buildings.

KEYWORDS: *Graphene oxide, Silica fume, Concrete, Mechanical properties, Microstructure*

1. Introduction

Concrete materials have been discovered for more than one hundred years. During this period, housing construction, roads and bridges, water conservancy and other industries have been greatly developed. However, the shortcomings of traditional concrete with low strength and durability have become increasingly difficult to meet the needs of construction. To solve this problem, researchers have tried different solutions, including adding fiber materials and nanomaterials, etc.

GO is a new type of carbon-based nanomaterial, and its surface contains a large number of hydrophilic functional groups such as hydroxyl, carboxyl and epoxy groups (Ghazizadeh et al., 2018). These hydrophilic functional groups can improve the surface activity and dispersion of GO in water. In addition, GO can participate in the hydration process of cement to promote the hydration reaction of cement, thus enhancing the mechanical properties of cement-based materials (de Souza et al., 2022).

SF is a mixture collected by a special device with the dust spilled from the waste gas in the smelting process such as silicon iron ore. In recent years, SF has been widely used in concrete production, mainly because SF can improve the particles gradation of cement-based materials, enhance the compactness of matrix and improve the mechanical properties of concrete (Golewski et al., 2021).

In this study, GO and SF were compounded with concrete and their effects on concrete properties were studied.

2. Materials

GO dispersion was provided by a company called Graphenea in Spain. Conch P.O42.5R cement was provided by Chongqing CSCEC Hailong Liangjiang Construction Technology Co., LTD. Silica fume was provided by Chengdu Yangtian Technology Co., Ltd. Mechanism medium sand was provided by Chongqing Nanchuan Xianglei Mine. The basalt gravel was used as a coarse aggregate of concrete. The powder-like polycarboxylate superplasticizer was Sika 540 P.

2.1 Concrete mix proportions

In the design of concrete mix proportions, the total mass of cementitious materials was kept unchanged. The dosage of GO and SF respectively was 0, 0.01%, 0.03%, 0.05% and 0, 2.5%, 5.0%, 7.5% of the total mass of cementitious materials. Due to the production of prefabricated building components requires that concrete has the characteristics of early strength, high strength and high durability. Therefore, reference group (A-0) and the highest 3d compressive strength of single-doped GO group (A-3), single-doped SF group (B-0) and composite-doped group (B-1) were selected for study in this paper.The mix proportions are listed in Table 1.

Table 1 Concrete test mix proportions

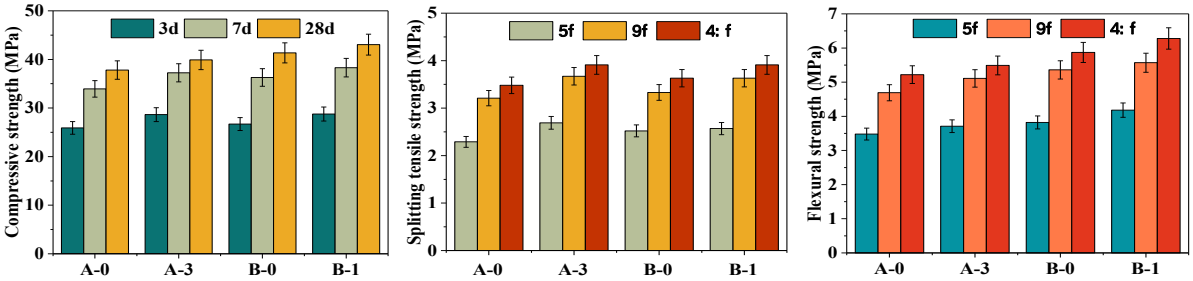
Number	SF (%)	GO (%)	Cement (kg)	SF (kg)	Water (kg)	Sand (kg)	Gravel (kg)	GO (kg)
A-0	0	0	330.00	0.00	165	838	1067	0.000
A-3	0	0.03	330.00	0.00	165	838	1067	0.099
B-0	2.5	0	321.75	8.25	165	838	1067	0.000
B-1	2.5	0.01	321.75	8.25	165	838	1067	0.033

2.2 Performance test

The workability of the concrete was measured through slump test and the slump of each group was consistent by adjusting the dosage of polycarboxylate superplasticizer, which was 180 ± 20 mm. Moreover, further mechanical characteristics were evaluated by determining the compressive strength, splitting tensile strength and flexural strength. The composition, microstructure of concrete were characterized by X-ray diffraction analysis (XRD), Scanning Electron Microscopy (SEM).

3. Results and discussion

3.1 Mechanical property



(a) Compressive strength **(b) Splitting strength** **(c) Flexural strength**

Fig. 1 (a)~(c) Mechanical properties of specimens.

As shown in Fig. 1, each group had improved the strength of concrete for 3d, 7d and 28d. Among them, the compressive, splitting tensile, flexural strength of B-1 group were increased by 11.04%, 12.23%, 20.11% compared with the reference group(A-0) after 3 days of curing. This is because both GO and SF promote the hydration of cement. In addition, GO promotes the pozzolanic reaction of SF, resulting in the formation of more hydrated calcium silicate gel, SF isolates GO and Ca^{2+} by mechanical action, which promotes the dispersion of GO, thus improving the mechanical property of concrete (Li et al., 2016).

3.2 XRD

The XED patterns of each group after 3 days of curing are shown in Fig. 2. It can be found that a large amount of calcium silicate hydrate (CSH), calcium hydroxide (CH), and incompletely hydrated tricalcium silicate (C_3S) were still retained in each group. By observing the diffraction peak of C_3S, it is found that the diffraction peak of C_3S in B-1 group was relatively low, which indicated that the amount of C_3S in the sample was relatively small. This is because the addition of GO and SF promoted the hydration of cement, making the hydration reaction more sufficient, so more C_3S was consumed. By analyzing the diffraction peak of CH in A-3 group, it can be seen that it was higher than other groups, which proved that more CH was generated in the sample. Compared with B-0 group, the diffraction peak of CH in B-1 group was relatively low, which indicated that the pozzolanic reaction of B-1 group was more sufficient, namely, GO and SF could enhance the pozzolanic reaction of the specimens (Liu et al., 2018).

Fig. 3 shows that after 28 days of curing, the diffraction peaks of and C_3S in the sample had almost disappeared, with only a small amount of residue. This showed that most of the cement clinker had been hydrated at 28 days. By observing the diffraction peak of CH, it is found that the diffraction peak of CH in A-0 group was the largest, while the sample doped with GO, SF and their compound were decreased. This is because the pozzolanic reaction of SF consumes part of CH and increases the amount of CSH gels. The carboxyl group (-COOH) on the surface of GO reacted with CH to form calcium carboaluminate hydrate, which reduced the content of CH (Mokhtar et al., 2017). In addition, the incorporation of GO can also promote the pozzolanic reaction of SF, thereby consuming more CH.

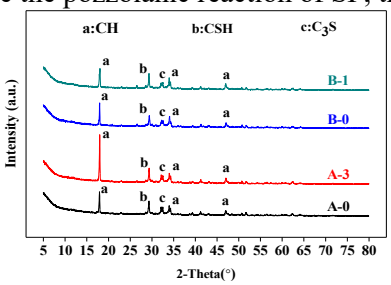


Fig. 2 XRD patterns of hydration for 3 days

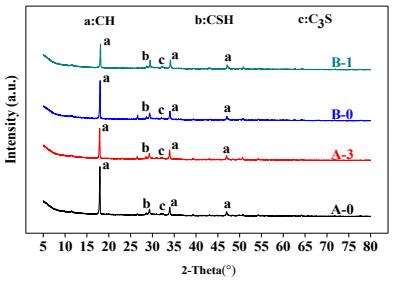
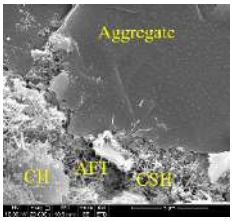


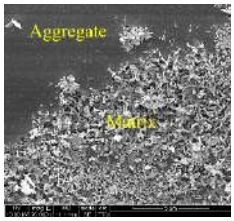
Fig. 3 XRD patterns of hydration for 28 days

3.3 SEM

The SEM patterns of each group after 3 days (a)~(d) and 28 days (e)~(f) of curing are shown in Fig. 4. From (a)~(d), it can be seen that there were large pores in the arrangement of hydration products of A-0 group, and there were obvious flake-like CH crystals and needle-like ettringite (AFt). The bonding between the matrix of the hydration products and aggregates was poor and the structure was loose. The hydration products of A-3 group showed obvious honeycomb structure in the interface transition zone, which was considered to be the CSH gel formed by cement hydration, and the combination of gel and aggregate was relatively dense. The structure of hydration products of B-0 group was dense and the matrix had a better adhesion to the aggregate. There were some CH crystals and AFt in the hydration products. The structure of the hydration products in B-1 group was more compact, the hydration products in the matrix were interlaced, and the interface transition zone between the aggregate and the matrix was well bonded.

As shown in Fig 4 (e)~(f), it can be seen that the hydration products of A-0 group were denser than those at 3d, but there were still large holes and unevenness. Meanwhile, there were wide cracks between the matrix and the aggregate. The connection between matrix and aggregate in A-3 group was relatively tight, but the matrix structure was also loose. The matrix of B-0 group was relatively smooth, and the connection between the matrix and the aggregate was relatively good, but the compactness of the matrix was still unsatisfactory, there were still many needle-like AFt in the matrix and the overall compactness of the matrix was relatively loose. The matrix of B-1 group had fewer pores, the matrix structure was dense and flat, and there was no obvious AFt in the matrix. The bonding between the matrix and the aggregate was better, and the interface transition zone was denser.









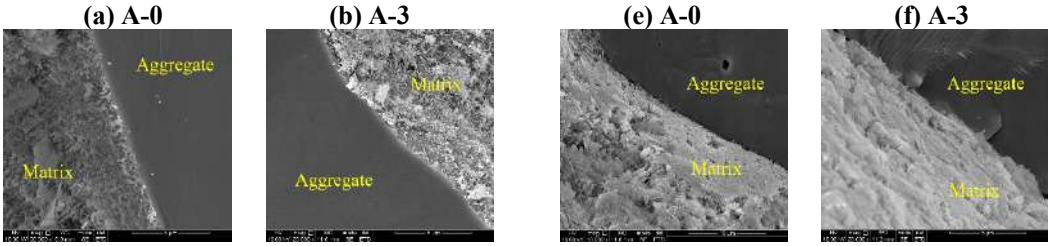


Fig. 4 (a)~(d) SEM patterns of hydration for 3 days. (e)~(h) SEM patterns of hydration for 28 days.

4. Conclusion

Based on these investigations, the following conclusions can be drawn:
(1) The compound of GO and SF has significantly improved the mechanical properties of concrete. The experimental data show that B-1 group has the greatest improvement on the compressive strength, splitting tensile strength and flexural strength of concrete. Among them, the compressive strength is 43.04 MPa after curing for 28 days and the growth rate is 13.80%. The splitting tensile strength is 3.91 MPa after curing for 28 days and the growth rate is 3.91%. The flexural strength is 6.28 MPa after curing for 28 days and the growth rate is 20.30%.
(2) The effects of GO and SF on the composition and microstructure of concrete were investigated by XRD, SEM. XRD patterns showed that in the early stage, the compound of GO and SF could consume more CH in the system. At 28 days, whether A-3, B-0 or B-1group decreased the amount of CH, and increased the amount of CSH gel. The SEM images showed that the compound of GO and SF can strengthen the interfacial transition zone of concrete, enhance the connection between aggregate and matrix, and strengthen the compactness of matrix.

Acknowledgment

This work was supported by the Chongqing Technology Innovation and Application Development Special General Project (cstc2020jscx-msxmX0084), Chongqing Construction Science and Technology Plan Key Project (Urban Science 2021,No.1-8) and Guangzhou Basic and Applied Basic Research Project (202201010750) .

References

de Souza F B, Yao X, Lin J, et al. (2022) “Effective strategies to realize high-performance graphene-reinforced cement composites”, *Construction and Building Materials*, 324: 126636.

Ghazizadeh S, Duffour P, Skipper N T, et al. (2018) “Understanding the behaviour of graphene oxide in Portland cement paste”, *Cement and Concrete Research*, 111: 169-182.

Golewski G L, Gil D M. (2021) “Studies of fracture toughness in concretes containing fly ash and silica fume in the first 28 days of curing”, *Materials*, 14(2): 319.

Li X, Korayem A H, Li C, et al. (2016) “Incorporation of graphene oxide and silica fume into cement paste: A study of dispersion and compressive strength”, *Construction and Building Materials*, 123: 327-335.

Liu H, Yu Y, Liu H, et al. (2018) “Hybrid effects of nano-silica and graphene oxide on mechanical properties and hydration products of oil well cement”, *Construction and Building Materials*, 191: 311-319.

Mokhtar M M, Abo-El-Enein S A, Hassaan M Y, et al. (2017) “Mechanical performance, pore structure and micro-structural characteristics of graphene oxide nano platelets reinforced cement” *Construction and Building Materials*, 138: 333-339.

The 16th International Congress on the Chemistry of Cement 2023 (ICCC2023)
"Further Reduction of CO_2 -Emissions and Circularity in the Cement and Concrete Industry"
September 18–22, 2023, Bangkok, Thailand

Comparison of the mode of action of a shotcrete accelerator in a slag cement and an OPC cement

U. Pott[1*], T. Dorn[1], C. Jakob[2], J. Neubauer[2], and D. Stephan[1]

[1] *Department of Civil Engineering, Chair of Building Materials and Construction Chemistry, Technische Universität Berlin, Berlin, Germany*
Email: u.pott@tu-berlin.de, t.dorn@tu-berlin.de, stephan@tu-berlin.de

[2] *Department of Geography and Geosciences, Friedrich-Alexander-Universität, Erlangen, Germany*
Email: cordula.jakob@fau.de, juergen.neubauer@fau.de

ABSTRACT

In the 3D concrete printing injection method, an accelerator is added to a printable mortar in the nozzle immediately before extrusion. The dosage of the accelerator can be adjusted to the necessity of the printing process. Shotcrete accelerators based on aluminium sulphates are particularly suitable for this application, as they accelerate the aluminate reaction and thus influence the early rheological material behaviour. The effect of these accelerators in pure OPC systems has already been well-studied. Since pure OPC systems will be used less in the future due to their poor environmental performance, other cement types are increasingly coming to the forefront of research. In this paper, the mode of action of a shotcrete accelerator on a slag cement is investigated and compared with the mode of action in an OPC cement. The results of the slow penetrating sphere test, isothermal heat flow calorimetry and compressive strength are compared, and differences are explained by the phase development measured by in-situ QXRD. Finally, an evaluation of the suitability of slag cement for the 3D concrete printing injection method is made.

KEYWORDS: *Shotcrete accelerator, slag cement, OPC cement, 3D-printing injection method*

1. Introduction

Large quantities of natural resources are consumed in the construction industry. As the market continues to grow, natural resources can no longer meet the demand alone (Netinger et al. 2016). In addition, OPC is not promising for the future due to the high CO_2 emission caused by the decarbonisation of the limestone during the manufacturing process. For this reason, there is a need to reduce the use of natural materials through the reuse of waste materials (Netinger et al. 2016; Ahmad et al. 2022). A possible substitute for OPC is ground granulated blast furnace slag, a by-product of pig iron production. In addition to the improved CO_2 balance of CEM III, slag can have a positive impact on the microstructure of the paste, mechanical properties, and durability (Ballim and Graham 2009; Ganesh and Ramachandra Murthy 2019). Thus, admixtures have a significant market advantage if they are robust enough to be used universally. For this reason, physical (SPS-test, compressive strength) and physiochemical (heat flow calorimetry, in-situ QXRD) results of a CEM III-based mortar were compared to the results of a mortar based on CEM I.

2. Material and Methods

The printable mortars consist either of 450 g CEM I 42.5 R or 450 g CEM III A 42.5 and additionally of 235 g limestone powder, 300 g crushed aggregate Ø 0.1-0.6 mm, 2 g fibres, 4.5 g defoaming agent, different dosages of a non-alkaline aluminium sulphate-based shotcrete accelerator with a reactive part of 54 wt.-% and 228.5 g deionised water. The amount of deionised water was reduced in the accelerated mortars by the amount of water in the accelerator (AC). AC dosages of 2, 3 and 4 wt.-% in relation to the cement content were investigated.

The mortars used for this study were prepared with a stand mixer. The sample preparation and the tests were performed under laboratory conditions (20.0 ± 0.3 °C, 65 % relative humidity). The liquid and solid components were mixed separately before being brought together and mixed for 4 min.
A slow penetrating sphere test (SPS-test) was performed in a threefold repetition with the device ToniSET Force with a speed of 0.005 mm/min. The mould (h = 80 mm; Ø = 60 mm) was filled with mortar and covered to prevent evaporation. Before the test, the sphere (Ø = 15 mm) was driven 15 mm into the sample. A detailed description of the test implementation can be found in (Pott and Stephan 2021).
A TAM air calorimeter was used to measure the isothermal heat flow evolution of the exothermic cement hydration in triplicate. The raw data were corrected by the Tian equation (Wadsö 2010).
In-situ XRD was used to measure the phase evolution. During the test, water evaporation and CO_2 uptake were prevented. The diffraction patterns were recorded every 15 min by a Bruker AXS D8 advance diffractometer with a Bragg-Brentano geometry from 7° to 55° 2θ and a step width of 0.0236° 2θ. The method was performed with a LYNXEYE detector and Cu Kα radiation. The power generator operated at 40 mA and 40 kV. The software TOPAS 5.0 was used for Rietveld analysis. The scattering contribution of each phase to the diffraction pattern was recorded, and the combination with the external standard G-factor method (Jansen et al. 2011) led to the absolute quantification of the phases.
Last, the compressive strength test was performed according to EN 196-1 (EN 196-1 2016). For the test, three prisms (4·4·16 cm³) per sample age were made and stored under water until tested. The compressive strength was determined on the six halves of the prisms.

3. Results

First, the penetration force was measured with the SPS-test. Fig. 1a shows the penetration force of the CEM I and CEM III mortar with AC dosages of 0, 2 and 4 wt.-%. The results clearly show that the acceleration of the CEM I mortar is more effective than that of the CEM III mortar.

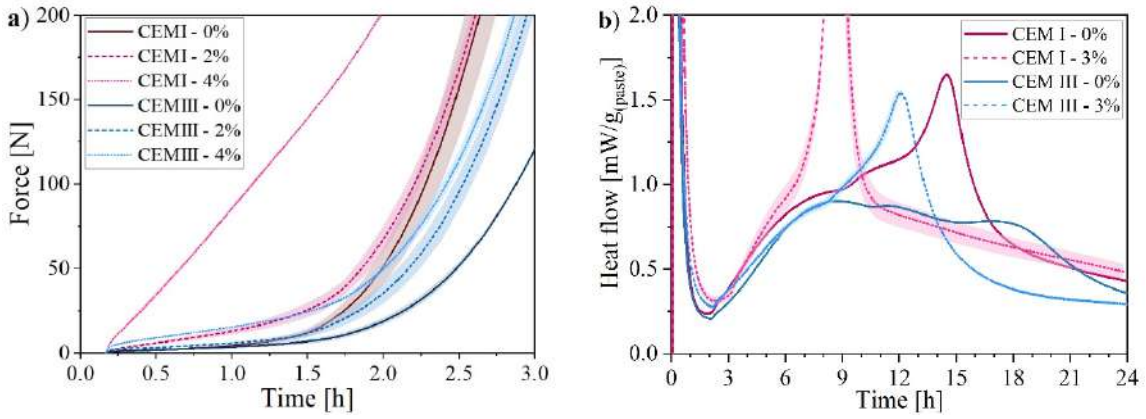


Figure 1: a) Penetration force of samples with 0, 2 and 4 wt.-% and b) heat flow of samples with 0 and 3 wt.-% of an accelerator of the CEM I and CEM III-based mortars

Fig. 1b shows the heat flow of specimens with 0 and 3 wt.-% of AC of the CEM I and CEM III-based mortar. For the calorimetry and the XRD, the AC dosage of 3 wt.-% was chosen to ensure comparability to the CEM I mortars investigated in a previous publication (Pott).
It is observable that both the accelerated and pure CEM III mortars release less heat than the corresponding CEM I mortars. The heat flow of the pure CEM III sample shows three peaks during the main reaction, similar to the CEM I sample, but at different times and with different intensities. The addition of the AC causes an accelerated aluminate reaction, which was already observed in (Pott). The heat flow clarifies that the AC can act more effectively in the CEM I mortars due to the higher OPC content. A comparison between Fig. 1a and b shows that the strong force increase is caused by the beginning of the acceleration period.
Fig. 2 presents the phase content in addition to the heat flow of the pure (Fig. 2a/b) and the accelerated (Fig. 2c/d) CEM I and CEM III mortars. The results of both CEM I mortars are presented for comparison, but were already intensively discussed in a previous publication (Pott). The pure CEM III mortar in Fig. 2b shows after the maximum heat release at 9 h, which is caused by C-S-H formation, a decreasing heat flow

until another peak appears at 17 h, caused by sulphate depletion. It can be assumed that the peak after about 11 h is not due to an exothermic reaction. It is rather a short-term dip in the decreasing heat flow after the main reaction of the alite, which can be explained by the endothermic solution of gypsum. This was also suggested in (Pott). Compared to the pure sample, the accelerated slag sample shows an increase in the aluminate reactions and the following higher ettringite precipitation caused by the additional sulphate of the AC. It can be seen that the peak of the second aluminate reaction at 13 h is significantly higher and superimpose the maximum of the silicate reaction. Following the course of the curve and not the silicate reaction, the subdivision between the acceleration and deceleration period was made after the second aluminate peak. After sulphate depletion, the ettringite content remains constant until 24 h. In summary, similar observations could be made in the CEM III mortar as in the CEM I mortar.

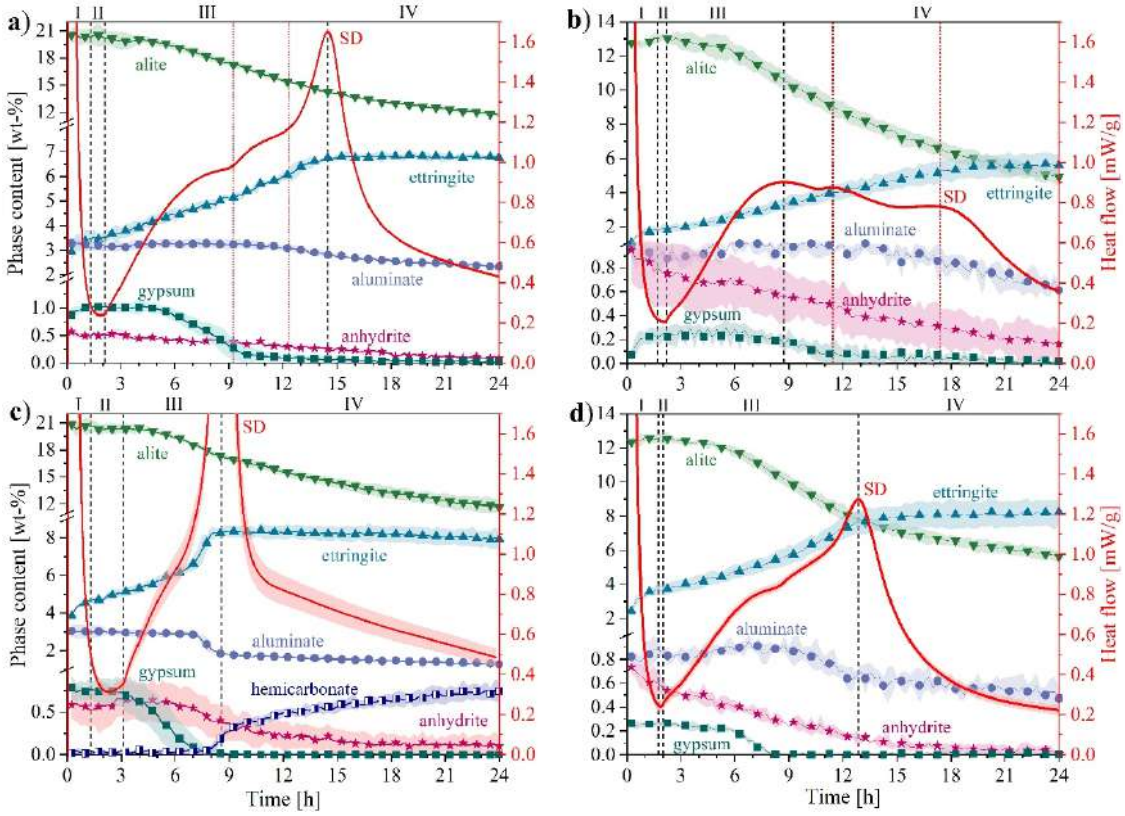


Figure 2: Phase content and heat flow of a) the pure CEM I mortar, b) the pure CEM III mortar, c) the accelerated (3 wt-%) CEM I mortar and d) the accelerated (3 wt-%) CEM III mortar; (I) initial period, (II) induction period, (III) acceleration period, (IV) deceleration period; sulphate depletion (SD)

Finally, compressive strengths were measured after 1, 2 and 7 d. The results are illustrated in Fig. 3. If first the pure samples are compared with each other, it is observable that the compressive strength of the CEM III mortar is significantly reduced compared to the CEM I mortar.

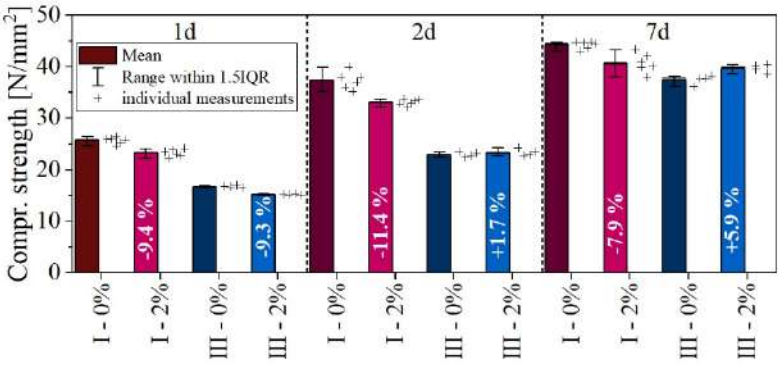


Figure 3: Compressive strength of a CEM I and CEM III mortar with 0 and 2 wt.-% accelerator after 1, 2 and 7 d.

Moreover, after 1 d, both accelerated mortars show lower compressive strength values than pure mortars. The relative decrease in compressive strength is almost the same, namely 9.4 % and 9.3 %. A decrease in compressive strength of the CEM I-based accelerated mortar is also observable after 2 and 7 d. In contradiction, in the case of the accelerated slag mortars, an increase in compressive strength of 1.7 % is recorded after 2 d, and even 5.9 % after 7 d.

4. Discussion

The results of the penetration test showed that the early rheological material behaviour could be strongly influenced by the addition of the AC, whereby the AC is more effective in the CEM I-based mortar. The early force increase is caused by ettringite formation, presented by a comparison of Fig. 2b and 2d. The heat flow curves in Fig. 1b show that the silicate reaction of the CEM III mortar is less negatively affected. The CEM I mortar demonstrates a slight delay in the silicate reaction, which does not occur with the CEM III mortar. Fig. 2 proves that the addition of the AC significantly increases the second aluminate reaction. However, compared to the CEM I mortar, the acceleration of the slag mortar is less. The compressive strength values in Fig. 3 show lower values of the CEM III-based samples caused by the lower OPC content compared to the CEM I-based mortar. However, the CEM III-based specimens show an increased strength after 2 and 7 d.

5. Conclusions

It can be concluded that the aluminium sulphate-based shotcrete accelerator is suitable for the 3D concrete printing injection method with a CEM III-based printable mortar, even though a less effective performance must be accepted. A higher dosage of the accelerator can presumably compensate for this disadvantage. In addition, some advantages were observed. First, the silicate reaction is not retarded by the addition of the accelerator, and second, the compressive strength is improved after 2 and 7 d. Both positive effects are beneficial for 3D concrete printing because a better performance of the long-term properties is ensured.

Acknowledgements

The authors thank DFG for funding the project “Tailored yield stress for 3D printing using low clinker cement” (386869775).

References

Ahmad, J., Kontoleon, K.J., Majdi, A., Naqash, M.T., Deifalla, A.F., Ben Kahla, N., Isleem, H.F. and Qaidi. S.M.A. (2022) “A Comprehensive Review on the Ground Granulated Blast Furnace Slag (GGBS) in Concrete Production”, *Sustainability*, 14:14

Ballim, Y. and Graham, P.C. (2009) “The effects of supplementary cementing materials in modifying the heat of hydration of concrete”, *Mater. Struct*., 42:803–811

EN 196-1: 2016, Methods of testing cement - Part 1: Determination of strength.

Ganesh, P. and Ramachandra Murthy, A. (2019) “Tensile behaviour and durability aspects of sustainable ultra-high performance concrete incorporated with GGBS as cementitious material”, *Constr. Build. Mater.*, 197:667–680

Jansen, D., Goetz-Neunhoeffer, F., Stabler, C., Neubauer, J. (2011) “A remastered external standard method applied to the quantification of early OPC hydration”, *Cem. Concr. Res.* 41:602–608.

Netinger Grubeša, I., Barišić, I., Fucic, A. and Bansode, S.S. (2016) “Characteristics and Uses of Steel Slag in Building Construction”, *Woodhead Publishing*, 1 ed.

Pott, U. and Stephan, D. (2021) “Penetration Test as a fast Method to Determine Yield Stress and Structural Build-up for 3D Printing of Cementitious Materials”, *Cem. Concr. Compos.* 121:104066.

Pott, U., Jakob, C., Dorn, T. and Stephan, D. (under review) “Investigation of a shotcrete accelerator for targeted control of material properties for 3D concrete printing injection method”

Wadsö, L. (2010) “Operational issues in isothermal calorimetry”, *Cem. Concr. Re.s* 40:1129−1137.

The 16th International Congress on the Chemistry of Cement 2023 (ICCC2023)
"Further Reduction of CO_2 -Emissions and Circularity in the Cement and Concrete Industry"
September 18–22, 2023, Bangkok, Thailand

3D-printable magnesium-silicate-hydrate cement composites: A feasibility study

Yiming Peng[1] and Cise Unluer[2*]

[1] *School of Engineering, University of Glasgow, Glasgow, G12 8LT, United Kingdom, Email: y.peng.3@research.gla.ac.uk*

[2] *Department of Mechanical, Aerospace and Civil Engineering, University of Manchester, Manchester M13 9PL, United Kingdom, Email: cise.unluer@manchester.ac.uk*

ABSTRACT

Magnesium-silicate-hydrate system is considered as an alternative cementitious binder due to its potentially lower environmental impact. This study evaluated the feasibility of using the MgO-SiO_2 system in the 3D printing of cementitious composites. The printability of the system was improved via the addition of a small amount of fly ash, Sodium hexametaphosphate (SHMP), and polycarboxylate superplasticizer (PCE), while the water-to-binder (w/b) ratio was kept at 0.38. The compressive strength and microstructure of samples at different ages were analyzed. The actual printed sample was close to the design height, where the size accuracy of the rectangular sample was higher than that of the circular sample. The compressive strengths of the corresponding MgO-SiO_2 pastes at 3, 7, and 28 days were 21.4, 28.6, and 46.5 MPa, respectively. SEM observations showed that silica particles generally dissolved after 7 days of curing, contributing to the formation of magnesium-silicate-hydrate (M-S-H). Overall, the results of this study highlighted the feasibility of using MgO-SiO_2 mixes in the development of 3D-printed cementitious composites with sufficient mechanical performance.

KEYWORDS: *Magnesium-silicate-hydrate system, 3D printing, compressive strength, microstructure*

1 Introduction

Magnesium-based materials are considered as an alternative binder system that could benefit from the lower calcination temperatures used in the production of MgO and potentially reduced carbon emissions (Walling and Provis, 2016). The use of light-burned magnesia (i.e. reactive magnesia), silica fume or other silica sources in the MgO-SiO_2 system leads to the formation of amorphous magnesium-silicate-hydrate (M-S-H) gel, which is similar to the strength gain mechanism provided by calcium-silicate-hydrate (C-S-H) gel, the principal hydration product of Portland cement (PC)-based mixes (Martini et al., 2017).

The global development of additive manufacturing (or 3D printing) using cementitious materials has accelerated during the past few years. The idea of digital concrete has evolved from a theoretical concept to a realizable field with significant research potential. It can significantly reduce labor expenses and increase resource utilization efficiency (Wangler et al., 2019). The fresh workability of 3D printing materials mainly include extrudability, flowability (pumpability) and buildability, which correspond to the static yield stress, dynamic yield stress and viscosity and the structural build-up from the perspective of

rheology (Peng and Unluer, 2022). Appropriate rheological adjustment is a crucial component for optimizing the printability of the applied materials.

This study investigated the feasibility of applying the MgO-SiO_2 system to 3D printing technology, assessed the fresh and hardened properties of the material via slump flow and compressive strength, and measured the buildability of the sample by comparing its actual size to its designed size. Finally, the hydration microstructure of the material was analyzed by using the scanning electron microscope. This study aims to provide experimental basis and new insights for the subsequent optimization of printability of MgO-SiO_2 mixes.

2. Materials and Methodology

2.1 Materials and mix proportions

The raw materials for this study include reactive magnesia cement (RMC) provided by Richard Baker Harrison (UK) and microsilica (MS) provided by Elkem. Their chemical compositions are shown in Table 1. Sodium hexametaphosphate (SHMP) was supplied by Sigma-Aldrich Company. The mix proportion of this study is shown in Table 2. In addition to RMC and MS, 8 wt.% fly ash (FA) is added to improve the fluidity of the paste. The water-to-binder ratio (w/b) is controlled at 0.38, and two superplasticizers (4 wt.% SHMP and 0.3 wt.% polycarboxylate superplasticizer PCE of powder weight) are added to reduce the water demand of the paste.

Table 1 Chemical and physical properties of RMC and MS

	Chemical composition								LOI
	MgO	SiO_2	CaO	Al_2O_3	Fe_2O_3	Na_2O	P_2O_5	SO_3	
RMC	88.9	2.86	2.23	0.63	0.90	0.15	0.18	0.28	3.6
MS	0.70	93.84	0.33	0.72	0.21	0.38	0.14	0.13	2

Table 2 Mix proportion of this study

Samples	Binder composition			w/b ratio	SHMP	PCE
	RMC	MS	FA			
1	50	42	8	0.38	4	0.3

2.2 Methodology

The 3D printing process of MgO-SiO_2 paste was completed with StoneFlower 4.0 Multimaterial 3D printer. The diameter of the printing nozzle is 7 mm. The printing speed is adjusted in the range of 30 mm/s-40 mm/s according to the path to construct the optimal structure. This study chose two types of printing shapes, i.e., a rectangular structure and a circular structure, to print their outlines.

The sample dimension for compressive strength test was 20×20×20 mm. The mixed paste was poured into the mold and covered with wet film to prevent moisture from volatilizing. After curing for 24 h, the samples were demolded and placed in a standard curing environment for the rest curing duration. Instron 3367 was used to measure its compressive strength at 3 d, 7 d and 28 d.

The microscopic morphology of the samples was obtained with the aid of Field Emission Scanning Electron Microscope (FESEM, ZEISS Sigma). The accelerating voltage during scanning was fixed at 5.00 kV, and the working distance was adjusted between 4.5-5.5 mm to obtain the clearest image. The surface of each sample was treated with gold coating before the tests.

3 Results and Discussion

3.1 3D printing

Fig. 1 shows the rectangular and circular structures obtained by using 3D printer. The total number of layers of each shape was 10, and the height was 5 cm. Combined with the previous slump test results, it can be found that the lower layer of the structure could sustain the pressure from the upper layer without significant deformation due to its large static yield stress, which showed good buildability. In addition, the printing structure had no instability such as wall collapse, and its general shape was highly consistent with the design shape. However, due to the faster rotation speed of the screw and the small amount of air contained in the pipe, there were obvious bubbles on the surface of the extruded paste, showing that it still needed further optimization. Compared with the rectangular structure, there was more obvious deformation at the bottom of the circular structure, which could also be verified from the actual height measurement results (Fig. 1(c)), where the height of the rectangular and circular printing structures was 4.68 cm and 4.57 cm respectively.



Fig. 1 Images of 3D-printed samples showing (a) rectangular sample and (b) circular sample and (c) height of 3D-printed rectangular and circular samples

3.2 Mechanical strengths

Fig. 2 depicts the stress-strain relationship of 3 d, 7 d, and 28 d of curing, respectively. Although the curing period varies, each sample exhibits a similar failure stage through the test curve. When the strain range is within 0.02 to 0.03, the relationship between stress and strain is essentially linear elastic. When the stress reaches a certain peak, it will drop precipitously. At this point, the sample has lost a portion of its bearing capacity, resulting in structural collapse. The peak stress in Fig. 2 indicates that the MgO-SiO_2 sample has reasonable strength (21.4 MPa) after 3 d of curing. After 7 d and 28 d, the average compressive strength of the sample is 28.6 MPa and 46.5 MPa, which is 33.6% and 117% higher than that at 3 d.

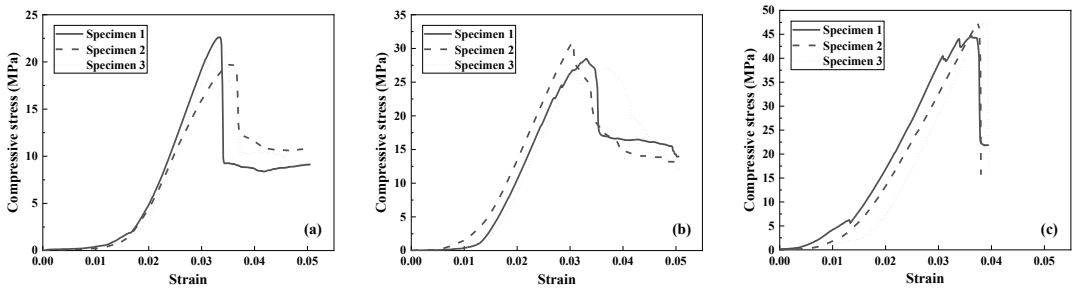


Fig. 2 Stress-strain curves under compressive test showing (a) 3 d of curing, (b) 7 d of curing and (c) 28 d of curing

3.3 Microstructure

Fig. 3 depicts the micromorphology of 3D-printed samples after 1 d, 3 d, 7 d, and 28 d of hydration, showing their microstructure under different hydration times varied significantly. As the image scales in Fig. 3 were all 200 nm, the majority of the detected phases are microsilica particles. At 3 d of hydration, the surfaces of microsilica particles were smooth without evident surface dissolution, which is consistent with previous results (Jia et al., 2016). In addition, microsilica particles were wrapped by certain fibrous hydrates and agglomerated to form flocculation structures. When the hydration period is increased to 7 d (Fig. 3(c)), the microsilica and MgO particles are mostly dissolved. many gel-like phases are bonded to the surface of MgO particles, which corresponds to the continual formation of MSH with the dissolution of microsilica and promotes the densification of microstructure. The MgO-SiO_2 paste in this study gained early strength fast, as seen by the microstructure after 3 d of hydration.

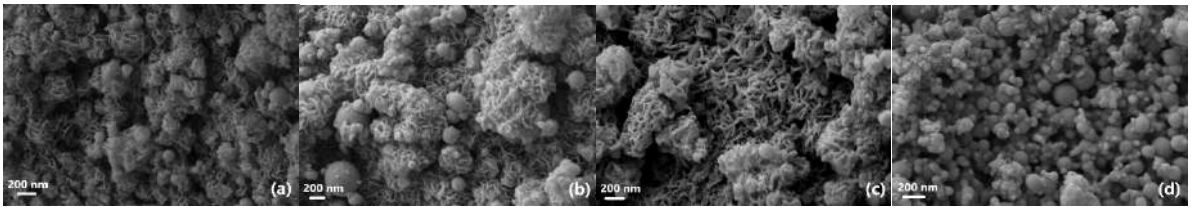


Fig. 3 Microstructure of 3D-printed MgO-SiO_2 pastes at (a) 1 d, (b) 3 d, (c) 7 d and (d) 28 d

4 Conclusions

This study discussed the feasibility of using MgO-SiO_2 mixes in the production of 3D printing components and investigated the workability, hardened mechanical properties and microstructure development of these mixes through slump flow, compressive strength and SEM analyses. The following conclusions were drawn:

(1) The printed structure used in this study showed good buildability. The height of the printed rectangular structure was closer to the design height than that of circular structure. The bottom layer of the circular structure had a significant deformation after being subjected to the pressure from the upper layers.

(2) The compressive strength of the MgO-SiO_2 pastes at 3, 7, and 28 days were 21.4, 28.6, and 46.5 MPa, respectively. The particle surface of microsilica in the MgO-SiO_2 system showed a certain degree of dissolution after 7 d of hydration and led to the formation of M-S-H gel, contributing to the densification of microstructure.

Acknowledgements

This study was funded by the Newton Fund Institutional Links project 623812328 provided by the British Council and China Scholarship Council (grant number: 202006370082).

References

Jia, Y., Wang, B., Wu, Z., Han, J., Zhang, T., Vandeperre, L.J. and Cheeseman, C.R. (2016) “Role of sodium hexametaphosphate in MgO/SiO2 cement pastes”, Cement and Concrete Research, 89, 63-71.

Martini, F., Tonelli, M., Geppi, M., Ridi, F., Borsacchi, S. and Calucci, L. (2017) “Hydration of MgO/SiO2 and Portland cement mixtures: A structural investigation of the hydrated phases by means of X-ray diffraction and solid state NMR spectroscopy”, Cement and Concrete Research, 102, 60-67.

Peng, Y. and Unluer, C. (2022) “Development of alternative cementitious binders for 3D printing applications: A critical review of progress, advantages and challenges”, Composites Part B: Engineering, 110492.

Walling, S.A. and Provis, J.L. (2016) “Magnesia-Based Cements: A Journey of 150 Years, and Cements for the Future?”, Chemical Reviews, 116(7), 4170-4204.

Wangler, T., Roussel, N., Bos, F.P., Salet, T.A.M. and Flatt, R.J., 2019. “Digital Concrete: A Review”, Cement and Concrete Research, 123.

The 16th International Congress on the Chemistry of Cement 2023 (ICCC2023)
"Further Reduction of CO_2 -Emissions and Circularity in the Cement and Concrete Industry"
September 18–22, 2023, Bangkok, Thailand

Evaluation of Internal Cracks and Three-Dimensional Deformation due to Different Nozzle Paths in a Material Extrusion 3D Printer

K. NAKASE[1*], K. HASHIMOTO[2], T. SUGIYAMA[3], K. KONO[4]

[1] *Environmental Material Engineering Laboratory, Graduate school of Engineering, Hokkaido University, Sapporo, Japan*

Email: k0utao121@eis.hokudai.ac.jp
[2] *Environmental Material Engineering Laboratory, Faculty of Engineering, Hokkaido University, Sapporo, Japan*

Email: hashimoto.k@eng.hokudai.ac.jp
[3] *Environmental Material Engineering Laboratory, Faculty of Engineering, Hokkaido University, Sapporo, Japan*

Email: takaf@eng.hokudai.ac.jp
[4] *TAIHEIYO CEMENT CORPORATION, Sakura, Japan*
Email: katsuya_kono@taiheiyo-cement.co.jp

ABSTRACT

3D Concrete Printing (3DCP) is an innovative technology that has been displaying remarkable development and application for the construction of concrete structures. It is significantly different from the conventional construction method and achieves the layer structure of cement-based material for building the designated shape without preparing formwork. It is potentially and promisingly expected that 3DCP provides the material characteristics and gives the mechanical performance to concrete structures, determining the nozzle path or the building process according to the stress distribution in the printed structure. However, even when constructing a structure with the appropriately designed material extrusion pattern from a 3D printer, the material interfaces/boundaries and their distributions are unavoidably formed between the layered system of extruded filament. The presence of the material interface and boundary affects the fracture process resulting in the formation of cracks under external stress conditions. In this study, designing the material extrusion nozzle path varied in several patterns of prism specimen followed by core-sampling the cylindrical specimen, and the propagation of the internal cracks in response to compressive stress was evaluated by X-ray computed tomography. In addition, using a 3D surface scanning system, the three-dimensional deformation was measured due to the fracture behavior of the printed materials using different nozzle paths.

KEYWORDS: *3D Concrete Printing, X-ray computed tomography, crack, deformation, nozzle path*

1. Introduction

3D Concrete Printing (3DCP) is an innovative technology construction, which is totally different from conventionally cast construction in terms of design freedom. Therefore, it is expected to be used in combination with topology optimization (Ohno (2022)). There must also be an optimal nozzle path to construct the structural form determined by topology optimization. However, even when the material is properly extruded from the 3D printer to construct the structure, voids and interfaces can be formed between the extruded filaments (Buswell et al. (2018), Le et al. (2012)). These voids cause the printed concrete to have anisotropic strength. Namely, it is still unknown how the nozzle path and its interface formation affect the fracture propagation of 3D-printed concrete. This paper focuses on the influence of void-induced interfaces caused by the printing nozzle path on the fracture process and crack propagation

in the printed specimen. To this end, the voids formed in the printed specimen are observed by X-ray computed tomography, and three-dimensional deformation is evaluated by 3D scanning.

2. Methods

2.1 Manufacturing of the printed specimens

Table.1 shows the mix proportion. In this study, RHPC (rapid hardening Portland cement) and LSP (limestone powder) were used as a binder, and silica sand was used as a fine aggregate. As an admixture, SP (super plasticizer) was used. The printed specimens (100 x 100 x 400 mm) were manufactured by two patterns of nozzle paths shown in Fig.1 using a material extrusion 3D printer. In pattern (I), after printing the outer surface layer, the inner layers were printed in the short side direction. In pattern (II), after printing the outer surface layer, the odd-numbered layers were printed in the long side direction and the even-numbered layers were printed in the short side direction. In other words, the pattern (I) specimen was printed in one direction in all layers and the pattern (II) specimen was printed alternately in two orthogonal directions. Finishing the preparation of the above-mentioned prism specimens, the cylinder specimens (ϕ 50 x 100 mm) were obtained by coring in the height direction at the dotted circle line in Fig.1.

Table.1 Mix proportion for printed specimen

W/B (%)	Water (kg/m^3)	RHPC (kg/m^3)	LSP (kg/m^3)	Sand (kg/m^3)	SP (B x %)
27	365	913	456	456	0.2



(I) One direction **(II) Two orthogonal direction**

Fig.1 Two patterns of the nozzle paths

2.2 Introduction of cracks

The top and bottom surfaces of the cylinder specimens were capped with high-strength gypsum, and cracks were introduced by compression loading. The loading rate was controlled to 5 MPa/min. The loading was stopped when fine cracks were visually observed on the surface of the specimen.

2.3 X-ray computed tomography

To observe the effect of the nozzle paths on the internal crack propagation behavior, X-ray computed tomography was used. The imaging conditions were the tube voltage of 100 kV and the tube current of 200 μA. The image (2864 pixel x 2864 pixel) was obtained. The image resolution was 24.86 μm/pixel.

2.4 3D scanning system

To evaluate the effect of the nozzle path on deformation in three dimensions, 3D scanning was conducted before and after compression loading. The conventional deformation measurement method using strain gauges evaluates the deformation locally at a specific point. However, Miyagawa et.al. (2022) used 3D scanning to evaluate deformation on the surface of an object rather than at a specific point, and it is also useful when the starting point of the fracture cannot be predicted. Also, Yamamoto et.al. (2021) used 3D scanning to evaluate how accurately 3D-printed specimens were manufactured compared to the designed geometrical data in three dimensions.

Fig.2 shows the 3D scanning process. The 3D scanner is a non-contact light projection method using a white LED as the light source. The pattern light is projected from the light source of the scanner, and the pattern reflected from the object's surface is captured by the scanning camera. This process provides three-dimensional coordinate data of the object's surface. By rotating the object during the measurement, the three-dimensional coordinates of the object's surface can be acquired. Since the specimen was not scanned from all directions in a single scan, multiple scans were performed by changing the direction in which the specimen was placed. After scanning, the point cloud data were combined in the software and converted to polygon data for analysis. The shortest distance from each vertex of the polygon data before loading to that after loading was calculated by using the two 3D scan data before and after loading, so that it can be defined as the amount of deformation due to loading.

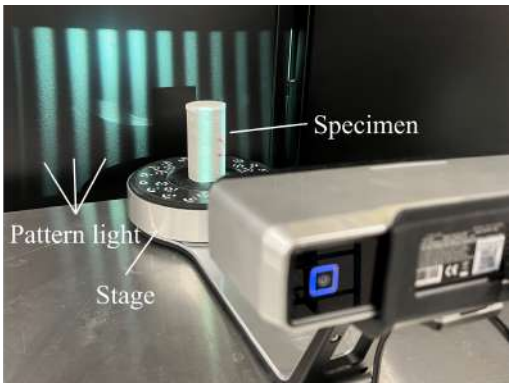


Fig.2 3D scanning process

3. Results and discussion

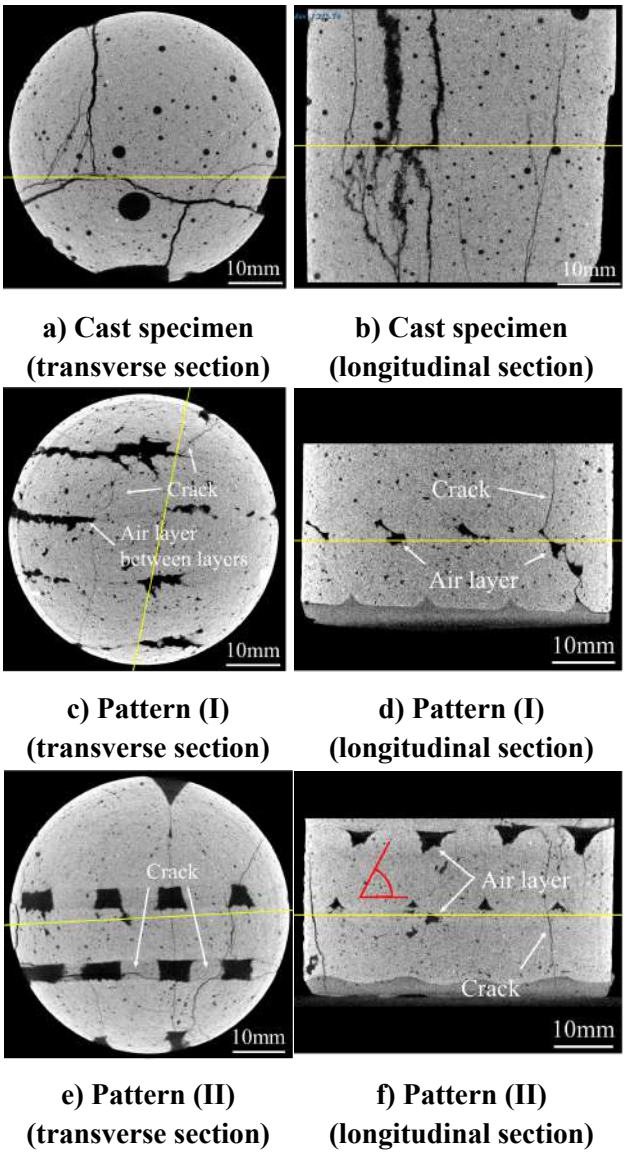
3.1 Internal crack propagation

Fig.3 shows the X-ray computed tomography images of the conventionally cast specimen and the 3D-printed specimens. The yellow line indicates the slice of the corresponding cross-section.

As for the cast specimen, Fig.3a) and b) show that the cracks propagate randomly in the cast specimen.

In the printed specimen with pattern (I) displayed in Fig. 3c) and d), the cracks propagate from the voids formed between the layers. This suggests that the voids which are the interfaces between the filament layers are the starting point for crack propagation.

In the printed specimens with Pattern (II) in Fig. 3e) and f), the voids formed between the layers are more complicated than those in Pattern (I). In addition, the cross-section of the printed filaments is inclined in the longitudinal direction as illustrated in red in Fig. 3f), the cracks in this layer propagate inside the filaments, not at the interface between the filaments.



a) Cast specimen (transverse section) **b) Cast specimen (longitudinal section)**

c) Pattern (I) (transverse section) **d) Pattern (I) (longitudinal section)**

e) Pattern (II) (transverse section) **f) Pattern (II) (longitudinal section)**

Fig.3 X-ray CT Images

3.2 Three-dimensional deformation

Fig.4 shows the cross-sectional images (from 5 mm, 25 mm, 45 mm, and 65 mm from the bottom of the specimen) obtained from X-ray computed tomography and surface polygon data provided before and after

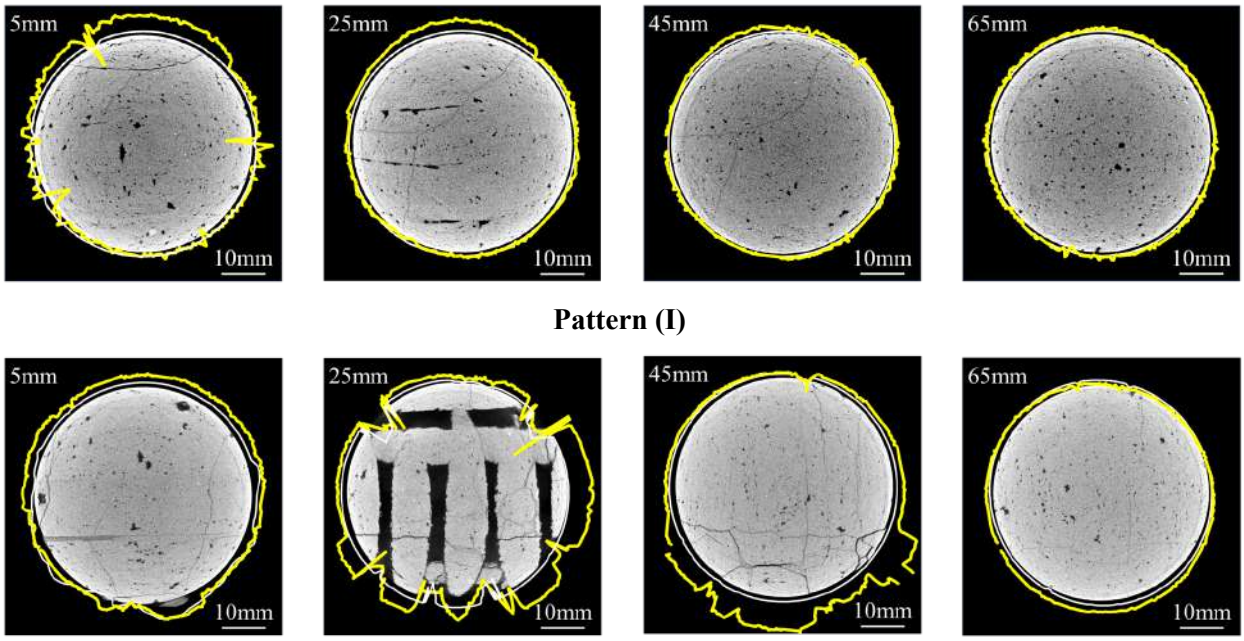


Fig.4 Deformation of each cross-section

loading from 3D scanning. The white lines show the surface geometry before loading and the yellow lines show the surface after loading.

In the pattern (I), the deformation is the largest at 5 mm from the bottom. Also, the shape of the voids between layers indicates that the specimen is printed in the left-right direction in the images. On the other hand, the specimen expands in the vertical direction, that is the deformation direction is orthogonal to the printed direction. This means that the printed direction has an influence on the fracture propagation of the printed specimen.

In Pattern (II), the specimen was largely deformed at 25 mm and 45 mm from the bottom. In their cross-sectional images, large cracks are observed due to the voids between the layers as shown in Fig.3e). Moreover, Pattern (I) expands in the direction perpendicular to the printed direction, whereas Pattern (II) is printed in two orthogonal directions, therefore there is no significant difference in the vertical and horizontal directions in the cross-sectional images.

4. Conclusions

In the investigation on the fracture process in 3D-printed specimens under compressive loading, the propagation behavior of internal cracks was evaluated by X-ray CT method and three-dimensional deformation by 3D scanning. As the results, the following items were obtained. The findings of this study show that the deformation direction can be controlled by designing the nozzle path.

- When the nozzle path is in one direction, the deformation is perpendicular to the printed direction.
- When the nozzle paths are orthogonal in two directions, there is no anisotropy in the deformation.

References

M. Ohno (2022) “Recent Progress and Applications of Topology Optimization for Concrete: A Review”, Concrete Journal, 60 (3): 282-290

R.A. Buswell, W.R. Leal de Silva, S.Z. Jones, and J. Dirrenberger (2018) “3D printing using concrete extrusion: A roadmap for research”, Cement and Concrete Research, 112: 37-49

T.T. Le, S.A. Austin, S. Lim, R.A. Buswell, R. Law, A.G.F. Gibb, T. Thorpe “Hardened properties of high-performance printing concrete, Cement and Concrete Research, 42: 558-566

S. Yamamoto, H. Ogura, H. Abe, and R. Kikuchi (2021) “Development and Practical Application of 3D Printing Technology for Construction”, Concrete Journal, 59 (8): 655-660

Y. Miyagawa, A. Shibayama, and K. Kanazawa (2022) “Displacement Distribution Measurement of Specimens and Real Structure with 3D scanner, Concrete Journal, 60 (9): 796-802

The 16th International Congress on the Chemistry of Cement 2023 (ICCC2023)
"Further Reduction of CO_2 -Emissions and Circularity in the Cement and Concrete Industry"
September 18–22, 2023, Bangkok, Thailand

Use of volcanic ash in an ECC material for 3D printing

F. Fernández[1,2], R. Jarabo[2], E. Asensio[1], and A. Guerrero[1]

[1] *Instituto de Ciencias de la Construcción Eduardo Torroja. IETcc-CSIC. Serrano Galvache, 4, 28033, Madrid, Spain*
Email: aguerrero@ietcc.csic.es eloyadl@ietcc.csic.es fdezluquefernando@gmail.com *
[2] *A3D Additive Printer SL. C/ Valgrande, 25, nave 13, 28108, Alcobendas, Madrid, Spain,*
Email: ffernandez@a3dprinter.es rjarabo@a3dprinter.es

ABSTRACT

The construction industry is one of the sectors that generate the most CO_2 emissions and waste. Therefore, new construction techniques have been developed, with 3D printing standing out, numerous materials have been developed to meet the requirements of 3D printing. One of the most interesting materials is ECC (Engineered Cementitious Composites), whose composition includes fly ash. This material has the capacity for autogenous self-recovery, i.e., the material can reduce and heal the microcracks generated by transport. However, various European laws call for the reduction of net greenhouse gas emissions by at least 55% by 2030. In Spain, the Agreement for a Just Transition stands out, intending to close all coal-fired power plants. Because of this drawback, this study seeks the replacement of fly ashes by volcanic ashes of La Palma, Spain, in 2021. The main goal is the design, development and evaluation of a self-healing and efficient cement-based material that can be used in additive manufacturing. This material has the characteristics to achieve structural integrity, reliability, and robustness of 3D printing.

This paper describes the experimental procedure of an ECC 3D material with volcanic ashes under the curing conditions of room temperature 34 ± 2% RH and 20 ± 2 ºC. Hardened properties are researched via compressive and flexural for up to 90 days. Meanwhile, the self-healing behavior of ECC is followed by optical microscopy.

This study describes the experimental study and shows the results that confirm that the material is 3D printable and the autogenous healing of ECC material at room temperature.

KEYWORDS: *ECC, Fly Ash, Volcanic Ash, 3D printing, Self-healing behavior*

1. Introduction

ECC (Engineered Cementitious Composites) is a new kind of High-Performance Fiber Reinforced Cementitious Composite (HPFRCC) with PVA fibers, micromechanically engineered to achieve a high tensile strain 3-5%, while maintaining fine crack width and possessing the ability to self-repair. The self-healing behaviour is known as autogenous recovery [1, 2]. In September 2021, the volcanic eruption of La Palma, Spain, occurred. The amount of volcanic ash that emerged, in some areas more than one million cubic meters, has sparked interest in its use as a replacement for fly ash, due to the Just Transition agreement in Spain, which aims to close all coal-fired power plants.
In this study, the replacement of fly ash with volcanic ash for a 3D printing ECC material is being studied. For this, the developed material must meet the basic specifications for printing in its fresh state; having consistency between 120 mm and 170 mm, an open time of more than 30 minutes, according to EN: 196-1 [3], having the ability to be extrudable and buildable layer upon layer, as well as reaching a value of at least 15 MPa in compression at one day of hydration age. At the same time, the mechanical

properties are studied up to 90 days of hydration age at RT (T: 20 ± 2°C; RH=35%). The self-healing behavior is supported by the following minicracks by optical microscopy.

2. Materials and Methodology

2.1. Materials

The binder material used in this study was composed of ordinary Portland cement (OPC), Volcanic Ash (LP), Microsilica (MS), and fines aggregates. OPC, designated CEM I 42.5R, was supplied by Cementos Portland Valderrivas, El Alto factory, Madrid. VA used during the experimental test was from the Parque natural de Cumbre Vieja volcano, La Palma Island, Spain.

Table 1. Mixture proportion for composite under investigation (percentage weight).

Mix	OPC	VA	MS	F. Agg.	PVA fibers	Additives	w/b
LP-3D	33.6	36.6	9.5	19	0.75	0.25	0.18

Table 1 shows the developed mixture, LP-3D. Additives used in the composition were a polycarboxylate ether-based superplasticizer (SP) to achieve the required flowability. To prevent segregation and increase the viscosity and thixotropy of fresh mixtures sepiolite was used. The quantity components are protected by a confidential document with a private company, A3D Additive Printer SL. The mixing water used in this work was distilled. The particle size distributions of OPC, VA, F. Agg., and MS are presented in Fig. 1a High strength and high modulus polyvinyl alcohol (PVA) fibers of 8 mm length were employed to reinforce the matrix for ECC material development, LP-3D. Figure 1b presents the chemical compositions of FA and LP, which were obtained by X-ray Fluorescence (XRF).

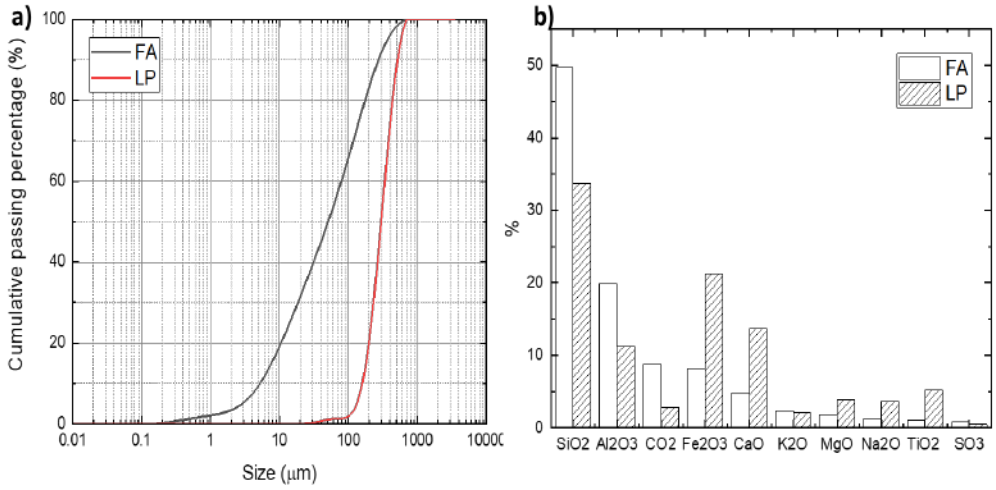


Figure 1. a) FA and LP particle size distributions. b) Chemical compositions of Fly Ash (FA) and Volcanic Ash (LP).

2.2 Methodology

2.2.1. Fresh and hardened properties

The workability of LP-3D is carried out using the flow table test according to the European Standard [3]. The loss of workability with time is carried out for one hour under slow speed agitation, the consistency of the material was measured at 0, 10, 20, 35, 45, and 60 minutes. Density is measured according to EN 1015-6 [4]. In addition, to complete the tests of the properties in fresh state, extrudability, and printability tests were performed. The extrudability and printability tests are carried out with a caulk gun, a layer on layer impression of 10 cm in length, and a layer width of 1 cm for a 4 cm long rectangular extruder, as D. G. Soltan et al. [5].

The key properties of impression materials in the hardened state are compressive and flexural strengths, which are measured according to the Standard [3]. The mechanical properties of the mixture to be studied will be carried out in the hydration time of one day to 90 days due at RT (T= 20 ± 2°C; RH=35%).

2.2.2 Evaluation of Self-healing

To observe the image of self-healing products in ECC-A3D cracked by optical microscopy (Olympus SZ61/ Olympus SC50), specimens were prepared just after the controlled cracks, and, to evaluate the effect of the curing time for both conditions, a morphology study is carried out at large days from the total of the mix.

3. Results and discussion

3.1. Fresh and hardened properties

The results of the open time test and consistency table are shown in Fig. 2a. The material presents a necessary balance from the point of view of workability, since a material with high fluidity, although workable, can cause a decrease in the retention capacity.
The initial consistency is 140 mm. This consistency remains almost constant during the test, reaching 137 mm after half an hour, and 136 mm at the end of the test. In fact, visual observation during the production handling of mixtures confirmed the good appearance of the material during the measurements.

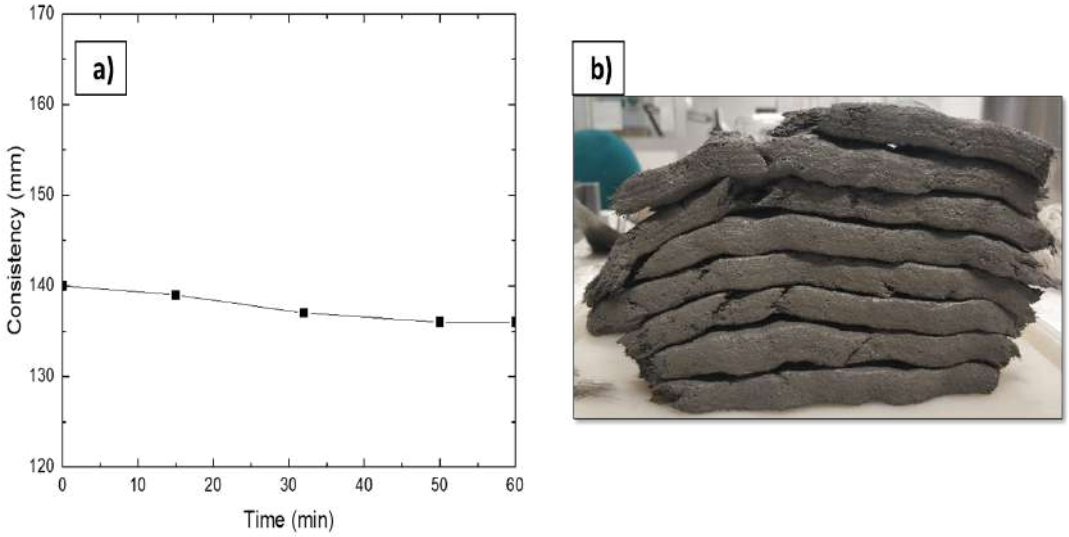


Figure 2. a) Open time test b) Buildability test.

Density of LP-3D was measured. Due to the particle size of the aggregate and the binder, Fig. 1, the density achieved by ECC-A3D is 1,767.9 kg/m^3.

Fig. 2b shows the printing process of ECC-A3D and an 8-layer printed using a caulking gun. It should be noted that the bottom layer of the printed sample was able to support the weight of the upper layers, 8 in total, allowing a layer upon layer rises without any deflection. As for the printing width, all layers around the 4 mm. Therefore, as shown in Fig. 2b, ECC-A3D exhibited good buildability and shape retention ability. Furthermore, ECC-A3D material showed good workability and rapid rebuilding that allowed both extrusion and buildability with minimal deformation of layers under the weight of subsequent layers.

Fig. 3a shows the evolution of the mechanical properties at room temperature up to 90 days of hydration time. In flexural strength, LP-3D shows a value of 7.12 MPa at one day. The flexural value increases after 28 days to 9.17 MPa and remains constant until 90 days of hydration. The compressive strength of LP-3D was also studied. At one day of hydration, the material shows a resistance of 29.13 MPa, much higher than the 15 MPa required. This value continues to increase reaching 57.48 MPa and 71.5 MPa at 28 and 90 days, respectively.

3.2. Evaluation of Self-healing

Fig. 3b and Fig. 3c show the evolution of the cracks generated at two days of hydration, up to 180 days, respectively. Fig 2c shows that the material is able to reduce cracks.

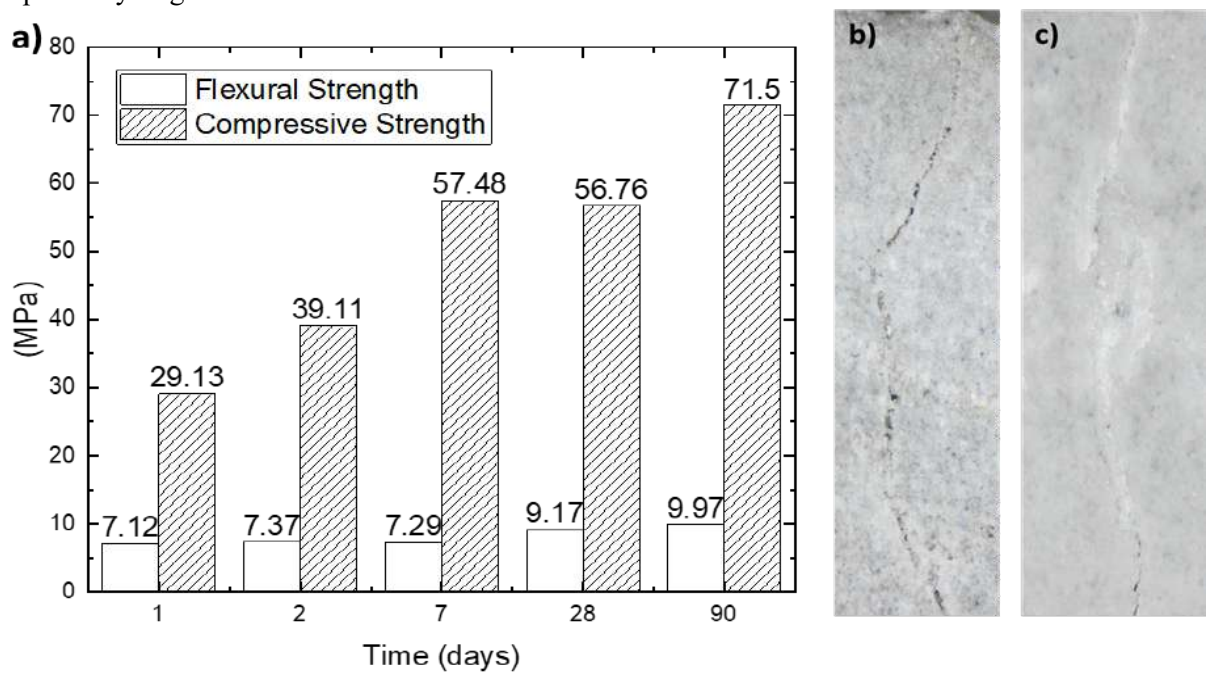


Figure 3. a) Mechanical Properties of LP-3D. Evolution of preloaded cracks b) 2 days. c) 180 days.

4. Conclusions

This paper attempt to investigate the fresh properties, mechanical properties, and self-healing behaviour of LP-3D. The following conclusions can be drawn from this study:

1. The development material, LP-3D, meets the requirements of 3D printing, since it shows good rheology, extrudability, and buildability.
2. Volcanic ash (LP) does not affect the mechanical properties.
3. It is observed by Optical Microscopy how the material is able to reduce the mini cracks generated during loading.

In future lines, a more exhaustive study of the self-healing behaviour will be carried out. A larger-scale 3D printing will be also performed.

Acknowledgments

Authors gratefully acknowledge the financial support of the PID2020-113223RB-100, funded by the Spanish Government (Ministerio de Ciencias e Innovación) to the Instituto de Ciencias de la Construcción "Eduardo Torroja" of the Spanish Research Council – IETcc-CSIC.

References

[1] Fischer, F, Wang, Li, V, Design of engineered cementitious composites (ECC) for processing and workability requirements, Brittle Matrix Composites 7, Woodhead Publishing, 2003, Pages 29-36, https://doi.org/10.1533/9780857093103.29.

[2] Li, Victor. Engineered Cementitious Composites (ECC) – Material, Structural, and Durability Performance. 2011.

[3] EN 196-1: Methods of testing cement – Part 1: Determination of strength.

[4] EN 1015-6: Methods of test mortar for masonry. Part 6: Determination of bulk density of fresh mortar.

[5] Soltan D.G, Li V.Ci, A self-reinforced cementitious composite for building-scale 3D printing, CCC, Volume 90, 2018, Pages 1-13, https://doi.org/10.1016/j.cemconcomp.2018.03.017.

The 16th International Congress on the Chemistry of Cement 2023 (ICCC2023)
"Further Reduction of CO_2 -Emissions and Circularity in the Cement and Concrete Industry"
September 18–22, 2023, Bangkok, Thailand

Future projection of carbon dioxide emission in calcium carbonate concrete (CCC) production

S. Fujimoto[1*], B. N. Kien[2], R. Kurihara[3], R. Kitagaki[4], T. Masuo[5], H. Hyoudou[6], H. Hirao[7], M. Kanematsu[8], M. Tsujino[9], Y. Kuroda[10], H. Nakazawa[11], M. Tamura[12], I. Maruyama[13] and T. Noguchi[14]

[1] *Utsunomiya University, Utsunomiya, Japan, fujim@cc.utsunomiya-u.ac.jp*

[2] *The University of Tokyo, Tokyo, Japan, kienbui@g.ecc.u-tokyo.ac.jp*

[3] *The University of Tokyo, Tokyo, Japan, ryo.kurihara@bme.arch.t.u-tokyo.ac.jp*

[4] *Hokkaido University, Sapporo, Japan, ryoma@eng.hokudai.ac.jp*

[5] *Masuo Recycle Co., Ltd, Tokyo, Japan, taka.m@masuo-group.com*

[6] *Taiheiyo Cement Corporation, Tokyo, Japan, Hikotsugu_Hyoudou@taiheiyo-cement.co.jp*

[7] *Taiheiyo Cement Corporation, Tokyo, Japan, Hiroshi_Hirao@taiheiyo-cement.co.jp*

[8] *Tokyo University of Science, Tokyo, Japan, manabu@rs.tus.ac.jp*

[9] *Shimizu Corporation, Tokyo, Japan, m.tsujino@shimz.co.jp*

[10] *Shimizu Corporation, Tokyo, Japan, y.kuroda@shimz.co.jp*

[11] *Shimizu Corporation, Tokyo, Japan, nakazawa.h@shimz.co.jp*

[12] *Kogakuin University, Tokyo, Japan, masaki-t@cc.kogakuin.ac.jp*

[13] *The University of Tokyo, Tokyo, Japan, i.maruyama@bme.arch.t.u-tokyo.ac.jp*

[14] *The University of Tokyo, Tokyo, Japan, noguchi@bme.arch.t.u-tokyo.ac.jp*

ABSTRACT

Carbon dioxide emission due to cement concrete accounts for considerable amount. To compensate the emission, authors have proposed a novel material, so called calcium carbonate concrete (CCC), in which carbon dioxide is absorbed during the production. Since the energy input is inevitable to achieve fast and controlled carbon capture, the balance of carbon dioxide emission and absorption should be appropriately evaluated. In contrast to the ordinary life cycle assessment (LCA), the difficulty in LCA for a novel material lies in the fact that the actual plant is not yet implemented, and measurement of the actual production processes is impossible. Therefore, this paper investigates such balance of carbon dioxide emission in several types of possible CCC production processes. Combination of experimental and partially theoretical approach was taken. Energy input to CCC specimen production was measured and collected, and possible carbon dioxide emission balance was projected based on assumptions in production systems and energy efficiency.

KEYWORDS: *Life cycle assessment for CR2 technologies, carbon dioxide emission, C^4S project, calcium carbonate concrete (CCC)*

1. Research background and objectives

Carbon dioxide emission due to cement concrete accounts for the considerable proportion of the global emission. To compensate the emission, Maruyama et.al. (2021) have proposed a novel material, so called calcium carbonate concrete (CCC), in which carbon dioxide is absorbed during the production. Because

the energy input is inevitable to achieve fast and controlled carbon capture, it is essential to quantify balance between carbon dioxide emission and absorption to evaluate environmental performance of the technology. This paper investigates such balance in several types of possible CCC production processes. Combination of experimental and partially theoretical approach was taken. Specifically, energy input to CCC specimen production was measured and possible carbon dioxide emission balance was projected.

2. Materials and methods

2.1 Overview of CO_2 emission accounting

The process-based inventory analysis was conducted for 3 types of CCC production in comparison with typical precast concrete production in winter. Considering the current pre-mature development stage of CCC, where construction method is not yet determined, the system boundary for inventory analysis was set as cradle-to-gate basis as shown in Figure 1 in reference to LCA (2020). The CO_2 emission coefficients for each energy source, i.e., kg-CO_2 emission per a unit energy consumption, were assumed the same for all types of production. CO_2 emission due to transportation was not considered. The CO_2 emissions for all types of production were estimated and compared for cubic meter of production. 2 different scenarios of CO_2 emission accounting were compared as explained in the next section.

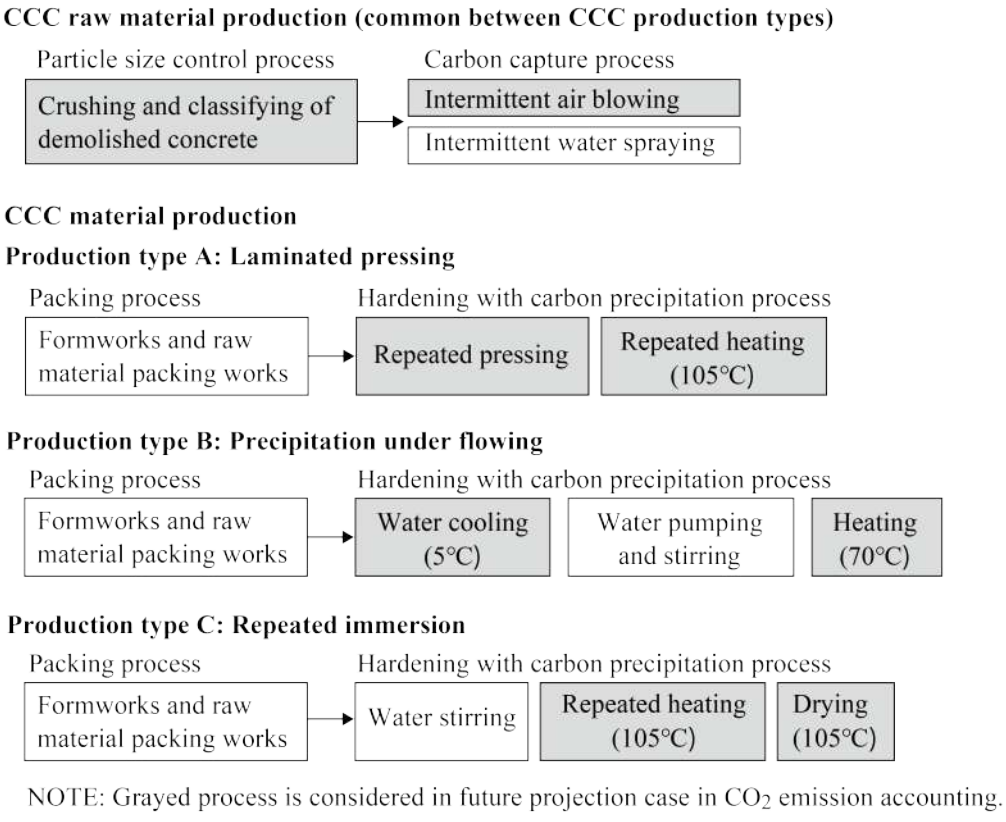


Figure 1 CCC and CCC raw material production processes

2.2 Assumptions in each scenario for CO_2 emission accounting

In the current accomplishment scenario, CO_2 emission intensity, that is, the emission per a unit volume of CCC was assumed the same between small specimen CCC production and full-scale production. The energy consumption for a CCC specimen in production type B was determined by electric consumption measurement of water cooling, pumping, stirring and specimen heating. Energy consumption for a CCC specimen in production type C was determined by accumulating nominal energy consumption of machineries for vibration, stirring, heating and drying. CO_2 emission per a cubic meter of CCC was

estimated by multiplying energy consumption with emission coefficients in NEDO (2022). Influence of specimen size was also investigated for production type B.

In the future projection scenario, optimal CO_2 emission for 1 cubic meter CCC was projected based on experimental resource input at CCC specimen production and on the assumptions of high energy efficiency. The list of assumptions made is shown as follow:

- ✓ 100% energy efficiency was assumed for material temperature change.
- ✓ Crushing and classification energy input (kWh/ton) for CCC raw material production was assumed the same as the energy input for recycled aggregate production measured at actual plant. Influence of particle distribution was neglected.
- ✓ Wind blowing energy input (kWh/min) for CCC raw material production was calculated based on nominal energy consumption of machineries assumed at current bench scale plant design.
- ✓ Energy input for water temperature change was calculated from water amount, specific heat, temperature difference in each type of production and energy intensity in NEDO (2022).
- ✓ Water spraying energy input for CCC raw material production was neglected due to lack of data.
- ✓ Formwork and particle packing energy was neglected for type B due to lack of data. Particle packing energy for type C (MJ/m^2) assumes the same as pressing at every 20cm thickness.
- ✓ The energy input for pressing was calculated from tile production data (MJ/m^2) in Ciacco (2017). Pressing of 0.5cm thickness and the same energy intensity as heating in NEDO (2022) was assumed.
- ✓ In type A, water input was estimated based on the water sprayed (g/m^2) for a specimen production. Water heating energy from 5 deg. to 105 deg. was considered.
- ✓ In type B, water input speed for specimen production was used to estimate minimum amount of water necessary for production. Energy input for water heating from 5 deg. to 70 deg. and cooling from 20 deg. to 5 deg. was considered. The water was assumed to be cooled down at outdoor from 70 deg. to 20 deg. Water pumping and stirring energy input was neglected.
- ✓ Energy input for CCC solids was calculated assuming 70% packing ratio and the same density and specific heat as ordinary concrete. Temperature change of CCC solids was assumed 20 deg. to 70 deg. for type B, and 35 times of 85 deg. difference for type C.
- ✓ In type C, energy input for water heating was calculated based on water evaporation estimated from mass difference at final drying per unit volume of specimen. Cooling at outdoor was assumed.

3. Results

3.1 Estimated CO_2 emission per a unit volume of CCC production

Figure 2 shows the estimated CO_2 emissions for each production type and scenario. The results of "current accomplishment scenario" revealed that CO_2 emission at current CCC specimen production system is significantly higher than precast concrete. However, the future projection scenario results implies that the CCC material has potential of CO_2 reduction in comparison with precast concrete production if optimal scaled-up production system could be implemented.

3.2 Possible reduction of CO_2 emission

Figure 3 (left) shows the time-dependent electric current for heating process in specimen production type B. Although overall energy consumption was linear to time, the intermittent energy consumption was observed for keeping the constant temperature. This tendency indicates possible reduction of energy consumption if appropriate insulation is implemented in heating process. Figure 3 (right) shows relationship between specimen size and CO_2 emission per CCC volume. In contrast to the assumptions made in 2.2, the declining trend in CO_2 emission increase was observed as specimen size increased. This result implies possible improvement in energy efficiency in the scale-up of production process.

4. Discussion

Energy efficiency decrease in real processes as well as improvements in scale-up remain as future works. Authors are currently working on estimating energy efficiency decrease of similar processes.

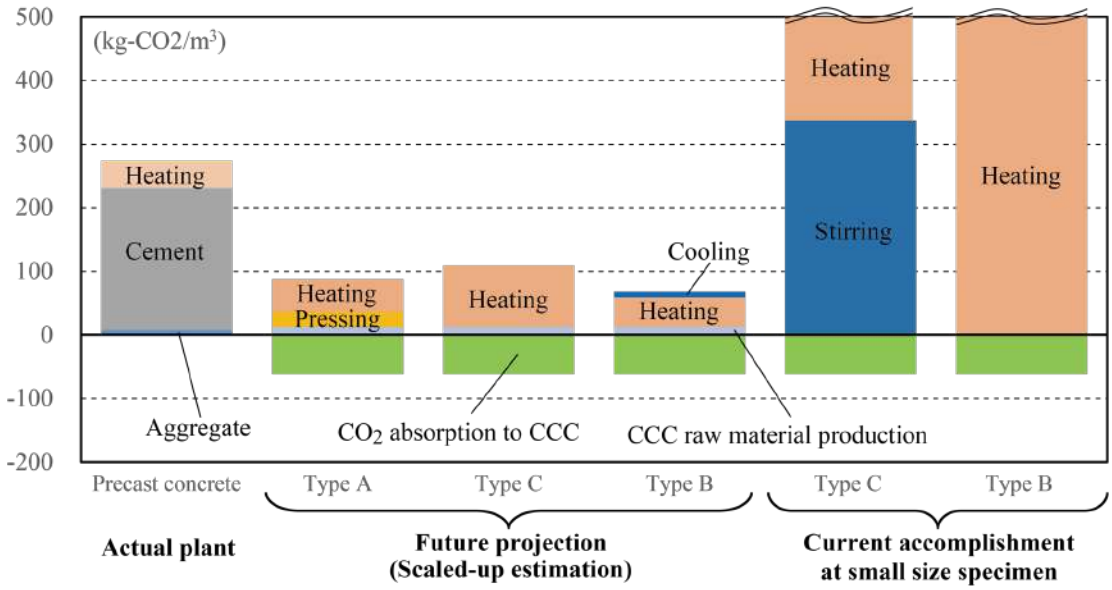


Figure 2 Estimated carbon dioxide emission of CCC in each scenario and production type in comparison with precast concrete production

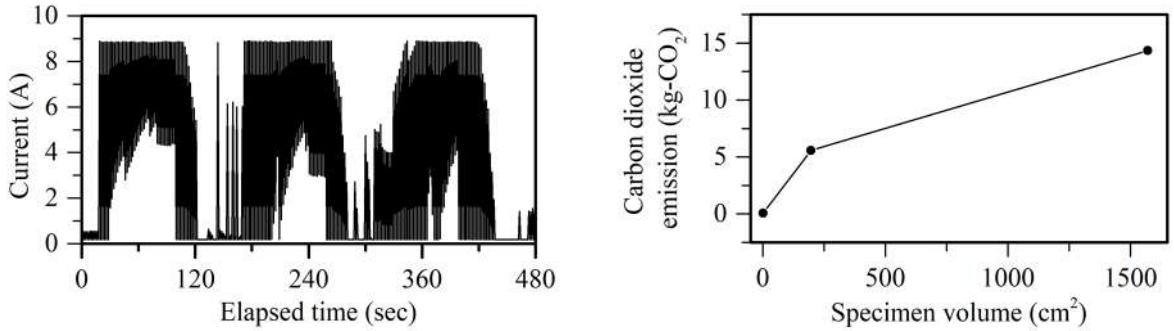


Figure 3 Intermittent electric consumption of heating process (left) and Relationship between estimated carbon dioxide emission and specimen size (right) - current accomplishment case in production type B -

5. Conclusions

Future projection of CO_2 emission for CCC produced under 3 different systems and 2 scenarios were estimated. The potential of CO_2 reduction of CCC in comparison with precast concrete production was suggested.

Acknowledgements

This research was funded by the NEDO Moonshot Project "C^4S Research and Development Project" (Project Manager: Prof. Takafumi Noguchi, The University of Tokyo).

References

Ciacco E.F.S. et. al. (2017), "The energy consumption in the ceramic tile industry in Brazil", *Applied Thermal Engin eering*, 113: 1283-1289

LCA Japan Forum (2020), "Guideline for carbon dioxide emission estimation of carbon removal and recycling (CR2) technologies based on life cycle assessment", https://lca-forum.org/research/nets/public.html (access 2023-2-28)

Maruyama I. et. al. (2021) "A New Concept of Calcium Carbonate Concrete using Demolished Concrete and CO_2", *Journal of Advanced Concrete Technology*, 19: 1052-1060

NEDO (2022), Simplified guideline for estimating life cycle CO2 emission for CCU technologies in initial develop ment stage, https://www.nedo.go.jp/library/ccuguideline.html

The 16th International Congress on the Chemistry of Cement 2023 (ICCC2023)
"Further Reduction of CO_2 -Emissions and Circularity in the Cement and Concrete Industry"
September 18–22, 2023, Bangkok, Thailand

Novel Soluble Boron Compounds to Improve Shielding of Cement Systems

Ashish D. Patel[1], Jerry M. Paris[2], Christopher C. Ferraro[3]*, Kyle A. Riding[4], Eric R. Giannini[3] Brian R. Strazisar[6]

[1]University of Florida, Gainesville, USA
Email: ashish.patel@ufl.edu
[2]US Army Corps of Engineers, Vicksburg, USA
Email: jerry.m.paris@erdc.dren.mil
[3]University of Florida, Gainesville, USA
Email: ferraro@ce.ufl.edu
[4]University of Florida, Gainesville, USA
Email: kyle.riding@essie.ufl.edu
[5]Portland Cement Association, Washington, USA
Email: egiannini@cement.org
[6] National Energy Technology Laboratory, Pittsburgh, USA
Email: Brian.Strazisar@netl.doe.gov

ABSTRACT

Nuclear power plants use concrete biological shields to protect plant personnel from excessive radiation dose uptake. Boron can be added to concrete shields to improve neutron attenuation. Effective neutron shielding requires high boron content and dispersion. Common boron compounds such as borate minerals are soluble and thus can be used to uniformly distribute boron in concrete. However, they also adversely affect setting and strength development which limit the amount of boron that can be incorporated into shields. Borane compounds, $K_2B_{10}H_{10}$ and $K_2B_{12}H_{12}$, are potential candidates for shield development due to their high boron content, solubility, and chemical stability. The borane compounds were assessed for solubility and impacts on early-age cement hydration properties. Results were compared to that of borax, a common borate mineral. Solubility of the boron compounds was measured in aqueous and lime-saturated solutions using inductively coupled plasma atomic emission spectroscopy (ICP-AES). Hydration kinetics and phase formation in portland cement pastes doped with the boron compounds were examined using isothermal conduction calorimetry and X-ray diffraction (XRD). Borane compounds were found to release more boron into aqueous and lime solutions than borax, suggesting that borane compounds can uniformly distribute boron into cement systems and thus enhance shielding homogeneity. Moreover, borane compounds had minimal impact on early hydration properties compared to the control while borax severely altered hydration. Results indicate that borane compounds can be used to incorporate larger quantities of soluble boron into cement systems than borates without degrading early-age cementitious properties.

KEYWORDS: *Boron, solubility, shielding, cement, kinetics*

1. Introduction

Boron enhances the neutron shielding properties of cementitious systems while reducing radioactivation (Solanti et al (2016), Tanaka et al (2022)). Boron removes neutrons from the radiation field through capture; after capture, neutrons no longer pose risks for workers or vital components near nuclear sources. The quantity of boron atoms in cementitious shields dictates neutron shielding efficiency. This is because the neutron capture probability of boron is approximately 100 to 1000x greater than elements

commonly found in concrete (Kharita et al (2011)). Two shields with the same mass proportion of boron theoretically have the same neutron shielding efficiency, regardless of the boron compound.

Higher boron dispersion in cementitious shields, though, has been shown to improve neutron attenuation (Soltani et al (2016)). Soluble boron compounds can provide a relatively uniform dispersion of boron in cementitious systems. Common borate minerals like colemanite, borax, and boric acid are soluble but strongly retard hydration, setting, and strength development in cementitious systems (Glinicki et al (2018)). Borate anions are thought to impede cement hydration and setting by rapidly forming an amorphous borate gel that adsorbs onto unreacted cement grains, preventing further dissolution and hydration (Glinicki et al (2018)). Techniques to accelerate hydration in borated cementitious systems have been studied but are generally inefficient (Li et al (2021)). Borates are, thus, impractical for use in large concrete shields.

Borane compounds, $K_2B_{10}H_{10}$ and $K_2B_{12}H_{12}$, are promising alternatives to borate minerals as they have higher boron mass fractions (55 to 59%) than those of borate minerals, which range from approximately 11 to 17%. Thus, less borane compounds are needed by mass to achieve equivalent boron content and neutron shielding as borate compounds. The borane compound, $K_2B_{12}H_{12}$ has been shown to release more boron into saturated aqueous solutions than a borate mineral across a range of temperatures which translates to effective dispersion of boron (Blake (2015)). However, these boranes have not been tested in cementitious systems despite being considered chemically stable (Knoth et al (1964)).

This study presents novel research on the effects of borane compounds on early-age cement hydration. Hydration kinetics and phase formation were tested in cement pastes doped with the borane compounds and borax. Boron mass content was equivalent in each mixture. This study provides a basis for the design of highly efficient cementitious neutron shields with normal setting behavior and uniform shielding properties.

2. Materials and Methodology

An ASTM C150 Type I/II ordinary portland cement (OPC) and ultrapure water (resistivity > 18.0 MΩ-cm) were used to prepare paste mixtures for isothermal calorimetry and X-ray diffraction (XRD) experiments. Borax pentahydrate ($Na_2B_4O_7•5H_2O$>99%) and the borane compounds, potassium decahydrodecaborate ($K_2B_{10}H_{10}$ >98%) and potassium dodecahydrododecaborate ($K_2B_{12}H_{12}$ >98%) were used to for this study.

Boron concentration in aqueous and lime-saturated solutions with borax and the borane compounds were measured using ICP-AES per the U.S. Environmental Protection Agency (EPA) method 6010C. To ensure solutions were saturated with the boron compounds, 0.5 g of each boron compound were mixed into 10 mL solutions consisting of deionized water with and without 0.1 g of lime ($Ca(OH)_2$).

The hydration kinetics and heat of hydration of paste mixtures were measured using an eight-channel isothermal calorimeter at 23 °C (TAM Air). Testing was performed in accordance with ASTM C1702. Paste mixtures were externally mixed using a vortexer at 2500 RPM for five seconds. Boron compounds were added to paste to achieve an elemental boron content of 2.5 kg/350 kg OPC. This boron dose was selected based on the neutron flux at the surface of an in-situ concrete shield with an OPC content of 350 kg/m^3. The dosages of $K_2B_{10}H_{10}$ and $K_2B_{12}H_{12}$ were, respectively, increased by factors of five and six. This allowed for testing of the borane compounds at higher doses and at equivalent molar additions. Equivalent molar additions of the borane compound allow for better comparison of the effects of the borane anions on hydration while controlling for the effects of potassium cations. Table 1 shows the mixture proportions of the paste mixtures used in this study.

Table 1. Isothermal Calorimetry and XRD Paste Mixture Design (g).

Mixture ID	OPC	Water	Boron Compound
Control	4.0000	2.0000	-
Borax	4.0000	2.0000	0.1925
$K_2B_{10}H_{10}$	4.0000	2.0000	0.0519
$K_2B_{12}H_{12}$	4.0000	2.0000	0.0485
$K_2B_{10}H_{10}$ x5	4.0000	2.0000	0.2595

$K_2B_{12}H_{12}$ x6	4.0000	2.0000	0.2908

Phase formation of paste mixtures with and without boron compounds were examined at 72 hours after mixing using XRD. Paste mixture proportions are shown in Table 1. Preparation of paste mixtures followed the same process for calorimetry specimens. Three days after mixing, the paste specimens were removed from their glass ampoules and ground using a mortar and pestle. Immediately after grinding, diffraction data were collected using a Panalytical X'Pert Powder instrument operating at 40 mA and 45 kV with CuKα radiation. Counts were collected over a 2θ scan range from 5 to 70° at increments of 0.008°/step and 20 s/step integration time.

3 Results and Discussion

Boron concentrations in solutions saturated with borax and the borane compounds are presented in Table 2. Borane compounds had substantially higher boron concentrations in the solutions compared to the borax-doped solutions. The boron solubilities of the borane compounds were similar in both types of solutions while borax exhibited lower boron solubility in the lime solution than in the aqueous solution. This indicates that the borane anions, $B_{10}H_{10}^{2-}$ and $B_{12}H_{12}^{2-}$, were likely not reacting in the lime-saturated solution to form precipitates. Moreover, this could also indicate that borane anions are less prone to react in cement pore solution than borates.

Table 2. Boron Concentrations in Deionized Water and Lime-Saturate Solutions (g/L).

Compound	B (aq)	B in lime (aq)
Borax	47.3	8.78
$K_2B_{10}H_{10}$	182	189
$K_2B_{12}H_{12}$	147	149

Thermal power and cumulative heat curves for the paste mixtures are shown in Figure 1. Borax retarded the main hydration peak by more than 72 hours while the borane compounds had minimal impact on peak time relative to the control at boron dosages of 2.5 kg/350kg OPC. Compared to the control, the $K_2B_{12}H_{12}$ mixture had a slightly higher main peak intensity but similar 72-hour cumulative heat. The $K_2B_{10}H_{10}$ mixture had similar main peak intensity and 72-hour cumulative as the control. At higher dosages, the $K_2B_{10}H_{10}$ and $K_2B_{12}H_{12}$ compounds delayed the main hydration peaks by approximately three hours. The $K_2B_{10}H_{10}$ 5x mixture exhibited lower peak intensity than the $K_2B_{12}H_{12}$ 6x and control mixtures. Since the number of moles of the borane compounds in the $K_2B_{10}H_{10}$ 5x and $K_2B_{12}H_{12}$ 6x paste mixtures were the same, the difference in reactivity is likely tied to the borane anions. Regardless, the borane compounds had similar or higher total heat production at 72-hours than the control at higher doses. This suggests that the borane compounds can be used to improve shielding efficiency without substantially degrading OPC reactivity.

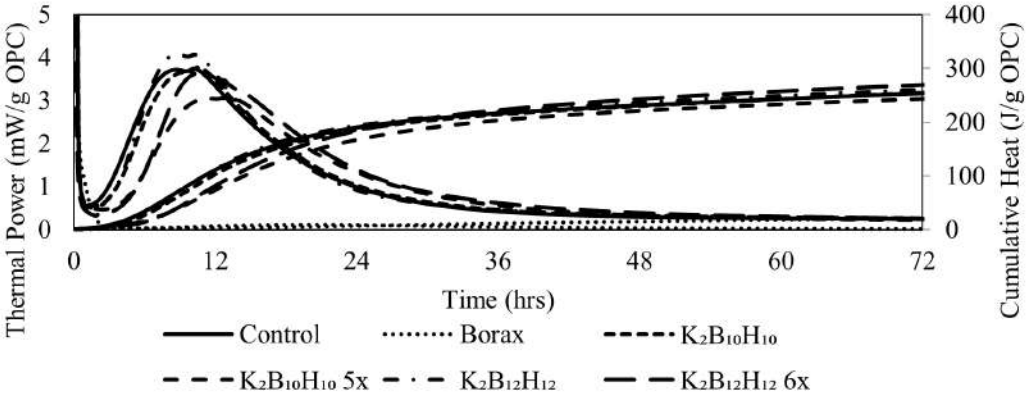


Figure 1. Thermal power and cumulative heat curves for paste mixtures

Diffraction patterns of anhydrous OPC and paste mixtures with and without the boron compounds are shown in Figure 2. The borax paste mixture lacks the portlandite peak and exhibits higher intensities for the alite and belite peaks than the other paste mixtures. Alite and belite peak intensities for the borax mixture are also slightly lower than those for anhydrous OPC. Calcium silicates likely underwent some dissolution in the borax mixture but were prevented from forming typical hydrate phases. It is likely that the borax interfered with the nucleation and growth of cement hydrate phases. Ettringite peaks are present in the borax doped mixture. The first ettringite peak is notably broader and slightly shifted to a higher 2Θ value which indicates that borax may have altered the structure of ettringite (Champenois et al (2015)). In contrast, the diffraction patterns of the control and borane-doped paste mixtures are nearly equivalent. Peaks corresponding to ettringite, portlandite, alite, and belite are present at similar intensities. This indicates that phase formation and, thus hydration, in the borane-doped paste mixtures were similar to the control at 72 hours after mixing.

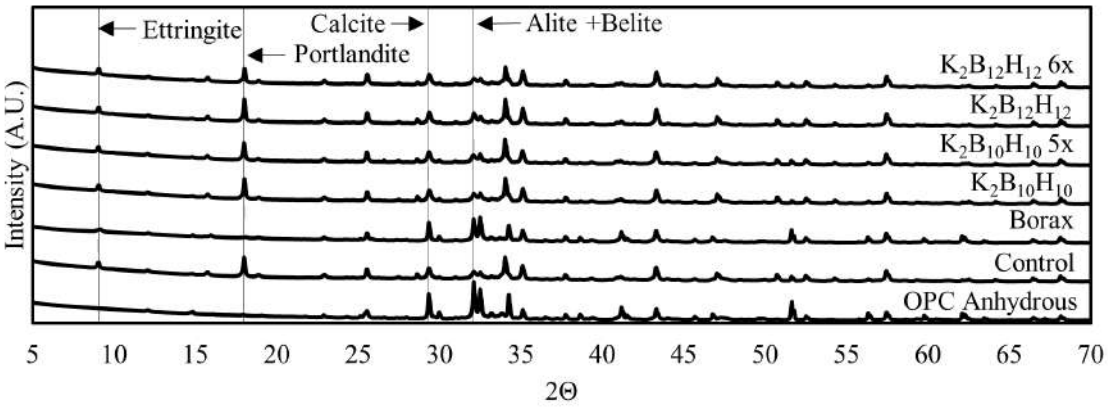


Figure 2. XRD diffraction plots of paste mixtures at 72 hours after mixing

3 Conclusion

Unlike borax, the borane compounds exhibited high boron solubility and chemical stability in lime-saturation solution and enabled the addition of higher boron content in cement paste with minor impacts on hydration kinetics and phase formation. Results suggest that the borane compounds can be used to develop highly efficient cementitious neutrons shields with uniform shielding characteristics. Further testing is needed to determine strength development, long-term durability, and neutron shielding properties.

References

Soltani, Z., Beigzadeh, A., Ziaie, F., Asadi, E. (2016) "Effect of particle size and percentages of Boron carbide on the thermal neutron radiation shielding properties of HDPE/B4C composite: Experimental and simulation studies", *Radiation Physics and Chemistry*, 127:182-187

Tanaka, S., Okuno, K., Takeuchi, Y., Tabara, T. (2022) "Development of a novel boron carbide-based coating material for reduction of activation in neutron application facilities", *Applied Radiation and Isotopes*, 181:110074

Kharita, M.H., Yousef, S., AlNassar, M. (2011) "Review on the addition of boron compounds to radiation shielding concrete", *Progress in Nuclear Energy*, 53(2):207-211

Glinicki, M.A., Antolik, A., Gawlicki, M. (2018) "Evaluation of compatibility of neutron-shielding boron aggregates with Portland cement in mortar", *Construction and Building Materials*, 164:731-738

Li, Q., Ma, H., Tang, Y., Chen, W. (2021) "Combined effect of $NaAlO_2$ and NaOH on the early age hydration of Portland cement with a high concentration of borate solution", *Cement and Concrete Research*, 144:106430

Blake, A. (2015) "Characterization of Boron Hydride Compounds for Potential Use in Pressurized Water Nuclear Reactors", MS Thesis, Pittsburgh State University

Knoth, W.H., Sauer, J.C., England, D.C., Hertler, W.R., Muetterties, E.L. (1964) "Chemistry of Boranes. XIX.1 Derivative Chemistry of $B_{10}H_{10}^{-2}$ and $B_{12}H_{12}^{-2}$", *Journal of the American Chemical Society*, 86:3973-3983

Champenois, J., Dhoury, M., Coumes, C.C.D., Mercier, C., Revel, B., Le Bescop, P., Damidot, D. (2015) "Influence of sodium borate on the early age hydration of calcium sulfoaluminate cement", *Cement and Concrete Research*, 70:83-93

The 16th International Congress on the Chemistry of Cement 2023 (ICCC2023)
"Further Reduction of CO_2 -Emissions and Circularity in the Cement and Concrete Industry"
September 18–22, 2023, Bangkok, Thailand

Constructing solutions using cement-based materials for energy harvesting and storage

J. S. Dolado[1]

[1] *Centro de Física de Materiales (CFM), CSIC-UPV/EHU, San Sebastián, Spain*
Email: j.dolado@ehu.eus

ABSTRACT

Concrete and cement-based materials are among the most widely used materials on Earth, second only to water. These versatile materials have shaped the modern landscape, from towering skyscrapers to highways and bridges. While their primary use has been structural, recent advancements have shown that their widespread presence can also be leveraged for energy conversion and storage. In recent years, various construction methods have been developed that use cementitious composites for energy solutions, such as rechargeable concrete batteries, cementitious thermal energy storage devices for concentrated solar plants, and the emergence of radiative cooling concretes. These novel applications of cement-based materials have the potential to revolutionize the way we think about energy storage and conversion in the built environment. For example, rechargeable concrete batteries could offer a sustainable and cost-effective solution for storing energy in buildings and infrastructure, while radiative cooling concretes could help reduce energy consumption and mitigate the urban heat island effect in cities. As we continue to explore the full potential of cement-based materials, we may uncover new ways to address some of the most pressing challenges facing our world today, including climate change and energy sustainability.

KEYWORDS: *Cement and Concrete, Energy, Batteries, Thermal Energy Storage, Radiative Cooling Concrete*

1. Introduction

Concrete has been used as a building material for thousands of years, dating back to ancient civilizations such as the Egyptians and Romans. Its primary use has been for constructing buildings, roads, bridges, and other infrastructure projects. However, with the increasing need for sustainable and renewable energy sources, concrete is now being used for energy storage and harvesting. This represents a significant shift in the way we think about concrete and its potential applications. The underlying idea of this new concept is the extensive character of energy. Regardless the kind of energy we refer to, the overwhelming volume of cementitious structures might compensate their *a priori* low energy density.
One paradigmatic possibility is the case of electrochemical energy. Materials such as lithium are scarce, unequally distributed around the planet, and extremely expensive. Could an electrochemical battery be produced using materials as abundant and cheap as cementitious materials? Could we build a building that functions as a giant battery? The answer is yes, as demonstrated by the seminal work of Meng and Chung (2010), though of course many things must be improved prior to become a reality.
The second example is the use of concrete in thermal energy storage systems. Concrete has a high thermal mass, which means it can absorb and store heat energy. This makes it ideal for use in heating and cooling systems for buildings. By using concrete as a thermal storage medium, energy can be stored during off-peak hours when electricity is cheaper and then released during peak hours when energy demands are higher. While this application in buildings is relatively well known, the thermal properties of concrete are also valuable in storing the energy produced in Concentrated Solar Power (CSP) Plants. Indeed, the applicability and performance of OPC concrete for TES have been largely investigated and validated in CSPs of first generation [eg. Laing et al (2006), Hoivik et al (2019)]. The challenge here is that differently

to the old (1st generation) CSPs that operate with storing temperatures lower than 450ºC, current 2nd generation CSPs operate at temperatures between 500 ºC and 700 ºC, making the use of OPC-based TES modules highly risky. And the things will be worse for the incoming 3rd generation CSPs whose running temperatures will lay between 700ºC and 1000ºC. Does this mean that concrete cannot continue being used in this application? Actually, it means that OPC-based concretes cannot. However other varieties of concretes might be valid for this application. Recent studies on CA concretes [Boquera et al (2022)] or geopolymer-based concretes [Rahjoo et al. (2022a)] make us be optimistic.

Another example is the use of concrete in photovoltaic energy harvesting systems. Concrete can be embedded with photovoltaic cells, allowing it to generate electricity from sunlight. This can be particularly useful in urban environments where there is limited space for solar panels. Here concrete, if correctly tuned, can cool the embedded solar cell (Cagnoni et al. (2022)). Keeping in mind that the performance and the service lifespan of the solar cell device are dramatically affected by temperature, it seems clear that the marriage of "cool" concretes and solar cells is a win-win case. The progress of cooling technologies has lately received a great deal of attention since the recent advent of daytime radiative cooling materials [Chu et al (2017)]. These materials are specifically engineered to use atmospheric transparency window (8-13 μm), called Atmospheric Window (AW), to passively dissipate heat from the Earth to outer space. The possibility of turning concrete into a daytime radiative cooling material is a big challenge with positive implications in building energy efficiency or combating the so-called urban heat island (UHI) effect [Kousis and Pisello (2020)].

Present work for ICCC 2023 aims to illustrate this novel application of cement-based materials, (i) reviewing some promising examples of the state of the art on rechargeable concrete batteries, and (ii) briefly presenting some ongoing research undertaken in my group in the field of cementitious thermal energy storage devices for CSPs and the emergence of radiative cooling concretes.

2. Cement-based batteries

The dream of cement-based batteries started after the work of Meng and Chung (2010). They used an OPC (Ordinary Portland Cement) cement paste with inclusions of Zn and MnO_2 particles, achieving energy densities of the order of 10^{-4} Wh/kg. While this energy density is much lower than that of a lithium battery (typically 10^2 Wh/kg), cementitious materials are usually associated with large structures, so the "deficit" in quality can be more than compensated for in quantity. For example, a typical battery (about 10 grams) houses 1 Wh. The same amount of energy could be stored in a cube of cement paste like the one used in Meng and Chung's work, but of 3 meters on each side.

Although the mentioned work demonstrated the feasibility of the concept, its implementation was not optimized. The proposed cementitious composite presented two main problems: on the one hand, the energy density was quite low, and on the other, the system was not rechargeable. Several works have been published in the state of the art afterwards, although two deserve a special mention, in my opinion:

Firstly, the work of Chen et al (2018), which proposed replacing the OPC cement matrix with the zeolitic matrix of alkali-activated cements. The structure of alkali-activated cement matrices is much more conducive to improving ionic conductivity since, in addition to having inherently more water, the zeolite cavities favor transport. It is not surprising that the obtained energy densities improved significantly, being of the order of 10^{-1} Wh/kg.

Secondly, the work of Zhang and Tang (2021), which improved the design of cementitious anodes and cathodes, allowing up to 6 cycles of charging and discharging and energy densities of about 10^{-2} Wh/kg. Essentially, this work proposed cementitious composites based on OPC cements, in which Zn inclusions (anode) and MnO_2 (cathode) are replaced by meshes of carbon fibers coated by electrodeposition by Fe and Ni, respectively.

3. Thermal energy storage

Differently to OPC concretes, those based on geopolymer and hybrid cements are known to withstand much higher temperatures [Qu et al (2020]. For that reason, Rajhoo et al (2022a) explored the heat capacity and the thermal diffusivity of a commercial Hybrid cement [Martauz et al. (2016)]. Motivated by the good behaviour of the geopolymer concrete at high temperature, we have recently undertaken a proof of concept study aimed at testing a TES module under realistic temperature charge and discharge cycles.

While the details can be found in Rahjoo et al. (2022b), Figure 1 (a) shows the details of the prototype employed. In essence, the design consisted of a concrete block with a steel pipe finished with two flanges. The TES module was flanged onto predetermined air heater tubes (see Figure 1 (b)). Later, four cycles of charges and discharges were conducted, with the inlet air temperature (T_{inlet}) varying between 200 ºC to 650 ºC. The temperatures measured in the three temperature probes of the TES module and the one of T_{inlet} can be seen in Figure 1 (c). As can be seen, the TES prototype withstood high running temperatures, always higher than 500 ºC. In fact, the prototype fitted well with the thermal requirements of the 2nd CSP generation, and has opened the door to improve the design by using FEM and AI methodologies (Rahjoo et al (2023)).

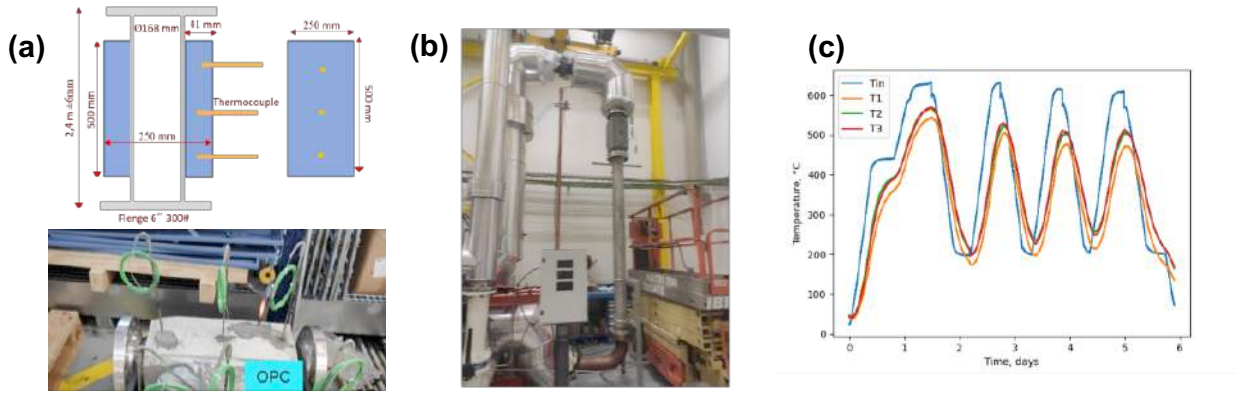


Figure 1. (a) Design of the TES prototype modules. (b) Experimental set-up within the air thermal loop. (c) Temperatures of the Geopolymer-based concrete TES module for T_{inlet} between 250ºC and 650ºC.

4. Radiative cooling concrete

Despite their widespread use, the potential for leveraging the innate radiative cooling properties of concrete has been largely overlooked. While many studies have sought to improve the albedo of concrete and pavements [e.g. Levinson and Akbari (2002], only few papers have examined the possibility of using cement-based materials for daytime radiative cooling [Lu et al. (2021), Cagnoni et al. (2022), Pérez-Escudero et al. (2023)]. The most significant difficulty lies in the complex structure of concrete, which comprises numerous constituents and a pore network of various sizes. To facilitate the analysis, we conducted a systematic study that examines the inherent response of relevant cementitious minerals and phases. For example, we recently measured and compared the reflectance of Tobermorite minerals with that of a typical white cement paste (refer to Figure 2). A cursory examination of Figure 2 reveals that the reflectance profile of white cement pastes resembles that of Tobermorite, but with two key differences. Firstly, the white cement paste exhibits a lower reflectance within the solar domain (0 µm-2.5 µm), and secondly, it has a greater emissivity (lower reflectance) within the AW. Both aspects can be attributed to pore and size effects [Dolado et al 2023], thus confirming the significant role of pore-size engineering in concurrently enhancing solar reflectance and emissivity in the AW [Pérez-Escudero et al. (2023)]

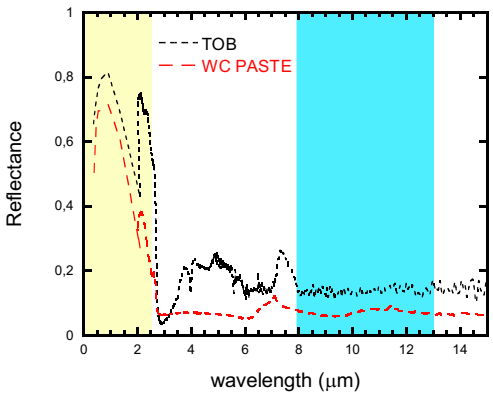


Figure 2. Reflectance of Tobermorite and a White Cement paste. Yellow and blue panels correspond to the solar domain and the AW.

5. Conclusions

The objective of the current study has been to demonstrate the innovative use of cement-based materials in energy storage and conversion. This includes highlighting successful examples such as rechargeable concrete batteries, cement-based thermal energy storage systems for concentrated solar plants, and the development of radiative cooling concrete. Overall, the use of concrete for energy storage and harvesting represents a significant shift in the way we think about this versatile material. It has the potential to play a critical role in the transition to a more sustainable and renewable energy future.

Acknowledgements

This undergoing research wouldn't be possible without the help and participation of the whole C2M group and the LTC Green Concrete members. Besides the acknowledgment is extended to my collaborators within the projects MIRACLE (GA 964450) and ECRETE (RTI2018-098554-B-I00)

References

Boquera L., Castro J. R., Fernandez A. G., Navarro A., Pisello A. L., Cabeza L. F. (2022) "Thermo-mechanical stability of concrete containing steel slag as aggregate after high temperature thermal cycles". Solar Energy 239: 59–73

Chen Y.H., Lin S. C., Wang J.A., Hsu S. Y, Ma C.M. (2018) "Preparation and Characterization of Geopolymer-Based Batteries with Electrochemical Impedance Spectroscopy (EIS) and Discharge Performance"Electrochem. Soc. 165 (13): 3029-3039

Chu, S., Cui, Y., Liu, N. (2017) "The path towards sustainable energy". Nature Mater 16: 16–22

Dolado J. S., Goracci G., Arrese-Igor S., Ayuela A., Torres A., Liberal I., Beruete M., Gaitero J. J., Cagnoni M., Cappelluti F. "Radiative cooling properties of Portlandite and Tobermorite: two cementitious minerals of great relevance in concrete science and technology", Under review

Hoivik, N.; Greiner, C.; Barragan, J.; Iniesta, A.C.; Skeie, G. (2019) "Long-term performance results of concrete-based modular thermal energy storage system". Energy Storage 74: 100735

Kousis I. and Pisello A. L. (2020) "For the mitigation of urban heat island and urban noise island: two simultaneous sides of urban discomfort" Environ. Res. Lett. 15 103004

Laing, D.; Steinmann, W.-D.; Tamme, R.; Richter, C. (2006) "Solid media thermal storage for parabolic trough power plants". Sol. Energy 80: 1283–1289

Levinson, R.; Akbari, H. (2002) "Effects of composition and exposure on the solar reflectance of Portland cement concrete". Cement and Concrete Research 32: 1679–1698

Lu G.; She W.; Tong X.; Zuo W.; Zhang Y. (2021) "Radiative cooling potential of cementitious composites: Physical and chemical origins". Cement and Concrete Composites 119: 104004 (11)

Martauz, P.; Janotka, I.; Strigác, J.; Bacuvcík, (2016) M. "Fundamental properties of industrial hybrid cement: Utilization in ready-mixed concretes and shrinkage-reducing applications". Materiales de Construcción 66: 322

Meng Q and Chung D.D.L (2010) "Battery in the form of a cement-matrix composite"; Cement & Concrete Composites 32: 829–839

Pérez-Escudero J. M., Torres-García A. E., Lezaun C., Caggiano A., Ignacio Peralta, Dolado J. S., Beruete M., Liberal I. (2023) "Suppressed-scattering spectral windows for radiative cooling applications" Optics Express 31 (4): 6314-6326

Qu B., Martín A., Pastor J. Y., Palomo A., Fernández Jiménez A. (2020) "Microstructural characterisation of hybrid cement after exposure to high temperatures". Construction and Building Materials 262: 120843

Rahjoo, M.; Goracci, G.; Martauz, P.; Rojas, E.; Dolado, J.S. (2022) "Geopolymer Concrete Performance Study for High-Temperature Thermal Energy Storage (TES) Applications". Sustainability 14: 1937

Rahjoo, M.; Goracci, G.; Gaitero, J.J.; Martauz, P.; Rojas, E.; Dolado, J.S. (2022) Thermal Energy Storage (TES) Prototype Based on Geopolymer Concrete for High-Temperature Applications. Materials 15: 7086

Rahjoo, M.; Goracci, G.; Gaitero, J.J.; Martauz, P.; Rojas, E.; Dolado, J.S. (2023) Under review

Zhang E. Q. and Tang L. (2021) "Rechargeable concrete battery" Buildings 2021, 11, 103

The 16th International Congress on the Chemistry of Cement 2023 (ICCC2023)
"Further Reduction of CO_2 -Emissions and Circularity in the Cement and Concrete Industry"
September 18–22, 2023, Bangkok, Thailand

Use of biomass ash in the fabrication of Self-healing engineered cementitious composites (ECC)

E. Asensio[1, *], F. Fernández[2], G. Pérez[3] and A. Guerrero[4]

[1]*Eduardo Torroja Institute for Construction Sciences, 28033, Madrid, Spain*
Email: eloyadl@ietcc.csic.es
[2]*Eduardo Torroja Institute for Construction Sciences, 28033, Madrid, Spain*
Email: fdezluquefernando@gmail.com
[3]*Eduardo Torroja Institute for Construction Sciences, 28033, Madrid, Spain*
Email: gperezaq@ietcc.csic.es
[4]*Eduardo Torroja Institute for Construction Sciences, 28033, Madrid, Spain*
Email: aguerrero@ietcc.csic.es

ABSTRACT

Construction sector is in continuous evolution, an evidence, is the design of cement-based matrices with self-healing properties. Concrete structures in service, are often subjected to drying shrinkage, temperature stress, humidity changes, static and dynamic loads, and other adverse external factors, resulting in different degrees of damage, manifested as cracks or micro-cracks in concrete. These problems can be reduced or partially solved using engineered cementitious composites (ECC). These new materials based on the incorporation of high content of fly ash (FA) in the formulation belong to a family of high performance fiber reinforced composites that offer higher ductility compared to normal concretes and can carry out the self-healing of the material with autogenous mechanisms.

Nowadays, in parts of the world, thermal power plants are shutting down what result in scarcity of fly ash that could be used in these formulations. Due to this situation, the current research presents the study of the viability of the total or partial substitution of the fly ashes by ashes from biomass burning (BA).

Four formulations of ECC were prepared increasing BA content until total replacement of the FA. Mortars were mixed and cured for 28 days at 98 ± 2% RH and 20 ± 2ºC. After curing time, mechanical behaviour (compressive and flexural strength) and self-healing capacity of the new cement based materials (by non-destructive methods: capillary water absorption test and visual characterization by optical microscopy) were measured.

Results show a good behaviour of these new matrices based on BA what allows their use in ECC and the new materials agree with new environmental policies and Circular Economy.

KEYWORDS: *ECC, Fly Ash, Biomass Ash, Self-healing behavior, Circular Economy*

1. Introduction

Construction sector is in continuous evolution. Engineered Cementitious Composites, ECCs, are a good example of that. These materials are a high performance fiber reinforced cementitious composites. In its formulation, they include PVA fibers, and a high percentage of fly ash, components that give the material the ability of self-healing [1–3]. On one hand, this kind of materials could solve different problems in concrete structures derived from the appearance of micro-cracks. On the other hand, thermal power plants are shutting down what result in scarcity of fly ash that could be used in these formulations. Due to this

situation, it is important the study of different options to the use of FA. One of these alternatives is the utilization of ashes from biomass burning (BA).
The current research presents the study of the viability of the total substitution of the FA by BA.

2. Materials and Methodology

2.1 Materials

The main materials used during this study are: CEM I 42.5R type Portland cement (OPC) [4] supplied from Portland Valderrivas, class F fly ash (FA) supplied by SOTO DE RIBERA (Spanish thermal power plant), biomass fly ash (BA) (from forest pruning) provided by a private entity (with a similar particle size in comparison to FA) and commercial sand with a silica content of over 98% and a particle size of under 1 mm. In addition during the research were used Poly Vinyl Alcohol (PVA) fibers and a superplasticizer "ViscoCrete 80" from SIKA.

2.2 Methodology

Four formulations of ECC were designed and are listed in Table 1. The reference formulation (R) is based on the composition defined in the literature as the optimum for ECC with enhanced self-healing behaviour [1] where ratio between ash and cement is 1.20. The other three compositions increase the percentage of BA as substitution of FA until a total replacement (sample C).

Table 1. Composition (% weight) of formulations designed

	CEM	FA	BA	Sand	PVA	SP
R	32.50	39.00	-	26.00	1.38	1.12
A	32.50	27.30	11.70	26.00	1.38	1.12
B	32.50	11.70	27.30	26.00	1.38	1.12
C	32.50	-	39.00	26.00	1.38	1.12

Solid materials were blended in order to reach a homogenous dry mix mortar, after that, the samples were mixed according to the European Standard, EN 196:1 [5] (superplasticizer was included in the mixing water) and casted into the prismatic molds (4x4x16 cm^3), demolded after 24 h and curing (T= 20 ± 2ºC and RH= 98 ± 2%) up to 118 days.

Research is based on two different batches of samples:

- Uncracked: specimens were mechanically tested after 28, 56 and 118 days of curing.
- Cracked: a crack was generated in specimens after 28d of curing (applying 65% of the maximum load of flexural strength obtained from uncracked specimens tested at 28d). After the generation of the crack, compressive strength was tested for 28 and 90 healing days (28+28d and 28+90d).

The results for R and C formulations will be shown in the following sections of this paper to compare the reference ECC material with a sample with the maximum replacement of FA by BA.

Mechanical behaviour (compressive strength), and non-destructive methods as capillary water absorption test and visual characterization by optical microscopy were measured to evaluate the self-healing capacity.

3. Results and discussion

Figure 1 shows mechanical behavior (compressive strength) for formulation R (100% FA) and formulation C (100% BA) at different hydration curing periods (56 and 118 days). Results compare specimens uncracked (56 and 118d) with cracked ones (28+28 and 28+90d).

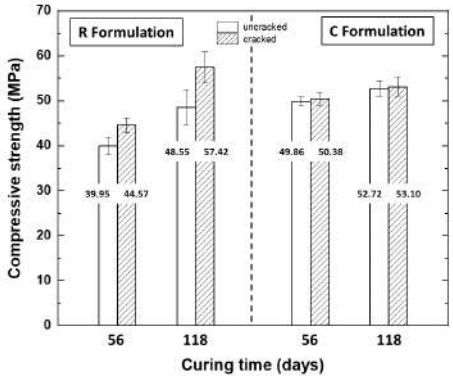


Figure 1. Compressive strength of specimens of formulation R and C

When FA is the base of the formulation is observed that compressive strength increases with the curing time. Cracked specimens reach higher strength than uncracked specimens what means that this kind of materials are able to heal the cracks previously produced and improve the mechanical behaviour.
The same performance is observed in formulations where FA is substituted by BA.
Results showed in Figure 1 indicates that BA reacts faster than FA, as a result, higher compressive strength at 56 days in C than in R. On one hand, although FA reacts more slowly, is able to continue reacting and improve the compressive strength at 118 in comparison to 56 days of curing time. On the other hand, compressive strength in formulation based on BA keeps almost constant.

One important point for the study of self-healing capacity of the ECC materials is the water absorption due to this test can give an idea about the healing of the cracks. During the present research work sorptivity test has been carried out according to the ASTM C1585-13 [6].
Figure 2 shows the variation of the absorption, I (mm) with the squared root of time ($s^{1/2}$) for formulation R (Figure 2a) and C (Figure 2b) when specimens were cracked at 28 days and have healing periods of 28 and 90 days.

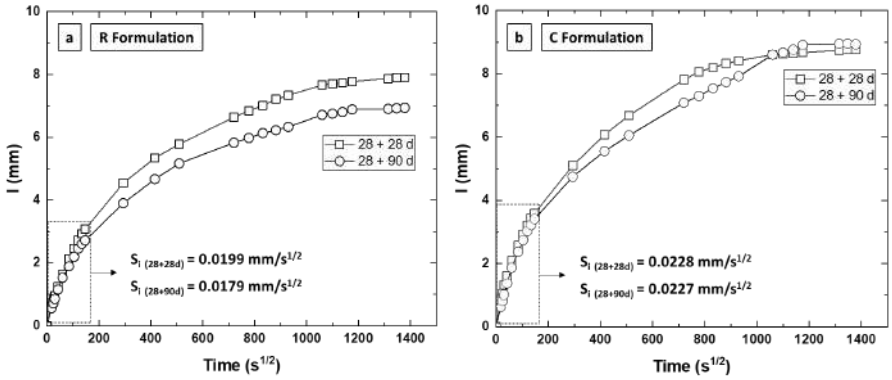


Figure 2. Sorptivity results for formulation R and C

In Figure 2, is also shown the initial rate (S_i) of water absorption (mm/$s^{1/2}$) that is defined by the slope of the linear regression analysis of the initial data (points from 1 min to 6 hours).
Results show that these ECC materials are able to seal cracks previously generated. After 90 days of healing, the water absorption decrease in comparison to the water absorption observed for healing periods of only 28 days.
Higher rates of water absorption are also observed for 28+28d in comparison to 28+90d of healing.
A small difference in initial rate (0.0228 mm/$s^{1/2}$ *vs* 0.0227 mm/$s^{1/2}$) is observed when the formulation incorporates 100% BA, result that is related to the small differences in mechanical behaviour for curing times of 28+28d and 28+90d (Figure 1). Mechanical behaviour and water absorption are directly related to porous structure of cementitious matrices.

As an example, Figure 3 shows optical microscopy images of the specimens.

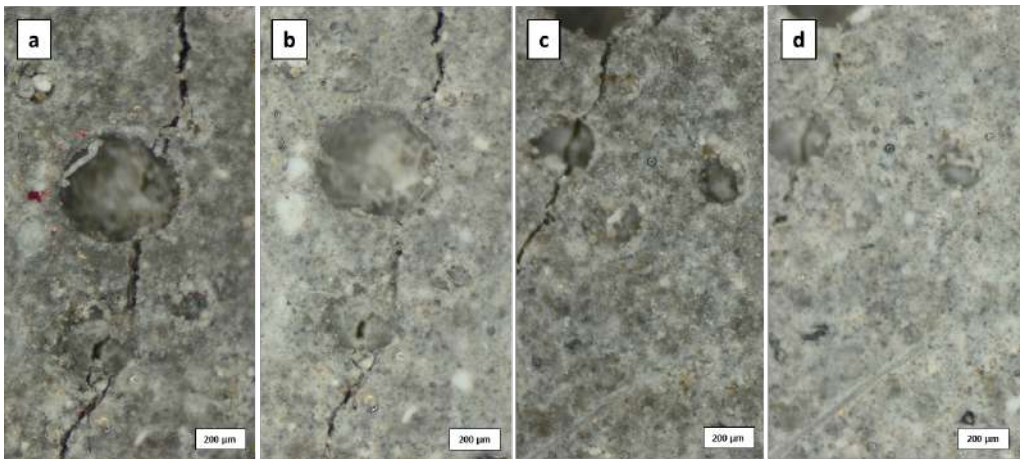


Figure 3. Optical microscopy images. a) R after the generation the crack at 28d, b) R after 28d of healing, c) C after the generation the crack at 28d and d) C after 28d of healing

Images show how after 28 days of healing, ECC materials are able to seal cracks. The substitution of 100% of FA by BA keep the self-healing capacity in the materials. These results are in consonance with the mechanical behaviour and water absorption.

3. Conclusions

- Sealing the cracks will give rise to denser matrices and therefore recover mechanical behavior and reduce water absorption.
- It is possible the total replacement of the FA by BA keeping the self-healing properties of the material.

Acknowledgements

Authors gratefully acknowledge the financial support of the PID2020-113223RB-100, funded by the Spanish Government (Ministerio de Ciencias e Innovación) to the Instituto de Ciencias de la Construcción "Eduardo Torroja" of the Spanish Research Council – IETcc CSIC.

References

[1] V. Li, Yang, Self-Healing in Concrete Materials, Self-Healing Materials: An Alternative Aproach to 20 Centuries of Materials Science. (2007) 161–193.
[2] J.L. García Calvo, G. Pérez, P. Carballosa, E. Erkizia, J.J. Gaitero, A. Guerrero, Development of ultra-high performance concretes with self-healing micro/nano-additions, Construction and Building Materials. 138 (2017) 306–315. https://doi.org/10.1016/j.conbuildmat.2017.02.015.
[3] Fernandez, F., Jarabo, R., Asensio, E., Guerrero, A., Study of Self-Healing at large ages for a 3D printable ECC Material, in: 2022.
[4] CEN-CENELEC, EN 197-1. Cement Part 1: Composition, specifications and conformity criteria for common cements, Brussels, Belgium, 2011.
[5] CEN-CENELEC, EN 196-1. Method of testing cement. Part 1: Determination of strength, Brussels, Belgium, 2018.
[6] ASTM International, ASTM C1585-13, Standard test methods for measurament of Rate of Absorption of Water by Hydraulic- Cement Concretes, (2020).

The 16th International Congress on the Chemistry of Cement 2023 (ICCC2023)
"Further Reduction of CO_2 -Emissions and Circularity in the Cement and Concrete Industry"
September 18–22, 2023, Bangkok, Thailand

Assessment of early-age drying induced microstructural changes in 3D printed cement mortar

A.V. Rahul[1*], M.K. Mohan[2], K. Van Tittelboom[3], and G. De Schutter[4]

[1]*Department of Civil and Environmental Engineering, Indian Institute of Technology Tirupati, Tirupati, India*
Email: rahulav@iittp.ac.in
[2]*Magnel-Vandepitte Laboratory, Department of Structural Engineering and Building Materials, Ghent University, Ghent, Belgium*
Email: Manu.KurungodMohan@ugent.be
[3]*Magnel-Vandepitte Laboratory, Department of Structural Engineering and Building Materials, Ghent University, Ghent, Belgium*
Email: Kim.VanTittelboom@UGent.be
[4]*Magnel-Vandepitte Laboratory, Department of Structural Engineering and Building Materials, Ghent University, Ghent, Belgium*
Email: Geert.DeSchutter@ugent.be

ABSTRACT

With the use of formwork-free digital construction techniques, the concrete is exposed to drying from a very early-age. In the current study, we assess the early-age drying induced microstructural changes in a Portland cement-slag based 3D printable mortar. Scanning electron microscope (SEM) analysis was performed on two cylindrical samples, one which was protected against drying and another which was continuously exposed to drying from the onset of casting until 24 hours. Following this, detailed image analysis was performed using MATLAB to threshold and quantify the porosity as well as the hydrated and unhydrated particles in the SEM images. Although the amount of unhydrated particles was found to be lower in the region close to the aggregates due to the "wall effect", the amount and distribution of unhydrated particles were similar for both samples protected against or exposed to drying. On the other hand, the amount of hydrated particles and the porosity were found to be significantly influenced by drying. Samples subjected to drying showed a much lower amount of hydrated particles and an increased porosity both close to and away from the aggregate surface. This study points out that even though early-age drying may not always result in structural problems such as cracking, it may adversely influence cement hydration leading to increased porosity in both the bulk region and the interfacial transition zone with the aggregate surfaces.

KEYWORDS: *early-age drying, scanning electron microscope, interfacial transition zone, image analysis, concrete 3D printing.*

1. Introduction

3D concrete printing is one of the latest developments in the construction industry. It involves fabricating construction components based on a computer model by the layerwise extrusion of a special concrete that can retain its shape after extrusion without formwork support. Although the elimination of formwork provides many advantages, such as reduced cost, time, and labour, and the possibility for structural optimization, one adverse effect associated with it is the early-exposure of fresh concrete to drying (Lim et al (2012), Mohan et al (2021a)).

Although there have been studies that have examined the effect of drying on the shrinkage behaviour of 3D printable systems (Moelich et al (2020), Rahul et al (2022)), very few studies could be found on how drying may influence the microstructure development of cementitious systems. Recently, Mohan et al (2023), using mercury intrusion porosimetry, indicated that 3D printed mixtures, when exposed to early-

age drying can have a larger size and higher volume of pores as compared to samples which are protected from early-age drying. In this work, we assess the effect of drying induced microstructural changes in 3D printable cementitious systems by using backscattering electron (BSE) images obtained with a scanning electron microscope (SEM) and a subsequent image analysis performed using MATLAB.

2. Materials and methods

The binder used in the study consisted of Portland cement (Blaine area of 408 m^2/kg and specific gravity of 3.15) and ground granulated blast furnace slag (Blaine area of 428 m^2/kg and specific gravity of 2.80). The aggregates used consisted of river sand with a maximum particle size of 2 mm and specific gravity of 2.60. The chemical admixtures used consisted of a polycarboxylic ether-based superplasticizer (SP) and a cellulose ether-based viscosity modifying agent (VMA). The design of the 3D printable mixture was based on a previous study by the same authors (Mohan et al (2021b)) and is indicated in Table 1.

Table 1: Mixture proportion of the 3D printable concrete used in the study

Material	Cement	Slag	Sand	Water	SP	VMA
Quantity (Kg/m^3)	378	378	1287	265	6.40	0.75

The concrete specimen was cast in a cylindrical mould (50 mm diameter and 10 mm height) and immediately demoulded after casting for exposure to early-age drying. Its top surface was covered with a thin plastic film with the same diameter of 50 mm (see Fig. 1). The inside of the plastic film was coated with a thin layer of paraffin wax so that film closely adhered to the specimen. The top surface was kept completely covered, ensuring a condition of unidirectional drying (drying only along the circumferential direction). Drying was allowed to occur for 24 hours in a temperature controlled room (temperature of 20 $^{\circ}$C and relative humidity of 60 %). After that, a sample of size 10 mm was cut out from the exposed surface (see Fig. 1) for SEM studies. A second sample was also prepared that was protected against drying. This sample was prepared by not immediately demoulding the cylindrical specimen. Demoulding was done only after 24 hours while cutting out the sample for the SEM analysis.

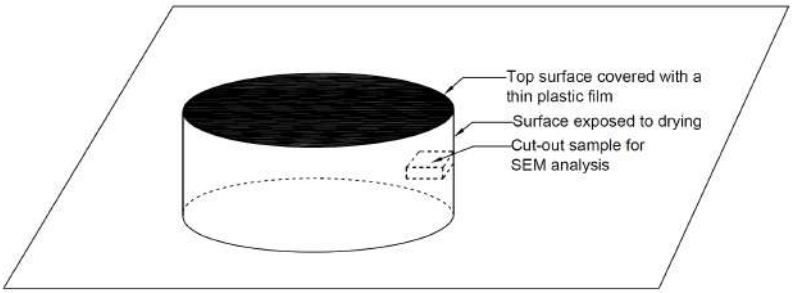


Figure 1: Preparation of the sample subjected to early-age drying for SEM analysis

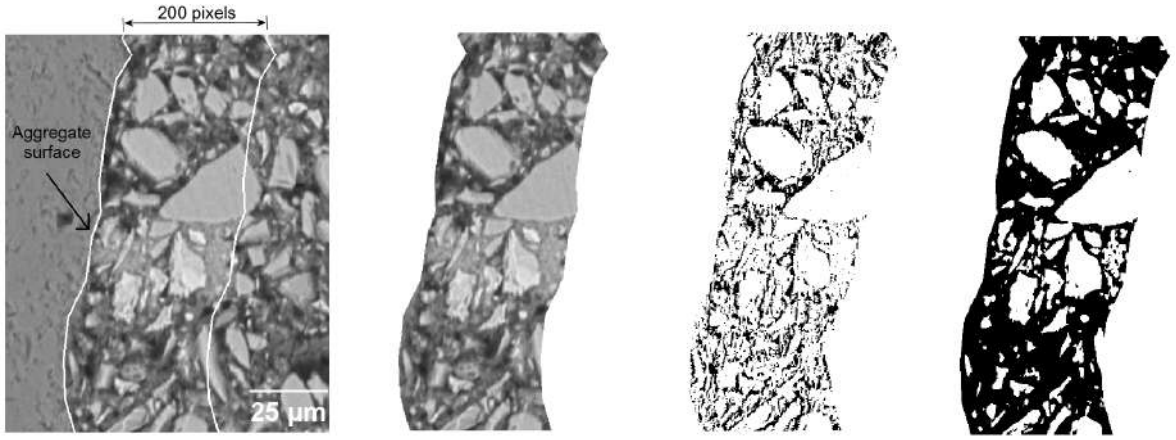
Hydration stoppage was performed on all samples at the age of 24 hours by the solvent exchange method. The SEM experiments were carried out using JEOL JSM-7400F. For each sample, around 20 BSE images were obtained and average values were taken to calculate the amount of porosity, hydrated and unhydrated cementitious particles.

2. Results and discussions

2.1 Image analysis

Fig. 2(a) shows a BSE-SEM image of the region close to the aggregate surface for the sample protected against drying. A 200-pixels wide region adjacent to the aggregate surface was selected as the region of interest (ROI), as shown in Fig. 2(b). The ROI consists of primarily three phases: (i) pores, (ii) hydrated cementitious particles, and (iii) unhydrated cementitious particles. To separate out the pores, ROI was first binarized with the pores assigned an intensity value of 0 (black colour) and all the solid phases assigned the intensity value of 1 (white colour), as shown in Fig. 2(c). The binarization was performed in

MATLAB based on Otsu's method (Otsu (1979)) using locally adaptive thresholding. Following this, the unhydrated particles were identified and the corresponding binary image is shown in Fig. 2(d). The threshold was manually done based on the image histogram of the ROI.



(a) (b) (c) (d)

Figure 2: SEM image of sample protected against drying- (a) HCP close to the aggregate surface, (b) ROI for image analysis, (c) pores in the ROI (black colour), and (d) unhydrated cementitious particles in the ROI (white colour)

2.1 Effect of drying on microstructure

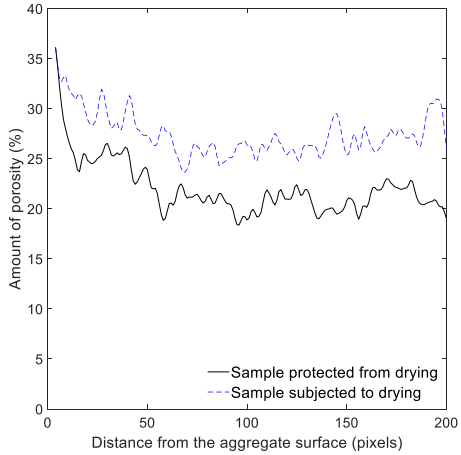
Fig. 3(a) shows the variation in porosity as the distance from the aggregate surface changes. Very close to the aggregate surface (called the "aureole"), the porosity is found to be much higher as compared to the bulk region. Similar observations have also been reported by other researchers and are attributed to the fewer amounts of unhydrated particles close to the aggregate surface arising from the wall effect (Scrivener et al (2004)). This can be seen in the distribution of unhydrated particles shown in Fig. 3(b). The more porous packing of anhydrous cement grains close to the aggregate surface favours the through solution deposition of hydration products (calcium hydroxide and C-S-H gel) in this region (Diamond and Huang (2001)), as depicted in Fig. 3(c).

Fig. 3 also shows the variation in porosity for samples exposed to and not exposed to early-age drying. Interesting, the amount of porosity both very close to the aggregate surface as well away from the aggregate surface (bulk region) is higher (by around 25 %) in the case of dried samples. This is due to the fewer amounts of hydrated cementitious particles formed in the case of dried samples (see Fig. 3(b)). Interestingly, the distribution of unhydrated particles is found to be similar irrespective whether the samples are exposed to drying or not (Fig. 3(c)). This indicates that a similar particle packing of anhydrous particles is found to occur in both cases. This indicates that the external water loss occurring due to drying can hinder the through solution deposition of hydration, resulting in a less densified ITZ and higher porosity. More studies evaluating the effect of early-age drying on hydration degree (both short-term and long-term), the influence of mineral admixture (that requires prolonged water availability for its reactivity), and the effect of various factors like relative humidity and temperature that influence drying needs to be examined through future studies.

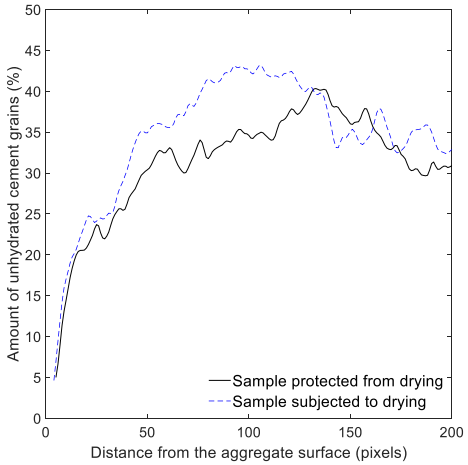
3. Conclusions

This paper examines the effect of early-age drying on the microstructure of 3D printable cementitious systems. Samples exposed and protected from drying were examined using a scanning electron microscope, and the images were subsequently examined based on a detailed image analysis procedure. For both sample types, a higher porosity is observed in the region very close to the aggregate surface. This can be attributed to the wall effect resulting in a lower amount of anhydrous particles close to the aggregate surface. Even though the sample subjected to drying and that protected from drying was found to have the same distribution of anhydrous particles, the former was found to have a significantly higher porosity in the interfacial transition zone and also in the bulk regions away from the aggregate surface.

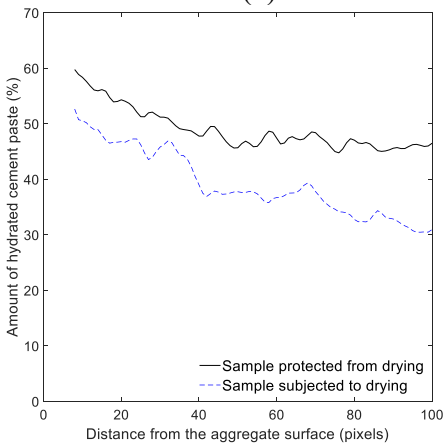
This can be attributed to the fewer amounts of hydrates formed by the through solution mechanism as a result of the external water loss occurring due to early-age drying. More studies need to be conducted to evaluate the long-term effect of early-age drying on the microstructure and durability of 3D printable cementitious systems.



(a) Variation in the amount of porosity



(b) Variation in the amount of unhydrated particles



(c) Variation in the amount of hydrated particles

Figure 3: Effect of drying on microstructure

References

Lim, S. Buswell, R.A. Le, T.T. Austin, S.A. Gibb, A.G. and Thorpe, T. (2012) "Developments in construction-scale additive manufacturing processes". *Automation in construction*, 21: 262-268

Moelich, G.M. Kruger, J. and Combrinck, R. (2020) "Plastic shrinkage cracking in 3D printed concrete", *Composites Part B: Engineering*, 200:108313

Mohan, M.K. Rahul, A.V. De Schutter, G. and Van Tittelboom, K. (2021a) "Extrusion-based concrete 3D printing from a material perspective: A state-of-the-art review" *Cement and Concrete Composites*, 115:103855

Mohan, M.K. Rahul, A.V. Van Tittelboom, K. and De Schutter, G. (2021b) "Rheological and pumping behaviour of 3D printable cementitious materials with varying aggregate content" *Cement and Concrete Research*, 139:106258

Mohan, M.K. Rahul, A.V. Villagran-Zaccardi, Y. De Schutter, G. and Van Tittelboom, K. (2023) "A rheometric approach to assess early age drying of cement-based materials" *Cement and Concrete research (under review)*

Rahul, A.V. Mohan, M.K.. De Schutter, G. and Van Tittelboom, K. (2022) "3D printable concrete with natural and recycled coarse aggregates: Rheological, mechanical and shrinkage behavior" *Cement and Concrete Composites*, 125: 104311

Otsu, N. (1979) "A threshold selection method from gray-level histograms" *IEEE transactions on systems, man, and cybernetics*", 9(1): 62-66

Scrivener, K.L. Crumbie, A.K. and Laugesen, P. (2004) "The interfacial transition zone (ITZ) between cement paste and aggregate in concrete", *Interface science*, 12: 411-421

Diamond, S. and Huang, J. (2001) "The ITZ in concrete–a different view based on image analysis and SEM observations", *Cement and concrete composites*, 23(2-3):179-188

The 16th International Congress on the Chemistry of Cement 2023 (ICCC2023)
"Further Reduction of CO_2 -Emissions and Circularity in the Cement and Concrete Industry"
September 18–22, 2023, Bangkok, Thailand

3D Printing Mortar and Concrete: Advancement and Application of Laboratory Test Protocol to Evaluate Properties physicochemical and mechanical.

Alexandre Cordeiro dos Santos[1*], Fabiano Ferreira Chotoli[2], Valdecir Angelo Quarcioni[3],

[1 1, 2, 3] *Technological Research Institute of the State of São Paulo - Housing and Buildings / Laboratory of Materials for Construction Products, São Paulo, Brazil*
[1] ** Email: alexcord@ipt.br*
[2] *Email: fchotoli@ipt.br*
[3] *Email: quarciva@ipt.br*

ABSTRACT

3D Printing (3DP) has garnered significant attention in the past decade and is still regarded as a disruptive Additive Manufacturing technology, often associated with the concept of Industry 4.0. 3DP involves the manufacturing process of depositing successive layers of a specific material until it takes the shape of a 3D product. The most groundbreaking aspects of this manufacturing process pertain to the properties of the mixture used for printing, which must possess certain characteristics. For instance, it should flow smoothly from the inside to the outside of the print head and solidify almost immediately after leaving the head, allowing it to receive another layer of material without significant deformation. This technology has started to be explored and gain commercial visibility in the construction industry, particularly in the utilization of mortar and concrete. Researchers in the field are investigating various mortar and concrete mixtures to create new 3D printed products with different mechanical properties and specific dimensions, by leveraging the physicochemical properties of the raw materials suitable for 3D printing. To gain expertise in applying mortars and concretes for 3D printing, it is recommended to develop protocols that involve routines for using mixtures in their fresh state and determining the supportive properties of the cementitious material. This study presents data on the physical and mechanical properties of cement mortar with partial clay additions, which have the potential for use in 3D printing (3DP). The aim is to comprehend the phenomena involved in the consolidation of paste and mortar mixtures for 3DP. The inclusion of gray clay in this study significantly enhanced the 3D printing process when the clay was mixed in a 5% ratio with the mixture. Finally, the squeeze-flow test method enabled the establishment of a minimum extrudable profile for the cementitious material, considering the 3D printer utilized.

KEYWORDS: *Additive manufacturing, mortar, clay, 3D printing, squeeze-flow.*

1. Introduction

Research on the use of cementitious materials (mortar or concrete) in Additive Manufacturing, commonly known as 3D Printing, was initially introduced by Pegna (1997). Subsequently, Khoshnevis implemented this technology on a larger scale, giving rise to the Contour Crafting (CC) method for manufacturing industrial molds, which was later adapted for the construction industry (Khoshnevis, 2004, and 2006). Additive Manufacturing involves depositing successive layers of a specific material under computer control to create a 3D product. It is a technology associated with the concept of Industry 4.0 and has garnered significant attention in the past decade as a disruptive technology for the future of manufacturing. In the construction industry, this technology is referred to as 3D Concrete Printing (3DCP) or Digital Construction (DC) and has the potential to address various challenges in conventional concrete construction. It can reduce the need for formwork, optimize construction time, lower costs, minimize material waste, and facilitate the construction of complex and customized designs (NERELLA et al., 2019).
Among the various 3DCP methods, the extrusion method is the most widely used and implemented. In this method, the material is pumped to the print head, where it is extruded through a nozzle to create the desired

object by depositing successive layers (JAYATHILAKAGE et al., 2022). It is important to note that, for this process to be successful, in addition to relevant parameters such as 3D printer configuration, nozzle geometry, and pump, the extrudable material must possess favorable rheological properties, flow characteristics, and workability. This means that the material should be easily transportable in the pumping system with minimal energy consumption, pass through the nozzle without blockages, segregation, or phase separation, and solidify almost immediately after extrusion to receive another layer without significant deformations (NERELLA et al., 2019; PERROT et al., 2012).

While Additive Manufacturing has gained commercial visibility in the construction industry using cementitious mortars and concretes, there are still numerous challenges to overcome for its widespread use in civil construction, particularly concerning the use of these materials (Bucli et al., 2018; Bos et al., 2022). Several researchers in the field are exploring mortar and concrete mixtures to develop new 3D printed products with distinct mechanical properties and specific dimensions, as evident from the literature (Buswell et al., 2018). To gain expertise in utilizing 3D Printing with cementitious materials, it is recommended to develop protocols that include routines for determining the properties of the fresh and hardened states of the cementitious material.

In this context, the present study provides data on the physical and mechanical properties of cementitious mortar (Portland limestone-cement) with partial clay additions, aiming to comprehend the phenomena involved in consolidating mortar mixtures for 3D Printing. Clay was chosen as an additive due to its good plasticity and extrudability, which have the potential to enhance 3D printing of mortars. The Squeeze-flow rheological method was employed to determine the ideal mixture with the minimum clay content for 3D printing.

2. Materials and Experimental Work

2.1 Materials

Portland limestone-cement (CEM II/A-L), fine quartz sand, fine and very plastic gray Ball Clay from the region of São Simão (State of São Paulo/Brazil), superplasticizer additive based on polycarboxylates and viscosity modifying additive were used to produce mortar mixes without clay (RM, Reference Mix) and with clay (Mix 1 to Mix 5).

2.2 3D printing Apparatus

- Mechanical mixer with a stainless steel vat with a capacity of 5 liters and a metal paddle that rotates around itself (140 ± 5 RPM and 285 ± 10 RPM) and in planetary motion (62 ± 5 RPM and 125 ±10 RPM) around the vat's axis, both in opposite directions.
- "3D Potter XLS-2 Scara" clay extruder printer with 4 liters capacity and 5 mm diameter nozzle.

2.3 Testing Protocol and Methods

Knowing that clay naturally presents good extrusion properties, mortars from cement, fine sand and admixtures (RM, Reference Mix) were produced with gradual incorporation of clay until obtaining an extrudable cementitious mixture. After preparing the mortars in the proportions of the materials according to Table 1, the test method called Squeeze-flow of the Brazilian Standard NBR 15839 (ABNT, 2018) was applied to determine a typical profile of a mortar with good extrudability and buildability, considering the 3D printer used in this work. Subsequently, specimens were produced by 3D printing for the physical and mechanical tests in the hardened state.

The Squeeze-flow test consists in compressing a cylindrical-shaped clay sample between two parallel plates to evaluate its rheological behavior. In this work, the cylindrical samples were made with a diameter of 100 mm and a thickness of 10 mm. The piston was positioned on top of the mortar and the test was performed by applying a velocity of 0.1 mm/s displacement.

Table 1: Proportion of materials used in mortars for use in the 3D Printer

Mix design	Constituents and amounts used in mixtures in grams (g)					
	Cement	Sand	Clay	Viscosity Modifying Agent	Superplasticizer	Water
RM	55.0	438.0	0.0	0.06	1.10	123.3
Mix 1	55.0	416.1	9.3	0.06	1.10	120.1
Mix 2	55.0	394.2	18.6	0.06	1.10	117.0
Mix 3	55.0	372.3	27.9	0.06	1.10	113.8
Mix 4	55.0	328.5	46.5	0.06	1.10	107.5
Mix 5	55.0	219.0	93.0	0.06	1.10	91.8

2.4 Tests in the hardened state

The mortar characterization tests after 3D print (3DP) are shown in Table 2. Adaptations have been made to allow the use of these specimens forms.

Table 2: Mixing methods and characterization tests of mortars in the hardened state

Test methods	Standards
Flexural and compressive strength	EN ISO 196-1 (BSI, 2016) [(a)]
Dry bulk density	EN ISO 1015-10 (BSI, 1999) [(a)]
Water absorption coefficient	EN ISO 15148 (BSI, 2016)

(a): general guidelines

3 Results and Discussion

3.1 Squeeze-flow rheology test to determine the extrusion capacity

In the Squeeze-flow rheology test, it was observed that only Mix 5 exhibited a rheological profile suitable for the 3D printer used in this study. This indicates that mixtures with extrusion forces ranging from 200 N to 700 N have the potential for 3D printing. Figure 1 presents the results of the Squeeze-flow test, which are further detailed in Figure 2. Furthermore, Figures 3 to 5 demonstrate the progression of extrusion with the minimum clay additions in 3D printing. Notably, there was an improvement in the extrusion conditions starting from Mix 3 onwards. However, it was only the minimum clay content of Mix 5 that enabled the successful 3D printing of the specimens.

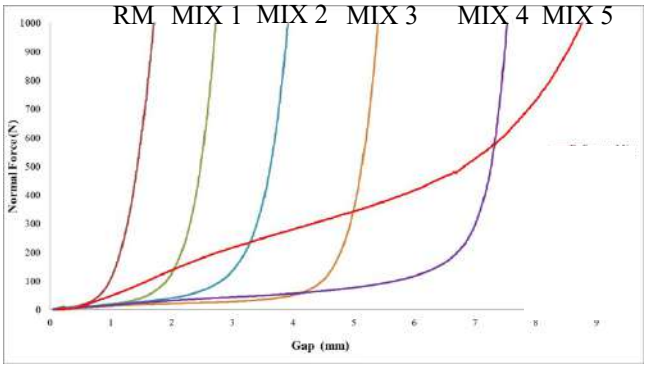


Figure 1: Squeeze-flow results with a speed of 0.1 mm/s



Figure 2: Squeeze-flow test detail



Figure 3: 3d printing with Mix 3



Figure 4: 3d printing with Mix 4



Figure 5: 3d printing with Mix 5

3.2 Tests in the hardened state

The results and corresponding determination methods for the hardened state of the 3DP specimens are outlined in Table 3. These results align with the literature regarding mortars used for masonry construction. Nonetheless, in order to enhance strength for 3D printing purposes, an increase in cement consumption is

required. Figures 6 to 8 illustrate the details of the test specimens obtained through 3D printing, as well details of the flexural and compressive strength tests.

Table 3: Results of tests in the hardened state from mix 5

Test Methods	Units	Results
Dry bulk density of hardened	kg/m³	1662.0
Flexural strength	MPa	2.9
Compression strength		10.7
Water absorption coefficient	kg/(m².h^{0,5})	W_{4h} =5.6



Figure 6: 3DP specimens (Mix 5)



Figure 7: Flexural strength test



Figure 8: Compression strength test

4. Conclusions

The results led to the following findings:

- São Simão clay enabled the use of the Reference Mix (RM) in the 3D printer, like Mix 5.
- The mix protocol and test methods, particularly the Squeeze-flow, determined the cementitious mixture with good extrusion capacity and buildability for the 3D printer. This method also defined the minimum extrudable profile with extrusion loads between 200 N and 700 N.

References

ASSOCIAÇÃO BRASILEIRA DE NORMAS TÉCNICAS. **NBR 13279**: Mortars applied on walls and ceilings - Determination of the flexural and the compressive strength in the hardened stage. Rio de Janeiro: ABNT, 2018 (Test method similar to EN ISO 196-1).

_____**NBR 13280**: Determination of the specific gravity in the hardened stage. Rio de Janeiro: ABNT, 2018.

_____**NBR 15839**: Rheological evaluation by squeeze-flow. Rio de Janeiro: ABNT, 2018.

_____**NBR 16541**: Preparation of mortar mixture for tests. Rio de Janeiro: ABNT, 2016.

Bos, F.P.; Menna, C.; Pradena, M.; Kreiger, E.; Silva, W.R. Leal da; Rehman, A.u.; Weger, D.; Wolfs, R.J.M.; Zhang, Y.; Ferrara, L. The realities of additively manufactured concrete structures in practice. Cement and Concrete Research, [S.L.], v. 156, p. 106746, jun. 2022. Elsevier BV. http://dx.doi.org/10.1016/j.cemconres.2022.106746.

Buchli, Jonas; Giftthaler, Markus; Kumar, Nitish; Lussi, Manuel; Sandy, Timothy; Dörfler, Kathrin; Hack, Norman. Digital in situ fabrication - Challenges and opportunities for robotic in situ fabrication in architecture, construction, and beyond. Cement and Concrete Research, [S.L.], v. 112, p. 66-75, out. 2018. Elsevier BV. http://dx.doi.org/10.1016/j.cemconres.2018.05.013

Buswell, R.A.; Silva, W.R. Leal de; Jones, S.Z.; Dirrenberger, J. 3D printing using concrete extrusion: a roadmap for research. Cement and Concrete Research, [S.L.], v. 112, p. 37-49, out. 2018. Elsevier BV. http://dx.doi.org/10.1016/j.cemconres.2018.05.006.

Jayathilakage, R.; Rajeev, P.; Sanjayan, J. Rheometry for Concrete 3D Printing: A Review and an Experimental Comparison. Buildings 2022, 12, 1190. https://doi.org/10.3390/buildings12081190

Khoshnevis, B. Automated construction by contour crafting—related robotics and information technologies. Autom. Constr. 2004, 13, 5–19.

Khoshnevis, B.; Hwang, D.; Yao, K.-T.; Yeh, Z. Mega-scale fabrication by contour crafting. Int. J. Ind. Syst. Eng. 2006, 1, 301–320.

Mechtcherine, V.; Bos, F.P.; Perrot, A.; da Silva, W.L.; Nerella, V.; Fataei, S.; Wolfs, R.J.; Sonebi, M.; Roussel, N. Extrusion-based additive manufacturing with cement-based materials–Production steps, processes, and their underlying physics: A review. Cem. Concr. Res. 2020, 132, 106037.

Nerella, V.; Näther, M.; Iqbal, A.; Butler, M.; Mechtcherine, V. Inline quantification of extrudability of cementitious materials for digital construction. Cem. Concr. Compos. 2019, 95, 260–270.

Pegna, J. Exploratory investigation of solid freeform construction. Autom. Constr. 1997, 5, 427–437.

Valencia, N. World's First 3D Printed Bridge Opens in Spain. 2017. Available online: https://www.archdaily.com/804596/worldsfirst-3d-printed-bridge-opens-in-spain (accessed on 1 August 2022

Perrot, A.; Mélinge, Y.; Rangeard, D.; Micaelli, F.; Estellé, P.; Lanos, C. Use of ram extruder as a combined rheo-tribometer to study the behaviour of high yield stress fluids at low strain rate. Rheol. Acta 2012, 51, 743–754.

The 16th International Congress on the Chemistry of Cement 2023 (ICCC2023)
"Further Reduction of CO_2 -Emissions and Circularity in the Cement and Concrete Industry"
September 18–22, 2023, Bangkok, Thailand

The Role of Belitic Calcium Sulfoaluminate Cement in Achieving Net-zero

T. Hanein[1]*, J. L. Gálvez-Martos[2], and E. Bescher[3]

[1] *Department of Materials Science and Engineering, University of Sheffield, Sheffield, United Kingdom*
Email: t.hanein@sheffield.ac.uk
[2] *Systems Analysis Unit, IMDEA Energy, Móstoles (Madrid), Spain*
[3] *Department of Materials Science and Engineering, University of California Los Angeles, Los Angeles, California, United States*

ABSTRACT
Alternative low-carbon cements can provide a short-term solution for emissions reduction but those cements gaining the most attention cannot achieve the highly desirable (and often necessary) early strength. Belitic calcium sulfoaluminate cement (BCSA) is a standalone cement that can provide this early strength, and that is its current unique selling point. In this communication, we discuss how BCSA can increase the eco-efficiency of net-zero cement production while contributing to the circular economy of the construction sector.

KEYWORDS: *BCSA, early strength, low-carbon cement, closed-loop recycling, Eco-efficiency*

1. Introduction

The cement industry is responsible for ~7 % of the global CO_2 emissions, coming mainly from the calcination of limestone (60 – 70%), and has the lowest margin to deal with abatement, as they produce around 7 kg of CO_2 per USD of turnover, quite high if compared to other carbon-intensive industrial sectors, such as iron and steel (1.5 kg CO_2 per USD turnover) or chemicals (0.3 kg CO_2 per USD turnover) (UNECE, 2022). The current decarbonisation roadmaps proposed by the main players of the cement industry, the Global Cement and Concrete Association, the International Energy Agency and/or cement maker associations rely heavily on the use of carbon capture and storage technologies, with different degrees of intervention on cement plants (Cembureau, 2020; Habert et al., 2020; International Energy Agency and Cement Sustainability Initiative, 2018). This aspect is due to the unavoidability of CO_2 emissions coming from limestone calcination in the production of conventional cements. A recent study showed how alternative formulations with lower associated greenhouse gases emissions are not only able to reduce the overall environmental footprint of cement-based products, but how they increase the eco-efficiency of the implementation of CCS technologies in the sector (Galvez-Martos et al., 2022).
The use of alternative formulations is still considered marginal within the future prospects of the industry. The future role of novel formulations is only associated to specialty applications and only 4 – 6% of market share is foreseen in prospective mixes of cement production (Cembureau, 2020). In this work, we discuss how alternative cements can increase the eco-efficiency towards net-zero cement-based products such as concrete, not only through the production of lower carbon footprint products, but with better performance results and with a better cost-efficiency in a theoretical large-scale production. We finally focus our discussion on the further contribution of that novel formulations towards the circular economy of the construction sector.

2. What is BCSA?

BCSA is a ye'elimite-based cement where belite is the major phase. As a rule of thumb, it constitutes <40wt.% ye'elemite and >40wt.% belite. BCSA differs from traditional calcium sulfoaluminate (CSA) cements where, in the latter, ye'elimite is the major phase (>70wt.%). Furthermore, unlike CSA, BCSA is a standalone cement. It is (as are all ye'elimite and aluminate rich clinkers) well-known for its rapid set/high early strength capability. The know-how for the efficient and safe placement of BCSA concrete does exist and technological advancements such as the development of volumetric concrete mixer trucks, or progress in the development of suitable concrete mix designs for ready-mix trucks allow for resolving

workability or delivery concerns. Technical know-how and practice related to the placement of BCSA concrete are now well-established. BCSA concrete mix designs for cold and hot weather placement, freeze-thaw resistance, low permeability, self-consolidation, or ultra-high-performance concretes have been developed and commercialized. Large scale infrastructure mix designs making use of suitable retarders such as citric acid (and ice) and superplasticizers can be used in volumetric trucks that need little retardation, or ready-mix trucks requiring haul times in excess of two hours. Let us also remember that ye'elimite-rich cements do not benefit from the decades of research into tailored chemical additives.

3. Sustainable Sourcing and Recycling

Ye'elimite-based cements are one of the most readily available, low carbon options for the production of low carbon cement-based products. Its production does not require major changes from Portland cement manufacturing, and its direct emissions are around 30% lower than Portland cement (PC) due to the lower temperature and lower limestone requirement (Hanein et al., 2018). However, ye'elimite-based cements require a higher amount of Al_2O_3 in comparison to conventional cements. This is the main factor negatively affecting the economics and the carbon footprint of their production, since the use of alumina-rich raw materias such as bauxite (for high ye'elimite cements) or bauxite-derived raw materials is required, and are concentrated in a few regions in the world. Recent studies showed that the distance to the location of the source of bauxite is "key to enable the eco-efficient character of CSA clinker" (Gálvez-Martos et al., 2020). If the cost of CO_2 avoidance is taken into account, only low ye'elimite CSA cements (i.e., BCSA) are suitable for an affordable transition towards descarbonisation, avoiding undesired pressure over proven reserves of bauxite in places such as Australia, Brazil, India, or the U.S. (Knutson, 2023). Bauxite is also considered a critical raw material by many regions and economies; therefore, decarbonisation of the cement sector cannot rely on its extended use (European Commission, 2020a).

A closer look is necessary to low ye'elimite(< 40%) CSA cements, where the main component is belite and are known as belitic CSA cements, or BCSA. The source of alumina in the formulation are common clays, which is a widely-available, non-critical resource (European Commission, 2020b; USGS, 2023), which may be supplemented with Al from other sources. In addition, the economic importance of BCSA is not only based on its capacity to substitute PC in many applications, but on its recyclability and its ability to provide highly-valuable early strength. It is often argued that the realistic replacement of traditional cement with calcium sulfoaluminate based cement is limited due to the [non] availability of the alumina source (normally considered to be bauxite), relative to global cement demand. However, this argument has created, within the cements community, a perception of alumina scarcity that is not real. Alumina is more available than calcium in the Earth's crust and what is scarce is our ability/technology to reap this alumina (see Figure 1).



Figure 1: Most abundant elements in the Earth's crust by mass, bar Oxygen (which is almost half of the weight).

BCSA can be produced from kaolinite; a raw feed of 59% limestone ($CaCO_3$), 11% gypsum, and 30% kaolinite will give 35% ye'elimite, 60% belite, and 5% $CaSO_4$ in the clinker under adequate processing conditions. The material efficiency is 68% and raw materials CO_2 emissions are 0.38 kg per kg clinker. Furthermore, BCSA is truly recyclable. The material produced in the kiln is [almost] the same material used to make concrete, apart from minor additions of chemical additives. If we achieve a truly circular process for BCSA production, and we can separate binder from sand efficiently, virgin raw materials will no longer be required. Regarding the latter, separation of hardened BCSA from aggregate may prove to be less energy intensive than that needed for PC, due to the lower breakdown temperature of ettringite.

4. Performance of Belitic Calcium Sulfoaluminate cements in rapid setting concretes

The global warming potential (GWP) of BCSA has been certified to be 0.671 kg CO_2-eq (CTS EPD), which is significantly lower than that of PC. However, BCSA is not currently sold based on its low GWP but on the basis of its fast-setting characteristics. As such, it competes with other fast-setting concretes like those made with accelerated Portland cement, or blends of high (>50wt%) CSA cement with PC. Generally, these concretes are able to compete against one another as long as they can achieve similar compressive or flexural strength within a few hours. For example, rapid strength concrete pavement specifications in California (Caltrans 2018) call for a pavement opening flexural strength of 400 psi (2.75 MPa) before opening to traffic. Concrete must be able to reach this strength within 4 hours. In this study, three concrete formulations based on BCSA, PC (accelerated), and PC+CSA cements that can achieve these strengths are studied. The mix designs for the three concretes are significantly different from one another (Table 1). A PC-based mix must have a high cement content (474 kg/m^3) in order to achieve high early strength. The PC+CSA mix and BCSA mixes have much lower but similar cement content (362 kg/m^3). Here, the concrete mixes used the same source of aggregates – the fine aggregate (washed concrete sand) from Hanson Aggregates, Irwindale Plant, and the coarse aggregate (9.53 mm pea gravel) from Vulcan Materials Company, San Bernardino Plant. The carbon footprint of each type of cement is calculated from their environmental product declarations: BCSA: 0.671 kg CO_2 eq per kg cement (CTS 2023); PC Type III 0.962 kg CO_2 per kg cement (PCA 2021) CSA – 0.559 kg CO_2 per kg cement (comprised of 72 wt% CSA with GWP of 0.728 kg CO_2 per kg cement and 28% anhydrite with GWP of 0.123 kg CO_2 per kg).

Table 1: Concrete mix designs for rapid setting concretes. FA = fine aggregate and CA = coarse aggregate.

1 Cubic Meter Batch Weight (SSD Basis)							
Cement Type	**Cement (kg)**	**FA (kg)**	**CA (kg)**	**w/c**	**Admixture 1**	**Admixture 2**	**Admixture 3**
BCSA	362	699	1098	0.46	1.47 l/m^3 Superplasticizer	1.10 L/m^3 Retarder	-
CSA+PC (CSA + type III 60/40)	362	698	1097	0.46	1.83 l/m^3 Superplasticizer	1.80 kg/m^3 Citric Acid	-
Accel. PC	474	646	1015	0.34	1.92 l/m^3 Superplasticizer	22.77 l/m^3 Accelerating admixture	0.12 l/m^3 Slump retainer

4.1 Eco-efficiency of rapid setting concretes

The ISO standard 14045 defines eco-efficiency as an "aspect of sustainability relating the environmental performance of a product system to its product value" (ISO, 2012; Simioni and da Silva, 2020). To determine the eco-efficiency within this study, the calculation of the carbon footprint of the proposed rapid-setting concretes was related to the early compressive and flexural strengths, as shown in Table 2. Considering the cement portion alone (everything else being equal) reveals some significant differences. Data in Table 2 show that the (carbon intensity) CI at 4 hours for BCSA is significantly lower than the accel. PC system or the CSA+PC system. PC also has the highest GWP (0.962 kg/kg cement) of the three systems. These factors lead to the accel. PC system having double the carbon intensity of the BCSA mix. These results indicate that BCSA is an excellent binder for its carbon intensity when compared with rapid setting concretes based on performance. Now arises the question: What is the price of early strength?

Table 2: Compressive and flexural strengths and associated carbon intensity for Concrete Mixes in Table 1

Mixes	**CO_2 emissions (kg/m^3)**	**4-hr Compressive Strength (MPa)**	**CI w.r.t 4-hr Compressive (kg/m^3.MPa)**	**4-hr Flexural Strength (MPa)**	**CI w.r.t 4-hr Flexural (kg/m^3.MPa)**
Accel. OPC	437.03	23	19.00	3.6	119.96
BCSA	242.90	36	6.75	4.3	55.89
CSA-OPC (CSA+Type III 60/40)	309.66	28	11.06	3.9	80.43

4.2 Cost of CO_2 Avoidance and Early Strength

Using generic cement manufacturing cost for CSA from the literature (Gálvez-Martos et al., 2021), shows that the cost of CO_2 avoidance and the cost of early strength of BCSA from conventional PC is remarkably lower than PC/CSA mixes.

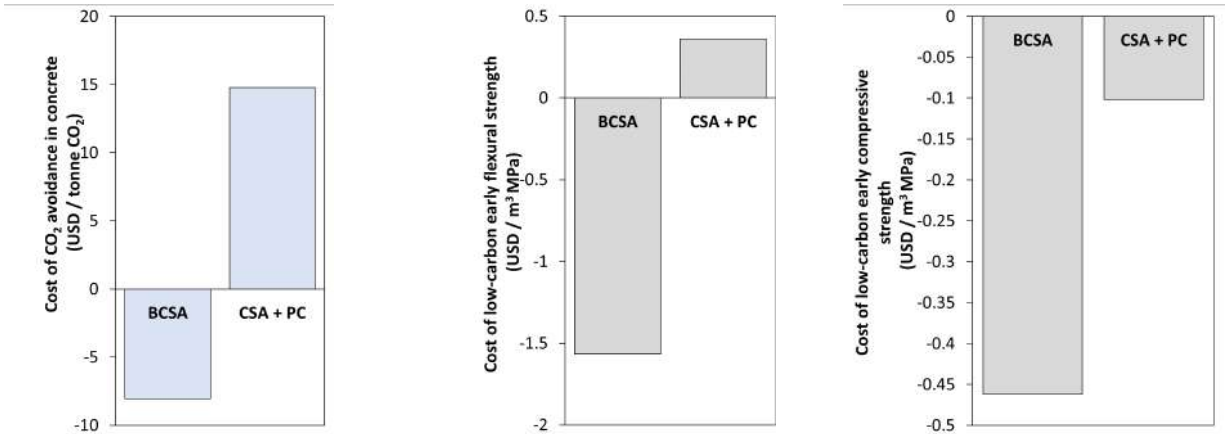


Figure 2: Cost of CO_2 avoidance (left), cost of early flexural strength (centre) and of early compressive strength (right) for CSA-bearing formulations in relation to accelerated Portland cement concrete.

5. Closing remarks

It is reasonable to ask the following questions: if the priority is to develop a low-carbon cement, should all its characteristics (which are otherwise compatible with existing PC manufacturing plants and concrete placement logistics) be compared to PC by mass? Are PC properties a suitable benchmark against those of low carbon alternatives or is the bar too low?

References

Caltrans- California Department of Transportation Standard Specifications, 2018.

Cembureau, 2020. Cementing the European Green Deal: Reaching Climate Neutrality Along the Cement and Concrete Value Chain by 2050.

CTS, 2023. Cement Manufacturing Corporation, Environmental Product Declaration for Rapid Set, https://www.ctscement.com/assets/doc/info/EPDlabel_RapidSet_Labeling_Sustainability_CTS_Cement.pdf

European Commission, 2020a. Study on the EU's list of Critical Raw Materials (2020): Critical Raw Materials Factsheets.

European Commission, 2020b. Study on the EU's list of Critical Raw Materials (2020): Non Critical Raw Materials Factsheets [WWW Document]. URL https://rmis.jrc.ec.europa.eu/uploads/CRM_2020_Factsheets_non-critical_Final.pdf

Gálvez-Martos, J.-L., Chaliulina, R., Elhoweris, A., Mwanda, J., Hakki, A., Al-horr, Y., 2021. Techno-economic assessment of calcium sulfoaluminate clinker production using elemental sulfur as raw material. J. Clean. Prod. 301. https://doi.org/10.1016/j.jclepro.2021.126888

Galvez-Martos, J.-L., Elhoweris, A., Chaliulina, R., Mwanda, J.A., Bannerman, C., AlHorr, Y., 2022. On the Eco-efficiency and Life Cycle Performance of Decarbonization Approaches of Cementitious Materials. https://doi.org/10.2139/ssrn.4282839

Gálvez-Martos, J.-L., Valente, A., Martínez-Fernández, M., Dufour, J., 2020. Eco-efficiency assessment of calcium sulfoaluminate clinker production. J. Ind. Ecol. 24, 695–706. https://doi.org/10.1111/jiec.12967

Habert, G., Miller, S.A., John, V.M., Provis, J.L., Favier, A., Horvath, A., Scrivener, K.L., 2020. Environmental impacts and decarbonization strategies in the cement and concrete industries. Nat. Rev. Earth Environ. 1, 559–573. https://doi.org/10.1038/s43017-020-0093-3

Hanein, T., Galvez-Martos, J.-L., Bannerman, M.N., 2018. Carbon footprint of calcium sulfoaluminate clinker production. J. Clean. Prod. 172, 2278–2287. https://doi.org/10.1016/j.jclepro.2017.11.183

International Energy Agency, Cement Sustainability Initiative, 2018. Technology Roadmap - Low-Carbon Transition in the Cement Industry.

ISO, 2012. ISO 14045: Eco-efficiency assessment of product systems: principles, requirements and guidelines. Geneva.

Knutson, C.Y., 2023. Bauxite and alumina (USGS Mineral Commodities Summary).

PCA, 2021. Environmental Product Declaration for Portland Cement. https://www.cement.org/docs/default-source/epds/pca_epd_portland_athena_final_revised_04082021.pdf?sfvrsn=3e4affbf_2

Simioni, F.J., da Silva, F.A., 2020. Eco-efficiency: Concept, Indicators and Applications, in: Leal Filho, W., Azul, A.M., Brandli, L., Özuyar, P.G., Wall, T., Affordable and Clean Energy. Springer International Publishing, Cham, pp. 1–11.

UNECE, 2022. Technology Brief. Carbon Neutral Energy Intensive Industries.

USGS, 2023. Clays (Mineral Commodity Summary) [WWW Document]. URL https://pubs.usgs.gov/periodicals/mcs2023/mcs2023-clays.pdf (accessed 3.3.23).

The 16th International Congress on the Chemistry of Cement 2023 (ICCC2023)
"Further Reduction of CO_2 -Emissions and Circularity in the Cement and Concrete Industry"
September 18–22, 2023, Bangkok, Thailand

Carbon neutral concrete based on a sea snail shell: a green solution for the urban heat island

G. Goracci[1*], M.B. Ogundiran[1,2], E. Saeed[1,3], and J.S. Dolado[1,4]

[1] *Centro de Física de Materiales, CSIC-UPV/EHU, P. Manuel de Lardizábal 5, 20018 San Sebastián, Spain*
[2] *Analytical/Environmental Unit, Department of Chemistry, Faculty of Science, University of Ibadan, Nigeria*
[3] *University of Bordeaux, CNRS, Bordeaux INP, ICMCB, UMR 5026, F-33600 Pessac, France*
[4] *Donostia International Physics Center, P. Manuel de Lardizabal 4,San Sebastián, Spain*

Email: guido.goracci@ehu.eus

Email: mbogundiran@gmail.com

Email: ebtisamtarek.saeed@ehu.eus

Email: j.dolado@ehu.eus

Abstract

Urban Heat Island (UHI) refers to the fact that the temperature in urban areas tends to be higher than in the rural landscapes surrounding them. This effect occurs because 30-45% of the area in the cities is paved and 20-25% is roofed. Therefore, the development of new materials for cool pavements and roofs with high solar reflectance properties is necessary to reduce transmitted heat (and thus reduce energy consumption for cooling) and improve human comfort. So far, various coatings and advanced materials have been proposed for mitigation of UHI. In this study, an innovative carbon-neutral building cementitious composite was produced using a natural, recycled material: Periwinkle shell ash. In fact, 70% of the concrete mix was made from the shell of the sea snail, commonly found worldwide, which consists mainly of portlandite and calcite. After a process of carbon capture, the periwinkle shell ash was added to a special cement mix to obtain a carbon neutral concrete with a competitive solar reflectance index (SRI) of 73, which can be used as a structural element for ecological UHI mitigation.

Keywords: *Carbon Capture, Urban Heat Island, Carbon Neutral Concrete, Solar Reflectance Index, Periwinkle Shell Ash.*

1. Introduction

Urban Heat Island (UHI) is a significant problem facing cities today, in which urban areas tend to be warmer than the rural areas surrounding them. The increased temperature in cities is primarily due to the high density of paved and roofed surfaces, such as roads, sidewalks, and building roofs, which absorb and retain heat. This phenomenon can result in increased energy consumption for cooling, reduced human comfort, and negative impacts on the local environment and biodiversity.

To mitigate the effects of UHI, it is essential to develop materials with high solar reflectance properties that can reduce the transmission of heat and improve the overall thermal comfort of urban areas. In recent years, various strategies have been proposed for mitigating the effects of UHI, including the use of reflective surfaces, green roofs, and cool pavements (e.g Pisello (2017)). However, these solutions have several limitations that have hindered their widespread adoption. For example, many reflective surfaces and cool roof membranes have a relatively short lifespan and require frequent maintenance, while green roofs can be expensive to install and maintain. Additionally, many of these solutions are limited in terms of their effectiveness, as they only reflect a portion of the solar radiation incident on the surface and do not address the underlying problem of heat retention in the urban areas.

In this study, an innovative carbon-neutral building cementitious composite was made from a natural, recycled material: the ash of Periwinkle shells. Periwinkles are a type of sea snail commonly found worldwide, and the shells they produce consist mainly of portlandite and calcite. After undergoing a process of carbon capture, the innovative cementitious material was produced by mixing 70%wt of the carbonated Periwinkle shell (CPS) ash with Ordinary Portland Cement (OPC), resulting in a concrete that captured 18% of its weight in carbon dioxide and a competitive Solar Reflectance Index (SRI) of ~73.

The use of this material presents a unique solution to the UHI problem as it utilizes a widely available natural resource in a sustainable and eco-friendly manner.

Table 1. Oxide composition of (wt.%) Periwinkle shell ash (PS) and OPC .

Mateial	SiO_2	Al_2O_3	Fe_2O_3	MnO	MgO	CaO	Na_2O	K_2O	Ti_2O	P_2O_5	SO_3
PS	1.28	0.52	0.42	0.05	0.70	59.5	0.48	0.15	0.02	0.10	0.17
OPC clinker	19.0	4.73	2.79	0.02	1.05	62.7	0.01	0.94	0.24	0.17	2.70

2. Materials and Method

The raw materials were ordinary Portland cement (OPC) CEM-1 52.5R (Rezola) and periwinkle shell (PS) ash. The oxide compositions of these materials are presented in Table 1. To prepare carbonated periwinkle (CPS), a CO_2 gas with a pressure of 0.4 bar was bubbled into a mixture of 5 g of periwinkle shell ash and 87.5 mL of distillated water in a sealed plastic tube with stirring at the speed of 1700 rpm. The carbonation duration of reaction was for 15 minutes at room temperature and pressure. The sample was kept in a water-rich CO_2 for one night. Afterwards, the carbonated periwinkle powder was obtained by centrifugation for 10 minutes and drying at 80 ºC overnight. The cement paste sample was produced by first mixing the cement with the carbonated periwinkle (OPCCPS) with a ratio cement-to-ash of 0.3, then adding water (w/c= 1) and superplasticizer (6%wt_{OPC}). The sample was mixed for 90 s, rest for 60 s, and then stirring again for 90 s, poured in a silicon mould, and removed after 24 h to cure it in a desiccator with relative humidity of 100%.
To identify the distinct phases, PS, CPS and OPCCPS were characterized using Fourier Transform Infrared (FTIR), a Jasco 6300, with a spectral range of 4000-500 cm^{-1}. The carbonation efficiency of the PS and OPCCPS was evaluated by thermogravimetric analysis (TGA) using a TGA-500. Approximately 10 mg of carbonated periwinkle shell powder was heated from room temperature to 900°C at a rate of 10°C/min under a flow of nitrogen gas. The Solar Reflective Index (SRI) of the cement paste was determined by measuring the solar reflectivity from ultraviolet (UV) to mid-infrared (MIR) using a portable spectrophotometer (410-SOLAR) and an integrated sphere mounted on FTIR (PIKE). The SRI was calculated using the ASTM E1980 standard method, which considers the reflectance in the visible and infrared regions. Three measurements were performed on different areas of each cement paste sample, and the average value was reported. Finally, OPCCPS was subjected to simulated solar radiation using a 500 W halogen lamp and compared with OPC and White Cement pastes. The distance between the lamp and sample was regulated to achieve a solar radiation power of 750 W/ while the temperature of the sample surface was measured using a thermocouple.

3. Results and Discussion

The results of the FTIR analysis showed that the Periwinkle shell (PS) was primarily composed of portlandite and calcite (Fig 1). After undergoing the carbon capture process, the resulting carbonated Periwinkle shell (CPS) was found to consist mainly of calcite.

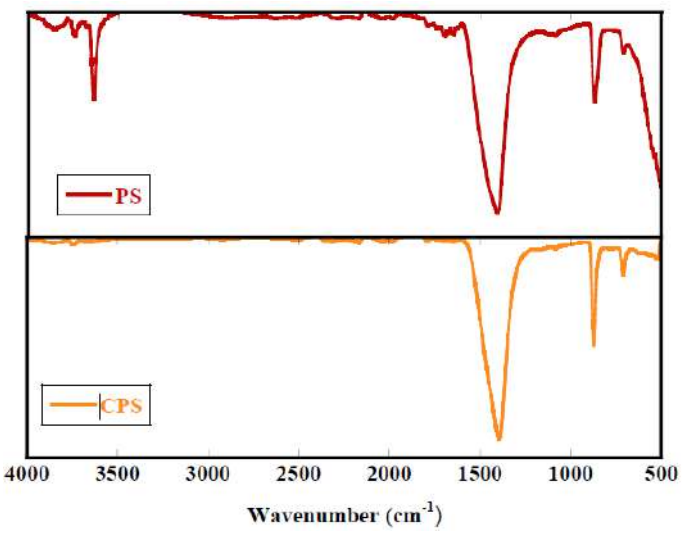
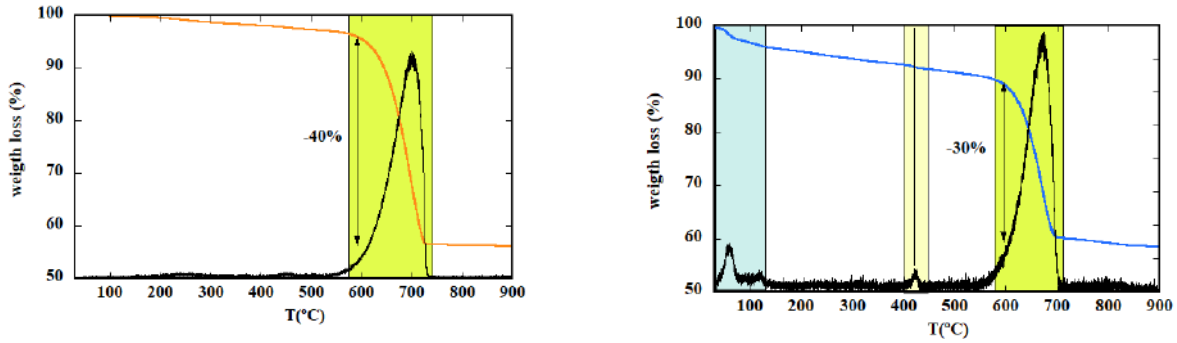


Fig 1. FTIR spectra of PS (top) and CPS (bottom)

The mineralization of CO_2 by portlandite, and subsequently converting to calcite, are well-documented in the literature (e.g. Shih (1999) and Falzone (2019). The TGA curve of CPS (Fig. 2a) displays a single significant decay between 600-700 ºC, indicating the decarbonation of the calcite formed by the carbonation reaction of the PS. The TGA curve of OPCCPS is shown in Fig. 2b. Weight loss due to bulk water evaporation was observed at T < 150 ºC. The dehydroxylation of Portlandite is found at ~400ºC. Since all portlandite in CPS reacts with CO_2 to form calcite, the contribution to the portlandite resulting from the OPC hydration process is associated with this finding. Finally, a significant decay in weight associated with the CO_2 lost is observed (18%wt carbon dioxide uptake). The decrease in intensity, compared with pure CPS, is consistent with the percentage of carbonated Periwinkle shell in the sample.



a) b)

Fig 2: TGA curves of CPS (a) and OPCCPS (b)

The reflectance R measured of OPCCPS is presented in Figure 3a. In the sun wavelength frequency range (yellow area), a pronounced peak in R is observed. To obtain the solar absorption (α) of the cementitious composite, data were normalized to the solar spectra (ASTM G173 Global Solar spectrum). From the calculation a value of α=0.38 was obtained. Regarding the frequency range in the atmospheric window (light blue area), an almost flat R can be observed. The emissivity *e* was calculated as 1-<R>, where <R> is the average of R in the atmospheric window. According to the active standard ASTM E1980, an SRI=73 is obtained for OPCCPS closely approaching values of "cool roofs" (SRI>78) (ASHRAE, 2011).

The high SRI value of the OPCCPS is due to the high solar reflectance of the CPS, which is mainly composed of calcite, a mineral with a high refractive index and low absorbance in the visible and near-infrared regions of the solar spectrum. Finally, the solar reflectance property of the cementitious composite was tested with and homemade experimental (fig.3b) setup and compared with OPC and White Cement paste. In Fig. 3c, a comparison of the temperature reached by the different specimen is shown. The OPCCPS has the same temperature profile of a White Cement paste and more than 5ºC colder than traditional OPC paste.

a) b) c)

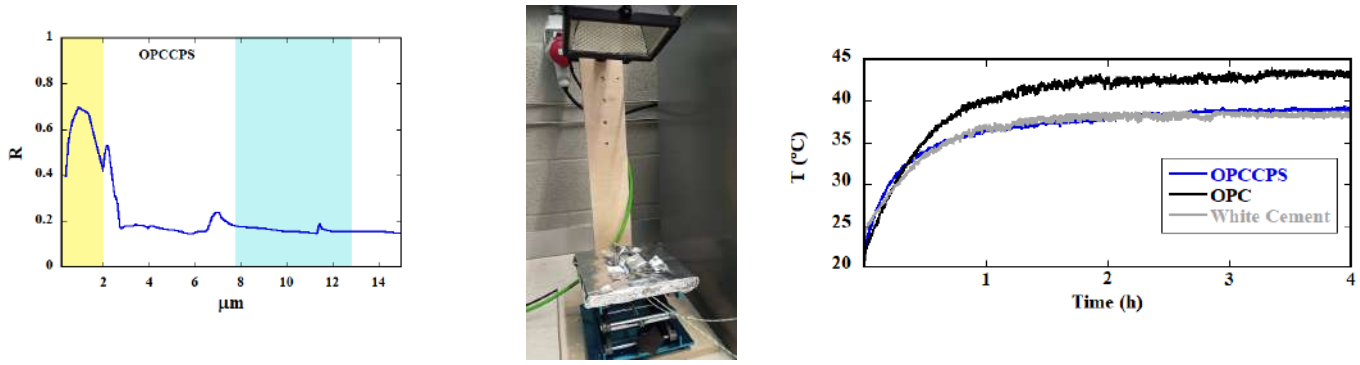


Fig 3: a) Measured reflectance of OPCCPS b) Homemade to simulate solar radiation on cement paste c) temperature profile of OPCPS, OPC and White Cement paste as a result of simulated solar radiation (750 W/m^2)

4. Conclusions

In this study, an innovative carbon-neutral building cementitious composite made from a natural, recycled material, the ash of Periwinkle shells, was developed. The carbonation of Periwinkle shell ash was successfully achieved, resulting in a material with a significant carbon dioxide uptake (18%wt in OPCCPS). The resulting cement composite exhibited a competitive Solar Reflective Index (SRI) of 0.73, comparable to reflective building materials commonly used to mitigate the urban heat island (UHI) effect. Solar radiation simulations demonstrated that the OPCCPS composite performed comparably to White Cement and was more than 5 ºC cooler than traditional OPC paste. Our findings highlight the potential of OPCCPS as a sustainable alternative to traditional cementitious materials, with the additional benefits of reducing waste and mitigating the UHI effect. Overall, our study contributes to the development of environmentally-friendly and sustainable building materials that can help combat the negative effects of climate change. Further research is needed to optimize the production and performance of OPCCPS, but the results of this study are promising and provide a basis for future investigations.

Acknowledgements

MBO appreciates sponsorship from Women for Africa Foundation to be part of this research.

References

Pisello, A. L. (2017). State of the art on the development of cool coatings for buildings and cities. Solar Energy, 144, 660-680.

Shih S-M, Ho C-S, Song Y-S, Lin J-P. Kinetics of the reaction of Ca(OH)2 with CO2 at low temperature. Ind Eng Chem Res. 1999;38(4)

Falzone, G., Mehdipour, I., Neithalath, N., Bauchy, M., Simonetti, D., & Sant, G. (2021). New insights into the mechanisms of carbon dioxide mineralization by portlandite. AIChE Journal, 67(5), e17160.

ASHRAE, Advanced Energy Design Guide for Small to Medium Office Buildings:Achieving 50% Energy Savings toward a Net Zero Energy Building, (2011).

The 16th International Congress on the Chemistry of Cement 2023 (ICCC2023)
"Further Reduction of CO_2 -Emissions and Circularity in the Cement and Concrete Industry"
September 18–22, 2023, Bangkok, Thailand

Prediction of Total Bond Order Density of Cement Crystals using Fermionic Hubbard Model and Bloch and Fermi Surface

Natt Makul

Department of Civil Engineering Technology, Faculty of Industrial Technology, Phranakhon Rajabhat University, 9 Changwattana Road, Bangkhen, Bangkok 10220, Thailand
Email: natt@pnru.ac.th

ABSTRACT

This work used quantum physics to predict how cement crystals' internal cohesiveness will evolve. At low temperatures, the electron-electron interactions of cement-based materials' internal cohesiveness may be more accurately predicted with the assistance of the Hubbard model. This model should make research on the bosonic version of the Hubbard model and the fermionic version possible. The total bond order density, or TBOD, is a quantum mechanical metric used to characterize C-S-H crystals. For a better understanding of cement crystal cohesiveness, this measurement considers geometric components and interatomic interactions. The orthogonalized linear combination of atomic orbitals (OLCAO) approach will be used to determine the source of internal cohesion in C-S-H crystals by comparing the bond order of an atom pair to the bond length of the pair. This study should contribute to the information on the internal cohesiveness of cement-based crystals and provide practical approaches to reinforce calcium-silicate-hydrate crystals in addition to contributing to the body of knowledge on cement-based crystals.

KEYWORDS: *Calcium-Silicate-Hydrate; Quantum-physical theory; Hubbard model; Total bond order density (TBOD); OLCAO*

1. Introduction

Portland cement consists of four distinct clinker phases: alite (Al_3SiO_5), belite (Ca_2SiO_4), ferrite (Al_xFe_{2-x}), and tri-calcium aluminate ($Ca_2(Al_xFe_{2-y})\ O_5$) ($Ca_3Al_2O_6$). C-S-H with varied compositions is the principal hydrate product responsible for cement-based concrete's strength, calculated as an average of the Ca/Si percentage and water content. The C-S-H phase with a large fraction of Ca/Si forms during the hydration of pure cement, as reported by Kunther et al. (2015).

Colloidal materials and systems commonly display net interactions between surfaces with the same electrical charge. The DLVO theory was first proposed by Derjaguin, Landau, Verwey, and Overbeek. In order to investigate the interactions between ions in space and their changing behavior, the theory depended on the mean-field approximation. This allowed the theory to capture some of the scenarios that were presented. However, it is generally agreed that the DLVO theory does not apply to cement hydration products such as C-S-H. This is because the ions that make up cement hydration products are of a multivalent nature (Ca^{2+}), and they can only be found on charged surfaces with a surface density of approximately 3 to 5 e/nm^2 in the hardened C-S-H phase. Given this information, the DLVO hypothesis cannot predict how the internal cohesiveness of cement crystals changes over time.

Molecular simulation of the extended Hubbard model for internal cohesion and direct measurement, on the other hand, has provided strong arguments on how to determine the surface forces supported with hydrated calcium ions, which are essential in the compressive strength of concrete. This is the case because the extended Hubbard model predicts that it is anticipated that this model will both facilitate research into the bosonic version of the Fermionic Hubbard model and promote research into the latter. In addition, the research will analyze the cohesiveness of cement-based crystals by classifying C-S-H crystals based on an ideal quantum mechanical metric known as total bond order density (TBOD)

(Kunther et al., 2015). In order to give a more in-depth understanding of the cohesiveness of cement-based crystals, this metric will take into account the influence of geometric parameters and interatomic interactions. In this particular scenario, the first-principles OLCAO approach will be used to compare the bond order (BO) in an atom pair and the bond length to discover the source of the internal cohesiveness in the C-S-H crystals. It is anticipated that this will give vital hints about modifying the cement's internal cohesiveness at the nano- and meso-structure levels. It is anticipated that the results of this research will significantly contribute to the expanding body of literature on the internal cohesion of cement-based crystals and will also provide valuable strategies for increasing the robustness of cement in the face of silicate and hydrate. This paper presents the data using an expanded Hubbard model adjusted for crystal polymerization. The data from crystalline phases may assist in understanding experimental spectroscopic results, leading to accurate models of the C-S-H phase in Portland cement.

2. Internal cohesion of cement crystals

Nineteen well-documented cement crystals are classified based on the increasing order of Ca/Si ratio into four groups (Zang et al., 2012). The first group includes anhydrous cement (a.1 (Belites) and a.2 (Alite)), and the groups b.x through d.x are C-S-H crystals (Mills et al., 2009) as shown in Table 1.

Table 1. Chemical characteristic of (a) Clinkers/Hydroxide phases, (b) Nesosubsilicates, (c) Sorosilicates and (d) Inosilicates (Zang et al., 2012).

Mineral Name	Chemical formulas	Ca/Si	Mineral Name	Chemical formulas	Ca/Si
(a) Anhydrous cement			(c) Sorosilicate		
a.1	Belites ($2(CaO)\ SiO_2$)	2.00	c.1	Rosenhahnites $Ca_3Si_3O_8(OH)_2$	1.00
a.2	Alite ($3(CaO)\ SiO_2$)	3.00	c.2	Suolunites $Ca_2[Si_2O_5(OH)_2]H_2O$	1.00
(b) Nesosubsilicates			c.3	Kilchoanites $Ca_6(SiO_4)(Si_3O_{10})$	1.50
b.1	Afwillite ($Ca_3(SiO_3OH)_2{\cdot}2H_2O$)	1.50	c.4	Killalaites $Ca_{6.4}(H_{O.6}Si_2O_7)_2(OH)_2$	1.60
b.2	α-C_2SH $Ca_2(HSiO_4)(OH)$	2.00	c.5	Jaffeites $Ca_6[Si_2O_7](OH)_6$	3.00
b.3	Dellaite ($Ca_6(Si_2O_7)(SiO_4)(OH)_2$)	2.00	(d) Inosilicates		
b.4	Ca Chondrodites ($Ca_5[SiO_4]_2(OH)_2$)	2.50	d.1	Nekoite $Ca_3Si_6O_{15}{\cdot}7H_2O$	0.50
Remark: Sorosilicate structures feature solitary (Q0) and finite (Q2) tetrahedra linked by 6- or 8-fold Ca atoms. Silicate tetrahedra pair each polymerization phase's (Qn) Si. Group d has the highest polymerization compared to C-S-H (Dharmawardhana et al. (2014).			d.2	T11 Å $Ca_4Si_6O_{15}(OH)_2{\cdot}5H_2O$	0.67
			d.3	T14Å $Ca_5Si_6O_{16}(OH)_2{\cdot}7H_2O$	0.83
			d.4	T9 Å $Ca_5Si_6O_{17}5H_2O$	0.83
			d.5	Wollastonites $Ca_3Si_3O_9$	1.00
			d.6	Xonotlites $Ca_6Si_6O_{17}(OH)_2$	1.00
			d.7	Foshagites $Ca_4(Si_3O_9)(OH)_2$	1.33
			d.8	Jennites $Ca_9Si_6O_{18}(OH)_6{\cdot}8H_2O$	1.50

3. Hubbard model, Bloch and Fermi surface of C-S-H

In this case, using the Hubbard model, the interaction between electrons in the crystals will involve a series of fractional filling factors. A quantum mechanics representation of the Hubbard model is presented in Eq. (1), considering the site repulsion (i) and nearest neighbor repulsion (j). Electron interactions in a 2-dimensional lattice crystal are summated using i and j to cover all pairs of nearest-neighbors sites; t represents the magnitude of *NN* interaction; U represents crystal interaction onsite.

$$H = -t\sum_{i,j} b_i^{+} b_j + \sum_{i,j} n_i U_{i,j} n_j - \mu \tag{1}$$

A general form of the Hamiltonian H, can be expressed as a product of $|\varphi> = \sum_{e,p} |e>_{e,i} * |p>_{pk}$, where e and p represent electronic interaction and the bosonic state of the crystal. This truncated bosonic version of the infinite crystal takes one electron for each crystal. In this case, we argue that the change of the internal cohesion of a crystal where another crystal is already present does not necessarily change the scenario of the interacting electrons qualitatively. In order to overcome this challenge, we considered a scenario where two electrons spin in the opposite direction. The

electrons were also restricted to one phonon operator identical $b_i^+|1_t>=|1_t>$; $b_i^+|0_t>=|1_t>$; $b_i|1_t>=|0_t>$; and $b_i|0_t>0$ where 1(0) represents a change in the internal cohesion of a cement crystal. To establish the effect of a pair electron interaction in the crystal, the study computed the electron-electron density correlation using the function $C(i-j)=<\varphi_0|n_i n_j|\varphi_0>$.

Bloch's theorem presents the one-dimensional symmetry of an infinite crystal through the absence of the aggregate electric current at an equilibrium state (Watanabe, 2022). Yamamoto (2015) applied Bloch's theorem to generic systems to gauge particles in symmetry to understand the chiral transport concept. The study investigates the fermionic and bosonic versions of the Hubbard model to determine changing internal cohesion in a lattice. From the findings, the study demonstrated the adoption of the theorem to a non-equilibrium state, which is similar to the integral quantum Hall effect. For the case of cement crystals, this concept remains valid as long as there are no topological variations in the internal cohesion subject to periodical conditions, as illustrated in $|\varphi(x)|^2 = |\varphi(x+a)|^2$. In case a crystal changes by '*a*' as illustrated in $\varphi(x+a)=C.\varphi(x)$, there should be no difference in the internal cohesion with the magnitude of C is equal to 1.0. This main feature of Bloch's theorem remains valid as the fermion interaction of the crystals considers the bosonic excitations perturbatively (Zhang & Zubkov, 2019). Using a periodic boundary condition, research assumes that an infinite crystal can transverse the entire lattice and return to its initial position. However, the empirical literature has not elaborated on the different forms that can be assumed by *C ()*. Suppose *s = 0, 1, 2, ..., N*, one of the forms assumed by $C\ is\ e^{i2\pi\frac{s}{n}}$, with no clear indication of the crystal momentum. Thus, the weak version of Bloch's theorem is underpinned by the notion that the total current vanishes in any system, provided that smooth modification of its gapped charged fermions and periodical boundary conditions do not change (Zhang & Zubkov, 2019).

4. Results and discussion

This section presents internal cohesion data for cement crystals. The research compared TBOD and C/S to investigate cement crystal internal cohesiveness. TBOD and C/S ratio are inversely related in Fig. 1. The identical C/S ratio crystals (≈ 1.7 of cement gel is chosen from the mean of Belites (a.1) and Alite (a.2)) have different TBOD values. TBOD does not affect four significant categories of cement crystal internal cohesion. Comparing the four groups, group c had the most C/S and TBOD. Group d had a limited cement crystal dispersion near hydrated cement in C/S compared to TBOD. Based on TBOD, cement crystals may be categorized as high, medium, or low. Due to their high C/S ratios, cement crystals a.1, b.4, and c.5 have a lower TBOD than b.1, c.1, c.2, d.1, d.2, and d.4 (group d). Group d's middle TBOD range contains the remaining cement crystals. The blending of Strunz groups and a poor link between TBOD and C/S ratio imply deteriorating internal cohesiveness in C-S-H structures. Interlayer hydroxyl, water, and HBs lowered cement's internal cohesiveness with reduced Qn chains in group d crystals. Variations in the silicate chain from one group to another alter the internal cohesiveness of C-S-H crystals.

This research also assessed the role of bonding order in cementing crystal internal cohesion using total bond order density (TBOD). No uniform rule for crystal bonding was found; however, several tendencies were detected. TBOD of cement crystals showed many features of its internal cohesion: (1) how bonding contributed to stiffness; (2) the dispersion of each bond type in the C-S-H phase; and (3) the vital importance of precise crystal structure. The standard criteria for distinguishing C-S-H crystals and their internal cohesiveness explained variances. Total bond order density (TBOD) was used to assess cement crystals' internal cohesion and strength using the extended Hubbard model, fermions, and Bloch's theorem.

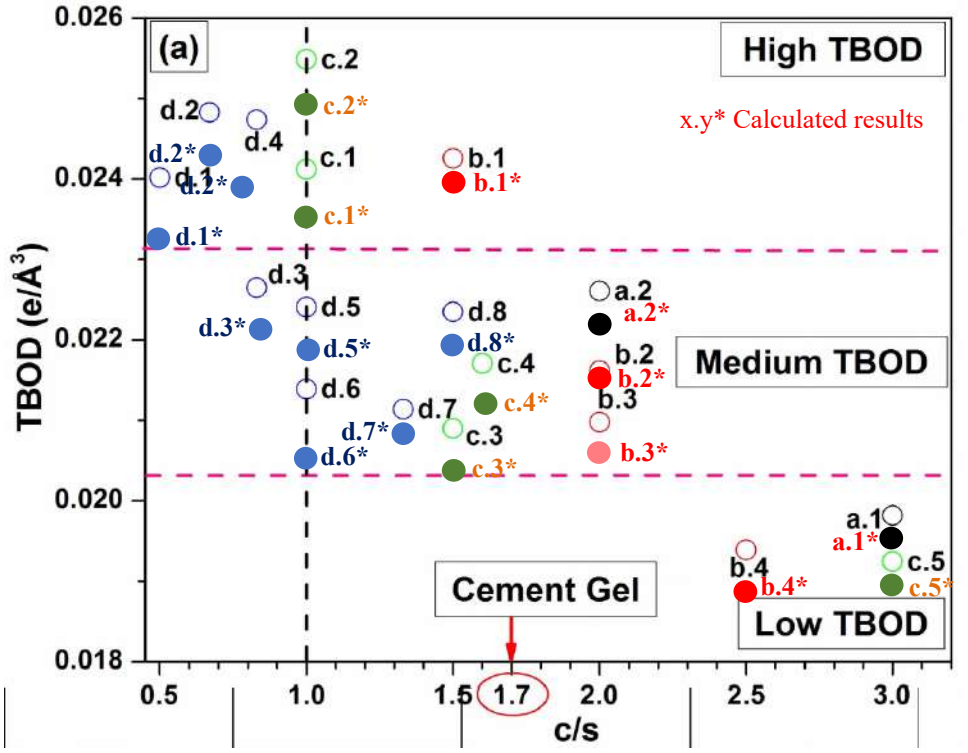


Fig. 1: The relationship between TBOD and the C/S ratio of cement-based crystals (Dharmawardhana, Misra, and Ching (2014))

5. Conclusion

Bloch and Fermi surfaces, and the TBOD to evaluate the changing internal cohesion of cement-based crystals. This method approximates crystal transition using geometric variables and interatomic interactions. TBOD evaluated the internal cohesiveness of several cement crystal classifications. There is no direct association between changing cement crystal cohesiveness and calculated TBOD. Using the fermi and Bloch spectral functions on 19 anhydrous and C-S-H crystals, affiliate (b.1) had the most internal cohesion.

Acknowledgements

This project is funded by National Research Council of Thailand (NRCT) and Phranakhon Rajabhat University (No. N42A660379).

References

Derjaguin, B. V., N. V. Churaev, and V. M. Muller. "The Derjaguin—Landau—Verwey—Overbeek (DLVO) theory of stability of lyophobic colloids." *Surface Forces*. Springer, Boston, MA, 1987. 293-310.

Dharmawardhana, C. C., Anil Misra, and Wai-Yim Ching. "Quantum mechanical metric for internal cohesion in cement crystals." *Scientific reports* 4.1 (2014): 1-8.

Kunther, Wolfgang, Barbara Lothenbach, and Jørgen Skibsted. "Influence of the Ca/Si ratio of the C–S–H phase on the interaction with sulfate ions and its impact on the ettringite crystallization pressure." *Cement and concrete research* 69 (2015): 37-49.

Watanabe, Haruki. "Bloch theorem in the presence of an additional conserved charge." *Physical Review Research* 4.1 (2022): 013043.

Yamamoto, Naoki. "Generalized Bloch theorem and chiral transport phenomena." *Physical Review D* 92.8 (2015): 085011.

Zhang, L., Lin, Z., Li, Z. “The Structure of Silicate Ions in C-S-H Discussed from Chemical Composition.” *Advances in Cement Research* (2012):24, 263-281.

The 16th International Congress on the Chemistry of Cement 2023 (ICCC2023)
"Further Reduction of CO_2 -Emissions and Circularity in the Cement and Concrete Industry"
September 18–22, 2023, Bangkok, Thailand

Digitalization in cement production: prediction of free lime content in clinker production

W.R. Leal da Silva[1*], J.P. Merino[1], and A.N. Dam[1]

1 FLSmidth A/S, Valby, Denmark
**Email: wilson.dasilva@flsmidth.com*

ABSTRACT

Portland cement production accounts for about 8.0% of the world's global CO_2 emissions and, if left unattended, this contribution is expected to increase to 26% by 2050. Thus, we need to rethink the current model of producing cement. Among various strategies supporting that, e.g. use of supplementary cementitious materials (SCM) and carbon capture, utilisation, and storage (CCUS) technologies, the advancements in artificial intelligence (AI) enables optimising cement production in a relatively fast and inexpensive manner. This is because the plants are already equipped with control system that capture production metrics e.g. process data and material characterization reports. With this in mind, we carried out a case study – using data from cement plants – focused on the development of an AI-based prediction models for free-lime content in clinker. We discuss the obtained results, identify the best performing models, and elaborate on the challenges in implementing AI-based solutions in cement production.

KEYWORDS: *artificial intelligence, cement production, digitalisation, machine learning.*

1. Introduction

Portland cement production accounts for circa 8.0% of the world's global CO_2 emissions and is expected to increase to 26% by 2050. Thus, there is an urgent need to rethink the current model of producing cement. Specifically, there are complementary strategies such as a) efficient utilization of cement in construction (Watari et al. 2022); b) supply-side technologies e.g. carbon capture, storage, and utilization (Plaza et al. 2020); and c) digital solutions to optimize the cement production (Stadler et al. 2011).
The first is heavily explored by industry and has made progress in material optimization (using performance-based design, topology optimization of structures, use of high-volume clinker replacement). The second is still in its infancy and requires large equipment and heavy capital investments to be implemented. The third – and the main topic of this article - has received increased attention lately (McKinsey, 2022) and corresponds to a solution with low capital and operational costs – considering that cement plants have control system that enable tapping into production metrics.
The challenge in implementing digital solutions derives from the complexity of cement production process. In particular, the raw materials (e.g. limestone and clay) are inherently variable, which means that system interventions (e.g. control free-lime content in the clinker, control kiln temperature) change over time. Hence, relying in control systems that are solely dependent on static rule-based architecture or that heavily depend on expert knowledge lack a high frequency and self-adapting capability that could lead to a more stable and reliable production process – yielding a more sustainable production. To overcome such limitation, the use of machine learning (ML) comes in handy, since models can be trained to identify correlations in data and used to make predictions. Examples of ML applications in cement industry are found in A. Kamalloo et al. 2010, Abubakar et al. 2019, and Yuan et al. 2012.
In this study, we aim at showing the benefits of using ML in the cement production process. To do so, we collected data from a cement plant and used ML to develop a prediction model for clinker quality parameters. Our focus was on using ML to predict Free Lime (f-CaO) in clinker production, since this metric is crucial to ensure the clinker has the right quality (Mtarfi et al. 2017). Currently, f-CaO measurements are carried out via laboratory testing, which results in a 2-4h delay from the production

window – with no viable solution for f-CaO prediction available in the market. There are several methods to measure f-CaO in clinker, e.g. Loss on ignition (LOI) and Titration method. All of these require sample collection and preparation, imposing limitations on the frequency at which f-CaO data is sent back to control systems.

2. Digitalisation applied to cement production

Our selected dataset contains 1096 f-CaO samples, representing three months of production data. The dataset has been inspected to identify outliers and whether the f-CaO datapoints were evenly distributed, see Table 1. Also, to assess the trained models' performances, we compare their results to the baseline model, which is a simple, fast, and reliable method that just uses the last known value as a prediction. This helps us measure how well our models perform compared to not doing anything. The models' performance metrics used in this study include Mean Absolute Error (MAE), Root Mean Square Error (RMSE), Trend Error (TE), and the Coefficient of Determination (R2).

Table 1. Dataset: f-CaO regions and Baseline model performance.

Limits	Boundaries [%]	# Datapoints	Baseline model	
Very Low	0.01 – 1.00	217	MAE	0.41
Low	1.00 - 1.30	258	RSME	0.64
Medium	1.30 - 1.80	368	TE	0.48
High	1.80 - 2.50	173	R2	0.36
Very High	2.50 – 8.00	80		
Total	0.01 – 8.00	1096		

The ML model types were selected to enable the exploration of diverse foundational functionalities, i.e. ensemble, forecasting, non-parametric and neural networks. Within each functionality, we selected model types with the highest potential for the given application (f-CaO prediction) using a supervised learning. The selected models and characteristics thereof are listed in Table 2. For all models, we used a time-series split method to divide the data into training and testing sets. This method is similar to a random split, but it ensures that the testing data is always more recent than the training data. This is a better way to evaluate the model's ability to make predictions, since in real life we cannot train a model using future data.

Table 2. ML models evaluated for f-CaO prediction in cement production.

Model	Type	Description
ARIMAX (Anggraeni et al. 2017)	Ensemble	Auto-Regressive Integrated Moving Average with EXogenous variables (ARIMAX) is widely used model for forecasting. The model incorporates information on previous values to model the temporal structures in time-series data. Advantages: easy to test / implement; widely used; designed to model time-series.
GP (Rasmussen, 2004)	Forecasting	Gaussian Process (GP) is a supervised method of solving regression problems in a probabilistic manner, utilizing kernels. This, however, requires some tuning, and the models can at times be computationally heavy. Advantages: versatility due to the use of kernels; direct interpolation of observations; estimation of noise distribution.
RF (Kam, 1995)	Non-parametric	Random Forest (RF) is a learning algorithm using fully grown trees in parallel (low bias, high variance). RF creates a large number of trees based on bagging. The basic idea is to resample the data over and over and train a new classifier for each sample. Advantages: easy to implement; fast training of models.
XGBoost (Zheng and Wu, 2019)	Neural Network	EXtreme Gradient Boosting (XGBoost) is a learning algorithm that uses weak learners boosted sequentially. It uses ensemble of weak learners (shallow trees/decision stumps) as base learners; while reducing variance, since multiple models are used (bagging), and bias by learning from subsequent models (boosting). Advantages: easy to implement; fast training of models.

3. Results and discussions

The models' performance metrics and corresponding f-CaO predictions of are shown in Table 3 and Figure 1, respectively. The overall trend showcasing the improvement of the model Coefficient of Determination (R^2) as the function of training data size is depicted in Figure 1 – all other metrics are omitted for the sake of brevity. Note that, while the models were trained with various dataset splits, the metrics from Table 3 relate to their performance when trained with 90% of dataset as training data.

Table 3. ML models performance (90% training data).

Model	MAE	RMSE	TE	R2
ARIMAX	0.20	0.26	0.73	0.71
GP	0.30	0.38	0.73	0.45
RF	0.26	0.37	0.64	0.64
XGBoost	0.25	0.35	0.66	0.60
Baseline	0.41	0.64	0.48	0.36

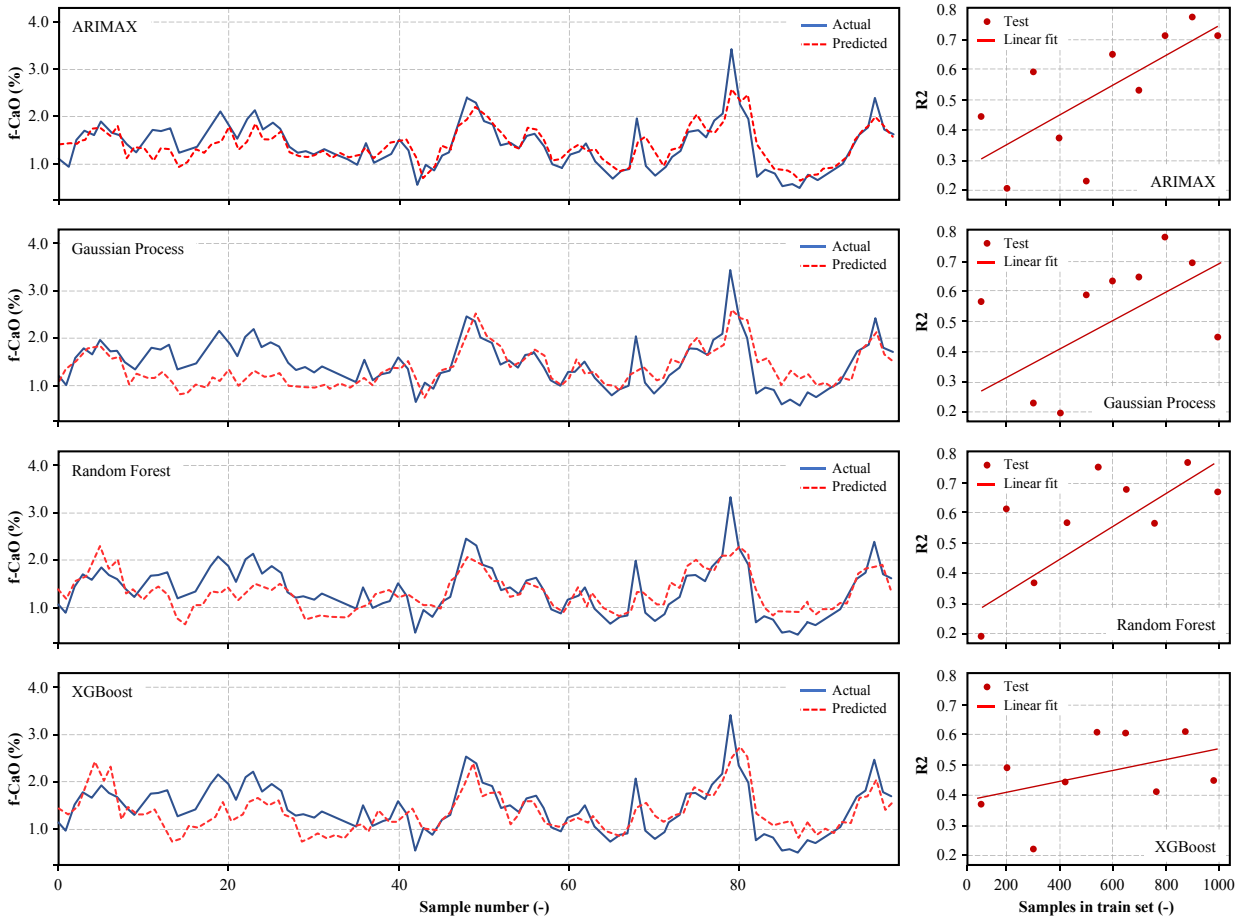


Figure 1. Model predictions and change in Coefficient of Determination (R^2) as a function of the training data size.

Table 3 shows that the ARIMAX model has the best performance when the R^2 coefficient is used the reference metric; nonetheless, the same model has the lowest performance from a RMSE standpoint. In fact, the ARIMAX model seems to perform better when predicting low f-CaO values. The same behaviour is observed for the RF and XGBoost models even if their metrics are slightly lower than that from ARIMAX. The GP model, conversely, performs poorly when in the low f-CaO domain, though it seems to follow the overall data trend with a slight drift – indicating that there is still much to be gained from model tuning. Altogether, the XGBoost presented the best-rounded average on the parameters after all the tests; as such, this is the preferred option to carry out an industrial site test.

Notice, however, that all models can be further optimised. The strategies to optimise the models include e.g. dedicated analysis of feature extraction and alignment, feature selection, and a hyper-parameter optimisation. These are expected to enable an overall improvement on RMSE by 10-30%. Also, note that the modelled process is variable between plants; thus, the inclusion of self-adapting features will likely ensure the more accurate predictions when compared to the current ones.

4. Conclusions

In this article, we demonstrated the use of ML models to predict f-CaO in clinker production. While the first iterations of the developed models still require further tuning to improve the prediction accuracy, our results serve as a steppingstone for the development of advanced control models with self-adapting capabilities, provided that enough production data is available for training. So far, the XGBoost model presented the best-rounded average on the parameters after all the tests, though the inclusion of additional refinements has been identified as necessary to increase the accuracy of the predictions.
It is important to bear in mind that since a) the physical sample sizes of material collected for material characterization are relatively small when compared to a cement plant's production rates, b) the sampling rate is relatively low, and c) the process relatively dynamic, there will always exist a level of uncertainty in the model prediction, thus the prediction can never be more accurate than the observation noise allows. In any case, this does not exclude the potential in developing models for predicting several quality metrics of cement in the production process rather than solely relying on irregular experimental characterisation.

References

A. Kamalloo, Y. Ganjkhanlou, S.H. Aboutalebi, H. Nuranian. (2010) "Modeling of compressive strength of Metakaolin based geopolymers by the use of artificial neural network. International Journal of Engineering, Transactions A: Basics. 23(-):145-152.

C.E. Rasmussen. (2004). Gaussian Processes in Machine Learning. In: Bousquet, O., von Luxburg, U., Rätsch, G. (eds) Advanced Lectures on Machine Learning. ML 2003. Lecture Notes in Computer Science, vol 3176. Springer, Berlin, Heidelberg.

H. Zheng, Y. Wu. (2019) "XGBoost Model with Weather Similarity Analysis and Feature Engineering for Short-Term Wind Power Forecasting". Applied Sciences 9(15):3019.

J. Yuan et al. (2012) "Prediction of free lime content in cement clinker based on RBF neural network." Journal of Wuhan University of Technology-Mater. Sci. Ed. 27: 187-190.

K.S. Stadler, J. Poland, E. Gallestey. (2011) "Model predictive control of a rotary cement kiln". Control Engineering Practice 19(1):1-9.

M.G. Plaza, S. Martínez, F. Rubiera. (2020) "CO_2 Capture, Use, and Storage in the Cement Industry: State of the Art and Expectations". Energies 2020, 13, 5692.

McKinsey & Company. (2022) "The 21st-century cement plant: Greener and more connected". Available at: https://www.mckinsey.com/industries/chemicals/our-insights/the-21st-century-cement-plant-greener-and-more-connected (Accessed on: August 2022).

M. A. Abubakar, A.S. Maihula, M.B. Jibril, A. Bashir. (2019) "Artificial Neural Network for forecasting the Initial Setting Time of Cement Pastes". International Journal of Recent Engineering Science, 6(4),13-17

N. H. Mtarfi, Z. Rais, M. Taleb. (2017) "Effect of clinker free lime and cement fineness on the cement physicochemical properties". Journal of Materials and Environmental Sciences 2017 JMES, 8(7):2541-48.

T. Watari, Z. Cao, S. Hata et al. (2022) "Efficient use of cement and concrete to reduce reliance on supply-side technologies for net-zero emissions". Nat. Commun. 13, 4158.

T.K. Ho (1995). Random Decision Forests (PDF). Proceedings of the 3rd International Conference on Document Analysis and Recognition, Montreal, QC, 14–16 August 1995. pp. 278–282.

W. Anggraeni, K.B. Andri, Sumaryanto, F. Mahananto. (2017) "The Performance of ARIMAX Model and Vector Autoregressive (VAR) Model in Forecasting Strategic Commodity Price in Indonesia". Procedia Computer Science 124(-):189-96.

The 16th International Congress on the Chemistry of Cement 2023 (ICCC2023)
"Further Reduction of CO_2 -Emissions and Circularity in the Cement and Concrete Industry"
September 18–22, 2023, Bangkok, Thailand

Method of Intensifying Cement Clinker Production

T. Staněk[1*], I. Khongová[1], A. Zezulová[1], A. Rybová[1] and M. Boháč[1]

[1] *Research Institute for Building Materials, Brno, Czech Republic*
Email: stanek@vush.cz, khongova@vush.cz, zezulova@vush.cz, rybova@vush.cz, bohac@vush.cz

ABSTRACT

The reduction of CO_2 emissions is one of the main themes of the present day, even in the case of cement production. One of the possibilities is to reduce the energy demand during clinker burning. A reduction in burning temperature due to chemical additives can contribute to this. The paper deals with the combined addition of lithium and sulfur compounds, which reduce the burning temperature by 100 to 150 °C. Both elements significantly affect the clinker melt's physical parameters, and sulfur stabilizes the more hydraulically active monoclinic modification of alite M_1. In addition, cement made from this clinker shows a significant increase in early strength compared to ordinary Portland cement. The compressive strengths after 1 day are about 100 % higher and after 2 days about 50 % higher than the reference Portland cement CEM I. It would allow a reduction of the clinker content in blended cements and thus further reduce CO_2 emissions. X-ray diffraction analysis and optical microscopy methods were mainly used for the research.

KEYWORDS: *clinker, intensifying, lithium, sulfur, low-energy*

1. Introduction

One way to reduce CO_2 emissions, which is also addressed in this paper, is using mineralisers to develop new types of clinkers that can be burned at lower temperatures with reduced energy consumption. In this case, it is the intensification of cement production by adding compounds containing lithium and sulphur, which will reduce the viscosity of the clinker melt and the burning temperature by up to 150 °C.
Today, our finding that a monoclinic modification of M_1 alite has higher hydraulic activity and higher compressive strengths than M_3 modifacation (Staněk and Sulovský (2002)) is now generally accepted and confirmed by many works (Li et al. (2012)). One factor that supports the formation of M_1 modification is the increased content of SO_3 in the clinker. SO_3 reduces the temperature of clinker melt formation and affects its viscosity and surface tension (Osokin and Potapova (1986, 1989a, 1989b)). In combination with other cation-forming elements that have intensifying effects, such as Li, the clinker melt can be affected even more dramatically. Lowering the viscosity and surface tension by combining lithium with sulfur will reduce the nucleation of the alite crystals and increase their growth rate, another factor promoting the formation of the M_1 modification. Smaller amounts of alite crystals will form and grow to larger sizes. The crystals will be defective and hydraulically active. The burning of normal alite clinker could then take place at even lower temperatures, around 1300 °C.
Lithium might behave differently from sodium or potassium because it tends to form a relatively nonvolatile oxide at elevated kiln temperatures (Bhatty (1995)). Li_2CO_3 addition decreases the decomposition temperature of $CaCO_3$ in a two-step process. When the addition of dopant is 1 %, CaO formed at low temperature reacts with SiO_2 to form the β-C_2S even at 750 °C. The reaction is completed at 1350 °C forming β-C_2S and small amounts of γ-C_2S. 5% of dopant decreases the reaction temperature to 1290 °C; the reaction products are β-C_2S and small amounts of C_3S (Kolovos et al. (2002)).
Small amounts of Li_2O were reported to improve the reactivity of the raw meal by lowering the temperature of the initial melt formation. However, if the concentration of Li_2O exceeds 1%, the combination of free lime is impaired, and the conversion of C_2S to C_3S is inhibited (Bhatty (1995), Mathur et al. (1992)). Studying the effect of various cation-forming oxides on the reactivity of the system

$CaO-SiO_2-Al_2O_3-Fe_2O_3$, a notably positive effect of Li_2O and CuO at 1200 °C has been monitored by the free lime content after burning under the same defined conditions (Saraswat et al. (1986)).
Kolovos et al. (2005) examined the addition of 2.5 % Li_2O into clinker raw meal. After sintering at 1450 °C, the samples were examined using SEM. Distinct differences compared to reference clinker were observed, specifically the size and shape of belite grains and alite crystals were very coarse. Li oxides easily form eutectic mixtures with SiO_2 and a unique belite configuration is formed.
Recent studies (Staněk et al (2018, 2019)) have confirmed the negative effect of lithium on alite formation, alite decomposition into a microcrystalline mixture of belite and free lime, depending on its content in clinker and the cooling rate. Nevertheless, cement was prepared from clinker with a content of 1 wt. % Li_2O at 1350 °C, which showed normal technological parameters as OPC.

2. Preparation and methods

A raw meal was prepared from ordinary cement raw materials to investigate the effect of the combination of the two oxides Li_2O and SO_3 on the phase composition of clinker. Silica sand was used to correct the lime saturation. The composition of the primary raw meal is given in Table 1.

Table 1. Composition of primary raw meal [wt. %]

Component	Content
Pure limestone	52.21
Contaminated limestone	27.48
Clay shale	16.02
Fe correction	1.51
FGD gypsum	0.82
Silica correction	1.96

The mixture of raw materials was ground in a laboratory ball mill. Chemically pure Li_2CO_3 was used as the lithium source and $(NH_4)_2SO_3$ as the sulfur source. Four raw meals were prepared with SO_3 contents of 1 and 3 wt. % and Li_2O contents of 0.25 and 0.75 wt. %. From the raw meals, tablets of 50 g and 40 mm in diameter were moulded and subjected to equilibrium burning in a superkanthal furnace. The burning was carried out on a Pt plate with a temperature rise of 10 °C/min firstly to 1400 °C with repeated grinding and tabletting and inserting back to the kiln at 1400 °C and continuing to 1450 °C with a dwell time of 4 hours. The phase composition of the clinkers was determined by X-ray diffraction analysis on a Bruker D8 Advance apparatus with a Cu anode ($\lambda K\alpha$ = 1.54184 Å) and variable divergence apertures at Θ-Θ reflection Bragg-Brentano para-focusing geometry. Quantitative phase analysis was determined by the Rietveld standardless method using Topas software. The area around the 2θ angle of 32° and 52° was examined to identify the alite modifications (Maki and Kato (1982)).
In the next stage, raw meals in the amount of 3 kg of doped Li_2O and SO_3 were prepared from common cement raw materials listed in Table 1. The compounds $CaSO_4$, $2H_2O$ and Li_2CO_3 were used for the by-product oxide doping. The raw materials were milled to fineness characterised by a residue on a 0.09 mm sieve: 13-16 wt. %. Tablets were moulded and burned at temperatures from 1300 to 1350 °C with the rate of 10°C/min and residence time 60-120 minutes. The clinkers were characterised by chemical analysis, the phase composition was analysed by microscopic point counting (Chromý (1978)) on a polished section etched with acetic acid fumes (Chromý (1974)). The specific gravities for the recalculation to weight percentages were: C_3S - 3.15; C_2S - 3.28; C_3A - 3.03; C_4AF - 3.77; free CaO - 3.35 $g.cm^{-3}$.
The burned clinkers were ground in a laboratory ball mill with the addition of 2 wt. % gypsum as a setting regulator with approximately the same specific surface area of 400 m^2/kg. The specific surface was determined by the permeable method of Lea and Nurse according to British Standard BS 12: 1958.
Cement samples were tested for normal consistency and setting (EN 196-3) and compressive strength (EN 196-1) after 1, 2, 28 and 90 days of hydration.

3. Results and discussion

The quantitative X-ray diffraction (QXRD) of the burned clinkers determined is given in Table 2. The results show that for the same Li_2O content, with an increase in SO_3 content, there is a decrease in alite

content, an increase in belite content and the appearance of free CaO and anhydrite. At a Li_2O content of 0.75 wt. %, Li_4SiO_4 appears. In all cases, alite modification appears to be M_1, the formation of which is promoted by SO_3 (Maki and Goto (1982), Staněk and Sulovský (2017)).
A summary of the characterising parameters of clinker and cement samples is shown in Table 3 including comparison with the CEM I 42.5 R. The determination of Li_2O content in clinker confirms the literature data (Bhatty (1995)) that lithium oxide is nonvolatile at these temperatures. An example of the microstructure of the doped clinker S4Li0.2AR is shown in Fig. 1.

Table 2. QXRD of equilibrium burned Li and S doped clinkers in %

Phase	0.25Li 1S	0.25Li 3S	0.75Li 1S	0.75Li 3S
C_3S (M_1)	70.0	62.1	66.0	65.3
ß-C_2S	18.1	25.7	17.6	18.9
C_3A cub.	3.3	3.4	0.1	2.3
C_3A orth.	0.0	0.1	0.8	1.1
C_4AF	8.6	7.4	10.6	7.8
Free lime	-	-	4.9	3.2
Anhydrite	-	1.3	-	1.4
Li_4SiO_4	-	-	trace	trace

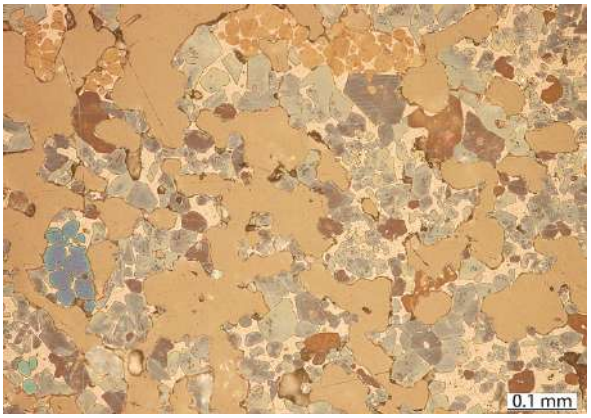


Fig. 1: Microstructure of S4Li0.2AR clinker, brown belite clusters (at the top), blue clusters of free CaO (left part), alite forms light blue to dark brown crystals, beige areas - pores closed by epoxy (reflected light, polished surface was etched in fumes of acetic acid)

Table 3. Parameters of Li and S doped clinkers and cements (Note on designation of samples: S – SO_3, Li –Li_2O, number – theoretical content in clinker, AR – a lower alumina ratio)

Cement	S4Li0.2AR	S4Li0.2	S3Li0.2	S3Li0.1	S4Li0.4	CEM I 42.5 R
Phase	**Phase composition of clinker [wt. %]**					
C_3S	58.3	67.5	40.2	48.2	42.8	69.6
C_2S	23.1	17.4	31.8	25.3	29.4	11.2
C_3A	2.9	3.2	8.7	9.6	10.8	8.7
C_4AF	13.0	10.5	12.4	10.8	10.8	9.0
C_{vol}	2.7	1.4	6.9	6.1	6.2	1.5
Parameter	**Chemical parameters of clinker**					
Li_2O [wt.%]	0.23	0.23	0.23	0.13	-	-
SO_3 [wt.%]	3.51	3.61	2.85	2.71	-	-
LSF [%]	102.0	103.6	100.1	99.8	-	-
SR	2.58	2.98	2.79	2.94	-	-
AR	1.16	1.57	1.65	1.69	-	-
Parameter	**Temperature and burning time [°C, min]**					
Temperature	1325	1325	1350	1330	1300	-
Burning time	120	120	60	120	120	-
Parameter	**Specific surface of cement [m^2/kg]**					
Specific surface	401	401	401	401	406	397
Hydration time	**Compressive strength [MPa]**					
1 day	33.6	36.3	26.7	29.2	29.9	18.7
2 days	36.1	40.8	32.6	36.0	32.8	27.3
28 days	51.5	53.9	51.1	54.3	49.7	49.3
90 days	57.0	61.5	57.0	58.9	52.2	60.2
Parameter	**Other technological parameters [%, min, min]**					
Normal consistency	29.0	28.7	29.3	29.0	30.7	29.7
Initial setting time	90	120	120	130	100	200
Final setting time	110	140	150	170	150	340

The combination of SO_3 and Li_2O oxides causes a decrease in the clinker melt formation temperature and viscosity, thus increasing the growth rate of clinker phase crystals, disturbing their crystal structure and increasing clinker hydraulic activity. It has also been found to promote the formation of monoclinic modification of alite M_1, which has higher hydraulic activity than the more common M_3 modification

(Staněk and Sulovský (2002)). Cements prepared from this clinker have compressive strengths up to 100 % higher than conventional Portland cement CEM I 42.5 R after 1 day and up to 50 % higher after 2 days of hydration. The long-term 90 days strengths of this cement have typical values. According to the appearance of the diffraction lines of the CEM I 42.5 R near the 32 and 52° 2θ angle reported by Maki and Kato (1982), the M_3 modification significantly dominates.

4. Conclusions

The effect of the combined addition of lithium and sulphur compounds on the clinker's phase composition and the cement's technological properties was tested under laboratory conditions. The hypothesis that alite clinker can be formed at lower temperatures than in conventional industrial production using these mineralisers and that alite in clinker is in more hydraulically active M_1 modification was verified.
This combined intensification will provide a reduction in the burning temperature of the clinker by 100 to 150 °C compared to the normal condition and an increase in the initial strengths of the cement produced from it by 50 to 100 % compared to conventional CEM I Portland cement. The increase in strength is probably caused by the stabilization of the M_1 modification and the rapid growth of defective alite crystals due to the reduced viscosity and surface tension of the melt due to the addition of Li and S.
In practice, sulphur-containing waste raw materials such as fluidised bed ash and FGD gypsum, and wastes from lithium mining and production could advantageously be used in cement raw meal.

Acknowledgements

This research was carried out within project No. 23-05082S, financed by the Czech Science Foundation.

References

Bhatty, J.I. (1995) *Role of Minor Elements in Cement: Manufacture and Use*, PC Association, Skokie.
Chromý, S. (1978) "Accuracy and precision of microscopic quantitative phase analysis of Portland clinkers" (in Czech), *Silikáty,* 22(3): 215-226
Chromý, S. (1974) "Anfärben des freiem CaO und Silikate in anschliffen von Portlandklinker", *Z-K-G*, 27(2): 79-84
Li, X., Huang, H., Xu, J., Ma, S. and Shen, X. (2012) "Statistical research on phase formation and modification of alite polymorphs in cement clinker with SO3 and MgO ", *Construction and Building Materials,* 37: 548-555
Kolovos, K., Tsivilis, T. and Kakali, G. (2002) "The effect of foreign ions on the reactivity of the CaO-SiO_2-Al_2O_3-Fe_2O_3 system" Part II: Cations, *Cement and Concrete Research,* 32(3): 463-469
Kolovos, K., Tsivilis, T. and Kakali, G. (2005) "SEM examination of clinkers containing foreign elements", *Cement and Concrete Composites,* 27(2): 163-170
Maki, I. and Goto, K. (1982) "Factors influencing the phase constitution of alite in Portland cement clinker", *Cement and Concrete Research* 12(3): 301–308
Maki, I. and Kato, K. (1982) "Phase identification of alite in portland cement clinker", *Cement and Concrete Research*, 12(1): 93-100.
Mathur, V.K., Gupta, R.S. and Ahluwalia, S.C. (1992) "Lithium as intensifier in the formation of C_2S phase", *Proc. 9th ICCC*, vol. 1, Delhi, India, 406-412
Osokin, A.P. and Potapova, E.N. (1986) "Alitbildung in zusammengesetzten Oxid-Salz-Schmelzen", *Silikattechnik,* 37(3): 79-80
Osokin, A.P. and Potapova, E.N. (1989a) "Alitbildung in Oxid-Salz-Schmelzen. Struktur und Eigenschaften der flüssigen Klinkerphase", *Silikattechnik,* 40(1): 4-6
Osokin, A.P. and Potapova, E.N. (1989b) "Alitbildung in Oxid-Salz-Schmelzen. Entmischungserscheinungen in Schmelzen", *Silikattechnik*, 40(5): 149-153
Saraswat, P. Mathur, V.K. and Ahluwalia, S.C. (1986) "Thermal studies of the $CaCO_3$:SiO_2 (2:1) system containing lithium as dopant", *Termochim Acta,* 97: 313-320
Staněk, T., Rybová, A., Zezulová, A. and Boháč M. (2018) "Properties of cement with increased lithium content", *Proc. SynerCrete'18,* Funchal, Portugal, *RILEM Proceedings* PRO 121, Paris, France, Vol. 1: 297-302
Staněk, T., Rybová, A., Zezulová, A. and Boháč M. (2019) "Formation of Clinker Containing Lithium", *Materials Science Forum*, vol. 955: 50-55
Staněk, T. and Sulovský, P. (2002) "The influence of the alite polymorphism on the strength of the Portland cement", *Cement and Concrete Research*, 32(7): 1169-1175
Staněk, T. and Sulovský, P. (2017) "The Impact of Basic Minor Oxides on the Clinker Formation", *Materials Science Forum*, vol. 908: 3-9

The 16th International Congress on the Chemistry of Cement 2023 (ICCC2023)
"Further Reduction of CO_2 -Emissions and Circularity in the Cement and Concrete Industry"
September 18–22, 2023, Bangkok, Thailand

Piezoresistive performance of GNP-modified highly deformable cementitious materials

N.X. Dang[1], Q. Zeng[1, 2*], and W.J. Zhao[1, 2]

[1] *College of Civil Engineering and Architecture, Zhejiang University, Hangzhou, China*
E-mail:12012079@zju.edu.cn (N.X. Dang); cengq14@zju.edu.cn (Q. Zeng)
[2] *Center for Balance Architecture, Zhejiang University, Hangzhou, China*
Email: cd@xxx.com

ABSTRACT

In-situ polymerization of materials can greatly improve the deformability of cementitious composites. The air-entrainment phenomenon that accompanies such process limits the application of polymers in cementitious materials. However, nanofillers could enable the application of in-situ polymerization in the construction industry. In this work, sodium acrylate was in-situ polymerized in cement mortars, while the conductive graphene nanoplatelets (GNP) were used as fillers. The mechanism of combining the two materials in cement-based materials is still not clear. Herein, GNP particles were used as conductive fillers in the dosage of 0.4 wt%, while the in-situ polymerized sodium acrylate (iPSA) was employed in the dosages of 0%, 2 wt%, 4 wt%, 6 wt% and 8 wt% to fabricate cementitious composites. The water-to-cement (w/c) ratio was 0.4 in all mixes. Because GNP particles are highly conductive, four-probe method was used to test piezoresistivity of the GNP-modified highly deformable cement-based composites. Scanning electron microscopy (SEM) was employed to study the microstructure of the fabricated composites. The enhancement mechanisms of piezoresistive by GNP on highly deformable cementitious materials were discussed. This research would provide a broad prospect for the application of structural health monitoring (SHM) in cement-based materials.

KEYWORDS: *GNP, In-situ polymerization, Piezoresistivity, Microstructure*

1. Introduction

Nano conductive fillers (NCF) have outstanding enhancement potentials of piezoresistivity of cementitious composites (Lan et al. 2018). Graphene nanoplatelets (GNP) are a great candidate as NCF owing to their excellent physical and mechanical properties, electric performance and carrier mobility (Dong et al. 2021). However, the GNP-modified cement composites are often fragile and easy to crack (Weis et al. 2019), hence, they are not widely used as a construction material. Polymers are known for their deformability improvement when added in cementitious systems (Hao et al. 2020, Chidiac et al. 2021). Therefore, the combined effect of GNP and polymers in cement-based materials could be an attractive option to produce highly deformable conductive cementitious composites. GNP-modified cement composites exhibit a high fragility and require the use of polymers (Safaei et al. 2015). Yet, the required dosage of polymers has a significant impact on the deformability of cementitious composites (Xu et al. 2022).

At present, with the continuous development of polymer industry, redispersible polymers such as styrene-butadiene rubber (SBR), epoxy resin (EP) and polyacrylate (PA) can be directly mixed with cement to make deformable cement-based materials (Pang et al. 2021). However, polymers are not always compatible with the hydration of cement clinker, which indicates a negative impact on the performance of macro structures (Chen et al. 2020). According to Liu et al. (2021), the use of in-situ polymerization could effectively improve the compatibility of polymers with cement-based materials. Therefore, the impact of dosages of

sodium acrylate (SA) on piezoresistivity and deformability of GNP-modified deformable cement composites (GNP-DCC) was discussed. Moreover, the mechanisms of piezoresistive enhancement on highly deformable cementitious materials in the presence of polymers were highlighted.

2. MATERIALS AND METHODS

2.1 Materials

Ordinary Portland cement (OPC) PI 42.5 and GNP powder purchased from XFNANO (Nanjing, China) were used. As a dispersant of GNP, melamine obtained from BASF Chemical Company (Germany) was used. Acrylic acid (AA) was purchased from Macleans Biochemical Technology Co., Ltd. (Shanghai, China), and sodium hydroxide (NaOH), ammonium persulfate (APS) and sodium bisulfite (SBS) were provided by Sinopharm Chemical Reagent Co., Ltd. (Shanghai, China). N,N'-methylene bisacrylamide (MBA) was obtained from China Shanghai Da Rui Fine Chemical Co., Ltd. (Shanghai, China). The water-to-cement (w/c) ratio was fixed at 0.4 for all mixes. Specimens with polymer-to-cement (m/c) ratios of 0%, 2%, 4%, 6% and 8% and a constant GNP dosage of 0.4 % were designed and labeled as SG-0, SG-2, SG-4, SG-6 and SG-8, respectively. Mixing proportions are presented in Table 1.

Table 1. Mix proportions (g)

Specimen	Cement	Water	AA	NaOH	APS	SBS	MBA	GNP	Dispersant
S-0	1000	400	0	0	0	0	0	0	0
SG-0	1000	400	0	0	0	0	0	3.5	1.75
SG-2	1000	400	15.3	20	0.5	0.5	0.02	3.5	1.75
SG-4	1000	400	30.6	40	1	1	0.04	3.5	1.75
SG-6	1000	400	45.9	60	1.5	1.5	0.06	3.5	1.75
SG-8	1000	400	61.2	80	2	2	0.08	3.5	1.75

2.2 Methods

Firstly, melamine dispersant was dissolved in distilled water, and GNP powder was gradually put into the melamine solution. After that, the GNP suspension was stirred with a tip ultrasonicator (Jiekang CE-9600, 70W) for 2 h. Then, NaOH was dissolved in the GNP suspension, and AA was added dropwise to obtain a mixed solution of GNP and SA. Note that the neutralization reaction between NaOH and AA was carried out in ice water (about 0 ^{o}C) to control the temperature of the mixed solution of GNP and SA and avoid the immediate SA polymerization. At the same time, the initiators (APS, SBS and MBA) were mixed with cement and stirred at low speed for 1 minutes before adding the GNP-SA solution. After mixing for 2 min, the fresh GNP-DCC slurries were cast into prism molds with the dimensions of 160 $\times$ 40 $\times$ 40 mm^3. Four copper electrodes with a size of 40 $\times$ 60 mm^2 were buried at fixed positions of each specimen during casting. After 24 h, specimens were demolded and stored in a standard curing condition (temperature 20$\pm$ 2◦C, relative humidity > 95%).

The piezoresistivity was tested by four-probe method after 7 d. A triangular-wave cyclic loading scheme (from 0 to 18.75 MPa) was designed. The signals of fractional resistance change (FCR) and strain ε of specimens were recorded. The piezoresistivity was presented by gauge factor (GF) which is expressed as:

$$GF = \frac{FCR}{\varepsilon} \tag{1}$$

The microstructure was observed by a scanning electron microscopy (SEM) after 27 d of curing. A plasmaspraying process was used to coat a gold film on each pre-dried GNP-DCC sample to enhance conductivity and visualization of the SEM images.

3. RESULTS AND DISCUSSION

3.1 Piezoresistivity and deformability of GNP-DCC specimens

Figure 1 demonstrates the results of the piezoresistivity and compression tests. The test setup of the four-probe method and the GF values are given in Figure 1a. When 0.4% of GNP were added to the mix SG-0 (no polymers), the GF value of the specimens increased by 163.3% compared with S-0. However, the use of polymers in the mixtures had the opposite effect, where the piezoresistivity of the polymer-modified specimens decreased with the increasing content of SA. The GF values of SG-2 and SG-4 were close to one another, showing an increase of nearly 56.3% and 60.3% compared with S-0, respectively. The GF values of higher polymer-to-cement ratios, namely SG-6 and SG-8, were 48.4% and 66.4% lower than that of S-0, respectively. Compression test setup and the compressive strain of the GNP-DCCs are displayed in Figure 1b. The specimens containing GNP shows a increase of deformable perfoemance. The strain of SG-0 increased by 38.9 % compared with S-0. With the addition of SA, the compressive strain of GNP-DCC specimens increased. For example, the strain of SG-4 increased by 65.6 % compared with S-0 and 19.3 % compared with SG-0. Slight increases in strain were observed for SG-2, SG-6 and SG-8 (by 9%, 23% and 22%, respectively). The reduction in compressive strain for SG-2, SG-6, and SG-8 may be induced by the large defects and/or pores due to the higher polymer content (see the pore structure evidence by SEM, Section 3.2).

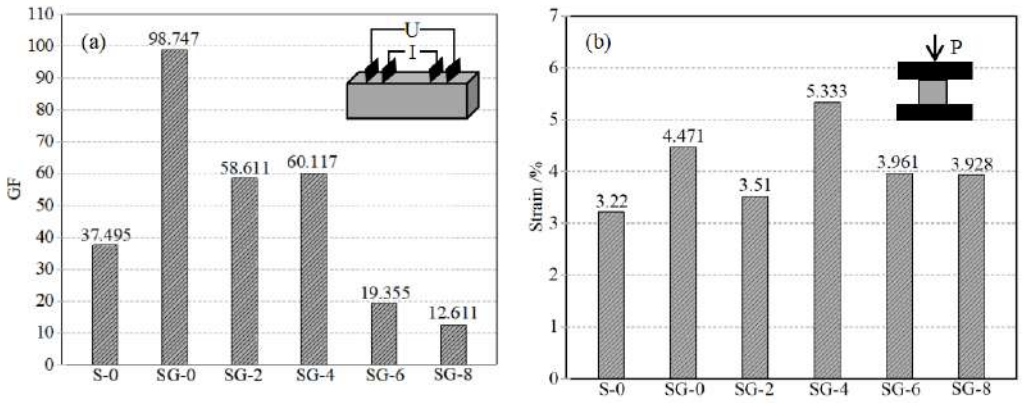


Figure 1. (a) GF of GNP-DCC specimens and arrangement of four-probe piezoresistive test, and (b) compressive strain and compression test setup of the GNP-DCC specimens.

3.2 SEM tests

Figure 2 demonstrates the typical micro morphology of the fractured GNP-DCC surfaces of small samples taken from SG-2, SG-4 and SG-6 specimens and the proposed mechanisms of piezoresistivity.

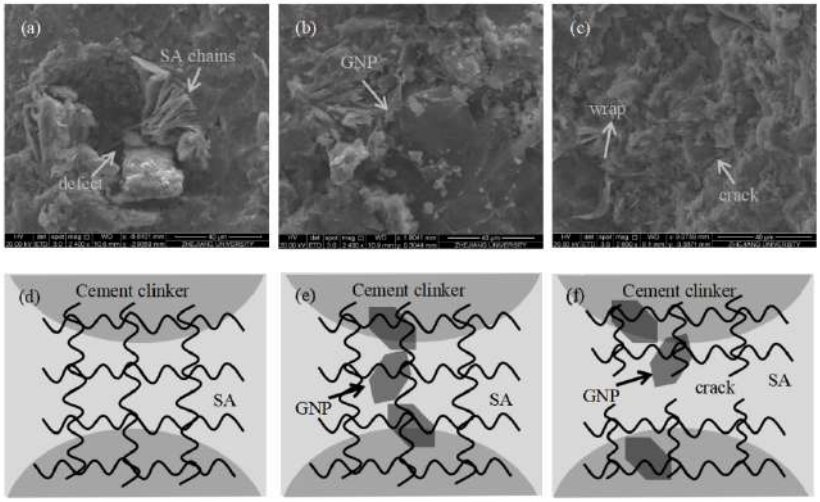


Figure 3 SEM images for matrix and hydrated products of (a) SG-2, (b) SG-4, (c) SG-6, and (d-f) mechanisms of piezoresistivity of GNP-DCC specimens.

SG-2 and SG-6 showed defects and cracks in their microstructures (Figure 2a and c), which may be attributed to the reduction in compressive strain (Ha et al. 2021). GNP sheets and SA chains can be observed in the micro morphology of the GNP-DCC samples (Figure 2b).

Figure 2d, e and f display schematic illustrations of the piezoresistivity mechanisms of different GNP-DCC specimens. Interaction between the cement matrix with the SA chains is observed in Figure 2d. It has been reported that the SA chains between cement clinkers could improve the deformability of GNP-DCCs (Xu et al. 2022). However, when GNP was added, the GNP particles in the cement composites form conductive paths (Figure 2e), which change the piezoresistivity behavior of GNP-DCC specimens (Jia et al. 2017). The excessive use of polymers in polymer-modified cementitious materials weakens the microstructure and facilitates the creation of defects and cracks that hinder the conductive paths of GNP particles.

4. Conclusions

GNP particles shows promising potentials owing to their electric properties which resulted in good piezoresistivity of cement composites. The results of this work showed that the addition of GNP in cement composites would improve the deformability sightly. The use of in-situ polymerization could decrease fragility and increase deformability of GNP-DCC. High SA content would decrease the piezoresistivity of GNP-DCC. The optimum mixture, however, was SG-4 indicating increase on both piezoresistivity by 60.3% and deformability by 65.6%.

References

Lan, C., Xiao, H., Liu, M., Wang, G., & Ma, M. (2018). Improved piezoresistivity of cement-based composites filled with aligned nickel powder. Smart Materials and Structures, 27(9), 095003.

Dong, W., Li, W., Wang, K., & Shah, S. P. (2021). Physicochemical and Piezoresistive properties of smart cementitious composites with graphene nanoplates and graphite plates. Construction and Building Materials, 286, 122943.

Weis, Johan Ek, Sophie Charpentier, and Aleksandra Kempinska. "Graphene Research and Advances Report December 2019." (2017)

Pan, H., She, W., Zuo, W., Zhou, Y., Huang, J., Zhang, Z., ... & Liu, J. (2020). Hierarchical toughening of a biomimetic bulk cement composite. ACS Applied Materials & Interfaces, 12(47), 53297-53309

Xu, C., Dai, Y., Peng, Y., Wang, J., Zhang, Z., Gui, Q., & Zeng, Q. (2022). Multi-scale structure of in-situ polymerized cementitious composites with improved flowability, strength, deformability and anti-permeability. Composites Part B: Engineering, 245, 110222

Safaei, M., Sheidaei, A., Baniassadi, M., Ahzi, S., Mashhadi, M. M., & Pourboghrat, F. (2015). An interfacial debonding-induced damage model for graphite nanoplatelet polymer composites. Computational Materials Science, 96, 191-199

Chidiac, S. E., Mihaljevic, S. N., Krachkovskiy, S. A., & Goward, G. R. (2021). Characterizing the effect of superabsorbent polymer content on internal curing process of cement paste using calorimetry and nuclear magnetic resonance methods. Journal of Thermal Analysis and Calorimetry, 145, 437-449.

Pang, B., Jin, Z., Zhang, Y., Liu, Z., She, W., Wang, P., ... & Gao, S. (2022). Ultraductile Cementitious Structural Health Monitoring Coating: Waterborne Polymer Biomimetic Muscle and Polyhedral Oligomeric Silsesquioxane‐Assisted C‐S‐H Dispersion. Advanced Functional Materials, 2208676

Chen, B., Qiao, G., Hou, D., Wang, M., & Li, Z. (2020). Cement-based material modified by in-situ polymerization: From experiments to molecular dynamics investigation. Composites Part B: Engineering, 194, 108036

Liu, Q., Lu, Z., Hu, X., Chen, B., Li, Z., Liang, R., & Sun, G. (2021). A mechanical strong polymer-cement composite fabricated by in situ polymerization within the cement matrix. Journal of Building Engineering, 42, 103048

Ha, K. H., Zhang, W., Jang, H., Kang, S., Wang, L., Tan, P., ... & Lu, N. (2021). Highly sensitive capacitive pressure sensors over a wide pressure range enabled by the hybrid responses of a highly porous nanocomposite. Advanced Materials, 33(48), 2103320

Jia, X. W., Zhang, X., Ma, D., Yang, Z. F., Shi, C. L., & Wang, Z. (2017). Conductive properties and influencing factors of electrically conductive concrete: A review. Mater. Rep, 31, 90-97.

The 16th International Congress on the Chemistry of Cement 2023 (ICCC2023)
"Further Reduction of CO_2 -Emissions and Circularity in the Cement and Concrete Industry"
September 18–22, 2023, Bangkok, Thailand

Research on the preparation of low-calcium Portland cement

Yuwei Li [1], Ying Ma [1,*], and Xiaodong Shen[1,2,*]

[1,] *College of Materials Science and Engineering, Nanjing Tech University, 211816 Nanjing, PR China*

[2] *The Synergetic Innovation Center for Advanced Materials, 211816 Nanjing, PR China*

Email: lwy19961106@163.com, maying@njtech.edu.cn, xdshen@njtech.edu.cn

ABSTRACT

Portland cement is the most used construction and building material worldwide, which also has the most carbon emissions and the highest consumption of limestone of all cement types. There is a request for the reduction of CO_2 emission in the cement industry by lowering the CaO content of Portland cement clinker to accomplish the national strategic goal of "carbon emission peak and carbon neutrality".
The reduction of CaO content requires the decrease of calcium silicate minerals (C_3S, C_2S) occupied 75% in clinker resulting in the reduction of the compressive strength of cement. This study aims to prepare low-calcium Portland cement through the optimization of calcination conditions and mineral phases. A small amount of ye'elimite is considered to be introduced into clinker to improve the early compressive strength of the cement. The low-calcium Portland cement has a reduction of 5% CaO in clinker and 28 days' compressive strength reaching 50 MPa.
This study details the preparation of low-calcium Portland cement clinker as well as its performance after 3 and 7 days.

KEYWORDS: *low-calcium Portland cement, Clinkering, Calcination conditions, Ye'elimite, Mineral optimization.*

1. Introduction

Carbon emissions reduction in the cement sector is a crucial step in implementing an environmentally friendly approach. It is the main research direction of many cement practitioners to realize the reform of cement industry by reducing the demand phase of calcite (Alite, C_3S) and introducing a new phase (Ye'elimite, $C_4A_3\$$) with low calcination temperature and high early strength (Gartner and Hirao (2015)). The cohabitation of alite and ye'elimite in new cement clinker is now a challenging subject to tackle.
Fluorite, as a flux and mineralizer, can coexist successfully with alite and yeelimite at 1300 ^oC (Altun (1999), De la Torre et al (2011), Hong et al (2007)). The addition of MgO and K_2O can promote the formation of alite and compensate for the decrease in alite production caused by SO_3 (Ludwig and Zhang (2015), Li et al (2012), Li et al (2014), Theodor and Petr (2017)). ZnO can transform coarse alite crystals into fine crystals, thus promoting the formation of alite (Li et al (2015), Pérez-Bravo et al (2014)).
In this study, the doping quantities of MgO, Na_2O, ZnO, CaF_2, and B_2O_3 are fixed, and the effect of K_2O and MnO_2 doping on clinker calcination is investigated. Ion doping and calcination system adjustment were used to study cement clinker containing alite and ye'elimite in a single calcination operation. To give theoretical direction for the development of an ecologically friendly cement sector and the implementation of the national strategy peak carbon dioxide emission and carbon neutrality.

2. Experimental

2.1 Raw materials

The raw materials used in the experiment include calcium carbonate ($CaCO_3$), silicon dioxide (SiO_2), aluminum oxide (Al_2O_3), and gypsum ($CaSO_4 \cdot 2H_2O$), which were all analytical grade reagents. The CaF_2, $ZnSO_4 \cdot H_2O$, K_2CO_3, Na_2CO_3, MgO, MnO_2 and B_2O_3 all from Sinopharm Chemical Reagent Co., Ltd. (Dongguan, China) were studied as mineralizers. Table 1 shows the ICSD collection codes for all clinker phases and design phase composition.

Table 1. ICSD collection codes for all clinker phases and design phase composition

Name	Polymorph/Phase	ICSD codes	Design phase composition
Alite	C_3S	64759	40
Belite	α-C_2S	81097	
	β-C_2S	81096	35
Ye'elimite	o-$C_4A_3\$$	80361	20
	c-$C_4A_3\$$	9560	
Tricalcium aluminate	c-C_3A	1841	
Mayenite	c-$C_{12}A_7$	241243	
Lime (CaO)	C	75785	
Periclase (MgO)	M	26958	
Anhydrite	C$	16382	5

2.2 Specimens preparation and curing

Clinker preparation: the raw materials were mixed in a blender mixer for 12 h to ensure raw mix homogeneity. A pressure of 20 MPa was applied to prepare 4 cm diameter cylindrical pellets. All pellets were dried at 110 ºC. The dried pellets were calcined at 900 ºC with a heating rate of 10 ºC/min and held for 30 min to completely decompose the calcium carbonate. Then, they were further heated at 1300 °C (at same heating rate) and held for 30 min. Finally, the samples were quenched using forced air convection. Four sample's raw materials dosage are given Table 2.

Cements were prepared by mixing 10 wt. % of $CaSO_4 \cdot 2H_2O$ to clinkers in a 500 ml mixing bowl at 100 rpm. Cement pastes were prepared with a 0.3 water to cement ratio and cast in a mold of 20 mm × 20 mm × 20 mm. All samples were curing at 20 ± 1 ºC and 95% RH for 24 hours. After demolding, the samples were still cured in cement standard curing box (20 ± 1 ºC and 95% RH) to a specific age (3 and 7 day). For XRD measurements, the hydration of small fractured samples was stopped by soaking in anhydrous ethanol. After that, the samples were dried in a vacuum drying oven at 40 ºC for at least one day. The samples were ground in an agate mortar until passing through a 75 μm sieve.

Table 2. Raw materials dosage

Sample	$CaCO_3$	SiO_2	Al_2O_3	MnO_2	MgO	K_2CO_3	Na_2CO_3	$ZnSO_4 \cdot H_2O$	$CaSO_4 \cdot 2H_2O$	CaF_2	B_2O_3
S	100.55	20.1	11.2	0	0.8	0	0.51	2.2	9.9	1.0	0.6
S-K	100.55	19.9	10.9	0	0.8	1.18	0.51	2.2	9.5	1.0	0.6
S-0.2M	99.84	20.0	10.9	0.2	0.8	1.18	0.51	2.2	9.5	1.0	0.6
S-0.8M	99.48	19.8	10.7	0.8	0.8	1.18	0.51	2.2	9.5	1.0	0.6

2.3 Test methods

The compressive strength of cement pastes was measured by an automatic strength testing machine (AEC-201-type) according to EN-196–1-2016. The loading rate was 2.4 kN/s. For XRD measurement, the specimens were crushed and ground by pestle in a agate mortar. In order to avoid the phase transformation or decomposition, ethanol was poured in the mortar when grinding the hydrated cement pastes. The ground powder was dried at 40 ºC for 12 h in oven The XRD analysis was performed by using Rigaku Smart Lab 3000 A diffractometer with Cu-Kα radiation. The test was conducted at an accelerating voltage of 40 kV and a current of 20 mA. The data of 2θ angle between 5º to 40º were recorded, and the scanning speed is 5º per minute.

3. Results

3.1 Phase Composition of Clinkers

The XRD patterns of the synthesized clinkers are shown in Fig. 1. Clinkers heated for 30 minutes at 1300 ºC include C_3S, a-C_2S, b-C_2S, $C_4A_3\$$, $C_{12}A_7$, and C_3A. Sample S has the highest $C_4A_3\$$ intensity, and sample S-0.8M has the highest α'$_H$-C_2S intensity. The phase compositions quantified through Rietveld analysis are shown in Table 3.

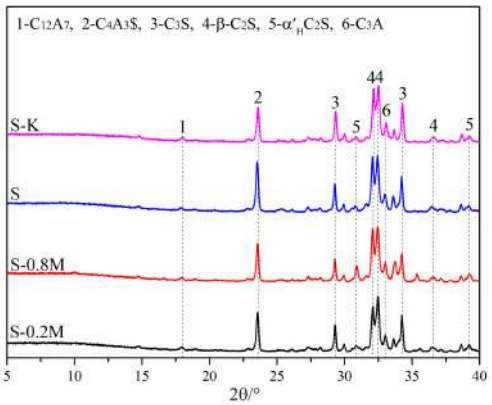


Fig. 1. X-ray diffraction pattern of clinkers.

Table 3. Phase composition measured by XRD-Rietveld refinement and Rwp values for all clinkers

Phase (wt. %)	S	S-K	S-0.2M	S-0.8M
C_3S	37.6	44.1	40.3	29.2
α'_H-C_2S	10.6	11.1	11.9	10.9
β-C_2S	25.5	21.5	26.8	36.0
c-C_4A_3\$	7.9	3.8		2.7
o-C_4A_3\$	12.0	10.6	17.8	12.6
c-C_3A	0.4	1.5	0.7	0.5
c-$C_{12}A_7$		3.2		
CaO	1.0	0.5		
MgO	1.3	1.1	0.7	0.3
$CaSO_4$	0.7		0.5	0.6
Rwp	6.54	7.03	7.45	9.00

3.2 Compressive Strength

Compressive strength data of cement pastes after hydration for 3 and 7 days were shown in Fig. 2. The compressive strength of S, S-K, S-0.2M and S-0.8M samples at 3d were 33.04, 15.54, 9.76 and 24.01, respectively. The compressive strength of S, S-K and S-0.8M samples increased at 7d compared with 3d, the growth rates of compressive strength are 123%, 76.6% and 174% respectively. Sample S has the highest compressive strength at both 3 and 7 days. The development of compressive strength of S-0.2M sample shows negative growth.

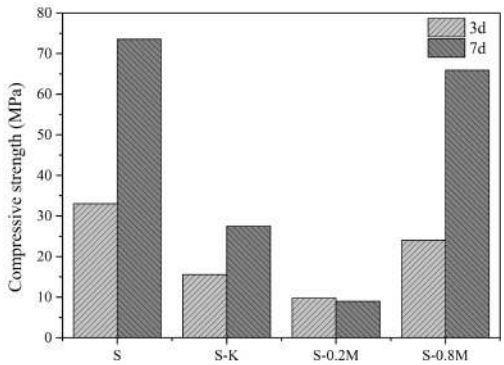
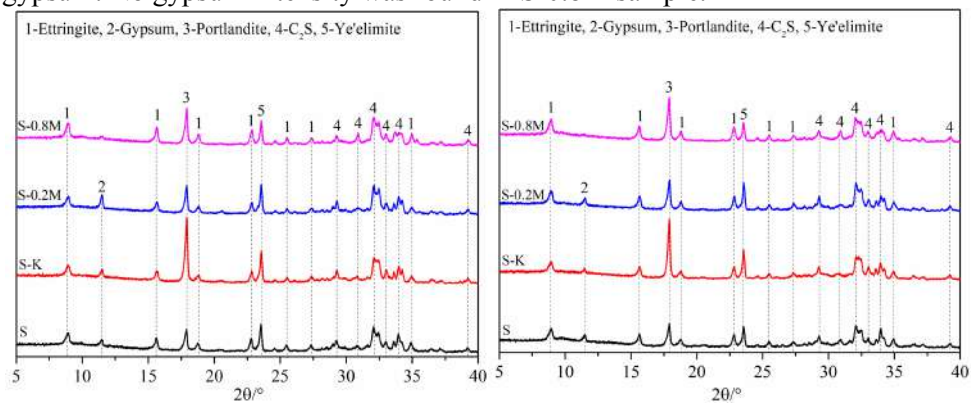


Fig. 2. Compressive Strength of clinkers at 3 and 7 days.

3.3 Phase Composition of the Hydrated Cement Paste

The XRD spectra of hydration of cements at 3d and 7d are listed in Fig. 3. At the early hydration, the remaining cement clinker phase assemblages included belite and ye'elimite phases. There is no discernible difference in hydration products between 3 and 7 days. The lowest portlandite intensity in sample S demonstrates the greatest degree of hydration, which is consistent with the strength

development. The portlandite intensity of sample S-K is the highest and sample S-0.2M has the highest intensity of gypsum. No gypsum intensity was found in S-0.8M sample.



(a) **(b)**

Fig. 3. Diffractograms of hydrated pastes of cement (a) 3d; (b) 7d.

4. Conclusions

In this paper, the influence of K_2O and MnO_2 doping on the calcination of alite and ye'elimit coexisting cement clinker was studied. The following conclusions have been drawn:

- By ion doping and adjusting the calcination system, cement clinker containing alite and ye'elimite may be effectively sintered at one time.
- The addition of K_2O can promote the formation of C_3S in clinker calcination, but it is not helpful for the early strength development. The addition of MnO_2 will promote the formation of β-C_2S during clinker calcination, and the early strength of clinker doping with high dosage MnO_2 develop better. The early strength development of clinker without K_2O and MnO_2 is the greatest.

Acknowledgements

The authors would like to acknowledge financial support from the National Key R & D Program of China (No. 2021YFB3802002), the National Natural Science Foundations of China (No. 51802151) and the Priority Academic Program Development of Jiangsu Higher Education Institutions (PAPD).

References

Gartner. E, Hirao, H. (2015), "A review of alternative approaches to the reduction of CO2 emissions associated with the manufacture of the binder phase in concrete", Cement and concrete research. 78: 126-142.

Altun, I.A. (1999), "Effect of CaF2 and MgO on sintering of cement clinker", Cement and concrete research. (29): 1847-1850.

De la Torre, A.G., Cuberos, A.J., Alvarez-Pinazo, G., et al. (2011), "In situ powder diffraction study of belite sulfoaluminate clinkering", J Synchrotron Radiat. 18(Pt 3): 506-14.

Hong, W.M., Li, J.H., Zhao, H.W., (2007), "Preparation of Sulphoaluminate-Alite Composite Mineralogical Phase Cement Clinker from High Alumina Fly Ash", Key Engineering Materials. 334-335,421-424.

Ludwig, H.-M., Zhang, W. (2015), "Research review of cement clinker chemistry", Cement and concrete research. 78: 24-37.

Li, X.R., Huang, H., Xu, J., et al. (2012), "Statistical research on phase formation and modification of alite polymorphs in cement clinker with SO3 and MgO", Construction and building materials. 37: 548-555.

Li, X.R., Xu, W., Wang, S., et al. (2014), "Effect of SO3 and MgO on Portland cement clinker: Formation of clinker phases and alite polymorphism", Construction and building materials. 58: 182-192.

Theodor, S., Petr, S. (2017), "The impact of basic minor oxides on the clinker formation", Materials Science Forum. (908): 3-9.

Li, X.R., Shen, X.D., Xu, J., et al. (2015), "Hydration properties of the alite–ye'elimite cement clinker synthesized by reformation", Construction and building materials. 99: 254-259.

Pérez-Bravo, R., G. Álvarez-Pinazo, J.M. Compana, et al. (2014), "Alite sulfoaluminate clinker: Rietveld mineralogical and SEM-EDX analysis", Advances in cement research. 26(1): 10-20.

The 16th International Congress on the Chemistry of Cement 2023 (ICCC2023)
"Further Reduction of CO_2 -Emissions and Circularity in the Cement and Concrete Industry"
September 18–22, 2023, Bangkok, Thailand

Determination of Clinker Performance with Chemical Additives by use of XRF, QXRD and Microscopy Analysis.

R.G Sibbick[1*], J.J. Thomas[2], and J.H. Cheung[3]

[1] *GCP Applied Technologies (SAINT-GOBAIN Construction Chemicals), Wilmington, USA*

Richard.sibbick@gcpat.com

[2] *GCP Applied Technologies (SAINT-GOBAIN Construction Chemicals), Wilmington, USA*

Jeffrey.Thomas@gcpat.com

[3] *GCP Applied Technologies (SAINT-GOBAIN Construction Chemicals), Wilmington, USA*

Josephine.H.Cheung@gcpat.com

ABSTRACT

Cement additives are chemicals that are added at the clinker grinding stage to improve grinding efficiency and enhance the performance, particularly the strength development, of the resulting finished cement. The response of Portland cement clinkers to strength enhancing cement additives is quite variable, with some clinkers exhibiting significant strength increases and others showing essentially no response. This variability is not linked to in any obvious way to compositional or performance criteria such as oxide composition, mineralogy, early and late age strength, set time, or water demand. For this study, Portland clinker samples were collected from around the world, and the response of each to strength enhancing additives was characterized. Those clinkers that exhibited a definitive positive or negative performance response were chosen for analysis by clinker microscopy, XRF, and QXRD. The resulting data were analyzed to see which factors were linked to positive or negative additive response. The results show that a positive response to chemical additives is strongly linked to a higher total aluminate (C_3A) content in the clinker and a corresponding negative chemical additive response is typically found associated with clinkers with low orthorhombic aluminate (C_3A) content of less than 1.5 %. Lower sulfate, higher total alkali, and higher total flux phase content were also associated with positive additive response. On the other hand, a negative response was associated with microscopic observations of high amounts of raw feed residue and other features associated with poor combinability of the raw feed during clinker manufacture.

KEYWORDS: *Chemical additive performance, aluminate, alkali, sulfate, XRF, QXRD, Microscopy.*

1. Introduction

Cement producers currently utilize a wide variety of techniques to monitor the composition and performance of their cement, including quantitative X-ray diffraction (QXRD) by Rietveld analysis, X-ray fluorescence (XRF), differential thermogravimetry (DTG), isothermal calorimetry, Blaine specific surface area (BSA), particle size distribution (PSD), flowability, set time, water demand, and strength testing. However, it has proven difficult to use this data to predict the response of a particular cement to additives, particularly strength improvements. The additives referred to in this paper are generally referred to as strength enhancing additives and they are added to the cement mill to improve both the grinding efficiency and the strength development. They are typically formulated from a range of organic and inorganic chemicals, such as alkanolamines, polyols, hydroxylated polymers, and inorganic salts.

2. Background information

Beginning in 2011, GCP laboratories began a program of assessing cement clinkers that demonstrated either a strong positive or negative response to strength enhancing additives with regards to strength development, referred to hereafter as positive or negative additive response. This was primarily

established by mortar strength testing of finished cement made from each clinker, to see the strength difference that resulted from the addition of the strength enhancing additives to the mix water. The clinkers were analyzed by QXRD by Rietveld, XRF, and optical clinker microscopy along with a chemical test for identifying clinker reduction. The 28 clinkers analyzed in this initial study were produced in cement plants throughout the world and the results were presented at the 2015 ICCC meeting [1]. That study did not identify any obvious compositional or mineralogical differences between the positive and negative performing clinkers. However, it was observed that negatively performing clinkers exhibited more atypical microstructural characteristics indicative of sub-optimal kiln burn conditions (e.g., light or hard burning) and/or raw feed-related issues such as difficulty in combinability as compared to the positive performers.

Some of the clinkers included in the original 2015 study demonstrated moderate or variable strength response to the additives tested and as such could not be clearly classified as positive or negative performers. In 2020 this original set of clinker data was revisited, along with several additional clinker samples that had been collected in the meantime. In this new study, only clinkers exhibiting strongly positive or negative strength response to the strength enhancing additives were included in the analysis. Positive response was defined as at least a 20% increase in strength at both early and late ages, while negative response was defined as no statistically significant increase in strength. Application of these stricter criteria reduced the number of clinkers in this new investigation to seventeen (eight positive and nine negative performers).

3. Results

All the clinker samples were analyzed by XRF, QXRD by Rietveld and whole clinker microscopy. XRF data was used in Figure 1 to show a clear relationship exists between alkali/sulfate ratio and additive response. Excess alkali is associated with positive additive response while excess sulfate is associated with negative additive response.

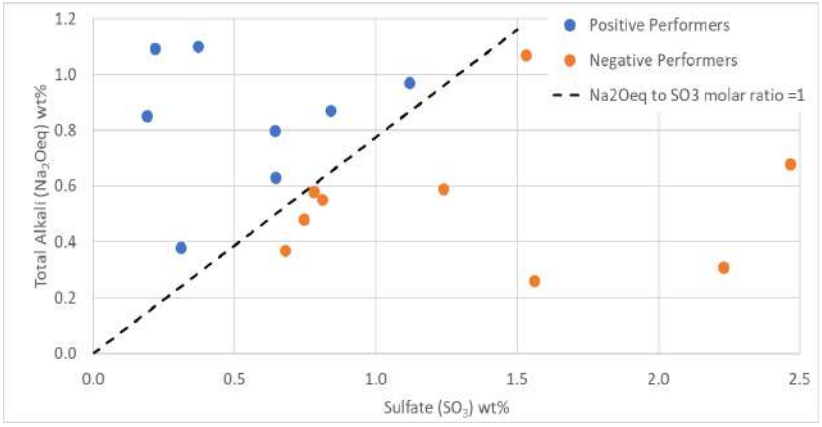


Figure 1: Total alkali (equivalent Na_2O wt%) content plotted against total sulfate (SO_3 wt%) content by XRF. The dashed line representing a molar ratio of Na_2O/SO_3 = 1.00 clearly separate the positive and negative performing clinkers.

The QXRD data show that positive clinker additive response is associated with higher total aluminate mineral content, and that a negative clinker additive response is typically associated with a lower orthorhombic aluminate (C_3A) content of less than 1.5 %, see Fig. 2. Comparison of the total aluminate content to total alkali and sulfate contents from XRF also shows clear relationships exist with regard to clinker performance, see Fig. 3. For the clinkers in this study, positive additive response is primarily associated with a total aluminate content greater than 7.0 %. Positive additive response is also associated with higher total alkali content, and lower sulfate content. These factors are linked, as Figs. 2 and 3 show that low orthorhombic C_3A aluminate contents of less than 1.5 % are correlated with both higher alkali content and, to a lesser degree, lower sulfate content. It is known that an excess of alkali over sulfate in the kiln results in more orthorhombic C_3A formation. Other compositional variables, such as the total flux content, the silica ratio, and the alumina ratio were also found to be associated with clinker additive response.

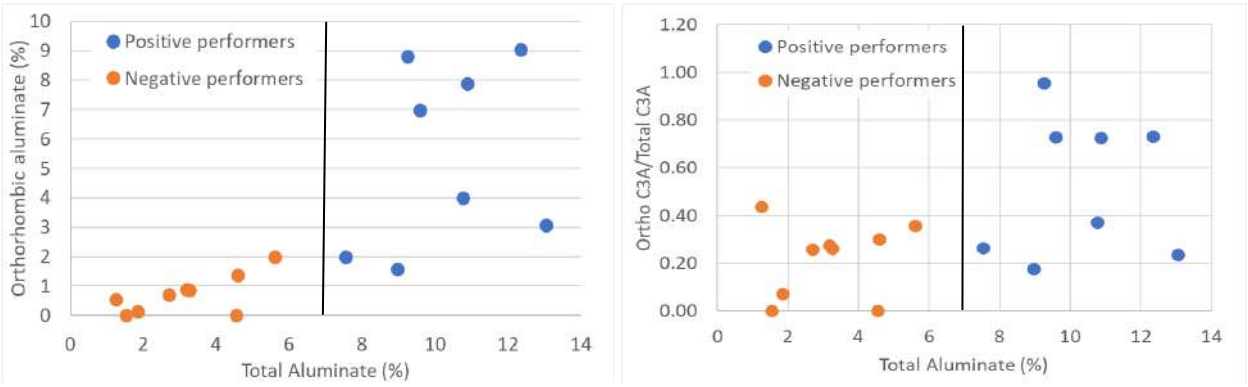


Figure 2: Left: Orthorhombic C_3A content plotted against total aluminate mineral content. Right: Ratio of orthorhombic C_3A/total aluminate plotted against total aluminate mineral content. Positive sample performers (blue) and negative sample performers (orange).

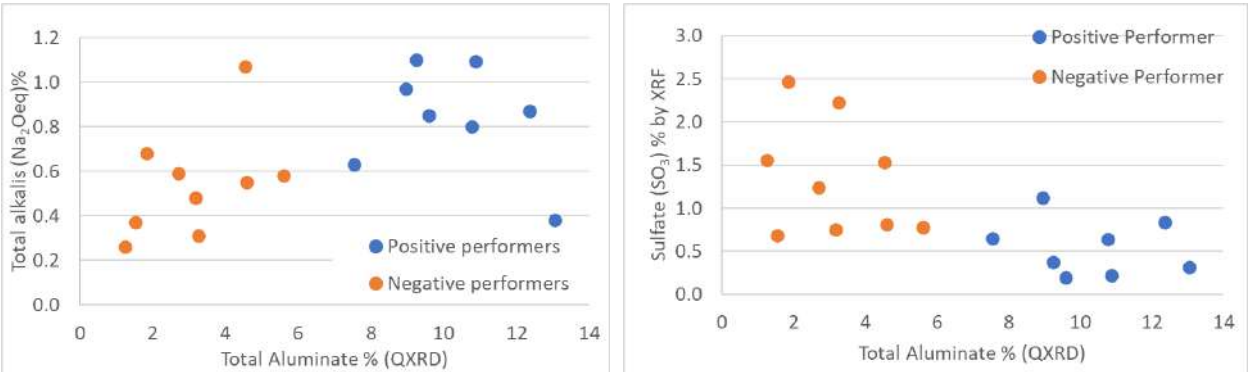


Figure 3: Total alkali (left) and total sulfate (right) contents derived from XRF plotted against total aluminate content from QXRD. Positive additive response (blue points) is primarily associated with higher aluminate content but is also associated to some degree with higher alkali content and lower sulfate content.

Whole clinker microscopical examinations were performed on all the samples, during which five features known to be associated with overall clinker quality were assessed, (see [2] for more details). Two features - the amount/size of raw feed residue (RFR) 'nest' features and the apparent combinability potential - were found closely associated with clinker additive response, as shown in Figure 4. The other features (apparent cooling rate, reduction, and degree of burning) were not obviously linked with clinker additive response. For the first two features, a qualitative visual-based rating from 1 (best) to 5 (worst) was assigned. As can be seen in Table 1, positive (lower) ratings for these microstructural features are closely associated with positive response to additives while negative (higher) ratings are associated with negative response.

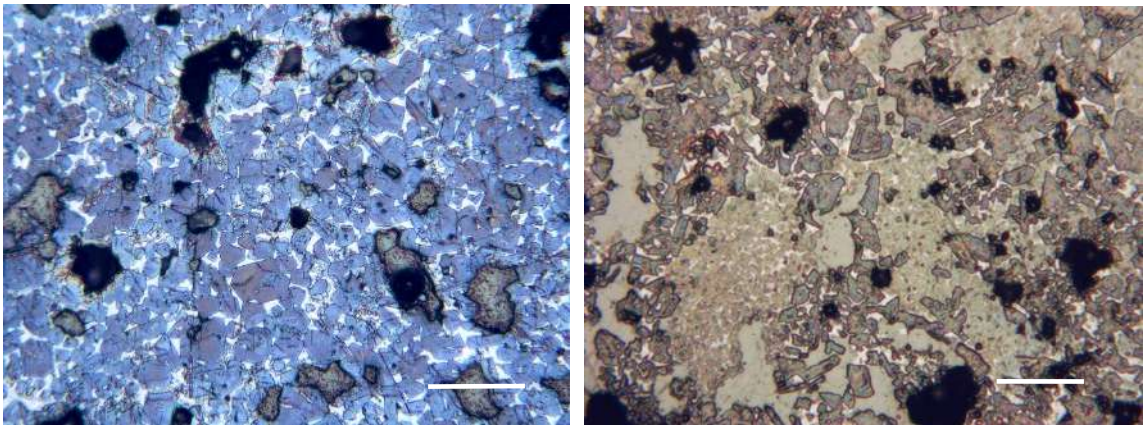


Figure 4: Left: Optical reflected light image of a positively performing clinker with a homogeneous, well combined, low small RFR microstructure. Right: Optical reflected light image typical of a negatively performing clinker with a more heterogeneous, poorly combined, and high RFR microstructure. Scale bars are 100 µm in length.

Table 1: Qualitative rating based on the microstructural assessments ranging between 1 (best) and 5 (worst) for two key features of the clinkers – Raw feed residue relative abundance and size, and features indicating difficulty in combinability.

Positive performing clinkers									Average
Raw feed residue	1.0	2.0	2.0	4.0	2.0	3.0	1.0	1.0	**2.0**
Combinability	1.0	2.0	2.0	3.0	1.0	3.0	1.0	1.0	**1.8**
Negatively performing clinkers									Average
Raw feed residue	5.0	5.0	1.0	3.0	3.0	3.0	5.0	3.0	3.0	**3.4**
Combinability	5.0	4.0	3.0	4.0	4.0	4.0	4.0	2.0	4.0	**3.8**

3. Conclusions

The objective of this study was to identify measurable clinker features that could be associated with the tendency to respond positively to strength-enhancing additives. It is important to note that this is distinct from the overall quality of the clinker. For example, a clinker that gives low absolute strengths but responds strongly to strength enhancing additives would be classified positively for this study.

The study was successful in identifying several compositional and morphological features associated with the response to additives. A strong positive relationship was found between the presence of a higher total aluminate (C_3A) content greater than about 7.0 wt%, and positive additive response. This relationship was further supported by the indication that a negative clinker additive response is associated with a low orthorhombic aluminate (C_3A) content less than about 1.5 %. A similar relationship was found between the total alkali content and positive additive response, with a positive response being typically associated with higher total equivalent Na_2O contents. Low intrinsic clinker sulfate content (i.e., prior to any gypsum addition) was also associated with positive additive response and higher aluminate content in this study. Sulfate balances alkali within the kiln, preventing alkali from forming and stabilizing orthorhombic C_3A.

Microstructural assessments of the clinkers reaffirmed previously reported [3] relationships between the response to additives and two specific clinker features: the extent and size of RFR features and the apparent combinability. In both cases, when these features indicate higher quality clinker (i.e., fewer/smaller RFR content and good combinability) there is an association with positive clinker response. Other microstructural features associated with overall clinker quality did not show obvious correlations to additive response.

These findings show that it may be possible to explain the additive response potential of some clinkers.

4. Acknowledgements

Steve Garrity and Eric Bala are thanked for help with sample preparation and testing. Finally, Derek Brown is thanked for the considerable time and patience in explaining whole clinker microscopy and the cement chemistry, mineralogy and manufacturing processes required to undertake this study.

5. References

[1] Sibbick, R.G and Cheung, J. (2015) "Cement Clinker Microscopy as an Aid to Determine Performance Differences in the Presence of Chemical Additives". Proceedings 14th International Conference on the Cement Chemistry (ICCC) conference in Beijing, PRC.

[2] Sibbick, R.G. (2017) "Cement Clinker Microscopy as a tool to aid the determination of kiln process and cement performance problems. 16th Euroseminar on Microscopy Applied to Building Materials, Les Diablerets, Switzerland.

[3] Sibbick, R.G and Cheung, J. (2014) "Cement Clinker Microscopy as an Aid to Determine Performance Differences in the Presence of Chemical Additives". 36th International Cement Microscopy Association (ICMA) conference, Milan, Italy, Copies of the proceedings from https://cemmicro.org/.

The 16th International Congress on the Chemistry of Cement 2023 (ICCC2023)
"Further Reduction of CO_2 -Emissions and Circularity in the Cement and Concrete Industry"
September 18–22, 2023, Bangkok, Thailand

Preparation and Characterization of Portland cement Clinker by High Magnesium Limestone and Iron Tailings

Tao Lu[1], Chao Zhu[1], Zhuqing Yu[1,2*], Liwu Mo[1,2*], and Xiaodong Shen[1,2]

[1] *College of Materials Science and Engineering, Nanjing Tech University, Nanjing, PR China*
[2] *State Key Laboratory of Materials-Oriented Chemical Engineering, Nanjing, P. R. China*
Email: zyu@njtech.edu.cn

ABSTRACT

As a key industry of CO_2 emission, cement industry urgently needs to seek a low-carbon development technological path. In view of the source of carbon emission during the production of Portland cement clinker, raw material substitution is an important way to reduce the emission of CO_2. Meanwhile, the traditional mineral resources for Portland cement clinker production are gradually exhausted, such as high quality limestone. Therefore, the use of low-grade raw materials and industrial wastes to produce Portland cement clinker is a tendency for reducing CO_2 emission.
In this study, high magnesium limestone and iron tailings are used as alternative raw materials to prepare Portland cement clinker in order to reduce the use of traditional limestone and clay. The replacement level of alternative raw materials, calcination system are taken into account. The chemical and mineral analysis of the prepared cement clinker is determined; the strength and chemical shrinkage of the clinker is also evaluated in order to prepare a kind of qualified Portland cement clinker.

KEYWORDS: *High magnesium limestone, Iron tailings, Mineralizer, Portland cement clinker*

1. Introduction

Carbon emission reduction is the only way for the green and sustainable development of cement industry, as well as the opportunity and challenge faced by the cement industry. Given the CO_2 source in cement production and the reduction of high quality raw materials, raw material substitution is an important low-carbon development path for the cement industry (Ishak et al (2015)). High magnesium limestone is a kind of low grade limestone, which can be used to produce cement clinker (Song et al (2021)). In the process of clinker calcination, the appropriate content of MgO can reduce the liquid phase formation temperature, increase the liquid phase content, and reduce the viscosity between the liquid phases (Li and Hong et al (2012)), thus promoting the formation of clinker (Li and Xu et al (2014)) and improving the color and properties of clinker (Segata et al (2019)). However, the solid solubility of MgO in Portland cement clinker is only about 2%. Excess MgO will exist in the form of periclase in cement clinker; the reaction of periclase is a volume expansion reaction, affecting the stability of cement clinker (Ren et al (2019)). The effective control of MgO formed in clinker is the key to produce qualified cement from high magnesium limestone, which can not only play the beneficial effect of MgO, but also reduce the harmful effect of MgO. Iron tailings, as a solid waste, is rich in silica and iron, and it has a major chemical composition similar to clay. It can be used as a silica or iron modification material to produce green and sustainable cement products. During the calcination of cement clinker, iron tailings also plays a role of mineralizing agent (Young and Yang (2019)). In this study, high magnesium limestone and iron tailings, instead of traditional raw materials partially, are used together to prepare Portland cement clinker.

2. Materials and methods

2.1 Raw materials

All raw materials were prepared in the laboratory by the process of crushing, grinding and sifting (75 μm

sieve). Table 1 shows the chemical composition of the used raw materials. Fig. 1 shows the XRD patterns of typical limestone and high magnesium limestone. The main mineral composition of typical limestone and high magnesium limestone is calcite, quartz and dolomite. The XRD pattern of iron tailings is shown in Fig. 2; its main composition is albite, quartz, calcite, etc.

Table 1 Chemical composition of raw materials /w%

	Typical limestone	High magnesium limestone	Sandstone	Iron ore fines	Fly ash	Iron tailings
Loss	39.29	41.19	3.18	2.77	9.43	-
SiO_2	7.44	5.83	80.6	59.23	45.45	45.335
Al_2O_3	1.82	1.34	8.31	4.43	28.8	16.995
Fe_2O_3	0.739	0.535	3.28	22.69	4.99	13.093
CaO	47.37	42.59	1.78	4.9	4.35	12.331
MgO	2.64	7.98	0.792	3.1	0.664	4.127
K_2O	0.427	0.289	1.24	0.828	0.989	1.445
Na_2O	-	-	0.187	0.893	0.416	4.307
Σ	99.726	99.754	99.569	98.841	95.089	97.633

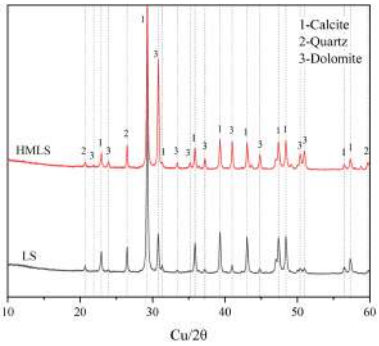


Fig. 1 XRD patterns of typical limestone (LS) and high magnesium limestone (HMLS)

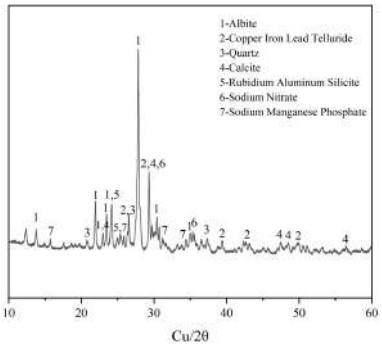


Fig. 2 XRD pattern of iron tailings

2.2 Preparation of raw meal and calcination system

In order to ensure the content of C_3S in the clinker mineral and improve the strength of high-magnesium cement clinker, the KH is set as about 0.92. The designed proportion of raw material is shown in Table 2.

Table 2 Designed proportion of raw material, wt. %

	Typical limestone	High magnesium limestone	Sandstone	Iron ore fines	Fly ash	Iron tailings	KH	SM	IM	MgO in clinker/%
A	88.220	-	4.480	3.500	3.800	-	0.920	2.80	1.81	2.60
B	60.750	27.400	4.460	3.520	3.870	-	0.919	2.81	1.80	6.17
C	60.100	27.400	2.100	4.450	5.950	-	0.919	2.40	1.80	6.17
D	62.050	25.700	4.900	1.650	1.700	4.000	0.920	2.81	1.80	6.12

The raw materials are dried at 105℃ for 12 h in a air dry oven and then mixed evenly in a ball mill. 5% deionized water of the raw meal is added into the mixed raw material. The mixed raw meal is pressed to a sample with Φ 60 mm×10 mm and dried again in a air dry oven at 105℃ for 10 h.

The dried sample is calcined in a furnace at a temperature of 1450℃ for 60 min. The heating rate is 5℃/min the cooling mode is rapid cooling. The cooled clinker is then ground and sieved.

2.3 Experimental methods

X-ray analysis

The prepared sample is determined by Rigaku Smart Lab 3000A diffractometer. The accelerating voltage is 40 kV. The accelerating current is 35 mA. The scanning range is from 5 to 70º with CuKa radiation source (wave length=0.154 nm), and speed is 5º/min with the step of 0.01º.

Chemical shrinkage

The prepared Portland cement clinker is mixed with deionized water at 600 rpm for 2 min. The mixed cement clinker paste is put into a glass bottle and vibrated to remove air bubbles. The glass bottle is sealed with a rubber plug equipped with a pipette (1 mL). 1-2 drops of oil is added to prevent the volatilization of deionized water. All samples are cured at 20℃.

Strength test

The prepared cement clinker with gypsum dihydrate (5% of the cement clinker) is mixed together to prepare cement paste with a size of 20 mm×20 mm×20 mm. The w/c (water to cement ratio) is 0.35. All sample is cured under water. The compressive strength is carried out after the curing age of 3 d and 7 d.

3. Results and discussion

3.1 XRD analysis

Fig. 3 shows the XRD pattern of the prepared clinker at the range of 25~45°. The results of quantitative phase analysis of main minerals for cement clinker by Rietveld method are shown in Table 3.As can be seen, after calcination at 1450 ℃ and rapid cooling, the main mineral phases of these four cement clinkers is C_3S, C_2S, C_3A, and C_4AF. In the sample of B, C, and D, the characteristic peak of periclase (f-MgO) is very clear due to the use of high magnesium limestone. During the calcination of cement clinker, MgO can not be completely solid dissolved in the clinker mineral phase; excess MgO exists in the form of periclase during the cooling process. In all samples, the characteristic peak of f-CaO is very weak. It indicates that these four raw meals have good burnability under the calcination system of 1450℃ and 1 h. In Fig. 3, it can be also seen that the sample D made with some iron tailings has a similar XRD pattern with the sample B. It means that it is feasible to prepare cement clinker with the use of iron tailings with high magnesium limestone.

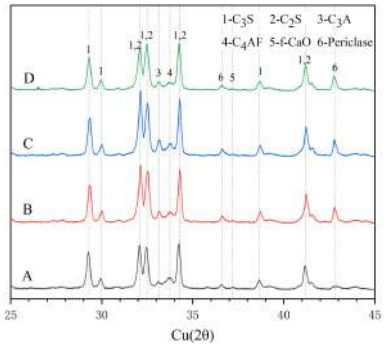


Fig. 3 XRD pattern of the prepared clinker

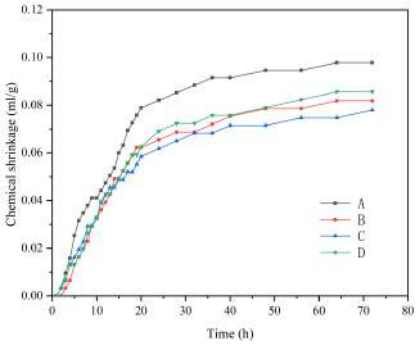


Fig. 4 The chemical shrinkage of the prepared clinker

Table 3 Quantitative phase analysis results of cement clinkers with the Rietveld method, wt. %

	C_3S	C_2S	C_3A	C_4AF	CaO	MgO
A	65.9	16.9	6.2	8.6	0.3	1.2
B	61.8	20.3	3.7	8.1	0.2	6.0
C	60.7	18.9	5.1	9.0	0.4	5.8
D	63.4	18.6	4.5	7.6	0.1	5.8

3.2 Chemical shrinkage analysis

Chemical shrinkage refers to the phenomenon that the absolute volume of hydration products of cement-based materials decreases in the hydration process compared to the total absolute volume of cement and water before hydration. The chemical shrinkage of the prepared Portland cement clinker is shown in Fig. 4. In the first 20 h, the chemical shrinkage of all samples increases rapidly; the hydration of cement clinker is very fast. After that, the increase of the chemical shrinkage of these four samples tends to slow. The chemical shrinkage of the samples made with high magnesium limestone (B, C and D) is less than that of the sample made without high magnesium limestone (A). As discussed in Fig. 3, the solid phase periclase is obviously found in the sample of B, C, and D. The reaction of periclase with water can form magnesium

hydroxide, which is expanded by 148% in volume. That can reduce the chemical shrinkage of the paste effectively. Furthermore, the reaction of periclase is a slow process and takes several months or even a year to be fully reacted. At 72 h, the chemical shrinkage of the sample B, C, and D is still showing an upward tendency. In addition, the effect of iron tailings on the chemical shrinkage of cement clinker is not obvious.

3.4 Compressive strength analysis

As seen in Table 4, the cement paste with a higher MgO content in clinker has a lower compressive strength at 3 d and 7 d. The main reason is that the presence of MgO can stabilize the alite formed in the cement clinker to a tendency of M3 with a relatively low strength (Ichikawa and Kanaya (1997)). The 3 d strength of specimen (B) with SM=2.8 is lower than that of specimen (C) with SM=2.4. When the value of SM decreases, the total amount of C_3A and C_4AF increases; the hydration of C_3A and C_4AF are rapid at 3 d resulting in a higher compressive strength within 3 d. When the value of SM is large, the total amount of silicate phase is high; C_3S and C_2S can provide the late strength. The sample of D prepared with iron tailings has a similar compressive strength with C at 7 d, further indicating the feasibility of iron tailings as an alternative raw material.

Table 4 The compressive strength of the cement paste at 3 d and 7 d, MPa

	A	B	C	D
3 d	12.68	10.16	10.33	9.87
7 d	32.14	29.96	28.50	28.44

4. Conclusion

(1) The use of high magnesium limestone can not affect the formation of minerals phases in clinker, but the presence of MgO can lead the formation of M3-type C_3S in Portland cement clinker, reducing the strength of clinker. Furthermore, the presence of f-MgO can reduce the chemical shrinkage of cement clinker in 72 h.

(2) The mineral composition, chemical shrinkage, and compressive strength of the clinker prepared by iron tailings are similar to that made with traditional raw materials. It indicates that the instead of clay raw materials with iron tailings has no obvious effect on the formation of clinker minerals and the gelling properties of clinker.

Acknowledgement

I hereby express gratitude for the financial support of the National Key R & D Program of China (Grant No. 2021YFF0500802), the Priority Academic Program Development of Jiangsu Higher Education Institutions (PAPD).

References

Ishak. SA. Hashim. (2015) “Low carbon measures for cement plant a review”, *J CLEAN PROD*, 103(-):260-274.

Song, Q. Su, J.H. Nie, J. Li, H. et al. (2021) “The occurrence of MgO and its influence on properties of clinker and cement: A review”, *Construction and Building Materials*, 293.

Li, X. Hong, H. Jie, X. et al. (2012) “Statistical research on phase formation and modification of alite polymorphs in cement clinker with SO_3 and MgO”, *Construction and Building Materials*, 37(37):548–555.

Li, X. Xu, W. Wang, S. et al. (2014) “Effect of SO_3 and MgO on Portland cement clinker: Formation of clinker phases and alite polymorphism”, *Construction and Building Materials*, 58:182–192.

Segata, M. Marinoni, N. Galimberti, M. et al. (2019) “The effects of MgO, Na_2O and SO_3 on industrial clinkering process: phase composition, polymorphism, microstructure and hydration, using a multidisciplinary approach”, *Materials Characterization*, 155.

Ren, X.H. Yao, Y. Zhang, W.S. et al. (2019) “Influence mechanisms of magnesium oxide on formation and properties of clinker (in Chinese)”, *J. Chin. Ceram. Soc.* 47 (08) 1137–1142.

Young, G. Yang M. (2019) “Preparation and characterization of Portland cement clinker from iron ore tailings”, *Construction and Building Materials*, 197:152-156.

Ichikawa, M. Kanaya, M. (1997) “Effects of minor components and heating rates on the fine textures of alite in Portland cement clinker”, *Cement & Concrete Research,* 27(7): 1123-1129.

The 16th International Congress on the Chemistry of Cement 2023 (ICCC2023)
"Further Reduction of CO_2 -Emissions and Circularity in the Cement and Concrete Industry"
September 18–22, 2023, Bangkok, Thailand

Production and Analysis of BYF Clinker Produced via the Combustion of Elemental Sulfur

A. Elhoweris[1*] , M.N. Campbell-Bannerman[2] , F. Winnefeld[3] , O. Abdalla[1] , R. Chaliulina[1] , and Y.M. Alhorr[1]

[1] GORD, Gulf Organization for Research and Development, Doha, Qatar
Email: a.elhoweris@gord.qa

University of Aberdeen, Department of Engineering, Aberdeen, UK

Email: m.campbellbannerman@abdn.ac.uk

[3] Empa, Swiss Federal Laboratories for Materials Science and Technology, Laboratory for Concrete and Asphalt, Dübendorf, Switzerland

Email: frank.winnefeld@empa.ch

ABSTRACT

Including calcium sulfoaluminate (CSA) cement associated phases in clinker can provide a useful approach to compensate for a lack of consistency in raw material compositions, such as high alumina contents in clays and shales as well as high sulfur levels in fuels. Furthermore, there are key advantages when comparing CSA clinker product with Ordinary Portland cement (OPC) clinker, such as lower clinkering temperatures and limestone requirements which lower process CO_2 emissions; it seems natural to explore the production of ye'elimite containing clinkers. Here, a production technique that utilizes sulfur as both a raw material and source of fuel was used to produce CSA clinker product. Low-cost high-alumina clays were used as the primary source of aluminum oxide and supplemented with bauxite to reach the target required to stabilize ye'elimite. A series of pilot-scale production trials were performed where the rotary kiln process conditions were optimized to produce belite-calcium ye'elimite ferrite (BYF) clinkers via a gas-to-solid mass transfer of gaseous sulfur. The composition of the produced clinker varied between 35–40 wt.% ye'elimite, 40–45 wt.% belite, and up to 5 wt.% anhydrite respectively. Samples from the obtained clinker were then blended with supplementary anhydrite to study the effect of the molar ratio of calcium sulfate to ye'elimite on hydration kinetics and strength development. An improvement in the compressive strength relative to OPC was reported after 1 and 2 days, while after 7 days (and beyond) comparable values were reached. Overall, the BYF clinker produced at pilot scale exhibited promising hydration and durability performance, where a large majority of the anhydrous phases were consumed after 182 days. In brief, the developed sulfurous fuel combustion technique was demonstrated to be a feasible and promising approach for the production of BYF clinker formulations with superior performance relative to OPC.

KEYWORDS: *Ye'elimite, BYF Clinker, hydration, durability, Rotary kiln*

1. Introduction

The inclusion of ye'elimite in the place of alite as the primary early age strength component of cement formulations can reduce CO_2 emissions of clinker production by 25-35% when compared to OPC (Hanein et al., 2018; Olivier, 2016). The most popular ye'elimite-based clinker formulations are Calcium Sulfoaluminate ($C\bar{S}A$) and Belite-Ye'elimite-Ferrite (BYF), although other formulations such as alite-ye'elimite cements do also exist. However, a common challenge observed when producing these clinker formulations is the difficulty of maintaining the stability of its mineralogical composition and, thus evidently the consistency of the resultant product quality. This is due to the fact that, at the low SO_2 partial pressures present in kiln atmospheres, SO_2 volatilisation from the clinker bed occurs as a result of the partial decomposition of the sulfate phases. Consequently, a production technique was developed wherein BYF or CSA clinker could be produced using sulfur as a fuel, that contributes towards the heat required for the production process and sequesters the SO_3 necessary for the formation the ye'elimite phase (Al Horr et al., 2017). The combustion of sulfur offers several advantages in terms of process and quality control of sulfate phases, as it creates a protective atmosphere that prevents sulfur volatilization and subsequent decomposition of ye'elimite. The use of this reactive atmosphere can even replace the solid sulfate provided by the gypsum/anhydrite typically found in raw mixes used for CSA production (Hanein et al., 2016). In previously reported pilot production trials, the produced clinkers exhibited a problematic fast-setting behavior. This fast-setting behavior was hypothesized to be due to the presence of calcium sulfate crystallites, which were formed as a result of SO_x and free lime combining in the last cooling stage of the kiln (Jen et al., 2017). This paper presents the follow-on pilot-scale trials which were conducted with the aim of preventing the previous observed false setting behaviour with a modified production method which targeted lower SO_2 partial pressures in the kiln environment. The pilot scale trials were conducted as an optimisation exercise focused on refining the developed requirements of the production technique while producing the required amount of clinker product for subsequent analyses which characterization, analysis of hydration behaviour, as well as physical, mechanical, and durability studies.

2. Methodology

The trial details are included in Table 1. The BYF clinkers produced in the pilot trials were analyzed using X-ray diffractometry (XRD) and X-Ray Fluorescence Spectrometry (XRF) to analyze the composition of the different phases via Rietveld refinement before being compared against thermodynamic predictions. The clinker samples were then mixed with different amounts of anhydrite (calcium sulfate/ye'elimite molar ratios = M-ratio) and hydrated with water with a w/c ratio of 0.5 and 1 to study the hydration behavior and of cement pastes through isothermal calorimetry. Mortar samples were also prepared as mortar and tested for their compressive and flexural strengths at ages up to 182 days.

Table 1: Raw feed design (left), target clinker composition (middle), and the kiln configuration (right).

Raw Feed	**w/w**		**Target clinker**	**w/w**		**Pilot kiln Configuration**			
Limestone	47.07%		$Ca_4Al_6SO_{16}$	40.00%		**Length**		7.4 m	
Bauxite	7.32%		Ca_2SiO_4	48.88%		**Inner diameter**		0.3 m	
Clay	25.53%		Ferrite	11.13%		**Refractory thickness**		5 cm	
Gypsum	20.17%					**Steel thickness**		5 mm	
Total	100.00%		**Total**	100.00%		**Inclination**	1°	**RPM**	1.8

3. Results and Discussion

Figure 1 presents the operating conditions of the kiln along with the clinker analysis on an hourly basis. There was a mechanical issue with the sulfur feeder during the trial, which lead to some issues with SO_2 partial pressure that affected composition, but otherwise the kiln smoothly operated, and product was collected throughout the green marked times in Figure 1. The average overall composition the produced BYF clinker is given in Table 2.

Table 2: Average phase composition of the BYF clinker produced, as determined by Rietveld refinement.

Phase	$C_4A_3\$$	C_2S	C_3A	$C_{12}A_7$	CA	C_4AF	$C_5S_2\$$	C_2AS	C	C$	CT
Wt%	36.8	40.9	1.9	2.6	0.3	2.5	2.8	5.7	0.1	5.1	1.3

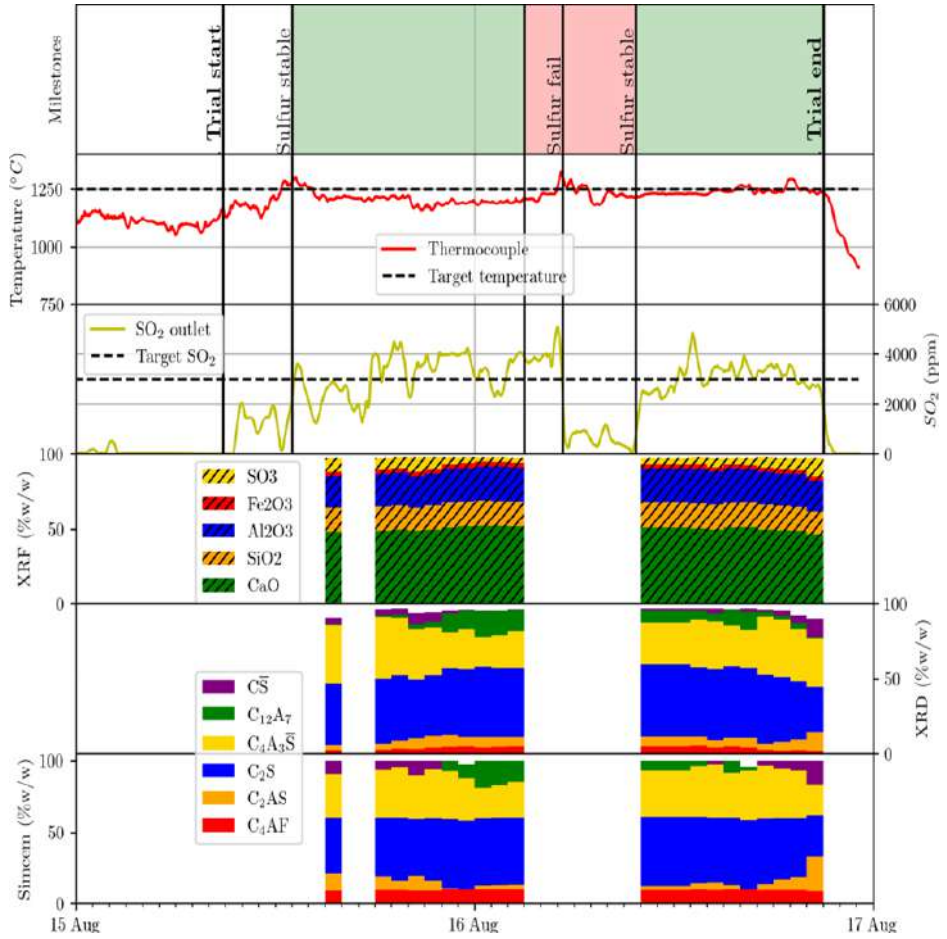


Figure 1: Aligned plots for the measured hot zone temperatures, the SO_2 concentration in the kiln gas exit, XRF and XRD data for the obtained hourly samples, and thermodynamic predictions (bottom).

Upon hydration of the obtained pilot clinker product, its setting and hydration behaviour was initially analysed with the use of varying additions of anhydrite. Higher w/c ratio had significant effect on hydration of different clinkers where it noticeably shortened the induction period, increased the heat flow, and shortened the width of main peak. This behaviour contradicted PC, where higher w/c ratio increase the induction period due to a decrease in pH of pore solution (Danielson, 1962). The compressive and flexural strengths of the pilot clinker (as mortar prisms) were also tested (Figure 2). The results clearly demonstrate that BYF mortars had a significantly higher compressive strength than Portland cement in the first two days due to the rapid hydration of ye'elimite. The flexural strength of BYF mortar was only better than PC in the first 24 hrs, after that Portland cement outperformed the BYF mortars. This could be associated with the formation of some microstructural damages due to micro-expansion at later ages (Chen et al., 2012).

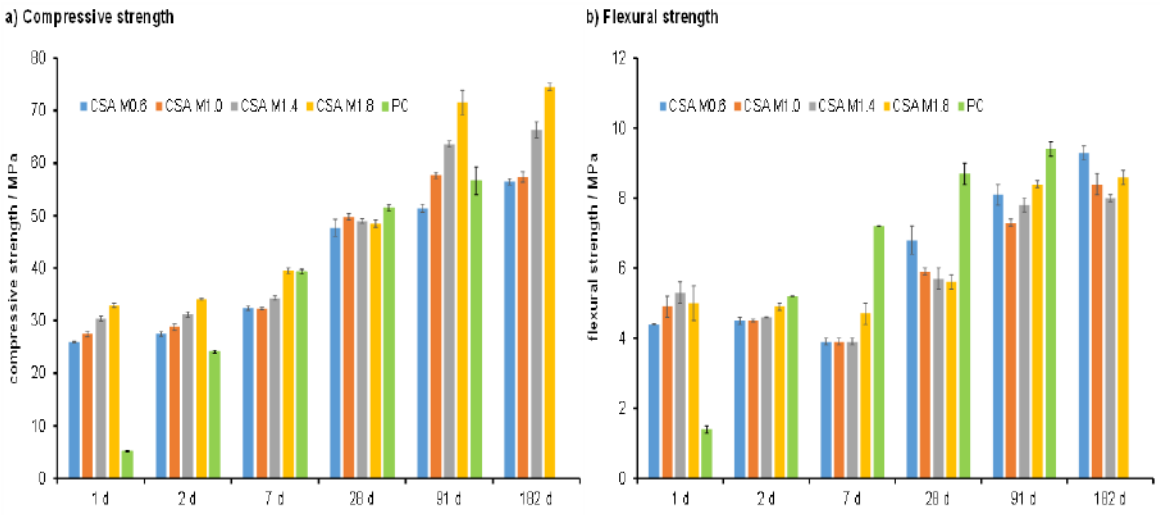


Figure 2: Compressive and b) flexural strength of EN 196-1 standard mortar prisms.

3. Conclusions

BYF clinker was successfully produced through the sequestration of sulfur from kiln combustion gas into clinker at operating temperatures around 1250°C, and previous fast-setting issues have been overcome. The positive outcome of this trial also illustrates that the use of computational thermodynamics in designing and creating formulations can greatly improve the development of processes. It was demonstrated that the necessary amount of sulfur needed to produce clinkers containing ye'elimite can be provided through the burning sulfur containing fuel or from sulfate such as calcium sulfate. The pilot scale trial was able to produce BYF clinkers with about 37% ye'elimite, 41% belite and some residual phases. Moreover, the addition of anhydrite had a retardation effect on the main hydration peak. The produced BYF clinkers demonstrated improved mechanical properties compared to Portland cement, especially in the first two days. Overall, BYF obtained from novel SO_2 containing conditions technology displayed promising superior properties when compared to Portland cement.

References

Al Horr, Y., Elhoweris, A., & Elsarrag, E. (2017). The development of a novel process for the production of calcium sulfoaluminate. *International Journal of Sustainable Built Environment*, *6*(2), 734–741.

Chen, I. A., Hargis, C. W., & Juenger, M. C. G. (2012). Understanding expansion in calcium sulfoaluminate–belite cements. *Cement and Concrete Research*, *42*(1), 51–60.

Danielson, U. (1962). Heat of hydration of cement as affected by water-cement ratio. *Proc. 4th Int. Symp. on the Chem. of Cem., Washington, 1962*.

Hanein, T., Galan, I., Elhoweris, A., Khare, S., Skalamprinos, S., Jen, G., Whittaker, M., Imbabi, M. S., Glasser, F. P., & Bannerman, M. N. (2016). Production of belite calcium sulfoaluminate cement using sulfur as a fuel and as a source of clinker sulfur trioxide: pilot kiln trial. *Advances in Cement Research*, *28*(10), 643–653.

Hanein, T., Galvez-Martos, J. L., & Bannerman, M. N. (2018). Carbon footprint of calcium sulfoaluminate clinker production. *Journal of Cleaner Production*, *172*, 2278–2287.

Jen, G., Skalamprinos, S., Whittaker, M., Galan, I., Imbabi, M. S., & Glasser, F. P. (2017). The impact of intrinsic anhydrite in an experimental calcium sulfoaluminate cement from a novel, carbon-minimized production process. *Materials and Structures*, *50*(2), 144.

Jos G.J. Olivier; Greet Janssens-Maenhout; Marilena Muntean; Jeroen A.H.W. Peters. (2016). *Trends in global CO2 emissions: 2016 Report*. 86.

The 16th International Congress on the Chemistry of Cement 2023 (ICCC2023)
"Further Reduction of CO_2 -Emissions and Circularity in the Cement and Concrete Industry"
September 18–22, 2023, Bangkok, Thailand

Effect of cooling rates on the properties of Portland cement clinkers in the presence of Mg

Z. Ren[1], F. Georget[2], J.L. Provis[1], A. Pisch[3], T. Matschei[2], and T. Hanein[1*]

[1] *University of Sheffield, Sheffield, United Kingdom*
Email: zren18@sheffield.ac.uk, j.provis@sheffield.ac.uk, t.hanein@sheffield.ac.uk
[2] *RWTH Aachen University, Aachen, Germany*
Email: Georget@ibac.rwth-aachen.de, matschei@ibac.rwth-aachen.de
[3] *Grenoble Alpes University, Laboratoire, SIMaP Grenoble, Grenoble, France*
Email: alexander.pisch@simap.grenoble-inp.fr

ABSTRACT
In order to enhance the performance of Portland cement clinker, this study investigates the effect of cooling rates on the mineralogical composition of cement clinkers containing magnesium (Mg), which is the most common minor element in raw materials (e.g., limestone). Three cooling regimes were considered to simulate industrial kiln processing conditions. MgO contents of 0, 3, and 6 wt.% were considered in this study. After synthesis of the clinkers, quantitative X-ray diffraction is used to investigate the mineralogical composition, as well, the phase amounts using the Rietveld method. The results show that rapid cooling and Mg doping can promote the formation of alite, and monoclinic alite can be stabilized via Mg ions. Slow cooling and Mg incorporation can stabilize γ- C_2S, but a rapid cooling rate is still effective to restrain the transformation from β-C_2S to γ-C_2S in MgO-doped clinker. The cooling rates do not influence the content of ferrite and C_3A obviously, but the MgO incorporation can enhance the ferrite formation and reduce the C_3A content. At a slow cooling rate, little Mg can dissolve in clinker phases, but the retention of MgO in clinker phases can be increased by a fast cooling rate. Therefore, the effect of MgO on the mineralization and the solubility of MgO is a function of cooling rates.

KEYWORDS: *Portland cement; clinker, magnesium; cooling rate.*

1. Introduction

With a decrease in the availability of high-purity raw materials and the need for emission reduction and material circularisation to achieve sustainability, the utilization of alternative raw materials and fuels in clinker production is unavoidable in various parts of the world. These alternative raw materials will introduce minor elements into the cement clinker, which can affect the formation and mineralogical composition of this clinker. Notably, magnesium is the most common guest element in raw meals for cement clinker manufacture. Additionally, the fate of magnesium oxide (MgO) in the clinker can be influenced by cooling rates

A MgO content in cement as high as 18.5% is still possible in some countries (Song et al (2021)). However, excess magnesium would form periclase (f-MgO), which would cause a 118% volume increase after hydration to form $Mg(OH)_2$ (Mo et al (2014)) and damage the concrete. Therefore, it is better to limit the formation of periclase. Conversely, the proper amount of MgO can reduce the burnability of raw meals (Zhao et al (2021)), since MgO can lower the liquidus temperature of cement clinker manufacture, which has a positive effect on reducing the consumption of fuels and the carbon dioxide footprint. Additionally, the solid solubility of MgO in clinker can be affected by cooling rates. Therefore, this study investigates the fate of Mg in cement clinker with different dosages and cooling regimes.

2. Materials and methods

2.1 Raw mixtures

The clinker composition is designed with fixed values of lime saturation factor (LSF), silica modulus (SM) and alumina modulus (AM) of 0.94, 2.5 and 1.4 respectively, and 0, 3, and 6 wt.% MgO was mixed into the raw materials. The synthesis of clinker involves of the utilization of high-purity natural limestone ($CaCO_3$) and silica flour (SiO_2), combined with chemical grades such as aluminium oxide (Al_2O_3), iron oxide (Fe_2O_3) and magnesium oxide (MgO).

Table 1. Information on the raw materials used in this study.

Chemicals	Purity (%)	Supplier
Limestone	99.3	Glassworks Services
Silica flour	99.7	Industrial Mineral Services Ltd
Aluminium oxide	99	Acros Organics
Iron oxide	96	Sigma Aldrich
Magnesium oxide	99.95	Thermo Scientific

2.2 Clinkering and cooling regimes

The raw materials were mixed for 10 min with a grinding speed of 300 rpm in a ball mill (Planetary Ball Mill PM100) which is equipped with an 80 ml jar and 5mm balls made of zirconia. The raw mix was compressed into pellets using a hydraulic press. The pellets were heated from 1000°C to 1450°C at a heating rate of 10 K/min, followed by an isothermal hold for 30 min at 1450°C in the elevator furnace (BLF 17/3, Carbolite Gero).

Following the heating process, the hot clinkers were cooled through three cooling rates respectively. 1) Slowly cool in the furnace at a cooling rate of 1 K/min; 2) Quench in the air with fan assistance; 3) Quench in water via a platinum crucible which holds the clinkers. The name of the samples is shown in Table 2.

Table 2. The Mg doped content and cooling regimes of the clinker.

Name	Mg doping (%)	Cooling regimes
0MgO-S	0	1 K/min
0MgO-A		Air
0MgO-W		Water
3MgO-S	3	1 K/min
3MgO-A		Air
3MgO-W		Water
6MgO-S	6	1 K/min
6MgO-A		Air
6MgO-W		Water

2.3 X-ray diffraction (XRD)

The resulting clinkers were characterized through XRD using a PANalytical X'Pert^3 powder diffractomerter operating at 45kV and 40 mA. The data were collected under a rotating mode, with a scanning range of 10-80° (2θ) and a step size of 0.013° (160 s per step). The powders were sieved to -63 μm. Topas v6 was used to execute Rietveld quantitative analysis.

3. Results and discussions

Figure 1 shows the XRD patterns of cement clinker doped with 0, 3, and 6 wt.% MgO and cooled at different cooling rates. The incorporation of MgO into the clinkers leads to a shift in the peak positions of alite, because Mg ions can promote the formation of high-temperature alite (monoclinic alite (M-alite))

which has higher peak positions than triclinic alite (T-alite). Whereas, a higher MgO content cannot widen the peak shift. In addition, slow cooling promotes the formation of γ-C_2S, and MgO cannot restrain the γ-C_2S formation.

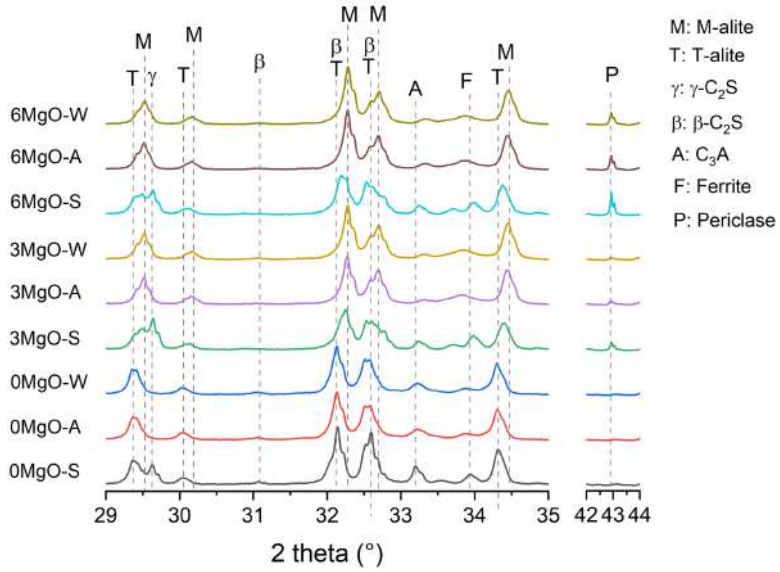


Figure 1. The XRD patterns of cement clinkers doped with 0, 3, and 6 wt.% MgO cooled at three cooling rates.

Figure 2 shows the phase contents of cement clinkers calculated through the Rietveld method; all the *Rwp* values are below 5% which indicates the reliability of the fittings. No significant difference in phase content can be observed between cooling in air and water, probably because the clinker cooled in water mainly dissipate the heat through air. The water just cooled the platinum crucible and just a small area of clinker touched the crucible. Therefore, in the following content, both cooling in air and water are called rapid cooling. The alite content decreased under a slow cooling rate, and Mg can increase the alite ratio. More Mg ions can retain in alite phase at a rapid cooling rate and Mg ions preferably substitute the Ca atoms in tricalcium silicate (C_3S), leading to the detachment of Ca ions. The released Ca ions combine with belite to form more alite, leading to the decrease of belite, shown in Figure 2. Whereas, the alite content does not show a noticeable difference in clinkers doped with 3 wt.% MgO and 6 wt.% MgO, because of the low solubility of Mg in clinker. Cooling rates also have a vital impact on the formation of belite. γ-C_2S can form in 0MgO-S clinker, and more γ-C_2S was observed in MgO-doping clinkers, which indicates the Mg ions can stablize γ-C_2S under slow cooling, which conforms to the results of Feng and Long (Feng and Long (1986)). Normally, γ-C_2S is not a desirable form in a Portland cement clinker because of its low hydration reactivity. Although Mg ions can stabilize γ-type C_2S, a rapid cooling rate is also effective to inhibit the formation of γ-C_2S, even in high-Mg concentration clinkers.

The cooling rates do not have an evident influence on the formation of tricalcium aluminate (C_3A). Additionally, MgO doping can reduce the C_3A content and increase ferrite content. The Fe and/or Al atoms in ferrite can be occupied by Mg ions (Zhao et al (2021)), and the escaped Fe and/or Al ions combine with C_3A to form more ferrite leading to a decrease in C_3A. A rapid cooling rate is also effective to increase the ferrite content, because Mg ions preserve in ferrite phase. However, increasing the content of MgO to 6 wt.% cannot further increase the ferrite content due to the low solution limit of MgO.

2.9 wt.% of MgO was observed in the 3MgO-S clinker, which indicates only a small amount of Mg was found to dissolve in the cement clinker phases, but the solubility can be increased by fast cooling. In this study, the solubility limit of MgO in cement clinker is about 1.1 - 1.5 wt.% which is in line with the published limit of 1.3 wt.% reported by Zhao (Zhao et al (2021)). And, the solid solution limit of MgO also relates to the AM value (Zhang et al (2022)). The calculated MgO value in 6MgO-S clinker is higher than the additive amount, probably because some amorphous in this group of clinker cannot be calculated

by XRD method. So, an internal standard is required to calculate a precise MgO content. All the clinkers have little lime, which means the good burnability of raw materials in this project. This agrees with the results (Zhang et al (2015)), who concluded that with a low doping level, MgO can decrease the content of free lime. Or, some lime is amorphous in the clinkers, and cannot be observed by XRD technique, so a solution rapid testing method is required to further determine the content of free lime.

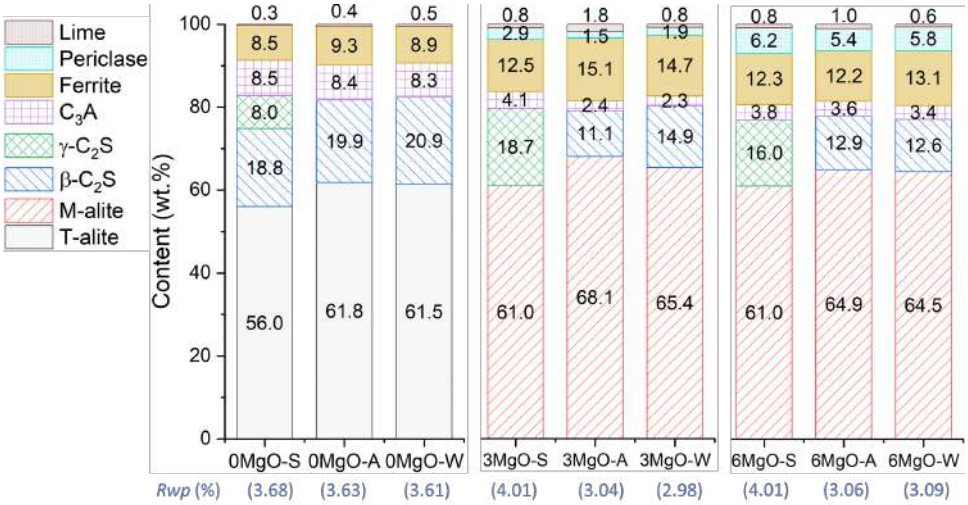


Figure 2. The phase content of clinkers doped with 0, 3, and 6 wt.% MgO at different cooling rates.

4. Conclusion

In summary, the MgO can influence the crystal forms of alite and belite, and the fate of MgO in cement clinker can be influenced by cooling regimes. MgO can enhance the formation of high-temperature alite (M-alite), while stabilize low-temperature belite (γ-C_2S). However, a rapid cooling rate can restrain the transformation of β-C_2S to γ-C_2S even in a high MgO-doped clinker. A high cooling rate is also beneficial to improve the retention of Mg in clinker phases.

Acknowledgements

This work is funded by Innovandi – The Global Cement and Concrete Research Network, a GCCA initiative.

References

Feng, X. and Long, S. (1986) "Investigation of the effect of minor ions on the stability of β-C_2S and the mechanism of stabilization", Cement and Concrete Research, 16(4): 587-601.

Mo, L., Deng, M., Tang, M., et al (2014) "MgO expansive cement and concrete in China: Past, present and future", Cement and Concrete Research, 57: 1-12.

Song, Q., Su, J., Nie, J., et al (2021) "The occurrence of MgO and its influence on properties of clinker and cement: A review", Construction and Building Materials, 293: 123494.

Zhang, J. et al (2015) "Effect of MgO on the composition and properties of belite-barium calcium sulphoaluminate cement in the presence of Na_2O and K_2O", Ceramics – Silikaty, 59(2): 135–144.

Zhang, W., Luan, Z., Ren, X, et al (2022) "Influence of alumina modulus on formation of high-magnesium clinker and morphological evolution of MgO", Cement and Concrete Research, 162: 106986.

Zhao, R., Zhang, L., Fan, G., Chen, Y., et al (2021) "Probing the exact form and doping preference of magnesium in ordinary Portland cement clinker phases: A study from experiments and DFT simulations", Cement and Concrete Research, 144: 106420.

The 16th International Congress on the Chemistry of Cement 2023 (ICCC2023)
"Further Reduction of CO_2 -Emissions and Circularity in the Cement and Concrete Industry"
September 18–22, 2023, Bangkok, Thailand

Effect of chlorides on the clinkering and reactivity of ye'elimite

V.K. Shenbagam[1] and T.Hanein[*]

[1] *Department of Materials Science and Engineering, University of Sheffield, S1 3JD, United Kingdom*
Email: v.shenbagam@sheffield.ac.uk and t.hanein@sheffield.ac.uk

ABSTRACT

Calcium sulfoaluminate (CSA) based cements are alternative low CO_2 binders to Portland cement (PC). CSA cement has ye'elimite ($Ca_4(AlO_2)_6SO_3$) replacing the limestone- and carbon-intensive phase alite (Ca_3SiO_5) in PC, contributing to the early age strength. However, the use of CSA has been limited due to the higher bauxite requirement which is relatively scarce and expensive. This could be overcome by using other alumina-rich alternatives that are locally available, such as aluminium oxide residue (AOR) from secondary aluminium production and aluminium salt slag recycling. The addition of these materials also unavoidably introduces some impurities or minor elements (such as Cl) which can affect the clinkering and reactivity of the resultant binder. The current study focuses on understanding the effect of Cl in the clinkering of the ye'elimite phase and its reactivity. Ye'elimite is synthesised from reagent-grade materials and doped with varying concentrations of $CaCl_2$. The clinkering of ye'elimite was studied using DSC and QXRD to quantify the different phases formed. Furthermore, the reactivity and the hydrated phase assemblages of the binders were studied using QXRD.

KEYWORDS: *CSA cement, Ye'elimite, Clinkering, Reactivity, Chlorine*

1. Introduction

Ye'elimite is the main reactive phase of Calcium sulfoaluminate (CSA) cement. CSA cement has a reduced carbon footprint mainly due to the lower limestone and maximum temperature required for the formation of ye'elimite (Gartner (2004)). The ye'elimite phase starts to form at about 1200 °C through the solid-state transitions (Khessaimi et al (2018)). At higher temperatures (>1300 °C), there can be an excessive loss in sulfate content due to desulphurization and the ye'elimite phase starts to decompose. Ye'elimite is highly reactive and hydrates rapidly to form the calcium sulfoaluminate phases monosulfate or ettringite depending on the availability of calcium sulfate (Ben Haha et al (2019)). CSA cement with ettringite as the main hydration product can have several interesting properties such as rapid hardening and sefl-stressing (Glasser and Zhang (2001)). These properties are highly dependent on the amount of ettringite and the time at which they are formed, which is controlled by the reactivity of ye'elimite. The reactivity of ye'elimite is affected by the presence of other phases such as calcium sulfate, calcium hydroxide or alkalis present in the cement (Shenbagam and Chaunsali (2022)).
The manufacturing of CSA cement requires a higher amount of alumina, which may not be available to make the cement economically viable. This could be overcome by using other alumina-rich alternatives that are locally available, such as aluminium oxide residue (AOR) from secondary aluminium production and aluminium salt slag recycling. Canbek and Erdoğan (2020) synthesised CSA cement using only alternative materials and were shown to attain sufficient strength levels. The addition of these materials also unavoidably introduces some impurities or minor elements (such as Cl) which can affect the clinkering and reactivity of the resultant binder. Simoni et al (2021) synthesized different clinker compositions containing chlorides and observed that ye'elimite and alinite phases did not co-exist; however, formed stable ye'elimite-chloromayenite-belite clinker. The presence of chloride phases thus can possibly be stable with ye'elimite. However, the effect of chlorides on the reactivity of the ye'elimite phase has not been studied. When using alternative materials for the synthesis of CSA cement, it is important to understand their effect on the reactivity of ye'elimite, the main hydrating phase. Hence, in

the current study, ye'elimite is synthesized using pure phases and doped with different levels of $CaCl_2$, to understand the role of chlorides on the formation and reactivity of ye'elimite.

2. Materials and methodology

The clinkers were synthesised using reagent-grade materials (CaO, Al_2O_3, $CaSO_4.2H_2O$ and $CaCl_2$). Two sets of clinkers were used in the study, the clinkers made using the stoichiometric proportions required for the formation of ye'elimite were termed Set A, with varying dosages of $CaCl_2$ (from A0 to A3). Set B consists of clinker made with the raw meal containing an addition (5% by weight) of sulfates. Similarly varying dosages of $CaCl_2$ were blended to obtain the clinkers B0 to B3. The $CaCl_2$ dosage in mole fraction was taken as 0, 0.05, 0.1 and 0.2 in the mixes B0 to B3 (Table 1).

Table 1 Raw meal composition of the different clinkers used in the study

Sample Name	Mole fraction of $CaCl_2$	Mix proportion (% weight)			
		Al_2O_3	CaO	$CaSO_4.2H_2O$	$CaCl_2$
A0	0	25.06	13.78	14.11	0.00
A1	0.05	24.95	13.49	14.04	0.45
A2	0.1	24.84	13.21	13.98	0.90
A3	0.2	24.62	12.64	13.86	1.79
B0	0	24.90	13.47	14.72	0.00
B1	0.05	24.79	13.18	14.65	0.45
B2	0.1	24.68	12.89	14.59	0.90
B3	0.2	24.46	12.33	14.46	1.78

The raw materials were batched in the required proportions and mixed using a planetary ball mill to ensure a uniform raw meal was obtained. The raw meal was then made into pellets of diameter 40mm and anout 5mm thick with each pellet weighing about 20 grams, under a 1-ton load. The pellets were sintered using a laboratory chamber furnace using alumina crucibles. The furnace was initially pre-heated to 900 °C and the samples were placed in the furnace at 900 °C. The furnace temperature was increased to 1300 °C at 5°C/min and held for one hour. The crucibles were then removed at the maximum temperature and air quenched to enable rapid cooling of the clinker. The clinker formed was ground into finer particles (<63 μm) and used for the study.

The hydration studies were done on selected samples (A0, A3, B0 and B3). The ground clinker samples were mixed with distilled water at a water-biner ratio of 0.5. Further additional gypsum (30% by weight) was added to the clinker to obtain a mix with a 2 molar ratio of calcium sulfate to ye'elimite to provide for sufficient sulfates for the hydration reaction of ye'elimite. The hydrated samples at the required ages (1 day and 7 days) were collected and the hydration stoppage was done by immersing the powdered samples in isopropyl alcohol for a duration of 3 days and further ground to be used for characterisation.

The phase composition in the clinker and the hydrated cement paste was determined using X-ray diffraction (XRD). The diffractograms were collected in Panalytical X'Pert instrument, in the two-theta range of 5° to 70°, and scanned with a step size of 0.013. The samples were blended with 20% rutile (TiO_2) to be used as an internal standard for the quantification of the amorphous phases. Simultaneous DSC/TG (Differential scanning calorimetry/Thermogravimetry) experiments were done in Q600 SDT of TA instruments, the sample was heated from room temperature to 1300 °C at 10 °C/min while being purged with compressed air (100 ml/min) in alumina crucibles.

3. Results and discussion

The diffractograms of the different clinkers used in the study are shown in Figure 1. Ye'elimite is the main phase formed in all the mixes, with the presence of other calcium aluminate phases such as krotite (CA: $CaO.Al_2O_3$), grossite (CA_2: $CaO.2Al_2O_3$), mayenite and some residual calcium sulfate (anhydrite). Mix A0 had a ye'elimite yield of about 80.7% with 3.9% calcium sulfate and 15.3% other calcium aluminate phases. Mix B had a higher amount of sulfate source present in the raw meal and the amount of other calcium aluminate phases formed reduced to 7.8%. However, Mix B also had a higher amount of

residual calcium sulfate (18.9%) in the clinker. The addition of $CaCl_2$ to the mix promoted the formation of chloromayenite. The amount of chloromayenite formed increased with the amount of $CaCl_2$ present in the raw meal. Mix B3 had the highest amount of chloromayenite (19.7%) with 61.8% ye'elimite, 6% calcium sulfate and 12.4% of the other calcium aluminate phases formed. The formation of ye'elimite was studied using DSC (Figure 1). At about 150 °C there is a small endothermic peak with mass loss, indicating the dehydration of gypsum losing water. In the temperature range of 850 °C to 1000 °C there is no mass loss with the heat flow remaining constant in both the samples. Beyond 1000 °C there is a constant reduction in heat flow and mass till 1200 °C, which could indicate the phase transformation and the formation of ye'elimite. The mass loss could be due to desulfurization of the unreacted calcium sulfate. The mass loss in B3 mix is higher than B0 which could be due to the vaporization of unreacted $CaCl_2$ in the mix. The presence of chlorides does not seem to significantly affect the formation of the ye'elimite phase but forms additional phases such as chloromayenite, reducing the yield of ye'elimite.

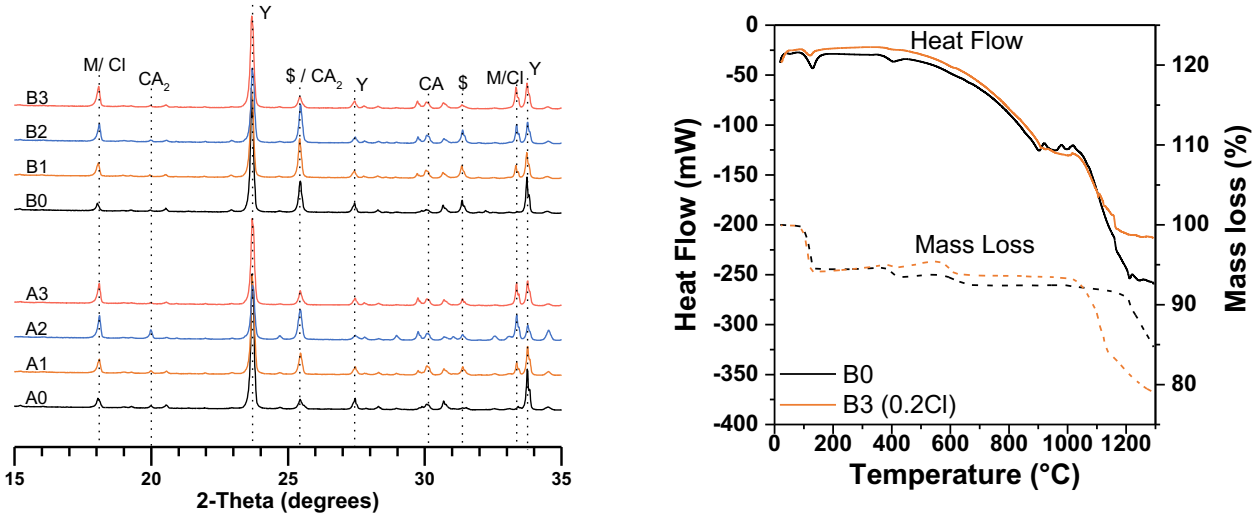


Figure 1 Diffractogram of Ye'elimite with increasing levels of Cl and differential thermal analysis of two selected clinkers (Ye'elimite and Ye'elimite_0.2Cl)
(Y: Ye'elimite, M/Cl: Mayenite/Chloromayenite, CA_2: Grossite, CA: Krotite, $: Calcium sulfate anhydrite)

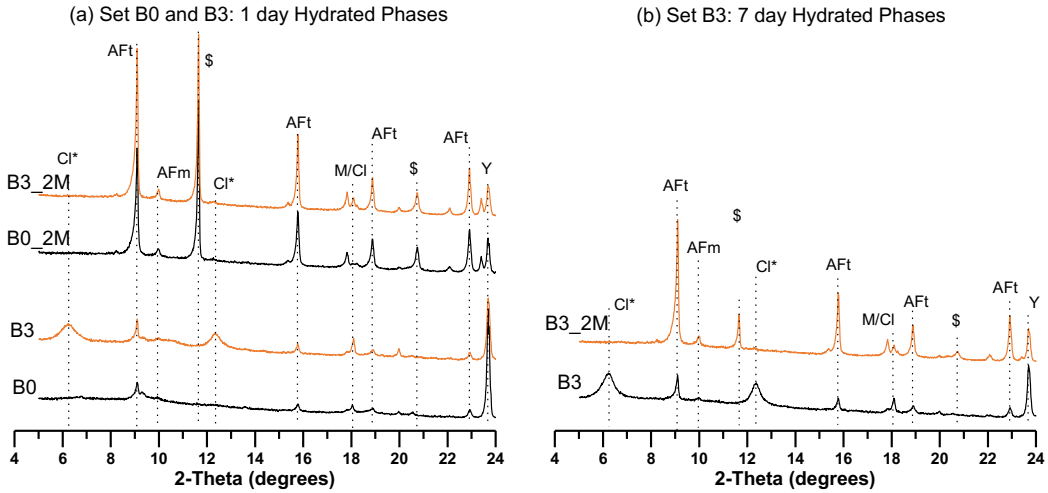


Figure 2 Diffractogram of the hydrated samples at 1 day (a) and 7 days (b)
B0: Ye'elimite; B0_2M: Ye'elimite+Gypsum; B3: Ye'elimite_0.2Cl; B3_2M: Ye'elimite_0.2Cl+Gypsum
(Y: Ye'elimite, M/Cl: Mayenite/Chloromayenite, $: Gypsum, AFt: Ettringite, AFm: Monosulfate, Cl*: Friedel's salt)

Ye'elimite phase hydrated rapidly and the reduction in the ye'elimite peak can be observed in 1 day (Figure 2). There is a significant reduction in the amount of ye'elimite remaining in B0 mix at 1 day with no presence of anhydrite. Ye'elimite hydrated to form monosulfate with a small amount of ettringite

formed as there is not sufficient sulfate source available. The B3 mix has the formation of Friedel's salt from 1 day from the hydration of the chloromayenite phase and the amount of ettringite formed seems to be higher than B0 (B3 has a lesser amount of ye'elimite than B0). The addition of calcium sulfate to the mix enhanced the reactivity of ye'elimite (Ben Haha et al (2019)), with the rapid formation of ettringite in 1 day. There is some unreacted ye'elimite and calcium sulfate present, which could be due to a lack of water for the hydration of ye'elimite (the water/binder ratio required for the complete hydration of ye'elimite with gypsum is about 0.64). Similarly, the B3 in the presence of gypsum (B3_2M) mix also had a significant formation of ettringite with the addition of gypsum. Although there is a reduction in the amount of chloromayenite there was no presence of Friedel's salt in the mix. The presence of a higher amount of calcium sulfate forming ettringite seems to suppress the formation of Friedel's salt. Ettringite has been shown to act as a sorbent in the anion removal for boron and fluoride ions (Tsunashima et al (2012)), similarly, the free chlorides present might be bound to ettringite in this case. Further characterisation studies have to be carried out to confirm the chloride binding in ettringite. Similarly with further hydration, B3 mix there is an increase in the amount of Friedel's salt formed and in the presence of calcium sulfate, there is only an increase in the amount of ettringite and no presence of Friedel's salt in the sample.

4. Conclusions

The role of chlorides on the clinkering and reactivity of ye'elimite was studied using ye'elimite synthesised from reagent grade simple oxides. The presence of chlorides (calcium chloride) promoted the formation of chloromayenite in place of ye'elimite. The hydration of the chloromayenite phase formed Friedel's salt from early ages only when availability of calcium sulfate was low. When higher amounts of calcium sulfate were available for the formation of ettringite, there was no formation of Friedel's salt, indicating that the chlorides were maybe bound to the ettringite formed and further work as to be done to confirm the same.

Acknowledgements

The authors would like to thank UK Research and Innovation grant (MR/V023829/1) for Green, Circular, and Smart Cement Manufacture which facilitated the study and the department of materials science and engineering at the University of Sheffield for the facilities and support in conducting the experiments.

References

Ben Haha, M., Winnefeld, F. and Pisch, A. (2019) "Advances in Understanding Ye'elimite-Rich Cements." *Cement and Concrete Research,* 123(July):105778

Canbek, O., Shakouri, S., and Erdoğan, S. T. (2020) "Laboratory production of calcium sulfoaluminate cements with high industrial waste content", *Cement and Concrete Composites*, 106

El Khessaimi, Y., El Hafiani, Y., Smith A., Trauchessec R., Diliberto C. and Lecomte A. (2018) "Solid-State synthesis of Pure Ye'elimite", *Journal of the European Ceramic Society,* 38(March):3401–11

Gartner, E. (2004). "Industrially interesting approaches to "low-CO2" cements." *Cement and Concrete Research*, 34, 1489–1498.

Glasser, F. P., and Zhang, L. (2001). "High-performance cement matrices based on calcium sulfoaluminate-belite compositions", *Cement and Concrete Research*, 31(12), 1881–1886.

Simoni, M., Hanein, T., Duvallet, T.Y., Jewell, R.B., Provis, J.L. and Kinoshita. H. (2021). "Producing Cement Clinker Assemblages in the System: CaO-SiO_2-Al_2O_3-SO_3-$CaCl_2$-MgO", *Cement and Concrete Research,* 144.

Shenbagam, V.K. and Chaunsali, P. (2022) "Influence of Calcium Hydroxide and Calcium Sulfate on Early-Age Properties of Non-Expansive Calcium Sulfoaluminate Belite Cement." *Cement and Concrete Composites,* 128

Tsunashima, Y., Iizuka, A., Akimoto, J., Hongo, T., & Yamasaki, A. (2012). "Preparation of sorbents containing ettringite phase from concrete sludge and their performance in removing borate and fluoride ions from waste water." *Chemical Engineering Journal*, 200, 338-343.

The 16th International Congress on the Chemistry of Cement 2023 (ICCC2023)
"Further Reduction of CO_2 -Emissions and Circularity in the Cement and Concrete Industry"
September 18–22, 2023, Bangkok, Thailand

Effect of Synthesis Conditions, Zn Doping and Al/Fe Ratio on Calcium [Alumino] Ferrite Structure

C. Pesce*, A. Baral, C. Utton, H. Kinoshita, N.A. Morley, J. L. Provis, T. Hanein

Department of Materials Science and Engineering, The University of Sheffield, Sheffield, UK
Email: c.pesce@sheffield.ac.uk; a.baral@sheffield.ac.uk; c.utton@sheffield.ac.uk; h.kinoshita@sheffield.ac.uk; n.a.morley@sheffield.ac.uk; j.provis@sheffield.ac.uk; t.hanein@sheffield.ac.uk

ABSTRACT
The use of steel waste for clinker production is a promising solution to reduce the environmental impact of Portland cement. While it is known that clinker produced from steel slag shows some advantageous properties e.g., lower burning temperature and reduced use of limestone, it is necessary to understand the formation and stability of iron-rich clinkers doped with the minor elements commonly found in steel wastes. In this study, pure ferrite phases were synthesized with varying Al/Fe ratios, burning temperature, cooling regimes, and in the presence of Zn as a minor element at various dosages. The phase assemblage and microstructure of the obtained ferrites were characterised by XRD/Rietveld and BSE-SEM/EDX. The results show that Zn is partially incorporated into the ferrite structure and partially replaces Al to form a Ca-Al-Zn phase. The Zn-incorporated ferrite leads to increased lattice parameter due to the bigger ionic radius of the dopant with respect to the substituted ions, and to increased crystallinity due to the increased ion mobility brought by ZnO which acts like a flux.

KEYWORDS: *Ferrite, Clinker, Zinc, Cooling rate, Firing temperature*

1. Introduction

Cement production is the major contributor to CO_2 emissions in the construction industry and accounts for 8% of total CO_2 emissions. Peys et al (2022) have recently proposed that the use of Fe-rich materials for cement production can be advantageous due to their ability to lower the clinkering temperature and to their cementitious properties, so far essentially unexplored, whilst upcycling largely available Fe-rich industrial by-products and residues, such as steel slags and bauxite residues. Fe in clinkers is usually found in the calcium [alumino] ferrite (or ferrite) phase, a solid solution with formula $Ca_2Fe_{2-x}Al_xO_5$ with $x \leq 1.4$. Only a few studies have been carried out on the synthesis of pure ferrite phases. In a ternary system CaO-Al_2O_3-Fe_2O_3, the final phase assemblage of ferrites is influenced by the Al/Fe ratio, burning temperatures, cooling rates, and the presence of minor elements in the raw materials. Ferrite accommodates substitution by different elements, including Zn, Mg, and Ti (Peys et al 2022; Murat and Sorrentino 1996; Chabayashi et al 2012). Zn is found in many of the major Fe-rich side streams potentially beneficial to use for clinker production (Peys et al 2022). In clinkers, Zn is known to be mainly incorporated in the aluminate and ferrite phases forming substitutional solid solutions. There is contradictory information regarding the solubility limit of Zn in clinkers, reported at 0.5-1 wt% (Barbarulo, Sorrentino, and Sing 2007), 2 mol% in C_4AF and 5 mol% in C_2F (Shevchenko and Jak 2019) and 0.7 wt% (Gineys et al 2011). Formation of C–Z–A phases has been reported in ferrites at Zn dosage ≥1.0 wt% (Bolio-Arceo and Glasser 1998; Barbarulo, Sorrentino, and Sing 2007; García-Díaz et al 2008) and >0.7 wt%. Understanding ferrite behaviour under different sintering conditions is key for the design of clinkers produced from Fe-rich resources and there is a clear need to gain insights on the effects of Zn as a minor element in clinkers. In this study, ferrites are synthesised at high temperatures varying Zn dosage, Al/Fe ratio, burning temperature, and cooling method, and characterised by powder X-ray diffraction (XRD)/Rietveld and scanning electron microscope/energy-dispersive X-ray spectroscopy (SEM/EDS) to obtain information on the phase assemblage, microstructure, and Zn distribution.

2. Materials and methods

Commercial reagents were used for the synthesis of ferrites: Al_2O_3 ≥99.7% (Thermo Scientific Chemicals), $Fe^{3+}{}_2O_3$ ≥96% (Sigma-Aldrich), $CaCO_3$ ACS reagent grade (Sigma-Aldrich), and ZnO 99.9% (Sigma-Aldrich). Mixtures were prepared at different A/F ratios within the $Ca_2(Fe_{2-x}Al_x)O_5$ solid solution at x=0, 0.33, 1, 1.67. For Zn-doped samples, the same mixtures were used and ZnO was added to the mixtures at 0.5 wt%, 1.0 wt%, and 2.0 wt%. The mixtures (~80g each batch) were prepared by weighing the reagents in the selected proportions and dry-mixing using a Retsch PM 100 ball mill. The mixtures were placed in a ZrO_2 80 mL jar with ZrO_2 ø 5 mm balls, and milled for 10 min at 200 rpm. The ground mixtures were then pressed into ø 16 mm pellets using a manual pellet press. The high-temperature synthesis was carried out in an electric muffle furnace at different firing temperatures (T_f): 1250°C, 1300°C and 1350°C. For all syntheses, the sample pellets were placed in a Pt crucible and put in the furnace at 900°C, then ramped up to the selected T_f at a heating rate of 5°C/min and dwelt at the selected T_f for 1 hour. Two cooling methods were studied: i) fan-assisted air quenching (AQ); ii) water quenching (WQ), carried out by taking the Pt crucibles containing the samples out of the furnace and placing them in a shallow stainless steel tray filled with water, so that only the crucible comes in contact with water but not the sample. The synthesised products were stored in a desiccator filled with silica gel until analysis. Table 1 shows the list of ferrites targetted. Hereinafter, samples are denominated after the target phase, ZnO wt%, firing temperature, and cooling method. For example, a mixture of C_4AF target doped with 1.0 wt% ZnO, fired at 1350°C and air quenched will be called C_4AF-1-1350-AQ.

The synthesis products were characterised by XRD. The instrument was a Panalytical X'Pert^3 Powder equipped with an Empyrean Cu tube (λ=1.54187 Å) used under the following operating conditions: 45 kV tube voltage, 40 mA tube current, 0.016726°2θ/s scan speed, 0.0131303°2θ step size, and 10-70°2θ scan range. The samples were manually ground with an agate pestle and mortar until all material could pass a 63 µm sieve. The powders were back-loaded to the sample holder, which was set to rotate at 15 rpm during the analysis. The phase analysis was carried out with the ICDD PDF4+/Sieve+ software. The Rietveld method interfaced with Diffrac.Topas 6 was used to perform Quantitative Phase Analysis (QPA) and to refine space group, crystallite size and strain, and lattice parameters. Analysis by SEM/EDS was performed on a polished cross-section of sample C_4AF-0.5-1350-AQ. To produce the polished surface, a broken fracture of the pellet was placed on a fitted plastic mould with the cross section facing the bottom. The mould was filled with a 3:1 v/v mixture of epoxy resin and hardener (Buehler EpoThin 2 resin and hardener) and cured at ambient conditions overnight. The mounted sample was ground and polished with a Buehler Automet 250 automatic grinder-polisher. Grinding steps were performed on SiC discs with increasing grit sizes of 220, 320, 400, and 600 and ethanol was used as lubricant. Polishing steps were performed on Buehler polishing cloths using diamond suspensions with sizes 15, 6, 3, 1, and 0.25 µm (MetPrep) and oil-based diamond lubricant (MetPrep). The polished section was carbon coated (10 nm) and stored in a desiccator until analysis. SEM/EDS analysis was performed on an FEI Inspect F50 equipped with an Oxford Instruments EDS detector. Images were taken in secondary electron/back-scattered electron modes at a voltage of 15.0 kV.

Table 1. List of synthesised ferrites. T_f=firing temperature; AQ=air quenched; WQ=water quenched.

A/F ratio $Ca_2Fe_{2-x}Al_xO_5$	Target phase	T_f (°C)	ZnO wt%	Cooling method
x=0	C_2F	1350	0.0/2.0	AQ
x=0.33	C_6AF_2	1350	0.0/2.0	AQ
x=1	C_4AF	1250	0.0/2.0	AQ
		1300	0.0/2.0	AQ
		1350	0.0/2.0	AQ/WQ
			0.5/1.0	AQ
x=1.67	C_6A_2F	1350	0.0/2.0	AQ

3. Results and discussion

Figure 1 shows the XRD diffractograms of ferrite samples. The highest intensity peaks of the (141) reflections of brownmillerite and the (100) of srebrodolskite were selected to evaluate shifts. In Figure 1a, the (141) peaks of brownmillerite show a slight shift towards wider d-spacing with increasing %wt Zn. This is likely due to the bigger ionic radius of Zn^{2+} (0.6-0.9 Å) with respect to Fe^{3+} (0.49-0.78 Å) (Shannon 1976). The Rietveld refinement of lattice parameters shows a monotonic increase in lattice parameter along the b axis. In Figure 1b, the (141) reflections of brownmillerite and the (100) of srebrodolskite show a

pronounced shift towards narrower d-spacing with increasing A/F ratio, both for undoped and Zn-doped ferrites. This is consistent with a Fe^{3+} substitution by the smaller Al^{3+} (ionic radius 0.39-0.535 Å) (Shannon 1976). Interestingly, all C-A-F phases show a slight shift towards wider d-spacing when doped with Zn however, the C_2F phase shows a slight shift towards smaller d-spacing when doped with Zn. This trend change is likely related to the space group change occurring at x~0.2-0.4 from *Pnma* (srebrodolskite) to *Ibm*2 (brownmillerite) and to the higher number of VI-coordinated Fe^{3+} ions (0.55-0.645 Å ionic radius) present in the srebrodolskite structure. Substitution with IV-coordinated Zn^{2+} (0.60 Å) would explain the observed reduction in the lattice parameter in Zn-doped C_2F. In Figure 1c, the effect of varying firing temperatures is shown. The position of the (141) reflection of brownmillerite does not show any significant trend with increasing firing temperatures, while the crystallinity increases with the firing temperature, and increases pronouncedly in the Zn-doped ferrites. The Rietveld crystallite size shows an increase from ~20 nm in the undoped ferrite fired at 1250°C to ~70 nm in the undoped ferrite fired at 1350°C. The increase in crystallite size in the Zn-doped ferrites is less pronounced. The results suggest that the presence of Zn is the major contributor with respect to firing temperatures in increasing the crystallinity. This is likely because ZnO acts as a flux, increasing the melt content (García-Díaz et al 2008; Andrade, Maringolo, and Kihara 2003) and therefore the kinetics of nucleation and growth of high-temperature phase crystals is increased with respect to a solid state reaction. In Figure 1d, the (141) reflections of brownmillerite in air-quenched and water-quenched ferrites are compared. It is confirmed that the presence of Zn is accompanied by a pronounced increase in crystallinity however, no clear effect of the cooling method on the brownmillerite structure could be observed.

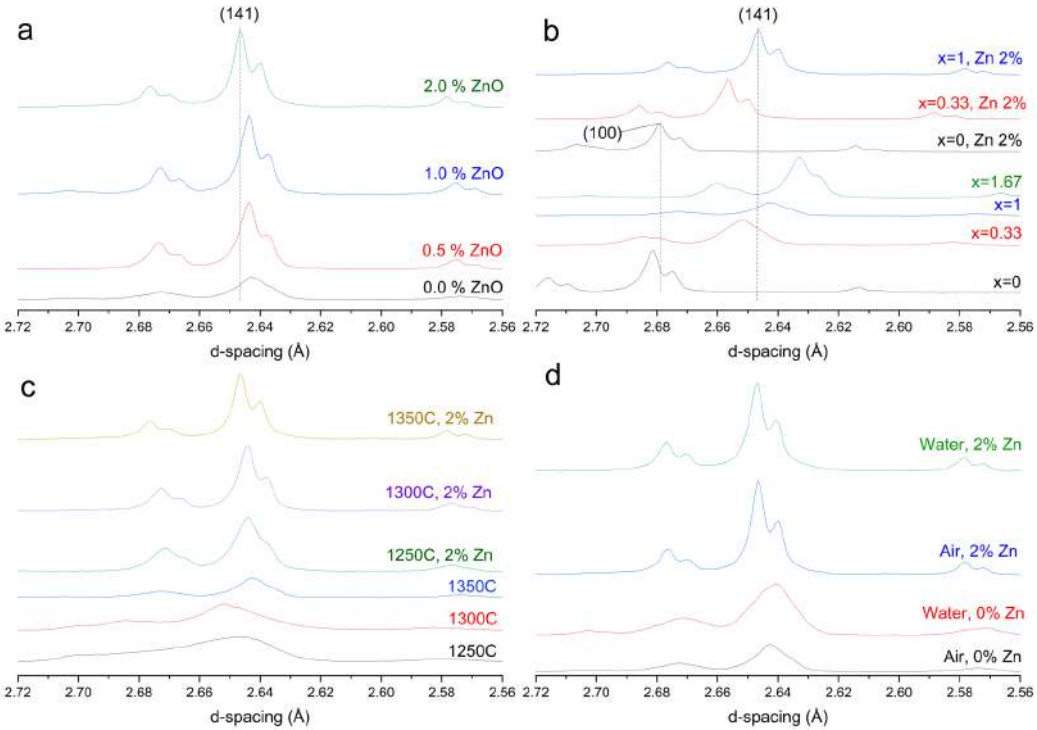


Figure 1. XRD scans showing the (141) reflections of brownmillerite (for C-A-F samples) and (100) reflection of srebrodolskite (for C_2F samples) in various conditions: a) increase in lattice parameter with increasing ZnO% of C_4AF-1350-AQ; b) decrease in lattice parameter with increasing A/F ratio of ferrites fired at 1350°C and air quenched; c) increase in crystallinity with increasing firing temperature and presence of Zn in C_4AF-AQ samples; d) no clear effect of cooling method (air quenched/water quenched) in C_4AF-1350.

The EDS mapping of a 30×26 µm area on the polished surface of sample C_4AF-0.5-1350-AQ is shown in Figure 2, displaying the mapping of elements Ca, Al, Fe, and Zn, along with the corresponding back-scattered electrons (BSE) image. The elements distribution does not appear homogeneous and there are areas where there is a higher concentration of Ca and Fe and other areas rich in Al and Zn. Two phases can be distinguished from the analysis: a major phase that is Ca-rich and has similar amounts of Fe and Al with traces of Zn, and a secondary phase Al-rich and with minor amounts of Ca and Zn. The major phase is consistent with a C_4AF phase doped with Zn, as expected by the stoichiometry of raw materials used and

confirmed by the brownmillerite pattern shown by XRD, with a slight shift towards wider d-spacing caused by the bigger ionic radius of Zn^{2+} replacing Al or Fe (Figure 1a). The secondary phase shows an average atomic composition determined by EDS similar to krotite ($CaAl_2O_4$) partially substituted by Fe ~2% and Zn ~1%. The secondary phase might also be part of the solid solution $Ca_{12}Al_{9-y}Zn_{5+x}O_{32\pm\delta}$, x = 5–5.76 and y = 8.1–8.73 (Kahlenberg and Krüger 2022). However, neither the main peak for krotite nor the main peak of $Ca_6Zn_3Al_8O_{15}$, which is the (044) reflection at 2.6350 Å (Bolio-Arceo and Glasser 1998), were detected in our XRD measurements. Furthermore, the formation of C-Z-A phases has been reported to start at higher Zn dosages, such as 1% (Bolio-Arceo and Glasser 1998; Barbarulo, Sorrentino, and Sing 2007; García-Díaz et al 2008) and 0.7% (Gineys et al 2011).

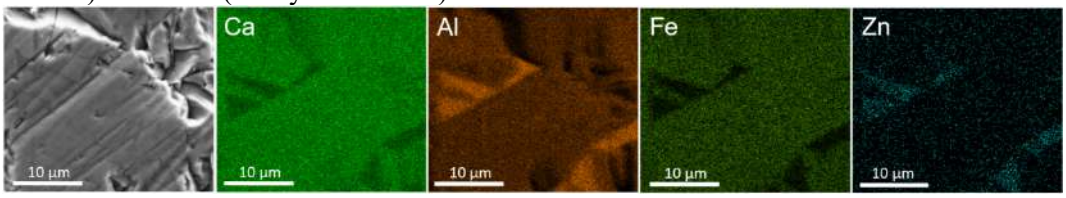


Figure 2. Back-scattered micrograph (left) and EDS mapping of elements Ca, Al, Fe, and Zn on the polished section of C_4AF-0.5-1350-AQ.

4. Conclusions

The effects of Zn on ferrite reported in the literature are often contradictory. In this study, Zn-doped ferrites were synthesised at varying conditions of A/F ratio, burning temperature, Zn dosage, and cooling method. The main findings are that i) Zn is incorporated in ferrites and its presence leads to an increase in lattice parameter due to the larger ionic radius of Zn^{2+} with respect to Al^{3+}, which on the contrary causes a decrease in lattice parameter with increasing A/F ratio. Higher firing temperatures and Zn dosages result in an increase in crystallinity, likely due to the higher melt content which aids crystallisation. No clear effects were observed in relation to the cooling method. Zn preferentially replaces Al in a Ca-Zn-Al phase.

Acknowledgements

This work was supported by the Engineering and Physical Sciences Research Council [grant number EP/W018810/1].

5. References

Andrade, F.R.D., V. Maringolo, and Y. Kihara. 2003. "Incorporation of V, Zn and Pb into the crystalline phases of Portland clinker", *Cement and Concrete Research*, 33: 63-71.

Barbarulo, R., F. Sorrentino, and C. Sing. 2007. "Impact of ZnO on clinker composition and reactivity-Coupling with MgO." *12th International Congress on the Chemistry of Cement*. Montreal, Canada.

Bolio-Arceo, H, and F.P. Glasser. 1998. "Zinc oxide in cement clinkering: part 1. Systems CaO-ZnO-Al_2O_3 and CaO-ZnO-Fe_2O_3", *Advances in Cement Research*, 10(1): 25-32.

Chabayashi, T., A. Nakamura, H. Kato, and K. Sada. 2012. "Influence of titanium oxide and magnesium oxide on the mineral composition and the properties of cement", *Cement Science and Concrete Technology*, 66(1): 211-16.

García-Díaz, I., F. Puertas, M. F. Gazulla, M. P. Gómez, and M. Palacios. 2008. "Effect of ZnO, ZrO_2 and B_2O_3 on clinkerization process. Part I. Clinkerization reactions and clinker composition", *Materiales de Construcción*, 58(292): 81-99.

Gineys, N., G. Aouad, F. Sorrentino, and D. Damidot. 2011. "Incorporation of trace elements in Portland cement clinker: Thresholds limits for Cu, Ni, Sn or Zn", *Cement and Concrete Research*, 41: 1177-84.

Kahlenberg, V., and H. Krüger. 2022. "High-temperature behavior and structural studies on $Ca_{14}Al_{10}Zn_6O_{35}$", *Zeitschrift für Kristallographie*, 237(6-7): 219-32.

Murat, M., and F. Sorrentino. 1996. "Effect of large additions of Cd, Pb, Cr, Zn, to cement raw meal on the composition and the properties of the clinker and the cement", *Cement and Concrete Research*, 26(3): 377-85.

Peys, A., V. Isteri, J. Yliniemi, A. S. Yorkshire, P. N. Lemougna, C. Utton, J. L. Provis, R. Snellings, and T. Hanein. 2022. "Sustainable iron-rich cements: Raw material sources and binder types", *Cement and Concrete Research*, 157: 106834.

Shannon, R. D. 1976. "Revised effective ionic radii and systematic studies of interatomic distances in halides and chalcogenides", *Acta Crystallographica*, A32: 751-67.

Shevchenko, M., and E. Jak. 2019. "Experimental Liquidus Studies of the CaO-ZnO-Fe_2O_3 System in Air", *Journal of Phase Equilibria and Diffusion*, 40: 779-86.

The 16th International Congress on the Chemistry of Cement 2023 (ICCC2023)
"Further Reduction of CO_2 -Emissions and Circularity in the Cement and Concrete Industry"
September 18–22, 2023, Bangkok, Thailand

Recent advances in understanding the hydration of limestone calcined clay cements (LC^3)

F. Zunino[1*], and K.L. Scrivener[2]

[1] *Physical Chemistry of Building Materials, Institute for Building Materials (IfB), ETH Zürich, CH-8093 Zürich, Switzerland*

Email: franco.zunino@ifb.baug.ethz.ch

[2] *Laboratory of Construction Materials, EPFL STI IMX LMC, Station 12, CH-1015 Lausanne, Switzerland*

Email: karen.scrivener@epfl.ch

ABSTRACT

Limestone and calcined kaolinitic clays are unique among supplementary cementitious materials due to their high and widespread availability. Furthermore, their combined reactivity enables substitutions of clinker of 50% (or more), while reaching comparable strength to PC (or pozzolanic cements) and enhanced durability properties. During the last 4 years, our understanding on the hydration mechanisms governing the behavior of these cementitious systems has evolved substantially, opening new possibilities for optimization and further development of the technology. The sulfate requirement of LC^3, which is commonly observed to be higher as conventional PC, has been proven to be controlled by sulfate adsorption mechanisms rather than the total reactive alumina content of the system.

The precipitation of hemi and monocarboaluminate in LC^3 was directly associated with the third hydration peak observed in isothermal calorimetry. Formation of carboaluminates is enhanced by the reaction of carbonates from limestone and alumina from metakaolin and has a significant contribution to strength gain and porosity reduction at early ages. Carboaluminates precipitate in pores remaining after clinker dissolution and remain stable in the long-term.

At later ages, it has been observed that the reaction of metakaolin slowdowns due to the lack of large-saturated pores where hydrates can precipitate. However, further reduction of the critical pore entry radius and total porosity was still observed, suggesting that precipitation might also take place in the pore solution film that lines the internal surface of partially saturated pores. In addition, precipitation of strätlingite was observed combined with a substantial reduction in Ca/Si ratio of C-A-S-H, in agreement with trends observed from thermodynamic modeling at equilibrium.

KEYWORDS: *sustainability, hydration, carboaluminates, sulfate requirement, porosity.*

1. Introduction

Sustainability in the cement industry is a major concern (Schneider et al., 2011). The most effective strategy to tackle this challenge on a worldwide scale is to reduce the clinker factor in cements based on Portland cement clinker (K. L. Scrivener et al., 2016). This has accelerated the adoption of blended cements that incorporate supplementary cementitious materials (SCMs) replacing part of the Portland cement (PC) fraction. Nowadays, blended cements are more common than PC. Among commonly used

SCMs are fine limestone, granulated blast furnace slag and fly ash (Lothenbach et al., 2011). Fly ash and slag are together available in amounts close to 15% of cement production (IEA & CSI, 2018). This means that we need to look for other materials to further reduce clinker factor, such as calcined clays.

Limestone calcined clay cements (LC^3) are one of the promising alternatives for high performance sustainable cements (K. Scrivener et al., 2017). LC^3 incorporates significant amounts of metakaolin, a reactive aluminosilicate phase (Antoni, 2011) formed after calcination of kaolinitic clays, and ground limestone ($CaCO_3$). Both materials are widely available and therefore are suitable to face the current shortage of SCMs (K. L. Scrivener et al., 2016). LC^3 can achieve equivalent strength to OPC at 7 days with a clinker content of only 50% if the kaolinite content of the calcined clay used is above about 40% (Antoni et al., 2012; Avet & Scrivener, 2018a; K. L. Scrivener et al., 2018). The high reactivity of metakaolin contributes to achieve a refined microstructure in LC^3 systems at early ages (Avet & Scrivener, 2018a), making LC^3 a particularly good cement in terms of resisting chloride ingress (Sui et al., 2019).

2. Sulfate requirement of LC^3 and cementitious systems

Calcium sulfate is added to clinker during grinding, to control the reaction of the aluminate phase. This addition is usually referred to as gypsum (Calcium sulfate dihydrate, $CaSO_4 \cdot 2H_2O$) although anhydrite and hemihydrates (plaster) may also be present in combination with minor amounts of alkali sulfates from clinker. The optimum sulfate addition is that which gives the highest strength PC (at 1 or 28 days).

The main purpose of adding gypsum to PC and blended cements is to control the reaction of C_3A and thus to prevent flash setting (Lerch, 1946), however it is also known to influence the hydration kinetics of C_3S/alite (Quennoz & Scrivener, 2013; Zunino & Scrivener, 2020a) and the morphology of C-(A)-S-H (Mota et al., 2015; Zunino & Scrivener, 2022a). In the presence of gypsum, the hydration reaction of C_3A shifts from the precipitation of calcium aluminate hydrates and ettringite is formed (RILEM T.C., 1986). The mechanism by which gypsum slows down the reaction of C_3A has been extensively studied but is still a matter of debate. Originally it was suggested that a diffusion barrier is formed of ettringite or Ca-Al hydrates, retarding the dissolution of C_3A (Collepardi et al., 1978; Corstanje et al., 1974). Recent work shows that there is no diffusion barrier and it is more tenable that the adsorption of sulfate (or Ca-S complexes) on C_3A active sites slows down the C_3A reaction (Geng et al., 2018; Minard et al., 2007; Myers et al., 2016). Usually, the adjustment of gypsum content is made based on the measurement of compressive strength at 24 hours in mortar specimens or by isothermal calorimetry (ASTM C563, 2018).

In LC^3 cements (and blended cements in general), the total sulfate content is lower due to the partial replacement of PC by SCMs. In some cases, undersulfation of the system is observed, where the aluminate peak occurs before the alite (main) hydration peak (Quennoz & Scrivener, 2013; Zunino & Scrivener, 2020a). The balance of the system can be restored by the incorporation of additional gypsum to retard the aluminate reaction (Antoni et al., 2012; Avet & Scrivener, 2018a; Zunino, 2020). For a given cementitious system (PC or blended cements), the sulphate balance can be associated with two main controlling factors established by Zunino and Scrivener (Zunino & Scrivener, 2020a):

- **Adsorption of sulfate on surfaces**, mainly C-(A)-S-H, during the induction and acceleration period (before the onset of the aluminate peak) (Zunino & Scrivener, 2019b). In LC^3 (and blended cements), an increased amount of C-(A)-S-H forms due to the enhanced reaction of alite (filler effect), leading to an earlier depletion of solid gypsum and thus an earlier aluminate peak (Bentz et al., 2017; Zunino, 2020; Zunino & Scrivener, 2020a, 2019b).

- **The formation of ettringite before gypsum depletion** (i.e., before the onset of the aluminate peak). The amount of ettringite formed depends on the reaction rate of C_3A and the solubility of the sulphate source (Zunino & Scrivener, 2020a). In a recent study, the authors showed that the contribution of alumina from SCMs to sulfate balance is second order compared to the effect on

alite hydration and C-(A)-S-H precipitation rate. Particularly, the contribution does not seem to be related to the alumina content of the SCM (Zunino & Scrivener, 2022c).

This mechanism has been extended to cementitious systems in general, including PC and blended cements with limestone (PLC) and slag (Zunino & Scrivener, 2022c), and it has been validated far beyond the original scope of the study, for example, with the addition of alkali salts as accelerators (Yan et al., 2021). It highlights that, in addition to dissolution and supersaturation, adsorption of species (sulfate complexes) in surfaces can also influence the hydration kinetics of cementitious systems.

3. Precipitation of carboaluminates and relationship with mechanical properties

A major factor contributing to this good performance is the higher amounts of carbo-AFm (CO_3-AFm) phases, which will be referred as carbo-aluminate phases. These carbo-aluminate phases are hemicarboaluminate ($C_4Ac_{0.5}H_{12}$, Hc) and monocarboaluminate (C_4AcH_{11}, Mc), which are formed in LC^3 systems due to the reaction between metakaolin and limestone (Antoni, 2011; Avet & Scrivener, 2018a).

As shown in Figure 1, carboaluminates precipitate in pores left after clinker hydration, significantly contributing to space filling and mechanical properties development. In a recent study (Zunino & Scrivener, 2021a), the authors showed that the precipitation of carboaluminates is related with a feature observed in calorimetry curves of LC^3 systems, namely the third peak of hydration. This peak relates to the reaction of metakaolin with limestone and occurs with a maximum between 2 and 4 days of hydration depending on the metakaolin content of the system. By comparing the total heat released (proportional to the overall reaction degree) and in-situ ultrasound pulse velocity (proportional to elastic modulus/strength), a relationship between strength development in LC^3 and the third peak of hydration was established. Moreover, a fundamental/mechanistic explanation for well-known relationship (Avet & Scrivener, 2018a) between metakaolin content (which influences the kinetics of the third peak) and compressive strength between 3 and 7 days was provided.

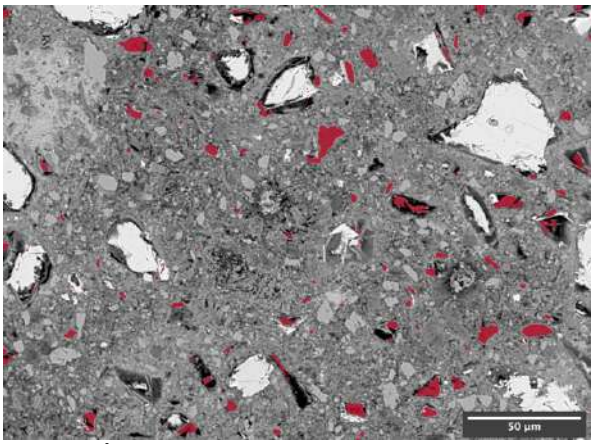


Figure 1: *BSE maps of a typical LC^3 system sealed-hydrated for 3 days with CO_3-AFm phase highlighted in red.*

In addition to the total metakaolin content of the system, the precipitation of carboaluminates is also influenced by the sulfate content of the system and the water to binder ratio (Zunino & Scrivener, 2021a). In LC^3 systems, the formation of ettringite is only limited by the availability of sulfate (gypsum), as alumina from metakaolin is generally present in excess. When the amount of sulfate in the system is increased so it is the amount of ettringite formed. Eventually, C_3A is depleted, and the reaction is then sustained with alumina from metakaolin. This pathway to ettringite (Eq, 1) is deficient in calcium compared to the classical reaction involving C_3A (Eq. 2) and therefore CH is consumed in the process. As a result, the formation of carboaluminates is suppressed until sulfate depletion.

$$AS_2 + 3CH + 3C\$H_2 + 23H \rightarrow C_6A\$_3H_{32} \quad (1)$$

$$C_3A + 3C\$H_2 + 26H \rightarrow C_6A\$_3H_{32} \quad (2)$$

4. Long-term hydration of LC^3 cements

In general, studies on LC^3 systems have focused on early-age performance, i.e., from mixing up to about 90 days (Avet & Scrivener, 2018b; Zunino & Scrivener, 2021a). Different aspects on raw material processing (Zunino et al., 2020; Zunino & Scrivener, 2020b, 2021b), blend design (Antoni et al., 2012) and sulfate balance (Zunino & Scrivener, 2019a, 2020c), rheology (Hou, 2021), hydration kinetics (Avet et al., 2018; Avet & Scrivener, 2018b), morphology and properties of hydrates (Avet et al., 2019; Zunino & Scrivener, 2021a), and the synergic reaction of metakaolin and limestone (Zunino & Scrivener, 2021a) have been described in detail over this period. Most of the studies concerning later-ages are related to durability aspects of LC^3 (Dhandapani et al., 2018, p. 3; Nguyen, 2020), rather than a detailed phase assemblage and microstructural assessment focused on hydration. In this regard, thermodynamic modelling is a useful tool to predict and extrapolate the phase composition of cements towards later ages (Lothenbach & Zajac, 2019). However, the complexity of LC^3 systems makes this process challenging, information on reaction kinetics is still required to accurately predict the phase assemblage over time (Lothenbach et al., 2019; Lothenbach & Zajac, 2019).

In a recent study (Zunino & Scrivener, 2022b), a systematic look on the microstructural development of LC^3 systems in the long term provided new insights in this regard. Strätlingite was observed for the first time in these types of binder in addition to Mc and Hc. More importantly, evidence for a continued (slow) reaction of metakaolin in the long term was provided, leading to an increased reduction in porosity between 90 days and 3 years. Based on CH consumption rates, it was estimated that the long-term reaction of metakaolin proceeds 10-to-20 times slower than at earlier ages.

Interestingly, the reaction of metakaolin seems to continue beyond depletion of CH. In this case, the required calcium to sustain the reaction is sourced from C-(A)-S-H, leading to a decrease in Ca/Si ratio. This observation, predicted by thermodynamic modeling before (Kunther et al., 2016), was confirmed experimentally for the first time in (Zunino & Scrivener, 2022b). The study also confirmed the long-term stability of Hc, despite the absence of this phase in thermodynamic modeling results. In a subsequent study, this stability is linked to the incorporation of sulfate in Hc (Georget et al., 2022). By comparing the pore size distribution with internal relative humidity, an hydration mechanism considering precipitation in the pore solution film lining the surface of larger pores was proposed (Zunino & Scrivener, 2022b).

5. Conclusions and perspectives

During the last 4 years, significant advances in the fundamental understanding of the hydration of LC^3 cements have been achieved. Clear answers have been provided to some outstanding questions regarding binder formulation and long-term hydration performance. Based on these findings, the following concluding remarks can be drawn:

- The sulfate requirement of LC^3 cements is associated with the surface area of the clay and limestone used, and not with the reactive alumina content of the system. Isothermal calorimetry appears as the most reliable method to assess and correct sulfation issues in complex binder formulations.
- Carboaluminates, as C-A-S-H, play a key role in the development of compressive strength in LC^3 binders. The kinetics of the carboaluminate precipitation was described and explained the relationship between metakaolin content and strength of LC^3 at early-age.
- The reaction of metakaolin continues in the long-term, leading to a decrease in the critical entry radius and a reduction in total porosity. While some conversion of Hc to Mc is observed, Hc is still present in significant amounts highlighting the long-term stability of this phase.

While progress has been significant, some open question remains. In general, our understanding on reaction kinetics and phase assemblage during the first 24 hours of hydration is limited compared to later ages. Shading light over this period is crucial to unveil outstanding issues for practice, such as workability (thixotropy, structural build-up, surface/admixture interactions) and early-age strength.

Acknowledgements

Dr. Zunino and Prof. Scrivener acknowledge the financial support provided by the Swiss Agency of Development and Cooperation (SDC), grant 81026665. Dr. Zunino is supported by the Swiss National Science Foundation (SNSF) through an Ambizione fellowship (grant 208719).

References

Antoni, M. (2011). *Investigation of cement substitution by combined addition of calcined clays and limestone*. École Polytechnique Fédérale de Lausanne.

Antoni, M., Rossen, J., Martirena, F., & Scrivener, K. (2012). Cement substitution by a combination of metakaolin and limestone. *Cement and Concrete Research*, *42*(12), 1579–1589. https://doi.org/10.1016/j.cemconres.2012.09.006

ASTM C563. (2018). *Standard Guide for Approximation of Optimum SO3 in Hydraulic Cement*. https://doi.org/10.1520/C0563-18.2

Avet, F., Boehm-Courjault, E., & Scrivener, K. (2019). Investigation of C-A-S-H composition, morphology and density in Limestone Calcined Clay Cement (LC3). *Cement and Concrete Research*, *115*, 70–79. https://doi.org/10.1016/j.cemconres.2018.10.011

Avet, F., Li, X., & Scrivener, K. (2018). Determination of the amount of reacted metakaolin in calcined clay blends. *Cement and Concrete Research*, *106*, 40–48. https://doi.org/10.1016/j.cemconres.2018.01.009

Avet, F., & Scrivener, K. (2018a). Investigation of the calcined kaolinite content on the hydration of Limestone Calcined Clay Cement (LC3). *Cement and Concrete Research*, *107*(January), 124–135. https://doi.org/10.1016/j.cemconres.2018.02.016

Avet, F., & Scrivener, K. (2018b). Investigation of the calcined kaolinite content on the hydration of Limestone Calcined Clay Cement (LC3). *Cement and Concrete Research*, *107*, 124–135. https://doi.org/10.1016/j.cemconres.2018.02.016

Bentz, D. P., Ferraris, C. F., Jones, S. Z., Lootens, D., & Zunino, F. (2017). Limestone and silica powder replacements for cement: Early-age performance. *Cement and Concrete Composites*, *78*, 43–56. https://doi.org/10.1016/j.cemconcomp.2017.01.001

Collepardi, M., Baldini, G., & Pauri, M. (1978). Tricalcium aluminate hydration in the presence of lime, gypsum or sodium sulfate. *Cement and Concrete Research*, *8*, 571–580.

Corstanje, W., Stevels, H. N., & Stevels, J. M. (1974). Hydration reactions in pastes C3S+C3A+CaSO4 2aq + water at 25ºC. *Cement and Concrete Research*, *4*, 417–431.

Dhandapani, Y., Sakthivel, T., Santhanam, M., Gettu, R., & Pillai, R. G. (2018). Mechanical properties and durability performance of concretes with Limestone Calcined Clay Cement (LC3). *Cement and Concrete Research*, *107*, 136–151. https://doi.org/10.1016/j.cemconres.2018.02.005

Geng, G., Myers, R. J., Yu, Y.-S., Shapiro, D. A., Winarski, R., Levitz, P. E., Kilcoyne, D. A. L., & Monteiro, P. J. M. (2018). Synchrotron X-ray nanotomographic and spectromicroscopic study of the tricalcium aluminate hydration in the presence of gypsum. *Cement and Concrete Research*, *111*(June), 130–137. https://doi.org/10.1016/j.cemconres.2018.06.002

Georget, F., Lothenbach, B., Wilson, W., Zunino, F., & Scrivener, K. L. (2022). Stability of hemicarbonate under cement paste-like conditions. *Cement and Concrete Research*, *153*, 106692. https://doi.org/10.1016/j.cemconres.2021.106692

Hou, P. (2021). Mechanisms dominating thixotropy in limestone calcined clay cement (LC3). *Cement and Concrete Research*, 13.

IEA, & CSI. (2018). *Technology Roadmap: Low-Carbon transition in the Cement Industry*. https://doi.org/10.1007/springerreference_7300

Kunther, W., Dai, Z., & Skibsted, J. (2016). Thermodynamic modeling of hydrated white Portland cement–metakaolin–limestone blends utilizing hydration kinetics from 29Si MAS NMR spectroscopy. *Cement and Concrete Research*, *86*, 29–41. https://doi.org/10.1016/j.cemconres.2016.04.012

Lerch, W. (1946). The influence of gypsum on the hydration and properties of portland cement pastes. *American Society for Testing Materials Journal*, *12*.

Lothenbach, B., Kulik, D. A., Matschei, T., Balonis, M., Baquerizo, L., Dilnesa, B., Miron, G. D., & Myers, R. J. (2019). Cemdata18: A chemical thermodynamic database for hydrated Portland cements and alkali-activated materials. *Cement and Concrete Research*, *115*(October 2018), 472–506. https://doi.org/10.1016/j.cemconres.2018.04.018

Lothenbach, B., Scrivener, K., & Hooton, R. D. (2011). Supplementary cementitious materials. *Cement and Concrete Research*, *41*(12), 1244–1256. https://doi.org/10.1016/j.cemconres.2010.12.001

Lothenbach, B., & Zajac, M. (2019). Application of thermodynamic modelling to hydrated cements. *Cement and Concrete Research*, *123*, 105779. https://doi.org/10.1016/j.cemconres.2019.105779

Minard, H., Garrault, S., Regnaud, L., & Nonat, A. (2007). Mechanisms and parameters controlling the tricalcium aluminate reactivity in the presence of gypsum. *Cement and Concrete Research*, *37*, 1418–1426. https://doi.org/10.1016/j.cemconres.2007.06.001

Mota, B., Matschei, T., & Scrivener, K. (2015). The influence of sodium salts and gypsum on alite hydration. *Cement and Concrete Research*, *75*, 53–65. https://doi.org/10.1016/j.cemconres.2015.04.015

Myers, R. J., Geng, G., Li, J., Rodríguez, E. D., Ha, J., Kidkhunthod, P., Sposito, G., Lammers, L. N., Kirchheim, A. P., & Monteiro, P. J. M. (2016). Role of adsorption phenomena in cubic tricalcium aluminate dissolution. *Langmuir*, *33*(1), 45–55. https://doi.org/10.1021/acs.langmuir.6b03474

Nguyen, Q. D. (2020). Mitigation of alkali-silica reaction by limestone calcined clay cement (LC3). *Cement and Concrete Research*, 14.

Quennoz, A., & Scrivener, K. L. (2013). Interactions between alite and C3A-gypsum hydrations in model cements. *Cement and Concrete Research*, *44*, 46–54. https://doi.org/10.1016/j.cemconres.2012.10.018

RILEM T.C. (1986). The hydration of tricalcium aluminate and tetracalcium aluminoferrite in the presence of calcium sulfate. *Materials and Structures*, *19*(2), 137–147. https://doi.org/10.1007/BF02481758

Schneider, M., Romer, M., Tschudin, M., & Bolio, H. (2011). Sustainable cement production—Present and future. *Cement and Concrete Research*, *41*(7), 642–650. https://doi.org/10.1016/j.cemconres.2011.03.019

Scrivener, K. L., Avet, F., Maraghechi, H., Zunino, F., Ston, J., Favier, A., & Hanpongpun, W. (2018). Impacting factors and properties of Limestone Calcined Clay Cements (LC3). *Green Materials*. https://doi.org/10.1680/jgrma.18.00029

Scrivener, K. L., John, V., & Gartner, E. M. (2016). *Eco-efficient cements: Potential, economically viable solutions for a low-CO2, cement-based materials industry*. United Nations Environmental Programme (UNEP).

Scrivener, K., Martirena, F., Bishnoi, S., & Maity, S. (2017). Calcined clay limestone cements (LC3). *Cement and Concrete Research*, *August 2017*, 1–8. https://doi.org/10.1016/j.cemconres.2017.08.017

Sui, S., Wilson, W., Georget, F., Maraghechi, H., Kazemi-Kamyab, H., Sun, W., & Scrivener, K. (2019). Quantification methods for chloride binding in Portland cement and limestone systems. *Cement and Concrete Research*, *125*(August). https://doi.org/10.1016/j.cemconres.2019.105864

Yan, Y., Scrivener, K. L., Yu, C., Ouzia, A., & Liu, J. (2021). Effect of a novel starch-based temperature rise inhibitor on cement hydration and microstructure development: The second peak study. *Cement and Concrete Research*, *141*, 106325. https://doi.org/10.1016/j.cemconres.2020.106325

Zunino, F. (2020). *Limestone calcined clay cements (LC3): Raw material processing, sulfate balance and hydration kinetics*. EPFL Thesis 8173.

Zunino, F., Boehm-Courjault, E., & Scrivener, K. (2020). The impact of calcite impurities in clays containing kaolinite on their reactivity in cement after calcination. *Materials and Structures*, *53*(2), 44. https://doi.org/10.1617/s11527-020-01478-9

Zunino, F., & Scrivener, K. (2019a). The influence of the filler effect on the sulfate requirement of blended cements. *Cement and Concrete Research*, *126*, 105918. https://doi.org/10.1016/j.cemconres.2019.105918

Zunino, F., & Scrivener, K. (2020a). Factors influencing the sulfate balance in pure phase C3S/C3A systems. *Cement and Concrete Research*, *133*(106085). https://doi.org/10.1016/j.cemconres.2020.106085

Zunino, F., & Scrivener, K. (2020b). Increasing the kaolinite content of raw clays using particle classification techniques for use as supplementary cementitious materials. *Construction and Building Materials*, *244*, 118335. https://doi.org/10.1016/j.conbuildmat.2020.118335

Zunino, F., & Scrivener, K. (2020c). Factors influencing the sulfate balance in pure phase C3S/C3A systems. *Cement and Concrete Research*, *133*, 106085. https://doi.org/10.1016/j.cemconres.2020.106085

Zunino, F., & Scrivener, K. (2021a). The reaction between metakaolin and limestone and its effect in porosity refinement and mechanical properties. *Cement and Concrete Research*, *140*. https://doi.org/10.1016/j.cemconres.2020.106307

Zunino, F., & Scrivener, K. (2021b). Assessing the effect of alkanolamine grinding aids in limestone calcined clay cements hydration. *Construction and Building Materials*, *266*, 121293. https://doi.org/10.1016/j.conbuildmat.2020.121293

Zunino, F., & Scrivener, K. (2022a). The influence of sulfate addition on hydration kinetics and C-S-H morphology of C3S and C3S/C3A systems. *Cement and Concrete Research*, *160*. https://doi.org/10.1016/j.cemconres.2022.106930

Zunino, F., & Scrivener, K. (2022b). Microstructural developments of limestone calcined clay cement (LC3) pastes after long-term (3 years) hydration. *Cement and Concrete Research*, *153*, 106693. https://doi.org/10.1016/j.cemconres.2021.106693

Zunino, F., & Scrivener, K. (2022c). Insights on the role of alumina content and the filler effect on the sulfate requirement of PC and blended cements. *Cement and Concrete Research*, *160*, 106929. https://doi.org/10.1016/j.cemconres.2022.106929

Zunino, F., & Scrivener, K. L. (2019b). The influence of the filler effect in the sulfate requirement of blended cements. *Cement and Concrete Research*, *126*. https://doi.org/10.1016/j.cemconres.2019.105918

The 16th International Congress on the Chemistry of Cement 2023 (ICCC2023)
"Further Reduction of CO_2 -Emissions and Circularity in the Cement and Concrete Industry"
September 18–22, 2023, Bangkok, Thailand

Microstructural mechanism involved in the expansion generated in cementitious materials with expansive agent type K

J.L. García Calvo*, P. Carballosa, F. Pedrosa and D. Revuelta

[1]*Institute for Construction Sciences Eduardo Torroja. IETcc-CSIC, Madrid, Spain*
Email: jolgac@ietcc.csic.es

ABSTRACT

In concrete elements exposed to the environment, shrinkage can promote cracking that compromises its durability due to a reduction of the mechanical properties along with the penetration of aggressive agents. One of the main purpose of developing expansive concretes is the mitigation of this shrinkage and the resulting cracking. Expansive concretes are usually fabricated by using expansive agent type K that is a powdered material with hydraulic properties. Expansive agent type K forms ettringite during its hydration process, but several aspects related to the microstructural mechanisms involved in the expansion performance of cement pastes with this type of expansive agent are not well known. In the present work, different microstructural techniques were considered to evaluate two issues related with this special type of material. The first one focuses on evaluating the possible microstructural mechanisms associated to the shrinkage observed in these expansive cementitious materials, even in isolated conditions or with outer water supply. The second one aims to appraise the influence of the pore microstructure content in the expansion obtained, to define the main microstructural mechanism involved in the generation of the expansion. The results obtained indicate that the transformation of low crystalline ettringite to low crystalline monosulfate could be responsible for the shrinkage detected after the maximum expansion is reached. Regarding the second issue, it seems that the main mechanism responsible for the expansion obtained is the in-situ precipitation of the constituent components from the expansive agent anhydrous grains components with the subsequent ettringite formation.

KEYWORDS: *Expansive cementitious materials; Hydration; Microstructure; Expansion performance; Porosity.*

1. Introduction

Drying shrinkage can promote cracking in concrete elements and reduce their durability (mechanical performance and penetration of aggressive agents). In this sense, expansive concretes are developed to mitigate this shrinkage and the resulting cracking. An effective means of reducing shrinkage is the development of expansive concretes with inorganic expansive agents, being the ettringite-based the most used ones (Klein et al (1961)). Despite its extended use, the mechanisms involved in the expansion promoted by this type of expansive agent are not yet fully understood. The crystallization pressure generated by the oversaturation of crystals (ettringite) when the agents hydrate would result in a significant expansion in the hardened state (Ogawa and Roy (1981)) and this phenomenon could partially explain the mechanisms involved. Other hypotheses put forward entail the "in situ" hydration of an anhydrous phase with the formation of hydrated phases, thereby forming coexisting pores by disintegration of expansive particles during hydration, the absorption of water by colloidal ettringite, etc (Okushima et al (1968); Hansen (1976)).

Previous studies have proven that without outer water supply, expansive concretes manufactured using type K agent undergo greater shrinkage than those cured in wet conditions (García Calvo et al (2017)). The above-mentioned concretes were cured under isolated conditions meaning the resulting shrinkage cannot be related to drying phenomena, rather to microstructural phenomena instead. In turn, recent

studies postulated that the expansion mechanism is a disruptive phenomenon that generates an initial microcracking in the cementitious matrix derived from the stresses produced by hydrates formation/precipitation in confined places by a cement matrix that already features a degree of stiffness, with this microcracking being initially alleviated by autogenous self-curing (Carballosa et al (2020)). Thus, the existence of confined places in the cement matrix seems to be essential to generate the expansion desired. Thereupon, the increase of porosity in the cement matrix should decrease the expansion obtained. Air-entraining admixture is used in this study to appraise the hypothesis postulated by modifying the pore content of the evaluated cement matrix.

2. Experimental program

Table 1 shows the chemical composition of the cement and the expansive agents. The X-ray diffractograms (XRDs) made, not shown, indicate that the expansive agents were mainly composed of anhydrite, ye'elimite and lime; the main differences between both agents were the higher ye'elimite content and the lesser lime content in K-1 agent. For evaluating the shrinkage observed under different curing conditions, cement pastes with 15% by weight cement of expansive agent type K-1 were manufactured, using w/c of 0.5. The manufactured paste samples were cured under two different free expansion conditions: F-1) cured in a humidity chamber (98%RH and 20ºC); F-2) wrapped in plastic film and maintained at 20ºC. The free expansion was assessed according to ASTM C157. The hydration of the cement pastes was also characterized at several curing ages: 1, 3, 7 and 28 days by stopping the hydration processes. Differential thermal analysis and thermogravimetric analysis (DTA/TGA), and Fourier-transform mid-infrared spectroscopy (FT-MIR) were used to evaluate the cement pastes' hydration.

Table 1. Main chemical composition (%) of the expansive agents used.

	CaO	*SiO_2*	*Al_2O_3*	*SO_3*	*Fe_2O_3*	*MgO*
Portland cement	60.3	17.4	4.68	3.17	5.08	1.78
Expansive agent K-1	54.0	1.88	13.6	26.5	0.49	1.33
Expansive agent K-2	69.2	1.84	6.48	17.3	0.84	1.45

Table 2. Cement pastes compositions to evaluate the influence of the pore microstructure in the expansion obtained.

	REF	*EXP*	*EXP+Air*
CEM I 42.5R (kg/m^3)	1394	1208	1208
Water (kg/m^3)	557	556	552
Air-entrainment additive (kg/m^3)	-	-	4.2
Expansive agent K-2 (kg/m^3)	-	181	181
(% by weight cement)	0%	15%	15%
w/c	0.40	0.46	0.46
w/b	0.40	0.40	0.40

The cement pastes defined in
Table 2 were fabricated for evaluating the influence of the porosity in the expansion obtained. Air entrainment additive was used in EXP+Air sample in order to increase the pore content of the cement paste. The restraining expansion was measured by filling steel tubes (∅100 x 70 mm size). Two strain gauges were placed diametrically opposed in the perimeter of the central section of each steel tubes. The circumferential expansion obtained was monitored on an hourly basis for 28 days by means of an electronic device. Cylindrical specimens (∅75 x 150 mm size) were produced to evaluate the hydration evolution of the cement pastes. The samples were cured wrapped in plastic film at 20ºC as to prevent any water exchange. The cement pastes' hydration was characterized at 2, 7, 28 and 365 days by means of XRD, DTA/TGA and BSEM (Backscattered scanning electron microscopy).

3. Results and discussion

3.1 Microstructural modifications related to the shrinkage detected.

The longitudinal free expansion behavior of the cement pastes was measured under curing conditions F-1 and F-2. As shown in Figure 2, the maximum expansion value was achieved on day 3, followed by an expansion decrease until 7 days of age. After that, the magnitude of the expansion was maintained during all the test period in both cases. The magnitude of the decrease is similar in both cases though slightly higher in F-2 conditions (29% versus 33%, in relative terms). Since drying shrinkage is not expected in any of the two curing conditions considered, certain microstructural modifications must be occurring. In the DTA analysis made, the most standout aspect is the existence of a signal between 220 and 270ºC which might be related to monosulfate dehydration. This signal appears after 3 days of curing and increases over time, so possibly some of the ettringite formed transforms to monosulfate. Moreover, if the weight loss associated to monosulfate signal at 28 days is calculated, the monosulfate content in the paste under F-2 conditions is slightly higher than the one of the cement paste under F-1 conditions. Therefore, wet curing may limit the ettringite conversion to monosulfate which concurs with the less relative expansion decrease detected in F-1 conditions with respect to those of F-2. The formation of calcium monocarboaluminate after 3 days of curing in both cases is also detected. The inclusion of type K expansive agent should significantly increase the availability of Al in the pore solution. Thus, even though aluminum ions take part in the formation of monocarboaluminate, there should be remaining Al that can react with ettringite to form monosulfate during the first days. However, since monocarboaluminate is also formed very fast in the evaluated pastes due to the high Al availability, the further formation of monosulfate from ettringite at longer ages is very limited. This initial lack of ettringite stabilization when monocarboaluminate is formed in the very short term has also been described in non-expansive ternary cement pastes when the C_3A content of the portland cement used is overly high (Fernández et al (2016)). The FT-MIR spectra made confirm the results already mentioned: regarding the "sulfate bands" (3530, 1120 and 610 cm^{-1}), clear modifications in the shape of the two firsts bands are detected, with the shoulder even beginning to disappear at 610cm^{-1}. This last band vanishes at 28 days in F-1 cement paste and at shorter time (7 days) in F-2 cement conditions. These phenomena should be related to the initial conversion of ettringite into monosulfate, being this conversion more evident in the absence of curing water (F-2 conditions).

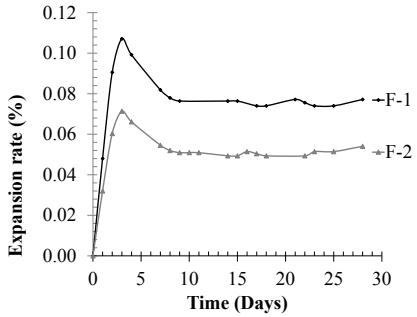


Figure 1. Free expansion regime measured in the cement pastes in F-1 and F-2 curing conditions.

3.2 Influence of the porous microstructure in the expansion obtained

Regarding the circumferential restrained expansion behavior of the cement paste filled tubes, the maximum expansion is detected after 5-6 days (slightly delayed in the EXP+Air tube) and, after that, expansion decrease is detected. The most noteworthy issue is the higher expansion detected in the expansive cement paste with air-entraining admixture. In the XRD made, any significant difference in the ettringite content was detected between EXP and EXP+Air sample, even if the former showed higher expansion. Moreover, the consumption of ye'elimite is very similar in both samples. DTA/TGA analysis do not show any significant difference between the cement pastes with expansive agent but higher ettringite content in both cases with respect to REF sample. Therefore, since similar ettringite content is detected in both cases and higher expansion is observed in EXP+Air sample, the pores formed by the air-entraining admixtures should not be filled by ettringite. This aspect is confirmed in the BSEM images shown in Figure 2 where it is evident that all the air pores generated with the air-entraining admixture are not filled by ettringite from the expansive agent but they are empty. This fact helps to confirm that the

main mechanism responsible for the expansion obtained is the in-situ precipitation of the constituent components of the ettringite with the subsequent ettringite formation.

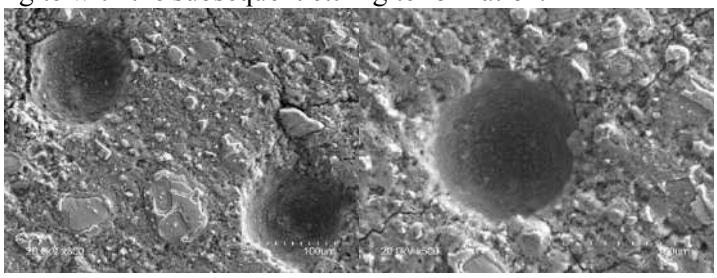


Figure 2. BSEM images of the air voids formed EXP+Air paste after 28 days of curing (x300 and x500).

4. Conclusions

The main conclusion drawn in each of the issues evaluated in this study is:
- The shrinkage detected after the maximum expansion value should be related to the transformation of low crystalline ettringite in low crystalline monosulfate. This transformation will cause lower volume of hydration products and it is closely related to the curing/environmental conditions.
- The higher expansion rate detected in the EXP+Air sample indicates that the air pores generated increase the expansion yet these pores are not filled by ettringite formed from the expansive additive. Consequently, the main mechanism responsible for the expansion obtained is not the diffusion of constituent components from the expansive agent anhydrous grains and further ettringite precipitation, but the in-situ precipitation of these components with the subsequent ettringite formation. In this sense, even if the air-entrained admixtures act in the fresh state, since the inclusion of the expansive agent significant decrease the setting times (both initial and final), the combination of both "additives" (air-entrained and expansive agent) can play an important role that generates this expansion. This fact must be evaluated in depth in further studies.

Acknowledgements

Authors gratefully acknowledge the Spanish Ministry of Science and Innovation for the financial support given to carry out this research as part of project PID2020-113223RB-I00. They would similarly like to express their gratitude to Cementos Portland Valderribas and IMCD for supplying the cement and expansive agents used in this study.

References

Carballosa, P., García Calvo, J.L. and Revuelta, D. (2020) "Influence of expansive calcium sulfoaluminate agent dosage on properties and microstructure of expansive self-compacting concretes", *Cement and Concrete Composites,* 107:103464

Fernández, Á., Alonso, M.C., García-Calvo, J.L., Lothenbach, B. (2016) "Influence of the synergy between mineral additions and Portland cement in the physical-mechanical properties of ternary binders", *Materiales de Construcción*, 66:e097

García Calvo, J.L., Carballosa, P., Revuelta, D. and Gutiérrez, J.P. (2017) "Comparison between the performance of expansive SCC and expansive conventional concretes in different expansion and curing conditions", *Construction and Building Materials*, 136:277–285

Hansen, W.C. (1976) "A discussion of the paper mechanism of expansion associated with ettringite formation", *Cement and Concrete Research,* 3:655-656

Klein, A., Karby, T. and Polivka, M. (1961) "Properties of an expansive cement for chemical prestressing", *ACI Journal Proceedings*, 58: 59–82.

Ogawa, K. and Roy D.M. (1982) "C_4A_3S hydration, ettringite formation and the expansive mechanism", *Cement and Concrete Research*, 12:247-256

Okushima, M.; Kondo, R.; Muguruma, H. and Ono, Y. (1968) "Development of expansive cement with calcium sulfoaluminous cement Clinker", Supplementary Paper 4-86, *Proc. Fifth International Symposium on the Chemistry of Cemen*t, 4:419-430

The 16th International Congress on the Chemistry of Cement 2023 (ICCC2023)
"Further Reduction of CO_2 -Emissions and Circularity in the Cement and Concrete Industry"
September 18–22, 2023, Bangkok, Thailand

The influence of free water removal approaches on the composition and morphologies of CAC hydrates cured at different temperatures

J. Zeng[1], Z. Zhang[2], S. Chu[3], Y. Mu[4], A. Zhang[5] and G. Ye[6]*

1 National Engineering Research Center for Advanced Polymer Processing Technology, Zhengzhou University, Zhengzhou 450001, China
Email: zengjinyan0811@163.com
2 School of Materials Science and Engineering, Zhengzhou University, Zhengzhou 450001, China
Email: 1345183859@qq.com
3 School of Materials Science and Engineering, Zhengzhou University, Zhengzhou 450001, China
Email: 1220732384@qq.com
4 School of Materials Science and Engineering, Zhengzhou University, Zhengzhou 450001, China
Email: myd1228@zzu.edu.cn
5 Luoyang Sanhe New Materials Technology Co. LTD., Luoyang 454000, China
Email: dongmeijin86@163.com
6 School of Materials Science and Engineering, Zhengzhou University, Zhengzhou 450001, China
Email: gtyezzu@zzu.edu.cn

ABSTRACT

The hydration of calcium aluminate cement (CAC) is highly dependent on the temperature and the various hydrates with diverse morphologies are generated by the hydration of CAC at different temperatures. Therefore, it is crucial to completely halt the hydration of CAC at the designated time to further investigate the composition and microstructure of CAC hydrates during the hydration process. This work aims to compare three commonly used drying techniques (freeze vacuum drying, isopropanol exchange followed by vacuum drying and oven drying) for arresting hydration of CAC and free water removal. The CAC pastes were cured at 10 ℃, 30 ℃ and 50 ℃, respectively, in order to obtain different hydrates CAH_{10}, C_2AH_8 and C_3AH_6 at varied hydration rates. The results show that the freeze vacuum drying terminates the hydration more effectively and brings little damage to the structure and component of hydrates, which should be the preferred technique of free water removal for CAC pastes. But as the isopropanol soaking is not able to thoroughly extract the free water, the subsequent oven drying and vacuum drying further accelerates the continued hydration of CAC to a bit higher extent. Moreover, the isopropanol replacement followed by vaccum drying even changes the phase composition of hydrate C_2AH_8.

KEYWORDS: *Calcium aluminate cement, Arresting hydration, Water removal, Hydrates structure*

1. Introduction

Calcium aluminate cement (CAC) is a versatile special cementitious material which is used in high performance applications (Ukrainczyk et al (2010), Shirani et al (2020)). The main mineral phases of CAC are anhydrous $CaO{\cdot}Al_2O_3$ (CA) and $2CaO{\cdot}Al_2O_3$ (CA_2), and it has been established that the hydration reactions of CA and CA_2 are highly dependent on temperature (Ukrainczyk et al (2010)). Halting the hydration of CAC at different temperatures reveals that the prism-shaped hydrate $CaO{\cdot}Al_2O_3{\cdot}10H_2O$ (CAH_{10}) is the main product at temperatures below 21 ° C, hydrates $2CaO{\cdot}Al_2O_3{\cdot}8H_2O$ (C_2AH_8) with plate-shaped structure and $Al_2O_3{\cdot}3H_2O$ (AH_3) gel are the main products at temperatures from 21 °C to 35 °C, and granular-shaped hydrates $3CaO{\cdot}Al_2O_3{\cdot}6H_2O$ (C_3AH_6) and AH_3 are generated at temperatures above 35 °C (Lee et al (2013), Zhang et al (2018)). And the hydration rate of CAC is also varying at different temperatures. Therefore, it is very important to completely terminate the hydration of CAC at the designated time to investigate its hydration behaviour.

However, there is sparse information about the effect of drying methods on the hydration halt of CAC at different temperatures. Thus, the purpose of this work is to compare three commonly used drying methods (freeze vacuum drying, isopropanol replacement followed by vacuum drying and oven drying) (Zhang et al (2019), Zhang et al (2011)) for arresting hydration of CAC and free water removal.

2. Experimental

A commercial CAC (Secar-71, Kerneos Aluminate Technologies Co. Ltd) was used in this work. The CAC pastes were fabricated by mixing Secar-71 with water in a ratio of 1:1. And then the mixed pastes were poured into the stainless-steel discs which were covered with a layer of plastic film to prevent free water from evaporating. Subsequently, the pastes were cured at 10 ℃, 30 ℃ and 50 ℃ for 24 h, 24 h and 3 h respectively to obtain different hydrates. The hydration of as-cured pastes with ~2 mm thick was terminated by freeze-vacuum drying, isopropanol exchange and followed by vacuum drying and oven drying. CAC paste samples were firstly frozen at -40 ℃ for 6 h and subsequently vacuum dried at a temperature of 40 ℃ and a vacuum of < 20 Pa for 12 h, which is the freeze-vacuum drying method. Isopropanol exchange is involved that the samples were immersed in isopropanol for 7 days at room temperature and then dried by vacuum drying and oven drying, respectively. Vacuum drying is the same as the vacuum drying mode in freeze-vacuum drying. Oven drying is to dry samples in an oven at 40 ℃ under an ambient pressure for 12 h.
The phase compositions and morphologies of paste samples after halting of hydration were characterized by X-ray diffraction (XRD; D8 Focus, Bruker, Germany) and field emission scanning electron microscopy (FE-SEM; SIGMA HD, Zeiss, Germany), respectively.

3. Results and discussion

Figure. 1a shows the XRD patterns of CAC pastes hydrated at 10 ℃ for 24 h subjected to different drying techniques. It is obvious that hydrate CAH_{10} is the main hydration product in all samples at 10 ℃, and there are also a lot of un-hydrated CA and CA_2. It is also found that the peaks for hydrate CAH_{10} in the freeze-vacuum drying are much lower than those in the solvent quenched samples. This indicates that a certain amount of free water is still present in the samples, since the organic solvents do not have the power to withdraw all the free water from the cement pastes (Luz et al (2011)). Therefore, the residual CA and CA_2 continues to hydrate and generate more CAH_{10} in the process of drying. It can be concluded that freeze vacuum drying removes the free water more effectively for CAC pastes cured at 10 ℃.

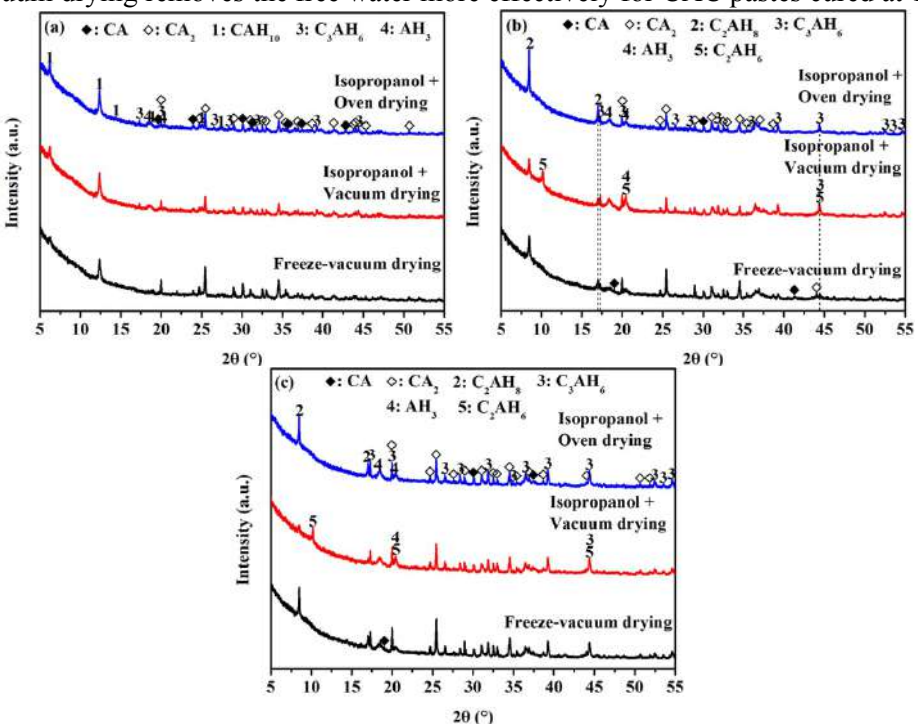


Fig. 1 Effect of drying techniques on the XRD patterns of CAC pastes cured at different temperatures: (a) 10 ℃ × 24 h, (b) 30 ℃ × 24 h and (c) 50 ℃ × 3 h.

Besides, comparing vacuum drying and oven drying after replacement, the peaks of hydrate CAH_{10} are relatively higher for oven drying. This is attributed to the fact that at the same drying temperature (40 ℃), the volatilization rate of free water in vacuum drying is much faster than that in oven drying, thus preventing the further hydration of residual CA and CA_2 at a relatively higher rate. Especially, oven drying at 40 ℃ even accelerates the continued hydration of un-hydrated CA and CA_2 to produce more hydrate CAH_{10} in **Fig. 1a**, as the peaks of residual CA and CA_2 are much lower than those in the other samples.

The microstructure of hydrate CAH_{10} in the paste samples after drying using the three different drying techniques are shown in **Figure. 2**. The hydrate CAH_{10} formed in all the samples are in the form of fine and long hexagonal prisms, and the CAH_{10} crystals have a size of roughly 200 nm in diameters. It can be seen from **Fig. 2** that these different drying methods have no noticeable effect on the morphology of CAH_{10} crystal.

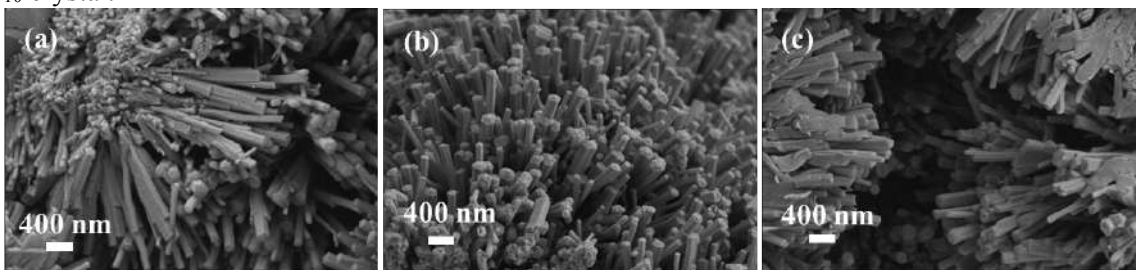


Fig. 2 Effect of drying techniques on the SEM micrographs of CAC pastes cured at 10 ℃ for 24 h: (a) freeze-vacuum drying, isopropanol replacement for 7 d and followed by (b) vaccum drying and (c) oven drying.

The XRD patterns of CAC pastes cured at 30 ℃ for 24 h subjected to different drying techniques are presented in **Figure. 1b**. It is seen that the peaks of hydrates C_2AH_8 and C_3AH_6 in the freeze-vacuum dried sample are much lower than that in the sample with solvent exchange followed by oven drying. Because the isopropanol soaking is not able to thoroughly extract the free water, the subsequent oven drying at 40 ℃ even accelerates the continued hydration of residual CA and CA_2 and formation of hydrates C_2AH_8 and C_3AH_6. Moreover, not only hydrates C_2AH_8 and C_3AH_6 but also hydrate C_2AH_6 is also produced in the sample with solvent exchange followed by vacuum drying in **Fig. 1b**. This is due to the dehydration and decomposition of hydrate C_2AH_8 to generate hydrate C_2AH_6 ($2CaO{\cdot}Al_2O_3{\cdot}8H_2O \rightarrow 2CaO{\cdot}Al_2O_3{\cdot}6H_2O + 2\ H_2O$). These results demonstrate that isopropanol exchange followed by vacuum drying can result in the dehydration of hydrate C_2AH_8 and is consequently not suitable for the free water removal of CAC samples.

Figure. 3 displays the SEM micrographs of the fractured surfaces of CAC pastes cured at 30 ℃ for 24 h where hydration is arrested by different drying techniques. Since the dehydration of hydrate C_2AH_8 to C_2AH_6 happens through solid-state reaction, the microstructure of crystal C_2AH_6 is the same as that of C_2AH_8 crystal. As clearly shown in **Fig. 3**, the characteristic plate-shaped crystals with about 200-800 nm in thickness are present in all samples. However, owing to the low content of hydrate C_3AH_6 (**Fig. 1b**), the typical granular C_3AH_6 cannot be seen in the samples. And it can be inferred from the SEM results that the different three drying methods also have little influence on the microstructure of C_2AH_8 and C_2AH_6 crystals.

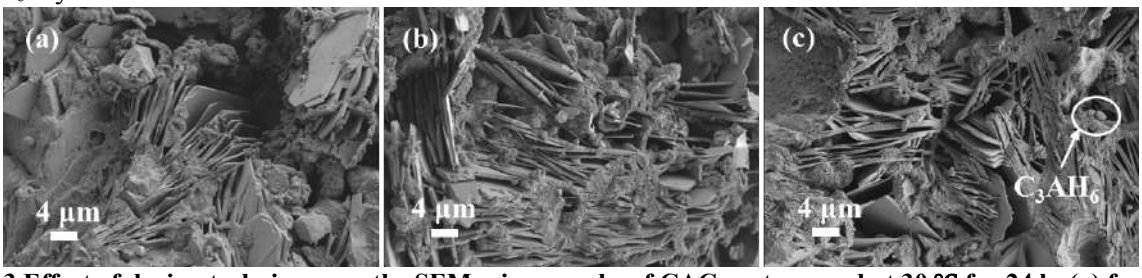


Fig. 3 Effect of drying techniques on the SEM micrographs of CAC pastes cured at 30 ℃ for 24 h: (a) freeze-vacuum drying, isopropanol exchange for 7 d and followed by (b) vaccum drying and (c) oven drying.

Figure. 1c presents the XRD patterns of CAC pastes hydrated at 50 ℃ for 3 h and subsequently subjected to different drying techniques. The peaks of hydrates C_2AH_8 and C_3AH_6 in the freeze-vacuum dried sample are much lower than that in the solvent replacement and followed oven dried sample. This illustrates that the remaining free water after isopropanol soaking enhances the hydration degree of CA

and CA_2 during the subsequent oven drying. Therefore, in a comparsion, freeze-vacuum drying halts the hydration of CAC more effectively.

In addition, the apparent difference in **Fig, 1c** is that hydration product C_2AH_8 is dominant in both the samples with freeze-vacuum drying and solvent exchange followed by oven drying, while the main hydration product is C_2AH_6 in the solvent replacement followed by oven dried sample. Similarly, the dehydration of hydrate C_2AH_8 leads to the formation of hydrate C_2AH_6 at 40 ℃, where the free water released is conducive to the hydration of residual CA and CA_2.

Figure. 4 shows the SEM images of fractured surfaces of CAC pastes hydrated at 50 ℃ for 3 h subjected to different drying techniques. Combined with XRD results, the typical plate-shaped C_2AH_8 or C_2AH_6 and granular C_3AH_6 are present in all samples. The SEM images further indicate that the three drying techniques have almost no effect on the morphologies of C_2AH_8, C_2AH_6 and C_3AH_6 crystals.

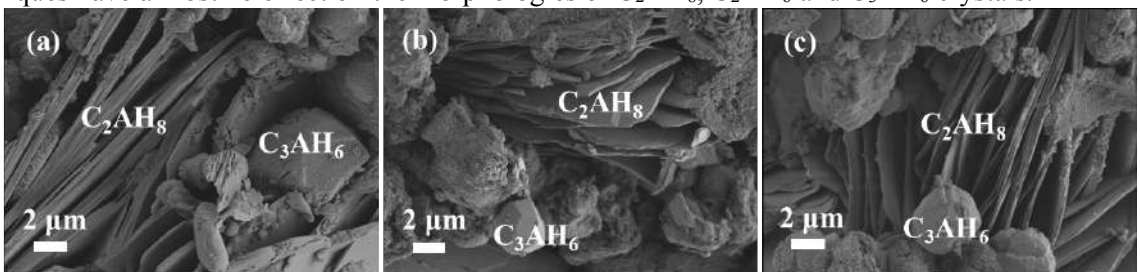


Fig. 4 Effect of drying techniques on the SEM micrographs of CAC pastes cured at 50 ℃ for 3 h: (a) freeze-vacuum drying, isopropanol replacement for 7 d and followed by (b) vaccum drying and (c) oven drying.

4. Conclusions

In order to fully understand the hydration behaviour of CAC at the designated time, it is vital to completely halt the hydration of CAC to further investigate the composition and microstructure of CAC hydrates during the hydration process. In this work, three commonly used drying methods (freeze vacuum drying, isopropanol replacement followed by vacuum drying and oven drying) were chosen to investigate their efficiencies in halting the hydration of CAC at the designated time. The CAC pastes were cured at 10 ℃ for 24 h, 30 ℃ for 24 h and 50 ℃ for 3 h, respectively, to obtain the different hydrates (CAH_{10} C_2AH_8 and C_3AH_6). The results indicate that the freeze vacuum drying removes the free water more effectively and brings little damage to the structure of hydrates, and thus it should be the preferred technique of hydration terminating for CAC pastes. Additionally, since the isopropanol soaking does not have the power to extract the all free water, the subsequent oven drying and vacuum drying further accelerate the continued hydration of residual CAC to a bit higher extent. The isopropanol exchange followed by vaccum drying results in the dehydration of hydrate C_2AH_8 to C_2AH_6.

Acknowledgements

This work was supported by the National Natural Science Foundation of China [grant number 52172030].

References

Lee, W.E., Vieira W. and Zhang, S. (2013) “Castable refractory concretes”, *Metallurgical Reviews*, 46(3):145-167.

Luz, A.P. and Pandolfelli, V.C. (2011) “Halting the calcium aluminate cement hydration process”, *Ceramics International*, 37(8): 3789-3793.

Shirani, S., Cuesta, A. and Torre, G. D. (2020) “Calcium aluminate cement conversion analysed by ptychographic nanotomography”, *Cement and Concrete Research*, 137: 106201.

Ukrainczyk, N. and Matusinović, T. (2010). “Thermal properties of hydrating calcium aluminate cement pastes”, *Cement and Concrete Research*, 40(1): 128-136.

Zhang, J. and Scherer, G.W. (2011) “Comparison of methods for arresting hydration of cement”, *Cement and Concrete Research*, 41(10): 1024-1036.

Zhang, Y., Gu, W.J. and Ye, G.T. (2018) “Conversion of calcium aluminate cement hydrates at 60°C with and without water”, *Journal of the American Ceramic Society*, 101(7): 2712-2717.

Zhang, Z. and Scherer, G.W. (2019) “Evaluation of drying methods by nitrogen adsorption”, *Cement and Concrete Research*, 120: 13-26.

The 16th International Congress on the Chemistry of Cement 2023 (ICCC2023)
"Further Reduction of CO_2 -Emissions and Circularity in the Cement and Concrete Industry"
September 18–22, 2023, Bangkok, Thailand

Effect of temperature rise inhibitor on heat evolution of cement-quartz system

Y.C. Zhou[1, a], C. Yu[2, b, *], Y. Yan[3, c], W.B. Wang[2, d], Y. Qin[4, e], J.P. Liu[1,2, f], K.C. Wang[5, g]

[1] *College of Materials Science and Engineering, Chongqing University, Chongqing, China*

[2] *State Key Laboratory of High Performance Civil Engineering Materials, Jiangsu Sobute New Materials Co., Ltd., Nanjing, China*

[3] *Department of Civil and Environmental Engineering, National University of Singapore, Singapore*

[4] *Chongqing Construction Engineering Quality Supervision and Testing Center Co., Ltd., Chongqing, China*

[5] *Guangdong Highway Construction Co., Ltd., Guangzhou, China*

[a] *zhouyc_cqu@163.com*

[b] *yucheng@cnjsjk.cn*

[c] *yan_yu@nus.edu.sg*

[d] *wangwenbin@cnjsjk.cn*

[e] *qinyuan13983626451@163.com*

[f] *liujiaping@cnjsjk.cn*

[g] *wangkc33@126.com*

ABSTRACT

Temperature Rise Inhibitor (TRI) is a highly effective approach for mitigating the risk of thermal cracking, while Supplementary Cementitious Materials (SCMs) play an indispensable role in the development of low-carbon cement-based materials. A comprehensive understanding of the interplay between TRI and SCMs with respect to cement hydration can enable the application of TRI in diverse practical conditions.

Isothermal calorimetry was utilized to investigate the hydration kinetics, which revealed that the replacement of quartz and reduction of clinker in the presence of TRI result in a significantly reduced heat flow in the cementitious materials. Nonetheless, the effect of TRI on cement hydration is alleviated by the enhancing effect of the inert filler. Moreover, the direct influence of TRI is restricted to the silicate phase in the process of cement hydration, causing a decline in formation of C-S-H and the adsorption of sulfate, which consequently hinders the aluminate reaction.

KEYWORDS: *temperature rise inhibitor, filler effect, heat release, aluminate hydration*

1. Introduction

Thermal cracking, caused by the strong silicate reaction during the first 24 hours, is a widespread problem of the cementitious materials. A novel starch-based admixture (Temperature Rise Inhibitor, TRI) is used to reduce the heat release during the first few days. The silicate reaction during the main peak is hindered due to the inhibition of TRI on nucleation of C-S-H, resulting in the decrease in the cumulative heat in the early age.

Supplementary cementitious materials (SCMs) are key components of sustainable, low carbon cements. The drive towards low-clinker cements with increasing proportion and number of SCMs will lead to the development of more complex, balanced hydrating systems since the presence and reactions of the SCMs influence the hydration kinetics of the clinker phases and the products formed.

The interaction between TRI and SCM on cement hydration can lead to slow development of strength in composite cementitious materials, thereby limiting the use of TRI in modern concrete. To address this issue, we selected quartz as an inert filler to study the interaction between the filler effect of SCM and TRI. In this paper, we focus on the effect of TRI on the heat of hydration of the composite system and propose a possible mechanism.

2. Materials and methods

Portland cement P•Ⅱ 52.5 and ultrapure water were used in all experiments of this study and cement paste was prepared with a water-to-cement ratio of 0.4. The temperature rise inhibitor (TRI) is a solid powder admixture prepared by acid hydrolysis of corn starch. The hydration kinetics have been characterized by isothermal calorimetry. Mortar samples with portland cement used in cement paste casting were prepared with standard sand according to GB/T 17671-2021 at a water-to-cement ratio 0.4.

3 Results

Fig. 1 illustrates the effect of TRI on the hydration kinetics of cement-quartz pastes. It is observed that the addition of TRI causes a notable decrease in the early-age hydration rate of cement, which becomes more apparent as the amount of TRI added increases. During the initial few hours, TRI addition leads to a slight prolongation of the induction period compared to the control system. Furthermore, the hydration of cement takes place at a reduced rate (i.e., the gentler slope and lower main peak of the acceleration period). Despite the reduction in the main peak, the cumulative heat of TRI-doped samples with appropriate levels of TRI and quartz can catch up with the control sample after several days. This is due to a higher heat flow after the end of the deceleration period in the cement paste with TRI (Fig. 2a). Thus, the incorporation of TRI results in a significant decrease in the early compressive strength due to the slower early hydration rate. However, the later compressive strength of mortar with TRI can reach a similar level compared to the control sample due to the ongoing hydration (Fig. 2b).

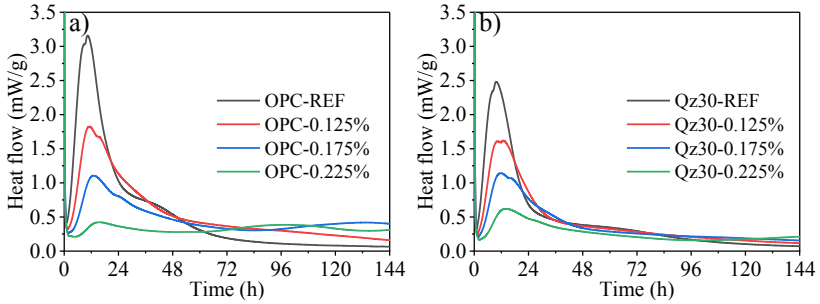


Fig. 1 Effect of increasing TRI in the different replacement quartz-cement pastes: a) OPC; (b) Qz30. All curves are normalized to the solid mass in the system.

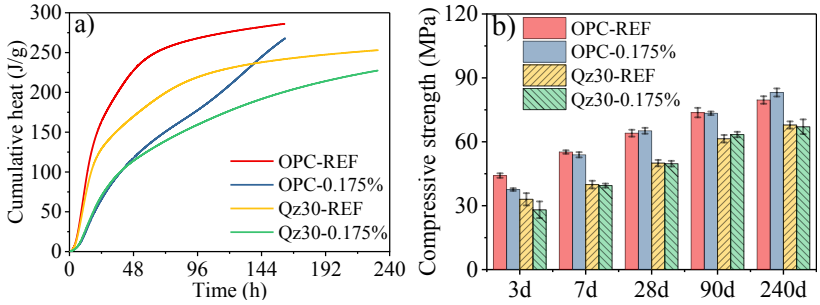


Fig. 2 Effect of TRI on the (a) accumulative heat and (b) compressive strength development.

Fig. 3a shows the relationship between the heat flow at peak time, and TRI dosage in all the systems studied, and it can still be observed that the heat flow decreases linearly with the increase of TRI dosage. An additional noteworthy finding is that a reduction in slope of "the peak value versus TRI dosage curves" as the quartz content increases This phenomenon implies that TRI's depressing effect on the peak value is weakened by the incorporation of quartz.

Blended cements enhance the hydration of cement by introducing surfaces that offer additional sites for heterogenous nucleation of C-S-H, known as the filler effect (Berodier and Scrivener 2014, Zunino, Bentz et al. 2018). The effect of quartz on the heat flow in TRI-doped cement pastes is depicted in Fig. 3. The heat flow is normalized by the cement mass, which is the only reactive component. As a result, the heat flow of cement increases with an increase in the replacement level of quartz, leading to a higher height of the main hydration peak and slope of the acceleration period. The addition of TRI does not alter the enhancement effect of quartz on cement hydration. In both TRI-containing and TRI-free systems, the presence of quartz led to higher heat release during hydration compared to systems without quartz.

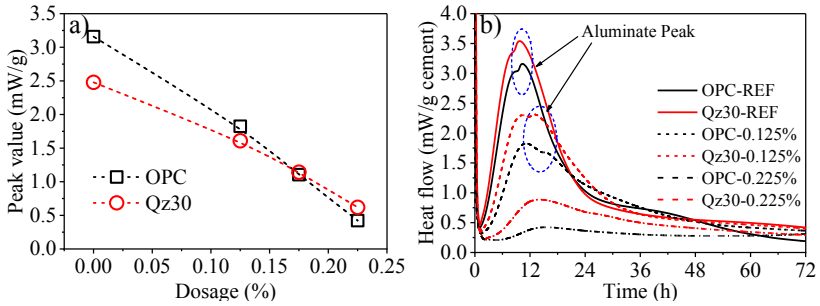


Fig. 3(a) Heat flow at the peak time versus TRI content for all the systems studied. The values are normalized to the solid mass. (b) Effect of increasing the replacement of quartz in cement pastes doped TRI. The values are normalized to the cement mass.

Furthermore, TRI appears to inhibit the aluminate reaction, which is characterized by the shoulder during the deceleration period (Fig. 3b). The onset time of the aluminate peak is delayed with an increase in TRI content. This is due to the decrease in the nucleation density of C-S-H caused by the depressing effect of TRI, which leads to the inhibition of the alite reaction (Yan, Ouzia et al. 2020). The deceleration of the silicate reaction results in a lower rate of C-S-H precipitation. Less C-S-H formation implies fewer sulfate ions adsorbed, which in turn, keeps the pore solution rich in sulfate ions. The delay in gypsum depletion results in the on-going inhibitory effect on the C_3A reaction (Minard, Garrault et al. 2007, Yan, Scrivener et al. 2021). Once the gypsum depletion occurs, the aluminate reaction becomes intense and the aluminate peak begins to arise. However, the enhancement effect of quartz on the aluminate peak does not disappear due to the presence of TRI. As the amount of quartz increases from 0% to 30% in the 0.175% TRI system, the onset time of the aluminate peak is shortened from 17.88 hours to 14.18 hours (Fig. 4a).

The cumulative heat generated during the acceleration period before gypsum depletion can function as a surrogate for C-S-H that has precipitated (Zunino and Scrivener 2019). Fig. 4b demonstrates the correlation between the heat flow at the onset of the aluminate peak and the TRI concentration in pure cement and blended 30% quartz systems. When the heat flow at the aluminate peak onset is normalized to the cement mass in the system, the cumulative heat flow at the acceleration period onset is equivalent across all studied systems. The introduction of TRI does not alter the heat flow at the time of aluminate peak onset, implying that TRI has no direct influence on the hydration kinetics of C_3A and gypsum consumption. In other words, TRI exclusively directly affects the hydration kinetics of the silicate phase in the quartz system, inducing a change in the hydration kinetics of the aluminum phase. According to this line of thought, it seems that the addition of other types of cementing materials, with ettringite as the main hydration product, may compensate for the early strength deficiency due to TRI. But this requires a balance between compressive strength gain and early heat release.

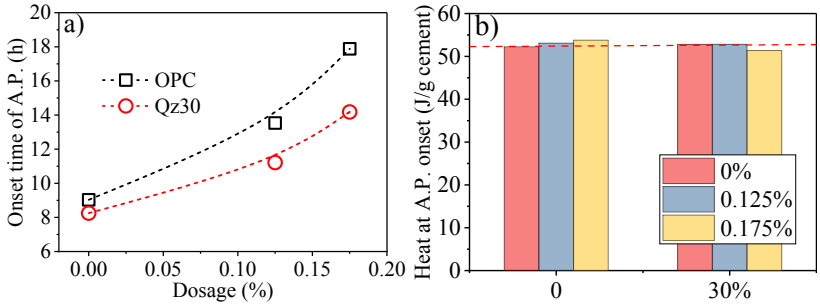


Fig. 4 (a) Effect of TRI on the onset time of aluminate peak. (b) Effect of TRI on the cumulative heat release at A.P. onset and cumulative heat is normalized to the mass of the cement in the system.

4 Conclusions

1) The use of TRI can efficiently reduce the heat release during the early stages of cement hydration by suppressing the main hydration peak without compromising the later development of compressive strength in the quartz system. However, the effectiveness of TRI in depressing cement hydration may be reduced by the enhancing effect of filler.
2) TRI does not directly affect the aluminate reaction. TRI decelerates the silicate reaction, leading to a slower rate of C-S-H precipitation. This reduction in C-S-H formation results in lower sulfate ion adsorption. The delayed depletion of gypsum has an ongoing depressing effect on the C_3A reaction.
3) Adding cementitious materials with ettringite as the main hydration product is a potential method for mitigating the negative impact of TRI on early compressive strength. This approach provides a practical solution for optimizing the use of TRI in engineering applications.

Acknowledgements

The authors gratefully acknowledge the financial support by the Guangdong Key Field R&D Program Project (No. 2019B111106002) and the National Natural Science Foundation of China (52008192).

References

Berodier, E. and K. Scrivener (2014). "Understanding the Filler Effect on the Nucleation and Growth of C-S-H." Journal of the American Ceramic Society **97**(12): 3764-3773.
Minard, H., S. Garrault, L. Regnaud and A. Nonat (2007). "Mechanisms and parameters controlling the tricalcium aluminate reactivity in the presence of gypsum." Cement and Concrete Research **37**(10): 1418-1426.
Yan, Y., A. Ouzia, C. Yu, J. Liu and K. L. Scrivener (2020). "Effect of a novel starch-based temperature rise inhibitor on cement hydration and microstructure development." Cement and Concrete Research **129**: 105961.
Yan, Y., K. L. Scrivener, C. Yu, A. Ouzia and J. Liu (2021). "Effect of a novel starch-based temperature rise inhibitor on cement hydration and microstructure development: The second peak study." Cement and Concrete Research **141**: 106325.
Zunino, F., D. P. Bentz and J. Castro (2018). "Reducing setting time of blended cement paste containing high-SO3 fly ash (HSFA) using chemical/physical accelerators and by fly ash pre-washing." Cement and Concrete Composites **90**: 14-26.
Zunino, F. and K. Scrivener (2019). "The influence of the filler effect on the sulfate requirement of blended cements." Cement and Concrete Research **126**: 105918.

The 16th International Congress on the Chemistry of Cement 2023 (ICCC2023)
"Further Reduction of CO_2 -Emissions and Circularity in the Cement and Concrete Industry"
September 18–22, 2023, Bangkok, Thailand

Influence of ferronickel slag on early hydration and microstructure of alkali-activated ground granulated blast furnace slag

Ruilin Cao[1], Yamei Zhang[2*]

[1] *School of Materials Science and Engineering, Jiangsu Key Laboratory of Construction Materials, Southeast University, Nanjing 211189, China*
Email: caoruilin1991@163.com
[2] *School of Materials Science and Engineering, Jiangsu Key Laboratory of Construction Materials, Southeast University, Nanjing 211189, China.*
Email: ymzhang@seu.edu.cn

ABSTRACT

Industrial metallurgical waste residue can be used as an activation precursor to prepare alkali-activated cements (AACs), which can realize the rational utilization of waste resources and bring huge environmental and economic benefits. In this study, ground granulated blast furnace slag (GGBS) as the major raw material and ferronickel slag (FNS) as the blending material were activated by sodium hydroxide (SH) and sodium silicate (SS), respectively. The hydration heat, mechanical strength and microstructure of alkali-activated ground granulated blast furnace slag-ferronickel slag binder (AASF) were investigated. The results show that the incorporation of FNS has no obvious effect on the reaction process of the SH-activated AASF system, but it will delay the reaction process of the SS-activated AASF system. Under the high curing temperature of 60°C, the delayed effect of FNS on the reaction process of the SS-activated AASF system is weakened. The Ca/Si and Ca/(Al+Si) of AASF are significantly decreased by the incorporation of FNS. Besides, the effect of FNS on the Na/Si and Na/(Si+Al) of hydration products in SS and SH-activated AASF systems is significantly different. The reaction degree of FNS is significantly increased in late age.

KEYWORDS: *Alkali-activated slag; Ferronickel slag; Hydration; Strength; Microstructure*

1. Introduction

In recent years, low-calcium and high-magnesium ferronickel slag (FNS) has been gradually used in the preparation of alkali-activated cements (AACs) (Huang et al., 2022; Cao et al., 2018; Huang et al., 2017; Bian et al., 2021). The mechanical strength of the alkali-activated pure FNS cement (AAFNS) is significantly lower than that of PC and AAS due to the poor reactivity of FNS. However, a class of alkali-activated composite binders with improved mechanical strength and durability can be made by combining other different kinds of solid wastes in AAFNS, including fly ash (Yang et al., 2014) and ground granulated blast furnace slag (GGBS) (Cao et al., 2018).

Alkali-activated slag (AAS) is now the most widely investigated in the field of AACs, with a focus on the hydration kinetics process (Cao et al., 2020) and microstructure (Jia et al., 2020), which are closely related to the macroscopic properties. The high shrinkage characteristic of AAS has become the key problem that limits the application of AAS in civil engineering (Kumarappa et al., 2018). At present, combining two or more kinds of precursor materials is an economical and efficient way to eliminate or mitigate the aforementioned defects of AACs. Therefore, the modifying effect and reaction mechanisms of the alkali-activated composite systems have received increasing attention. Existing research has demonstrated a strong correlation between the chemical composition of GGBS and the reaction process, hydration products and mechanical properties of AAS (Haha et al., 2011; Haha et al., 2012).

Up to now, the reaction kinetics of alkali-activated GGBS-FNS composite system (AASF) has not yet been systematically studied in depth. Based on the above, this study employed isothermal conduction

calorimetry (ICC) to characterize the heat release of AASF and investigated the effect of FNS on the hydration process and microstructure of AAS.

2. Experimental programs

2.1 Raw materials and mix proportions

The chemical composition of GGBS and FNS used in this study was determined by X-ray fluorescence spectrometry, as shown in Table 1. The chemical composition of FNS is mainly composed of SiO_2, MgO and Fe_2O_3, with a small amount of Al_2O_3 and CaO. The primary chemical components of GGBS are CaO, SiO_2 and Al_2O_3, with a combined content of 87.24%. The mix proportions of different AASF pastes are listed in Table 2. 'SH', 'SS1.2' and 'SS2.0' represent sodium silicate activator solutions with modulus 0 (i.e. sodium hydroxide activator solution in this study), 1.2 and 2.0, respectively.

Table 1 Chemical compositions of FNS and GGBS/ wt.%.

Oxides	MgO	CaO	Al_2O_3	SiO_2	Fe_2O_3	SO_3	K_2O	Na_2O	P_2O_5	MnO	Cr_2O_3	TiO_2
FNS	15.94	11.49	6.56	47.61	13.24	0.52	0.18	0.80	1.86	0.81	0.70	0.24
GGBS	3.90	36.05	16.52	34.67	0.29	2.53	0.33	-	4.95	0.20	-	0.55

Table 2 Mix proportions of different AASF pastes

Activator types	FNS /wt.%	GGBS /wt.%	Modulus	Na_2O /wt.%	Temperature ℃	Water/binder ratio	Sand/binder ratio
SH	0	100	0	4	25	0.4	0.5
	20	80	0	4	25	0.4	0.5
	40	60	0	4	25	0.4	0.5
	60	40	0	4	25	0.4	0.5
SS1.2	0	100	1.2	4	25/60	0.4	0.5
	20	80	1.2	4	25/60	0.4	0.5
	40	60	1.2	4	25/60	0.4	0.5
	60	40	1.2	4	25/60	0.4	0.5
SS2.0	0	100	2.0	4	25	0.4	0.5
	20	80	2.0	4	25	0.4	0.5
	40	60	2.0	4	25	0.4	0.5
	60	40	2.0	4	25	0.4	0.5

2.2 Experimental methods

The hydration evolvement of different AASF pastes under various reaction conditions was precisely detected by an eight-channel isothermal calorimeter. The heat of hydration data was automatically recorded by a calorimeter for 72 h.

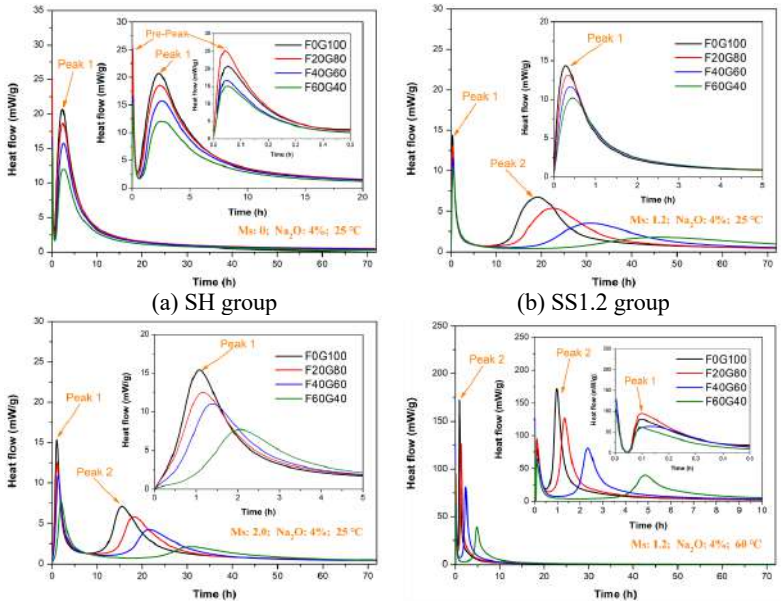
The AASF mortar samples with the size of 40 × 40 × 160 mm^3 were prepared following Chinese standard GB/T 17671-1999 at room temperature. Part of the samples was cured at 20 ± 2°C and RH = 90 ± 5% relative humidity until they were used for the mechanical strength tests of AASF cured at room temperature. The remaining molded samples were utilized to test the mechanical strength of AASF cured under high temperature. Following a resting period of 2 h to achieve a specific mechanical strength, the AASF samples were steam cured at 60°C for 7 h. After demolding, the above samples continued to be cured under standard conditions until testing. For each group, three parallel specimens were prepared and the strengths were determined by taking the arithmetic means.

The microstructure characteristics and elemental composition of AASF were examined by using scanning electron microscopy equipped with energy-dispersive X-ray spectra (SEM-EDS, Nova Nano SEM 450, FEI Company). The samples were dried and sprayed with gold for 360 s before testing. In this study, at least 30 points from each group of AASF samples were randomly chosen for EDS analysis of hydration products.

3. Results and discussion

3.1 Hydration heat of AASF

Fig. 1 shows the heat flow of different AASF pastes activated with SH, SS1.2, and SS2.0. As shown in Fig. 1 (a), the calorimetric curves of the SH group present an initial pre-exothermic peak and a primary exothermic peak, named Pre-Peak and Peak 1, respectively. The calorimetric curves of the SS groups have two primary exothermic peaks, named Peak 1 and Peak 2, respectively, as illustrated in Fig. 1 (b), (c) and (d). The Pre-Peak is not observed in the calorimetric curves at 25℃ in the SS groups but appeared at 60℃ (Fig. 2 (d)). In the SH group, the blending of FNS does not significantly change the occurrence time of Pre-peak and Peak 1. However, the emergence of Peak 1 and Peak 2 in the SS groups is delayed with the addition of FNS. Compared with the calorimetric curves at 25℃, the exothermic peaks of the AASF paste are sharper and the corresponding values are significantly increased at 60 ℃. However, as the hydration reaction rate of AASF increases under a high-temperature environment, the delay effect of FNS on the reaction process of the AASF system activated by SS is weakened.



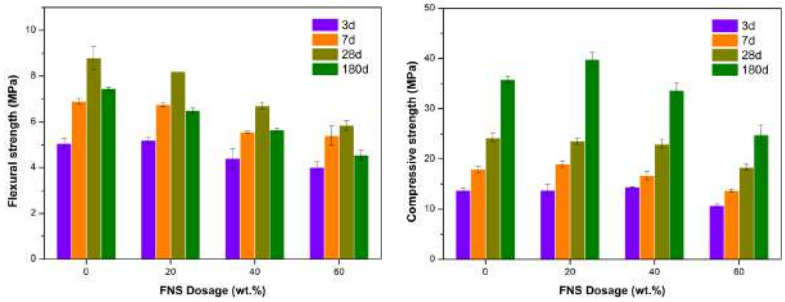
(a) SH group (b) SS1.2 group

(c) SS2.0 group (d) SS1.2 group (60℃)

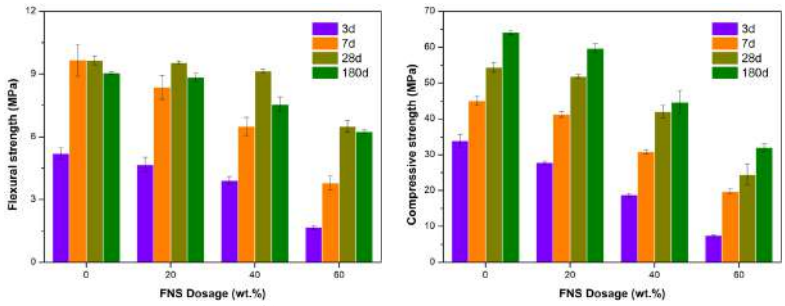
Fig. 1. Heat flow of per unit mass of different AASF pastes activated with various activators

3.2 Mechanical strength of AASF

The flexural and compressive strengths of various AASF mortars at different ages are shown in Fig. 2. The compressive strength of the SS group is higher than that of the SH group at all ages, although the activators employed in all AASF samples have the same alkali content. The highest compressive strength in the SH group is 39.85 MPa for the AASF mortar with 20%FNS content at 180 d, which is much lower than 59.7 MPa for the AASF mortar containing the same FNS content at 180 d in the SS group. The flexural and compressive strengths of AASF generally tend to decline as FNS content increased. The content of Al and Ca in FNS is much lower than that in GGBS, the incorporation of FNS inevitably leads to the deficiency of calcium and aluminum components in the AASF system, resulting in the reduction of the formation of C-(A)-S-H gel phase, which is the main contributor to the strength development.



(a) Ms: 0; Na_2O: 4%; 25℃



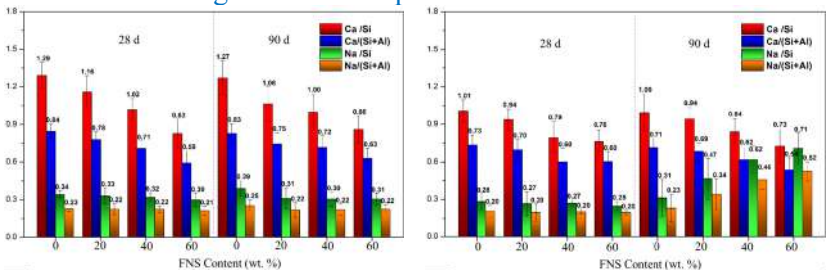
(b) Ms: 1.2; Na_2O: 4%; 25°C

Fig. 2. Mechanical strength of AASF mortars under different parameters

3.3 Microstructural analysis of AASF

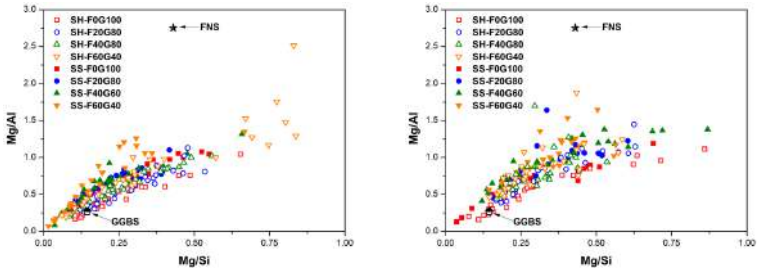
Fig. 3 shows the compositions of hydration products in different AASF samples at 28 and 90 d, including Ca/Si, Ca/(Si+Al), Na/Si and Na/(Si+Al). The Ca/Si and Ca/(Si+Al) of the SH group are larger than those in the SS1.2 group. The Ca/Si and Ca/(Si+Al) of AASF reveal a considerable reduction trend with the incorporation of FNS because of the low calcium content in FNS. In addition, the curing age has no obvious effect on the Ca/Si and Ca/(Si+Al) of AASF. The Na/Si and Na/(Si+Al) of the AASF pastes activated by SH and SS1.2 at 28 d have no obvious relationship with the FNS content. However, the Na/Si and Na/(Si+Al) of the hydration products in the SS1.2 group steadily increase with the rise of FNS content at 90 d, while there is no appreciable change in the SH group. The type of alkali activator has a significant effect on the reaction process and the composition of hydration products of AACs.

Fig. 4 plots the atomic Mg/Al ratio against Mg/Si ratio of the hydration products in different AASF pastes at 28 d and 90 d. It can be seen that the relationship points of Mg/Al and Mg/Si of the hydration products in AASF were close to GGBS particles at 28 d, but closer to FNS particles at 90 d. This finding provides further evidence that the reaction degree of FNS improved at later times.



(a) SH group (b) SS1.2group

Fig. 3. Ca/Si, Ca/(Si+Al), Na/Si and Na/(Si+Al) of different AASF pastes



(a) 28 d (b) 90 d

Fig. 4. Mg/Al vs Mg/Si of different AASF pastes

4. Conclusions

The addition of FNS significantly reduces the cumulative heat but has no impact on the reaction process of the SH-activated AASF system. In the SS-activated AASF system, the incorporation of FNS results in a reduction in the cumulative heat and a delay in the reaction progress. The delayed effect of the addition of FNS on the reaction process of the SS-activated system is weakened when the curing temperature increases from 25°C to 60°C. The reaction degree of FNS in the late age is significantly higher than that

in the early age in AASF. Therefore, FNS exerts significantly different effects on the composition of hydration products in the early and late stages of AASF.

Acknowledgements

The funding from the National Natural Science Foundation of China (Nos. 51972057 and 52202019) and the Excellence Project Funds of Southeast University are greatly appreciated.

References

Bian, Z., Jin, G., and Ji, T. (2021). Effect of combined activator of Ca $(OH)_2$ and Na_2CO_3 on workability and compressive strength of alkali-activated ferronickel slag system. *Cement and Concrete Composites,* 123, 104179.

Cao, R., Li, B., You, N., Zhang, Y., and Zhang, Z. (2018). Properties of alkali-activated ground granulated blast furnace slag blended with ferronickel slag. *Construction and Building Materials,* 192, 123-132.

Cao, R., Zhang, S., Banthia, N., Zhang, Y., and Zhang, Z. (2020). Interpreting the early-age reaction process of alkali-activated slag by using combined embedded ultrasonic measurement, thermal analysis, XRD, FTIR and SEM. *Composites Part B: Engineering,* 186, 107840.

Haha, M. B., Lothenbach, B., Le Saout, G. L., and Winnefeld, F. (2011). Influence of slag chemistry on the hydration of alkali-activated blast-furnace slag—Part I: Effect of MgO. *Cement and Concrete Research,* 41(9), 955-963.

Haha, M. B., Lothenbach, B., Le Saout, G. L., and Winnefeld, F. (2012). Influence of slag chemistry on the hydration of alkali-activated blast-furnace slag—Part I: Effect of MgO. *Cement and Concrete Research,* 41(9), 955-963.

Huang, Y., Wang, Q., and Shi, M. (2017). Characteristics and reactivity of ferronickel slag powder. *Construction and Building Materials,* 156, 773-789.

Huang, Z., Wang, Q., and Lu, J. (2022). "The effects of cations and concentration on reaction mechanism of alkali-activated blast furnace ferronickel slag". *Composites Part B: Engineering,* 236, 109825.

Jia, Z., Chen, C., Zhou, H., and Zhang, Y. (2020). The characteristics and formation mechanism of the dark rim in alkali-activated slag. *Cement and Concrete Composites,* 112, 103682.

Kumarappa, D. B., Peethamparan, S., and Ngami, M. (2018). Autogenous shrinkage of alkali activated slag mortars: Basic mechanisms and mitigation methods. *Cement and Concrete Research,* 109, 1-9.

Yang, T., Yao, X., and Zhang, Z. (2014). Geopolymer prepared with high-magnesium nickel slag: characterization of properties and microstructure. *Construction and Building Materials,* 59, 188-194.

The 16th International Congress on the Chemistry of Cement 2023 (ICCC2023)
"Further Reduction of CO_2 -Emissions and Circularity in the Cement and Concrete Industry"
September 18–22, 2023, Bangkok, Thailand

Synthesis and characterization of iron and aluminium-containing AFm phases

A. Lechevallier[1,2,3,a,*], M. Chaouche[2,d], J. Soudier[1,b], E. Prat[1,c] and G. Renaudin[3,e]

[1] *Sika, Zürich, Switzerland*
[a] *aurore.lechevallier@parex-group.com,* [b] *jerome.soudier@parex-group.com,* [c] *prat.evelyne@fr.sika.com*
[2] *Université Paris-Saclay, Gif-sur-Yvette, France*
[d] *mohend.chaouche@lmt.ens-cachan.fr*
[3] *Université Clermont Auvergne, Clermont INP, Clermont-Ferrand, France*
[e] *guillaume.renaudin@sigma-clermont.fr*

ABSTRACT

With the aim of properly characterising hydration products of new low-CO_2 binders, containing nitrate anions from accelerator additives, a series of AFm phases of the composition $Ca_4Al_{2-x}Fe_x(OH)_{12}\cdot(NO_3)_2\cdot 4H_2O$ (with $x \in [0;2]$) were synthesised by the coprecipitation method. Their purity was assessed using Raman spectroscopy and X-ray diffraction (XRD). Very low amounts of calcium carbonate and CO_3-containing AFm were observed, due to the CO_2 contamination from the air. Rietveld refinements evidenced that the AFm phases admit a trigonal $P\bar{3}c1$ space group. The existence of a solid solution has been highlighted in the complete range of $x \in [0;2]$ by following the evolution of the *a* lattice parameter. The *c* lattice parameter shows a decrease with Fe^{3+} substituting Al^{3+} which is due to a flattening of the octahedral layers. Finally, an in-situ XRD thermal study displayed that the Fe-AFm phase is less stable over temperature than its Al-analogue. The two AFm end-members keep a layered structure when rising the temperature (up to 175°C for the Fe-AFm and 200°C for the Al-AFm) but show different reorganisations of their interlayer regions.

KEYWORDS: *Low-CO_2 binder, hydraulic binder, Layered Double Hydroxides, AFm phase, solid solution*

1. Introduction

The increase of anthropogenic CO_2 emissions and their impact on the greenhouse effect result in rising social awareness as well as in business & economic paradigms change. The CO_2 footprint becomes then a product selection choice. This concerns in particular Ordinary Portland Cement (OPC), as the cement industry accounts for about 8% of global CO_2 emissions.
In this context, several new types of more environmentally friendly hydraulic binders have been studied and suggested as potential Ordinary Portland Cement substitutes. Many of them are composed of iron and aluminium oxides, and generally exhibit the $Ca_4Al_{2-x}Fe_{2+x}O_{10}$ (i.e. C_4AF) phase. Calcium layered double hydroxide (i.e. Ca-LDH or AFm phases) can be formed during the hydration process. Their structure consists of a positively charged main layer $[Ca_2M^{III}(OH)_6]^+$ with M^{III}=Al^{3+} or Fe^{3+}. The positive charge is balanced by anions X^- together with *n* water molecules organised in interlayers $[X\cdot nH_2O]^-$. Among possible anions are CO_3^{2-}, SO_4^{2-}, Cl^-, NO_3^-, etc. This work focuses on the NO_3^- anions as $Ca(NO_3)_2$, which is known as a C_4AF phase hydration accelerator (Chikh et al. (2008)), resulting in the rapid formation of AFm phases containing nitrate anions. Regarding the cations of the AFm phases; Al-based AFm-NO_3 phases (represented in Figure 1) have been extensively considered in the literature (Balonis et al. (2011); Renaudin and François (1999)) while only a few studies have been reported on the Fe-based AFm-NO_3 phases (Al-Jaberi et al. (2015)). Solid solutions of LDH may occur with substituting divalent and trivalent cationic positions within the main layer. In the case of Ca-AFm, it appears probable to substitute Al^{3+} ($R_{Al^{3+}}$ = 0.535 Å) with Fe^{3+} ($R_{Fe^{3+}}$ = 0.645 Å) that have close ionic radii. Investigating such model systems is considered to be a prerequisite to properly characterize the hydration products of the above-mentioned new low-CO_2 binders.

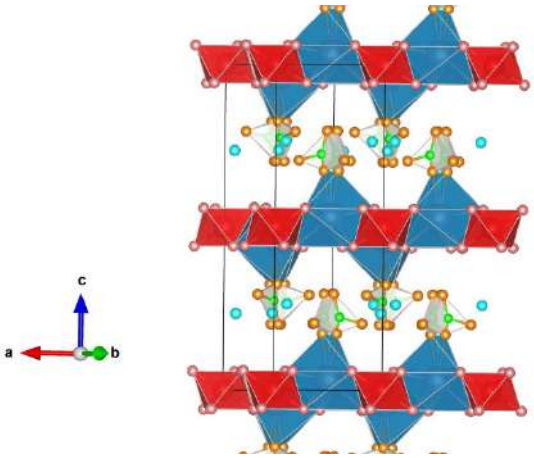


Figure 1. Structural representation of the Al-based AFm-NO_3 phase; red and blue polyhedrons are, respectively, sixfold Al and sevenfold Ca polyhedron. Red, blue, orange and green spheres represent, respectively, hydroxyl anions, water molecules, and O and N atoms from nitrate anions.

2. Materials and Methods

2.1 Synthesis of AFm phases

A series of AFm phases of the composition $Ca_4Al_{2-x}Fe_x(OH)_{12}\cdot(NO_3)_2\cdot 4H_2O$ with x = 0, 0.33, 0.67, 1.00, 1.33, 1.67 and 2.00 were synthesised by the coprecipitation method (Rousselot et al. (2002)) at constant pH. $Ca(NO_3)_2\cdot 4H_2O$; $Al(NO_3)_3\cdot 9H_2O$ and/or $Fe(NO_3)_3\cdot 9H_2O$ were put into solution in distilled water with a Ca/(Al+Fe) molar ratio of 2. 25mL of 0.3M salt solution were added into a reactor containing 100mL of a 0.2M NaOH solution under vigorous stirring. All synthesis steps were performed under a nitrogen gas flow to minimise carbonate contamination from the air. The pH was maintained at 13.5 by a controlled addition of a 2M NaOH solution (Al-Jaberi et al. (2015)). The suspension was aged for 24h in a reactor. The slurry was then centrifuged and washed three times with ethanol to remove any sodium or nitrate salt residue and dried in a desiccator (Rousselot et al. (2002)).

2.2 Analytical Methods

The crystal structure and purity of the phase were determined by X-ray powder diffraction (XRD), using a PANalytical X'Pert-Pro diffractometer in a θ-θ geometry, with a Cu Kα radiation (λ = 1.54155 Å) and an X'celerator detector. The crystal structure of AFm phases was refined, admitting a trigonal symmetry.
Raman spectroscopy was used to identify the intercalated anion and verify phase purity. Analyses were recorded on a T64000 Jobin Yvon spectrometer equipped with an Olympus BX41 confocal microscope at a x100 magnification.

3. Results and discussion

3.1. Purity of the synthesised AFm-NO_3 phases

The purity of the synthesised AFm phases was first controlled by XRD. Peak positions observed on diffractograms in Figure 2(a) confirm the formation of the layered $Ca_4Al_{2-x}Fe_x(OH)_{12}\cdot(NO_3)_2\cdot 4H_2O$ phase. Samples from the Al-rich side present AFm-CO_3 and calcite impurities due to CO_2 contamination from the air during the washing process.
Raman analyses were performed to identify the anion intercalated in the interlayers of the AFm phases. Renaudin et al. (2000) reported that the $Ca_4Al_2(OH)_{12}\cdot(NO_3)_2\cdot 4H_2O$ phase shows a vibration band corresponding to the symmetric stretching mode ν_2 at 1059 cm^{-1}. This vibration mode presents a second contribution at 1048 cm^{-1} by introducing Fe in agreement with Al-Jaberi et al. (2015); see Figure 2(b). Very low amounts of carbonate impurities in some synthesised mixed AFm are observed: 1094 cm^{-1} for calcite and 1070 cm^{-1} for AFm-CO_3 (Mesbah et al. (2011)).

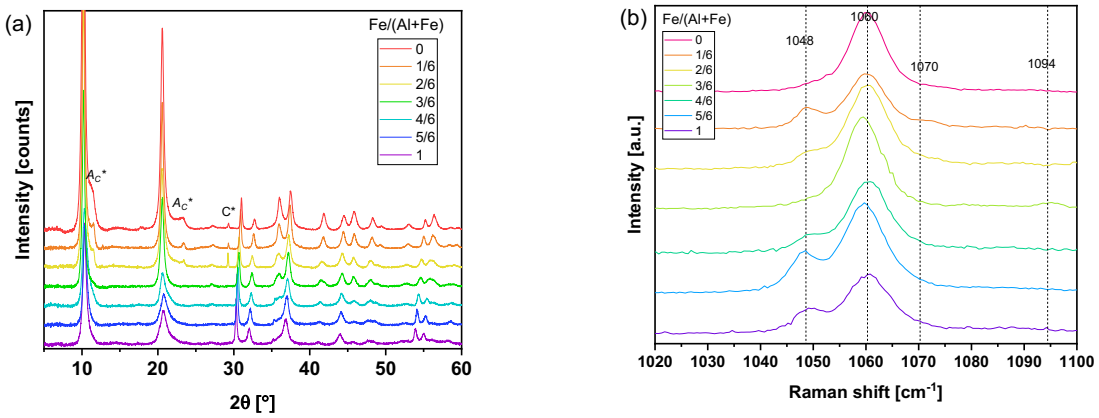


Figure 2. (a) XRD patterns of mixed $Ca_4Al_{2-x}Fe_x(OH)_{12}\cdot(NO_3)_2\cdot 4H_2O$ phases showing impurities A_C*= AFm-CO_3 and C*= calcite; (b) Raman spectra of mixed $Ca_4Al_{2-x}Fe_x(OH)_{12}\cdot(NO_3)_2\cdot 4H_2O$ corresponding to the anion ν_2 symmetric stretching mode.

3.2. Rietveld refinement

The X-ray powder patterns are representative of LDH material and identified as AFm-NO_3 phases which were systematically refined using the trigonal $P\bar{3}c1$ group space (Renaudin and François (1999)). The evolution of the refined cell parameters *a* and *c*/2 (d_{002}) are presented in Figure 3Figure 3. Lattice parameter *a* corresponds to the main layer's plan and is sensitive to the substitution of Fe over Al. The linear regression observed in Figure 3(a) tends to prove the existence of a complete solid solution between the two pure end-members. Half of the cell parameter *c* relates to the interlayer distance (Figure 3(b)). The interlayer distance depends on the number of water molecules and the anion's location. The slight decrease from 8.61 to 8.53 Å when introducing Fe^{3+} can be explained, although nonlinear, by its more flattened octahedron than that of Al^{3+}.

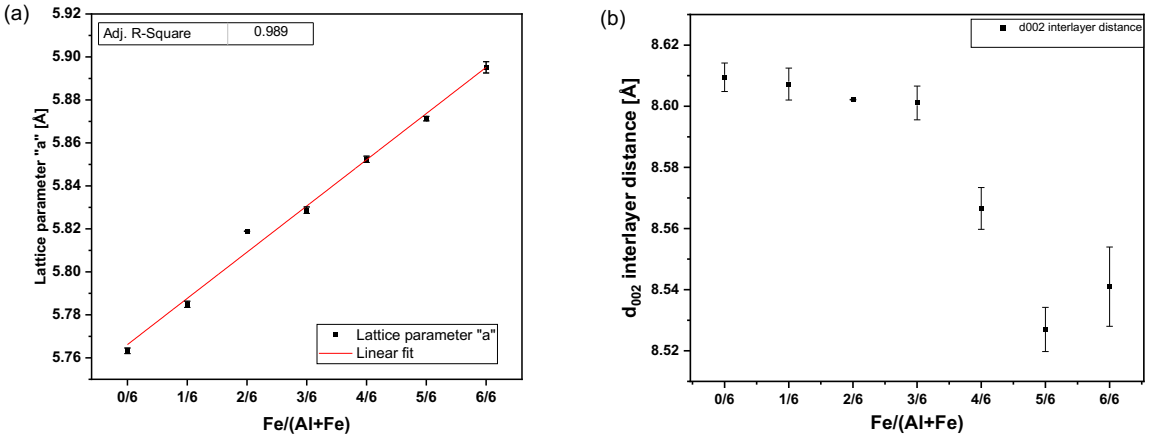


Figure 3 Representation of lattice parameters as a function of the Fe/(Al+Fe) ratio, (a) lattice parameter *a* and (b) d_{002} interlayer distance (*c*/2).

3.3. Thermal behaviour of the two pure end-members

In situ XRD experiments were performed over temperature to assess the stability of the AFm phases (Figure 4). An XRD pattern was recorded every 25°C up to 200°C and every 50°C beyond. XRD patterns highlight that the two pure end-members behave differently.

The Fe-AFm phase (Figure 4(a)) shows a decrease of the interlayer distance (from 8.54Å to 7.34Å) over temperature, which is in accordance with a progressive loss of the 4 water molecules. The dehydration of the interlayer is complete at 75°C. The Fe-AFm phase keeps its characteristic layered structure up to 175°C,

before becoming amorphous at 200°C.
The Al-AFm phase (Figure 4(b)) presents a very different behaviour. The phase starts losing water molecules above 50°C, decreasing the interlayer distance from 8.61Å to 7.43Å. The intermediate AFm hydrate – $Ca_4Al_2(OH)_{12}\cdot(NO_3)_2\cdot 2H_2O$ (Renaudin et al. (2000)) – remains stable up to 150°C. Above 150°C, the Al-AFm phase reorganises again, increasing its interlayer distance. This phenomenon is linked to the loss of the last water molecules and due to a change of nitrate bonding configuration with the main layer. And finally, the Al-AFm is almost amorphous from 250°C.
The two anhydrous AFm-analogues have different interlayer distances: 7.34 Å for Fe-AFm and 7.93 Å for Al-AFm.

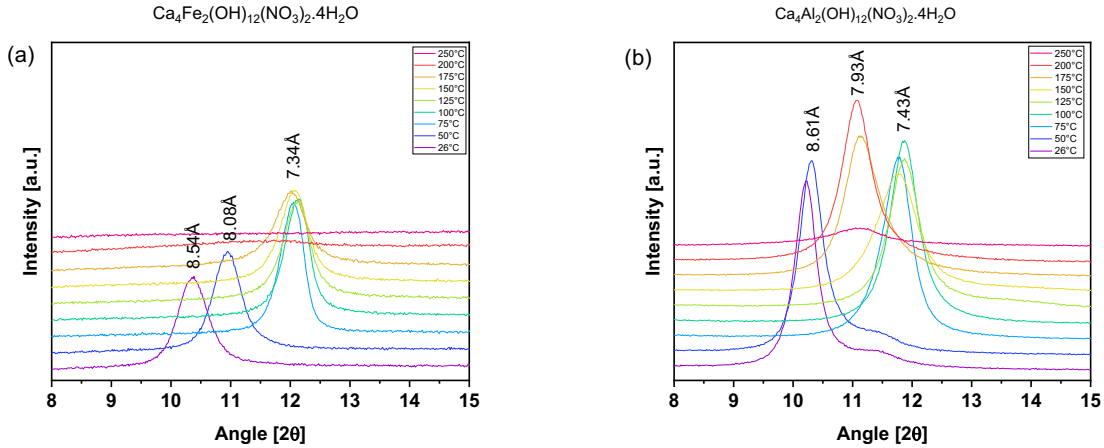


Figure 4. XRD patterns of (a) $Ca_4Fe_2(OH)_{12}\cdot(NO_3)_2\cdot 4H_2O$ and (b) $Ca_4Al_2(OH)_{12}\cdot(NO_3)_2\cdot 4H_2O$ over temperature.

4. Conclusions

The present work comes within the framework of general understanding and characterisation of hydration products of new CO_2-low binders, potentially containing nitrate anion sources as an accelerator. By Rietveld refinement, the existence of a complete solid solution between the two pure end-members of $Ca_4Al(OH)_{12}\cdot(NO_3)_2\cdot 4H_2O$ and $Ca_4Fe(OH)_{12}\cdot(NO_3)_2\cdot 4H_2O$ bounded to Fe/Al mixed oxide hydration was shown.
A thermal study also showed that the two end-members behave differently over temperature. The Al-AFm phase displays superior thermal stability. Moreover, the Al-AFm phase reorganises, and exhibits an intermediate hydrate. Further work about the stability of these AFm phases under various weathering conditions will complete this study in order to focus on durability for these CO_2-low binders.

References

Al-Jaberi, M., Naille, S., Dossot, M. and Ruby, C. (2015) 'Interlayer interaction in Ca–Fe layered double hydroxides intercalated with nitrate and chloride species', *J. Mol. Struct.* 1102, 253–60

Balonis, M., Mędala, M. and Glasser, F.P. (2011) 'Influence of calcium nitrate and nitrite on the constitution of AFm and AFt cement hydrates', *Adv. Cem. Res.* 23, 129–43

Chikh, N., Cheikh-Zouaoui, M., Aggoun, S. and Duval, R. (2008) 'Effects of calcium nitrate and triisopropanolamine on the setting and strength evolution of Portland cement pastes', *Mater. Struct.* 41, 31–36

Mesbah, A., Cau-dit-Coumes, C., Frizon, F., Leroux, F., Ravaux, J. and Renaudin, G. (2011) 'A New Investigation of the Cl−–CO32− Substitution in AFm Phases', *J. Am. Ceram. Soc.* 94, 1901–10

Renaudin, G. and François, M. (1999) 'The lamellar double-hydroxide (LDH) compound with composition 3CaO.Al2O3.Ca(NO3)2.10H2O', *Acta Crystallogr. Sect. C* 55, 835–38

Renaudin, G., Rapin, J.-P., Humbert, B. and François, M. (2000) 'Thermal behaviour of the nitrated AFm phase Ca4Al2(OH)12(NO3)2 • 4H2O and structure determination of the intermediate hydrate Ca4Al2(OH)12(NO3)2 • 2H2O', *Cem. Concr. Res.* 30, 307–14

Rousselot, I., Taviot-Guého, C., Leroux, F., Léone, P., Palvadeau, P. and Besse, J.-P. (2002) 'Insights on the Structural Chemistry of Hydrocalumite and Hydrotalcite-like Materials: Investigation of the Series Ca2M3+(OH)6Cl·2H2O (M3+: Al3+, Ga3+, Fe3+, and Sc3+) by X-Ray Powder Diffraction', *J. Solid State Chem.* 167, 137–44

The 16th International Congress on the Chemistry of Cement 2023 (ICCC2023)
"Further Reduction of CO_2 -Emissions and Circularity in the Cement and Concrete Industry"
September 18–22, 2023, Bangkok, Thailand

Effect of titanium dioxide nanoparticles on hydration and mechanical properties of mortar based on a ternary binder system

D.M. Le[1*], M. Michel[2], E. Prud'homme[3] and T.N. Baranger[4]

[1] *Université de Lyon, Université Lyon 1, LMC2-EA7427, F-69622 Villeurbanne, France*

Email : duc-manh.le@univ-lyon1.fr

[2] *Université de Lyon, Université Lyon 1, LMC2-EA7427, F-69622 Villeurbanne, France*

Email : marie.michel@univ-lyon1.fr

[3] *Université de Lyon, INSA Lyon, CNRS, MATEIS, UMR5510, 69621 Villeurbanne, France*

Email : elodie.prudhomme@insa-lyon.fr

[4] *Université de Lyon, Université Lyon 1, LMC2-EA7427, F-69622 Villeurbanne, France*

Email: thouraya.baranger@univ-lyon1.fr

ABSTRACT:

Cement and concrete structures are daily exposed to many organic pollutants that make their surface dirty. To handle this problem, titanium dioxide nanoparticles (NT) are incorporated into cementitious materials to create new multifunctional, self-cleaning materials.
With the combination of Portland cement (PC), calcium aluminate cement (CAC), and calcium sulfate, a ternary binder system was developed for its use in fast-setting repair mortar and composite materials. In order to research a multifunctional mortar based on a ternary binder system and NT, this paper presents the influence of NT on hydration and mechanical performances of the mortar by conducting X-ray diffractions (XRD) and mechanical strength tests. The microstructure of mortars was also investigated by using a scanning electron microscope (SEM).

KEYWORDS: ternary binder, nano titanium dioxide, hydration, microstructure, ettringite

1. Introduction

In recent decades, titanium dioxide nanoparticles (NT) have been applied in building materials to benefit their depolluting and self-cleaning properties, but some investigations revealed that these nanoparticles also have influences on the hydration, microstructure, and mechanical properties of cementitious materials. However, the knowledge about these influences is still in debate. The impact of NT on the hydration and mechanical properties of cement can be positive according to Li et al., (2018), or negative according to Kurihara & Maruyama (2016). Otherwise, most of the previous studies are limited to the mineral matrix based on ordinary Portland cement, and research about the impact of NT on others cement such as calcium aluminate cement, calcium sulfoaluminate cement, or mixed cement is rare.
On a different note, a ternary binder consisting of calcium aluminate cement, Portland cement, and calcium sulfate was developed to be used in construction. It was referred to as "ettringite binder" in some research since one of its main hydration products is ettringite ($C_6A\$_3H_{32}$) (Prud'homme, et al., (2014)). This binder provides some advantages such as rapid development in early-age strength and early-age shrinkage compensation. Furthermore, it has been specifically designed for some applications on composite materials. (Homoro, et al., (2022))
To design a new multifunctional mineral matrix based on ettringite binder and NT, the characterization of the matrix is essential. This article reports an experimental campaign to investigate the influence of NT on the mechanical strength of the matrix besides a study on the impact of NT on its hydration process and its microstructure.

2. Experimental

2.1 Raw materials

The composition of the base matrix was given in Table 1. The ettringite binder is a proportional mix of calcium aluminate cement (CAC), calcium sulfate (Plaster), and White Portland cement (WPC). The mineral skeleton consisted of quartz powder, limestone filler, and ground granulated blast-furnace slag (GGBS). The admixture consisted of a viscosity modifying agent, a dispersed resin, and a superplasticizer.

Table 1. Composition of the base matrix (liquid/solid = 0.308).

Component	CAC	Plaster	WPC	Quartz	Limestone filler	GGBS	Admixture
% weight	24.05	2.67	3.28	48.24	9.38	9.38	3

A commercialized photocatalytic suspension (CristalACTiV-S5-300B from Tronox France) (18.5% NT) was used as the source of NT. It is important to note that the photocatalytic suspension was not considered as a part of mixing water. The amount of suspension was calculated so NT was added at 1%, 2%, and 3 % by weight of the ettringite binder, which corresponded to the changes in the liquid/solid ratio to 0.324, 0.34, and 0.356, respectively. The sample was denoted as TiS_1, TiS_2, and TiS_3 respectively. The control sample was denoted as REF.

2.2 Sample preparation

Powder contents were mixed in a dry condition for 30 seconds at 80 r.p.m in a bowl mixer. Slowly, the pre-mix of water and suspension was added into the mixture while it was continuously mixed for 1 minute. Speed then was increased to 160 r.pm for 1 minute and turned back to 80 r.p.m for 1 additional minute. The mortar was cast as cylindrical specimens of 54 mm in height and 30 mm in diameter. Samples were demolded after 24 hours and stored at 20 ± 1°C and 100% RH until the day of the test.

2.3 Mechanical strength test

Compressive strength test and simple splitting tensile strength test were undertaken at the age of 7 days of the matrices using an MTS Criterion Series 40 machine. A displacement control mode was applied with the crosshead's displacement rate fixed at 2 mm/min. Compressive strength (R_c) and splitting tensile strength (R_t) were calculated using the equation:

$$R_c = F_{max} / (\pi \times r^2) \text{ and } R_t = F_{max} / (\pi \times r \times h) \quad (1)$$

Where F_{max} is the maximum value of the force corresponding to the test, r is the radius and h is the height of the specimen. The apparent density of the specimen was calculated by dividing its weight by its volume.

2.4 X-ray diffraction

The composition of hydrated matrices powder at 7-day age was characterized by X-ray diffraction using a Bruker D8 Advance diffractometer with CuKα X-ray source (λKα = 1.540 Å). The scanning range of 2θ is from 5° to 50° with a step size of 0.022° and a time per step of 1 second. Phase identification was fulfilled on DIFFRAC EVA software. Semi- quantitative analyses were performed on MAUD software with crystallography data that can be found on Crystallography Open Database.

2.5 Scanning electron microscope

The study of the microstructure of matrices at 28-day age was conducted using a Tescan Vega Microscope. A secondary electron scanning mode was considered in this study (HV = 10kV).

3. Results

3.1 Effect of NT on hydrated phases

Table 2 shows the XRD phase quantification of different formulations at 7-day age. The addition of NT admixture did not induce any discernible changes in the composition of the hydrated matrix. However, the increase in weight fraction of ettringite ($C_6A\$_3H_{32}$) and the decrease in weight fraction of Grossite (CA_2) on TiS_x formula indicates a higher reactivity of the phase CA_2 in calcium aluminate cement due to the addition of NT admixture. The reaction of CA_2 can be expressed by equation below, further information about the reactions can be found in the study of Nguyen (2015).

$$3CA_2+3C\$H_x + (47-3x)H \rightarrow C_6A\$_3H_{32} + 2AH_3 \quad (2)$$

Table 2. XRD quantification results.

XRD phase	% weight			
	REF	TiS_1	TiS_2	TiS_3
Ettringite	6.53	8.29	8.46	8.73
Quartz	63.33	61.831	63.47	62.55
Calcium monocarboaluminate	3.59	3.089	1.66	2.85
Calcium monocarboaluminate	4.48	4.91	5.02	3.84
Grossite	10.18	9.53	8.28	8.64
Gibssite	0.74	1.43	2.14	0.98
Calcite	11.15	10.92	10.97	12.41

3.2 Effect of NT on the microstructure of the matrix

SEM images of different matrix formulas were shown in Figure 1. Only observations on the REF sample and TiS3 sample were presented in this article. In the REF formula, Ettringite was observed in the form of massive pieces and sometimes "incomplete" hexagonal prism, suggesting a partially crystallization. However, in TiS_x formulas ettringite "needles" were observed and they were found nucleated on the surface of mineral aggregate. This finding agrees with the study of Guo, et al., (2020) which reported that the addition of NT can enhance the crystallinity and nucleation of its hydrated product in the cementitious material.

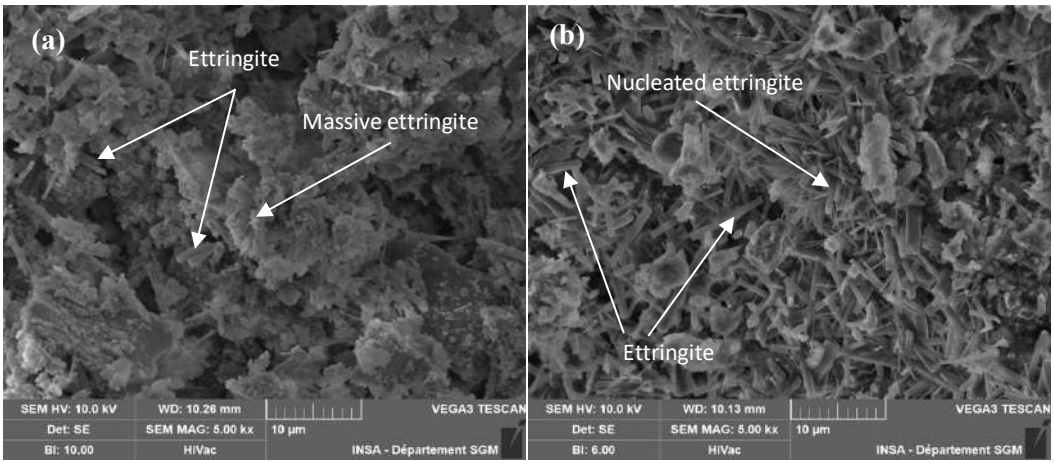


Figure 1. Microstructure of (a) REF matrix, (b) TiS_3 matrix

3.3 Effects of NT on mechanical strength

Figures 2a and 2b illustrate the compressive strength and the splitting tensile strength of 4 formulations. The addition of NT was found to significantly reduce the compressive strength of the matrix. This point can be explained that the addition of NT through a liquid suspension created a significant amount of air void in the matrix that leads to a weakness in its microstructure. The decrease in apparent density of TiS samples indicates the presence of excessive air voids in these formulations. However, the tensile strength of the matrix does not seem to be affected by the addition of the suspension. The reason for it can be attributed to the change in the microstructure of the matrix, caused by the intertwining of ettringite crystals in many directions, improving the material's resistance to splitting force. The reinforcing effect of NT on the tensile strength of cementitious matrix was also reported in the study of (Yang, et al., 2015)

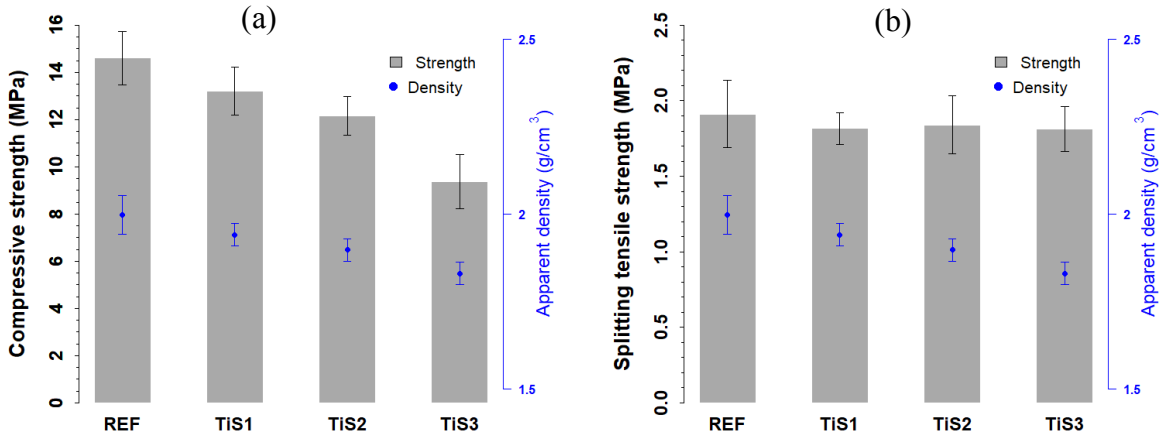


Figure 2 . (a) Compressive strength of the matrices at 7-day age

(b) splitting tensile strength of the matrices at 7-day age

4. Conclusions

An experimental campaign has shown an acceleration effect of NT on the hydration rate of mineral matrix based on ettringite binder. The compressive strength of the modified matrices was reduced due to the increase in their air-void content when a supplementary amount of liquid was added as the NT suspension. However, the addition of NT has a positive impact on the splitting tensile strength of the matrix, as evidenced by changes to its microstructure. The substitution of mixing water by NT suspension can be considered, as it will not affect the density of the matrix but it is important to take into account the impact on the workability of the mixture.

References:

Li, Z. et al., 2018. Multifunctional cementitious composites modified with nano titanium dioxide: A review. *Composites Part A: Applied Science and Manufacturing,* Volume 111, p. 115–137.

Kurihara, R. & Maruyama, I., 2016. Influences of nano-TiO2 particles on alteration of microstructure of hardened cement. *Tech. Paper,* Volume 38, p. 219–224.

Prud'homme, E. et al., 2014. Investigation of Ettringite Binder Hydration at Early Age for Glass Fiber Reinforced Concrete Application. In: *Developments in Strategic Materials and Computational Design V*. s.l.:John Wiley & Sons, Ltd, pp. 111-123.

Homoro, O., Michel, M. & Baranger, T. N., 2022. Improvement of the mechanical properties of a glass multifilament yarn reinforced ettringitic matrix using an innovative pre-impregnation process. *European Journal of Environmental and Civil Engineering,* Volume 26, p. 1977–1992.

Nguyen, N. L., 2015. *Étude de la microstructure des liants ettringitiques influence sur les propriétés macroscopiques: Résistance et variation dimensionnelle. PhD thesis*

Guo, C. et al., 2020. Characterization and mechanism of early hydration of calcium aluminate cement with anatase-TiO2 nanospheres additive. *Construction and Building Materials,* Volume 261, p. 119922.

Yang, L. Y., Jia, Z. J., Zhang, Y. M. & Dai, J. G., 2015. Effects of nano-TiO2 on strength, shrinkage and microstructure of alkali activated slag pastes. *Cement and Concrete Composites,* Volume 57, p. 1–7.

The 16th International Congress on the Chemistry of Cement 2023 (ICCC2023)
"Further Reduction of CO_2 -Emissions and Circularity in the Cement and Concrete Industry"
September 18–22, 2023, Bangkok, Thailand

Role of Gypsum on Early Age Hydration of Alite Polymorphs (TI and TIII): A Temporal X-ray PDF Analysis

C. Kothari, H. Jee, and N. Garg*

Department of Civil and Environmental Engineering, University of Illinois Urbana-Champaign, Urbana, United States

Email: chirayu4@illinois.edu, hjee3@illinois.edu, nishantg@illinois.edu

ABSTRACT

Alite, a solid solution of tricalcium silicate (C_3S) and other foreign ions (Mg^{+2}, Fe^{+3}, Al^{+3}, Zn^{+2}, etc.), is the major constituent of Ordinary Portland cement. The impurities in the raw materials chemically modify C_3S (polymorphs) and influence its hydration kinetics. Additionally, gypsum, primarily added to control the flash setting of reactive aluminates, also affects the hydration kinetics of C_3S. The effect of impurities and gypsum on the early-age hydration of C_3S has yet to be adequately understood. Here, we investigated the role of gypsum addition on the hydration kinetics of TI and TIII polymorphs of C_3S. Time-dependent phase evolution was observed via in-situ total X-ray total scattering and atomic pair distribution function (PDF) analysis. We analyzed the peak position shift and peak intensity evolution for hydrating C_3S (TI and TIII) systems with and without gypsum. Upon gypsum addition, the evolution was relatively lower for the first ~6 h and ~9 h for TI and TIII C_3S polymorphs, respectively. However, this trend was reversed at a later age, indicating a prolonged induction period but a higher degree of hydration. The findings will be useful for the sulfate optimization for the early age performance of blended cementitious systems.

KEYWORDS: *Tricalcium Silicate, hydration, polymorphs, gypsum, atomic pair distribution function*

1. Introduction

The higher CO_2 footprint of conventional OPC cement has led to the widespread acceptance of blended cement. Alite, the solid solution of C_3S and foreign ions, is the primary constituent of blended systems. The presence of these foreign ions causes polymorphism in tricalcium silicate (C_3S), altering its reactivity and hydraulic behavior. Sulfate addition controls early-age behavior and strength during the hydration of the blended systems. Previous studies have shown that gypsum not only regulates the hydration of aluminate phases but also influences the hydration kinetics of C_3S (Zunino and Scrivener (2022)). The presence of gypsum prolongs the induction period and a higher hydration rate at an early age. However, there is still significant debate surrounding the underlying mechanisms that govern this phenomenon. Hence, further investigation into the effect of gypsum on the hydration behavior of different polymorphs is required for optimizing sulfate content in blended systems.

X-ray total scattering and atomic pair distribution (PDF) analysis-based synchrotrons studies have effectively been used for exploring the reaction kinetics of cementitious materials involving gel formation, carbonation, and drying (Morandeau and White (2015), Garg and White (2017)). In-situ X-ray scattering experiments and subsequent PDF analysis enable tracking of time-dependent reaction kinetics and nanostructural evolution of cementitious systems due to its high resolution and quick data gathering.

Here, X-ray PDF analysis has been used to investigate the impact of gypsum addition on the hydration of two polymorphs of C_3S. Atom-Atom correlations were analyzed to understand the hydration behavior of C_3S. Further, this study observed the reaction kinetics between two polymorphs (TI and TIII) of C_3S and the effect of gypsum on the induction period and C_3S hydration degree based on the PDF evolution.

2. Materials and Methods

2.1 Material Synthesis and Sample Preparations

High purity C_3S (TI, wt.% > 94%) was synthesized in the lab by heating the stoichiometric proportion of $CaCO_3$ (99+% pure, Thermo Fisher Scientific, CAS No. 471-34-1), and fumed silica (SiO_2, Sigma Aldrich, CAS No. 112945-52-5) at 1600°C. The sample was air quenched after sintering it for 7 hrs. Similarly, C_3S (TIII) was synthesized using $CaCO_3$ (98 % pure, Alfa Aesar, CAS No. 471-34-1) with Mg (0.6% MgO) present as an impurity. Both synthesized C_3S were ground using an agate mortar and pestle and sieved through a 45 μm sieve. 2 more samples of both C_3S were prepared with the addition of 3% gypsum (G) after C_3S synthesis. The w/b ratio was kept at 0.5.

2.2 Synchrotron X-ray Scattering Experiment and PDF Analysis

High-Energy Synchrotron X-ray total scattering experiments (E = 58 keV, λ = 0.2112 Å) were performed on the beamline 11-ID-B at Advanced Photon Source, Argonne National Laboratory. A Perkin Elmer amorphous silicon imaging plate was used to detect the X-ray scattering data. The samples were mixed with a vortex mixer in the HDPA containers and immediately loaded into a 1 mm polyamide capillary. Capillaries were sealed with epoxy to avoid water loss and carbonation. The in-situ hydration measurements were performed every ~1.5 hours for a duration of ~33 h after mixing the paste (3 min scan on each sample). The data conversion from 2D to 1D was carried out via the Fit2D program with CeO_2 as a calibration material. PDF (g(r)) data was obtained via PDFgetX3 software with a maximum Q cutoff of 24 $Å^{-1}$.

3. Results and Discussion

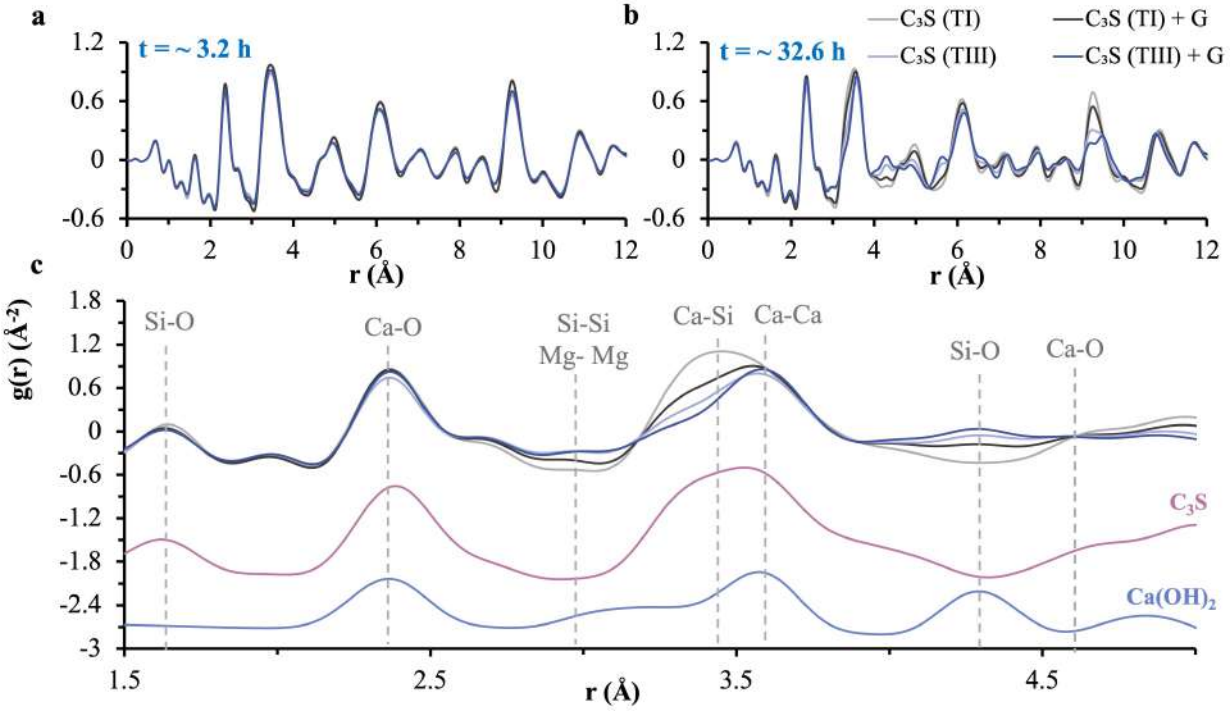


Figure 1 In-situ X-ray PDFs of (i) C_3S (TI) (ii) C_3S (TI) + G, (iii) C_3S (TIII), and (iv) C_3S (TIII) + G at (a) ~ 3.2 hrs, and (b) ~ 32.6 hrs of hydration displaying the data up to 12Å. (c) Experimental PDF of all 4 samples at ~ 32.6 hrs with attributed atom-atom correlation along with PDF data of C_3S and $Ca(OH)_2$ to understand their contribution.

We utilized in-situ PDF analysis to track the atomic ordering of cement hydration. X-ray PDF of 4 samples at ~ 3.2 hrs and ~32.6 hrs of hydration are shown in Figure 1(a) and Figure 1(b), respectively. The PDF difference in the range 3 Å-5 Å, indicates the reduction in C_3S and formation of C-S-H and $Ca(OH)_2$. The difference in PDF at a longer range can correspond to the fraction of crystalline phases. Figure 1(c)

illustrates atom-atom correlations based on previous studies (Meral et al., 2011; Skinner et al., 2010). The PDF curves for the samples were similar at ~3.4h. At ~32.6 hrs, a significant difference between the PDF of the 4 samples was observed, especially at r > 2.5 Å. The hydration of C_3S results in the formation of Calcium-Silicate-Hydrate (C-S-H) and Calcium Hydroxide ($Ca(OH)_2$). Hence, the experimental PDF curves are a combination of X-ray scattering from C_3S, $Ca(OH)_2$, and C-S-H. Polymorphism in C_3S and the presence of sulfate influence its hydration, as observed by the difference in PDF curves in Figure 1(c). The peak at ~2.9Å corresponds to the Si-Si and Mg-Mg correlations. At ~32.6 h, higher ~2.9Å peak intensity for C_3S -TIII in comparison with that of C_3S -TI indicates a higher reaction degree or incorporation of Mg ions in the C-S-H gel. Further investigation is required for validation.

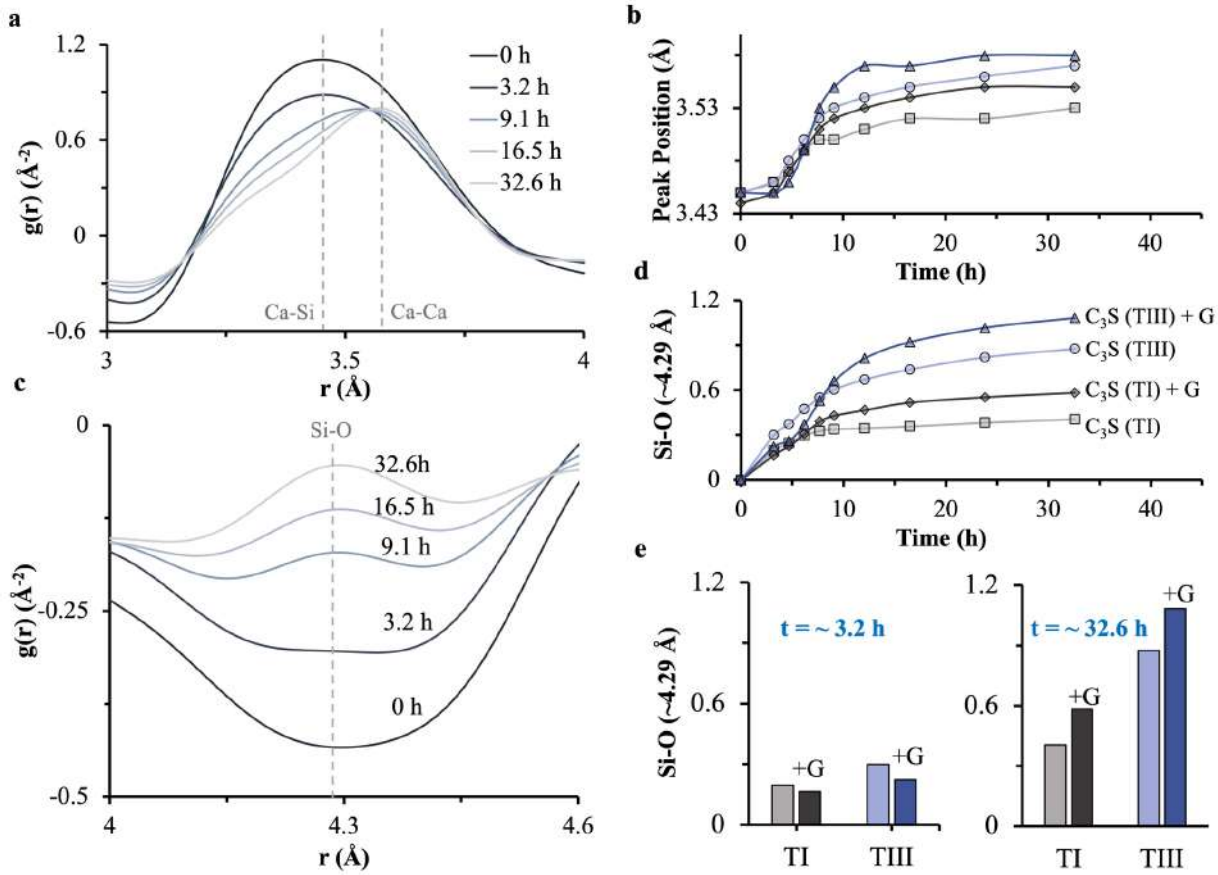


Figure 2: (a) PDF evolution of peak located in the range ~ (3.4 -3.7) Å in PDF analysis of C_3S(TIII) + G. The peak comes from the overlap of the Ca-Si and the Ca-Ca correlations. (b) The shift in the peak position in the range ~ (3.4 -3.7) Å with time is related to C_3S hydration (c) Evolution of the peak located at 4.29 Å in the PDF analysis of C_3S(TIII) + G (d) Change in the Si-O intensity (~ 4.3 Å) normalized at t =0 is related to extent of hydration (e) Normalized intensity at ~ 4.29 Å can be used as a measure of hydration degree. Samples with gypsum have lower normalized intensity at ~ 3.2 h and higher intensity at ~32.6 h, confirming a longer induction period and a higher rate of hydration upon the addition of gypsum.

C_3S hydration involves a reduction in C_3S (~2.4Å and ~3.45Å) and the formation of C-S-H and $Ca(OH)_2$ (~3.6Å). Figure 2(a) depicts the PDF evolution resulting from the hydration of C_3S (TIII) with gypsum, which shows a peak overlap in the Ca-Si and Ca-Ca correlation peaks. A shift in peak position was observed from the Ca-Si correlation to the Ca-Ca correlation upon hydration as depicted in Figure 2 (b). Additionally, the Si-O (~4.29Å) correlation intensity corresponding to the Si and O in the next nearest neighbor increased with hydration, as shown in Figure 2(c). This intensity normalized to t = 0 h was plotted against time (Figure 2(d)), and increased intensity can correspond to more CSH. The change in peak position in the range ~ (3.4 -3.7) Å and Si-O (~4.29Å) peak intensity upon hydration can be attributed to the extent of hydration. Finally, based on Figure 2(b), Figure 2(d) and Figure 2(), the extent of hydration at ~32.6 h can be given the order: C_3S (TI) < C_3S (TI) + G < C_3S (TIII) < C_3S (TIII) + G. However, due to the presence of multiple phases other than C-S-H, quantitative analysis and further characterization shall be performed for conformity on the

extent of hydration. Though both the polymorphs were sieved through 45-µm sieves, it is possible that the higher degree of reaction for the TIII polymorph could have been caused by the difference in particle size distribution.

Zunino and Scrivener (2022) have shown that the presence of gypsum results in a prolonged induction period during C_3S hydration. During the initial ~6h and ~9 h of hydration for the TI and TIII polymorphs of C_3S, respectively, the change in peak position in the range ~ (3.4 -3.7) Å was lower in the presence of gypsum compared to pure C_3S (Figure 2(b)). In addition, a similar trend of lower Si-O peak (~4.29Å) intensity was observed for C_3S with gypsum (Figure 2(d)), indicating the delayed formation of C-S-H during the early hours of hydration. However, after ~6h and ~9 h of hydration for the TI and TIII polymorphs, respectively, the trend was reversed with a higher shift in ~ (3.4 -3.7) Å peak position and (~4.29Å) intensity for samples with added gypsum, indicating that gypsum promotes C_3S hydration and C-S-H formation. The trend reversal was confirmed by comparing the normalized Si-O peak (~4.29Å) intensity of the four samples at ~3.2h and ~32.6h (Figure 2(e)). The lower intensity for the samples with gypsum at ~3.2h was due to the prolonged induction period, while the higher intensity at ~32.6 h indicated a higher amount of C-S-H and a higher degree of hydration. Therefore, the presence of gypsum prolongs the induction period and increases the extent of C_3S hydration. Overall, in-situ PDF analysis can be utilized to observe the effect of gypsum on both the induction period and hydration degree. Further verification of the influence of gypsum on C_3S hydration can be performed via isothermal calorimetry and microscopy-based methods.

4. Conclusions

This study investigated the hydration behavior of TI and TIII polymorphs of C_3S, with and without gypsum, using in-situ X-ray scattering experiments and PDF analysis. The results showed that the TIII polymorph exhibited a higher degree of hydration which may be attributed to the presence of Mg ions as observed at Si-Si/ Mg-Mg correlations (~ 2.9 Å) or due to smaller particle size distribution than TI polymorphs. Additionally, the study found that the addition of sulfate lowered the evolution of ~ (3.4 -3.7) Å peak position and (~4.29Å) peak intensity before ~6 hours and ~9 hours for TI and TIII C_3S polymorphs, respectively. However, for later ages, the trend for peak evolution was reversed for the samples with gypsum addition. This indicates the prolongation of the induction period and led to a higher hydration degree at a later age. Further experiments are needed to understand the reason for the higher reactivity of the TIII polymorph. With crystalline systems present in the system, deconvolution and quantitative analysis shall be performed to understand the influence of sulfate on the atomic ordering of C-S-H gel. Overall, these results provide valuable insights into the hydration behavior of C_3S and offer new directions for the development of blended systems.

Acknowledgments

We are thankful to Dr. Tiffany Kinnibrugh for their assistance and guidance at the beamline (11-ID-B). Use of the Advanced Photon Source at Argonne National Laboratory was supported by the US Department of Energy, Office of Science, Office of Basic Energy Sciences, under Contract No. DE-AC02-06CH11357.

References

Zunino, F. and Scrivener, K. (2022) "The influence of sulfate addition on hydration kinetics and C-S-H morphology of C3S and C3S/C3A systems", *Cement and Concrete Research,* 160, 106930.

Morandeau, A.E., and White, C.E. (2015) "In situ X-ray pair distribution function analysis of accelerated carbonation of a synthetic calcium-silicate-hydrate gel, *Journal of Material Chemistry A*, 3(16): 8597-8605.

Garg, N. and White, C. E. (2017) "Mechanism of zinc oxide retardation in alkali-activated materials: an in situ X-ray pair distribution function investigation", *Journal of Materials Chemistry A*, 5(23): 11794-11804

Meral, C., Benmore, C.J. and Monteiro, J.M. (2011) "The study of disorder and nanocrystalline in C-S-H, supplementary cementitious materials and geopolymers using pair distribution function analysis", *Cement and Concrete Research*, 41(7): 696-710

Skinner, L. B., Chae, S. R., Benmore, C. J., Wenk, H. R., and Monteiro, P. J. M. (2010) "Nanostructure of calcium silicate hydrates in cements", *Physical review letters*, 104(19): 195502

The 16th International Congress on the Chemistry of Cement 2023 (ICCC2023)
"Further Reduction of CO_2 -Emissions and Circularity in the Cement and Concrete Industry"
September 18–22, 2023, Bangkok, Thailand

Adsorption of Ca^{2+} at Micro Aggregate Surface and Its Effect on Particle Interaction, C-S-H Formation and Adhesion

X. Ouyang*, C. Lin, S. Xu, J. Li, L. Wang, Y. Ma and J. Fu

Research Center for Wind Engineering and Engineering Vibration, Guangzhou University, Guangzhou, 510006, China
Email: xwouyang@gzhu.edu.cn

ABSTRACT

Aggregates and fibers with diverse chemical properties have been applied to develop green, high-performance and smart concrete, such as manufactured sand, functional aggregates and recycled aggregates. It is of great significance to clarify the mechanism for the influence of these materials' chemical properties on the performance of cement-based materials. In this study, the interaction between the micro aggregates (i.e., limestone, quartz and magnesite) and cement particles, C-S-H formation and adhesion at the interface were studied at the micro-scale. At the nano-scale, the adsorption of ions (mainly Ca^{2+}) at the aggregates' surface was investigated with zeta potential measurement. Finally, the atomic structure of the micro aggregates and their effect on ion adsorption was discussed. The results showed that the adsorption of Ca^{2+} at the interface, which depends on the surface atomic structure, plays a dominant role in the particle interaction, C-S-H formation and adhesion. The limestone's surface is dominated by CO_3^{-2}. This enables its surface to chemically adsorb Ca^{2+}. It weakens the interparticle attraction in the solution, facilitates C-S-H nucleation and growth, and results in a chemical adhesion between C-S-H and the limestone's surface. On the contrary, magnesite's surface is dominated by Mg^{+2}, which is not conducive to the adsorption of Ca^{2+}. It leads to its poor performance as a micro aggregate. In the case of quartz, its surface is hydrolyzed into SiO^- in the alkaline solution. The interaction between Ca^{2+} and quartz is governed by electrostatic forces. Quartz's interaction with Ca^{2+} is inferior to limestone but better than magnesite. The performance of micro aggregates in cement paste is constant with the adsorption of Ca^{2+}.

KEYWORDS: *cement-based materials, aggregate, rheology, hydration, interfacial strength*

1. Introduction

Aggregates and fibers with diverse chemical properties are utilized to develop eco-friendly, high-performance and smart concrete. The surface chemical properties of these materials affect the inter-particle force, the formation and adhesion of hydration products at the interface, and ultimately, the rheology, hydration and interfacial strength of cement-based materials. For instance, it was demonstrated that the yield stress and viscosity of the fresh cement paste mixed with limestone powder are reduced and its fluidity is improved to some extent, while the addition of quartz powder has little effect on the rheology of cement paste (Bentz et al., 2017). In addition, surface chemical properties significantly affect the nucleation and growth of C-S-H, thus the hydration of cement. The surface of materials such as limestone promotes the formation of C-S-H, while others hinder it (Berodier and Scrivener, 2014; Juhart et al., 2019). Besides, it was found that the bonding between limestone surfaces and hydration products is significantly stronger than that between quartz surfaces and hydration products (French and Mokhtarzadeh, 1993). Despite the reported experimental evidence on the relationship between surface chemical properties and the performance of cement-based materials, including rheology, hydration and strength, the fundamental mechanism underlying these observations is not yet fully understood. Moreover, literature reports are scarce with regard to the (electro) chemical transformations on the surface of these materials, especially when interactions in the pore solution of fresh cement paste are concerned. In this study, the interaction between the micro aggregates (i.e., limestone, quartz and magnesite) and

cement particles, C-S-H formation and adhesion at the interface were studied at the micro-scale. At the nano-scale, the adsorption of ions (mainly Ca^{2+}) at the aggregates' surface was investigated with zeta potential measurement. Finally, the atomic structure of the micro aggregates and their effect on ion adsorption and their performance in cement-based materials were discussed.

2. Experimental

To assess the inter-particle forces, Atomic Force Microscopy (AFM) measurements were conducted on model solutions. To simulate the cement particle, a silicon dioxide sphere was glued onto tip-less triangular cantilevers, as they have similar surface charge properties (Ouyang et al., 2017). The aggregates were cut, ground, and polished to serve as a test base. $Ca(OH)_2$ solution was used as the model solution.

The morphology of hydration products in cement pastes containing 30% micro aggregates with a water/binder ratio of 0.4 after 7 h of curing was observed using a scanning electron microscope (Phenom, FEI). Additionally, the cracks in the pastes were examined after 28 d of curing.

Zeta potential tests were conducted to investigate the interaction between the surface of micro aggregates and ions in the pore solution of cement paste, using a potential analyzer (Malvern Zetasizer Nano). A model solution was prepared to facilitate the tests, with $Ca(OH)_2$ solutions ranging from 0.2 to 20 mmol/L.

3. Results and discussion

3.1 Particle interaction

Results on AFM dispersion forces as a function of distance were collected in a 4.0 mmol/L $Ca(OH)_2$ solution, as shown in Fig. 1. It is noted that the attraction forces between the magnesite substrate and silicon dioxide tip were significantly larger than those between the quartz substrate and silicon dioxide tip, while limestone showed the smallest attraction forces with the silicon dioxide tip. This indicates that cement paste with limestone powder has better rheological performance than that with quartz or magnesite powder. These findings are consistent with previous reports (Bentz et al., 2017).

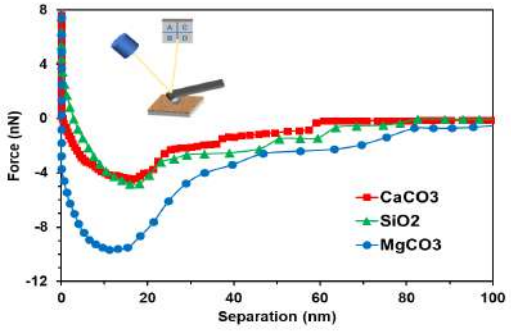


Fig. 1 The interaction forces between aggregates' surfaces and a silicon dioxide probe in $Ca(OH)_2$ solution.

3.2 C-S-H formation

Fig. 2 shows the surface morphology of limestone, quartz, and magnesite particles at 7 h. The surface of the limestone is densely covered with hydration products, mainly C-S-H, which exhibit directionality in their growth. On the surface of the quartz, a large amount of non-directional C-S-H is attached. Conversely, the surface of magnesite particles has only a small amount of hydration products, indicating that the surface of magnesite is not conducive to the nucleation and growth of C-S-H.

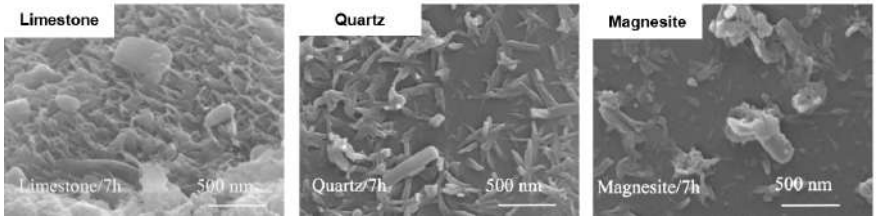


Fig. 2 SEM images demonstrating the morphology of hydration products at the surfaces of limestone, quartz and magnesite particles at 7 h.

3.3 C-S-H adhesion

The main factors influencing the development of micro-cracks in hardened cement paste, as reported in studies (van Mier, 2007), are local stress and weak connections between hydrates and aggregates. Micro-cracks tend to propagate along weak interfaces under certain pressure. Fig. 3 illustrates the crack development in hardened cement containing 30% limestone, quartz, and magnesite powders at a curing age of 28 d with a water-to-binder ratio of 0.4. The cracks rarely propagate alone the limestone particles, instead, they propagate through it. In contrast, tortuous cracks that tend to propagate around the quartz and magnesite particles were observed. These observations suggest that the interface between limestone and the hydration products is much stronger than the interface between quartz or magnesite particles and the hydration products.

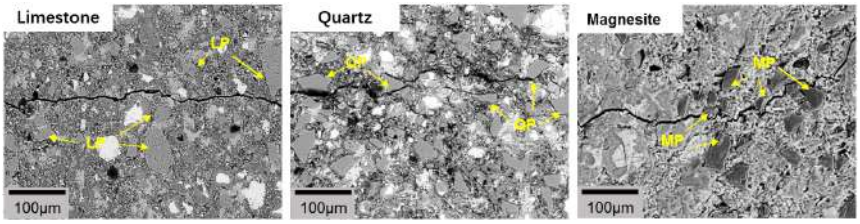


Fig. 3 BSE images illustrating the cracks in the cement paste blended with 30% limestone, quartz and magnesite powders at 28 d.

3.4 Ions interaction

The zeta potentials of the particles as a function of $Ca(OH)_2$ solutions are shown in Fig. 4. At the same Ca^{2+} concentration, limestone particles exhibit a higher zeta potential than quartz and magnesite particles, indicating that the limestone surface has a stronger adsorption capacity for Ca^{2+}. Moreover, the zeta potential of magnesite particles gradually increases from -22 mV to +10 mV as the Ca^{2+} concentration increases from 0.2 mmol/L to 20 mmol/L, due to the increase in the amount of Ca^{2+} adsorbed. However, the increase in potential slows down after the Ca^{2+} concentration exceeds 6 mmol/L. This suggests that the adsorption of Ca^{2+} on the surface of the magnesite is close to saturation at a Ca^{2+} concentration of around 6 mmol/L. These observations imply that the adsorption capacity of the magnesite for Ca^{2+} is weak, resulting in a significantly lower saturation potential compared to limestone and quartz.

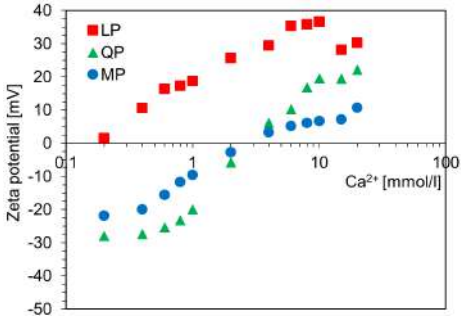


Fig. 4 Zeta potential of limestone (LP), quartz (QP) and magnesite (MP) particles in Ca $(OH)_2$ solutions.

3.5 Discussion

Based on the study, Fig. 5 depicts the influence of the chemical properties of micro aggregates on the particle interaction, C-S-H formation and adhesion at the surface, and ultimately the rheology, hydration and strength of the cement-based material. On the surface atomic structure of limestone, CO_3^{-2} predominates, which allows for the chemical adsorption of Ca^{2+} (Huang et al., 1991). This enhances the electrostatic repulsion between the particles in the solution, leading to better particle dispersion and improved flowability of the cement paste. Additionally, it promotes the growth of C-S-H, leading to faster hydration. The chemical adsorption of Ca^{2+} on the surface of limestone results in the formation of chemical bonds between the surface and the C-S-H, leading to a strong interface.

In an alkaline solution, the surface of quartz undergoes hydrolysis, generating SiO^- and making the particle surface negatively charged (Vikan and Justnes, 2007). This results in the physical electrostatic adsorption of Ca^{2+} similar to that of the cement particles, leading to less significant changes in the flowability of the cement paste when quartz powder is added (Bentz et al., 2017). The surface of the quartz particles has less Ca^{2+}, resulting in a less pronounced promotion of C-S-H nucleation. The physical

electrostatic adsorption of Ca^{2+} on the surface of quartz results in relatively weaker interfacial bonding compared with that between limestone's surface and C-S-H.

On the surface atomic structure of dolomite, Mg^{+2} predominates (Tang et al., 2020), which is not favorable for the adsorption of Ca^{2+}. This greatly weakens the electrostatic repulsion between the particles, resulting in poorer flowability. Additionally, it is not conducive to the growth of C-S-H. The primary adhesion force between the surface of magnesite and the C-S-H is a weak physical bond, which leads to the formation of a weak interface.

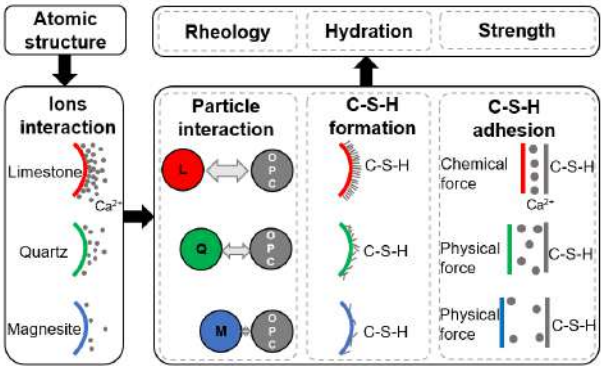


Fig. 5 Schematic diagram of the influence of chemical properties of micro aggregates.

4. Conclusions

The interactions of the aggregate surface with Ca^{2+}, which depend on the surface atomic structure, play a key role in understanding the influence of the chemical properties of aggregates on concrete performance. When a surface has strong adsorption of Ca^{2+} (such as limestone), it promotes particle repulsion in solution, nucleation and adhesion of C-S-H at the interface, which improves flowability, hydration, and strength development of cement-based materials. Conversely, magnesite has the weakest adsorption on Ca^{2+}, resulting in poor performance as an aggregate in cement-based materials. Quartz's interaction with Ca^{2+} is not as strong as limestone, but it is better than magnesite. The performance of micro aggregates with different chemical properties in cement-based materials is constant with the adsorption of Ca^{2+}.

Acknowledgements

The authors would like to acknowledge the financial support from the National Nature Science Foundation of China (Grant No.52008119), and the Natural Science Foundation of Guangdong Province (Grant No. 2021A1515012624).

References

Bentz, D. P., Ferraris, C. F., Jones, S. Z., Lootens, D., and Zunino, F. (2017) "Limestone and silica powder replacements for cement: Early-age performance", *Cement and Concrete Composites, 78*: 43-56

Berodier, E., and Scrivener, K. (2014) "Understanding the Filler Effect on the Nucleation and Growth of C-S-H", *Journal of the American Ceramic Society, 97*(12): 3764-3773

French, C. W., and Mokhtarzadeh, A. (1993) "High strength concrete: Effects of materials, curing and test procedures on short-term compressive strength", *PCI Journal, 38*(3): 76-87

Huang, Y. C., Fowkes, F. M., Lloyd, T. B., and Sanders, N. D. (1991) "Adsorption of calcium ions from calcium chloride solutions onto calcium carbonate particles", *Langmuir, 7*(8): 1742-1748

Juhart, J., David, G.-A., Saade, M. R. M., Baldermann, C., Passer, A., and Mittermayr, F. (2019) "Functional and environmental performance optimization of Portland cement-based materials by combined mineral fillers", *Cement and Concrete Research, 122*: 157-178

Ouyang, X., Koleva, D. A., Ye, G., and Van Breugel, K. (2017) "Insights into the mechanisms of nucleation and growth of C–S–H on fillers", *Materials and Structures, 50*(5): 213

Tang, Y., Kelebek, S., and Yin, W. (2020) "Surface chemistry of magnesite and calcite flotation and molecular dynamics simulation of their cetyl phosphate adsorption", *Colloids and Surfaces a-Physicochemical and Engineering Aspects, 603*: 125246

van Mier, J. M. (2007) "Multi-scale interaction potentials (F − r) for describing fracture of brittle disordered materials like cement and concrete", *International Journal of Fracture, 143*(1): 41-78

Vikan, H., and Justnes, H. (2007) "Rheology of cementitious paste with silica fume or limestone", *Cement & Concrete Research, 37*(11): 1512-1517

The 16th International Congress on the Chemistry of Cement 2023 (ICCC2023)
"Further Reduction of CO_2 -Emissions and Circularity in the Cement and Concrete Industry"
September 18–22, 2023, Bangkok, Thailand

In Situ X-ray Total Scattering Study on the Impact of Gypsum in C_3S-Metakaolin-Limestone Systems

H. Jee, C. Kothari, and N. Garg*

Department of Civil and Environmental Engineering, University of Illinois Urbana-Champaign, Urbana, United States

Email: hjee3@illinois.edu, chirayu4@illinois.edu, nishantg@illinois.edu

ABSTRACT

Tricalcium aluminate and metakaolin cause high aluminate contents in limestone calcined clay cement (LC^3), requiring a higher gypsum content than conventional ordinary Portland cement. Although gypsum primarily controls the reaction of aluminate phases, it also affects the hydration of calcium silicate phases such as tricalcium silicate (C_3S). However, the effect of gypsum on the calcium silicate phases in the blended system is not clearly understood. In this study, we investigate the impact of gypsum on hydration and the nanostructure development of three systems: (i) synthetic C_3S, (ii) C_3S with metakaolin, and (iii) C_3S with metakaolin and limestone in the presence and absence of gypsum via *in situ* synchrotron-based X-ray total scattering and pair distribution function (PDF) analysis. The Ca-T PDF peak shift located at ~3.4 Å showed that adding gypsum accelerated the hydration of all systems; however, the effect of gypsum was the most prominent for the pure C_3S systems with clear acceleration after ~7.5 h. Moreover, the evolution of the T-O peak (~1.6 Å) suggested that adding gypsum hampered the aluminum incorporation in the C-S-H structure. The results indicate the effect of gypsum on C_3S hydration differs in pure C_3S and blended systems, and the structure of the main binder gel alters in the presence of gypsum.

KEYWORDS: *Limestone calcined clay cement (LC^3), gypsum, calcium silicate, hydration, pair distribution function.*

1. Introduction

As the world population grows, so does ordinary Portland cement (OPC) usage. However, the high CO_2 emissions associated with OPC production necessitate alternative construction materials. Limestone calcined clay cement (LC^3) is a recently developed sustainable construction material, which is ternary blended cement with OPC, calcined clay, and limestone (Sharma et al., 2021). Since LC^3 includes high alumina contents due to the presence of calcined clay, typically, LC^3 contains higher gypsum contents than the OPC system. The main role of gypsum is to regulate the hydration kinetics of alumina sources; however, gypsum also affects the hydration behavior of calcium silicate phases such as tricalcium silicate (Neto et al., 2022). Thus, more investigation is needed to understand the effect of gypsum on the hydration behavior and structural evolution of calcium silicate phases in a blended system such as LC^3.

Synchrotron-based X-ray total scattering and pair distribution (PDF) analysis have been demonstrated to be powerful characterization technologies for probing the reaction kinetics of cementitious materials (Garg and White, 2017). Owing to high resolution and rapid data acquisition, in situ X-ray scattering experiments and subsequent PDF analysis enable the tracking of time-dependent reaction kinetics and the nano-structural development of cementitious systems.

In this study, we assessed the effect of gypsum on the hydration behavior of blended systems, including (i) pure C_3S, (ii) C_3S with metakaolin, and (iii) C_3S with metakaolin and limestone. A synchrotron-based X-ray scattering method and PDF analysis were used to investigate the hydration behavior and structural

development of final gel products. The PDF evolution results showed that adding gypsum accelerated the reaction kinetics for all three systems. However, whereas the gypsum addition significantly accelerated the hydration of C_3S after ~7.5 h, the presence of metakaolin and limestone curtailed the acceleration effects of gypsum. Lastly, the evolution of T-O peaks at ~1.6 Å indicated that adding gypsum or limestone consumed aluminum and hindered the incorporation of aluminum in C-S-H gel.

2. Materials and Methods

2.1 Materials and Sample Preparation

Pure C_3S (TIII) was experimentally synthesized in the lab by mixing the stoichiometric proportion of $CaCO_3$ (Alfa Aesar, CAS No. 471-34-1) with fumed silica (SiO_2, Sigma Aldrich, CAS No. 112945-52-5) and calcining at 1600°C. Metakaolin was prepared by calcining the pure kaolinite (KGa-1b) at 900°C. Pure $CaCO_3$ powder was used as limestone. A total of six paste samples were analyzed: (i) pure C_3S, (ii) C_3S with metakaolin, and (iii) C_3S with metakaolin and limestone in the presence and absence of gypsum. For the blended samples, metakaolin replaced 35 wt.% of C_3S, and limestone replaced 15 wt.% of C_3S. For the samples with gypsum addition, gypsum replaced 3 wt.% of C_3S. The w/b ratios were 0.55 for the C_3S samples and 0.7 for the blended samples.

2.2 X-ray Scattering Experiment and Pair Distribution Function Analysis

High-energy X-ray total scattering experiments were performed on the beamline 11-ID-B at the Advanced Photon Source, Argonne National Laboratory. The energy of the X-ray was 58 keV, and the wavelength (λ) of the X-ray was 0.2112 Å. X-ray scattering data were collected for 3 min, and *in situ* data was obtained up to ~33 h. An amorphous silicon imaging plate (XRD 1621, Perkin-Elmer) was used to collect the X-ray scattering data. 2D data were converted to 1D via Fit2D program with CeO_2 as a calibration material. PDF (g(r)) was obtained via PDFgetX3 software. The maximum Q cutoff was 24 $Å^{-1}$.

3. Results and Discussion

3.1 PDF Results of C_3S and Blended Systems with and without Gypsum

PDF analysis has been an important characterization method to scrutinize the atomic ordering of materials. For example, *in situ* PDF enables the analysis of real-time nano-structural growth in cementitious materials. In this study, the effects of gypsum on pure C_3S and blended C_3S systems were investigated by comparing the structure development obtained via PDF analysis.

Fig. 1 (a, c, and e) depict the *in situ* PDF curves of the C_3S and blended systems with and without the addition of gypsum at 3.4 h and 32.8 h hydration. Based on previous studies, the atom-atom correlations in PDF patterns were assigned (Garg and White, 2017; Skinner et al., 2010). For all systems, the structures were similar at the early hour (3.4 h), indicating the effect of gypsum was minor. As the reaction progressed, the nano-structural differences increased. In particular, pure C_3S specimens showed significant structural differences in presence of gypsum. For example, a large difference in the T-O* peak centered at ~4.2 Å was observed, which is the second-nearest atom-atom correlation between tetrahedral atoms (Si, Al) and oxygen.

To further investigate the effect of gypsum on the reaction kinetics and structural development, the shift of the peak position of Ca-T atom-atom correlations (~3.4 Å) was analyzed, as plotted in Fig. 1 (b, d, and f). The Ca-T peak is the nearest Ca and tetrahedral Si/Al correlation within C-(A)-S-H gel structure (Garg and White, 2017). Thus, the evolution of the Ca-T peak can reflect the formation of the C-(A)-S-H gel. For the pure C_3S systems (Fig. 1 (b)), adding gypsum slightly decelerated the structural development at the early hour (~7.5 h). However, after ~7.5 h, the presence of gypsum significantly accelerated the hydration of C_3S. In the case of both C_3S blended with metakaolin and ternary systems (Fig. 1 (d, f)), the deceleration effect was not observed, and the hydration of both systems was accelerated with adding gypsum. However, the effect of gypsum was less prominent than the pure C_3S systems. These results

indicate the influence of gypsum on C_3S hydration is suppressed when metakaolin and limestone are added to the systems, and the gypsum mainly reacts with alumina sources in metakaolin.

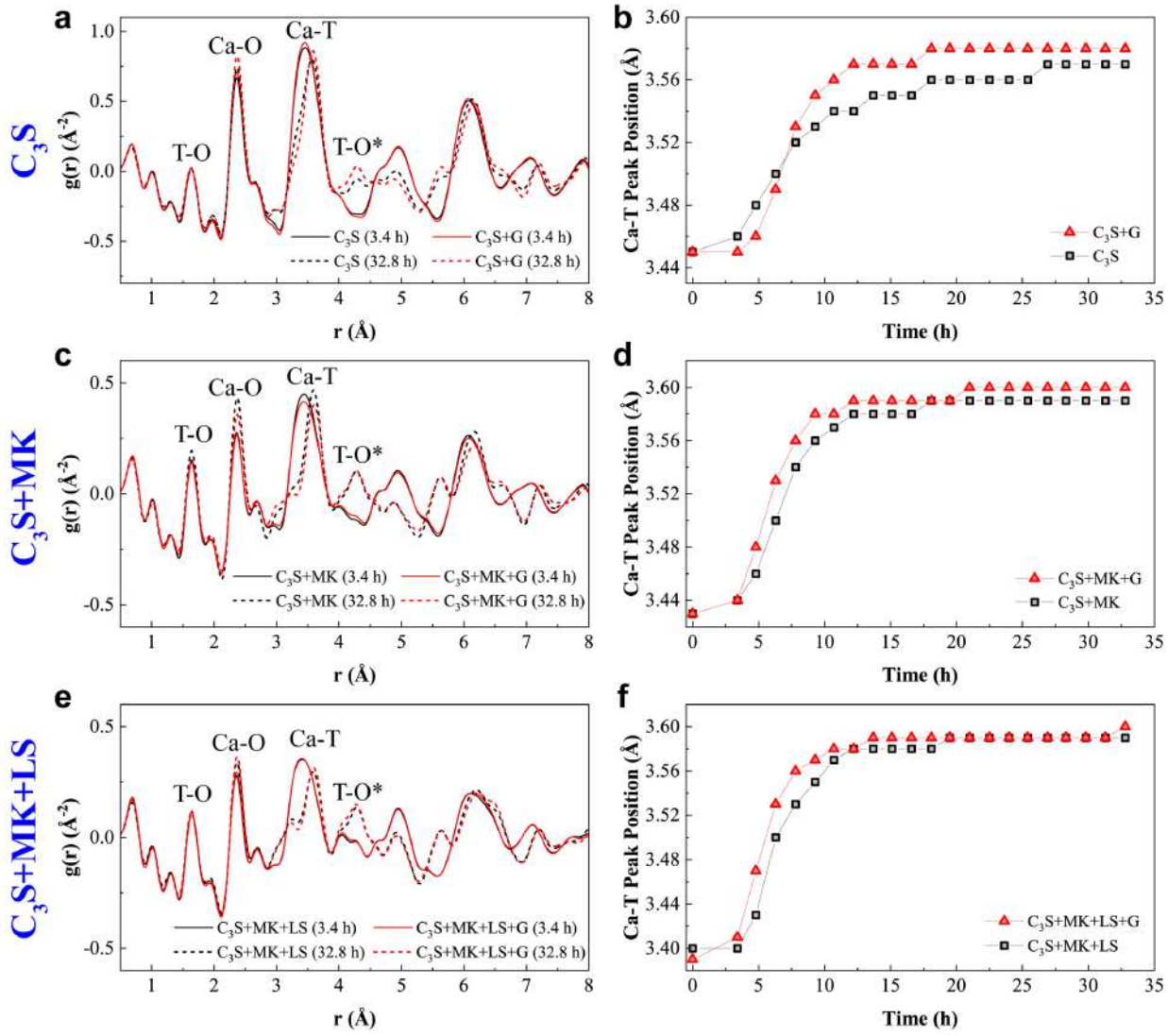


Figure 1. *In situ* X-ray pair distribution function results of (a) C_3S, (c) C_3S with metakaolin (MK), and (e) C_3S with metakaolin and limestone (LS), with and without gypsum (G) at ~3.4 h and ~ 32.8 h of hydration. The shift of Ca-T peak position of (b) C_3S, (d) C_3S with MK, and (f) C_3S with MK and LS, with and without gypsum. The symbol T indicates tetrahedral atoms such as Si and Al.

3.2 Aluminum Incorporation in C-S-H Gel Structure

Fig. 2 (a-d) shows the growth of the T-O peak located at ~1.6 Å in PDF curves of C_3S-metakaolin and ternary blended systems with and without gypsum. This evolution of the T-O peak intensities is depicted in Fig. 2 (e). A clear evolution of T-O peak intensity was observed in the blended C_3S-metakaolin system without gypsum as the reaction progressed. On the other hand, the T-O peak intensity remained similar when gypsum was added to the system. For the ternary blended systems, the T-O peak did not significantly evolve for both with and without gypsum.

Generally, the evolution of the T-O peak at ~1.6 Å in cementitious systems indicates the incorporation of aluminum in the C-S-H gel structure. Thus, the results indicate that in the C_3S-metakaolin system without gypsum, Al-incorporated C-(A)-S-H gel was formed. In contrast, Al was not incorporated into C-S-H gel in the other three systems due to the formation of other phases such as ettringite (AFt) or monocarboaluminate (Mc), as shown in Fig. 2 (f).

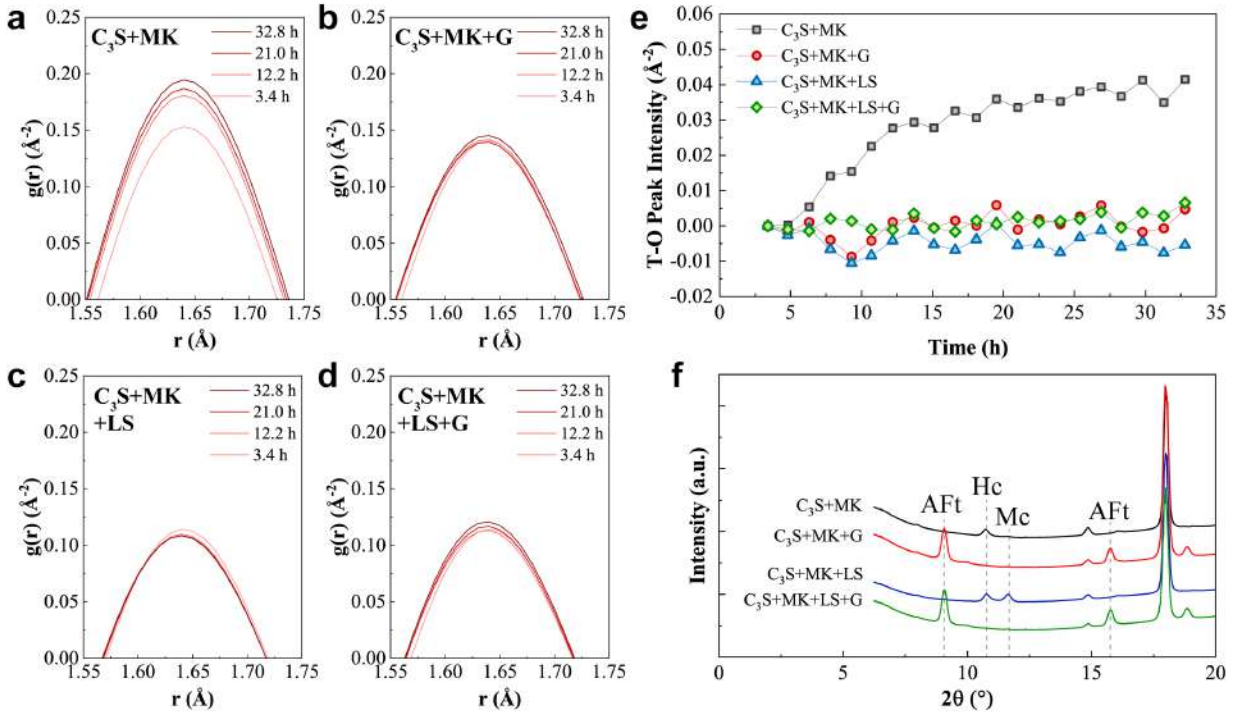


Figure 2. Evolution of T-O peak located at ~1.6 Å in pair distribution function analysis of (a) C_3S with metakaolin (MK), (b) C_3S with metakaolin and gypsum (G), (c) C_3S with metakaolin and limestone ($CaCO_3$), and (d) C_3S with metakaolin, limestone, and gypsum. (e) the evolution of T-O peak intensity and (f) X-ray diffraction pattern of the four blended systems. The symbol T indicates tetrahedral atoms such as Si and Al.

4. Conclusions

In this study, we investigated the influence of gypsum on the hydration of C_3S, C_3S-metakaolin, and ternary C_3S-metakaolin-limestone via *in situ* X-ray PDF analysis. Although the presence of gypsum slightly decelerated the early hydration of C_3S in pure C_3S systems, the clear acceleration effect was observed after ~7.5 h. On the other hand, the acceleration effect of gypsum on C_3S was less prominent in the blended systems. Moreover, adding gypsum and/or limestone in the C_3S-metakaolin systems impeded the Al incorporation in the C-S-H structure. Understanding the reaction mechanism of calcium silicate in blended systems is important to fully utilize sustainable construction materials such as LC^3. Thus, further investigation will be done by utilizing other characterization methods, such as isothermal calorimetry, to scrutinize the effect of gypsum on blended cementitious materials.

Acknowledgments

We are grateful for the assistance and guidance provided by 11-ID-B staff Dr. Tiffany Kinnibrugh. Use of the Advanced Photon Source at Argonne National Laboratory was supported by the U. S. Department of Energy, Office of Science, Office of Basic Energy Sciences, under Contract No. DE-AC02-06CH11357.

References

Garg, N. and White, C. E. (2017) "Mechanism of zinc oxide retardation in alkali-activated materials: an in situ X-ray pair distribution function investigation", *Journal of Materials Chemistry A*, 5(23): 11794-11804

Neto, J. S. A., Rodríguez, E. D., Monteiro, P. J., Angeles, G., and Kirchheim, A. P. (2022) "Hydration of C_3S and Al-doped C_3S in the presence of gypsum", *Cement and Concrete Research*, 152: 106686

Sharma, M., Bishnoi, S., Martirena, F., and Scrivener, K. (2021) "Limestone calcined clay cement and concrete: A state-of-the-art review", *Cement and Concrete Research*, 149: 106564

Skinner, L. B., Chae, S. R., Benmore, C. J., Wenk, H. R., and Monteiro, P. J. M. (2010) "Nanostructure of calcium silicate hydrates in cements", *Physical review letters*, 104(19): 195502

The 16th International Congress on the Chemistry of Cement 2023 (ICCC2023)
"Further Reduction of CO_2 -Emissions and Circularity in the Cement and Concrete Industry"
September 18–22, 2023, Bangkok, Thailand

Hydration of CAC pastes at high temperature

A. Pachón-Montaño[1*], M.M Alonso-López[1], S. Chhaiba[1], Q.B Marzal-García[1], J.A Jimenez[2], I. Llorente[2] and M.T Blanco-Varela[1]

[1] *CSIC. Eduardo Torroja Institute for Construction Science (IETcc-CSIC), Madrid, Spain*
Email: apachon@ietcc.csic.es
[2] *CSIC, National Center for Metallurgical Research (CENIM-CSIC), Madrid, Spain*
Email:jimenez@cenim.csic.es

ABSTRACT

Calcium aluminate cements or CACs are of great interest in a wide range of areas, such as industrial applications, waste encapsulation and even restoration of heritage sites. The hydration products of CAC are known to vary as a function of temperature and humidity conditions. In this study, the hydration process of a CAC cured at 70°C under high humidity conditions and different water/cement ratios has been investigated. The aim of using these conditions was to directly obtain katoite-type cubic hydrates, together with the development of gibbsite. The different water/cement ratios used have given rise to different proportions of crystalline and amorphous hydrated phases. The percentages of hydration products formed have been identified and quantified in relation to the mechanical strength and porosity of the pastes at different curing ages. The stability of the pastes subjected to two curing conditions, under water and in laboratory conditions, for 2 years, has also been studied.

KEYWORDS: *Calcium aluminate cement, hydration, high curing temperature*

1. Introduction

Calcium aluminate cement has different application such as industrial uses, waste encapsulation and even restoration of heritage sites (De Gasparo et al., 2009; Sang & Liu, 2010; Maier. S, 2009). Mixes of CAC and water develop different phases depending on the temperature and humidity at which this cement hydrated. When hydration takes place at low and moderate temperatures, the metastable hexagonal hydrates CAH_{10}, C_2AH_8 and AH_3 are formed, as shown in reactions (1-2), whereas when hydration takes place at a temperature above 45ºC the cubic stable phases such as C_3AH_6 and AH_3 are formed, as shown in reaction (3). (Scrivener, K, 2004; Glasser F. P, 1992).

$$CA + 10H \rightarrow CAH_{10} \quad (1)$$
$$2CA + 11H \rightarrow C_2AH_8 + AH_3 \quad (2)$$
$$3CA + 12H \rightarrow C_3AH_6 + 2AH_3 \quad (3)$$

Under certain conditions of high humidity, hexagonal metastable hydrates are transformed over time into stable cubic hydrates, with a consequent reduction in volume and decrease in mechanical strength (Scrivener, K, 2004). One way to avoid such transformation and its undesirable consequences is the direct formation of cubic stable reaction products by hydrating at 50-70ºC and using low w/c ratios.
Most studies about hydration of CAC pastes, focus on the formation of its phases at room temperature or at high temperatures with long curing times (Rivas Mercury, J. M, 2006), but if the curing time at high temperature is short and the reached degree of hydration is not complete, the evolution of mineralogy and mechanical strengths of such a pastes is not clear. This work studies the influence of w/c ratio and hydration time on the mineralogical composition and mechanical behaviour of CAC pastes hydrated at

70ºC for only one hour and them at 22ºC and RH 30% until 28 days. The pastes were characterised by means of XRD, mercury intrusion porosimetry and DTA-TG, determining the role that the different phases play in the development of the mechanical strengths from 0 to 28 days.

2. Methodology

In this study one CAC was used whose chemical characterisation is shown in Table 1.

Table 1. wt% Chemical composition of CAC.

	K_2O	SiO_2	Al_2O_3	MgO	Fe_2O_3	CaO	P_2O_5	TiO_2	MnO	LOI
CAC	0.09	4.40	37.90	0.76	14.93	39.10	0.15	1.80	0.19	0.68

Througth XRD, main phases identified were CA, brownmillerite, maghemite, larnite, ghelenite and perouvskite.
Specimens of size 3x3x3cm^3 of CAC pastes with three different water/cement ratio of 0.21, 0.30 and 0.40 were elaborated. Initial curing, was carried out at a temperature of 70°C for one hour and therefore another hour in a humidity chamber at a temperature of 30°C and 90% R.H. Afterwards, the specimens were cured at room temperature with an average temperature of 22ºC and 30% R.H until testing age (3 hours and 28 days). At these ages, hydration was stopped and compressive strength values were obtained under the conditions described in EN-197-1. Pastes were characterised by different techniques such as X-ray diffraction (XRD) with Rietveld refinement, and mercury intrusion porosimetry (MIP). DTA-TG was also carried out with a temperature ramp between 25 and 1000°C at a rate of 10°C/min and with an N_2 atmosphere of 100 ml/min. Moreover, additional specimens of 1x1x6 cm^3 with a water/cement ratio of 0.21 were also prepared. Half of these specimens were left uncovered and half specimen remained under water for 2 years. Hydration was stopped and the pastes were characterised.

3. Results and discussion

Table 2 shows the compressive strength and total porosity values for CAC pastes at 3hours and 28 days of curing in all water/cement ratios studied. Pastes have high mechanical strengths just after curing at 70ºC for one hour. However, as the w/c ratio increases, these resistances at 3h decrease due to the expected increase in porosity (Mehta, P, 2005).

Table 2. Mechanical compressive strength and total porosity values.

Sample	w/c	Compressive strength (MPa)		Total porosity (% vol)	
		3h	28 d	3h	28 d
Sample 1	0.21	49	74	13	12
Sample 2	0.30	34	56	18	18
Sample 3	0.40	17	32	28	27

In turn, after 28 days of curing the resistance of the samples increase by 57%, 63% and 87% for samples 1, 2 and 3 respectively, being these increases accompanied by no consequent reduction in porosity, which remains practically constant.

The main mass losses in the TG curves of the pastes were recorded between 200ºC and 600ºC, the temperature range in which both katoite and gibbsite lose their constituent water (Scrivner, K, 2016). Table 3 shows the gibbsite and katoite content calculated, from the mass losses between 200 and 600ºC. The amount of hydrates increases both with the curing time and with the w/c ratio.

Through the XRD results, two types of cubic hydrates (katoite/katoite grossular) as well as gibbsite (Figure 1) and to a lesser extent strätlingite (Aranda, M, 2021) were identified as main reaction products in pastes just after the thermal treatment (Figure 1a). At 28d of hydration, the identified phases are the same as at 3h, and no hexagonal hydrates were identified, (Figure 1b). These results indicate that the increase of compressive strength is due to hydration of remaining anhydrous CAC with formation of

crystalline katoite/grosular, gibbsite and strätlingite while no hexagonal hydrates are formed during the said 28 days.

Table 3. wt% of main phases by DTA-TG.

	w/c=0.21		w/c=0.30		w/c=0.40	
	3h	28 days	3h	28 days	3h	28 days
Katoite	25.80	26.32	28.10	29.01	30.17	31.24
Gibbsite	21.27	21.70	23.17	23.92	24.88	25.76
Total hydrates	47.07	48.02	51.27	52.93	55.05	57.00

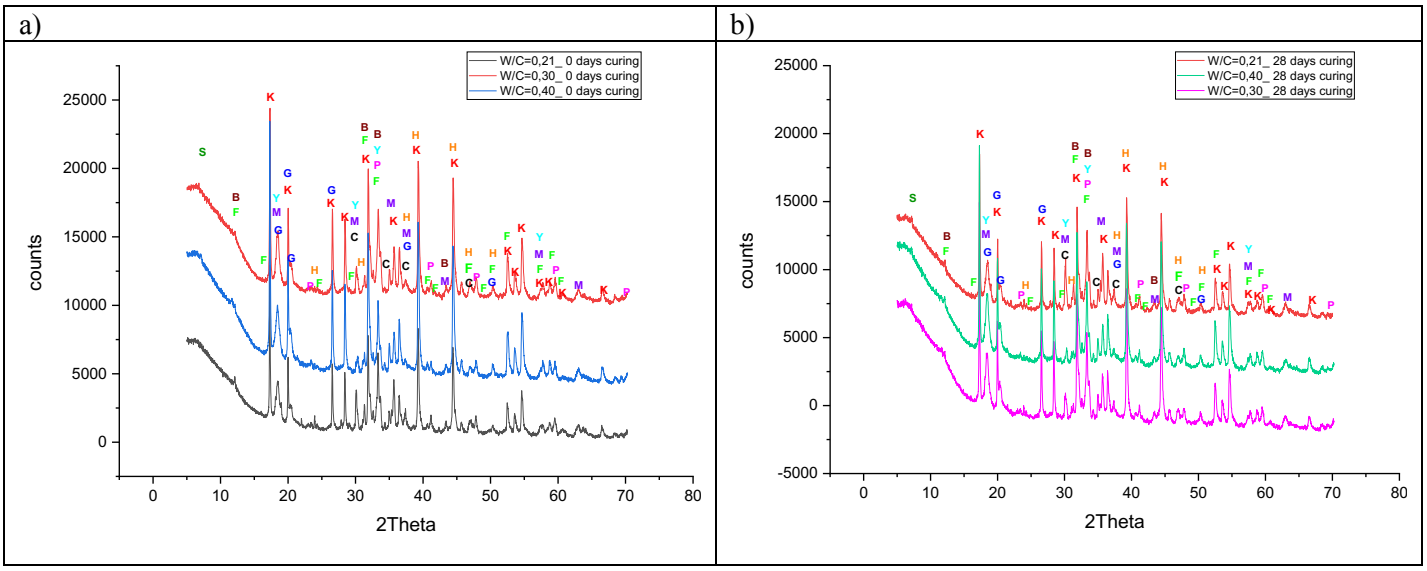


Figure 1. X-ray spectra of the samples 1, 2 and 3 tested at a) 3 hours and b) 28 days with identified phases. (C=CA; K=Katoite (C_3AH_6)/Grossular($Al_2Ca_3H_{10,96}O_{12}Si_{0,26}$); G=Gibbsite ($AH_3$), F= C_4AF, P=Perouvskite ($CaTiO_4$), M=Mahemite (Fe_2O_3), H=Ghelenite, Y= Mayenite ($Al_{14}Ca_{12}O_{33}$, B=Brownmillerite ($AlCa_2FeO_5$) and S=Strätlingite (C_2ASH_8)($Ca_2Al_2*SiO_7*8H_2O$/$2CaO*Al_20_3*SiO_2*8H_20$))

Using X-ray diffraction and Rietveld refinement (Table 3), a lower proportion of crystalline gibbsite is obtained than that calculated by DTA-TG and lower than expected if hydration were to occur throughout equation (3). However, the proportion of cubic hydrates (katoite and katoita-grossular), determined by both methods were similar. These results would indicate that a large part of the gibbsite is amorphous or has very low crystallinity. Increases in the amorphous gibbsite content with time would also justify the increase~~s~~ of mechanical strengths.

Table 3. wt% of gibbsite by XRD Rietveld refinement.

	w/c=0.21		w/c=0.30		w/c=0.40	
	3h	28 days	3h	28 days	3h	28 days
Gibbsite	7.2	10.5	9.2	10.6	10.9	10.8

Figure 2 shows the XRD of both samples prepared with the mentioned thermal treatment and cured for 2 years, one in open air (22ºC and RH 30%) and the other underwater. A remarkable result is that in both samples no hexagonal phases were identified, which implies that the initial curing has promoted that the phases developed over time and despite the presence of water were stable cubic phases and therefore the hydrated mixture presents a great stability over time.

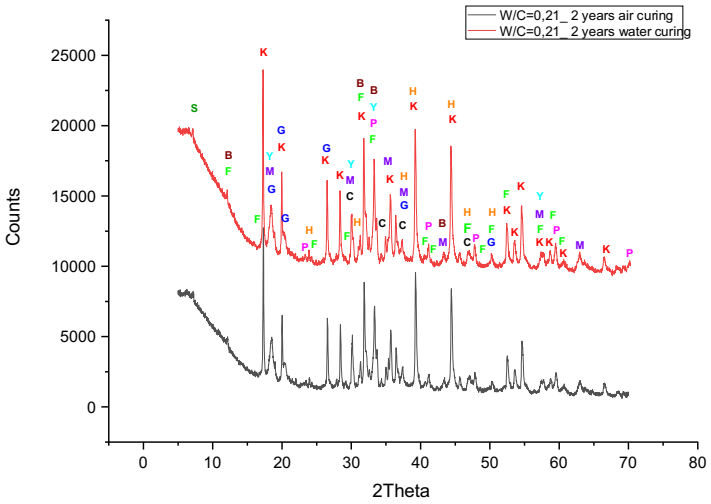


Figura 2. X-ray spectra of the samples curing under water and uncovered for two years.

3. Conclusions

The mechanical strengths of CAC pastes increase with the curing time. However, as the water/cement ratio increase, the mechanical strengths decrease and the porosity of samples increase. Preliminary results show that the gibbsite (crystalline and amorphous) and katoite increase both with the curing time and with the w/c ratio, justifying the increase of mechanical strengths of samples from 3h to 28d. Hexagonal phases were not identified, which implies that the initial curing at 70ºC has promoted the direct later formation of katoite and gibbsite during hydration of remaining CAC at 22ºC.

Acknowledgements:

The authors wish to thank the support of Project PID2020-116002RB-100/AEI/10.13039/501100011033 (HORRADIONEX)

References

Aranda, M., De la Torre, A., & Leon-Reina, L. (2012). "Rietveld Quantitative Phase Analysis of OPC Clinkers, Cements and Hydration Products". Reviews in Mineralogy and Geochemistry, 74, 169-209.

De Gasparo, A., Herwegh, M., Zurbriggen, R., & Scrivener, K. (2009). Quantitative distribution patterns of additives in self-leveling flooring compounds (underlayments) as function of application, formulation and climatic conditions. *Cement and Concrete Research*, *39*(4), 313-323.

Glasser F. P. and Jappy T. G. "Phase and density changes during the "conversión" reaction of high alumina cement ". *Materiales de Construcción*. Vol. 42, n.° 228, octubre/noviembre/diciembre 1992.

Maier, S. *"Ternary system: Calcium Aluminate cement-Portland cement-Gypsum"* Proceedings Calcium Aluminate Cements: Centenary Conference Avignon (2008).

Mehta, P., & Monteiro, P. J. M. (2005). *Concrete: Microstructure, Properties, and Materials*. McGraw-Hill Education.

Pachón-Montaño, A., Alonso-López, M. del M., Chhaiba, S., Marzal-García, Q. B., Jimenez, J. A., Llorente, I., and Blanco-Varela, M. T. Evolution of calcium aluminate cement hydration phases after high temperature of curing. "*In preparation*".

KYONO, Atsushi, y Shubhi ARORA. 2019. «Crystal structure change in grossular–Si–free katoite solid solution: Oxygen position splitting in katoite». *Journal of Mineralogical and Petrological Sciences* 114(4): 189-200.

Rivas Mercury, J. M., Turrillas, X., de Aza, A. H., and Pena, P. (2006). "Calcium aluminates hydration in presence of amorphous SiO2 at temperatures below 90°C". Journal of Solid State Chemistry, 179(10), 2988-2997.

Sang, G. C., & Liu, J. P. (2010). Study of properties of Portland and aluminate cementitious composited grouting material. *Materials Research Innovations*, *14*(3), 200-205.

Scrivener, K., Capmas, A. "Lea's Chemistry of cement and concrete" Ed. Elsevier Science & Technology Books, chapter "Calcium aluminate cements" pag. 713-782 (2004).

Scrivner, K., Snellings, R., & Lothenbach, B. "A Practical Guide to Microstructural Analysis of Cementitious Materials" CRC Press; 1er edición (2016).

The 16th International Congress on the Chemistry of Cement 2023 (ICCC2023)
"Further Reduction of CO_2 -Emissions and Circularity in the Cement and Concrete Industry"
September 18–22, 2023, Bangkok, Thailand

A Combined Calorimetry and XRD Study of The First 15 Minutes of Portland Cement Hydration

Tobias Lange[1], Daniel Axthammer[1], Daniel Jansen[2] and Torben Gädt[1*]

[1] *Chair Chemistry of Construction Materials, School of Natural Sciences, Technical University of Munich, Garching, Germany*
Email: torben.gaedt@tum.de
[2] *Chair of Mineralogy, Department of Geography and Geosciences, Friedrich-Alexander-Universität, 91054 Erlangen, Germany*
Email: sdjans@fau.de

ABSTRACT

Isothermal heat flow calorimetry is a powerful method to study the kinetics of Portland cement hydration. Most calorimetric studies are based on external mixing of water and binder to form a paste followed by insertion into the calorimeter after at least 5 – 10 minutes. To include the first minutes of cement reaction, we evaluate three different purpose-built mixing devices which allow mixing of a cement paste inside the calorimeter. In particular, we determine the heat flow due to the initial hydration reactions, the thermal inertia of the mixing device and estimate the thermal contribution of the mixing process due to viscous dissipation. Finally, we combine the calorimetry data for the first 15 minutes with an in-situ QXRD phase analysis of the cement paste. Based on the changes in phase composition, we calculate the expected heat development. We show that the best prediction of the experimental heat is achieved if only the heat corresponding to the observed ettringite quantity and the dissolution of the sulfate compounds is considered.

KEYWORDS: ***C****alorimetry, In-situ, Heat of hydration, Ettringite, C_3A*

1. Introduction

Experimental data for the first 15 minutes of the reaction of ordinary Portland cement (OPC) with water is surprisingly scarce. The reaction of OPC usually has a duration of months (if not years) to reach full conversion and is generally referred to as hydration. It is generally accepted that hydration is driven by simultaneous dissolution of cement clinker and calcium sulfate phases on the one hand and precipitation of hydrate phases on the other hand. The two most important reactions in the first hours of cement hydration are the formation of ettringite from C_3A and calcium sulfate (equation (1)) and the formation of CSH and CH from C_3S (equation (2)).

$$C_3A + C\bar{S} + 32\,H \longrightarrow C_6A\bar{S}_3H_{32} \quad (1)$$

$$C_3S + 5.3\,H_2O \longrightarrow C_{1.7}SH_4 + 1.3\,CH \quad (2)$$

Common methods to study cement hydration are quantitative x-ray diffraction (QXRD), thermogravimetry (TGA), chemical shrinkage (CS), heat flow calorimetry or infrared spectroscopy (IR). In general, all these methods have in common the necessity to mix a suspension from a solid precursor (i.e., cement) and water prior to mounting the sample on the analytical instrument. The mixing step intrinsically creates an initial dead time that bars the experimenter from observing the initial reaction, i.e., at least the first 5 minutes of cement hydration are missing.

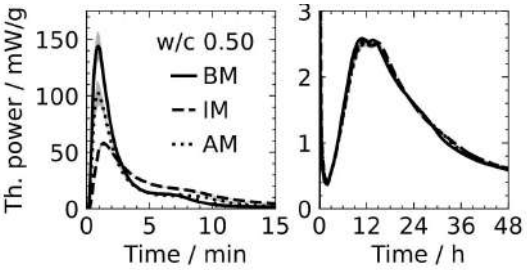
This initial dead time due to mixing is often not considered to be a major problem as the initial state of the reacting cement paste can be accurately determined (by Rietveld refinement of the dry cement) and lab methods such as QXRD have a minimum temporal resolution of a few minutes anyway. If, however, the details of the initial reactions are to be resolved analytically at a resolution on the order of seconds, experimental techniques which allow the mixing of a suspension while simultaneously being able to record meaningful analytical data are required. Here, a suitable method is (isothermal) calorimetry equipped with an in-situ mixing device (Wadsö, 2005). Heat flow calorimetry captures the sum of the heat associated to all underlying reactions and can be combined with in-situ XRD data. If the temporal phase development of clinker and hydrate phases has been obtained from QXRD, it becomes possible to calculate the corresponding reaction heat (using thermodynamic data available via the CEMDATA database)(Lothenbach et al., 2019). A comparison between calculated heat (from QXRD) and experimentally observed heat (from calorimetry) then allows the assignment of the heat flow events to the underlying reactions. While a number of combined QXRD and calorimetry studies are available, the first stage of cement hydration, i.e., the reactions happening during the first minutes, has not been mechanistically interpreted based on the combined data.
To accurately determine the initial heat, we evaluate three in-situ mixers. Two mixers were custom-built types and are compared to the commercial mixer manufactured by the instrument supplier. To separate the heat associated to the chemical reactions in the first 15 minutes from the total signal, we also determined the heat associated with mechanical friction and viscous dissipation.
Finally, we combine the initial heat flow data with in-situ XRD data obtained from Rietveld refinement. In summary, we address the following questions: 1. How do different mixers affect the heat flow in the first 15 minutes (and beyond)? 2. What is the contribution of a) mechanical heat due to friction and viscous dissipation and b) chemical hydration heat? 3. Which chemical reactions are responsible for the initial reaction heat?

2. Materials and Methods

The cement pastes were prepared using a commercial Portland cement CEM I 42.5 R (d_{50} = 16.0 µm, d_{90} =45.8 µm, Blaine specific surface of 3650 cm^2g^{-1}, phase composition via Rietveld refinement: 50.8% C_3S, 22.0% C_2S, 10.6% C_3A, 7.3% C_4AF, 1.0% Anhydrite, 2.9% Hemihydrate) and deionized water. The cement was stored in tightly sealed screw-cap bottles with a minimum air volume and stored in a desiccator over silica gel under a small vacuum. For calorimetry experiments with inert solids, cement was substituted by a fine quartz powder (d_{50} = 12.1 µm, d_{90} = 37.6 µm).
Three different in-situ mixers were used: a device available from the manufacturer of the calorimeter(TA instruments) under the name Admix ampoule stirrer (AM), a custom mixer developed at the University of Erlangen called InMixEr (IM)(Hertel et al., 2016), and a custom mixer with three rotating paddles in a planetary configuration, Bohr-O-Mir 4000 (BM) available from Technisch Zeichnen Grassl (Berchtesgaden). For pastes, 4.0000g ± 0.0005g of cement and for inert samples 3.3650g ± 0.0005g of quartz powder were weighed into sample vials and the required water amount (w/c dependent) was dosed from syringes after thermal equilibration overnight. The calibration factor for each setup was determined using a heating resistor. To correct the experimentally recorded thermal power of the initial rapid cement reaction for the inertia of the calorimeter, the Tian correction was employed(Wadsö, 2010). Additionally, we carried out an estimation of the mixing energy by mixing inert quartz suspensions at the same volume fraction compared to cement pastes.
X-Ray diffraction was performed with a Bruker D8 Advance diffractometer in Bragg-Brentano geometry, equipped with a Cu-source, which was operated at 40mA and 40kV. The phase quantification was performed by Rietveld refinement (TOPAS 5.0, Bruker AXS) and the external standard approach.

3. Results and Discussion

A German CEM I 42.5 R Portland cement was mixed with water in the calorimeter (w/c=0.5, 0.4 and 0.3) using three different mixing systems. The Tian corrected data obtained at w/c 0.5 for the different mixers is shown in Figure 1. No significant differences between the mixing setups are found for the C_3S reaction. For the first 15 minutes however, the observed differences indicate both the variation in



mixing energy (the BM mixer shows the largest heat flow) or different qualities of the Tian correction (in the case of the IM mixer).

Figure 1: Heat flow data for three different in-situ mixers at w/c 0.5. The characteristic instrument constants were: AM mixer, calibration factor ε=1.088, time constant τ = 329 s, mixing energy pure quartz suspension at highest volume fraction 51.4% Q_{SiO2}=1.4 J; IM mixer, ε=1.138, τ = 421 s, Q_{SiO2}=3.0 J; BM mixer ε=1.059, τ = 329 s, Q_{SiO2}=7.1 J.

It is noteworthy, that the initial reaction only lasts for less than 5 minutes. To clarify the influence of the w/c value on the heat flow, we mixed cement pastes at w/c 0.4 and 0.3 (with the AM mixer). The data is shown in Figure 2 together with the heat flow data of corresponding inert quartz suspensions with identical volume fractions. Clearly, the heat flow of the cement pastes is an order of magnitude larger than the heat flow for the inert suspensions. The heat in the inert suspensions is mostly due to viscous dissipation during mixing and partly due to the heat of wetting the quartz surface. For cement pastes, we inspected all vials after the calorimetric measurement to visually assess mixing homogeneity. All mixers produced visually homogeneous pastes at w/z 0.5 and 0.4 (flat surfaces) and all pastes at 0.3 were stuck to the walls of the vials due to the high yield stress (data not shown here).

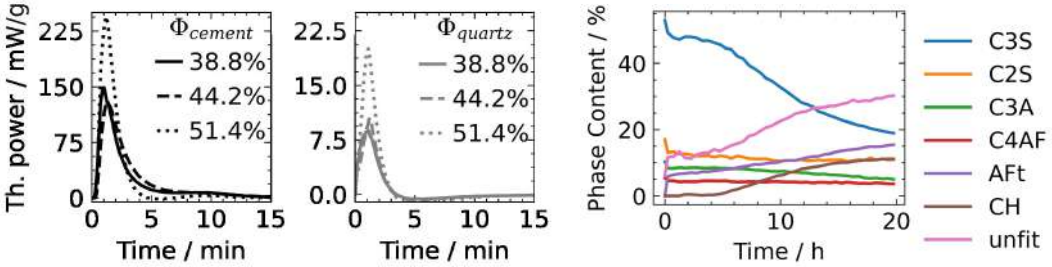


Figure 2, left: in-situ heat flow data AM mixer at w/c 0.5, 0.4 and 0.3 (ϕ=38.8%, 44.2% and 51.4%). Middle: heat flow data obtained by mixing a fine quartz suspension at identical volume fractions. Right: QXRD Rietveld data for the phase composition of the reacting cement paste.

The chemical heat Q^*_{15min} after the first 15 minutes of reaction is very similar for the three mixers and ranges between 18.9 and 20.4 Jg^{-1} (Table 1). Averaging over the three mixers yields a heat of 19.8 Jg^{-1} ± 0.6 Jg^{-1} after 15 minutes.

Table 1: Total heat Q after 1 and 15 min and after 48 h including the standard deviation in parentheses. Additionally Q^*_{15min} gives the chemical heat after correction for the mechanical heat due to mixing.

	Q_{1min} / Jg^{-1}	Q_{15min} / Jg^{-1}	Q^*_{15min} / Jg^{-1}	Q_{48h} / Jg^{-1}
BM	6.4 (0.0)	20.7 (0.3)	18.9 (0.4)	257.1 (0.2)
IM	2.1 (0.1)	20.9 (0.2)	20.2 (1.0)	266.2 (1.7)
AM	5.0 (1.0)	20.7 (0.2)	20.4 (0.3)	268.6 (12.5)

In order to ascribe the observed heat after 15 minutes to the different chemical processes happening in that period, we combine the phase composition obtained from Rietveld refinement of the dry cement with in-situ XRD data. To calculate the heat from the changes in phase composition obtained by this combination of QXRD data, we sum over the known reactions linked to the respective phases (e.g., ettringite formation from C_3A, anhydrite and water, etc. Details not shown here for brevity). When we consider the QXRD degrees of hydration of the silicate (C_3S and C_2S), aluminate (C_3A and C_4AF) and sulfate phases (Gypsum, Hemihydrate, Anhydrite and Arcanite), we obtain a resulting heat of −40.5 Jg^{-1} after 15 min. This value is twice as large as the experimentally observed value of −19.8 Jg^{-1}. Since it is safe to assume (given our results and commonly assumed errors during Rietveld refinement) that the calorimetric data has a significantly smaller experimental error than the Rietveld quantification and the

corresponding calculated heat, we focus our discussion on explanations for the difference and possible error sources of the heat calculation from QXRD data. In terms of the individual heat contributions from the different ongoing reactions, the largest fractions are due to the C_3A hydration to ettringite ($-17.3\ Jg^{-1}$), and the C_3S hydration to portlandite and C-S-H which amounts to $-17\ Jg^{-1}$ for the observed C_3S reduction. However, the observed drop in C_3S and C_2S is most likely an artifact of the QXRD method. Using in-situ calorimetry on pure C_3S, Bergold et al. found $2.7\ Jg^{-1} \pm 1.0\ Jg^{-1}$ for C_3S at a w/s = 1 after 15 minutes.(Bergold et al., 2015) We repeated this experiment with pure C_3S and found $1.7\ Jg^{-1}$ (after correction for viscous dissipation).

In search of an alternative approach to explain the measured heat, we recalculate the heat based on the reduction of the C_3A phase and the sulfate phases alone. This leads to a heat of $-26.4\ Jg^{-1}$, which is still about 33% higher than the measured value. However, there is evidence in the literature that C_3A dissolves in an incongruent fashion (Myers et al., 2017). Therefore, we argue that the reduction of C_3A observed via QXRD is comprised of two components: a) partial dissolution of C_3A which releases calcium and aluminate into solution and b) partial amorphization of the crystalline C_3A due to incongruent dissolution. Therefore, we recalculate the heat by only considering the dissolution of alkali sulfates and the hydration of the fraction of C_3A which corresponds to the observed ettringite amount and neglect the residual C_3A loss, effectively assuming that partial amorphization is significantly less exothermic.

$$\Delta H_{calc} = m'_{\mathrm{AFt}} \cdot \Delta H^{\circ}_{(\mathrm{C_3A\ +\ 3\,C\bar{S}\ +\ 32\,H\ \longrightarrow\ AFt})} + m_{\mathrm{K\bar{S}}} \cdot \Delta H^{\circ}_{\mathrm{K\bar{S}\ \longrightarrow\ K_{aq}\ +\ \bar{S}_{aq}}}$$

The resulting recalculated heat amounts to $-20.1\ Jg^{-1}$, which matches the detected amount of heat ($-19.8\ Jg^{-1} \pm 0.6\ Jg^{-1}$) very well.

4. Conclusions

The evaluated in-situ mixing setups yield very comparable values for the initial chemical heat production from the hydration of the chosen cement of approx. $20\ Jg^{-1}$. The measured thermal power was reproducible for repeated experiments with the same type of mixer and for different mixing devices. In order to explain the chemical contributions to the observed heat of the initial reaction, we investigated the phase changes by in-situ QXRD and calculated the corresponding heat from thermodynamic data. The results showed that the total heat calculated from the in-situ QXRD phase data is approximately twice as large as the experimentally observed heat. However, considering only the dissolution of the sulfate carriers, the ettringite crystallization and the amount of C_3A dissolution necessary for the experimentally observed ettringite amount, good agreement between XRD and calorimetry data is achieved. The exact reasons for the intensity loss for crystalline C_3S, C_2S and also partially C_3A as detected via XRD will need to be studied in the future.

References

Bergold, S. T., Goetz-Neunhoeffer, F., & Neubauer, J. (2015). Mechanically activated alite: New insights into alite hydration. *Cement and Concrete Research*, *76*, 202–211.

Hertel, T., Neubauer, J., & Goetz-Neunhoeffer, F. (2016). Study of Hydration Potential and Kinetics of the Ferrite Phase in Iron-Rich CAC. *Cement and Concrete Research*, *83*, 79–85.

Lothenbach, B., Kulik, D. A., Matschei, T., Balonis, M., Baquerizo, L., Dilnesa, B., Miron, G. D., & Myers, R. J. (2019). Cemdata18: A chemical thermodynamic database for hydrated Portland cements and alkali-activated materials. *Cement and Concrete Research*, *115*, 472–506.

Myers, R. J., Geng, G., Rodriguez, E. D., da Rosa, P., Kirchheim, A. P., & Monteiro, P. J. (2017). Solution chemistry of cubic and orthorhombic tricalcium aluminate hydration. *Cement and Concrete Research*, *100*, 176–185.

Wadsö, L. (2005). Applications of an eight-channel isothermal conduction calorimeter for cement hydration studies. *Cement international*, *5*, 94–101.

The 16th International Congress on the Chemistry of Cement 2023 (ICCC2023)
"Further Reduction of CO_2 -Emissions and Circularity in the Cement and Concrete Industry"
September 18–22, 2023, Bangkok, Thailand

Comparative study of the hydration kinetics of oil well cement and model cement retarded by tartaric acid at elevated temperatures

Fang Sun[1], Xueyu Pang[1,2*], Jing Zeng[1], Shenglai Guo[1,2]

[1] *School of Petroleum Engineering, China University of Petroleum (East China), Qingdao 266580, PR China*

Email: x.pang@upc.edu.cn

[2] *Key Laboratory of Unconventional Oil & Gas Development (China University of Petroleum (East China)), Ministry of Education, Qingdao 266580, PR China*

Email: x.pang@upc.edu.cn

ABSTRACT

Tartaric acid is commonly used as set retarder for cementing in wells at elevated temperature conditions. However, adding tartaric acid to cement slurry often cause abnormal gelation (premature setting) such that there is an increase in viscosity of cement slurry but no increase in compressive strength. To elucidate the reason of the abnormal gelation caused by tartaric acid, we investigated the hydration kinetics of oil well cement and model cement (consists of alite and belite) retarded by tartaric acid using isothermal calorimetry (IC) method in the elevated temperature range from 60 °C to 89 °C. Results show that, high dosages of tartaric acid change the typical shape of the oil well cement hydration heat flow curve fundamentally: two additional exothermic peaks appear before the main hydration peak. The appearance of the first peak in heat flow curves was found to be able to lead to premature setting. Meanwhile, a polyphase clinker composed of alite and belite was prepared and its hydration kinetics was compared with that of oil well cement in the presence of tartaric acid. The shape of the heat flow curve of this polyphase clinker without aluminate and ferrite phases was not changed by tartaric acid under the same test condition, suggesting that the two additional exothermic peaks were all related to the hydration of aluminate and ferrite phases. In addition, it was found that the second peak observed in this study was the sulfate-depletion peak commonly occurring after the main hydration peak, which can be depressed and eliminated by adding gypsum to the oil well cement slurry containing tartaric acid.

KEYWORDS: *hydration kinetics, isothermal calorimetry, premature setting, tartaric acid*

1. Introduction

Oil well cementing is one of the most important procedures performed during the drilling and completion of oil and gas wells (Pang, Cuello Jimenez, et al (2013)). During cementing, the prepared cement slurry is injected into the wellbore annulus between the steel casing and the wellbore to form a cement sheath. The cement sheath with mechanical strength can ensure zonal isolation and prevent the migration of fluid between different formations, as well as stabilizing and securing the casing in the wellbore. The evolution of the engineering properties of oil well cement, including rheology, fluid loss and setting time, is highly related to the continuous hydration of cement (Lu et al (2020)). In order to regulate the setting time of the cement, adding retarders to cement slurry is commonly applied in cementing, which can retard the hydration of cement slurry for prolonging the pumpable time until cement slurry is placed in a desired portion of wells (Pang et al (2014)). Tartaric acid is a hydroxy carboxylic acid and traditionally used as a retarder for the hydration of Portland cement (Bishop and Barron (2006); Cheung et al (2011)). However, premature setting often happens for cement slurries retarded by tartaric acid when the slurry is placed in a certain temperature range (≤93 °C) (Rodrigues (1995)). Premature setting causes the consistency of the cement slurry to increase without increases in compressive strength. Hence, it is worthwhile to fully investigate the reason

why tartaric acid can cause permature setting and elucidate the mechanism behind this abnormal phenomenon for the safety during cementing operations.

Portland cement is composed of multiple different phases, and its hydration is a complex process due to the interaction between different phases, even more so at elevated temperatures (Pang et al (2021)). Model cement with controlled composition has been widely used to simplify the study of cement hydration (Bergold et al (2017); Quennoz and Scrivener (2013)). In this paper, in the elevated temperature range from 60 to 89 °C, the abnormal gelation during the viscosity/consistency evolution of cement slurries containing tartaric acid before setting was continuously monitored by using an atmospheric consistometer. In addition, the hydration processes of these cement slurries and a ployphase clinker composed of alite and belite were also studied comparatively by using the isothermal calorimetry method. Finally, the mechnisam related to premature setting was explained from the view of cement hydration kinetics.

2. Experimental materials and methods

An API Class G cement provided by Jiahua Special Cement Co., Ltd. was used in this study. A polyphase composed of alite and belite was synthesized by sintering a compacted powder of calcium carbonate, silica fume, nano-alumina, magnesium oxide and boric acid at 1450 °C. The phase compositions, determined by quantitative X-ray diffraction analysis, of the cement and the polyphase are displayed in Table 1. The median particle size of the cement and the polyphase are 14.9 μm and 5.8 μm, respectively.

Table 1 Phase compositions (by mass of percentage) of the Class G cement and the synthesized polyphase

Phases	C_3S	C_2S	C_3A	C_4AF	Gypsum	Hemihydrate	Anhydrite	Periclase	Calcite
Cement	48.9	28.7	2.4	13.0	2.7	1.7	0.5	1.1	0.9
Polyphase	66.5	33.5							

Cement slurries with a water-to-cement ratio (w/c) of 0.4 were prepared according to standard API tests (API RP 10B, 2013), which is an optimized design from our previous study (Pang et al (2021)). The dispersant used has a weak retardation effect and can ensure an enough dormant period of the reference slurry at elevated temperatures. To detect the heat of hydration profile as complete as possible at elevated temperatures within 72 h, mixing different amounts of tartaric acid for cement slurry and polyphase paste is needed. For the cement paste admixed with tartaric acid, the dosage of the tartaric acid was 0.2% by weight of cement (bwoc). To the measurement on polyphase paste, the mass ratio of water to solid was fixed at 0.6 and the dosage of tartaric acid was 0.075%. The evolution of viscosity of cement slurries were tested by an atmospheric consistometer. The hydration kinetics of cement slurries and the polyphase paste were tested by an isothermal calorimeter (model: I-Cal Ultra).

3. Test results and analysis

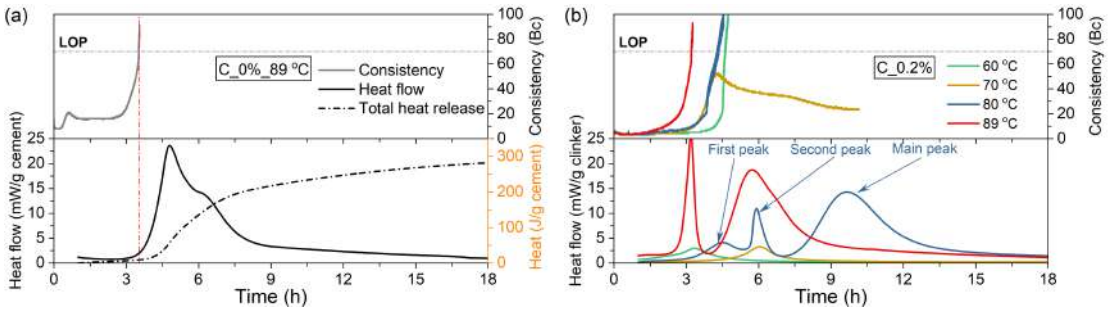


Fig.1 Consistency evolution and the corresponding hydration kinetics of cement slurries: (a) the reference cement slurry tested at 89 °C, (b) the cement slurry admixed with 0.2% tartaric acid tested at different temperatures.

Fig.1 shows the comparative test results of the cement slurry consistency evolution and corresponding hydration heat profiles with and without tartaric acid. As shown in Fig.1a, for the reference cement slurry, 3.5 h is the time to reach the limit of pumpability (LOP), and this timing exactly corresponds to the beginning of the acceleration period. However, as shown in Fig.1b, the slurry admixed with 0.2% tartaric acid presented an abnormal thickening phenomenon when tested at 70 °C: the consistency first increased rapidly, and then decreased gradually. In addition, the shape of the heat flow curves of cement hydration was fundamentally changed by tartaric acid: additional exothermic peaks occurring before the main peak

could be observed in the heat flow curve at 80 and 89 °C. Notably, it seemed that the timing of the increase in consistency of this retarded cement slurry was in line with the appearance of the "first peak".

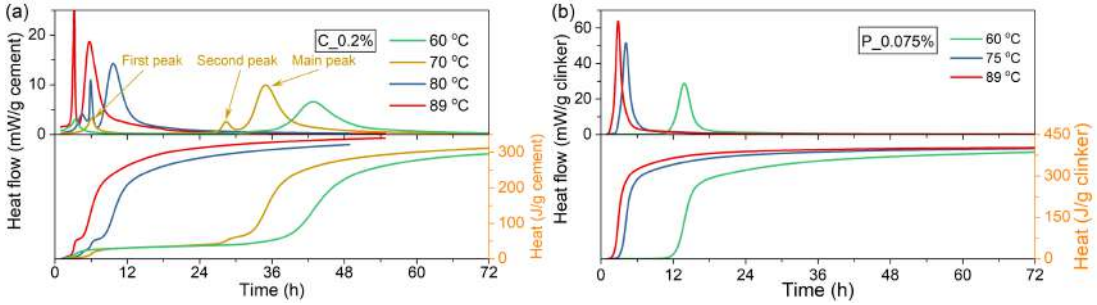


Fig.2 Hydration kinetics of the Class G cement (a) and the polyphase clinker (b) with tartaric acid addition at elevated temperatures.

In order to understand the effect of tartaric acid on cement hydration, the hydration of model cement composed of alite and belite containing tartaric acid was also tested and shown in Fig.2. In the same elevated temperature range from 60 to 89 °C, only the main hydration peak was observed for the model cement hydration. Hence, it can be concluded that the appearance of the additional exothermic peaks observed in the cement hydration all can be attributed to the hydration of aluminate and ferrite phases.

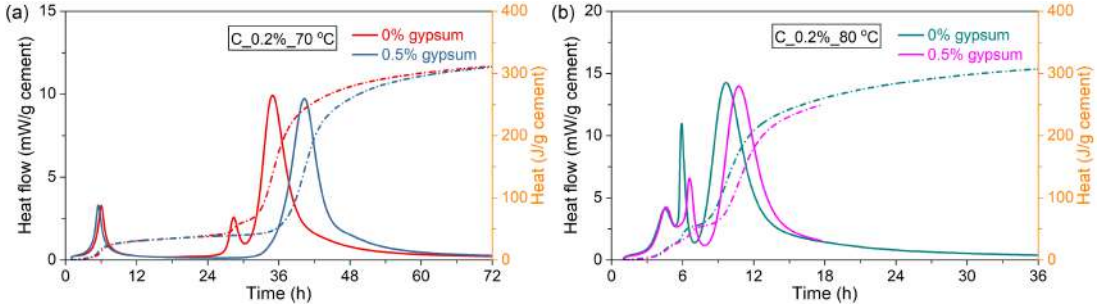


Fig.3 Effect of gypsum on the hydration kinetics of the cement slurry containing tartaric acid at 70 °C and 80 °C.

Fig.3 shows the effect of gypsum on the hydration kinetics of cement with tartaric acid added at 70 °C and 80 °C. Adding gypsum is often used to probe the relative position of the sulfate-depletion peak caused by the renewed dissolution of aluminate phases on heat flow curves (Quennoz and Scrivener (2013)). As shown in Fig.3, when 0.5% gypsum was admixed, the "second peak" was eliminated at 70 °C and was significantly depressed at 80 °C. Therefore, the origin of the "second peak" observed on the heat flow curves appear to be the renewed hydration of aluminate and ferrite phases after gypsum depletion.

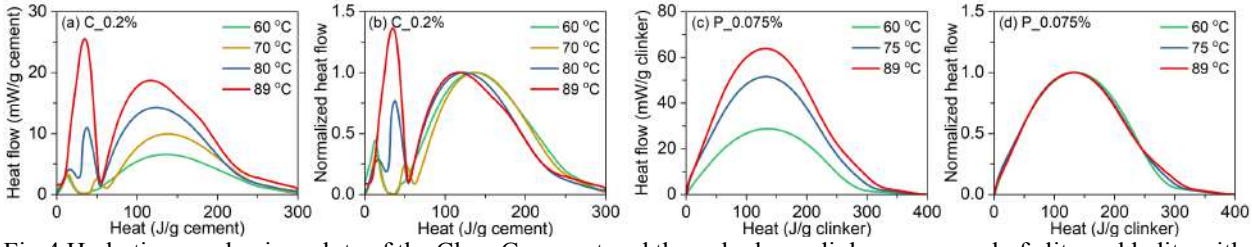


Fig.4 Hydration mechanism plots of the Class G cement and the polyphase clinker composed of alite and belite with tartaric acid addition: (a) and (c) before normalized, (b) and (d) after normalized by respective main peaks.

Fig.4(a) and (b) show the hydration mechanism plots of the cement with 0.2% tartaric acid before and after being normalized by the main hydration peak, respectively. It can be seen that with the temperature increasing, the first two exothermic peaks tend to merge, i.e. only one additional peak was observed at 89 °C. The additional peaks characterizing the aluminate/ferrite hydration mainly occurred before cumulative heat reached about 60 J/g. During the stage of hydration beyond 60 J/g cement, the cement hydration mechanism plots at different temperatures were similar, suggesting that the mechanism of silicate hydration was not changed by increasing temperature. The shapes of hydration mechanism plots of the polyphase clinker, shown in Fig.4 (c) and (d), were very similar and converged excellently when normalized. Therefore, it can be concluded that the significantly advanced hydration of the aluminate/ferrite phases in comparison to silicate phases is responsible for the premature setting of cement during this study. Based on the isothermal calorimetry results obtained above, apparent activation energies can be calculated based on a previously proposed scale factor model (Pang et al (2013)) and the values are reported in Table 2.

Table.2 Apparent activation energies (Ea) of Class G cement and polyphase clinker at elevated temperatures

Class G cement			Polyphase clinker		
T_r-T [a], °C	Scale factor [b] C	Ea, kJ/mol	T_r-T, °C	Scale factor C	Ea, kJ/mol
60-70	1.51	39.4	60-75	1.79	37.6
70-80	1.44	36.5	75-89	1.24	16.0
80-89	1.31	32.1			

[a] T_r-T means the temperature changing from T_r to T; [b] derived by the peak hydration rate method.

The apparent activation energies of Class G cement and polyphase clinker were both found to decrease with increasing curing temperature. In the temperature range from 60 to 75 °C, the apparent activation energy of the polyphase clinker was 37.6 kJ/mol, which was close to the two values of Class G cement estimated by using the three tests performed at 60, 70 and 80 °C. Meanwhile, there is a significant decrease of activation energy for the polyphase from 75 to 89 °C. However, this significant decrease of apparent activation energy could not be observed for the Class G Cement, which may be due to the fact that there was still some aluminate/ferrite contributions at the main peak in the heat flow curve obtained at 89 °C, leading to an overestimation of the apparent activation energy.

4. Conclusions

To clarify the premature setting caused by tartaric acid at elevated temperatures, the hydration kinetics of a Class G cement and a synthesized model cement containing no aluminate/ferrite phases were comparatively investigated. The shape of heat flow curves of the Class G cement could be significantly changed by the addition of tartaric acid (0.2% bwoc); additional exothermic peaks was detected before the main hydration peak, whose appearance can cause cement slurry viscosity increase and premature setting. By comparison with the hydration kinetics test results for the model cement, the additional peaks can be attributed to the hydration of aluminate/ferrite phases. The apparent activation energies of Class G cement and the polyphase clinker both decrease with increasing curing temperature, and a significantly lower value was observed for the polyphase clinker in the temperature range from 75 ℃ to 89 °C.

Acknowledgements

The authors gratefully acknowledge the financial support provided by National Natural Science Foundation of China (Grant No. 51974352).

References

API RP 10B. 2013. *Recommended Practice for Testing Well Cements*, second edition. Washington, DC, API.

Bergold, S. T., Goetz-Neunhoeffer, F. and Neubauer, J. (2017). Interaction of Silicate and Aluminate Reaction in a Synthetic Cement System: Implications for the Process of Alite Hydration. *Cem. Concr. Res.*, 93: 32-44.

Bishop, M. and Barron, A. R. (2006). Cement Hydration Inhibition with Sucrose, Tartaric Acid, and Lignosulfonate: Analytical and Spectroscopic Study. *Ind. Eng. Chem. Res.*, 45(21): 7042-7049.

Cheung, J., Jeknavorian, A., Roberts, L. and Silva, D. (2011). Impact of Admixtures on the Hydration Kinetics of Portland Cement. *Cem. Concr. Res.*, 41(12): 1289-1309.

Lu, Z., Kong, X., Jansen, D., Zhang, C., Wang, J., Pang, X. and Yin, J. (2020). Towards a Further Understanding of Cement Hydration in the Presence of Triethanolamine. *Cem. Concr. Res.*, 132: 106041.

Pang, X., Boontheung, P. and Boul, P. J. (2014). Dynamic Retarder Exchange as a Trigger for Portland Cement Hydration. *Cem. Concr. Res.*, 63: 20-28.

Pang, X., Cuello Jimenez, W. and Iverson, B. J. (2013). Hydration Kinetics Modeling of the Effect of Curing Temperature and Pressure on the Heat Evolution of Oil Well Cement. *Cem. Concr. Res.*, 54: 69-76.

Pang, X., Meyer, C., Darbe, R. and Funkhouser, G. P. (2013). Modeling the Effect of Curing Temperature and Pressure on Cement Hydration Kinetics. *ACI Mater. J.*, 110(2): 137-147.

Pang, X., Sun, L., Sun, F., Zhang, G., Guo, S. and Bu, Y. (2021). Cement Hydration Kinetics Study in the Temperature Range from 15 °C to 95 °C. *Cem. Concr. Res.*, 148: 106552.

Quennoz, A. and Scrivener, K. L. (2013). Interactions between Alite and C3A-Gypsum Hydrations in Model Cements. *Cem. Concr. Res.*, 44: 46-54.

Rodrigues, K. A. (1995). *Setting Retardant for Cement-containing Mixes*, Halliburton Co, USA, 1995, p. 18, pp.

Yan, Y., Wang, R., Wang, W., Yu, C. and Liu, J. (2021). Effect of Starch-Based Admixtures on the Exothermic Process of Cement Hydration. *Constr. Build. Mater.*, 289, 122903.

The 16th International Congress on the Chemistry of Cement 2023 (ICCC2023)
"Further Reduction of CO_2 -Emissions and Circularity in the Cement and Concrete Industry"
September 18–22, 2023, Bangkok, Thailand

Hydration of tricalcium aluminate-sulphate systems in presence of alkanolamines

M. Magistri[1*], M.C. Dalconi[2], M. Monti[1] and L. Valentini[2]

[1] *Mapei SpA, Milan, Italy*
Email: m.magistri@mapei.it
[2] *Department of Geoscience and CIRCe Centre, University of Padova, Padua, Italy*
Email: mariachiara.dalconi@unipd.it

ABSTRACT

The reduction of CO_2 emissions is the biggest challenge that global cement industry has to face nowadays. In the end, this means to strive for a higher reactivity of blended cements. Needless to say, this requires a step forward in the understanding of basic mechanisms of cement reactivity, with particular interest to main clinker phases and to their interactions with secondary cementitious materials. Among the available strategies for having more reactive cements, the use of chemical activators is known and implemented in the industrial practice since a long time. From a theoretical point of view, the presence of chemical admixtures introduces a further level of complication for the understanding of hydration mechanisms responsible for optimum strength development and acceptable rheology of fresh mortars and concrete. The hydration of tricalcium aluminate and in general of aluminate phases in Portland cement has been widely described in recent publications. Target of the present paper is to focus on the effect of alkanolamines on the hydration of C_3A/sulphate systems, on both pure phases and real cements. Particular attention is given to the morphology of hydration products: although being a fundamental parameter, it seems that this aspect has received in scientific literature less attention than what it deserves.

KEYWORDS: *Hydration, Tricalcium aluminate, Alkanolamines*

1. Introduction

The hydration of tricalcium aluminate (and calcium alumino-ferrite) contained in commercial clinkers and cements has been widely described in several publications. Type, structure, thermodynamical stability and kinetics of formation of hydration products (AFm - Alumino-ferrite mono and AFt - Alumino-ferrite tri depending on the molar ratio of anions to alumina), are the subject of fundamental publications in scientific literature (Scrivener et al. (2019)). It has also been described that some chemical admixtures regularly used as process additives in manufacturing of commercial cements have an impact on aluminate hydration. Alkanolamines (of which triethanolamine is the most common) are an important class of chemicals used in the formulation of grinding aids and performance enhancers. After pioneering works, more recent papers have been dedicated to the effect of triethanolamine during cement hydration, with very specific and detailed investigations. Further confirmations of the fact that triethanolamine is an effective chelating agent in alkaline media for Al^{3+} ion have been provided (Yaphary et al. (2017)). The present paper is aimed to give an additional contribution in understanding the effect of triethanolamine on model systems composed of tricalcium aluminate and calcium sulphates.

2. Experimental part

Pure tricalcium aluminate (C_3A) was obtained from Mineral Reasearh Processing, France. Commercially available ground natural gypsum and bassanite were used. Since C_3A is sensitive to ageing that reduces reactivity due to partial hydration with ambient humidity, part of this material was calcined in a laboratory furnace at 950°C for three hours. Fineness of C_3A was characterised by air-jet 40 μm sieve

(Hosokawa Alpine LS200 N, sieving time: 6 minutes, pressure drop: 4750±250 Pa, reproducibility: ±1.0%). Commercial grade triethanolamine with 99% purity was used.
Several blends of C_3A (before and after calcination), gypsum (G) and bassanite (B) were prepared and mixed with water in a closed plastic vial, with and without the presence of triethanolamine (TEA). Compositions of all blends and quantity of triethanolamine were decided according to a 2^3 Design of Experiment (Leardi (2009)) and details are summarized in Table 1. The logic behind the DoE is to check the effect of three main parameters: 1) ratio C_3A/total calcium sulphate, 2) replacement of natural gypsum with bassanite and 3) presence of TEA. Quantities were chosen to approach content of C_3A, gypsum, bassanite and TEA in commercial cements, where reasonably C_3A (if we exclude sulphate resisting cements) is in the range 5-10%, total calcium sulphate is around 5% (hence C3A/sulphate ratio is in the range 50/50 to 70/30) and dehydration of total natural gypsum can reach 50% of its starting amount. Normal dosage of alkanolamines used as grinding aid is around 100-200 ppm referred to cement, that corresponds to 2000 ppm (0,2%) if referred to C_3A/calcium sulphate only.

Tab. 1 - Composition of blends C_3A/G/B/TEA used in the investigation. Data are expressed as mass %, while TEA amount is expressed as mass % referred and in addition to the total mass of solid. All blends were prepared with both normal and calcined C_3A.

Blend number	1	2	3	4	5	6	7	8	9
C_3A	70%	50%	70%	50%	70%	50%	70%	50%	60%
Gypsum	30%	50%	15%	25%	30%	50%	15%	25%	30%
Bassanite	-	-	15%	25%	-	-	15%	25%	10%
TEA	-	-	-	-	0,2%	0,2%	0,2%	0,2%	0,1%

For each mix, isothermal calorimetry (TAM/Air calorimeter, T=23°C) was run. Water/solid ratio was set at 2:1 for normal C_3A and 10:1 for calcined C_3A (data normalised to total solid). For some selected mixes, hydration (water/solid 2:1 for both normal and calcined C_3A) was stopped after 24h with a "quenching" procedure. Quenched hydrated-pastes were characterised with X-Ray Powder Diffraction (XRPD) and scanning electron microscope (SEM). The Rietveld method, as implemented in Topas v 2.1, was used for quantitative phase analyses. Secondary electron (SE) images of dried powders (dispersed on a conductive tape and sputtered with carbon) were collected using a Tescan Solaris scanning electron microscope (SEM) equipped with a field emission electron source. Details of the methods are available upon request.

3. Result and discussion

3.1 Materials characterisation

According to XRD analysis, C_3A used in this study is mainly composed of cubic polymorph (86.9±0.2%), with traces of mayenite $C_{12}A_7$ and 11.8±0.1% hydrogarnet C_3AH_6. Loss on ignition of C_3A (weight decrease after calcination) is 5.4%. Residual at 40 μm is 4.8%. Effect of calcination is the elimination of partial hydration, with conversion of hydrogarnet to C_3A (98.2±0.1% cubic C_3A after calcination). Gypsum and bassanite used contain some anhydrite and other minor phases.

3.2 Isothermal calorimetry

Heat flow curves as obtained with isothermal calorimetry for blends 1 to 9 (C_3A before calcination) are reported in figure 1a. Although all of them can be divided in three stages usually referred to as initial dissolution, induction period and sulphate depletion, as widely described in recent publications (Shiju et al. (2019)), there are relevant differences in terms of maximum heat flow in stage 1 and 3 and time at which the maximum heat flow in stage 3 is reached (the latter being an indirect measure of the "induction period" length). In the present work, thanks to the DoE approach the effect of the blend composition (relative quantities of C_3A and total calcium sulphate, conversion of natural gypsum to bassanite and presence of TEA) on the hydration profile can be quantitatively described. It emerges that maximum heat

flow at stage 1 is proportional to the amount of bassanite in the blend and to the presence of TEA, the maximum heat flow at stage 2 is proportional to the C_3A content of the blend and the time at which the maximum heat flow in stage 3 is reached is proportional to the amount of sulphate and to the presence of TEA, hence there is a delay in the sulphate depletion that is also related to the presence of alkanolamine. Up to some extent, quantitative predictions can be made, as described in figure 1b that reports isoresponse surfaces for the time at which maximum heat flow in stage 3 is reached.

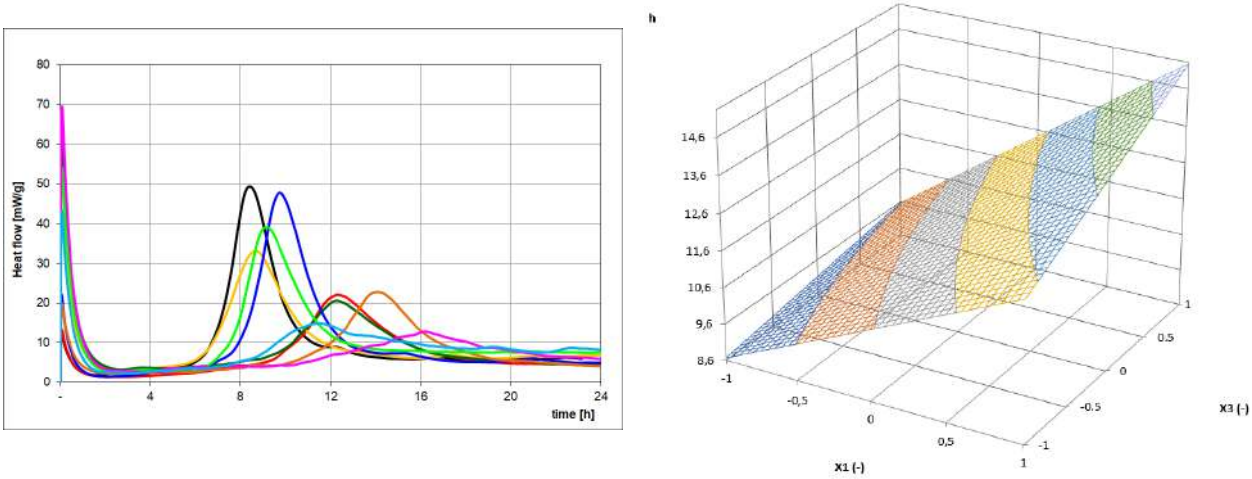


Figure 1a (left) - Heat flow obtained from blends 1 to 9. Stage 1: from 0 to 2 hours, stage 2: 2 to 6 hours, stage 3: after 6 hours. Curve colour-blend number: black-1, red-2, yellow-3, dark green-4, blu-5, orange-6, green-7, magenta-8, pale blu-9. Figure 1b (right) - Isoresponse surface for the time at which maximum heat flow in stage 3 is reached. Total time span (y-axis): between 8,6 and 14,6 hours. X1: total calcium sulphate content. X3: presence of TEA. Coloured surfaces represent composition areas with 1h difference in sulphate depletion. Longer delay in sulphate depletion is obtained with sample with highest sulphate and presence of TEA.

3.3 X-ray diffraction of hydrated blends

Hydrated C_3A/G/B pastes at 24 h are composed of remaining C_3A and calcium sulphate contained in the original blend, with variable amounts of ettringite, monosulphate, hydrogarnet and low crystallinity grade hydroxy-AFm phases as hydration products (Table 2).

Tab. 2 - XRD analysis of hydrated pastes. All data in mass %.

	Blend 3 C_3A not calcined	Blend 3 calcined C_3A	Blend 7 C_3A not calcined (with TEA)	Blend 7 calcined C_3A (with TEA)	Blend 4 C_3A not calcined	Blend 4 calcined C_3A	Blend 8 C_3A not calcined (with TEA)	Blend 8 Calcined C_3A (with TEA)
C_3A Cubic	34.9±0.4	17.6±0.5	32.4±0.1	15.1±0.3	31.5±0.2	20.0±0.2	30.8±0.2	19.7±0.2
$C_{12}A_7$ Mayenite	1.2±0.1	0.6±0.2	0.6±0.1	0.3±0.1	0.5±0.1	0.7±0.1	0.6±0.1	0.5±0.1
C_3AH_6 Hydrogarnet	7.7±0.3	16.0±0.4	6.0±0.2	15.3±0.3	2.8±0.2	8.9±0.1	4.9±0.1	17.4±0.2
Gypsum	14.6±0.3	6.4±0.3	14.4±0.5	5.9±0.1	34.3±0.2	27.8±0.2	34.1±0.2	25.4±0.2
Anhydrite	3.3±0.2	1.8±0.2	3.1±0.4	1.5±0.2	4.0±0.1	4.2±0.1	3.7±0.1	3.8±0.1
Ettringite	17.5±0.4	21.0±0.6	16.6±0.7	21.9±0.5	20.9±0.2	16.0±0.2	16.3±0.2	11.4±0.2
Monosulphate	9.3±0.4	22.5±0.7	10.3±0.4	22.6±0.5	2.5±0.2	10.7±0.3	3.6±0.2	8.4±0.3
Hydroxy-Afm	11.5±0.6	14.0±0.6	16.6±0.8	17.6±0.6	2.5±0.2	11.8±0.4	4.2±0.3	13.3±0.4

The effect of TEA (e.g. by comparing Blend 3 and 7, or 4 and 8) can be noticed in the increased C_3A consumption and in the higher amount of OH-AFm and hydrogarnet, while formation of sulphate

containing AFt and AFm (ettringite and monosulphate) is not particularly affected. All blends prepared with calcined C_3A show increased reactivity, with lower unreacted C_3A and higher formation of hydration products. Although mass fractions of pastes and original powders are not directly comparable, the high gypsum content in pastes obtained from blends with high bassanite content suggests that a strong recrystallisation of secondary gypsum has occurred.

3.4 SEM morphology of hydrated blends

Morphology of hydrated C_3A/G/B pastes is mainly characterized by a large number of ettringite crystals in forms of rods (1-2 mm length, tenth of nm thickness), hexagonal plates probably composed of monosulphate. Cubic structures typical of hydrogarnet can be observed in particular in samples prepared with calcined C_3A. By comparing same C_3A/G/B pastes with and without TEA (e.g. pastes from blend 3 and 7, figure 2a and 2b), a difference in the morphology of ettringite can be seen: the increased reactivity of C_3A (obtained either by addition of TEA or by calcination) promotes smaller ettringite crystals.

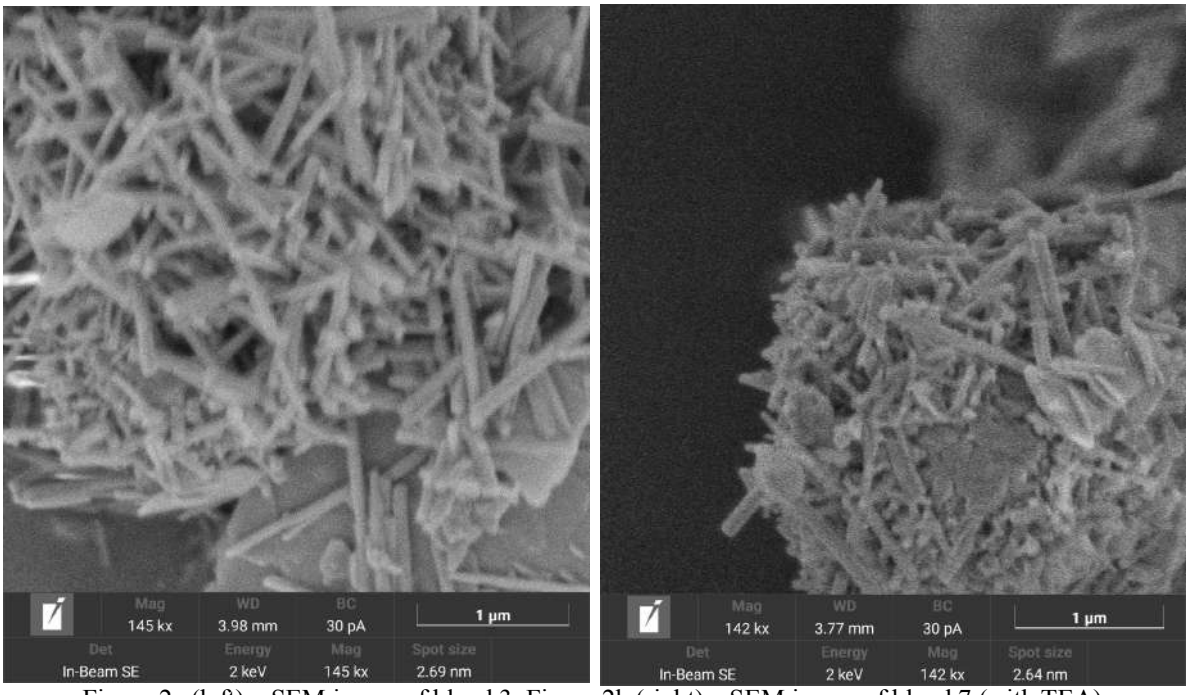


Figure 2a (left) – SEM image of blend 3. Figure 2b (right) – SEM image of blend 7 (with TEA)

4. Conclusions

Effects of TEA on C_3A/sulphate blends have been investigated and a quantitative correlation between hydration profile and C_3A/sulphates, bassanite and presence of TEA can be retrieved. In general, TEA tends to accelerate the consumption of C_3A with formation of OH-AFm and hydrogarnet. A different morphology of ettringite when C_3A hydration is accelerated (thanks to the presence of TEA or following calcination) can be noticed, with implication in nucleation/growth mechanism that could be present also in real cements.

References

Leardi R. (2009) "Experimental design in chemistry: A tutorial", Analytica Chimica Acta 652: 161-172

Scrivener K.L., Ouzia A., Juilland P, Aslam Kunhi M. (2019) "Advances in understanding cement hydration mechanisms", *Cement and Concrete Research* 124: 105823

Shiju J., Skibsted J., Özlem C. (2019) "A quantitative study of the C3A hydration", *Cement and Concrete Research* 115: 145-159

Yaphary Y.L., Zechuan Yu, Lam R.H.W., Denvid Lau (2017) "Effect of triethanolamine on cement hydration toward initial setting time", *Construction and building materials* 141: 94:103

The 16th International Congress on the Chemistry of Cement 2023 (ICCC2023)
"Further Reduction of CO_2 -Emissions and Circularity in the Cement and Concrete Industry"
September 18–22, 2023, Bangkok, Thailand

Thermogravimetric analysis on the effect of SAP addition on the microstructure of cement based materials

L.B. Agostinho[1*], E.F. Silva[2], and V.M. S. Capuzzo[3]

[1] *Federal University of Uberlândia, Uberlândia-MG, Brazil*

Email: liviaborba@ufu.br
[2] *University of Brasília, Brasília-DF, Brazil*

Email: eugenia@unb.br
[3] *University of Brasília, Brasília-DF, Brazil*

Email: valdirenemaria@unb.br

ABSTRACT

To mitigate autogenous shrinkage, the effectiveness of the superabsorbent polymer (SAP) is proven in scientific papers. Even so, several researchers mention that SAP can cause a reduction in the mechanical properties of concrete (compressive strength and elasticity modulus), because where before there was a polymer swollen with water, after supplying this water to the capillaries, a pore remains. Many works penalized SAP, as they compared mixtures containing SAP with a higher w/c ratio than the reference mix, as extra internal curing water was added. Even though is proved that internal curing water participates in hydration reactions and, therefore, should be considered in the mix for comparative purposes. For this reason, in this research, the mixtures present the same total w/c ratio. Despite the presence of isolated pores, the use of SAP is justified by its high effectiveness in mitigating autogenous shrinkage in high strength mixtures, and the impact of this material in the formation of microstructure of cement based materials is studied in this paper by thermogravimetric analysis. The thermogravimetric analysis shows that the higher the levels of SAP the higher was the consumption of CH.

KEYWORDS: *superabsorbent polymer, thermogravimetric, microstructure, cement hydration.*

1. Introduction

The use of superabsorbent polymers (SAP) in cementitious materials is justified by its high effectiveness in mitigating autogenous shrinkage in high strength mixes. But also, several researchers mention that SAP can cause a reduction in the mechanical properties of concrete (compressive strength and elasticity modulus), because where before there was a polymer swollen with water, after supplying this water to the capillaries, a pore remains. Many works blame SAP for these losses, but they compared mixtures containing SAP with a w/c ratio greater than that of the reference mix, as extra internal curing water was added. Manzano (2016) and Borges (2019) proved that internal curing water participates in hydration reactions and, therefore, should be considered in the mix for comparative purposes. Ma et al. (2017) and Hasholt e Jensen (2015) concluded that the comparison on SAP effectiveness should be based on the same total w/c ratio.

As the internal curing water participate on the hydration process, it is desirable that some microstructural analysis techniques be used to identify how SAP can interfere with the microstructure of cementitious materials. According to Taylor (1997), Thermogravimetry (TG) is one of the most suitable techniques for determining the amount of calcium hydroxide (CH) in Portland cement pastes, measuring the mass loss of the sample between temperatures of 425 and 550ºC.

2. Methodology

In this study, 3 samples were tested, being the reference and two samples containing SAP (0.15% and 0.30% SAP in relation to the cement mass) at the ages of 1, 3, 7 and 28 days. All samples in this experimental program have the same total w/c ratio, that is, internal curing water (extra) was not added to the mixtures, as it is considered that this water also participates in the hydration reactions. As the purpose of this work is to evaluate the formation of the microstructure, it was adopted as a research premise the parameter of all pastes having equal total w/c ratio, fixed spreading by using the mini-slump of 100±10mm, following the methodology of Kantro (1980) and variable superplasticizer additive content, seeking to analyze the influence of the SAP addition.

The experiments were performed on the Simultaneous SDT Q600 equipment from TA Instruments. Around 10mg of previously ground sample were used in an alumina crucible and the test was carried out from room temperature to 1000°C with a heating rate of 10°C/min in a nitrogen atmosphere (N_2) with a flow rate of 100ml/min.

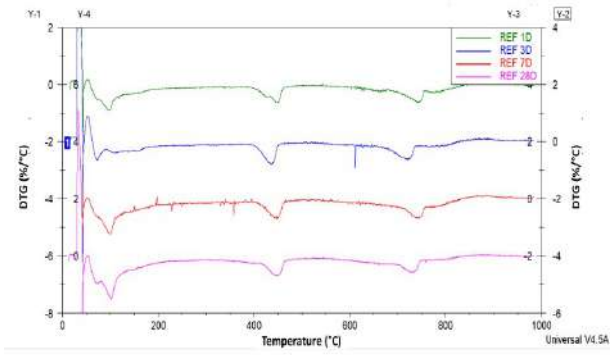
This technique was used with the aim of monitoring the hydration process of the pastes over time by calculating the CH content, which can be derived directly from the stoichiometry of the dihydroxylation(Ldx) of this product. The temperature range considered for dehydroxylation (Ldx), or decomposition of CH, was between 380ºC and 500ºC suggested by Oliveira (2019). Between these temperatures, CH decomposes into H_2O and CaO. The mass loss reported by thermogravimetry is due to the volatilization of water. Thus, with the values obtained by the TG curve and with stoichiometric calculations, it is possible to determine the amount of calcium hydroxide in a certain hydrated Portland cement paste. The calculation was performed according to (1) proposed by the RILEM TC 238-SCM committee (LEFEVER et al., 2020).

$$CH(\%) = \frac{ML_{CH}}{M_F} . \frac{MM_{CH}}{MM_{H2O}} \quad (1)$$

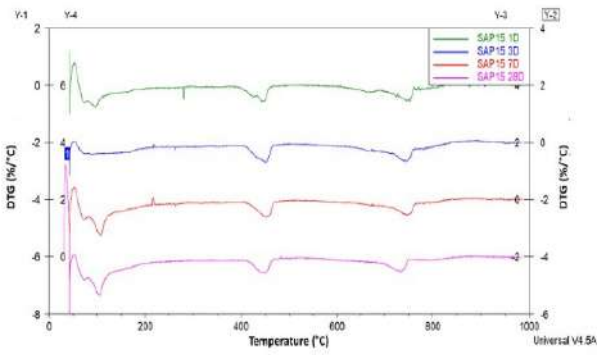
Where:
ML_{CH} = Mass loss in the temperature range of decomposition of CH
M_F = Final mass
MM_{CH} = Molecular mass of CH
MM_{H2O} = Molecular mass of water

3. Results and Analysis

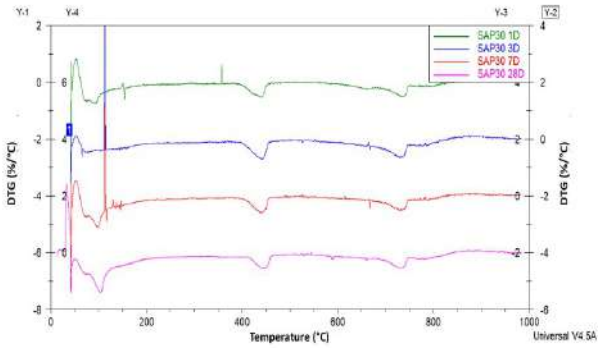
In general, the curves of the pastes at all ages showed similarity, that is, forming the same types of hydrates, but in different amounts according to age and content of SAP, this means that the presence of SAP does not create new hydrates (Figure 1).



(a)



(b)



(c)

Figure 1 - DTG curves from: REF samples (a); SAP15 samples (b) and SAP30 samples (c) at the ages of 1,3, 7 and 28 days.

Table 1 shows the calculated results of the CH content and the percentage in relation to the reference (Figure 2) for all pastes proposed in the experimental program at the ages of 1, 3, 7 and 28 days.

Table 1 - Results calculated from the thermogravimetry test of CH content and percentage in relation to the reference for the proposed pastes in the experimental program for the ages of 1, 3, 7 and 28 days.

PASTE	1 DAY	% REF	3 DAYS	% REF	7 DAYS	% REF	28 DAYS	% REF
REF	10,0%	100,0%	10,0%	100,0%	10,3%	100,0%	10,3%	100,0%
SAP15	8,5%	85,2%	10,4%	104,1%	8,9%	86,1%	8,4%	81,6%
SAP30	7,5%	75,3%	10,1%	100,8%	8,3%	80,9%	7,9%	76,5%

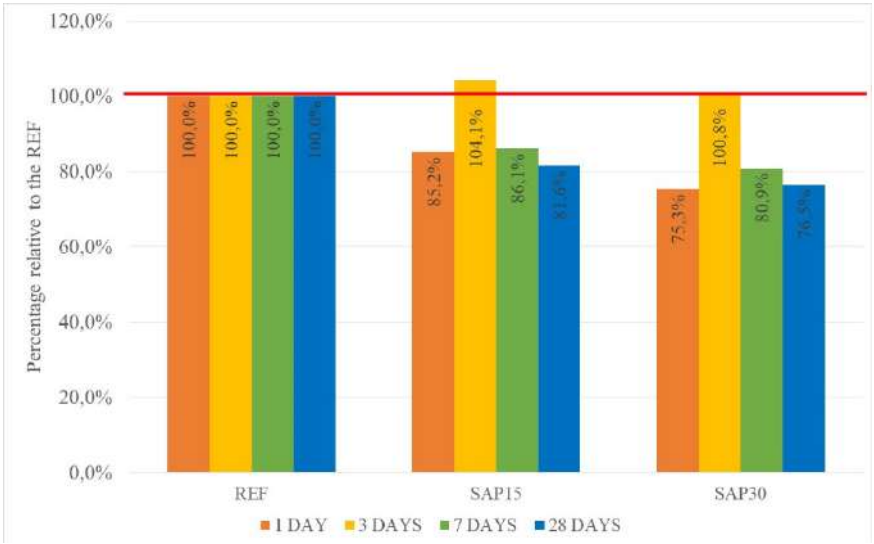


Figure 2 - Percentage in relation to the reference for the proposed pastes in the experimental program for the ages of 1, 3, 7 and 28 days.

It is observed that only at the age of 3 days did the pastes containing SAP show higher levels of CH than the REF paste and that at the other ages, the greater the presence of SAP, the lower the CH content when compared to the reference. It is then understood that the delay in the availability of part of the water (internal to the SAP), altered the formation and consumption of CH over time.

The increase in the percentage of CH observed from 1 day to 3 days can be justified by Taylor (1997) and Lothenbach and Zajac (2019), who states that within the first 24 hours of hydration, only about 30% of the cement reacts. Also, according to Agostinho (2021), in the isothermal conduction calorimetry test, at the end of 24 hours of testing, the curves are still in the acceleration period, that is, it did not reach the peak of

hydration reactions, which may justify the higher levels of CH at the age of 3 days compared to the age of 1 day.
Even so, the results on the ages of 7 days and 28 days, corroborate the results found by Snoeck et al. (2015) and Esteves (2011) that concluded that SAP caused the CH content to decrease in all samples with different contents and types of SAP, maybe because after releasing all the internal curing water, the SAP particles form spherical voids homogeneously distributed in the cementitious matrix and these pores can act as points to promote pozzolanic activity, consequently greater consumption of CH. Manzano (2016), found that the internal curing water, absorbed by the SAP, promotes the pozzolanic activity of the mixtures, mainly up to 7 days of age. Esteves et al. (2014) concluded that the presence of SAP influences the development of hydrates in their chemical nature. Perhaps it was this influence that altered the amount of CH at all ages when compared to the REF paste, even though the mixtures had the same total w/c ratio.
It seems that the availability of water interferes with the development of hydration products, because, even with the same amount of total water in all mixtures, pastes containing SAP which have part of the water internal to the polymer and return this water to the system as the hydration reactions advances, showed a higher consumption of CH than the reference paste.

3. Conclusions

Using the thermogravimetry technique, the moment of water availability interferes in the formation and consumption of CH and the higher the levels of SAP the greater the consumption of CH, because part of the water was retained in the SAP and was only returned to the system after the hydration reactions had progressed.

Acknowledgements

The authors thank Federal University of Uberlândia and University of Brasilia for the partnership in this research.

References

Agostinho, L. B. (2021) "Análise microestrutural de pastas de cimento Portland de alta resistência contendo polímero superabsorvente e nanosílica." *Doctoral Thesis*, University of Brasilia.

Borges, J. G. (2019) "Metodologia Dos Tubos Corrugados Para Determinação Da Retração Autógena Em Materiais Cimentícios De Alto Desempenho Contendo Polímero Superabsorvente (SAP)". *Masters Dissertation*, University of Brasilia.

Esteves L. P. (2011) "On the hydration of water-entrained cement–silica systems: Combined SEM, XRD and thermal analysis in cement pastes." *Thermochimica Acta*, Vol. 518, Iss. 1–2, p. 27–35.

Esteves, L.P.; Lukošiūtė, I.; Čėsnienė, J. (2014) "Hydration of cement with superabsorbent polymers." *Journal of Thermal Analysis and Calorimetry*, vol. 118, no 2, p. 1385-1393.

Hasholt, M. T.; Jensen, O. M.(2015) "Chloride migration in concrete with superabsorbent polymers." *Cement and Concrete Composites*, v. 55, p. 290–297.

Kantro, D. (1980) "Influence of water reducing admixtures on properties of cement paste." *Cement, Concrete and Agregates*, v. 2, n. 2, p. 95-102.

Lefever, G.; Aggelis, D. G.; De Belie, N.; Raes, M.; Hauffman, T.; Van Hemelrijck, D.; Snoeck, D. (2020) "The contribution of elastic wave NDT to the characterization of modern cementitious media." *Sensors (Switzerland)*, v. 20, n. 10.

Lothenbach, B. And Zajac, M., (2019) "Application of thermodynamic modelling to hydrated cements." *Cement and Concrete Research*, 123.

Ma, X.; Liu, J.; Wu, Z; Shi, C. (2017) "Effects of SAP on the properties and pore structure of high performance cement-based materials." *Construction and Building Materials*, v. 131, p. 476–484.

Manzano, M. A. R. (2016) Estudo Experimental de Materiais Cimentícios de Alta Resistência modificados com Polímeros Superabsorventes (PSAs) como Agentes de Cura Interna. *Doctoral Thesis* - Brasília-DF: University of Brasília.

Snoeck, D., Velasco L.F., Mignon A., Van Vlierberghe S., Dubruel P., Lodewyckx P., De Belie, N., (2015) "The effects of superabsorbent polymers on the microstructure of cementitious materials studied by means of sorption experiments." *Cement and Concrete Research*, v. 77, p. 26–35.

Taylor, H.F.W. (1997) "Cement Chemistry." 2. Ed. London: Thomas Tellford.

The 16th International Congress on the Chemistry of Cement 2023 (ICCC2023)
"Further Reduction of CO_2 -Emissions and Circularity in the Cement and Concrete Industry"
September 18–22, 2023, Bangkok, Thailand

Sodium sites and hydration state in C-S-H phases synthesized under alkaline conditions from ^{1}H and ^{23}Na MAS NMR experiments

S.Y. Yang [1], and J. Skibsted[1*]

[1] *Department of Chemistry, Aarhus University, 8000 Aarhus, Denmark*
Email: syyang@chem.au.dk; jskib@chem.au.dk

ABSTRACT

C-S-H samples with Ca/Si ratios of 0.8 and 1.4 have been synthesized from $Ca(OH)_2$ and colloidal silica by curing in a 0.5 M NaOH solution for 1.5 months. The ^{23}Na NMR spectra (14.1 T) are dominated by a featureless resonance at 0.9 ppm, which reflects sodium coordinated to water in $[Na(H_2O)_6]^+$ complex ions. De-hydration of the samples in a convection oven, by storage at different humidities, or by long-term MAS spinning results in a systematic shift of the main resonance towards lower frequency (0.9 to -5.5 ppm), reflecting the removal of H_2O from the sodium hydration shell. Rehydration by a change in humidity shows that water can be incorporated into the hydration shell again. ^{23}Na MAS and MQMAS NMR spectra at different magnetic fields (14.1 and 22.3 T) allow identification of three distinct sodium environments in the C-S-H samples from which ^{23}Na isotropic chemical shifts and quadrupolar product parameters have been determined with good accuracy. A tentative assignment of the three resonances is proposed.

KEYWORDS: *C-S-H phase, alkali adsorption, sodium hydration state, dehydration, ^{23}Na NMR*

1. Introduction

Portland cements include typically 0.2 – 2.0 wt% alkali oxides (Na_2O and K_2O) which increase pH during the initial hydration and affects the solubility of the principal phases. After prolonged hydration, the alkali ions are adsorbed on the surface of the hydration products and possibly incorporated into the structure of the calcium-silicate-hydrate (C-S-H) phase. Synthesized C-S-H samples have been widely used to explore the composition, structure and properties of this principal binding phase, often using equilibrated samples in alkaline solutions. However, current models lack a detailed description of the exact location of alkali ions associated with the C-S-H structure, including their level of hydration in different potential sites. Sodium can easily be detected by ^{23}Na NMR spectroscopy, and this work reports a detailed analysis of the ^{23}Na resonances, observed for synthesized C-S-H samples, with a main focus on the sodium hydration state, *i.e.*, $[Na(H_2O)_{6-x}]^+$, under different experimental conditions.

2. Sample Preparation

The C-S-H samples were prepared by mixing colloidal SiO_2 and $Ca(OH)_2$, targeting the molar ratios of Ca/Si = 0.8 and 1.4, in a 0.5 M NaOH solution, followed by curing at room temperature for 1.5 months.

3. Results and Discussions

3.1 Characterization of C-S-H samples by ^{23}Na MAS NMR. ^{23}Na MAS NMR has been used in relatively few studies to characterize sodium associated with the C-S-H phase (Viallis et al. (1999), Renaudin et al. (2009), Yang et al. (2021)), utilizing the high NMR sensitivity for ^{23}Na and the possible detection of sodium in less-ordered systems. The ^{23}Na chemical shift and quadrupolar broadening depend mainly of on the nearest coordination environments and thereby on the local bonding network for sodium.

The ^{23}Na MAS NMR spectra of the C-S-H phases synthesized with the initial ratios, Ca/Si = 0.8 and 1.4, and equilibrated in 0.5 M NaOH solution are shown in Figure 1. The spectra reveal a clear difference in chemical shifts and linewidths, as the resonance for the high-Ca/Si C-S-H sample is narrower and shifted to slightly higher frequency (0.9 ppm) as compared to the centerband for the low-Ca/Si sample at -0.7 ppm. These differences may reflect variations in the amount of water surrounding sodium or in the location of Na in the structure, potentially related to differences in silicate structure at low and high Ca/Si ratio. In this context, it is noted that high-Ca/Si C-S-H phases may have H_2O/Si of 1.5 ~ 1.8 whereas ratios of 1.1 ~ 1.3 are reported for low-Ca/Si C-S-H's (L'Hôpital et al. (2016)). For the Ca/Si = 1.4 sample, this can lead to a higher number of water molecules in the Na hydration shell and increased mobility for the Na^+ ions, which results in a narrowing of the ^{23}Na resonance.

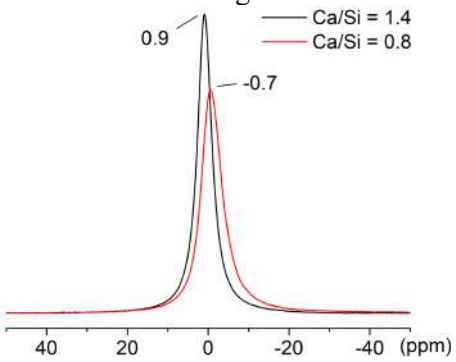


Figure 1. ^{23}Na MAS NMR spectra (14.1 T, ν_R = 12.0 kHz) of the C-S-H phases with Ca/Si = 0.8 and 1.4 cured in 0.5 M NaOH solutions for 1.5 months.

3.2 De-hydration of C-S-H samples. To investigate the sodium hydration shell in more detail, a series of drying experiments have been conducted by (*i*) heating the synthesized samples in a convection oven, (*ii*) storing the samples at different humidities, and (*iii*) by exposure to long-term MAS spinning. Heat-treatment (40 – 200 °C) of the samples results in a systematic shift of the main resonance towards lower frequency with increasing temperature, as observed in ^{23}Na NMR spectra obtained at 14.1 T (-0.9 to -5.5 ppm) and at 22.3 T (1.4 to 0 ppm) and shown in Figure 2. The differences at 14.1 and 22.3 T reflect the direct and inverse proportionality of the chemical shift and the second-order quadrupolar broadening with the magnetic field strength, respectively. A gradual broadening of the main resonance at 14.1 T is also found with increasing temperature, indicating a reduction in local symmetry of the sodium nuclei upon dehydration. In addition, a sharp resonance at higher frequency but with lower intensity is observed at both magnetic fields, which remains at the same frequency at all temperatures. This resonance may originate from a sodium site, which is stronger bonded in the C-S-H structure, whereas the changes upon heating for the dominating peak indicate the loss of water molecules in the first coordination shell, $[Na(H_2O)_6]^+$, for a more loosely bound Na site.

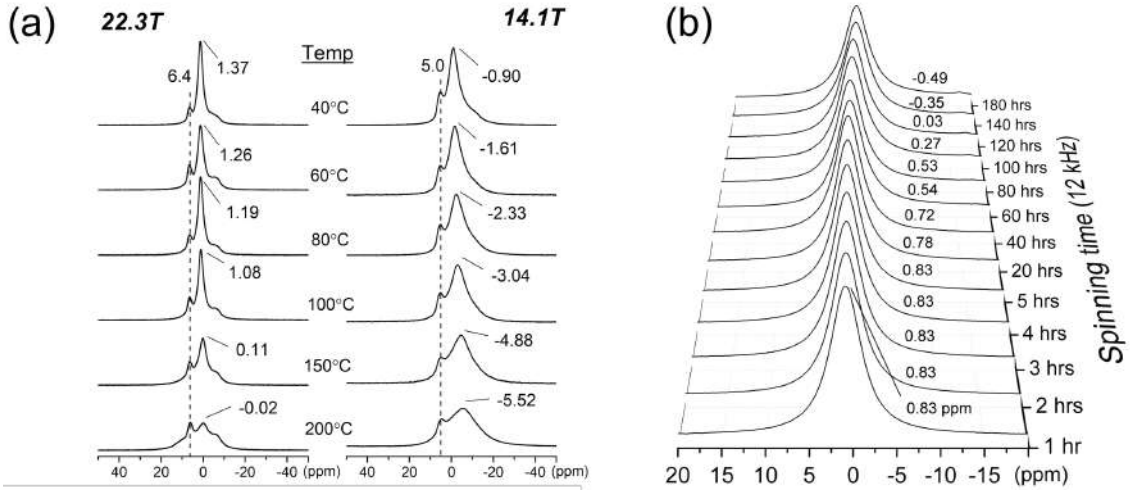


Figure 2. (a) ^{23}Na MAS NMR spectra recorded at 22.3 T (ν_R = 20.0 kHz) and 14.1 T (ν_R = 12.0 kHz) for the C-S-H phase with Ca/Si = 1.4 heated for one hour in an oven at temperatures of 40, 60, 80, 100, 150 and 200 °C. (b) ^{23}Na MAS NMR spectra (14.1 T) for the C-S-H phase with Ca/Si = 1.4, corresponding to *in-situ* drying of the sample in the 4 mm zirconia rotor spinning at 12.0 kHz for up to 180 hours. Each spectrum represents 896 scans acquired with a 4-s relaxation time (~1 hour per spectrum).

Similar investigations of samples stored at different humidities (data not shown) are consistent with the results shown in Figure 2, although longer storage times in the desiccators are required to achieve the same level of dehydration. An *in-situ* study of the drying process has been achieved by long-term MAS spinning of one sample in a 4 mm zirconia rotor at a spinning frequency of 12.0 kHz, corresponding to as sample temperature of 50 ºC in the actual NMR probe. This drying has been followed by ^{23}Na NMR by acquiring spectra for one hour over a period of 180 hours. Selected spectra following this process are shown in Figure 2, where it is seen that the broad resonance shifts slightly from 0.8 ppm to -0.5 ppm over the 180 hours, whereas the narrow component is not clearly resolved. The spectra reflect a mild type of drying via MAS spinning, where only weakly bonded water molecules will be released from the nearest coordination sphere. Although the shifts induced by MAS are smaller than those observed for the heat-treated samples at higher temperatures, the trend is the same and it can be ruled out that a thermal degradation of the C-S-H samples takes place.

3.3 Identification of different Na sites. Apart from two clearly resolved resonances, a tail towards lower frequency is also seen for the main peak in the ^{23}Na NMR spectra (Figure 2), indicating the presence of a third type of sodium species. To further improve the spectral resolution, ^{23}Na multiple-quantum (MQ) MAS NMR has been applied to remove effects from second-order quadrupolar broadening of the resonances. ^{23}Na MQMAS spectra recorded at 22.3 T are shown in Figure 3 as a function of the heating temperature for C-S-H samples with Ca/Si = 1.4. From 40 °C to 150 °C, two ^{23}Na sites are clearly identified from the contours, denoted Na(a) and Na(b), which correspond to the above-mentioned sharp and broad resonances, respectively. However, these spectra do not show any obvious sign of a third resonance, which is possibly due to a low quantity of these species in the structure. For the sample heated at 200 °C sample, a ^{29}Si NMR spectrum (not shown) reveals that a phase separation or partly decomposition of the C-S-H sample has occurred, since the presence of dicalcium silicate hydrate is observed. This may explain the absence of the Na(b) site in the ^{23}Na MQMAS spectrum. The ^{23}Na MQMAS NMR spectra also provide a valuable estimate of the isotropic chemical shifts (δ_{iso}) and the quadrupolar product parameters ($P_Q = C_Q(1+ \eta^2/3)^{1/2}$) for the Na(a) and Na(b) sites at different temperatures, as summarized in Table 1.

Further insight about the third Na resonance is achieved from simulations of the single-pulse ^{23}Na NMR using the DMfit software (Massiot et al. (2002)) that includes a Czjzek distribution for the electric field gradients (d'Espinose de Lacaillerie et al. (2008)) and thereby consider the less-ordered structural environments for these Na sites. The parameters of δ_{iso} and P_Q, determined from the ^{23}Na MQMAS NMR spectra for Na(a) and Na(b), are employed as the starting values for further optimizations. The optimum simulations by least-squares fitting to the ^{23}Na NMR spectra (22.3 T) for the Ca/Si = 1.4 C-S-H samples are also illustrated in Figure 3, resulting in chemical shifts of δ_{iso} = -5.3 to -6.1 ppm and P_Q values of approximately 1.0 MHz (Table 1) for the third Na resonance, denoted as Na(c).

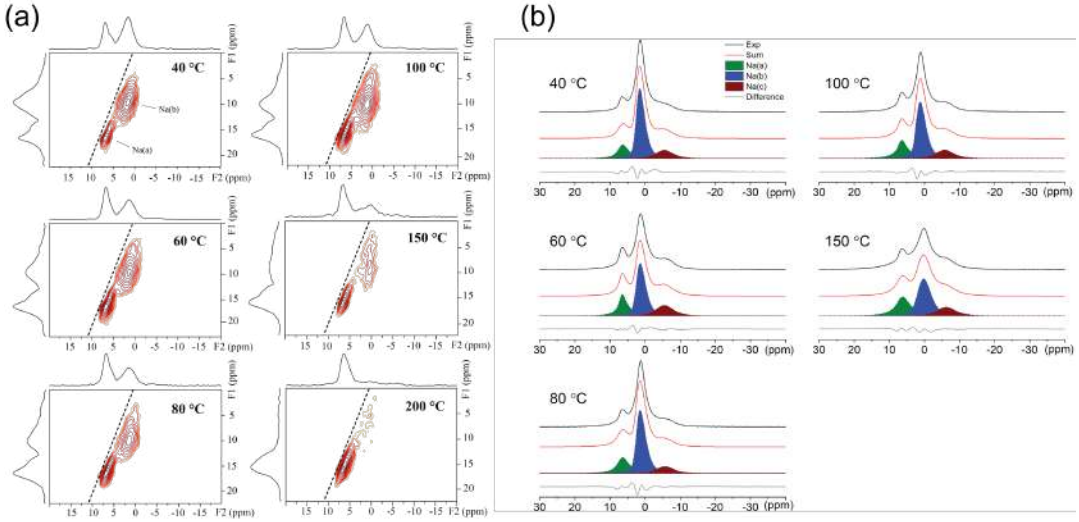


Figure 3. (a) Contour plots of ^{23}Na MQMAS NMR spectra (22.3 T, ν_R = 20.0 kHz) with sum projections in both dimensions for the C-S-H phases with Ca/Si = 1.4 after oven-heating at temperatures of 40, 60, 80, 100, 150 and 200 °C for one hour. The pure chemical shift direction (*i.e.,* P_Q = 0) is indicated by dashed lines. (b) ^{23}Na MAS NMR spectra (22.3 T, ν_R = 20.0 kHz, black lines) of the same C-S-H samples and their optimized least-squares simulations (red lines) corresponding to the sum of three Czjzek distributions shown by the color-filled peaks. Difference plots are given below the simulated spectra.

No variation in P_Q is observed for the Na(c) site upon increasing curing temperature, which suggests that the nearest coordination environments are rather stable and also symmetric due to the small P_Q value. Thus, we assign Na(c) to an interlayer Na site, associated with a fixed number of water molecules, that is not directly bonded to the silicate chains or pairs of silicate tetrahedra in the C-S-H structure, since the local environments are rather symmetric. The δ_{iso} values determined from simulations of the single-pulse spectra for Na(a) and Na(b) are systematically shifted by approx. 0.6 ppm to lower frequency relative to the values determined from the ^{23}Na MQMAS NMR spectra. This difference is ascribed to the two different models used for determination of δ_{iso} and P_Q, *i.e.*, the analysis of the MQMAS spectra assumes single, well-defined sites whereas the simulations of the single-pulse spectra employ a distribution in chemical shifts and quadrupole coupling parameters as outlined by the Czjzeck model. Despite this deviation, similar trends in the variation of δ_{iso} and P_Q are observed for the data from the two methods.

Table 1. ^{23}Na Isotropic Chemical Shifts (δ_{iso}, ppm) and Quadrupolar Product Parameters (P_Q, MHz) for the Distinct Na Sites in C-S-H Phases Synthesized with Ca/Si = 1.4 from ^{23}Na MQMAS and MAS NMR spectra acquired at 22.3 T.

	Na(a)				Na(b)				Na(c)	
	δ_{iso}[a]	P_Q[a]	δ_{iso}[b]	P_Q[b]	δ_{iso}[a]	P_Q[a]	δ_{iso}[b]	P_Q[b]	δ_{iso}[b]	P_Q[b]
40 °C	7.38	1.49	6.80	1.40	3.41	2.27	2.80	2.05	-5.25	0.95
60 °C	7.32	1.35	6.83	1.40	3.36	2.30	2.75	2.10	-5.30	0.96
80 °C	7.25	1.38	6.80	1.40	3.42	2.37	2.80	2.15	-5.45	0.95
100 °C	7.24	1.37	6.80	1.45	3.44	2.44	2.77	2.23	-5.51	1.02
150 °C	7.10	1.31	6.60	1.40	2.92	2.67	2.25	2.45	-5.93	1.06

[a] Values determined from the ^{23}Na MQMAS NMR spectra.
[b] Values determined from simulations of the ^{23}Na single-pulse NMR spectra.

3. Conclusion

The sodium environments in C-S-H phases with low (0.8) and high (1.4) Ca/Si ratios have been analyzed by ^{23}Na MAS and ^{23}Na MQMAS NMR at two different magnetic fields. The ^{23}Na chemical shift is found to reflect the hydration state of the Na^+ ion, as observed by studying C-S-H samples exposed to different de-hydration schemes. Three distinct Na resonances are identified by ^{23}Na NMR, and their ^{23}Na isotropic chemical shifts (δ_{iso}) and quadrupolar product parameters (P_Q) have been determined from ^{23}Na MQMAS NMR and Czjzeck simulations of the single-pulse ^{23}Na NMR spectra. The three distinct resonances are tentatively assigned to a surface Na site surrounded by mobile water molecules, an interlayer Na site associated with the silicate network, and a second interlayer Na site, which is not directly bonded to the silicate tetrahedra in the C-S-H structure.

Acknowledgements

The NANOCEM consortium is acknowledged for financial support to this project. The authors thank the Carlsberg-foundation for an equipment grant (no. CF14-0138).

References

d'Espinose de Lacaillerie, J.-B., Fretigny, C. and Massiot, D. (2008) "MAS NMR spectra of quadrupolar nuclei in disordered solids: The Czjzek model", *Journal of Magnetic Resonance*, 192(2): 244–251.

L'Hôpital, E., Lothenbach, B., Kulik, D.A. and Scrivener, K. (2016) "Influence of calcium to silica ratio on aluminium uptake in calcium silicate hydrate", *Cement and Concrete Research*, 85: 111–121.

Massiot, D., Fayon, F., Capron, M., King, I., Calvé, S.L., Alonso, B., Durand, J.-O., Bujoli, B., Gan, Z. and Hoatson, G. (2002) "Modelling one- and two-dimensional solid-state NMR spectra", *Magnetic Resonance in Chemistry*. 40(1): 70–76.

Renaudin, G., Russias, J., Leroux, F., Cau-dit-Coumes, C. and Frizon, F. (2009) "Structural characterization of C–S–H and C–A–S–H samples—Part II: Local environment investigated by spectroscopic analyses", *Journal of Solid State Chemistry*, 182(12): 3320–3329.

Viallis, H., Faucon, P., Petit, J.-C. and Nonat, A. (1999) "Interaction between Salts (NaCl, CsCl) and Calcium Silicate Hydrates (C−S−H)", *Journal of Physical Chemistry B*, 103(25): 5212–5219.

Yang, S.-Y., Yan, Y., Lothenbach, B. and Skibsted, J. (2021) "Incorporation of Sodium and Aluminum in Cementitious Calcium-Alumino-Silicate-Hydrate C-(A)-S-H Phases Studied by ^{23}Na, ^{27}Al, and ^{29}Si MAS NMR Spectroscopy", *Journal of Physical Chemistry C,* 125(51): 27975–27995.

The 16th International Congress on the Chemistry of Cement 2023 (ICCC2023)
"Further Reduction of CO_2 -Emissions and Circularity in the Cement and Concrete Industry"
September 18–22, 2023, Bangkok, Thailand

Effect of irradiation on Portland cement pastes: impact on mineralogy, mechanical properties, and microstructure

R. Hoarau Belkhiri[1,2]*, S. Poyet[2], M. Neji[1], E. Leoni[3], S. Esnouf[3], A. Dauzères[1], T. Charpentier[4]

[1] *Institut de Radioprotection et de Sûreté Nucléaire (IRSN), PSE-ENV/SEDRE/LETIS, Fontenay-aux-Roses, France r.hoaraubelkhiri@irsn.fr; mejdi.neji@irsn.fr; alexandre.dauzeres@irsn.fr*

[2] *Des-Service de recherche en corrosion et comportement des matériaux (S2CM), CEA, Université Paris-Saclay, Gif-sur-Yvette, France stephane.poyet@cea.fr*

[3] *Des-Service de Physico-Chimie (SPC), CEA, Université Paris-Saclay, Gif-sur-Yvette, France elisa.leoni@cea.fr; stephane.esnouf@cea.fr*

[4] *NIMBE, CEA, CNRS, Université Paris-Saclay, CEA Saclay, F-91191 Gif-sur-Yvette cedex, France thibault.charpentier@cea.fr*

ABSTRACT

In the framework of radioactive waste management, Low and Intermediate Level radioactive waste immobilisation are frequently carried out using cement-based materials; this process implies exposure of the immobilising binder to ionising radiation during setting and hardening. However, available data in the literature is scarce and conflicting, and mechanisms of cement hydration under irradiation still need to be assessed and understood. Contradictions in mechanical properties and mineralogy evolution were reported, likely due to differences in experimental procedures, radiation-induced temperature, and drying phenomena being sometimes overlooked.
In this study, C_3S and CEM I (OPC) pastes undergoing hydration were subjected to gamma radiation at a dose rate of 2.5 kGy/h for 14 days, with a radiation-induced temperature of 35°C. For each material, mineralogy, mechanical properties, and microstructure were determined and systematically compared to two analogous control pastes, cured at 20 and 35°C, respectively. Mineralogy investigation was performed by NMR, TGA, and XRD analyses while microstructural properties were measured by MIP and nitrogen adsorption. Early results suggest that the impact of gamma irradiation on the setting of these materials is limited to a temperature-induced hydration kinetic increase.

KEYWORDS: *Irradiation; Hydration; Cement; Ionizing radiation; Radioactive waste; Repository; Immobilization.*

1. Introduction

From radiotherapy to nuclear-driven electricity generation, radiation, albeit helpful, produces radioactive waste. Such waste contains radionuclides for which no further use is planned or intended implying that their management is a crucial issue in the nuclear industry. Some handling strategies consider transferring problematic and hazardous waste, e.g., Low-Level Waste–Long-Life, Intermediate Level Waste–Long Life, to long-term disposal. Their incorporation into an immobilising binder, acting as a chemical and physical barrier, is needed beforehand; cement-based materials are commonly used for this application. The immobilisation process involves exposure to ionising radiation along the material hydration. Only a few studies have addressed this issue; conflicting findings on both mechanical properties, reported by Glinicki et al. (2021) and Khmurovska et al. (2018), and microstructural ones, as in Burnham et al. (2016) and Khmurovska et al. (2018), were observed. In addition, published studies conducted on gamma-exposed cement paste reported shrinkage and carbonation phenomenon, suggesting gamma heating and drying as their causes. Where similar findings could be proposed for early-age exposition, differences in experimental procedures hinder such conclusion; the extent of irradiation on cement paste hydration remains thus to be determined.

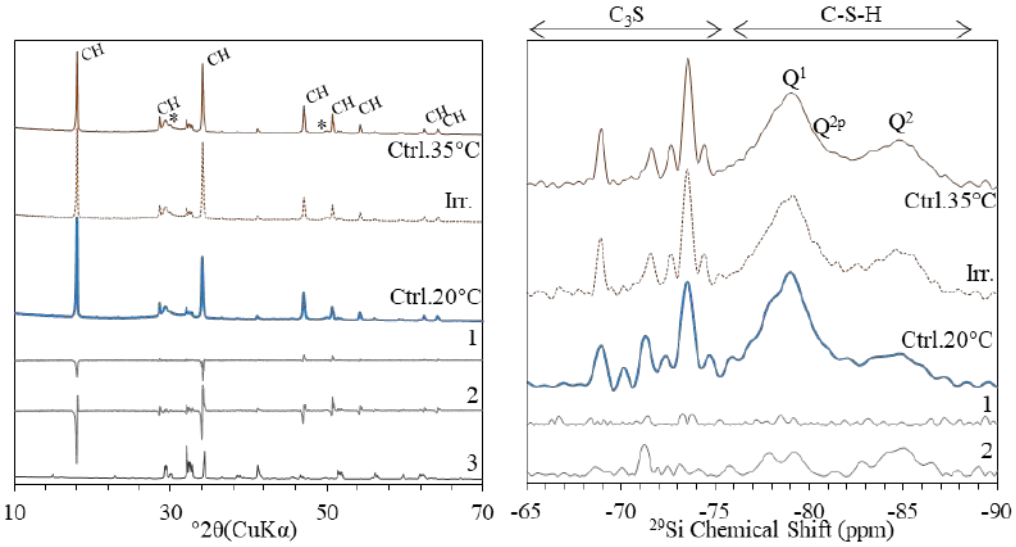
Accordingly, the guideline of this work is to assess potential macroscopic modification, whether directly or indirectly induced by ionising radiation, on the properties of the cementitious matrix and its effect on the resulting hardened binder properties.

2. Methods

The experimental procedure was chosen to avoid carbonation during hydration and to mitigate the radiation-induced temperature influence. C_3S and CEM I pastes were exposed to gamma irradiation in a sealed vessel directly after casting for 14 days; the cumulated dose reached 840 kGy with an average temperature of 35°C within the irradiation room. Two control samples batch were prepared in similar conditions and set to cure at 20 and 35 °C for the exposition duration. Subsequently, sealed vessels were opened, irradiated, and control samples were wrapped in parafilm and then stored in a vacuum bag at room temperature. After the 28th day of hydration, samples were freeze-dried and disposed of likewise until analysis.
The mineralogical study was performed using XRD analyses coupled with TGA and NMR investigations. Samples microstructure was assessed by MIP associated with nitrogen gas adsorption measurement. Mechanical properties were determined by nano and micro indentation testing.
All analyses were duplicated to ensure results consistency and reliability. The authors focused this paper on C_3S investigation through XRD, MIP and NMR results; nonetheless, similar phenomenologies were found on CEM I cement pastes; findings from other analytic techniques considered support the results presented herein.

3. Discussion

The irradiated and associated control sample, cured at 35°C, exhibit a similar XRD pattern (figure 1a) with very slight variations in peak heights and widths that can be attributed to the measurement uncertainty. This observation implies similarity in both proportion and crystallography for the anhydrous and hydrated phases. In contrast, the sample cured at 20 °C shows marked differences in residual C_3S and portlandite (CH) peak heights with respect to the 35 °C one, suggesting a higher hydration degree of the latter. These observations are in agreement with the literature as in Lothenbach et al. (2007). Furthermore, no carbonated phases were identified.

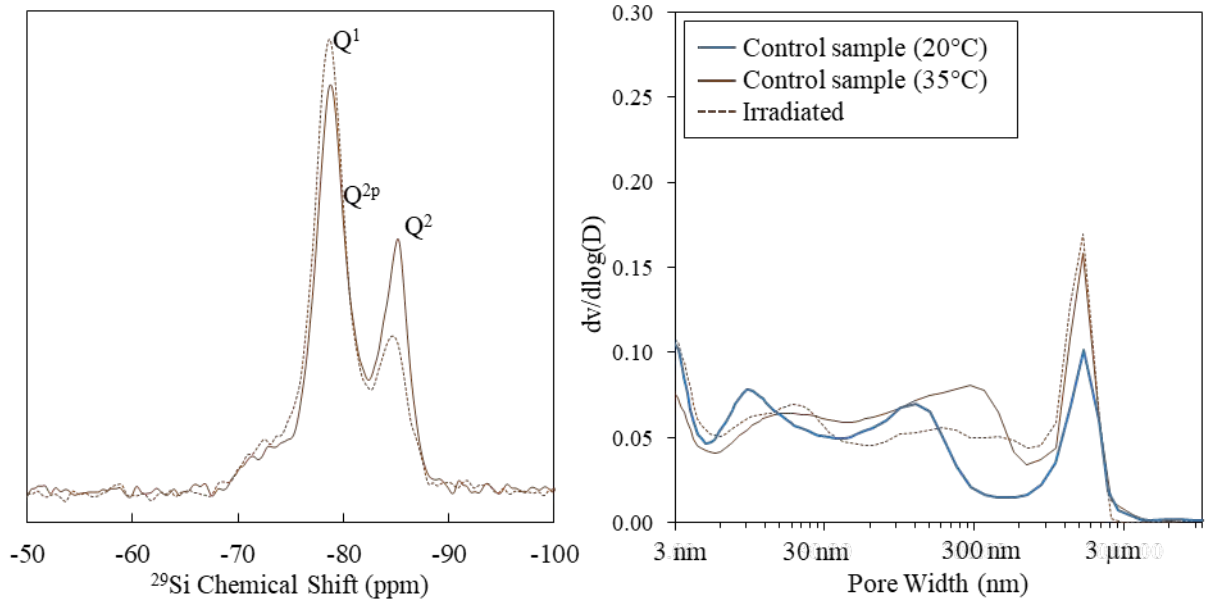


a) XRD pattern gathered *b) MAS ^{29}Si NMR results*

Figure 1 Mineralogical investigation performed on C_3S pastes
1. Diff. plot Irr. - Ctrl.35°C; 2.Diff. plot Ctrl. 35°C - Ctrl.20°C; 3. Anhydrous C_3S.
*Legend: CH → Portlandite; * → C-S-H*

MAS ^{29}Si NMR results suggest a similar atomic structure for both samples cured at 35°C; measured differences do not highlight significant variations in C_3S and C-S-H structure (Figure 1b). This structural

similarity between samples cured at 35°C emphasises the absence of the direct impact of irradiation on their consecutive mineralogical phases.
On the other hand, the difference plot between the two control samples (Figure 1B) features the influence of temperature curing on material structure. The 35 °C control sample measurement indicates a slightly higher resonance between -87 and -82 ppm, adding a lower resonance between -82 and -76 ppm, corresponding to the chemical shift range of Q^2 sites and both Q^1 and Q^{1B}, respectively. These observations are likely to be related to C-S-H chains lengthening on the corresponding sample. Along with this elongation, a decrease in the Ca/Si ratio could occur, as Roosz et al. (2016) indicated. Changes are also noticeable on the resonances corresponding to C_3S, between -75 and -70 ppm, which may suggest a lower dissolution rate during the hydration of the sample cured at 20 °C, in agreement with XRD findings.
However, cross-polarization (CP) MAS ^{29}Si NMR analyses (Figure 2a) revealed a different behaviour of C-S-H bound water after gamma-ray exposure. Irradiated and control 35 °C samples show a different proton environment at the C-S-H vicinity, as measured intensities between - 88 and - 73 ppm revealed. A higher intensity between -74 and -82 ppm and a lower intensity between -83 and -88 ppm, Q^1 and Q^2 sites, respectively, is measured on the irradiated sample with respect to the control one. This difference, unmeasurable in direct acquisition (Figure 1b), suggests a different amount of water bound to C-S-H silicate groups between samples cured at 35°C, despite atomic structure similarity.
The values provided by the MIP measurements (Figure 2b) show that the irradiated sample displays a pore amount, reachable to mercury, lower than the control one. This decrease is between 50 and 700 nm and is limited to this pore range. Such a phenomenon was reported by Glinicki et al. (2021); authors have also noted a refinement of the porosity below 100 nm, which has not been observed here. On the other hand, it should be pointed out that no "new" family of pores can be distinguished from these measurements; it would be a decrease in the accessible capillary porosity without creating measurable defects at the mesoscopic scale. The influence of curing temperature is noticeable when both control samples are considered (Figure 2B), with results falling in agreement with Bahafid et al. (2018) but does not support the discrepancy between irradiated and its control analogue.



a) CPMAS ^{29}Si NMR results *b) Pore size distribution gathered by MIP measurement*

Figure 2 C-S-H bound water and microstructural investigations of C_3S pastes

This effect might be attributed to water consumption caused by radiolysis, i.e., chemical dissociation and decomposition of a water molecule, during the hydration process. A decrease in available water at an early age would thus decrease the W/C ratio of the suspension, influencing the hydrating paste capillary porosity according to mechanisms described in Atahan, Oktar, and Taşdemir (2009) and Chen and Wu (2013).
At present, the mechanisms behind this phenomenon have not yet been elucidated with certainty, although having been rigorously carried out, experimental biases in the measurements cannot be excluded given the

number of analyses carried out and the sample preparation techniques employed.

4. Conclusions

This study addresses the influence of ionising radiation during hydration in the framework of nuclear waste immobilisation. C_3S and CEM I were irradiated immediately after casting, and their resulting properties were subsequently assessed. Discrepancies measured among investigated samples are mainly located between the samples subjected to different curing temperatures. The mineralogical and microstructural differences between the non-irradiated models are consistent with phenomenologies reported in published studies. Aside from the thermally induced variations, no significant differences between the irradiated material and its control analogue could be found. Irradiation effect on both pastes during hydration could thus be limited to a cure temperature increase. No drying or carbonation phenomena under radiation were detected in this study.
Nevertheless, a subtle effect was identified using NMR and MIP measurements. A lower amount of water bound to C-S-H could be measured, in addition to a decrease in accessible capillary porosity. As the phenomena leading to these effects may be synchronous with or after precipitation, investigations on fully hydrated pastes are necessary.

References

Glinicki, Michał A. et al. 2021. 'Gamma Irradiation Sensitivity of Early Hardening Cement Mortar'. *Cement and Concrete Composites*: 104-327.

Khmurovska, Yuliia et al. 2018. 'The effect of gamma-ray irradiation on mechanical properties of early-age cement mortar'. *Stavební obzor - Civil Engineering Journal* 27(3): 357–63.

Burnham, et al. 2016. 'Examining the Effect of Gamma Radiation Exposure in Early Stage of Concrete Curing on Its Strength and Long-Term Durability'. In *Volume 5: Student Paper Competition*, Charlotte, North Carolina, USA: American Society of Mechanical Engineers.

Lothenbach, Barbara et al. 2007. "Effect of Temperature on the Pore Solution, Microstructure and Hydration Products of Portland Cement Pastes." Cement and Concrete Research 37(4): 483–91.

Roosz, C. et al. 2016. "Distribution of Water in Synthetic Calcium Silicate Hydrates." Langmuir 32(27): 6794–6805.

Glinicki, Michał A. et al. 2021. "Gamma Irradiation Sensitivity of Early Hardening Cement Mortar." Cement and Concrete Composites: 104327.

Bahafid, Sara et al. 2018. "Effect of the Hydration Temperature on the Pore Structure of Cement Paste: Experimental Investigation and Micromechanical Modelling." Cement and Concrete Research 111: 1–14.

Atahan, Hakan Nuri, Osman Nuri Oktar, and Mehmet Ali Taşdemir. 2009. "Effects of Water–Cement Ratio and Curing Time on the Critical Pore Width of Hardened Cement Paste." Construction and Building Materials 23(3): 1196–1200.

Chen, Xudong, and Shenxin Wu. 2013. "Influence of Water-to-Cement Ratio and Curing Period on Pore Structure of Cement Mortar." Construction and Building Materials 38: 804–12.

Influence of TiO_2 on the kinetic reaction of white Portland cement suspensions

S.R.A. Dantas[1], M.H. Maciel[2], R.C.O. Romano[2], R.G. Pileggi[2], L.F.M. Sanchez[1]
[1]Structure - uOttawa, [2]LME - USP

Introduction

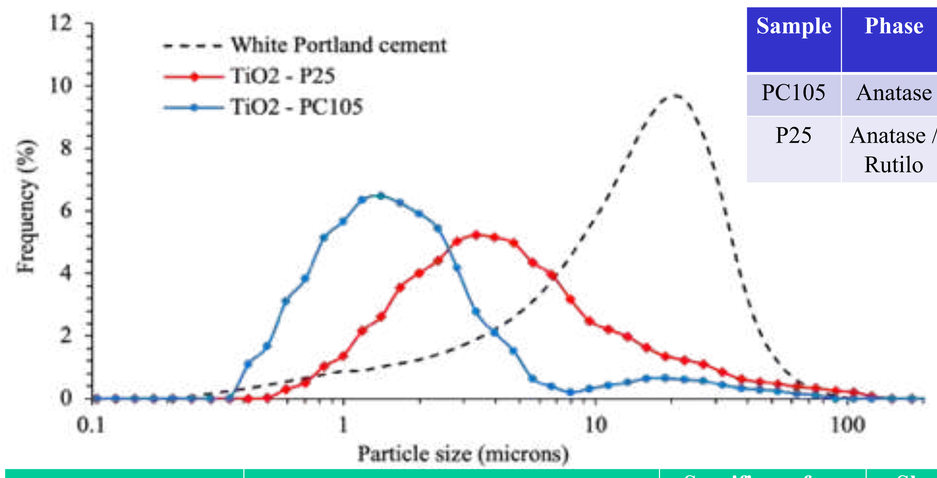
- TiO_2 nanoparticles (NPs-TiO_2) are commonly used in photocatalytic processes.
- NPs-TiO_2 is highly efficient and has high potential in promoting the hydration degree and additional nucleation sites.
- The hydration kinetics of white Portland cement (WPC) with adding NPs-TiO_2 follows dissolution-precipitation dynamics, similar to that of ordinary Portland cement (OPC) but with certain peculiarities.
- In addition to the physical characteristics, the mineralogy of titanium can also affect the hydration kinetics.

Objective

To evaluate the influence of NPs-TiO_2 on WPC suspensions and its participation in the kinetics regarding the type and its physicochemical characteristics.

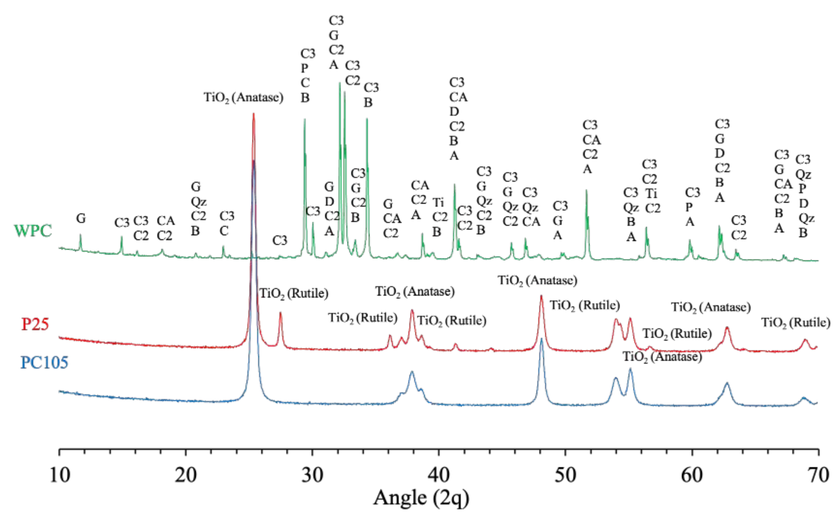
Raw material

❑ Cementitious suspensions materials:
- ❖ WPC (WHITE CEM I 52.5R EN 197-1).
- ❖ Commercial TiO_2 powder samples (P25 and PC105).
- ❖ Reference suspension without TiO_2.
- ❖ WPC with 10% mass replacement by TiO_2.
- ❖ Constant water/solid ratio



Sample	Phase	ICSD code	%
PC105	Anatase	93098	100
P25	Anatase / Rutilo	202243 / 51938	87.8 / 12.2

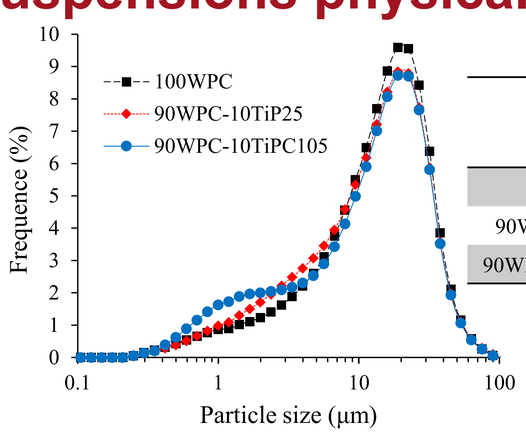
Materials	Characteristics diameter (µm)			Specific surface area (SSA)	Shape Factor	Real density (RD)
	d_{10}	d_{50}	d_{90}	(m^2/g)		(g/cm^3)
WPC	2.60	17.7	19.5	0.86	2.4	3.05
TiO_2 (PC105)	0.66	1.50	4.59	79.8	65.6	3.62
TiO_2 (P25)	1.38	3.90	17.7	49.4	99.3	3.84



Alite / Hatrurite (C3)
Akermanite - Gelenite (A)
Bassanite (B)
Belite / Larnite (C2)
Calcite (C)
C3A-ortho (CA)
Dolomite (D)
Gypsum (G)
Portlandite (P)
Quartz / Cristobalite (Qz)
TiO2 - Anatase
TiO2 - Rutile

Materials	Fe_2O_3	CaO	K_2O	Na_2O	SO_3	SiO_2	Al_2O_3	MgO	TiO_2	LOI
WPC	0.33	67.5	0.61	0.53	2.83	21.6	4.60	0.59	---	2.48
TiPC105	0.03	---	---	---	---	---	0.12	---	99.6	---
TiP25	0.02	---	---	---	---	0.25	---	---	99.7	---

Suspensions physical characteristics

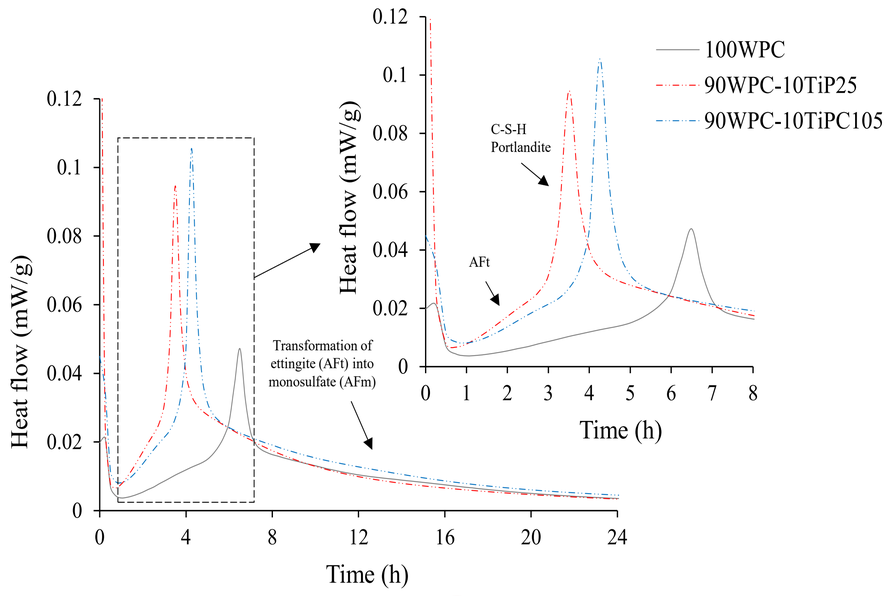


	Real density (g/cm^3)	SSA (m^2/g)
100WPC	3.05	0.86
90WPC-10TiP25	3.13	5.71
90WPC-10TiPC105	3.11	8.75

Methodology

❑ Suspensions preparation:
1. Powder homogenization (manual)
2. Adding water
3. Mechanical high-energy stirring (10,000 rpm) - 1 min.

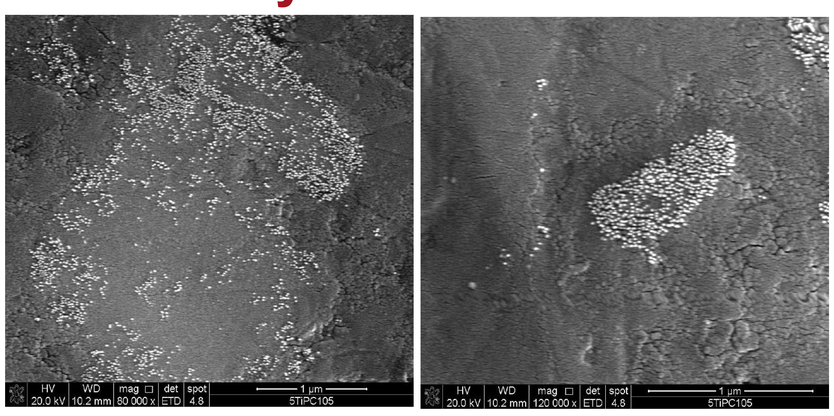
Heat Flow – Chemical reaction



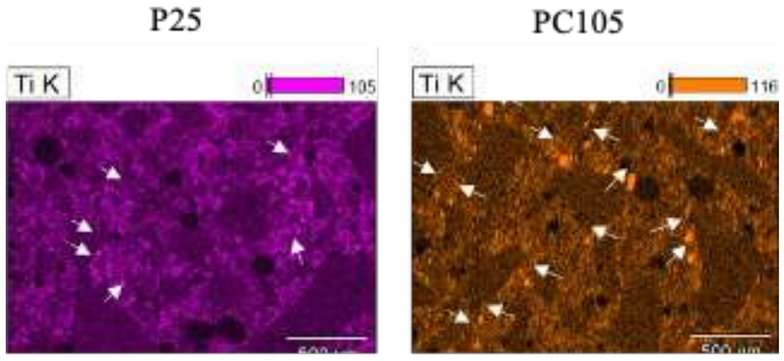
Due to particle characteristics such as SSA, PSD and distinct mineralogy reactions are changed mainly between 1h and 8h after the NPs-TiO_2 addition.

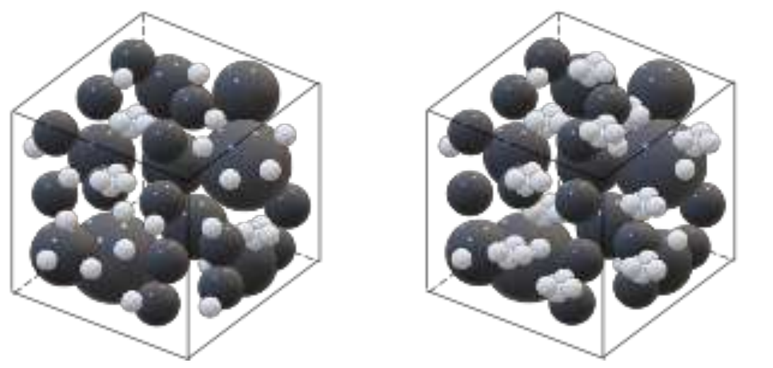
SEM Analysis

The agglomerate sites allow:
- Decrease of the effective surface area.



TiPC105 agglomeration particles





- Decrease nucleation sites for the hydrate formation.
- Interfering in the chemical reaction.
- Early reaction kinetics is lower to PC105 than P25, even with the higher SSA of the first one.

Conclusions

- ✓ The calorimetry results indicate the TiO_2 influence on the Kinect reaction of WPC suspensions;
- ✓ For TiP25 suspension, the hydrate formation Kinect at first hours is more accelerated than TiPC105;
- ✓ The finer titanium (TiPC105) has a lesser effect on early hydration due to its higher agglomeration kinetics, decreasing its effect on hydration kinetics.
- ✓ In general, the influence is decisively more physical than chemical.

Publications

[1] M.S.Döndüren, M.G. Al-Hagri, A review of the effect and optimization of use of nano-TiO_2 in cementitious composites, Res. Eng. Struct. Mater. (2022); [2] M. Pérez-Nicolás, Í. Navarro-Blasco, J.M. Fernández, J.I. Alvarez, The Effect of TiO_2 Doped Photocatalytic Nano-Additives on the Hydration and Microstructure of Portland and High Alumina Cements, Nanomaterials. 7 (2017) 329; [3] F. Sanchez, K. Sobolev, Nanotechnology in concrete – A review, Constr. Build. Mater. 24 (2010) 2060–2071; [4] M. H. Maciel, G. S. Soares, R.C.O. Romano, M. A. Cincotto, Monitoring of Portland cement chemical reaction and quantification of the hydrated products by XRD and TG in function of the stoppage hydration technique, Journal of thermal analysis and calorimetry, 136 (2019) 1269-1284; [5] E. Berodier, K. Scrivener, Understanding the Filler Effect on the Nucleation and Growth of C-S-H, J. Am. Ceram. Soc. 97 (2014) 3764–3773.

µStructure · uOttawa · LME Laboratório de Microestrutura e Ecoeficiência de Materiais – Departamento de Engenharia de Construção Civil · USP

The 16th International Congress on the Chemistry of Cement 2023 (ICCC2023)
"Further Reduction of CO_2 -Emissions and Circularity in the Cement and Concrete Industry"
September 18–22, 2023, Bangkok, Thailand

Early hydration and rheological behavior of the calcium aluminates mixtures in the presence of gypsum

W. Barbosa [1*], E. B. C. Costa[2], and K. F. Portella[3]

[1] *Universidade Positivo, Curitiba – Parana, Brazil*
Email: waleska.barbosa@up.edu.br
[2] *Faculty of Civil Engineering, Federal University of Uberlandia, Uberlandia – Minas Gerais, Brazil*
Email: elianebetania@ufu.br
[3] *LACTEC, Instituto de Pesquisa para o Desenvolvimento de Estruturas Civil, Curitiba – Parana, Brazil*
Email: portella@lactec.org.br

ABSTRACT

The aluminate phases (tricalcium aluminate-C_3A and tetracalcium aluminoferrite - C_4AF) are present in Portland cement and its hydration kinetics is strongly dependent on its relationship with calcium sulphate. The incorporation of calcium sulphate leads to retardation early-age hydration in the aluminates phases of cement preventing a rapid drying and increase of rigidity of the freshly mixed paste. In this study, the synergistic effect of aluminate phases and gypsum ($CaSO_4$. $2H_2O$) in eight binary (C_3A-gypsum; C_4AF-gypsum) and three ternary systems (C_3A-C4AF-gypsum) were investigated. The experiments were isothermal calorimetry, in situ X-ray diffraction, and rheological tests. The effect of calcium sulphate dihydrate content was also studied for the binary systems. Both C_3A and C_4AF systems, the slow initial formation of AFm phase followed by ettringite formation during the period when the sulphate ions are consumed; with the depletion of sulphate ions, the amount of ettringite decreased for formation of AFm phases. For ternary systems, in the higher sulphate ions content, the reaction rate was controlled by the aluminate phase present in greater amount. Pastes with higher C_3A content showed lower flow resistance, viscosity, and yield stress in relation to C_4AF systems. The presence of C_4AF reduced the workability time of the pastes.

KEYWORDS: *Hydration, Kinetics, Rheology, C_3A, C_4AF.*

1. Introduction

The hydration of aluminate phases (C_3A and C_4AF) has significant effect on the setting and workability of cement paste. Gypsum plays a crucial role in adjusting the reaction rate of aluminate phases, which can be delayed by minutes to hours depending on the aluminate to calcium sulfate ratio in cement. The reaction of C_3A with water in the presence of gypsum can be described in three stages according to calorimetry curves: (1) an initial reaction characterized by an initial dissolution peak, followed by a stage of low heat release within the first minutes. It corresponds to the reaction between C_3A and gypsum, yielding a pour crystalline AFm-phase that coats the C_3A particles that are quickly masked by needle-like ettringite precipitates (Geng et al, 2018); (2) a period of slow reaction in which the concentration of sulfate ions decreases, and (3) renewal hydration of C_3A featured by a hydration peak reflecting an acceleration and deceleration period; the ettringite becomes unstable converting to AFm phases. The hydration of C_3A usually does not enter the third period until the exhaustion of solid gypsum in the system (Liu et al, 2020). Recent studies have been developed to understanding and clarify the mechanisms of retardation of tricalcium aluminate in the presence of gypsum (Quennoz; Scrivener, 2012; Myers et al, 2017; Geng et al, 2018; Joseph; Skibsted; Cizer, 2019; Liu et al, 2020). Nonetheless, there is still no consensus. The currently most accepted hypothesis is that the coexistence of calcium and sulfate ions absorbed at the C_3A surface is more likely to dominate the retardation of C_3A hydration in the presence of gypsum (Geng et al., 2018; Joseph et al, 2019;

Scrivener et al, 2019; Liu et al, 2020), rather than the alleged physical barrier mechanism caused by the precipitation of hydration products (Gartner et al, 2001; Minard et al, 2007). According to Scrivener et al (2019), there is no evidence that ettringite is a diffusion barrier. The behavior of hydration of the two aluminate phases is similar (Taylor, 1997; Gartner et al, 2001; Lin et al, 2019). However, it is suggested that the reaction rate of C_3A is higher than that of C_4AF, but Gartner et al (2001) pointed out that this may not necessarily be true because the reactivity of C_3A depends on the alkali content in Portland cement. The ferrite phase has essentially the same role as Al_2O_3 in which iron replaces part of the aluminum in the hydration product to form a solid solution of calcium sulfoaluminate hydrate and calcium sulfoferrite hydrated or hydrated calcium aluminate and hydrated iron calcium solid solution (Lin et al, 2019). Huang, Mu and Wang (2019) pointed out that the Al/Fe ratio in ferrite phases and the gypsum content have a significant influence on the hydration progress of the ferrite phase. The early hydration of C_3A-C_4AF-gypsum systems is not well investigated. It is known that in C_3A-C_4AF-gypsum systems, C_3A phase competes more efficiently for sulfate ions, and with the depletion of gypsum C_4AF reacts to form monosulfoaluminate (Gartner et al, 2001).

The appropriate amount of gypsum required to balance the aluminate phases should be adjusted based on the content, species, and characteristics of aluminates in the cement system (Andrade Neto et al, 2022). It is crucial to understanding the fundamentals of the aluminate phases-gypsum reaction to comprehend the early hydration of cement, primarily because of its effects on the rheology of cementitious matrices. Thus, the main objective of this study is to investigate how the gypsum content can influence the hydration of C_3A and/or C_4AF systems and its impacts on the viscosity of pastes to contribute to knowledge and the development of new cementitious materials.

2. Materials and Methods

The synthesis of C_3A and C_4AF phases and characterization of raw materials were conducted following the procedure described in Barbosa and Portela (2019). Table 1 presents the different formulations that were studied. Distilled water was used for the mixes. For binary systems, the water-to-solid ratio (w/s) was fixed at 0.75 by weight, while for ternary systems a ratio of 1.0 was used since it is the most common ratio used for C_3A pastes. This ratio is enough to fully hydrate the C_3A and promote adequate workability as pointed out by Andrade Neto et al. (2022). The w/s ratio used in this study does not consider the chemically bound water present in gypsum, as it will not be available during mixing and the beginning of the reaction.

Table 1 – Formulations studied.

Mixtures	C_3A_ G1	C_3A_ G2	C_3A_ G3	C_3A_ G4	C_4AF_ G1	C_4AF_ G5	C_4AF_ G6	C_4AF_ G7	AP1_ G8	AP2_ G8	AP2_ G8
C_3A	96.0	85.9	72.8	56.5	-	-	-	-	22.9	36.0	48.0
C_4AF	-	-	-	-	96.0	90.8	82.2	71.5	49.1	36.0	24.0
Gypsum	4.0	14.1	27.2	43.5	4.0	9.3	17.8	28.5	28.0	28.0	28.0
w/s	0.75	0.75	0.75	0.75	0.75	0.75	0.75	0.75	1.0	1.0	1.0

The hydration of aluminate phases and gypsum was monitored by calorimetry at 23°C using an isothermal calorimeter: *TAM Air* from *TA instruments*. The pastes were manually mixed outside the calorimeter, using an L-shaped plastic propeller following this sequence: distilled water was added to anhydrous materials in 10 s and homogenized for 50 s. The samples were introduced into the calorimeter 10 minutes after mixing. The heat flow was recorded for 3 and 120 days according to the reactivity of each mixture.

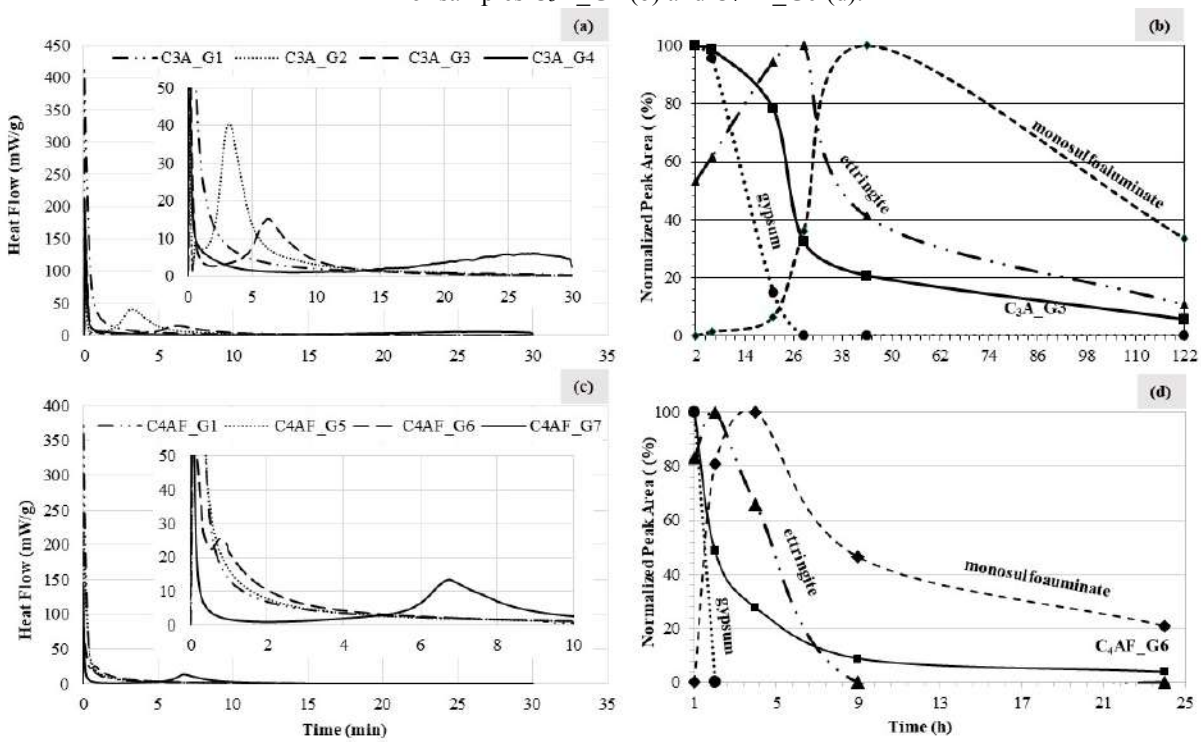
In-situ XRD analyses were performed using a Philips X-ray diffractometer, model X'PERT Pro MPD, at room temperature. The experimental conditions consisted of Cu-Kα radiation (λ = 1,4187 Å), 40 kV and 40 μA, with a 2θ angle range of 7 to 70° and a step of 0.017° 2θ. The identification and further refinement of crystalline phases using the Rietveld method were performed using HighScore 3.0 software. For the in-situ XRD, the anhydrous materials (~3 g of solids) were manually mixed with distilled water according to water-solid ratio presented in Table 1. The sample holder was filled to the brim with a part of the paste and covered with a Kapton film to reduce evaporation of mixing water. Mechanical mixing and rheological tests were conducted following the methodology applied by Barbosa et al (2018).

3. Results

Figure 1 shows the results of isothermal calorimetry and XRD of C_3A and C_4AF pastes with different gypsum contents. The heat flow of the C_3A samples depended on the amount of calcium sulfate used. The increase in gypsum content promotes a reduction in the dissolution of C_3A, which in turn enhances the hydration kinetics, as shown in Fig. 1 (a). Therefore, higher gypsum contents lead to a greater induction period and a widening of the base of the main peak (acceleration and deceleration curve of the reactions), as well as the reduction in the intensity of the heat flow released in this peak. This phenomenon has been observed in previous studies (Quennoz; Scrivener, 2012; Andrade Neto et al, 2022). Figure 1 (b) shows the monitoring of the dissolution and precipitation of phases in sample C_3A_G3 using XRD. It can be seen that the C_3A dissolution is accelerated as gypsum goes extinction. Maximum ettringite precipitation occurs at the end of gypsum dissolution, and the monosulfoaluminate (AFm14) formation begins at this time. Subsequently, ettringite enters a dissolution process, and the sulfates are consumed in the formation of the AFm14 phase. Other phases, such as AFm12 and AFm hydroxide, were also observed. However, these phases show greater influence than other phases, as overlaps occur in the main peak area, making the analysis difficult.

Samples of C_4AF with gypsum showed the same trend as those of C_3A and gypsum, as shown in Fig. 1 (c) and (d). The higher the amount of gypsum, the longer the induction period and the lower the intensity of the heat flow during the acceleration and deceleration period of the reactions, resulting in a widening of the peak base. When examining the formed phases, we can also observe the same relationship in the consumption of gypsum for the formation of ettringite and, consequently, the precipitation of monosulfoaluminate. However, the low gypsum content in this sample resulted in the rapid dissolution of C_4AF.

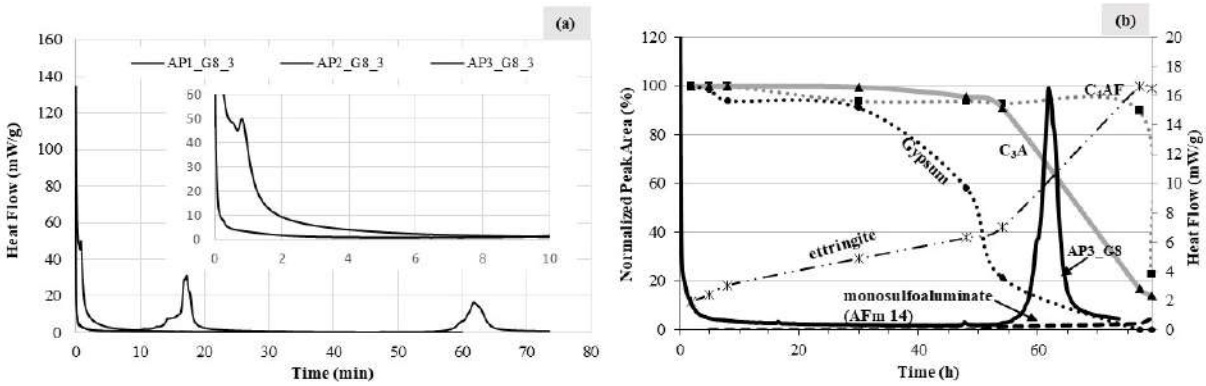
Figure 1 – Heat Flow curve for samples from C_3A_G1 to C_3A_G4 (a) and C_4AF_G1, C_4AF_G5 to G7 (c), as well as XRD for samples C_3A_G4 (b) and C_4AF_G6 (d).



The reaction rate of samples containing aluminate phases followed the trend of the predominant phase. Therefore, the higher the amount of C_4AF (AP_1), the faster the hydration reactions, with the peak heat flow occurring around 1 hour after contact with water, as shown in Figure 2 (a). In the sample with a similar ratio of C_3A and C_4AF (AP_2), the heat flow was slower compared to samples C_3A_G3 and C_4AF_G7, approximately 2.5 times slower, with peak acceleration and deceleration between 5 and 10 hours and using gypsum content equivalent to that used in AP_2 (28%). On the other hand, a higher amount of C_3A (AP_3) resulted in longer time for acceleration and deceleration reactions, with the peak of heat flux occurring at

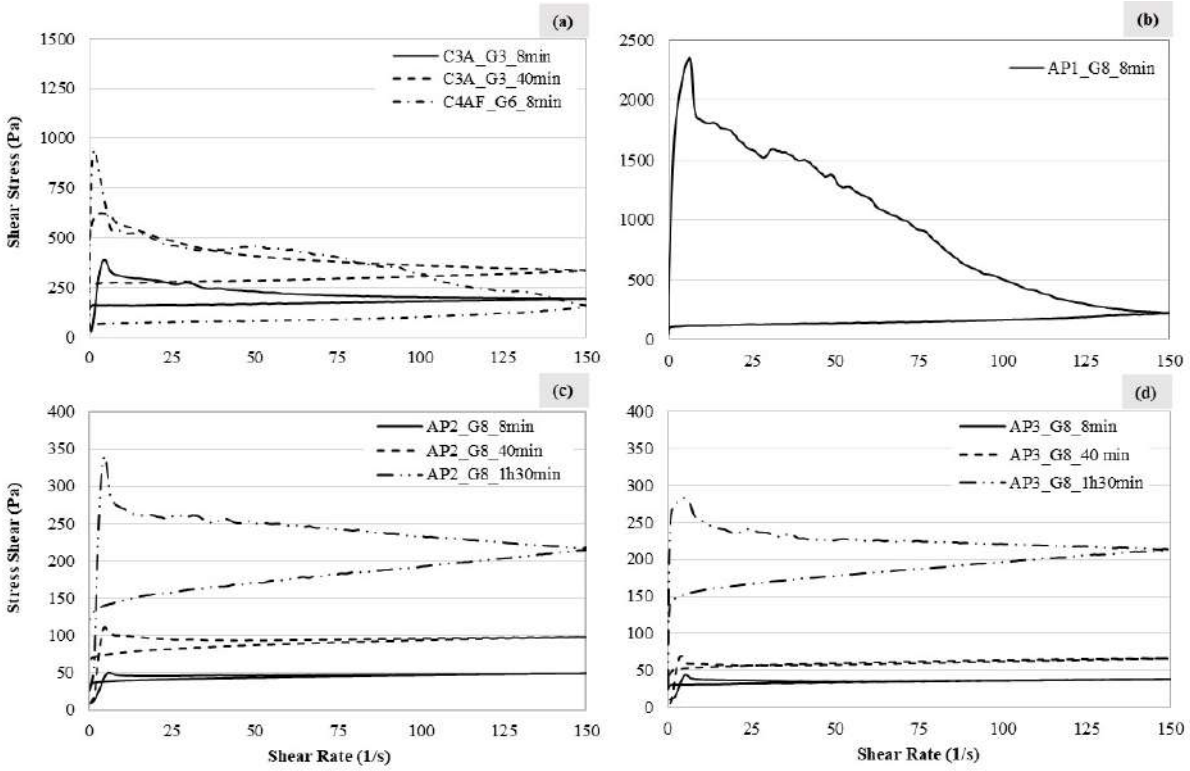
the approximately 62 hours. To understand the hydration kinetics of sample AP_3, we performed the XRD analysis, and the results are presented in Figure 2 (b). The initial dissolution of gypsum and C_4AF is mainly responsible for the formation of ettringite up to approximately 30 hours. From this point, there is an acceleration in the consumption of gypsum and the beginning of the dissolution of C_3A, leading to an increase in the rate of ettringite formation. Monusulfoaluminate slowly begins to form after 55 h of hydration.

Figure 2 – Heat Flow curve (a) for samples AP1_G8, AP2_G8 and AP3_G8 and XRD (b) for sample AP3_G8.



In Figure 3, we can see the rheological results of the flow curves analyzed for some samples. All samples showed the same behaviour in terms of shear rate acceleration (upper curve) and deceleration (lower curve).

Figure 3 – Flow curve for 8 min, 40 min, and 1 h 30 min after mixing: a) C_3A_G3 e C_4AF_G6; b) AP1_G8; c) AP2_G8; and d) AP3_G8.



In the rheological analysis of samples C_3A_G3 and C_4AF_G6, with approximately 28% and 17.8% of the gypsum, respectively, as shown in Fig. 3 (a), we can observe that the flow curve for 8 minutes presents the same trend observed in the XRD, with shorter time for gyspum dissolution and rapid precipitation of ettringite. This fact promotes greater hardening in the C_4AF_G6 sample, making the flow in the paste difficult, and is confirmed in the rheological analysis by the greater area of hysteresis between the acceleration and deceleration curve. However, after breaking the flocculated particles, the shear stress is lower than that of sample C_3A_G3. In the latter, it was still possible to perform the 40 min test, which showed an increase in shear stress and hysteresis area with time, indicating greater consolidation in the

system. After this period (40 minutes) the sample showed greater stiffness than the load cell. The same occurred with sample C_4AF_G6 after 8 minutes of mixing.
In the aluminate and gypsum phase systems (AP) from the flow curve analyses, shown in Fig. (b), (c), and (d), the C_4AF content directly influences the flow resistance. The higher the content, the greater the shear stresses, as well as the hysteresis area in the analyzed periods. The AP1_G8 sample with 49.1% of C_4AF could only be evaluated for a duration of 8 min.

4. Conclusion

The kinetics of hydration in binary systems are strongly influenced by the phase-to-gypsum ratio, where a higher amount of gypsum leads to a slower reaction acceleration process, and the maximum formation of ettringite is directly related to the total consumption of gypsum. In ternary systems, the hydration process is greatly affected by the ratio between the aluminates. A decrease in the C_4AF phase prolongs the induction period and delays gypsum dissolution and ettringite formation. Initially, there is a greater dissolution of C_4AF, and later, the reactions are governed by the dissolution of C_3A. Rheological analyzes followed the same trends observed in calorimetry and XRD, making it a technique with great potential for expanding its use in paste hydration analysis studies.

Acknowledgements

The authors are either grateful for the infrastructure and technical support from Votorantim Cimentos (Dra. Silvia Regina S. S. Vieira and Viviane Magalhães), PANalytical (Luciano Gobbo and Eduardo Macaiba), Institutos Lactec (Betina Lepretti) and Universidade Federal do Paraná/PIPE. The authors would also like to thank the financial resources from CAPES PhD scholarship (process number 1522224) and the CNPq scholarship for DT (process number 302672/2016-8).

References

Andrade Neto, J. S.; Matos, P. R.; De la Torre, A.; Campos, C. E. M.; Gleize, P. J. P.; Monteiro, J. M.; Kirchheim, A. P. (2022) "The role of sodium and sulfates sources on the rheology and hydration of C_3A polymorphs". Cem. Concr. Res., 151: 106639.

Banfill, P. F. G. (1991) Rheology of fresh cement and concrete. Rheol. Rev. 10.4324/9780203473290.

Barbosa, W.; Portella, K. F. (2019) "Synthesis and characterization of mineral phases C_3S, C_2S, C_3A and C_4AF for use in Portland cement". Ceramica 65: 373. (In Portuguese).

Barbosa, W.; Ramalho, R. P.; Portella, K. F. (2018) "Influence of gypsum fineness in the first hours of cement paste: Hydration kinetics and rheological behaviour". Construction and Building Materials 184: 304-310.

Gartner, E. M.; Young, J. F.; Damidot, D. A.; Jawed, A. (2001) *Hydration of Portland cement*. In: "Structure and Performance of Cements", Chapter 3, Editors: Bensted, J.; Barnes, P, 2nd Edition, CRC Press.

Geng, G.; Myers, R. J.; Yu, Y-S.; Shapiro, D. A.; Winarski, R.; Levitz, P. E.; Kilcoyne, D. A. L.; Monteiro, P. J. M. (2018) "Synchronton X-ray nanotomographic and spectromicroscopic study of the tricalcium aluminate hydration in the presence of gypsum". Cem. Concr. Res., 111: 130-137.

Huang, X.; Mu, Y.; Wang, F. (2019) "Brownmillerite hydration in the presence of gypsum: The effect of Al/Fe ratio and sulfate ions". J. Am. Ceram. Soc., 102: 5545−5554.

Joseph, S.; Skibsted, J.; Cizer, O. (2019) "A quantitative study of the C3A hydration". Cem. Concr. Res., 115: 145-159.

Lin, Z.; Xing, W.; Chen, W. (2019) *Cementitious Materials Science: Theories and Applications*. Wuhan University of Technology Press, Wuhan and Walter de Gruyter GmbH, Berlin/Boston.

Liu, X.; Feng, P.; Lyu, C.; Ye, S. (2020). "The role of sulfate ions in tricalcium aluminate hydration: New insights", Cem. Concr. Res., 130: 105973.

Minard, H.; Garrault, S.; Regnaud, L.; Nonat, A. (2007) "Mechanisms and parameters controlling the tricalcium aluminate reactivity in the presence of gypsum". Cem. Concr. Res., 37 (10): 1418-1426.

Quenoz, A.; Scrivener, K. (2012) "Hydration of C_3A-gypsum systems". Cem. Concr. Res., 42 (7): 1032-1041.

Scrivener, K.; Ouzia, A.; Julliand, P. Mohamed, A. K. (2019) "Advances in understanding cement hydration mechanisms". Cem. Concr. Res., 124: 105823

Taylor, H. F. (1997) *Cement chemistry*, Thomas Telford, London.

The 16th International Congress on the Chemistry of Cement 2023 (ICCC2023)
"Further Reduction of CO_2 -Emissions and Circularity in the Cement and Concrete Industry"
September 18–22, 2023, Bangkok, Thailand

Elucidation of hydration reaction of blended OPC by the utilization of alkanolamine-base grinding agent

Sungjin Jung[1], Hyunuk Kang[1], Juhyuk Moon[1,2*]

[1] *Department of Civil and Environmental Engineering, Seoul National University, Seoul 08826, Republic of Korea*

[2] *Institute of Construction and Environmental Engineering, Seoul 08826, Republic of Korea*

* *Corresponding authors. E-mail addresses: juhyukmoon@snu.ac.kr*

ABSTRACT

The grinding agent (GA) can be utilized as a chemical activator, which can result in improvement in the mechanical properties of concrete. The results revealed that the chemical activation induced by GA led to the remarkable enhancement in OPC hydration. To be specific, GA predominantly enhanced the ferrite (C_4AF) hydration at both the initial and later stages. As a result, the accelerated formation of ettringite (Ett) at 1 day and monocarboaluminate (Mc) from 2d were observed respectively. The promoted formation of Mc indicated that GA also indirectly activated the calcite dissolution, which is generally having very low solubility in OPC hydration. Furthermore, the quantified amorphous phases were relatively higher with GA from 1 day, which gradually became more conspicuous as time elapsed. This indicated that the formation of hydrates from OPC hydration was promoted with GA, which was dominantly ascribed to the enhanced C_4AF reaction. Therefore, it was concluded that the enhancement of OPC hydration from the addition of GA is mostly due to the favorable changes in hydration kinetics.

KEYWORDS: *Alkanolamine; hydration; C4AF reaction; heat evolution; Rietveld refinement method*

1. Introduction

Grinding agents (GA) have been widely used in the cement industry to meet the demand for energy savings and reduction of carbon emissions being recently confronted. GA is capable of improving the grin dability of OPC particles in grinding process. Thus, it enables the reduction of the energy required for the production of OPC by adopting an exceptionally small quantity of the GA. Meanwhile, GA also acts as a chemical activator which has the potential to alter the OPC hydration kinetics, thus resulting in the improv ement in the mechanical properties of concrete.

The main objective of this study is to demonstrate the favorable change of hydration kinetics induce d by the alkanolamine GA at both early and later stages in OPC hydration. The improvement of compressive strength of OPC mortar, associated with changed hydration kinetics, was systematically investigated by u sing analytical techniques, such as X-ray powder Diffraction (XRD), quantitative X-ray powder diffractio n (QXRD), isothermal calorimetry. This further investigation of alkanolamine GA would lead to a better u nderstanding of the role of alkanolamine GA as a chemical activator in OPC hydration.

2. Materials and sample preparations

2.1 Material

In this study, the KS L 5201 type Ⅰ OPC was used. The Blaine fineness of OPC was set to be 3700c m^2/g. The chemical compositions of the OPC were obtained using X-ray fluorescence (S8 Tigre, Bruker C o. Ltd., Land Baden- Württemberg, Germany) analysis, and the mineralogical composition was determine d using the Rietveld refinement method (Table 1).

The investigated alkanolamine GA (commercial product name is GA) was supplied by Silkroad C&T Co., Ltd. (Seoul Republic of Korea). The adopted quantity was 0.026wt.% by OPC weight.

Table 1. Chemical and mineralogical composition of the OPC used.

Oxide	CaO	SiO_2	Al_2O_3	Fe_2O_3	MgO	SO_3	K_2O	LOI	
Wt.%	60.1	21.5	6.05	2.66	2.64	2.59	0.73	2.82	
Phases	C_3S	C_2S	C_4AF	C_3A	Gypsum	Arcanite	Periclase	Quartz	Calcite
Wt.%	46.9	27.1	9.8	4.3	3.7	0.8	1.4	0.9	4.8

2.2 Paste and mortar preparation

The pastes were adopted with a water-to-cement ratio of 0.5 for all the experiments. The pastes were stored in the curing chamber with a relative humidity of 60 % at 20 ℃. After curing, the hardened pastes were crushed into fine particles and immersed in isopropyl alcohol and diethyl ether respectively for hydr ation stoppage by solvent exchange method. The crushed pastes were then dried in an oven at 40 ℃ durin g 40 min. The degree of hydration of pastes were analyzed using XRD for curing times of 3h, 16h, 1d, 2d, 3d, 7d, and 28d respectively.

The mortars were prepared by mixing the cement with ISO-standard sand and pure water. The cemen t, water, and sand were mixed by weight ratio of 1: 0.5: 3. The other preparation procedures were identical to the case of pastes preparation.

3. Results and discussion

Fig.1 presents quantified each phase through Rietveld refinement method. The calculated results from Rietveld refinment were normalized to the anhydrous OPC by using chemically bound water. Thus, The mass ratio above 100% in each quantification result is contributed to the chemically bound water.

The most noticeable difference in quantification results was C_4AF between woGA and wGA. Furthermore, in Fig. 2, wGA exhibited a lower quantity of C_4AF even from 3 h. It is generally accepted that C_4AF has a very low reactivity in early hydration due to the formation of a rim of amorphous gel with a high surface area around the C_4AF grain, which hinderes further hydration [1]. The strong complex formed between alkanolamine GA and ferric ions of C_4AF might lead to the higher solubility of amorphous gel surrounding the C_4AF grain, eventually the transport of ferric ions was more readily occured [1]. Thus, it can be estimated that the GA significantly enhanced the solubility of C_4AF through the complex formation.

As a result, wGA exhbited the accelerated ettringite (Ett) formation at 1 d. This indicated that enhanced C_4AF reaction led to the faster release of Al or Fe ions. Meanwhile, after the sulfate depletion, the additional formation of Ett ceased irrespective of GA addition, and then hemi/monocarboaluminate (Hc/Mc) formation was observed due to the presence of calcite contained in OPC [2]. Correspondingly, wGA exhibited the promoted formation of Hc/Mc. This indicated that GA indirectly led to the more active calcite dissolution due to the more release of Al ions from C_4AF [2].

The quantified amorphous was significantly higher in wGA compared to woGA. Especially, it was most conspicuous during 7 to 28 d. However, the difference in silicates (C_3S and C_2S) was negligible between woGA and wGA at 28 d, while the quantified C_4AF showed a significant difference between woGA and wGA. This indicated that the higher quantified amorphous during 7 to 28 d might be contributed to more formation of Fe-containing hydrates, such as Fe-containing siliceous hydrogarnet or hydrotalcite, which generally show very weak signal in XRD pattern [3]. As a result of enhancement in OPC hydration in both early and later stages, the enhanced heat evolution was observed in Fig. 2.

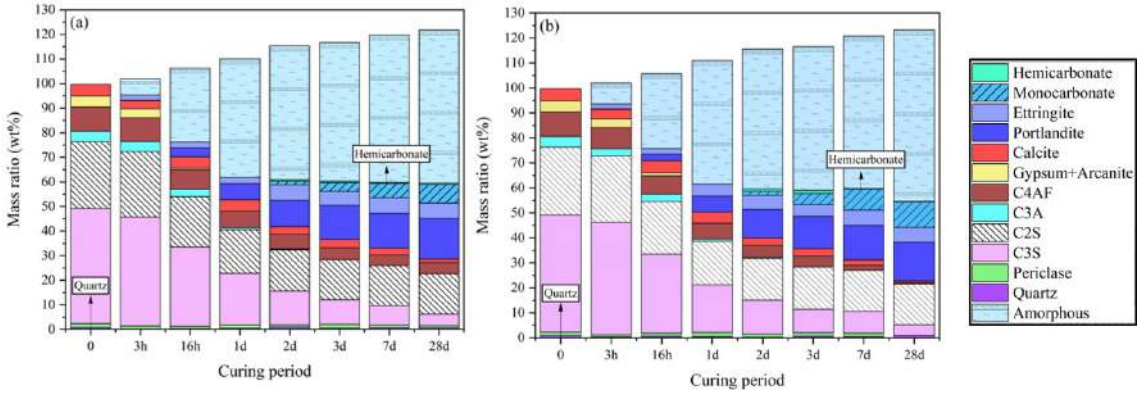


Fig. 1. Results of quantitative analysis of hydrated OPC with and without GA for curing times of 3 h, 16 h, 1 d, 2 d, 3 d, 7 d, and 28 d.

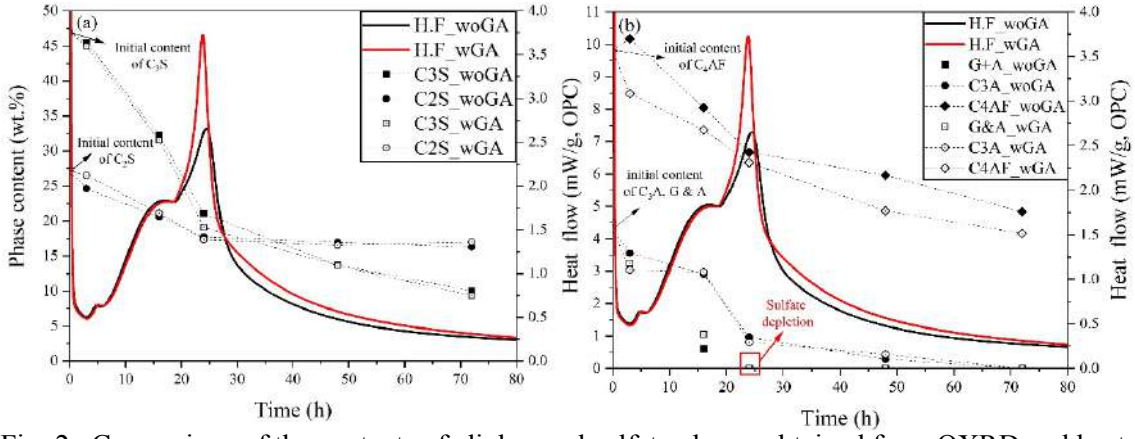


Fig. 2. Comparison of the contents of clinker and sulfate phases obtained from QXRD and heat flow results of OPC hydration at initial periods, (a) silicate phases, (b) aluminate & sulfate phases. G+A: summation of gypsum and arcanite contents, H.F: heat flow.

4. Conclusion

This study substantiated that the GA significantly enhanced the initial hydration as well as later. The most dominantly influenced phase in OPC by incorporation of alkanolamine GA was confimred as C_4AF. Thus, it can be estimated that OPC containing more C_4AF would lead to a greater enhancement in the degree of OPC hydration by utilizing the GA (e.g., ferrite-rich portland cement).

Acknowledgements

This work was supported by the Industrial Strategic technology development program-Development of m anufacturing technology of hardened cement with carbonation curing (RS-2022-00155662, Development of manufacturing and application technology of 1,000 ton/year class hardened cement with carbonation cu ring) funded By the Ministry of Trade, industry & Energy (MOTIE, Korea).

References

1. Gartner, E. and D. Myers, *Influence of tertiary alkanolamines on Portland cement hydration.* Journal of the American Ceramic Society, 1993. **76**(6): p. 1521-1530.
2. Lothenbach, B., et al., *Influence of limestone on the hydration of Portland cements.* Cement and Concrete Research, 2008. **38**(6): p. 848-860.
3. Dilnesa, B., et al., *Fe-containing phases in hydrated cements.* Cement and Concrete Research, 2014. **58**: p. 45-55.

The 16th International Congress on the Chemistry of Cement 2023 (ICCC2023)
"Further Reduction of CO_2 -Emissions and Circularity in the Cement and Concrete Industry"
September 18–22, 2023, Bangkok, Thailand

An insight on the effect of $KAlO_2$ on hydration kinetics and mechanical properties of ternesite

X. Ren[1], L. Liu[1,2*], J. Ye[1], H. Zhang[1], Z. Luo[2] and W. Zhang[1]

[1] *State Key Laboratory of Green Building Materials, China Building Materials Academy, Beijing, China*

Email: renxue968@163.com; liulei_cbma@163.com; yejiayuan2017@163.com; wensheng_zhang01@163.com
[2] *School of Materials Science and Engineering, Zhengzhou University, Zhengzhou, China*
Email:liulei_cbma@163.com; luozhongtao@126.com

ABSTRACT

Potassium aluminate ($KAlO_2$) can be used to accelerate hydration of Portland (PC) and Calcium sulfoaluminate (CSA) cements. Here, the hydration behaviour of ternesite ($C_5S_2\$$) in 0.1, 0.5 and 1.0 M $KAlO_2$ solutions was investigated. Hydration kinetics were measured via isothermal conduction calorimetry (ICC) and scanning electron microscopy (SEM). The reaction products were characterised with X-ray diffraction (XRD) analysis. The results showed that whilst $C_5S_2\$$ hydration kinetics were significantly accelerated in the presence of $KAlO_2$, the resulting pastes with 1.0 M $KAlO_2$ had lower 120 d mechanical strength than the pastes hydrated with water and exhibited severe decay in some cases. An analysis of the hydration products revealed the presence of gypsum in the water hydrated $C_5S_2\$$ pastes, whereas under $KAlO_2$ conditions the main hydration products detected were ettringite. Examination under SEM indicates a significant difference in C-S-H morphology and composition in the presence of $KAlO_2$.

KEYWORDS: *Ternesite; Potassium aluminate; Hydration kinetics; Mechanical strength; Products*

1. Introduction

Alternative clinkers are being developed with decreased environmental footprint and energy consumption that are chemically different from Ordinary Portland Cement (OPC) clinkers. These may result in very significant reductions in limestone use and CO_2 savings (Gartner and Sui (2018)). Belite-Ye'elimite-Ternesite (BYT) clinker, as a promising alternative clinker, is prepared based on the basic mineral composition of Calcium Sulfoaluminate Belite (CSAB) cement clinker by partially replacing belite with ternesite (Hanein et al (2017), Shen et al (2015), Dienemann et al (2013)). Moreover, ternesite ($C_5S_2\$$) has been further discovered to be a reactive clinker phase in the presence of soluble aluminum sources (Montes et al (2018), Shen et al (2021), Skalamprinos et al (2018), Shen et al (2018)). It hydrates, then, in their presence, yielding ettringite and C-S-H respectively. Thus, properly controlling the activity of ternesite in BYT cements can combine the early age strength contribution of Calcium Sulfoaluminate (CSA) cements with the durability of OPC cements.
In the presence of $Al(OH)_4^-$, the pore solution was undersaturated with regard to Ca^{2+}, SO_4^{2-} and SiO_3H^-, which promoted the dissolution of ternesite (Haha et al (2015)). The dissolution of ternesite was accompanied with the release of Ca^{2+} and SiO_3H^- that could consume $Al(OH)_4^-$ to precipitate strätlingite(Haha et al (2015), Bullerjahn et al (2014)). Further dissolution of ternesite promoted the ettringite or calcium monosulfoaluminate hydrate formation. Zhang et al. reported the activation of ternesite hydration by alkali metal ions doping (Li^+, Na^+ and K^+) (Zhang et al (2023)). Potassium aluminate ($KAlO_2$) is an important composition of the alkaline accelerators, which can provide both $Al(OH)_4^-$ and K^+ sources in cement hydration and significantly promote the early hydration of cement (Salvador et al (2016)).

In the present study, to explore the coupling effect of alumina and alkali sources on ternesite in BYT cement, some experiments have been implemented to describe the impact of $KAlO_2$ addition in the pore solution on the resulting hydrates assemblage and microstructure of ternesite.

2. Experimental

2.1 Materials and preparation of ternesite

Ternesite was prepared by sintering a stoichiometric mixture of AR grade $CaCO_3$, SiO_2, and $CaSO_4 \cdot 2H_2O$ by a solid solution reaction process. The mixtures were pressed into 115 mm diameter cylindrical pellets. The prepared pellets were heated at 5 ℃/min from room temperature to 1200 ℃ in an elevator furnace, and holding for 12 h. The pellets were followed by air quenching and ground to pass through a 75 μm sieve. The free lime (f-CaO) content of obtained samples was less than 0.1%, and the quantitative phase analysis result shows that the purity of resulting ternesite was nearly 98%.

2.2 Paste preparation and characterization methods

Four different ternesite pastes were prepared with different solutions: $C_5S_2\$$ mixed with deionized water 0.1, 0.5 and 1.0 M (mol/L) $KAlO_2$ solution, respectively. The liquid to solid mass ratio was 0.4 for all the pastes. Cubic $C_5S_2\$$ pastes (20×20×20 mm) were prepared for microstructure and hydration products test. Then, cubic $C_5S_2\$$ pastes (40×40×40 mm) were obtained for mechanical strength test. The specimens were all removed from the molds after 24 h of initial curing at 20±1℃ and 99% relative humidity, then stored in a climatic chamber under the same conditions until the test age.
The crushed ternesite pastes were stored in ethanol to stop the hydration reaction and then dried in a vacuum oven at 40℃. Finally, the tried samples were ground for X-ray diffraction (XRD) analysis. unground samples were taken for scanning electron microscopy (SEM) observation. Isothermal conduction calorimetry (ICC) was used to monitor the early hydration at 20±1℃. Controlling the liquid/solid of 0.4, all samples were mixed with different solutions into the reaction vessel. Data was recorded until 72 h.

3. Results and discussion

3.1 Isothermal conduction calorimetry (ICC) analysis

The heat flow curves for the hydration of ternesite with deionized water and $KAlO_2$ solutions are shown in **Fig. 1**. An initial exothermic peak (1st peak) appeared mainly corresponding to the heat of dissolution of ternesite. Then, a following dormant period appeared. The 2nd peak appeared mainly attributes to the rapid hydration of ternesite. It could be observed that the intensity of 1st peak was higher for the $KAlO_2$ activated paste. The higher concentration of $KAlO_2$ solution results in higher hydration rate. The cumulative heat evolved was much higher in the case of samples mixed with $KAlO_2$ solutions, especially for 8 h after the beginning of the hydration. The difference in heat released between the deionized water hydrated paste and $KAlO_2$ activated pastes decreased with the hydration process. This indicated that $KAlO_2$ has the greater acceleration effect for the initial hours of ternesite hydration.

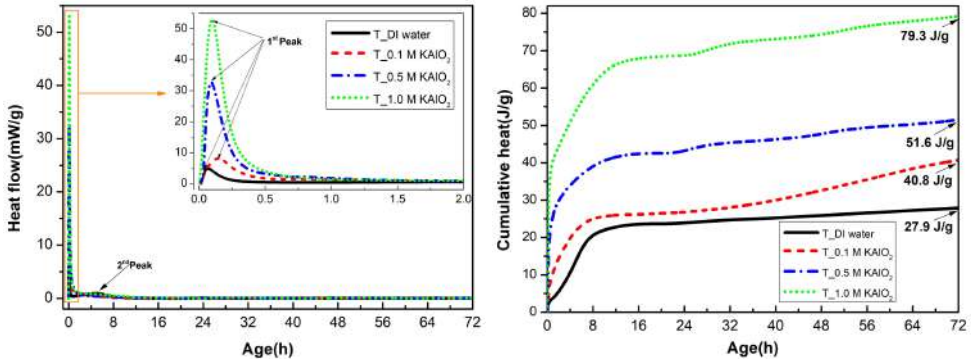


Fig. 1 Calorimetric measurements of ternesite mixed with different solutions.

3.2 X-ray diffraction (XRD) analysis

The diffraction patterns of the hydrated pastes of ternesite mixed with different solutions were presented in **Fig. 2**. $C_5S_2\$$, β-C_2S and gypsum ($C\$H_2$) were identified in all pastes cured for 28 d. It can be observed that the intensities of diffraction peaks for $C_5S_2\$$ decreased during the hydration in all pastes. While, for $KAlO_2$ activated pastes, ettringite (AFt) and portlandite (CH) were identified in addition. Interestingly, the intensities of diffraction peaks for these hydrates increased with the increase of $KAlO_2$ solution concentration. It was proved that the addition of $KAlO_2$ solution promoted the hydration of $C_5S_2\$$ and changed the composition of hydration products.

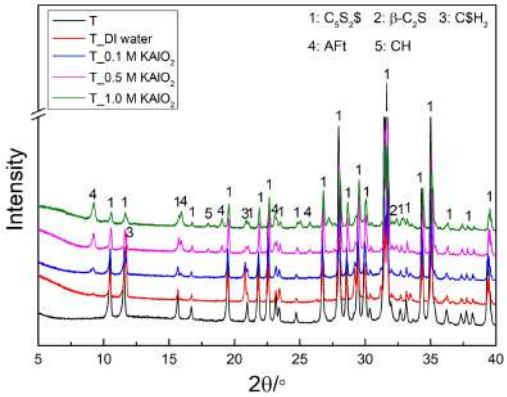
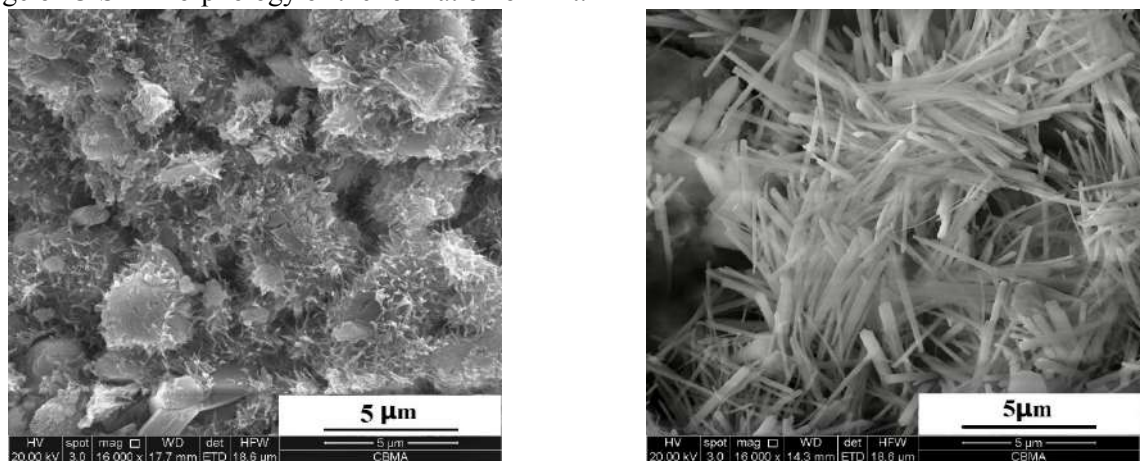


Fig. 2 X-ray diffraction patterns of ternesite and hydrated pastes after 28 days hydration.

3.3 Scanning electron microscopy (SEM) analysis

The morphology of hydrated samples after 28 days hydration are shown in **Fig. 3**. The morphology of C-S-H was fiber-like structure when hydrated with deionized water, as shown in **Fig. 3a**. While needle-like and prismatic structure of products was observed in $KAlO_2$ activated paste, as shown in **Fig. 3b**. The morphological transition of products might be attributed to the change of hydrate compositions, i.e., the change of C-S-H morphology or the formation of AFt.



(a) Deionized water (b) 1 M $KAlO_2$ solution

Fig. 3 SEM of hydrated ternesite pastes for 28 days.

3.4 Mechanical strength

Compressive strength of ternesite pastes with deionized water and $KAlO_2$ solutions cured for different ages is shown in **Fig. 4**. As the hydration developed the strength of $KAlO_2$ activated paste were higher than that of deionized water hydrated pastes in the early ages. For the hydrated paste with deionized water, the compressive strength was 6.8 MPa at 28 days hydration. Whereas 1.0 M $KAlO_2$ activated paste increased from 6.8 MPa to 13.1 MPa at the same curing days. However, the resulting pastes with 1.0 M $KAlO_2$ had lower 60 days and 120 days mechanical strength than the pastes hydrated with water and exhibited severe decay in some cases.

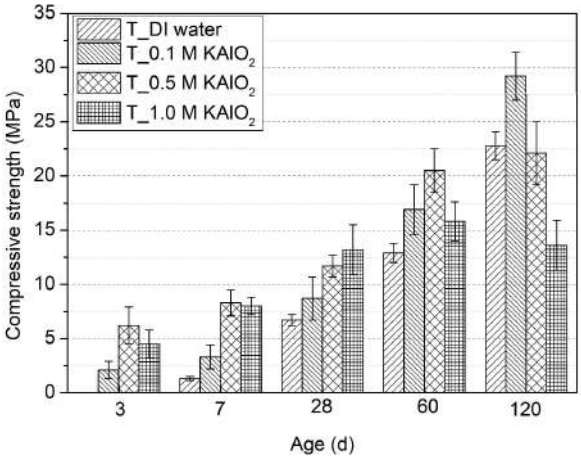


Fig. 4 Compressive strength of ternesite pastes cured for different ages

4. Conclusions

In this study, we investigated the influence of $KAlO_2$ on the hydration of ternesite. The primary findings of the study can be summarized as follows:
(1) The addition of $KAlO_2$ solution significantly accelerated the hydration and raised the degree of reaction of ternesite.
(2) The hydration of ternesite mixed with deionized water leaded to the formation of C-S-H and CH_2 products, whereas the addition of $KAlO_2$ solution promoted the formation of AFt in the paste.
(3) The strength of $KAlO_2$ activated paste were higher than that of deionized water hydrated pastes in the early ages. However, the resulting pastes with 1.0 M $KAlO_2$ had lower 60 days and 120 days mechanical strength.

Acknowledgements

The present work has been supported by the National Natural Science Foundation of China (No. 51832006) and the Key Technologies R&D Program of CNBM (No. 2021HX0304).

References

Bullerjahn, F., Schmitt, D. and Haha, M.B. (2014) "Effect of raw mix design and of clinkering process on the formation and mineralogical composition of (ternesite) belite calcium sulphoaluminate ferrite clinker", *Cement and Concrete Research*, 59: 87-95

Dienemann, W., Schmitt, D., Bullerjahn, F. and Haha, M.B. (2013) "Belite-Calciumsulfoaluminate-Ternesite (BCT)-a new low carbon clinker technology", *Cement International*, 11: 100-109

Gartner, E. and Sui, T. (2018) "Alternative cement clinkers", *Cement and Concrete Research*, 114: 27-39

Haha, M. B., Bullerjahn, F. and Zajac, M. (2015) "On the reactivity of ternesite", in: 14th ICCC, Pekín

Hanein, T., Galan, I., Glasser, F.P., Skalamprinos, S., Elhoweris, A., Imbabi, M.S. and Bannerman, M.N. (2017) "Stability of ternesite and the production at scale of ternesite-based clinkers", *Cement and Concrete Research*, 98: 91-100

Montes, M., Pato, E., Carmona-Quiroga, P.M. and Blanco-Varela, M.T. (2018) "Can calcium aluminates activate ternesite hydration?", *Cement and Concrete Research*, 103: 204-215

Salvador, R.P., Cavalaro, S.H.P., Senacio, I., Figueiredo, A.D. and Pérez, J. (2016) "Early-age hydration of cement pastes with alkaline and alkali-free accelerators for sprayed concrete", *Construction and Building Materials,* 111: 386-398

Shen, Y., Qian, J., Huang, Y. and Yang, Y.D. (2015) "Synthesis of belite sulfoaluminate-ternesite cements with phosphogypsum", *Cement and Concrete Composities*, 63: 67-75

Shen, Y., Chen, X. and Zhang W. (2018) "Influence of ternesite on the properties of calcium sulfoaluminate cements blended with fly ash", *Construction and Building Materials,* 193: 221-229

Shen, Y., Wang, P., Chen, X., Zhang, W. and Qian, J. (2021) "Synthesis, characterisation and hydration of ternesite", *Construction and Building Materials*, 270: 121392

Skalamprinos, S., Jen, G., Galan, I., Whittaker, M., Elhoweris, A. and Glasser, F. (2018) "The synthesis and hydration of ternesite, $Ca_5(SiO_4)_2SO_4$", *Cement and Concrete Composities*, 113: 27-40

The 16th International Congress on the Chemistry of Cement 2023 (ICCC2023)
"Further Reduction of CO_2 -Emissions and Circularity in the Cement and Concrete Industry"
September 18–22, 2023, Bangkok, Thailand

Synthesis of sodium iron silicate hydrate (N-F-S-H)

M. Zhang [1], E. Bernard[2], M.H.N. Yio[1], C.R Cheeseman[1], and R.J. Myers[1,*]

[1] *Department of Civil and Environmental Engineering, Imperial College London, London, UK*

*Email:m.zhang22@imperial.ac.uk, marcus.yio@imperial.ac.uk, c.cheeseman@imperial.ac.uk, *r.myers@imperial.ac.uk.*

[2] *Empa, Laboratory for Concrete and Asphalt, 8600 Dübendorf, Switzerland*

Email:ellina.bernard@empa.ch

ABSTRACT

Alumina production generates a bauxite residue by-product that can be processed into a Fe-rich cementitious material, for example, as a precursor for alkali-activated materials (AAMs). Typically, AAMs use Ca-poor precursors to produce a binder composed of a nanocrystalline zeolite-like alkali aluminosilicate (hydrate) phase, often described as N-A-S-(H) gel. However, the chemistry of AAMs based on Fe-rich precursors like bauxite residue are poorly understood. For example, it is unclear whether Fe can play an analogous role to Al in the binding gel phase.

In this study, results are reported for samples with Fe to Si mol ratios from 0.1-0.3, synthesised at 50°C, targeting the precipitation of a sodium iron silicate hydrate (N-F-S-(H)) phase. NaOH is added to maintain a high pH to increase Fe solubility. At pH values of ~12, Fourier-transform infrared (FTIR) results reveal that initially amorphous FeO(OH) and N-F-S-H are formed. At higher Fe/Si mol ratios, more of these hydrates are formed. FTIR spectroscopy results show that the band related to Si-O internal stretching vibrations in N-F-S-H shifts to lower frequencies, indicating silica network rearrangement and Fe participation in the silica network. We report complementary XRD, TGA and FTIR, results for these samples, and discuss them together to improve understanding of the formation and stabilisation of N-F-S-H.

KEYWORDS: *iron-rich materials, alkaline condition, N-F-S-H gel, micro-analysis.*

1. Introduction

Bauxite residue (BR) is the main by-product of alumina production, which contains iron minerals and other non-alumina bearing bauxite minerals as well as the liquor desilication product from the Bayer process cycle. Currently, less than 3% of the annual worldwide BR production is reused, while there is a considerable amount of cumulatively stockpiled material. Therefore, with the gradual exhaustion of space and social tolerance towards landfilling, there is a global concern about finding an alternative pathway and bulk applications for BR.

Fe-rich resources such as BR can be used as raw materials for Portland clinker production, supplementary cementitious materials (SCMs) to substitute cement, and as a raw material for alternative binders like alkali-activated materials (AAMs) through exploiting its cementitious properties (Peys et al., 2022). As the key element in BR, the role and extent of the contribution of Fe in different utilisation routes should be assessed. Some literature has confirmed the function of Fe in calcium silicate hydrates (C-S-H). Here, it has been shown that the strength of Fe-O ionic bonds is stronger than that of Al-O bond to C-S-H phases (Mancini et al., 2020). A molecular dynamics (MD) simulation has also been developed for the effect of Fe(III) on the structure of C-S-H by Hou et al (2021), indicating that the high Fe concentration is

in tetrahedral coordination in the C-S-H. It was suggested that the iron in AAM reaction products is partially in the Fe^{3+} oxidation state, and that the configuration of this Fe^{3+} is similar to Al in an N-A-S-H or C-A-S-H (Lemougna et al., 2013; Peys et al., 2019). At the same time, MD was used to create N-A-S-H gel models by quenching various oligomers with different Si/Al ratios and configurations to mimic the geopolymerisation process by Guan et al (2022). However, the incorporation of iron-rich materials in AAMs-based models remains unclear and whether Fe can play an analogous role to Al in the binding gel phase is not well understood.

In this study, the formation of N-F-S-H gel was studied and investigated by XRD, TGA, and FT-IR. Goethite (FeO(OH)) was synthesised to improve understanding of the reaction process.

2. Methodology

2.1 Materials and methods

Iron (III) chloride hexahydrate (Sigma-Aldrich ACS reagent, 97%), fumed silica (Evonik, Aeroil 200), and sodium hydroxide (Honeywell ACS Reagent, pellets(anhydrous),>=98%) were chosen as starting materials. Goethite was prepared with a pH value of 12 and cured for 7 days. For synthesising N-F-S-H gel, the total Fe/Si mol ratio varied from 0.1 to 0.3, and sodium hydroxide was used to provide sufficient alkaline conditions with pH values of ~12. All samples were prepared in Polytetrafluoroethylene (PTFE) containers using deionised water, and experiments were performed in a glove box under N_2 to avoid CO_2 contamination. The samples were equilibrated at 50 °C and manually shaken twice per week.

After 7 and 28 days of equilibration, the samples were separated by vacuum filtration using syringes and 0.45 μm filters. The solutions extracted were used to measure pH and stored in a 3 °C fridge for further characterisation. The solids were washed with ethanol (>=99.8% wt.% alcohol) to eliminate adsorbed ions and were then dried by freezing with liquid nitrogen for further 7 days in a freeze dryer. The solid characterizations were performed after further equilibration in N_2-filled desiccators over saturated $CaCl_2$ solution to ensure ~30% relative humidity and NaOH solution to avoid sample carbonation.

For comparison with the N-F-S-H samples, goethite was synthesised at a pH of 12 after an equilibration time of 7 days and 50°C. Here, NaOH solution was prepared at ambient temperature for the pH correction.

2.2 Analytical techniques

XRD data were collected using a Malvern PANalytical Empyrean diffractometer in the Bragg-Brentano configuration, using a Cu X-ray source at 40 mV voltage and 40 mA current. The samples were scanned between 5 and 85 degrees 2-theta with a PIXcel detector. TGA was carried out on ground powder (~20 mg) with a NETZSCH STA 449F5 using a heating rate of 20 °C/min from 35 to 1050 °C. FT-IR spectra were recorded in the mid-region on a Nicolet iN10 MX FT-IR spectrometer between 400 and 4000 cm^{-1} with a resolution of 4 cm^{-1} by transmittance directly on of power (~0.1 g).

3 Results

Fig. 1 shows the XRD results for goethite synthesised at 50 °C and equilibrated for 7 days, and the samples with initial Fe/Si mol ratios of 0.1 and 0.3 equilibrated at 50 °C for 7 and 28 days. Goethite (FeOOH)(ICDD:00-029-0713) and halite (ICDD:01-080-3939) are present in the goethite sample but not in the other four N-F-S-H samples. This indicates that no crystalline FeO(OH) is present in the N-F-S-H samples. However, since some of the solids synthesised had a brownish colour, we expect that some of the samples contain traces of poorly crystalline iron hydroxide phases. In the N-F-S-H samples, a broad hump is present with a peak at 32 degrees 2-theta, indicating the presence of N-F-S-H gel. Since the solids were washed with ethanol to eliminate dissolved ions, the amount of halite remaining is relatively low.

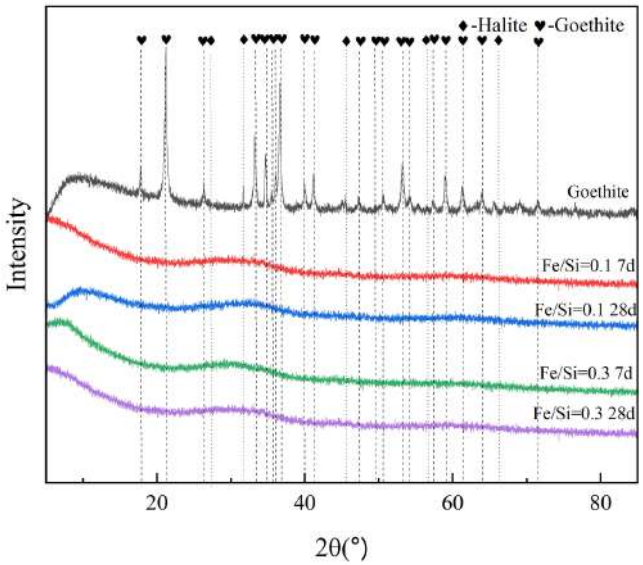


Fig.1. XRD patterns of goethite synthesised at 50 °C cured for 7 days and samples with Fe/Si mol ratios of 0.1 and 0.3 cured at 50°C equilibrated for 7 and 28 days

Fig.2 presents the FT-IR spectra of the N-F-S-H samples equilibrated at 50 °C for 7 and 28 days. Fumed silica, iron(III) chloride hexahydrate, and goethite cured at 7 days are shown for comparison. Unreacted silica can be identified based on the bands at ~1075 cm^{-1} (Si-O stretching band), 803 cm^{-1} (Si-O bending band), and 455 cm^{-1} (Si-O rocking band) (Fig.2). The Si-O stretching band of the N-F-S-H samples is centred at 936 cm^{-1}. This effect can be related to Fe^{3+} binding as a network former in the silicate network. This interpretation is consistent with the results of Peys et al. (2017).

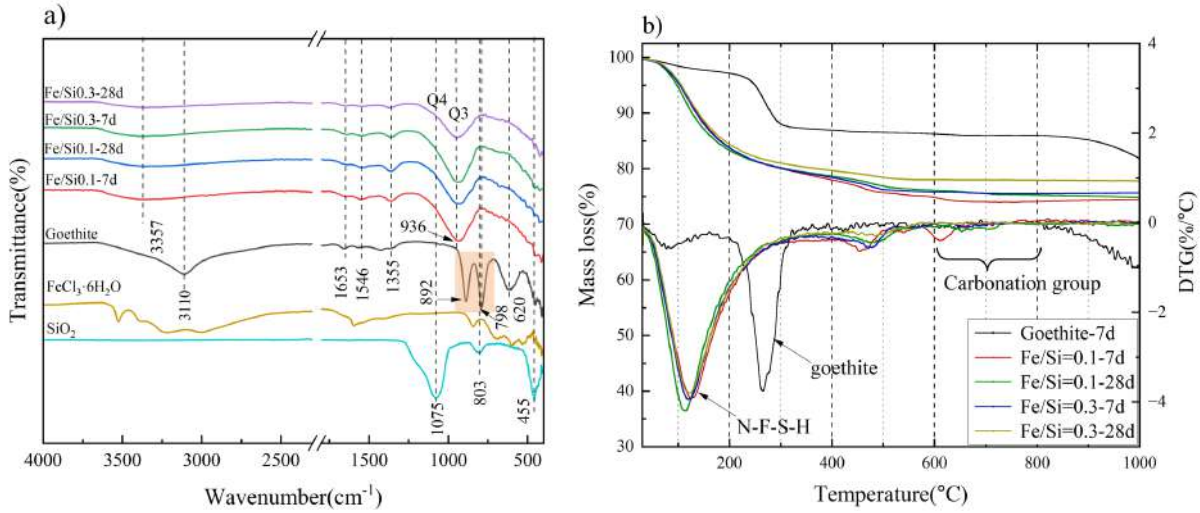


Fig.2 a) FT-IR spectra of the starting materials (fumed silica and Iron (III) chloride hexahydrate), goethite cured for 7 days, and N-F-S-H samples with Fe/Si of 0.1, 0.3 equilibrated for 7 and 28 days. The shaded areas show characteristic regions for goethite. b) Thermogravimetric analysis of goethite aged of 7 days and N-F-S-H samples synthesized at 50 °C, Fe/Si = 0.1, 0.3 aged at 7 days and 28 days, respectively.

In the FT-IR spectrum of the goethite, two intense peaks seen between 700 cm^{-1} and 900 cm^{-1} corresponding to Fe-O stretching bond, and another at 620 cm^{-1}, are characteristic peaks for goethite.
In the FT-IR spectra for N-F-S-H samples, the O-H stretching bond ranged from 3700-3000 cm^{-1} is broader compared to the signal of the unreacted $FeCl_3.6H_2O$ (centred at 3110 cm^{-1}). The broad signal centred at 3357 cm^{-1} in the spectra of the N-F-S-H samples is caused by sorbed H_2O molecules on the solids, usually poorly or nanocrystalline solids as C-S-H or N-A-S-H. The peaks at 1355 cm^{-1} correspond to C=O stretching, indicating slight carbonation of the goethite and N-F-S-H samples during their synthesis, storage, and characterisation. The small band observed at around 1653 cm^{-1} for each sample that is assigned to O-H of the bending H_2O molecules.

The TGA results in Fig.2b show that the N-F-S-H samples contain gel water (as indicated in the FT-IR spectra), which is identified by the peaks at 120 °C (Bernal et al., 2011), suggesting that N-F-S-H might be present in these samples after 7 days of equilibration. Comparing the N-F-S-H samples to TGA data for the goethite sample, which has a well-defined weight loss in the temperature range centred at 265 °C in Fig. 2b, shows that goethite is not present in the N-F-S-H samples. These results are consistent with the XRD measurements (Fig. 1), which confirm the presence of FeO(OH) (reflections peaks in the XRD patterns (Fig.1)) in the goethite samples, and the presence of N-F-S-H gel in the N-F-S-H samples through broad humps with peaks at ~34 2-theta and 936 cm^{-1} by FTIR.

4. Conclusions

In summary, this paper has shown that N-F-S-H gel forms at Fe/Si mol ratios of 0.1 and 0.3 in samples equilibrated at 50 °C in alkaline conditions for at least 7 days. This result is supported by XRD, FT-IR, and TGA measurements, which we describe here.

The XRD result shows that no crystalline goethite is formed in this system. However, since some of the solids synthesised had a brownish colour, we expect that some of the samples contain traces of poorly crystalline iron hydroxide phases. The FT-IR data confirm Fe incorporation in the silicate network since the Si-O stretching band is shifted compared with unreacted fumed silica. The TGA results show the mass loss of goethite centred at 265 °C and that of N-F-S-H samples centred at 120 °C, which is in good agreement with other characterisation techniques mentioned above.

Acknowledgements

The research leading to these results has been performed within the ReActiv project and received funding from the European Community's Horizon 2020 Programme (H2020/2014-2020) under grant agreement n° 958208.

References

Bernal, S.A., Rodríguez, E.D., Mejía de Guti´errez, R., Gordillo, M. and Provis, J.L. (2011) "Mechanical and thermal characterisation of geopolymers based on silicate-activated metakaolin/slag blends", *Journal of Material Science,* 46(16):5477–86.

Guan, X.W., Jiang, L., Fan, D., et al,. (2022) "Molecular simulations of the structure-property relationships of N-A-S-H gels", *Construction and Building Materials,* 329:127166

Hou, D.S., Zhang, W., Sun, J., et al,. (2021) "Structure, dynamics and mechanical properties evolution of calcium silicate-hydrate induced by Fe ions: A molecular dynamics study", *Construction and Building Materials,* 287:122875

Lemougna, P.N., MacKenzie, K.J.D., Jameson, G.N.L., et al. (2013) "The role of iron in the formation of inorganic polymers (geopolymers) from volcanic ash: a 57Fe M¨ossbauer spectroscopy study", *Journal of Material Science,* 48: 5280–5286

Mancini, A., Wieland, E., Geng, G., et al,.(2020) "Fe(III) uptake by calcium silicate hydrates", *Applied Geochemistry,* 113:104460

Peys, A., Isteri, V., Yliniemi, J, et al,. (2022) "Sustainable iron-rich cements: Raw material sources and binder types", *Cement and Concrete Research,*157:106834

Peys, A., Douvalis, A.P., Hallet, V., et al,. (2019) "Inorganic polymers from CaO-FeOx-SiO2 slag: the start of oxidation of Fe and the formation of a mixed valence binder", *Frontiers in Materials,* 6:212

Peys, A., Arnout, L., Hertel, T., et al,. (2017) "The use of ATR-FTIR spectroscopy in the analysis of iron-silicate inorganic polymers", *5th International Slag Valorisation Symposium*

Nucleation of C-S-H from Molecular Dynamics

Xabier M. Aretxabaleta[1]*, Jon Lopez-Zorrilla[1], Iñigo Etxebarria[1], and Hegoi Manzano[1]*

[1] *Fisika saila, Euskal Herriko Unibertsitatea UPV/EHU, Sarriena Auzoa z/g, 48940 Leioa, Basque Country, Spain*

corresponding authors: xabier.mendez@ehu.eus, hegoi.manzano@ehu.eus

ABSTRACT

The nucleation and growth of C-S-H plays a prominent role in cement hydration and the microstructure development of the hardened cement paste. Understanding the nucleation could help us to control the kinetics of the process, designing for instance smart additives. Unfortunately, the characterization and modeling of nucleation is a very challenging problem, and despite recent advances the are still many uncertainties. In this work we present a study of the formation of C-S-H pre-nucleation clusters (PNC) using molecular dynamics (MD) simulations. It is known that the C-S-H nucleation, is a non-classical process taking place in several steps, and the PNCs are form in the initial stages. It has been demonstrated for other minerals like portlandite that the PNC formation may be (des)stabilised, changing the kinetics of nucleation. Therefore understanding the PNCs formation is a key technological step. Using MD simulation with ReaxFF empirical potentials we explore the aggregation of complexes as a function of the solution composition (Ca/Si ratio) and the presence of aluminum complexes. We used realistic system densities based on homogeneous nucleation experiments as starting point. From the MD trajectories we characterize the structure of the PNCs from radial distribution functions and radius of gyration. We discuss as well the speciation of the PNCs and their aggregation free energies.

KEYWORDS: ***C-S-H, nucleation, molecular dynamics, aggregates***

1. Introduction

Calcium silicate hydrate (C-S-H) is the most important binder in cement-based materials and plays a crucial role in their mechanical properties. Understanding the prenucleation pathways of C-S-H can provide insights into the formation and growth of cement-based materials, which is important for designing better and more sustainable construction materials.

Complexes, primary particles and prenucleation clusters play a critical role in the nucleation and growth of materials. These clusters/particles are small aggregates that have not yet reached the size or configuration required to form a stable nucleus, and can be stable. They represent an intermediate stage in the nucleation process, and their formation and behavior can have a significant impact on the final properties and characteristics of the resulting material.

In the case of the C-S-H gel, the structure, properties, and kinetics of the primary particles is still unknown. Recent experimental studies suggested a non-classical nucleation route, yet they focused on the transformation of an amorphous "spheroid" into a well defined C-S-H structure (panels c and d of figure 1). Characterizing the initial primary particles (figure 1b) is very challenging task, and even if in-situ characterization has been possible for other materials like $CaSO_4$ (Stawski et al 2016), atomistic simulation is a common and valuable tool for this scale. Recently, several approaches have started to explore the formation of complexes and aggregates using DFT (Manzano et al. 2007, Yang and White 2021, Li et al. 2022) or MD simulations (Galmarini et al. 2016, Aretxabaleta et al. 2022).

In this study, we investigated the C-S-H prenucleation pathways using molecular dynamics (MD) simulation with the ReaxFF force field. We started from silicate dimers obtained from density functional theory (DFT) calculations and study their aggregation reproducing the experimental compositions. We observed

the formation of elongated aggregates, similar to those observed in the formation of calcium carbonates or sulphates.

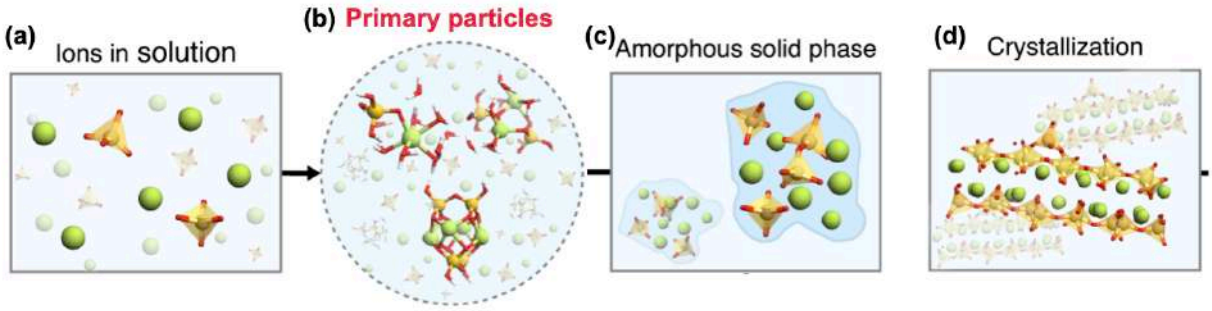


Fig 1. Schematic representation of the C-S-H nucleation stages. This work focuses on the PNC species and primary particles, corresponding to panel (b)

2. Methodolgy

We made 4 different systems by randomly placing 8 $Ca_2Si_2H_{20}$ dimers (see fig 2a) with water and 8 additional $Ca(OH)_2$ groups were added to reach a Ca/Si =1.5. The system reproduces the experimental silicate density estimated in reference (Krautwurst et al. 2018), ~19 times lower than the final silicate density in tobermorite. The dimers were selected as the lower energy ones from a search of the configurational space using evolutionary algorithms (presented in this conference by Xabier M. Aretxabaleta).
The Molecular Dynamics simulation was performed using the LAMMPS package (Singraber et al. 2019) and the ReaxFF force field (Manzano et al 2012). ReaxFF is a reactive force field that allows for the description of chemical reactions and bond breaking and formation. Each simulation was carried our for 6 ns in the NPT ensemble at room temperature and pressure, with a timestep of 0.2fs and the verlet integration method. The thermostat and barostat constraints were applied each 100 and 1000 steps respectively.

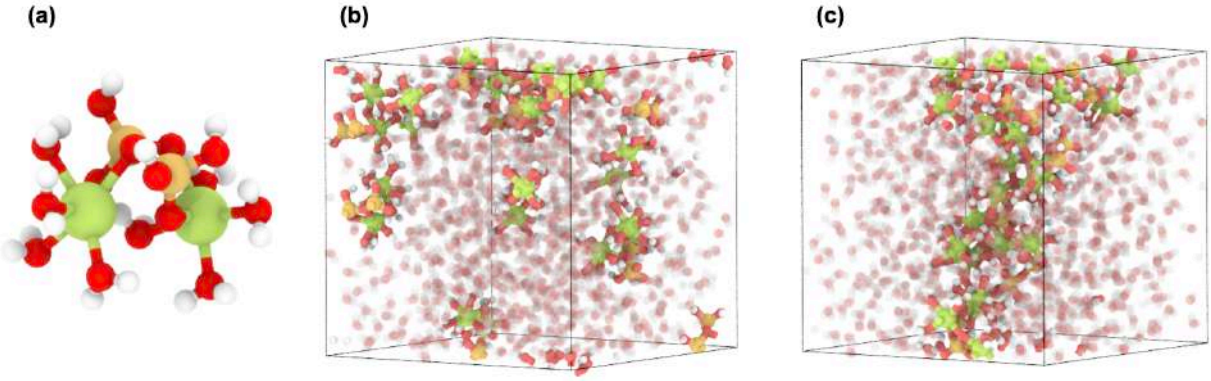


Fig 2. (a) $Ca_2Si_2H_{20}$ dimeric particles used as starting point. (b) Evolution of the system after 0.05 ns and (c) 6 ns. Ca in green, Si in orange, O in red and H in white. The free water molecules are showed as transparent particles.

3. Results

We observe in our simulations a very fast (within 6 ns) aggregation of the dimeric particles to form aggregates. The size of the aggregates, computed by the number of atoms that form it, is in average 6 times larger than that of the dimers (fig 3a). The aggregates do not display any recognizable structure like layers, they are amorphous. This is not surprising as the simulation time is not enough to develop internal order.

The final density of the system is 1.02 g/cc, close to liquid water, which suggest a liquid-like nature of the system.
There is a constant increase of the free water content over time, see fig 3b. We defined as free water any water molecule that is not directly coordinated to a Ca atom. The free water increases due to the aggregation of small clusters by two processes. On the one hand, the Ca ions in solution coordinate to each other or with the $Ca_2Si_2H_{20}$ dimers, sharing OH groups and thus reducing the water molecules in their coordination shell. On the other hand, condensation reactions between the Ca-OH and Si-OH groups take place, generating additional water molecules. This make us suggest that water release could be one of the key steps in the formation of amorphous aggregates and in the posterior crystallization.
The aggregates are mainly elongated aggregates. In fig 3c we show the asphericity of the aggregates as a function of the aggregate size. The asphericity quantifies how much a structure deviates from a symmetric shape, being zero for spheres or cubes and increasing as the shape is less symmetric. For the aggregates in this work it is clear that they tend to be elongated as they increase their size. This has been attributed to a maximization of the water-Ca coordination.

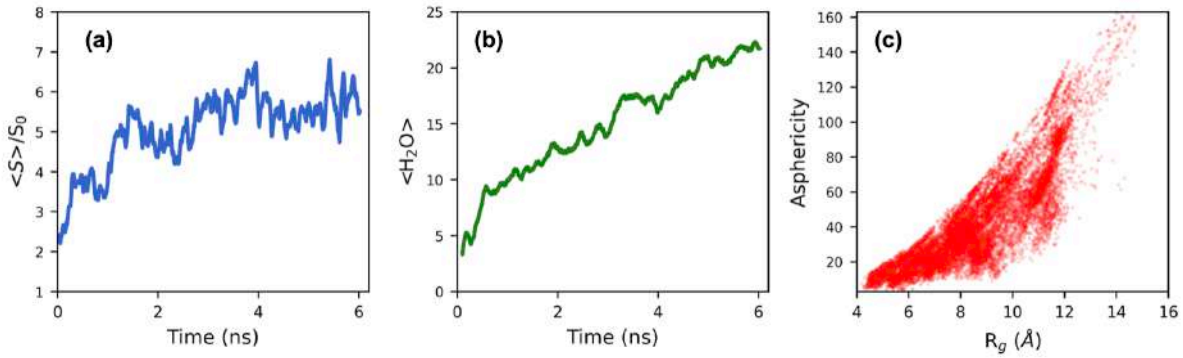


Fig 3. (a) Size of the aggregates over time. (b) Free water increase as the dimeric clusters aggregate due to condensation reactions. (c) Asphericity of the particles as a function of size.

3. Conclusions

In this study, we investigated the C-S-H primary particles using MD simulation with ReaxFF force field. We observed the formation of elongated aggregates, similar to those observed in the formation of calcium carbonate or sulphates. The simulations suggest that condensation reactions and dehydration are key steps in the formation of the aggregates. Our study provides insights into the formation and growth of cement-based materials, which is important for designing better and more sustainable construction materials. Our study also highlights the utility of MD simulation with ReaxFF force field for investigating the prenucleation pathways of materials, which can have a wide range of applications in materials science and

Acknowledgements

This work was supported by the “Departamento de Educación, Política Lingüística y Cultura del Gobierno Vasco” (Grant No. IT1458-22), the "Ministerio de Ciencia e Innovación" (PID2019-106644GB-I00 and TED2021-130860B-I00), the University of the Basque Country UPV/EHU (Colab22/06) and the Transnational Common Laboratory “Aquitaine-Euskadi Network in Green Concrete and Cement-based Materials” (LTC-Green Concrete). The authors thank for technical and human support provided by SGIker (UPV/EHU/ ERDF, EU). X.M.A. acknowledges the financial support from the University of the Basque Country, UPV/EHU (PIF17/118), and J.L.-Z. the financial support from the Basque Country Government (PRE\2019\1\0025).

References

Aretxabaleta, X. M., López-Zorrilla, J., Labbez, C., Etxebarria, I., & Manzano, H. (2022). A potential CSH nucleation mechanism: atomistic simulations of the portlandite to CSH transformation. Cement and Concrete Research, 162, 106965.

Galmarini, S., Kunhi Mohamed, A., & Bowen, P. (2016). Atomistic simulations of silicate species interaction with portlandite surfaces. The Journal of Physical Chemistry C, 120(39), 22407-22413.

Krautwurst, N., Nicoleau, L., Dietzsch, M., Lieberwirth, I., Labbez, C., Fernandez-Martinez, A., ... & Tremel, W. (2018). Two-step nucleation process of calcium silicate hydrate, the nanobrick of cement. Chemistry of Materials, 30(9), 2895-2904.

Li, Y., Pan, H., & Li, Z. (2022). Ab initio metadynamics simulations on the formation of calcium silicate aqua complexes prior to the nuleation of calcium silicate hydrate. Cement and Concrete Research, 156, 106767.

Manzano, H., Ayuela, A., & Dolado, J. S. (2007). On the formation of cementitious C–S–H nanoparticles. Journal of computer-aided materials design, 14, 45-51.

Manzano, H., Moeini, S., Marinelli, F., Van Duin, A. C., Ulm, F. J., & Pellenq, R. J. M. (2012). Confined water dissociation in microporous defective silicates: mechanism, dipole distribution, and impact on substrate properties. Journal of the American Chemical Society, 134(4), 2208-2215.

Singraber, A., Behler, J., & Dellago, C. (2019). Library-based LAMMPS implementation of high-dimensional neural network potentials. Journal of chemical theory and computation, 15(3), 1827-1840.

Stawski, T. M., Van Driessche, A. E., Ossorio, M., Diego Rodriguez-Blanco, J., Besselink, R., & Benning, L. G. (2016). Formation of calcium sulfate through the aggregation of sub-3 nanometre primary species. Nature Communications, 7(1), 11177.

Yang, K., & White, C. E. (2021). Modeling of aqueous species interaction energies prior to nucleation in cement-based gel systems. Cement and Concrete Research, 139, 106266.

The 16th International Congress on the Chemistry of Cement 2023 (ICCC2023)
"Further Reduction of CO_2 -Emissions and Circularity in the Cement and Concrete Industry"
September 18–22, 2023, Bangkok, Thailand

Study of early age hydration behavior of sulfate-rich belite sulfoaluminate cements with anhydrite and gypsum

Xuehong Ren[1], Lixue Cao[1], Jiayuan Ye [1], Hongtao Zhang [1], and Wensheng Zhang [1]

[1] *State Key Laboratory of Green Building Materials, China Building Materials Academy, Beijing 100024, China*
Email: caolixue1216@163.com

ABSTRACT

Excess SO_3 contributes to the formation of cubic ye'elimite in belite sulfoaluminate (BSA) clinker. In this study, BSA clinker containing 0, 5, and 10 wt.% f-$CaSO_4$ were synthesized, and samples mixed with anhydride and gypsum were prepared separately. The early age hydration process and products of these samples were analyzed X-ray diffraction(XRD), thermogravimetric analysis(TGA) and isothermal calorimetry. The BSA clinker with 10 wt.% f-$CaSO_4$ has the minimum initial and final setting time and the highest compressive strength in 3 days. The experiment of XRD and TGA showed that the clinker with more f-$CaSO_4$ expresses higher hydration activity, resulting in higher crystallinity of ettringite. Calorimetry indicated that the effects of anhydrite and gypsum on the hydration of clinker with or without f-$CaSO_4$ showed different patterns. For the BSA clinker containing f-$CaSO_4$, gypsum may slow down hydration kinetics. While the clinker without f-$CaSO_4$, ye'elimite hydrated faster with gypsum than with anhydrite.

KEYWORDS: *Sulfate-rich Belite sulfoaluminate clinker, Early age hydration, f-$CaSO_4$, Gypsum, Anhydrite*

1. Introduction

The issues affecting the global cement business are getting worse. While retaining the effectiveness of cement and concrete, the accompanying CO_2 emissions must be reduced. Conventional Portland cement could potentially be replaced with calcium sulfoaluminate cements (CSAC), a low-carbon cement clinker (OPC). CSAC can reduce CO_2 emissions by around 30% and utilize less limestone than OPC since they have a lower fire temperature. However, the global availability of aluminum and sulfursources suitable for the production of CSA cements is limited. Based on CSAC, belite sulfoaluminate (BSA) cement is made from clinkers having 40-70% C_2S and 20-50% C_4A_3\$. In addition to ye'elimite, belite is a significant mineral phase in BSA cements. In contrast to traditional CSA cement, BSA cement can be produced with less material since industrial by-products including aluminum-rich fly ash, anodization mud, and red mud can be utilized in place of bauxite(Sahu, et al,1994; Arjunan, et al,1999; Pace, et al 2011).

This study synthesized various f-$CaSO_4$ concentrations of sulphate-rich BSA cements from natural (limestone and bauxite) and waste resources (fly ash). Using X-ray diffractometry, the physical phase composition of the synthesized clinker was examined. From a hydration hardening standpoint, the impact of f-$CaSO_4$ in the clinker, externally blended anhydrite and gypsum on the early performance of CSA cement was examined. The goal of this study was to examine how gypsum affects sulfate aluminate cements and to offer insights into the prospective usage of sulfate-rich BSA cements as a replacement for PC in the future.

2. Experimental

2.1 Raw materials

In this experiment, limestone, fly ash, bauxite and hard gypsum were used to fire the BSA clinker. Natural hard gypsum, natural gypsum were used for the external gypsum mixing. The chemical composition of each material is shown in Table 1.

Table 1 Chemical composition of experimental materials/%

Experimental materials	CaO	SiO_2	Al_2O_3	SO_3	Fe_2O_3	Loss
Limestone	55.9	0.61	0.05	0.42	0.19	42.64
Fly ash	4.80	52.47	34.02	0.27	2.92	2.32
Bauxite	/	21.72	52.40	/	7.63	16.00
Anhydrite	38.61	1.03	1.19	49.89	0.25	6.12
Gypsum	24.50	1.72	5.29	29.80	1.96	/
Desulfurization gypsum	29.80	2.89	0.69	44.20	0.41	/

2.2 Synthesis of sulfate-rich BSA clinkers

Experiments were designed and fired into BSA clinker with 0%, 5% and 10% f-CaSO4 content respectively. The early hydration activity of each mineral in the system was considered comprehensively in order to avoid variations in the f-$CaSO_4$ content causing the composition of each of the other mineral phases in the clinker system. As the early strength of CSA is mainly dependent on the rapid reaction of C_4A_3\$, while the hydration activity of C_2S is low and hardly reacts within 3d [7]. Therefore, when designing the mineral composition of the clinker, the content of C_4A_3\$ and C_4AF was kept constant and only the content of C_2S and C\$ was adjusted. The raw materials are accurately weighed and mixed in proportion to each other, put into a test mould and pressed into a wavy round cake of ø12cm x 0.5cm using a hydraulic press. The sample is placed on a platinum sheet and placed in a high temperature silicon-molybdenum rod furnace, where it is heated to 1350°C at a constant rate of 10°C/min and held for 60min.

Table 2 Phase compositions of BSA clinkers/%

Number	C_4A_3\$	C_2S	C_4AF	C\$
C-1	45	45	10	0
C-2	45	40	10	5
C-3	45	35	10	10

3. Results and discussion

The XRD results were quantified by the Rietveld method, as shown in Table 3. Compared to the design composition of the clinker in Table 2, there are differences in each component due to the firing process and raw material composition, etc. Due to the low design content of f-$CaSO_4$ and the phenomenon of volatilisation of anhydrite in high temperature environment, the S content in the system during clinker firing is insufficient, which affects the production of C_4A_3\$, so the C_4A_3\$ content in the clinker of group C1 is 1% lower than the design. When the design content of free gypsum was increased to 5% and 10%, C_4A_3\$ was able to solidify Fe^{3+} under high SO_3 environment, and the C_4A_3\$ content was 1% higher than the design value in both cases. After solid solution of Fe^{3+}, the orthorhombic crystalline type Pcc2 (o-C_4A_3\$) shifted to cubic crystalline type I-43m (c-C_4A_3\$), and the solid solution of Fe^{3+} increased with the increase of SO_3 content in the system. Thus the C3 group has a higher c-C_4A_3\$ content than the C2 group.

Table 3 Rietveld quantitative analysis of actual mineral composition of clinker/%

Number	C_4A_3\$		C_2S	C_4AF	C\$	*Rwp*
	C_4A_3\$-c	C_4A_3\$-o				
C-1	1.21	42.66	46.28	9.83	0.02	7.567
C-2	6.10	40.12	39.76	9.45	4.30	6.005
C-3	8.07	38.63	34.35	9.27	9.43	6.321

The Figure 1. depicts the compressive strength and setting time data for the three clinker groups C1-C3. The C3 group had the shortest initial and final setting times, as well as the highest intensity (3 days). Gypsum significantly accelerates the hydration process of BSA clinker and promotes the development of early strength; however, it can inhibit the early hydration of sulfate-rich BSA cement.

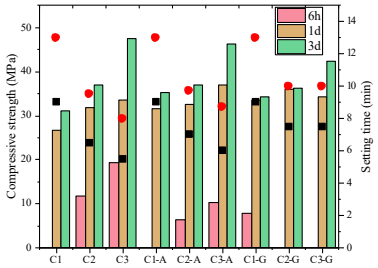


Fig.1 Compressive strength, Initial and final setting time of clinker with different f-$CaSO_4$ content

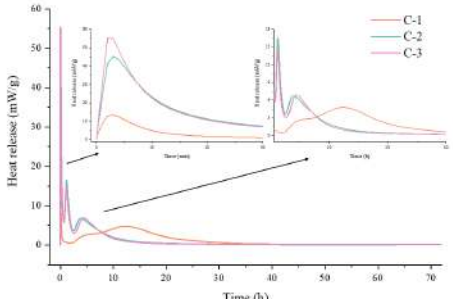


Fig.2 Isothermal conduction calorimetry of clinker with different f-$CaSO_4$ content

Firstly, we studied the hydration of the three groups of clinker itself. The isothermal calorimetric results for the three f-$CaSO_4$ content clinkers over 72h are shown in Figure 2. The first exothermic peak was formed from the start of mixing with water to 10 min for the three sample groups. The initial exothermic peak may be a combination of the initial dissolution of the clinker and precipitation of the hydration products. the presence or absence of f-CaSO4 directly influences the heat flow profile of the samples after the initial peak. the samples in groups C-2 and C-3 containing f-$CaSO_4$ have a higher initial exothermic peak, which may be related to the dissolution and hydration of the highly reactive cubic crystalline $C_4A_3\$$ in the clinker.This stage may result in the formation of calcium alumina (AFt) and an amorphous aluminium hydroxide gel with the reaction equation in equation (1).After the initial exotherm, two exothermic peaks appeared in the samples of groups C-2 and C-3 after only a short induction period, with peaks at 1.15h, 1.16h, 3.7h and 4.1h respectively. The induction period for the clinker of group C-1 was much longer, with hydration starting at 2.4h, followed by a continuous broad exothermic peak of hydration, reaching a maximum exothermic peak at 12.6h. The hydration products at this stage are mainly monosulphur type hydrated calcium sulphate aluminate (AFm), aluminium hydroxide microcrystals, whose hydration reaction is shown in equation (2). In addition, due to the presence of f-$CaSO_4$ in C-2 and C-3, calcium alumina and amorphous aluminium hydroxide may also be present in the samples, and their hydration reactions are shown in equation (3).

$$3\ C_4A_3\$ + 98\ H \rightarrow C_6A\$_3H_{32} + 6\ CAH_{10} + 2\ AH_{3\ \text{amorphous}} \quad (1)$$

$$C_4A_3\$ + 18\ H \rightarrow C_4A\$H_{12} + 2\ AH_{3\ \text{gibbsite-like}} \quad (2)$$

$$C_4A_3\$ + 2C\$ + 38\ H \rightarrow C_6A\$_3H_{32} + 2\ AH_{3\ \text{amorphous}} \quad (3)$$

While the diffraction peaks of AFt and AFm grew stronger with time, the intensity of the calcium sulfate aluminate diffraction peaks steadily decreased. Group C1 had much lower intensity of the early hydration products of clinker diffraction peaks than the other two groups. Over the interval of 10 min. to 2 h., the intensity of the calcium aluminate group C1 diffraction peaks was quite low. When combined with the TG-DTA findings, it can be concluded that less AFt produced than in groups C2 and C3 during this time period and that clinker hydration was low. The diffraction peaks of AFt in group C1 clinker dramatically increased after 2 hours, indicating that the material had begun the accelerated hydration phase. Also, around 12 hours, the XRD pattern began to show AFm diffraction peaks, indicating that the clinker entered the primary hydration reaction stage at this time, which is consistent with the results of the hydration calorimetry.

$$C_G = 0.13 \times Y/S_g \times M\text{-}A \quad (1)$$

C_G: The ratio of gypsum/anhydrite to clinker; Y: The content of $C_4A_3\$$ in the clinker; S_g: The content of SO_3 in gypsum/anhydrite; M: the M value, with reference to sulphoaluminate cements; A: Content of C$ in the clinker.

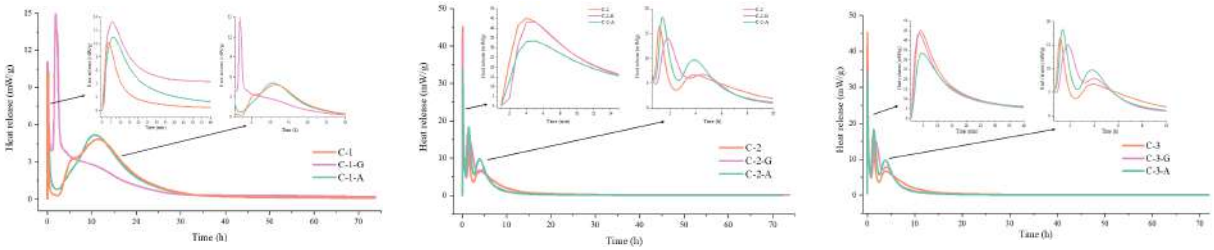


Fig.3 Isothermal conduction calorimetry of C1-C3 with anhydrite or gypsum

Considering the different f-$CaSO_4$ content of each group of clinker, the M value of 0.8 was set and different groups were added with different contents of gypsum and anhydrite respectively according to equation 1. A broad main hydration peak that appeared after 3 hours and reached a maximum after 12 indicate a slow rate of hydration (Fig. 3). As opposed to the sample containing hard gypsum, the system including gypsum dihydrate displayed a greater heat flow profile in the early hours. On the heat flow profile, a maximum had already developed after 1.5 hours. In comparison to clinker without f-CaSO4, the exothermic pattern of hydration in the clinker with f-CaSO4 compounded with gypsum was noticeably different. Gypsum delays the second stage of hydration and does not begin to serve as a facilitator until after the third stage, but hard gypsum speeds up the development of the second exothermic peak of the hydration reaction in the C2 and C3 groups of clinker. The TG-DTG results also show that anhydrite and gypsum has a delaying impact on the early hydration of C2 and C3 samples. According to the XRD results(Figure 4), the blended gypsum in the C3 sample was hardly participate in the hydration process. The rapid dissolution of f-$CaSO_4$ may raises the concentration of Ca^{2+} and SO_4^{2-} ions in the system while inhibiting gypsum decomposition and reaction.

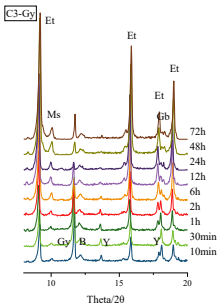


Fig.4 XRD patterns of the early hydration products of C3 samples with gypsum (Et:ettringite,Y:yelimitie,Gy:gypsum,Gb:gibbsite,B:belite,Ms: monosulphate)

4. Conclusions

To determine how f-$CaSO_4$ content affects the early cement characteristics, early hydration rates and hydration products of sulphate-rich BSA cements synthesized from fly ash with various f-$CaSO_4$ levels were examined. The following is a summary of the key findings.

(1) In comparison to regular BSA cement, sulfate-rich BSA cements have increased early hydration activity.

(2) Ye'elimite dissolves more quickly in sulfate-rich BSA cement, which also supplies the calcium and sulfate ions required for the ye'elimite process.

(3) Both gypsum and anhydrite slow down the early hydration of sulfate-rich BSA cement. When f-$CaSO_4$ reaches 10%, gypsum hardly participates in the early hydration of sulfate-rich BSA cement.

References

Sahu S, Majling J.(1994)"Preparation of sulfoaluminate belite cementfrom fly-ash", *Cement and Concrete Research*, 24(6):1065–72.6.

Arjunan P, Silsbee MR, Roy DM.(1999)“Sulfoaluminate-belite cementfrom low-calcium fly ash and sulfur-rich and other industrial by-products”, *Cement and Concrete Research*, 29(8):1305–11.7.

Pace ML, Telesca A, Marroccoli M, et al.(2011)“Use of industrialbyproducts as alumina sources for the synthesis of calcium sul-foaluminate cements”, *Environmental Science & Technology*, 45(14):6124–8.

The 16th International Congress on the Chemistry of Cement 2023 (ICCC2023)
"Further Reduction of CO_2 -Emissions and Circularity in the Cement and Concrete Industry"
September 18–22, 2023, Bangkok, Thailand

Identification of Phases in Cementitious Materials at Critical Elevated Temperatures

L. Zemberekci[1], M.C.G. Juenger[2], and S.D. Nair[3*]

[1] *Cornell University, Ithaca, New York, USA*
Email: lz549@cornell.edu
[2] *University of Texas at Austin, Austin, Texas, USA*
Email: mjuenger@mail.utexas.edu
[3] *Cornell University, Ithaca, New York, USA*
Email: sn599@ cornell.edu

ABSTRACT
Calcium silicate hydrates (C-S-H) and calcium alumina silicate hydrates (C-A-S-H) are temperature-dependent hydration products in which certain stoichiometries are chemically unstable at critical temperatures in the range of (100 – 150 ˚C). This metastability phenomenon is especially important for cement slurries subjected to high-pressure (HP) and high-temperature (HT) environments. Wells drilled to tap into geothermal energy for direct use, a renewable source of energy, tend to operate at this temperature range, directly influencing the early-age cementing operation and the long-term durability of the cemented annulus. At such temperatures, the conversion of cement phases into porous, weaker phases leads to the unwanted migration of fossil fuels along the cemented annulus. Therefore, there is a need to identify the chemical phases that form at critical temperatures in cementitious systems and to improve their stability by designing temperature-tolerant cement-based formulations.
This study focuses on sample preparation and characterization techniques to fundamentally understand phases forming in cement-based slurries cured under HPHT conditions. Phases present in slurries containing various supplementary cementitious materials are compared to synthetic counterparts prepared with varying calcium-to-silica and alumina-to-silica ratios. Scanning electron microscopy in conjunction with energy-dispersive X-ray spectroscopy and X-ray diffraction were employed for this analysis. Identification of phases is an important step toward conducting thermodynamic modeling to predict the long-term stability of phases formed under HPHT environments.

KEYWORDS: *hydration products, pure phase synthesis, chemical reactions, aluminosilicates, high temperature*

1. Introduction

Cementing of sub-surface infrastructure, such as enhanced geothermal systems (EGS), requires durable formulations to maintain the structural integrity of the well. Such formulations are expected to withstand elevated temperatures compared to cement-based materials that are designed for above-ground infrastructure projects. For example, sub-surface hydrothermal reservoirs can reach temperatures up to 500 ˚C, whereas EGS wells tend to operate at a lower temperature range of 80–120 ˚C (Bergen et al. (2022)). This is a critical temperature range that impacts the stability of portland cement hydrated phases. Although there is existing knowledge regarding the composition and morphology of stable geological minerals, there are uncertainties regarding the phases that form under subsurface conditions in cement-based systems. In this study, we aim to identify these phases that form in supplementary cementitious materials (SCM)-containing cement samples with the long-term goal of evaluating their thermal stability.
In a previous study, the rheological behavior of slurries with varying aluminum oxide and silicon dioxide compositions was systematically modified with retarders and superplasticizers to achieve appropriate pumping times, while maintaining acceptable 2-day compressive strengths at 80–120 ˚C and 24 MPa (Zemberekci et al. (2022)). For example, at these elevated temperatures and under high pressure, SCMs can enable the formation of tobermorite, a calcium silicate hydrate (C-S-H) morphology that remains stable

over long timescales up to 150 ˚C (Kalousek (1955)) along with the formation of calcium alumina silicate hydrates (C-A-S-H). Additionally, we explore sample preparation for the synthesis of phases that form under high-pressure (HP) and high-temperature (HT) conditions. This work is a step towards correlating micro-scale observations with the long-term performance of cementitious materials exposed to extreme subsurface environments.

2. Materials and Methods

Class H cement, Class F fly ash, and ground granulated blast furnace slag were used in this study, and their oxide compositions are shown in Table 1. Blended cement slurries with 17.5% fly ash and 17.5% slag by weight of cement at a water-to-cementitious materials ratio of 0.3, with naphthalene-based superplasticizer and sodium glucoheptonate, were prepared according to American Petroleum Institute standard 10B-2. Slurries were cured under downhole EGS conditions in 5.1×5.1×5.1 cm^3 molds at a pressure of 24 MPa and temperatures of 80 ˚C and 120 ˚C for 2 days. At 2-days cubes were tested for compressive strength.

Table 1. Cement and supplementary cementitious materials oxide analyses

	CaO (%)	SiO_2 (%)	Al_2O_3 (%)	Fe_2O_3 (%)	Na_2O (%)	K_2O (%)	MgO (%)	SO_3 (%)	Loss on Ignition
Class H Cement	63.6	21.5	3.2	4.5	0.27	0	2.7	2.9	1.1
Slag (Grade 100)	39.0	37.0	9.0	0.8	0.19	0.56	9.2	2.1	1.4
Class F Fly Ash	12.4	54.3	21.0	5.0	0.37	1.00	2.6	0.6	0.4

To track the ratios of elements from phases that form under EGS conditions, ex-situ characterizations were performed on fractured samples following previously established procedures (Stutzman and Clifton (1999)). According to the discussion in Winnefeld F. (2016), ethanol or isopropyl alcohol have been found to be better solvents than methanol and acetone to stop hydration. For scanning electron microscopy (SEM), the samples were epoxied and polished for backscattered imaging only. X-ray powder diffraction (XRD) patterns were obtained using Cu-K_α radiation on a fractured sample crushed with a pestle and mortar, with the addition of rutile for quantitative analysis.

After the elements and hydration products in cement slurry samples cured at 80 ˚C and 120 ˚C were identified, synthetic phases were produced under HT and HPHT conditions. Steps laid out in previous work by Williamson et al. (2018) regarding the formation of synthetic phases at lower temperatures were followed in this research for higher temperatures. Sample preparation was carried out entirely inside a nitrogen-filled glovebox. Colloidal silica suspension (SiO_2, 50 wt. % in H_2O) with a surface area of 140 m^2/g, aluminum oxide (Al_2O_3) with a particle size < 50 nm, and calcium carbonate ($CaCO_3$, >99%) were used. Decarbonated and degassed Milli-Q water was used to disperse all particles. Calcium oxide (CaO) was synthesized at 1000 ˚C for 12 hours. The sintering profile of mono calcium aluminate ($CaAl_2O_4$ or CA) was as such: Al_2O_3 and $CaCO_3$ were ball-milled dry and then reacted at increasing temperatures of 800 ˚C for 2 hours, 1000 ˚C for 4 hours (5 ˚C/min), 1400 ˚C for 8 hours (4 ˚C/min) then cooled down to room temperature (5 ˚C/min) (Yang et al. (2021)).

All phases were synthesized for 2 days to match the curing conditions of the cement slurry. Two different preparation procedures were explored in this study as shown in Table 2. 50 ml tubes were sealed in the N_2 glovebox and then rotated at 80 ˚C under ambient conditions. Additionally, samples were also prepared under hydrothermal conditions at 120 ˚C under pressure. The samples at 120 ˚C were placed in a vacuum oven, where the vacuum was maintained at –29 mm Hg. XRD patterns were obtained on the final synthesized product after washing with ethanol and drying in the vacuum oven at 70 ˚C for ~ 12 h.

Table 2. Synthesis conditions of C-A-S-H samples

Temperature	Pressure	Ca/Si	Al/Si	Atmosphere	Synthesis Method
80 ˚C	0.1 MPa	1.0, 2.0	0.05	Ambient	Continuously rotated at 50 rpm
120 ˚C	≤ 3 MPa	1.0, 2.0	0.05	Vacuum	Vacuum oven, stationary

3. Results and Discussion

3.1 Assessment of Cementitious Phases under HPHT EGS condition

This section focuses on the assessment of phases forming in real samples that were cured under EGS conditions. With 35% replacement of cement with SCMs by weight of cement, the compressive strengths of the cured specimens were measured to be 66.4± 2 MPa at 80 ˚C and 66.1± 2.3 MPa at 120 ˚C. Figure 1 displays the SEM results of a specimen cured at 80 ˚C and 24 MPa. The morphology of hydration products can be seen in Figure 1 (a), where CH can be identified with its characteristic hexagonal crystal structure along with the dominant presence of calcium in the EDS map shown in Figure 1 (b).
C-A-S-H is specifically identified with a distribution of silicon, aluminum, and calcium in the EDS maps (Figure 1 (b)). The average ratios of formed C-A-S-H were obtained via EDS patterns at multiple locations and were found to be in the range of Ca/Si ≃ 2–2.4 and Al/Si ≃ 0.03–0.05, where an example spectrum is shown in Figure 1 (c).

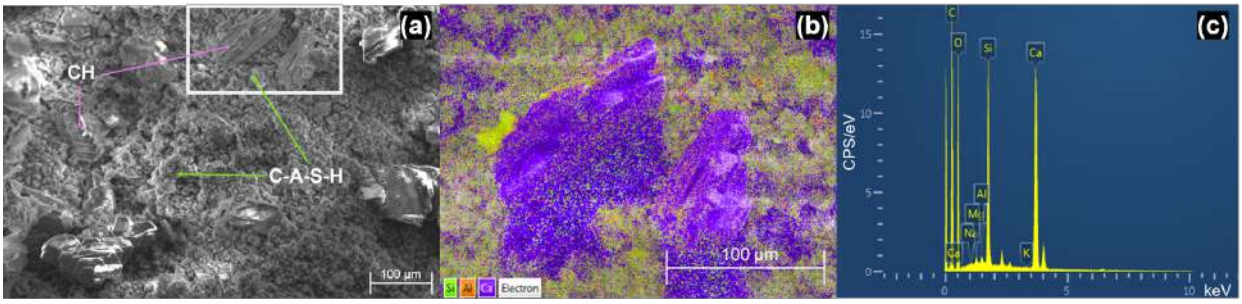


Figure 1. a) SEM of an unpolished fractured sample cured at 80 ˚C and 24 MPa showing the morphology of C-A-S-H and CH b) an EDS map showing the distribution of Ca (purple), Si (green), and Al (orange) over a selected region, c) an EDS pattern a polished sample cured under the same conditions showing Ca, Si, and Al with apparent concentrations of 31.56, 14.39, and 0.46, respectively.

3.2. Characterization of HT/HPHT Synthetic Phases

The C-A-S-H and CH phases were synthesized according to the procedure described in Section 2 by selecting appropriate Ca/Si and Al/Si starting ratios from the EDS spectra obtained on samples cured under EGS conditions. The XRD patterns of the synthesized phases are illustrated in Figure 2(a) for a 2θ range of 5–45˚. The phases of synthesized materials were first selected via Jade Software and existing literature (L'Hôpital et al. (2015); Myers et al. (2015)). The patterns demonstrate the dependence of CH on the starting Ca/Si ratio (PDF #00-004-0733). A Ca/Si ratio of 1 showed little to no CH at both temperatures, whereas the amount of CH significantly increased with a ratio of 2. At 120 ˚C the intensity of CH peaks was higher relative to 80 ˚C, indicating the preferential formation of CH over C-S-H/C-A-S-H at elevated temperatures. Since Al/Si was kept constant, the formation of CH could be independent of the amount of aluminum but was not investigated in this study. It is noteworthy to mention that peaks for CH were identified in the cement slurry sample with 35% SCMs cured at 80 ˚C (Figure 2(b)). CH is detrimental to the integrity of hardened cement slurries as it has an adverse effect on strength at all temperatures (Bergen (2022)).
Characteristic peaks for a 14 Å tobermorite structure (PDF# 00-029-0331, a high-temperature phase of C-S-H) were identified in the XRD patterns shown in Figure 2. Although 11 Å tobermorite and other crystalline stoichiometries have been reported in literature as in Myers et al. (2015), they were not identified in both the XRD patterns for the synthesized phases and the cement slurry samples studied here. In the tobermorite structure, silicon sites could be substituted with aluminum, and the substitution rate is dependent on temperature (Yang et al. (2021); Myers et al. (2015)). Current studies are underway to determine the elemental composition of the synthesized tobermorite and other amorphous phases.

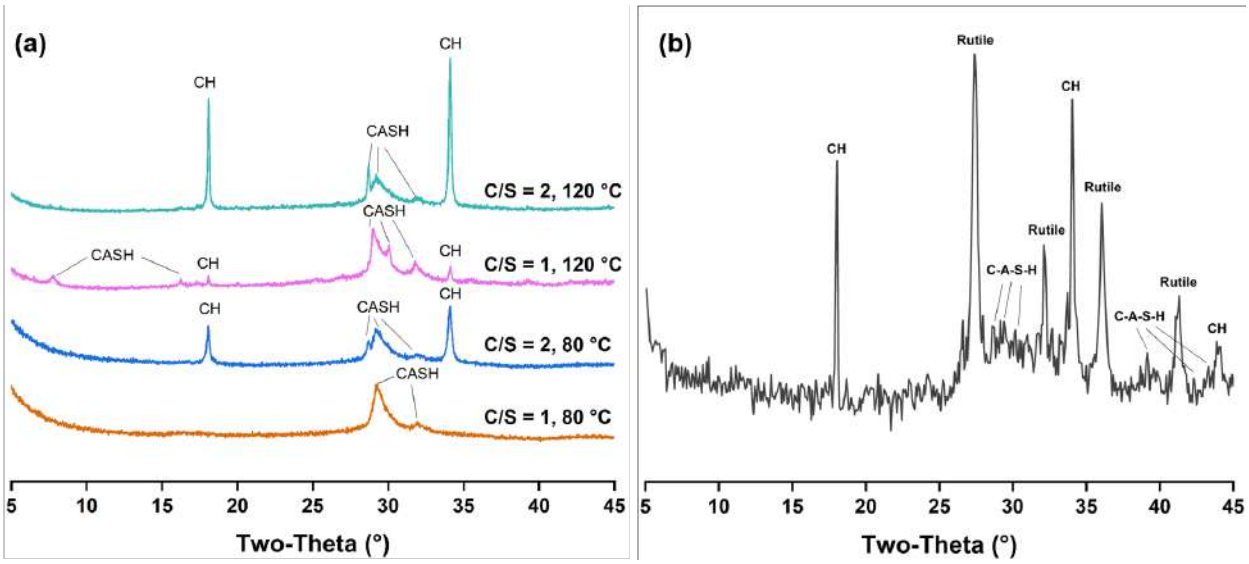


Figure 2. XRD patterns obtained using a Cu-K$_\alpha$ source of a) pure phases synthesized at 80 ˚C and 120 ˚C with starting ratios of Ca/Si = 1 and Ca/Si = 2, and Al/Si was kept constant at 0.05, and b) a fractured sample cured under EGS conditions from Section 3.1 that was crushed into powder.

4. Conclusions

The hydration products or HPHT phases that form in SCM-containing cementitious systems are complex and depend on the chemical composition and morphology of the SCMs. Identifying phases in "real" samples and matching them to synthesized counterparts is necessary to develop a database of phases. In this study, using synthesized materials and cementitious hydration products at 2 days, we demonstrated the identification of C-A-S-H that has the characteristics of 14 Å tobermorite. However, early-age performance may not be sufficient to assess the stability of phases subjected to elevated temperatures over long periods. For this, future studies are necessitated to assess the parameters that are required for thermodynamic modeling under hydrothermal environments.

References

Bergen, S.L., Zemberekci, L. and Nair, S.D. (2022) "A Review of Conventional and Alternative Cementitious Materials for Geothermal Wells." *Renewable and Sustainable Energy Reviews*. Elsevier Ltd. https://doi.org/10.1016/j.rser.2022.112347.

Kalousek G.L. (1955) "Tobermorite and Related Phases in the System CaO-SiO2-H2O." *Journal of the American Concrete Institute* 51 (6): 989–1011.

L'Hôpital, E., Lothenbach, B., Le Saout, G., Kulik, D., and Scrivener, K. (2015) "Incorporation of Aluminium in Calcium-Silicate-Hydrates." *Cement and Concrete Research*. Elsevier Ltd. https://doi.org/10.1016/j.cemconres.2015.04.007.

Myers, R.J., L'Hôpital, E., Provis, J.L. and Lothenbach,B. (2015) "Effect of Temperature and Aluminium on Calcium (Alumino)Silicate Hydrate Chemistry under Equilibrium Conditions." *Cement and Concrete Research* 68: 83–93. https://doi.org/10.1016/j.cemconres.2014.10.015.

Stutzman, P.E., and Clifton, J.R. (1999) "Specimen preparation for scanning electron microscopy." *Proceedings of the international conference on cement microscopy*. Vol. 21. International Cement Microscopy Association.

Williamson, T., Han, J. Katz, L. Sant, G. and Juenger , M.C.G. (2018) "Method for Experimentally Determining N-a-s-(H) Solubility." *RILEM Technical Letters* 3 (July): 104–13. https://doi.org/10.21809/rilemtechlett.2018.63.

Winnefeld F., Schöler A., Lothenbach B. (2016) "*Sample preparation. In: Scrivener KL, Snellings R, Lothenbach B (eds) A practical guide to microstructural analysis of cementitious materials.*" CRC Press, Boca Raton, pp 1–36

Yang, S.Y., Yan, Y. Lothenbach, B. and Skibsted, J. (2021) "Incorporation of Sodium and Aluminum in Cementitious Calcium-Alumino-Silicate-Hydrate C-(A)-S-H Phases Studied by 23Na, 27Al, and 29Si MAS NMR Spectroscopy." *Journal of Physical Chemistry C* 125 (51): 27975–95. https://doi.org/10.1021/acs.jpcc.1c08419.

Zemberekci, L., Moneeb G., and Nair, S.D. (2022) "Rheology-Based Approach to Design Cement Slurries for Enhanced Geothermal Wells." *Transactions - Geothermal Resources Council* 46: 1579–89.

The 16th International Congress on the Chemistry of Cement 2023 (ICCC2023)
"Further Reduction of CO_2 -Emissions and Circularity in the Cement and Concrete Industry"
September 18–22, 2023, Bangkok, Thailand

Time resolved synchrotron X-ray diffraction investigations of LC3 hydration in the presence of hydroxyethyl methyl cellulose ethers

E. Qoku[1*], A.P. Wilkinson[2,3], and K.E. Kurtis[1,3]

[1]*School of Civil and Environmental Engineering, Georgia Tech, 30332, Atlanta USA*

[2] *School of Chemistry and Biochemistry, Georgia Tech, 30332, Atlanta USA*

[3] *School of Material Science and Engineering, Georgia Tech, 30332, Atlanta, USA*

Emails: eqoku3@gatech.edu , aw42@gatech.edu and kkurtis@gatech.edu

ABSTRACT
The interaction of hydroxyethyl methyl cellulose (HEMC) with limestone calcined clay blends (LC3) was investigated to better understand their physico-chemical interactions during early hydration. Coupled measurements, using in-situ X-ray synchrotron diffraction and isothermal calorimetry, were carried out during the first 48 hours of hydration for a LC^3 blend at a water-to-solid ratio (w/s) of 0.55. Two types of HEMC, with similar molecular weight but with different degrees of substitution (DS) were added to the blends at 0.2 and 0.45% by mass, respectively, with a 0% case serving as a control. In all samples, the main crystalline hydration products identified from XRD were ettringite, portlandite and hemicarboaluminate hydrate. The heat evolution curves were characterized by two main peak events, with the second one delayed in the presence of HEMC. A retardation of ~3 hours was observed in the presence of the high DS admixture at 0.45%, but in presence of the low DS HEMC the delay was 5 hours, as compared to a reference sample with no HEMC. Ettringite was observed as early as the first hour of hydration for all samples. The use of HEMC delayed the initial precipitation of hemicarboaluminate and the termination of ettringite formation occurred later in the samples containing additives.

KEYWORDS: *Limestone Calcined Clay (LC3), Cellulose ethers, Hydration, In-Situ X-ray, synchrotron*

1. Introduction

The main challenge facing the cement industry is reducing the CO_2 emissions from cement production. One way to achieve this is reducing the clinker factor. Limestone Calcined Clays (LC3) are of interest as they could reduce CO_2 emission by 50% compared to Portland cement (PC) and still yield comparable physiochemical properties and good (and potentially even better) durability according to Scrivener et al. (2018).
In the dry-mix mortar industry, several types of organic admixtures are used to tailor rheological properties, set time, durability and strength development. Among others, polysaccharides and especially cellulose ethers (CEs) are used to control water retention and act as excellent thickening agents (Palacios and Flatt (2016)). CEs are synthesized from cellulose by etherification, a process in which the C-2, C-3 and C-6 OH groups of the anhydroglucose units are partially substituted. The number of substituent groups can be characterized by two important molecular parameters, namely the degree of substitution (DS) and the molar degree of substitution (MS). The degree of substitution DS refers to the number of OH groups of an anhydroglucose unit etherified on average, whereas MS refers to the molar ratio of alkoxy groups in the side chains of the cellulose. The main effect of cellulose ethers on Portland cement is a retardation of the hydration and lengthening of setting time. A lower DS leads to stronger retardation (Palacios and Flatt (2016), Pourchez et al. (2006). Pourchez et al. (2009), Pourchez, et al. (2010)). They concluded that the delay in hydration may relate to the adsorption of cellulose ethers on cement grains. CEs were found to particularly hinder the precipitation of C-S-H and portlandite, due to their high adsorption affinity for these phases. According to Ridi et al. (2005), CEs may also alter the hydration of C_3A and C_4AF, due to the adsorption of the polymers on the surfaces of OH-AFm phases.
The prior literature focuses on Portland cement and its phases. To date, the role of CEs in the hydration of LC3 has received little attention (Chen et al. 2020). Herein, first observations into the effect of hydroxyethyl methyl cellulose ether (HEMC) on phase formation during the first 48 hours of LC3 hydration are presented through

coupled measurements, using in-situ X-ray synchrotron powder diffraction and isothermal calorimetry. The selected HEMCs have similar molecular weight (noted Mw), but different substitution patterns.

2. Materials and methods

The mixture design for the LC3 was based on the LC3 – 50 system. The metakaolin-to-limestone ratio was fixed at 2 to 1, and 2% gypsum by mass of binder was added to achieve an adequate sulphate balance after Canbek et al. (2022). An ASTM C150 Type I/II PC (Argos Cement, Atlanta, GA), a high purity metakaolin (BASF, Gordon, GA) and limestone powders (Imerys, GA) were used in this study. Two types of HEMCs with identical Mw but different DS and MS were used at mass contents in the total mineral mix of 0.2 and 0.45%. Their molecular parameters are reported in Table 1. A water-to-solid ratio (w/s) of 0.55, based on mineral content, was used for all samples.

Table 1: Molecular parameters of the HEMC

Parameters	**HEMC1**	**HEMC2**
Viscosity (mPa.s)	43000	38900
Degree of substitution (DS)	1.75-2.20	1.25-1.50
Molecular subsitution (MS)	0.33-0.55	0.05-0.22
Molecular weight Mw (Dalton)	40000	

Heat flow calorimeter
Heat evolution from the blended cement pastes was measured using an isothermal calorimeter (TAM Air, TA Instruments) according to ASTM C1679. Approximately 8.5 g of paste was prepared outside the calorimeter at room temperature (23 ± 2 ^{o}C) and then loaded into the calorimeter. The heat evolution was followed up to 48 hours of hydration.

In-situ synchrotron X-ray powder diffraction (SXRPD)
Powder diffraction data were collected at the 11-IDB beamline of the Advanced Photon Source (APS), Argonne National Laboratory, Illinois, USA. A 0.5 mm x 0.5 mm X-ray beam with $\lambda = 0.2116$ Å was used along with a Perkin-Elmer amorphous silicon 2D detector located ~750 mm from the sample. The detector position was calibrated using diffraction data from a CeO_2 standard sample. Cement paste samples were loaded into 1.56 mm diameter polyimide capillary tubes, which were sealed at both ends with modelling clay. The tubes were mounted vertically in a rack, which allowed up to 60 samples to be examined in an automated fashion. During data collection, the sample tubes were moved up and down in the beam to improve diffracting particle statistics. Each sample was remeasured at ~6 minute intervals over a 2θ interval 0.3 to 13.9. Rietveld analysis was carried out making use of quartz as an internal standard.

3. Results

Figure 1 shows the heat flow for each of the LC3-50 pastes during the first 48 hours of hydration. Each curve is characterized by two main peak events related to the silicate reaction and aluminate reaction respectively. With increasing HEMC addition, some retardation of the main hydration peak events is observed. In the presence of HEMC1, which has a higher DS, the retardation is most noticeable for the aluminate peak. As the addition increases from 0.2 to 0.45%, the aluminate peak is delayed by almost 3.5 hours compared to the LC^3-50 paste with no additive. However, the silicate peak is largely unaffected, and the cumulative heat of hydration is quite similar for all HEMC1 pastes up to ~10 h. In contrast, HEMC2 leads to a stronger retardation than HEMC1 for both the silicate and aluminate peak events. The maximum of the aluminate peak occurs ~ 5 hours after that for the reference LC3. This reassembles the effect of HEMC in Portland cement, where a lower DS leads to stronger retardation .

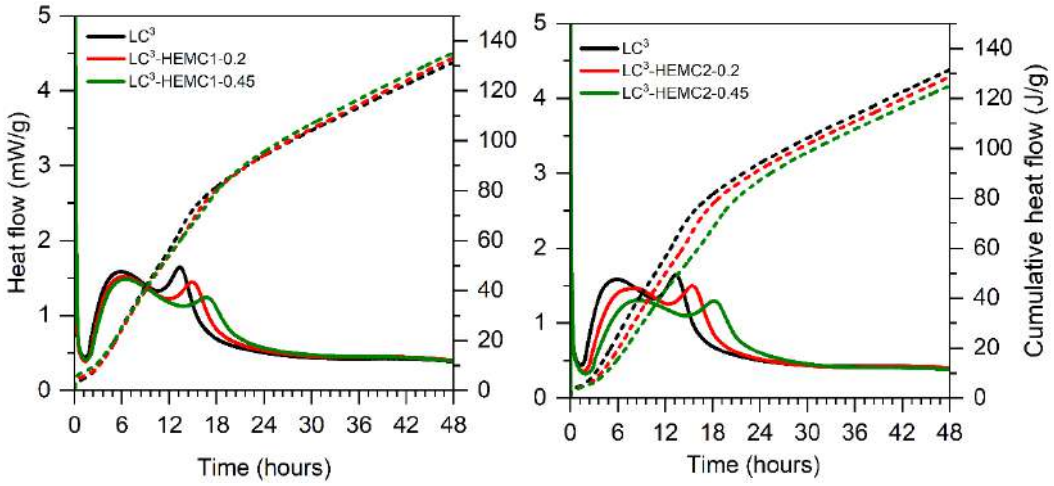


Fig.1: Heat flow curves and cumulative heat for LC3-50 with different amounts of each of the additives.

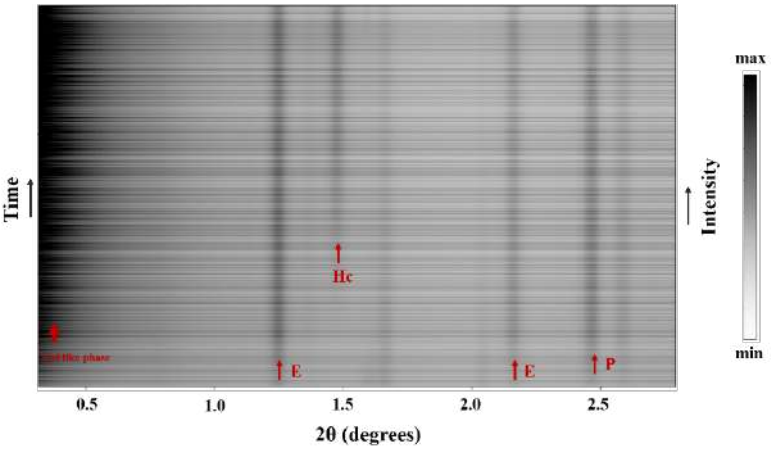


Fig. 2: 2D plot of the in-situ synchrotron X-ray powder diffraction data for a hydrating LC3 paste. The main hydrate phases have been indicated. E = Ettringite, P = Portlandite Hc = Hemicarbonate and a gel like phase.

Figure 2 shows the in-situ X ray synchrotron powder diffraction data for hydrating pure LC3 (data sets for the samples with additives are not shown due to space constraints). The main hydrate peaks occur in the range 0.31-2.78 ° 2θ. From the X-ray data, ettringite, portlandite and hemicarboaluminate are identified as the main hydration products. Besides the presence of the above mentioned phases, in the low angle scattering region (2θ 0.35 – 0.7°) an increase in scattered intensity is observed. This is associated with the presence of a gel-like phase(s). C_3S, C_2S, C_4AF, C_3A, gypsum, quartz, calcite and traces of anatase were identified as anhydrous phases.

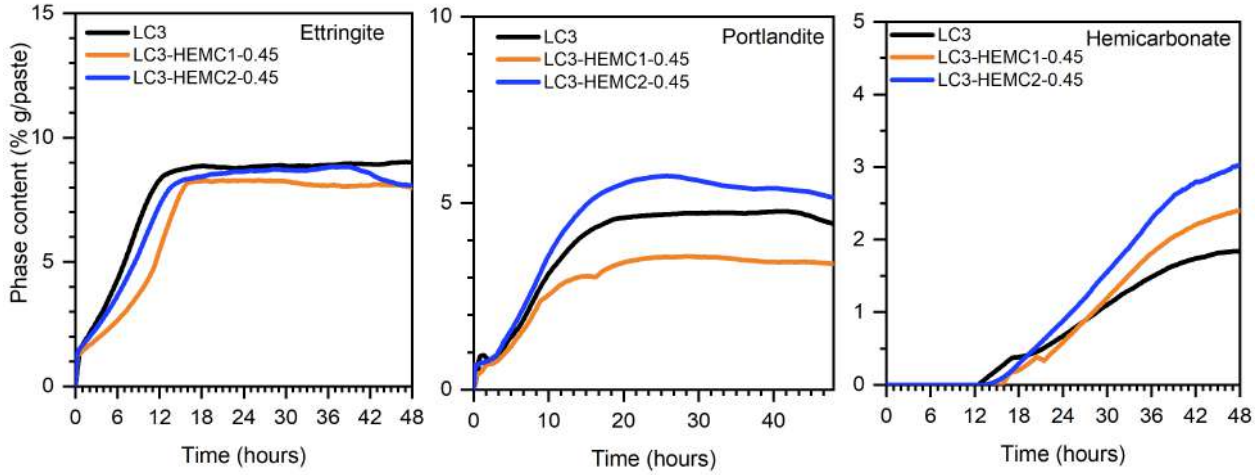


Fig.3: Comparison of the ettringite, portlandite and hemicarbonate phase content over time for the LC3, LC3-HEMC1-0.45 and HEMC2-0.45 pastes.

Figure 3 compares the time evolution of the main hydrate phases for the LC3, the LC3 - HEMC1-0.45, and the LC3-HEMC2-0.45% samples. In each case, the formation of ettringite starts in the first minutes of hydration. However its formation in the LC3 paste finishes ~ 1.5 hours earlier as compared to the samples containing

HEMC. Pourchez et al. (2009) has argued that there is no significant adsorption of CE on ettringite, whereas Müller (2006) suggests that the retardation of ettringite formation is indireclty linked to CH concentration in the solution. The ultimate ettringite content of the LC3 paste is slightly higher than that of the pastes with additives. Additionally, the use of HEMC2 at 0.45% leads to a decrease of ettringite content with time, which could be due to its conversion to monosulphate. Although the strongest retardation is observed in the presence of HEMC2, the highest portlandite and hemicarboaluminate contents are observed in the LC3-HEMC2-0.45 paste. The hemicarboaluminate is first identified at ~ 12.5 hours of hydration for the control LC3 paste, whereas for those with additives, hemicarbonate is first observed at ~ 17 hours of hydration, thus suggesting, that the interaction between the HEMC additives and LC3 plays a key role in the rate of the aluminate hydration and AFm phase formation.

4. Summary

- The use of HEMCs in LC3 influences the heat evolution. From the calorimetry data, it is evident that a lower DS leads to stronger retardation of the main peak events. The retardation is most pronounced for the aluminate peak.
- The use of HEMCs delays the appearance of hemicarboaluminate. The termination of ettringite formation is achieved latter in the presence of additives. Although the strongest retardation is observed in presence of HEMC2, these cement pastes evolve the highest content of portlandite.
- In addition to the formation of the crystalline hydrates ettringite, portlandite and hemicarbonate, the time dependence of scattering in the low angle area, indicates the formation of nanostructured gel-like phase(s).

Acknowledgements

Financial support for this work was provided by Dow Chemical Company. This research used resources of the Advanced Photon Source, a U S Department of Energy (Office of Science user facility operated for the DOE Office of Science by Argonne National Laboratory under Contract No. DE-AC-02-06CH11357. We are grateful to Leighanne C. Gallington of 11-I-DB beamline at the Advanced Photon Source for experimental assistance. Any opinions, findings, and conclusions expressed in this document are those of the authors and do not necessarily reflect those of the sponsor.

References

Canbek, Oğulcan et al. (2022) "Predicting the Rheology of Limestone Calcined Clay Cements (LC3): Linking Composition and Hydration Kinetics to Yield Stress through Machine Learning." *Cement and Concrete Research* 160.

Chen, Yu et al. (2020) "Improving Printability of Limestone-Calcined Clay-Based Cementitious Materials by Using Viscosity-Modifying Admixture." *Cement and Concrete Research* 132; 106040

Müller, Ingo. (2006) "Influence of Cellulose Ethers on the Kinetics of Early Portland Cement Hydration." Schriftenreihe des Instituts für Mineralogie und Geochemie, Universität Karlsruhe.

Palacios, M., and Robert J. Flatt. (2016) "Working Mechanism of Viscosity-Modifying Admixtures." In *Science and Technology of Concrete Admixtures*, Elsevier Inc., 415–32.

Pourchet, S., L. Regnaud, J. P. Perez, and A. Nonat. 2009. "Early C_3A Hydration in the Presence of Different Kinds of CalciumSulfate." *Cement and Concrete Research* 39(11): 989–96.

Pourchez, J. et al. 2006. "HPMC and HEMC Influence on Cement Hydration." *Cement and Concrete Research* 36 (2): 288–94.

Pourchez, J., P. Grosseau, and B. Ruot. 2010. "Changes in C3S Hydration in the Presence of Cellulose Ethers." *Cement and Concrete Research* 40(2): 179–88.

Ridi, Francesca, Emiliano Fratini, Francesca Mannelli, and Piero Baglioni. 2005. "Hydration Process of Cement in the Presence of a Cellulosic Additive. A Calorimetric Investigation." *Journal of Physical Chemistry B* 109(30): 14727–34.

Scrivener, Karen L., Vanderley M. John, and Ellis M. Gartner. (2018) "Eco-Efficient Cements: Potential Economically Viable Solutions for a Low-CO_2 Cement-Based Materials Industry." *Cement and Concrete Research* 114(June): 2–26.

The 16th International Congress on the Chemistry of Cement 2023 (ICCC2023)
"Further Reduction of CO_2 -Emissions and Circularity in the Cement and Concrete Industry"
September 18–22, 2023, Bangkok, Thailand

Mineral dissolution mechanism of different polymorphs of alite from ReaxFF molecular dynamics simulation

Haoyi Li[1, 2],Zhizong Tian[1, 2], Qianqian Wang[1, 2*], Xiaodong Shen[1, 2]

[1] College of Materials Science and Engineering, Nanjing Tech University, Nanjing 210009, CHINA

[2] State Key Laboratory of Materials-Oriented Chemical Engineering, College of Materials Science and Engineering, Nanjing Tech University, Nanjing 210009, CHINA

E-mail: haoyili@njtech.edu.cn, zztian@njtech.edu.cn, qqwang@njtech.edu.cn, xdshen@njtech.edu.cn

ABSTRACT

Cement remains the world's largest building material, and China's cement-based cement material accounts for more than 60 percent of the world's total production. The quality of cement clinker is still the key to improving the performance and durability of concrete cementite. Alite is the mineral phase that has the greatest influence on the early properties of cement clinker. Therefore, the research on the hydration mechanism of alite (tricalcium silicate) is still a hot topic in recent years. In this experiment, the hydration processes of different crystalline types of tricalcium silicate were analyzed by molecular dynamics simulation. Two kinds of C3S with different crystal types were selected for hydration simulation analysis, and the radial distribution function, hydroxylation degree and system energy were comprehensively compared. We found that there were hydration differences between the C_3S of two different crystal types, which might be related to the difference in crystal structure. The change of energy in the system also more directly reflects the transmission of proton and energy in the system. The research on cement clinker hydration can effectively reduce carbon emission in the cement production process and improve the quality of cement clinker(Chen, et al. 2020).

KEYWORDS: *Calcium silicate, crystal surface, hydration, molecular dynamics, proton transfer*

1. Introduction

Improving the sustainability of cement production by reducing the amount of carbon dioxide produced and the amount of energy used is an important and persistent challenge. One strategy in the current social context is to modify Portland cement to reduce the calcination temperature and thus reducing energy consumption. Reducing CO_2 emissions through the use of "carbon capture and storage", or "carbon capture and reuse" technologies in cement production has become an attractive and active area of research, but remains uneconomic. Alternative approaches focus on replacing Portland cement in the composition of concrete, particularly using cement based on alkali-activated adhesives. Often referred to as inorganic polymers or geopolymers, however, these new non-Portland cement lack building codes and data on their long-term durability, so studies of new Portland cement and early hydration mechanisms have been conducted (Chen, et al. 2020, Kumar, et al. 2017, Meng, et al. 2017).

Silicate minerals are not only the most widely distributed minerals on the Earth's surface but also the world's most common manufacturing materials, including refractories, photoelectric materials and cement. The performance of concrete can also be improved by incorporating industrial by-products, such as fly ash and iron blast furnace slag, to replace some Portland cement, and there is great interest in this new source of supplementary cement that can be scaled up worldwide. A comprehensive study shows that calcined clay is an excellent source. The use of these alternative materials, combined with the optimization of silicate hydrate (the main binding phase of concrete matrix), is a promising approach to achieving enhanced and more durable concrete(Bazzoni, et al. 2014). The life cycle of concrete structures can be more flexible and

sustainability can be improved by improving the material performance, combining the structural design with risk-based durability modeling and the optimized construction method. Recent improvements in material properties also include the use of multi-scale fiber-reinforced materials, improved corrosion resistance, advanced chemical admixtures to improve the rheological properties of freshly mixed concrete, and the creation of self-healing concrete that is, concrete containing limestone produces polymer microcapsules capable of repairing micro-cracks, And the development of ultra-light cement composites with low thermal conductivity for use in energy-efficient buildings(Manzano, et al. 2013).

2. Computational methods and parameters

The molecular dynamics simulation was carried out using the ReaxFF reaction force field by the LAMMPS software package in this work. The ReaxFF force field parameters for Si-O-H and Ca-O were developed by Fogarty and Manzano. They are widely used to study the structural and mechanical properties of amorphous silicate materials, crystalline calcium silicate hydrates, clay, and so on.

First, cell optimization for M3-C_3S(Golovastikov, et al. 1975) and T1-C_3S(Yang, et al. 2008) was performed using the Polak−Ribiere conjugate gradient algorithm with an energy cutoff tolerance of 10-5 kcal/mol. After reasonably optimized cells were obtained, different low-index surface models were constructed based on their surface energies and surface areas in the Wulff shapes.

Table 1

Wulff shapes the surface area of M3-C_3S and T1-C_3S

Phase	Wulff shapes surface area (Å^2)						
	(100)	(001)	(010)	(110)	(101)	(011)	(111)
M3-C_3S	8.12	9.77	5.45	5.07	2.49	0.98	0.48
T1-C_3S	5.84	7.92	5.98	3.11	4.47	3.19	0.24

Surface energy was calculated after the optimization process with the same parameters of bulk optimization. Then, the water-surface interface model was constructed with a water density of 1 g/cm3. After structure optimization, Molecular dynamics simulation for the reaction process between water and mineral surfaces was carried out in the canonical ensemble at 298 K and 1 atm for 3 ns(Álvarez, et al. 2013). Wherein, the middle parts of the mineral surfaces were constrained. A Nose−Hoover thermostat method was used to modify the system temperature every 20 fs and the motion equations were integrated using the velocity−Verlet algorithm(Manzano, et al. 2015) with a time step of 0.2 fs. The initial velocities for every atom were generated from a Gaussian distribution at 300 K. To avoid energy transfer to zero-frequency modes, the velocity of the center of masses was removed every 10^3 steps, which is the same as the methods in(Lentz, et al. 2019).

3 Results and discussion

3.1 Surface hydroxylation process

In the process of hydration, the water molecules in the water molecular layer will decompose continuously, forming free Ow atoms and H atoms and getting closer to the solid surface(Chen, et al. 2021). The free Ca atoms and Oi atoms in the solid surface will get closer to the water molecular layer. In the process of contact, new bonds will be formed, and the Ow atoms in the water molecular layer will form Ca-Ow bonds with the free Ca atoms on the solid surface. The H atom generated by the decomposition of water molecules will bond with the free Oi atom on the solid surface and the Os atom in the silico-oxygen tetrahedron on the solid surface. The formation of this bond means that the surface will be hydroxylated in the hydration process.Fig 1 shows the difference in the percentage of water molecules decomposed and the degree of hydroxylation between the two crystal types and the six crystal faces. It can be observed from the figure that the degree of water decomposition of the two crystalline forms is the same, and there are differences between different crystal faces. We can infer that the influence of C_3S crystalline forms on the degree of water molecular decomposition is limited, but there is a certain difference in the rate of water

decomposition. This is because the crystalline activity of M3-C_3S is greater than that of T1-C_3S, and its hydration activity is also stronger than that of T1. In the process of water decomposition, it can be observed that it is not a continuous process, but a gradual process, indicating that the hydration of C_3S is not a continuous process, but at the same time of water decomposition, some water molecules are decomposed into water molecules again(Dupuis, et al. 2019). In the initial stage of hydration, the rate is very fast, and the degree of hydration has been nearly 70% in the initial stage of about 0.5ns. Both the number of water decomposition and the degree of hydroxylation conform to this characteristic, indicating that the hydration process is a very rapid stage. The solid surface is rapidly hydrated just after contact with the water molecular layer and enters the slow hydration process after about 0.5ns, which is similar to the slow setting time of cement. The difference in hydration activity between different crystal faces of the same crystal type may be related to surface energy(Manzano, et al. 2015).

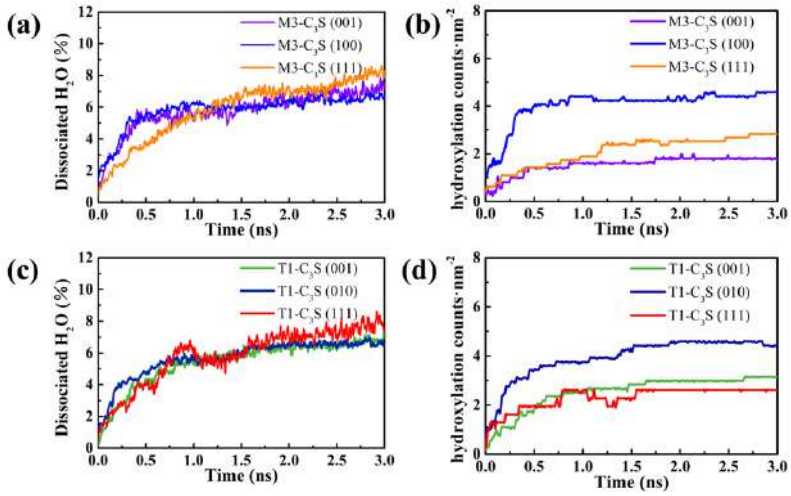


Fig. 1(a) and (c) Percent of dissociated water molecules in the interface models. (b) and (d) Hydroxylation counts calculated from Os-H and Oi-H per nm2 (The cutoff distance: 1.25 Å).

3.2 Bonding characteristics

To better judge the bonds formed in the hydration process, the radial distribution function is a better demonstration of the conditions and strength of the bonds formed in the hydration reaction. Fig 2 shows RDF pictures of several of the more common bonds in the M3-C_3S crystal, with different bonds varying between hydration times of 0ns and 3ns. As can be observed in Fig 2, a part of Ca-Ow bonds has been generated at the initial stage of the hydration process. This is because the solid surface has strong hydration when it comes into contact with the water molecular layer, so a part of Ca-Ow bonds is generated in the process of just contact. As the hydration process progresses, the number and strength of Ca-Ow bonds will become stronger and stronger. This is consistent with the observed phenomenon of hydration surface. A small number of Ca-Ow bonds are generated in the initial stage of hydration, and more Ca-Ow bonds are generated in the later stage of hydration. Moreover, we can observe that the number of water molecules decomposed in different crystal faces in M3-C3S is similar to the number of Ca-Ow bonds generated. This indicates that the number of Ow generated by water decomposition is related to the number of Ca-Ow bonds formed. The more water molecules decomposed, the more Ca-Ow bonds are generated. The formation of the Oi-H bond and Os-H bond is similar to the degree of hydroxylation. In the initial stage of hydration, different crystal faces do not form narrow and slender peaks, indicating that Os-H and Oi-H have no strong interaction in the initial stage of hydration. However, after 3ns, narrow and thin peaks are formed, indicating that with the progress of hydration, The decomposed H ions in the water molecular layer continuously pour into the solid surface, and form bonds with the free oxygen atoms Oi on the solid surface and the Os atoms in the silico-oxygen tetrahedron, which is similar to the protonation phenomenon.

By analyzing the radial distribution function of the six crystal faces of the two crystal types, it can be seen that a small amount of Si-Ow bonds are formed, which is similar to the hydration process. The peak height of Si-Ow bonds generated by M3-C_3S is higher than that of T1-C_3S crystals, indicating that this is

related to the hydration phenomenon of different crystals, and the C_3S hydration degree of M3 crystals is more intense. The situation of the Ow atom entering and forming pentahedral coordination with silico-oxygen tetrahedron is also more intense(Xu, et al. 2017).

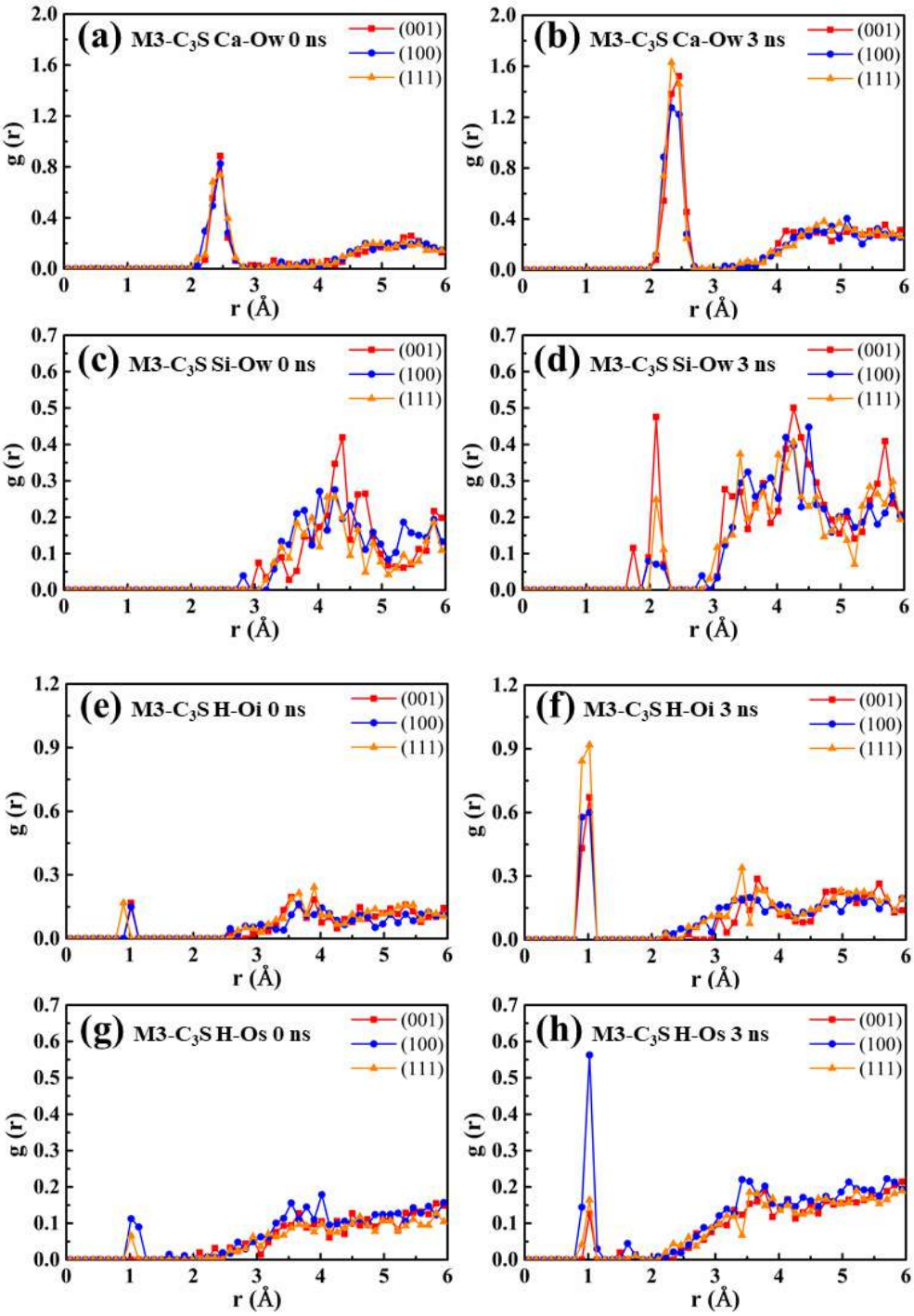


Fig. 2 Radial distribution functions of different chemical bonds at 0 ns and 3 ns in different interfaces for M3-C3S hydration

4. Conclusions

By using molecular dynamics simulation, this work studied the differences in the initial hydration processes of C_3S of M3 and T1 crystal surfaces and compared the hydration differences, structure analysis, bonding conditions, and radial distribution functions of the six crystal surfaces of the two crystal types in the hydration process. Si-Ow bond was generated in the hydration process, which is a phenomenon that is

hard to see. Therefore, we analyzed the energy change of [SiOsOw] on the surface of M3-C_3S(001) and the surrounding environment of silicon atoms forming pentetate. Based on the above analysis results and phenomena, we put forward the following conclusions:

(1) The water decomposition of C_3S of the two crystal types is similar, but there is a certain difference in the rate, indicating that the crystal type has a small impact on the degree of hydration, but a greater impact on the rate of hydration. The hydration rate of C_3S of the M3 crystal type is faster than that of the T1 crystal type.

(2) The water decomposition percentage and hydroxylation degree of the six crystal faces of the two crystal types were compared, and it was found that the decomposition of more water molecules did not mean a higher hydroxylation degree, indicating that H_3O^+ was generated in the hydration process, which was caused by the existence of the Grotthuss mechanism.

Ca-Ow bonds are generated when the interface is just in contact with the water molecular layer, showing strong interaction, while Os-H bonds and Oi-H bonds are not generated in the initial structure, and the radial distribution functions at 3ns are improved to a certain extent, indicating that these bonds and,

Acknowledgements

The authors thank for the financial support from the National Natural Science Foundation of China (No. 52072171), and the Priority Academic Program Development of Jiangsu Higher Education Institutions (PAPD). The computational resources generously provided by the High-Performance Computing Center of Nanjing Tech University are greatly appreciated.

References

A. Álvarez, R. Trujillano and V. Rives, Differently aged gallium-containing layered double hydroxides, Applied Clay Science, 80-81 (2013) 326-333

A. Bazzoni, S. Ma, Q. Wang, X. Shen, M. Cantoni, K. L. Scrivener and G. Scherer, The Effect of Magnesium and Zinc Ions on the Hydration Kinetics of C3

S, Journal of the American Ceramic Society, 97 (2014) 3684-3693

J. Chen, P. E. Martín, Z. Xu, H. Manzano, J. S. Dolado and G. Ye, A dissolution model of alite coupling surface topography and ions transport under different hydrodynamics conditions at microscale, Cement and Concrete Research, (2021)

X. Chen, S. Wei, Q. Wang, M. Tang, X. Shen, X. Zou, Y. Shen and B. Ma, Morphology prediction of portlandite: Atomistic simulations and experimental research, Applied Surface Science, 502 (2020)

R. Dupuis, L. K. Béland and R. J.-M. Pellenq, Molecular simulation of silica gels: Formation, dilution, and drying, Physical Review Materials, (2019)

N. I. Golovastikov, R. Matveeva and N. Belov, Crystal structure of tricalcium silicate, 3CaO.SiO2 = C3S, (1975)

A. Kumar, B. J. Walder, A. Kunhi Mohamed, A. Hofstetter, B. Srinivasan, A. J. Rossini, K. Scrivener, L. Emsley and P. Bowen, The Atomic-Level Structure of Cementitious Calcium Silicate Hydrate, The Journal of Physical Chemistry C, 121 (2017) 17188-17196

J. Lentz and S. H. Garofalini, Role of the hydrogen bond lifetimes and rotations at the water/amorphous silica interface on proton transport, Phys Chem Chem Phys, 21 (2019) 12265-12278

H. Manzano, E. Durgun, I. Lopez-Arbeloa and J. C. Grossman, Insight on Tricalcium Silicate Hydration and Dissolution Mechanism from Molecular Simulations, ACS Appl Mater Interfaces, 7 (2015) 14726-33

H. Manzano, E. Masoero, I. Lopez-Arbeloa and H. M. Jennings, Shear deformations in calcium silicate hydrates, Soft Matter, 9 (2013)

Q. Meng and H. Yan, Theoretical study on the topotactic transformation and memory effect of M (II) M (III)-layered double hydroxides, Molecular Simulation, 43 (2017) 1338-1347

S.-M. Xu, H. Yan and M. Wei, Band Structure Engineering of Transition-Metal-Based Layered Double Hydroxides toward Photocatalytic Oxygen Evolution from Water: A Theoretical–Experimental Combination Study, The Journal of Physical Chemistry C, 121 (2017) 2683-2695

H. G. Yang, C. Sun, S.-z. Qiao, J. Zou, G. Liu, S. C. Smith, H. M. Cheng and G. Q. Lu, Anatase TiO2 single crystals with a large percentage of reactive facets, Nature, 453 (2008) 638-641

The 16th International Congress on the Chemistry of Cement 2023 (ICCC2023)
"Further Reduction of CO_2 -Emissions and Circularity in the Cement and Concrete Industry"
September 18–22, 2023, Bangkok, Thailand

Hydration of Calcium [Alumino] Ferrite with Limestone

A. Baral[1*], C. Pesce[2], C. Utton[3], H. Kinoshita[4], N. A. Morley[5], J. L. Provis[6], and T. Hanein[7]

[1-7] Department of Materials Science and Engineering, The University of Sheffield, Sheffield, UK
Email: [1]a.baral@sheffield.ac.uk, [2]c.pesce@sheffield.ac.uk, [3]c.utton@sheffield.ac.uk, [4]h.kinoshita@sheffield.ac.uk, [5]n.a.morley@sheffield.ac.uk, [6]j.provis@sheffield.ac.uk, [7]t.hanein@sheffield.ac.uk

ABSTRACT
Ferrite has the lowest embodied CO_2 among the four major phases found in Portland cement, so increasing the ferrite content of the clinker would improve its CO_2 footprint. Ferrite hydration is known to depend on the cooling regime during the production, Al/Fe ratio, and minor element uptake, and thus, their effects have to be fully understood to increase the composition of this phase in the Portland cement and assure their good hydration properties. Here, ferrites with different Al/Fe ratios (0, 0.5, 1, and 2), and minor elements (Zn) has been synthesized at two different burning temperatures, 1250 °C and 1350 °C and hydrated in presence of excess $CaCO_3$ for 1 and 3 days. The ferrite with Al/Fe = 0 did not form any hydration product after 3 days of hydration, while Al-monocarbonate was the only hydration product in the other systems. The hydration kinetics increased with Al/Fe ratio, and when the burning temperature was increased. Comparing XRD and TGA data, the Al-monocarbonate formed from the ferrite with Al/Fe = 2 was found to be more amorphous than other ferrites. ZnO doping up to 2 wt.% had no prominent effect on hydration, implying that raw materials with Zn can be utilised in high-ferrite cement. These results indicate that high-ferrite limestone cement could be a promising solution to reduce cement the CO_2 emission.

KEYWORDS: *Limestone, Ferrite, Monocarbonate, Hydration, ZnO doping*

1. Introduction

Portland cement (PC) generates ~8% of anthropogenic CO_2 emissions (Monteiro et al., 2017), and one of the ways to reduce CO_2 footprint of cement includes designing PC clinker containing a higher ferrite ($Ca_2Fe_{2-x}Al_xO_5$, x = 0 - 1.4) content as it lowers the clinkering temperature by ~100°C and requires less limestone calcination because of less calcium content (Gartner, 2004). Currently, high ferrite cement is already being used in oil-well cement and sulphate-attack-resistant cement. However, the reactivity of ferrite is less than alite and tricalcium aluminate, thus one of the drawbacks of high-ferrite cements is their lower early-age strength. The reactivity of ferrite is known to be affected by the Al/Fe ratio and synthesis conditions (sintering temperature, cooling rate) as well as the presence of minor elements in the raw materials, such as Zn, Mg, Cr, Ti, and Mn. Out of these elements, Mg, Ti, and Cr generally reduce the ferrite reactivity. The presence of Mn has been shown to improve ferrite reactivity through an increase in the initial dissolution (Zhong et al., 2022), but the effect of Zn is still debated. ^{27}Al MAS NMR and Raman spectroscopy indicated that in the presence of Zn, the Fe speciation changes from $[FeO_4]$ to $[FeO_6]$ (Zhang et al., 2019) and DFT showed that an increase in effective charge of Fe in the presence of Zn is responsible for higher reactivity (Tao et al., 2020). Most of the studies investigate the ferrite hydration process only in the presence of calcium sulphates, as calcium sulphate is well-known to react with ferrite to form monosulphate or ettringite. However, the cement industry is currently rapidly moving towards producing Portland Limestone Cement (PLC) containing up to 15% limestone. Limestone is expected to react with ferrites because it reacts with tricalcium aluminates, but there is no detailed study in the literature about the hydration kinetics and hydration products formed when ferrites react with calcium carbonate.
In this paper, we have synthesised ferrites with four different Al/Fe ratios, two different burning temperatures, and ZnO doped at four different quantities. The ferrites were hydrated in presence of excess limestone to evaluate their hydration product formation using X-ray diffraction and thermal analysis.

Briefly, we found that ferrites ($x \geq 0.5$) react with calcite to form Al-monocarbonate, and the reactivity of ferrite increases with increasing Al/Fe ratio, or increasing sintering temperature from 1250 °C to 1350 °C.

2. Materials and Methods

2.1. Ferrite synthesis and its hydration

Ferrites with different Al/Fe ratio, ZnO doping, and burning temperatures (Table 1) were synthesized by mixing $CaCO_3$ (Sigma-Aldrich, 99.5%), Al_2O_3 (Acros Organics, 99%), Fe_2O_3 powders (Sigma-Aldrich, >96%) and ZnO powders (Sigma-Aldrich, 99.9%) in a ball mill for ~10 minutes and compressing them into pellets. The pellets were introduced in a Carbolite 1600 furnace using platinum crucibles at 900 °C and heated to a final burning temperature of 1250 or 1350 °C at 5 °C/min and were held at the final burning temperature for one hour. The pellets were subsequently water quenched while still in the platinum crucible to avoid direct contact with water. Finally, the pellets were ground into powder passing through a 63-micron sieve using mortar and pestle. The ferrite samples were subsequently characterised using X-ray diffraction to ensure their purity.

Previous studies (Fukuhara et al., 1981) evaluated the hydration reaction of C_4AF and gypsum, as shown in Eq. 1, where 2 mols of $Ca_2Al_xFe_{2-x}O_5$, x = 1, react with 4 mols of gypsum and 35.33 mols of water.

$$2Ca_2Al_xFe_{2-x}O_5 + 4\,CaSO_4 \cdot 2H_2O + 35.33\,H_2O \rightarrow \frac{4}{3}Ca_6(Al_{1.5}Fe_{0.5})(SO_4)_3 \cdot 31\,H_2O + \frac{2}{3}Fe_2O_3.3H_2O \quad (1)$$

In this paper, the synthesised ferrites ($Ca_2Al_xFe_{2-x}O_5$) were mixed with $CaCO_3$ and water at 2:8:43.33 molar ratio to form Fe-carbonate-Aft, $C_6(A_{0.75}F_{0.25})\bar{C}_3H_{31}$, where $\bar{C}$ represents CO_3. Twice the minimum required amount of $CaCO_3$ was used to encourage the formation of $C_6(A_{0.75}F_{0.25})\bar{C}_3H_{31}$. Although the existence of this compound has not been proven, a very similar compound, called carbonate-ettringite with chemical formula $Ca_6Al_2(CO_3)_3(OH)_{12}\cdot 26H_2O$ has been observed in the past (Barnett et al., 2001).

Table 1: Ferrite Test Sample Matrix

Sample Name	0AF1350	0.5AF1350	1AF1350	2AF1350	1AF0.5Zn1350	1AF1Zn1350	1AF2Zn1350	1AF1250
Burning Temperature	1350	1350	1350	1350	1350	1350	1350	1250
Extra ZnO added (wt.% of raw meal)	0	0	0	0	0.5	1.0	2.0	0
Al/Fe	0	0.5	1	2	1	1	1	1

2.2. Characterisation of clinkers and hydration products

X-ray diffraction patterns of the un-hydrated and hydrated ferrites were obtained using a Panalytical Xpert[3] that operates using a Cu source (Kα ~ 1.5406 Å) at 45 kV and 40 mA and a PIXcel1D-Medipix3 detector. The samples were backloaded into a 16 mm dia. sample holder rotating at 4 s per revolution. For the hydrated samples, ~20% rutile (Alfa Aesar, 99.5%) by mass was added as an internal standard and 2θ values ranged from 5 to 80° with a step size of 0.013°, with a ¼° divergence slit and a ⅛° anti-scatter slit with a total scan time of ~2.5 h. Thermogravimetric analysis of the hydrated samples was performed using a Pyris 1 TGA with alumina crucible in between 40 and 1000 °C at 10 °C/min using 10±0.5 mg samples with 20 mL/min nitrogen flow. The derivative of the weight loss was calculated using cubic spline regression.

3. Results and Discussions

The X-ray diffraction data (Figure 1a) showed that no AFt or hydrogarnet phases formed in any of our samples as no peaks below 2θ = 10° or at around 17° were observed. Even though there is no existing detailed crystal structure of Fe-carbonate-Aft in the literature, the crystal structure of Fe-carbonate-Aft can be expected to be similar to Fe-ettringite, and thus the samples are expected to have a peak at around 2θ = 9° (Fe-ettringite's (100) peak location is at 9.139°) had Fe-carbonate-Aft formed. The XRD detected only one hydrated phase, Al-monocarbonate with 11 mols of water (Al-Mc, $3CaO\cdot Al_2O_3\cdot CaCO_3\cdot 11H_2O$), in all the samples. As the lattice parameter is expected to change by less than 1% when Fe completely replaces

Al in Al-monocarbonate, the formula of the hydrate could be $3CaO{\cdot}yAl_2O_3{\cdot}(1\text{-}y)Fe_2O_3{\cdot}\ yCaCO_3{\cdot}11H_2O$ (y>0). However, we are confident that the hydration product is not Fe-monocarbonate with 12 mols of water ($3CaO{\cdot}Fe_2O_3{\cdot}CaCO_3{\cdot}12H_2O$) as it is rhombohedral, and Al-Mc, with 11 mols of water is triclinic, leading to different diffraction patterns (Dilnesa et al., 2011). SEM-EDS measurements will be performed in the future to determine the Al/Fe ratio in the monocarbonate.

The samples synthesised at 1350 °C and with Al/Fe ≥ 1 were almost fully hydrated just after 1 day of hydration as no ferrite peaks were visible in the XRD data. The 0.5AF1350 and 1AF1250 show a considerable increase in Al-monocarbonate peak intensity from 1 to 3 days of hydration. The 1AF1250 clinker sample had a smaller crystallite size and more disorder than the 1AF1350 clinker, which might explain the lower reactivity. The sample with Al/Fe = 0 on the other hand, does not show any reactivity as no hydrated products were detected in the XRD data. The lower reactivity of ferrite with Al/Fe = 0 is expected as previously it took ~7-days for a mix of C_2F and $CaCO_3$ in a highly alkaline solution to form Fe-hemicarbonate, and about 180 days to start forming Fe-monocarbonate (Dilnesa et al., 2011). In general, for all the samples, an increase in the Al-monocarbonate peak was accompanied by a decrease in the calcite and ferrite peaks. However, for Al/Fe =2, even though the calcite peak intensity was lower than the Al/Fe =1 samples for both 1 and 3-days of hydration, implying a greater reactivity, the Al-monocarbonate peak intensity was not higher than the Al/Fe =1 samples, indicating "amorphous AFm" formation (Lothenbach et al., 2008). In terms of the effect of ZnO addition, there were no obvious trends in the Al-monocarbonate peak intensity.

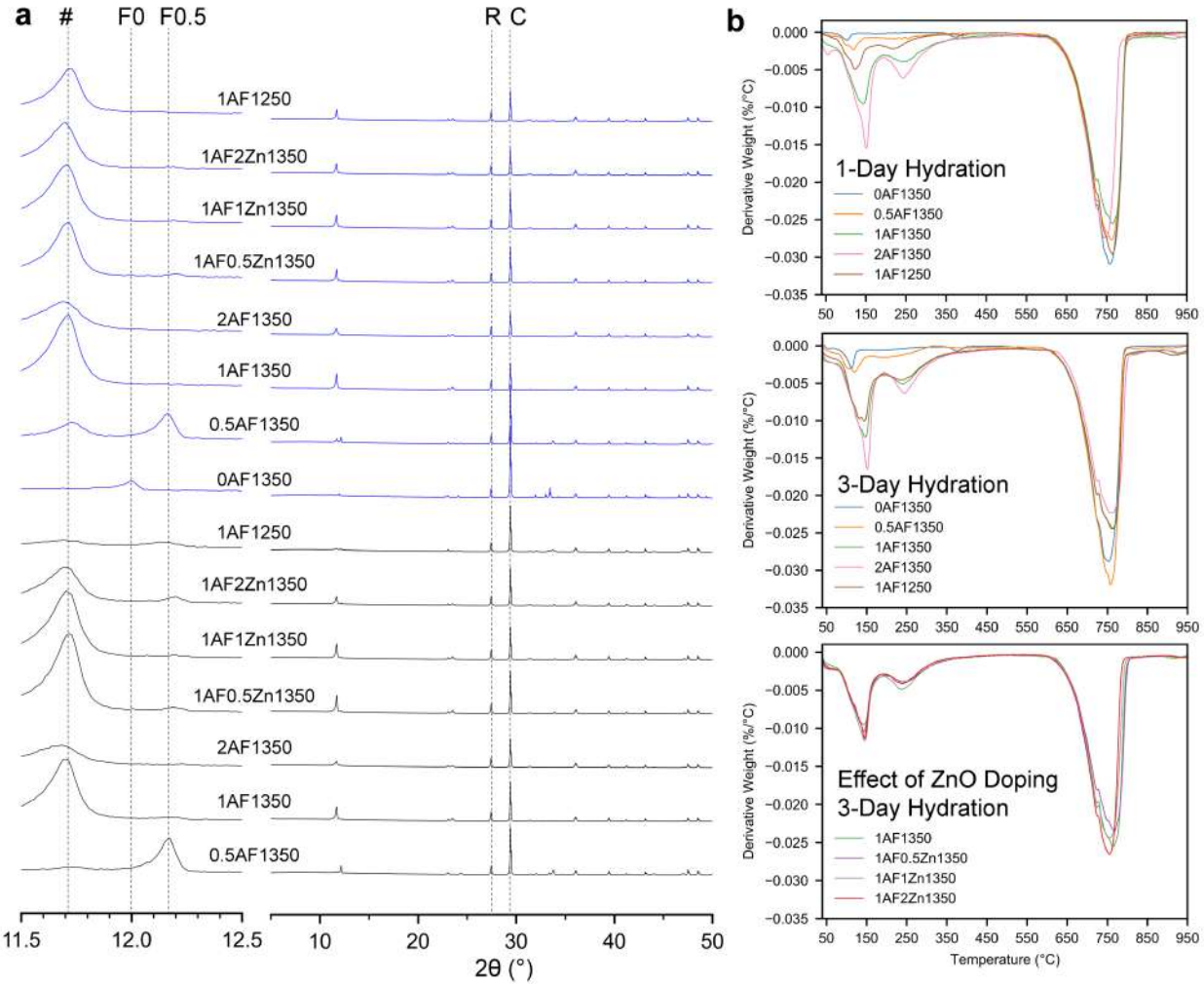


Figure 1. XRD and TGA results of the hydration products. (a)XRD patterns of hydration products of ferrites with $CaCO_3$ after 1-day (black) and 3-day (blue) hydration (#: Al-monocarbonate, F0: ferrite with Al/Fe =0, F0.5: ferrite with Al/Fe = 0.5, R: rutile, and C: calcite). (b) DTG curves of the hydration products.

3.2. Thermal Analysis

The thermal analysis of the hydrated samples (Figure 1b) mostly confirmed the XRD observations. The twin-peaks in the DTG data commonly associated with Al-monocarbonate were observed in the DTG data, where Al-monocarbonate loses five interlayer water molecules in between 50 and 200 °C, and six water molecules from the octahedral layer in between 200 and 300 °C (Lothenbach et al., 2008). The 0AF1350 sample showed minimal water mass loss indicating little hydration product formation, and the amount of mass loss related to Al-monocarbonate increased with the Al/Fe ratio, including Al/Fe = 2, further indicating that there is more amorphous AFm formation in the 2AF1350 sample compared to other samples. Further, the DTG peak area of the 0.5AF1350 and 1AF1250 increased from 1 day to 3-day of hydration implying continual hydration process between 1 and 3-day for those samples, whereas the DTG peak did not change a lot in between 1 and 3 days for 1AF1350 and 2AF1350 samples showing the hydration reaction was mostly completed within 1 day. Finally, there was no pronounced effect and trends of ZnO doping on the hydration product formation in general, however, the sample with 1% ZnO doping showed a slight increase in DTG peak area. As Zn-doping did not change the ferrite reactivity, raw materials containing minor amounts of Zn can be used in cement with high ferrite content.

4. Conclusions

Ferrites with different Al/Fe ratios, sintering temperatures, and ZnO doping were synthesised and hydrated in presence of excess $CaCO_3$ in this paper, and the hydration product was characterised using TGA and XRD. Four major conclusions were drawn from the experiments — first, Al-monocarbonate forms when ferrites with Al/Fe = 0.5, 1 and 2 react with excess calcium carbonate, with the reaction kinetics accelerating with Al/Fe ratio, and the hydration reaction being almost completed just after 1-day hydration for Al/Fe = 1 and 2, when a sintering temperature of 1350°C is used. No AFt or hydrogarnet phases were observed in the XRD data. Second, the hydration kinetics is slower when a sintering temperature of 1250 °C is used instead of 1350 °C for ferrite with Al/Fe = 1, as the hydration reaction was continued between 1 day and 3 days for the sample synthesised at 1250 °C. Third, the Al-monocarbonate formed from the ferrite with Al/Fe = 2 is potentially more amorphous and/or contains more disorder than other ferrite samples. Finally, ZnO doping did not alter the hydration product formation and hydration kinetics prominently showing that Zn containing raw materials can be utilised for high ferrite cements. These results indicate that high-ferrite limestone cement could be a promising solution to reduce cement CO_2 emission by reducing both clinker factor and clinker carbon footprint.

Acknowledgements

This research was funded by the EPSRC project, “Developing iron-rich cement clinker & understanding ferrite for the valorisation upcycling of steel slags (FeRICH)” (EP/W018810/1).

References

Barnett, S. J., Adam, C. D., & Jackson, A. R. W. (2001). An XRPD profile fitting investigation of the solid solution between ettringite, $Ca_6Al_2(SO_4)_3(OH)_{12}\cdot 26H_2O$, and carbonate ettringite, $Ca_6Al_2(CO_3)_3(OH)_{12}\cdot 26H_2O$. *Cement and Concrete Research*, *31*(1), 13-17.

Dilnesa, B. Z., Lothenbach, B., Le Saout, G., Renaudin, G., Mesbah, A., Filinchuk, Y., Wichser, A., & Wieland, E. (2011). Iron in carbonate containing AFm phases. *Cement and Concrete Research*, *41*(3), 311-323.

Fukuhara, M., Goto, S., Asaga, K., Daimon, M., & Kondo, R. (1981). Mechanisms and kinetics of C_4AF hydration with gypsum. *Cement and Concrete Research*, *11*(3), 407-414.

Gartner, E. (2004). Industrially interesting approaches to “low-CO_2” cements. *Cement and Concrete Research*, *34*(9), 1489-1498.

Lothenbach, B., Le Saout, G., Gallucci, E., & Scrivener, K. (2008). Influence of limestone on the hydration of Portland cements. *Cement and Concrete Research*, *38*(6), 848-860.

Monteiro, P. J., Miller, S. A., & Horvath, A. (2017). Towards sustainable concrete. *Nature materials*, *16*(7), 698-699.

Tao, Y., Zhang, W., Li, N., Ching, W.-Y., Wang, F., & Hu, S. (2020). Atomic-level insights into the influence of zinc incorporation on clinker hydration reactivity. *Open Ceramics*, *1*, 100004.

Zhang, K., Wang, F., Rao, M., Zhang, W., & Huang, X. (2019). Influence of ZnO-doping on the properties of high-ferrite cement clinker. *Construction and Building Materials*, *224*, 551-559.

Zhong, H., Zhang, K., Yang, L., Wang, F., Hu, S., Lv, M., & He, J. (2022). In-depth understanding the hydration process of Mn-containing ferrite: A comparison with ferrite. *Journal of the American Ceramic Society*, *105*(7), 4883-4896.

The 16th International Congress on the Chemistry of Cement 2023 (ICCC2023)
"Further Reduction of CO_2 -Emissions and Circularity in the Cement and Concrete Industry"
September 18–22, 2023, Bangkok, Thailand

Deciphering the defects of alite particles at the single-atom level

Q. Zheng[1], C.Y. Liang[2], J.Y. Jiang[3], and S.F. Li[4*]

[1] *Department of Civil and Environmental Engineering, University of California, Berkeley, CA, 94720, USA*

Email: qizheng@berkeley.edu

[2] *Department of Civil and Environmental Engineering, University of California, Berkeley, CA, 94720, USA*

Email: icyliang@berkeley.edu

[3] *School of Materials Science and Engineering, Southeast University, Nanjing 211189, P.R.China*

Email: jinyangjiang@163.com

[4] *Department of Civil and Environmental Engineering, University of California, Berkeley, CA, 94720, USA*

Email: shaofan@berkeley.edu

ABSTRACT

Crystallographic defects play a crucial role in cement hydration, with initial dissolution being dominated by the formation of etch pits that rely on the intersection of defects on surfaces. However, the defects present in cement particles have remained a mystery without direct observation. In this study, we used scanning transmission electron microscopy to unravel the defects in alite particles at the atomic level. Our observations identified different types of defects, including vacancies, doping, dislocations, twinning, grain boundaries, and more. Our findings indicate that defects in cement particles may serve as reactive sites during early hydration, facilitating the initial dissolution and providing nucleation sites for C-S-H. This work provides insight into the secrets of cement defects at the single-atom level and opens up new opportunities for tuning the hydration process through defect engineering of cement particles.

KEYWORDS: *Alite structure, defect, atomic resolution, scanning transmission electron microscopy*

1. Introduction

With an estimated yearly consumption of 30 billion tons (Monteiro et al., 2017), Portland cement concrete is the world's most widely used manufactured material. Fundamental questions regarding its hydration mechanisms, such as the dissolution of cement grains or the nucleation and growth of calcium silicate hydrate (C-S-H), remain unsolved. Tricalcium silicate (C_3S) is the primary constituent in Portland cement (50-70%) that governs the hydration kinetics at an early age with the reaction with water leading to the formation of Portlandite and C-S-H. C_3S is commonly used in the study of hydration mechanisms considering its simplicity in chemical component. For example, the initial fast dissolution of C_3S can be explained by the geochemistry theory (Juilland et al., 2010), which is governed by the defects from the particles. However, very few studies have been reported on the defect types and evolutions in tricalcium silicate. Groves et al. studied the crystalline structure of cement phases by means of transmission electron microscopy while only twin bands and planar defects were observed at moderate resolution.
In this study, we resolved the crystallographic defects present in pure M1-C_3S samples at the atomic level using transmission electron microscopy. Different types of defects were identified. The effect of these defects will be related with the hydration behavior of C_3S and our findings provide new opportunities for tuning the hydration process by engineering defects in cement particles.

2. Materials and Methods

Sample preparation. Tricalcium silicate (C_3S) was prepared following a reported protocol (Dvořák et al., 2023): we used a 3:1 stoichiometric mixture of calcium carbonate ($CaCO_3$) and high-purity quartz

powder (SiO_2) purchased from Sigma Aldrich. Some minor impurities (<3% wt) including Al_2O_3, Fe_2O_3, and SO_3 may be introduced. The powders were pressed into pellets, followed by a two-step burning synthesis process, and finally ground into grains.

Transmission electron microscope. The Thermo Fisher Scientific ThemIS TEM was used in characterizing the morphology at low magnitude. The microscope was operated at 300 keV with the image aberration corrector fully corrected for coherent axial aberrations up to 3rd order. The Bruker EDS detector, with a solid angle of 0.7 steradian, enabled high count rates with minimal dead time for fast STEM-EDS mapping. Here, the dwell time was set 20 µs with drift correction enabled. For bright field imaging, the electron dose rate was ~11 $e \cdot Å^{-2} \cdot s^{-1}$. For electron diffraction, a 50 µm C2 aperture was used to limit the illuminated area.

High-angle annular dark-field imaging, scanning transmission electron microscopy (HAADF-STEM). Atomic resolution STEM images of the C_3S particles were acquired on a FEI Titan 80-300 microscope (energy: 200 keV; spherical aberration: 1.2 mm; illumination semi-angle, 10.7 mrad). The 100-pA electron beam was focused to a probe with a 50-mm probe-forming aperture (C2) and rastered over the sample. The scattered electrons were captured by a Fischione 3000 HAADF detector.

Diffraction pattern simulations. CrystalMaker software was used for the visualization of the crystal structures as well as simulating the diffraction patterns at different zone axes with all parameters consistent with the experiment setups.

3. Results and Discussions

The C_3S grains were irregularly shaped with sharp edges (**Figure 1A**) due to the milling and annealing process (Bazzoni et al., 2014), and the average size of C_3S powder was found to be 21.28 µm with a normal distribution from 0.1 to 200 µm. For STEM characterization, we focused on ~1 µm C_3S grains for better resolution. In **Figure 1B**, we observe dislocation patterns as dark lines resulting from the lattice distortion around dislocation cores. Some of the dislocations are regularly distributed at a moderate density, likely due to imperfections from the synthesis process (Bazzoni et al., 2014). Meanwhile, tangled dislocations are observed in regions with concentrated stress domains, indicating active glides and mechanical twinning with an extremely high dislocation density. These defects can promote the dissolution of C_3S, as dislocations aid etch pit formation during C_3S hydration (Juilland and Gallucci, 2015) and activate the onset of the induction period (Juilland et al., 2010). Furthermore, the electron diffraction pattern (**Figure 1C**) reveals that the C_3S grain exhibits a single-crystal feature with slight lattice distortions resulting from lattice misfits. The C_3S powder used in our experiments was identified to be monoclinic (M1) tricalcium silicate (Nishi et al., 1985), a typical phase that we used to explore its defects.

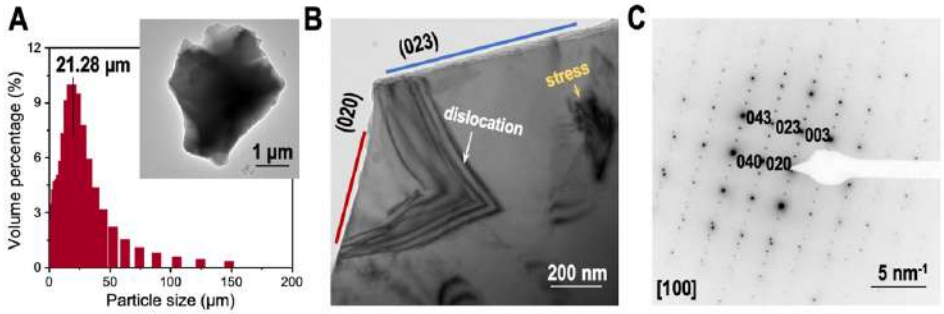


Figure 1. Characterization of C_3S grains. (**A**) Morphology and particle size distribution of C_3S grains. (**B**) Bright-field TEM image of a C_3S grain with distinct dislocation patterns. (**C**) Electron diffraction pattern with single crystal features.

Aimed to investigate the defects present in small C_3S grain < 1 µm, we successfully captured its crystal structure at the atomic resolution. The bright dots **Figure 2** represents the atom columns in perfect lattices. The atomic arrangement of C_3S particle at different zone axes were captured with its distinct species highlighted. Note that the indexing in the diffraction patterns was based on the physical distances of each spot and the angle between respective spots. The Best-fit pattern with the smallest sum-of-squares error was regarded as the perfect indexing.

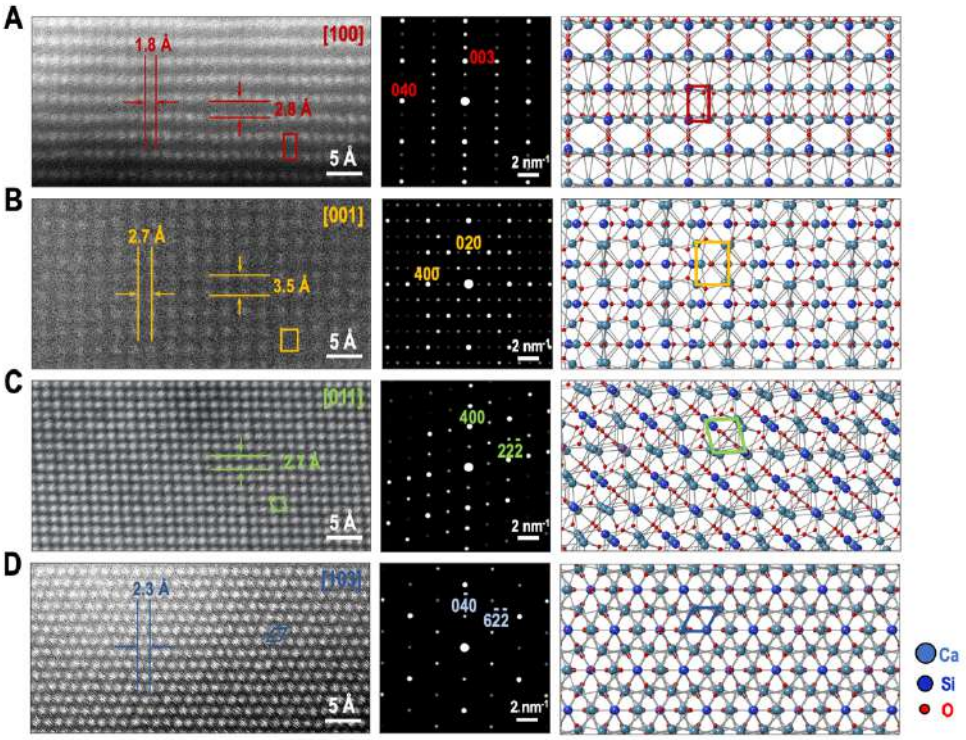
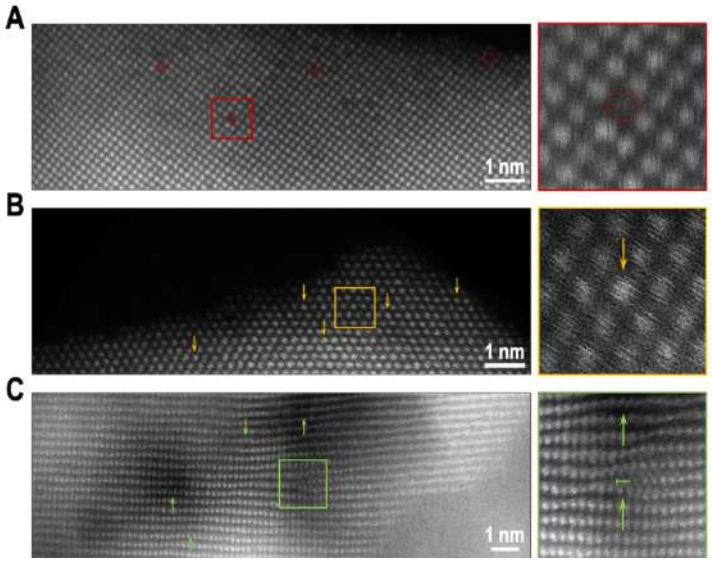


Figure 2. STEM images of C_3S particle at different zone axes. Atomic resolution STEM image; simulated diffraction pattern; crystal structure at (**A**) [100], (**B**) [001], (**C**) [011], and (**D**) [103] zone axes.

Different defect types can be discerned including vacancy, doping, dislocation, twinning and grain boundary. It is possible some foreign ions such as sulfur, aluminum ions act as substitutional impurities to distort the calcium silicate lattice (**Figures 3A & B**). In fact, these ions can significantly stabilize the M1 alite polymorph by affecting the calcium to oxygen bond lengths, and the orientation of SiO_4 tetrahedra (Maki et al., 1992; Manzano et al., 2011). Some point defects may develop into planar dislocations (**Figure 3C**) or twinning structures (**Figure 3D**). **Figure 3D** reflects a high density of defects. The twinning of the cubic array oriented along the <110> zone axis on the {112} plane introduced a high density of misfit dislocations. An interphase boundary between two domains had another misfit dislocation in **Figure 3E**. Due to the high-temperature processing involved in alite preparation, these defects may serve as preferable pathways for energy release and act as reactive sites during initial dissolution.



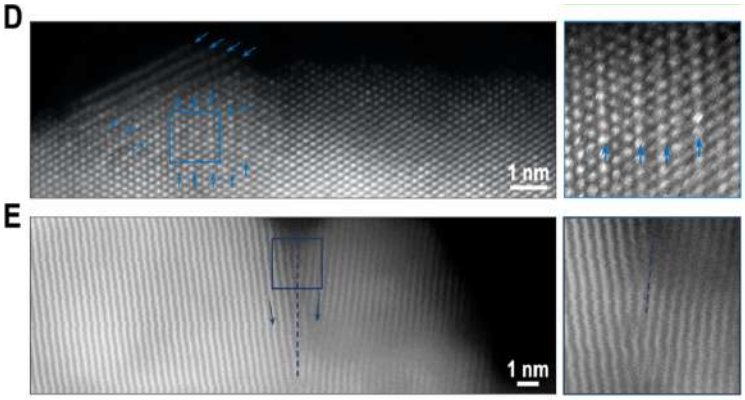


Figure 3. Various defects found in different C_3S domains, including (**A**) vacancy, (**B**) doping, (**C**) dislocation, (**D**) twining, and (**E**) grain boundary.

4. Conclusions

In this study, we utilized scanning transmission electron microscopy to investigate the intrinsic defects present in alite particles. Based on our findings, the following conclusions can be reached:
(1) Point defects including vacancies and doping were deciphered at the atomic level in alite particles. These defects can be introduced from substitutional impurity during the calcination process; (2) Some plane defects such as edge dislocations, twinning were commonly identified in the particle which could potentially serve as reactive sites for initial dissolution; (3) Our analysis showed that alite particles were polycrystalline and had distinct grain boundaries. Furthermore, we found that planar interfaces within the particles disrupted the long-period cubic-stacking sequences.
This work provides a comprehensive analysis of cement defects at the atomic level, shedding light on their fundamental properties and characteristics, as well as presents new avenues for manipulating the hydration process by engineering defects in cement particles.

References

Bazzoni, A., Cantoni, M. and Scrivener, K.L. (2014) "Impact of annealing on the early hydration of tricalcium silicate", *Journal of the American Ceramic Society*, 97(2): 584–591

Dvořák, K., Všianský, D., Ravaszová, S. and Jančíků, A. (2023) "Synthesis of M1 and M3 alite polymorphs and accuracy of their quantification", *Cement and Concrete Research*, 163: 107016

Juilland, P. and Gallucci, E. (2015) "Morpho-topological investigation of the mechanisms and kinetic regimes of alite dissolution", *Cement and Concrete Research*, 76: 180–191.

Juilland, P., Gallucci, E., Flatt, R. and Scrivener, K. (2010) "Dissolution theory applied to the induction period in alite hydration", *Cement and Concrete Research*, 40(6): 831–844.

Maki, I., Fukuda, K., Yoshida, H. and Kumaki, J. (1992) "Effect of MgO and SO_3 on the impurity concentration in alite in Portland cement clinker", *Journal of the American Ceramic Society*, 75(11): 3163–3165

Manzano, H., Durgun, E., Abdolhosseine Qomi, M.J., Ulm, F.-J., Pellenq, R.J.M. and Grossman, J.C. (2011) "Impact of chemical impurities on the crystalline cement clinker phases determined by atomistic simulations", *Crystal Growth & Design* 11(7): 2964–2972.

Monteiro, P.J.M., Miller, S.A. and Horvath, A. (2017) "Towards sustainable concrete", *Nature Materials* 16(7): 698–699

Nishi, F., Takeuchi, Y. and Maki, I. (1985) "Tricalcium silicate $Ca_3O[SiO_4]$: the monoclinic superstructure" *Zeitschrift für Kristallographie-Crystalline Materials*, 172(1-4): 297–314

The 16th International Congress on the Chemistry of Cement 2023 (ICCC2023)
"Further Reduction of CO_2 -Emissions and Circularity in the Cement and Concrete Industry"
September 18–22, 2023, Bangkok, Thailand

The Influence of Aluminum Uptake on the Mechanical Properties of Calcium Silicate Hydrate

Z. Zhang[1*], G. Geng[2]

[1] *National University of Singapore, Singapore*
Email: zhangzhe@u.nus.edu

ABSTRACT

Supplementary cementitious materials (SCMs) are widely used in cement-based materials, which reduces the amount of cement usage and provides a solution to reduce the amount of CO_2 emitted in construction industries. In addition, it can enhance final strength and durability of concrete. However, the mechanism of this enhancement is unclear. Having a better understanding of the mechanism is helpful for mix design improvement. Incorporating SCMs in cement-based materials often modifies cement paste by incorporating aluminum to calcium silicate hydrate (C-S-H). Previous research explains how aluminum modifies the nanostructure of C-S-H. In molecular scale, Al takes up a bridge position on silica chains, elongates the main silicate chain length, and can even form cross-linking structure among interlayers of C-A-S-H. How these structure changes influence mechanical properties are still unclear. In this research, hydrothermally synthesized C-A-S-H powders were used to study the effect of aluminum on the multi-scale mechanical properties with a series of methods including Superficial Rockwell hardness and Vickers hardness. Among the mechanical properties in different length scales, a relationship between chemical composition especially Al/Si ratio and strength would be built and explained in detail.

KEYWORDS: *C-A-S-H, Mechanical Properties, Aluminum, Multi-scale*

1. Introduction

Incorporation of supplementary cementitious materials (SCMs) in cement-based materials alters the pore network and composition of the primary hydration product, calcium (-aluminate)-silicate-hydrate (C(-A)-S-H) (Güneyisi et al (2012) and Duan et al (2013)). While numerous studies have investigated the impact of chemical composition, particularly the Ca/Si ratio, on the multiscale mechanical properties of C-S-H, few have focused on the influence of aluminum uptake. A few experiments suggest that the presence of Q_3(Al) in the C(-A)-S-H interlayer is a critical factor affecting the micromechanical properties.
Geng et al (2017) confirmed that the incorporation of aluminum increases the crystallinity of C-(A-)S-H, particularly along the c-axis, as observed through Rietveld refinement. Cross-linking induced by aluminum was observed in C-A-S-H synthesized at 80 °C, resulting in a similar basal spacing of 11 Å to tobermorite increasing the overall bulk modulus. Hunnicutt et al (2016) demonstrated that the increased mean coordination number (MCL) and crosslinking of C-A-S-H contribute to a lower viscous response compared to C-S-H.
In order to accurately analyze the influence of aluminum uptake on the strength of C-A-S-H, well-controlled porosity, and chemical composition of samples is needed (Zhang et al (2022)).
In this study, we attempt to generate a C-A-S-H pellet from C-A-S-H powders produced by hydrothermal reaction. Through this practice, we aim to investigate the effect of chemical conditions on the strength of compacted C-A-S-H pellets. Hardness in different length scales were measured to study the influence of controlled Al/Si, porosity and water content on mechanical properties.

2. Materials and methods

2.1 Materials

C-A-S-H powders were synthesized by mixing silica fume (99.09% SiO_2), calcium oxide, and monocalciumaluminate (synthesized from $CaCO_3$ and Al_2O_3) and deionized water. The synthesis involved an initial bulk Ca/(Si+Al) of 1.1 and a water-to-solid ratio of 20. One set of samples utilized KOH solution instead of deionized water to investigate pH effects. Further sample details are provided in Table 1.

Table 1 Sample information

Sample	CASH_1	CASH_2	CASH_3	CASH_4	CASH_5
Al/Si ratio	0	0.05	0.1	0.2	0.2
KOH (mol/L)	0	0	0	0	0.5

The mixtures were stored in high density polyethylene bottles at 80 °C for 2 months to accelerate the reaction (Myers et al., 2015). Afterward, the products underwent vacuum filtration and isopropanol washing using 0.45 μm filter papers in an N_2-filled glovebox to prevent carbonation. The filtered C-A-S-H was then stored in a vacuum oven (up to 0.1 MPa) at 40 ℃ for 15 days. Each of the four C-S-H powders were divided into two groups and transferred to desiccators with RH of 8% and 100% respectively.
Subsequently, the powder was compressed at 500 MPa, 1000 MPa, and 2000 MPa using a hydraulic press to create dense C-S-H pellets for further investigations.

2.2 Methods

The microscale morphology of the C-A-S-H powders was imaged using a Hitachi Regulus 8230 field emission scanning electron microscope (FE-SEM) in secondary electron mode with an accelerating voltage of 5 kV. The major crystalline phases were identified using a Shimadzu diffractometer (LabX XRD-6000) with a Cu-Kα 2θ range of 5°-45°, a scan rate of 1.5°/min, and operating parameters of 40 kV and 30 mA.
The hardness test is advantageous for evaluating the mechanical properties of materials independently of initial defects such as voids or cracks, providing a reliable measure of bulk strength. For macro hardness testing, Superficial Rockwell hardness was employed, while Vickers hardness (HMV SHIMADZU) was chosen for micro hardness assessment.

3. Results

3.1 Morphology of C-A-S-H powders

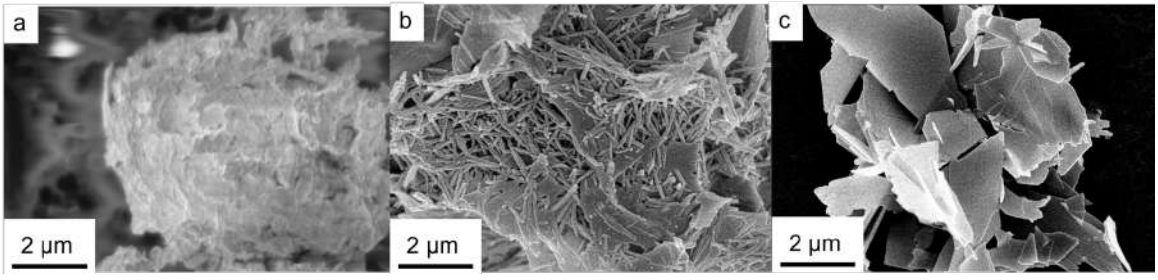


Figure 1 Morphology of C-A-S-H powders of (a) CASH_1 (b) CASH_4 and (c) CASH_5

Figure 1 demonstrates that C-S-H powders exhibit a foil-like shape, while the inclusion of aluminum leads to the formation of needle-like structures in C-A-S-H. Higher pH values result in the transformation

of needle-like structures into plate-like shapes, enhancing the crystallinity of C-A-S-H. This is corroborated by the XRD findings presented in Figure 2, where the intensity of the 002 peak is notably strengthened when aluminum is incorporated, particularly under higher pH conditions.

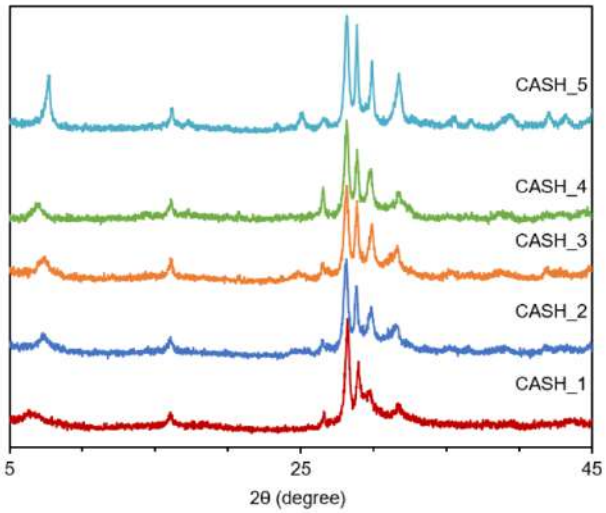


Figure 2 XRD reuslts of C-A-S-H powders

3.2 Hardness of C-A-S-H monoliths

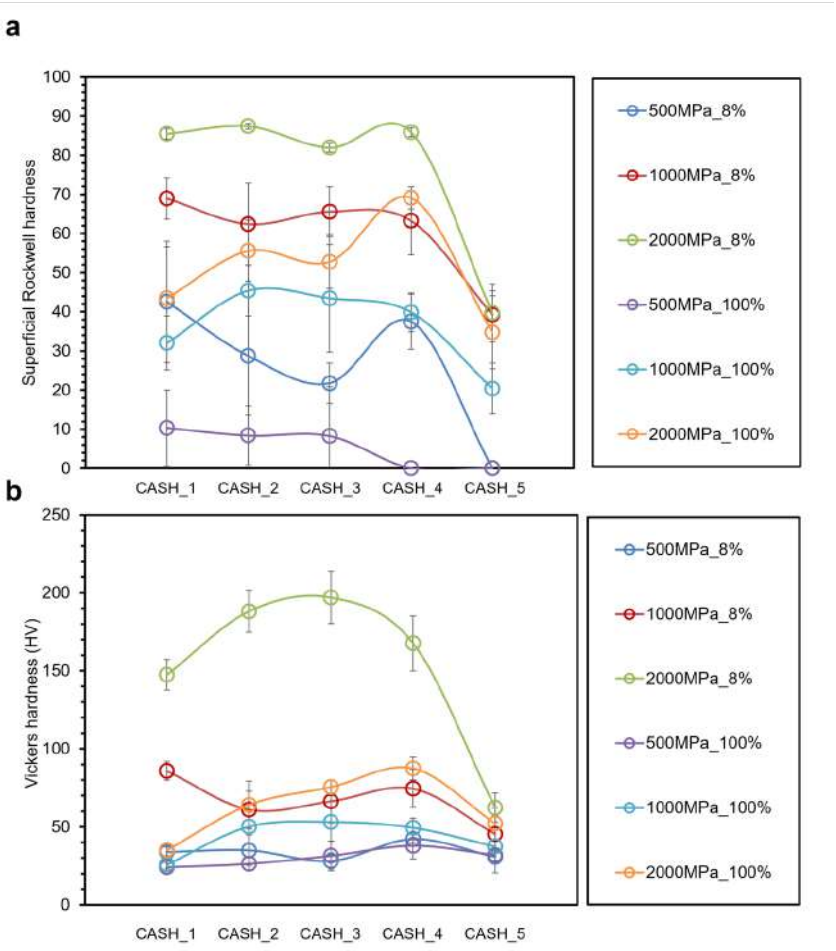


Figure 3 (a)Superficial Rockwell hardness and (b) Vickers hardness of C-A-S-H monoliths

Two length scales of hardness were employed to assess the impact of aluminum incorporation on the mechanical properties of C-S-H. Figure 3 illustrates that increasing the compacting pressure from 500 MPa to 2000 MPa results in a noticeable enhancement of both macro and micro hardness in all samples. Additionally, a higher water content leads to a decrease in macro and micro hardness. The changing pattern of macro hardness among different samples is similar to that of micro hardness. Notably, a higher pH value has a significant detrimental effect on hardness when comparing the hardness of CASH_4 and CASH_5.

Regarding the influence of Al/Si ratio, the micro hardness of samples cured under 100% RH conditions increases as the Al/Si ratio increases. However, for samples cured under 8% RH conditions, only the micro hardness of samples made at 2000 MPa (with the least porosity) exhibits an increasing trend with increasing Al/Si ratio. Samples made at 500 MPa and 1000 MPa show a slight decreasing trend. The regulation of macro hardness follows a similar pattern, albeit with some exceptions due to the formation of larger-scale cracks.

4. Conclusions

In conclusion, this paper investigates the impact of aluminum uptake in C-S-H on morphology and mechanical properties. The study examines multiscale mechanical responses and C-S-H particle shapes based on initial chemical conditions (Al/Si ratio and moisture content). The findings reveal that aluminum uptake enhances the crystallinity of C-S-H, as does a higher pH value. However, a higher pH value reduces the hardness of C-A-S-H. The strengthening effect of aluminum uptake on hardness is particularly evident in higher water content or lower porosity. The underlying reasons for these influences warrant further exploration. This paper offers a new direction for understanding the effects of surface chemistry on the mechanical properties of C-A-S-H, which could guide the design of cement with improved performance.

Acknowledgements

This research is funded by the MOE Tier 1 project in Singapore under WBS A-0009288-01-00.

References

Güneyisi, E. et al. (2012) “Strength, permeability and shrinkage cracking of silica fume and metakaolin concretes”, *Construction and Building Materials*, 34: 120–130

Duan, P. et al. (2013) “Effects of metakaolin, silica fume and slag on pore structure, interfacial transition zone and compressive strength of concrete”, *Construction and Building Materials*, 44 :1–6

Geng, G. et al. (2017) “Aluminum-induced dreierketten chain cross-links increase the mechanical properties of nanocrystalline calcium aluminosilicate hydrate”, *Scientific Reports*, 7(1): 44032

Hunnicutt, W.A., Mondal, P. and Struble, L.J. (2016) “Effect of Aluminum Substitution in C-S-H on Viscoelastic Properties: Stress Relaxation Nanoindentation”, *1st International Conference on Grand Challenges in Construction Materials*

Zhang, Z. et al. (2022) “Endowing strength to calcium silicate hydrate (C-S-H) powder by high pressure mechanical compaction”, *Cement and Concrete Research*, 159:106858

Myers, R.J. et al. (2015) “Effect of temperature and aluminium on calcium (alumino)silicate hydrate chemistry under equilibrium conditions”, *Cement and Concrete Research*, 68: 83–93

The 16th International Congress on the Chemistry of Cement 2023 (ICCC2023)
"Further Reduction of CO_2 -Emissions and Circularity in the Cement and Concrete Industry"
September 18–22, 2023, Bangkok, Thailand

New steel production processes and their consequences for slag utilization in cement

A. Ehrenberg[1*], D. Algermissen[1]

[1] *FEhS - Institut für Baustoff-Forschung e.V., Duisburg, Germany*
a.ehrenberg@fehs.de, d.algermissen@fehs.de

ABSTRACT

The main challenge of the steel industry for the next decade is the steel production transformation process, starting in Europe. The CO_2 intensive blast furnace/basic oxygen furnace (BOF) route will be substituted by a combination of Direct Reduced Iron (DRI), based on natural gas, later on "green" hydrogen, with an Electric Arc Furnace (EAF) or a Submerged Arc Furnace (SAF), heated with renewable energy. Thus, the well-known latent-hydraulic granulated blast furnace slag (GBS) being successfully used in cement and concrete since more than 140 years will vanish step by step! GBS is used as a SCM not only, but in particular, due to its clinker reduction and from there its CO_2 reduction potential for the cement and concrete production. Whereas the DRI process itself does not generate any slag, EAF and SAF will do. These slags will be very different. Moreover, the new EAF slags will be different compared to today's EAF slag based only on scrap re-melting, too. For example, the heavy metal content will be lower, but still much higher compared to GBS. However, specific slag/metal ratios, resulting slag volumes, chemical and mineralogical compositions and physical properties of the new slags are yet unknown. Thus, also their cementitious and environmental properties are still unknown. Different projects being already started or which are expected to start within the next time aim mainly to create slags being similar to today's GBS. The main objective is to offer furthermore a material with latent hydraulic properties to the cement and concrete industry.

KEYWORDS: ***blast furnace slag, steel slag, direct reduced iron, CO_2 reduction, SCM***

1. Introduction

The "Green deal" strategy of the European Commission from 2019 aims to reduce the net CO_2 emissions to zero until 2050. In order to reach this task breakthrough technologies have to be implemented, as well for the steel as other energy and CO_2 intensive industries, like cement production. Worldwide steel production is responsible for about 7-9 % of all man-made CO_2-emissions which is comparable to the contribution of the cement industry (5-8 %). The main CO_2 source is the Carbon in coke and coal being used as well as reduction agent as energy carrier in the blast furnaces. Thus, the main challenge of the steel industry for the future is related to the steel production transformation process, starting in Europe. Several steel producers defined ambitious strategies to substitute the blast furnace/BOF route by a combination of DRI, based on natural gas (later on "green" hydrogen) with an EAF or a SAF, heated with renewable electric energy. Since decades blast furnace slag is used mainly as a cementitious material (if it is glassy due to a quenching process for the liquid slag) or as an aggregate for concrete and road construction (if it is crystalline due to slow cooling in a slag pit), as it is described e.g. by Ehrenberg (2021). This slag utilisation saves natural resources as well as primary energy and it significantly reduces the CO_2 footprint of cement and concrete (CEMBUREAU (2020a, 2020b)). Due to the lack of hydraulic properties the crystalline steel slags are mainly used as road making aggregates substituting natural materials. It is of high importance to qualify the new slags to fulfil the same ecological and technical tasks in order to avoid negative consequences for the cement, concrete and construction industries.

2. Today's steel and slag production

According to Worldsteel (2022) the worldwide crude steel production was 1950 million tons in 2021. On average 71 % were produced by the blast furnace/BOF route and 29 % by the EAF route using mainly scrap. Other processes are negligible. The pig iron production was 1354 million tons whereas the direct reduced iron production was only 114 million tons. The shares of the different routes differ from country to country. While in the EU the shares were 56 % and 44 %, respectively, the shares in the USA were 31 % and 69 %, respectively, and in China - with 1033 million tons by far the biggest steel producer - the shares were 89 % and 11 %, respectively. Thus, also the resulting blast furnace and steel slag volumes differ from region to region. In total it can be estimated that in 2021 worldwide about 325 million tons of GBS, 110 million tons of air-cooled blast furnace slag, 145 million tons of BOF slag and 70 million tons of EAF slag have been produced. It is expected by ESTEP (2019) that the maximum world steel production might be 2.8 billion tons in 2070. Then, without any changes regarding process technology, slag/metal ratios, market shares etc., the resulting total slag volume would culminate in about 1 billion tons!
Assuming that 1 ton of GBS substitutes 1 ton Portland cement clinker and considering average specific CO_2 emissions (122 kg/t for GBS, 900 kg/t clinker) it can be calculated that for 2021 cement production about 250 million tons CO_2 emissions were avoided and that about 500 million tons of natural raw materials for clinker burning have been saved! Therefore, beside other activities the further reduction of the clinker content in cement, e.g. by the intensified use of metallurgical slags, is an integral part of the CO_2 road maps of the cement and concrete industry (CEMBUREAU (2020b), GCCA (2021), VDZ (2020)).
The different steel making routes cause different specific CO_2 emissions (table 1). The EAF process, based on scrap, causes only about 455 kg/t. However, the scrap recycling is limited and scrap availability is time-delayed. Moreover, not all high grade steel qualities can be efficiently produced. Thus, a significant further switchover from the blast furnace/BOF route to the classical EAF route cannot be expected in Europe and other countries with noteworthy EAF steel production. Other measurements, e.g. the use of hydrogen in the blast furnace instead of coke and coal, are very limited and are intended to be used only as bridge technologies. Thus, only the implementation of breakthrough technologies might be able to achieve the ambitious CO_2 reduction goals.

Table 1: Different steel making routes and the belonging specific CO_2 emissions (Boston (2013, Arens (2017))

Route	kg CO_2 per ton hot rolled coil
Blast furnace (coke and coal based) / BOF (pig iron and scrap based)	1888
EAF (scrap based)	455
DRI (natural gas based) / EAF	1487
Melting reduction (coal based)	1349

3. The new processes

The basic idea of the new processes is to substitute the CO_2 intensive blast furnace process by a gas based solid state direct reduction process of natural iron ores and pellets combined with a downstream electrical smelting of the direct reduced iron as it is (DRI) or as hot briquetted iron HBI (Bartholmé (2022)). The significant difference of the processes is the electrical smelting method. Alternative 1 uses a conventional EAF as it is used today for scrap melting. DRI/HBI will be melted batchwise together with a certain scrap volume in an oxidising atmosphere. The products are crude steel and a modified EAF slag. The existing BOF steel shop will be omitted. Alternative 2 uses a SAF in a continuous process in a reducing atmosphere, as it is given in a blast furnace. The products are "electric" hot metal and a SAF slag being similar to a typical blast furnace slag. The existing BOF steel shop and all other metallurgical process steps will remain. Today SAFs are mainly used for ferro alloys and non-ferrous metal production (SMS (2015)).
Different steel companies decided to follow different alternatives. The cost-intensive programs are named e.g. "SALCOS" (Salzgitter), "XCarb" (ArcelorMittal), "HYBRIT" (SSAB), "tkH2Steel" (thyssenkrupp Steel) or "Zeremis" (Tata Steel). Regarding the time scale the goals are very ambitious. Already in 2025/2026 the first blast furnaces should be closed and e.g. "SALCOS" should result finally in a 95 % CO_2 reduction, compared to 2018, in 2033! More and more contracts on "green steel" are agreed between steel

producers and customers, e.g. from the automotive or white goods industries. Depending on the individual blast furnace capacity yearly 150-800 thousand tons of GBS will vanish together with each substituted blast furnace! This will result in drastic consequences for the cement producers. In Germany the market share of Portland slag and blast furnace cements was 37 % in 2021, and other composite cements include GBS, too (VDZ (2022)).

4. The new slags

All new steel production routes will produce new types of slags. But specific slag/metal ratios, resulting total slag volumes, chemical and mineralogical composition and physical properties of the new liquid and solidified slags are yet unknown. Thus, also their technical and environmental properties are still unknown. Volumes and properties depend on the future ore and pellet quality, the electrical smelting process (EAF or SAF), the DRI/scrap ratio (DRI/EAF route), the slag adjustment according to metallurgical and cementitious requirements, a potential separate slag treatment in order to reduce the high iron oxide and heavy metal content (DRI/EAF route) and - of course - the cooling process of the liquid slag (wet/dry granulation or slag pit). Based on the current knowledge and expectations table 2 summarises the most relevant aspects regarding the new slags. It is quite clear that the differences compared to GBS may result in more or less significant differences of the cementitious properties.

Table 2: Properties of the new slags compared to granulated blast furnace slag

Route	DRI/EAF	DRI/SAF
Slag/metal ratio (after slag processing, if necessary)	> scrap based EAF slag (≈ 130 kg/$t_{crude\ steel}$) << GBS	≈ 150 kg/$t_{electric\ hot\ metal}$ << GBS (≈ 300 kg/$t_{pig\ iron}$)
Original basicity CaO/SiO_2	1.8-2.2 >> GBS (∅ 1.1) Decrease necessary	< GBS Increase necessary
Heavy metal content (in particular Cr-III)	< scrap based EAF slag >> GBS	≈ GBS (very low)
Fe oxide content	>> GBS	≈ GBS (very low)
Glass content (if granulated)	≈ GBS	≈ GBS (very high)
Colour	dark	bright

It is expected that the the DRI/SAF route will create a slag being very similar to GBS, if it is granulated. But a very important topic is that within the DRI/EAF route not only DRI is used as iron source but also scrap. The scrap share might differ between 30-50 % in relation to the Fe input into the EAF. The consequence is that the heavy metal input into the new slags will increase significantly. In particular, the Chromium content will be much higher compared to GBS. Today German scrap based EAF slags have a total Chromium content of about 4300 mg/kg (as a median value after aqua regia dissolution). However, it has to be stressed that iron and steel slags do not contain Chromium-VI, but only Chromium-III. Moreover, the results of leaching tests according to different test procedures (e.g. EN 12457-4 or NEN 7373) show very low values fulfilling the relevant German or Dutch requirements. Nevertheless, as well the cement industry itself as some national authorities must rethink whether requirements regarding solid contents have really an additional benefit for securing the environmental compatibility!
Different projects being already started or which are expected to start within the next time aim mainly to create slags being similar to today's GBS. The main objective is to offer the cement and concrete industry furthermore a material with latent hydraulic properties. For example, FEhS co-operates with Salzgitter, Holcim et al. on alternative 1 ("DRI-EOS") and with thyssenkrupp Steel, HeidelbergMaterials et al. on alternative 2 ("SAVE CO_2"). Moreover, additional projects aim to qualify the remaining scrap based EAF slags or the BOF slags and slag from the smelting reduction HIsarna® process (Meijer (2015)) for cementitious applications. For the common EAF and BOF slags as well chemical as cooling process modifications are necessary in order to generate hydraulic properties. Figure 1 shows a water granulation test of FEhS in a scrap based EAF steel plant. The basicity CaO/SiO_2 of the liquid slag was decreased from about 2.2 to 1.51 to enable the glass formation. In this specific case a glass content of only 68 wt.-% was achieved, measured by XRD. Due to the high iron oxide content the slag grains were very dark (figure 2).

Despite the below average glass content (compared to GBS), cementitious tests according to EN 196 confirmed a latent hydraulic reactivity comparable to GBS.



Figure 1: Water granulation of modified scrap based EAF slag



Figure 2: Granulated EAF slag

5. Conclusions

The goals of some steel producers to reduce their CO_2 emissions by implementation new processes are very ambitious and will have a strong impact on generation and use of slags in cement and concrete. However, the time schedule differs in the different world regions. The running and upcoming projects aim to solve the technical and metallurgical tasks, also regarding handling, treatment, quality and utilisation of the new slags. Even though their specific and total volumes are expected to be lower compared to today, it is quite clear that dumping will be avoided and that the preferred task must be to generate a latent hydraulic substitute for GBS and consequently for clinker. Moreover, in order to compensate the stepwise decrease of GBS it is an option to qualify also the remaining scrap based EAF and the BOF slags for cementitious applications. However, many questions regarding technical, economical and political frame conditions have still to be answered. In addition, in some countries the environmental requirements for building materials have to be focused on the potential release of heavy metals instead of their content in the solid state.

References

Arens, M. et al. (2017) "Pathways to a low-carbon iron and steel industry in the medium-term - the case of Germany", *Journal of Cleaner Production*, 163: 84-98

Bartholmé, J. et al. (2022) "Flexibility of the direct reduction routing for a CO_2 reduced steel making while enabling the production of a high quality slag", in *9. Berliner Konferenz - Mineralische Nebenprodukte und Abfälle*, Neuruppin

Boston Consulting Group and Steel Institute VDEh (2013) "Steel's contribution to a low-carbon Europe 2050", Boston

CEMBUREAU (2020a), "Environmental Product Declaration (EPD) for blast furnace cement (CEM III) produced in Europe", Brussels

CEMBUREAU (2020b), "Cementing the European Green Deal", Brussels

Ehrenberg, A. (2021) "Iron and steel slags - from wastes to by-products of high technical, economical and ecological advantages", in *Industrial Waste. Characterization, Modification and Applications of Residues*, edited by H. Pöllmann, de Gruyter, Berlin

ESTEP - European Steel Technology Platform (2019) "Green Steel by EAF", workshop report, Bergamo

GCCA - Global Cement and Concrete Association (2021) "Concrete future - The GCCA 2050 cement and concrete industry roadmap for net zero concrete", London

Meijer, K. et al. (2015) "The HIsarna ironmaking process", METEC, Düsseldorf

SMS group (2015) "SAF Bulletin", 3rd ed., Düsseldorf

VDZ - Verein Deutscher Zementwerke (2020) "Decarbonising cement and concrete: A CO_2 roadmap for the German cement industry", Düsseldorf

VDZ - Verein Deutscher Zementwerke (2022) "Zahlen und Daten 2022", Berlin

Worldsteel (2022) "World steel in figures 2022", Brussels

The 16th International Congress on the Chemistry of Cement 2023 (ICCC2023)
"Further Reduction of CO_2 -Emissions and Circularity in the Cement and Concrete Industry"
September 18–22, 2023, Bangkok, Thailand

The effect of iron phases on the performance of calcined clays in calcined clay-limestone cement

T.R. Muzenda[1*], F. Georget[2], T. Matschei[3]

Institute of Building Materials Research, RWTH Aachen University, 52062 Aachen, Germany

1. muzenda@ibac.rwth-aachen.de

2. georget@ibac.rwth-aachen.de

3. matschei@ibac.rwth-aachen.de

ABSTRACT

The increasing use of calcined clay limestone cement (CCLC) requires an understanding of the effect of kaolinitic clay secondary phases on overall performance of the cement blends. In this study, we investigate fresh and early hydration properties of CCLC using kaolinitic clays with a wide range of chemical and mineralogical composition. The results indicate that early performance of calcined clays is not only dependent on kaolinite content but that specific surface area (SSA) plays a key role in the onset and evolution of rheological properties and early hydration. Furthermore, when the same calcination and grinding protocol is applied, there appears to be a correlation between the resulting SSA of calcined clays and the initial content of iron phases in raw clays.

Key Words: Kaolinitic clay secondary phases, Rheology, Early hydration

1. Introduction

The need to cut down on carbon-footprint in the cement and concrete industry has led to an increased use of supplementary cementitious materials (Juenger et al. 2011). Previous research has convincingly shown that even at a substitution rate of 45 wt.%, the combination of calcined clay and limestone ensures comparable mechanical properties to OPC at as early as 7 days (Antoni et al. 2012; Scrivener et al. 2018).

The phase composition of natural raw clays is always more than just kaolinite. Secondary phases such as quarts, iron (hydr)oxides, and secondary clay phases, for example, illite, montmorillonite, and smectite, are always present. However, the effects of these secondary phases on the physiochemical properties of the resulting calcined clay as well as the impact on the performance of calcined clay limestone cement (CCLC) has not been widely studied.

In this study, clays with a wide range of phase compositions were analyzed. The focus of this part of the research is to show how secondary phases in the calcined clays affect rheological properties and early hydration.

2. Materials and methods

Pastes made from clinker and gypsum blended with calcined clay and limestone were used. Eight clays with different chemical and mineral compositions (three of which are shown in Table 1) are studied. Calcination was carried out at 800 °C for 2 h after an initial drying at 105 °C for at least 48 h and

crushing to a diameter of less than 2 mm. After calcination, grinding was carried out using a steel ball mill for 90 min in batches of 2.5 – 4.0 kg. A PCE-based superplasticizer was used to adjust flow and to allow for the measurement of rheological properties possibly up to 3 h.

Rheology tests were carried out using an Anton Paar MCR 102 modular compact rheometer. The rheometer is stress-controlled and operates with a maximum torque of 200 mNm. A geometry consisting of a sand blasted cup (to prevent slippage on the walls) with an inner diameter of 28 mm and a helix of a stirrer 24 mm in diameter was used. Static yield stress (logarithmic stress ramp) and dynamic yield stress (Bingham model) are reported. Thermogravimetric analysis was also carried out to determine the portlandite quantity and bound water up to 7d. A heating rate of 10 °C/min was used, and the measurement cell was flushed with 50 mL/min nitrogen gas. $Ca(OH)_2$ content was determined using the tangential method between 400 and 550 °C, and mass losses were normalized and reported to the sample mass at 550 °C, which was considered to be the dry binder mass that remains constant during cement hydration.

Table 1: Phase composition and physical parameters for the 3 main clays studied.

		MK72	MK47	MK23
Phase composition (wt.%)				
Kaolinite	XRD	69.6	47.5	21.2
	TGA	73.2	46.6	23.4
Illite/Muscovite		2.7	-	14.4
Silicates & Aluminosilicates		10.8	22.6	57.5
Fe (hydr)oxides		-	6.5	0.6
BET surface area (m^2/g)		15.6	34.7	15.1

3. Results and discussion

Rheology results for static yield stress (SYS) and dynamic yield stress (DYS) are shown in Fig. 1. As expected (Kawashima et al. 2013; Muzenda et al. 2020), both SYS and DYS increase with hydration time. In addition, for MK47, the rheology tests could only be carried out up to 1 h, beyond which the sample was too stiff to load reliably (homogenously) into the measuring cup. The SYS and DYS results show late structural growth for MK23 and MK72 (between 2 and 3 h) when compared to MK47 (between 5 min and 1 h).

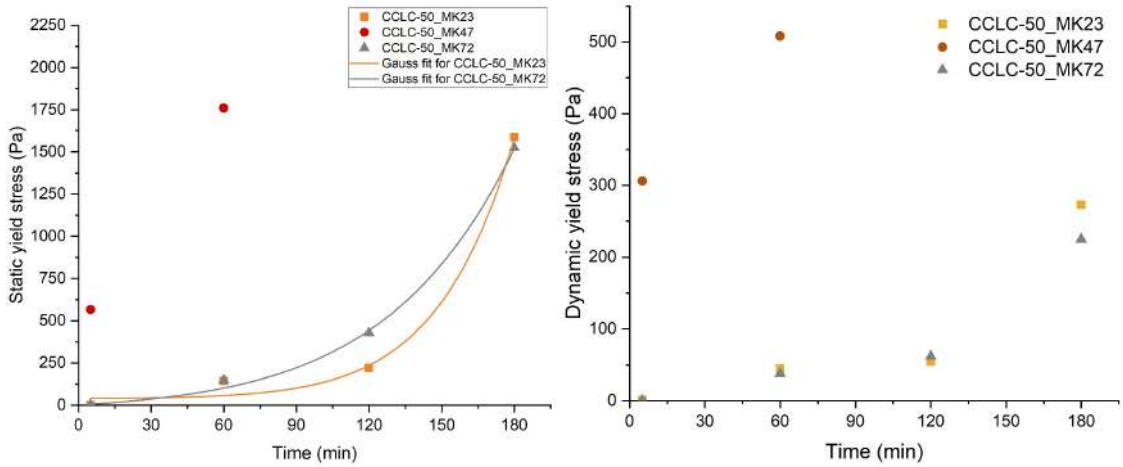


Figure 1. Change of static yield stress (left) and dynamic yield stress (right) up to 3 h for varying clays.

Table 1 shows that MK47 had almost double the BET specific surface area (SSA) of MK72 and MK23 even though the same calcination and grinding protocol was utilized for all clays. The effects of the higher SSA are also seen in early hydration in addition to the rheology. Fig. 2 shows that up to at least 3 days MK47 has superior portlandite consumption (which indicates pozzolanic reactivity) when compared to MK72. The contribution of the filler effect (which is largely dependent on SSA) on early hydration has been widely reported (Berodier and Scrivener 2014; Zunino and Scrivener 2019). The results presented here also suggest that early hydration of CCLC is not only dependent on metakaolin content and that SSA has a significant contribution.

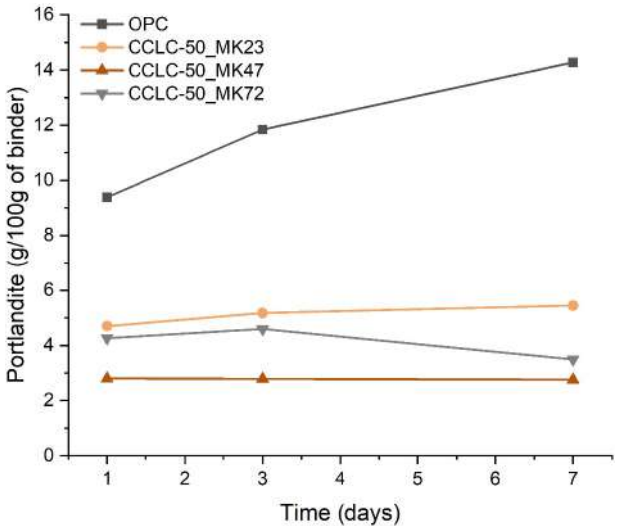


Figure. 2. Portlandite consumption as measured by TGA.

The follow up question is that if the same calcination and grinding protocol was applied what could be the cause of the difference in resulting SSA? Five more clays of various composition were investigated to answer this question. The rheology and early hydration results were consistent with those reported earlier – SSA through the filler effect had a significant impact on early performance of the clays. This seems to suggest that the development of fresh properties and early hydration kinetics for natural clays is not as dependent on metakaolin content as 'lab-prepared clays' based on highly pure metakaolin appear to be. In the latter case, the surface of the highly pure metakaolin dominates the overall surface leaving an impression that water demand could be related to metakaolin content of calcined clays when it may mainly be an issue of the overall SSA, which tends to go down with substitution of the metakaolin by other materials.

An interesting correlation appeared to also appear as we looked at the phase composition of the clays studied (Fig. 3). There are several possible reasons why iron phases seem to affect SSA and, consequently, rheology and hydration. For example, it may have to do with the effect on calcination, the easy of grindability or probably an impact on nucleation. The presence of iron phases in kaolinitic clays results in substitution of Al by Fe in the kaolinite structure (Murad and Fabris 2010). This leads to a disordered structure which may increase reactivity and may also contribute to the increase in SSA. Additionally, it has been reported previously that iron phases, goethite in particular, are considerably easier to grind than quartz (Akande, Adebayo, and Akande 2013) which would likely increase the SSA of iron-containing clays. Two hypotheses have been presented, and the real effect is currently under investigation.

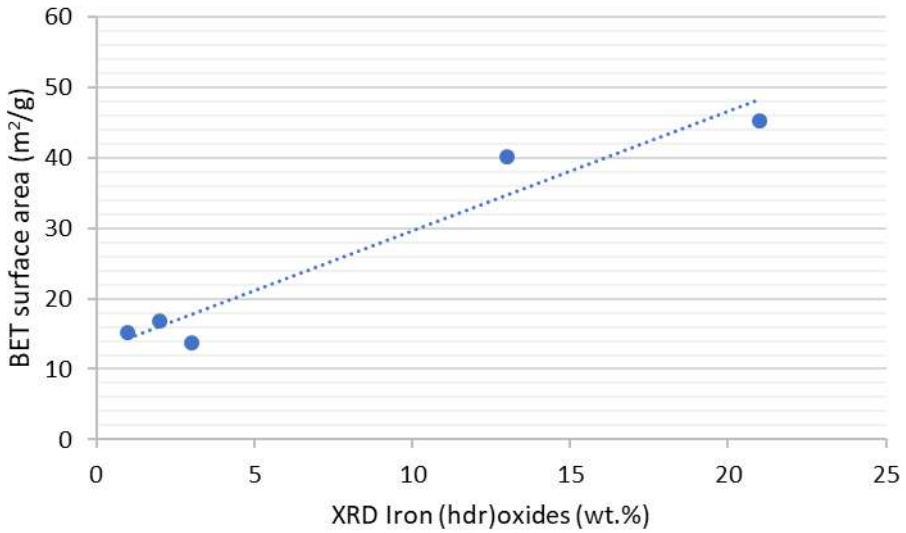


Fig. 3. Correlation of BET surface area and iron (hydr)oxides determined by QXRD.

4. Conclusions

The impact of the SSA of calcined clays on rheology and early hydration of calcined clay limestone cements (CCLC) was analyzed by several techniques in this study. The results suggest that SSA has a significant impact on the onset and evolution of rheological properties and early hydration, and that these properties depend not only on metakaolin content but also on the content of secondary phases. Further experiments also indicated that given the same calcination and grinding protocol, clays with high amounts of iron phases tend to end up with significantly higher specific surface area which in turn impacts early performance in CCLC.

Acknowledgement: The authors would like to express appreciation for the support of INNOVANDI (GCCA) under core projects 5-7 (2021).

References

Akande, S., Adebayo, B., and Akande, J.M. (2013) 'Comparative Analysis of Grindability of Iron- Ore and Granite' *Journal of Mining World Express* 2 (3): 55-62.

Antoni, M., Rossen, J., Martirena, F., and Scrivener, K. (2012) 'Cement Substitution by a Combination of Metakaolin and Limestone'. *Cement and Concrete Research* 42 (12): 1579–89.

Berodier, E., and Scrivener, K. (2014) 'Understanding the Filler Effect on the Nucleation and Growth of C-S-H'. *Journal of the American Ceramic Society* 97 (12): 3764–73.

Juenger, M.C.G., F. Winnefeld, Provis, J.L., and Ideker. J.H. 2011. 'Advances in Alternative Cementitious Binders'. *Cement and Concrete Research* 41 (12): 1232–43.

Kawashima, S., Chaouche, M., Corr, D.J., and Shah, S.P. (2013) 'Rate of Thixotropic Rebuilding of Cement Pastes Modified with Highly Purified Attapulgite Clays'. *Cement and Concrete Research* 53: 112–18.

Murad, E., and Fabris, J.D. (2010) 'Kaolin mining and beneficiation: The role of iron'. *Journal of Physics: Conference series* 217: 012066.

Muzenda, T.R., Hou P., Kawashima, S., Sui, T., and Cheng, X. (2020) 'The Role of Limestone and Calcined Clay on the Rheological Properties of LC3'. *Cement and Concrete Composites* 107: 103516.

Scrivener, K., Martirena, F., Bishnoi, S., and Maity, S. (2018) 'Calcined Clay Limestone Cements (LC3)'. *Cement and Concrete Research* 114: 49–56.

Zunino, F., and Scrivener, F. (2019) 'The Influence of the Filler Effect on the Sulfate Requirement of Blended Cements'. *Cement and Concrete Research* 126: 105918.

The 16th International Congress on the Chemistry of Cement 2023 (ICCC2023)
"Further Reduction of CO_2 -Emissions and Circularity in the Cement and Concrete Industry"
September 18–22, 2023, Bangkok, Thailand

Dilution Effects in Cementitious Matrices by Using Calcined Clay and Limestone for Reduced Clinker Factors

A.H. Ahmed[1], S. Nune[1,2], M. Liebscher[1*], V. Mechtcherine[1]

[1] *Technische Universität Dresden, Dresden, Germany*
ameer_hamza.ahmed@tu-dresden.de
marco.liebscher@tu-dresden.de
mechtcherine@tu-dresden.de
[2] *Sonocrete GmbH, Cottbus, Germany*
swamynune@outlook.com

ABSTRACT

With the addition of supplementary cementitious materials (SCMs) in ordinary Portland cement (PC) systems at a certain specific water-to-binder ratio, the resultant water-to-cement ratio increases, generating additional space for clinker hydrates to precipitate – the "dilution effect". This effect becomes more and more pronounced as more cement is replaced by SCMs. This study investigates the dilution effect caused by the reducing clinker factor by coupled substitution of limestone and calcined clays – commonly known as limestone calcined clay cement (LC^3). It was found that 30% replacement of PC (i.e., LC^3-70) yields similar mechanical properties and critical pore sizes as the pure PC system at 28 days. Beyond this replacement level, the dilution effect becomes more pronounced leading toward reduced mechanical response and less dense microstructure. However, between 7- and 28 days the recovery in the overall porosity, critical pore sizes, and mechanical properties were more pronounced in LC^3 blended systems with dilution effects as compared to plain PC and LC^3-70.

KEYWORDS: *Clinker factor, LC^3, dilution effects, compressive strength, porosity.*

1. Introduction

The blend of limestone and calcined clays as supplementary cementitious materials (SCMs) in conjunction with Portland cement (PC) has led to the development of a promising novel ternary blended cement known as limestone calcined clay cement (LC^3) (Antoni et al., 2012). LC^3 not only reduces the clinker factor and thus lowers the CO_2 emissions from clinker production, but also maintains the mechanical performance and improves durability compared to traditional Portland cement (PC) system (Scrivener 2014, Scrivener et al. 2018, and Sharma et al. 2021).
Recent advances in cementitious materials and application technologies, such as Engineered Cementitious Composites (ECC), Textile Reinforced composites (TRC), and 3D Printable Concrete (3DPC) - as reviewed by Mechtcherine (2013) and Zhang et al. (2021) - led to the design of fine-grained cementitious matrices incorporating high volumes of SCMs to compensate for high cementitious masses due to the absence of coarse aggregates in their mix design. Since the availability of the conventional SCMs (fly ash, slags, etc.) becomes less, LC^3 can be a suitable alternative cement for further developing these composites, as limestone and calcined clays are available in abundance. However, when high-volume substitutions are rehearsed in blended systems, the dilution effects get more pronounced due to the increased water-to-clinker ratio at a certain water-to-binder ratio. LC^3 can effectively recoup these dilution effects through the pozzolanic reaction of aluminosilicates (metakaolin in calcined clay), as well as the additional synergetic reaction between metakaolin and carbonates (from limestone), precipitating C-(A)-S-H and AFm-carbonate phases (K. Scrivener et al., 2018; Sharma et al., 2021), respectively. To maximize the benefits of LC^3 in these high substitution scenarios, it is recommended to use low-grade

(less reactive) calcined clays to ensure that the availability of portlandite does not impede the ongoing reactions (Krishnan et al. 2020).
This article investigates the dilution effects caused by the different substitutions of low-grade limestone and calcined clays and looks into the strength and microstructure development of different LC^3 mortars between 7 and 28 days of hydration using standard compression test and mercury intrusion porosimetry (MIP).

2. Materials and experimental methods

2.1 Characterization of raw materials

A commercially available PC, CEM I 52.5 R-SR3/NA from Holcim GmbH, Germany, and calcined clay from Liapor GmbH & Co. KG, Hallendorf Germany were used in this study. It is a low kaolinite clay with a kaolinite content of ≤ 25 wt.% and consists of other clay minerals and impurities before calcination (Beuntner 2017). After calcination, the quantified amorphous content from XRD-Rietveld analysis is 65.7 wt.%. A dolomite-rich limestone, Saxodol 90 LE from sh minerals GmbH, Germany, was used. It had 54 wt.% calcite and 44 wt.% dolomite content. A high-purity gypsum (99%) from Grüssing GmbH, Germany was attained and used for proper sulfation of the investigated mortars. For detailed physical, chemical, and mineralogical characterization of raw materials, refer to (Wang et al., 2021).

2.2 Mixture design

Table 1 shows the mix proportions of four different substitution levels of limestone and calcined clay, along with a reference PC mixture. The ratio between the calcined clay and limestone was kept constant (2:1) and quartz sand was used as a source of fine aggregate. The ratio of sand-to-binder was kept low. PCE-based superplasticizer (Glenium ACE 460 from Master Builders Solution GmbH, Germany) and viscosity modifying agent (Sika Unterwasser-Compound 100) were added for workability purposes. A fixed water-to-binder ratio of 0.4 was used for all the mixes and the resultant water-to-cement ratio is in the table.

Table 1. Mixture composition of investigated blends. The values expressed in wt. %.

Raw materials	PC	LC^3-70	LC^3-50	LC^3-35	LC^3-25
Portland cement	100	70	50	35	25
Calcined clay	-	18	31	41	48
Limestone	-	9	16	21	24
Gypsum	-	3	3	3	3
Sand-to-binder	0.23	0.23	0.23	0.23	0.23
Water-to-binder	0.40	0.40	0.40	0.40	0.40
Water-to-cement	0.40	0.57	0.80	1.14	1.60

2.3 Sample preparation and testing

Compression tests were performed according to EN 196-1 standard on two halves of 40x40x160 mm^3 prisms at 7 and 28 days. Samples were sealed-cured at 20 °C until the testing date. Porosity was characterized by MIP using Pascal 140/440 porosimeter on crushed pieces of a few millimeters in size at similar ages. Before MIP measurements, the pieces were dried via solvent exchange with iso-propanol and vacuum desiccator. Mercury with a contact angle of 140° was intruded into the dried samples up to 400 MPa with a 6-14 MPa/min pressure ramp.

3. Results and discussion

The compressive strength of the investigated mortar compositions was evaluated at 7 and 28 days, the results are presented in **Fig. 2(a)**. To compare the strength of different compositions, the data were normalized with respect to the reference PC strength and plotted as the strength activity index (SAI) in

Fig. 2(b). The dashed lines in this plot represent the theoretical strength of the compositions based on the PC replacement level. For instance, the compressive strength of a pure PC system is 100%, indicating that when 30% PC is replaced (i.e., LC^3-70), the theoretical strength should be 70% of pure PC mortar. However, in all the blended compositions, the actual strength exceeded the theoretical one at both investigated ages, indicating the physical and chemical interaction of added supplementary materials to the hydrating PC system.

The LC^3-70 composition exhibited the highest strength at 7 days, and its strength at 28 days was similar to the reference PC. The high early strength is likely due to the accelerant and dilution effects of adding supplementary materials, which promote clinker hydration. Between 7 and 28 days of age, LC^3-70 exhibited the least gain in strength out of all the studied compositions, which is attributed to the limited availability of spaces for continued hydration and precipitation of hydrates after a certain age, as indicated by the MIP results (**Fig. 3**). Specifically, the critical pore entry size (the peak value in differential pore volume curve) of LC^3-70 composition was similar to plain PC mortar at 28 days. It was between 10-12 nm, which is slightly higher than the 6-8 nm, found by Berodier & Scrivener (2015) for blended and plain cement systems. Note, the differences in sample preparation, curing, or hydration stoppage methods can explain this disparity. These critical radius values typically reach the maximum after 14 days of hydration, which slows down further reaction rates and subsequent strength gains (Berodier & Scrivener, 2015). These implications arise specifically due to the fact that when the radius of curvature is high (for smaller pore sizes), a higher degree of supersaturation levels of pore solution is needed for hydrates to precipitate there (Steiger, 2005).

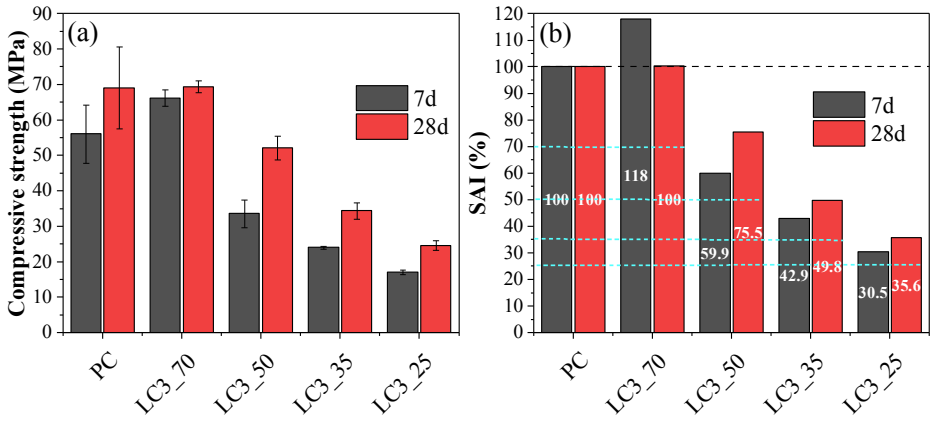


Fig 2. (a) Compressive strength, and (b) strength activity index (SAI) of the investigated compositions.

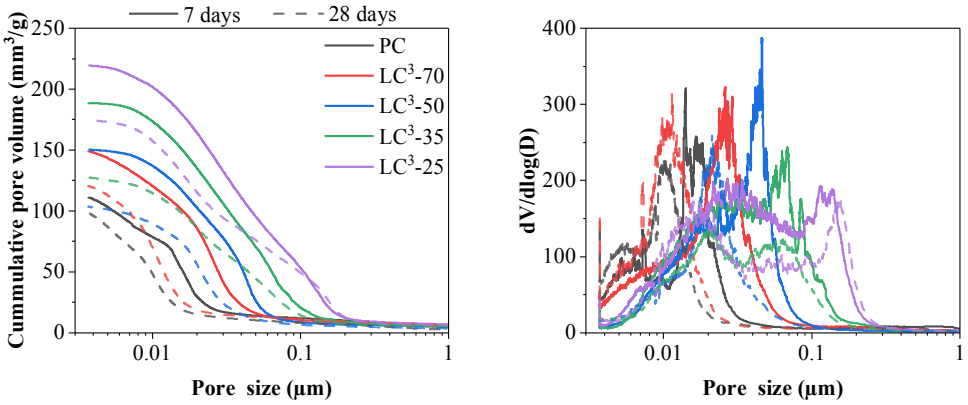


Fig 3. Porosity measured by MIP for PC and LC^3 mortars at 7 and 28 days.

For compositions with 50% or greater PC replacement, such as LC^3-50, LC^3-35, and LC^3-25, the dilution effects were evident in the mechanical properties and the pore structure build-up at the investigated ages. For these compositions, due to pronounced dilution effects, the critical pore entry sizes did not reach the 10-12 nm range, resulting in a higher and prolonged degree of hydrations for these blends, as evident by the pronounced recovery in mechanical strengths and refinement in pore structure between 7 and 28 days.

It is noteworthy that the overall porosity was higher in blended compositions, which is attributed to the fact that the volume that clinker hydrates can fill is not similar to one of the supplementary material's hydrates (Berodier & Scrivener, 2015). Moreover, under pronounced dilution effects, the degree of reaction of clinker phases enhances, but the reaction of added supplementary materials is delayed further in time resulting in a lower degree of reaction of SCMs in blended systems (Lam et al., 2000). This delay is more pronounced as more PC is substituted. Additionally, the amount of clinker can be a limiting factor for the further development of microstructure when high volumes of substitutions are rehearsed.

4. Conclusions

This study aimed to investigate the strength development and pore structure evolution in LC^3 blended mortars with dilution effects for reduced clinker factors. The findings indicate that the accelerant and dilution effects resulting from the addition of limestone and calcined clay in hydrating PC systems can yield higher early strengths than plain PC systems at optimum substitution levels (in this case 30% replacement of PC: LC^3-70). However, the strength development can significantly slow down once maximum critical pore radius values similar to pure PC systems are reached. Contrarily, when high volume substitution levels of PC are rehearsed (LC^3-50, LC^3-35, and LC^3-25), the reduction in mechanical properties is evident because the maximum critical pore sizes don't reach similar values as plain PC systems. However, relatively higher gains in strengths and densification of pore structure were observed in systems with pronounced dilution effects as compared to neat PC systems and LC^3-70. As long as critical pore sizes are below maximum and clinker hydrate doesn't become a limiting factor, the microstructure development can continue.

Acknowledgments

The authors greatly acknowledge the financial support by the German Research Foundation (DFG) for funding project 455631638. Moreover, this research was co-financed by tax funds on the basis of the budget adopted by the Saxon State Parliament.

References

Antoni, M., Rossen, J., Martirena, F., & Scrivener, K. (2012). "Cement substitution by a combination of metakaolin and limestone", *Cement and Concrete Research*, *42*(12), 1579–1589.

Berodier, E., & Scrivener, K. (2015). "Evolution of pore structure in blended systems", *Cement and Concrete Research*, *73*, 25–35.

Beuntner, N. (2017). "*Zur Eignung und Wirkungsweise calcinierter Tone als reaktive Bindemittelkomponente im Zement*". 207.

Krishnan, S., Dhoopadahalli, G. R., & Bishnoi, S. (2020). "Why Low-Grade Calcined Clays Are the Ideal for the Production of Limestone Calcined Clay Cement (LC3)", In S. Bishnoi (Ed.), *Calcined Clays for Sustainable Concrete*. Springer.

Lam, L., Wong, Y. L., & Poon, C. S. (2000). "Degree of hydration and gel/space ratio of high-volume fly ash/cement systems", *Cement and Concrete Research*, *30*(5), 747–756.

Mechtcherine, V. (2013). "Novel cement-based composites for the strengthening and repair of concrete structures", In *Construction and Building Materials* (Vol. 41, pp. 365–373).

Scrivener, K. L. (2014). "Options for the future of cement", *Indian Concrete Journal*, 11–21.

Scrivener, K., Martirena, F., Bishnoi, S., & Maity, S. (2018). "Calcined clay limestone cements (LC3)", In *Cement and Concrete Research* (Vol. 114, pp. 49–56).

Sharma, M., Bishnoi, S., Martirena, F., & Scrivener, K. (2021). "Limestone calcined clay cement and concrete: A state-of-the-art review", *Cement and Concrete Research*, *149*.

Steiger, M. (2005). "Crystal growth in porous materials - I: The crystallization pressure of large crystals", *Journal of Crystal Growth*, *282*(3–4), 455–469.

Wang, L., Ur Rehman, N., Curosu, I., Zhu, Z., Beigh, M. A. B., Liebscher, M., Chen, L., Tsang, D. C. W., Hempel, S., & Mechtcherine, V. (2021). "On the use of limestone calcined clay cement (LC3) in high-strength strain-hardening cement-based composites (HS-SHCC)", *Cement and Concrete Research*, *144*.

Zhang, C., Nerella, V. N., Krishna, A., Wang, S., Zhang, Y., Mechtcherine, V., & Banthia, N. (2021). "Mix design concepts for 3D printable concrete: A review", *Cement and Concrete Composites*, *122*(February), 104155.

The 16th International Congress on the Chemistry of Cement 2023 (ICCC2023)
"Further Reduction of CO_2 -Emissions and Circularity in the Cement and Concrete Industry"
September 18–22, 2023, Bangkok, Thailand

Study on Calcined Clay-Recycled Concrete Powder Composite as Supplementary Cementitious Material

Shusen Li[1], Jiaping Liu[2]*, Zhen Li[3], Cheng Yu[3], Weixiao Xie[2]

[1] *College of materials science and engineering, Chongqing University, Chongqing, CHINA*
E-mail: Shusen Li 20200901043@cqu.edu.cn
[2] *School of materials science and engineering, Southeast University, Nanjing, CHINA*
E-mail: Jiaping Liu liujiaping@cnjsjk.cn, Weixiao Xie xieweixiao@seu.edu.cn
[3] *Sobute New Materials Co., Ltd., Nanjing, CHINA*
E-mail: Zhen Li lizhen@cnjsjk.cn, Cheng Yu yucheng@cnjsjk.cn

ABSTRACT

Recycled concrete powder (RCP) contains a large amount of calcium carbonate, which means it can be used as a calcium carbonate source in calcined clay (CC) -limestone cement system (LC^3). This method will reduce the dependence of LC^3 cement on natural limestone and improve the utilization rate of construction demolition waste. In this study, by adjusting the ratio and dosage of CC/RCP, hardened matrix properties and hydration products of the CC-RCP cement system were characterized. The results show that the compressive strength index of mortar could reach 0.87 when 30% of cement was replaced with CC. When CC and RCP were used together, the mortar's compressive strength could get 86% of that when CC was used alone. The reduction in cement content has almost no effect on the flexural strength of mortar after 28d. From XRD, the mixed-use of CC and RCP could promote the conversion of C_4AH_{13} into hemicarboaluminate (Hc) and monocarboaluminate (Mc) in hydration products. These results validates the potential of RCP to be used to produce LC^3 cement.

KEYWORDS: *calcined clay, recycled powder, mechanical properties, hydration product*

1. Introduction

Today, fly ash and slag are the most widely used supplementary cementitious materials (SCMs). With the promotion of clean energy and decreasing demand for pig iron, the output of fly ash and slag is expected to decrease. Thus, more readily available and environmentally friendly alternatives are essential (Skocek et al (2020)). Kaolinite-rich clay is widely available on the Earth's crust. When calcined at half the temperature of calcined cement, a highly reactive pozzolan can be obtained. Compounding CC with limestone in a ratio of 2 to 1 will lead to a 50% total clinker substitution without significantly affecting the cement quality (Cancio Díaz et al (2017)). Therefore, calcined clay and limestone have the potential to meet the demand for SCMs and the low-carbon requirements of the cement and concrete industry. This new green cement system is also known as LC^3 cement (Sánchez Berriel et al (2016)).

Recycled concrete powder (RCP) is a by-product produced in crushing and recycling waste concrete, which contains a large amount of aggregate debris and a small amount of cement paste. The main mineral composition of RCP is calcium carbonate and SiO_2 with no pozzolanic, which will lead to the degradation of performance when added to cement alone (Duan et al (2020), Prošek et al (2019)) . In this study, RCP was used to replace limestone as the source of calcium carbonate in LC^3 cement. The influence of the mixture proportion and content on hardened matrix was explored, indicating the feasibility of the waste mixture as an SCM. It is significant to broaden the raw material source of LC^3 cement and the utilization range of RCP.

2. Experiment

2.1 Raw materials

The cement used in this study was Ordinary PII52.5 cement. The precursor of RCP was C30 concrete beam demolition waste from construction in Beijing. The RCP was obtained after the industrial powder passed through 200 sieves. And calcined clay was produced at a factory in New Delhi, India. Superplasticizer (SP) made from Sobute New Materials Co., Ltd., Nanjing. The water-reducing rate of SP is 30%, and its solid content was diluted to 10% before being used.

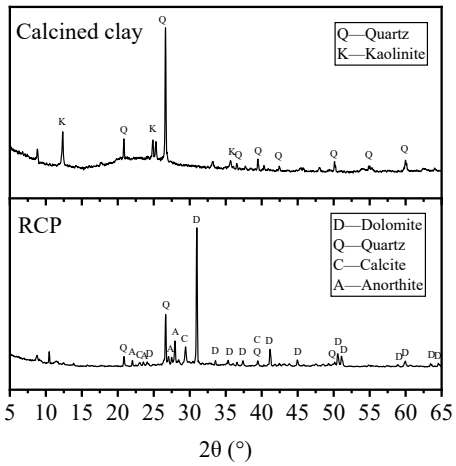


Fig. 1 Mineral composition of raw materials

Fig. 1 shows the mineral composition and chemical composition of raw materials measured by XRD. RCP is rich in calcium and silicon elements and consists of dolomite, quartz, and some calcite and feldspar minerals, which are common in aggregate of concrete. The total calcium carbonate content is about 40% (according to thermogravimetric analysis). In addition, the main crystalline phases of calcined clay are quartz and kaolinite, and the protruding curves of 15~30° indicate the presence of many amorphous phases.

2.2 Mixtures

In the LC^3 cement system, metakaolin reacts with limestone in a molar ratio of 1:1, so the optimal mass ratio is usually designed to be 2:1.

$$A + C\bar{C} + 3CH \rightarrow C_3A\bullet C\bar{C}\bullet H_{11} \quad (1)$$

The mixture of CC and RCP will replace 15, 30 and 45% weight of the cement, which were successively labeled as groups A, B, and C. The CC to RCP mass ratio was designed to be 1:0, 2:1, and 1:1 at 30% cement replacement. Table 1 shows the proportions of each group of cementitious materials. Each group was weighed proportionally and placed in the mixer for dry mixing for 5h before being used.

Table 1 Proportions of cementitious materials

	Cement replacement	CC:RCP	Material (wt%)			
			Cement	CC	RCP	Gypsum
Ref	0	-	100	0	0	0
A	15	2:1	84	10	5	1
B_1	30	1:0	68	30	-	2
B_2	30	2:1	68	20	10	2
B_3	30	1:1	68	15	15	2
C	45	2:1	52	30	15	3

2.3 Method

The 40*40*40mm paste samples were molded at w/c of 0.4, removed from the mold after 24h, and then cured in water at 20±1 °C for 27 days. After that, the hydrated paste samples were broken into 3~5mm small pieces and immersed in isopropanol to terminate hydration. After drying at 60°C in a

drying cabinet, the samples were ground to pass through a 200-mesh screen. German Brock D8 ADVANCE XRD was used to analyze the mineral composition of the hydration products. The target material was Cu, and the scanning parameter was at a speed of 2°/min from 5 ° to 80 °.

The mortar samples preparation method and strength test method are referred to GB/T 17671 (GB/T 17671(1999)). A water-cement ratio of 1:2 and a cement-sand ratio of 1:3 were used to prepare the mortar samples, and the sand used was ISO standard sand. SP was used to adjust the fluidity of each mortar sample to 240±5 mm. Then, the 40*40*160 mm matrixes formed were cured under the same condition as the paste samples.

3. Results and discussion

3.1 Mechanical properties

Unsurprisingly, the compressive strength of mortar at all ages decreases with the increase of cement substitution, as shown in Fig.2(a). Fig.2(b) shows the compressive strength of mortar with different CC: RCP at 30% cement substitution. The mortar strength decreased by 10% when half or 1/3 of CC was replaced by RCP compared with CC alone. Those were since that RCP contained a large amount of quartz which only acts as an inert filler。 In previous studies (Antoni et al (2012)), the reduced value was 5% when limestone was used instead of metakaolin under the same conditions. Therefore, a 10% reduction in strength was considered acceptable in this experiment using low-grade raw materials.

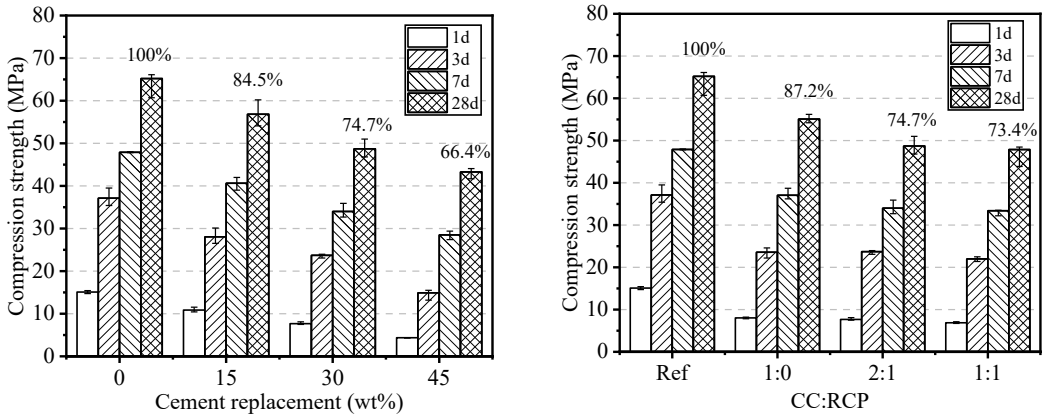


Fig. 2 Compressive strength of mortars: (a) with different cement replacement, (b) with different ratio of CC to RCP

Fig.3 shows the flexural strength of the mortar samples. As can be seen from Fig.3(a), CC/RCP mixture replacing cement resulted in a decrease in the flexural strength of mortar in the early stage but had little effect on the strength of 28d. In addition, Fig.3(b) shows that the ratio of CC/RCP has little effect on the flexural strength at 30% cement substitution. This indicates that CC/RCP mixtures cement are more suitable for load-bearing bending than bearing pressure.

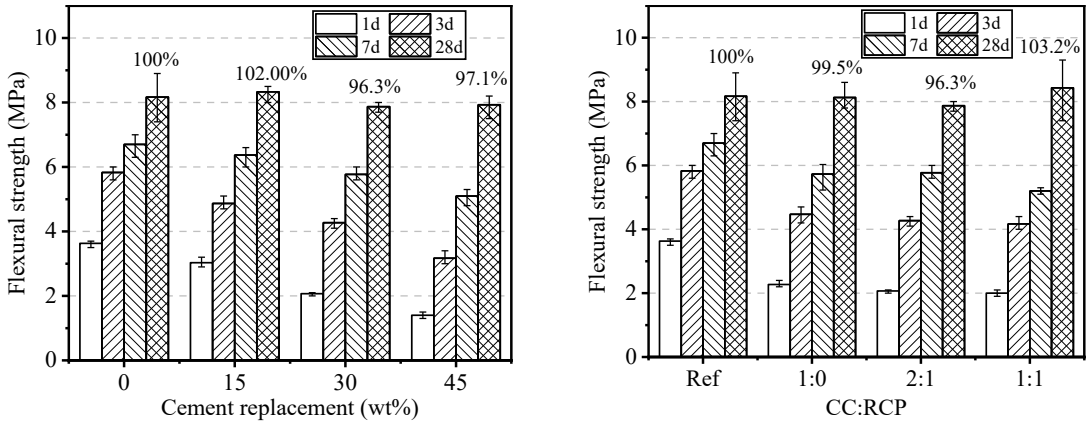


Fig. 3 Flexural strength of mortars: (a) with different cement replacement, (b) with different ratio of CC to RCP

3.2 Hydration products

As can be seen from Fig.4(a), with the increase in CC-RCP content, the diffraction peak of gypsum decreased, and the diffraction peak of AFt increased, indicating that CC was doubly excited by alkali and sulfate, which generate more AFt (Taha et al (1985)). In addition, the diffraction peak of C_4AH_{13} gradually disappeared, while the Hc peak slowly appeared. There are two reasons for this. First, due to the decrease in cement content, the alkalinity of the system decreased, resulting in a change of the reaction type between CC and CH. At low alkalinity, the hydration reaction no longer generated C_4AH_{13} (Ding and Zhang (1997), Tironi et al (2014)). Second, due to the increased calcium carbonate content in the system, the generated C_4AH_{13} would also be transformed into Hc and Mc (Ferreiro et al (2017)). This point could also be seen in Fig (b). Under the same amount of cement substitution, the generation of C_4AH_{13} decreased while the Hc and Mc increased with the increase in RCP ratio.

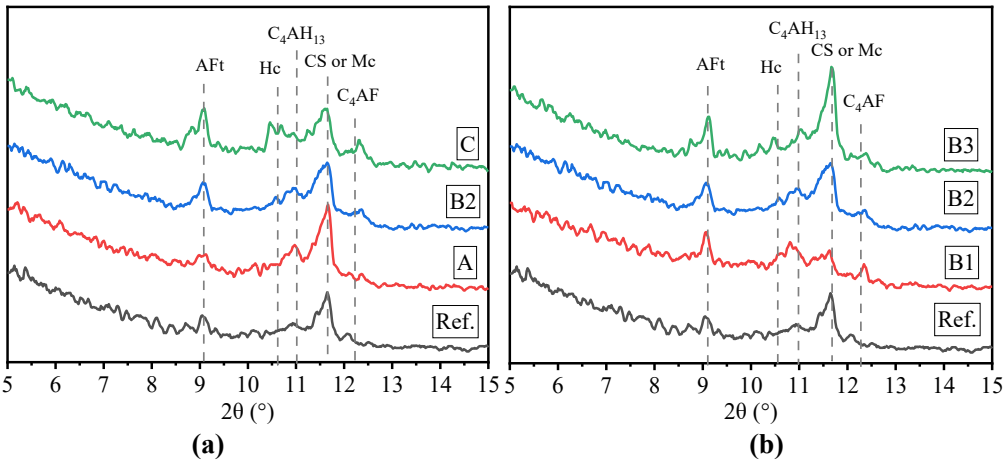


Fig. 4 Mineral composition of hydration product of 28d pastes: (a) with different cement replacement, (b) with different ratio of CC to RCP

4. Conclusion

1) By combining CC with RCP, more AFt and Mc were generated. When a mixture of CC and RCP replaced 15, 30, and 45% of cement in the sample, the 28d strength losses were only about 12%, 26%, and 35%.

2) An increase in the proportion of RCP in the SCM mixture lead to a decrease in mortar strength due to the RCP's inert composition and the decrease in CC content. With 30% cement substitution, the

mortar compressive strength was reduced by 10% by using RCP to replace half or 1/3 of CC, which is acceptable for low-grade raw materials.

References

Skocek J., Zajac M. and Ben Haha M. (2020) "Carbon Capture and Utilization by mineralization of cement pastes derived from recycled concrete", *Scientific reports*, 10(1): 5614

Cancio Díaz Y., Sánchez Berriel S. and Heierli U. et al. (2017) "Limestone calcined clay cement as a low-carbon solution to meet expanding cement demand in emerging economies", *Development Engineering*, 2: 82–91

Sánchez Berriel S., Favier A. and Rosa Domínguez E. et al. (2016) "Assessing the environmental and economic potential of Limestone Calcined Clay Cement in Cuba", *Journal of Cleaner Production*, 124: 361–369

Duan Z., Hou S. and Xiao J. et al. (2020) "Study on the essential properties of recycled powders from construction and demolition waste", *Journal of Cleaner Production*, 253: 119865

Prošek Z., Nežerka V. and Hlůžek R. et al. (2019) "Role of lime, fly ash, and slag in cement pastes containing recycled concrete fines", *Construction and Building Materials*, 201: 702–714

GB/T 17671-1999, (1999) "Method of testing cement-Determination of strength", Beijing: Standards Press of China

Antoni M., Rossen J., and Martirena F. et al. (2012) "Cement substitution by a combination of metakaolin and limestone", *Cement and Concrete Research*, 42(12): 1579-1589

Taha A.S., Serry M.A. and El-Didamony H. (1985) "Hydration characteristics of metakaolin—lime—gypsum", *Thermochimica Acta*, 90: 287–296

Ding Z. and Zhang D.C. (1997) "Research and Application of Pozzolanic Activity of Metakaolin", *Bulletin of the Chinese Ceramic Society*, 4: 57~62

Tironi A., Castellano C.C. and Bonavetti V.L. et al. (2014) "Kaolinitic calcined clays – Portland cement system: Hydration and properties", *Construction and Building Materials*, 64: 215–221

Ferreiro S., Herfort D. and Damtoft J.S. (2017) "Effect of raw clay type, fineness, water-to-cement ratio and fly ash addition on workability and strength performance of calcined clay – Limestone Portland cements", *Cement and Concrete Research*, 101: 1–12

The 16th International Congress on the Chemistry of Cement 2023 (ICCC2023)
"Further Reduction of CO_2 -Emissions and Circularity in the Cement and Concrete Industry"
September 18–22, 2023, Bangkok, Thailand

Study of filler effect of VGP on cement hydration

Y. Ren[1*], A. Tomoyose[1], R. Kurihara[1] and I. Maruyama[1, 2]

[1] *The University of Tokyo, Graduate School of Engineering, Department of Architecture, Tokyo, Japan*
Email: renyuqi1996@g.ecc.u-tokyo.ac.jp
Email: tomoyose@bme.arch.t.u-tokyo.ac.jp
Email: ryo.kurihara@bme.arch.t.u-tokyo.ac.jp
Email: i.maruyama@bme.arch.t.u-tokyo.ac.jp
[2] *Nagoya University, Department of Environmental Engineering and Architecture, Nagoya, Japan*

ABSTRACT

Nowadays, reducing CO_2 emissions is an important goal for society. In the field of concrete, one of the strategies is the use of supplementary cementitious materials (SCMs). However, most conventional SCMs, such as fly ash (FA) and blast furnace slag (BFS) come from industrial wastes. According to the SDGs, those waste emissions should be reduced, and FA and BFS may disappear. Therefore, new SCMs should be developed. With the publication of JIS A 6209 in Japan, volcanic glass powder (VGP) was identified as an SCM. VGP is manufactured from volcanic sediments. It is not a by-product of industrial waste like FA and BFS but a green material that doesn't contribute to the pollution of the earth. For the concrete mixed with SCMs, the initial strength development is often an issue in construction. The filler effect of SCMs accelerates cement hydration and contributes to strength development at an early age. Therefore, it is necessary to understand the filler effect of VGP. The experimental results showed that the filler effect of VGP is more effective than that of FA or BFS. This is due to the complex texture of VGP and its high specific surface area.

KEYWORDS: *Volcanic glass powder, Filler effect, Hydration, Calorimetry, XRD/Rietveld analysis*

1. Introduction

Supplementary cementitious materials (SCMs) have a long history of use in the construction industry. They offer two key benefits: first, they allow for a reduction in the amount of cement used, which leads to a decrease in carbon dioxide emissions and mitigation of the greenhouse effect (Snellings 2016). Second, many SCMs are derived from the by-products of heavy industries, such as fly ash and blast furnace slag, and using them helps to address industrial waste. However, as the energy sector transitions to renewable sources, the traditional SCMs may become more difficult to obtain. For example, wind and solar power may replace thermal power generation, leading to a decrease in the production of fly ash. In light of this, it is crucial to develop new, environmentally friendly SCMs to ensure a sustainable future for construction.

Volcanic Glass Powder (VGP) was introduced as a supplementary cementitious material in 2020 in Japan. VGP is created from raw volcanic ejecta known as Shirasu found in Kagoshima, Japan (Sodeyama et al. 2017). This innovative material has many advantages over traditional supplementary cementitious materials. For example, the volcanic glass powder is more environmentally friendly, as it is derived from a natural source and does not produce harmful emissions during production. In addition, its unique properties, such as its high silica content, give it the potential to enhance the performance of concrete. The widespread availability of raw volcanic ejecta throughout Japan and the world makes VGP a promising environmentally friendly alternative to conventional SCMs.

The hardened mortar containing VGP showed a good compressive strength result even at an early age (Tomoyose et al. 2018). It indicated that VGP has a filler effect accelerating the hydration of cement. Hardened cement systems mixing with SCMs are subjected to the filler effect, which has been pointed out

Table 1 Mineral composition of OPC and VGP

Type	Mineral composition (wt%)								
OPC	C_3S	C_2S	C_3A	C_4AF	Gypsum	Bassanite	Anhydrite	Calcite	SUM
	63.54±1.1	15.94±0.1	5.64±0.1	7.58±0.1	2.25±0.1	0.67±0.1	0.52±0.1	3.87±0.1	100.00
VGP	Quartz		Magnetite		Albite		Glass		SUM
	1.88±0.1		0.56±0.1		4.97±0.2		92.59±1.1		100.00

by many studies. The filler effect has been summarized into two aspects (Deschner et al. 2012). Using SCMs to replace a part of cement increases the effective water-to-cement ratio. Additionally, SCMs provide additional nucleation sites for the hydrates. In the Proceedings of the Japan Concrete Institute 2022, experimental results proved that VGP particles accelerate the hydration of cement by providing additional nucleation sites (Ren, Cheng, and Maruyama 2022). More experiments need to do to verify the filler effect of VGP and to make the mechanism clear. This paper was designed to determine the filler effect of VGP.

2. Experimental programs

The materials used in this study are ordinary Portland cement (OPC) and JIS A 6209 type 2 VGP. The mineral composition of the OPC and VGP determined by XRD/Rietveld analysis is given in Table 1. Specific surface area of VGP is 6.9m^2/g, OPC is 1.0 m^2/g. Four mixes: 100wt%OPC, 90wt%OPC + 10wt%VGP, 80wt%OPC + 20wt%VGP, 70wt%OPC + 30wt%VGP (denoted as OPC, VGP10, VGP20 and VGP30, respectively) were prepared. The water-to-binder ratio was 0.4. A twister II Nr.1826 vacuum mixer was used to mix the paste, with a spiral speed of 300rpm for 5 minutes. The paste was mixed by hand for a further 1 hour to avoid bleeding. All the samples were sealed in Aluminum foil bags (completely covered by the polyester film) and cured in a 20±1℃ room until the experiments were performed. The hydration was followed by isothermal calorimetry (TAM Air Isothermal Calorimeter, TA Instruments, MODEL 605000). The ambient temperature is 20℃. The water injection times were uniform for all samples.

When the curing finished, the samples were crushed into pieces of less than 5mm. The pieces were immersed in isopropanol for 24 hours. Then, the isopropanol was removed by an aspirator pump for 10 minutes. Subsequently, the pieces were placed in an 11%RH 20℃ desiccator for 14 days. After the 11%RH drying, all the pieces were ground with a ball mill. The powder sample was used to conduct the TG, XRD, and selective dissolution experiments (Asaga et al. 1982; Maruyama and Igarashi 2014).

3. Experimental results and discussion

Isothermal calorimetry results (Fig.2) showed that VGP significantly accelerated the hydration of cement within the first 12 hours due to the filler effect. With increasing the replacement ratio of VGP, the acceleration period of hydration came earlier, and the peak of specific heat flow was larger. This phenomenon was confirmed by the development of the hydration degree (Fig. 4 (a)). However, the hydration time between 12 and 24 hours, the hydration rate entered a deceleration period. The filler effect of VGP cannot prevent the deceleration period coming.

According to the previous study on the filler effect of fly ash or other inert materials (De Weerdt et al. 2011; Wu et al. 2021), the specific heat flow from those papers is totally different with the present study. For example, the fly ash did not accelerate the hydration during the acceleration period. The main hydration peak was delayed, although it was enlarged. However, the present study showed that the VGP particles accelerated the rate of the heat of hydration at the acceleration period. VGP is barely reactive at the early hydration time, which can be seen as an inert material same as fly ash (Fig.4 (d)). The difference between VGP and fly ash in the early hydration period is derived from their shape differences. Fig.3 is an SEM image of VGP which clearly shows the structure and complex texture of VGP particles. (Berodier and Scrivener 2014) have pointed out that the nucleation of C-S-H has a high correlation with the total surface area of the solids. In the present study, the specific surface area (SSA) of VGP is 6.9 m^2/g, which is much higher than the OPC of 1.0 m^2/g. VGP particles extremely increased the total surface area, so the hydration of cement was accelerated during the acceleration period, in other words, during the C-S-H nucleation period. Those studies of the filler effect of fly ash only gave the particle distribution of used

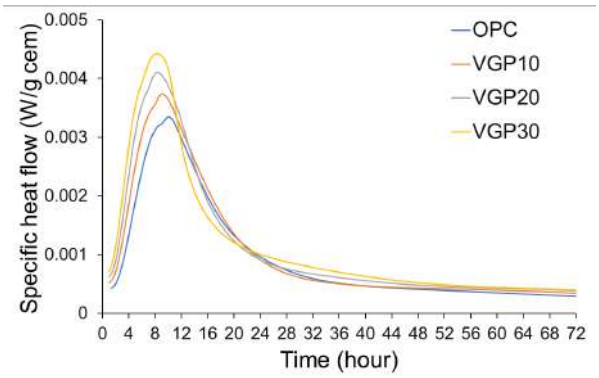


Fig.2 Specific heat flow

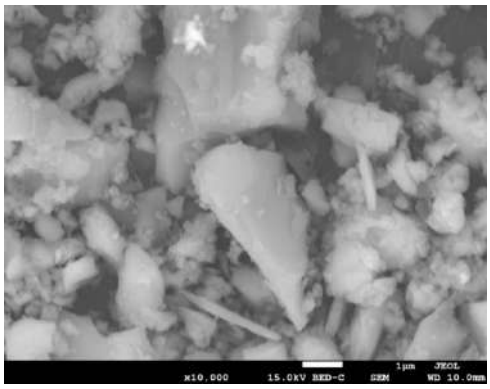


Fig.3 SEM image of VGP

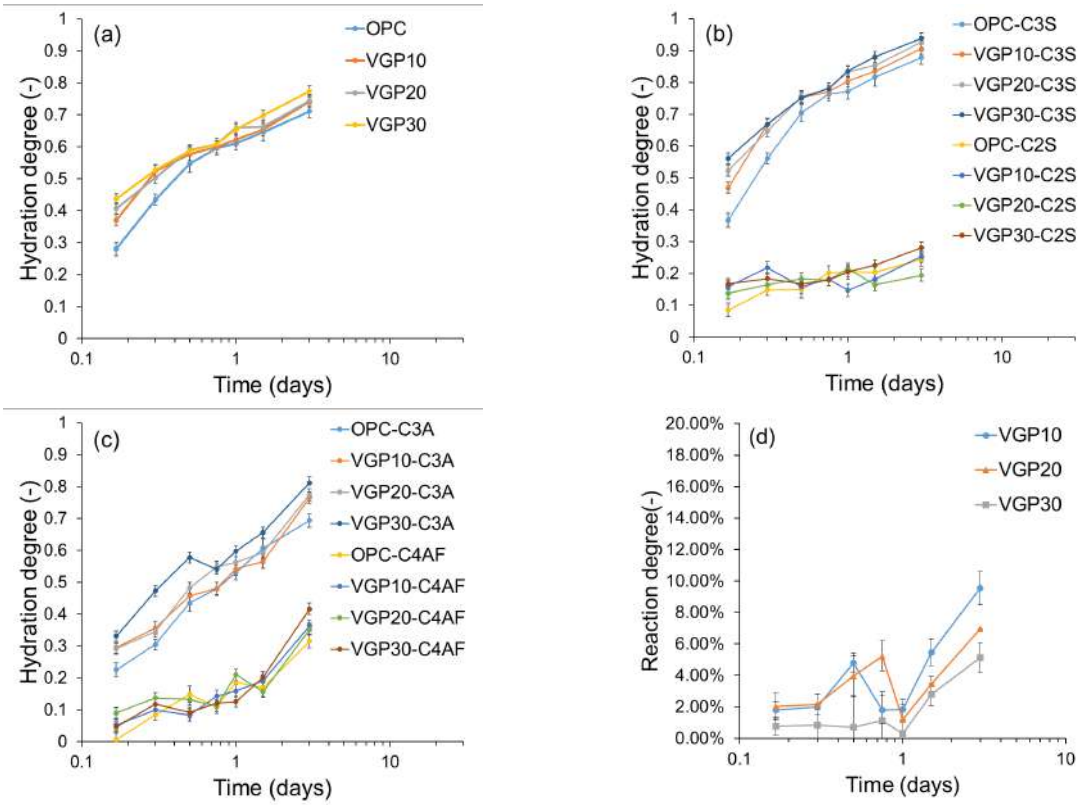


Fig. 4 Hydration degree of cement (whole system and individual clinker) and reaction degree of VGP

materials but did not mention the SSA. Because fly ash is approximately spherical, the SSA of fly ash maybe lower than that of cement. Therefore, the total surface area was not increased but decreased after the fly ash replaced cement. It caused the delay of the main hydration peak.

However, both VGP and fly ash enlarged the main hydration peak. This is not very much related to the nucleation sites. Bazzoni's C_3S experiment (A. Bazzoni 2014) showed that a higher W/C ratio delayed the main hydration peak but increased the peak value and expanded the width of the peak. The replacement of cement by VGP or fly ash can increase the efficient W/C ratio which is the second function of the filler effect. Thus, the broadened main hydration peak was caused by the effect of the efficient W/C ratio.

The development of the hydration degree and reaction degree of VGP was given in Fig.4. The hydration of C_3S was accelerated in the VGP-OPC system (Fig.4 (b)). At 18 hours, however, the hydration degrees of all the systems tended to the same value, around 77%. It seems that the hydration degree of C_3S reached a threshold. This time corresponded to the end of the main hydration peak. According to Ouzia's C-S-H nucleation and growth theory (Ouzia 2019), the main hydration peak represents the formation of outer C-S-H. At the end of the main hydration peak, the outer C-S-H stops growing and the inner C-S-H starts to form. The transformation process of C-S-H morphology may lead to a temporary cessation of

C_3S dissolution. Additionally, it indicated that the filler effect of VGP did not affect the growth of C-S-H. Because the VGP-OPC system and OPC system reached the threshold at the same time. After 24 hours, the renewed hydration of C_3S was observed. The hydration degree of the VGP-OPC system is slightly higher than that of the OPC system. The hydration of C_2S was not accelerated by the filler effect of VGP. Either the additional nucleation sites or the efficient W/C ratio did not affect the hydration rate of C_2S.
From an overall view, the hydration of C_3A was accelerated in the VGP-OPC system (Fig.4 (c)). Unlike the hydration of C_3S, the hydration of C_3A did not stagnate. The hydration rate of C_3A did not decrease during the deceleration period of the main hydration peak. Although the hydration degree of C_3A dropped obviously for the VGP30 at 18 hours and the hydration degrees of C_3A for the VGP20 and VGP10 were lower than that of OPC at 36 hours, it could be an experimental error. It was observed that the hydration of C_4AF was accelerated from 36 hours for all systems. The hydration degree of C_4AF in the VGP-OPC system was relatively high, but it is difficult to verify that it was caused by the filler effect of VGP.
According to the results of the selective dissolution experiment (Fig.4 (d)), VGP was barely reactive before 24 hours. Therefore, it can be treated as an inert material. However, the reaction degree of VGP has an obvious increasing trend after 24 hours, which indicated that VGP became active after 24 hours.

4. Conclusions

The present study determined the filler effect of VGP:

1. The filler effect of VGP has two effects on the hydration of cement. First, VGP has a large specific surface area, which provides additional nucleation sites for hydrates. Secondly, the replacement of VGP increases the efficient W/C ratio. It enlarges the main hydration peak.
2. The hydration degree of C_3S and C_3A is accelerated by the filler effect of VGP. The hydration degree of C_2S and C_4AF is not affected.
3. The selective dissolution experiment shows that VGP is barely reactive before 24 hours. It ensures that the hydration of cement is not affected by the VGP reaction.

In summary, volcanic glass powder is a promising new supplementary cementitious material that offers many advantages over traditional materials. Its environmentally friendly origins, combined with its potential to enhance concrete performance, make it an attractive option for sustainable construction.

References

A. Bazzoni. 2014. “Study of Early Hydration Mechanisms of Cement by Means of Electron Microscopy.” École Polytechnique Fédérale de Lausanne.

Asaga, Kiyoshi et al. 1982. 90 Journal of the Ceramic Association Determination of Uncombined Quartz in Hydrothermal Reaction of Quartz and Portland.

Berodier, E., and K. Scrivener. 2014. “Understanding the Filler Effect on the Nucleation and Growth of C-S-H.” Journal of the American Ceramic Society 97(12): 3764–73.

Deschner, Florian et al. 2012. “Hydration of Portland Cement with High Replacement by Siliceous Fly Ash.” Cement and Concrete Research 42(10): 1389–1400. http://dx.doi.org/10.1016/j.cemconres.2012.06.009.

Maruyama, Ippei, and Go Igarashi. 2014. “Cement Reaction and Resultant Physical Properties of Cement Paste.” Journal of Advanced Concrete Technology 12(6): 200–213.

Ouzia, Alexandre Reda Constantin Willian Caleb. 2019. “Modeling the Kinetics of the Main Peak and Later Age of Alite Hydration.” : 263.

Ren, Yuqi, Luge Cheng, and Ippei Maruyama. 2022. “Fundamental Study on Filler Effect of Volcanic Glass Powder.” Proceedings of the Japan Concrete Institute 44: 118–123.

Snellings, Ruben. 2016. “Assessing, Understanding and Unlocking Supplementary Cementitious Materials.” RILEM Technical Letters 1: 50.

Sodeyama, Kenichi, Atsushi Tomoyose, Takafumi Noguchi, and Kazuro Higashi. 2017. “Total Utilization of Shirasu as Construction Materials through Dry Gravity Classification and Pulverization.” Journal of the Society of Materials Science, Japan 66: 574–81.

Tomoyose, Atsushi, Takafumi Noguchi, Kenichi Sodeyama, and Kazuro Higashi. 2018. “Utilization of Volcanic Ejecta as a High-Performance Supplementary Cementitious Material by Gravity Classification and Pulverization.” RILEM Technical Letters 3: 66–74.

De Weerdt, K. et al. 2011. “Hydration Mechanisms of Ternary Portland Cements Containing Limestone Powder and Fly Ash.” Cement and Concrete Research 41(3): 279–91. http://dx.doi.org/10.1016/j.cemconres.2010.11.014.

Wu, Meng et al. 2021. “Analyzing the Filler and Activity Effect of Fly Ash and Slag on the Early Hydration of Blended Cement Based on Calorimetric Test.” Construction and Building Materials 276.

The 16th International Congress on the Chemistry of Cement 2023 (ICCC2023)
"Further Reduction of CO_2 -Emissions and Circularity in the Cement and Concrete Industry"
September 18–22, 2023, Bangkok, Thailand

Reactivity of alternative supplementary cementitious materials assessed by the R^3 method

M. Ranger[1,2*], J. Duchesne[3]

[1] *Department of Environmental and Resource Engineering, Technical University of Denmark, Kgs. Lyngby, Denmark*
Email: maug@dtu.dk
[2] *Danish Road Directorate, Copenhagen, Denmark*
[3] *Department of Geology and Geological Engineering, Laval University, Quebec City, Canada*
Email: josee.duchesne@ggl.ulaval.ca

ABSTRACT

The necessity to reduce carbon emissions in concrete production has accelerated the partial replacement of Portland cement by Supplementary Cementitious Materials (SCMs). As the range of SCMs studied is constantly expanding, screening tests to evaluate their reactivity have gained considerable attention. One example is the R^3 method, which consists in quantifying the chemical reactivity of an SCM in a simplified mixture simulating the environment of a cement paste. Different parameters measured by various techniques have been proposed in previous work: heat release, bound water, portlandite consumption and chemical shrinkage.

In the present study, the R^3 method was applied to both traditional and alternative SCMs, to further investigate the validation range of the method. The experimental matrix included limestone, fly ash, calcined clays, biomass ashes, crushed brick, glass beads and sewage sludge ash. Three parameters were measured: heat release by isothermal calorimetry, bound water by oven-drying and portlandite consumption by thermogravimetry. The results indicated that both heat release and bound water correlated well with the relative compressive strength at 28 days, even for alternative SCMs. Thus, the R^3 method appears as an efficient screening test to identify promising SCMs. In addition, the study confirmed the potential of bound water, which can be measured with basic equipment available in many laboratories.

As most SCMs were first tested as received, the particle size varied significantly between the materials. Crushing the SCMs did not always improve the reactivity, presumably only when the amorphous part was affected. Finally, the effect of sulphates and carbonates on the reactivity was tested. Both compounds influenced the measured parameters, but no conclusion could be drawn regarding the correlation with the compressive strength. Thus, it is suggested to keep both sulphates and carbonates in the R^3 mix design, following the initial idea of mimicking a cement paste environment.

KEYWORDS: *Reactivity tests, Supplementary cementitious materials, Heat release, Bound water, Compressive strength*

1. Introduction

Supplementary Cementitious Materials (SCMs) are major assets for limiting the CO_2 emissions associated with the production of concrete. However, the availability of traditional SCMs, such as fly ash or blast furnace slag, is expected to be reduced, because of the global trend towards reducing the use of fossil resources and increasing the recycling of waste materials. To ensure a sufficient supply for the concrete industry, it is necessary to find alternative materials and assess their suitability as SCMs. Many binder properties should be tested, but the compressive strength is among the first characteristics to document. In the process of developing new binders, a screening test able to determine the potential of a material to be

used as an SCM is of major interest. This is the purpose of the R^3 method, which was one of the key topics of RILEM TC 267-TRM, see Li et al. (2018). The method consists of reactivity measurements of a paste made of portlandite, SCM, alkalis, sulphates, carbonates, and water, aiming at isolating the SCM reaction while simulating the environment of a cement paste. After 7 days of curing at 40°C, the SCM reactivity can be quantified by different parameters: heat release, bound water, portlandite consumption and chemical shrinkage. Previous work has already shown a fairly good correlation of heat release and bound water with the relative compressive strength at 28 days for traditional SCMs, see Londono-Zuluaga et al. (2022).

2. Research significance

The present study focused on assessing whether the R^3 method is effective with alternative SCMs. Two materials were ground finer in an attempt to increase their reactivity and study the effect on R^3 results. Finally, the influence of sulphates and carbonates on two SCMs was also investigated.

3. Materials and methods

The chemical composition of the SCMs measured by X-Ray Fluorescence (XRF) is shown in Table 1.

Table 1: Chemical composition of the SCMs (measured by XRF). *: spherical particles.

Oxide	Limestone	Fly ash	Calcined clay		Biomass ash		Sewage sludge ash	Crushed brick	Glass beads*
	LL	FA	CC1	CC2	BA1	BA2	SSA	CB	GB
SiO_2	2.0	56.2	46.6	49.0	25.5	23.2	56.8	63.4	72.0
Al_2O_3	0.4	23.8	17.4	17.3	4.8	4.3	8.4	11.2	0.7
Fe_2O_3	0.12	6.90	9.58	9.74	1.80	1.93	19.57	4.32	0.17
MgO	0.3	1.8	2.5	2.5	3.5	4.0	0.9	1.2	3.8
CaO	54.2	3.9	9.7	10.1	34.1	30.9	1.4	9.0	9.1
Na_2O	0.03	0.49	0.92	0.81	0.87	0.71	1.03	2.81	13.63
K_2O	0.06	1.64	2.47	2.66	4.93	7.35	2.43	0.43	0.21
TiO_2	0.03	0.93	0.97	0.97	0.28	0.29	1.54	0.63	0.07
P_2O_5	0.11	1.02	0.21	0.24	2.91	3.03	2.97	0.15	0.01
SO_3	0.08	0.79	0.97	0.98	4.58	12.66	0.38	0.63	0.24
Na_2O_{eq}	0.07	1.57	2.54	2.55	4.12	5.55	2.63	2.91	13.77
LOI	42.52	1.57	7.97	4.94	15.83	10.26	3.77	5.37	0.09
Sum	100.0	99.6	99.8	99.7	99.8	99.6	99.4	99.8	100.0
Density [kg/m^3]	500	2300	2700	2700	2620	2650	2650	2640	2500
d_{50} [µm]	4	18	10	39	16	70	11	43	67

R^3 pastes were prepared by mixing the constituents in the following proportions: 11.11 g of SCM, 33.33 g of portlandite, 60.00 g of deionised water, 0.24 g of KOH, 1.20 g of K_2SO_4 and 5.56 g of calcite.

3.1 Compressive strength

The compressive strength at 28 days was tested on mortar bars containing 65 % of CEM I 52.5 N and 35 % of SCMs. The relative compressive strength was calculated with respect to a mix containing 100 % CEM I. A correction was made for the air content, on the basis of 5 % strength loss for 1 % of air.

3.2 Techniques to quantify reactivity

Isothermal calorimetry was performed at 40°C on a paste sample of approximately 30 g (Calmetrix I2000). Heat release was measured for up to 7 days. For bound water, paste samples of approximately 8 g were cast into plastic vials and cured at 40°C. After 7 days, the samples were crushed and dried for 24h at 40°C followed by 2h at 350°C. Bound water was defined as the mass loss between 40 and 350°C.

On the same samples as for bound water, hydration was stopped after 7 days using the double solvent exchange method. The amount of portlandite was quantified by thermogravimetric analysis (NETZSCH STA 449 F3 Jupiter®, from 30 to 950°C at 10°C/min) using the tangential method. The results were corrected for the portlandite purity (86 %).

4. Results and discussion

Figure 1 shows the relative compressive strength at 28 days plotted against the different R^3 parameters. The best correlation is obtained with heat release (R^2 = 0.79), followed by bound water (0.73) and portlandite consumption (0.59). This is consistent with the trends reported by Li et al. (2018), confirming that both heat release and bound water are well correlated with the compressive strength. Portlandite consumption presents some inconsistencies for biomass ashes, which might be latent hydraulic materials. This is similar to previous results obtained for blast furnace slag, see Li et al. (2018). It should be noted that SCMs may behave differently in mortars and R^3 pastes, e.g. because of the filler effect or the particle shape.

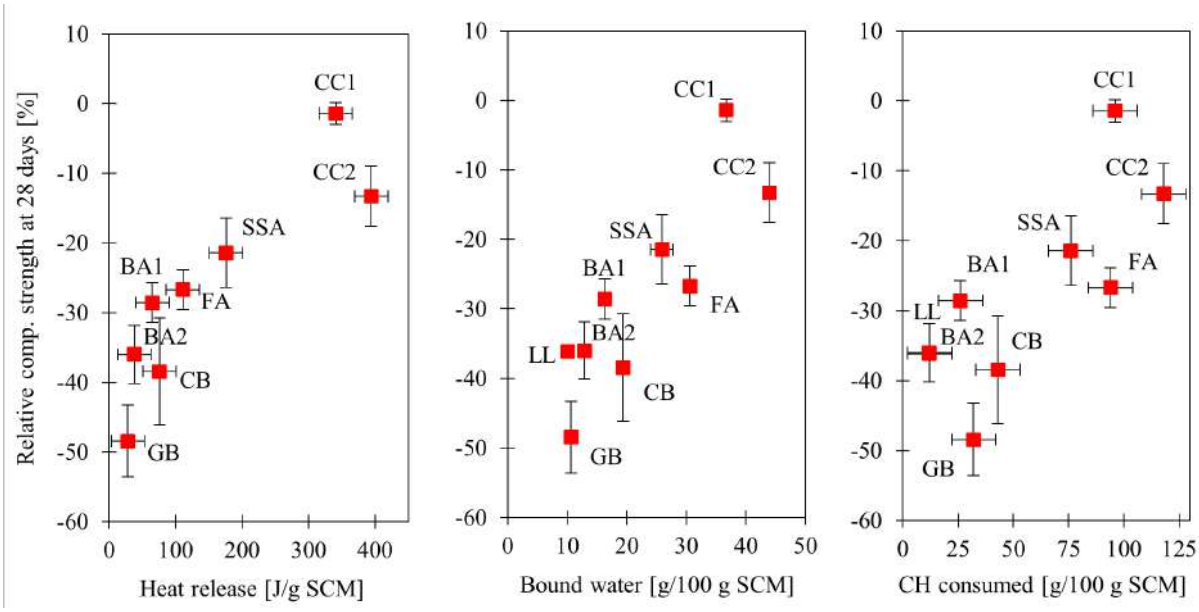


Figure 1: Relative compressive strength at 28 days plotted against R^3 results at 7 days: heat release (left), bound water (centre), portlandite consumption (right). Note: the heat release was not measured for LL.

As heat release and bound water lead to similar conclusions, the latter appears to be a promising parameter for screening potential SCMs on an industrial scale. As the method requires basic and affordable laboratory equipment, it could be useful to identify new potential SCMs and estimate their reactivity. In this respect, an important parameter is the particle size of the SCM, which affects the specific surface area and thus the dissolution rates. As shown in Table 2, the bound water content more than doubles when the glass particles are crushed to cement-like particle sizes. Conversely, no changes are observed when reducing the particle size of brick powder. This is probably because crushing only affects the crystalline non-reactive phases, while the amorphous phases are already fine enough. Thus, R^3 tests can also be used in a pre-optimisation process to assess whether the gain in reactivity with a finer material is worth the energy used for grinding.

Table 2: Bound water at 7 days as a function for different particle sizes. *For glass, coarse particles are spherical, while fine particles are more angular due to grinding.

Material	Glass beads*		Crushed brick	
Particle size (d_{50})	Coarse (67 µm)	Fine (9 µm)	Coarse (43 µm)	Fine (13 µm)
Bound water at 7 days [g/100 g SCM]	11	25	19	17

Table 3 shows the results obtained with regular R^3 pastes, and modified R^3 systems without sulphates and no carbonates. For both calcined clay and fly ash, the presence of sulphates and carbonates increases bound

water and portlandite consumption, but reduces heat release. These changes are likely due to changes in the phase assemblage. In the absence of sulphate, ettringite is not formed as shown in Avet et al. (2016), which could explain the lower amount of bound water. In the presence of calcite, Avet et al. (2022) reported a slightly lower heat release, which is in agreement with the present results. However, it is not possible to conclude on the influence of sulphates and carbonates on the correlation with the compressive strength. In the absence of further evidence, and because the current mixture already gives satisfactory results, it is proposed to follow the regular R^3 design and include both sulphates and carbonates in the mixture.

Table 3: R^3 results for mixes with and without sulphate and carbonates. BW = bound water, HR = heat release, CHC = portlandite consumption.

Sulphates and carbonates	Fly ash			Calcined clay 2		
	BW [g/100 g SCM]	HR [J/g SCM]	CHC [g/100 g SCM]	BW [g/100 g SCM]	HR [J/g SCM]	CHC [g/100 g SCM]
With	31	111	94	44	394	118
Without	24	135	59	39	407	83

5. Conclusions

As alternative SCMs attract increasing attention due to the expected shortage of traditional SCMs, screening test methods can help identify the most promising materials. In the present work, the R^3 method was successfully applied to a range of alternative SCMs and showed a satisfactory correlation with the relative compressive strength at 28 days. The influence of the particle size of the SCMs on the reactivity was also studied, illustrating the possibility to use the R^3 method to assess whether pre-processing the materials is worthwhile. Finally, no clear conclusion can be drawn regarding the effect of sulphates and carbonates on the correlation with the compressive strength. However, the phase assemblage is probably more realistic in their presence. Unless proven otherwise, it is suggested that they should be kept in the mix.

Acknowledgements

The work presented is part of an industrial PhD project financed by the Danish Road Directorate and a joint grant from Innovation Fund Denmark (Innovationsfonden) and Realdania under the program Circular Built Environment. This financial support is gratefully acknowledged. The Research and Quality Centre of Aalborg Portland is warmly thanked for XRF analyses.

References

Avet, F., Snellings, R., Diaz, A.A., Ben Haha, M., Scrivener K. (2016), "Development of a new rapid, relevant and reliable (R^3) test method to evaluate the pozzolanic reactivity of calcined kaolinitic clays", *Cement and Concrete Research*, 85: 1-11

Avet, F., Li, X., Ben Haha, M., Bernal, S.A., Bishnoi, S., Cizer, Ö., Cyr, M., Dolenec, S., Durdzinski, P., Haufe, J., Hooton, D., Juenger, M.C.G., Kamali-Bernard, S., Londono-Zuluaga, D., Marsh, A.T.M., Marroccoli, M., Mrak, M., Parashar, A., Patapy, C., Pedersen, M., Provis, J.L., Sabio, S., Schulze, S., Snellings, R., Telesca A., Thomas, M., Vargas, F., Vollpracht, A., Walkey, B., Winnefeld, F., Ye, G., Z., Zhang, S., Scrivener, K. (2022) "Report of RILEM TC 267-TRM phase 2: optimization and testing of the robustness of the R3 reactivity tests for supplementary cementitious materials", *Materials and Structures*, 55(3): pp. 92

Li, X., Snellings, R., Antoni, M., Alderete, N.M., Ben Haha, M., Bishnoi, S., Cizer, Ö., Cyr, M., De Weerdt, K., Dhandapani, Y., Duchesne, J., Haufe, J., Hooton, D., Juenger, M., Kamali-Bernard, S., Kramar, S., Marroccoli, M., Joseph, A.M., Parashar, A., Patapy, C., Provis, J.L., Sabio, S., Santhanam, M., Steger, L., Sui, T., Telesca A., Vollpracht, A., Vargas, F., Walkey, B., Winnefeld, F., Ye, G., Maciej, Z., Zhang, S., Scrivener, K.L. (2018) "Reactivity tests for supplementary cementitious materials: RILEM TC 267-TRM phase 1", *Materials and Structures*, 51(6): pp. 151

Londono-Zuluaga, D., Gholizadeh-Vayghan, A., Winnefeld, F., Avet, F., Ben Haha, M., Bernal, S.A., Cizer, Ö., Cyr, M., Dolenec, S., Durdzinski, P., Haufe, J., Hooton, D., Kamali-Bernard, S., Li, X., Marsh, A.T.M., Marroccoli, M., Mrak, M., Muy, Y., Patapy, C., Pedersen, M., Sabio, S., Schulze, S., Snellings, R., Telesca, A., Vollpracht, A., Ye, G., Zhang, S., Scrivener, K.L. (2022) "Report of RILEM TC 267-TRM phase 3: validation of the R^3 reactivity test across a wide range of materials ", *Materials and Structures*, 55(5): pp. 142

The 16th International Congress on the Chemistry of Cement 2023 (ICCC2023)
"Further Reduction of CO_2 -Emissions and Circularity in the Cement and Concrete Industry"
September 18–22, 2023, Bangkok, Thailand

Activation of LC^3 low-carbon cements by C-S-H seeding

A. Morales-Cantero[1*], A.G. De la Torre[1], A. Cuesta[1], I. Santacruz[1], O. Mazanec[2], A. Dalla-Libera[2], S. Dhers[2], P. Schwesig[2], P. Borralleras[3] and M.A.G. Aranda[1]

[1] *Departamento de Química Inorgánica, Universidad de Málaga, Málaga 29071, Spain*
Email: alejandrom@uma.es, mgd@uma.es, a_cuesta@uma.es, isantacruz@uma.es, g_aranda@uma.es

[2] *Master Builders Solutions Deutschland GmbH, Albert-Frank Str, 32, 83308 Trostberg, Germany*
Email: oliver.mazanec@mbcc-group.com, alessandro.dalla-libera@mbcc-group.com, sebastien.dhers@mbcc-group.com, peter.schwesig@mbcc-group.com

[3] *Master Builders Solutions España S.L.U., Carretera de l'Hospitalet, 147-149, Edificio Viena, 1ª planta, 08940 Cornellà de Llobregat, Spain*
Email: pere.borralleras@mbcc-group.com

ABSTRACT

Portland-based Limestone Calcined Clay Cements (LC^3) are attracting a lot of the attention from scholars and field applications due to the reduction in CO_2 emissions. However, their low mechanical strengths at early ages are a key bottleneck for their widespread use. Calcined clays can also lead to a strong reduction of the fluidity in the first hours after mixing, which is an important second drawback. Here, these two issues have been addressed. Three LC^3 binders were prepared based on a PC-52.5R cement and three calcined clays, with variable amounts of kaolinite in the raw materials ranging 29-74 wt%. The particle sizes of the calcined clays were adjusted by milling to $D_{v,50}$=13±2 μm. The results show that the loss of fluidity of LC^3 mortars during the first hours can be solved by a recently developed PCE-based superplasticizer, specifically tailored for this application. Moreover, the compressive strengths at 1 day for LC^3 mortars have been boosted by a C-S-H nucleation seeding admixture and the gains are maintained at 28 days. It is noted that the compressive strengths at 1 day and room temperature were increased by 45-100 %, when compared to the corresponding unseeded mortars.

KEYWORDS: *Calcined clay, admixtures, superplasticizer, CO_2 footprint, mechanical strength*

1. Introduction

Calcined clays are a type of widely-available supplementary cementitious material that, combined with Portland cements, are starting to contribute in the reduction of the CO_2 emissions (Juenger et al., 2019). However, the main drawbacks of the resulting LC^3 binders are their poor mechanical strengths at early ages, i.e. 1-2 days (Scrivener et al., 2018), and their severe loss of fluidity during the first hours of hydration (Akhlaghi et al., 2017).

In this work, these two challenges have been addressed with tailored admixtures. On the one hand, and in order to avoid the loss of fluidity during the first hours of hydration, a new commercially available PCE-based superplasticizer, specially designed for this application, was employed. The amounts of this superplasticizer have been optimized for each sample. The performances have been compared to that of a typical PCE. On the other hand, and to improve the mechanical strength at early ages, a commercial accelerator admixture based on C-S-H nucleation seeding has been used (Morales-Cantero et al., 2022a, 2022b).

2. Materials and Methods

2.1 Starting material

A commercial Portland cement, CEM-I 52.5R (PC-Ref) with $D_{v,50}$=12(1) μm and three raw clays with different kaolinite content, ~74 (CC1), ~49 (CC2) and ~29 (CC3) wt%, have been used to fabricate the LC^3 binders. The clays were calcined at 860 ºC during 4 h, and milled down to $D_{v,50}$=13±2 μm. Subsequently,

the calcined clays were used to prepare the LC^3-50 binders (52 wt% PC-Ref, 30 wt% calcined clay, 15 wt% limestone and 3 wt% $CaSO_4 \cdot 2H_2O$), (LC^3-CC#). An additional reference sample was prepared by replacing the calcined clay by quartz (inert), with $D_{v,50}$=16(1) μm (PC-Qz).
Three commercially-available admixtures from Master Builders Solutions have been employed in this work, two PCE-based superplasticizers and one C-S-H based strength enhancement agent. SP-1 is a standard one used for years for concrete rheology optimisation. SP-2 is a new superplasticizer specially designed to avoid the loss of fluidity during the first hours of LC^3 hydration. Finally, Master X-Seed 130 (XS130) was used for strength enhancement.

2.2 Analytical techniques

2.2.1 Slump retention

Mortars have been prepared with a water-to-binder mass ratio (w/b) of 0.40 and with a sand-to-binder mass ratio of 1.78, at 20 ºC. For all samples, an optimized amount of SP for an initial constant self-flow, i.e. 200±15 mm, was added. For the samples containing the accelerator, a 2.00 wt% of XS130 by the weight of binder (referred to the commercial suspension) was added. For the mortar preparation, a mortar mixer (Matest, mod. E095) was used according to the following procedure: Step 1: 60 s at 140 rpm (solid, i.e. sand + binder and 80 wt% water); Step 2: 30 s to add the SP and 20 wt% of water for samples without C-S-H seeding or 10 wt% of water for samples with seeding; Step 3: 60 s at 285 rpm; Step 4 (only for samples incorporating C-S-H seeding): 30 s to add the admixture and the 10 wt% of water left; Step 5: 120 s at 285 rpm. After mixing, the mortar was poured in the truncated cone (bottom diameter: 100 mm, top diameter: 70 mm, height: 60 mm) in two steps. The first one, filling up half of the cone and the air bubbles were taken out with a glass rod with 30 vertical punctures. In the second step, the cone was filled up completely and punctured again 30 times. Slump was measured at t_0, 30 and 60 min, at the lab. temperature, 20(2) ºC.

2.2.2 Isothermal calorimetry

An eight channels Thermal Activity Monitor (TAM) instrument with glass ampoules was used. The pastes were prepared with a w/b ratio of 0.35 with the same amount of SP optimized for the mortar slump measurements. Pastes were prepared with a mechanical stirrer (IKA, mod. RW20-D) according to the following procedure: Step 1: 60 s at 800 rpm (binder + 80 wt% water); Step 2: 30 s to add the SP and 20 wt% of water for samples without C-S-H seeding or 10 wt% of water for samples with seeding; Step 3: 60 s at 800 rpm; Step 4 (only for samples with C-S-H seeding): 30 s to add the seeding and the 10 wt% of remain water; Step 5: 60 s at 800 rpm. The heat flow curves were collected up to 7 days at 20 ºC. The first 45 minutes after mixing were not collected to ensure the stabilisation of the equipment.

2.2.3 Compressive strength

Mortars were prepared as described in section 2.2.1. After mixing, the mortars were poured in 4×4×16 cm moulds in two steps, the first, filled up half of the volumes of the moulds. Then, the air bubbles were taken out with a glass rod with 60 vertical punctures. In a second step, the moulds were filled completely and punctured again for 60 times. The moulds were kept in a humidity chamber at 20 ºC and 99 %R.H. during the first 24 h. After that time, they were demoulded and kept underwater up to the selected age. The compressive strength was measured according to EN196-1 in a press (Model Autotest 200/10 W, Ibertest) at a rate of 1.5 $MPa \cdot s^{-1}$. The mortars (three prisms per age) were measured at 1, 7 and 28 days. The reported compressive values are the average of the six specimens, which resulted after flexural tests.

3. Results and discussion

The amounts of SP required for an initial (target) self-flow of 200±20 mm are given Table 1. Moreover, to evaluate the slump retention, the flow values were also measured at 30 and 60 minutes after water mixing. Three main conclusions can be drawn from these data. (1) As previously reported, the fluidity loss for standard PCEs, i.e. SP-1, is extreme for clays containing relatively high amount of kaolinites and/or high BET surfaces. (2) Also as previously published, the amount of required SP is a function of the kaolinite content in the pristine clay which usually correlates with BET surfaces. (3) The novel result here is that SP-2 successfully solved the slump retention problem, see Table 1.

Once the slump retention issue was successfully cleared up, the second drawback was addressed, i.e. the low mechanical strengths at early ages. In order to do so, initially the heat released by the corresponding pastes during the first 7 days were studied. Figure 1 shows the heat flow traces and cumulative heat curves of the pastes without and with C-S-H seeding admixture. Firstly, LC^3 pastes release less heat compared to the PC-Ref, as expected. Secondly, the total heat released by the second reference, PC-Qz, which contains quartz instead of the calcined clay, is lower than that of all LC^3 pastes. After approximately 12 h, the three LC^3 pastes released more heat than PC-Qz which might indicate that the pozzolanic reactions are starting to develop at about 12 hours. Finally, it should be noted that the heat released by PC-Qz is higher than the expected value (i.e. 48% less heat due to dilution), which is very likely due to the filler effect.

Table 1: Optimized amounts of SPs, and slump values, at the given times, for the studied mortars. Values in brackets indicate the standard deviation of the measurements.

Mortars	SP-1 (wt%)	SP-2 (wt%)	Slump /mm (at t_0)	Slump /mm (at 30min)	Slump /mm (at 60min)
PC-Ref-a	0.34	-	183(1)	156(1)	143(2)
PC-Ref-b	-	1.20	190(1)	264(1)	288(1)
PC-Ref-c	-	0.80	156(1)	203(1)	231(4)
LC^3-CC1	1.00	-	196(2)	106(2)	100(1)
LC^3-CC1	-	1.20	186(3)	210(1)	196(1)
LC^3-CC2	-	1.00	214(2)	271(1)	284(1)
LC^3-CC3	-	0.50	210(1)	267(1)	276(3)
PC-Qz	-	0.40	211(1)	266(1)	283(1)

After C-S-H nucleation seeding with XS130, a clear cement hydration acceleration effect is observed. Firstly, the induction periods are shortened in the seeded pastes as shown by the vertical purple lines (left bottom of Figures 1a and 1c). These times ranged 1.3-2.8 h for the unseeded pastes and 1.0-2.0 h for the seeded ones. Secondly, the seeded samples show higher slopes in the acceleration periods, see oranges lines in Figures 1a and 1c. Thirdly, the C-S-H seeded pastes present larger main peaks at earlier times, see Figures 1a and 1c. This is reflected in larger accumulated heat released at 1 day of hydration, see inset in Figures 1b and 1d. Finally, larger and shaper aluminate-related peaks are observed for the seeded pastes, see Figures 1a and 1c. Because this peak is smaller in PC-Qz, which has the same amount of cement, it is concluded that the C-S-H seeding is also accelerating/enhancing the aluminate dissolution from the calcined clays.

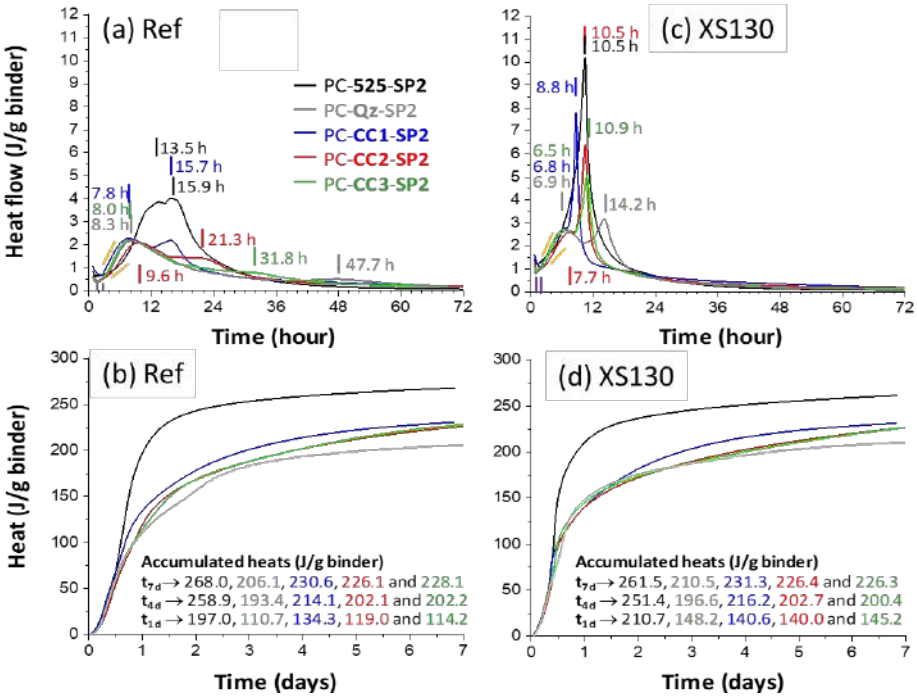


Figure 1: Calorimetric curves for pastes with w/b= 0.35. (a) Heat flow and (b) total heat released for pastes without seeding. (c) Heat flow and (d) total heat released for pastes with seeding.

Finally, the effect of the C-S-H nucleation seeding admixture on the mechanical properties of the mortars was studied. Figure 2a shows the compressive strength values for the studied mortars at 1, 7 and 28 d of hydration. Figure 2b depicts the percentages of compressive strength variation referred to PC-Ref at the

same ages. On the one hand, the strengths strongly decrease for the LC^3 binders at 1 day of hydration. The 50% dilution would imply ≈22 MPa at 1 day, but smaller values were measured. Furthermore, clays with lower amounts of kaolinite give lower strengths, as expected. This variation is damped at later ages but invariably LC^3 binders showed lower compressive strengths. On the other hand, the C-S-H seeded mortars showed a very important increase of the compressive strengths, see Figure 2. It is worth noting that the LC^3 binder with high kaolinite content, 74 wt%, surpassed the reference PC at 28 days. It is also remarkable that the LC^3 binder based on a low-content kaolinite clay, 29 wt%, can develop more than 20 MPa at 1 day.

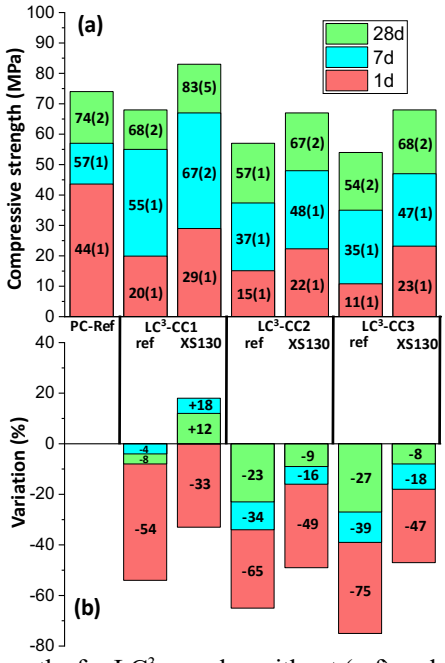


Figure 2: (a) Mortar compressive strengths for LC^3 samples without (ref) and with 2 wt% C-S-H seeding (XS130); (b) Variation of compressive strengths with respect to PC-Ref. Values in the brackets are the standard deviations.

4. Conclusions

Two main conclusions can be drawn from this work.

♦ Firstly, the new PCE-based superplasticizer, specially designed to avoid loss of fluidity during the first hours, successfully solved the slump retention problem of the studied LC^3 binders.

♦ Secondly, C-S-H nucleation seeding boosted the compressive strengths of LC^3 binders at 1 day of hydration by 45-100% respect to the unseeded mortars. The C-S-H seeded LC^3 mortars developed 22-29 MPa at 1 day, which are competitive values for field applications. Moreover, the compressive strength improvements are noticed at all ages. For instance, the relative improvements at 28 days ranged 18-26 %.

Acknowledgements

Financial support from PID2020-114650RB-I00 research grant, co-funded by FEDER, is acknowledged.

References

Akhlaghi, O., Aytas, T., Tatli, B., Sezer, D., Hodaei, A., Favier, A., Scrivener, K.L., Menceloglu, Y.Z., Akbulut, O. (2017) "Modified poly(carboxylate ether)-based superplasticizer for enhanced flowability of calcined clay-limestone-gypsum blended Portland cement", *Cem. Concr. Res.* 101: 114–122.

Juenger, M.C.G., Snellings, R., Bernal, S.A. (2019) "Supplementary cementitious materials: New sources, characterization, and performance insights", *Cem. Concr. Res.* 122: 257–273.

Morales-Cantero, A., Cuesta, A., De la Torre, A.G., Santacruz, I., Mazanec, O., Borralleras, P., Weldert, K.S., Gastaldi, D., Canonico, F., Aranda, M.A.G. (2022a) "C-S-H seeding activation of Portland and Belite Cements: an enlightening in situ synchrotron powder diffraction study", *Cem. Concr. Res.* 161: 106946.

Morales-Cantero, A., Cuesta, A., Torre, A.G.D. la, Mazanec, O., Borralleras, P., Weldert, K.S., Gastaldi, D., Canonico, F., Aranda, M.A.G. (2022b) "Portland and Belite Cement Hydration Acceleration by C-S-H Seeds with Variable w/c Ratios", *Materials* 15: 3553.

Scrivener, K.L., Martirena, F., Bishnoi, S., Maity, S. (2018) "Calcined clay limestone cements (LC3)", *Cem. Concr. Res.* 114: 49-56.

The 16th International Congress on the Chemistry of Cement 2023 (ICCC2023)
"Further Reduction of CO_2 -Emissions and Circularity in the Cement and Concrete Industry"
September 18–22, 2023, Bangkok, Thailand

Nucleation Effects of Biologically Architected Calcium Carbonate in Portland Limestone Cements

D.N. Beatty[1], and W.V. Srubar[1,2*]

[1] *Materials Science and Engineering Program, University of Colorado, Boulder, USA*
Email: danielle.beatty@colorado.edu
[2] *Department of Civil, Environmental, and Architectural Engineering, University of Colorado, Boulder, USA*
Email: wsrubar@colorado.edu

ABSTRACT

The production of portland cement accounts for 7% of global annual greenhouse gas emissions. One of the most utilized approaches to reduce emissions is to reduce the amount of portland cement in concrete mix designs using supplementary cementitious materials (SCMs) or ground limestone ($CaCO_3$) fillers. Ground $CaCO_3$ fillers can be used to replace 5-15 wt% (ASTM C595) (6-35 wt%, EN 197-1) of cement in concrete mix designs. The resulting portland limestone cement has a reduced carbon footprint due to reduced cement clinker content. The ground limestone also improves other cement properties (e.g., workability) and can lead to accelerated hydration kinetics due to the filler effect. In this work, two sources of photosynthetically produced, biologically architected $CaCO_3$ with high surface areas (produced by macroalgae and microalgae) were investigated as potential nucleation seeds and CO_2-storing mineral replacements for ground limestone in portland limestone cement. The particle size, morphology, and mineralogy of each biogenic $CaCO_3$ source were characterized using particle size analysis, scanning electron microscopy, and X-ray diffraction, respectively. Then, cement pastes were prepared using 5 wt% or 15 wt% cement replacement with biogenic $CaCO_3$. The reaction kinetics and 7-day and 28-day compressive strength were assessed and compared to plain cement paste and portland limestone cement pastes containing a non-biogenic $CaCO_3$ replacement control. Characterization results reveal that the high surface areas (8.26 m^2/g (macroalgal) and 12.22 m^2/g (microalgal)) of biogenic $CaCO_3$ induce nucleation and seeding effects during cement hydration, thereby accelerating cement hydration kinetics, without altering compressive strength. Results substantiate that biogenic $CaCO_3$ produced using photosynthesis can be used to produce portland limestone cement, highlighting an opportunity for substantial CO_2 storage in portland limestone cements and concretes.

KEYWORDS: *Portland Limestone Cement, $CaCO_3$, Nucleation, Hydration, Compressive Strength*

1. Introduction

The production of portland cement accounts for 7% of global annual greenhouse gas emissions (de Brito and Kurda (2021), Rissman et al (2020)). One of the most common strategies to reduce emissions of cement or concrete projects is to replace a fraction of cement clinker in each mix design with limestone filler materials (International Energy Agency (2018), Juenger and Siddique (2015), Portland Cement Association (2021)). The use of limestone fillers in cement to produce portland limestone cement (PLC) is standardized in the US (15% replacement)(ASTM International (2021)), Canada (15% replacement)(Canadian Standards Association (2018)), Europe (35% replacement)(European Standards (2011)), and China (25% replacement)(Technical Supervision and Research Center of Building Materials Industry (2010)).

Apart from emissions and cost reductions, there are four tangible effects that limestone fillers impart in cement: the filler effect, the dilution effect, the nucleation effect, and the chemical effect. These effects have been well studied and reported in the literature (Bentz et al (2017), Berodier and Scrivener (2014), Oey et al (2013)), and recent review articles have detailed these effects in both cement (Ahmad et al (2022), Dhandapani et al (2021), Wang et al (2018a)) and concrete (Panesar and Zhang (2020), Wang et al (2018b)). The dilution effect refers to the dilution of cement in paste or concrete when replaced by other particles. The filler effect refers to the addition of particles of different sizes to the cementitious matrix, which leads

to increased particle packing, increased density, compressive strength, and durability of cementitious materials (Briki et al (2021), Knop and Peled (2016)). The nucleation effect refers to the tendency of filler materials to act as nucleation sites for hydration product formation, which leads to higher early age strength and decreased setting time (Knop and Peled (2016), Moon et al (2017)). The chemical effect refers to the chemical reactions induced by fillers that can occur during cement hydration. Various studies have shown that limestone is a better nucleating agent than other filler materials (Berodier and Scrivener (2014), Kumar et al (2017), Ouyang et al (2017), Zhang et al (2020)), which is attributed to the $CaCO_3$ surface structure and interfacial properties, specifically in the calcite phase (Bentz et al (2015)). The most important property of filler particles, which affects both their filler and nucleation responses, is particle size and surface area. Finer particles, with correspondingly larger surface areas, generally lead to higher hydration product nucleation and can lead to higher particle packing density (Briki et al (2021), Cook et al (2020), Knop et al (2014), Knop and Peled (2016), Vehmas et al (2017), Zhu et al (2022)).

While limestone fillers reduce clinker content, and, therefore, emissions, limestone is obtained through open pit mining, which leads to pollution and ecosystem damage (Ganapathi & Phukan, 2020). Limestone must also be ground to the micron scale before use in cement or concrete, which is a highly inefficient and costly process (Admin (2020), Napier-Munn (2015), Zhang et al (2022)). To address these limestone challenges, it is possible to return to the original method for limestone production: photosynthesis. Limestone rocks were originally produced over eons of time by marine organisms, including photosynthetic microorganisms such as coccolithophores. Coccolithophores absorb dissolved CO_2 (in the form of HCO_3^- ions) and convert it to $CaCO_3$ through the process called microbially induced calcium carbonate precipitation (Beatty et al (2022)), which results in highly intricate, ordered $CaCO_3$ particles (coccoliths).

There is significant potential to utilize such biogenic, micron-scale, high surface area $CaCO_3$ particles produced by coccolithophores as high nucleation, carbon storing limestone filler in PLCs. Using photosynthetic sources of limestone has the potential to further reduce emissions associated with cement and concrete projects and eliminate the challenges associated with limestone mining and grinding. In this work, we explore the use of micron-scale, biologically architected $CaCO_3$ with high surface area, produced by coccolithophores, as limestone fillers up to 15% replacement in PLC. We compare these filler results to PLCs made with photosynthetic macroalgae-produced $CaCO_3$ and non-biogenic $CaCO_3$ filler controls.

2. Materials and Methods

Reagent grade $CaCO_3$ and two sources of biologically architected $CaCO_3$ were compared as fillers for portland limestone cement. Reagent grade $CaCO_3$ (>99.0%) was purchased from Sigma Aldrich. $CaCO_3$ produced by photosynthetic macroalgae *Lithothamnion* sp. was purchased from Stauber. $CaCO_3$ produced by photosynthetic microalgae *Emiliania huxleyi* was purchased from the Algal Resource Collection at the University of North Carolina, Wilmington. *E. huxleyi* $CaCO_3$ also contained biomass alongside inorganic minerals and was treated to remove organics following a protocol similar to that used by Jakob et al (2017).

Each $CaCO_3$ source was imaged using a Hitachi SU3500 scanning electron microscope (SEM). Samples were coated in platinum prior to imaging to ensure sufficient conductivity. $CaCO_3$ sources were imaged in secondary electron mode using 15 keV accelerating voltage and < 9 mm working distances.

Surface area analysis was conducted using a Micromeritics 3Flex system at the University of Utah Materials Characterization Lab. Specific surface area of each $CaCO_3$ source was calculated using the Brunauer-Emmett-Teller (BET) method. Prior to analysis, samples were flow degassed for 4 hours at 105 °C. The particle size distribution of each CaCO3 source was measured using laser diffraction in a Malvern Panalytical Mastersizer3000, following ultrasonic dispersion in ultrapure water.

To assess the effectiveness of each $CaCO_3$ source as a filler for portland limestone cement, cement pastes with 5% and 15% (ASTM International (2021)) $CaCO_3$ replacement by weight of cement were prepared. Cement hydration was analyzed using isothermal conduction calorimetry (ICC). Compressive strength was analyzed by testing 1 cm^3 cubes of each PLC cement paste at 7 and 28 days after hydration. To make the paste, $CaCO_3$ was first thoroughly mixed with OPC powder (Quikrete Type I/II) for 5 min. Water was then added and the paste was mixed by hand for two minutes. A water-to-cementitious materials ratio (w/cm) of 0.5 was used for all samples; *E. huxleyi* $CaCO_3$ showed enhanced water demand and additional water was added to the 15% replacement mix to achieve workability (effective w/cm = 0.6).

ICC was completed at 25 °C using an 8 channel Thermometric TAM Air calorimeter, with siliceous sand as a reference. Twenty-gram batches were made for each mix and samples were run in duplicate. Heat

of hydration and total heat data were collected for 72 hours. Data were then normalized by weight of cement powder in each sample. Fifteen grams of cement paste was mixed and poured into 1 cm^3 silicone cube mold tray to create cubes for compression testing. The cube mold was placed in a >98% humidity chamber created according to ASTM International (2020). Cubes were allowed to cure for 24 hours and then removed from the molds and placed into oversaturated $Ca(OH)_2$ solution. After curing for 7 or 28 days, cubes were removed from the saturated $Ca(OH)_2$ solution and thoroughly dried using a paper towel. Compressive strength of cement cubes was measured using an Instron Universal Testing machine with a 50 kN load cell and a 0.1 mm/sec compression rate. Three cubes were tested for each mix design. One-factor ANOVA analysis was used to assess the variability in results between $CaCO_3$ filler sources.

3. Results

Scanning electron micrographs, particle size analysis results, and BET surface area analysis results of reagent grade $CaCO_3$, *Lithothamnion* sp. $CaCO_3$, and *E. huxleyi* $CaCO_3$ are shown in Figure 1. Reagent grade $CaCO_3$ particles are larger, more angular particles, with correspondingly low surface area, as compared to biogenic $CaCO_3$ sources. *Lithothamnion* sp. $CaCO_3$ are a range of particle sizes, and *E. huxleyi* $CaCO_3$ particles are the expected small, intricate, and uniform shapes of coccoliths. *E. huxleyi* $CaCO_3$ particles are the smallest of the three, with the highest surface area. Though larger than those of *E. huxleyi* $CaCO_3$, *Lithothamnion* sp. $CaCO_3$ particles also exhibit relatively small size and high surface areas.

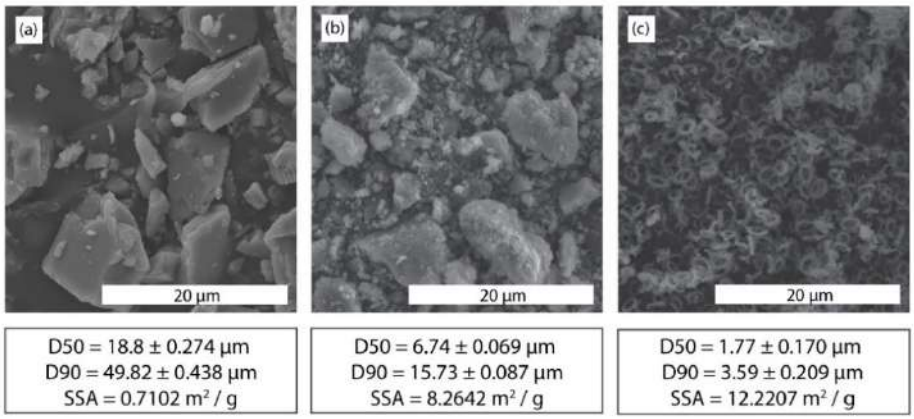


Figure 1: Scanning electron micrographs of (a) reagent grade $CaCO_3$, (b) *Lithothamnion* sp. $CaCO_3$, and (c) *E. huxleyi* $CaCO_3$. Particle sizes (D50 and D90), measured by particle size analysis, and specific surface area (SSA) values measured by the BET method are also included for each $CaCO_3$ source.

ICC data collected for each PLC paste (Figure 2) were used to analyze hydration kinetics. Initial and final set time were estimated from ICC using previously published methods (Hu et al., 2014; Vishavkarma & Harish, 2022). Initial and final set times differed slightly for each PLC paste, but all differed from OPC control paste by less than 0.5 hr. PLCs made with *Lithothamnion* sp. $CaCO_3$ and *E. huxleyi* $CaCO_3$ had no significant effect on initial set time. PLC with 5% *Lithothamnion* sp. $CaCO_3$ increased final set time and PLC with 15% *Lithothamnion* sp. decreased final set time. Both PLCs made with *E. huxleyi* $CaCO_3$ decreased final set time. All PLCs showed increased peak heat compared to OPC control cement paste, except 5% *Lithothamnion* sp. $CaCO_3$ PLC. PLC with *E. huxleyi* $CaCO_3$ showed significant peak heat increases (>20% increase for 15% PLC). PLC with 15% *E. huxleyi* $CaCO_3$ also showed a >12% increase in max cumulative heat at 72 hrs.

Statistical results, calculated through one factor ANOVA analysis, revealed that all PLC pastes achieved statistically similar strength after 7 days of hydration (Figure 2c). For 28 days of hydration, PLC pastes with 5% *Lithothamnion* sp. $CaCO_3$ and 5% *E. huxleyi* $CaCO_3$, were statistically different (i.e., higher) than the OPC control and other PLC pastes. All other 28-day strength results were statistically similar to the OPC control.

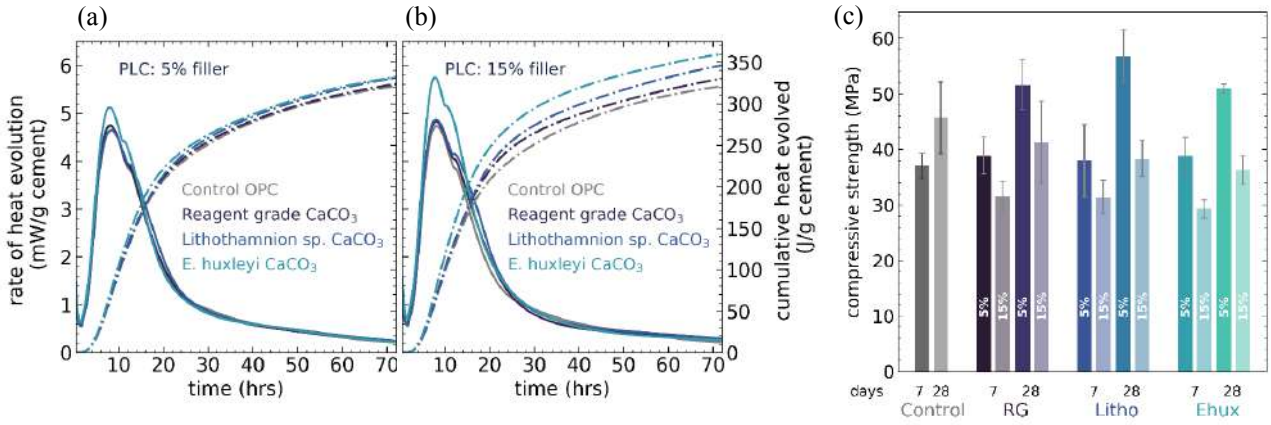


Figure 2: Isothermal conduction calorimetry results for OPC Control compared to PLCs incorporating (a) 5% or (b) 15% reagent grade $CaCO_3$ (RG), *Lithothamnion* sp. $CaCO_3$ (Litho), or *E. Huxleyi* $CaCO_3$ (Ehux), and (c) compressive strength results for PLCs with each $CaCO_3$ filler.

4. Discussion

Both biogenic sources of $CaCO_3$ studied here act as effective fillers for PLC up to 15% cement replacement. Both *Lithothamnion* sp. $CaCO_3$ and *E. huxleyi* $CaCO_3$ consisted of >93% and >97% (respectively) $CaCO_3$ as measured by XRD and TGA (data not shown). These $CaCO_3$ values exceed purity requirements for limestone fillers, as specified by ASTM International (2021).

Lithothamnion sp. $CaCO_3$ and *E. huxleyi* $CaCO_3$ also exhibited increased surface areas. High surface area and low density fillers can result in high water demand in cementitious pastes, thus limiting their replacement values or requiring the use of superplasticizer to control workability (Bost et al (2016), Knop et al (2014), Poudyal et al (2021), Wang et al (2014)). In the case of *E. Huxleyi* $CaCO_3$ at 15% replacement studied here, adding additional water was enough to achieve a workable paste for hydration and strength testing. Despite additional water added to 15% *E. huxleyi* $CaCO_3$ PLC, this $CaCO_3$ showed the greatest nucleation effects (increased peak heat and highest cumulative heat at 72 hrs), and statistically similar strength results at both 7 and 28 days. High surface areas (increased water demand) may limit industrial use at higher cement replacements; however, the high nucleation effects, and energy efficient production process (photosynthesis) show promise for use of this material in place of precipitated calcium carbonate or C-S-H nucleation seeds. Despite relatively high surface area of *Lithothamnion* sp. $CaCO_3$, pastes with this filler showed limited nucleation effects in ICC. This lack of nucleation may be due to agglomeration, which can limit nucleation (Knop and Peled (2016), Kumar et al (2017), Oey et al (2013)), or surface area that was too large to induce as significant a nucleation effect. However, PLC with 5% *Lithothamnion* sp. $CaCO_3$ showed increased compressive strength at 28 days of hydration, indicating evidence of nucleation or other filler, dilution, or chemical effects. Reagent grade $CaCO_3$ behaved as expected for an inert limestone filler; ICC and compressive strength results were similar to those of the OPC control paste.

5. Conclusions

This study is the first to test photosynthetic $CaCO_3$ produced by macro and micro algae as limestone fillers in PLCs. Hydration kinetics and compressive strength of PLCs with 5% and 15% replacement of cement by *Lithothamnion* sp. (macroalgae) $CaCO_3$ and *E. huxleyi* (microalgae) $CaCO_3$ were analysed. Results reveal statistically similar compressive strength values for both biogenic PLCs at 7 days of hydration and increased compressive strength for both 5% biogenic PLCs at 28 days of hydration. Early age hydration and reaction kinetics reveal significant nucleation for PLC with *E. huxleyi* $CaCO_3$ and slight nucleation for PLC with *Lithothamnion* sp. $CaCO_3$, both due to increased surface areas. This study was limited to 15% cement replacement, as dictated by US standards. *E. huxleyi* $CaCO_3$ introduced increased water demand at 15% cement replacement, which could limit the application of microalgae $CaCO_3$ to low replacement levels or require superplasticizers to achieve pastes with higher replacement levels (up to 35% to meet EU standards).

This study reveals that biogenic $CaCO_3$ can be used as a filler for PLC. Biogenic $CaCO_3$ produced by photosynthetic organisms is net-carbon storing and may lead to further CO_2 reduction for PLCs if industrially implemented. More research is needed to investigate sustainable, cost-effective scale-up of biogenic $CaCO_3$ production for industrial use in the construction industry.

Acknowledgements

This research was supported in part by the Colorado Shared Instrumentation in Nanofabrication and Characterization (COSINC): the COSINC-CHR (Characterization), College of Engineering & Applied Science, University of Colorado Boulder. The authors would also like to acknowledge the help of scientists at the University of Utah Materials Characterization Lab. This material is based upon work supported by the National Science Foundation under Grant No. CMMI-1943554, the National Science Foundation Graduate Research Fellowship under Grant No. DGE 2040434, the Advanced Research Projects Agency - Energy under Award No. DE-AR0001629, and the Breakthrough Energy Foundation under Explorer Grant number AWD-22-05-0179. Any opinions, findings, and conclusions or recommendations expressed in this material are those of the authors and do not necessarily reflect the views of the National Science Foundation, the Advanced Research Projects Agency, or the Breathrough Energy Foundation.

Declaration of Competing Interest

W.V.S. is a listed co-inventor on a patent application (PCT/US2020/020863) filed by the University of Colorado on April 3, 2020, related to biomineralized building materials. W.V.S. is a co-founder and shareholder of Prometheus Materials, Inc. and Minus Materials, Inc. and a member of their scientific advisory boards. D.N.B. is a co-founder, consultant to, and shareholder of Minus Materials, Inc.

References

Admin. (2020, May 15) "The four major costs associated with cement production", INFINITY FOR CEMENT EQUIPMENT.

Ahmad, I., Shen, D., Khan, K. A., Jan, A., Khubaib, M., Ahmad, T., and Nasir, H. (2022) "Effectiveness of Limestone Powder in Controlling the Shrinkage Behavior of Cement Based System: A Review", *Silicon*, 14(2): 359–371

ASTM International. (2020) "ASTM E104-20a: Standard Practice for Maintaining Constant Relative Humidity by Means of Aqueous Solutions", ASTM International.

ASTM International. (2021) "ASTM C595/C595M-21: Standard Specification for Blended Hydraulic Cements", ASTM International.

Beatty, D. N., Williams, S. L., and Srubar, W. V. (2022) "Biomineralized Materials for Sustainable and Durable Construction", *Annual Review of Materials Research*, 52(1): 411–439

Bentz, D. P., Ardani, A., Barrett, T., Jones, S. Z., Lootens, D., Peltz, M. A., Sato, T., Stutzman, P. E., Tanesi, J., and Weiss, W. J. (2015) "Multi-scale investigation of the performance of limestone in concrete", *Construction and Building Materials*, 75: 1–10

Bentz, D. P., Ferraris, C. F., Jones, S. Z., Lootens, D., and Zunino, F. (2017), "Limestone and Silica Powder Replacements for Cement: Early-Age Performance", *Cement & Concrete Composites*, 78: 43–56

Berodier, E. and Scrivener, K. (2014) "Understanding the Filler Effect on the Nucleation and Growth of C-S-H", *Journal of the American Ceramic Society*, 97(12): 3764–3773

Bost, P., Regnier, M., and Horgnies, M. (2016) "Comparison of the accelerating effect of various additions on the early hydration of Portland cement", *Construction and Building Materials*, 113: 290–296

Briki, Y., Zajac, M., Haha, M. B., and Scrivener, K. (2021) "Impact of limestone fineness on cement hydration at early age", *Cement and Concrete Research*, 147: 106515

Canadian Standards Association. (2018) "A3000-18: Cementitious materials compendium", Canadian Standards Association.

Cook, R., Ma, H., and Kumar, A. (2020) "Influence of size-classified and slightly soluble mineral additives on hydration of tricalcium silicate", *Journal of the American Ceramic Society*, 103(4): 2764–2779

de Brito, J. and Kurda, R. (2021) "The past and future of sustainable concrete: A critical review and new strategies on cement-based materials", *Journal of Cleaner Production*, 281" 123558

Dhandapani, Y., Santhanam, M., Kaladharan, G., and Ramanathan, S. (2021) "Towards ternary binders involving limestone additions—A review", *Cement and Concrete Research*, 143: 106396

European Standards. (2011) "DIN EN 197-1: Cement—Part 1: Composition, specifications and conformity criteria for common cements", Eurpean Standards.
Ganapathi, H. and Phukan, M. (2020) "Environmental Hazards of Limestone Mining and Adaptive Practices for Environment Management Plan", *Environmental Processes and Management: Tools and Practices*: 121–134. Springer International Publishing.
Hu, J., Ge, Z., and Wang, K. (2014) "Influence of cement fineness and water-to-cement ratio on mortar early-age heat of hydration and set times", *Construction and Building Materials*, 50: 657–663
International Energy Agency. (2018) "Technology Roadmap—Low-Carbon Transition in the Cement Industry – Analysis"
Jakob, I., Chairopoulou, M. A., Vučak, M., Posten, C., and Teipel, U. (2017) "Biogenic calcite particles from microalgae—Coccoliths as a potential raw material", *Engineering in Life Sciences*, 17(6): 605–612
Juenger, M. C. G. and Siddique, R. (2015) "Recent advances in understanding the role of supplementary cementitious materials in concrete", *Cement and Concrete Research*, 78: 71–80
Knop, Y. and Peled, A. (2016) "Setting behavior of blended cement with limestone: Influence of particle size and content", *Materials and Structures*, 49(1): 439–452
Knop, Y., Peled, A., and Cohen, R. (2014) "Influences of limestone particle size distributions and contents on blended cement properties", *Construction and Building Materials*, 71: 26–34
Kumar, A., Oey, T., Falzone, G., Huang, J., Bauchy, M., Balonis, M., Neithalath, N., Bullard, J., and Sant, G. (2017) "The filler effect: The influence of filler content and type on the hydration rate of tricalcium silicate", *Journal of the American Ceramic Society*, 100(7): 3316–3328
Moon, G. D., Oh, S., Jung, S. H., and Choi, Y. C. (2017) "Effects of the fineness of limestone powder and cement on the hydration and strength development of PLC concrete", *Construction and Building Materials*, 135: 129–136
Napier-Munn, T. (2015) "Is progress in energy-efficient comminution doomed?", *Minerals Engineering*, 73: 1–6
Oey, T., Kumar, A., Bullard, J. W., Neithalath, N., and Sant, G. (2013) "The Filler Effect: The Influence of Filler Content and Surface Area on Cementitious Reaction Rates", *Journal of the American Ceramic Society*, 96(6): 1978–1990
Ouyang, X., Koleva, D. A., Ye, G., and van Breugel, K. (2017) "Understanding the adhesion mechanisms between CSH and fillers", *Cement and Concrete Research*, 100: 275–283
Panesar, D. K., and Zhang, R. (2020) "Performance comparison of cement replacing materials in concrete: Limestone fillers and supplementary cementing materials – A review", *Construction and Building Materials*, 251: 118866
Portland Cement Association. (2021) "PCA Roadmap to Carbon Neutrality", Portland Cement Association.
Poudyal, L., Adhikari, K., and Won, M. (2021) "Mechanical and Durability Properties of Portland Limestone Cement (PLC) Incorporated with Nano Calcium Carbonate (CaCO3)", *Materials*, 14(4): 905
Rissman, J., Bataille, C., Masanet, E., Aden, N., Morrow, W. R., Zhou, N., Elliott, N., Dell, R., Heeren, N., Huckestein, B., Cresko, J., Miller, S. A., Roy, J., Fennell, P., Cremmins, B., Koch Blank, T., Hone, D., Williams, E. D., de la Rue du Can, S., and Helseth, J. (2020) "Technologies and policies to decarbonize global industry: Review and assessment of mitigation drivers through 2070", *Applied Energy*, 266: 114848
Technical Supervision and Research Center of Building Materials Industry. (2010) "JC/T 600-2010 Limetsone Portland Cement", Ministry of Industry and Information Technology of the People's Republic of China.
Vehmas, T., Kronlöf, A., and Cwirzen, A. (2017) "Effect of Additional Surfaces on Ordinary Portland Cement Early-Age Hydration", *Materials Sciences and Applications*, 8(12): Article 12.
Vishavkarma, A. and Harish, K. V. (2022) "Using Isothermal Calorimetry to Predict Setting Time of Cement-Based Materials (CBMs)", Recent Advancements in Civil Engineering: 341–349. Springer.
Wang, D., Shi, C., Farzadnia, N., Shi, Z., & Jia, H. (2018) "A review on effects of limestone powder on the properties of concrete", *Construction and Building Materials*, 192: 153–166
Wang, D., Shi, C., Farzadnia, N., Shi, Z., Jia, H., and Ou, Z. (2018) "A review on use of limestone powder in cement-based materials: Mechanism, hydration and microstructures", *Construction and Building Materials*, 181: 659–672
Wang, X., Wang, K., and Tanesi, J. (2014) "Effects of Nanomaterials on the Hydration Kinetics and Rheology of Portland Cement Pastes", *Advances in Civil Engineering Materials*, volume 3.

Zhang, Z., Wang, Q., Zhang, M., Huang, Z., and Zhuang, S. (2020) "A new understanding of the effect of filler minerals on the precipitation of synthetic C–S–H", *Journal of Materials Science*, 55(35): 16455–16469

Zhang, Z.-X., Sanchidrián, J. A., Ouchterlony, F., and Luukkanen, S. (2022) "Reduction of Fragment Size from Mining to Mineral Processing: A Review", *Rock Mechanics and Rock Engineering*, 56: 747-778

Zhu, P., Jiang, L., Chu, H., Yu, Y., Shi, Y., Xu, N., and Liu, M. (2022) "Cement with high-volume limestone powder: Effect of powder fineness on packing density, strength and hydration behaviour", *Advances in Cement Research*, 34(7): 311–323

The 16th International Congress on the Chemistry of Cement 2023 (ICCC2023)
"Further Reduction of CO_2 -Emissions and Circularity in the Cement and Concrete Industry"
September 18–22, 2023, Bangkok, Thailand

Dune sand powders characterization for their use in cement-based materials

J.H. Niu[1], Z. Wang[2*]

[1] *Chongqing university, Chongqing, China;Shihezi University, Shihezi, China*
Email: niujinghang@126.com
[2] *Chongqing university, Chongqing, China*
Email: cquwangzhi@126.com

ABSTRACT

Based on an ongoing experimental programme, this research focuses on the effect of dune sand powders (DSP) as supplementary cementitious materials (SCMs) at various grinding method on the microstructure and mechanical property of blended mortar. A series of characterization experiments was conducted to evaluate the potential application of DSP in cement-based materials.
The paper primarily considers the characteristics of DSP, including their physical property and chemical composition, by different grinding method with same time. In addition, the activity of DSP in cement was evaluated by mortar strength test. The hydration heat release of Portland cement incorporated with DSP is studied by isothermal calorimetry test. Microstructural investigations, such as thermogravimetric analysis, were also used to support the explanation for these mechanisms.
The results of this research work confirm that dry grinding of DSP is more advantageous than wet grinding as a partial substitute for Portland cement. As an inert admixture, the promotion effect of DSP on cement hydration is mainly manifested by heterogeneous nucleation of micro-powder particles.

KEYWORDS: *Dune sand powder, Portland cement, Supplementary cementitious materials, Hydration, Compressive strength.*

1. Introduction

Manufacturing of Portland cement consumes a considerable amount of energy and natural resources. As a substitute for Portland cement in concrete, the use of supplementary cementitious materials(SCMs) in modern concrete mixtures is nearly ubiquitous. SCMs currently serve as one of the primary tools for reducing carbon dioxide emissions associated with concrete production (WBCSD and IEA (2009)). Variety of waste materials including tire rubbers (Pacheco-Torgal et al (2012)), lime stone (Ghrici et al (2007)), silica fume (Bhanja and Sengupta (2002)), fly ash and blast furnace slag(Li and Zhao (2003)) have been used in concrete production. These wastes have a beneficial effect on the performance of concrete. These benefits include mechanical and durability aspects.
However, the use of these materials lead to some disadvantages including: slow rate of strength development; increased water demand; and increased superplasticizer dosage (Ghrici et al (2006)). At the same time, some SCMs are becoming more expensive and difficult to obtain in market (Erdem and Kirca (2008)). Due to above mentioned reasons, researchers are seeking for cheap and easily available cement replacement materials.
Dune sand (DS) is an abundant natural material, with high content of quartz silica (Zhang et al (2022)). For a long time, it has been widely believed in the construction industry that DS cannot be used to prepare concrete because of its fine particles and poor gradation. therefore, it has been used as partial replacement for fine aggregate only (Al-Harthy et al (2007)). A very limited work has been carried out to study the possibility of using dune sand powders (DSP) as cement replacement materials (Zhang et al (2022)).
The aim of this work is to study natural DS obtained from the Gurbantunggut Desert by grinding them to form DSP, which present some interesting properties for their different fineness and grinding method in

cement-based materials. The outcome of study is expected to encourage the use of DSP as a cement replacement material in concrete industry.

2. Materials and methods

DS used in this work was obtained from Gurbantunggut Desert in Xinjiang, China. Dry grinding and wet grinding processes were used to prepare DSP by ball mill. The pulp concentration of wet grinding is 50%, and the sand ball ratio for dry grinding is 1:1. The grinding times were 60, 90, 120, and 150 minutes. The physical properties of DSP with different grinding times are shown in Table 1. The particle size data were measured by BT-9300HT laser particle size distributor and the specific surface area was obtained by a Quadrasorb 2MP specific surface analyzer.

Table 1 physical properties of DSP

Serial number	DSP1	DSP2	DSP3	DSP4	DSP5	DSP6	DSP7	DSP8
Grinding process	Dry grinding				Wet grinding			
Grinding time / min	60	90	120	150	60	90	120	150
D50 / um	14.680	8.718	6.445	6.608	5.29	6.303	3.544	3.57
Mean particle size / um	22.68	12.76	8.794	9.057	6.913	8.391	4.364	4.403
Specific surface area / (m^2/kg)	543.8	758.0	853.6	851.0	939.2	832.5	1184	1187

A Portland cement from Chongqing Xiaonanhai Cement Plant was used, and its specific gravity and specific surface area is 312 kg/m^3 and 452 m^2/kg, respectively. The chemical composition of DS and Ordinary Portland cement (OPC) as obtained by XRF is presented in Table 2. The SEM image and XRD analysis of DSP is shown in Figures 1 and 2, respectively.

Table 2 Chemical analysis (%) of the materials used

	SiO_2	Al_2O_3	CaO	Fe_2O_3	K_2O	Na_2O	MgO	TiO_2	LOI
OPC	21.51	6.98	61.68	5.01	0.96	0.26	3.32	-	2.67
DS	70.06	12.63	3.79	4.66	3.46	2.58	1.59	0.63	-

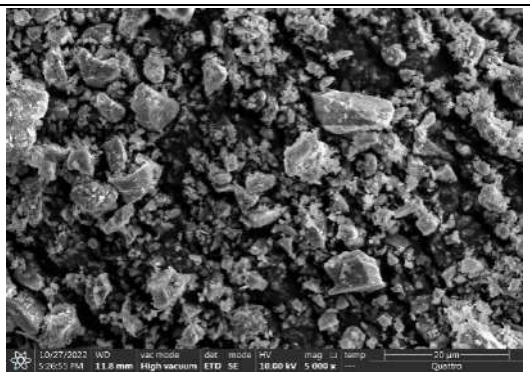


Fig.1. SEM image of DSP

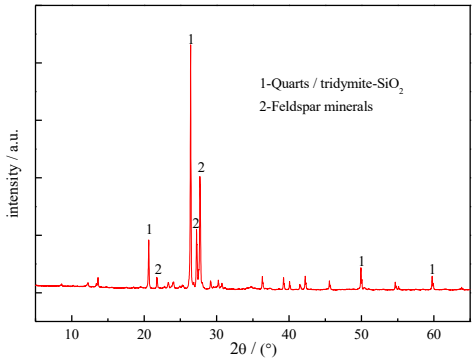


Fig.2. XRD analysis of DSP

Control (CTRL) group contained only Portland cement as binder material and labelled 0. In the other mixtures, 30% (by weight) of the cement was replaced with DSP and the mixture were labelled as DSP1-8 respectively (Table 1). Cement paste specimens were cast into cube of 20 mm and compacted on a vibration table for about 10 seconds. All specimens were covered with plastic sheets and stored in air at 23±5 °C for 24 hours. The specimens were then demolded and cured in water to test age. The specimens were tested by the procedure specified in GB/T17671-2021. The cement replacement rate of mortar specimens was also 30%, standard sand was used as aggregate, and the preparation process, curing and test method stipulated by GB/T17671-2021 are strictly followed.

3. Result and discussion

3.1 Compressive strength

Figure 3 shows the results of compressive strength of cement paste. The influence of DSP obtained by different grinding methods on the strength of cement paste is completely different.Although the wet grinding method can obtain smaller particles of DSP, the strength of the specimen at the same age is much lower than that prepared by dry grinding DSP. This effect is more significant in the early age, possibly

because the physical combination of DSP with water molecules weakens the micro-aggregate effect of DSP in the mixture at the same water-cement ratio. No matter dry grinding or wet grinding, the fineness of DSP in micron scale has no significant effect on the strength of the paste. Obviously, when used as SCMs, the DSP obtained by dry grinding has less influence on the strength loss of binder than the pulp obtained by wet grinding, the micro-aggregate effect (Lawrence et al (2003)) may explain this phenomenon.

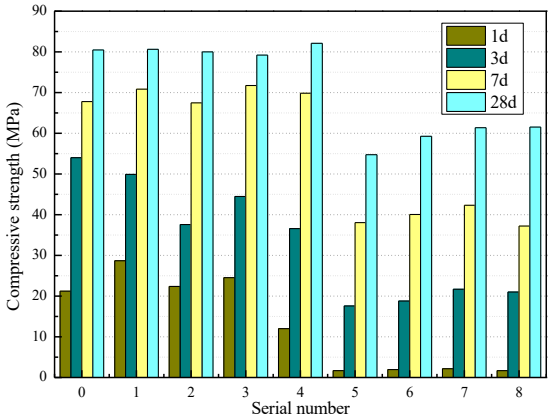


Fig.3. Compressive strength of cement paste

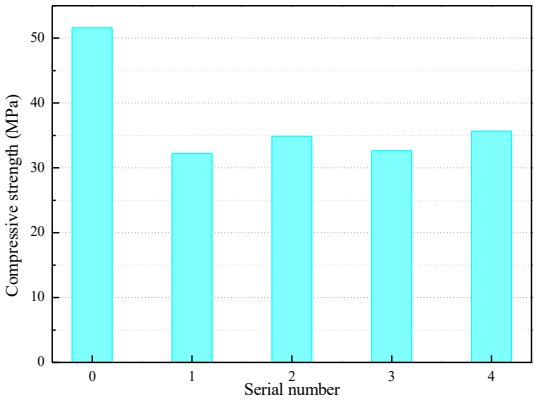


Fig.4. Compressive strength of Mortar

In order to further understand the activity of DSP as SCMs, strength test was conducted by preparing mortar specimens, and the results were shown in Figure 4. The activity index of DSP obtained by mechanical grinding is not more than 70%, which cannot meet the activity requirements of SCMs. The activity index of DSP has little relationship with particle fineness, but closely with grinding method.

3.2 Calcium hydroxide content

The weight loss of samples at different temperatures after 28d was measured by thermogravimetric analysis. The calcium hydroxide content of each sample was calculated by water loss. Figure 5 shows the calcium hydroxide content at 28d for all tested materials. It can be seen that the grinding method of DSP has an effect on the hydration process of the binder. In contrast, the generation of calcium hydroxide during the hydration of binders is less affected by dry grinding. As additional nucleation sites for cement particles are provided by dry grinding DSP in the mixed system, it can promote the hydration process of cement (Guettala and Mezghiche (2011)), another possible reason is that some of the active ingredients in the DSP participate in the hydration reaction, which produces additional calcium hydroxide (Guettala and Mezghiche (2011)).

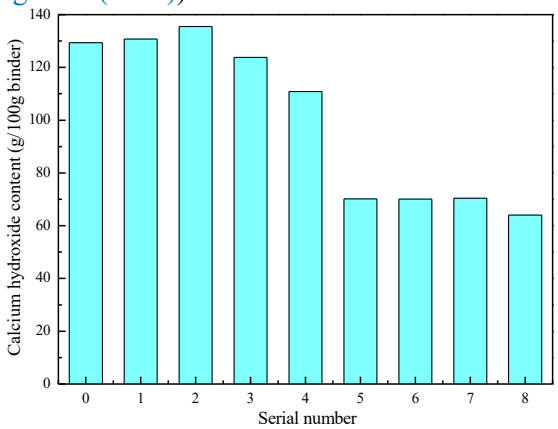


Fig.5. Calcium hydroxide content at 28d for all binders

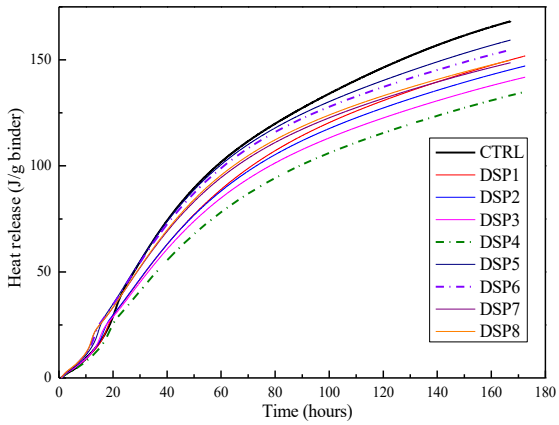


Fig.6. Heat release of cement in binders

3.3 Heat release

Figure 6 shows the cumulative heat release (J/g of binder) for cement and DSP. Obviously, DSP partial replacement of cement reduces the total heat release of the binder, but increases the hydration heat release per gram of cement. This finding is in conformity with the literature results (Suraneni and Weiss (2017)), demonstrating once again that the DSP with a main composition of SiO_2 has very low activity and is mainly

inert. Nonetheless, it can provide nucleation sites for cement hydration, which will promote cement hydrate more quickly. The analysis results of DSP4 and DSP6 with the same particle fineness show that dry grinding has more significant influence on the early hydration process of cement. The complexity of the influence of DSP on the early hydration of cement is proved again (Lawrence et al (2003)).

4. Conclusions

The research on the application of dune sand in cement concrete as SCMs has not many achievements at present, but future research opportunities are significant. The properties of DSP produced by mechanical grinding (dry and wet) as SCMs were examined based on the mechanochemical theory. The effectiveness of grinding can be increased in wet grinding by using water as a dispersion medium, according to particle size analysis. The pulp produced by wet grinding, however, greatly affects the strength of cement paste because it prevents cement from fully hydrating, as shown by thermogravimetric analysis and hydration heat release. Therefore, grinding dune sand with the wet approach is not recommended. The results of the mortar strength index test show that DSP constitutes the majority of the inert filler in the mixture. It can scatter cement particles and create nucleation sites, which helps cement hydrate. At the same time, DSP can exhibit some activity when its particle size is tiny enough, demonstrating that it has the potential for activity and can be stimulated by chemical excitation.
Dune sand has a complicated composition that is primarily crystalline, and mechanical grinding has little impact on its activity. However, as mineral admixture, it not only acts as inert filler in the mixture system, but also shows certain activity, which has the potential to improve the activity.

Acknowledgements

The research reported in the paper is supported by the National Natural Science Foundation of China (NSFC, Grant No.52268034) and the Chongqing Natural Science Foundation of China (Grant No. CSTB2022NSCQ-MSX0647). The financial support is highly appreciated.

References

WBCSD and IEA (2009) “Cement Technology Roadmap 2009: Carbon Emissions Reductions up to 2050”

Pacheco-Torgal, F., Ding Y.Y. and Jalali, S. (2012) “Properties and durability of concrete containing polymeric wastes(tire rubber and polyethylene terephthalate bottles):An overview”, *Construction and Building Materials*, 30: 714–724

Ghrici, M., Kenai, S., and Said-Mansour, M. (2007) “Mechanical properties and durability of mortar and concrete containing natural pozzolana and limestone blended cements”, *Cement and Concrete Composites*, 29(7): 542–549

Bhanja, S. and Sengupta, B. (2002) “Investigations on the compressive strength of silica fume concrete using statistical methods”, *Cement and Concrete Research*, 32(9): 1391–1394

Li, G.Y. and Zhao, X.H. (2003) “Properties of concrete incorporating fly ash and ground granulated blast-furnace slag”, *Cement and Concrete Composites*, 25(3): 293–299

Ghrici, M., Kenai, S. and Meziane, E. (2006) “Mechanical and durability properties of cement mortar with Algerian natural pozzolana”, *Journal of Materials Science*, 41(21): 6965–6972

Erdem, T. K. and Kirca, O. (2008) “Use of binary and ternary blends in high strength concrete”, *Construction and Building Materials*, 22(7): 1477–1483

Zhang, M.h. et al. (2022) “Utilization of desert sand in the production of sustainable cement-based materials: A critical review”, *Construction and Building Materials*, 327: 001-018

Al-Harthy, A. S. et al. (2007) “The properties of concrete made with fine dune sand”, *Construction and Building Materials*, 21(8): 1803–1808.

Lawrence, P., Cyr, M. and Ringot, E. (2003) “Mineral admixtures in mortars - Effect of inert materials on short-term hydration”, *Cement and Concrete Research*, 33(12):1939-1947

Guettala, S. and Mezghiche, B. (2011) “Compressive strength and hydration with age of cement pastes containing dune sand powder”, Construction and Building Materials, 25(3):1263-1269

Suraneni, P. and Weiss, J. (2017) “Examining the pozzolanicity of supplementary cementitious materials using isothermal calorimetry and thermogravimetric analysis”, *Cement and Concrete Composites*, 83:273-278

Pore structure refinement of calcium-sulfate-aluminate--Portland cement mortars by early-age CO_2 curing

Y. Lan[1], Q. Zeng[2*], Z.D. Zhang[3]

[1] *College of Civil Engineering and Architecture, Zhejiang University, Hangzhou, China*

Email: 22112049@zju.edu.cn

[2] *College of Civil Engineering and Architecture, Zhejiang University, Hangzhou, China*

Email: cengq14@zju.edu.cn

[3]*Institute for Building Materials, ETH Zurich, Zurich, Switzerland*

Email: zhidongz@ifb.baug.ethz.ch

ABSTRACT

This work focuses on the pore structure alterations of calcium-sulfate-aluminate--Portland cement (CSA-PC) mortars at early age induced by CO_2 curing. Three CSA:PC ratios of 100:0, 75:25, and 50:50 were adopted to fabricate mortars with a constant water-to-cement (w/c) ratio of 0.45. A CO_2 curing scheme of 0.5 MPa for 24 h was designed to deeply carbonate the CSA-PC hybrid mortars after the primary curing for 1 day. Pore structure of the mortars with and without the CO_2 treatment was characterized by mercury intrusion porosimetry (MIP) and Nitrogen adsorption/desorption (NAD). Pore characteristics, i.e., total porosity, mean pore size, and specific surface area (SSA), were used to quantify the changes of pore structure of the CSA-PC hybrid mortars after CO_2 curing. Pore size distributions (PSD) interpreted by Barrett-Joiner- Halenda (BJH) and Non-local density functional theory (NLDFT) models were specifically chosen to understand how CO_2 curing altered the pore structure of the CSA-PC hybrid mortars measured by NAD tests. Our data testify the significant pore refinements of CSA-PC hybrid mortars treated by CO_2 curing at early age. The finding of this work would deepen the knowledge in mechanism of microstructural benefits of CSA-PC cement mortars cured by CO_2 at an early age.

KEYWORDS: *CSA-PC hybrid, Carbonation, pore structure, Non-local density functional theory*

1. Introduction

Due to the lower sintering temperatures of calcium-sulfate-aluminate (CSA) cement clinkers compared with those of Portland cement (PC) clinkers, CSA cement is regarded as a greener binder for constructions. However, due to the fast hardening, low alkalinity, poor leaching resistance of CSA paste, it is not feasible to simply replace PC by CSA for in the construction industry. The CSA-PC hybrids may be an attractive construction material owing to their balanced engineering properties (Wolf et al (2021)). Nowadays, with the increase of CO_2 emissions, the influence of carbonation on the properties of CSA-PC hybrid materials has received increasing attention. It has been reported that the CO_2 gas could penetrate into the cementitious materials through their connected pores and react with the hydration products to form carbonates (Rostami et al (2012), Zhang et al (2017)). The carbonation reactions induce mineralogical phase alterations and influence the pore structure, which play a critical role in determining the mechanical properties and durability of cement-based materials (Beaudoin et al (1994), Neves et al (2015)). However, the existing researches on carbonation of CSA-PC hybrids are limited to the long-term CO_2 curing or CO_2 curing after 28 days of hydration (Bertola et al (2022), Gastaldi et al (2018), Hargis et al (2017)). Since the engineering performance strongly relates to the pore structures, it is essential to understand the pore structure changes of CSA-PC based materials caused by early age carbonation towards the reliable design and fabrication of sustainable construction materials.

To this end, the pore structure of CSA-PC cement mortars at early age with and without CO_2 curing was comparatively investigated. Pore structure of the mortars was characterized by mercury intrusion porosimetry (MIP) and Nitrogen adsorption/desorption (NAD). Pore size distributions (PSD) and the pore characteristics, i.e., total porosity, mean pore size, and specific surface area (SSA) were used to quantify the changes of pore structure of the CSA-PC hybrid mortars after CO_2 curing.

2. Materials and methods

The binders were PC (PI 42.5) and CSA (52.5). The chemical components of the two cements, as tested by X-ray fluorescence (XRF), were listed in Table 1. Standard sand that meets the Chinese standards GSB 08-1337-2018 was used to produce mortar specimens.

Table 1. Oxides of the PI 42.5 and CSA 52.5 cement types (wt.%).

Oxides	CaO	Al_2O_3	SO_3	SiO_2	Fe_2O_3	MgO	TiO_2	Loss
CSA	35.28	22.91	16.72	14.32	2.67	2.68	0.93	2.65
PC	64.02	4.69	2.09	21.14	3.15	2.57	-	1.36

Three CSA:OPC ratios of 100:0, 75:25 and 50:50 were designed to prepare mortars with constant water-to-cement (w/c) ratio of 0.45 and sand to cement ratio of 2.7. According to the mix proportions of both cement types, the three groups of mortars were named as C100P0, C75P25 and C50P50, respectively. Mortars were cast in cylindrical molds of 15 mm diameter and 40 mm height. After casting, the cylindrical specimens were covered with a plastic film to prevent water evaporation during the first 18 h of hydration. After that, the specimens were demolded and dried at 40 ℃ for 4 h to remove 40% of free water and reach an appropriate CO_2 curing state. Specimens were then placed in a carbonation chamber for early age carbonation curing under high pressure of 0.5 MPa for 24 h. Right after the carbonation treatment, mortars were crushed into small samples with a thickness of 5 mm and dried at 40 ℃ for 48 h. For all three groups, the standard hydrate (non-carbonated) mortars were cast at the same time as the reference. Small samples were collected from the carbonated and non-carbonated specimens and used for pore structure analysis.

Pore structure of the samples (~ 5 g) was acquired by MIP tests in AutoPore IV 9510 instrument (Micromeritics Instruments Corp., USA). Smaller mortar segments (~ 2 g) were used for NAD tests in an ASAP 2020 apparatus. Barrett-Joyner-Halenda (BJH), Brunauer-Emmett-Teller (BET) models and non-local density functional theory (NLDFT) were used to interpret the NAD data. Porosity, mean pore size and SSA were investigated for characterizing the pore structure of CSA-PC mortars after carbonation.

3. Results and discussions

Fig.1 showed the PSD spectra of the carbonated and non-carbonated samples analyzed by three different approaches. Fig.1(a-b) displays the PSD curves obtained by MIP with pore sizes ranging from 3 nm to 360 μm. Among the non-carbonated mortars (Fig.1(a)), the PSD curves of C100P0 and C75P25 showed a similar trend, with the peak pore size at 226 nm and 350 nm, respectively. A distinct peak at pore size around 5 nm was found for C100P0. The PSD of C50P50 mortar, however, was extremely different from the other two groups showing an almost unimodal distribution with the peak pore size centered at 95 nm. The volume of the pores in the range of 50-200 nm accounted for 46.9% of the total pore volume of C50P50. After carbonation (Fig.1(b)), the peak pore size gathered at 62 nm for C100P0, 12 nm for C75P25 and 95-150 nm for C50P50. The peak pore size for the carbonated mortars decreased significantly. The volume of the pores in the range 50-200 nm only occupied 31.5%, and the PSD peak intensity was greatly depressed for C50P50.

Fig.1(c-d) display the NLDFT PSD spectra of the mortars with the pore size in the range of 2-150 nm. The differential NLDFT PSD curves showed the minimum intensities around 23 nm that clearly separated pores into thin pores (2-23 nm) and coarse pores (23-150 nm). For thin pores, it demonstrated similar pore volume and distribution intensity for the non-carbonated mortars (Fig.1(c)), while for the carbonated mortars the amount of thin pores increased significantly and the peak pore size centered at around 9 nm (Fig.1(d)). For coarse pores, the main pore size in all non-carbonated and carbonated mortars gathered at 34 nm, but the carbonated mortars showed a lower peak intensity. The reduction of the coarse pores and the increase of the thin pores indicated the transformation of pores from large to small sizes. Among the three groups, the C50P50 mortar always showed the largest pore volume.

Fig.1(e-f) presents the differential PSDs of CSA-PC mortars probed by BJH model. The desorption stage is more likely to be in liquid-vapor thermodynamic equilibrium during condensation (Thommes et al (2015)), so the desorption branches of BJH result were adopted to estimate the pore characteristic. For the non-carbonated mortars (Fig.1(e)), two peaks appeared at 3.5 nm and 29.5 nm in each PSD curve.

C100P0 mortar showed the highest distribution intensity and pore volume rising rate at around 3.5 nm, followed by C75P25 and then C50P50. C50P50 mortar had the highest distribution intensity and pore volume rising rate at a pore size of 29.5 nm, followed C100P0 and then C75P25. For the carbonated mortars (Fig.1(f)), two peaks were observed at 3.5 nm and 12.6 nm. The distribution intensity at 3.5 nm increased significantly for all mortars after carbonation, and C100P0 mortar still showed the highest peak intensity. The PSD curves of the three mortars had the same distribution intensity at a peak pore size around 12.6 nm.

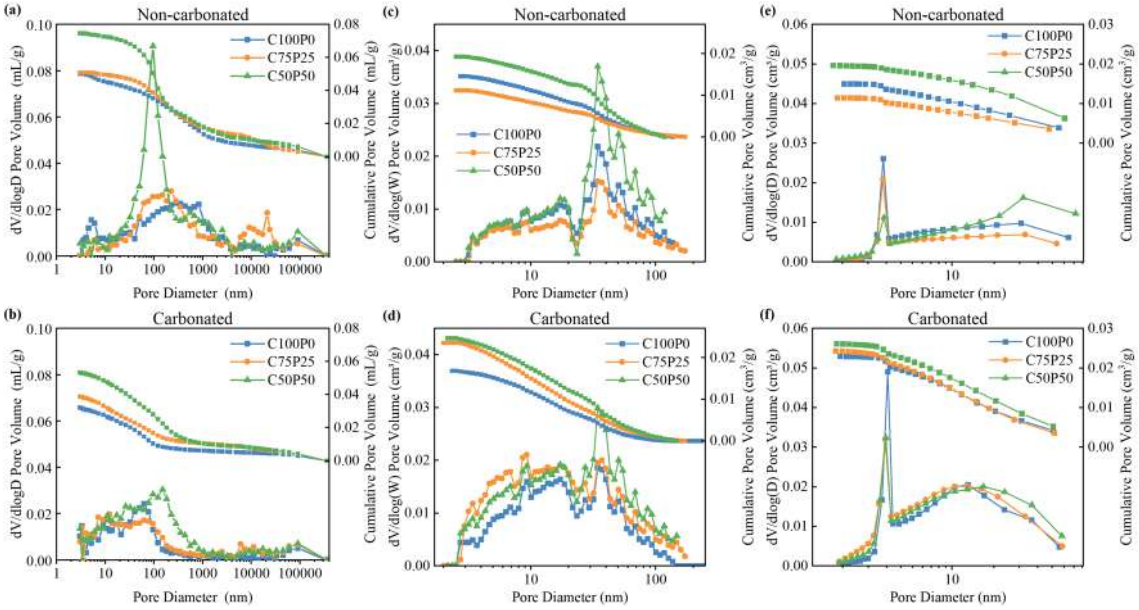


Fig.1 PSD spectrum of non-carbonated/carbonated mortars obtained from MIP and NAD tests.

The total porosities for the carbonated and non-carbonated mortars were depicted in Fig.2(a). On one hand, the porosity of the non-carbonated C100P0 and C75P25 mortars were very close (11.4% and 11.5%, respectively), which was consistent with their PSD curves. The C50P50 mortar, however, showed the highest porosity (16.3%) among the non-carbonated mortars with a large fraction of the pores in size of 50-200 nm. On the other hand, the porosity of the carbonated C100P0, C75P25 and C50P50 mortars decreased to 7.6%, 9.0% and 12.0 %, respectively. The total porosity dropped by 33.3% for C100P0, 21.7% for C75P25 and 26.4% for C50P50. This indicated that carbonation curing resulted in the reduction of the total pore volume for all tested CSA-PC mortars. Fig.2(b) demonstrates a comparison of mean pore size in each group. The non-carbonated C75P25 mortar had the largest mean pore size of 89.1 nm possibly owing to the appearance of the peak around 21 μm (Fig.1(a)), followed by non-carbonated C50P50 with a mean pore size of 69.2 nm, and finally the non-carbonated C100P0 with the smallest mean pore size of 40.9 nm. After CO_2 curing, the mean pore size dropped to 20.6 nm for C100P0, 21.9 nm for C75P25, 30.0 nm for C50P50. C75P25 mortar showed the most significant mean pore size densification by roughly 75.4%. Fig.2(c) presents SSA of the mortars calculated from the NAD tests using BET model. Overall, there were small differences in the BET surface area of mortars with different CSA/PC ratios. The difference in BET surface area was mainly caused by carbonation. Early age carbonation curing increased the BET surface area from 3.2 m^2/g to 7.0 m^2/g (2.2 times) for C100P0, from 2.6 m^2/g to 7.2 m^2/g (2.8 times) for C75P25 and from 3.8 m^2/g to 7.3 m^2/g (1.9 times) for C50P50. The gain in BET surface area after carbonation is mainly attributed to the refinement of the pore structure. Generally, the higher fraction of small pores contributes to the larger SSA. The alteration of pore parameters here are in line with the PSD changes (Fig.1(a-f)).

The same conclusions were found elsewhere (Morandeau et al (2014)). The paper revealed the carbonation mechanism of cement material in term of microstructure. When hydration products like calcium hydroxide (CH) and calcium silicate hydration (CSH) are submitted to CO_2, the carbonation reactions occur to form calcium carbonate ($C\bar{C}$). Owing to the larger molar volume of the $C\bar{C}$ than CH and CSH, the precipitation of $C\bar{C}$ finally leads to the porosity reduction and pore structure change in carbonated cement.

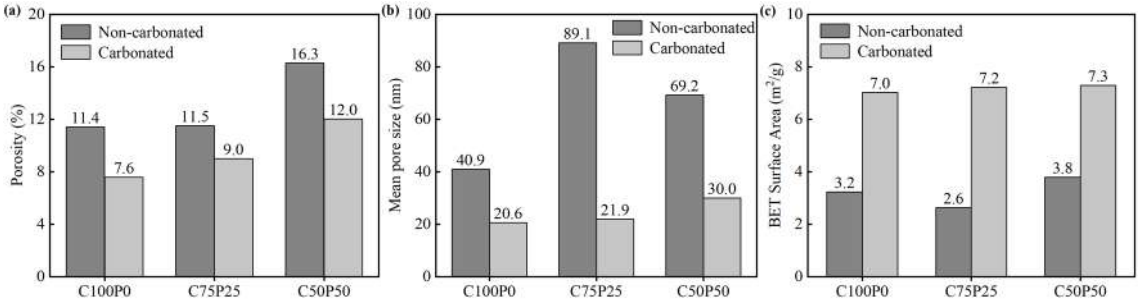


Fig.2 Comparisons of pore characteristics between carbonated and non-carbonated mortars.

4. Conclusions

The analysis of PSD spectrum obtained from MIP and NAD tests consistently showed that pore structure refinement occurred in carbonated CSA-PC cement mortars. The main characteristic pores size of the carbonated mortars dropped significantly compared with those of the non-carbonated mortars. Besides, the total porosity of the hybrid CSA-PC mortars decreased after carbonation, with the rate of 21.7%~33.3%. The mean pore size decreased by 49.6%~ 75.4% and the BET surface area increased by 1.9-2.8 times after CO_2 curing.

Acknowledgements

The authors acknowledge the financial support from Zhejiang University Global Partnership Fund.

References:

Beaudoin,J.J., Feldman,R.F. andTumidajski,P.J. (1994) "Pore structure of hardened portland cement pastes and its influence on properties", *Advanced Cement Based Materials*, 5: 224-236

Bertola,F., Gastaldi,D.,Irico,S., Paul, G. and Canonico, F. (2022)"Influence of the amount of calcium sulfate on physical/mineralogical properties and carbonation resistance of CSA-based cements", *Cement and Concrete Research*, 151: 106634

Gastaldi,D.,Bertola,F.,Canonico,F., Buzzi, L., Mutke, S., Irico, S., Paul, G., Marchese, L., and Boccaleri.(2018) "A chemical/mineralogical investigation of the behavior of sulfoaluminate binders submitted to accelerated carbonation", *Cement and Concrete Research*, 109: 30–41

Hargis,C.W.,Lothenbach,B., Müller,C.J. and Winnefeld, F. (2017)"Carbonation of calcium sulfoaluminate mortars", *Cement and Concrete Composites*, 80: 123-134

Morandeau, A., Thiéry, M. and Dangla, P. (2014) "Investigation of the carbonation mechanism of CH and C-S-H in terms ofkinetics, microstructure changes and moisture properties", *Cement and Concrete Research*,56: 153–170

Neves, A., Toledo, R.D., Fairbairn, E.D.R, and Dweck, J. (2015)"The effects of the early carbonation curing on the mechanical and porosity properties of high initial strength Portland cement pastes", *Construction and Building Materials*, 77: 448–454

Rostami, V., Shao, Y., Boyd, A.J. and He, Z. (2012)"Microstructure of cement paste subject to early carbonation curing", *Cement and Concrete Research*, 42(1): 186-193

Thommes, M., Kaneko, K., Neimark, A.V., Olivier, J.P., Rodriguez-Reinoso, F., Rouquerol, J. and Sing, K.S.W. (2015) "Physisorption of gases, with special reference to the evaluation of surface area and pore size distribution", *Pure and Applied Chemistry*, 87(9–10):1051–1069

Wolf,J.J., Jansen, D., Goetz-Neunhoeffer, F. and Neubauer, J. (2021)"Relating phase transitions to pore size distributions and mechanical mortar properties in CSA-OPC-C$ based systems – The potential impact of delayed straetlingite formation", *Cement and Concrete Research*, 147: 106496

Zhang, D.,Ghouleh, Z. and Shao, Y.X. (2017)"Review on carbonation curing of cement-based materials", *Journal of CO_2 Utilization*, 21: 119–131

Simulation of sulfate attack on carbonated Portland cement-blast furnace slag binary cement

N.S. Melaku[1*], and S. Park[2]

[1] *Pukyong National University, Busan, South Korea*
Email: naspknu@pukyong.ac.kr
[2] *Pukyong National University, Busan, South Korea*
Email: solmoi.park@pknu.ac.kr

ABSTRACT

Carbonation of cement paste results in numerous physiochemical changes that have a detrimental impact on the concrete structure, such as pH reduction which causes corrosion of reinforcement bars. Sulfate attack on cement paste results in the formation of phases that leads to development of expansive cracks. Both of these are natural occurrences that can cause a premature failure of a concrete structure. This study aims to describe and compare the effects of exposure of a carbonated Portland cement-blast furnace slag blend to various sulfate solutions. Thermodynamic modeling was used as a predictive method to determine the resulting phase assemblage of the binary blend system. The binary mix was exposed to Na_2SO_4 or $MgSO_4$ solutions. Various discrete levels of carbonation were simulated with sulfate solution up to 10^4 ml / 100g of binder. As the extent of carbonation increased, the hydration products destabilized and formed amorphous aluminosilicate, calcite and gypsum prior to the additions of sulfate solutions. On the other hand, exposure to different levels of sodium solutions resulted in the precipitation of various phases depending on the extent of carbonation. The pH level was observed to reduce as C-S-H starts to destabilize either due to carbonation or exposure to a higher level of sodium solutions.

KEYWORDS: *Portland cement, Blast furnace slag, Sulfate attack,* and C*arbonation*

1. Introduction

Concrete structures are often exposed to environmental conditions that can cause durability issues, with sulfate attack being a prime example. The sulfate ions react with C_3A and portlandite from the Portland cement to form ettringite and gypsum, leading to the expansion and degradation of the concrete. The type of cement used, the type of sulfate involved, the concentration of sulfate, and the quality of the concrete are some of the major factors that can influence the impact of sulfate attack. Additionally, studies have shown that a lower water-to-cement ratio reduces porosity and limits the transportation of sulfate ions in the concrete, thereby improving the sulfate resistance of concrete structures, (Omar (2002)).

To improve the sulfate resistance of cement and cementitious materials, researchers have explored the use of supplementary cementitious materials such as fly ash, silica fume, and blast furnace slag. These materials contribute to the development of resistance by reducing the expansion of cement in sulfate attack. However, the effectiveness of blast furnace slag depends on its Al_2O_3 content, with higher content resulting in reduced resistance to expansion (Higgins (2003)).

Another environmental condition that causes durability issues is the exposure of concrete structures to CO_2. When cement structures are exposed to CO_2, the hydrated phases carbonate leading to shrinkage, cracking, and corrosion of reinforcement bars in the concrete (Reddy, Melaku and Park (2022)). Sulfate attack and carbonation are common durability issues. However, there have been only a limited number of studies that have investigated the combined effect of sulfate attack and carbonation of cement and cementitious materials. As such, further investigations are required to better understand their impact. This research aims to explain the

microstructural phase changes that occur when a carbonated PC-slag blend is exposed to $MgSO_4$ and Na_2SO_4 solutions.

2. Methods

Thermodynamic analysis was conducted using Gibbs free energy minimization software GEM-Selektor v.3.7. CEMDATA 18 database was selected, with an extended Debye-Hueckel equation for the aqueous electrolyte model. KOH was chosen as the background electrolyte, with common ion size and short-range interaction parameters of 3.67 Å and 0.123 kg/mol, respectively.
The compositions of ASTM Type I cement and BFS used in the simulation are listed in Table 1. BFS was introduced as a 10% replacement with a water-to-cement ratio of 0.6. A hydration period of one year was assumed and Parrot and Killoh's hydration model was used to determine the degree of reactivity of PC for such a date. For slag, the degree of reactivity was obtained from separate thermodynamic modeling (Degefa, Yang and Park (2023)). To simulate carbonation, CO_2 was added at discrete levels of 0, 1, 5, 10, 20 and 30g per 100g binder. Sulfate solutions of $MgSO_4$ and Na_2SO_4 were used in the simulation keeping the concentration of the sulfates as 10%. The sulfate solution was increased from 0 to 10,000 g per 100g of binder to simulate extreme conditions.

Table 1: Compositions of PC and BFS

PC	C_3S	C_2S	C_3A	C_4AF	$CaSO_4$	Other phases				
	55	19	10	7	4.2	4.8				
BFS	CaO	SiO_2	Al_2O_3	SO_3	MgO	K_2O	Fe_2O_3	Na_2O	TiO_2	LOI*
	47.49	30.59	13.19	3.15	3.01	0.54	0.51	0.1	0.69	0.66

3. Results and discussions

Prior to sulfate attacks and the addition of CO_2, the hydration products of Portland cement are C-S-H, portlandite, monosulfate and hydrogarnet. when Portland cement comes in contact with $MgSO_4$, the hydrated phases become destabilized and lead to the precipitation of new phases. As shown in **Figure *1***, in the presence of extra sulfate provided by $MgSO_4$, monosulfate is converted into ettringite and hydrotalcite, while portlandite produces brucite and gypsum. Ettringite possesses a higher density, making it beneficial for reducing the porosity of concrete (Schmidt, Lothenbach, Romer, Neuenschwander, Scrivener (2009)). However, its expansion can also bring negative effects. Similarly, gypsum has an expansive behavior that can result in concrete deterioration. As the amount of ettringite and gypsum increases, the concrete expands to a point where it causes cracking and fracture (Santhanam, Cohen and Olek (2002)). This results in a reduction of the strength of the concrete. Further sulfate attack causes ettringite to destabilize into hydrotalcite and gypsum. Finally, the sulfate attacks C-S-H and replaces the calcium, forming magnesium silicate hydrate (M-S-H) which has no binding property. Its continuous formation leads to a loss of cohesiveness of the concrete, ultimately resulting in a reduction of strength. Upon destabilization of C-S-H, the pH level starts to decline.

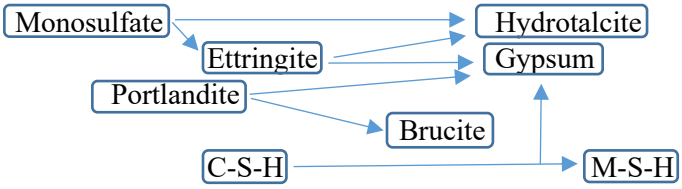


Figure 1: Illustrations of phase changes due to MgSO4 attack on PC

Adding 1g of CO_2 /100g binder causes monosulfate to transform into hemicarbonate and monocarbonate, which later forms ettringite and calcite when $MgSO_4$ is added. The remaining hydrated phases at this stage follow the same pattern as in the case of no carbonation. As the carbonation degree reaches 5 g/100g binder, calcite becomes a carbonation product before the destabilization of monosulfate from $MgSO_4$ reactions. With the addition of $MgSO_4$, calcite forms gypsum and magnesite. Further carbonation reduces the quantity of portlandite while increasing the quantity of calcite. The reduction of portlandite however brings an undesirable effect on the concrete. As portlandite reduces, the pH level also declines resulting in the disappearance of a protective oxide layer around the reinforcement bars in concrete structures. This exposes the reinforcement bars to corrosion (Revert, Weerdt, Hornbostel and Geiker (2018)). Carbonation level of 20 g/100g binder results in the complete carbonation of portlandite and thus the absence of brucite from the final list of phases due to $MgSO_4$ attack. Portlandite acts as a buffering agent preventing the carbonation of C-S-H. when portlandite vanishes, CO_2 starts to react with C-S-H and form calcite. After carbonation level of 20 g/ 100g, the quantity of C-S-H reduces even before the addition of $MgSO_4$ resulting in a lesser sulfate requirement for its destabilization. As a result, the joint occurrence of carbonation and sulfate attack can be considered to have the worst impact than the impact of individual conditions. As the carbonation level reaches 30 g/100g binder, amorphous aluminosilicate becomes a carbonation product while monocarbonate completely carbonates. Carbonation also affects the pH level as it reduces the quantity of C-S-H. The higher the carbonation level, the lower pH gets.

In PC-slag blended cement, C-A-S-H, portlandite, monosulfate, ettringite and hydrogarnet are the hydration products. The addition of slag results in the formation of C-A-S-H instead of C-S-H due to the higher availability of aluminum and silica, which create favorable conditions for the formation of C-A-S-H. However, the quantity of C-A-S-H that formed is less than C-S-H from PC due to the reduction of PC clinkers when slag is added. A lesser quantity of C-A-S-H implies lower resistance to carbonation and sulfate attacks. Ettringite forms as a hydration product in 10% slag replacement which increases in quantity with the addition of sulfate. The sulfate attack from $MgSO_4$ tends to lead to the same phases at 10 % replacement as it did in 0 % replacement but with a lesser requirement of sulfates to cause destabilization.

The sulfate attack from Na_2SO_4 results in the formation of gypsum, ettringite, hydrogarnet and C-S-H as final products (**Figure *2***). The quantity of gypsum formed here is much less than the one observed in $MgSO_4$ attacks and ettringite and C-S-H are more stable in these conditions. Portlandite also requires more quantities of sulfate solution to destabilize from Na_2SO_4 attack. This results in the requirement of even higher quantities of sulfate to destabilize C-S-H. Additionally, the total volume of the mixture after Na_2SO_4 attack is about one-third of the volume in $MgSO_4$ attack. Lesser volume implies that the expansion from the Na_2SO_4 attack is not as big as it is in $MgSO_4$ attack which leads to fewer cracks and less exposure of reinforcement bars. The reduction of pH is also much less in Na_2SO_4 attack, contributing to better resistance against corrosion of reinforcement bars. Overall Portland cement has better resistance capabilities against $NaSO_4$ attack than $MgSO_4$ attack.

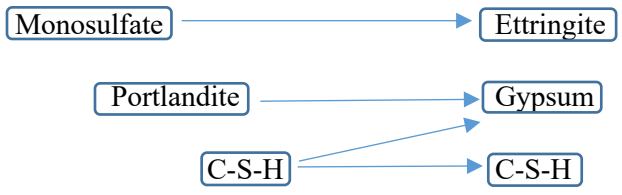


Figure 2: Illustrations of phase changes due to Na_2SO_4 attack on PC

Carbonation amplifies the effect of sulfate attacks. As the level of carbonation increases, the hydration phases start to destabilize even before the addition of sulfate. The quantity of C-S-H and portlandite reduces, leading to lower resistance capacity against sulfate attacks. At higher carbonation levels (20 g/100g binder), gypsum no longer forms from Na_2SO_4 attack due to the complete carbonation of portlandite. Further carbonation and addition of sulfate result in the reduction of ettringite and C-S-H quantities. The use of slag at zero or lower carbonation levels has little impact on the results of Na_2SO_4 attack. However, the 10 % slag replacement results

in a reduction of the resistance abilities of cement when exposed to carbonation and Na_2SO_4 attack. At higher carbonation levels, gypsum becomes more stable in lower sulfate attack levels, while ettringite forms from gypsum and C-A-S-H at higher sulfate attack levels before transforming back to gypsum.

4. Conclusion

The thermodynamic modeling results for a PC-slag blended cement exposed to carbonation and sulfate attacks after one-year hydration is summarized as follows.

1. C-S-H, portlandite, monosulfate and hydrogarnet are hydration products of PC. Addition of slag results in the formation of C-A-S-H instead of C-S-H due to the presence of higher quantities of aluminum and silica in slag.
2. 10 % slag replacement results in the reduction of the resistive capabilities of cement against sulfate attack.
3. Carbonation accelerates the effects of sulfate attack.
4. $MgSO_4$ attack is more severe than Na_2SO_4 attack. It converts C-S-H into a non-binding M-S-H phase resulting in a reduction of strength.

Acknowledgments

This work was supported by the National Research Foundation of Korea (NRF) grant funded by the Korean government (MSIT) (NRF-2021R1A4A3033128 and 2022R1C1C1007498).

References

Omar, S.B.A. (2002) “Attack on plain and blended cements exposed to aggressive sulfate environments”, Cement & Concrete Compositions, 24: 305-316

Higgins, D.D. (2003) “Increased sulfate resistance of ggbs concrete in the presence of carbonate”, Cement & Concrete Compositions, 25: 913-919

Reddy, K.C., Melaku, N.S. and Park, S. (2022) “Thermodynamic Modeling Study of Carbonation of Portland Cement”, materials, 15(14), 5060

Degefa, A.B., Yang, B., Park, S. (2023) “Predicting the degree of reaction of supplementary cementitious materials in hydrated Portland cement”, Submitted.

Schmidt, T., Lothenbach, B., Romer, M., Neuenschwander, J. and Scrivner, K. (2009) “Physical and microstructural aspects of sulfate attack on ordinary and limestone blended Portland cements”, cement and concrete Research, 39: 1111-1121

Santhanam, M., Cohen, M.D. and Olek, J. (2002) “Mechanisim of sulfate attack: A fresh look – Part 1; Summary of experimental results”, Cement and Concrete Research, 32: 915-921

Revert, A.B., Weerdt, D.K., Hornbostel, K. and Geiker, M.R. (2018) “Carbonation-induced corrosion: Investigation of the corrosion”, Construction and Building Materials, 162: 847-856

The 16th International Congress on the Chemistry of Cement 2023 (ICCC2023)
"Further Reduction of CO_2 -Emissions and Circularity in the Cement and Concrete Industry"
September 18–22, 2023, Bangkok, Thailand

A Study on Hydration Properties of Cement Matrix according to Limestone Content for Portland Cement

In.Gyu. Kang[1], Sang.Chul. Shin[2], and Jin.Man. Kim[3*]

[1] *Kongju National University, Cheonan, Republic of Korea*

Email: kik4098@naver.com
[2] *Eco Friendly Concrete Research Center, Cheonan, Republic of Korea*

Email: hiykhj@kongju.ac.kr
[3] *Kongju National University, Cheonan, Republic of Korea*

Email: jmkim@kongju.ac.kr

ABSTRACT

This study investigated the hydration properties of cement matrix while changing the admixture content for Portland cement as prescribed in the Korean cement standards (KS L 5201). Currently, cement additive is allowed up to 10% in South Korea, and specifically, it is stipulated that blast furnace slag, fly ash, or pozzolan can be used up to 5%, and limestone up to 5%. This study focused on the change in the content of limestone, and the cement was manufactured in the laboratory using clinker, gypsum, ground granulated blast furnace slag (GGBFS), and limestone commercially used by Korean cement manufacturers. The results of the study showed that, when the content of limestone increased, various advantages (e.g., securing fluidity, shortening setting time, promoting initial hydration, acquiring equal compressive strength, and reducing shrinkage) could be obtained due to various mechanisms (i.e., filler, nucleation, and chemical effect).

KEYWORDS: *Portland Cement, Limestone, Carbon Neutrality, Additive, Action Mechanism*

1. Introduction

Portland cement is one of the most widely used building materials worldwide and accounts for approximately 6 to 8% of global CO_2 emissions due to a large amount of cement production each year(Boden, et al. 2017). In cement manufacturing, most CO_2 emission occurs in the process of decarbonization limestone to produce clinker. Therefore, reducing the production and usage of clinker and increasing the use of supplementary cementitious materials (SCMs) to replace clinker are most effective in reducing CO_2 emissions in the cement industry. The International Energy Agency (IEA) also reported that this strategy would play a prominent role in reducing CO_2 in the cement industry. Various inorganic materials (e.g., ground granulated blast furnace slag, fly ash, pozzolanic materials, and limestone) have been used SCMs in many countries in recent years, and related standards have also been established. Among them, if limestone is used as a raw material for manufacturing clinker, it emits a large amount of CO_2. However, when it is used as an SCM, it reduces final CO_2 emission because it does not undergo a decarbonization process during the calcinating process. Although limestone does not have hydration properties, it promotes the initial hydration reaction of clinker by filling the pores between the cement particles and acting as a nucleation seed for the precipitation of hydration products. Moreover, it reduces the voids in the cement matrix by increasing the volume of hydration products through the formation of carbo-aluminate phases(Senhadji, et al. 2014). Even though using SCMs instead of clinker reduces activity by decreasing the amount of reactive particles in cement, limestone has a positive impact on solving the dilution effect due to the decrease in the clinker-to-cement ratio by participating in the hydration of cement, as well as serving as a filler.

It was a fundamental study to investigate the hydration properties of cement with a low clinker-to-cement ratio by using a additive that can replace clinker while the international community aimed for carbon neutrality. The main objective of this study was to examine the hydration properties of carbon-neutral Portland cement, which had higher limestone content than the cement additive ratio established in Korean Industrial Standards.

2. Materials and methods

2.1 Mix proportion and experimental methods

Table 1 shows the mixing ratio according to the limestone content set in this study. Paste and mortar were mixed at a water-to-binder ratio (w/b) of 0.5 according to KS L ISO 679. The mortar used consists of 1 part binder and 3 parts of sand proportioned by mass. The Plain mixing ratio refers to Ordinary Portland Cement (KS L 5201), and the limestone content increases by 2.5% from the plain mixing ratio from L7.5 to L15.

Table 1. Mix proportion of cement

Mixture ID	w/c	b:s	Content (wt %)			
			Clinker	Gypsum	Limestone	GGBFS
Plain	0.5	1:3	85.5	4.5	5	5
L7.5			83.125	4.375	7.5	5
L10			80.75	4.25	10	5
L12.5			78.375	4.125	12.5	5
L15			76	4	15	5

2.2 Raw materials

This study used clinker, gypsum, GGBFS, and limestone as raw materials to manufacture lab-scale cement, and the materials used were provided by cement and steel companies. The lab-scale ball mill was used for mixed intergrinding, and the chemical composition of the raw materials and manufactured cement was measured by X-ray fluoresce (Table 2). Table 3 shows the results of particle size analysis (measured by laser diffraction), specific surface (measured by air permeability apparatus), and density measurement. It was found that the fineness of the mixed and ground final cement increased as the limestone content was higher because limestone has a higher grinding efficiency.

Table 2. Chemical composition of raw materials and manufactured cement

Sample	Content (wt %)							
	CaO	SiO_2	Al_2O_3	MgO	Fe_2O_3	K_2O	SO_3	LOI
Clinker	64.2	17.1	4.0	2.5	3.4	1.3	3.5	2.1
Gypsum	32.4	1.7	0.7	0.3	0.8	0.1	37.6	24.4
GGBFS	44.2	33.2	13.2	3.3	0.8	0.6	1.8	0.92
Limestone	52.0	0.3	0.1	0.5	0.1	0.02	0.03	47
Plain	62.6	17.5	4.7	2.3	3.1	1.2	3.7	3.4
L7.5	63.1	16.9	4.6	2.1	3.1	1.2	3.5	4.1
L10	62.9	16.3	4.4	2.1	2.9	1.0	3.4	5.5
L12.5	63.1	15.7	4.3	2.0	2.9	1.0	3.4	6.4
L15	63.5	14.9	4.2	1.9	2.9	1.0	3.2	7.3

Table 3. Physical properties

Sample	D [0.1]	D [0.5]	D [0.9]	D [4,3]	SSA [cm^2/g]	Density [g/cm^3]
Plain	2.060	9.876	34.665	14.671	3,693	3.15
L7.5	1.987	9.233	21.756	13.516	3,825	3.14
L10	2.205	9.627	33.166	14.108	3,823	3.15
L12.5	1.935	8.707	31.321	13.149	3,940	3.14
L15	1.818	8.597	32.005	13.278	4,001	3.14

2.3 Test methods

Flow, setting time, and compressive strength were tested according to Korea Industrial Standards. To measure the compressive strength, the samples were cured in water and measured on days 1, 3, 7, and 28. Drying shrinkage was measured at 24-hour intervals according to ASTM C596. The heat of hydration was measured using a TAM Air isothermal calorimeter at 21℃, and XRD analysis was conducted at a scanning speed of 2°/ min and a scanning range from 5° to 80° (2θ).

3 Results and Discussion

3.1 Heat of hydration

Figure 1 shows heat flow curves and total heat release curves according to various limestone contents. The increase in limestone content accelerated the main peak of C_3S(Briki, et al. 2021), while the main hydration peaks of L7.5, L10, and L12.5, except for L15, were lower than the main hydration peak of Plain. Meanwhile, clear C_3A peaks could be identified in all samples after C_3S peaks. The 48-hour total heat release curves of L7.5, L10, L12.5, and L15 were lower than that of Plain due to the dilution effect (decreased reactive particles) in the cement matrix because clinker was replaced with limestone.

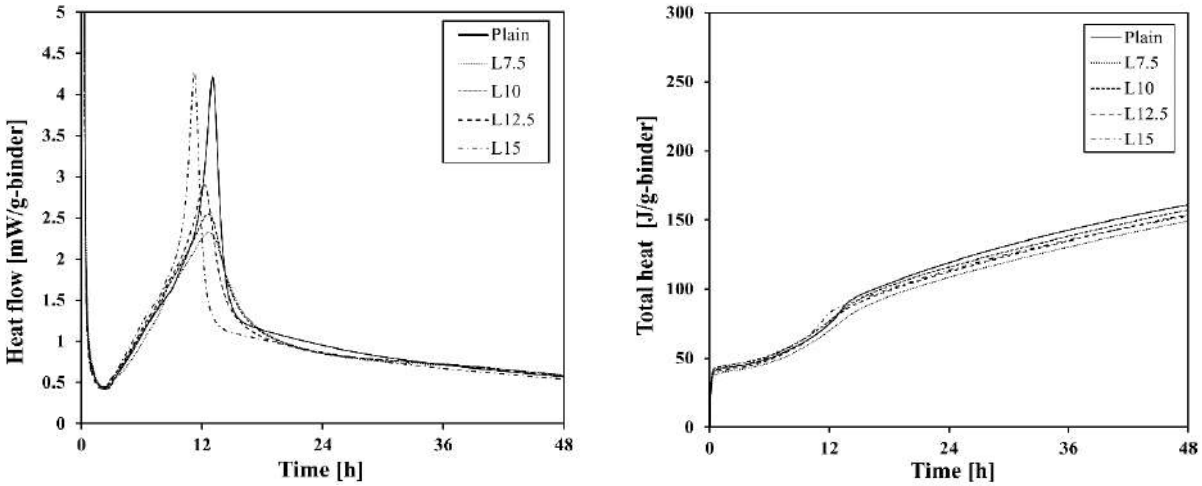


Figure 1. Heat flow (left) and total heat release (right) curves

3.2 Physical properties of cement mortar

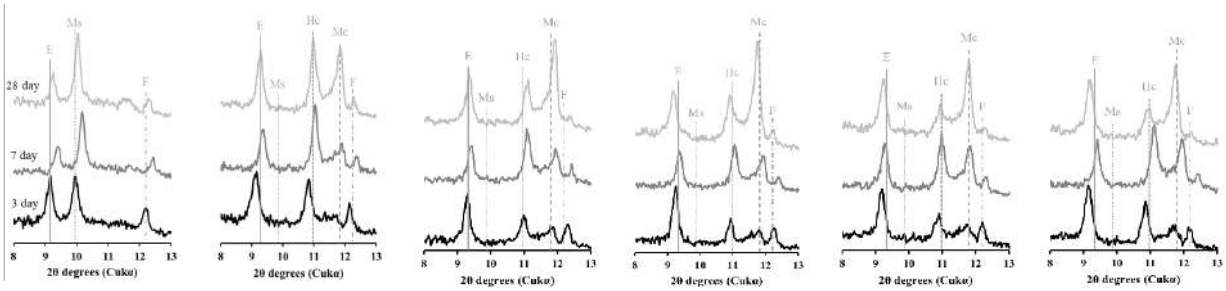
Table 4 shows the physical properties of cement mortar depending on limestone content. The effects of increased limestone content on flow decreased by approximately 10mm compared to Plain. However, it was found that there was no distinctive effect on workability, and similar fluidity was observed in all mixtures. It was also found that setting time shortened with an increase in limestone content. It was believed that the setting time was reduced because of the accelerated hydration response of initial C_3S due to an increase in limestone content. Limestone is known to promote the initial hydration of C_3S among clinker phases owing to the filler effect and nucleation effect at an early age. However, compressive strength measurements revealed that strength decreased compared to Plain on day 1 as the limestone content increased. After that, until day 28, the strength of L7.5, L10, and L12.5 was similar to that of Plain. Especially, the strength of L7.5 and L10 was higher than that of Plain. It was believed that alumina and limestone in cement reacted to form carbo-aluminate phases and carbo-aluminate phases contributed to the expression of strength. The results of this study revealed that dry shrinkage decreased as the content of limestone increased. Dry shrinkage is affected by the loss of physical adsorption water of C-S-H due to the humidity difference between the cement paste and its environment and the evaporation of water in the capillary voids. Therefore, drying shrinkage could be reduced by the filler effect of limestone and the decrease in cement paste due to the replacement of clinker with limestone.

Table 4. Physical properties of cement mortar

Sample	Flow [mm]	Setting time [h]		Compressive strength [MPa]				Drying shrinkage [%]			
		Initial	Final	1d	3d	7d	28d	7d	14d	21d	28d
Plain	180	9.1	12.2	6.2	20.8	30.4	42.5	0.032	0.06	0.072	0.078
L7.5	169	8.9	11.8	4.6	22.3	31.2	42.9	0.032	0.058	0.071	0.077
L10	171	8.4	11.9	4.2	19.4	29.2	43.3	0.031	0.058	0.071	0.077
L12.5	171	8.3	11.5	4.0	19.4	27.7	41.3	0.028	0.056	0.068	0.074
L15	170	7.7	10.4	3.9	18.2	24.6	37.7	0.028	0.055	0.066	0.072

3.3 XRD-patterns

Figure 2 shows the XRD measurements of the examined samples by age. Sample (a) is cement prepared using only clinker and gypsum. Sample (a) formed Ettringite (E) and monosulfoaluminate (Ms), and it was confirmed that E was converted to Ms as the age increased by consuming gypsum. On the other hand, hemicarboaluminate (Hc) and monocarboaluminate (Mc) were formed in samples (b) – (f) by the reaction of alumina and limestone due to the addition of limestone(Lothenbach, Et al. 2008). It was confirmed that Hc was formed first at an early age, and it was converted into Mc, which was thermodynamically more stable, due to further dissolution of carbonate as age increased. In addition, the formation of carbo-aluminate phases stabilized E, and, as a result, no clear Ms peak was observed.



(a) clinker+gypsum (b) Plain (c) L7.5 (d) L10 (e) L12.5 (f) L15

Figure 2. XRD patterns for different additions of limestone at 3, 7, 28 days

4. Conclusions

This study presented the experimental results of cement hydration properties after increasing limestone content in the cement additive ratio established in Korean Industrial Standards while the world aims for global carbon neutrality. The experiment results showed that the filler and nucleation effect of limestone accelerated the initial hydration of C_3S and stabilized Ettringite through the formation of carbo-aluminate phases. Particularly, the compressive strength of samples up to 10% limestone content was equivalent to that of Plain after day 3. It was also confirmed that limestone samples showed properties similar to the Plain sample because it positively affected the physical properties of cement by offsetting the possible dilution effects caused by the use of SCMs through diverse various mechanisms. However, since low strength was expressed at an early age, it would be necessary to additionally consider various methods (e.g., increased fineness, alumina content, and C-S-H nucleation seed) to improve initial strength. Consequently, it is believed that cement with higher limestone content can play an important role, as Korea's low-carbon cement, in achieving the carbon neutrality goal of the cement industry because it can reduce CO_2 emission due to low clinker usage compared to the conventional OPC and it shows equivalent results in hydration and mechanical properties.

Acknowledgements

This research was supported by the National Research Foundation of Korea (NRF) grant funded by the Ministry of Education (No. 2020R1A2C2013161).

References

Boden, T.A., Marland, G. and Andres, R. J. (2017) "National CO_2 Emissions from Fossil-fuel Burning, Cement Manufacture, and Gas Flaring", *Carbon Dioxide Information Analysis Center, Oak Ridge National Laboratory, US Department of Energy*, :1751-2014

Senhadji, Y., Escade illas, G., Mouli, M., Khelafi, H. (2014) "Influence of natural pozzolan, silica fume and limestone fine on strength, acid resistance and microstructure of mortar", *Powder technology* , 254: 314-1007

Briki, Y., Zajac, M., Haha, M. B. and Scrivener, K. (2021) "Impact of limestone fineness on cement hydration at early age", *Cement and Concrete Research*, 147: 106515

Lothenbach, B., Saout, G.L., Gallucci, E. and Scrivener, K. (2008) "Influence of limestone on the hydration of Portland cements", *Cement and Concrete Research*, 38(6): 848-860

The 16th International Congress on the Chemistry of Cement 2023 (ICCC2023)
"Further Reduction of CO_2 -Emissions and Circularity in the Cement and Concrete Industry"
September 18–22, 2023, Bangkok, Thailand

Mineralogical analysis of BOF slag with different grinding characteristics

Seohyun Kim[1], and Juhyuk Moon[2,*]

[1] *Department of Civil and Environmental Engineering, Seoul National University, Seoul 08826, Republic of Korea*

Email: ksh0128706@snu.ac.kr

[2] *Department of Civil and Environmental Engineering / Institute of Construction and Environmental Engineering, Seoul National University, Seoul 08826, Republic of Korea*

Email: juhyukmoon@snu.ac.kr

ABSTRACT

Although Basic Oxygen Furnace (BOF) slag contains cementitious mineral components such as C_2S, and brownmillerite (C_2F), it has not been largely utilized in cement or concrete industry due to its low grindability as well as low chemical compatibility with cement-based materials. This study investigates the mineralogical and chemical properties of BOF slag with different grindability of low and high grindability groups. Low grindability group is named as Hard Steel Slag (HSS), and high grindability group is named as Soft Steel Slag (SSS). By applying proper grinding time, similar particle size distributions of both groups could be achieved. Therefore, it can eliminate the physical effect (i.e., from identical particle size) so chemical effect can be fairly compared. The mineralogy of both samples was determined by repeating X-Ray Diffraction (XRD) for 10 times so that it can minimize the non-homogeneity of steel slag. Also, isothermal calorimetry test was used to measure chemical reactivity of both sample groups. The XRD result shows that HSS group contains a larger amount of C_2S, C_2F, RO phase. Amorphous phase and reactive phases such as C_2S, C_2F in HSS group resulted in higher cumulative heat than SSS group from isothermal calorimetry test.

KEYWORDS: *BOF slag, Grindability, X-ray diffraction, Calorimetry*

1. Introduction

Basic Oxygen Furnace (BOF) slag is an industrial by-product with low recycling rate, globally. About 15% by mass of steel making process output is steel slag. The BOF slag is composed of CaO (30–50%), SiO_2 (10–20%), Fe_2O_3 (20–40%), Al_2O_3 (1–7%), MgO (4–10%), MnO (0–4%), P_2O_5 (1–3%) and TiO_2 (0–2%), with a mineral assemblage of C_2S, C_3S, $C_2(A,F)$, RO phase (CaO–FeO–MgO–MnO solid solution, crystallized in wuestite structure), and free lime (CaO). Some steel slag contains kirschsteinite which has low alkalinity. Among them, C_2S and $C_2(A,F)$ have potential to react with water. The utilization of BOF slag in concrete is further limited due to the volume instability problems caused by the presense of free CaO and low hydraulic acitivity.

In this study, we investigated mineralogical and chemical analysis of BOF slag with different grinding efficiency. By the result of XRD analysis, C_2S, C_2F and RO phase are contained more in HSS than SSS due to their strong hardness. Especially C_2S and C_2F are reactive phases in steel slag. Therefore, by the isothermal calorimeter experiment, HSS showed higher cumulative heat release than SSS due to its higher amount of reactive phases.

2. Materials and methods

2.1 Materials

To control the particle size distribution of steel slag, a lab-scale micro ball mill device (McCrone micronizing, McCrone Scientific LTD., Leighton Road London, UK) and desktop ball mill were used. The grinding process is described in Fig. 1. SSS is obtained by grinding raw steel slag with desktop ball mill for 3 hours. HSS is obtained by grinding raw steel slag with desktop ball mill for 3 hours, seived over 1.18mm, and additional grinding with desktop ball mill for 10 hours

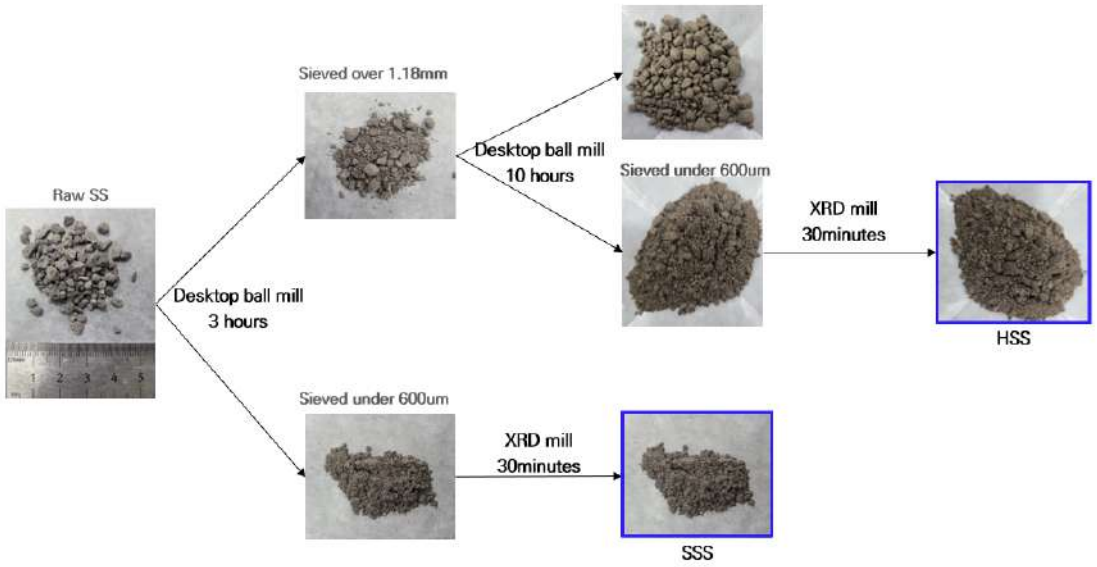


Fig. 1. The grinding process of SSS and HSS

Fig. 2 shows the particle size distribution of SSS and HSS after milling process. The similar particle size distributions were obtained in both groups.

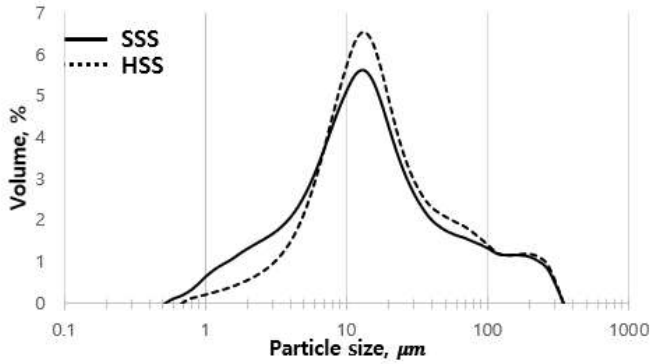


Fig. 2. The particle size distribution of SSS and HSS

Table. 1 shows the chemical composition determined by Energy Dispersive X-Ray Fluorescence (ED-XRF) analysis.

Table. 1. Chemical composition of SSS and HSS

SSS		HSS	
Oxide	**Content (wt%)**	**Oxide**	**Content (wt%)**
CaO	35.59	CaO	37.29
Fe_2O_3	33.82	Fe_2O_3	33.59
SiO_2	14.6	SiO_2	13.4
MgO	5.06	MgO	5.51
MnO	3.7	MnO	3.53
Al_2O_3	3.52	Al_2O_3	3.19
P_2O_5	1.99	P_2O_5	2.09
SO_3	0.33	SO_3	0.16
Cr_2O_3	0.29	Cr_2O_3	0.315
V_2O_5	0.21	V_2O_5	0.23

2.2 Methods

2.2.1 X-ray powder diffraction/Quantitative X-ray Diffraction

The degree of hydration and the phase development were analyzed through X-ray patterns measured from the X-ray diffractometer (D2 Phaser, Bruker Co. Ltd, Land Baden- Württemberg, Germany) equipped with Cu- Kα radiation (λ = 1.5418 Å) in the range of 2θ between 5˚ and 60˚.
For accurate quantitative XRD analysis, SSS and HSS were milled with micro ball mill for 30 minutes. Also, to minimize the non-homogeneity effect of steel slag, XRD measurement was conducted 10 times for each group.

2.2.2 Isothermal calorimetry

The hydration heat evolution and kinetics of SSS and HSS were analyzed through heat evolution measured from calorimeter (TAM Air, TA Instruments, New Castle, DE, USA). Cumulative heat flow was obtained in 40°C for 7 days.

3. Results

3.1 Quantitative X-ray Diffraction

Fig. 3 shows the mineralogical contents of SSS and HSS with 10 wt.% of internal standard(Rutile, TiO_2). HSS contains higher amount of C_2F, C_2S, RO phase, and amorphous phase than SSS. Especially, amorphous phase and reactive phases such as C_2F and C_2S are 5.9%, 2.9% and 4.8% more in HSS than in SSS respectively. Also, kirschsteinite which has low alkalinity is contained more in SSS than HSS. Other mineral contents such and portlandite, free lime, and so on are excluded due to their low amount (under 3 wt.%).

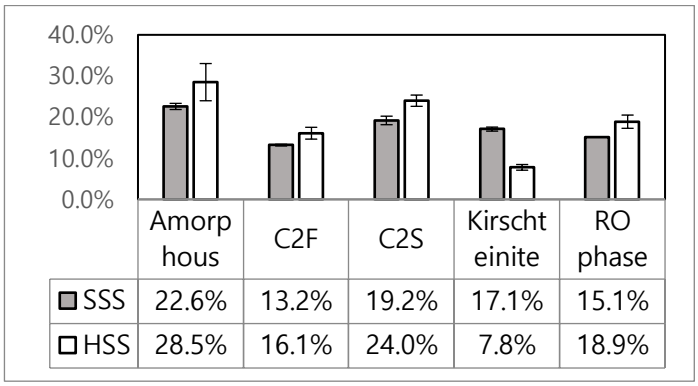


Fig. 3. QXRD results of SSS and HSS

3.2 Isothermal calorimetry

Fig. 4 shows the cumulative heat release of SSS and HSS. The cumulative heat of SSS is about 65 J/g, and that of HSS is about 90 J/g which is 38% higher than that of SSS. The higher cumulative heat of HSS is presumed to be due to higher amount of C_2S and C_2F and lower amount of kirschsteinite.

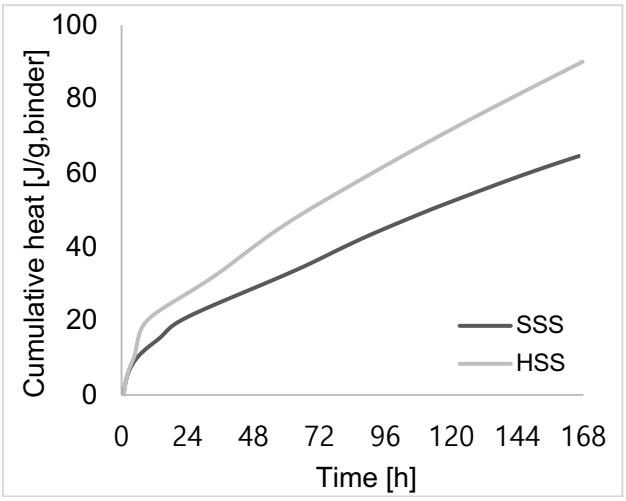


Fig. 4. Cumulative heat release of SSS and HSS

4. Conclusion

In this paper, the mineralogical and chemical analysis of steel slag sorted by different grinding efficiency were investigated. Soft Steel Slag powder is obtained by 3 hour grinding and Hard Steel Slag powder is obtained by 13 hour grinding.

i. According to quantitative X-ray diffraction result, Hard Steel Slag (HSS) contains larger amount of C_2F, C_2S, wuestite than Soft Steel Slag (SSS) and has lower amount of kirschsteinite. The reason is that C_2F, C_2S, and wuestite has strong hardness. Among them, C_2F and C_2S has potential to react with water.

ii. The cumulative heat of SSS for 7 days is 65 J/g and that of HSS is 90 J/g. This data correspond to the QXRD results in which HSS contains a larger amount of reactive phases such as C_2F, C_2S.

iii. Above results show that HSS is more reactive so that it is good to use as cementitious materials.

Acknowledgements

This work was supported by the Industrial Strategic technology development program-Development of manufacturing technology of hardened cement with carbonation curing (RS-2022-00155662, Development of manufacturing and application technology of 1,000 ton/year class hardened cement with carbonation curing) funded By the Ministry of Trade, industry & Energy (MOTIE, Korea).

References

A. van Zomeren, S.R. van der Laan, H.B.A. Kobesen, W.J.J. Huijgen, R.N.J. Comans. (2011), “Changes in mineralogical and leaching properties of converter steel slag resulting from accelerated carbonation at low CO2pressure,” Waste Manag., 31(11), pp. 2236-2244

D. Wang, J. Chang, and W. S. Ansari. (2019), “The effects of carbonation and hydration on the mineralogy and microstructure of basic oxygen furnace slag products,” *J. CO2 Util.*, vol. 34, pp. 87–98

The 16th International Congress on the Chemistry of Cement 2023 (ICCC2023)
"Further Reduction of CO_2 -Emissions and Circularity in the Cement and Concrete Industry"
September 18–22, 2023, Bangkok, Thailand

Cement Hydration Kinetics of LC3 Paste Synthesized with Biologically Architected $CaCO_3$

N.D. Dowdy[*], J. Ren[2], and D.N. Beatty[3], W.V. Srubar III[4]

[1] *University of Colorado Boulder, Boulder, Colorado, USA*
Email: nicolas.dowdy@colorado.edu
[2] *University of Colorado Boulder, Boulder, Colorado, USA*
Email: jie.ren@colorado.edu
[3] *University of Colorado Boulder, Colorado, USA*
Email: danielle.beatty@colorad.edu
[4] *University of Colorado Boulder, Boulder, Colorado, USA*
Email: wrubar@colorado.edu

ABSTRACT

Portland cement (PC) is one of the most used materials in the world, and its production is projected to increase over the next several decades. However, the manufacture of PC results in 7% of the world's CO_2 emissions. Replacing fractions of PC with supplementary cementitious materials (SCMs), such as limestone and calcined clays, can reduce the emissions associated with PC production. This study investigated the use of biologically architected calcium carbonate ($CaCO_3$) in the synthesis of limestone calcined clay cement (LC3). We used $CaCO_3$ produced by two photosynthetic algae, *Lithothamnion corallioides* (*L. corallioides*) and *Emiliania huxleyi* (*E. huxleyi*) that exhibit a small particle size and high specific surface area compared to reagent-grade $CaCO_3$. $CaCO_3$ was combined with Type I/II PC, metakaolin, and polycarboxylate superplasticizer (SP) to ensure workability of all samples. The reaction kinetics during cement hydration of these systems were measured using isothermal conductive calorimetry (ICC). ICC data show biologically architected $CaCO_3$ induce higher peak heat and higher cumulative heat compared to the control PC and LC3 pastes, likely due to the smaller particle sizes, high specific surface areas, and composition of the biologically architected $CaCO_3$ compared to reagent-grade $CaCO_3$. Future research on the microstructure and mechanical properties of LC3 pastes is needed to develop a more comprehensive understanding of the effects that biologically architected $CaCO_3$ may have on the structure and properties of LC3.

KEYWORDS: *LC3, isothermal calorimetry, calcium carbonate, L. corallioides, E. huxleyi*

1. Introduction

Cement and concrete production accounts for approximately 8%-9% of global greenhouse gas (GHG) emissions (Miller et al. (2016)). This problem is unlikely to be solved from the demand side due to the projected increase in building design and construction over the next few decades (OECD, 2019). The use of supplementary cementitious materials (SCMs) has emerged as a best-practice strategy for reducing GHG emissions of cement and concrete production in the near term. A wide variety of SCMs have been investigated. The most common SCMs include industrial byproducts, such as fly ash and slag. Other SCMs include quarried minerals, such as limestone and clays (de Brito & Kurda (2021)).

Limestone calcined clay cement (LC3) is a high-volume SCM cement produced by replacing portland cement (PC) with limestone and calcined clay. These cementitious systems are produced using 55% PC, 15% limestone, and 30% calcined clay (Scrivener et al. (2018)). Replacing 45% of PC in a cement paste significantly reduces the GHG emissions required to produce LC3 (Zhu et al. (2020)). Another benefit of using LC3 over PC binders is that the clay purity requirements, which are relatively low, enable

developing regions to produce these cements (Juenger et al. (2019)). Other benefits include strength and durability enhancements due to increased C-S-H gel formation *via* the pozzolanic reaction and lower porosity of LC3 systems compared to PC (Antoni et al. (2012), Mansour & Al Biajawi (2022)).

Limestone fillers can enhance the properties of cement by acting as nucleation seeds, owing to the small particle size and calcium-rich chemistry of limestone (*i.e.*, $CaCO_3$). To understand how $CaCO_3$ surface area affects LC3 hydration, this study investigated the use of biologically architected $CaCO_3$ in the synthesis of limestone calcined clay cement (LC3). We used $CaCO_3$ produced by two photosynthetic algae, *Lithothamnion corallioides* (*L. corallioides*) and *Emiliania huxleyi* (*E. huxleyi*) that exhibit a smaller particle size and higher specific surface area as compared to conventional ground limestone. The smaller particle size, larger surface area, and variable composition of the biogenic $CaCO_3$ sources have the potential to increase heat flow and cumulative heat development of hydrating LC3 pastes. The results of this work contribute new knowledge regarding potential nucleation effects that can be induced in LC3.

2. Materials & Methods

2.1 Materials

ASTM C150 Type I/II PC was supplied by Quikrete. Reagent-grade (RG) $CaCO_3$ (>99%) was obtained from Sigma Aldrich. Lithothamnion Powder (*L. corallioides*) was purchased from Aquamin (Ireland). Lyophilized *E. huxleyi* biomass ($CaCO_3$ and organic cell matter) was purchased from the Algal Resource Collective (ARC) at the University of North Carolina, Wilmington, USA. The organics were removed from the *E. huxleyi* biomass using a modified procedure (Jakob et al. 2017). MK was obtained from BASF Chemical Corporation (Georgia, USA). PCE superplasticizer (ADVA® Cast 575) was obtained from GCP Applied Technologies (Cambridge, MA, USA). The composition of all raw materials was analyzed using ICP-OES (Table 1). The median particle size of the reagent grade, *L. corallioides*, and *E. huxleyi* $CaCO_3$ were 18.8 ± 0.274 μm, 6.74 ± 0.069 μm, and 1.77 ± 0.170 μm, respectively, as measured by laser diffraction. The specific surface areas of the reagent grade, *L. corallioides*, and *E. huxleyi* $CaCO_3$ were 0.71 m^2/g, 8.26 m^2/g, and 12.22 m^2/g, respectively, as measured by BET analysis.

Table 1. Oxide composition of raw materials from ICP-OES analysis as percentages.

	Al_2O_3	CaO	Fe_2O_3	K_2O	MgO	Na_2O	P_2O_5	SiO_2	TiO_2	Other
PC	4.21	62.7	3.99	0.695	0.877	0.19	0.18	19.0	0.187	7.97
Metakaolin	41.8	0.0476	0.393	0.199	0.028	0.38	0.030	49.6	1.47	6.05
RG $CaCO_3$	<0.01	56.4	<0.007	<0.006	0.02	0.015	<0.01	<0.267	<0.0008	43.6
L. corallioides	0.756	41.7	1.10	0.110	3.8	1.16	0.060	3.4	0.149	47.8
E. huxleyi	0.011	51.9	0.0114	<0.006	0.058	0.11	0.055	<0.267	<0.0008	47.9

2.2 Methods

One PC control paste and three LC3 paste samples were prepared, yielding a total of four mixture formulations. All samples were prepared using a water-to-cementitious ratio (*w/cm* = 0.5). Each LC3 mixture was prepared using the same proportions of PC (55%), MK (15%), and $CaCO_3$ (15%) by mass. The differentiating factor between the four mixes was the type of $CaCO_3$ integrated into the corresponding mix. To prepare the mixtures, first, all dry materials in each sample mixture were combined and hand-mixed for five minutes. Then, the samples were mixed with water for 2 minutes. Lastly, SP was added to the mixes to ensure workability of all mixtures at ~1.5% mass. Once the mixtures were prepared, ~ 7 g of each paste were placed into an ampoule. Heat flow and cumulative heat were measured using isothermal conductive calorimetry (ICC). Testing was performed using a modified ASTM C1702-17. Data were collected over the course of 7 days. Each paste sample was tested in duplicate.

3. Results & Discussion

3.1 Scanning electron microscopy

SEM micrographs of the RG $CaCO_3$, *L. corallioides*, and *E. huxleyi* are shown in Figure 1. The morphologies and the particle sizes differ between the $CaCO_3$ sources. In particular, the biogenic sources are both smaller and less angular than the RG $CaCO_3$. These images substantiate the mean particle size and surface area data obtained *via* laser diffraction and BET, respectively (see Section 2.1).

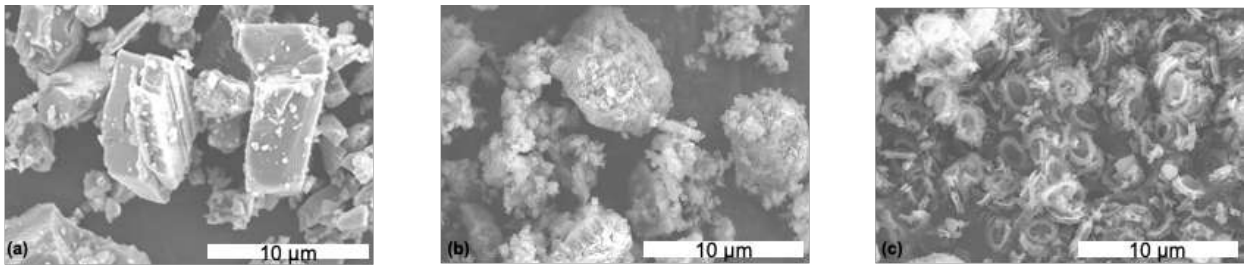


Figure 1. SEM micrographs of (a) RG $CaCO_3$, (b) *L. corallioides*, and (c) *E. huxleyi* $CaCO_3$.

3.2 Isothermal conduction calorimetry

Normalized heat flow and cumulative heat data for all samples are shown in Figure 2. As shown in Figure 2a, all LC3 pastes exhibited a higher peak heat compared to PC, which was expected (Antoni et al. (2012), Parashar & Bishnoi (2021)). In addition, the LC3 pastes containing biogenic $CaCO_3$ demonstrated higher peak heats than the LC3 control, owing to a possible nucleation effect due to smaller particle size and higher specific surface areas. The higher peaks at 60 h induced by the LC3 pastes containing biogenic $CaCO_3$ have been shown to correspond to the latent aluminate hydration peaks, specifically the formation of monocarboaluminate and hemicarboaluminate phases (Zunino & Scrivener, 2021). The *L. corallioides* sample has higher fractions of silica and alumina than the other $CaCO_3$ sources, which supports the hypothesis that higher heat flow and cumulative heat are causally linked with composition (see Table 1). Existing literature substantiates that alumina present in calcined clays leads to the formation of early carboaluminate phases instead of sulfoaluminate phases (Zunino & Scrivener, 2021). Formation of carboaluminates could lead to an increase in sulfate available for ettringite formation. As shown in Figure 2b, the LC3 samples containing biologically architected $CaCO_3$ exhibited the highest total cumulative heats, indicating an overall higher degree of reaction compared to the PC and LC3 controls. A higher degree of reaction could be caused by the nucleation effects induced by these particles (due to their higher surface areas), along with higher quantities of carboaluminate phases that form at later ages, although further study is required to confirm these hypotheses.

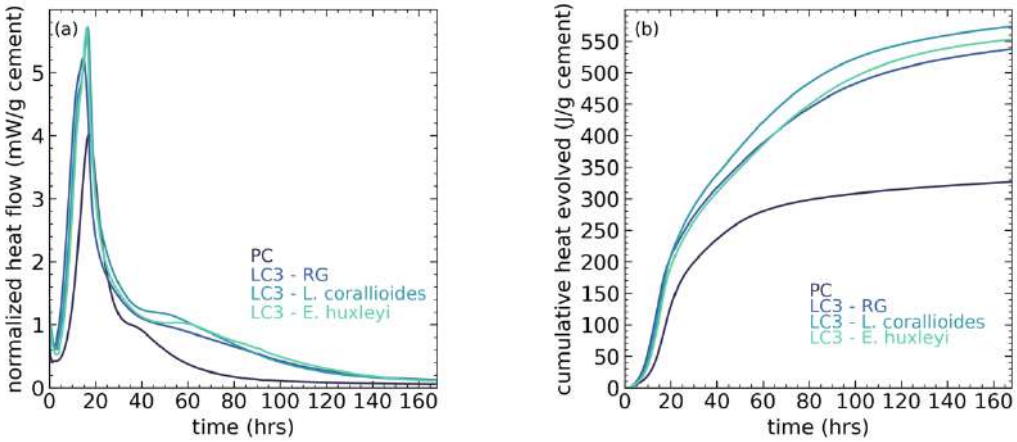


Figure 2. (a) normalized heat flow and (b) cumulative heat development for PC and LC3 pastes.

4. Conclusions & Future Work

This study illustrates how different $CaCO_3$ sources can have a significant impact on the heat flow and heat evolved in LC3 systems. LC3 pastes that incorporate biologically architected limestone from

L. corallioides and *E. huxleyi* with small particle sizes, high surface areas, and different chemical compositions exhibit higher cumulative heat compared to LC3 pastes produced using reagent-grade $CaCO_3$. More specifically, biologically architected $CaCO_3$ affects the kinetics of cement hydration at 60 hours in LC3 systems, owing to the possible formation of additional carboaluminate phases and enhanced nucleation due to small particle sizes and increased surface areas. Future work will further interrogate the effects of biogenic $CaCO_3$ on paste mineralogy, morphology, and compressive strength.

Acknowledgments

This research was conducted in partnership with the Colorado Shared Instrumentation in Nanofabrication and Characterization (COSINC) facility at the University of Colorado Boulder. This research was financially supported, in part, by the National Science Foundation (Grant No. CMMI-1943554), the National Science Foundation Graduate Research Fellowship under Grant No. DGE 2040434, and the Breakthrough Energy Foundation. Any opinions, findings, and conclusions or recommendations expressed in this material are those of the authors and do not necessarily reflect the views of the sponsors. The authors acknowledge Hazen Research for conducting the ICP-OES analysis.

References

Antoni, M., Rossen, J., Martirena, F., & Scrivener, K. (2012) "Cement substitution by a combination of metakaolin and limestone" *Cement and Concrete Research*, *42*(12), 1579–1589. https://doi.org/10.1016/j.cemconres.2012.09.006

de Brito, J., & Kurda, R. (2021) "The past and future of sustainable concrete: A critical review and new strategies on cement-based materials" *Journal of Cleaner Production*, *281*, 123558. https://doi.org/10.1016/j.jclepro.2020.123558

Jakob, I., Chairopoulou, M. A., Vučak, M., Posten, C., & Teipel, U. (2017) "Biogenic calcite particles from microalgae—Coccoliths as a potential raw material" *Engineering in Life Sciences*, *17*(6), 605–612. https://doi.org/10.1002/elsc.201600183

Juenger, M. C. G., Snellings, R., & Bernal, S. A. (2019) "Supplementary cementitious materials: New sources, characterization, and performance insights" *Cement and Concrete Research*, *122*, 257–273. https://doi.org/10.1016/j.cemconres.2019.05.008

Mansour, A. M., & Al Biajawi, M. I. (2022) "The effect of the addition of metakaolin on the fresh and hardened properties of blended cement products: A review" *Materials Today: Proceedings*, S2214785322045400. https://doi.org/10.1016/j.matpr.2022.06.521

Miller, S. A., Horvath, A., & Monteiro, P. J. M. (2016) "Readily implementable techniques can cut annual CO2 emissions from the production of concrete by over 20%" *Environmental Research Letters*, *11*(7), 074029. https://doi.org/10.1088/1748-9326/11/7/074029

OECD. (2019). *Global Material Resources Outlook to 2060: Economic Drivers and Environmental Consequences*. OECD. https://doi.org/10.1787/9789264307452-en

Parashar, A., & Bishnoi, S. (2021) "Hydration behaviour of limestone-calcined clay and limestone-slag blends in ternary cement" *RILEM Technical Letters*, *6*, 17–24. https://doi.org/10.21809/rilemtechlett.2021.134

Scrivener, K., Martirena, F., Bishnoi, S., & Maity, S. (2018) "Calcined clay limestone cements (LC3). *Cement and Concrete Research*, *114*, 49–56" https://doi.org/10.1016/j.cemconres.2017.08.017

Zhu, H., Zhang, D., Wang, T., Wu, H., & Li, V. C. (2020) "Mechanical and self-healing behavior of low carbon engineered cementitious composites reinforced with PP-fibers" *Construction and Building Materials*, *259*, 119805. https://doi.org/10.1016/j.conbuildmat.2020.119805

Zunino, F., & Scrivener, K. (2021) "The reaction between metakaolin and limestone and its effect in porosity refinement and mechanical properties" *Cement and Concrete Research*, *140*, 106307. https://doi.org/10.1016/j.cemconres.2020.106307

The 16th International Congress on the Chemistry of Cement 2023 (ICCC2023)
"Further Reduction of CO_2 -Emissions and Circularity in the Cement and Concrete Industry"
September 18–22, 2023, Bangkok, Thailand

Effect of silica fume on long-term hydration and compressive strength of UHPC under different curing regimes

D.S. Xu[1], J.H. Tang[2], C. Yu[3*], J.P. Liu[4]

[1] *Southeast University, Nanjing, China*
Email: xudisheng@seu.edu.cn
[2] *Southeast University, Nanjing, China*
Email: 101012824@seu.edu.cn
[3] *Jiangsu Sobute New Materials Co., Ltd., Nanjing, China*
Email: yucheng@cnjsjk.cn
4 Southeast University, Nanjing, China
Email: liujiaping@cnjsjk.cn

ABSTRACT

Thermal curing is widely used in ultra-high performance concrete (UHPC) to achieve good mechanical properties due to the acceleration of hydration of both cement and silica fume. In this paper, the effects of silica fume content, varying from 0% to 25% by mass, on long-term hydration and compressive strength of UHPC under different curing temperatures were investigated. The experimental results showed that the maximum reaction degree and compressive strength can be obtained when the content of silica fume was 20%. Compared with normal temperature curing for 1 year, the degree of hydration (DOH) of cement, degree of pozzolanic reaction (DOPR) of silica fume and compressive strength after 90 °C thermal curing was increased by 5.8%, 20.6% and 25.9% respectively. After thermal curing, the DOH of cement remained basically unchanged, the DOPR of silica fume increased slightly, while the compressive strength decreased slightly.

KEYWORDS: *Ultra-high performance concrete, thermal curing, silica fume, hydration, compressive strength*

1. Introduction

Ultra-high performance concrete (UHPC) is a new type of cement-based composite material with ultra-high strength, good toughness and excellent durability. In addition, it can be widely used in prefabricated components and repair structures due to its slenderness and lightness. As a result, raw material can be saved while performance is improved, thereby reducing carbon emission. Silica fume has become an indispensable constituent of UHPC due to its ultra-fine particle size and active pozzolanic effect (Lee et al (2018), Xi et al (2022)). Many studies (Wu et al (2016), Sadrmomtazi (2018)) have proved that the addition of silica fume plays an important role in improving the mechanical properties of UHPC, and there would be an optimal silica fume content. Besides, thermal curing can greatly accelerate the reaction of cement and silica fume, compact pores and enhance the performance of UHPC. However, although the content of silica fume had obvious significance for the improvement of hydration and mechanical properties under thermal curing, the performance change of UHPC after thermal curing required further discussion. The main purpose of this paper is to study the effect of silica fume content on long-term reaction degree of cement and silica fume of UHPC by thermal curing, and its relationship with compressive strength.

2. Experimental Procedure

2.1 Materials and Curing Regimes

The chemical compositions (by XRF) of the Portland Cement and gray silica fume (SF) used in this paper are given in Table 1. A polycarboxylate-based high range water reducer with a solid mass content of 50% was adopted. Natural river sand with the fraction 0-1.12 mm was used. the mix proportions of UHPC are shown in Table 2. In order to eliminate the additional influence of superplasticizer, the dosage of it was maintained at 1.8% (by mass of binder), which could ensure that the mini slump flow of all mixtures except SF25 (180 mm) was 250 ± 20 mm. Sand was removed from the mix of hydration test samples.

First, all the solid components were mixed dry at 140 r/min for 3 min with homogeneous mixing. Then, Water and superplasticizer were added and mixed at the same speed for 2 min until the slurry started to flow. Finally, the slurry was mixed for a high speed at 280 r/min for another 2 min until the mixture appeared uniform. The fresh mortar was poured into the molds (40 × 40 ×160 mm), while the paste was cast into cylinder molds and demolded after 1 day. They were cured under three curing regimes: 1) normal temperature curing at 20 ± 2 °C until testing age; (2) thermal curing at 60 °C for 2 d; (3) thermal curing at 90 °C for 2 d. After thermal curing, the curing method was the same as normal temperature curing.

Table 1. Chemical compositions of cement and SF (wt%).

Oxide	CaO	SiO_2	Al_2O_3	MgO	SO_3	Fe_2O_3	K_2O	MnO	LOI (950°C)
Cement	66.44	19.17	4.24	1.31	3.34	3.91	0.91	0.14	2.97
SF	0.11	98.01	0.56	0.11	0.51	0.25	0.24	0.01	1.89

Table 2. Mixture proportioning of UHPC mixes (kg/m^3).

Sample	Cement	Silica fume	Natural river sand	water	Superplasticizer*
SF0	1200	0	1100	193.2	21.6
SF5	1140	60	1100	193.2	21.6
SF10	1080	120	1100	193.2	21.6
SF15	1020	180	1100	193.2	21.6
SF20	960	240	1100	193.2	21.6
SF25	900	300	1100	193.2	21.6

[Note] Superplasticizer*: the total mass of liquid-based superplasticizer

2.2 Analytical methods

The compressive strength measurement was carried out according to the Chinese Standards GB/T 17671-1999. The DOH of cement was obtained by XRD and Rietveld analyses, and the scanning angular range was 5-70° with a step size 0.02°/s, as well as it could be calculated by Eq. (1). The DOPR of silica fume was evaluated by the selective dissolution, which was calculated by Eq. (2). Dilute nitric acid was used as the solution and it dissolved cement and hydration products without dissolving silica fume. All tests were performed for 3 d, 28 d and 360 d with 0-25% silica fume at 20 °C, 60 °C and 90 °C curing.

$$\mathrm{DOH(t)} = 1 - \frac{(C_3S+C_2S+C_3A+C_4AF)(t)}{(C_3S+C_2S+C_3A+C_4AF)(t=0)} \tag{1}$$

$$\alpha_{SF}=1-\frac{\left[\frac{w_{SD\text{-}EXP}}{1-w_{BW}}(1-w_{SF})\times w_{SD\text{-}REF}\right]/w_{SD\text{-}SF}}{w_{SF}}\times 100\% \tag{2}$$

Where α_{SF} is the reaction degree of silica fume (%); w_{SF} is the content of silica fume in the mixture; w_{BW} is the chemically bound water; $w_{SD\text{-}EXP}$ and $w_{SD\text{-}REF}$ are the residual amount of experimental group (SF5-SF25) and reference group, respectively; $w_{SD\text{-}SF}$ is the amount of silica fume left after dissolution.

3. Result and Discussion

3.1 Compressive strength

Fig. 1 presents the effect of silica fume content on compressive strength of UHPC at 20 °C, 60 °C and 90 °C curing. For one thing, from Fig. 1(a) at 20 °C curing, the compressive strength of UHPC exerts a significant increase at early ages, in details, such as SF20 increases from 104.7 MPa at 3 d to 129.5 MPa at 28 d. However, the growth rate decreases significantly at later ages, and it only increases by 4.7 MPa in 1 year compared with

28 d. Additionally, the compressive strength increases with the dosage of silica fume. Nevertheless, it should be noted that when the content of silica fume is more than 20%, the compressive strength decreases slightly after 28 d, this may be explained by the introduction of additional air entrapment and formation of micro-cracks (Wu et al (2016)). For another, it can be seen that the highest strength of the samples is obtained at 3 d of thermal curing as shown in Fig. 1(b) and (c). Thereafter, it shows a trend of first decreasing and then slightly increasing after thermal curing. As for the content of silica fume, the impact trend is relatively consistent with 20 °C curing.

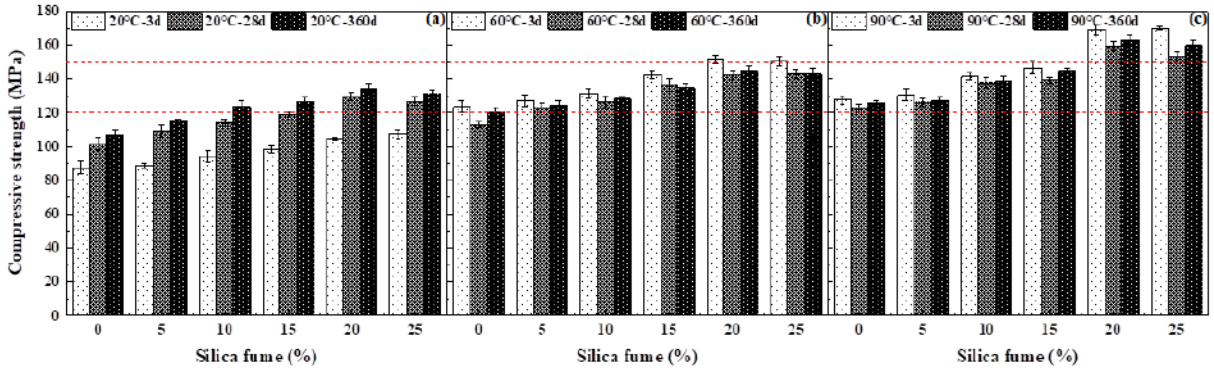


Fig. 1. Compressive strength of a) 20 °C curing, b) 60 °C curing and c) 90 °C curing.

3.2 The reaction degree of cement and silica fume

Fig.2 shows the effect of silica fume content and curing age on the reaction degree of cement and silica fume at 20 °C, 60 °C and 90 °C curing. As shown in Fig. 2(a), the DOH of cement of reference group reaches the maximum after thermal curing, which is mainly because more cement can be hydrated under thermal curing without silica fume wrapping water, while it increases with silica fume from 5% to 25% due to the nucleation effect of silica fume. However, it should be noted that the DOH of cement decreases when the dosage exceeds 20% of thermal curing, which is consistent with compressive strength. In addition, the hydration degree at different ages becomes closer under thermal curing, indicating that there is very little hydration after heat curing. The DOPR of silica fume decreases continuously with the increase of silica fume. When the dosage is 5%, the DOPR of silica fume (except 20 °C curing for 3 d) reached more than 95%, implying curing temperature has little effect with low dosage. When the dosage is 10% or 15%, the results after curing at 20 °C for 1 year under these two dosages can reach 94.7% and 87.9% of those after curing at 90 °C, respectively. However, when the dosage is 20% or 25%, the difference in results due to the curing temperature become larger. At this time, the results after curing at 20 °C for 1 year only reached 77.5% and 79.3% of those after curing at 90 °C under these two high dosages. Overall, high temperature can better promote the reaction of silica fume with high dosage of silica fume, and significantly increase the degree of pozzolanic reaction.

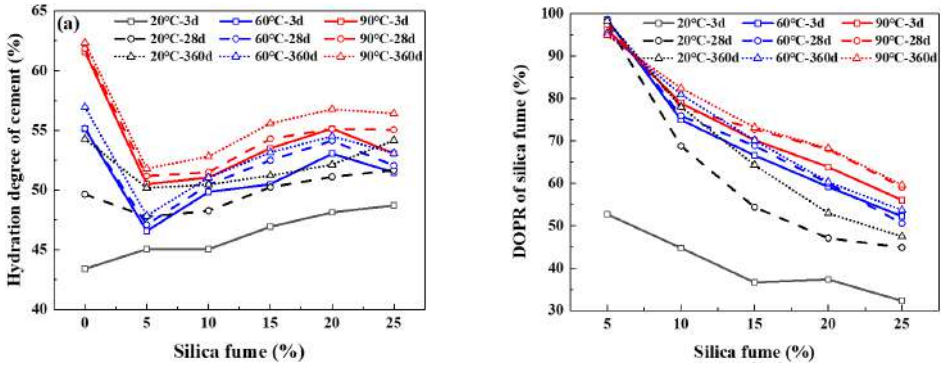


Fig. 2. The reaction degree of a) cement and b) silica fume.

3.3 The relationship between hydration and compressive strength

According to previous study (Kazemi-Kamyab (2013)), the pozzolanic reaction of silica fume occurred less under normal or low temperature curing. However, the pozzolanic effect is significantly improved under thermal curing, which has been also proved in Fig. 2(b). The compressive strength seen in Fig. 1 have shown that 20% dosage is the best dosage, but the impact mechanism of silica fume content on compressive strength is different

under thermal curing. The discrepancy of compressive strength, DOH of cement and DOPR of silica fume after thermal curing with 0-25% silica fume compared with 20 °C curing is analyzed in Fig. 3, and the relative index is obtained by dividing each value of thermal curing for 3 d by the corresponding value of 20 °C curing for 1 year. As can been seen from Fig. 3(a), thermal curing all increases the compressive strength. However, the reasons for the increase seems to be different. For SF0 group without silica fume, the increase of compressive strength is due to the significant increase in the DOH of cement. For SF5 and SF10 groups with low dosages of silica fume, the compressive strength increases by about 10%, but the relative value of reaction degree fluctuates around 100%. At this time, the increase in compressive strength may be attributed to the rapid reaction under initial thermal curing, which directly leads to the refinement of pore size and reduction of porosity even comparing with 20 °C curing for 1 year. For SF15, SF20 and SF25 groups with high dosages of silica fume, although the DOH of the cement changes little, its significantly increased DOPR of silica fume still promotes a substantial increase of compressive strength. An interesting phenomenon is that the relative compressive strength index of SF25 group is upward compared with SF20, while the relative index of reaction degree decreases. This indicates that the possible adverse effects of over-doped silica fume on mechanical properties of normal temperature curing are more obvious, and thermal curing can slightly compensate for the defects.

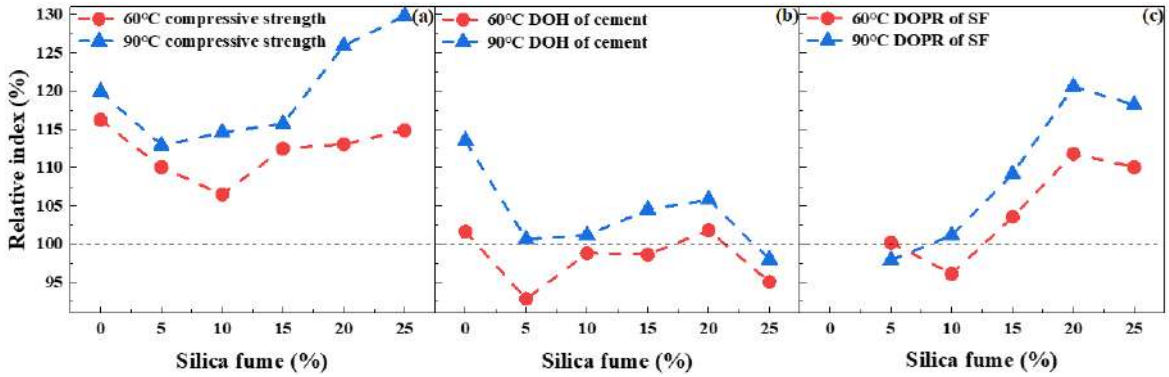


Fig. 3. Relative index of a) compressive strength, b) DOH of cement and c) DOPR of silica fume.

4. Conclusions

The use of UHPC can not only enhance structural performance, but also save the material, which is of great significance to energy saving and emission reduction in building materials. This paper quantitatively compares the effect of silica fume content on the reaction degree of cement and silica fume under different curing temperatures and its relationship with compressive strength. This has referential value for the mix design and selection of thermal curing in subsequent research and application of UHPC. Compared with 20 °C curing, thermal curing significantly improves the compressive strength of UHPC, up to about 30%. Under thermal curing, when the silica fume content is not higher than 10%, the increase in compressive strength is mainly due to the increase of cement hydration, thereby promoting the reduction of porosity; when the silica fume content exceeds 10%, the compressive strength has been greatly improved due to silica fume reaction. After thermal curing, the compressive strength shows a slight decrease first and then a slow increase trend, and subsequent increase is related to still a small amount of silica fume reaction.

References

Kazemi-Kamyab, H. (2013) "Autogenous Shrinkage and Hydration Kinetics of SH-UHPFRC under Moderate to Low Temperature Curing Conditions", *Doctoral Dissertation*, EPFL.

Lee, N.K., Koh, K.T., Kim, M.O. and Ryu, G.S. (2018) "Uncovering the Role of Micro Silica in Hydration of Ultra-High Performance Concrete (UHPC)", *Cement and Concrete Research*,104: 68-79.

Sadrmomtazi, A., Tajasosi, S. and Tahmouresi, B. (2018) "Effect of Materials Proportion on Rheology and Mechanical Strength and Microstructure of Ultra-High Performance Concrete (UHPC)", *Construction and Build Materials*, 187: 1103-1112.

Wu, Z., Shi, C. and Khayat, K.H. (2016) "Influence of Silica Fume Content on Microstructure Development and Bond to Steel Fiber in Ultra-High Strength Cement-Based Materials", *Cement and Concrete Composites*, 71: 97-109.

Xi, J., Liu, J., Yang, K., Zhang, S., Han, F., Sha, J. and Zheng, X. (2022) "Role of Silica Fume on Hydration and Strength Development of Ultra-High Performance Concrete", *Construction and Build Materials*, 338.

The 16th International Congress on the Chemistry of Cement 2023 (ICCC2023)
"Further Reduction of CO_2 -Emissions and Circularity in the Cement and Concrete Industry"
September 18–22, 2023, Bangkok, Thailand

Variation of Fluidity of Calcined Clay Limestone Cements by Power Ultrasound and Gypsum Addition

C. Rößler[1], J. Kocis[2], M. Heinemann[1], F.Kleiner[1], T. Sowoidnich[1] and H.-M. Ludwig[1]

[1] *Bauhaus-University, Weimar, Germany*
Email: christiane.roessler@uni-weimar.de, melanie.heinemann@uni-weimar.de, thomas.sowoidnich@uni-weimar.de horst-michael.ludwig@uni-weimar.de

[2] *Friedrich-Schiller-University, Jena, Germany*
Email: jackson.robert.kocis@uni-jena.de

ABSTRACT

The substitution of Portland cement clinker with a combination of limestone, calcined clays and set regulator (calcium sulphates) is a promising way to reduce CO_2 emissions of concrete. These cements are described as Limestone Calcined Clay Cement (LC3). Calcined clays are known to have a high specific surface area, which results in an increased water demand and thus reduced workability of mortars and concretes made from them. In practice, the reduced workability, among other things, means that these cements are rarely used. The advantage of calcined clays is their pozzolanic reactivity, so they contribute to hydration and thus to strength development. Previous work has shown that the amount of set regulator has significant effects on workability and strength development. For Portland cement, it is known that a brief exposure to power ultrasound during the mixing process improves workability and accelerates setting.

Here we show how power ultrasound affects the fluidity of LC3 cements. This is compared with the effect of gypsum on the cement fluidity by measuring the slump of cement suspensions. The dispersing effect of ultrasound in cements is imaged in the scanning electron microscope (SEM) using high pressure frozen samples, that are sectioned using a focused ion beam (FIB). This allows to visualize agglomeration and deagglomeration of sub-micron scaled particles in a close-to native state. Result show that PUS strongly de-agglomerates LC3 cements leading to a significantly increased specific surface area. Furthermore, the very early hydration (≤ 5 h) of cements is monitored by in-situ X-ray diffraction. The effects of sonication on hydration and particle dispersion on fluidity of cements pastes are discussed.

KEYWORDS: *calcined clay cements, fluidity, power-ultrasound, cryo-FIB-SEM*

1. Introduction

It is no surprise that climate change has influenced the course of scientific research towards the development of low(er)-carbon solutions for sources of anthropologically generated carbon emissions.
Born of this realization, researchers from Cuba, India, and Switzerland began development in the late 2000's of a low-clinker cement not reliant on industrial waste. This research would eventually result in what are known as Limestone Calcined Clay Cements, or LC3 for short (https://lc3.ch/). LC3s function by replacing 50% of the clinker with a mixture of hydraulically active calcined clay (30%, usually metakaolin), ground limestone (15%), and gypsum (5%) while obtaining similar engineering performances as Ordinary Portland cement (Sharma et al. 2021).
These cements are made from globally abundant materials (clays, limestones) and can, in comparison to Ordinary Portland cement (OPC), reduce emissions associated with production by up to 40% while maintaining comparable long-term strength, costs, while sometimes even exceeding the lifespans of OPCs, depending on the application (Scrivener et al. 2022, Scrivener et al. 2019, Pillai et al. 2019, Nguyen et al.

2020). These benefits are however checked by the generally poorer, and unpredictable rheology LC3 concretes exhibit (Tregger et al. 2010, Mousavi et al. 2021). Workability is amongst the most crucial factors to consider when laying, casting, or pouring cement products and is naturally of particular importance to the construction sector who steadfastly rely on uniform and predictable rheological outcomes from their cements.
The application of Power Ultrasound (PUS) has been shown in previous studies to improve the rheological behaviour, increase early strength gain, and accelerate setting time in OPC mortars and concretes (Peters 2016, Remus et al. 2018).
In preliminary tests PUS was shown however to greatly worsen the rheology in pure, metakaolin based LC3s. The present work is therefore targeted on trying to understand the origin of the loss in workability experienced by LC3s when given PUS treatment. In addition, it will be evaluated whether to what extent additions of gypsum might stymy this process or whether it can be used towards a more predictable rheological outcome.

2. Materials and Methods

2.1 LC3 cement

The LC3 Reference (Ref) is used and characterised for the Deutsche Forschungsgesellschaft (DFG) funded project "Opus Fluidum Futurum" (https://www.spp2005.de/), which seeks to build a foundation for rheology-based design of cements as well as the development of sustainable construction materials. The Ref LC3's preparation was done by project partner Heidelberg Materials. The LC3 Ref contains 52.0 wt.-% CEM I, 30.0 wt.-% calcined clay, 15.6 wt.-% limestone and 5.0 wt.-% of set regulator (C$ = anhydrite + gypsum + hemihydrate). Samples LC3 Ref +C$ and ++C$ contained 5.7 and 6.7 wt.-% C$, respectively. Further details on LC3 Ref properties can be found elsewhere (Pott et al. 2023).
The uncalcined clay contained 5.6 wt.-% calcite, 18.6 wt.-% quartz, 7.5 wt.-% muscovite, 31.9 wt.-% illite, 32.0 wt.-% kaolinite and 4.4 wt.-% montmorillonite. After calcination the amorphous content of the calcined clay was approximately 45 wt.-%, the LOI is < 10-15 %, reactive silica content is ≥ 33 %. The calcined clay is available as Liapor® Calcined Clay.

2.2 Slump test and Setting times

The production of mortars (w/c 0.5) tested for their slump bases itself on DIN 196-1 but deviates from the norm in several ways to accommodate the extra step of applying PUS to the cement pastes while maintaining the highest degree of comparability. The measurement of slump itself follows DIN EN 1045-3. The slump of each mortar, with and without the addition of PUS, was measured 20 minutes after the initial addition of water. The determination of setting time was carried out using an automatic Vicat device (RatioTEC) following DIN 196-3. Measurements were made every 10 minutes over the course of 15 hours.

2.3 Power Ultrasound

Sonication proceeded using an ultrasound processor and generator (UIP1000hd, Hielscher) connected to an amplifier (Booster B2-2.2, Hielscher) and Sonotrode (BS2d34, Hielscher). The maximum amplitude was set at 42.4 µm for all experiments. To ensure all treated sample received the same amount of energy, a voltmeter (Energy-Check 3000, Voltcraft) was first used to determine the amount of energy delivered to samples.

2.4 XRD and SEM

In-situ XRD measurements were performed (D8 diffractometer, energy-dispersive Sol-X detector Siemens) using Cu radiation at 40 kV and 30 mA. The scanning was set at a step width of 0.015° 2θ over an angular range from 8° to 56° 2θ with 19.2 s counting time per step. The samples were sealed with a Kapton foil and placed on a Peltier-cooled sample holder to maintain a stable reaction temperature of 25°C. After mixing with water the sample was immediately placed and sealed on the XRD sample holder. The first XRD scan was taken approximately 5 min after water addition and following after every hour.
Cryo-SEM on 20 min hydrated cement suspensions was carried out using a high-pressure freezing (HPM 100, Leica) procedure as described elsewhere (Holzer et al. 2007). For obtaining a section and recording of backscattered electron images (BSE) a high-resolution scanning electron microscope equipped with a focused ion beam (SEM-FIB, Helios G4 UX, ThermofisherScientific) was used.

3. Results

Results in Figure 1 show that PUS worsened workability across all C$ levels. Important to note as well, is that additional C$ did only improve the slump for the sonicated sample. Interestingly the error bars in the sonicated sample are reduced compared to the non-sonicated LC3 Ref.
The second effect of sonication is an acceleration of setting of cement pastes as shown by results in Table 1. These findings furthermore reveal that additional C$ has a minor influence on this acceleration effect.

Table 1: Set times of cement pastes (Vicat).

	w.o. PUS	*w. PUS*
LC3	480 min	360 min
LC3++C$	480 min	360 min

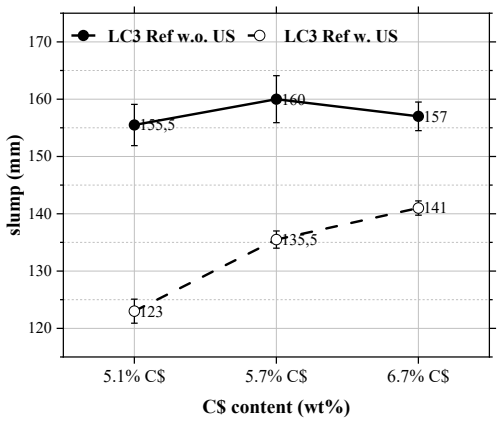


Figure 1: Slump of mortars in dependence of sonication and gypsum (C$) content.

The phase formation during early (≤ 5 h) hydration of the sonicated and non-sonicated LC3 samples were investigated by in-situ XRD **(**Figure 2**).** Results show that within the investigated hydration time sonication does not introduce other phases (AFm for example) or accelerates gypsum consumption and that the intensities of the ettringite and gypsum reflections are very similar. This indicates that sonication does not alter the LC3 phase assemblage to a verifiable extent.



Figure 2: Stacked in-situ X-ray diffractograms for 2 Theta range from 7.8-17.2°, reflections labels: Ett-ettringite, C$-gypsum, A) LC3 Ref, B) LC3 w. PUS.

To further unravel the cause of the fluidity reduction caused by sonication of cement suspensions, cryo-SEM investigations on 20 min hydrated LC3 pastes have been carried out. In order to view LC3 particle distribution in the aqueous phase without the necessity to sublimate the sample, the high-pressure frozen suspension was sectioned in the SEM using a focused ion beam. Results are shown in Figure 3. The BSE images in Figure 3A and B clearly show that in the sonicated sample the particles are dispersed and more homogenously distributed within the amorphous ice. To analyse the particles, images were segmented (Figure 3C & D) and particle size distributions were determined (Figure 4). As indicated by the images in Figure 3, the sonication leads to a dispersion of particles, and thus to a shift in particle size distribution towards smaller particles (Figure 4). In the non-sonicated LC3 reference sample these particles are probably agglomerated.

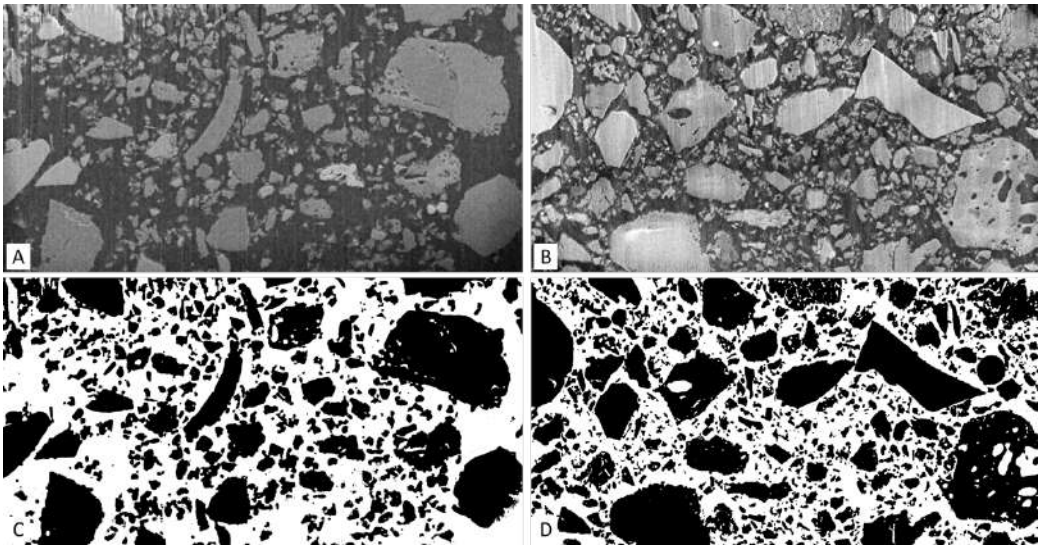


Figure 3 Cryo-SEM images of high-pressure frozen, FIB sectioned LC3 cement suspension (w/c = 0.5, 20 min hydrated): A, Reference B, Sonicated. C, D) segmented particles (Image width 46.3 µm resp. 44.8 µm).

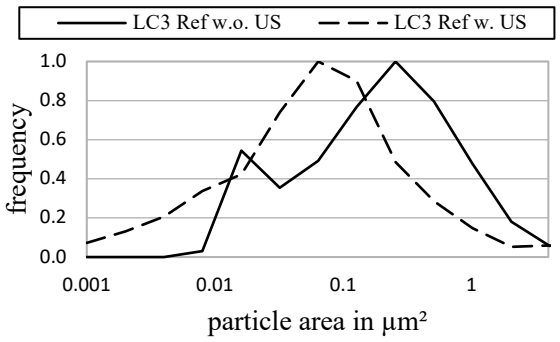


Figure 4: Particle size distribution determined from segmented images Fig. 3C & D.

4. Conclusions

Results of the investigation show:

1. Sonication of LC3 cement leads to a slump reduction, which is in contrast to observations with OPC.
2. Nevertheless, sonication leads to an acceleration of LC3 setting.
3. Phase assemblage investigated by in-situ XRD is mostly unaffected by sonication.

Cryo-FIB-SEM imaging revealed that sonication caused a dispersion of particles shifting the particle size distribution to smaller sizes. This is consistent to OPC. However, the dispersion of particles is associated with improved slump in OPC, whereas in LC3 a reduction was shown. The reason for this behaviour needs to be investigated in more detail.

References

Holzer L., Gasser P., Kaech A., Wegmann M., Zingg A., Wepf R., Muench B., Cryo-FIB-nanotomography for quantitative analysis of particle structures in cement suspensions, *Journal of Microscopy*, 227 (2007) 216-228.

Mousavi S.S., Bhojaraju C., Ouellet-Plamondon C., Clay as a Sustainable Binder for Concrete — A Review, *Construction Materials* 1 (2021) 134 – 168.

Nguyen Q.D., Kim T., Castel A., Mitigation of alkali-silica reaction by limestone calcined clay cement (LC3), *Cement and Concrete Research* 137 (2020) 106176.

Peters S., The Influence of Power Ultrasound on Setting and Strength Development of Cement Suspensions: Doctoral Dissertation, Bauhaus-Universität Weimar, 2016 https://doi.org/10.25643/bauhaus-universitaet.2744

Pillai R.G., Gettu R., Santhanam M., Rengaraju S., Dhandapani Y., Rathnarajan S., Basavaraj A.S., Service life and life cycle assessment of reinforced concrete systems with limestone calcined clay cement (LC3), *Cement and Concrete Research* 118 (2019) 111 – 119.

Pott, U., Crasselt, C., Fobbe, N., Haist, M., Heinemann, M., Hellmann, S., ... & Stephan, D. (2023). Characterization data of reference materials used for phase II of the priority program DFG SPP 2005 "Opus Fluidum Futurum–Rheology of reactive, multiscale, multiphase construction materials". *Data in Brief*, 108902.

Remus R., Rößler Ch., Ludwig H.-M. "Power Ultrasound-Assisted Concrete Production—Workability, Strength Development, and Durability." *ACI Special Publication 330* (2018): 135-150.

Scrivener K.L., Laffely J. D, Favier A., Cement Plant Environmental Handbook 3rd Edition: LC3 – Limestone Calcined Clay Cement, *Tradeship Publications Ltd*, UK, 2022.

Scrivener K., Avet F., Maraghechi H., Zunino F., Ston J., Hanpongpun W., Favier A., Impacting factors and properties of limestone calcined clay cements (LC 3), *Green Materials* 7 (2019) 3 – 14.

Sharma M., Bishnoi S., Martirena F., Scrivener K., Limestone calcined clay cement and concrete: A state-of-the-art review, *Cement and Concrete Research* 149 (2021).

Tregger N.A., Pakula M.E., Shah S.P., Influence of clays on the rheology of cement pastes, *Cement and Concrete Research* 40 (2010) 384 – 391.

The 16th International Congress on the Chemistry of Cement 2023 (ICCC2023)
"Further Reduction of CO_2 -Emissions and Circularity in the Cement and Concrete Industry"
September 18–22, 2023, Bangkok, Thailand

Effect of solid wastes with different activities on the rheological properties of 3D printing low carbon concrete

Lutao Jia[1], Zijian Jia[2], Zhenzhong Tang[3], Yamei Zhang[4]*

[1] *Jiangsu Key Laboratory of Construction Materials, School of Materials Science and Engineering, Southeast University, Nanjing, 211189, China*

Email: jialutaoseu@163.com
[2] *Jiangsu Key Laboratory of Construction Materials, School of Materials Science and Engineering, Southeast University, Nanjing, 211189, China*

Email: jzjjzj18@163.com
[3] *China Resources Cement Technology R&D Co., Ltd, Guangzhou, 510460 ,China*

Email: TANGZHENZHONG@crcement.com
[4] *Jiangsu Key Laboratory of Construction Materials, School of Materials Science and Engineering, Southeast University, Nanjing, 211189, China*

Email: ymzhang@seu.edu.com

ABSTRACT

Partially replacing cement with solid wastes in 3D printing concrete (3DPC) is an effective way to reduce carbon footprint. It is therefore of great importance to understand the effect of solid wastes on the rheological properties of 3DPC due to its high requirement for printability. In this paper, ground granulated blast furnace slag (GGBFS) with high activity and tungsten tailing powder (TTP) with low activity were selected as supplementary cementitious materials. The effects of these solid wastes with different activities on the rheological properties of 3DPC were investigated from the perspective of hydration kinetics and the state and distribution of water in the mixture. GGBFS improved the initial static yield stress by reducing the freedom degree of water and content of free water due to the adsorption and flocculation effect. GGBFS promotes the early hydration and increases the growth rate of static yield stress with time while TTP play opposite effect by weakening cement hydration.

KEYWORDS: *3D printing concrete, Low carbon concrete, Rheological properties, Hydration kinetics, Water state*

1. Introduction

3D printing concrete (3DPC) technology is a new intelligent construction technology combining 3D printing technology and concrete material technology. Compared with traditional casting and molding process, 3DPC technology has the advantages of mold-free, high degree of automation, labor saving and time saving (Wang et al. 2022). 3DPC technology will play an increasingly important role in the development of industrialized and intelligent buildings.

The special manufacturing method of 3DPC determines that the material must have suitable static yield stress and other rheological properties to ensure the good printability of fresh material. In order to meet the demand for printability, the content of cementitious materials in 3D printing concrete is generally higher than that in ordinary concrete (Zhang et al. 2021). Approximately, one ton CO_2 is emitted from the production of one ton of ordinary Portland cement (Lee et al. 2021). The high content of cement in 3D printed concrete leads to high material costs, high carbon footprint and high shrinkage. Therefore, it is an urgent need to find suitable supplementary cementing materials (SCMs) to partially replace cement in 3D printing concrete and it is of great significance to the performance control of 3D printing low carbon concrete and utilization of solid waste.

In this study, the GGBFS and TTP were used as SCMs in 3D printing low carbon concrete, and their effects on the rheological properties of blended cement pastes were tested. In addition, TAM Air isothermal calorimeter and ^{1}H low-field nuclear magnetic resonance (low-field NMR) were used to comprehensively study the influence mechanisms of the RBPs on rheological properties. The results will give a better understanding on utilization of GGBFS and TTP in 3DPC.

2. Materials and experiments

2.1 Materials

The cement used in this study is P·O 52.5R, which complies with GB175-2007. GGBFS and TTP were used as SCMs to reduce the cement content in 3DPC. The chemical compositions of cement, GGBFS and TTP are shown in Table.1.

Table.1 Chemical composition of Portland cement, GGBFS and TTP (wt%)

	CaO	SiO_2	Al_2O_3	MgO	Fe_2O_3	SO_3	Na_2O
Cement	65.74	17.23	5.53	1.39	4.58	2.97	0.15
GGBFS	40.23	27.91	17.77	9.73	0.42	2.13	0.28
TTP	29.35	36.97	8.85	3.61	16.49	0.95	0.38

The particle size distribution of the cementitious materials is shown in Fig.1. The medium dimeters of cement, GGBFS and TTP particle are 16.4 μm, 2.33 μm and 62.8 μm, respectively.

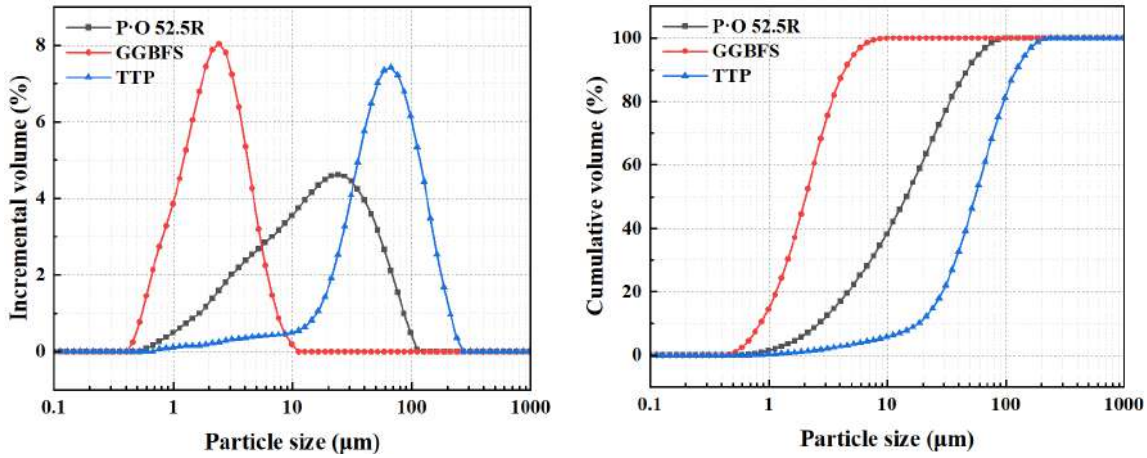


Fig.1. Particle size distributions of cement, GGBFS and TTP: (a)incremental and (b) cumulative volume

Table.2 shows the density and specific surface area of the cementitious materials.

Table 2 Physical parameters of P·II 52.5 and RBPs

	P·O 52.5 R	GGBFS	TTP
Density （g/m^3）	3.185	2.934	3.400
Specific surface area （m^2/g）	1.268	2.580	0.952

2.2 Experimental methods

2.2.1 Static yield stress

A rotational rheometer RST-CC (Brookfield, United States) equipped with a four-bladed rotor (10 mm width and 40 mm height for each blade) was used to test the rheological behaviors of blended cement pastes. A tiny shear rate ($0.01s^{-1}$) was applied to the sample, and the peak shear stress was recorded as the static yield stress during static rheology test.

2.2.2 Hydration heat

TAM -Air isothermal calorimeter was used to measure the hydration heat release of the paste samples. 10 g of freshly mixed paste was injected into an ampoule bottle with an internal diameter of 25.4 mm. The bottle was sealed and placed in the calorimeter, where the heat flow and cumulative hydration heat could be continuously recorded in a 20 °C atmosphere.

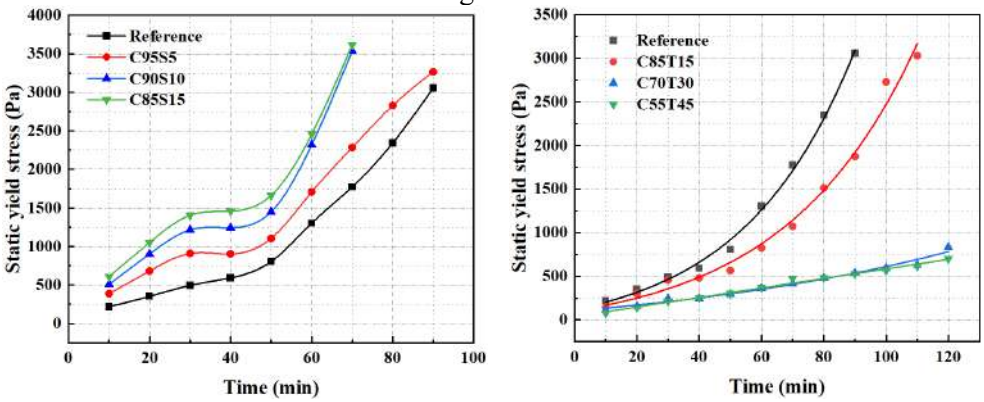
2.2.3 Low-field NMR

The signal value information of water in blended pastes were tested using the MesoMR12-060V-1 low field nuclear magnetic system, with a 0.3T magnetic field intensity (12MHz). The normalized signal value is created by dividing the measured signal value by the total mass of water in the sample.

3. Experimental results

3.1 Effect of GGBFS and TTP on static yield stress

Fig.2 shows the effects of GGBFS and TTP on the static yield stress evolution of different pastes with time, it can be seen that the initial static yield stress and the growth rate of static yield stress of blended cement pastes increased with the increase of GGBFS dosage and decreased with the increase of TTP dosage.



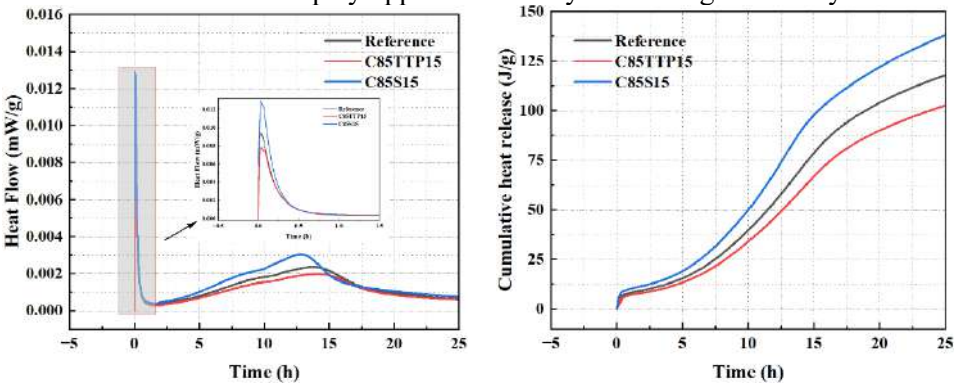
(a) (b)

Fig.2. Static yield stress evolution of different pastes with time: (a) GGBFS and (b) TTP

3.2 Effect of GGBFS and TTP on hydration heat

The structure formation and development of cement paste is a complex process involving physical and chemical actions such as particle force and cement hydration. Hydration is the most important factor affecting the structural build-up of cement and hydration heat reflect the hydration process of cement pastes (Yuan et al. 2018). Heat flow and cumulative heat release curves of blended cement pastes determined during 24 h after mixing are given in Fig.3. As can be observed, GGBFS considerably increased the dissolving heat release peak during the initial reaction period and the main heat release peak during the acceleration period while TTP play opposite effect.

The cumulative heat release of reference, C85S15 and C85TTP15 group are 9.48 J/g, 11.65 J/g and 8.16 J/g during the first 2 h, respectively. GGBFS promotes the early hydration and increases the growth rate of static yield stress with time while TTP play opposite effect by weakening cement hydration.



(a) (b)

Fig.3. Heat flow(a) and cumulative heat release(b) curves of different pastes

3.2 Effect of GGBFS on water state and water distribution in pastes

Fig.4 shows the T_2 relaxation distributions of GGBFS-cement blended paste at the time of 10 min after the initial contact of dry powders and water. The smaller the T_2 at the peak of the curve, the higher the binding degree of water, the smaller the freedom degree of water. The peak area under the curve represents the relative volume of different water conditions (Liu et al. 2022). Compared with the reference group, the peak T_2 values shift to the left after the addition of GGBFS, which means lower degree of water freedom and higher flocculation degree. This result can explain that the static yield stress of slurry increases with the addition of GGBFS.

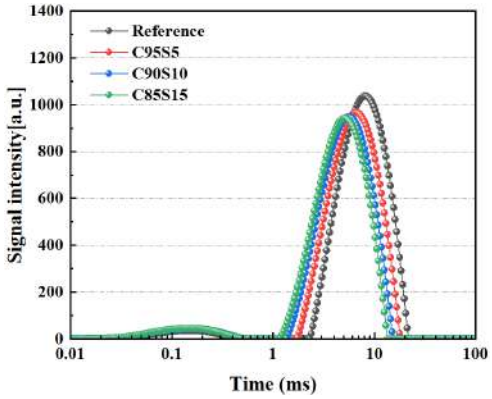


Fig.4. Initial T_2 spectrums of GGBFS-cement pastes

The low-field NMR test was not performed for the group mixed with TTP because the content of iron oxide in TTP is very high, which will affect the accuracy of the test.

4. Conclusions

Solid wastes with different activities have different influence on the rheological properties of 3D printing low carbon concrete. The influence mechanism is explained from the perspective of hydration process, water state and migration of blended pastes. The main conclusions can be drawn as follows:

(1) GGBFS with higher specific surface area can improve the initial static yield stress of blended cement pastes while the TTP plays opposite effect.

(2) GGBFS promotes the early hydration due to the nucleation effect and increases the growth rate of static yield stress with time while TTP plays opposite effect by weakening cement hydration due to dilution effect.

(3) The incorporation of GGBFS reduces the water freedom degree and free water amount by promoting the formation of flocculation, which increases the initial static yield stress of blended cement pastes.

Acknowledgements

This work is supported by National Natural Science Foundation of China (No.52130210).

References

Wang, X., L. Jia, Z. Jia, C. Zhang, Y. Chen, L. Ma, Z. Wang, Z. Deng, N. Banthia and Y. Zhang (2022). *"Optimization of 3D printing concrete with coarse aggregate via proper mix design and printing process."* Journal of Building Engineering 56: 104745.

Zhang, C., V. N. Nerella, A. Krishna, S. Wang, Y. Zhang, V. Mechtcherine and N. Banthia (2021). *"Mix design concepts for 3D printable concrete: A review."* Cement and Concrete Composites 122: 104155.

Lee, J., T. Lee, J. Jeong and J. Jeong (2021). *"Sustainability and performance assessment of binary blended low-carbon concrete using supplementary cementitious materials."* Journal of Cleaner Production 280: 124373.

Yuan, Q., D. Zhou, B. Li, H. Huang and C. Shi (2018). *"Effect of mineral admixtures on the structural build-up of cement paste."* Construction and Building Materials 160: 117-126.

Liu, C., Y. Chen, Y. Xiong, L. Jia, L. Ma, X. Wang, C. Chen, N. Banthia and Y. Zhang (2022). *"Influence of HPMC and SF on buildability of 3D printing foam concrete: From water state and flocculation point of view."* Composites Part B: Engineering 242: 110075.

The 16th International Congress on the Chemistry of Cement 2023 (ICCC2023)
"Further Reduction of CO_2 -Emissions and Circularity in the Cement and Concrete Industry"
September 18–22, 2023, Bangkok, Thailand

Assessing the activity of potential SCM's using the R3 test method

M.Batog[1*], A.Golda[2], D.Dziuk[3], B.Batog[4], and K.Synowiec[5*]

[1] *phD, Dąbrowa Górnicza, Poland*
Email: maciej.batog@betotech.pl
[2] *phD, Dąbrowa Górnicza, Poland*
Email: artur.golda@betotech.pl
[3] *phD, Dąbrowa Górnicza, Poland*
Email: damian.dziuk@betotech.pl
[4] *MSc, Dąbrowa Górnicza, Poland*
Email: barbara.batog@betotech.pl
[5] *phD, Dąbrowa Górnicza, Poland*
Email: katarzyna.synowiec@betotech.pl

ABSTRACT

The political and economic situation in Europe is challenging the cement industry to source new alternative raw materials for cement production. Driving to reduce the carbon footprint of industrial activities, including power generation results in the limited availability of commonly used fly ash and granulated blast furnace slag. To effectively replace these materials, it is necessary to find raw materials with similar activity. In the comparative assessment of the chemical reactivity of potential SCMs, the R3 test can be used - a rapid, relevant, reliable test developed on the basis of ASTM C1702 standard by RILEM Technical Committee 267-TRM. The test involves calculating the total heat released by the hardening/binding paste under isothermal conditions and water bound. Raw materials with predicted pozzolanic properties, such as calcined clays, coal shale, stockpiled ash-slag, and recycled concrete powder (RCP), were subjected to preliminary activity evaluation. For comparison, a classic activity index determination, based on results of compressive strength of standard mortars, has also been carried out. The paper attempts to find a relation between the results obtained.

KEYWORDS: *cement, supplementary cementitious materials, activity, R3 test*

1. Introduction

Many years of positive experience in the use of fly ash and granulated blast furnace slag, both as constituents in cement and concrete, has led to a steady increase in demand and a shrinking supply of good quality products. Economic reasons and environmental aspects are not insignificant for such a state of matters. Growing demand to cut CO_2 emissions from the cement and concrete sector is driving industry to find new material solutions, Avet et al (2016), Flegar et al (2020). Technical aspects dictated by the effects of alternative raw materials known from practice, such as improved workability and long-term durability, point in the direction of the search for materials with pozzolanic (pozzolanic-hydraulic) properties. Environmental aspects, on the other hand, focused on the need to reduce the carbon footprint of the product, indicate the need to source decarbonized, non-carbonate raw materials, Londono-Zuluaga et al (2022). Increased interest is being observed in the subject of calcined clay as natural calcined pozzolana (Q), as well as waste materials from the energy and mining industries set aside in landfills and industrial wastes not used previously, Avet et al (2016, 2022), Blotevogel et al (2020). Thus a rapid, relevant and reliable test for assessment of activity of such materials in comparison to well-known fly ash and granulated blast furnace slag is needed, Parashar et al (2022). Activity index test is dedicated for fly ash (EN 450-1:2012) and granulated blast furnace slag (EN 15167-1:2006) but there are different replacement rates and different requirements for results obtained for these components. R3 test developed

on the basis of ASTM C1702-17 standard by RILEM Technical Committee 267-TRM gives the possibility to asses chemical activity in the model system composed of $Ca(OH)_2$, the SCM along with calcite, alkali and sulphate, which are invariably present in real cement, Avet et al (2020), Li et al (2018), Londono-Zuluaga et al (2022).

2. Tests methods

2.1. R3 test

Detailed R3 test procedure can be found in ASTM C1897-20. The R3 method is two step verification for chemical reactivity of SCMs in Portland cement blends (paste sample incorporating SCMs acc. the mix design of the model paste shown in Table 1), Avet et al (2020), Li et al (2018), Londono-Zuluaga et al (2022).

Table 1. Mass proportions of the R3 test model paste

Ingredient	SCM	Calcium hydroxide	Calcium carbonate	Potassium solution*
Mass (g)	10,0	30,0	5,0	54,0
*The potassium solution consists of 4,00 g/L KOH and 20,0 g/L of K_2SO_4 dissolved in deionized water				

First step consist of total heat measurements over 7 days carried out by isothermal calorimetry at 40°C. The cumulative heat release per gram of SCM (H_{SCM}) was calculated with Eq. (1), where H is the cumulative heat from 75 min after mixing until 7 days, m_p is the mass of the paste in the calorimeter vial, and 0.101 is the mass fraction of the SCM in the paste specimen.

$$H_{SCM} = H / (m_p \times 0{,}101) \ [J/g_{SCM}] \quad (1)$$

Second step is calculation of water bound while hardening for 7 days. Hardened pastes were crushed and sieved on a 2 mm sieve and dried in an oven at 40°C for 24 h, then dehydrated at 350°C for 2 h and cooled in a desiccator. The bound water (for hydrates, excluding portlandite) was calculated according to Eq. (2), where w_0 is the total mass of the dried paste and vial, w_h is the total mass of the 350°C—dehydrated paste and vial, and w_c is the mass of the empty vial.

$$H_2O_{bound} = (w_0 - w_h)/(w_0 - w_c) \ [\%] \quad (2)$$

2.2. Activity index

Activity indices were determined after 7, 28 and 90 days curing, in accordance with EN 450-1 standard, but proportions of the mortar component were modified. Mortars were prepared with 30% SCMs (as cement CEM I 42,5R substitution by mass) and water content was adjusted due to water demand of SCMs (determined on the basis of flow table test). The modification of the mortar composition is based on past experience. It has been observed that materials with a higher water demand (porous or high fineness) absorb water, thus reducing the w/c in the mortar and falsely presenting an increase in strength. For this reason, the authors consider strength measurement with corrected w/c to be more representative.

3. Samples description

Analyzed as possible SCMs, there were samples of calcareous fly ash (W), calcined clay (CC), coal shale (CS), stockpiled ash-slag mix (AS) and recycled concrete powder (RCP). Common used fly ash (V) and ground granulated blast furnace slag (S) were chosen as a reference samples. Chemical composition of tested SCMs samples is shown in Table 2. Clay and coal shale samples were calcined to boost activity. Three calcination temperatures were analyzed for CC sample (800°C, 850°C and 900°C) and the temperature of 700°C was established for CS.

Table 2. Chemical composition of SCMs

SCM	Chemical composition [% mass]							
	LOI	SiO_2	Al_2O_3	Fe_2O_3	CaO	MgO	Na_2O	K_2O
GGBFS	nd	42,20	7,41	0,67	41,40	7,02	0,46	0,38
FA (V)	1,90	53,04	26,97	5,74	3,27	2,59	1,33	3,15
FA (W)	4,05	30,08	22,25	8,6	26,64	1,14	0,08	0,13
CC	7,25	62,61	21,74	5,32	0,83	1,94	< 0,01	3,63
CS	21,91	57,34	26,77	5,23	0,63	1,55	0,56	3,19
AS	13,35	48,00	24,48	5,21	1,70	2,11	0,58	2,84
RCP	nd	47,3	13,5	5,1	28,8	2,0	1,0	2,4

3. Results and discussion

R3 tests results are presented in Table 3 and compressive strength and activity indices results in Table 4.

Table 3. R3 test results

Sample	Heat released H_{SCM} [J/g]	Bound water H_2O_{bound} [%]
GGBFS	393	6,1
FA (V)	221	4,4
FA (W)	414	7,2
CC 800	244	6,2
CC 850	288	6,8
CC 900	258	6,4
CS 700	344	6,2
AS	252	4,1
RCP	101	nd

Table 4. Compressive strength and activity indices results

Sample	Water demand [%]	Compressive strength [MPa]			Activity index [%]		
		7 days	28 days	90 days	7 days	28 days	90 days
GGBFS	100,0	39,8	54,4	62,3	78,9	91,4	95,4
FA (V)	100,0	28,9	40,2	54,0	59,8	67,6	85,3
FA (W)	110,7	43,0	56,2	70,3	85,3	94,5	107,7
CC 800	114,2	27,2	42,1	46,6	57,1	70,8	73,5
CC 850	111,5	27,6	45,0	55,5	58,0	75,6	87,5
CC 900	108,9	29,5	46,8	61,1	62,0	78,7	96,4
CS 700	110,7	27,2	43,1	48,6	55,7	69,8	71,1
AS	101,3	36,2	50,6	67,4	69,0	79,6	97,3
RCP	112,4	37,7	46,7	51,9	69,9	75,2	76,3

Despite higher water demand calcined clay samples reveal chemical activity at the level of siliceous fly ash, and even better. Bound water amount for CC samples is higher, reaching the level of GGBFS. For stockpiled ash-slag mix (AS) the level of heat released and bound water are very close to common used siliceous fly ash (V). Results obtained for calcareous fly ash (W) indicate on its latent hydraulic properties and show even higher chemical activity when compared to GGBS, especially when bound water result is investigated. Similarly coal shale (CS) reveals beneficial activity level. On the other hand RCP sample almost do not reveal chemical activity, as the heat level was the lowest and bound water determination was impossible because paste sample was non-hardened.

Activity indices results gives similar output. Effect of thermal treatment of clay on its activity after 28 and 90 days seems promising, as well as 90 days results for stockpiled ash-slag mix. Activity index results of CS sample do not reveal beneficial activity in opposition to chemical activity by means of R3 method, thus further tests to clarify this issue are ongoing including effects of thermal treatment.

Taking into account presented results some attempts to find a relationship between R3 test and activity indices were made. Linear correlation between results of R3 test ie. total heat and bound water was

determined but model fit factor R2 was quite low. An improvement in model fit factor R2 performance can be observed, by dividing the samples results into two series (pozzolanic SCMs samples and latent hydraulic SCMs samples) and setting H_{SCM}=300 as the limit.
The same has been observed for correlation between R3 test results and activity indices. Fig. 1. presents model fit factor for correlation on total heat released H_{SCM} [J/g] and the rate of increase in compressive strength over time per 1g of SCMs (Δ_S) calculated acc. Eq. (3) where f_7 – compressive strength after 7 days, f_{28} – compressive strength after 28 days, 135 – SCM mass [g] in mortar sample (30% of 450g).

$$\Delta_S = (f_{28}-f_7)/135 \text{ [MPa/g]} \quad (3)$$

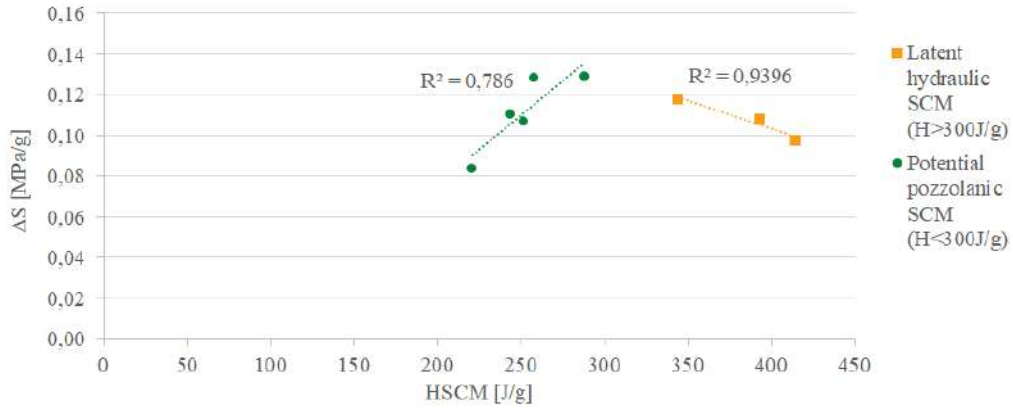


Fig. 1. Correlation between R3 test and activity indices results

3. Conclusions

R3 test method is quite simple procedure to assess the activity of SCMs. It is much less time-consuming and results are obtained much faster when compared to classic activity index assessment. It gives the opportunity to compare possible SCMs regardless the impact of cement properties. Nevertheless, it still needs to be comparable to other activity assessment methods and suitable for wide range of materials not used so far or completely unknown as possible SCMs. Thus much more tests and their verification needs to be done.

References

Avet, F., Li, X., Ben Haha, M. et al. (2022) "*Report of RILEM TC 267-TRM phase 2: optimization and testing of the robustness of the R3 reactivity tests for supplementary cementitious materials"*. Materials and Structures, 55, 92

Avet F., Snellings R., Diaz A. A., Ben H., Scrivener K., (2016) "*Development of a new rapid, relevant and reliable (R3) test method to evaluate the pozzolanic reactivity of calcined kaolinitic clays*" Cement and Concrete Research, Volume 85, Pages 1-11,

Blotevogel S., Ehrenberg A.s, Steger L., Doussang L., Kaknics J., Patapy C., Cyr M., (2020), "*Ability of the R3 test to evaluate differences in early age reactivity of 16 industrial ground granulated blast furnace slags (GGBS)*", Cement and Concrete Research, Volume 130

Flegar M., SerdarM., Londono-Zuluaga D., Scrivener K., (2020) *"Screening Regionally Available Natural Resources and Waste Streams as Potential Supplementary Cementitious Material"* Proceedings of the 3rd RILEM Spring Convention and Conference

Li, X., Snellings, R., Antoni, M. et al. (31 more authors) (2018) *"Reactivity tests for supplementary cementitious materials: RILEM TC 267-TRM phase 1"*. Materials and Structures, 51, 151

Londono-Zuluaga, D., Gholizadeh-Vayghan, A., Winnefeld, F. et al. (2022) "*Report of RILEM TC 267-TRM phase 3: validation of the R3 reactivity test across a wide range of materials*". Materials and Structures 55, 142

Parashar, A., Vollpracht, A., Haufe, J. et al. (2022) "*Report of RILEM TC 267—TRM: Improvement and robustness study of lime mortar strength test for assessing reactivity of SCMs*". Materials and Structures 55, 96

The 16th International Congress on the Chemistry of Cement 2023 (ICCC2023)
"Further Reduction of CO_2 -Emissions and Circularity in the Cement and Concrete Industry"
September 18–22, 2023, Bangkok, Thailand

The effect of ionic environment of cement pore solution on the PCE's molecular conformation, adsorption and performance

B. Li[1], L. Wang[1]*, and Z. D. Wang[1]

[1] China Building Materials Academy, Beijing, China
Email: libin@cbma.com.cn
Email: wangling@cbmamail.com.cn
Email: wzhendi@163.com

ABSTRACT

In this paper, the influence of cement pore solution's ionic concentration and type on PCE's molecular conformation, adsorption thermodynamics and kinetics by cement particle, and dispersing performance are investigated in detail.

The ionic concentration ranges and ionic types of low-clinker cement (blended with mineral admixtures) and ordinary Portland cement' pore solutions are studied by Inductively Coupled Plasma Optical Emission Spectra (ICP-OES). According to the ICP-OES test results, a series of simulated cement pore solutions with concentration gradient are prepared by dissolving a certain amount of NaOH, KOH, $Al(OH)_3$ and other soluble salts. Moreover, ether-type macromonomer HPEG and acrylic acid (AA) are used to synthesize PCEs with different anionic charge density and molecular weight. The structure of synthesized PAA-HPEG (HPCE) are characterized by FT-IR, ^{1}H NMR and GPC. The effect of ion's concentration and type of cement pore solution on HPCE's hydrodynamic radius and adsorption process by cement particle are revealed by DLS and TOC. This paper reveals the influence of cement's composition on PCE's properties and mechanism from perspective of ionic environment.

KEYWORDS: *ionic concentration; pore solution; low-clinker cement; molecular weight; charge density*

1. Introduction

The scientific community has discussed the low environmental performance of conventional concrete due to the high CO_2 emissions in the production of Portland cement. The partial replacement of Portland cement by low impact supplementary cementing materials (SCM) is one of the most effective methods. Polycarboxylate superplasticizer (PCE) as a new generation superplasticizer is widely used in concrete production. PCEs are adsorbed onto the positively charged surface sites of cement particles, and positive sites of other supplementary particles and hydration products like ettringite (Aft) (Kanchanason et al. 2018). It is well-known that the dispersion mechanisms of PCEs is exclusively due to steric hindrance. The use of mineral admixtures in cement blends would remarkably modify the ion's concentration and type of cement pore solution, which could affect flow properties of the cementitious system (Franco et al. 2020). This work consists of an investigation of the influence of PCE's molecular parameters on the properties of Portland cement pastes containing mineral admixtures. The main objectives were to reveal the influence of cement's composition on PCE's properties and mechanism from perspective of ionic environment.

2. Experimental section

2.1 Materials

Sodium hydroxide (NaOH) (analytical grade, Aladdin); h; L-ascorbic acid (97%, Aladdin); thioglycolic acid (Aladdin); 2 – methyl allyl polyoxyenthylene (HPEG) with molecular weight 2400 g/mol (Industrial-grade, Liaoning Oxiranchem Co., Ltd. of China); hydrogen peroxide (H_2O_2) (Aladdin); acrylic acid (AA) (99%, Aladdin); Type I ordinary Portland cement (OPC) was adopted. Class II fly ash (FA) was used. Chemical/mineral compositions of cement and FA are shown in Table 1.

Table 1 Chemical and mineral composition of cement/fly ash

	SiO_2	Al_2O_3	Fe_2O_3	CaO	MgO	SO_3	Na_2O_{eq}	Loss	C_3S	C_2S	C_3A	C_4AF
Cement	25.10	6.38	4.19	54.87	2.61	2.66	0.56	2.18	59.88	17.49	6.22	10.55
FA	56.70	4.92	2.73	3.76	1.70	0.38	1.12	4.67	/	/	/	/

2.2 Synthesis process of PCEs

The preparation of PCEs was carried out through free radical polymerization. A certain amount of AA and HPEG were placed in a 50 ml three-necked flash, and deionized water was poured into the flash to form HPEG solution. When the system was heated to 60 ℃, the initiator H_2O_2 was added. Next, the acrylic acid (AA) and ascorbic acid (Vc)/thioglycolic acid (transfer agent, TA) solution were added dropwise into the HPEG solution for 2 and 2.5 h, respectively. Then the system was reserved for a heat preservation reaction that lasted for 1.5 h. When the reaction was completed, the polymer solution's pH was adjusted to 7.0 by 30 wt% NaOH. Their chemical compositions were shown in Table 2.

Table 2 Chemical compositions of PCEs

Sample	Molar ratio of [AA : HPEG]	H_2O_2 (wight of HPEG, %)	Molar ratio of (Vc : H_2O_2)	Molar ratio of (TA : AA)
PCE-1	2:1	0.5	1:5.8	0.030:1
PCE-2	4:1	0.5	1:5.8	0.015:1
PCE-3	6:1	0.5	1:5.8	0.010:1
PCE-4	4:1	0.5	1:5.8	0.030:1
PCE-5	4:1	0.5	1:5.8	0.007:1

2.3 Test method for characterization of the molecular structure of synthesized polymers

Fourier transform infrared (FTIR), ^{1}H Nuclear magnetic resonance (^{1}H NMR), and Gel permeation chromatography (GPC) were used to characterize the structure of synthesized polymers.

FTIR test: Dried samples were embedded in KBr pellets at a concentration 1 mg/100 mg, scanned by TENSOR 27 Infrared spectrometer (Bruker Co.,), the range of wavelength was 400 ~ 4000 cm^{-1}

^{1}H NMR test: An AVANCE Digital 400 MHz NMR spectrometer (Bruker Co., German) was used. The chemical shift values were expressed in d values (ppm) relative to tetramethylsilane (TMS) as an internal standard. A certain amount of specimen was dissolved in DMSO and tested.

GPC test: The number-average molecular weight (Mn), weight average molecular weight (Mw), and dispersity (PDI) of the samples were performed using a Shimadzu GPC system (using low dispersity polyethylene glycol as the standard)

Hydrodynamic diameter test: The concentration of PCEs solution is diluted to 0.5 wt ‰ by DI water and the pH is adjusted to 12 by NaOH. The calcium concentration of the solution is from 0 to 20 mM.

2.4 Test method of the fluidity for cement paste/ low-clinker cement paste with superplasticizer

The fluidity of cement paste/low-clinker cement paste containing superplasticizer was measured by the mini-slump test according to Chinese standard GB/T 8077–2012. The water/cement ratio is 0.32 and 0.2 wt.% PCEs were added. For revealing the effect of Ca^{2+} on the dispersing performance of PCE, a certain amount of $CaCl_2$ was dissolved in mixing water firstly. Fluidity was measured as the above procedure.

2.5 Test method for adsorption behavior of PCEs on cement particles

The adsorption behavior of PCEs on cement particles is evaluated by TOC method, and detailed procedures refer to (Li et al. 2021). For revealing the effect of Ca^{2+} on the adsorption behavior of PCE by cement particle, a certain amount of $CaCl_2$ was dissolved in PCE soultion firstly.

2.6 The ICP-OES analysis

In our study, the ICP-OES's test method was referred to F. Caruso et al.'s work (Caruso et al. 2017). The low-clinker cement paste samples were prepared through replacing 20%, 40% and 80% cement with FA, respectively. The pore solution of samples was prepared in PP containers by mixing 100 g of cement/cement-FA, and 50 g of Ultra pure water (w/c ratio=0.5). Afterwards, the cement paste (around 120 g) was put in the barrel (Vmax = 200 mL) of a stainless steel pressure filter holder previously mounted with a nylon 0.45 μm membrane filter. The test results were shown in Table 3.

Table 3 The ionic concentration ranges and ionic types of cement-FA and cement' pore solutions

Sample	Al mmol/L	Ca mmol/L	K mmol/L	Na mmol/L	S mmol/L	Si mmol/L
100% OPC	0.037	0.674	1.259	0.499	1.291	0.036
80% OPC + 20% fly ash	0.036	0.615	1.028	0.508	1.207	0.033
40% OPC + 60% fly ash	0.035	0.604	0.997	0.624	1.170	0.032
20% OPC + 80% fly ash	0.033	0.552	0.788	0.907	1.033	0.032

3. Results and Conclusions

3.1 The characterization of PCEs

The FTIR of PCEs are shown in Figure 1. In FTIR of PCEs, vibration absorption at 1646.20 cm^{-1} (which corresponds to the absorption peaks of -C=C- group) almost disappeared, indicating that the HPEG was copolymerized with AA. Meanwhile, the absorption peaks observed at 1109.87 cm^{-1} and 1725.04 cm^{-1} correspond to -C-O-C- and -C=O, respectively. All of the above findings demonstrated that the PCEs with different molecular parameters have been successfully synthesized.

The ^{1}H NMR of PCEs are shown in Figure 2. The characteristic peaks corresponding to H atoms of the vinyl group at 4.88 ppm almost disappeared, which indicated that monomers were polymerized. The peaks in range of 3.40 ~ 3.50 ppm and 3.60 ~ 4.10 ppm correspond to the H atoms of polyoxyethylene ether. The peak at 1.63 ppm corresponds to the H atoms of methyl linked to the backbone.

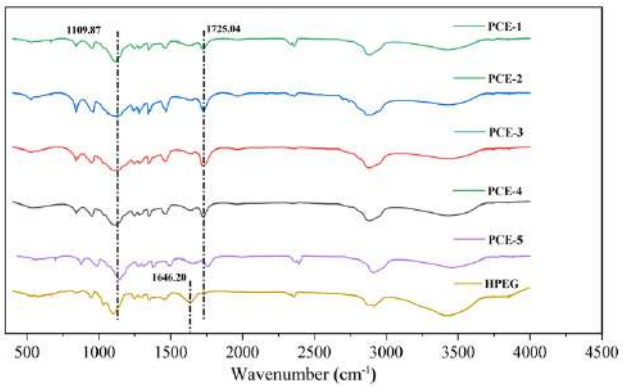


Fig. 1 The FT-IR spectra of PCEs

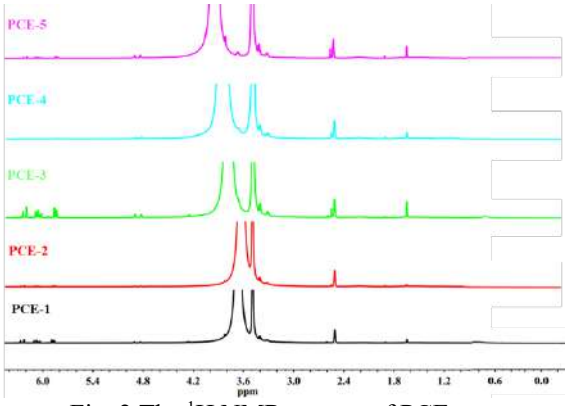


Fig. 2 The ^{1}H NMR spectra of PCEs

Furthermore, GPC was employed to measure the molecular weights and distributions of PCEs and test results were listed in Table 4. The molecular weight (Mn) of the synthesized PCEs were increased with molar ratio of AA/HPEG increasing. Moreover, through adjusting the dosage of TA, a series of PCEs with different molecular weights were synthesized. The PDIs of all PCEs are around 1.50 ~ 1.56.

Table 4 Molecular weight of PCEs

Sample	Mn (g/mol)	Mw (g/mol)	Dispersity (Mw/Mn)
PCE-1	20400	30500	1.50
PCE-2	38200	58000	1.52
PCE-3	43900	65700	1.50
PCE-4	29800	46500	1.56
PCE-5	46000	69500	1.51

The effect of FA's content on the fluidity of cement-FA paste containing PCEs with different molecular parameters was shown in Figure 3. It can be seen that for PCE-1, PCE-2, PCE-4, and PCE-5, with content of FA increasing, the fluidity was also increased. It can be attributed to the ball-bearing effect of FA. However, the fluidity of cement-FA paste containing PCE-3 (lower side-chain density) has decreased, when the content of FA was over 20%. The introduction of FA decreased the concentration of cations, such as Ca^{2+} K^{+} (as shown in Table 3), which decreased the cationic strength of solution. Therefore, the interaction between cement/fly ash particle and PCE would be decreased. Meanwhile, the PCE-3 has higher charge density, which may make PCE be more sensitive to the cations' concentration.

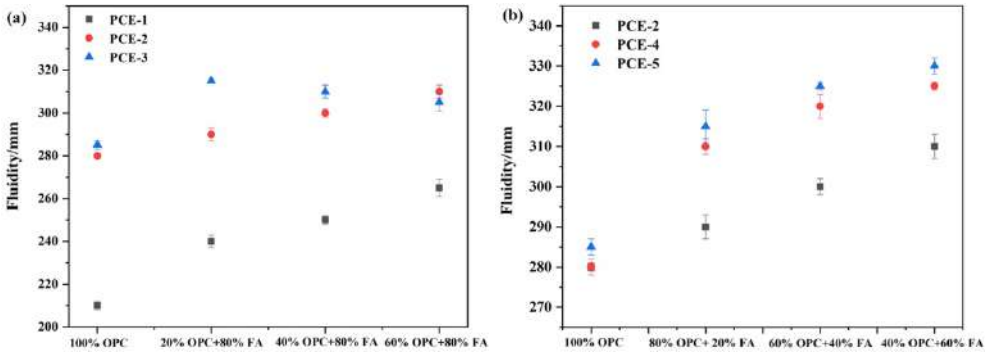


Fig.3 The fludity of cement-FA paste containing PCEs with different density of side chains (a); with different molecular weights (b)

The introduction of FA obviously affected the concentration of cations. Therefore, the influence of the concentration of Ca^{2+} on PCE's dispersing performance, adsorption amount by cement particle and hydrodynamic diameter were tested. From Figure 4a, the fluidity of cement paste was increasing firstly and then decreased with Ca^{2+} concentration increasing. When the introduced molar of Ca^{2+} was 0.9 mmol, the fluidity of cement paste with PCE-3 has decreased 14.04%, but the cement paste containing PCE-1 almost has no change. With the ionic concentration raises, the adsorption amount of PCEs by cement particles has a little increase. More importantly, the R_h of PCE-3 significantly increased, while only a slight increase was observed for PCE-1 and PCE-2. The higher R_h of PCE-3 could be attributed to the bridging effect by Ca^{2+}, which reduced its dispersing efficiency. This result implies that the concentration of Ca^{2+} makes impact on the conformation of PCEs, especially for higher-charge density PCE. Above results indicated that PCE with higher charge density was more sensitive to the concentration of Ca^{2+}.

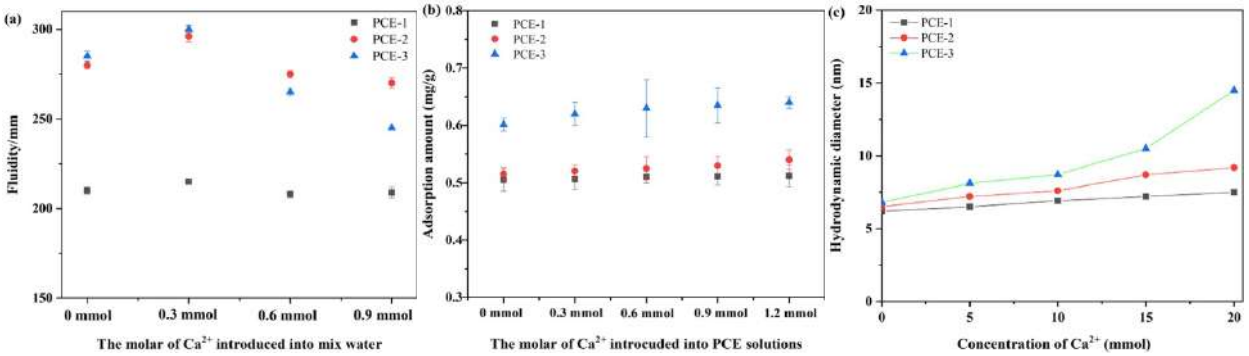


Fig. 4 The fluidity of cement pastes containing PCEs (a); adsorption amount of PCEs by cement particle (b), and hydrodynamic diameter of PCEs (c)

4. Conclusions

- The introduced FA decreased the concentration of Al^{3+}, Ca^{2+}, K^{+}, SO_4^{2-}in pore solution.
- The PCE with higher charge density is more sensitive to the concentration of Ca^{2+}.

Acknowledgements

Thanks for the financial support from the self-supporting projects of State Key Laboratory of Green Building Materials (ZA-81).

References

Kanchanason, V. Plank, J. (2018) "Nucleation and growth of C-S-H - PCE used as strength enhancer in cement", *Am. Concr. Institute,* 67– 75.

Franco, J. M. Schmidt, W. Kühne, H. C. Peixoto, R. A. F. (2020) "Influence of high-charge and low-charge PCE-based superplasticizers on Portland cement pastes containing particle-size designed recycled mineral admixtures". *Journal of Building Engineering*, 32:101515.

Li, B. Wang, L. (2021) "Synthesis and performance of a novel polycarboxylate superplasticizer through grafting the β-cyclodextrin on the side chain by click reaction" *J. Appl. Polym. Sci.* 51524.

Caruso, F. Mantellato, S. Palacios, M. Flatt, R.J. (2017) “ICP-OES method for the characterization of cement pore solutions and their modification by polycarboxylate-based superplasticizers,” *Cement Concr. Res*. 91: 52–60.

The 16th International Congress on the Chemistry of Cement 2023 (ICCC2023)
"Further Reduction of CO_2 -Emissions and Circularity in the Cement and Concrete Industry"
September 18–22, 2023, Bangkok, Thailand

Performance of calcined anthill clay as a supplementary cementitious material

J. O. Ukpata[1*], D. E. Ewa[2], and R. O. Ogirigbo[2]

[1] *Department of Civil Engineering, Cross River University of Technology, Calabar, Nigeria*
Email: joeukpata@unicross.edu.ng
[2] *Cross River State Ministry of Works, Calabar, Nigeria*
Email: desmondewa4sky@gmail.com
[3] *University of Benin, Benin City, Nigeria*
Email: okiemute.ogirigbo@uniben.edu

ABSTRACT

Reduction in the Portland clinker components of binders has been a major part of efforts to improve environmental sustainability, including lowering the high cost of conventional cement production. This study investigates the suitability of incorporating calcined anthill clays (CAHC) in Portland cement. Calcination of the anthill clay was carried out using locally made furnace, which was fired up to 800 ºC temperature. The investigation involved characterization for the physical and chemical properties of anthill clay, determination of fresh properties of blended mortars and mechanical properties of hardened mortar samples, namely: compressive and flexural strengths of mortar samples produced by using different replacement levels of CAHC ranging from 5 to 30%. Water sorptivity of mortar samples was also investigated to understand the durability characteristics of the CAHC-blended mortars. The performance of CAHC mortars were compared with those of conventional Portland cement (CEM I 42.5N). The results show that CAHC-blended binders can be suitably applied with comparable mechanical properties up to 30% replacement in CEM I. The compressive strengths of CEM I mortars ranged from 33.3 to 50.8N/mm2, from 3 to 28 days of age, while CAHC showed compressive strengths ranging from 17.3 to 48.6N/mm2, within the same period, and replacement levels ranging from 5 to 30%. Similar trends were observed for flexural strengths. Also, the sorptivity of CAHC-blended mortars showed lower water absorption rates for blended samples compared with plain Portland cement. The study has shown that local environments can be improved with the useful application of anthill clay soil in cement production.

KEYWORDS: *Anthill. Cement, Binder, Mortar, Performance*

1. Introduction

Conventional Portland cement (OPC) is expensive and have been known to contribute about 7% of anthropogenic carbon dioxide into the atmosphere, leading to worsening climate change effects (Kamau et al. 2018). Besides, housing deficit in Nigeria and most developing countries, due to high cost of building materials such as cements, remains a huge challenge to the building industry (Akanni et al. 2014).

Mounts of anthill soil from the nest of termite are common features around grassland areas, especially where there is high level of compost materials from dead plants. The physical structure of the anthill mount indicates some level of bonding between the particles of soil, as it is hard and difficult to break, particularly when dry. It also exhibits some resistance to abrasion and water penetration is low. Studies have shown that anthills can endure hot daytime tropical temperatures and low night temperatures, including heavy tropical rainfall. The soil is said to be coated with secretions of chemicals indicative of those found in cement, namely: oxides of calcium (CaO), silicon (SiO_2), aluminium $Al2O_3$) and magnesium (MgO) (Kamau et al. 2018, Kipsanai et al. 2017). Understanding the performance of anthill soil in concrete binders will encourage its application, thereby reducing the costs of buildings and other infrastructure development for local communities, where anthills presently constitute a nuisance to the people.

2. Materials and methods

The samples collected from the field were put in clay pots and placed inside a locally made furnace. The furnace was fuelled by natural gas and had a thermometer inserted into it with an external display. The furnace was fired up to 800°C temperature (Sabir, Wild and Bai 2001), for approximately 2 hours to calcine the ant hill soil after which the firing was put out and samples were allowed to cool throughout the night till the next day. Figure 1(a-e) shows the calcination processes.

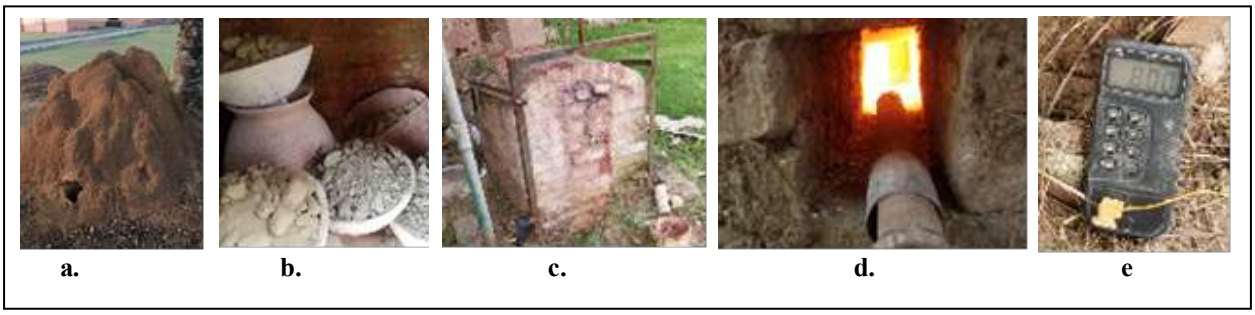


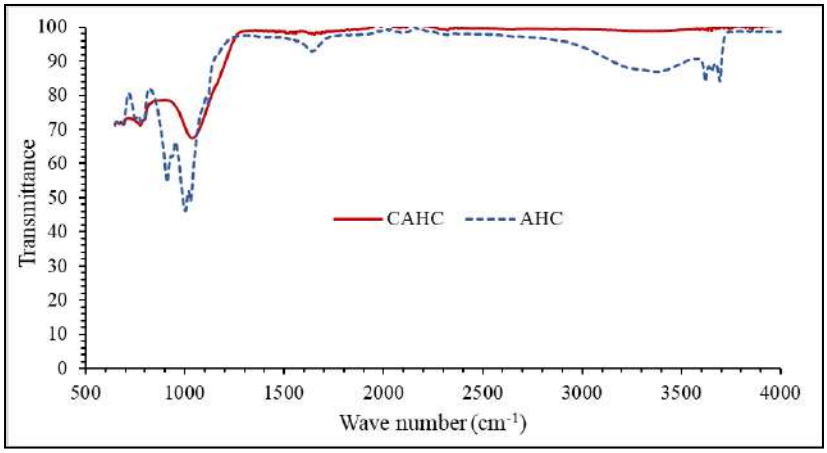
Figure 1. a: Anthill mount, b: Samples inside furnace, c: Closed furnace, d: Furnace fired, c- Thermometer

The calcined samples were then pounded in a local mortar and pestle to have the required fineness used for the experiments. The physical and chemical properties of the calcined anthill soil and control Portland cement are shown in Tables 1 and 2. Oxide compositions were obtained using Xray Fluoresence. Fourier Transform Infrared (FTIR) spectra comparing raw anthill clay soil (AHC) and calcined anthill clay (CAHC) is shown in Figure 2.

Table 1: Physical properties of the binders

Binder	**Residue/ seive size** (in microns)			**Specific Gravity**
	45	**90**	**212**	
OPC 42.5N	7.1	1.0	0.0	3.38
CAHC	91.1	80.9	52.6	2.94

The peaks decreased from 11 to 3 following calcination. Initial and final setting time of pastes were



carried using automatic Vicat Apparatus.

Figure 2. FTIR spectra for calcined (CAHC) and raw anthill soil (AHC)

Table 2: Chemical properties of the binders

OXIDES	**SiO_2**	**Al_2O_3**	**Fe_2O_3**	**CaO**	**MgO**	**SO_3**	**K_2O**	**Na_2O**	**TiO_2**	**LOI**
OPC 42.5N	17.61	4.02	2.94	60.40	2.10	2.22	0.88	0.03	0.22	8.39
CAHC	68.65	13.20	4.06	1.01	0.07	0.25	0.19	-0.16	0.99	4.01

The tests for flexural and compressive strengths of mortars (160x40x40mm) were conducted inline with BS EN 196-1 (2005). Portland cement, grade 42.5N and CEN standard sand were mixed using distilled water in line with. Table 3.

Table 3: Mix Proportions for mortar production

S/N	% Replacement	OPC (g)	CAHC (g)	Standard Sand (g)	Water (g)
1	OPC 42.5 (0%)	450.0	0.0	1350.0	225
2	5%	427.5	22.5	1350.0	225
3	10%	405.0	45.0	1350.0	225
4	30%	315.0	135.0	1350.0	225

Sorptivity test on mortar prisms were conducted after 28 days of curing and additional drying period of 7 days, in line with previous study (Ukpata, Basheer and Black 2019).

3. Results and Discussion

3.1 Setting time

Table 4 shows comparisons between the setting times of Portland cement and CAHC-blended pastes. Setting times delayed with increase in the contents of CAHC in the blended systems, suggesting slow hydration of CAHC. This behaviour is similar to most supplementary cementitious materials (SCMs).

Table 4: Setting times of OPC compared with CAHC-blended binders

Binder	Percentage of replacement	Water Demand (mls)	Consistency (%)	Setting time	
				Initial (mins)	Final (mins)
OPC (42.5N)	0%	138.0	27.6	165.0	220.0
CAHC	5%	137.0	27.4	165.0	225.0
	10%	136.0	27.2	180.0	240.0
	30%	132.0	26.4	230.0	295.0

3.2 Compressive and Flexural Strengths

Figures 3 and 4 show the results of compressive and flexural strengths developments up to 28 days hydration period, also showing the effects of replacements with CACH. With up to 10% replacement of portland cement by CAHC, both compressive and flexural strengths compared favourably with the control OPC. However, significant decrease in strengths were observed when percentage replacement was increased to 30%. Nevertheless, the compressive strengths at 30% replacement were still above 30N/mm^2 from 14days of age, suggesting that 30% replacement was suitable for structural applications (BS 8110-1 1997).

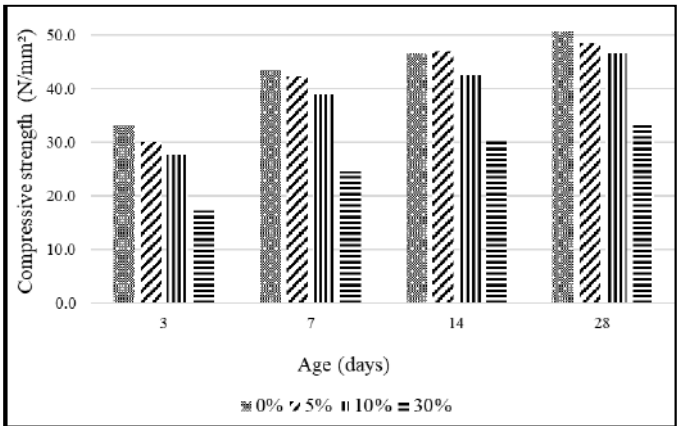


Figure 3. Comparison of compressive strengths at various replacements of CAHC and curing age

A slight difference can be observed between compressive and flexural strengths. Unlike compressive strength, no significant decrease in flexural strength was shown due to the presence of up to 10% of CAHC. This indicates more robustness to flexural than compressive stresses.

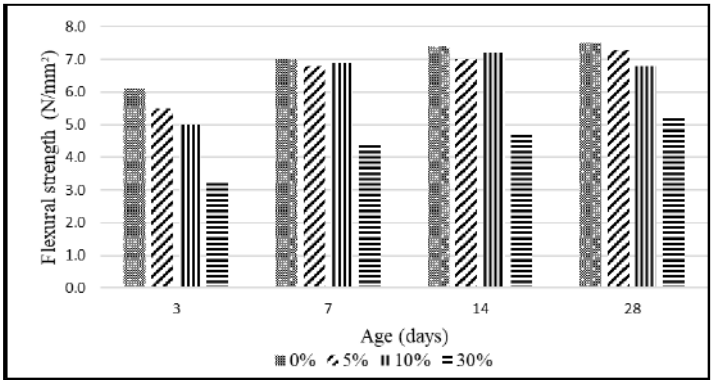


Figure 4. Comparison of flexural strengths at various replacements of CAHC and curing age

3.3. Sorptivity (Rate of water absorption)

The rates of water absorption for different mortar samples are shown in Figure 5. 10% blended mortars showed the lowest rate of water absorption. Generally, the blended systems showed lower rate of water absorption than the control OPC, suggesting a refinement of microstructure, inhibiting water ingress (Frias et al. 2013). This suggests potential for more durable blended systems than plain OPC.

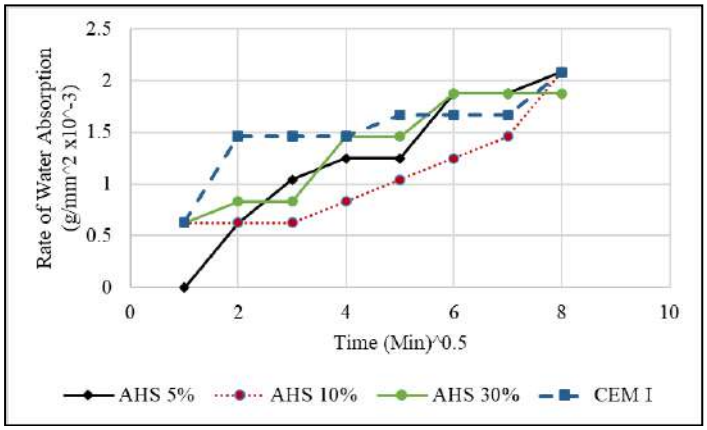


Figure 5. Rate of water absorption for Calcined Anthill Clay (CAHC) and OPC 42.5N (CEM 1) mortars

4. Conclusions

This study has demonstrated the suitability of calcined anthill clay as a supplementary cementitious material, to support the development of low-cost concrete binders from locally available materials. Calcination was achieved with the help of a locally fabricated clay furnace with potential for cost reduction. Calcination temperature was about half of what is used for Portland clinker production with much less energy requirement and tendency for reduced CO_2 contribution to the atmosphere.

Though the presence of CAHC showed longer setting times, suggesting slow early age hydration, the mechanical properties shown by compressive and flexural strengths suggest that the blend can well serve for structural use, while also improving durability characteristics as shown by decreased rate of water absorption.

Acknowledgements
The authors gratefully acknowledge Lafarge Cement for providing the laboratory facilities for this study.

References

Akanni, P. O., A. E. Oke and O. J. Omotilewa. (2014). "Implications of Rising Cost of Building Materials in Lagos State Nigeria." *SAGE Open* 2014:1-7.

BS 8110-1. (1997). "Structural Use of Concrete." Pp. 1-123 in *Part 1: Code of practice for design and construction*, Vol. BS 8110-1. London: BSI.

BS EN 196-1. (2005). "Methods for Testing Cements." in *Part1: Determination of strengths*.

Frias, M., S. Goñi, R. García and R. Vigil de La Villa. (2013). "Seawater Effect on Durability of Ternary Cements. Synergy of Chloride and Sulphate Ions." *Composites. Part B, Engineering* 46:173-78. doi: 10.1016/j.compositesb.2012.09.089.

Kamau, John, Ash Ahmed, Paul Hirst and Joseph Kangwa. (2018). "Suitability of Anthill Soil as a Supplementary Cementitious Material." *European Journal of Engineering Research and Science* 3(7):5-11.

Kipsanai, Janet J., Saul S. Namango and Alex M. Muumbo. (2017). "A Study of Selected Kenyan Anthill Clays for Production of Refractory Materials." *International Journal of Scientific and Research Publications* 7(9):169-79.

Sabir, B. B., S. Wild and J. Bai. (2001). "Metakaolin and Calcined Clays as Pozzolans for Concrete: A Review." *Cement & Concrete Composites* 23(2001):441-54.

Ukpata, Joseph O., P.A. Muhammed Basheer and Leon Black. (2019). "Expansion of Cem I and Slag-Blended Cement Mortars Exposed to Combined Chloride-Sulphate Environments." *Cement and Concrete Research* 123(2019):1-13.

The 16th International Congress on the Chemistry of Cement 2023 (ICCC2023)
"Further Reduction of CO_2 -Emissions and Circularity in the Cement and Concrete Industry"
September 18–22, 2023, Bangkok, Thailand

Reactivity of alternative SCMs from Nordic Countries – Input for the R^3 test

T. Danner[1*], H. Justnes[1], and K.O. Kjellsen[2]

[1] *SINTEF Community, Trondheim, Norway*

Email: tobias.danner@sintef.no, harald.justnes@sintef.no
[2] *Heidelberg Materials Sement Norge AS, Brevik, Norway*

Email: knut.kjellsen@heidelbergmaterials.com

ABSTRACT

About 20 different alternative Nordic SCMs were examined with the aim to be used in future cement products with high clinker replacement. The materials were screened regarding practical production considerations, composition, chemical reactivity, strength development and durability parameters. After the overall assessment natural volcanic pozzolan from Iceland was ranked as the most promising alternative to currently used fly ash. A good correlation between accelerated chemical reactivity test (R^3 bound water) and 28-day strengths in mortars with 20% cement replacement was only found when dividing the tested materials in different material groups. Calcined clays with higher amount of reactive alumina besides reactive silica appeared to achieve much higher values in bound water without increasing 28-day compressive strength compared to other reactive SCMs. The reactivity did not only depend on the amorphous content, but the general chemical composition and crystalline mineral phases present besides the fineness of the materials.

KEYWORDS: *Alternative SCMs, natural pozzolan, pozzolanic reactivity, compressive strength*

1. Introduction

About 2.5% of the total Norwegian CO_2 emissions can be tracked back to the two cement producing plants in Norway. Currently about 15-20% of the Portland clinker are replaced by fly ash in about 80% of the cement produced for the domestic market. For known reasons the long-term supply of fly ash is expected to decrease in Europe, while an even higher clinker replacement will be needed in the future to reach targeted sustainability goals. For this reason, a Norwegian research project was established to screen alternative SCMs for future cements. While in other parts of the world calcined clay is one of the most promising alternatives, Nordic clays are often of inferior reactivity due to high contents of illite, chlorite and/or smectite. Hence, besides calcined clays, natural volcanic materials from Iceland (partly amorphous), industrial by-products like ashes and slags, and other processed rocks like mine tailings (high crystallinity) were investigated.

2. Materials

The alternative SCMs that were investigated can be categorized in 4 different groups:
1) Ashes: different types of bio coal fly ash (Bio) and oil shale ash (T); **2) Calcined clays**: illite (I), smectite (S) and a kaolin reference (K); **3) Volcanic rocks**: rhyolite (R), pumice (P), basalt (B), hyaloclastite (H); **4) Other rock types**: (norite (N), aplite (A), phyllite (Ph). Table 1 shows the chemical composition, amorphous content and d_{50} values of the materials. The main crystalline phases in all materials were typically quartz, feldspars and pyroxenes and mullite in the fly ashes.

Table 1: Chemical composition (XRF), amorphous content (XRD) and d_{50} value for the investigated SCMs

Type	Abbr.	SiO_2	Al_2O_3	Fe_2O_3	CaO (%)	K_2O	Na_2O	MgO	SO_3	Amorph. (%)	d_{50} (µm)
REF	**FA**	55.1	21.6	7.0	5.3	2.1	0.9	2.2	0.2	82	15
	LL	13.2	3.3	1.9	44.4	0.8	0.2	1.7	0.6	n.a.	16
Ash	**Bio1**	46.0	21.8	4.5	10.5	5.6	0.6	2.8	0.7	79	14
	Bio2	56.0	17.8	5.3	8.8	3.4	0.8	3.4	0.5	72	17
	T	34.3	8.2	4.6	31.5	3.7	0.0	4.8	6.3	33	12
Calc. Clay	**I**	62.8	18.5	7.1	0.6	6.3	0.1	2.5	0.1	41	16
	S	49.6	18.1	10.6	14.1	2.4	0.7	2.9	n.d	n.a.	n.a.
	K	62.6	26.6	3.9	0.2	3.7	0.1	0.5	0.0	52	28
Volc. rocks	**P**	65.8	14.8	6.5	3.3	2.0	4.6	0.5	0.0	91	14
	R	60.4	13.8	8.0	4.8	1.6	2.7	2.3	0.0	50	14
	B	47.9	14.7	11.9	12.1	0.3	1.8	8.6	0.1	39	6
	H	47.8	14.4	11.9	11.8	0.3	1.8	9.2	0.1	83	6
Rocks	**N**	43.0	15.5	12.5	6.6	0.9	3.4	6.8	n.d.	0	5
	A	81.7	8.8	0.9	1.0	3.0	2.4	0.1	n.d.	0	7
	Ph	n.a.								n.a.	n.a.

3. Methods

The chemical composition of the materials was determined by XRF on molten glass plates. The amorphous content was determined by QXRD with the external standard method. Particle size distributions were measured with lasergranulometry; materials were immersed in iso-propanol and treated with ultra sound for 1 min. The materials were ground with a ball mill. The chemical reactivity of the SCMs was measured with the R^3 test (Avet et al. 2016) by hydrating pastes for 2 days at either 20 or 40 ºC. Hydration was stopped by solvent exchange and the amount of bound water was measured with thermogravimetry (TGA) as the weight loss between 40-350 ºC. Bound water test was chosen as this might be the easiest method to be implemented in plants without investing in characterization equipment. Mortars were cast with 80% PC (CEM I 52.5R) and 20% SCM and compressive strength tested according to EN 196-1. If necessary, superplasticizer was added to adjust the flow to that of the reference with FA.

4. Results and Discussion

Figure 1 shows the collected results of bound water (R^3 paste) versus the 28-day compressive strength of mortars with 20% replacement of PC. There is a general trend of increasing compressive strength with increased amount of bound water. Still, there is also quite some scatter in the results. The red symbols are the results obtained with the FA reference. It can be seen that there are some materials with high amount of bound water without increasing the compressive strength in mortars. Especially the kaolin clay did increase the amount of bound water without increasing contribution to strength compared to the other most reactive materials, e.g. hyaloclastite, pumice, oil shale ash and the smectite clay (Danner et al. 2018). This shows that care needs to be taken in interpreting R^3 results when mixing several different material groups. A good correlation of the bound water is only achieved when dividing the materials in different material groups, e.g. calcined clays (brown circle). The ashes are shown in the black circle, while the volcanic materials are within the green circle. Fillers (blue circle) do also show one particular outlier which is the limestone filler (black symbol). Due to their high crystallinity, the rock types limestone, norite, applite and phyllite (also calcined phyllite) did act as inert fillers. However, besides not showing any amount of bound water, limestone still gave a good contribution to 28-day compressive strength. The reason might be the surface morphology of limestone providing extra nucleation sites for hydration products (Berodier & Scrivener 2014). Obviously, chemical and mineralogical composition are decisive for the reactivity of a material. Reactivity is often closely related to the amount of amorphous phase content. Still, the chemical composition of the amorphous phase is also important to take into account. The TGA curves of all R^3 pastes are shown in Figure 2. It can be seen that most materials bind

water in form of C-S-H phases (peak around 100 ºC). Ash type materials showed similar behaviour as the volcanic rocks shown in Figure 2 (left). Calcined clays on the other hand, bind a significant amount of water also in AFm phases (200 ºC). The reason is the higher amount of reactive alumina in the amorphous phase content. Besides composition, the fineness of the material can increase the reactivity as it is shown for natural volcanic materials. For other materials like oil shale ash, increased fineness did not increase the reactivity.

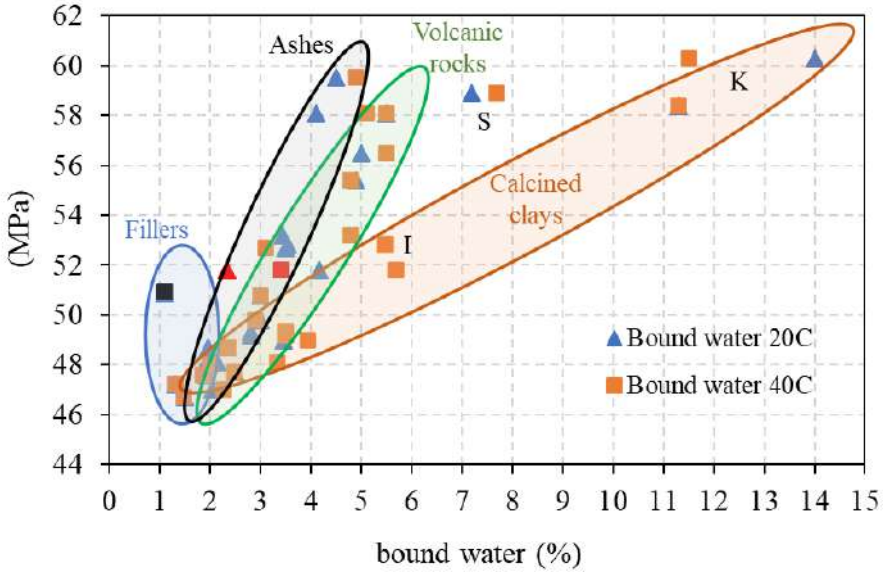


Figure 1: 28-day compressive strength (20% SCM 80% PC) vs. Bound water (R^3). Black: LL; Red: FA

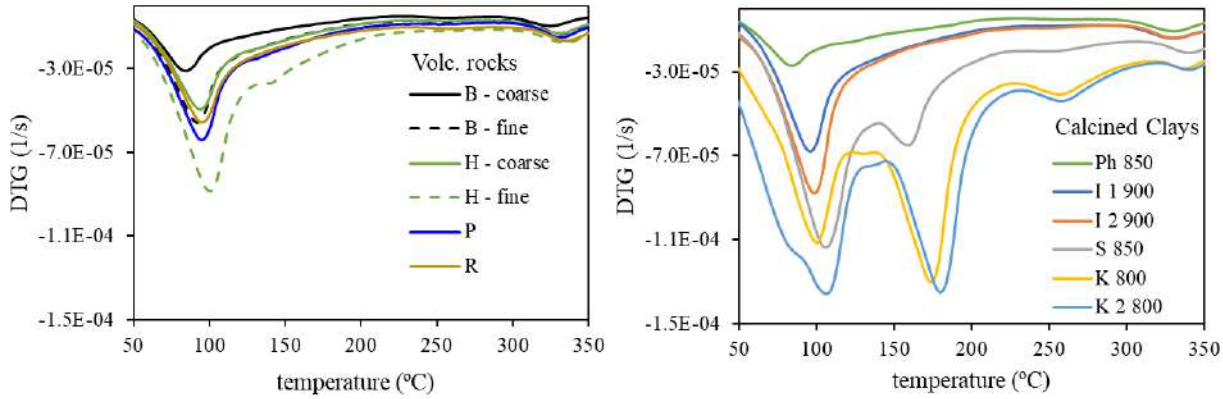


Figure 2: DTG curves of a selection of R^3 pastes covering area of bound water

Another reason for a general scattering of results might be that the hydration of R^3 pastes was stopped at 2 days and with that potentially too early. The amount of bound water is also in relation to the cumulative heat evolved in R^3 pastes. Different materials show different kinetics of reaction. Figure 3 indicates that when comparing different material types, results after 1 or 2 days might give a wrong impression when comparing the reactivity of materials. For calcined kaolin clays a similar relation between clays with different kaolin content was found from 1 day onwards (Avet et al. 2016). However, for different material types, reliable relations might not be obtained before 5-7 days of hydration. Due to some SCMs reacting relatively slowly (e.g. FA), a correlation to 91 day strength might also improve results.

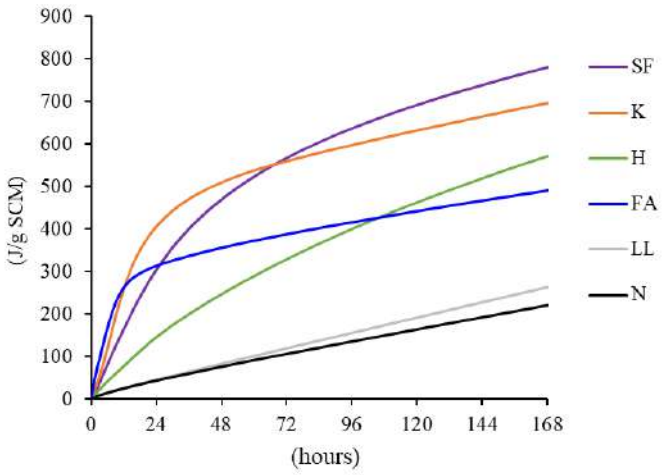


Figure 3: Cumulative heat of R^3 pastes with different SCMs

5. Conclusions

The reactivity of different alternative SCMs available in nordic countries (natural and industrial by products) was investigated. Several materials showed similar or higher reactivity compared to FA. The correlation between amount of bound water and compressive strength was good when dividing the SCMs in different material groups. Care should be taken when interpreting R^3 results of different material types together. Initial isothermal calorimetry is recommended to evaluate the optimum time of stopping hydration if bound water is the preffered test method in practice.

5. Perspective for future nordic cements

Besides reactivity and meachanical properties, durability parameters (carbonation, chloride diffusion, salt-frost scaling and alkali silica reactions) were tested according to current European standards. All SCMs except oil shale ash showed similar or better performance than fly ash. After an overall assessment including practical considerations, natural volcanic pozzolan is curently the most promising alternative SCM to fly ash in future norwegian binders. Recently, a PhD study focusing on hydration and microstructural development in systems with 22% replacement of PC by natural volcanic pozzolan was finished (Zuschlag 2022). In the second phase of the research project clinker replacement levels of up to 50% or more will be investigated and measures to optimize fresh and hardened properties of concrete.

Acknowledgements

The presented research is part of the projects NEWSCEM and ZeroCarbCon, financed by Norcem, the Research Council of Norway (P-Nr.:282578 & 336953). Project partners were NTNU, Heidelberg Materials Global R&D Dept., IBRI, Mapei, Skanska, Cementa, Rambøll, Spenncon, NorBetong.

References

Avet F., Snellings R., Alujas Diaz A. Ben Haha M., Scrivenere K. (2016) " Development of a rapid, relevant and reliable (R3) test method to evaluate the pozzolanic reactivity of calcined kaolinitic clays", Cement and Concrete Research, 85:1-11

Berodier E., Scrivener K. "Understanding the filler effect on the nucleation and growth of C-S-H", Journal of the American Ceramic Society, 97 (12): 3764-3773

Danner T. Norden G. Justnes H. "Characterisation of calcined raw clays suitable as supplementary cementitious materials", Applied Clay Science, 162: 391-402

Zuschlag P. "The impact of curing temperatures on Portland composite cements – hydrate assemblage, porosity, and compressive strength, Doctoral thesis, NTNU, 2022:374

The 16th International Congress on the Chemistry of Cement 2023 (ICCC2023)
"Further Reduction of CO_2 -Emissions and Circularity in the Cement and Concrete Industry"
September 18–22, 2023, Bangkok, Thailand

New Insights on the Use of Sewage Sludge Ashes as Supplementary Cementitious Materials

D. Shehadeh[1*], A. Govin[1], L. Bessette[2], H. Krour[2], G. Zeigler[3], and P. Grosseau[1]

[1] *Mines Saint-Etienne, Univ Lyon, UMR 5307 LGF, Centre SPIN, F-42023 Saint-Etienne, France*
Email : danahshehade@gmail.com, govin@emse.fr, grosseau@emse.fr
[2] *VICAT, 4 rue Aristide Bergès, 38080 L'Isle d'Abeau, France*
Email : laetitia.bessette@vicat.fr, hichem.krour@vicat.fr
[3] *FMI Process, 22 rue de Garat, 42152 L'Horme, France*
Email: gz@fmi-process.com

ABSTRACT

This study explores the feasibility of using sewage sludge ashes (SSA) as a partial substitution for Ordinary Portland Cement in cement-based materials. SSA is a powdery by-product produced from the calcination process of sewage sludge. SSA production is expanding globally and its reuse in various fields has become a significant challenge. A characterization study of SSA was conducted to evaluate SSA effect on cement hydration at different replacement levels (10, 20 and 30wt%), with a constant water-binder ratio of 0.5. Furthermore, mechanical properties and strength activity index (SAI) of the prepared mixes were assessed. The results confirmed the presence of phosphorus, sulfate, lime, and heavy metals in SSA. The modified SSA-cement pastes exhibit a delay in early hydration period. The impact was most significant with 30% substitution rate. A long-term positive effect on mechanical properties of mortars was noticed, with SAI of 86% at 28 days, highlighting the potential of SSA incorporation.

KEYWORDS: *Sewage sludge ash, Portland cement, circular economy, hydration, mechanical properties*

1. Introduction

Sewage sludge (SS) residue coming from waste water treatment has seen a significant increase generated globally. As a result, effective management and sustainable utilization of SS have become crucial to minimize its environmental impact and ensure its safe disposal. Because SS contains a variety of substances that can be potentially harmful, it is often disposed of through incineration which eliminates pathogens, organic matter, odorous substances, and reduces the volume up to 90-95% (Lynn et al (2018)). The incineration process generates a nonhazardous mineral residue known as sewage sludge ash (SSA). SSA is often studied for its potential use in the construction industry, used as a replacement for a binder or as a mineral addition in both mortars and concretes, which helps reduce CO_2 footprints per ton of cement produced. The use of SSA in cementitious composites can also present some challenges, mainly related to the high variability in SSA composition, caused by differences in SS characteristics and incineration conditions, and which might affect the performance of cementitious composites (Lynn et al (2018)). SSA can also contain contaminants such as heavy metals, which can cause environmental and health risks if not properly managed. According to Danish & Ozbakkaloglu (2022), a high percentage of SSA has an adverse effect on their mechanical properties. The aim of this study is to investigate the potential of using SSA as a partial substitution for Ordinary Portland Cement (OPC) in cement-based composites. The work done helped characterizing the properties of SSA and assessing the mechanical properties of cement paste with different rates (10, 20 and 30%) of CEM I substitution by SSA.

2. Materials and methods

The studied SSA originated from the Rhône-Alpes region in France, produced in fluidized bed furnaces at 850°C, by FMI process. The OPC used was a standard CEM I 52.5 R CE CP2 NF with a minimum clinker content of 95%, provided by the company VICAT. The oxide composition and physical properties of the CEM I used are presented in Table 1.

2.1 Characterization of SSA

The Mastersizer 3000 (Malvern Panalytical) was utilized to determine the particle size distribution of the SSA powder under a pressure of 4 bars and a vibration rate of 20% via laser diffraction analysis. The oxide composition was determined using X-Ray Fluorescence spectrometry, and mineralogical content X-Ray diffractometry (Bruker D8-A25) using the internal standard method (ZnO) to quantify the amorphous phase content in the powder. The inorganic element content of SSA was quantified by inductively coupled plasma (ICP-MS, Agilent). R^3 method was done according to Li et al (2018), in order to characterize the pozzolanic behaviour of SSA.

2.2 Characterization of cementitious paste

The hydration of cement pastes with partial substitution of CEM I by SSA was investigated using isothermal calorimetry (TAM air) at 20°C. Cement pastes were prepared with different substitution rates (10%, 20%, and 30% by weight of CEM I), with a water to binder ratio of 0.5 and a mixing duration of 60 seconds. The hydration of water-SSA paste was also studied with W/SSA ratio of 0.9 (due to the high-water demand of SSA). The mechanical properties of the mortars were characterized by calculating the strength activity index (SAI) of specimens prepared with 25 wt% substitution of CEM I by SSA. The mortars were prepared in a 40 mm x 40 mm x 160 mm molds, according to French Standard NF EN 450-1. The compressive strength of the prisms was measured at 1, 2, 7, and 28 days after demolding. Under the same conditions, pure cement pastes with 10, 20 and 30% of substitution rates were prepared and casted in cube molds of 20 mm x 20 mm x 20 mm. Compressive strength tests were conducted on three samples of each specimen at 1, 7, and 28 days, using a loading rate of 50 N/s.

3. Results and discussions

3.1 Characterization of SSA

Table 1 presents the physical properties, chemical composition, and mineralogical composition of SSA. The results indicate that SSA particles are larger than those of cement, and that the high specific surface area of SSA is likely due to its non-uniform morphology, resulting in greater porosity between its elemental particles. The chemical composition and the mineralogical content of SSA, are presented in table 1.

Table 1. Physical properties, oxide and mineralogical composition, and inorganic content of CEM I and SSA.

Physical properties	**Density (g/cm^3)**	**Specific surface area (m^2/g)**	**D_{50} (µm)**
CEMI	3.2	1.9	10.5
SSA	3.0	7.8	23.5

Oxide %	**SiO_2**	**Al_2O_3**	**Fe_2O_3**	**CaO**	**MgO**	**SO_3**	**K_2O**	**Na_2O**	**P_2O_5**	**TiO_2**	**MnO**	**Cl**	**LOI**
CEMI	19.2	4.9	3.7	62.4	2.1	3.8	1.0	0.2	0.1	0.3	0.1	0.05	1.6
SSA	20.0	6.4	15.4	30.8	1.5	5.3	1.3	0.4	10.3	0.6	0.1	0.1	7.6

Phase wt%	**Amorphours**	**Whitlockite**	**Calcite**	**Quartz**	**Hematite**	**Anhydrite**	**Lime**	**Portlandite**
SSA	21.0	23.0	16.0	12.0	11.0	9.0	7.0	2.0

Elements (PPM)	**Cr**	**Mn**	**Cu**	**Zn**	**As**	**Sr**	**Sn**	**Sb**	**Pb**
SSA	223	1762	509	1177	131	377	62	18	133

The results indicate the presence of a fraction of heavy metals originating from the SS, that, if leachable, could have two major impacts: (i) perturbation of the hydration reaction of the composite, and (ii) pollution of the environment by the leaching mechanism of heavy metals into the soil (Lynn et al., 2015). The quantification results obtained by XRD proves the presence of 21% of an amorphous phase of unknown composition. We notice the presence of soluble phases such as anhydrite ($CaSO_4$), portlandite ($Ca(OH)_2$), and lime (CaO), having a possible impact on the hydration reaction after SSA incorporation. The 11.7% quartz (SiO_2) content, inert mineral, originates from the fluidized bed during the incineration process. Whitlockite ($H_{0.8}Ca_{9.1}Mg_{0.6}Fe_{0.4}(PO_4)_7$), poorly soluble, presents the highest percentage of 22.6, containing Ca, Mg, Fe and P elements. The hematite (Fe_2O_3) content in SSA gives a red shade coloring to SSA. The anhydrite ($CaSO_4$) and calcite ($CaCO_3$) content are 8.9 and 9% respectively. While sulfate essential for cement hydration, an excess of sulfate in the cement matrix could hinder the hydration reaction, specifically the transformation of ettringite into monosulfate.

3.2 Hydration of prepared pastes

During the pre-induction period, the dissolution of C_3S releases a significant amount of heat within the first few minutes. As presented in Figure 1a, the control paste exhibits a heat flow of 35.5 mW/g during wetting, whereas the SSA-paste reaches 58 mW/g due to its highly soluble phases (anhydrite and lime). SSA-paste does not contribute significantly to the hydration as there was no detectable heat release over the time (Figure 1a-100%SSA). This finding is consistent with Chen & Poon (2017) research, and with the done R^3 method confirming that the material did not undergo a significant activity on their own. Following that, a low heat flow induction period is observed for cement pastes, before the onset of the second peak. This low heat flow value is 0.8 mW/g at 1.3h for the reference paste, and increases with the incorporation of SSA to reach 1.1 mW/g at 3h with 30% SSA. A more exothermic reaction is noticed due to the dissolution of SSA soluble phases. The extension in the induction period could be due to a lower undersaturation of C_3S in the bulk solution. The end of the induction period is generally linked to the formation of portlandite and the extension could be due to a delay in its formation. The main exothermic peak (end of acceleration period) is mainly attributed to the acceleration rate of CSH nucleation and growth. As the SSA rate in the sample increases, the hydration peak consistently decreases from 4 mW/g (reference) to 2.8 mW/g (30% SSA). On one hand, this is a consequence of the replacement of a portion of CEM I by SSA, resulting a dilution effect. On another hand, the presence of heavy metals in SSA (Table 1) could delay CSH growth. The second peak in the hydration period corresponds to the depletion of sulfate, which leads to the secondary formation of ettringite. The sulfate depletion peak occurs at 12 h in reference and 18 h in the presence of 30%SSA, due to an increase in sulfate content in the cement matrix, and results in additional ettringite precipitation.

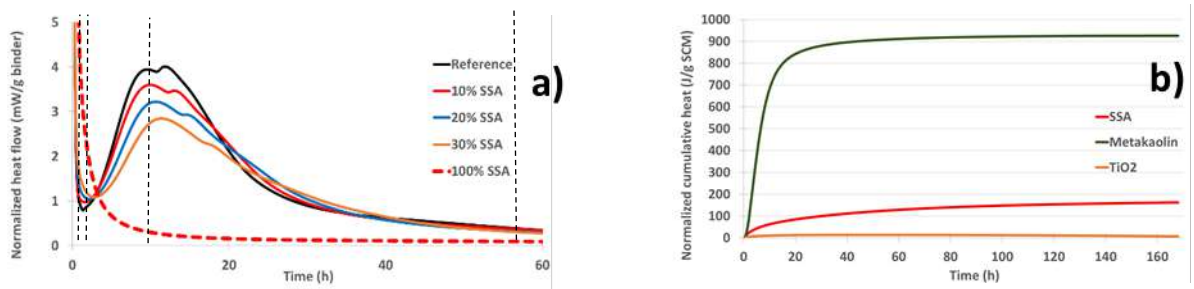


Figure 1. Calorimetry curve of a) 0, 10, 20, 30 and 100% SSA modified paste 20°C, b) R^3 method of SSA 40°C.

3.3 Strength activity index

Figure 2a presents the SAI test outcomes for blended mortars containing 25% SSA, with a 100% OPC sample used as the reference. Mortars containing SSA exhibited a maximum SAI of 86% at 28 days, surpassing 75% which is the minimum requirement imposed by European standards. However, as presented in figure 1b, the R^3 method conducted on SSA showed a low 7d cumulative heat compared to metakaolin (MK, highly reactive SCM) and approaches TiO_2 results (inert material). SSA presents then a low reactivity and have rather a filler effect in the composite. Given these results, several mechanisms could be studied in order to enhance the reactivity and performance of SSA and therefore the early age mechanical strength

such as: thermal or mechanical modification in SSA fabrication process (Oliva et al., 2019), or incorporating other activators (Chang et al., 2020).

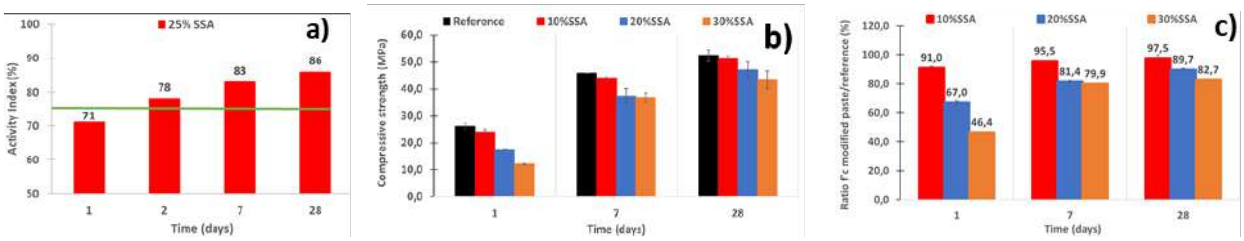


Figure 2. a) SAI, b) Mechanical properties, c) Compressive strength ratio of the SSA-cement paste.

3.4 Compressive strength of cement pastes

Figure 2b illustrates the compressive strength at 1, 7 and 28 days. We notice that at all ages, the increase in SSA incorporation rate decreases the mechanical properties. This is related to the presence of fewer hydrates in the paste, responsible for the compressive strength. The decrease in strength was detected at early ages and even more significant with 30% SSA having a value of 12 MPa against 26 MPa for the reference at 1 day. At 28 days, the compressive strength reaches 43 MPa against 52 MPa for the control. SSA may possess porosity within its particles resulting in a reduction in the mechanical properties. Figure 2c presents the compressive strength ratio of modified cement pastes with respect to the reference. The ratio was low with 30% SSA at 1days (46% against 91% for 10% SSA) but increases to 82.7% at 28 days (against 97.5% for 10% SSA). The results suggest that SSA has better mechanical properties at later age, which is consistent with the SAI test. Despite this loss at early age, the findings are interesting and prove a potential for CEM I substitution by SSA.

4. Conclusion

This study investigates the use of SSA as a partial replacement for OPC. According to the presented experimental results, the presence of heavy metal or soluble phases are factors that affect the hydration mechanism. For 30% SSA incorporation we observe 82.7% in mechanical strength at 28 days, with respect to the reference paste. Overall, the findings of the study demonstrate the potential use of SSA as SCM for developing sustainable building materials, and reducing the environmental impact and carbon footprint of cement production through circular economy practices. However, further studies are to be considered in order to determine the microstructure and hydrates formation, explain the delay observed, assess the durability of concrete samples and evaluate the leaching of heavy metals for SSA-cement composites.

References

Chang, Z., Long, G., Zhou, J. L., & Ma, C. (2020). Valorization of sewage sludge in the fabrication of construction and building materials: A review. In *Resources, Conservation and Recycling* (Vol. 154). Elsevier B.V.

Chen, Z., & Poon, C. S. (2017). Comparative studies on the effects of sewage sludge ash and fly ash on cement hydration and properties of cement mortars. *Construction and Building Materials*, *154*, 791–803.

Danish, A., & Ozbakkaloglu, T. (2022). Greener cementitious composites incorporating sewage sludge ash as cement replacement: A review of progress, potentials, and future prospects. In *Journal of Cleaner Production* (Vol. 371). Elsevier Ltd.

Li, X., Snellings, R., Antoni, M., Alderete, N. M., ben Haha, M., Bishnoi, S., Cizer, Ö., Cyr, M., de Weerdt, K., Dhandapani, Y., Duchesne, J., Haufe, J., Hooton, D., Juenger, M., Kamali-Bernard, S., Kramar, S., Marroccoli, M., Joseph, A. M., Parashar, A., … Scrivener, K. L. (2018). Reactivity tests for supplementary cementitious materials: RILEM TC 267-TRM phase 1. *Materials and Structures/Materiaux et Constructions*, *51*(6).

Lynn, C. J., Dhir, R. K., & Ghataora, G. S. (2018). Environmental impacts of sewage sludge ash in construction: Leaching assessment. *Resources, Conservation and Recycling*, *136*, 306–314.

Lynn, C. J., Dhir, R. K., Ghataora, G. S., & West, R. P. (2015). Sewage sludge ash characteristics and potential for use in concrete. *Construction and Building Materials*, *98*, 767–779.

Oliva, M., Vargas, F., & Lopez, M. (2019). Designing the incineration process for improving the cementitious performance of sewage sludge ash in Portland and blended cement systems. *Journal of Cleaner Production*, *223*, 1029–1041.

The 16th International Congress on the Chemistry of Cement 2023 (ICCC2023)
"Further Reduction of CO_2 -Emissions and Circularity in the Cement and Concrete Industry"
September 18–22, 2023, Bangkok, Thailand

Impact of Ca/Si and Al/Si ratio on the alumina-silica gel formed by wet carbonation of synthesized C-S-H phases

Jiayi Song[1*], Maciej Zajac[2], Mohsen Ben Haha[2] and Jørgen Skibsted[1]

[1] *Department of Chemistry and Interdisciplinary Nanoscience Center (iNANO), Aarhus University, Langelandsgade 140, DK-8000 Aarhus C, Denmark*
E-mail: jiayi_song@chem.au.dk, jskib@chem.au.dk
[2] *Global R&D HeidelbergCement AG, Oberklamweg 2-4, 69181 Leimen, Germany*
E-mail: maciej.zajac@heidelbergcement.com, mohsen.ben.haha@heidelbergcement.com

ABSTRACT

Recent studies have shown that enforced carbonation of recycled concrete fines from end-of-life concrete can bind a substantial amount of CO_2, giving a product with very favorable properties as a supplementary cementitious material in new composite cement. The carbonation products are $CaCO_3$ and an amorphous alumina-silica gel with an unknown alumino-silicate structure, containing different types of $Q^3(n\text{Al})$ ($0 \leq n \leq 3$) and $Q^4(m\text{Al})$ ($0 \leq m \leq 4$) silicate species and aluminum in four-fold coordination as $Al(\text{-O-Si})_4$ sites.

To improve our knowledge on the structure and composition of the amorphous alumina-silica gel, the present work investigates aqueous carbonation of synthesized C-S-H phases where the Ca/Si and Al/Si ratios are varied during the carbonation process by the addition of portlandite ($Ca(OH)_2$) and ettringite ($Ca_6[Al(OH)_6]_2(SO_4)_3 \cdot 26H_2O$). The C-S-H was prepared by hydration of α-$Ca_2SiO_3(OH)_2$ for 28 days using a water/binder ratio of 0.40. The resulting C-S-H was carbonated under aqueous conditions in a 0.25 M Na_2SO_4 solution, using 10 g solid in 150 g solution and a gas composition of 25% CO_2 / 75% N_2 with a flow of 100 L/h. The carbonation process was followed from 10 s to 6 hours, and solid samples at different carbonation times were analyzed by ^{27}Al and ^{29}Si NMR, TGA, XRD, and in-situ pH measurements. It is observed that the overall Ca/Si ratio has only a small effect on the amorphous silica structure. Samples with high Al/Si ratios, obtained by the addition of 20 - 80 wt% ettringite, were also studied after carbonation for 6 hours. The current results show that a high content of Al caused a structural change in the alumina-silica gel and leads to the formation of an alumina gel with Al in octahedral coordination for the carbonated samples containing the highest ettringite content.

KEYWORDS: *Carbonation, alumina-silica gel, C-S-H phases, ettringite, NMR spectroscopy*

1. Introduction

Reduction in CO_2 emissions represents an urgent demand for the cement industry in order to meet society's green economy goals. Several approaches are being developed, where partial replacement of Portland clinkers by supplementary cementitious materials (SCMs) such as fly ashes, slags and calcined clays represent a direct and effective pathway, which attracts significant attention and is widely implemented on the industrial scale (Skibsted and Snellings 2019). Considering the limitations of the traditional SCMs, new SCM materials with comparable or even preferable properties to fly ashes and slags are envisioned. Recent studies show that recycled concrete paste displays favorable properties as an SCM in new composite cements (Zajac et al. 2020a). A significant amount of CO_2 can be bound in recycled concrete paste (~25 g CO_2 per 100 g cement paste) by enforced aqueous carbonation methods (Zajac et al. 2020b). This process transfers the hydrated cement phases into calcium carbonate and an amorphous alumina-silica gel (Lu et al. 2018, Zajac et al. 2021) with an unknown alumino-silicate structure, containing different types of $Q^3(n\text{Al})$ ($0 \leq n \leq 3$) and $Q^4(m\text{Al})$ ($0 \leq m \leq 4$) SiO_4 species and

aluminum in four-fold coordination present as $Al(-O-Si)_4$ sites. To improve our knowledge on the structure and composition of the amorphous alumina-silica gel, the present work investigates aqueous carbonation of synthesized C-S-H phases where the Ca/Si and Al/Si ratios are varied during the carbonation process by the addition of portlandite and ettringite to the reaction blend. The carbonated samples were analyzed by ^{27}Al and ^{29}Si NMR, TGA, and XRD, and in-situ pH measurements were used to follow the carbonation process. The ^{27}Al and ^{29}Si NMR spectra can provide direct structural information about the SiO_4 and AlO_4 environments in the alumina-silica gel, which are analyzed in detail by numerical simulations, giving information about the evolution of the different SiO_4 and AlO_4 species with carbonation time. On the other hand, TGA provides the fractions of $CaCO_3$, $Ca(OH)_2$ and bound water in the samples.

2. Materials and methodology

The synthesized C-S-H phase, used for aqueous carbonation, is produced by hydration of a highly reactive multiphase binder of x-belite (Figure 1), which is achieved by annealing of alpha-dicalcium silicate hydrate (α-$Ca_2SiO_3(OH)_2$: α-C_2SH), following an earlier reported recipé (Link et al. 2015). The basic structure for α-C_2SH and x-belite have been confirmed by XRD (not shown). For the last step of the synthesis, the hydration gives samples with a degree of hydration of 89%, mainly consisting of C-S-H, as determined by TGA and ^{29}Si NMR.

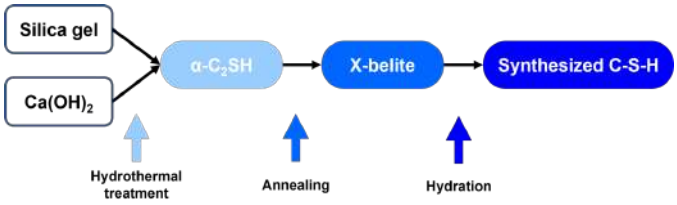


Figure 1: Process for the synthesis of the C-S-H phase.

The synthesized C-S-H samples were carbonated under enforced aqueous conditions along with additions of 20 wt% portlandite (sample denoted CSH-CH) or 20 - 80 wt% ettringite (denoted as CSH-XEtt) to achieve different Ca/Si and Al/Si ratios for the suspension in the carbonation reactor. The carbonation experiments used an earlier developed setup (Zajac et al. 2020b) and the following conditions: (*i*) 25% vol CO_2/75% vol N_2 gas blend, (*ii*) a flow of 100 L/h flow through the suspension, (*iii*) a starting solution of 0.25 M Na_2SO_4, (*iv*) 10 g solid in 150 g solution, and (*v*) 20°C for a maximum of 6 hours.

3. Results

3.1 Impact of Ca/Si ratio

The ^{29}Si NMR spectra following the carbonation of the pure C-S-H phase without and with portlandite addition are shown in Figure 2. The initial molar Ca/Si ratio of the C-S-H sample before carbonation was calculated to 1.72, according to a XRF measurement, whereas the Ca/Si ratio of the CSH-CH sample is 2.58. The evolution of the spectra reveals that the silicate chains of the C-S-H phase (Q^1 and Q^2 silicate species) are consumed and transfer in to broadened resonances from Q^3 and Q^4 sites at prolonged CO_2 exposure time. The Q^2/Q^1 ratio increases with increasing carbonation time as well as at a higher Ca/Si ratio during the carbonation process, reflecting a gradual decalcification of the C-S-H phase. The system with high Ca/Si reaches full decomposition of the C-S-H phase at 1 hour, which is earlier than for the pure C-S-H phase. After 2 and 6 hours of carbonation, no significant differences are clearly apparent in the spectra, indicating that the change in Ca/Si ratio has a limited impact on the final structure and composition of the amorphous silica gel.

The evolution of the fractions of Q^0 - Q^4 sites for the two series of ^{29}Si NMR spectra is shown in Figure 3 as a function of carbonation time. It can be clearly seen that the amorphous silica phase consisting of Q^3 and Q^4 silicate tetrahedra is formed earlier in the CSH series as compared to the CSH-CH samples. This observation suggests that the decomposition of the C-S-H phase is retarded by the increase of the Ca/Si

ratio for the overall system. This is in agreement with the fact that portlandite carbonates readily and preferentially, prior to the C-S-H in mixtures of the two phases. This reflects that the reaction between portlandite and aqueous CO_2 is an acid - base neutralization, which is more direct than the two-step decomposition of the C-S-H phase upon carbonation.

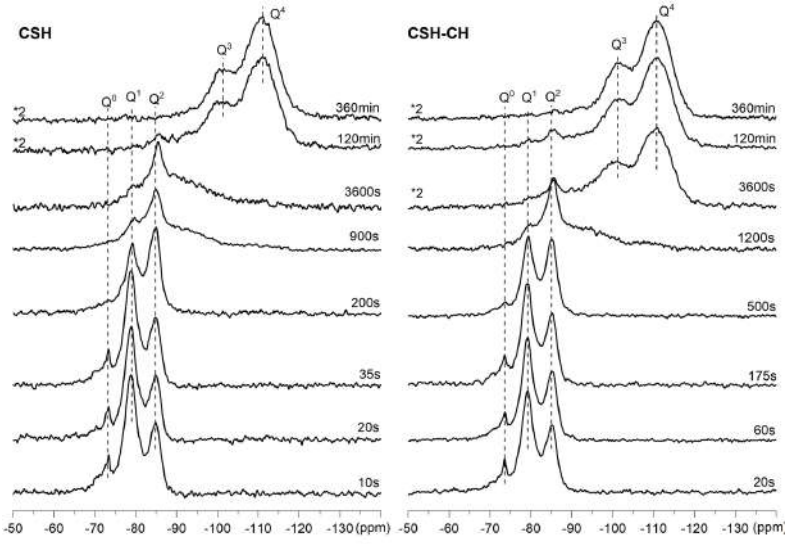


Figure 2: ^{29}Si NMR spectra (9.4 T, spinning frequency of 10.0 kHz) of the pure C-S-H (CSH) and C-S-H/portlandite (CSH-CH) samples carbonated for up to 360 minutes. Q^0 denotes an impurity from the anhydrous alpha-dicalcium silicate hydrate, Q^1 and Q^2 refer to the silicate sites from the C-S-H phase, and Q^3, and Q^4 relate to the condensed silica gel formed up on carbonation.

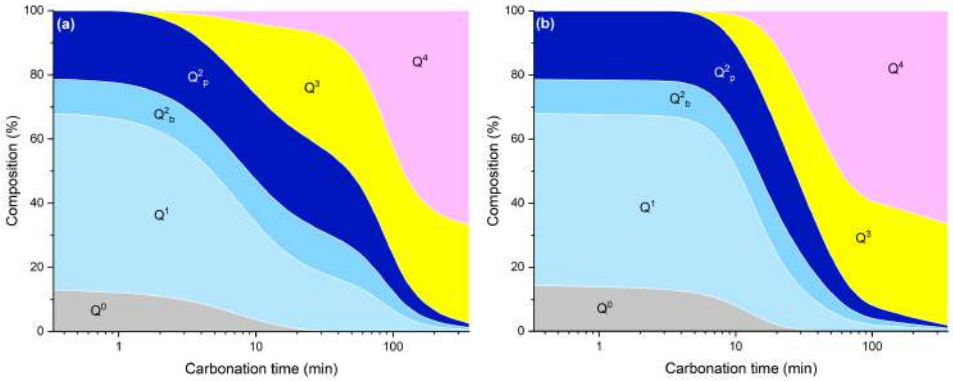


Figure 3: Fractions of Q^0 – Q^4 silicate intensities obtained by deconvolution of the ^{29}Si NMR spectra of (a) pure C-S-H and (b) a mixture of C-S-H and portlandite as a function of carbonation time.

3.2 Varying Al/Si ratio impact

Figure 4 shows the ^{29}Si and ^{27}Al NMR spectra of the carbonated pure C-S-H phase partially replaced by 0 - 80 wt% of ettringite after 6 hours of carbonation. The ^{27}Al NMR spectra show that ettringite has been fully carbonated for all samples. The carbonation of the C-S-H phase is strongly affected by the presence of ettringite, as the ^{29}Si NMR spectra for ettringite contents of 40 wt% and above show an intermediate state with a mixture of decomposed C-S-H phase and an amorphous alumina-silica gel. A full decomposition of the C-S-H phase is only observed for the 20 wt% replacement by ettringite. This indicates that ettringite has priority to the C-S-H phase in the sequence of carbonation in such blends. Moreover, the ^{27}Al NMR spectra reveal a shift of the Al(IV) resonance for the alumina-silica gel by 4 ppm from 20 wt% to 80 wt% ettringite as well as the presence of five-fold Al in the sample with the highest ettringite content. In analogy to ^{27}Al NMR studies of alumino-silicate glasses, this may reflect that Al replaces some tetrahedral silica sites, forming Si-O-Al(IV) linkages, and that the resonance shifts to a higher

frequency when the number of Si-O-Al(IV) linkage increases. Finally, it is noted that the CSH-XEtt samples (Figure 4) show slower kinetics for the carbonation process for higher ettringite contents, as compared to the carbonation of the pure C-S-H sample (Figure 2), as the presence of an alumina gel incorporating octahedral Al only.

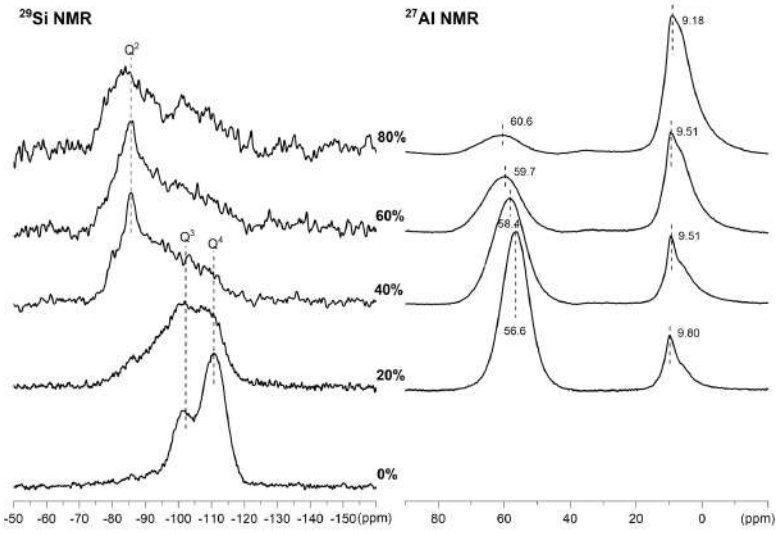


Figure 4: ^{29}Si NMR spectra (9.4 T, 10.0 kHz spinning frequency) and ^{27}Al NMR spectra (14.1 T, 13.0 kHz spinning frequency) of the carbonated C-S-H phase with different proportions of ettringite (CSH-XEtt). The values (0% - 80%) show the weight proportion of ettringite. The numbers on the ^{27}Al NMR spectra denote peak positions.

3. Conclusions

The carbonation of different C-S-H phases with varying Ca/Si and Al/Si ratios has been studied in this work. The change of the Ca/Si ratio for the overall system only has minor effects on the structure and composition of the amorphous silica gel whereas significant effects are observed when the Al/Si ratio is increased. The C-S-H phase, in the presence of a high Al content from ettringite, displays a significantly hindered carbonation process. Moreover, a shift by 4 ppm for the Al(IV) resonance from the alumina-silica gel is observed with increasing ettringite content and in addition, indications of a separate aluminate gel including six-fold coordinated Al sites only seen in the ^{27}Al NMR spectra.

Acknowledgements

J. Song and J. Skibsted acknowledge Heidelberg Materials, Leimen, Germany, for financial support to this research project.

References

Link, T., Bellmann, F., Ludwig, H. M., Ben Haha, M. (2015) "Reactivity and Phase Composition of Ca_2SiO_4 Binders Made by Annealing of Alpha-Dicalcium Silicate Hydrate", *Cement and Concrete Research*, 67: 131-37.

Lu, B., Shi, C., Zhang, J., Wang, J. (2018) "Effects of Carbonated Hardened Cement Paste Powder on Hydration and Microstructure of Portland Cement". *Construction and Building Materials*, 186 (October): 699-708.

Skibsted, J., Snellings, R. (2019) "Reactivity of Supplementary Cementitious Materials (SCMs) in Cement Blends", *Cement and Concrete Research*, 124 (October): 105799.

Zajac, M., Skocek, J., Durdzinski, P., Bullerjahn, F, Skibsted, J., Ben Haha, M. (2020a) "Effect of carbonated cement paste on composite cement hydration and performance", *Cement and Concrete Research*, 134 (October): 106090.

Zajac, M., Skibsted, J. Durdzinski, P., Bullerjahn, F., Skocek, J., Ben Haha, M. (2020b) "Kinetics of Enforced Carbonation of Cement Paste", *Cement and Concrete Research*, 131 (May): 106013.

Zajac, M., Skibsted, J., Ben Haha, M. (2021) "Effect of Alkalis on Enforced Carbonation of Cement Paste: Mechanism of Reaction", *Journal of the American Ceramic Society*, 104 (2): 1076-87.

The 16th International Congress on the Chemistry of Cement 2023 (ICCC2023)
"Further Reduction of CO_2 -Emissions and Circularity in the Cement and Concrete Industry"
September 18–22, 2023, Bangkok, Thailand

About The Effect Of Portland Cement Activation On Supersulfated Cements Properties

L. André[1,2*], C. Bacquie[1,2], T. Wattez[1,2], C. Patapy[1,3] and M. Cyr[1,3]

[1] *ORISON LabCom, Université de Toulouse, UPS, INSA, Toulouse, France*

[2] *ECOCEM Materials Ltd., Paris, France*

Email: landre@ecocem.ie

Email: cbacquie@ecocem.ie

Email: twattez@ecocem.ie

[3] *LMDC, Université de Toulouse, UPS, INSA, Toulouse, France*

Email: patapy@insa-toulouse.fr

Email: cyr@insa-toulouse.fr

ABSTRACT

Supersulfated cements (SSC) were first discovered more than hundred years ago, but were abandoned after the 70's. Nowadays, this technology is experiencing a new boom, due to its durability towards sulfate attacks and to its ultra-low carbon footprint. These cements are composed of ground granulated blast-furnace slag (GGBS), calcium sulfate, and less than 5% Portland clinker (PC) according to the European standard. However, despite numerous studies on this subject, the role of PC content on the hydration of SSCs is still not well controlled and understood. As PC content increases, nonlinear and sometimes pessimum effects are observed for strength development in the short- and long-terms.
In this study, the effect of PC content variation is assessed with GGBS from various origins. It is shown that the optimized PC content for strength development is dependent on GGBS chemistry. Slight variations of PC content can lead to either optimum or pessimum of activation. With some GGBS sources, a 0.5%wt. increase of PC could lead to a 50% diminution of compressive strength of SSC at 28 days. Variations of mechanical strength cannot be correlated to hydration heat alone. Water accessible porosity and hydrates formation are also assessed to try to understand these phenomena.

KEYWORDS: *Supersulfated cement, activation, hydration, isothermal calorimetry, porosity*

1. Introduction

Supersulfated cement (SSC) technology is described in the European standard EN 15743-1+A1 (AFNOR (2015)), where it must contain at least 75%wt. of ground granulated blast-furnace slag (GGBS), between 5 and 20%wt. of calcium sulfate, and less than 5%wt of Portland clinker. Despite this normative definition, the formulation principles detailed in the literature are often empirical and the effect of each component is sometimes unclear. While the calcium sulfate content as well as the GGBS nature have been more carefully evaluated (e.g. Gruskovnjak et al (2008), Angulski da Luz and Hooton (2019)), the impact of the Portland cement activator is still under debate. The nature and content of activators have been studied by several authors, with sometimes contradictory observations. Bijen and Niel (1981) found that increasing clinker content from 2 to 5%wt. led to loss of strength while Baux et al (2014), showed the opposite. Angulski da Luz and Hooton (2019) found out that, with one GGBS source, increasing the activator content (KOH) led to better results, but it was the opposite with a second source. Kondo et al (1980) and Rubert et al (2018) also showed the high sensitivity of SSC to non-Portland activator content ($Ca(OH)_2$ and KOH respectively). Unfortunately, all these authors often performed only few activator content variations, on few different

GGBS sources. Thus, it remains difficult to analyse the role of activator and how SSC should be formulated to optimize its strength development.
This study aims to show the sensitivity of SSC to OPC dosage, with 8 different clinker contents and 3 GGBS of different origins. A methodology is proposed, by comparing compressive strength, isothermal calorimetry, hydrates formation and water accessible porosity.

2. Materials & Methods

Table 1 presents main characteristics of the materials used in this study. Three granulated slag sources were used. Source A was milled in two different ways: industrially with a vertical mill and in laboratory with a ball mill to have the comparison with other sources. The activation of SSC was realized with an ordinary Portland cement (OPC), and natural anhydrite served as a calcium sulfate source (Cs). All SSC were formulated by keeping a constant GGBS/Cs ratio equals to 7.33.

Table 1: Materials properties

	physical properties		Chemical composition (%wt)									
	grinding	d50 (µm)	CaO	SiO_2	Al_2O_3	Fe_2O_3	MgO	TiO_2	Na_2O	K_2O	SO_3	LoI
GGBS - A1	Vertical Mill	10.1	43.1	37.5	10.0	0.4	6.6	0.6	0.2	0.4	0.9	-
GGBS - A2	Ball Mill	5.5	42.9	36.9	10.6	0.4	6.8	0.6	0.3	0.4	1.0	-
GGBS - B	Ball Mill	4.7	42.2	33.9	14.6	0.9	6.0	0.5	0.2	0.3	1.1	-
GGBS - C	Ball Mill	5.4	35.7	36.4	18.1	1.0	6.1	0.6	0.3	0.4	0.9	-
OPC	-	10.4	63.4	20.4	3.8	3.0	1.5	0.2	0.2	0.9	3.2	1.2
Anhydrite	-	7.9	37.9	4.3	0.0	0.4	2.1	0.0	0.2	0.4	40.8	0.6

Compressive strength of SSC was either realized on mortars, (cured at 20°C, under water after 24h according to EN 196-1 standard), or on cement pastes (with 6 cubes of dimensions 2cm x 2cm x 2cm, per age of test). All pastes were cast with a water-to-binder ratio of 0.40 and cured at 20°C in autogenous conditions until tested. Hydration heat was followed by isothermal calorimetry. X-Ray diffraction (XRD) was performed at 28 days after hydration was stopped by solvent exchange. SSC dry powder was mixed with ~5%wt. of fluorite as internal calibration standard for Rietveld refinement. Water accessible porosity was estimated on paste, using a protocol consisting in drying at 50°C, after imbibition under vacuum.

3. Results

Figure 1 presents the influence of OPC content on SSC mortars' compressive strength at 1, 7 and 28 days, depending on GGBS source. For GGBS A, it appeared that the best OPC content to optimize both 1- and 28-days strength was around 0.25 to 0.5%wt. A pessimum phenomenon emerged for an OPC content of

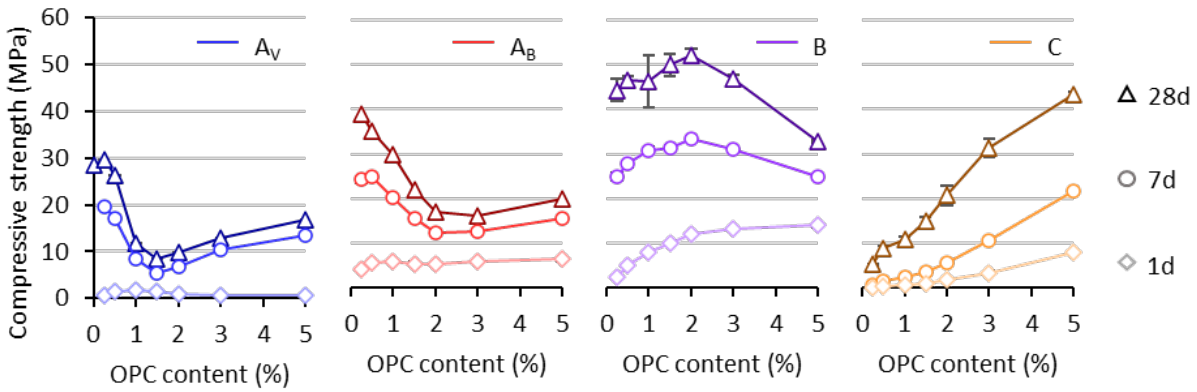


Figure 1: Compressive strength on standardized mortars of SSC at 1, 7 and 28d, depending on the GGBS source and OPC content in their formulation

1.5 to 2%wt. While grinding method had an impact on absolute strength development (A_B>A_V) at all curing ages, it had little to no consequence on OPC optimal content. GGBS B led to high strength due to its high Al_2O_3 and CaO content and presented an optimum effect for 2%wt. OPC. With GGBS C, considering the limits of formulation set by the standard, 5%wt. of OPC led to the best results. For the three GGBS tested, a linear correlation appeared between the optimal OPC content that would maximize long term strength and the Al_2O_3/CaO ratio of the GGBS.

Complementary analyses to understand the role of OPC on SSC hydration were only realized on GGBS A_V for the moment.

Figure 2a shows the normalized heat flow of SSC pastes made with GGBS Av and variable OPC content. OPC content influenced the duration of induction period, the evolution of the hydration heat flow, and the time of appearance and value of maximum heat release. Increasing the OPC from 0.5 to 2%wt. extended the induction period, leading to a delayed maximum, single, heat flow peak. However, with 5%wt. OPC, at least 2 main peaks of hydration were visible. Without any OPC, SSC hydration started after 96h or later in some repetition trials.

Figure 2b presents the corresponding 7-day compressive strength plotted in function of the heat of hydration. Represented linear trend line do not consider the point without OPC as confidence interval on heat of hydration was too important. As revealed by the low R^2 value, despite a general tendency linking strength with hydration heat, it did not explain the zone where a small change of OPC content led to the largest loss in strength development (from 0.25 to 1.5%wt).

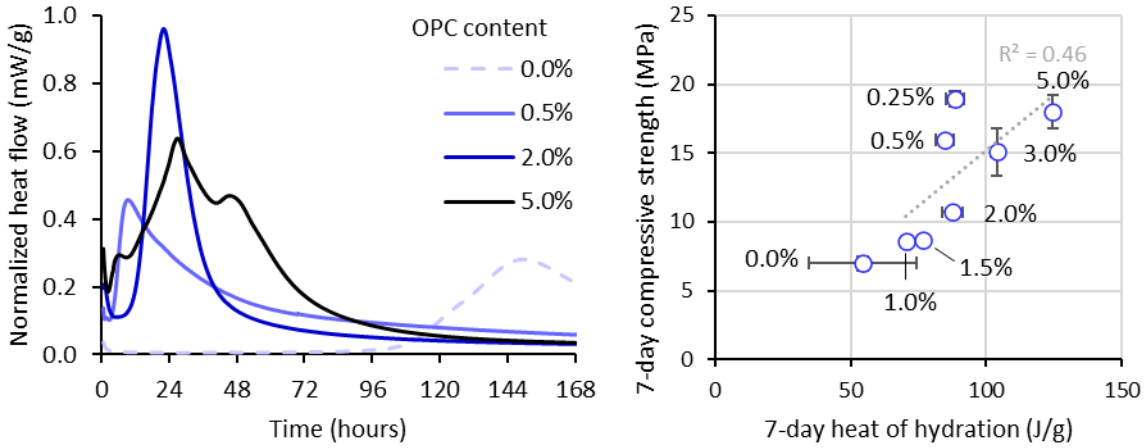


Figure 2: a) Normalized heat flow of SSC pastes made with GGBS A_v and variable OPC content and b) corresponding 7-day compressive strength plotted in function of the heat of hydration – indexed numbers corresponds to the OPC content

Figure 3 presents the XRD patterns obtained after 28days of hydration of SSC paste made with GGBS A_v and various OPC contents. Diagrams were truncated in intensity so that all the hydrates are visible without being overwhelmed by the larger anhydrite and fluorite (used as reference) peaks. It was observed that these SSCs still contained unreacted anhydrite, and small gypsum content (coming from anhydrite surface hydration). Unsurprisingly, main crystallized hydrate was ettringite, but a poorly crystallized tobermorite like C-(A)-S-H phase could also be identified around 29° (Grangeon et al. (2016)). No modification in hydrates nature was identified for different OPC contents. However, ettringite production appeared to be positively correlated with the OPC dosage in SSC. After a Rietveld refinement, ettringite content was found to be around 5%wt. in all mixes with an OPC content below 1%, and 9%wt. for the SSC paste made with 5%wt. OPC (also correlated with a diminution of anhydrite).

Figure 4 shows the 28-day compressive strength of SSC pastes made with GGBS A_V, versus estimated water accessible porosity. This porosity was calculated after drying the samples at 50°C until mass stabilization, instead of 105°C as usually recommended (to avoid ettringite deterioration). Obviously, this method tends to reduce the calculated porosity since part of the smallest pores are not emptied at such a low temperature. If the 5%wt. of OPC point is set aside, it was observed that compressive strength was well correlated with SSC porosity at 28 days.

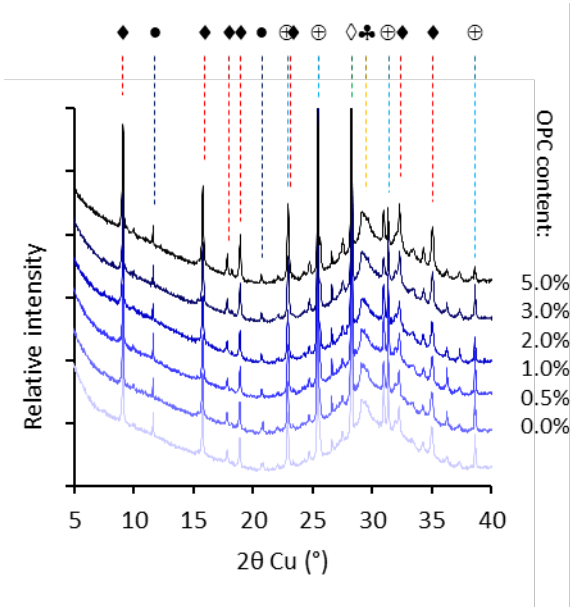


Figure 3: XRD of hydrated SSC pastes made with GGBS Av and variable OPC content after 28 days – mineral phases are illustrated as follows: ⊕ Anhydrite ♦ Ettringite ◊ Fluorite • Gypsum ♣ Tobermorite

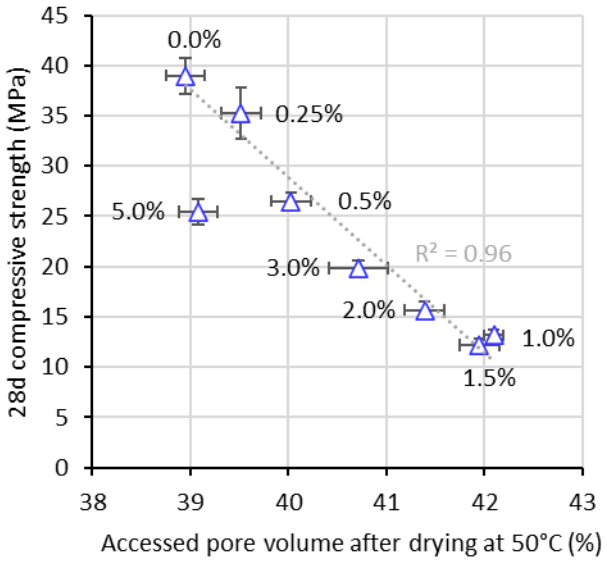


Figure 4: 28-day compressive strength of SSC pastes made with GGBS A_v and variable OPC content plotted in function of the water accessible porosity estimated after drying the samples at 50°C

4. Conclusions

Several conclusions were drawn from this study:

- The optimal OPC content to maximize SSC compressive strength was highly dependent on GGBS source. The chemical composition could have a preponderant influence.
- For a given GGBS, increasing OPC above 1% led to more ettringite formation. However, cumulative heat (associated to hydration rate) was not well correlated to compressive strength development. Thus, it would seem the degree of hydration alone could not explain why a major loss of strength can appear for a slight OPC variation.
- Strength was mostly driven by porosity development. It would suggest that along hydration of GGBS, formation of ettringite in the paste structure could be the main factor influencing its porosity. More in-depth analyses, realized on several GGBS sources, would be required to precise this phenomenon.

References

AFNOR (2016) "NF EN 196-1, Methods of testing cement - Part 1: Determination of strength"

AFNOR (2015) "NF EN 15743-1+A1, Supersulfated cement - Composition, specifications and conformity criteria"

Angulski da Luz C. and Hooton R. D. (2019) "Influence of Supersulfated Cement Composition on Hydration Process" *Journal of Materials in Civil Engineering*, 31: 1–6.

Baux, C., Phelipot-Mardelé, A., Lanos, C. and Pierre, A. (2014) "Mechanical performances of super sulfated cements" *Key Engineering Materials*, 617: 32-35

Bijen, J. and Niël, E. (1981) "Supersulphated cement from blastfurnace slag and chemical gypsum available in the Nerherlands and neighbouring countries" *Cement and Concrete Research*, 11: 307–322

Grangeon, S., Claret, F., Roosz, C., Sato, T., Gaboreau, S. and Linard, Y. (2016) "Structure of nanocrystalline calcium silicate hydrates: insights from X-ray diffraction, synchrotron X-ray absorption and nuclear magnetic resonance" *Journal of Applied Crystallography*, 49: 771–783

Gruskovnjak, A., Lothenbach, B., Winnefeld, F., Figi, R., Ko, S.-C., Adler, M. and Mäder, U. (2008) "Hydration mechanisms of super sulphated slag cement" *Cement and Concrete Research*, 38: 983–992.

Kondo, R., Daimon, M., Song, C.-T. and Jinawath, S. (1980) "Effect of Lime on the Hydration of Supersulfated Slag Cement" *American Ceramic Society Bulletin*, 59: 848–851.

Rubert, S., Angulski da Luz, C., F. Varela, M.V., Pereira Filho, J.I. and Hooton, R.D. (2018) "Hydration mechanisms of supersulfated cement" *Journal of Thermal Analysis and Calorimetry*, 134: 971–980.

The 16th International Congress on the Chemistry of Cement 2023 (ICCC2023)
"Further Reduction of CO_2 -Emissions and Circularity in the Cement and Concrete Industry"
September 18–22, 2023, Bangkok, Thailand

Determining the reaction kinetics of supplementary cementitious materials for input into thermodynamic-kinetic models

T. Zhu[1], O.B. Isgor[2], M.C.G. Juenger[3*], and L.E. Katz[4]

[1] *University of Texas at Austin, Austin, Texas, USA*
Email: tongren@utexas.edu

[2] *Oregon State University, Corvallis, Oregon, USA*
Email: Burkan.Isgor@oregonstate.edu

[3] *University of Texas at Austin, Austin, Texas, USA*
Email: mjuenger@mail.utexas.edu

[4] *University of Texas at Austin, Austin, Texas, USA*
Email: lynnkatz@mail.utexas.edu

ABSTRACT

Thermodynamic simulation is a powerful tool to predict hydrated cement phase assemblages; however, the reaction kinetics of specific components in SCMs are generally unknown, impeding accurate incorporation of SCMs into thermodynamic-kinetic calculations. This study measured elemental contributions from SCMs in simulated pore solutions and tracked selective dissolution of SCMs in cement pastes over time. SCM dissolution rates in the dilute systems were matched to the dissolution rates in the pastes, allowing a realistic temporal representation of elements contributed to the pore solution from the dissolving SCMs. A modified Parrot-Killoh model was fit to the data to obtain empirical kinetic parameters. The empirical kinetic parameters can be used to model the reaction kinetics of OPC-SCM pastes, providing inputs for thermodynamic-kinetic simulations.

KEYWORDS: *thermodynamic modeling; supplementary cementitious materials; dissolution kinetics*

1. Introduction

Strategic blending of supplementary cementitious materials (SCMs) into ordinary portland cement (OPC) helps reduce greenhouse gas emissions from concrete production (Juenger *et al.* 2019). Thermodynamic simulation is powerful in predicting hydrated phase assemblages in OPC-SCM systems, facilitating the prediction of properties of SCM-containing concrete. However, the reaction kinetics of specific components in SCMs are generally unknown, impeding accurate incorporation of SCMs into thermodynamic-kinetic simulations. Prior work on thermodynamic-kinetic simulations with SCMs used degree of reaction data from literature studies that used selective dissolution, nuclear magnetic resonance, and scanning electron microscopy with energy dispersive X-ray spectroscopy analysis (Glosser *et al.* 2020a; Glosser *et al.* 2020b). The obtained results were then used to obtain kinetic parameters for oxide components in SCMs in a modified Parrot-Killoh (MPK) model. In this study, an experimental method based on coupling results from SCM dissolution in simulated cement pore solution (Aughenbaugh *et al.* 2013; Snellings 2013) and selective dissolution of hydrated OPC-SCM pastes (Haha *et al.* 2010, Luke and Glasser 1987) was evaluated as an approach to obtain the contribution of elements from SCMs to cement paste pore solution over time. These results are used to obtain the kinetic parameters for the MPK model for the soluble elements in the SCMs and compared with the parameters obtained with other empirical approaches in the literature. The proposed approach is intended to provide a practical and efficient way to predict the MPK parameters.

2. Materials and Methods

Although the methodology used in this study is applicable to all SCMs, this paper focuses on obtaining empirical kinetic parameters of soluble components of calcined clay. X-ray fluorescence was used to measure oxide composition of the calcined clay, and quantitative x-ray diffraction with Rietveld analysis was used to quantify all crystalline phases. The composition of the amorphous phase was determined by comparing the crystalline composition with the oxide composition. Particle size analysis was determined by laser diffraction. The following steps are summarized below.

Step 1: The contribution of elements to pore solution by the calcined clay was determined by its dissolution in a simulated pore solution (0.3 N NaOH and liquid to solid ratio of 1000) in conventional batch reactors. Concentrations of dissolved metals (Al, Ca, Fe, K, Mg, and Si) from calcined clay were measured over a period of up to 28 days along with total mass loss of the materials after dissolution.

Step 2: The kinetics of calcined clay dissolution was assessed using experiments on pastes through a selective dissolution procedure. Pastes were prepared using OPC with 20% replacement of calcined clay using a water/binder ratio of 0.5. The prepared pastes were cured in a fog room for up to 90 days. To obtain reactivity at a certain time, paste samples were taken out of the fog room to stop hydration. The dried paste samples were then crushed and sieved before undergoing selective dissolution in EDTA/NaOH (Ben Haha *et al.* 2010, Luke and Glasser 1987). The change in mass of the sieved hydration products before and after the dissolution process was used to determine the degree of reaction of the calcined clay.

Step 3: The results from Steps 1 and 2 were used as inputs to obtain the coefficients used in the MPK model for thermodynamic-kinetic modeling (Glosser *et. al.* 2020b). The MPK model extends the original Parrot-Killoh (PK) model to include the components for the reactive SCM phases (i.e., Al_2O_3, SiO_2, and CaO) in addition to the four OPC clinker phases (i.e., C_3S, C_2S, C_3A, and C_4AF). In the MPK model, different stages of binder kinetics are described by rates that are calculated using empricial coefficients. Table 1 provides these coefficients for OPC (Parrot and Killoh 1984). The coefficents K_1, N_1, and K_2 define early-stage kinetics (hours to days) while K_3 and N_3 define the later age kinetics.

Table 1: PK parameters and activation energy for clinker phases (Parrot and Killoh 1984)

Phases	K_1	N_1	K_2	K_3	N_3	H	E_i **(J/mol)**
C_3S	1.5	0.7	0.05	1.1	3.3	2	41,570
C_2S	0.5	1.0	0.02	0.7	5.0	1.55	20,785
C_3A	1.0	0.85	0.04	1.0	3.2	1.8	54,040
C_4AF	0.37	0.7	0.015	0.4	3.7	1.65	34,087

Empirical kinetic parameters (K_1, N_1, and K_2) for Al_2O_3 and SiO_2 (calcined clay did not have CaO) contributed by the calcined clay were obtained in this study by fitting the elemental contributions from Step 1 with time component from Step 2 with the Levenberg-Marquardt method in Matlab. The parameters K_3 and N_3, which govern the long-term reactivity, were not captured in this study and are not reported. In Table 1, H is a parameter that accounts for the impact of water to binder ratio (w/b). Because this study did not vary the *w/b* ratio, H was not fit.

3. Results and Discussion

An example of determining the degree of reaction of SCMs over time using results from simulated pore solution and pastes is shown in Fig. 1 for a calcined clay containing metakaolin and quartz. In Step 1a, dissolved elements from the SCM into the simulated pore solution over time are shown. In Step 1b, the

mass loss of the SCM in the simulated pore solution over time is shown; the time in these experiments is not representative of the dissolution kinetics in real systems, so experiments in pastes were then performed. In Step 2, the mass loss in paste samples over time is shown; these mass loss values were matched to the mass losses in Step 1b to determine the realistic kinetics of dissolution. Since in this example, only Al and Si were released in significant quantities, only these elements were used to understand the degree of reaction of the SCM. In Step 3, the total mass loss of the SCM is shown on the x-axis, and the y-axis represents the mass loss from the presumed oxide components of the bulk amorphous phase in the SCM. These values were determined by subtracting the contribution from readily dissolvable crystalline phases (e.g., anhydrite and gypsum) and assuming that the rest of the elements released in Step 1a came from the bulk amorphous phase. The y-axis in Step 3 then represents the percentage of Al_2O_3 and SiO_2 dissolved from the bulk amorphous phase. In Step 4, the y-axis data from Step 3 are combined with the time from Step 2 to represent the degree of reaction of components in the bulk amorphous phase over time. The data from Step 4 were used to obtain the MPK parameters.

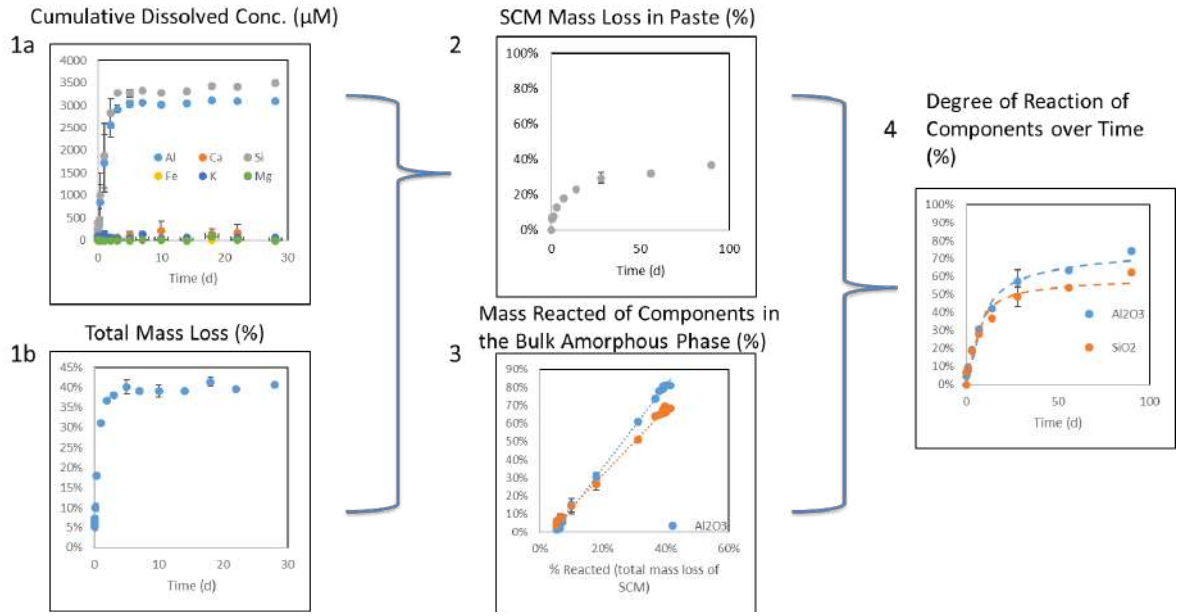


Figure 1: Example results of determining reactivity of oxides in the bulk amorphous phase in calcined clay based on dissolution on simulated pore solution and mass loss of SCM from paste.

The results of the fitting to obtain the MPK parameters K_1, N_1, and K_2 for calcined clay are shown in Table 2, along with the coefficients obtained from that literature that used selective dissolution, nuclear magnetic resonance, and scanning electron microscopy with energy dispersive X-ray spectroscopy analysis (Glosser *et al.* 2020a; Glosser *et al.* 2020b). As shown in Table 1, the fitted parameters are in reasonable agreement with the results obtained using other methods. The differences in K_1 and N_1 could be attributed to the resolution of the data collected in early stages of the dissolution experiments. Increasing the number of data collected within the first 3 hours is expected to improve the K_1 and N_1 fits, which are related to the initial stage processes of nucleation and precipitation.

Table 2: Estimated MPK parameters and of individual oxide components in bulk amorphous phases.

Calcined Clay	**This study**		**Glosser et al. 2020b**	
Phases	**Al_2O_3**	**SiO_2**	**Al_2O_3**	**SiO_2**
K_1	0.65	0.64	0.50	0.49
N_1	0.91	0.81	0.70	0.63
K_2	0.05	0.05	0.05	0.05
R^2	0.97	0.97	0.99	0.99

4. Conclusions

In this study, an improved method based on the MPK model to determine inputs for thermodynamic/kinetic simulations was established. Reactivity of SCMs (total mass loss) in simulated pore solution dissolution and OPC-SCM paste hydration studies was linked and used to obtain the reactivity of individual oxide components in the bulk amorphous phases in cement hydration. The proposed approach provides a practical and efficient way of obtaining the MPK coefficients.

Acknowledgements

The authors thank Advanced Research Projects Agency–Energy (ARPA-E) Grant DE-AR0001143 and National Science Foundation (NSF) Award CMMI-1903457 for financial support of the study presented in this paper.

References

Aughenbaugh, K.L., Chancey, R.T., Stutzman, P., Juenger, M.C., & Fowler, D.W. (2013). An examination of the reactivity of fly ash in cementitious pore solutions. *Materials and Structures*, 46, 869–880

Bharadwaj, K., Isgor, O. B., & Weiss, W. J. (2022). A Simplified Approach to Determine Pozzolanic Reactivity of Commercial Supplementary Cementitious Materials. *Concrete International*, *44*(1), 27-32.

Durdziński, P. T., Snellings, R., Dunant, C. F., Haha, M. B., & Scrivener, K. L. (2015). Fly ash as an assemblage of model Ca–Mg–Na-aluminosilicate glasses. *Cement and Concrete Research*, *78*, 263-272.

Glosser, D., Isgor, O.B., & Weiss, W.J. (2020a). ACI Materials Journal, 117(6), 111-123.

Glosser, D., Suraneni, P., Isgor, O. B., & Weiss, W. J. (2020b). Estimating reaction kinetics of cementitious pastes containing fly ash. *Cement and Concrete Composites*, *112*, 103655.

Haha, M. B., De Weerdt, K., & Lothenbach, B. (2010). Quantification of the degree of reaction of fly ash. *Cement and Concrete Research*, *40*(11), 1620-1629.

Juenger, M.C.G., Snellings, R., & Bernal, S.A. (2019). Supplementary cementitious materials: New sources, characterization, and performance insights. *Cement and Concrete Research*, *123*, 257-273.

Lothenbach, B., Le Saout, G., Gallucci, E., & Scrivener, K. (2008). Influence of limestone on the hydration of Portland cements. *Cement and Concrete Research*, *38*(6), 848-860.

Luke, K., & Glasser, F. P. (1987). Selective dissolution of hydrated blast furnace slag cements. *Cement and Concrete Research*, *17*(2), 273-282.

Parrot, L.J. & Killoh, D.C. (1984). Prediction of cement hydration. *Br. Ceramics Proc.*, 35, 41-53.

Snellings, R. (2013). Solution-controlled dissolution of supplementary cementitious material glasses at pH 13: the effect of solution composition on glass dissolution rates. *Journal of the American Ceramic Society*, *96*(8), 2467-2475.

The 16th International Congress on the Chemistry of Cement 2023 (ICCC2023)
"Further Reduction of CO_2 -Emissions and Circularity in the Cement and Concrete Industry"
September 18–22, 2023, Bangkok, Thailand

Characterization of (A/F) H_3 Phase Microstructure with Different Al/(Fe+Al) Ratios based on Calcium Sulfoaluminate Cement

Jiangchuan Li[1], Jun Chang[2*], Tian Zeng[3] and Zhiqi Hu[4]

[1,2,3,4]*School of Civil Engineering, Dalian University of Technology, Dalian, 116024, China*
[1]*E-mail: jclidut@163.com,* [2*]*E-mail: mlchang@dlut.edu.cn,* [3]*E-mail:*2922234940@qq.com, [4]*E-mail:* anshanhzq@126.com

ABSTRACT
The hydration product $Fe(OH)_3$ gel phase or Al-containing $Fe(OH)_3$ ($(A/F)H_3$) gel phase enables calcium sulfoaluminate cement (CSA) to obtain excellent cementitious properties. In order to enable the influence relationship between the ratio of Al and Fe and the gel phase was thoroughly investigated. In this study, $(A/F)H_3$ with different Al/(Fe+Al) ratios was synthesized from its chemical composition by sol-gel method, and its microstructure was characterized to determine the formation process of this phase. The results show that Fe in $Fe(OH)_3$ was substituted by Al to form the $(A/F)H_3$ phase of goethite crystal structure at pH=12.5. The gradual increase of Al/(Fe+Al) ratios significantly changed the crystal structure parameters of $(A/F)H_3$, and the adsorption capacity and desorption temperature of OH- groups were improved. When the ratio was greater than 40 mol%, the crystal structure of $(A/F)H_3$ was transformed, and the crystallinity was significantly reduced. In addition, the substitution of Al resulted in a significant decrease in the aspect ratio of the $(A/F)H_3$ phase particles, the microscopic morphology changed from needle-rod to granular, and a larger specific surface area was obtained.

KEYWORDS: *Calcium sulfoaluminate cement, Al/(Fe+Al) ratios, (A/F) H_3 phase, Crystal, Microstructure*

1. Introduction

Calcium sulfoaluminate cement (CSA) has received extensive attention from researchers due to its potential environmental protection effects and functional properties. The properties of CSA are closely related to the content of clinker minerals and $C_4A_3\$$ (Wang et al. 2017), $C_4A_3\$$ reacts very quickly with water, and AFt and AH_3 phase are the main hydration products, which enables the cement products to obtain high early strength (Berger et al. 2011). In previous studies, it was found that the AH_3 phase in CSA hydration products had a crystal-like structure, which was microcrystalline rather than amorphous, and had good packing and densification effects(Zhang et al. 2018). This significantly improving the pore structure and compressive strength of cement products. In the hydration products of CSA, in addition to the AH_3 gel phase, the FH_3 phase is inevitably generated. The hydration product FH_3 of the iron phase provides further potential for the improvement of the performance of CSA. Previous studies have shown that the FH_3 phase has gel properties and can fill the pores, which can effectively improve the strength, wear resistance, impact resistance and seawater erosion resistance of cement (Ferenc et al. 2015). The oxides of Fe and Al have similar chemical properties they can be substituted for each other under certain conditions (Idrissi et al. 2010). Zhang et al. (2021) found that the vitrified C_4AF was hydrated to form the FH_3 phase, and the Al phase precipitated into the iron-containing gel (FH_3) along with the hydration. Buenfeld et al. (2003) found that the iron phase hydrates to form $C3(A,F)H_6$ and $(A,F)H_3$. Although some researchers have found the formation of $(A,F)H_3$ in hydration products, the microstructure and properties of $(A,F)H_3$ are still unclear. The related work on the substitution of Fe^{3+} and Al^{3+} in FH_3 and AH_3 to generate $(A/F)H_3$ in cement hydration obviously needs to be improved. Therefore, the purpose of this work is to investigate the AH_3-FH_3 gel phase binary system by regulating the Al/Fe molar ratio to understand the effect of Al and Fe contents on the microstructure of $(A/F)H_3$. This work can play an important role in the promotion and application of calcium sulfoaluminate cement series products.

2. Experimental procedure

2.1 Materials and preparation of Al-substituted ferric hydroxide

The chemical reagents used in the experiment are $AlCl_3{\cdot}6H_2O$ (≥99%), $FeCl_3{\cdot}6H_2O$ (≥98%) and NaOH (≥99%) produced by Sinopharm Group. These reagents are AR grade and require no further purification before use. To obtain different Al-substituted ferric hydroxides ($(A/F)H_3$), a mixture of 0.1 mol/L $FeCl_3{\cdot}6H_2O$ and $AlCl_3{\cdot}6H_2O$ was mixed with 500 ml deionized water in a beaker, and the weight of $FeCl_3{\cdot}6H_2O$ and $AlCl_3{\cdot}6H_2O$ was adjusted to obtain mixtures with different Al/(Fe+Al) ratios. Ten series of mixtures with different Al substitution amounts (0 mol%, 10 mol%, 20 mol%, 25 mol%, 30 mol%, 40 mol%, 60 mol%, 80 mol%, 100 mol%) were placed in different beakers with continuous stirring to

dissolve them, which were named FA0, FA10, FA20, FA25, FA30, FA40, FA60, FA80, FA100. After complete dissolution, 3 mol/L NaOH solution was added dropwise to the beaker at a constant rate with continuous stirring until the pH of the solution is controlled at 12.5.

2.2 Characterization method

Dried powder samples were tested at 5°-80° in steps of 0.02° with a single-step dwell time of 0.5 s in an X-ray diffractometer (Bruker D8 advance) equipped with Cu Kα radiation. Thermogravimetric (TGA) was tested by the METTLER TOLEDO TGA/DSCI thermal analyzer at a measurement temperature of 50-800°C and a N_2 atmosphere at a heating rate of 10°C/min. The microstructure of the synthesized samples was observed by an FEI NOVA Nano 450 scanning electron microscope (SEM). The microstructure and lattice images (HRTEM) of the samples prepared on the copper mesh after ultrasonic dispersion with absolute ethanol were obtained by field emission transmission electron microscopy (JEM-F200). In addition, energy dispersive X-ray spectroscopy (EDS) was also analyzed. Samples pelleted with KBr were measured by Nicolet iS10 Fourier transform infrared spectroscopy(FTIR) within 400–4000 cm^{-1} with an accuracy of 4 cm^{-1} to analyze functional groups. BET-specific surface area (SSA) of the samples was determined by a physical adsorption analyzer.

3. Results and discussion

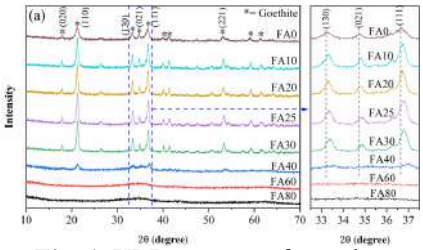


Fig. 1 XRD patterns of samples

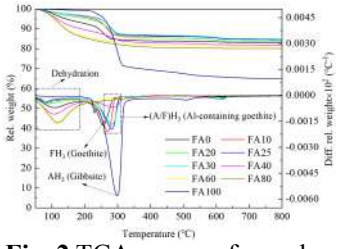


Fig. 2 TGA curves of samples

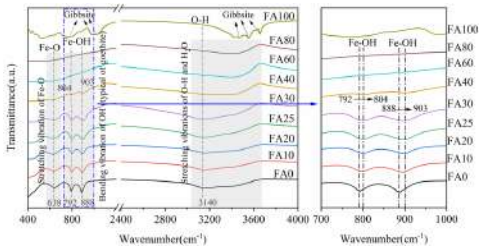


Fig. 3 FTIR patterns of samples

Table 1. d-Spacings and unit cell parameters of samples with different Al/(Fe+Al) ratios

Samples	Al/(Fe+Al) (mol%)	d-Spacings (Å)					Unit cell parameters (Å)			Cell volume ($Å^3$)	Crystal density (g/cm^3)
		020	110	130	021	111	a	b	c		
FA0	0	4.954	4.192	2.688	2.577	2.449	4.627	9.907	3.018	138.35	4.248
FA10	10	4.952	4.190	2.687	2.575	2.447	4.624	9.905	3.015	138.09	4.253
FA20	20	4.951	4.183	2.685	2.574	2.445	4.614	9.904	3.013	137.71	4.257
FA25	25	4.942	4.173	2.679	2.570	2.441	4.604	9.884	3.009	136.93	4.260
FA30	30	4.940	4.167	2.678	2.568	2.437	4.593	9.883	3.006	136.46	4.262

Figure 1 shows the X-ray diffraction patterns of $(A/F)H_3$ with different Al/(Fe+Al) ratios. It can be seen that different samples have diffraction peaks, which indicates that $(A/F)H_3$ has a crystal structure. According to the qualitative analysis of XRD, the diffraction peak of FA0 (the content of Al 0 mol%) is determined to be goethite. The positions of all diffraction peaks observed in XRD of samples FA10, FA20, FA25, FA30, and FA40 are the same as those of goethite, and no diffraction peaks of other Fe or Al phases are observed. This means that $(A/F)H_3$ has a mixed crystal structure of Al and goethite. With the increasing Al/(Fe+Al) ratio, the intensity of diffraction peaks in XRD gradually increased, and when the ratio was 40 mol%, the intensity of diffraction peaks showed a decreasing trend. The diffraction peaks of FA60 and FA80 are broadened when Al/(Fe+Al) is 60 and 80 mol%, respectively. This indicates that the increase of Al/(Fe+Al) ratio (≥40 mol%) reduces the crystallinity, and the high content of Al is not conducive to the formation of goethite crystals. More importantly, the 2θ of the diffraction peak of $(A/F)H_3$ shifts higher with increasing Al/(Fe+Al) ratio, which is more clearly seen from the selected enlarged XRD patterns from 32.5(2θ) to 37.5(2θ). This indicates that the replacement of Fe by Al changes the interplanar spacing of goethite, which is embodied in the gradual decrease of the d-spacing. In order to more clearly reflect the shift of the diffraction peaks to analyze the certainty of Al entering goethite to form $(A/F)H_3$ phase, TOPAS software was used to perform Rietveld refinement to obtain the results of d-spacing and unit cell parameters (Table 2). It can be seen that the interplanar spacing (d-spacing) gradually decreases with the increase of Al substitution, and the unit cell parameters (a, b, c) are also gradually reduced. At the same time, with the increase of Al substitution amount, the unit cell volume also gradually decreased, while the crystal density gradually increased. These changes are closely related

to the radius of Al^{3+} and Fe^{3+}, the substitution of Fe^{3+} by Al^{3+} leads to the distortion of the unit cell and reduces the spacing of the crystal facets (Shannon 1976), which causes the diffraction peak to shift to a higher 2θ.

Figure 2 shows the TG-DTG curves of samples with different Al/(Fe+Al) ratios, In the first stage of weight loss, it is mainly the loss of physically adsorbed water. The weight loss peaks were shifted due to different Al substitutions, which implied that Al substitution contributed to the adsorption of water. The substitution of Al less than 40 mol% has the effect of reducing the content of adsorbed water, but high substitution of Al (≥40 mol%) will cause the opposite effect. The second stage of weight loss is mainly dehydroxylation by structural water. The weight loss peak of FA0 without Al is about 255°C, which is mainly due to the decomposition of goethite. When Fe is replaced by Al in FH_3, the weight loss peak shifts to higher temperature, and the weight loss peak of FA10, FA20, FA25, FA30, FA40 are approximately 270, 280, 282, 285 and 290℃, respectively, This is mainly caused by the decomposition of Al-containing goethite ($(A/F)H_3$). This suggests that Al substitution makes the thermal stability of $(A/F)H_3$ gradually improve. When the Al substitution amount increased to 60 mol%, the weight loss peaks of FA60 and FA80 at approximately 115 °C. This indicates that high content of Al is not conducive to the formation of Al-containing goethite, which is consistent with the results of XRD.

Figure 3 shows the FTIR spectra of different samples. It can be seen that the absorption peak at 638 cm^{-1} is the stretching vibration of Fe-O. The absorption peaks at 792 cm^{-1} and 888 cm^{-1} are the bending vibrations of Fe-OH. The absorption peak at 3140 cm^{-1} is the stretching vibration of -OH. With the increase of Al/(Fe+Al) ratios, the absorption peaks at 638 cm^{-1}(Fe-O), 792 cm^{-1}(Fe-OH), 888 cm^{-1}(Fe-OH) and 3140 cm^{-1}(-OH) gradually broadened and their intensity became weaker, and the wavenumber gradually shifted to the high wavenumber in the direction of 4000 cm^{-1}. When the Al/(Fe+Al) ratio is 40 mol%, the wavenumber of Fe-OH increases from 792 cm^{-1} and 888 cm^{-1} to 804 cm^{-1} and 903 cm^{-1}, respectively. This is caused by the change of the goethite structure caused by the substitution of Fe by Al in FH_3, and the increase of the substitution amount of Al leads to the increase of the binding force of -OH. When the Al/(Fe+Al) ratio is greater than 40 mol%, the absorption peak at 638 cm^{-1},792 cm^{-1},888 cm^{-1} and 3140 cm^{-1} disappears, which is closely related to the substitution amount of Al. This indicates that high content of Al is not conducive to the formation of goethite. When the Al substitution amount was 100 mol%, the absorption peak was observed at about 770, 979,1020, 3470, 3537, 3650 cm^{-1}, which is caused by the OH vibration of gibbsite (AH_3). FTIR and XRD showed consistent results.

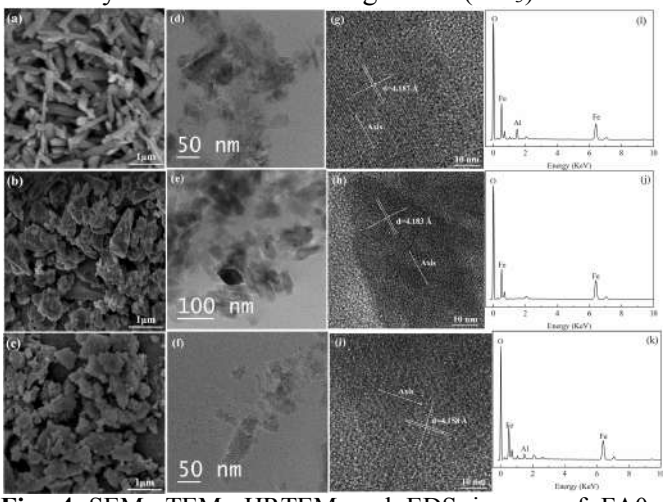


Fig. 4 SEM, TEM, HRTEM and EDS images of FA0 (a,d,g,j), FA25 (b,e,h,k) and FA40 (c,f,I,l)

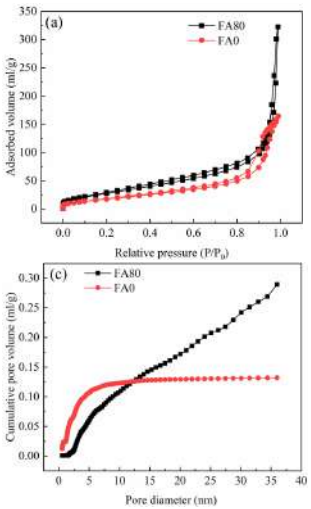


Fig.5 N_2-adsorption curves: (a) adsorption-desorption isotherms; (b) cumulative surface area; (c) cumulative pore volume

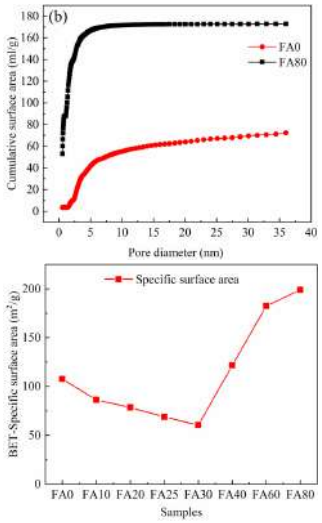


Fig.6 SSA of samples

SEM and TEM images of different samples FA0, FA25, FA40 are shown in Figure 4. The samples all have regular particle morphology, and they have obvious morphological differences. It can be seen that FA0 (without Al substitution) shows a typical needle-like structure of goethite, and the average particle size (length) of FA0 obtained by Imag-Pro Plus statistical measurement was approximately 375 nm. As the Al/(Fe+Al) ratio gradually increases, the typical needle-like structure of goethite was disturbed by the

substitution of Al, the width of the needle-like structure gradually increases, and the aspect ratio gradually decreases, transforming into a rod-like or granular shape. This indicates that the substitution of Al for $Fe(OH)_3$ changes the microstructure of the $(A/F)H_3$ phase. In addition, EDS results show that the main elements in FA0, FA25, FA40 are Fe, Al, O, and Al shows an increasing trend, which was similar to the actual content of Al. The lattice fringes in Fig. 4(g, h, i) show that the samples all have good crystal structures, and the lattice spacings (d) of FA0, FA25, and FA40 are 4.187 Å, 4.183 Å and 4.158 Å, respectively, which correspond to the 110 crystal face of the goethite crystal. The d-spacings gradually decreases with the increase in the amount of Al substitution, which has similar results to the theoretical values in Table 1. This further indicates that the $(A/F)H_3$ phase formed by Al substitution has a crystal structure, and the crystal structure changes with Al substitution.

Figure 5 is the nitrogen adsorption curve for samples. It can be seen that the samples without Al have the lowest adsorption-desorption isotherms, while the samples with Al show higher curves. The hysteresis loop of the sample is closed, which indicates that the sample is porous. In addition, the cumulative surface area and pore volume curves of the samples show that FA80 is higher than FA0, which is closely related to the Al content. Figure 6 shows the change in SSA. The SSA of sample FA0 is 107.6 m^2/g, and with the increase of Al/(Fe+Al) ratios, the SSA gradually decreases. When the Al content is greater than 30 mol%, the SSA gradually increased from 121.6 m^2/g (FA40) to 198.9 m^2/g (FA80), and the samples with high Al content (>30 mol%) had large SSA. This indicates that the Al content significantly affects the SSA of the samples, which seems to be related to the microscopic morphology of the samples. The incorporation of Al makes the needle like structure of $(A/F)H_3$ crystals gradually transform into rod-like and granules, which leads to the broadening of the crystal structure and the reduction of the aspect ratio, which changes the SSA. The length and width of goethite are one of the key factors affecting the SSA, and the decrease of the length and the increase of the width will lead to the decrease of SSA. However, goethite with smaller particle size and length will increase the SSA (Boily et al. 2014).

4. Conclusions

$(A/F)H_3$ has an Al-containing goethite crystal structure. Al substitution of Fe changed the crystal structure and crystalline morphology of $(A/F)H_3$. With the increase of Al/(Fe+Al) ratios, the interplanar spacing (d-spacing), unit cell parameters (a, b, c) and unit cell volume gradually decreased, while the crystal density increased. When the Al/(Fe+Al) ratio is greater than 40 mol%, it is unfavorable for the formation of goethite crystal structure.

Al substitution improves the thermal stability of $(A/F)H_3$ crystals and the binding capacity of OH-groups and reduces the content of adsorbed water, but high Al content (>40 mol%) will have the opposite effects.

$(A/F)H_3$ has remarkably regular microscopic morphology. With the increase of Al substitution, the aspect ratio of $(A/F)H_3$ crystals decreased gradually, and changed from needle-like to rod-like or granular shape. In addition, with the increase of Al/(Fe+Al) ratios, the specific surface area of $(A/F)H_3$ gradually decreased, and when it was greater than 30 mol%, the specific surface area gradually increased.

Acknowledgements

This research was supported by the National Natural Science Foundation of China (52172015).

References

Berger, S., Coumes, C., Bescop, P. L., et al. (2011) “Influence of a thermal cycle at early age on the hydration of calcium sulphoaluminate cements with variable gypsum contents”, *Cement & Concrete Research*, 41(2):149-160.

Buenfeld, N. R. (2003) “Structure and performance of cements, 2nd edition”, *Engineering Structures*,25(1):127.

Boily, J. F., Kozin, P. A. (2014) “Particle morphological and roughness controls onmineral surface charge development”, *Geochimica et Cosmochimica Acta*, 141: 567-578.

Ferenc, D., Tamás, A. V. (2015) “A Mössbauer study on the hydration of brownmillerite ($4CaO{\cdot}A1_2O_3{\cdot}Fe_2O_3$)”, *Cement & Concrete Research*, 3(5):575-581.

Idrissi, M., Diouri, A., Damidot, D., et al. (2010) “Characterisation of iron inclusion during the formation of calcium sulfoaluminate phase”, *Cement and Concrete Research*, 40(8):1314-1319.

Shannon, R. D. (1976) “Revised effective ionic radii and systematic studies of interatomic distances in halides and chalcogenides”, *Acta Crystallographica Section A*, 32:751-767.

Wang, P., Nan, L., Xu, L. (2017) “Hydration evolution and compressive strength of calcium sulphoaluminate cement constantly cured over the temperature range of 0 to 80 °C”, *Cement and Concrete Research*, 100:203-213.

Zhang, Y., Chang, J., Zhao, J., et al. (2018) “Nanostructural characterization of Al $(OH)_3$ formed during the hydration of calcium sulfoaluminate cement”, *Journal of the American Ceramic Society*,101:4262-4274.

Zhang, G., Ren, Q., He, J., et al. (2021) “New understanding of early hydration of C_4AF under surface vitrification”, *Powder Technology*, 377:372-378.

The 16th International Congress on the Chemistry of Cement 2023 (ICCC2023)
"Further Reduction of CO_2 -Emissions and Circularity in the Cement and Concrete Industry"
September 18–22, 2023, Bangkok, Thailand

Restraining strength retrogression of silica-cement at high temperature above 200 ℃ using flint clay and graphite

H.T. Liu[1*], Z.R. Zhang[2], C.Q. Li[3], Y.J. Yu[4], F.Z. Q[5] and Y.C. Ke[6]

[1] *CNPC Engineering Technology R&D Company Limited, Beijing, China*
Email: liuhtdr@cnpc.com.cn
[2] *CNPC nano-Chemistry key laboratory, College of Science, China University of Petroleum, Beijing, China*
Email: zzr130618@163.com
[3] *Petro China Southwest Oil & Gasfield Company, Chengdu, China*
Email: lichengq@petrochina.com.cn
[4] *CNPC Engineering Technology R&D Company Limited, Beijing, China*
Email: yuyongjindri@cnpc.com.cn
[5] *CNPC Engineering Technology R&D Company Limited, Beijing, China*
Email: qfzh69dri@cnpc.com.cn
[6] *CNPC nano-Chemistry key laboratory, College of Science, China University of Petroleum, Beijing, China*
Email: key@cup.edu.cn

ABSTRACT

Strength retrogression phenomenon of silica-cement systems subjected to high pressure and high temperature above 200 ℃ is common, which is not conducive to the sealing integrity of cement ring and long-term exploitation of high-temperature oil and gas wells. In this paper, the effects of individual flint clay (FC), graphite and its hybrid combination on the silica-cement cured at 240 ℃ and 20.7 MPa for different ages were studied. The decline of controlled sample's compressive strength was obvious, ranging from 32.4 MPa at 2 days to 16.5 MPa at 28 days. Compared with the control, the compressive strength of FC2 cement and G3 cement increased by 182.4% and 187.9% at 28 days, respectively. High-temperature cement containing 15% FC and 2% graphite showed higher mechanical strength which is 52.8 MPa for 28 days than the FC2 or G3 cement. The mechanism is probably due to the high crystallinity hydration products formed via the volcanic ash reaction of FC, the fill effect and interface effect of graphite, and the synergy of the two forms a more stable and dense internal structure. To sum up, flint clay and graphite had excellent effects to increase the strength of silica-cement cured at 240 ℃, which provided a way to restrain strength retrogression of silica-cement at high temperature above 200 ℃.

KEYWORDS: *flint clay, graphite, mechanical behavior at high temperature, strength retrogression, oil well cement*

1. Introduction

With the development of oil and gas well exploration and, there are more and more.deep wells and super-deep wells. In high temperature cementing operation, serious problems such as cement strength retrogression and cement ring seal integrity failure occurred, which is extremely bad for production. It is found that adding silica sand can retard the strength decline of cement at high temperature ranged from 110 to 200 ℃ (Kanchanason et al (2019)). However, the strength of silica sand cement systems still decline severely at high temperature above 200 ℃, which is not conducive to the long-term exploitation of super high-temperature oil and gas wells. Therefore, it is particularly important to study the new high-temperature resistance strength decay material and the enhancement mechanism.

Flint clay is a kind of refractory clay, the main chemical composition are Al_2O_3 and SiO_2, the main mineral is kaolin. They can produce the volcanic ash effect with CH, significantly accelerate the hydration reaction. Graphite is a hexagonal lamella structure, with the characteristics of high temperature resistance, good toughness, and good chemical stability at room temperature (Liu et al (2021)). The unique properties of graphite-based materials prove to improve the properties of cemented nanocomposites (Le et al (2014)), so as to achieve higher or even super high mechanical and physical properties (Dimov et al (2018)). Relevant studies have found that metakaolin and graphite can inhibit the

decline of cement strength (Zhang and Yang (2020)). The current study has not fully solved the strength decline of cement under high temperature conditions, and the mechanism of resistance decline is not clear. In this paper, the effects of FC and graphite on compressive strength of SC cement were investigated. And microscopic morphology, pore structure changes and hydration products were studied. The research results have important reference value for cement slurry design of high-temperature and ultra-deep wells.

2 Materials and methods

2.1 Materials

The following raw materials were used: API class G oil well cement was obtained from Sichuan Jiahua Cement Factory (Leshan, China). Silica sands were got from Jingxi petroleum Engineering Co., Ltd. The study subject was 50% mass fraction sand-added class G oil well cement, which was used to prepare all samples. Flint clay was purchased from Shijiazhuang Yunwang Mineral Products Co., Ltd (Hebei, China). The chemical composition and physical properties are shown in Table 1. Graphite was obtained from Qingdao Yanhai Carbon Materials Co., Ltd (Shandong, China). Dispersing agent DRS-1S are made by the cementing research Institute of CNPC Engineering Technology Research Institute Co., LTD.

Table 1 Chemical Composition of FC

Chemical composition	Al_2O_3	Fe_2O_3	K_2O+Na_2O	TiO_2	Refractoriness/°C
content（wt%）	45~48	≤1.15	≤0.3	≤0.8	≥1770

2.2 Slurry sample preparation

Oil-well cement slurries were prepared and cured according to Chinese standard GB/T 19139-2012. Given the curing formulation of all samples in Table 2. The cement slurry was stored in standard curing molds at 240 ºC, 20.7 MPa, RH 95% for 2, 7 and 28 days.

Table 2 Mix compositions of different silica cement systems

Sample number	Cement(g)	silica sand	FC content(wt%)	Graphite content(wt%)	Dispersant(wt%)	Water(g)
SC	400	200	0	0	1.5	232
FC2	400	200	15	0	1.5	232
G3	400	200	0	2.0	1.5	232
FC2G3	400	200	15	2.0	1.5	232

2.3 Characterization

The universal pressure tester is used to test the compressive strength of the cube, and the average value is calculated. Using x-ray powder diffraction instrument (XRD, Bruker Corporation, D8 ADVANCE) (Cu target, K-alpha rays (λ = 0.154nm)), the scan range of 2θ is 5-90°, and the scan rate is 7°/min. The sample was broken with compressive specimen and ion sputtering metal film was coated on the surface of the cement was characterized via scanning electron microscopy (SEM, Hitachi SU8010, Japan), and the change of interface performance of the cement was evaluated. The pore structure of cement was tested with automatic mercury pressure aperture analyzer (AutoPore IV 9510, McMurray, USA).

3. Results and discussion

3.1 Compressive Strength

The compressive strength of SC, FC2, G3 and FC2G3 cement at 2, 7, and 28 days is shown in Fig. 1. The results showed that the compressive strength of FC2G3 cement increased significantly at 7 days curing ages, and did not decline at 28 days. At 240 ℃, the compressive strength of FC2 cement increased by 23.8%, 22.3% and 182.4%, respectively, compared with the SC cement. At 2, 7 and 28 days, the compressive strength of G3 cement has been increased 7.7%, 39.0% and 187.9, respectively, compared with SC cement. The compressive strength of FC2G3 cement is 52.4 MPa and 52.8 MPa at 7 and 28 days, increased by 23.9% and 13.3%, respectively, compared with FC2 cement. It shows that the addition of FC and graphite can improve the strength of cement, and the two play a synergistic role, which can effectively alleviate the decline of cement strength under high-temperature. In the following sections, we will study the crystalline phase components, micro-structure and pore structure changes, which can explain the mechanical results to some extent.

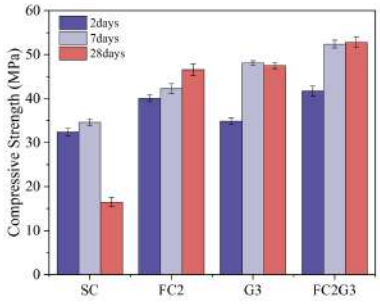


Fig. 1. Compressive strengths of SC, FC2, G3 and FC2G3 cement

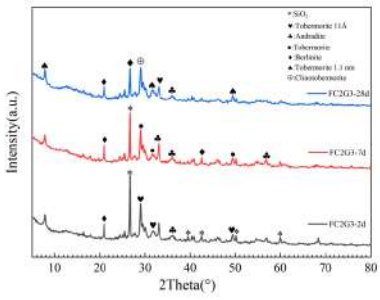


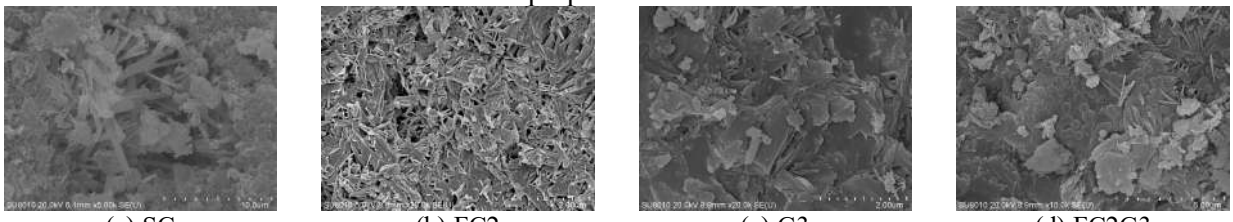
Fig. 2. Representative XRD profiles of FC2G3 cement at various curing age

3.2 XRD Analysis

In order to study the influence of flint clay and graphite on cement hydration products, XRD analysis of FC2G3 cement was performed. The representative XRD test results are shown in Fig. 2. The pattern shows that the main hydration products are tobermorite, andradite, tobermorite 1.1 nm and berlinite. Berlinite has good temperature resistance, which is conducive to the strength development of cement. And the qualitative analysis showed that the crystal form of the C-S-H changed, such as 2 days is tobermorite 11 Å ($Ca_5H_{10}O_{23}Si_6$), and 7 days becomes tobermorite ($Ca_{2.25}H_{3.5}O_{10}Si_3$), which has lower Ca/Si. At 28 days curing time, the characteristic peaks of tobermorite and clinomorite were identified, these hydrated phases have higher stability, and the strength of cement does not decline at high-temperature and long curing ages. Some studies (Bu and Du (2016)) have found that, tobermorite and andradite suppress the reduction in cement strength because they can fill the structure tightly and have high stiffness. The characteristic peak of CH is not observed, which is caused by the secondary hydration reaction.

3.3 Micro-structure Analysis

Fig. 3 shows the fracture surface morphology characteristics of SC(a), FC2(b), G3(c) and FC2G3(d) cement at 240 ℃, 28 days curing time. There are obvious micro-cracks, micro-gaps, lots of holes and aggregates (Fig. 3a). These agglomerates may be the hydration products with low crystallinity and poor stability produced by the hydration reaction. It is one of the important reasons for the decline of high-temperature cement strength. Fig. 3b appears tobermorite and needle-like xonotlite. Tobermorite has good temperature resistance and high strength, plays the role of filling in cement, so as to inhibit the strength decline of cement under high-temperature. Needle-like xonotlite can make the structure of cement denser. The denser structure and high stiffness are important factors hindering the reduction of cement strength (Bu and Du (2016)). Fig. 3c shows that graphite and cement matrix are strong bonding. The different layers of graphite are connected by van der Waals force, it will form cracks at the interface between the cement and graphite. Also, sliding between the graphite sheets to offset the strain force, resulting in stress relaxation of the crack tip. Graphite plays a physical filling role, and forms better adhesion with the cement matrix, which increases the roughness of the interface (Fig. 3d). Meanwhile, SiO_2 and Al_2O_3 have a secondary hydration reaction with CH, and form stable C_3S, C_2ASH_8 and C_4AH_{13}. The high stability of hydration products increases the strength of high-temperature cement and engenders the interface effect. This is consistent with the above mechanical properties and XRD results.



(a) SC (b) FC2 (c) G3 (d) FC2G3

Fig. 3. SEM images of silica cement systems at 28 days curing ages

3.4 MIP Analysis

Cement composites is a porous material with numerous air voids and capillary voids, which may be detrimental to the mechanical properties (Liu and Jin (2020)). MIP test method was used to characterize

the pore structure of cement. The porosity results of SC and FC2G3 cement was shown in Table 3. The total porosity of FC2G3 cement decreased 14.8%, compared to SC cement. The pore diameter of SC cement is mainly distributed in above 200 nm, accounting for 36.79%. The aperture of FC2G3 cement is mainly distributed in 20-50 nm, accounting for 30.01%. Compared with SC cement, the total porosity of FC2G3 cement changed from 42.76% to 36.43%, which reduced by 14.8%. This result may be the filling effect of graphite and FC, the synergistic effect of the two optimize the aperture distribution, make the pore structure get denser. This is one of the reasons to suppress the decline of high-temperature strength.

Table 3 Porosity and pore size distribution of SC and FC2G3 cement

Sample	Curing time	Total porosity/%	Distribution of pore size /%					
			>200nm	100-200nm	50-100nm	50-20nm	10-20nm	<10nm
SC	28d	42.76	36.79	23.95	18.43	14.65	5.03	1.15
FC2G3	28d	36.43	13.18	19.52	21.48	30.01	12.72	3.09

3.5 The mechanism to restrain strength retrogression of silica-cement at high temperature

Flint clay is a good quality kind of clay, the main components are Al_2O_3 and active SiO_2, which can react with the CH generated in the hydration process of cement, produce high-temperature resistant stable crystal phase, and inhibit the transition of tobermorite to xonotlite. FC mainly achieves the effect of high-temperature strength decline through volcanic ash reaction and pore filling effect. Graphite has a layered structure and rough surface. And the bond between graphite and the cement matrix is better. It manifested as the embedded form, fracturing through a similar fiber extraction effect to suppress the expansion of the cement crack. Because of its good compressibility, it can provide development space for hydration products in the hydration process, and optimize the crystalline phase structure of high temperature cement, improve the aperture distribution, micro-structure and density of cement effectively. In addition, there is Van der Waals force between graphite layers, and the combination force is weak, which make it have lubricity. This characteristic makes the graphite can slide in the cement matrix and offset the strain force, so as to reduce the production of cracks, which may be an important reason for its effective improvement of the mechanical strength of oil well cement under high-temperature.

4. Conclusion

1. The compressive strength decline of silica cement was obvious, ranging from 32.4 MPa at 2 days to 16.5 MPa at 28 days. Compared with SC cement, the compressive strength of cement increases by 23.8%, 22.3% and 182.4% cured at 2, 7, and 28 days with 15% FC, and increases by 7.8%, 39.0% and 187.9% with 2% graphite, respectively.
2. Flint clay plays a filling role and reduces the formation of micro-cracks. The hydration reaction of Al_2O_3 and SiO_2 in FC and Ca^{2+}, accelerates the hydration process of cement, promotes the formation of stable hydration phase. The graphite particles can produce mechanical binding force on the surface of the matrix, which is conducive to the interface and hindering the destruction of external force, thus inhibiting the strength decline of high temperature cement.
3. Flint clay and graphite had excellent and synergistic effects to increase the strength of silica-cements, which provided a way to restrain strength retrogression of silica-cement at high temperature above 200 ℃.

Acknowledgements

General Project of National Natural Science Fund (Approval No.51974339); The authors would like to acknowledge the co-financial support by CNPC Science and Technology Project (2021DJ4403).

References

Bu, Y., Du, J., Guo, S., Liu, H., & Huang, C. (2016). Properties of oil well cement with high dosage of metakaolin. CONSTRUCTION AND BUILDING MATERIALS, 112, 39-48.

Dimov, D., Amit, I., Gorrie, O., Barnes, M.D., Townsend, N.J., Neves, A.I.S., Withers, F., Russo, S., & Craciun, M.F. (2018). Ultrahigh Performance Nanoengineered Graphene-Concrete Composites for Multifunctional Applications. ADVANCED FUNCTIONAL MATERIALS, 28, 1705183.

Kanchanason, V., & Plank, J. (2019). Effect of calcium silicate hydrate – polycarboxylate ether (C-S-H–PCE) nanocomposite as accelerating admixture on early strength enhancement of slag and calcined clay blended cements. CEMENT AND CONCRETE RESEARCH, 119, 44-50.

Le, J., Du, H., & Pang, S.D. (2014). Use of 2D Graphene Nanoplatelets (GNP) in cement composites for structural health evaluation. Composites Part B: Engineering, 67, 555-563.

Liu, H., Jin, J., Yu, Y., Liu, H., Liu, S., Shen, J., Xia, X., & Ji, H. (2020). Influence of halloysite nanotube on hydration products and mechanical properties of oil well cement slurries with nano-silica. CONSTRUCTION AND BUILDING MATERIALS, 247, 118545.
Liu, L., Zhang, X., Xu, L., Zhang, H., & Liu, Z. (2021). Investigation on the piezoresistive response of carbon fiber-graphite modified asphalt mixtures. CONSTRUCTION AND BUILDING MATERIALS, 301, 124140.
Zhang, H., Yang, Y., Yu, W.Y., Li, L.K., & Zhang, X.G. (2020). "A Cementing Slurry Used in Alternating Ultra-High Temperatures." Drilling Fluid & Completion Fluid 37 (06): 771-776.

The 16th International Congress on the Chemistry of Cement 2023 (ICCC2023)
"Further Reduction of CO_2 -Emissions and Circularity in the Cement and Concrete Industry"
September 18–22, 2023, Bangkok, Thailand

Influence of mineralogical composition on the calcinability of shales

K. Dvořák[1*], S. Ravaszová[1], A. Jančíků[1], O. Šrámek[1]

[1] *Brno university of technology, Brno, Czechia*

Email: dvorak.k@fce.vutbr.cz

ABSTRACT

The use of pozzolanic admixtures in cement production is a possible way to reduce emissions, especially CO_2. A good example is the technogenic pozzolan metakaolin. The disadvantage is its high price and resource constraints. One alternative may be another type of phyllosilicate, which is shale. Shales are relatively available, but they have undergone metamorphosis and their calcinability may be limited. Calcinability will depend strongly on the mineralogical composition. The work is focused on the influence of mineralogical composition on the calcinability of shales. Suitable type of sedimentary shale was selected. Petrographic analysis and chemical analysis were carried out. Mineralogical composition of shale sample was performed by XRD analysis using glycolation for accurate identification of clay minerals. In the second part, calcinability of shale under different burning temperatures was studied. The pozzolanic activity was evaluated by Chapelle test. In the third part, blended cement mortars were made and the efficiency indices for replacing of 30 % Portland cement were determined. As a result, the effective calcination temperature, and the relationship of the mineralogical composition with the increase of pozzolanic activity were evaluated.

KEYWORDS: *Blended cement, Calcination, Shale, Pozzolanic activity, Phyllosilicates*

1. Introduction

From the chemical point of view, pozzolans are materials that contain amorphous SiO_2 and reactive silicates, aluminates, and aluminosilicates. The reaction rate is dependent on the respective state of the CaO component with water, the reaction kinetics, and the temperature of the water Duda (1975).
The pozzolanic activity of shales is primarily influenced by their mineralogical compositions, which are like those of calcined clays Taylor (1997). It is an alternative source of pozzolans activated by a group of phyllosilicate minerals. Shales are predominantly composed of clay minerals that are altered during the transformation process to pozzolanic products. Nowadays, there is a lot of shale waste in the world, which is being investigated by the cement industry as a suitable admixture for cement as a pozzolanic substance Frias et al (2013), Cheng et al (2012) Poussardin et al (2023).
The pozzolanic activity is enhanced by the fact that the slates are activated at an appropriate temperature, which produces hydration products in the form of C-S-H, C-A-H or C-S-A-H gels. For this to work, the T-O-T layers must be properly breached to produce as many strength-bearing gels as possible. The damaged T-O-T layers should react in an alkaline environment with calcium hydroxide and form the appropriate gels, Sabir et al (2001). This destruction of the T-O-T structure occurs at the temperature range from 500 to 1100 °C Nevrátilová (2013). The pozzolanic reaction is relatively slow, using up $Ca(OH)_2$ and reducing pore size. Methods for determining the pozzolanity are divided into direct and indirect methods. Direct methods deal with the reaction of a substance where $Ca(OH)_2$ plays the most important role Moore et al (1997). Calcium hydroxide is a strong hydroxide and is completely dissociated into ions in aqueous media. In this case, the amount of $Ca(OH)_2$ that decreases during the pozzolanic reaction is monitored using appropriate analyses. They are based on the measurement of the concentration of portlandite by mixtures of cement and pozzolan. Direct methods include the Frattini or Chapelle test Irassar et al (2019).

2. Materials and Methods

The experiment was divided into three main sections. In the first section, the petrographic analysis and mineralogical and chemical composition of the shale sample was carried out. In the second section, the calcinability of the shale was carried out at different temperatures and the pozzolanic activity was determined by the modified Chapelle test. In the third section, blended cement pastes were made, and the activity index was determined by compressive strength. To determine the sufficiency of calcination, the shale samples were fired in a Classic 2017 S 20 L furnace between 100 and 900 °C (with 100 °C steps) and residence time for 30 min. The XRD analysis was performed on a PANalatical Empyrean XRD device, CuKα anode, total time per scan 1 hour. Qualitative evaluation was performed using HighScore plus software (3.0e, PANanlytical B.V., The Netherlands) with the ICSD database (released in 2012). Clay minerals were identified using oriented sample (e.g. Moore and Raynolds, 1997).
The shale samples were ground on a Retsch RS 200 vibratory disc mill at the same specific surface area of 400 $m2 \cdot kg^{-1}$ as referral Portland cement CEM I. The specific surface area was measured at ZEB PC-Blaine Star automatic Blaine apparatus according to ČSN EN 196-6. In the last part the activity indices were determined. The cement pastes were prepared for the efficiency indices evaluation. To increase the influence of the admixture, the replacement amount was increased to 30%. The recipe of the reference cement paste and the three blended cement are at the table 1. The water/binder ratio was determined according to ČSN EN 196-3 was always at 0.31.

Table 1: Reference cement paste recipe

	Dosage [g]		
	Cement	Shale 25 °C, 600 °C, 800 °C	Water
Reference	76.3	-	23.7
B25 (shale 20 °C)	53.4	22.9	23.7
B600 (shale 600 °C)	53.4	22.9	23.7
B800 (shale 800 °C)	53.4	22.9	23.7

For the compressive strength test, prisms of 10 x 10 x 30 mm were prepared and cured under the wet conditions. The mixed cement paste was compacted with 10 taps on a ceramic table to produce a uniform texture. The compressive strength was determined on a hydraulic press at 7, 28, 56 and 90 days.

3. Results and Discussion

The raw material used is powdery slate with graphite from slate/shale mine Lhotka near Lhotka u Vítkova, Moravian-Silesian Region in Czech Republic. It is a potentially significant source of shale in the Czech Republic and a relatively typical representative of metamorphosed shales with low $CaCO_3$ content. The microstructure is aleuritic with a noticeable preferential orientation, with cross-arrangement of phyllosilicate flakes in places. The binder consists of a clay matrix, Quartz and carbonate cement. The minerals identified were Quartz, carbonate, graphite, clay minerals, Muscovite, Biotite, Chlorite, Plagioclase, Alkali feldspar, iron oxyhydroxides, Tourmaline and Zircon.
The chemical analysis of the shale revealed a high content of SiO_2 with a value of about 59 %. In addition, Al_2O_3 was present with a value of around 18 % and other oxides with a value close to 7 % and alkali with a value of around 6 %. Measured oxides and other companion compounds in lower amounts are shown in Table 2.

Table 2: Measured content of oxides

Sample	Representation of oxides in %										
name	SiO_2	Al_2O_3	Fe_2O_3	FeO	MnO	CaO	MgO	K_2O	Na_2O	∑ Other	∑
Sample 1	56.84	17.89	2.23	4.64	0.08	1.47	3.42	3.39	2.15	7.89	100

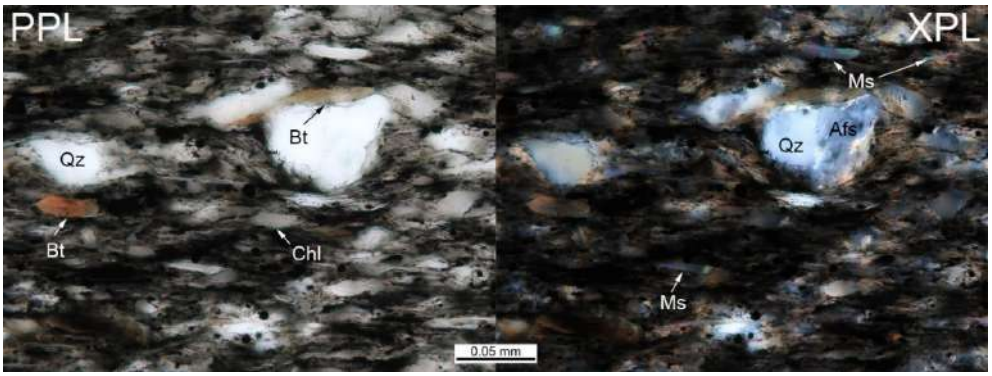


Figure 1: PPL a XPL shale; Qz – quartz, Bt – biotite, Chl – chlorite, Ms – muscovite, Afs – alkalic feldspar

On a glycolated sample at an angle of 5° degrees, the mineral smectite was separated from the mineral chlorite. At an angle of about 6 degrees, chlorite was identified, because the reflexion was affected neither by ethylene glycol treatment, nor by heating. No kaolinite was identified. However, kaolinite (0 0 1) reflection may be overlain by a peak of chlorite at 12.5°. When heated to 400°C, no significant difference was observed from the air-dried sample, only smectite basal layers collapsed. The collapse of the basal layers could contribute to the pozzolanic activity.

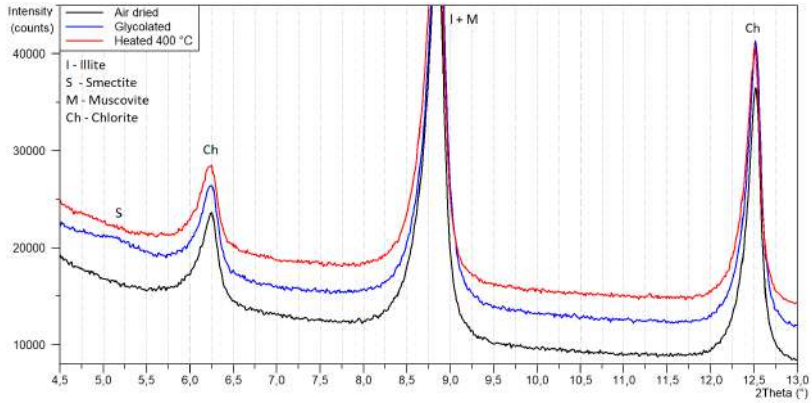


Figure 2: XRD analysis of the shale (glycolated)

The following minerals were identified on the samples, fired from 100 to 900 °C (in increments of 100 °C) with residence time for 30 min., by XRD analysis: Chlorite, Muscovite, Quartz, Albite. The main mineral here is chlorite, whose T-O-T layers disintegrate between 600 and 800 °C. At 900 °C, the beginning of mica degradation is observed, see Figure 3. For the reason of Chlorite structural changes and the highest chance of C-S-H gel formation in cement paste, the temperatures of 600 °C and 800 °C were selected as suitable for the thermal activation of shale.

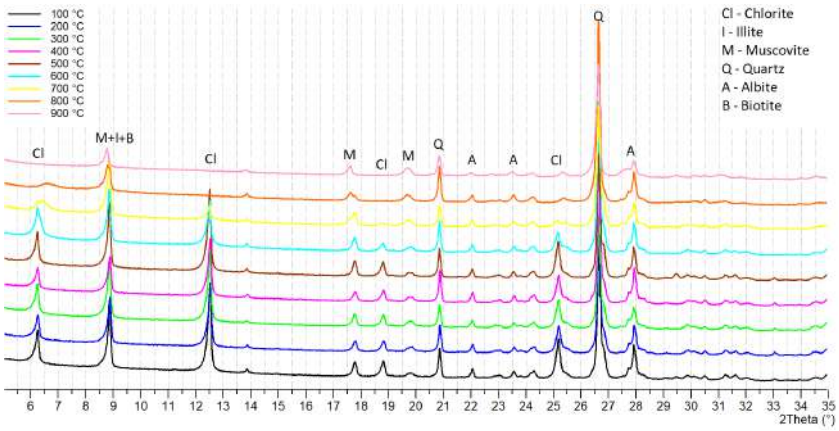


Figure 3: XRD analysis at specific thermal activation of shale.

The shales thermally activated at 600 °C and 800 °C and not activated shale were tested for pozzolanic activity by the modified Chapelle test according to the French standard NF P 18-513. The prone to thermal activation of this shale has not been very high, for example typical value of metakaoline is around 1000 g $Ca(OH)_2$/g pozzolana and the highes value in this case was only aroud 380. This value was obtained for the shale activated at 800 °C, see at table 3. Surprisingly, there is not much difference between 600 °C and 800 °C.

Table 3: Determination of pozzolanic activity by modified Chapelle test.

	B25	B600	B800
Chapelle test [g $Ca(OH)_2$/g pozzolana]	251	359	382

The result of compressive strength of reference and blended cements is given in Table 4. The increase in compressive strength was slower for the blended cements than for the reference. However, it reached 75% after 90 days. The contribution of calcination was evident in the initial stages up to 28 days. This was probably due to the disturbed structure of the calcined minerals. However, the long-term strengths of the cement with this shale were already comparable.

Table 4: Compressive strength and efficiency index of blended cement pastes and reference cement paste

	Ref	B25	B600	B800
Compressive strength [MPa]				
- 7 days	32.2	24.8	21.5	22.5
- 28 days	49.1	27.2	30.2	32.6
- 56 days	50.5	38.7	37.1	37.7
- 90 days	51.3	38.5	38.5	39.0
Efficiency index [%]				
- 7 days	-	77.0	68.0	69.8
- 28 days	-	55.4	66.6	66.4
- 56 days	-	75.0	73.9	74.6
- 90 days	-	75.0	75.0	76.0

4. Conclusion

A typical type of sedimentary shale from the Lhotka locality was selected for this experiment. The selected shale contains mainly Chlorite, Smectite, Muscovite, Illite and of course Quartz and some feldspars. The main mineral here was Chlorite, whose T-O-T layers gradually disintegrate during calcination between 600 °C and 800 °C. Smectite also decomposes at the same temperature. At these temperatures, the pozzolanic activity increased from 250 in the uncalcined shale to 380 g $Ca(OH)_2$/g pozzolana in the shale calcined at 800 °C. Chlorite and Smectite/Illite therefore appeared to be the effective minerals in this case. However, compared to metakaolin, which normally reaches values around 1000, this value is low.

The result of the mechanical properties up to day 28 was consistent with the results of the pozzolanic activity determination. But in the case of the selected shale, the higher calcination temperature was not effective. Moreover, in the long term (after 90 days), even the blended cement with non-calcined shale matched the compressive strength of the blended cement with calcined shale. It is possible that even finely ground metamorphosed uncalcined shale may have some pozzolanic ability.

Acknowledgements

We acknowledge the financial support of Czech Science Foundation under the project “The role combination of fluxes and mineralizers on properties of low-energy clinker ” (23-05122S)

References

ČSN EN 197-1: Cement Composition, specifications, and conformity criteria for common cements.

Cheng, An, Sao Jeng Chao, and Wei Ting Lin. "Effect of Calcination Temperature on Pozzolanic Reaction of Calcined Shale Mortar." Applied Mechanics and Materials. Trans Tech Publications, Ltd., May 2012. https://doi.org/10.4028/www.scientific.net/amm.174-177.843.

Duda H.W., Cement Data-book, Bauverlag GmbH Wiesbaden und Berlin, 1975. pp. 173-176.

Frias, M., R.V. De La Villa, R. Garciá, M.I.S. De Rojas a A.J. Valdés. The Influence of Slate Waste Activation Conditions on Mineralogical Changes and Pozzolanic Behavior published: 20 May 2013, https://doi.org/10.1111/jace.12387

Irassar, E.F., Bonavetti, V.L., Castellano, C.C., Trezza, M.A., Rahhal, V.F., Cordoba G., and Lemma. R., Calcined illite-chlorite shale as supplementary cementing material: Thermal treatment, grinding, color and pozzolanic activity, Applied Clay Science, Volume 179, October 2019, 105143, https://doi.org/10.1016/j.clay.2019.105143

Moore, D.M. and Reynolds, R.C.,1997. X-Ray Diffraction and the Identification and Analysis of Clay Minerals. Oxford, New York: Oxford University Press. ISBN 0 19 508713 5

Navrátilová E., Methods for Determination of Pozzolanic Activity, Faculty of chemistry, Brno University of technology

NF EN 206-1 pour la production de béto, NF P18-513 Standard, August 2012, Addition for concrete - Metakaolin - Specifications and conformity criteria.

Poussardin, V., Paris, M., Wilson, W., Tagnit-Hamou, A., Deneele, D. (2023). Calcination and Reactivity of Marlstones: A Comparison Between Palygorskite and Smectite Bearing Marlstones. In: Escalante-Garcia, J.I., Castro Borges, P., Duran-Herrera, A. (eds) Proceedings of the 75th RILEM Annual Week 2021. RW 2021. RILEM Bookseries, vol 40. Springer, Cham. https://doi.org/10.1007/978-3-031-21735-7_3

Sabir, B.B., S. Wild a J. Bai. Metakaolin and calcined clays as pozzolans for concrete, Cement and Concrete Composites, Volume 23, Issue 6, December 2001, Pages 441-454, https://doi.org/10.1016/S0958-9465(00)00092-5

Taylor, H.F.W, 1997. Cement chemistry. 2. edition. London: Thomas Telford Publisching. pp. ISBN 0 7277 2592 0.

The 16th International Congress on the Chemistry of Cement 2023 (ICCC2023)
"Further Reduction of CO_2 -Emissions and Circularity in the Cement and Concrete Industry"
September 18–22, 2023, Bangkok, Thailand

A New Soluble Alkali Test to Predict the Alkali Contribution of SCMs to Concrete Pore Solution

M. Sharbaf[1], and F. Rajabipour[2*]

[1] *Ph.D. Student, Pennsylvania State University, University Park, PA, USA*
Email: m.r.sharbaf@psu.edu
[2] *Professor of Civil Engineering, Pennsylvania State University, University Park, PA, USA*
Email: farshad@psu.edu

ABSTRACT

Clinker substitution with supplementary cementitious materials (SCMs) is a pillar of decarbonizing cement and concrete. SCMs are also often used to improve the durability of concrete, such as to mitigate the alkali-silica reaction (ASR) in concrete containing reactive aggregates. Many non-conventional and rapidly growing SCMs (such as natural pozzolans, marginal coal ashes, and ground glass) have a high alkali content (Na_2O_{eq} > 3.0%). The ASR-mitigation effectiveness of these SCMs is uncertain as some of those alkalis may be soluble in the concrete pore solution. This paper introduces a new soluble alkali test to quantify the soluble fraction of alkalis in an SCM. The test was applied to 11 natural pozzolans and coal ashes, and their alkali release was monitored over 90 days. The results are compared with ASTM C311's Available Alkali Test and the pore solution compositions of cement pastes made with the 11 pozzolans. Recommendations are made on predicting the hydroxyl ion concentration (or pH) of concrete's pore solution based on the SCM reactivity, chemical composition, and soluble alkalis.

KEYWORDS: *Available alkalis, ASR, Natural pozzolan, Calcined clay, Pozzolanic reactivity*

1. Introduction

Supplementary cementitious materials (SCMs) are commonly employed in cement and concrete production due to their ability to improve the sustainability, durability, and long-term strength of concrete. However, traditional SCMs such as coal fly ash and slag cement are facing supply shortages (e.g., due to retirement of coal fuel power plants). This has led to an urgent need for exploration and rapid commercialization of alternative SCMs, including natural pozzolans, marginal coal ashes, and ground glass (Yoon et al., 2022). Despite their potential benefits, many such pozzolans contain high levels of alkalis with a Na_2O_{eq} above 3.0%wt. This has raised questions about the efficacy of such high alkali pozzolans in mitigating the alkali-silica reaction (ASR) in concretes containing reactive aggregates. If soluble, such SCM alkalis may increase the concentration of OH^- ions in the pore solution of concrete, and potentially exacerbate ASR.

Conventional SCMs generally mitigate ASR through alkali dilution, alkali binding by pozzolanic C-(A)-S-H, contributing Al ions which depress silica dissolution, reducing availability of portlandite, and reducing the water permeability of concrete (Shafaatian et al., 2013; Thomas, 2011). For high alkali SCMs, the net alkali contribution of the SCM to the pore solution of concrete (i.e., the available alkalis of the SCM), should be quantified. For this purpose, ASTM C311 (2022) presents a test method for measuring the available alkalis in SCMs. This method involves preparation and curing of a lime-pozzolan paste, followed by demolding and grinding at 28 days, washing and vacuum filtering the powder using hot deionized water, and measuring the dissolved alkalis in the filtrate. However, several shortcomings of the test have been identified, including the short duration of the test (i.e., some alkalis may be released beyond 28 days) and the low pH of the test (~12.5), while the pH of concrete generally ranges from 13.2 to 13.9, resulting in higher alkali solubility from SCM (Kalina, 2019, Kasaniya & Thomas, 2022).

Therefore, a new test method is proposed in this work to better investigate the soluble fraction of alkalis from an SCM. The test was applied to 11 non-conventional pozzolans and the results are compared with those obtained from the ASTM C311 test and the pore solution OH^- concentrations of cement pastes incorporating these pozzolans.

2. Materials and Methods

2.1 Materials

ASTM C150 Type I portland cement was used having the following characteristics: CaO=64.40%, SiO_2=18.64%, Al_2O_3=5.24%, Fe_2O_3=2.25%, SO_3=3.44%, Na_2O=0.33%, K_2O=1.08% by mass, and Blaine fineness=436 m^2/kg. 11 non-conventional pozzolans were tested included 3 calcined clays (CC1, CC2, CC3), 3 volcanic ashes (VA1, VA2, VA3), 3 ground bottom ashes (GBA1, GBA2, GBA3), and 2 fluidized bed combustion fly ashes (FBC1, FBC2). Due to space constraints, the detailed analysis of the chemical and physical properties and the pozzolanic reactivity of these 11 pozzolans are not included here but can be found in the study by Yoon et al. (2022).

2.2 Methods

A new test method was developed to determine the soluble alkali content of SCMs. In this method, 6.70 g of SCM is added to 280.0 ml of either 1 N NaOH or 1 N KOH solution in an airtight HDPE bottle, resulting in a solution/SCM volumetric ratio of approximately 112 (this ratio depends on the SCM density and was in the range 101 to 125, with an average of 112). The NaOH solution was used to monitor the release of K ions from the SCM while the KOH solution was used to monitor the release of Na ions from the SCM. A separate bottle was used for each test date to avoid carbonation/contamination of the solution during the sample extraction. The bottles were kept at 38±2 °C with periodic agitation/flipping. At designated test dates (28, 56, and 90 days), a 5.0 ml solution sample was extracted from each bottle using a syringe. The sample was filtered through a 0.2 µm non-cellulose filter, diluted/acidified using a 3.0% HNO_3 solution, and analyzed using ICP-AES to measure the concentration of dissolved Na and K ions. Matrix-matched calibration standard solutions were also prepared to minimize the matrix effect in the ICP analysis results.

In addition, ASTM C311 (2022) procedure was followed to determine the available Na and K contents of each SCM. For both soluble and available alkali test methods, the equivalent sodium oxide content ($Na_2O_{eq} = Na_2O + 0.658\ K_2O$) was calculated and reported in the results section.

Cement pastes were also prepared with a w/cm=0.48, and 20% cement replacement with SCM. Two additional pastes, one with 20% replacement of cement with quartz flour, having 0.0% alkalis, and one with 100% cement, were also prepared, referred to as “inert” and “cement” mixtures in the results section. The pastes were poured into airtight containers and sealed-cured in a 100% relative humidity room at 23±2 °C. The fresh pore solution of the pastes was extracted using high pressure air filtration, while the 7, 28, 56, and 90-day pore solutions were extracted using a high-pressure die operated at a maximum pressure of 800 MPa. After extraction, each pore solution was filtered using a 0.2 µm filter and acid titrated using 0.085 M HCl with phenolphthalein indicator to determine its hydroxyl ion concentration ($[OH^-]$).

3. Results and Discussion

3.1 Soluble and ASTM C311 available alkalis

The total (via XRF), the available (via ASTM C311), and the soluble (via the new test method) alkalis of the 11 SCMs are shown in Figure 1 (error bars represent ±1 st. dev.). The soluble alkalis were measured after 28, 56, and 90 days. To enable straightforward comparison, the results were expressed in terms of Na_2O_{eq}. The data reveals that calcined clays had the lowest soluble and available alkali contents, while volcanic ashes had the highest. A significant fraction (16 to 66%) of the total alkalis are in fact soluble at 90 days. This is especially important for volcanic ashes that have high total alkali content. For the VAs, the soluble alkali content continued to increase over time, surpassing the C311 results. This suggests that the 28-day test period for ASTM C311 may be inadequate. Individual Na and K release results are not presented here due to space limitations.

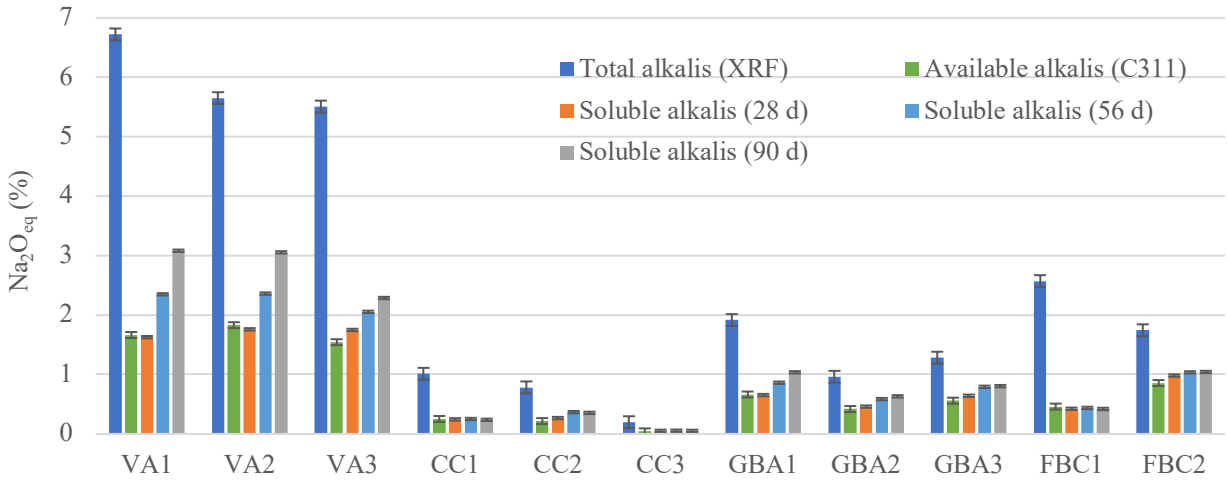


Figure 1 – Total, C311 available, and soluble alkalis of the 11 SCMs

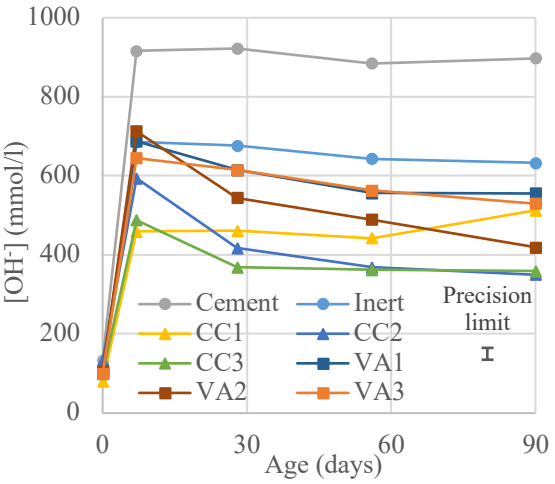


Figure 2a- CCs and VAs

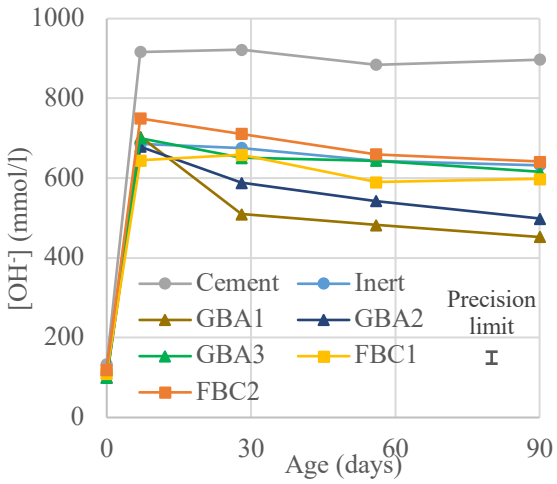


Figure 2b- GBAs and FBCs

Figure 2 – [OH^-] of cement pastes incorporating SCMs (precision limit represents the average range for each point)

3.2 Pore solution of cement pastes

As previously discussed, a high level of soluble alkalis in an SCM does not necessarily translate to a higher [OH^-] or pH in the concrete pore solution. The alkali binding capacity of the SCM (via its pozzolanic reaction) should also be considered. Figure 2 shows the OH^- concentration in the pore solution of cement pastes containing the 11 SCMs. For comparison, the results of the "cement" and "inert" pastes are also included. The "inert" paste represents the alkali dilution effect (20% cem. is replaced with a filler). Ideally, an SCM should reduce [OH^-] to below that of the "inert" paste to suggest a net alkali sink/binding. For high alkali SCMs, [OH^-] may be above that of the "inert" paste, suggesting a net alkali contribution.

The results in Figure 2 show that, 8 SCMs (all but FBC1, FBC2, and GBA3) consumed [OH^-] to below that of the "inert" paste. The other three pastes are comparable with the "inert" paste. Among the SCMs tested, CC2, CC3, and VA2 were the most effective in reducing [OH^-]. Despite their high total and soluble alkali contents, VA1, VA2, and VA3, were able to effectively reduce the [OH^-] in the pore solution of the pastes by 38.1%, 53.3%, and 40.9%, respectively, in comparison with the [OH^-] of the "cement" mixture. The findings imply that a considerable portion of the VAs' alkalis are soluble in the pore solution, but the enhanced alkali binding due to the pozzolanic reaction of the VAs compensates for their higher alkali content. This finding agrees with a low available alkali content of VAs reported by Kalina et al. (2021). Notably, despite the cement's high alkali content (Na_2O_{eq}=1.04%), CC2 and CC3 reduced the [OH^-] to a level below the ASR safe limit of 398 mmol/l (pH=13.6), suggested by Kaladharan et al. (2021).

3.3 Discussion

Several factors influence the pH of the pore solution in concretes containing SCMs. These include the w/cm, the SCM dosage (wt% cement replacement), the soluble alkalis of the cement and SCM, and the bulk chemistry and pozzolanic reactivity of the SCM. An attempt was made here to predict the $[OH^-]$ of the pastes containing SCM at 90 days using a regression analysis. $[\text{Na or K}]_{\text{bound}} = [\text{Na or K}]_{\text{inert}} - [\text{Na or K}]_{\text{SCM}}$ at 90 days was considered as the dependent variables. The input variables for the regression function were the 90-day soluble Na and K of each SCM, the SCM pozzolan reactivity, and its Ca/(Si+Al). The latter two are known to determine the alkali binding capacity of an SCM as a result of its pozzolanic reaction (Hong & Glasser, 2002). The pozzolanic reactivity of each SCM was determined using the R^3 test (ASTM C1897) in terms of the cumulative 7-day heat release, and is reported in Yoon et al. (2022).

An analysis of variance (ANOVA) suggested that soluble Na and K contents, pozzolanic reactivity, and Ca/(Si+Al) oxides mass ratio were significant factors at a 90% confidence level. Two regression equations were developed separately for predicting $[\text{Na}]_{\text{bound}}$ and $[\text{K}]_{\text{bound}}$ at 90 days. Due to the charge balance, the sum of the two regression functions represents the $[\text{OH}]_{\text{bound}}$, as shown in Eq. (1). A relatively high correlation was observed, with an R-squared value of 0.91. It is noted that Eq. (1) is preliminary and is only applicable to the cement tested and at a 20% replacement of cement with SCM. Future research is needed to collect data and develop a more comprehensive model applicable to a wide range of cements, SCMs, and replacement levels.

$$[\text{OH}]_{\text{bound}} = [\text{OH}]_{\text{inert}} - [\text{OH}]_{\text{SCM}} = 72.74 + 256.1 \times \text{Reactivity} - 51.84 \times \text{Sol. Na} - 48.15 \times \frac{\text{Ca}}{\text{Si+Al}} - 399.0 \times \text{Sol. K} \times \frac{\text{Ca}}{\text{Si+Al}} \quad (1)$$

3. Conclusions

A new test was developed to quantify the soluble fraction of alkalis in SCMs. It was observed, based on testing 11 natural pozzolans and coal ashes, that a significant fraction of their total alkalis (16 to 66%) were soluble into concrete's pore solution. However, the pozzolanic reaction of the SCMs binds the dissolved alkalis and removes them from the pore solution. Among the SCMs tested, 8 were found to be a net alkali sink and the other 3 were alkali neutral while still served to dilute the alkali contribution of cement. A preliminary regression analysis suggested that the $[OH^-]$ of pore solution is significantly dependent on the soluble alkalis, pozzolanic reactivity and Ca/(Si+Al) mass ratio of the SCM. The test method and proposed model warrant further refinement and expansion in subsequent studies.

Acknowledgments

Funding for this project was provided by the United States Department of Transportation, under FHWA Award# 693JJ31950019, granted to a team of researchers at Purdue, Penn State, and Clarkson Universities.

References

Hong, S. Y., and Glasser, F. P. (2002) "Alkali sorption by C-S-H and C-A-S-H gels: Part II. Role of alumina", Cement and Concrete Research, 32(7), 1101–1111

Kaladharan, G., Szeles, T., Stoffels, S.M. and Rajabipour, F. (2021) "Novel admixtures for mitigation of alkali-silica reaction in concrete", Cement and Concrete Composites, 120, p.104028

Kalina, R. D. (2019) "Evaluation of test methods and specifications for supplementary cementitious materials for concrete", University of Texas at Austin

Kalina, R. D., Al-Shmaisani, S., Seraj, S., Cano, R., Ferron, R. D., and Juenger, M. C. G. (2021) "Role of Alkalis in Natural Pozzolans on Alkali-Silica Reaction", ACI Materials Journal, 118(3)

Kasaniya, M., and Thomas, M. D. A. (2022) "Role of the alkalis of supplementary cementing materials in controlling pore solution chemistry and alkali-silica reaction", Cement and Concrete Research, 162, 107007

Shafaatian, S. M. H., Akhavan, A., Maraghechi, H., and Rajabipour, F. (2013)"How does fly ash mitigate alkali–silica reaction (ASR) in accelerated mortar bar test (ASTM C1567)?" Cement and Concrete Composites, 37, 143–153

Thomas, M. (2011) "The effect of supplementary cementing materials on alkali-silica reaction: A review. Cement and concrete research, 41(12), 1224-1231

Yoon, J., Jafari, K., Tokpatayeva, R., Olek, J., Peethamparan, S., and Rajabipour, F. (2022) "Characterization and quantification of pozzolanic reactivity of natural and non-conventional pozzolans", Cem. Con. Comp. 133, 104708

The 16th International Congress on the Chemistry of Cement 2023 (ICCC2023)
"Further Reduction of CO_2 -Emissions and Circularity in the Cement and Concrete Industry"
September 18–22, 2023, Bangkok, Thailand

Sensitivity of the Modified Chapelle test for measuring the reactivity of different types of clays calcined under different conditions

Mehnaz Dhar[1*], Shashank Bishnoi[2]

[1] *Indian Institute of Technology Delhi, India*
Email: dharmehnaz08@gmail.com
[2] *Indian Institute of Technology Delhi, India*
Email: bishnoi@iitd.ac.in

ABSTRACT

Clays have shown an excellent potential for the production of low carbon cements if the thermal treatment and reactivity are understood. The present work investigates the performance of the modified Chapelle test to measure the pozzolanic reactivity across a wide range of clays. Raw clays were calcined at four different temperatures ranging from 400 °C to 1000 °C using the static calcination method in a laboratory muffle furnace. It was observed that this test method can differentiate the effect of different calcination temperatures on the pozzolanic reactivity. All the clays exhibited the highest pozzolanicity at 800 °C, which means the optimum burning temperature for clays to be used as SCM. The influence of the chemical and mineralogical composition of clays on the reactivity measurement was also studied. The results showed the kaolinite content and reactivity have only a fair degree of linear correlation (R^2=0.57), indicating that reactivity is controlled by other mineral phases as well. The iron impurity seems to contribute to pozzolanicity as higher reactivity was obtained for clays with greater iron content. The results from the modified Chapelle test were compared with the thermogravimetric analysis and a good correlation was obtained. However, it was observed that the chemical composition of clays affects the reactivity measurements especially at the lower calcination temperature. The reactivity measurements can be overestimated as this method takes into account both pozzolanic consumption and adsorption effect in the calculations of the pozzolanic activity.

KEYWORDS: *calcination, clay minerals, impurities, reactivity, modified Chapelle test*

1. Introduction

The use of calcined clay as supplementary cementitious material provides an opportunity to produce low-carbon cement due to the availability of large quantities sufficient to fulfill the growing cement demand. Clay minerals are phyllosilicates and possess a well-ordered arrangement of tetrahedral and octahedron structures in their original state. So, thermal treatment is required to induce the disorder in the crystal lattice and transforms into pozzolanic material (Sabir et al. 2001). However, the determination of optimum calcination temperature is not the straightforward as dehydroxylation process occurs during a specific temperature range and further increase in temperature will result in recrystallization (Lopez 2009). The quality of clay calcination can be checked from thermogravimetric analysis and X-ray diffraction or using standard SCM reactivity tests like lime reactivity, modified Chapelle test, Frattini test (Li et 2018). Unlike most of the test methods that require more than 24 hours to assess the pozzolanicity, modified Chapelle test gives reactivity results within one day. For this reason, this test method can be considered to be feasible to evaluate the quality of clay calcination. The present study explores the influence of varying calcination temperatures on the reactivity of different types of clays using modified Chapelle method. The optimum calcination temperature of clays for use as SCM was determined. In this study, thermogravimetric analysis was considered as benchmark test and reactivity values were compared to assess the sensitivity of modified Chapelle test.

2. Materials and Methods

For the present study, six raw clay samples that were procured from external suppliers were selected. The chemical and mineralogical composition of clay samples was determined from X-ray fluorescence, thermogravimetric analysis and X-ray diffraction techniques. The chemical composition of raw clays (Figure 1) fulfilled the specifications of Class N pozzolans as mentioned in ASTM C618 as SiO_2+ Al_2O_3+Fe_2O_3 >70%. Thermal curves indicate the presence of kaolinite clay mineral as the dehydroxylation process was noticed in all clays. For the quantitative analysis of clay mineral content, the decomposition temperature range was selected from the first derivative curves as it gives better resolution and helps to differentiate adjacent thermal phenomena. The results of mineralogical compositions indicate that B2 clay has maximum kaolin content while D1 has the lowest kaolin content. Except for D3 clay, kaolinite was found to be a major clay mineral present in all clays with various other minor mineral phases as listed in table 1. Calcination was done in laboratory muffle furnace at 400 °C, 600 °C, 800 °C and 1000 °C.

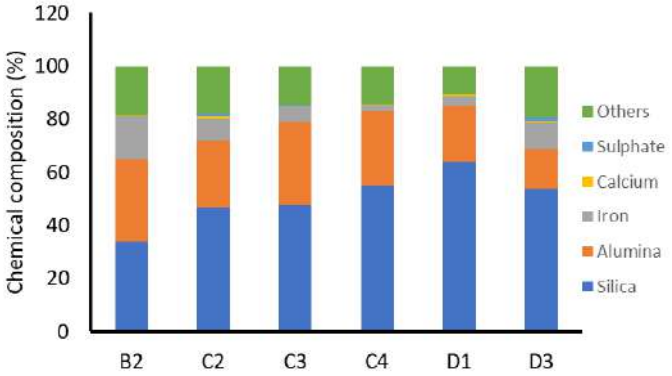


Figure 1: XRF results of different clays used in the study

Table 1: Composition of clays

Clay name	Major mineral phase	Minor mineral phases
B2	Kaolin (73%)	Goethite
C2	Kaolin (57%)	Quartz
C3	Kaolin (53%)	Quartz + Goethite
C4	Kaolin (43%)	Quartz + 2:1 clay
D1	Kaolin (34%)	Quartz
D3	Smectite	kaolin

The modified Chapelle test was performed on all calcined clay samples according to NF P18-513. In this test, 1 g of clay and 2 g of calcium oxide is mixed in 250 ml of deionised water and heated at 90 °C for 16 hours. The setup also includes a reflux condenser to prevent water loss during heating. The solution is then cooled down and 250 ml of sucrose solution is added to dissolve the unreacted portlandite for 30 minutes. Finally, the suspension is filtered and titrated with 0.1N Hcl using phenolphthalein as an indicator. The reactivity is calculated using equation 1 and results are expressed in terms of calcium hydroxide fixed per gram of calcined clay. The efficiency of the calcination process was also determined using thermogravimetric analysis. In this study, TGA experiments were performed on Setaram Instruments at a heating rate of 15 °C/ minute in nitrogen environment. The conversion process of kaolinite to metakaolin was determined by calculating the mass loss in calcined clay samples.

$$\text{Reactivity} = 2\times((V1-V2))/V1\times 74/56\times 1000 \quad (1)$$

V1=Volume of Hcl required in the blank solution (ml)
V2= Volume of Hcl required in the sample solution (ml)

3 Results and Discussion

The effect of calcination temperature on the reactivity of calcined clay samples was observed in the results of modified Chapelle test. It was observed that an increase in the calcination temperature from 400 °C to 800 °C, has a positive influence on the pozzolanicity as evident from Figure 2. This is because the crystalline structure transforms into amorphous till 800 °C and is responsible for an increase in the reactivity of clays. However, reactivity was found to decrease as the calcination temperature reached 1000 °C. This is because the structure of metakaolin becomes unstable at 1000 °C and starts to convert into stable crystalline phases that show lower reactivity (Lopez 2009). Thus, 800 °C can be considered as an optimum calcination temperature to achieve pozzolanic activity in the clays.

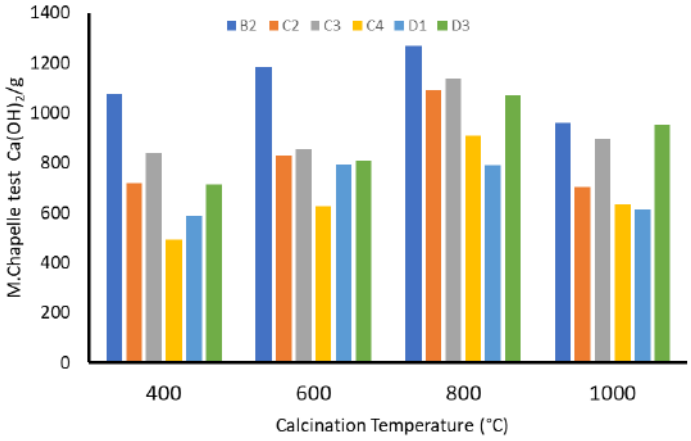


Figure 2: Pozzolanic activity of clays at different calcination temperatures

The influence of the chemical and mineralogical composition of raw clays on pozzolanicity was assessed. As shown in Figure 3 (a), the higher the kaolinite content, higher is the reactivity of calcined clays. The linear correlation was found to be moderate with $R^2 = 0.57$, which implies that reactivity is governed by several other parameters as well. The B2 clay showed the highest reactivity as it contains maximum kaolinite content. Although C2, C3 and D3 have a large difference in the kaolinite content, similar reactivity was observed. This is because of the difference in the mineralogical composition of the clays. D3 clay contains smectite as a major clay mineral and modified Chapelle test appears to over-estimate the reactivity for smectite clays (Hollanders et al. 2016).

Figure 3(b) shows the direct relationship between the chemical composition (iron content) and pozzolanic activity. The results indicate a better degree of correlation (R^2= 0.7) which confirms the contribution of iron impurities to the reactivity properties.

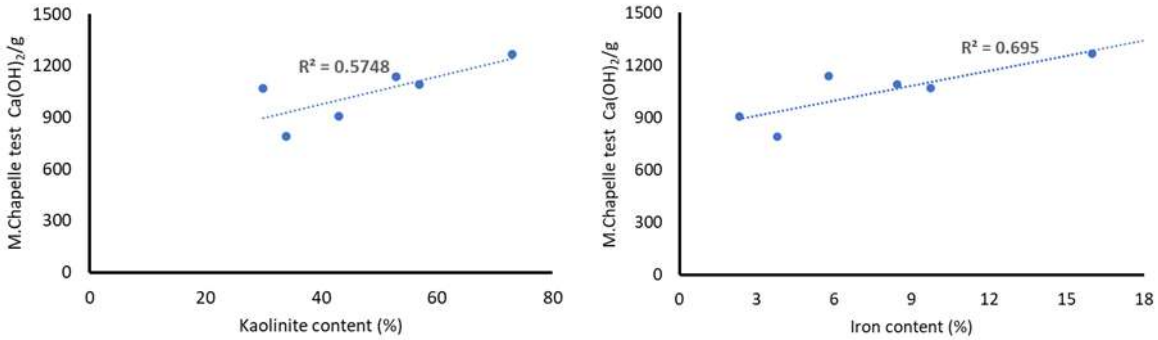


Figure 3: Relationship between (a): reactivity and mineralogical composition, (b): reactivity and chemical composition

The reactivity results obtained from modified Chapelle test were compared with the thermogravimetric analysis. The dehydroxylation process was found to start approximately from 380 °C and a calcination temperature of 400 °C is too low to cause any appreciable change in the structure of kaolinite and thus low reactivity values are obtained. The dehydroxylation degree increased rapidly as the calcination temperature was increased to 600 °C (Figure 4) and a similar trend is expected to be followed in the reactivity. The difference between the pozzolanic activity of C2, C4 and D1 clay at 400 °C and 600 °C

was evident which is consistent with the degree of dehydroxylation process. However, unexpectedly, B2, C3 and D3 clays showed a similar reactivity values at 400 °C and 600 °C. It is possible that a higher adsorption of ions on the surface of iron-rich clays leads to these higher apparent reactivity values. Thus it implies that reactivity results determined from the modified Chapelle test are affected by the chemical composition of clays and the results need not have a direct correlation with the reactivity of the calcined clay in cements. Nonetheless, modified chapelle test can be used as a qualitative measure of the quality of calcination.

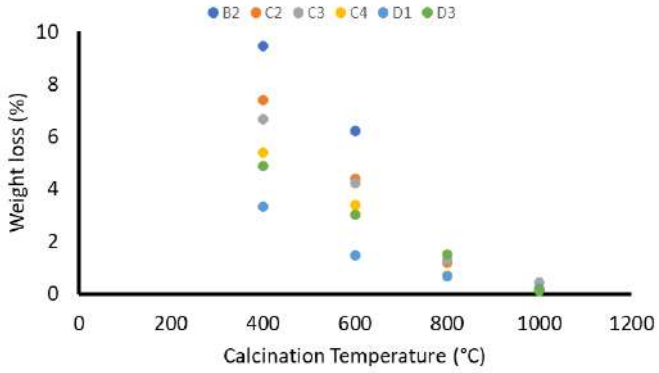


Figure 4: TGA results of calcined clay samples

4 Conclusions

A study on the applicability of modified Chapelle test to predict the reactivity of different types of clays calcined under various conditions was performed in this paper. The results were compared with the thermogravimetric analysis for validating the reactivity values and the following conclusions were drawn:

1.The pozzolanic reactivity was found to be maximum at 800 °C for all the clays and TGA results also confirmed the end of the dehydroxylation process. Thus, 800 °C can be considered as optimum calcination temperature for production of clays suitable as SCM.
2. The effect of increase in the calcination temperature from 600 °C to 1000 °C on the reactivity results of modified Chapelle test was noticed in all clays. Moreover, this test can be used to identify over-calcined clays as lower reactivity was observed after calcination at 1000 °C.
3. The chemical and mineralogical composition of clays influences the reactivity. The results suggest that higher the iron content, the greater is the reactivity of calcined clays. However, the reactivity does not appear to be proportional to the degree of dehydroxylation in the iron-rich clays.
4. The modified Chapelle test measures the consumption of calcium ions, and does not differentiate the adsorption and the reactivity phenomena. The adsorption of ions on the higher surface of the clays may lead to misleading values of reactivity from the modified Chapelle test.

Acknowledgements
The authors would like to acknowledge INNOVNADI for providing financial support and Cementir for making the FutureCem technology available to us.

References

ASTM C618. (2022) “Standard Specification for Coal Fly Ash and Raw or Calcined Natural Pozzolan for Use in Concrete”
Fernandez Lopez, R. (2009) “Calcined clayey soils as a potential replacement for cement in developing countries” Thesis, EPFL
Hollanders, S., Adriaens, R., Skibsted, J., Cizer, Ö., and Elsen, J. (2016) “Pozzolanic reactivity of pure calcined clays”, *Applied Clay Science*, 132–133, 552–56
Li, X., Snellings, R., Antoni, M.,Parashar, A., … Scrivener, K. L. (2018). “Reactivity tests for supplementary cementitious materials: RILEM TC 267-TRM phase 1”. *Materials and Structures*, 51(6). 55:3
NF P18-513.(2012) “Additions pour béton hydraulique Métakaolin Spécifications et critères de conformité”
Sabir, B. B., Wild, S. and Bai, J. (2001) “Metakaolin and calcined clays as pozzolans for concrete: a review”,*Cement and Concrete Research*, 23: 441-454L

The 16th International Congress on the Chemistry of Cement 2023 (ICCC2023)
"Further Reduction of CO_2 -Emissions and Circularity in the Cement and Concrete Industry"
September 18–22, 2023, Bangkok, Thailand

Use of alkaline salts to improve the reactivity of cements with high fly ash content: hybrid alkaline cements

F. Almeida[1*], A. Fernández-Jiménez[2], C.S. Vieira[3], N. Cristelo[4], and M.L. Lopes[5]

[1] *CONSTRUCT, Faculty of Engineering of University of Porto, Porto, Portugal*
Email: filipe.almeida@fe.up.pt
[2] *Instituto de Ciencias de la Construcción Eduardo Torroja (IETcc-CSIC), Madrid, Spain*
Email: anafj@ietcc.csic.es
[3] *CONSTRUCT, Faculty of Engineering of University of Porto, Porto, Portugal*
Email: cvieira@fe.up.pt
[4] *CQ-VR, University of Trás-os-Montes e Alto Douro, Vila Real, Portugal*
Email: ncristel@utad.pt
[5] *CONSTRUCT, Faculty of Engineering of University of Porto, Porto, Portugal*
Email: lcosta@fe.up.pt

ABSTRACT

It is known that the activities carried out throughout the production cycle of Portland cement result in serious environmental impacts. This negative circumstance must be counteracted by introducing into the cement industry and the building and construction sector more sustainable practices that could meet the principles of circular economy and the targets of the Sustainable Development Goals included in the United Nations 2030 Agenda for Sustainable Development. A possible solution within this context is to foster the use of hybrid cements, a combination of Portland cement with alkaline cements, in which a significant amount of supplementary cementitious materials is used for replacing the former. The effect of adding a mixture of alkaline salts (Na_2SO_4 + NaCl) to improve the development of early-age mechanical strengths in cements having high contents of fly ash (45% and 65%) in place of Portland cement was analysed in this work. The mechanical strength values of those cement pastes were determined for curing ages of 2, 28, 90 and 180 days and compared to the behaviour of an ordinary Portland Cement CEM I 42,5R. The rate of heat release and total heat were determined by isothermal conduction calorimetry. The reaction products were characterized by X-ray diffraction and scanning electron microscopy. The results of the mechanical strength tests indicated that the hybrid alkaline cement having 45% of fly ash showed a similar behaviour to the reference cement for a curing age of 28 days, which is an interesting achievement. The findings of the investigation allow considering the possibility of using these types of cements in non-strucutural concrete products within the context of the precast concrete industry. Such solution will be an important green deal between the cement industry and the environment and will aid the introduction of circular and sustainable practices within the building and construction sector.

KEYWORDS: *Hybrid alkaline cements, fly ash, alkaline salts, mechanical strength, microstructural characterization.*

1. Introduction

Worldwide efforts are being carried out to introduce into the different economic sectors circular and sustainable practices that could provide a more pleasant quality of life to society. The United Nations 2030 Agenda for Sustainable Development, which includes the 17 Sustainable Development Goals (UN, 2022), is serving as a compass to achieve such outcome.
The building and construction sector is responsible for generating serious environmental impacts caused by the large-scale consumption of natural resources and energy. To counteract this scenario, it is important to foster the use of alternative binders to ordinary Portland cement. Hybrid alkaline cements

might be a step towards that goal. These cements are composed by a combination of Portland clinker with a significant amount of supplementary cementitious materials (SCMs), as a source of aluminosilicate compounds, such as fly ash, and an alkaline activator (Qu *et al*., 2016; Sanchéz-Herrero *et al*., 2019).
The main goal of this work was the study of hybrid alkaline cements using fly ash as SCM and a mixture of two alkaline salts (Na_2SO_4 + NaCl) to perform the role of activator. Two hybrid alkaline cements were investigated by carrying out mechanical strength tests, isothermal conduction calorimetry, X-ray diffraction (XRD) and blackscattered scanning electron microscopy (BSEM)/energy dispersive X-ray (EDX). An ordinary Portland cement hydrated with water was also prepared for comparison purposes.

2. Experimental

Ordinary Portland cement CEM I 42,5R (OPC), fly ash (FA) provided by a Portuguese coal power plant and a combination of the alkaline salts Na_2SO_4 and NaCl from Panreac, which were provided in the anhydrous form, were used to prepare the cements. The chemical composition of OPC and FA, determined by X-ray fluorescence using a BRUKER S8 Tiger spectrometer, can be consulted in Table 1. FA was ground in a ball mill, leading to a circumstance in which around 99% of its particles were below 32 μm (the particle size distribution was evaluated using laser diffraction technique on a Coulter LS 130). In the case of the original FA, only about 65% of the particles were below that dimension.

Table 1. Chemical composition of OPC and FA.

Material	Compound (weight %)											
	Al_2O_3	SiO_2	CaO	Na_2O	Fe_2O_3	SO_3	Cr_2O_3	MgO	TiO_2	K_2O	Other	LOI[a]
OPC	4.64	18.40	61.60	0.28	3.27	3.23	0.01	1.32	0.47	0.97	5.81	4.00
FA	21.44	56.11	1.30	1.12	8.20	0.66	5.05	1.46	1.15	2.81	0.70	5.05

[a]Loss on ignition

Hybrid alkaline cements including the precursors OPC and FA and a combination of Na_2SO_4 and NaCl in solid form were prepared in accordance with Table 2. For comparison purposes, it was also manufactured a reference cement including exclusively OPC. After mixed with water, the pastes were casted into prismatic moulds 1 × 1 × 6 cm. The workability of the cements was evaluated by conducting mini-slump tests according to Kantro (1980). Results have showed quite similar behaviours: consistencies of 76, 74 and 67 mm were found to BOPCR, BOPC50 and BOPC30, respectively.

Table 2. Composition of the cement pastes.

Paste	Raw material (weight %)				w/b[a]
	OPC	FA	Na_2SO_4	NaCl	
BOPCR	100	—	—	—	0.28
BOPC50	50	45	2.5	2.5	0.28
BOPC30	30	65	2.5	2.5	0.28

[a]w/b = water/binder ratio (binder corresponds to the sum of OPC, FA and activator)

Five samples of each cement were submitted to compressive strength tests on a IBERTEST AUTOTEST 200/10 SW under displacement control at a rate of 0.07 $kN \cdot s^{-1}$ for 2, 28, 90 and 180 days (the results, which show the standard deviation, are presented without outliers). After each curing age, samples were ground and forwarded to characterization by XRD on a BRUKER D8 ADVANCE diffractometer under CuKα radiation (40kV y 30 mA). The rate of heat release and total heat of the cements were monitored on a conduction isothermal calorimeter from TAM AIR working at a temperature of 25ºC. In addition, the reaction products were submitted to BSEM analysis on a Hitachi S-4800 scanning electron microscope (20 kV) prepared with an Oxford LINK-ISIS X-ray energy dispersive analyser.

3. Results and discussion

The results of the compressive strengths displayed in Figure 1 show that there were meaningful losses of resistance for the cements in which OPC was replaced by FA at early-age curing ages. The presence of the alkaline salt prevented the losses from being even higher. However, the increase of the curing time

tended to neutralize those differences, especially in the case of BOPC50, which showed a similar behaviour to the reference cement from 28 days onwards (compressive strengths above 60 and 40 MPa were found after 28 days for, respectively BOPC50 and BOPC30).

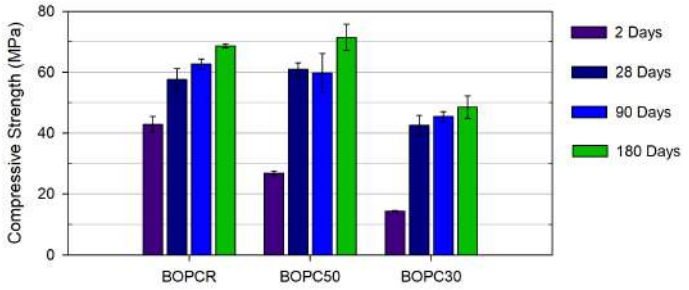


Figure 1. Compressive strength of the cements.

The heat flow and total heat released by the cements provided in Figure 2 show similar calorimetric responses for all cements: a first very intense peak, very difficult to detect, followed by a short induction period and then a second peak, much broader than the first one. The second peak is associated with the precipitation of the C-S-H gel, while the shoulder of that peak is related to the reaction of aluminates with sulfates to form AFt or AFm phases (sulfate depletion) (Scrivener *et al*., 2015). The presence of FA instead of OPC resulted in a lower total heat release by BOPC50 and BOPC30 compared to BOPC.

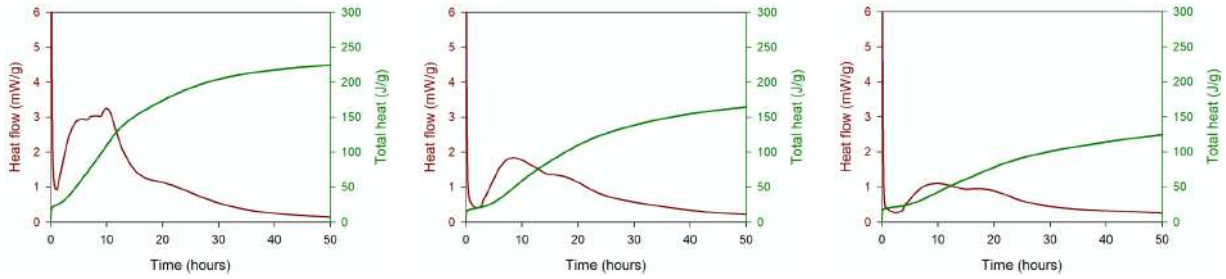


Figure 2. Heat flow and total heat released by (a) BOPCR, (b) BOPC50 and (c) BOPC30.

The XRD patterns of the cements and also the anhydrous OPC and FA is exhibited in Figure 3. It was noticed that the signals referring to the crystalline phases of FA the did not disappear overtime. The peaks associated with clinker phases (alite, belite, tricalcium aluminate and ferrite) tended to disappear with the curing time, or their intensity decreased.

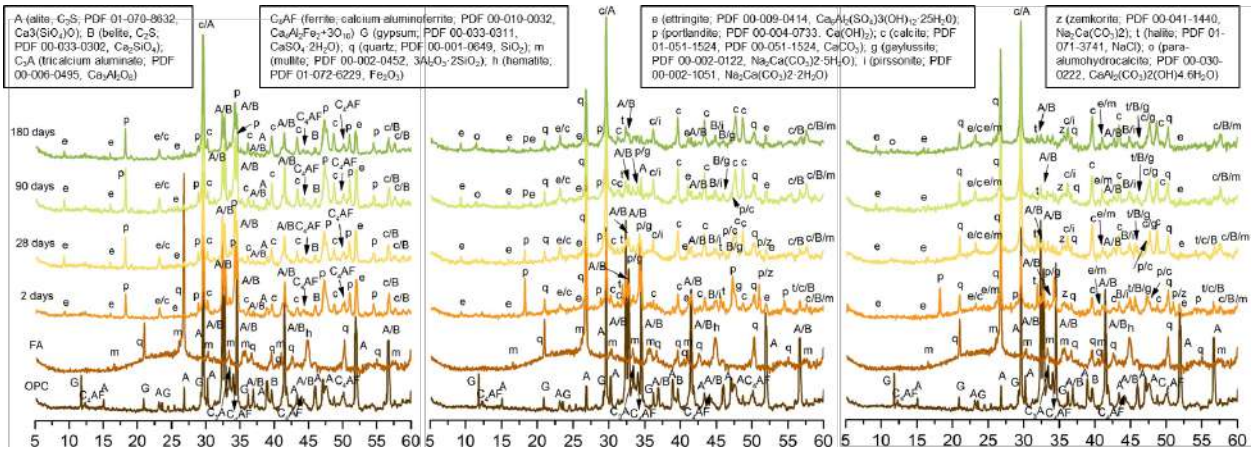


Figure 3. XRD patterns for (a) BOPCR, (b) BOPC50 and (c) BOPC30.

The intensity of portlandite-related peaks is lower in BOPC50 and BOPC30, which could be explained by: 1) lower cement content, lower portlandite generation; 2) portlandite consumption by the reaction between this phase and the alkaline salt, to generate *in situ* alkalinity; 3) the reaction with FA at highest curing ages (pozzolanic reaction) or 4) carbonation: the intensity of the peaks associated with calcite tended to increase with curing time for hybrid cements. For these cements, the presence of other carbonates such as gaylussite, pirssonite or zemkorite was also observed.
The BSEM/EDX analysis performed for BOPC30 at 28 days, and that is displayed in Figure 4, shows the coexistence of a mixture of cementitious gels C-A-S-H/(N,C)-A-S-H, which is the main reaction product of these types of hybrid cements. The composition of the gels included in the matrix were influenced by the presence of OPC/FA particles. Close to OPC particles, the gel had high contents of Ca and Si and a minor amount of Al. On the other hand, high contents of Si and Al and smaller amounts of Ca were noticed around FA particles. A common element of these gels is Na, which was provided by the alkaline salts used as activator.

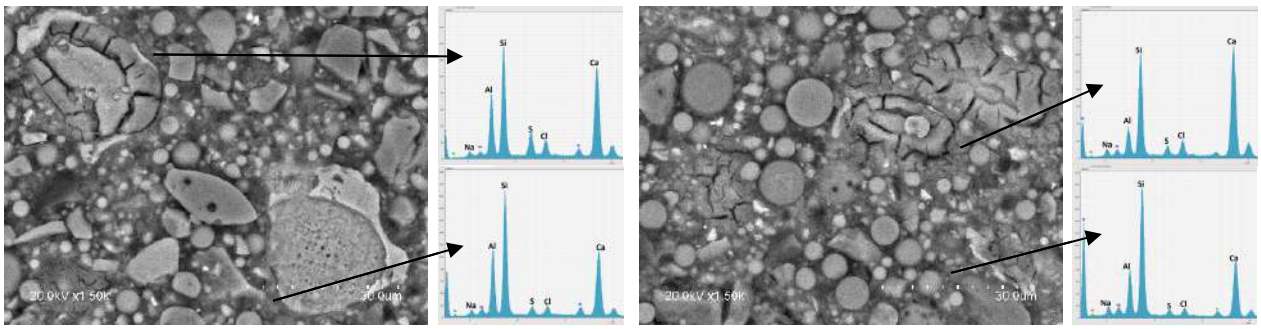


Figure 4. BSEM micrographs and EDX analyses for BOPC30 after 28 days of curing.

4. Conclusions

Cements including residues as raw materials should be studied in order to develop sustainable alternatives to OPC. The hybrid alkaline cements using fly ash in large amounts as SCM and a mixture of Na_2SO_4 + NaCl as activator investigated in this work showed potential to play that role. It should be highlighted the quite interesting mechanical behaviour of these cements from 28 days onwards. The reason for this outcome is the coexistence in the matrix of the main reaction product of these cements, which were the cementitious gels C-A-S-H/(N,C)-A-S-H. These results might act as a lever to promote the use of these cements in the manufacture of non-structural concrete products (without reinforcement).

Acknowledgements

This work was financially supported by Base Funding – UIBD/04708/2020 of the CONSTRUCT – Instituto de I&D em Estruturas e Construções – funded by national funds through the FCT/MCTES (PIDDAC). The authors would like to thank Eng. André Cruz for having speeded up the supply of the fly ash and Dr. Carlos Tavares from SEMAT/UM. Filipe Almeida wish to thank FCT – Fundação para a Ciência e a Tecnologia for his research grant (SFRH/BD/05956/2021). The support from PDC2021-120771-I00, (REVERDECE)/ AEI / 10.13039/501100011033/ Unión Europea NextGenerationEU/PRTR is also acknowledged.

References

Kantro, D.L. (1980) "Influence of water-reducing admixtures on properties of cement paste – a miniature slump test", *Cement, Concrete and Aggregates*, 2(2): 95-102

Qu, B., Martin, A., Pastor, J.Y., Palomo, A. and Fernández-Jiménez, A. (2016) "Characterisation of pre-industrial hybrid cement and effect of pre-curing temperature", *Cement and Concrete Composites*, 73: 281-288

Sánchez-Herrero, M.J., Fernández-Jiménez, A. and Palomo, A. (2019). "Studies About the Hydration of Hybrid "Alkaline-Belite" Cement", *Frontiers in Materials*, 6(66): 9p.

Scrivener, K.L., Juilland, P., Monteiro, P.J.M. (2015). "Advances in understanding hydration of Portland cement", *Cement and Concrete Research*, 78: 38-56

UN (2022) *The Sustainable Development Goals Report 2022*, United Nations – Department of Economic and Social Affairs (DESA), New York, United States of America

The 16th International Congress on the Chemistry of Cement 2023 (ICCC2023)
"Further Reduction of CO_2 -Emissions and Circularity in the Cement and Concrete Industry"
September 18–22, 2023, Bangkok, Thailand

Reduced OPC content in limestone calcined clay cement (LC^3) with C-S-H seeding

Xuerun Li*, Joachim Dengler and Christoph Hesse

BASF Construction Additives GmbH, 83308 Trostberg, Germany

Email: xuerun.li@basf.com

ABSTRACT
Solutions in cement industry to reduce the CO_2 emission could significantly reduce the global CO_2 emission because cement industry accounts ~ 8% of the global manmade CO_2 emission. Limestone calcined clay cement (LC^3 cement) attracts lots of attention from both academia and industry due to its high potential in reducing CO_2 emission of cement industry. Even though LC^3 cement could provide decent late strength development to similar or even higher strength than ordinary Portland cement (OPC), the early strength still needs to be improved due to the relatively low clinker content (typically 40-60 wt% clinker).
Impact of C-S-H seeding on LC^3 cement was investigated. The main goals are achieving similar compressive strength in the blended cement compared to neat ordinary Portland cement (OPC) using C-S-H seeding. The lower limit of OPC content (equivalent to clinker content, or clinker factor) was also explored. EN standard mortar compressive strength were carried out.
Results showed that C-S-H seeding dramatically enhanced the hydration and strength of LC^3 cement. OPC content can be lower than 50% in LC^3 with C-S-H seeding obtaining similar strength until 28 days to neat OPC. Impact of the C-S-H seeding on the mortar flow were also investigated.
Due to the enhanced strength by using C-S-H seeding, there are more freedom to optimize the binder mix design in favor of the CO_2 footprint or the rheology properties depends on the application needs.

KEYWORDS: *LC^3 cement, C-S-H seeding, mortar flow, compressive strength*

1. Introduction

To enhance the early-age strength of LC^3, there are two main solutions: optimizing the binder mix design and using accelerators such as C-S-H seeding. In addition to strength optimization, the rheology challenges of LC^3 should also be considered in application scenarios.
Several research studies have demonstrated that C-S-H (calcium silicate hydrate) seeding can enhance the early hydration and strength of OPC (Nicoleau 2013, John, Matschei et al. 2018) and blended cement (Kanchanason and Plank 2019, Li, Bizzozero et al. 2022). In calcined clay blended cement, hydration acceleration using C-S-H seeding has been reported. A significant enhancement of early-age clinker hydration and strength was demonstrated. Additionally, C-S-H seeding enhanced the late strength of calcined clay blended at an age of 28 days.
Here, we investigated the impact of C-S-H seeding in calcined clay blended cement. One goal was to examine the potential of C-S-H seeding to produce blended cements with similar or better strength than that of neat OPC (CEM I 42.5 N type). Another goal was to explore the concepts lor lowering OPC content (CEM I 42.5 N type, equivalent to clinker content) in calcined clay blended cement, especially the LC^3 system and the so-called LC^{3+} system (combination of calcined clay and slag in the LC^3 system), to obtain strength development similar to that of neat OPC.

2. Experiments

CEM I 42.5N with a low alkali content (Na_2O equivalent 0.39 wt%) was used in this study. Calcined clay (CC), GGBFS (SL) and limestone powder (LS) were used to make blended cement according to the mix design.
A commercial product of synthetic C-S-H (HyCon® S 7042 F) was used as C-S-H seeding material. The 3% of C-S-H was added refer to the total solid. A Melflux® 2500 L liquid additive was used as a dispersant for the standard mortar test, the dosage was based on the product refer to the total solid.
The mortar strength test was conducted according to EN 196-1, except that curing was performed at 23 °C instead of 20 °C. A flow table test was made based on a standard mortar according to EN 196-1 by following the protocol described in EN 1015-3. Fifteen shocks were applied before measuring the spread of the fresh mortar at 5, 15, 30 and 60 min.

2.1 Testing program

We investigated the original LC^3 cement and a modified LC^3 system with more than one SCM. As there were more than one SCMs, the modified LC^3 system was called LC^{3+}.

Table 1 Overview of the mix design plan (wt.%).

	OPC	Calcined clay	GGBFS	Anhydrite	$Ca(OH)_2$	Limestone powder
Label	OPC	CC	SL	Anh.	CH	LS
LC^3 low OPC	50-25	30		5		15-40
LC^{3+} (1:1) low OPC	50-20	30-15	30-15	3		17
LC^{3+} (1:1) with Portlandite	20	30	30	3	5	12

3 Results

3.1 LC^3

The OPC was replaced by an equivalent amount of limestone in the LC^3 system to explore its lower limit for blended cement used in this study while maintaining strength like that of neat OPC. The compressive strength results are given in Figure 1 (a) and (b). The binder mix design of these experiments is shown in Figure 1 (c). Varying components are labeled by the arrow, and the binder refers to the sum of OPC, SCMs and sulfate source in the pie chart.
The addition of 3 wt% C-S-H seeding to the LC^3 blended system made it possible to reduce the OPC content to ~40 wt% by using more limestone. In contrast, the reference blended cement without C-S-H seeding could not achieve strength development like that of the neat OPC reference across all replacement levels investigated here (from 25 wt% to 50 wt%). Even in the LC^3-50 sample, the reference showed slightly less strength than neat OPC. This was due to the reactivity of calcined clay and the low alkalinity (sodium equivalent, Na_{eq} ~0.6 wt%) environment of the OPC used for this experiment.

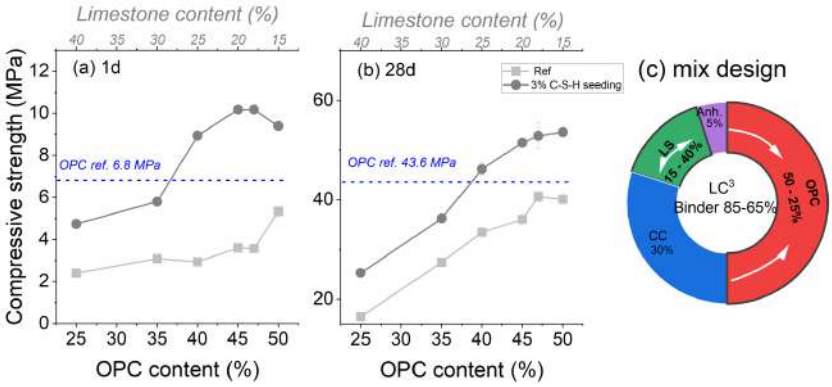


Figure 1 Compressive strength vs. OPC content in the LC^3 blended cement: (a) and (b). (c) shows the mix design of the experiments. The calcined clay and anhydrite contents were kept constant at 30 wt% and 5 wt%, respectively. An equivalent amount of OPC was replaced by more limestone. The strength of the pure OPC reference at the corresponding ages is indicated with a blue dashed line.

3.2 LC^{3+} with two SCMs – combining calcined clay with slag

The total binder was fixed to 83 wt% while more SCM was used to replace the OPC. The 1-day strengths did not depend much on the OPC content in either the reference or C-S-H seeded samples, as shown in Figure 2. There was more dependence of the strength on the OPC content after 7 days, i.e., more OPC resulted in greater late strength.

The combination of calcined clay, GGBFS and 3 wt% C-S-H seeding brought the lower limit of the OPC content in LC^{3+} cement down to 25 wt% based on the strength results until 28 days. Such low OPC content was not possible in the standard LC^3 mix design using only calcined clay as the SCM (as shown in Figure 1). The extended lower OPC content in the LC^{3+} compared to the LC^3 mix design could be explained by a higher total binder (from 83 wt% to 60 wt%, see Figure 1). Another factor could be the synergetic effect from the combination of calcined clay and GGBFS in the blended cement, as previously reported (Anuj and Shashank 2021, Wang, Hou et al. 2021).

Portlandite (5%, plotted as star in Figure 2) enhanced the late strength in the extremely low OPC content (20 wt%) system in this paper. This was because of the enhanced calcined clay reaction, which required portlandite. The added portlandite content played a critical role when there was not enough portlandite produced by cement hydration.

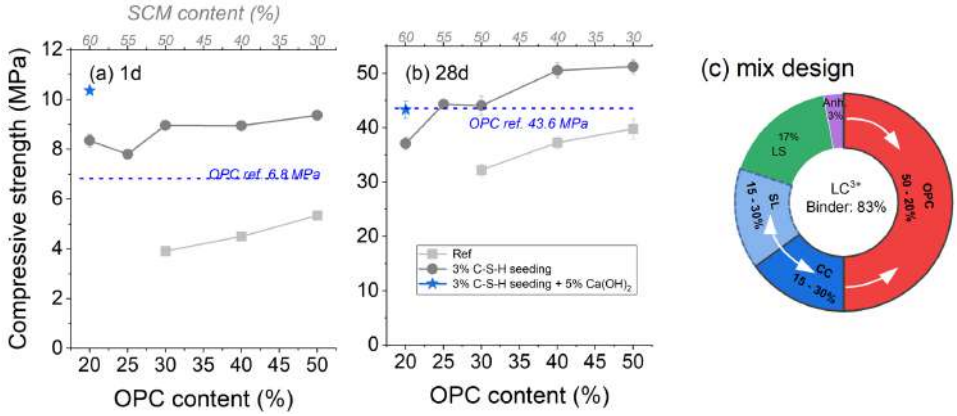


Figure 2 Strength of OPC replaced by SCMs for the LC^{3+} system: (a) and (b). (c) shows the mix design of the experiments. Two-component SCM (calcined clay to slag ratio is 1:1) replaced cement, and the corresponding total SCM content is labeled in the figure. The limestone content was kept constant at 17 wt%, and the total binder was kept constant at 83 wt%. The OPC reference at the corresponding ages is indicated with a blue dashed line.

3.4. Mortar flow

Figure 3 shows the impact of GGBFS replacement on the flow behavior in samples with (a) only dispersant (Melflux® additive) and (b) both dispersant and 3 wt% C-S-H seeding. Replacing 10 wt% of the calcined clay with GGBFS already showed an obvious improvement in the flow behavior for both the reference and C-S-H seeded samples. Increasing the GGBFS amount from 10 wt% to 15 wt% further improved the flow behavior.

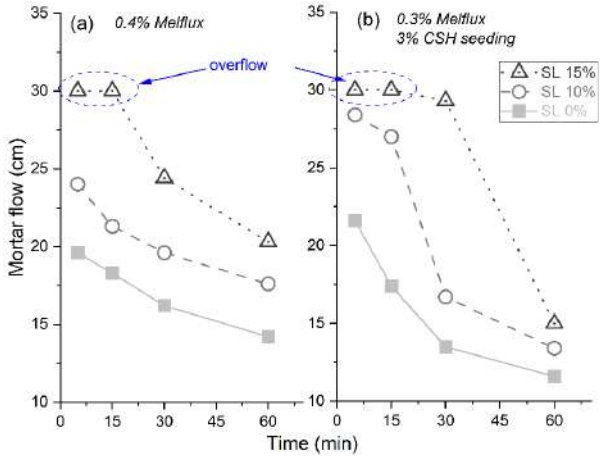


Figure 3 Mortar flow after 15 shocks of limestone calcined clay cement with 50 wt% OPC, 0, 10 and 15 wt% of slag (SL) replacing part of the calcined clay, and the total SCM was fixed to 30 wt%: (a) flow test with 0.4 wt% dispersant (Melflux® additives) and (b) flow test with 0.3 wt% dispersant and 3 wt% C-S-H seeding. Values of 30 cm, labeled as "overflow" in the dashed blue circle, refer to flow values equal to or greater than 30 cm, i.e., the maximum diameter of the testing plates.

4. Conclusions

The OPC content (equivalent to the clinker factor) in the blended cement could be dramatically reduced when 3 wt% C-S-H seeding was used in the LC^3 and LC^{3+} cement (combination of calcined clay and GGBFS). The lowest OPC content with 3% C-S-H seeding (with a similar strength until 28 days compared to neat OPC) could be concluded for the SCM and cement investigated in this paper:

- 40 wt% OPC for LC^3
- 25 wt% OPC for LC^{3+}
- 20 wt% OPC for LC^{3+} with 5% $Ca(OH)_2$

Replacing part of the calcined clay with GGBFS resulted in a significant improvement in workability.

Acknowledgements

Mr. Bernhard Mayr, Ms. Franziska Bichler and Ms. Cornelia Kronast from BASF Construction Additives GmbH are acknowledged for their experimental work.

References

Anuj, P. and B. Shashank (2021). "Hydration behaviour of limestone-calcined clay and limestone-slag blends in ternary cement." RILEM Technical Letters **6**(0).
John, E., T. Matschei and D. Stephan (2018). "Nucleation seeding with calcium silicate hydrate – A review." Cement and Concrete Research **113**: 74-85.
Kanchanason, V. and J. Plank (2019). "Effect of calcium silicate hydrate – polycarboxylate ether (C-S-H–PCE) nanocomposite as accelerating admixture on early strength enhancement of slag and calcined clay blended cements." Cement and Concrete Research **119**: 44-50.
Li, X., J. Bizzozero and C. Hesse (2022). "Impact of C-S-H seeding on the hydration of slag blended cement." Cement and Concrete Research **161**: 106935.
Nicoleau, L. (2013). "The acceleration of cement hydration by seeding: influence of the cement mineralogy." ZKG INTERNATIONAL **01**: 40.
Wang, H., P. Hou, Q. Li, S. Adu-Amankwah, H. Chen, N. Xie, P. Zhao, Y. Huang, S. Wang and X. Cheng (2021). "Synergistic effects of supplementary cementitious materials in limestone and calcined clay-replaced slag cement." Construction and Building Materials **282**: 122648.

The 16th International Congress on the Chemistry of Cement 2023 (ICCC2023)
"Further Reduction of CO_2 -Emissions and Circularity in the Cement and Concrete Industry"
September 18–22, 2023, Bangkok, Thailand

Novel strength enhancing cement additives to enable production of low-clinker cements

J.J. Thomas[1], R.G. Sibbick[2], J.F. Detellis[3], and J.H. Cheung[4]

[1] *GCP (SAINT-GOBAIN Construction Chemicals), Wilmington (MA), USA*
Email: jeffrey.thomas@gcpat.com

[2] *GCP(SAINT-GOBAIN Construction Chemicals), Wilmington (MA), USA*
Email: richard.sibbick@gcpat.com

[3] *GCP (SAINT-GOBAIN Construction Chemicals), Wilmington (MA), USA*
Email: joshua.detellis@gcpat.com

[4] *GCP (SAINT-GOBAIN Construction Chemicals), Wilmington (MA), USA*
Email: josephine.h.cheung@gcpat.com

ABSTRACT

The effect of a powerful strength enhancing additive on the hydration kinetics, strength, microstructure, and composition of mortars made with two different cements was investigated. It is anticipated that new strength enhancers of this general type will be increasingly employed by cement manufacturers to reduce cement clinker contents and thus CO_2 emissions. This study found that there were important microstructural differences related to the amount and morphology of the calcium hydroxide (CH) phase, with the mortars made with the additive having finer CH crystals as well as fewer larger CH prismatic crystals in the interfacial transition zones. The capillary pore structure was also more refined in the mortars made with the additive. These differences could well be related to the higher strengths of these samples. Use of the additive also resulted in less total CH as measured by thermogravimetry.

KEYWORDS: *Cement additives, strength enhancement, clinker reduction*

1. Introduction

The dilution of Portland cement clinker with less reactive materials such as supplementary cementitious materials and limestone is currently the primary lever for reducing the carbon footprint of cement manufacture, and this is projected to be the case for several years to come. However, aggressive reductions in clinker content are limited by associated reductions in strength, creating an urgent need for chemicals that provide significant strength enhancement when the cement is used to make concrete. Therefore, cement manufacturers are increasingly choosing to use a new class of strength enhancers designed for low carbon cements. Their use can enable clinker reductions of 10 % or more while maintaining equivalent strength development, creating significant CO_2 emission reductions. Alternatively, they allow cement manufacturers to significantly reduce the cement fineness, which reduces specific grinding energy and increases production rates. The focus of this paper is on the compositional and microstructural changes associated with the response of mortars to these new types of strength enhancers, to better understand the source of the strength enhancement.

2. Experimental

Mortar samples for microstructural examination were mixed and cured according to the ASTM C109 standard, using two different commercial Type I/II cements made in North America, denoted cement A and cement B. These cements were manufactured using glycol-based grinding aids without strength

enhancing additives. Characterization of the mineral composition of the cements by QXRD and the particle size distribution by laser PSD analysis is given in Table 1. Cement A has a typical mineral composition for a Type I/II cement, while Cement B has low C_3S and C_3A contents.

For each cement, a commercial GCP cement additive product designed to maximize the strength of limestone blended cements was admixed at a dosage of 2000 ppm into the mix water of one set of mortars, while another set was made with no additive as a blank control. The additive is an aqueous blend of alkanolamines (including EDIPA), organic retarders, and inorganic salts with a total active concentration of 52 %. At ages of 1 day, 3 days, and 28 days, hydration was stopped by immersing samples in isopropyl alcohol. To prepare samples for optical microscopy, thin sections were impregnated with fluorescent resin and polished to a thickness of 25 µm. For scanning electron microscopy (SEM) analysis, samples were impregnated with a low-viscosity resin and polished. For more experimental details see Sibbick and Silva (2019). Isothermal calorimetry tests on paste specimens made with and without additive were conducted using a TAM-Air calorimeter at 21°C. Thermogravimetric analysis (TA Instruments model Q500) was conducted on crushed paste specimens using a heating rate of 10°C /min to a maximum temperature of 900°C. Mortar strength tests had previously been conducted for the same cements and additive according to the EN-196 standard at the ages of 1 day, 2 days, and 28 days.

Table 1: Characterization of the cements. Left: mineral composition by QXRD (wt%). Right: laser PSD analysis.

	Cem A	Cem B		Cem A	Cem B
Alite	60.1	51.5	Dx (10) (µm)	1.72	1.73
Belite	15.7	23.6	Dx (50) (µm)	11.5	11.5
Ferrite	7.5	10.6	Dx (90) (µm)	35.1	29.8
Aluminate - Cubic	3.6	1.9	Below 32 µm (%)	86.8	92.6
Aluminate - Orthorhombic	1.4	1.1	Below 45 µm (%)	96.7	99.7
Portlandite	0.8	0.4	SSA (m²/kg)	477	485
Calcite	3.9	4.6			
Periclase	1.7	0.3			
Arcanite	0.6	1.1			
Gypsum	2.1	1.5			
Bassanite	2.1	2.8			

3. Results and Discussion

Isothermal calorimetry results for Cements A and B are shown in Figure 1. The effect of the chemical strength enhancer can be seen in both cases, although the effects are slightly different depending on the cement. For cement A the main hydration peak is significantly enhanced, particularly the secondary shoulder that is typically associated with C_3A hydration. For cement B the main peak is slightly enhanced but then an additional later peak at about 24 hours appears. The difference in the response to the strength enhancer is likely related to differences in the C_3A content and sulfate level of these cements.

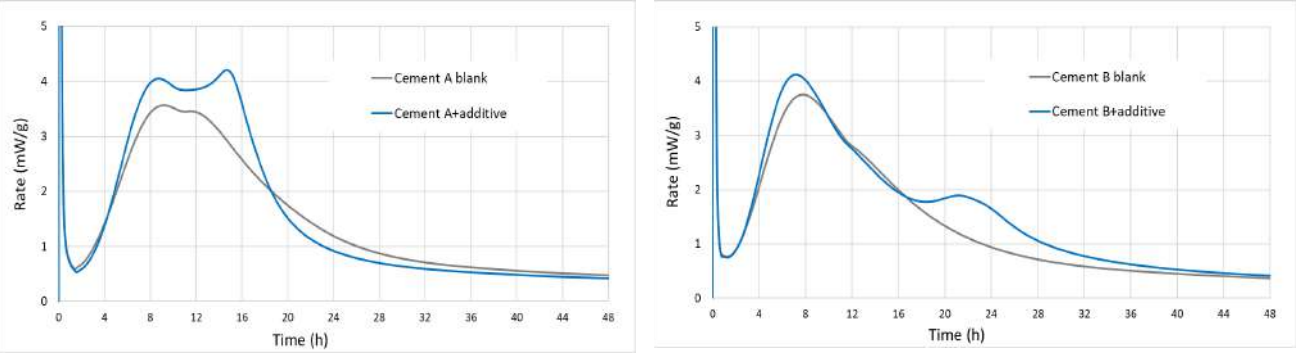


Figure 1: Isothermal calorimetry results for Cement A (left) and Cement B (right).

Table 2: Mortar strength results for blank and strength-enhanced mortars.

	Strength (MPa)			*Strength Gain (MPa)*		
	1D	2D	28D	1D	2D	28D
Cement A blank	17.2	30.3	65.5			
Cement A+additive	22.7	37.9	75.0	5.5	7.6	9.5
Cement B blank	21.9	32.9	63.0			
Cement B+additive	28.2	38.7	69.4	6.3	5.8	6.5

The mortar strength results are provided in Table 2. Both cements exhibit significant strength gains due to the additive at all ages tested, ranging from about 5-10 MPa. For cement A, the absolute strength gain increases with age, while for cement B the absolute strength gain is approximately constant with age.

Selected optical micrographs (transmitted light) for Cement A at the ages of 1 days and 28 days are shown in Figure 2. Based on the overall examination of multiple areas of the samples, the following general observations can be made. The strength-enhancing additive appears to accelerate the degree of hydration at 1 day, resulting in additional hydration product and less residual cement material as compared to the blank. Overall, there are lower amounts of the larger CH prismatic crystals present in the ITZ regions of the pastes made with the additive, which could well be related to the higher strengths of these samples. Another significant observation is that more of the CH crystals are visible in the presence of the additive, primarily as fine-sized and evenly distributed needle-like crystals in a 'lattice-like' formation within the cement paste matrix rather than the more typical larger prismatic CH crystals. Overall there appears to be lower total amounts of CH in the samples produced with the additive than the blank samples.

Backscatter SEM micrographs for Cement B at the ages of 3 days and 28 days are shown in Figure 3. Based on the overall examination of multiple areas of the samples, some general observations can be made, which are generally similar to the findings from the optical images. Without the strength-enhancing additive, the pastes are quite heterogeneous with a high abundance of residual cement grains, especially

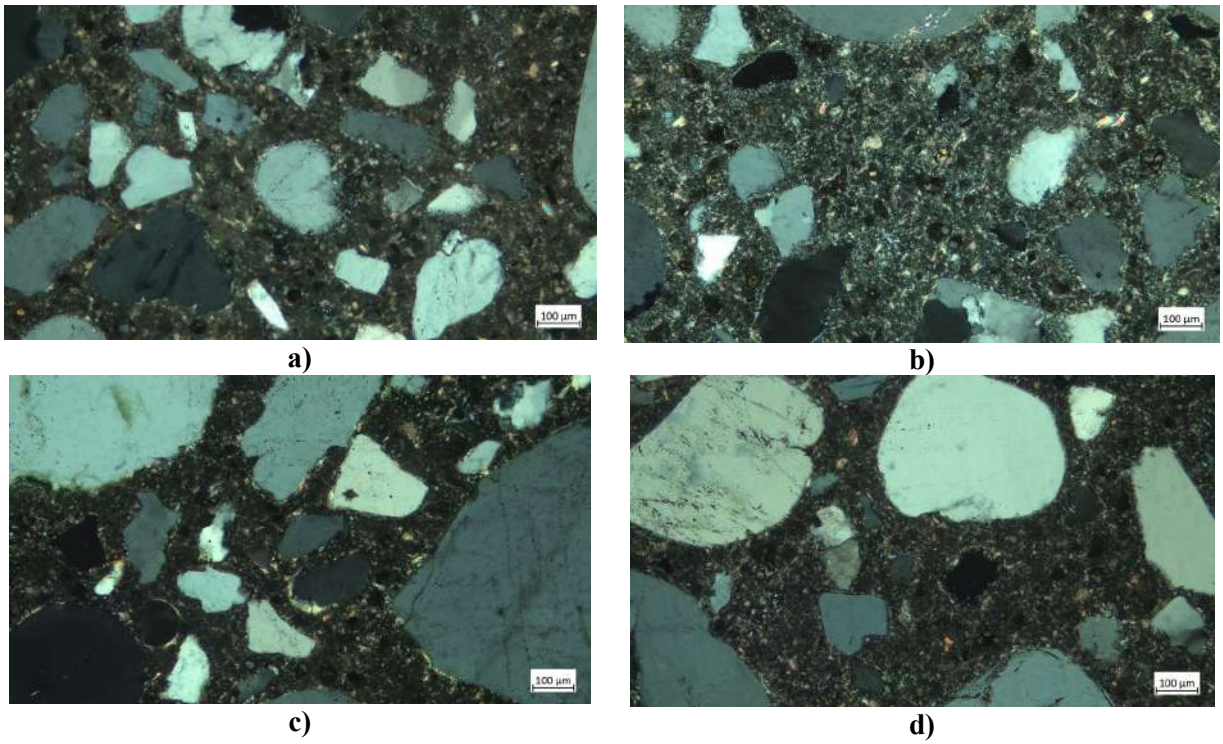


Figure 2: Thin-section optical cross-polarized transmitted light microscopy images of mortars made with Cement A. a) Blank at 1 day. b) Strength-enhanced at 1 day. c) Blank at 28 days. d) Strength-enhanced at 28 days. The light yellow, fine-sized crystals distributed throughout the cement paste primarily represent CH crystals.

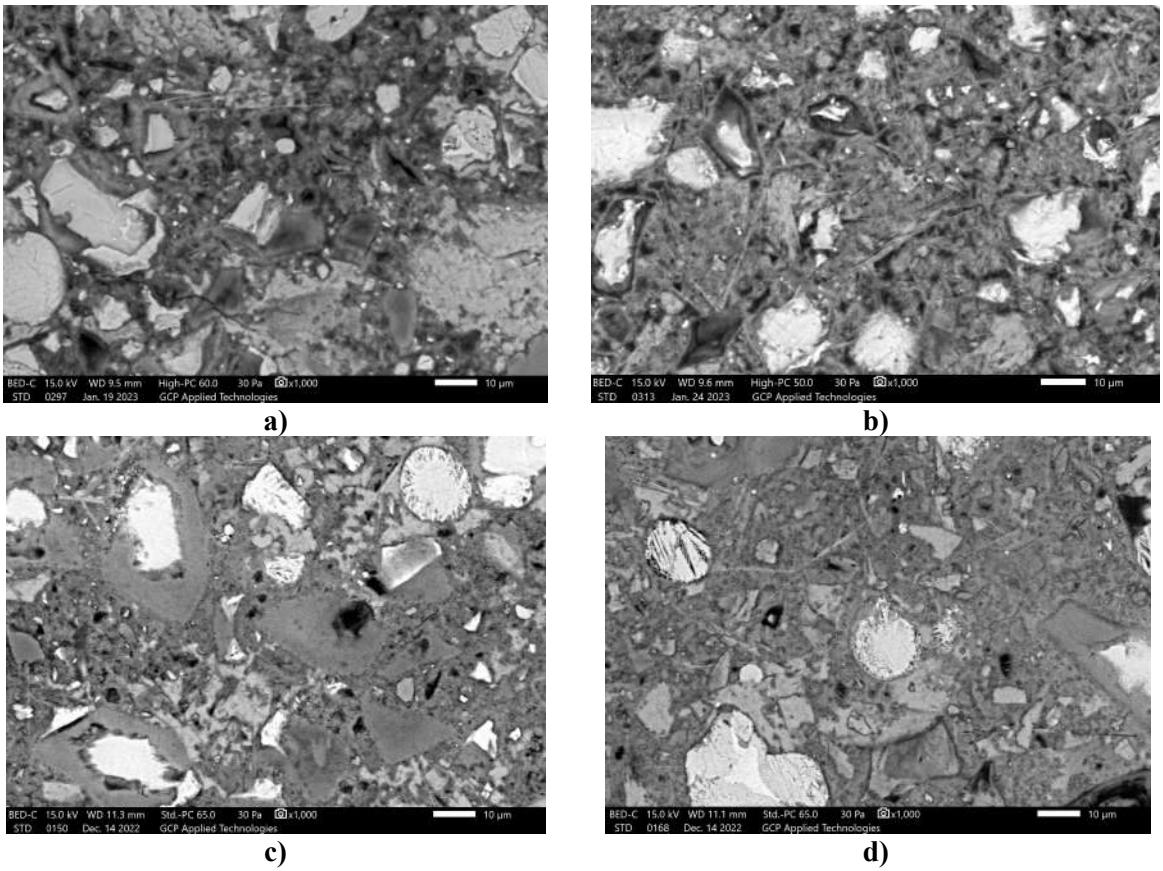


Figure 3: Backscatter SEM images of mortars made with Cement B. a) Blank at 3 day. b) Strength-enhanced at 3 day. c) Blank at 28 days. d) Strength-enhanced at 28 days.

belite crystals. Most CH is present as coarse prismatic crystals developing on aggregate ITZ and in the body of the cement paste, with finer needles appearing only rarely. With the additive, the paste appears more homogeneous and there is a slight reduction in the amount of residual cement grains, a reduction of larger prismatic crystals (particularly in the ITZ), and an increase in fine, randomly oriented needle-like CH crystals in the matrix. There are also clear differences in the pore structure, with the additive samples having overall reduced capillary porosity and finer average pore size. This is particularly apparent at the earlier age. Similar microstructural effects with pure amines have been reported previously (Riding et al. (2010), Jardine and Cheung (2015)). It is likely that amines such as DEIPA and TEA have a direct effect on the growth process of portlandite resulting in changes in the crystal morphology, and a mechanism for this was proposed by Zhang *et al*. (2016). As discussed by Berodier *et al*. (2019), alkanolamines likely increase strength through a few different mechanisms, including reduced CH amount and crystal size, reduced porosity, and increased hydration of the aluminate and ferrite phases.

To further investigate the effects of the additive on the overall hydration and on the CH phase, thermogravimetric analysis was performed on pastes made with cement A with and without the additive (see Table 3). While there are only minor differences in the total weight loss between room temperature and 900°C, the amount of CH (measured from the decomposition peak near 400°C) is distinctly lower in the pastes made with additive (despite a presumed higher degree of hydration). A similar reduction in CH content was reported for pure alkanolamine additions by Riding et al. (2010), who noted that this could be caused either by an increase in the Ca/Si ratio of the C-S-H phase, or by an increase in fine nanoscale CH intermixed with C-S-H.

Table 3: TGA analysis of hydrated cement pastes

	Total weight loss (%)			Calcium hydroxide (wt%)		
	1D	3D	28D	1D	3D	28D
Cement A blank	14.5	18.7	23.6	13.0	15.1	17.1
Cement A+additive	14.7	18.5	24.6	11.9	12.8	16.4

4. Conclusions

Use of a powerful strength-enhancing additive created microstructural differences in mortars at both early and late age. There was a reduction in the amount of larger prismatic CH crystals in both the matrix and the ITZ, while there was in increase in the amount of fine, needle-like CH in the matrix. The capillary pore structure was more refined, in that the total porosity appeared lower and the average pore size smaller. These observations could be related to the significantly higher strength at a given age. Thermogravimetric analysis indicated that the total amount of CH formation at 1D and at 3D was reduced, despite the accelerating effect of the additive.

Acknowledgements

The authors thank Steve Garrity for preparing the samples for microscopy and Tariq Khairalla for the TGA analysis.

References

Berodier, E., Gibson, L.R., Burns, E., Roberts, L., and Cheung, J. (2019). "Robust production of sustainable concrete through the use of admixtures and in-transit concrete management systems," *Cement and Concrete Composites*, 101: pp. 52-66.

Jardine, L. and Cheung, J.H. (2015) "Faster cement hydration," *International Cement Review*, October: 83-85.

Riding, K., Silva, D.A. and Scrivener, K. (2010) "Early age strength enhancement of blended cement systems by $CaCl_2$ and diethanol-isopropanolamine," *Cement and Concrete Research*, 40(6): 935-946.

Sibbick, R.G. and Silva, D.A. (2019) "Microscopic assessment into causes for early age strength gain with various amine-based admixtures in concrete," *17th Euroseminar on Microscopy Applied to Building Materials*, Toronto, Canada, pp. 54-60.

Zhang, Y.-R., Kong, X., Lu, Z.-C., Lu, Z.-B., Zhang, Q., Dong, B. and Xing, F. (2016) "Influence of triethanolamine on the hydration product of portlandite in cement paste and the mechanism," *Cement and Concrete Research* 87(5): 64-76.

The 16th International Congress on the Chemistry of Cement 2023 (ICCC2023)
"Further Reduction of CO_2 -Emissions and Circularity in the Cement and Concrete Industry"
September 18–22, 2023, Bangkok, Thailand

How siderite ($FeCO_3$) might be a future low-CO_2 reactive binder component for composite cements

F.R. Steindl[1,2*], M. Sakoparnig[1], L. Briendl[1], I. Galan[2], F. Mittermayr[1]

[1] *Graz University of Technology, Institute for Technology and Testing of Building Materials, Graz, Austria*

Email: florian.steindl@tugraz.at, m.sakoparnig@tugraz.at, briendl@student.tugraz.at, f.mittermayr@tugraz.at
[2] *Graz University of Technology, Institute of Applied Geosciences, Graz, Austria*

Email: florian.steindl@tugraz.at, igalangarcia@tugraz.at

ABSTRACT

While demand for reduced CO_2 emission and increased resource efficiency in the cement industry is growing steadily, certain "traditional" supplementary cementitious materials (SCMs), such as blast-furnace slag or coal fly ash, are expected to be of short supply in future years. Therefore, investigations for new possible SCMs are necessary. This contribution covers the characterisation of the iron carbonate mineral siderite, sourced from the world's largest deposit in the Styrian Erzberg mine in Austria, with respect to its utilisation potential as an energy-efficient reactive binder component. After chemical and mineralogical characterisation of the initial material, the hydration behaviour was investigated according to the R^3 reactivity test. Subsequently, hydration products were analysed by thermogravimetry and powder X-ray diffraction followed by Rietveld refinement. These analyses showed a significant hydration contribution of siderite, leading to the consumption of portlandite and siderite in favour of calcite and other iron-bearing phases such as $Fe(OH)_2$, FeO(OH) and Fe-bearing AFm phases. By repeating the R^3 test protocol using a 3% H_2O_2 solution, it was found that the type of iron-bearing hydrates was heavily depending on the redox conditions in the test regime. Siderite, in analogy to the classic pozzolanic reaction of traditional SCMs, exhibits a "ferrolanic" reaction within the cement system, consuming portlandite and potentially increasing compressive strength and durability of hardened concrete. These results highlight a potentially promising pathway of siderite and other iron carbonates being used as a reactive binder component to support a CO_2-reduced cement and concrete production and alleviate shortages of traditional SCMs.

KEYWORDS: *Clinker reduction, SCM development, hydration, CO_2-reduced cement additions*

1. Introduction

Reducing the CO_2 impact of cement and concrete is one of the main pillars of establishing a sustainable building economy. Supplementary cementitious materials (SCMs) are commonly used to substitute cement clinker in the binder and improve strength, durability and/or workability of the resulting concrete (Habert et al. 2020; Lothenbach et al. 2011). However, traditional SCMs such as blast-furnace slag or fly ash are expected to be of short supply in future years due to increased demand coinciding with the shutdown of coal-fired power plants and the transformation of the steel production from blast furnaces towards direct reduction and electric arc furnaces. Other hydraulic SCMs such as calcined clays or upcycled industrial wastes (Doschek-Held et al. 2022; Steindl et al. 2023) help to mitigate these supply shortages, but their processing and thermal activation is energy intensive.
Siderite ($FeCO_3$) has to date mainly been mined as iron ore, for example at the largest known deposit, the Styrian Erzberg mine in Austria. Economic considerations impose high cut-off values for the Fe content of the ore, meaning that mined rock with a relatively high siderite content is landfilled as gangue and would be easily available as an SCM. The siderite-rich material would require little processing and no thermal activation, thus causing very little additional CO_2 emissions.

Knowledge about the reactivity and effects of siderite in cementitious systems is almost inexistent. Zdiri et al. (2010) concluded that siderite fines can act as inert filler materials with potential strength-enhancing properties. To our best knowledge, hydraulic reactivity of siderite has not been mentioned in published literature before. In this contribution, we present a study on the reactivity of siderite in a cementitious system and characterise reaction products.

2. Materials and Methods

For the experiments, siderite ore concentrate was sourced from the Styrian Erzberg mine (VA Erzberg company) and powdered in a Retsch RS1 vibratory disc mill for 40 s at 1400 rpm without grinding aid. To avoid premature oxidation, the material was freshly ground shortly before each test and stored in sealed glass bottles. Chemical, mineralogical and physical material parameters of the resulting siderite powder are given in Table 1. The siderite powder contained some impurities of other carbonate and silicate minerals.

Table 1: Chemical and mineralogical composition and physical properties of the siderite powder used.

Oxide composition (wt-%)		Crystalline phases (wt-%)		Physical properties	
SiO_2	3.88	calcite	1.5	Blaine fineness (cm^2g^{-1})	5240
TiO_2	0.06	phlogopite	0.7	BET spec. surface (m^2g^{-1})	3.38
Al_2O_3	0.84	quartz	3.2	ρ ($g \cdot cm^{-3}$)	3.56
Fe_2O_3	-	siderite	84.3		
FeO	49.64	ankerite	5.1		
MnO	2.65	illite	3.0		
MgO	3.26	ferrihydrite	2.2		
CaO	2.44				
K_2O	0.15				
Na_2O	-				
P_2O_5	0.08				
SO_3	0.08				
loss on ignition	36.92				

To study the hydraulic reactivity of the powdered siderite, the R^3 test according to (Li et al. 2018) was conducted at 40°C by mixing siderite, portlandite and limestone powder in appropriate ratios with solutions of KOH and K_2SO_4 in distilled H_2O. To investigate the influence of a more oxidative environment on the system, the R^3 test was repeated with 3 wt-% H_2O_2 (hydrogen peroxide) in the solution. The resulting hydrated material was hydration-stopped after 7 and 28 d of reaction time by solvent exchange with isopropanol and subsequent drying at 40°C. These samples were analysed by thermogravimetry (TG) for phase identification and to determine the bound water content (between 105 and 350°C) with a Nietzsch STA 409 EP instrument (N_2 atmosphere, T range 30-1050°C, heating rate 10 K min^{-1}). Furthermore, X-ray powder diffraction was applied using a PANalytical X-Pert PRO diffractometer (Co-K_α radiation, 40 kV, 40 mA) in the range of 4 and 85°2θ with 0.008°2θ step size and 45 s count time per step. Rietveld refinement with Highscore Plus 3.0.5 was used for phase quantification of crystalline phases. The activity index of the powdered siderite was determined (without H_2O_2 addition) on standard mortar prisms fabricated according to EN 196-1, using a binder containing 75% standard cement (CEM I 42.5 R) and 25% powdered siderite.

3. Results and Discussion

The thermogravimetric curves (shown in Figure 1) reveal the major components in the reacted R^3 materials and significant differences between the tests conducted with and without peroxide. Besides portlandite, siderite and calcite from the initial materials, DTG peaks of hydrated phases can be ascribed to FeO(OH) (Koga et al. 1995) and Fe-containing AFm phases (monocarbonate Fe-MC, hemicarbonate Fe-HC, possibly monosulfate Fe-MS) (Dilnesa et al. 2012, 2011). These phases are mostly apparent from the test conducted

with peroxide. Calculating portlandite consumption was not possible, as the dehydroxylation peak of $Ca(OH)_2$ overlaps with the decarbonation peak of siderite. The amounts of bound water, as a result of the R^3 test, are given in Table 2. The addition of peroxide causes a higher amount of bound water, likely due to the oxidation of siderite and Fe^{2+} hydroxides, leading to increased formation of Fe^{3+}-hydroxides and Fe-AFm-phases, as detected by TG. At least part of the Fe^{3+} hydroxides, such as FeO(OH), was probably not formed during the test but during hydration stoppage by the oxidation of Fe^{2+} hydroxides like $Fe(OH)_2$.
The diffractograms recorded by XRD corroborate the TG results, verifying the formation of Fe-bearing AFm-phases (Fe-monosulfate, Fe-monocarbonate, Fe-hemicarbonate; possibly limited solid solution formation) and calcite (see Figure 2).

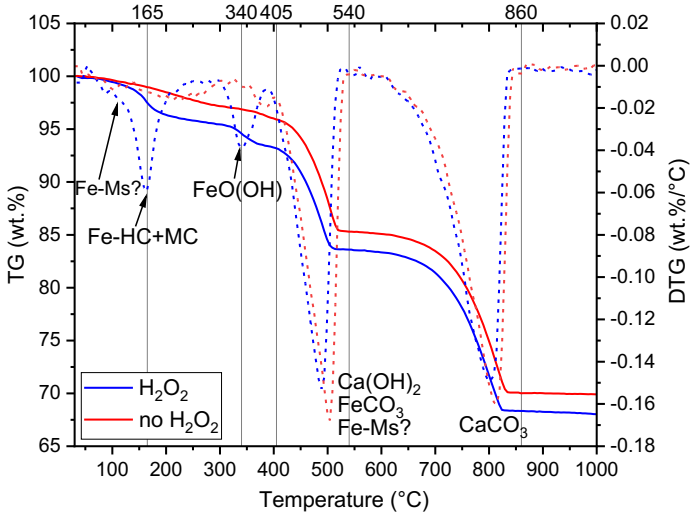


Figure 1: TG analysis curves of R^3 material after 7 d of reaction with and without H_2O_2.

Table 2: Bound water as determined in the R^3 reactivity test after 7 d of reaction time.

Sample type	bound water (g/100g dry paste)
Siderite (H_2O_2)	5.2
Siderite (no H_2O_2)	2.8

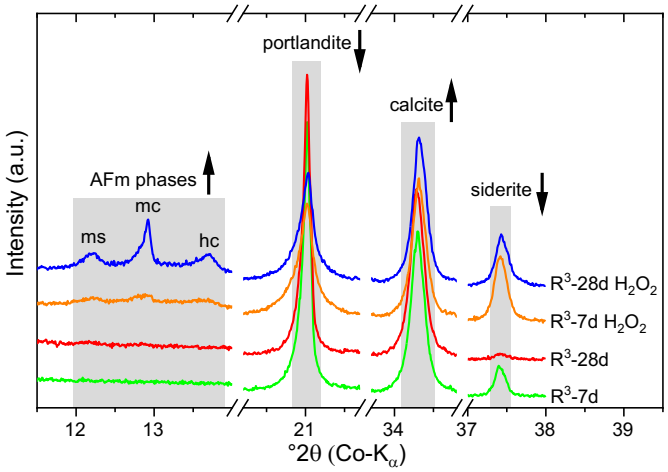


Figure 2: Details of diffractograms obtained from R^3 material reacted with and without H_2O_2 for 7 and 28 d. Black arrows indicate the formation of AFm phases and calcite and the consumption of portlandite and siderite, which is found both with and without H_2O_2.

Rietveld refinement showed that, in accordance with TG, these phases are readily formed if H_2O_2 was added during mixing, leading to a total of 9.7 and 17.5 wt-% of Fe-bearing AFm phases after 7 and 28 d, respectively. In contrast, only 1.6 wt-% of such phases were detected without H_2O_2 after 28 d.

Simultaneously, portlandite and siderite are consumed by the "ferrolanic" reactions. The almost complete consumption of siderite without H_2O_2 suggests a second reaction mechanism, possibly the formation of X-ray-amorphous phases such as amorphous $Fe(OH)_2$, which could oxidise to poorly crystalline Fe^{3+} hydroxides and thus be not easily detected with TG.
The activity index of cement-siderite blends was determined at 69% after 28d of hydration, increasing to 83% after 90d of hydration. In comparison to inert fillers, siderite could therefore result in strength loss at early ages but significantly contribute to strength after later ages when more siderite has reacted.

4. Conclusions

Siderite has until recently not been considered as a potential reactive binder component for Portland cement systems. Our findings provide first evidence of a "ferrolanic" reaction of siderite, consuming portlandite in favour of hydrated Fe-bearing phases in analogy to classic pozzolans. The type of phases formed is controlled by the redox regime: the formation of Fe-AFm-phases depends on the provision of Fe^{3+} by oxidation, while other phases such as $Fe(OH)_2$ could also form without oxidation by a reaction of siderite with portlandite. The discovered reaction pathways open possibilities for siderite (and potentially other iron carbonates) being used as reactive SCMs. The formation of hydrated phases could potentially contribute to concrete strength, especially at later ages. Probably more importantly, the consumption of portlandite and the incorporation of Fe in AFm phases are likely improving durability against for example Ca leaching or sulfate attack. Future research is planned to investigate the effects of siderite on Portland cement hydration and the durability of the resulting mortars and concretes.

Acknowledgements

The authors want to thank the VA Erzberg Company for providing the investigated materials. Support by the Austrian Research Promotion Agency (FFG) within the research project "SpOC – Sprayed optimised concrete" (Grant-No. FO999896972) is gratefully acknowledged.

References

Dilnesa, B.Z., Lothenbach, B., Le Saout, G., Renaudin, G., Mesbah, A., Filinchuk, Y., Wichser, A., and Wieland, E. (2011) "Iron in carbonate containing AFm phases", *Cement and Concrete Research,* 41(3): 311–323

Dilnesa, B.Z., Lothenbach, B., Renaudin, G., Wichser, A., and Wieland, E. (2012) "Stability of Monosulfate in the Presence of Iron", *Journal of the American Ceramic Society,* 95(10): 3305–3316

Doschek-Held, K., Mimra, C., Sattler, T., and Steindl, F.R. (2022) "Behandlung von Steinwolle zur stofflichen Verwertung als Sekundärzumahlstoff in der Baustoffindustrie (Recycling of rock wool as a binder component in the building materials industry)". In: Pomberger, R. (Ed.), *Recy&DepoTech 2022*. Montanuniversitaet Leoben, Chair of Waste Processing Technology and Waste Management, Leoben

Habert, G., Miller, S.A., John, V.M., Provis, J.L., Favier, A., Horvath, A., and Scrivener, K.L. (2020) "Environmental impacts and decarbonization strategies in the cement and concrete industries", *Nature Reviews Earth & Environment,* 1(11): 559–573

Koga, N., Takemoto, S., Okada, S., and Tanaka, H. (1995) "A kinetic study of the thermal decomposition of iron(III) hydroxide oxides. Part 1. α-FeO(OH) in banded iron formations", *Thermochimica Acta,* 254(C): 193–207

Li, X., Snellings, R., Antoni, M., Alderete, N.M., Ben Haha, M., Bishnoi, S., Cizer, Ö., Cyr, M., De Weerdt, K., Dhandapani, Y., Duchesne, J., Haufe, J., Hooton, D., Juenger, M., Kamali-Bernard, S., Kramar, S., Marroccoli, M., Joseph, A.M., Parashar, A., Patapy, C., Provis, J.L., Sabio, S., Santhanam, M., Steger, L., Sui, T., Telesca, A., Vollpracht, A., Vargas, F., Walkley, B., Winnefeld, F., Ye, G., Zajac, M., Zhang, S., and Scrivener, K.L. (2018) "Reactivity tests for supplementary cementitious materials: RILEM TC 267-TRM phase 1", *Materials and Structures,* 51(6): 151

Lothenbach, B., Scrivener, K., and Hooton, R.D. (2011) "Supplementary cementitious materials", *Cement and Concrete Research,* 41(12): 1244–1256

Steindl, F.R., Doschek-Held, K., Weisser, K., Juhart, J., Grengg, C., Wohlmuth, D., and Mittermayr, F. (2023) "Mineral residues and by-products upcycled into reactive binder components for cementitious materials", *Synercrete 2023,* (accepted):

Zdiri, M., Ouezdou, M. Ben, Abriak, N., and Neji, J. (2010) "Contribution of Siderite fines additions on the Roller Compacted Concrete (RCC) strength", *Journal of Engineering and Technology Research,* 2(1): 13–23

The 16th International Congress on the Chemistry of Cement 2023 (ICCC2023)
"Further Reduction of CO_2 -Emissions and Circularity in the Cement and Concrete Industry"
September 18–22, 2023, Bangkok, Thailand

A Particle Packing Approach for Eco-efficient Ultra High-Performance Concrete (E-UHPC)

B. Baten[1], H. Samouh[1], and N. Garg[1*]

[1] *Department of Civil and Environmental Engineering, University of Illinois at Urbana Champaign, Urbana, IL*
Email: bbaten2@illinois.edu, hsamouh@illinois.edu, nishantg@illinois.edu

ABSTRACT

Conventional design methods of Ultra-High-Performance Concrete (UHPC) usually involve high cement content (900-1100 kg/m^3) to enhance the mechanical and durability performance. However, the associated cost and environmental impact have limited its widespread usage. This study reports an efficient particle-packing approach in designing eco-efficient UHPC (E-UHPC) mixes with lower cement content while ensuring good rheological and mechanical properties. A total of five (5) UHPC mixes with different 'packing factors (PF)' (32.9 to 46.0) were designed by optimizing different commonly used supplementary cementitious materials (SCMs). The experimental results show that the packing factor strongly influences the workability (flow and yield stress), regardless of the binder types. Moreover, optimizing the packing factor resulted in a dense E-UHPC microstructure with open porosity of 3.67% at 28 days. The results also confirms that the packing factor govern the strength-porosity relationship of UHPC mixes with a higher strength development at PF:32.9. Furthermore, this study signifies that using packing factor and binder coefficient (BC) as design parameters can effectively allow cement replacement of >50% with adequate compressive strength ($f'_{c,28d}$: 118 MPa) and workability (flow: 230 mm). This implies an eco-efficient optimization method for designing low-cost E-UHPC (BC: 5.99 kg/m^3/MPa) with very low cement content (<50%) and thereby with significantly lower carbon footprint.

KEYWORDS: ***E-****UHPC, Packing factor, SCMs, Binder coefficient, Binder optimization.*

1. Introduction

The conventional design method of Ultra-High-Performance Concrete (UHPC) relies on a combination of very high cement content, low water-binder ratio, and high volume of steel fibers to ensure its enhanced mechanical properties and durability (Arora et al. (2018)). However, such elevated cement content increases the material's overall cost and carbon footprint. Hence, it is a significant incentive to replace cement with commonly used supplementary binders (SCMs) and fillers to make UHPC more sustainable and environmentally friendly (Huang et al. (2017)). As such, estimating the maximum cement replacement criteria and proportions is vital without compromising the mechanical and durability properties. This study used a packing model to investigate the extent of cement replacement with common SCMs while ensuring adequate packing, rheological and mechanical properties. With an inherently low w/b ratio, adequate packing of the microstructure plays a dominant role over the limited degree of hydration in governing the characteristic properties of UHPC. This concept was used to design five UHPC mixes with different replacement proportions of fly ash (≤ 35%), ground granulated blast furnace slag (≤20%), and silica fume (≤20%) to represent different ranges of packing density. The role of packing density on UHPC performance was investigated through fresh properties (flow and yield stress) and mechanical properties (porosity and compressive strength) at different ages. This study confirms that the packing model is more effective in optimizing the binder composition for a UHPC mix incorporating low cement content. Ensuring a microstructure with higher packing also exhibited enhanced flow and significantly higher compressive strength, even with lower cement requirements. This study also reveals that the 'binder coefficient' reflects an ideal evaluation tool of cement consumption in a UHPC function in terms of its performance. It was possible to reduce the cement consumption to one-third (5.99

kg/m^3/MPa) by enhancing the packing density through binder optimization. This design concept has significant potential in reducing the overall carbon footprint of UHPC mixes while maintaining its intended performance and making it applicable for sustainable construction practice.

2. Experimental Program

2.1 Materials

The binders used in this study include Type-I ordinary Portland cement (OPC), ultra-fine class-F fly ash (UFFA), slag (GGBS), and silica fume (SF). Masonry sand, sieved below 600 μm, was used as the fine aggregate. The particle size distribution (Fig. 1a) of each constituent was determined by using Laser Diffractometer to be used in the packing model. This study used an ultra-fine fly ash sample for a higher packing density. In addition, a polycarboxylate-based high-range water reducer (ADVA Cast 593) was used to reduce water demand and ensure adequate workability.

2.2 Mix Design based on Packing Model

In this study, five (5) UHPC mixes (M1-M5) were designed, with M1 being the control mix and Mix M2-M5 with varying replacement proportions of cement (up to 55%) with different SCM content (Table-1).

Table 1: Mix Details of UHPC Mix (M1-M5). The nomenclature represents the proportion in % of each constituent (represented by each letter) in the mix.

ID	Nomenclature	Mix Constituents (kg/m^3)						
		OPC	SF	UFFA	GGBS	Sand	Total Binder	S/B Ratio
M1	**C100**	1575	0	0	0	1325	1575	1
M2	**C70S5F10G15**	1103	55	131	221	1325	1509	1
M3	**C45S5F30G20**	709	55	392	295	1325	1450	1
M4	**C45S20F35**	788	244	508	0	1178	1539	0.8
M5	**C45S20F35**	709	220	457	0	1325	1386	1

A constant w/b ratio and HRWR dosage of 0.18 and 5% (wt. of binder), respectively, were used. Each mix's 'packing factor' was measured from the deviation between the ideal curve from Modified Anderson and Andreasen model (Yu et al. (2015)), using q=0.23, and the composite particle size distribution (Fig. 1a). Fig. 1b shows the variation of the packing factor with Mix M5 having the highest packing.

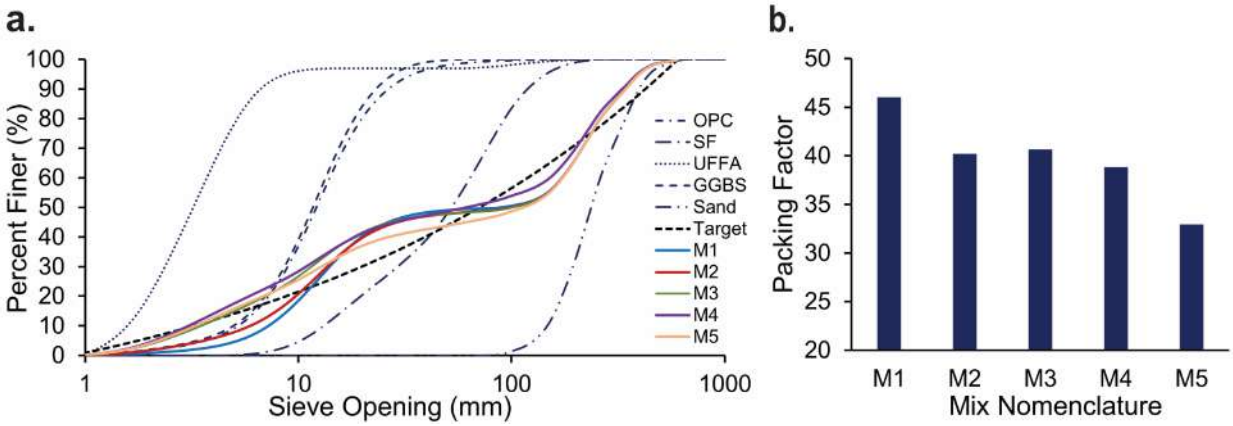


Figure 1. (a) Particle size distribution of the mix constituents used in designing the UHPC mixes. The composite particle size distribution of UHPC mixes, M1-M5, are represented in solid lines compared to the target curve from the Modified Anderson and Andreasen Model, (b) Packing factor of M1-M5 representing packing of the mixes.

3. Experimental Methods

The fresh properties of the UHPC mixes were measured through the modified flow test (ASTM C1611). The rheological properties (yield stress and plastic viscosity) were also evaluated using a TA DHR-3

Rheometer with a vane in cup geometry at 25±1 °C. A logarithmic shear sweep with a broad ramp-up phase of 0.1/s to 200/s was used to measure yield stress and viscosity accurately.
The compressive strength of 50 mm cube specimens was determined at different cured ages (3d, 7d, 14d, and 28d) following ASTM C109. The open porosity of the mixes was also determined at the same ages using AccuPyc 1330 Pycnometer at a constant pumping pressure (Kumar and Garg (2022)).

4. Results and Discussion

The stress-strain behavior, shown in Fig. 2a, reflects a significant influence of particle packing on the rheological behavior of UHPC mixes containing high SCM content.

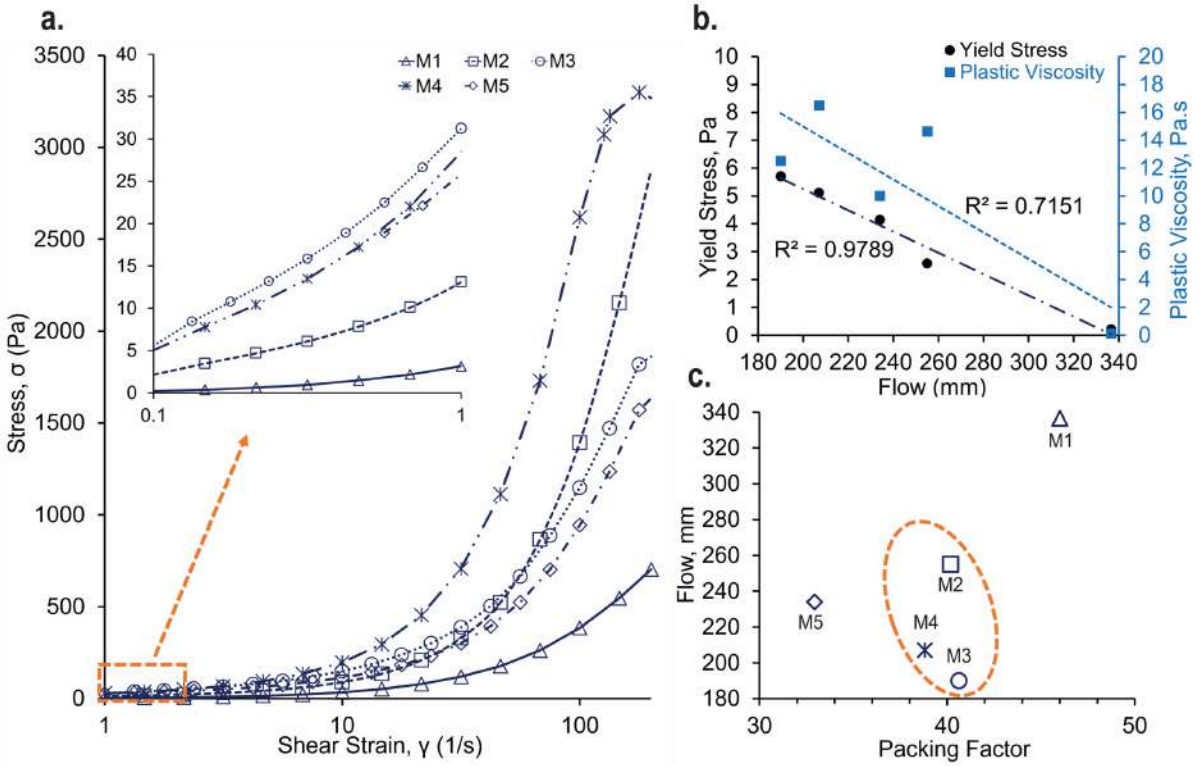


Figure 2. (a) Rheological behavior of the UHPC mixes for a logarithmic stress-strain sweep (0.1-200 s^{-1}) in a co-axial rheometer, (b) correlations developed between the flow and the rheological parameters (yield stress and plastic viscosity) and (c) role of packing density in influencing the rheological parameters of the mixes.

The presence of high SCM content increased the HRWR demand, resulting in much higher yield stress and flow than the control mix (M1). Meanwhile, M5 exhibits the highest packing (lowest packing factor), contributing to lower inter-particle voids and a higher amount of free water for enhancing flow despite much less cement content. This also explains a lower flow value and higher yield stress for Mix M4, which had similar mix composition but lower packing due to a lower s/b ratio of 0.8. While particle packing certainly governs the rheological behavior of UHPC mixes, HRWR demand should also be considered for an appropriate mix selection, as shown for Mix M2-M4 (marked zone) in Fig. 2c. Although M2 and M3 showed similar packing, however, the high UFFA content of M3 and higher HRWR demand resulted in lower flow spread and the highest yield stress. A similar trend was observed in all the rheological parameters, although flow values showed a better correlation (Fig. 2b) with the yield stress of any UHPC mix. This confirms that packing and HRWR dosage govern the inter-particle contact and friction, determining the water-film thickness required to initiate flow.
The effect of packing is more dominant on the mechanical behavior of UHPC mixes, as shown in Fig. 3. Although all the mixes showed a strong negative correlation between compressive strength and open porosity, however, it was found that the packing factor highly governs the relationship (Fig. 3a). Evidently, mix M5 showed the lowest porosity and the steepest slope along with a reducing slope with decreasing packing (lower PF value from left to right). This reflects that higher particle packing resulted in a refined microstructure and increased strength, even at an early age, and also contributed to higher

strength gain at later ages due to further pore refinement. Meanwhile, the control mix (M1) with lowest packing showed a broader change in porosity due to hydration. However, it still resulted in much lower strength ($f'_{c,28d}$: 77 MPa) compared to M5 ($f'_{c,28d}$: 118 MPa) with only 45% OPC content, as shown in Fig. 3b. This suggests that in UHPC mixes with low w/b ratio and degree of hydration, ensuring higher packing governs the mechanical properties and should be key in designing the mix. Most importantly, it offers an efficient approach to reducing the binder requirement and the associated environmental impact of UHPC. To justify the same, this study suggests evaluating the binder coefficient (amount of cement requirement per MPa strength) as a more appropriate parameter for comparing mix efficiency. With a reduced packing factor, the binder coefficient could be reduced by three folds (20.2 kg/m^3/MPa to 5.99 kg/m^3/MPa). Hence, considering the packing factor and binder coefficient as mix design criteria ensure low-cement UHPC with adequate performance.

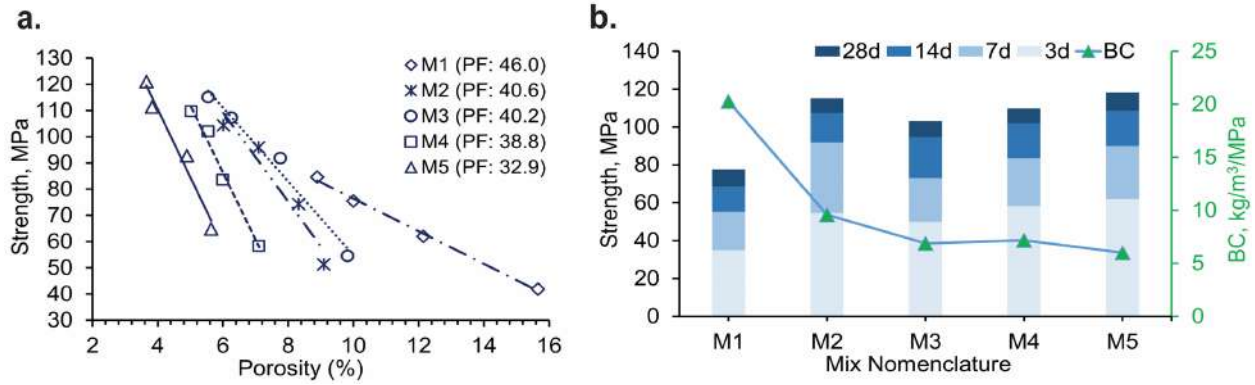


Figure 3. (a) Effect of packing factor on the strength-porosity relationship of the UHPC mixes (M1-M5) at different ages and (b) Compressive strength of the mixes at different ages as a function of the binder coefficient (BC)

5. Conclusions

This study demonstrated the significance of the packing factor in designing UHPC mixes with low binder content based on rheological and mechanical properties. Although the packing factor primarily governs the yield stress and flow of fresh UHPC mix, the amount of fines and HRWR dosage should also be considered while considering rheological criteria. Meanwhile, the packing factor has a more dominant effect in governing the strength-porosity development of UHPC mixes. This study also showed how ensuring a packed microstructure through a low packing factor can replace more than 50% cement without comprising strength (118 MPa) and rheology (flow: 230 mm). Moreover, optimizing the binder coefficient by ensuring a lower packing factor is a more effective approach to ensure an eco-efficient UHPC with low cement content and a significantly lower carbon footprint.

Acknowledgements

The authors acknowledge the support from the Illinois Center for Transportation (ICT) and Illinois Department of Transportation (IDOT) for funding the project (ICT R27-232)

References

Arora, A., Aguayo, M., Hansen, H., Castro, C., Federspiel, E., Mobasher, B. and Neithalath, N. (2018) "Microstructural packing-and rheology-based binder selection and characterization for Ultra-high-Performance Concrete (UHPC)", *Cement and Concrete Research*, 103: 179-190.

Huang, W., Kazemi-Kamyab, H., Sun, W. and Scrivener, K. (2017) "Effect of cement substitution by limestone on the hydration and microstructural development of ultra-high-performance concrete (UHPC)", *Cement and Concrete Composites*, 77: 86-101.

Kumar, V., and Garg, N. (2022) "The chemical and physical origin of incineration ash reactivity in cementitious systems", *Resources, Conservation and Recycling*, 177, 106009.

Yu, R., Spiesz, P. H. J. H. And Brouwers, H. J. H. (2015) "Development of an eco-friendly Ultra-High-Performance Concrete (UHPC) with efficient cement and mineral admixtures uses", *Cement and Concrete Composites*, 55: 383-394.

The 16th International Congress on the Chemistry of Cement 2023 (ICCC2023)
"Further Reduction of CO_2 -Emissions and Circularity in the Cement and Concrete Industry"
September 18–22, 2023, Bangkok, Thailand

Production of Low-Heat Cement from Industrial Waste

G.V.P.Bhagath Singh[1*]

[1*] *Assistant Professor, Department of Civil Engineering, SRM University, AP, Andhra Pradesh, India*
Email: bhagathsingh.g@srmap.edu.in

ABSTRACT

The partial or fully utilization of industrial waste materials in cement production became an interest due to environmental regulations. The current paper explores the production of clinker and low-heat composite cement using different industrial waste materials. Lime sludge generated by the paper mill industry and sponge iron collected from the iron industry is used as primary source materials along with pharma and chemical industry wastes. A large-scale vertical kiln is used to produce clinker for initial evaluation. Carbon in the sponge iron was used as an energy source to burn the raw materials, which helped reduce the required fuels. The outcome of clinker composition is belite rich. Low-heat cement is produced by inter-grinding the clinker with silico-manganese slag and fly ash, and performance was compared with commercially available Ordinary Portland Cement (OPC). Different analytical techniques were used to characterize the raw materials, clinker, and composite cement. The ultimate strength of composite and OPC cement concrete is the same. This work provides a basis for efficiently utilizing industrial waste materials in making alternative cement for various construction activities.

KEYWORDS: *Industrial waste materials, Low heat cement, clinker, Composite cement, Concrete.*

1. Introduction

The growing infrastructure required significant quantities of cement. Currently, the cement consumption level is about 4.2 million tons per year, and it is expected to reach 4.4 billion metric tons by the end of 2020 (Cement industry trends report (2017), Scrivener (2014)). Cement production involves consuming virgin materials and releasing anthropogenic CO_2 into the atmosphere. Due to the high demand for cement, particularly in developing countries, there is an increasing demand for a source of raw materials in the required quantities. A large quantity of post-industrial waste materials are available in and around the industries, and disposal of these materials has become a challenge. Due to the large generation of these materials, it is challenging to identify permanent land for disposal. Hence, there is an increasing interest in using these materials for different applications. Researchers have used different waste materials over the past few years to produce clinker and cement. Steel slag was used with a combination of limestone, sand, clay, and bauxite materials to produce clinker (Tsakiridis et al. (2008)). Another researcher used sewage waste in clinker production. The produced sewage waste-based cement has shown similar chemical composition to regular conventional ordinary portland cement. The higher sewage dosage in the cement was shown to be higher in the setting time and lower in strength (Lin et al. (2012)). An eco-portland clinker was produced using different combinations of biological sludge, lime mud, and fly ash (Buruberri et al. (2015)).

The current paper explores clinker and composite cement production using post-industrial waste materials, the characterization of materials, and the cement evaluation. Different waste materials such as lime sludge, sponge iron, and pharmaceutical wastes were used to produce the clinker. Composite cement (CC) is produced by blending clinker with fly ash and silico-manganese slag. Finally, concrete is produced using composite cement and compared with conventional cement.

2. Materials and methods

Lime sludge waste and sponge iron were used as primary raw materials to produce the clinker. Composite cement was produced by combining the clinker with other waste materials from different industries, such as fly ash, silico-manganese slag, gypsum, and pharmaceutical waste containing sodium sulfate and sodium hydroxide.

All the waste materials used in this study were collected from different industries in southern India. The lime sludge was collected from a paper mill industry. The sponge iron generated during the first stage of iron production was collected from the sponge iron unit and contained half-burnt coal along with the iron. It had a gross calorific value of 2500-3000 kJ/kg. Clay used in clinker production was collected from a locally available aggregate crusher plant. Fly ash was obtained from the thermal power station. The silico-manganese slag was collected from a ferroalloy plant. Gypsum was collected from a fertilizer plant. Pharmaceutical waste was collected from producers of intermediaries for drug manufacture.

A vertical kiln was used to produce clinker at a maximum temperature of 1400^{o}C. The raw mixture for clinkering consisted of a combination of lime sludge: clay: sponge iron in the proportion of 70: 6: 20.5. The calcination zone temperature varies between 600 to 1400^{o}C. Composite cement is produced by inter-grinding 65% clinker with other materials such as 22% fly ash, 10% silico-manganese slag, 2% gypsum, and 0.5% of a pharmaceutical waste solution consisting of sodium sulfate and sodium hydroxide.

The oxide composition of all the source materials, the clinker, and the composite cement was determined using an S2-ranger (Bruker) X-ray Fluorescence Spectrometer (XRF). A D2 phaser (Bruker) XRD was used to determine the spectrum of the samples. The diffraction measurements were performed between the 2θ angles from 10 to 70^{o} with a 0.02^{o} increment. The total measurement time is about 30 minutes. Quantification was performed using TOPAS 5 software using an external standard (Corundum) approach (Bhagath Singh and Subramaniam (2016a and 2018)). Heat signatures were measured using TAM AIR Isothermal calorimetry.

Concrete mix design was prepared to achieve a slump of 60 mm and a mean target strength of 33 MPa as per BIS 10262 (BIS 10262 (1982)). The composite cement (CC), fine and coarse aggregate contents in the concrete mixture were 340 kg/m^3, 767kg/m^{3,} and 1146 kg/m^3. The water-to-CC mass ratio was 0.43. Standard 150 mm cubes were prepared to evaluate the compressive strength of concrete. Immediately after casting, the concrete specimens were cured at 25^{o}C and 95% relative humidity till the day of testing. Compressive strength was determined using the concrete cubes at 1, 3, 7, 14, 28, and 90 days.

3. Results and discussion

3.1 Oxide composition of source materials

The oxide compositions of source materials are listed in Table 1. Clay, sponge iron, and silico-manganese slag contain significant quantities of silica, alumina, iron, and calcium. Along with these oxides, the silico-manganese slag also contains alkalis, such as sodium and potassium. The fly ash primarily contains silica, alumina, and iron oxides with the very low calcium content. Based on the oxide composition, fly ash is classified as siliceous (class F) fly ash (ASTM C618 (2017), BIS 3812(1981)). The purity of gypsum and sodium sulfate are 99% and 98%, respectively. The sodium hydroxide solution from the pharmaceutical industry contains 3.97%Na, 1.03% Si, and 0.98% K, while Br, Cl, and S are present in trace quantities.

Table 1. Oxide composition of the industrial waste materials (% by mass).

Compound name	SiO_2	Al_2O_3	Fe_2O_3	CaO	TiO_2	K_2O	MgO	P_2O_5	Na_2O	SO_3	MnO	LOI
Lime sludge	0.69	0	0.27	96.66	0	0.32	0.77	0.63	0	0.22	0.02	0.11
Sponge iron	26.64	14.45	20.94	7.27	2.07	1.98	1.73	1.09	0	3.35	0.18	17.89
Clay	43.6	12.29	9.49	27.89	1.07	1.47	1.78	0.46	0	0.93	0.1	0.21
Silico-manganese slag	28.42	9.22	2.32	22.34	1.59	13.15	3.75	0.14	13.21	1.21	3.5	0.31
Fly ash	54.89	27.54	5.88	0.85	2.14	3.95	0.87	0.45	1.72	0.54	0.02	0.76

3.2 Characterization of clinker and composite cement

3.2.1 Oxide composition

The oxide composition of clinker and composite cement are shown in Table 2. The composition of a typical commercially available OPC (Grade 43 cement as per BIS 8112 (BIS 8112 (1989)) is also shown in the table for comparison. Similar oxides are present in composite cement and clinker in varying quantities. In composite cement, Al_2O_3 and SiO_2 contents are increased and reduced CaO content slightly. The main reason for the changes in the addition of fly ash and silico-manganese slag, which increase the SiO_2 and Al_2O_3 contents in the composite cement as these are the predominant contents present in these two materials. The composition of the composite cement was comparable to the OPC 43-grade cement with a difference in the CaO content. The reduction in CaO content was expected to influence the early

strength gain in the system, which is required for the reaction of the fly ash and Silicomanganese slag in the composite cement.

Table 2. Oxide composition of clinker, composite cement, and OPC (% by mass).

Compound name	SiO_2	Al_2O_3	Fe_2O_3	CaO	TiO_2	K_2O	MgO	P_2O_5	SO_3	MnO	ZnO	Na_2O
Clinker	13.64	4.39	5.99	67.45	0.4	1	1	0.73	3.24	0.03	0.89	0.88
Composite cement	22.06	9.11	5.58	52.69	0.79	1.24	0.96	0.85	4.11	0.15	0.79	1.09
OPC	22.37	5.98	3.81	62.77	0.39	0.7	1.44	0.19	1.97	0.15	0	0.19

3.2.2 Identification and quantification of phases present in clinker and composite cement

The X-ray diffraction patterns of clinker and composite cement are shown in Figure 1. The refined crystalline phases are also shown in Figure. The obtained phase quantities are listed in Table 3. The clinker composition indicates a belite-rich cement. Significant quantities of calcite and portlandite were available in the clinker. The presence of calcite in the clinker is due to the lime sludge waste, which did not completely decompose. Portlandite content occurred due to the available free lime likely reacting with the available moisture. In composite cement, along with the crystalline phases, a small hump is attributed over the 2θ range, as shown in Figure 1 (b). The hump is attributed due to the diffuse scattering of the glassy phases in fly ash and silico-manganese slag. Comparing the other phases, the quantities of C_3S and C_2S in composite cement are smaller than in clinker. Significant quantities of calcite and portlandite are available in the composite cement. Calcite in the composite cement is contributed primarily by the clinker. Portlandite is likely formed when pharmaceutical waste is added, which is an alkaline solution. The available free lime probably reacted with the available moisture to form portlandite.

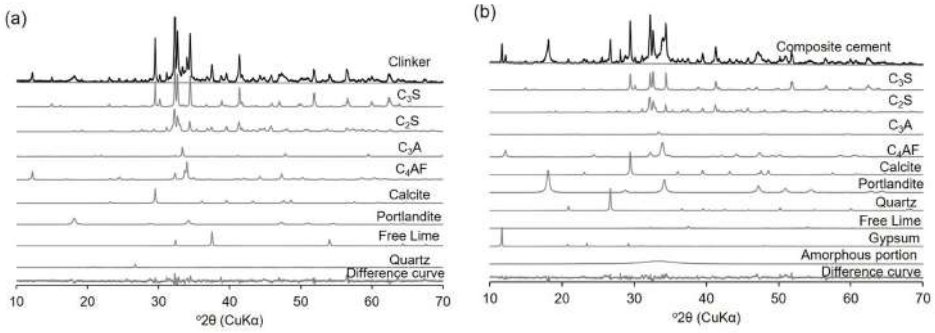


Figure 1. XRD intensity patterns of the (a) clinker and (b) composite cement.

Table 3. Phase composition of clinker and composite cement (% by mass).

Phase Name	C_3S	C_2S	C_3A	C_4AF	Gypsum	Lime	Calcite	Portlandite	Quartz	Glassy content
Clinker	35.56	31.45	4.11	14.44	0	3.47	6.16	4.24	0.57	0
Composite cement	20.12	18.32	2.17	13.02	1.36	0.44	8.35	13.16	5.1	17.96

3.3 Compressive strength of composite cement

Compressive strength development in concrete is shown in Figure 2. The strength achieved by concrete with identical mixture proportions made with commercially available Portland cement (OPC 43 grade cement) is also shown in the Figure for comparison. The initial rate of strength development in the composite cement concrete was slower than the concrete with OPC. The strength achieved by the composite cement concrete was also lower than the conventional concrete with OPC up to 90 days. The 90-day compressive strengths of the OPC and composite cement concretes were 40 MPa and 34 MPa, respectively. The compressive strength gain in OPC concrete indicated an asymptotic trend after 28 days, with little further increase after 90 days. The compressive strength development in the composite cement concrete indicates a continued increase after 90 days. The trend in the compressive strength gain attained by the composite cement concrete showed a continuous increase after 90 days, eventually approaching the strength achieved by the OPC cement concrete strength. The ultimate strengths achieved in both systems are comparable at lateral ages. The composite cement system will take much longer to achieve similar strength gain as the OPC since the pozzolanic reactions involving the fly ash and slag and the available calcium hydroxide (Bhagath Singh and Subramaniam (2016b)). in the system are slower.

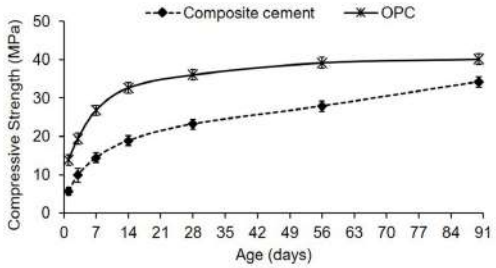


Figure 2. Compressive strength of concrete with age.

3.4 Heat evolution of clinker and composite cement

Heat evolution curves from the hydration of clinker and composite cement are shown in Figure 3(a). As shown in the Figure, the very early narrow peak is due to the wetting and dissolution of particles. This peak occurred immediately after adding water to the cement. The second peak in the heat flow measurement is associated with the acceleration stage of the hydration reaction, which follows a dormant period. The heat flows measured from the different types of cement are nominally similar with differences in the duration of the individual stages of the hydration reaction and the intensities of heat release in each stage of the hydration reaction. The composite cement system showed a smaller heat flow at the acceleration period's peak than the clinker. The reduced heat flow is due to the clinker substitution with fly ash, which is less reactive. The cumulative heat release in the composite cement and clinker paste are shown in Figure 4(b). The hydrating clinker produces higher heat than the composite cement paste. Results show that the composite cement has a lower heat of hydration and requires a longer period to complete the hydration.

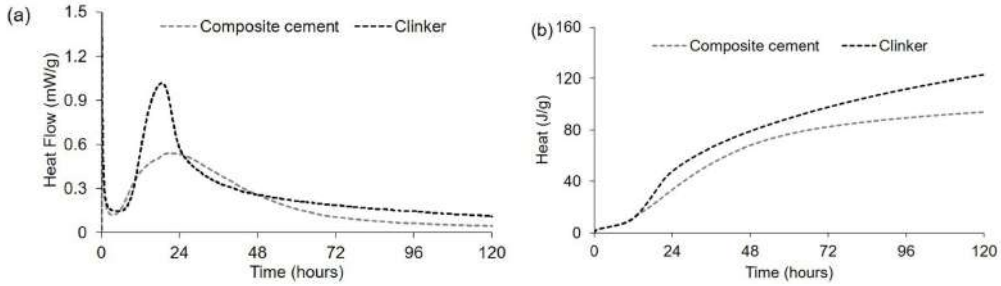


Figure 3. (a) Heat flow and (b) heat released during the hydration of clinker and composite cement.

4. Conclusions

Composite cement is produced by inter-grinding clinker made using post-industrial waste with silico-manganese slag, fly ash, and pharmaceutical waste. The source materials obtained from the post-industrial waste primarily contribute reactive species of CaO, SiO_2, Al_2O_3 and Fe_2O_3. Clinker produced using waste materials are shown belite rich clinker. The combination of belite-rich clinker, fly ash, and slag produces low-heat composite cement. The hardened composite cement concrete attains a compressive strength of 33MPa is achieved at 90 days. The composite cement concrete attains strength, which is 90% of the compressive strength of OPC concrete. The trend in compressive strength gain and the availability of slower-reacting belite, fly ash, and silico-manganese slag in the composite cement indicate a continued increase in strength after 90 days.

References

ASTM C618-17a. (2017). "Standard Specification for Coal Fly Ash and Raw or Calcined Natural Pozzolan for Use in Concrete", ASTM International, West Conshohocken, PA, United States.

Bhagath Singh, G.V.P. and Subramaniam, K.V.L. (2016) "Quantitative XRD Analysis of Binary Blends of Siliceous Fly ash and Hydrated Cement", *Journal of Materials in Civil Engineering (ASCE)*, 28(8): 040160421-7.

Bhagath Singh, G.V.P. and Subramaniam, K.V.L. (2018) "Characterization of Indian fly ashes using different experimental Techniques", *Indian Concrete Journal*, 92: 10-23.

Buruberri, L.H., Seabra, M.P., and Labrincha, J.A. (2015) "Preparation of clinker from paper pulp industry wastes", *Journal of Hazardous Materials*, 286: 252-260.

Cement Industry Trends Report. (2017). The Energy and Resources Institute, New Delhi, India.

Lin, Y., Zhou, S., Li, F., and Lin, Y. (2012) "Utilization of municipal sewage sludge as additives for the production of eco-cement", *Journal of Hazardous Materials*, 213-214: 457-465.

Scrivener, K.L. (2014) "Options for the future of cement", *Indian Concrete Journal*, 88: 11-21.

Tsakiridis, P.E., Papadimitriou, G.D., Tsivilis, S., and Koroneos, C. (2008) "Utilization of steel slag for Portland cement clinker production", *Journal of Hazardous Materials*, 152: 805-811.

The 16th International Congress on the Chemistry of Cement 2023 (ICCC2023)
"Further Reduction of CO_2 -Emissions and Circularity in the Cement and Concrete Industry"
September 18–22, 2023, Bangkok, Thailand

Hydration of ternary blended cements comprising co-calcined bauxite residue and kaolinitic clay

N. Pires-Martins[1*], A. Peys[1], Y.A. Villagrán-Zaccardi[1], R. Snellings[2,3,1]

[1] *Sustainable Materials Management, Flemish Institute for Technological Research (VITO), Mol, Belgium*
Email: natalia.piresmartins@vito.be; arne.peys@vito.be; yury.villagranzaccardi@vito.be
[2] *Department of Earth and Environmental Sciences, KULeuven, Leuven, Belgium*
[3] *Department of Materials Engineering, KULeuven, Leuven, Belgium*
Email: ruben.snellings@kuleuven.be

ABSTRACT

The Bayer-process for alumina extraction results in an alkaline iron oxide-rich residue, so-called bauxite residue (BR). Presently 160 Mt/y of BR is generated and several Gt is stored in landfills. If suitably processed, bauxite residue would be an interesting candidate supplementary cementitious material (SCM) and reduce risks and costs related to current landfilling or storage practices. In nature, bauxite ore is often found associated with or in the proximity of kaolinitic clays. Earlier findings showed that co-calcination of bauxite residue and kaolinitic clay results in a pozzolanically reactive material with promising potential as a novel SCM for high-level clinker replacement (30-50 wt.%). In the present study, the hydration and performance of ternary blended cements comprising co-calcined BR are studied in order to optimize the cement formulation. Co-calcined BR was blended with Portland cement, limestone filler and calcium sulfate. The hydration kinetics and evolution of hydrate assemblages of the blended cement pastes was characterized by means of isothermal calorimetry, X-ray diffraction, and thermogravimetric analysis in complement to compressive strength testing on mortar bars, to better understand the reactivity and performance contribution of the co-calcined BR in ternary blends. Finally, the feasibility and potential impact of ternary blended cements comprising co-calcined BR is discussed.

KEYWORDS: *red mud, co-calcination, ternary blended cement, reactivity, industrial symbiosis.*

1. Introduction

The global generation of bauxite residue (BR), or red mud, is estimated at 160 Mt/y, which corresponds to 4% of cement production (IAI, 2020). The cement industry, which is in the search for a new generation of high-quality supplementary cementitous materials (SCMs) (Habert et al., 2020), offers one of the most promising opportunities for the high-volume utilization of this waste (IAI, 2020).

BR is the mineral residue resulting from the digestion of the bauxite ore using caustic soda (NaOH) for alumina production. During digestion, reactive silicate minerals present in the bauxite ore dissolve and precipitate as phases of the sodalite/cancrinite group, generically called desilication products (DSP). These phases, together with iron (hydr)oxides, titanium phases (perovskite or oxides), hydrogarnet, and undissolved alumina hydroxides are the main components of BR. The Na_2O contents in BR are typically 1-10% (Danner & Justnes, 2020), partly bound in the sparingly soluble DSP phases and partly in soluble forms (Evans, 2016). The latter represents a major challenge for the direct utilization of BR in cement-based materials.

Among the strategies explored to improve the suitability of BR for application as a partial replacement for cement, a co-calcination process with kaolinitic clay showed to succesfully bind most of the soluble Na_2O and minimize alkali-induced acceleration of cement hydration (Danner & Justnes, 2020; Peys et al., 2022). Co-calcination of BR with as low as 10 wt.% of kaolinitic clay is already sufficient to avoid fast

setting and acceleration. Moreover, the co-calcined product shows a moderate/high reactivity and blended cements produced with 30 wt.% replacement present good technical performance and environmental compatibility. Interestingly, the reactivity of the SCM derives greatly but not solely from the calcined kaolin fraction. The contribution of BR to the reactivity of the co-calcined product has been previously demonstrated using the calorimetric R3 test in a comparison with a metakaolin-quartz mix (Peys et al., 2022). The present article aims at further developing this new SCM by investigating the hydration of blended cements comprising the co-calcined product and additions of anhydrite and limestone filler.

2. Materials and methods

The BR used was supplied by the Mytilineos alumina plant, in Greece. The kaolinitic clay was kaolin Bole white (VWR). Both materials were homogeneously mixed (80 wt.% BR, 20 wt.% kaolinitic clay) and calcined following the procedure described by (Peys et al., 2022) to produce the SCM used in this study, henceforth referred to as Myt80/K. The Portland cement used was a CEM I 52.5N (Holcim). The chemical composition of CEM I and Myt80/K are shown in Table 1. The SCM contained an amorphous fraction (38 wt.%, corresponding partly to metakaolin), in addition to hematite (51 wt.%), cancrinite (5 wt.%) – one of the zeolitic DSP phases-, muscovite/illite (3.5 wt.%), and minor amounts of quartz, anatase, corundum, grossular, and albite. The d_{50} and d_{90} were 5.2 µm and 19.2 µm for the SCM and 10.6 and 27.2 µm for CEM I, respectively.

Table 1. Chemical composition of the SCM and CEM I, measured by X-ray fluorescence (XRF) on glass beads.

%	Na_2O	MgO	Al_2O_3	SiO_2	P_2O_5	K_2O	CaO	TiO_2	Fe_2O_3	LOI
MYT80/K	3.6	<1	25.1	14.9	<0,6	0.5	0.6	5.6	47.3	0.9
CEM I 52.5N	<0,7	1.2	6.1	20.1	0.9	0.7	61.3	0.2	2.5	1.2

The SCM was mixed with CEM I to produce blended cements at different cement replacement ratios (10, 30, and 50 wt.%). All blends contained an addition of 2 wt.% of reagent grade $CaSO_4$ and one of them also contained 10 wt.% of reagent grade $CaCO_3$ as limestone filler. The cement blends and distilled water were mixed using a high speed mixer to produce pastes (water:solids 0.5) that had their heat release measured by isothermal calorimetry (TAM Air calorimeter) at 20 ºC. Two additional pastes were measured as references: a pure CEM I paste and a CEM I paste containing 30 wt.% of an inert filler (Quartz M400, from Sibelco). They were produced using the same water:solids ratio (0.5).

The pastes were cast and cured in sealed cylindrical containers at 20 ºC. At certain ages, the hydrated pastes underwent hydration stoppage before being measured under N_2 atmosphere by thermogravimetric analysis (TGA). X-ray diffraction (XRD) measurements were performed on freshly cut disks on a PANalytical Empyrean with a Co source (40 kV/45 mA), using a step size of 0.0131° 2θ and a counting time of 0.02 s/step. Qualitative analysis was done in HighScore X'Pert software using the PDF-4 database. The performance of the blended cements was evaluated based on the compressive strength of mortars (following the EN 196–1). A superplasticizer (Master Glenium 51) was added to reach the same mortar flow of 20.25 ± 1 cm (measured according to EN 1015–3) as the CEM I reference sample.

3. Results

The hydration kinetics of the blended cements, studied by isothermal calorimetry, is shown in Figure 1. With the increase in the replacement ratio, two main effects are observed in the heat flow curves (Figure 1 (a)). First, a slightly steeper slope and earlier position of the first heat flow peak, denoting that the hydration is accelerated. This has been previously observed and is attributed to the known accelerating effect of soluble sodium present in BR (Danner & Justnes, 2020). Although the calcination process significantly decreases the content of soluble sodium in the co-calcined product (Danner & Justnes, 2020; Peys et al., 2022), this observation could be a result of unbound and soluble sodium remaining after calcination. In fact, crystalline and nano-crystalline cancrinite ($Na_6Ca_2[(CO_3)_2|Al_6Si_6O_{24}]\cdot 2H_2O$) were still present in Myt80/K (see Figure 2 (a)). It should be noted, however, that the observed acceleration could partly result from a filler effect introduced by the fine particles of the co-calcined product. In fact, when

comparing the Myt80/K S2 30% paste with the reference CEM I Q30 paste, in which the same proportion of CEM I was replaced by an inert filler (quartz), only a slight acceleration is observed. The second main effect observed in Figure 1 (a) is the shift of the second heat flow peak, which is associated with the clinker aluminate reaction. Its onset represents the depletion of anhydrite. As the replacement ratio increases, the aluminate peak becomes more prominent and takes place earlier in time. This is most likely due to the high surface area of co-calcined BR, which ultimately leads to the earlier depletion of sulfate (Zunino & Scrivener, 2019). For Myt80/K S2 30% and Myt80/K S2 L10 30% the second peak occurs several hours after the first peak, which is indicative of appropriate sulfation.

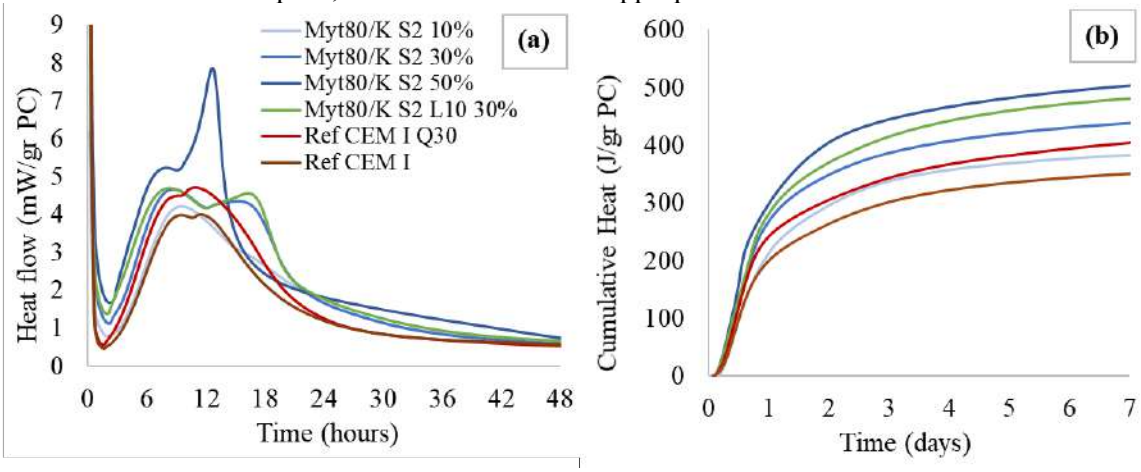


Figure 1. (a) Heat flow and (b) Cumulative heat measured at 20 °C on blended cement pastes and CEM I. S2 refers to 2 wt.% of anhydrite; L10 refers to 10 wt.% limestone; Q30 refers to 30 wt.% of quartz; X% refers to the replacement ratio with CEM I.

In the cumulative heat curves (Figure 1 (b)), the Myt80/K S2 30% paste shows a higher heat release than the reference CEM I Q30 paste. This suggests that the contribution of the co-calcined product takes place already at early age. The beneficial effect of limestone filler is highlighted in Figure 1 (b), where the limestone-containing blend shows a higher heat release in comparison to the Myt80 K S2 30% blend.

The XRD patterns of the blended cement pastes hydrated for 2 and 28 days are plotted in Figure 2 (a). Among the hydration products, portlandite, ettringite and AFm phases were identified, in addition to the XRD-amorphous contribution of C(-A)-S-H. A lower portlandite content is observed with the increase in the replacement ratio. This is a result of the lower content of CEM I in the blends and the consumption of portlandite as the pozzolanic reaction of Myt80/K advances. The contribution of poorly crystalline AFm in the 2-day patterns is visible in Figure 2 (a) as a broad reflection between 2θ 11.0 º and 12.9 º. With the increase in the replacement ratio, the broad reflection becomes more prominent and the ettringite/AFm ratio decreases. In the limestone-containing blend (Myt80/K S2 L10 30%), the formation of well-crystallized carbo-aluminate phases, i.e, initially hemicarbonate and at 28 days also monocarbonate, provides sulfate for the stabilization of ettringite. As a result, the ettringite content at both 2 and 28 days is higher than in the Myt80/K S2 30% paste.

Traces of crystalline cancrinite are detected only in the Myt80/K S2 50% paste hydrated for 2 days. Considering that the amorphous fraction of cancrinite reacts at least as fast as the crystalline fraction, nearly full reaction is obtained within the first 2 days in that blend. This more detailed study of the early reaction kinetics of the co-calcined BR indicates that cancrinite reacts faster than previously anticipated (Peys et al., 2022). The previous results were obtained on 7-day hydrated R^3-like pastes and they showed that cancrinite fully reacted within that period (Peys et al., 2022).

The compressive strength of the mortars produced from all blends continuously increase up to 28 days (Figure 2 (b)), despite the use of high replacement ratios. When the absolute strength values are compared to the calculated strength relative to the CEM I content in the blends (represented by the yellow lines in Figure 2 (b)) to account for the CEM I dilution, the contributions of Myt80/K and limestone filler become evident. For 28-day cured mortars, the obtained strength is at least 78% that of the reference sample, even for a 50% replacement ratio.

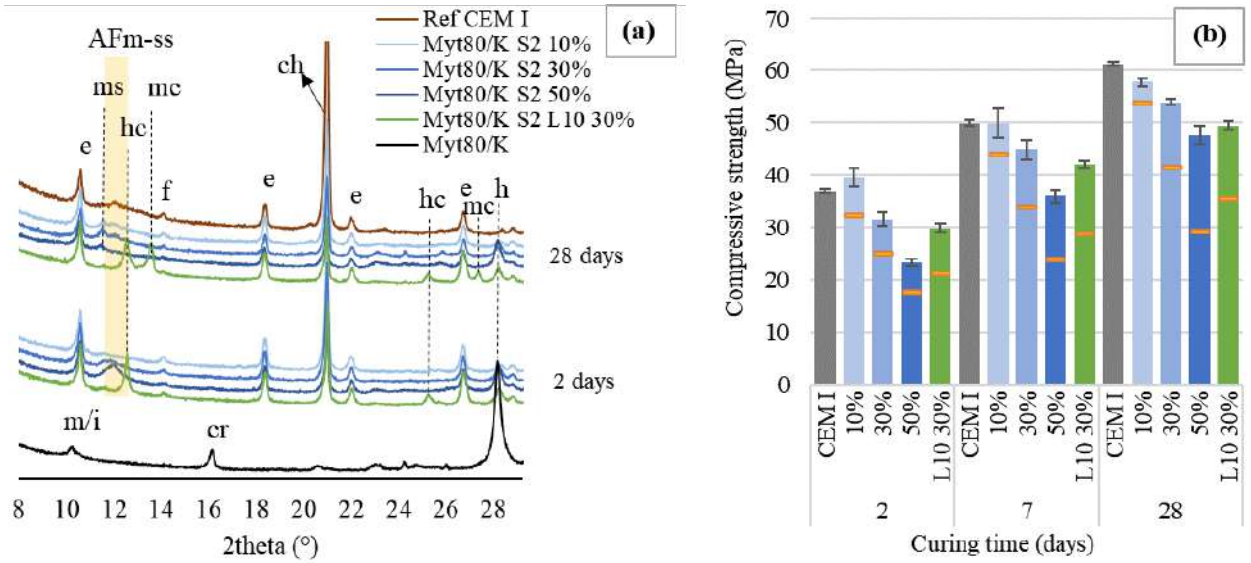


Figure 2. (a) XRD patterns of blended cement pastes hydrated for 2 and 28 days. The XRD pattern of anhydrous Myt80/K was included to indicate the cancrinite peak at 16.2 ° 2theta. e: ettringite; ms: monosulfate; hc: hemicarbonate; mc: monocarbonate; AFm-ss: AFm solid solutions; f: C_4AF; ch: portlandite; m/i: muscovite/illite; cr: cancrinite; h: hematite. (b) Compressive strength of blended cement mortars compared to a reference CEM I mortar. Results shown are the average of 3 measurements. The yellow lines represent the compressive strength of CEM I scaled by its content in each blend.

4. Conclusions

This contribution described the hydration and performance of blended cements containing a reactive product of co-calcination of bauxite residue with kaolinitic clay. Results show that the combination of the co-calcined BR product with calcium sulfate and limestone filler is beneficial to the hydrated phase assemblage of blended cement pastes and that the co-calcined product has a noteworthy contribution to the strength development of mortars at early age and up until 28 days. The synergy between limestone, calcium sulfate and co-calcined BR enables to reach higher cement substitution levels and enhances the potential of the use of co-calcined BR as an SCM.

Acknowledgements

The authors are thankful to Willem Stuyck, Myrjam Mertens, Jan Van Loy, Jo Lievens, Bo Peeraer, Anne-Marie De Wilde, and Hilde Leppens for the experimental work. The research leading to these results has been performed within the REACTIV project and received funding from the European Community's Horizon 2020 Programme (H2020/2014-2020) under grant agreement n° 958208.

References

Danner, T., & Justnes, H. (2020). Bauxite Residue as Supplementary Cementitious Material – Efforts to Reduce the Amount of Soluble Sodium. *Nordic Concrete Research*, *62*(1), 1-20. https://doi.org/doi:10.2478/ncr-2020-0001 %U https://doi.org/10.2478/ncr-2020-0001

Evans, K. (2016). The History, Challenges, and New Developments in the Management and Use of Bauxite Residue. *Journal of Sustainable Metallurgy*, *2*(4), 316-331. https://doi.org/10.1007/s40831-016-0060-x

Habert, G., Miller, S. A., John, V. M., Provis, J. L., Favier, A., Horvath, A., & Scrivener, K. L. (2020). Environmental impacts and decarbonization strategies in the cement and concrete industries. *Nature Reviews Earth & Environment*, *1*(11), 559-573. https://doi.org/10.1038/s43017-020-0093-3

IAI, I. A. I. (2020). *Technology Roadmap: Maximising the use of bauxite residue in cement*.

Peys, A., Hertel, T., & Snellings, R. (2022). Co-Calcination of Bauxite Residue With Kaolinite in Pursuit of a Robust and High-Quality Supplementary Cementitious Material [Original Research]. *Frontiers in Materials*, *9*. https://doi.org/10.3389/fmats.2022.913151

Zunino, F., & Scrivener, K. (2019). The influence of the filler effect on the sulfate requirement of blended cements. *Cement and Concrete Research*, *126*, 105918.

The 16th International Congress on the Chemistry of Cement 2023 (ICCC2023)
"Further Reduction of CO_2 -Emissions and Circularity in the Cement and Concrete Industry"
September 18–22, 2023, Bangkok, Thailand

Effect of chloride salts on cement hydration: influence of the cation - part II

P. Forni[1*]

[1] *Mapei S.p.A., Milan, Italy*

Email: p.forni@mapei.it

ABSTRACT

Chloride salts are used as cement hydration accelerators in mortar or concrete since decades. Their use in chemical activators formulations is even more important as clinker substitution is mandatory in the current scenario. Sodium and calcium chlorides are traditionally the most widespread, mainly due to their limited cost and vast availability. However, no thorough studies of the effect of the cation on the hydration kinetics and strength increase effect were carried out. The first part of the study (presented in 15th ICCC in Prague, 2019) concentrated on the comparison of the effect of different cations at the same level of chloride ion dosage. The second part concentrates on the comparison of the effect of different cations at the same level of cations equivalents. Dosage efficiency, heat of hydration, strength development profiles, setting times are some of the parameters to judge the effect of the addition. The study is performed on several Portland cements prepared in the laboratory with different clinkers, which are analysed for their chemistry and mineralogy.

KEYWORDS: *Cement, Chlorides, Hydration*

1. Introduction

In cement production, the use of chemical additives to lower manufacturing costs has become normal practice worldwide. These additives can be simple grinding aids (providing decreased energy costs for grinding) or hydration activators, able to influence the reaction of cement with water. In the latter case, higher potential for savings is given by the possibility to substitute clinker with secondary cementitious materials, as for example pozzolanas, blastfurnace slag, fly ash and limestone. The use of chloride salts (traditionally, sodium and calcium chloride), often coupled with alkanolamines (as for example triethanolamine), is well-known to impart grinding effect together with early strength enhancement of cement mortars. However, most of the scientific studies have regarded the effect on concrete and have been made at such high dosages of chemicals so to be insignificant for the grinding stage addition point of view (e.g. Rapp (1935), Dodson (1990)). Particular care has been given to the effect of chlorides on concrete reinforcement bars (e.g. MJ Kim et al (2016)). A few studies concentrated on proposed mechanisms (Ramachandran (1971)) and chloride migration (Wowra & Setzer (1997)), but again at very high dosages (in the order of magnitude of units of weight %).
Other studies have been carried out on the effect of chemical activators in cement at typical cement additive dosages, but they were not specifically focused on different sources of chlorides (e.g. Huang & Shen (2011), Huang et al (2010), Katsioti (2009)).
Basically though, no agreement exists on the actual mechanism of action of chlorides, apart from the common acceptance that it is a catalytic type of mechanism, due to the very low amounts of chemicals required and their absent/minimal consumption.
At this stage, it was not the purpose of this study to inquire further about these mechanisms. On the other hand, the focus has been to verify the effect of different forms of chlorides at the typical dosages used in the cement grinding stage. The first part of this work, presented at ICCC 2019 (Forni (2019)), offered the

conclusion that the well-known early strength effect of these chemicals is confirmed. However, at dosages typical of addition during the grinding stage, this seems to be limited to 24 hours, flattening out afterwards, even as early as 2 days. The cation plays a role in the mechanism, with calcium and sodium as the most effective on strength development and heat of hydration, but only calcium able to decrease initial setting time (however limited to 12 minutes on average).

2. Experimental

2.1 Materials

The following materials were selected for the investigation:

- eight Portland cement clinkers (coded C8831, C8606, C8792, C8718, C8440, C8593, C8747 and C8669)
- a natural calcium sulfate (in dihydrate – gypsum - form)

Criteria followed in choosing were to avoid any very particular material, trying to select a wide range of clinkers with "typical" characteristics, so to be closer to the field of application. Clinkers come from different geographical areas.

2.2 Preparation and analysis methods

Clinker and gypsum were ground together in a steel-ball laboratory mill for a standard time, in the w/w ratio of 95:5. Fineness of the finished cements so prepared is comparable to the one of commercial Ordinary Portland Cements (OPCs).
Finished cements were analyzed for their chemical composition by X-Ray fluorescence (XRF), and for their mineralogical composition by quantitative X-Ray diffraction with Rietveld method. Details on the equipment and method are available upon request.
Compressive strength was measured in mortar according to standard EN-196/1, so with fixed water/cement ratio of 0.5 and standard sand/cement ratio of 3:1. Siliceous sand was used according to the norm. For the determination of strengths in the presence of chemicals, the latter were added directly in the mixing water by weighing the appropriate amount of each.
Setting time determination was carried out in paste according to standard EN-196/3. Standard consistency was determined for each cement without chemical additions, and the water/cement ratio obtained was kept constant for all determinations with different chemicals on that specific cement. Again, chemicals were added directly in the mixing water by weighing the appropriate amount of each.

2.3 Chemical additions

On each cement, the following compositions were added (dosages refer to cement weight):
1. triethanolamine (TEA) 5% and sodium chloride 17%, in demineralised water, dosage 3000 ppm
2. triethanolamine (TEA) 5% and calcium chloride 16%, in demineralised water, dosage 3000 ppm
3. combination of 1. with 3000 ppm of 12% NaOH solution
4. combination of 2. with 330 ppm of powder $Ca(OH)_2$

The concentration of the different chloride salts is such to always have 10% chloride ion (w/w) in the solutions. Dosage was dictated by the average actual use of these chemicals in practical use.
Analytical grade of all chemicals was used.

3. Results

3.1 Analytical data

XRF results of the finished cements are reported in Table 1. Full analytical results of XRD-Rietveld are available upon request. Mineralogy of the clinkers is quite varied: total C_3S is generally >58-60%, with C_2S under 20%. This is in accordance with the good level of compressive strengths and reactivity found for all the cements. Total C_3A is generally within the range 4÷7%, with a few exceptions at higher values.

Some samples contain a significant amount of orthorhombic aluminate. C_4AF content is quite varied, ranging from 7 to 12%.

Table 1 – cement XRF results (% composition)

Cement code	Na_2O	MgO	Al_2O_3	SiO_2	SO_3	K_2O	CaO	Fe_2O_3	TiO_2	P_2O_5
C8440	0.47	1.20	3.52	21.00	3.55	0.58	65.29	4.72	0.26	0.12
C8593	0.17	2.27	5.12	20.61	3.22	0.72	64.97	2.86	0.30	0.17
C8747	0.21	2.50	5.03	19.25	4.58	0.54	63.65	3.39	0.44	0.08
C8669	0.18	1.01	5.28	23.09	2.64	0.55	64.10	2.79	0.24	0.18
C8718	0.20	1.32	5.02	20.73	3.27	0.72	64.55	3.51	0.30	0.27
C8792	0.25	2.21	5.34	19.60	2.92	0.79	64.14	3.80	0.32	0.18
C8606	0.24	1.32	4.95	20.00	3.21	0.80	65.13	3.43	0.27	0.07
C8831	0.15	0.89	5.40	20.60	2.88	0.39	65.63	3.12	0.24	0.15

3.2 Compressive strengths and setting time data

Compressive strengths values (at 1, 2 and 28 days, in MPa) and setting time data (IST, initial setting time, and FST, final setting time, in minutes) are reported in Table 2.

Table 2 – mortar strength data

	Average % strength increase vs blank			Average % setting time vs blank	
	1D	2D	28D	IST	FST
blank					
TEA + NaCl	10.1	9.6	-4.2	-3.8	-11.3
TEA + $CaCl_2$	9.5	7.7	-3.5	-4.2	-14.5
TEA + NaCl + NaOH	12.2	9.1	-5.3	-11.7	-23.4
TEA + $CaCl_2$ + $Ca(OH)_2$	7.6	6.5	-5.1	-5.5	-16.2
	Averaged strength value (MPa)			Averaged setting time value (mins)	
	R1	R2	R28	IST	FST
blank	20.4	29.2	55.1	124	178
TEA + NaCl	22.3	31.4	52.7	113	151
TEA + $CaCl_2$	22.0	30.8	53.1	113	150
TEA + NaCl + NaOH	22.4	31.2	52.2	104	134
TEA + $CaCl_2$ + $Ca(OH)_2$	21.9	30.5	52.2	110	146

All cements tested (with one exception, C8440) yielded significant strength increases at 1 and 2 days with all the formulations tested. Sodium chloride mixes gave very good average gains. At 2 days, the strength enhancing effect was somewhat less. Late strength tends to decrease. As for setting times, no significant differences were apparent between sodium or calcium chloride, with an average 10 minutes acceleration. The presence of additional alkali does not seem to give any additional advantage on strength development; for sodium, data show a stronger setting time acceleration in the presence of free NaOH.

4. Conclusions

As a continuation of the study presented in ICCC 2019, the purpose of the work was to assess the effect of changing cation in chloride-based activation of cement, and specifically at dosages typical of process grinding additives used industrially in cement manufacturing. To our knowledge, no such study exists or is divulged. The first step (2019) was focused on studying the difference between sodium, calcium, and potassium chloride activation. This further step regarded the simultaneous addition of sodium or calcium chloride with a corresponding strong alkali (sodium hydroxide or calcium hydroxide). This subject is quite interesting from the application point of view, since low-carbon cement require development of new chemical activators, and alkaline activation is one of the possible routes. Exploring the effect of strong alkali at the selected dosages can clarify the range of practical use of this approach.
The present study, while confirming the favourable effect of sodium and calcium chloride as early strength activators of cement, allowed to make clear that the simultaneous addition of free sodium or calcium hydroxide at dosages typical of grinding aid additions doesn't contribute significantly to strength development. Sodium hydroxide may accelerate setting time further to the effect of sodium chloride, but the extent of this is limited.

References

Dodson V (1990). Concrete Admixtures. Van Nostrand Reinhold. pp 84-86.

Forni P (2019). ICCC 2019 proceedings.

Huang H, Shen X, Zheng J (2010). Modeling, analysis of interaction effects of several chemical additives on the strength development of silicate cement. Construction and Building Materials, Volume 24, Issue 10, pp 1937-1943.

Huang H, Shen X (2011). Statistical study of cement additives with and without chloride on performance modification of Portland cement. Progress in Natural Science: Materials International, Volume 21, Issue 3, pp 246-253.

Katsioti M, Tsakiridis PE, Giannatos P, Tsibouki Z, Marinos J (2009). Characterization of various cement grinding aids and their impact on grindability and cement performance. Construction and Building Materials, Volume 23, Issue 5, pp 1954-1959.

Kim, MJ, Kim KB, Ann KY (2016). The Influence of C3A Content in Cement on the Chloride Transport. Advances in Materials Science and Engineering, Volume 2016, Article ID 5962821.

Rapp, P (1935). Effect of calcium chloride on Portland cements and concretes. Journal of Research of the National Bureau of Standards, Volume 14, pp 499-517.

Ramachandran VS (1971). Possible states of chloride in the hydration of tricalcium silicate in the presence of calcium chloride. Mat. Constr., Volume 4, Issue 1, pp 3-12.

Wowra O, Setzer MJ (1997). Sorption of chlorides on hydrated cements and C3S pastes. Frost resistance of concrete, E & FN Spon. pp 155-162.Leung, C.K.Y. and Cao, Q. (2010) "Development of Pseudo-ductile Permanent Formwork for Durable Concrete Structures", *RILEM Materials and Structures*, 43(7): 993-1007

The 16th International Congress on the Chemistry of Cement 2023 (ICCC2023)
"Further Reduction of CO_2 -Emissions and Circularity in the Cement and Concrete Industry"
September 18–22, 2023, Bangkok, Thailand

Correlating initial chemistry, reaction degree and phase assemblage in alkali-activated systems

L. Miranda de Lima[1*], J.L. Provis[2], and G. Ye[1]

1 Delft University of Technology, Faculty of Civil Engineering and Geosciences, the Netherlands

Email: L.MirandadeLima@tudelft.nl / G.Ye@tudelft.nl

2 University of Sheffield, Department of Materials Science and Engineering, United Kingdom

Email: j.provis@sheffield.ac.uk

ABSTRACT

The present study investigated the influence of binder chemistry on the phase assemblage and overall reactivity of alkali-activated systems up to 7 days, focusing on individual precursors. Pastes were prepared with four synthetic glasses resembling blast furnace slags and coal fly ashes, with fixed Si/Al (1.5) and variable Ca/Si (0.2-1.1) ratios, activated with sodium hydroxide and waterglass. The degree of reaction of hardened pastes was evaluated with grayscale images obtained by scanning electron microscopy. The content of Ca provided a direct indication of reaction degree, which increased from 32.7 to 48.2 % (wt%Ca of 12.6 and 42.5, respectively). Through selective dissolution of hardened pastes and X-ray diffraction analysis, it was possible to distinguish the nature of reaction products in different systems. While calcium-(alumino)silicate hydrate (C-(A-)S-H) gels were dominant in percalcic systems, precipitation of sodium-aluminosilicate (N-A-S-H) gel was found to be inversely proportional to Ca/Si ratios. The content of N-A-S-H gel increased from 0 to 61.7 wt% of reaction products (Ca/Si of 0.94 and 5.02 respectively), according to selective dissolution tests. Additionally, two different secondary reaction products were identified in only three mixtures, with a maximum content of katoite (C_3AH_6) up to 11 % in one of them, indicating that gel phases dominate hardened microstructures. Novel nucleation indices were proposed to measure the potential of precipitation of the two main hydrated gels and to correlate them to the reaction degree, in agreement with the chemistry of mixtures. The current results demonstrate a connection between the initial features of blended precursors and characteristics of mature microstructures of alkali-activated systems, facilitating the proposal of mixtures tailor-designed to attend specific performance requirements.

Key-words: *Phase assemblage; Degree of reaction; Quantitative X-ray diffraction; Scanning electron microscopy; Selective dissolution.*

1. Introduction

Despite being the subject of extensive research for decades, with successful examples of practical applications in real-condition projects, the technology of alkali-activated materials (AAMs) still poses problems for practical conditions. The diverse list of potential raw materials, in the sense of activators and precursors, presents additional challenges in the design of standardized mixtures with reliable performance estimation. Through the years, several authors have attempted to create subclasses of these type of materials, mainly classifying them by their chemical composition (Palomo et al., (2014)). However, high variability in chemistry and mineralogy can be expected even for precursors belonging to the same class.
Depending on the initial characteristics of the binders, different reaction mechanisms take place leading to variable microstructure features. Generically, precursors in which Ca is the main component (blast furnace slags, calcium rich ashes) present accelerated reaction and different phase assemblage compared to low-Ca materials (coal fly ashes, biomass ashes, waste glass, calcined clays), and precursors activated with waterglass display a more homogeneous matrix in comparison with sodium hydroxide activation. Moreover, use of less reactive activators, such as sulfates or carbonates, promotes a slower development of

the matrix and lower degrees of reaction, thus delaying the performance development (Provis and Van Deventer (2014)).
The performance and durability of AAMs depend significantly on the nature and amount of reaction products present in the hardened binder. Therefore, a connection between the characteristics of the raw materials and the final microstructure would have a positive effects on the industry, as the application characteristics and service life of structures made with AAMs could be easily estimated and optimized. The aim of this paper is to propose nucleation indices that can correlate the binder chemistry with the phase assemblage, accurately predicting the quantities of the main reaction products in alkali-activated systems.

2. Materials and methods

2.1 Obtainment of synthetic glasses

Stoichiometrically controlled quantities of SiO_2, Al_2O_3 and $CaCO_3$, were used for the synthesis of glasses with simplified chemistry resembling blast furnace slags (S1 and S0.9), calcareous fly ash (S2) and siliceous fly ash (S4). Reagent grade source materials were mixed in a Retsch PM100 planetary ball mill in a 1:1 isopropanol suspension for 2 h, at 200 rpm, and dried overnight at 105 ºC. The dry mixtures were hand pressed in alumina crucibles and heated using a Carbolite HTF1700 furnace. The samples were heated up to 950 ºC (5 ºC/min; dwell time of 1 h) to allow slow decarbonation, followed by a second heating ramp up to 1600 ºC (10 ºC/min; dwell time of 2 h). The molten samples were removed from the oven at the maximum temperature and immediately poured in a water bath. Dried glass particles were ground to a D_{50} of approximately 20 µm and stored in a vacuum desiccator prior to use. The chemical compositions of the synthetic glasses were determined using a Panalytical Axios Max wavelength disperser X-ray fluorescence device and the particle size distribution was measured by laser diffraction analysis. The specific surface area was determined with nitrogen adsorption by the Brunauer-Emmet-Teller method, using a Micromeritics Gemini VII device. The results of the glass characterization are given in Table 1.

Table 1: Chemical composition and physical characteristics of synthetic glasses.

Glass	Glass Type	Atomic ratios				D_{50} (µm)	BET (g/m^2)
		Si/Ca	Si/Al	Al/Ca	Ca / (Si +Al)		
S4	Siliceous fly ash	4.16	1.51	2.75	0.15	22.1	13.09
S2	Calcareous fly ash	2.04	1.47	1.39	0.29	17.2	11.79
S1	Blast furnace slag	1.00	1.56	0.64	0.61	21.5	11.18
S0.9	Blast furnace slag	0.93	2.05	0.46	0.72	16.6	7.77

2.2 Preparation and characterization of hardened pastes

Two different activating conditions were used for the casting of cementitious pastes. Each one of the synthetic glasses was mixed with sodium hydroxide and sodium silicate – 8 wt% Na_2O per mass of glass in both activators, and a silicate modulus of 1.5 in the latter –, with a water/precursor ratio of 0.35 for glasses S4 and S2 and 0.4 for glasses S1 and S0.9. The pastes were cured in sealed conditions, at 20 ºC, for 7 days. Surface-polished hardened pastes were analysed with scanning electron microscopy (SEM), using a FEI Quanta FEG 650 instrument with an acceleration voltage of 15 kV in low vacuum conditions. A total of 20 backscattered electron images (BSE) were obtained for each paste, and the degree of reaction was estimated using grayscales (Scrivener et al., (2016)). Finely-crushed/ground pastes were subject to a selective dissolution method using salicylic acid and methanol solutions according to (Puligilla and Mondal, (2015)) aiming the dissolution of Ca-based phases. The measured weight loss, normalized to the degree of reaction, was used to quantify the amount of sodium aluminosilicate hydrate (N-A-S-H) gel. Finely ground pastes were also characterized with quantitative X-ray diffraction analysis (QXRD) using a Bruker D8 Advance diffractometer with Cu-Kα radiation (λ = 1.54 Å), with ZnO as standard material. Quantitative

analysis were performed using the SIeve+ software to determine the nature and quantities of the resulting reaction products.

3. Results

A direct correlation of the reaction potential with binder chemistry has been observed for pastes prepared with individual precursors, after a curing time of 7 days. As observed in Fig. 1a, the degree of reaction increased from 32.7 % for the paste S4-N8S12, to 47.6 % for the paste S0.9-N8S0 (Ca/(Si+Al) ratios of 0.16 and 0.85). The overall amount of Ca in the mixture was also observed to be proportional to the phase assemblage of hardened binders. The calculated quantity of N-A-S-H gel (Fig. 1b) was inversely proportional to the quantity of Ca. The presence of aqueous silicate species from the activator showed a competitive effect with other Ca-based hydrates. In waterglass activated systems, the potential of precipitation of N-A-S-H gel was observed to be enhanced, as all glasses, except S0.9, showed residual Na-based gel after selective dissolution. However, the maximum calculated quantity of N-A-S-H gel was only 61.7 %, indicating that there is ample room for the precipitation and growth of the Ca-based phases. Contrarily, the precipitation and growth of calcium (alumino)silicate gels (C-(A-)S-H) (Fig. 1c) increased linearly with the initial content of Ca, as determined by QXRD analysis. The amount of Ca-based gel varies from 38.3 %, in the paste S4-N8S12 to being the sole reaction product observed in the mixture S0.9-N8S12.

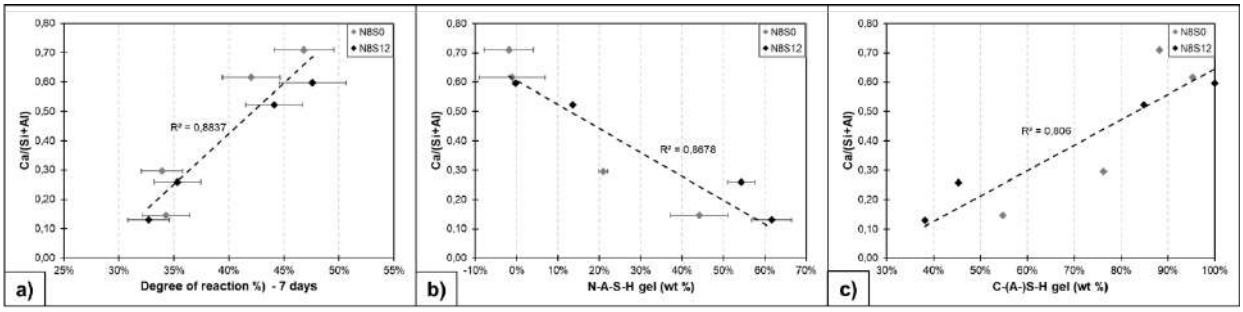


Figure 1: Correlation of initial Ca/(Si+Al) ratio of the binders with characteristics of hardened pastes: a) degree of reaction; b) quantity of N-A-S-H gel; and c) quantity of C-(A-)S-H gel.

In view of the observed linear correlation between binder chemistry, degree of reaction and reaction products, nucleation indices were proposed to predict the quantitative formation of the two main gel phases, by considering the atomic fractions of the elements associated with each. In the C-(A-)S-H term, shown in Eq. 1, two correction factors were considered for the chemistry of C-S-H and C-A-S-H: 1) regarding the Ca/Na ratio, as gels with Na as the main charge-balancing element are favored in systems with low supply of Ca; and 2) regarding the ratio of Si/Al, as higher contents of Al can favor the precipitation of secondary layered-double hydroxide phases, among others (L'Hôpital et al., (2015)). Similarly, the N-A-S-H index (Eq. 2) presents other two correction factors regarding the presence of aqueous silicate species: 1) ratio between total Si and the Si fraction only in the precursor; and 2) a conditional factor considered for systems activated with waterglass, considering the silicate modulus (Ms) of the mixture. The two indices were proportionally normalized to their sum, in order to deliver the predicted quantitative distribution of each.

$$\text{C-(A-)S-H index} = \left[\frac{xCa+xSi}{xCa+xSi+xAl+xNa} + \frac{xCa+xAl+xSi}{xCa+xSi+xAl+xNa}\right] \cdot \frac{xCa}{xNa} \cdot \frac{xSi}{xAl} \qquad (1)$$

$$\text{N-A-S-H index} = \left[\frac{xAl+xSi_{total}+xNa}{xCa+xSi_{total}+xAl+xNa} + \frac{xAl+xSi_{total}}{xCa+xAl+xSi_{total}}\right] \cdot \frac{xSi_{total}}{xSi_{precursor}} \cdot Ms \qquad (2)$$

The accuracy of the proposed nucleation indices were verified and compared with the quantitative determination of the two groups of phases. The charts displayed in Fig. 2 indicate that both indices presented a good relationship with the experimental analysis. Most of the experimentally determined quantities are within a 10 % margin of agreement with the calculated indices, and the R^2 of these values with respect to the indices is of 0.89. The amount of N-A-S-H gel was slightly overestimated, especially in slag-like systems. While systems S1-N8S0, S0.9-N8S0 and S0.9-N8S12 did not show any residual Na-

based gel, the N-A-S-H index estimated a formation of up to 17 % of the total matrix. Since the quantitative analysis were performed after only 7 days of curing, an increased N-A-S-H presence in the microstructure can be expected at longer periods given the slower kinetics of formation of such phases (Walkley et al., (2016)). A better agreement was observed for the C-(A-)S-H index due to the presence of secondary phases. Out of the three systems that did not present N-A-S-H, the precipitation of 11.3 % katoite (C_3AH_6) and 5.8 % strätlingite (C_2ASH_8) was observed for pastes S0.9-N8S0 and S1-N8S12, respectively. The observed quantities of both phases, especially for the former, suggest that they could also be included as additional nucleation indices.

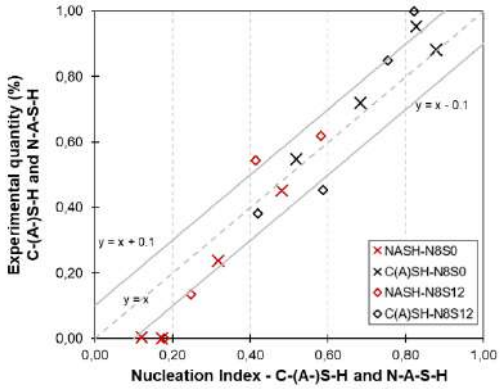


Figure 2: Correlation of the nucleation indices with experimental quantitative determination of N-A-S-H and C-(A-)S-H gels.

3. Conclusions

The present study showed that binder chemistry has a direct impact on the phase assemblage of alkali-activated materials. By combining the selective dissolution treatment with quantitative X-ray diffraction, it was possible to observe a linear relationship in between the Ca content and the amount of the main reaction products, following the evolution in the degree of reaction. The proposed nucleation indices proved to be successful on the forecasting of phase assemblage, as they were mostly within 10% of experimental observations for pastes prepared with individual precursors. Since both indices take into account the entire chemistry of the binder and are mutually normalized, it can be concluded that the distribution of reaction products within the hardened microstructure of alkali-activated materials can be accurately predicted, delivering a powerful tool for further modelling of performance AAMs.

Acknowledgements

This project has received funding from the European Union's Horizon 2020 research and innovation programme under grant agreement No 813596 DuRSAAM. The opinions expressed in this document reflect only the author's view and reflect in no way the European Commission's opinions.

References

L'Hôpital, E., Lothenbach, B., Le Saout, G., Kulik, D., & Scrivener, K. (2015). "Incorporation of aluminium in calcium-silicate-hydrates". *Cement and Concrete Research*, 75: 91–103

Palomo, A., Krivenko, P., Garcia-Lodeiro, I., Kavalerova, E., Maltseva, O., & Fernández-Jiménez, A. (2014). "A review on alkaline activation: New analytical perspectives". *Materiales de Construccion*, 64(315)

Provis, J. L., & Van Deventer, J. S. J. (eds.) (2014). "Alkali-activated materials: State-of-the-Art Report of RILEM TC 224-AAM", RILEM/Springer, Dordrecht.

Puligilla, S., & Mondal, P. (2015). "Co-existence of aluminosilicate and calcium silicate gel characterized through selective dissolution and FTIR spectral subtraction". *Cement and Concrete Research*, 70, 39–49

Scivener, K., Snellings, R., Lothenbach, B. "A Practical Guide to Microstructural Analysis of Cementitious Materials". CRC Press, Taylor & Francis Group

Walkley, B., San Nicolas, R., Sani, M. A., Rees, G. J., Hanna, J. V., van Deventer, J. S. J., & Provis, J. L. (2016). "Phase evolution of C-(N)-A-S-H/N-A-S-H gel blends investigated via alkali-activation of synthetic calcium aluminosilicate precursors". *Cement and Concrete Research*, 89, 120–135

The 16th International Congress on the Chemistry of Cement 2023 (ICCC2023)
"Further Reduction of CO_2 -Emissions and Circularity in the Cement and Concrete Industry"
September 18–22, 2023, Bangkok, Thailand

Preliminary Selection Criteria of Clays for Limestone Calcined Clay Cement

Aastha Singh[1*] and Shashank Bishnoi[2]

[1] *Department of Civil Engineering, Indian Institute of Technology, Delhi, India*
Email: aasthasingh1411@gmail.com
[2] *Department of Civil Engineering, Indian Institute of Technology, Delhi, India*
Email: bishnoi@iitd.ac.in

ABSTRACT
Among all potential materials, calcined clay is the only energy-efficient material that is abundant in the earth's crust and can replace clinker in cement. Kaolinitic clays from the kaolin group are most suitable as a supplementary cementitious material. It is a 1:1 clay mineral with the chemical formula $Al_2O_3(SiO_2)_2.2H_2O$. In this paper, the criteria for the selection of clays suitable as cement substitutes for the production of limestone calcined clay cement are explained based on the correlation between chemical and mineralogical composition. Although XRF is not the most appropriate technique for estimating the kaolinite content in a clay, data of clays from more than 200 locations in India were analysed to compare kaolinite content with chemical composition. Based on this analysis, the limits of relative composition that can be used to identify suitable clays, were ascertained. It was found that these limits can be plotted in the form of graphs, which provide an initial assessment of the suitability of clays for use in cement. The relationships between the kaolinite content and the ratio of alumina to silica, the kaolinite content and the loss on ignition,the ratio of alumina to silica and the kaolinite content of the clays are examined. These relationships are based on the kaolinite content threshold, i.e. 40%, which ensures that the alumina content is ≥ 15.8%, the Al/Si content is ≥ 0.2, and the loss on ignition is ≥ 5.6.

KEYWORDS: *Kaolinite content, loss on ignition, alumina to silica ratio, selection criteria.*

1. Introduction

Kaolin is often used as a trade name for a low-iron claystone composed mainly of kaolinite or similar clay minerals. It is characterised by its white or near-white colour, even after calcination, and its commercial value is determined by its particle size distribution and whiteness. However, the targeted clays are not necessarily white, contain other impurities such as iron, quartz, etc., and have a kaolinite content of 40 to 60%. As for LC^3 production with a clinker replacement of 50%, clays with a kaolinite content between 40 and 60% give comparable results to ordinary Portland cement. Since the regions with the highest population growth are also rich in kaolinite, the development of kaolinitic clays as a source of SCM (compared to other clays) makes sense from a geographical, reservational and mineralogical point of view.
For practical use in relation to SCM, the broader term kaolinitic clay is preferred to kaolin. It can be said here that reserves for kaolin clay have been identified, but these clays are not the focus of the search and therefore the information on reserves for kaolinitic clays is limited. While current inventories of global reserves generally refer to high-grade kaolin, global resources of kaolinitic clays suitable as sources of SCM due to their clay mineral content are considered extremely large, but at the same time are largely undiscovered or not properly classified.

2. Reserves of kaolin clays versus suitable kaolinitic clays

The global distribution (Figure 1) shows that the mineral kaolinite is abundant throughout the soil profile in tropical and humid regions, while cooler and arid regions have few kaolinitic clays (Alujas Diaz *et al.*, 2022). This global distribution also shows that the mineral kaolinite is present in very small quantities in

India. This is due to the fact that so far the focus has been on kaolinite clays with a high purity of more than 80%, suitable for the ceramics and paper industries. However, literature on limestone calcined clay cement indicates that the high purity kaolinite clays are not required for cement production. In general, clays with a kaolinite content between 40% and 60% are suitable.

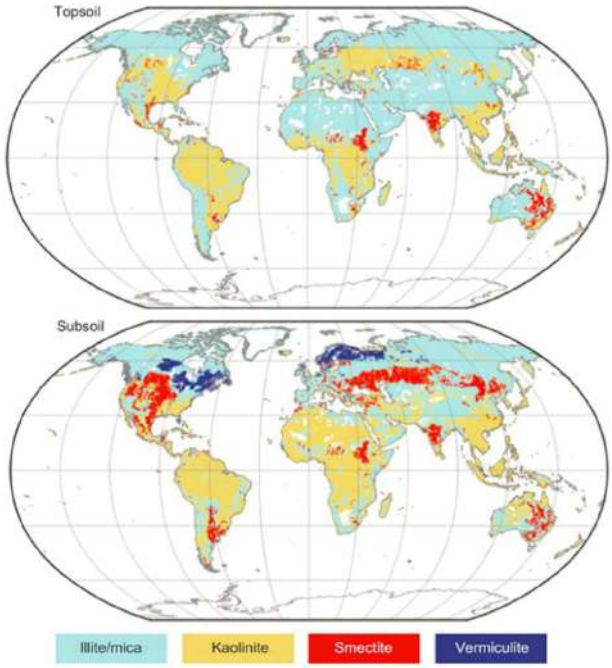


Fig-1: Global Distribution of clay minerals in topsoil and subsoil [(Alujas Diaz et al., 2022), (Ito and Wagai, 2017)]

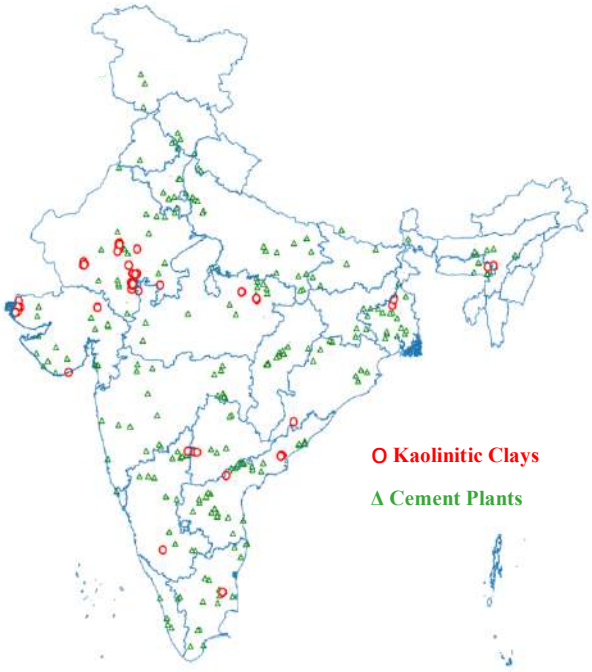


Fig-2: Map of India showing kaolinitic clays and cement plants.

Based on the existing knowledge of kaolin deposits in India, the geographical coordinates were determined and the clays were extracted from the existing deposits and nearby mines in India. Figure 2 shows the distribution of identified and tested kaolinitic clays and overall cement plants in India (CemNet 2022). The map of India shows that the clays studied occur in the states where there are a large number of cement plants, such as Gujarat, Rajasthan, West Bengal, and Madhya Pradesh. Table 1 shows the clays with different kaolinite contents in each state, with the range starting from the minimum kaolinite content of 40%. It also shows the impurities present in the clays in a particular state.

Table-1: Kaolinitic clay range with other minerals in different states.

State	Kaolinitic range (%)	Other minerals
Gujarat	40-80	Quartz, Muscovite, Gibbsite
Rajasthan	40-90	Quartz, Calcite, Muscovite
West Bengal	40-60	Quartz, Muscovite, Gibbsite
Meghalaya & Assam	60-80	Quartz
Madhya Pradesh	40-80	Quartz, Gibbsite, muscovite, calcite, hematite
Andhra Pradesh	40-60	Quartz, Muscovite
Orissa	40-85	Quartz, Muscovite
Karnataka	40-80	Quartz
Tamil Nadu	40-65	Quartz

In addition to the clays of the kaolinite group, mica, smectites, and chlorites are other clay minerals commonly found in kaolinitic clay deposits. Iron oxides are also commonly associated with kaolinitic clay minerals in the non-clay fraction occurrence of quartz and feldspars is common. Depending on the

formation, small amounts of titanium oxides, carbonates, and sulfates may also be present (Alujas Diaz et al., 2022). The value of using kaolinitic clays as SCM sources is primarily related to their content of clay minerals from the kaolinite group, which are among the most reactive SCMs known when properly activated. Due to their worldwide distribution and occurrence, the low activation temperature and large thermal activation window compared to other clay minerals are advantageous factors for their processing on an industrial scale (Fernandez, Martirena and Scrivener, 2011). In addition, the calcination-activated products of clay minerals from the kaolinite group are an excellent source of reactive alumina.
As an SCM source, clay need not be of the highest purity, and the availability of a comparatively high percentage of impurities as clay or non-clay mineral is acceptable. High clinker replacement is possible by using lower quality kaolinite clay. Because of the lower clinker factor, less calcium hydroxide is formed, so less activated kaolinitic clay is required for the pozzolanic reaction.
Similarly, cement with high clinker factor can be replaced with high quality kaolinitic clay (Krishnan and Bishnoi, 2020). Once the clay mines and clay collection are identified, the criteria for selecting clays suitable for use as SCM in a ternary blend of limestone calcined clay cement must be established.

3. Preliminary selection of the clays for LC^3

For the development of ternary cements from calcined clays, robust techniques are needed to define the selection criteria for clays based on their mineralogical and elemental composition. This not only helps in identifying potentially suitable clays based on kaolinite content, but is also important for clays that have relatively high levels of impurities, particularly ferrous phases, which are abundant but have little use in most of the common applications of the kaolin industry.

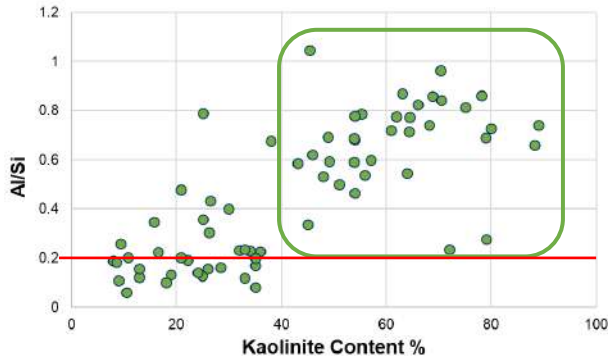


Fig-3a Correlating Al/Si to kaolinite content of clays

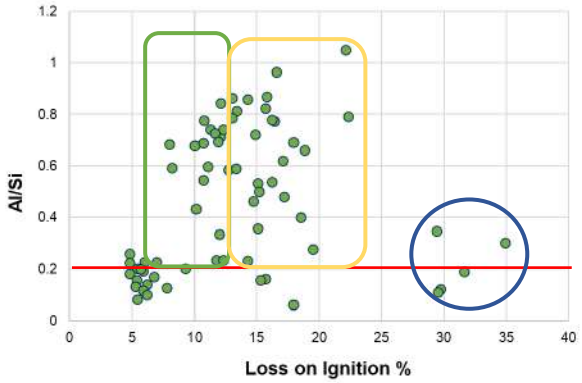


Fig-3b: Correlating Al/Si to loss on Ignition of clays

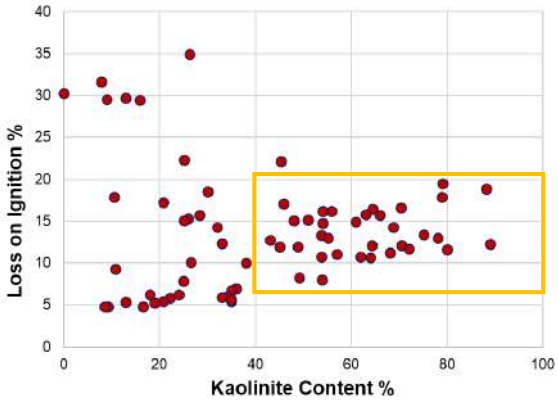


Fig-3c: Comparing Loss on Ignition to Kaolinite content of clays

Fig-3: Preliminary selection criteria of clays by correlationg different parameters

After obtaining the clay samples, they are first dried in an oven and a particular batch is homogenized to reduce the particle size of the clay to below 90 µm. The determination of the oxide composition using the X-ray fluorescence technique is the first characterization method for the analysis of a clay, as it is readily

available in cement plants and gives a first impression of the nature of the clay. The threshold for kaolinite content in a clay is 40%, which means that the alumina content is ≥ 15.8%, the Al/Si content is ≥ 0.2, and the loss on ignition is ≥ 5.6. These criteria do not give a clear picture of the clay's minerology, but they help in the preliminary evaluation of clays at the cement plant level.
Preliminary selection criteria of clays by correlationg different parameters is shown in Figure 3. The relationships between kaolinite content and the ratio of alumina to silica for the clays studied (Figure 3a). The green box shows that clays with an Al_2O_3/SiO_2 (Al/Si) content greater than 0.2 have a kaolinite content of at least 40%, ensuring that the alumina content is ≥ 15.8%. Clays with an Al/Si content of ≥ 0.2 but a kaolinite content of less than 40% indicate the presence of other clay impurities such as muscovite, gibbsite, etc. Correlating Al/Si content with loss on ignition (Figure 3b), the green box shows the kaolinitic clays with low impurities suitable for use as SCM, the yellow box shows the presence of alumina-containing impurities along with other carbonate impurities, and the blue circle shows the impurities that have high LOI due to decomposition of calcium carbonate. Similarly, Figure 3c shows a yellow box containing kaolinitic clays with a content greater than 40% and an LOI ≥ 5.6%. A high LOI within this box indicates a high content of alumina or carbonate impurities, just as a high LOI outside the box indicates carbonate impurities. Thus, when analysing a clay, these limits should be considered.
After a preliminary evaluation using XRF, to confirm that the main clay mineral belongs to the kaolinite group, the clay should be examined for its mineral composition. This is done using X-ray diffraction (XRD), which can identify highly complex clays and clay minerals, allowing both high-resolution identification of clay and other minerals and accurate quantification of phases using the Rietveld method.

4. Conclusions

The identification of kaolinite clay mines is the key factor for the development of limestone calcined clay cement. The existing kaolin clay database has helped to begin the search for clays suitable for LC^3. Using the X-ray fluorescence method to determine oxide composition and loss on ignition, an initial evaluation of clays at the cement plant level is possible. Robust selection criteria should be introduced and a clay should only be selected if it meets all the required parameters. This work has shown that there are large clay deposits throughout India.

Acknowledgements

The authors acknowledge that this study which is a part of Low carbon cement project is financially supported by Swiss Development Cooperation (SDC) and Cementir for making the FutureCem technology available to us.

References

Alujas Diaz, A. *et al.* (2022) 'Properties and occurrence of clay resources for use as supplementary cementitious materials: a paper of RILEM TC 282-CCL', *Materials and Structures/Materiaux et Constructions*, 55(5). Available at: https://doi.org/10.1617/s11527-022-01972-2.

CemNet (2022) *Global cement report 14th Edition* accessed 31 August 2022

Fernandez, R., Martirena, F. and Scrivener, K.L. (2011) 'The origin of the pozzolanic activity of calcined clay minerals: A comparison between kaolinite, illite and montmorillonite', *Cement and Concrete Research*, 41(1), pp. 113–122. Available at: https://doi.org/10.1016/j.cemconres.2010.09.013.

Ito, A. and Wagai, R. (2017) 'Global distribution of clay-size minerals on land surface for biogeochemical and climatological studies', *Scientific Data*, 4(1). Available at: https://doi.org/10.1038/sdata.2017.103.

Krishnan, S. and Bishnoi, S. (2020) 'A numerical approach for designing composite cements with calcined clay and limestone', *Cement and Concrete Research*, 138.

The 16th International Congress on the Chemistry of Cement 2023 (ICCC2023)
"Further Reduction of CO_2 -Emissions and Circularity in the Cement and Concrete Industry"
September 18–22, 2023, Bangkok, Thailand

Scientific dosage of self-compacting concretes containing ternary cement mixtures

M.M.L. Pereira[1*], V.M.S. Capuzzo[2], R.M. Lameiras[3], and A. A. P. Silva[4]

[1] *University of Brasilia, Postgraduate Program in Structures and Civil Construction, Brasilia, Brazil*
Email: maramonaliza19@gmail.com
[2] *University of Brasilia, Postgraduate Program in Structures and Civil Construction, Brasilia, Brazil*
Email: valdirenemaria@unb.br
[3] *University of Brasilia, Postgraduate Program in Structures and Civil Construction, Brasilia, Brazil*
Email: rmlameiras@gmail.com
[4] *University of Brasilia, Postgraduate Program in Structures and Civil Construction, Brasilia, Brazil*
Email: eng.aviz@gmail.com

ABSTRACT

Several studies have investigated the incorporation of granite waste and supplementary cementitious materials (SCMs) in cement, with the aim of significantly reducing CO_2 emissions and improving the energy and technical characteristics of concrete. In this study, the main objective was the performed an optimization of the granular mixture for the dosage of self-compacting concretes (SCC), using marble and granite waste as part of ternary cement mixtures. For that, it was developed an experimental program with four mixtures of SCC, using three types of binders and incorporated granite waste, whose dosage was performed through Bétonlab Pro 3, which is based on the Compressible Packing Model (CPM). It was evaluated the behavior of concrete in the fresh state, with the intention of classifying the SCC according to the self-compacting criteria presented in ABNT NBR 15823-1:2017. The test results indicated that from the self-compacting criteria and dosage parameters used, it was possible to classify all concrete as self-compacting. Thus, the results found indicated that from the dosage strategy used it is possible to successfully dose self-compacting concretes with granite waste and SCMs. All the concretes dosed attended to the self-compacting criteria, with high fluidity and without risk of exudation and segregation.

KEYWORDS: *Self-compacting concrete, Marble and granite waste, Ternary cement mixtures, Dosage, Reduction of CO_2.*

1. Introduction

In the literature, there are several methods for the formulation of SCC that are based mainly on experimental and analytical investigation (Sebaibi et al., 2013). In this research, the chosen model was the Compressive packing model (CPM) which is the third generation of packing models developed at Laboratoire Central des Ponts et Chaussées (LCPC) and has been adopted for the mixture proportion of different families of concretes (Amario et al., 2017). CPM was introduced by De Larrard (1999) to estimate the packing density of aggregates, cement, and cementitious materials along with properties of fresh and hardened concrete, and considers the combined effects of shape, texture, and grading of particles. In addition, CPM é relatively complex since includes the compaction method to describe the actual packing density of the mix (Moghaddam and Baaj, 2017). According to the literature, many studies (Nanthagopalan and Santhanam, 2012; Sebaibi et al., 2013; Andrade et al., 2020) have investigated the optimum mix performance field by determining optimum aggregate gradation to perform an important role in the maximum filling of voids between the particles of cement mix. Thus, the main objective of this paper was utilizing CPM as a potential method to dosage SCC, using marble and granite waste as part of ternary cement mixtures, by optimizing the granular mixture. In this study, the use of the CPM searched mainly optimizes the cement consumption with a focus on the reduction of the clinker, and consequently, emission reduction of CO2, besides conservation of quarries when it proposed reintroducing a residue in the production cycle and use it in the production of a good quality SCC.

2. Materials and methods

For the development of the proposed objective used in the experimental program the following materials: (1) Mineral additions: limestone filler, metakaolin, marble and granite waste; (2) Three different types of cement: CPV-ARI cement that was a high initial resistance cement, the ternary cement CP-MLF produced with 50% Portland cement, 30% metakaolin, 15% limestone filler, and 5% calcium sulfate, and the ternary cement CP-MMG with 50% Portland cement, 30% metakaolin, 15% marble and granite waste, and 5% calcium sulfate used; (3) fine and coarse aggregate; (4) superplasticizer, and (5) water. Also, the calcium sulfate in the ternary mixtures was used in a corrected amount from the assumption that for each 100% of Portland cement produced, there was 5% gypsum. All characterizations of these materials can be found in the study by Pereira et al. (2022).

2.1. Mixture proportioning approach: the compressible packing model

The concrete mixes were designed with the Compressible Packing Model (CPM), proposed by De Larrard (1999), using the Bétonlab Pro 3 software. The CPM was developed for describing the packing density achieved by a granular mixture. Since the packing density of the granular mixture is governed by the shape, surface texture, and size of the aggregate particles, the packing density of each class size of the aggregates employed in the mixture should be experimentally measured. Thus, in this study, both fine and coarse aggregates were separated into classes in which the packing density test was performed in accordance with the methodology proposed by De Larrard (1999), through the experimental compactness, whereas aggregates with particles larger than 100 μm are performed through the mechanical compaction and vibration test. The classes of "mono-size" material were: Class 1 (12.50 mm > d > 9.50 mm), Class 2 (9.50 mm > d > 6.30 mm) Class 3 (6.30 mm > d > 4.75 mm), and Class 4 (4.75 mm > d > 0 mm) for coarse aggregates; Class 1 (4.75 > d > 2.36 mm), Class 2 (2.36 mm > d > 1.18 mm), Class 3 (1.18 mm > d > 0.60 mm), and Class 4 (0.60 mm > d > 0 mm) for natural sand. The experimental compactness was also performed for materials with particles smaller than 100 μm, i.e., the different types of cement and the marble and granite waste, using the water demand test. This test was also performed on pastes produced with a superplasticizer additive, in which the superplasticizer dosage used was determined through the saturation point test. The results of the measured packing density for all materials are reported in Table 1.

Table 1 – Actual packing density of fine and coarse aggregate, cements and marble and granite waste.

	Fine aggregate	**Coarse aggreate**
Class 1	0.681	0.601
Class 2	0.658	0.610
Class 3	0.631	0.628
Class 4	0.606	0.709
	Without superplasticizer	**With superplasticizer (saturation amount)**
CPV-ARI cement	0.538	0.593
CP-MLF cement	0.496	0.577
CP-MMG cement	0.505	0.581
Marble and granite waste	0.537	0.548

Besides the determination of the experimental compactness, another experimental procedure essential for the application of the Compressible Packing Model (CPM) is the calibration of two parameters, p and q, of compressive strength related to the aggregates. The parameter p is related to the paste-aggregate interface, while the parameter q refers to the intrinsic strength of the aggregate. As the calibration considers the largest grains in the mixture, concrete was produced for the calibration of the coarse aggregate parameters and mortar for the calibration of the fine aggregate parameters. Furthermore, since this research used three different types of cement, it was necessary to produce concrete and mortar mixtures for each one, with different strengths (low strength and high strength). In this aim, three cylindrical specimens, with dimensions 100 x 200 mm for concrete mixtures and 50 x 100 mm for mortar mixtures, were tested for each strength class under compressive loads after 1, 7, and 28 days de curing. Based on the composition of the mixtures and on the results of compressive strengths, it was possible to calibrate the p and q parameters for the coarse and fine aggregate, as can be seen in Table 2.

Table 2 – *p* and *q* values for fine and coarse aggregates.

CPM parameters	Fine aggregate			Coarse aggreate		
	CPV-ARI	CP-MLF	CP-MMG	CPV-ARI	CP-MLF	CP-MMG
p	1.2280	2.2127	1.6329	1.0832	1.1603	1.0790
q (Mpa^{-1})	0.00853	0.03714	0.01891	0.00810	0.00000	0.00000

The highest value of *p* was achieved for the CP-MLF which means that the paste-aggregate interface was better for this type of ternary cement mixture in comparison with other cement used in this study. Regarding parameter *q*, the values obtained for the two ternary cement mixtures were equal to zero and this means that these particles presented the highest intrinsic strength. After completing the calibration step of parameters *p* and *q*, it was possible to start simulations of the dosages of self-compacting concrete.

2.2 Simulations of SCC with ternary cement mixtures

Simulations for four mixtures compositions were performed by using the Bétonlab Pro 3 software in which the CPM is implemented. In this program, it was possible to perform the dosage of concrete optimizing four different mixtures and also to estimate some properties of the mixture in the fresh and hardened states. In order to use the Bétonlab Pro 3 software, it was necessary to specify some parameters to optimize the concrete mixes. Some of these parameters with established values, yield stress ≤ 400 Pa, plastic viscosity ≥ 200 Pa.s, fine contribution ≥ 3.3, and coarse aggregates contribution ≤ 1.4, were defined by De Larrard (1999) and provided in the program's manual so that it was possible to perform simulations of concretes with self-compacting characteristics. Also, the mixture proportioning procedure was optimized by minimizing the consumption of cement, and the proportion of coarse and fine aggregates was chosen based on the ACI 237R-07 (2007) criteria, in which the values of 52 e 48%, respectively, served as a basis for the mixing adjustments. In addition, according to the ACI 237R-07 (2007), the maximum recommended value for the water/cement in order to obtain self-compacting concrete is 0.45. Thus, in this study, it was adopted a water/cement ratio fixed equal to 0.45 for the adjustments of mixtures. For each mix, dosage simulations were performed, varying the type of binder and inserting the marble and granite waste in the mixture as fine.

2.3. Fresh properties

From the defined compositions, all SCC mixtures were produced to evaluate the behavior in the fresh state using the test methods for workability properties of SCC recommended by Brazilian standard NBR 15823–1 (2017). The flowability, apparent plastic viscosity, and passing ability were determined through Slump flow, V-funnel, and L-box, respectively.

3. Results

As mentioned, four SCC mixtures were simulated that differed in the type of cement and only the SCC CP did not have marble and granite waste in the mixture as fine. During the dosing process, difficulties arose to find a solution in the software that would present the greatest contribution of fines to the established SCC parameters. Despite the difficulties found, the mixtures are presented in Table 3 with their properties estimated.

Table 3 – Mixture proportioning of SCC with the estimated properties (adapted from Pereira et al., 2022).

Mixture proportions and properties	SCC CP	SCC CP-MGW	SCC CP-MLF	SCC CP-MMG
Coarse aggregate (kg/m^3)	882.7	847.9	844.8	840.9
Fine aggregate (kg/m^3)	785.8	754.8	752.1	748.6
Cement (kg/m^3)	469.1	469.1	478.6	480.9
Marble and granite waste (kg/m^3)	0	64.6	22.9	17.5
Superplasticizer (kg/m^3)	3.13	3.56	7.35	7.35
Water (kg/m^3)	215.6	215.1	216.7	217.7
Superplasticizer content (%)	0.2	0.23	0.46	0.46

Efficient water (kg/m³)	211.1	211.1	215.4	216.4
Total air (%)	1.0	1.0	1.1	1.1
Coarse aggregate/fine aggreate ratio	1.123	1.123	1.123	1.123
Shear yield stress (Pa)	400	400	400	400
Plastic viscosity (Pa.s)	95	128	126	123
Segregation index (confined)	0.973	0.97	0.961	0.958
Packing index of unconfined concrete	5.805	6.085	6.084	6.08
Fines contribution (K'f)	2.278	2.92	2.92	2.92
Coarse aggregate contribution (K'gg)	0.979	0.936	0.935	0.926
Aggregate packing (g*)	0.7832	0.7832	0.7832	0.7832

In order to verify the efficiency of the software in simulating SCC with ternary cement mixtures, the properties of the fresh state of the obtained mixtures were evaluated. Table 4 presents a summary of the results of the tests performed to evaluate the criteria for SCC of the studied mixes.

Table 4 – Testing results of fresh characteristics of SCC mixtures (Pereira et al., 2022).

Test	**SCC CP**	**SCC CP-MGW**	**SCC CP-MLF**	**SCC CP-MMG**
t_{500} (s)	1.96	1.09	1.70	1.90
Slump flow test (mm)	670	700	680	670
V-funnel – T_{10sec} (s)	4.38	4.58	5.94	6.33
V-funnel – T_{5min} (s)	4.90	4.89	7.97	8.68
L-box	0.90	0.95	0.95	0.95
Superplasticizer content (%)	0.49	0.59	1.41	1.40

Evaluating the behaviour in the fresh state, it was found that all the mixes stabilized in the self-compacting concrete and fit all the self-compacting parameters, making it possible to fit them into one of the classes defined by ABNT NBR 15823-1 (2017). Also, it was observed that the mixes containing the ternary cement mixtures had a higher demand for superplasticizer.

3. Conclusions

Despite the difficulties encountered in the dosage process using the Bétonlab Pro 3 software, the Compressible Packing Model (CPM) proved to be efficient, since, based on pre-established parameters, it was possible to obtain concrete that fit the self-compacting criteria, with high fluidity and without risk of exudation and segregation, using ternary cement mixtures in its composition.

References

Amario, M., Rangel, C. S., Pepe, M. and Filho, R. D. T. (2017) “Optimization of normal and high strength recycled aggregate concrete mixtures by using packing model”, *Cement and Concrete Composites,* 84: 83-92

American Concrete Institute. ACI 237R-07: Self-Consolidating Concrete. 2007.

Associação Brasileira de Normas Técnicas, NBR 15823–1: Concreto autoadensável: Classificação, controle e aceitação no estado fresco, ABNT, Rio de Janeiro, 2017.

Andrade, G. P., Polisseni, G. C., Pepe, M. and Filho, R. D. T. (2020) “Design of structural concrete mixtures containing fine recycled concrete aggregate using packing model”, *Construction and Building Materials,* 252

De Larrard, F., Concrete Mixture Proportioning: A Scientific Approach, CRC Press, Series: Modern Concrete Technology, 1999, 448 pages.

Moghaddam, T. B. and Baaj, H. (2018) “Application of compressible packing model for optimization of asphalt concrete mix design”, *Construction and Building Materials,* 159: 530-539

Nanthagopalan, P. and Santhanam, M. (2012) “An empirical approach for the optimisation of aggregate combinations for self-compacting concrete”, *Materials and Structures,* 45: 1167-1179

Pereira, M. M. L., Capuzzo, V. M. S. and Lameiras, R. M. “Evaluation of use of marble and granite cutting waste to the production of self-compacting concrete”, *Construction and Building Materials,* 345

Sebaibi, N., Benzerourm, M., Sebaibi, Y. and Abriak, N.E. (2013) “Composition of self compacting concrete (SCC) using the compressible packing model, the Chinese method and the European standard”, *Construction and Building Materials,* 43: 382-388.

The 16th International Congress on the Chemistry of Cement 2023 (ICCC2023)
"Further Reduction of CO_2 -Emissions and Circularity in the Cement and Concrete Industry"
September 18–22, 2023, Bangkok, Thailand

Impact of curing time on carbonation of low-clinker binders

E. L'Hôpital[1,a*], I. Outras[1,b], and K. Malaga[1,c]

[1] *Research Institute of Sweden, Borås, Sweden*
[a]*Email: emilie.lhopital@ri.se*
[b]*Email: ilias.outras@ri.se*
[c]*Email: katarina.malaga@ri.se*

ABSTRACT

The project studies low-clinker/high-supplementary cementitious materials (SCMs) systems exposed to early-age carbonation, starting within the first week of hydration. In practice, concrete starts its field exposure and carbonation at a very young age, i.e. just a few days old. As the binders are shifted towards a lower amount of clinker and a higher amount of SCMs (which increase the carbonation risk), the investigation of the impact of carbonation on the early-age microstructures becomes increasingly relevant. The goal of the study is to identify the negative impacts of early-age carbonation to achieve good concrete with low-clinker binders. The project will investigate the impact of carbonation on a young binder containing 40% of cement, 45% of slag, and 15% of limestone. Short curing times (3 and 7 days) were compared to the regular curing time (28 days). Two different relative humidity (75 and 98 % RH) were investigated to determine the effect of the environment on the carbonation rate. For each condition, the experiments were carried out in the presence of atmospheric CO_2 and compared to a reference experiment with CO_2 free atmosphere. After 60 days of exposure, the samples were investigated at the surface and powder by XRD and TGA. The carbonation is mainly located at the surface of the samples at 98% RH as ettringite and portlandite are not observed while powder samples show a similar amount of bound water, portlandite, and CO_3. At 75% RH, portlandite remains at the surface. However, the powder sample shows a decrease in the portlandite amount and a higher carbonation rate.

KEYWORDS: *low-clinker binders, short curing time, carbonation, supplementary cementitious material*

1. Introduction

The use of SCMs (supplementary cementitious materials) in cement and concrete is a common practice for decades. In recent years, the focus has shifted towards new binders, with combinations of SCM, new types of SCM, and higher clinker substitutions to help reach the climate goals towards carbon neutrality. Nowadays, numerous studies on carbonated binders were carried out on systems relatively well-hydrated cementitious systems, after 28 days (e.g. Shah 2018) but these results might not be representative of concrete which is exposed to ambient CO_2 after a few days. Since the removal of the concrete formwork may imply an early and drastic relative humidity (RH%) drop, the immature binder becomes exposed to a combination of drying and carbonation. Early carbonation disturbs hydration kinetics, phase assemblage, and porosity, leading to changes in transports and mechanical properties (e.g. Herterich 2017, Soja 2019). This study aims to identify the impact of carbonation and RH on the microstructure of a binder containing slag and limestone with a short curing time.

2. Material and method

A binder paste containing 40% Portland cement (CEM I 52.5 R from Cementa), 45% powder granulated blast furnace slag (Merit from Swecem), and 15 % limestone (Limus 25 from Nordkalk) was mixed with a water-to-binder ratio of 0.4. The paste was cast and cured at 20ºC for 3, 7, and 28 days in 50 ml sealed plastic cylindrical molds of a diameter of 37 mm and height of 45 mm. After curing, the cylinders were cut into slices with a thickness of 4 ± 1 mm. The samples were exposed to two different relative humidity

(RH) in the presence and absence of atmospheric CO_2. The exposure chambers were airtight containers with internal ventilation to homogenize the atmosphere. The RH was maintained with saturated salt solutions of sodium chloride and potassium sulfate to obtain 75% and 98% RH respectively. For the carbonated curing chambers, the ambient air was firstly equilibrated to the appropriate RH by bubbling through the corresponding saturated salt solution and then the air was injected with a pump into the chamber. The CO_2 free curing chamber was controlled with soda lime used as a CO_2 trap.

After 60 days of exposure in a controlled chamber, the hydration of the samples was stopped by isopropanol solvent exchange. The surface of the sample was analysed by XRD. The same sample was ground and called powder sample and analysed by XRD and TGA. X-ray diffraction (XRD) was carried out by a Rigaku Miniflex 600 with a CuK*a* source and a fast 1d solid-state detector with time delay integration. The X-ray tube worked at 40kV and 15mA. The Bragg-Brentano configuration included a fixed divergence slit of 1.25 ˚ and a Soller slit of 2.5˚. The sample powder was prepared by a front-loading method in a sample holder of 1 mm deep and 4 cm diameter. The sample was scanned between 3 and 73˚ (2θ) with an increasing step of 0.02 and a scanning speed of 1˚/min.

Thermogravimetric analyses were realized with a Mettler Toledo TGA/DSC 3+. The weight loss of the samples was recorded from 30°C to 1000°C with a heating rate of 10 K/min. The bounded water was quantified from the weight loss between 30°C to 500°C and the $CaCO_3$ between 500°C and 850°C. If the weight loss of calcite is observed around 680ºC, vaterite and aragonite are observed at earlier temperatures ranging around 500˚C, as shown by previous research (Vogler 2022). The different amounts of bound water (BW), portlandite (CH), and $CaCO_3$ are calculated as shown in equations 1, 2, and 3.

$$BW_{\text{measured, per 100g anhydrous}} = \frac{WL_{BW} * 100}{100 - WL_{BW}} \quad (1)$$

$$CH_{\text{measured, per 100g anhydrous}} = \frac{WL_{CH} * 100}{100 - WL_{BW}} x \frac{74\ (M_{CH})}{18\ (M_{water})} \quad (2)$$

$$CaCO_{3\ \text{measured}} = WL_{CaCO_3}\ x\ \frac{100}{44} \quad (3)$$

3. Results and discussion

The diffractograms of the sample's surface are shown in Figure 1. In the absence of CO_2, calcite is associated with the presence of limestone in the binder. In the presence of atmospheric CO_2, calcite and vaterite are observed at both RH, while aragonite is only observed at 75% RH. In addition to limestone, calcite is strongly associated with the carbonation of portlandite (Steiner 2020). At 98% RH, the portlandite is below the detection limit indicating that the portlandite was dissolved. At 75% RH, portlandite is detected in all the samples. It confirms the fact that the effect of carbonation on other hydrates can start before the complete consumption of portlandite. Vaterite and aragonite are associated with the carbonation of hydrates such as calcium silicate hydrate (C-S-H) and ettringite (Steiner 2020). Ettringite is dissolved and cannot be observed in the presence of CO_2, while it is present in CO_2 free atmosphere after 7 and 28 curing at 75% RH. Moreover, a small hump at 20.7º 2θ could be explained by a trace of gypsum that would agree with the carbonation of ettringite. At 98% RH, most of the ettringite is carbonated after 28 days of curing as only some traces are visible after carbonation while it is present in the CO_2-free sample.

The results of the powder samples are presented in Figure 2 and Table 1. In the absence of CO_2, no significant difference is observed between the samples. Similar hydrates, amount of bound water, portlandite, and $CaCO_3$ are observed. In the carbonated sample, calcite is observed at both RH but vaterite is observed as a trace, only at 98% RH. However, the TGA shows a similar amount of bound water, portlandite, and $CaCO_3$ at different curing times in the presence and absence of CO_2 meaning that the carbonation is relatively low. At 75% RH, when the curing time decreases from 28 days to 3 days, the bound water decreases by 39%, the amount of portlandite decreases by 51 % and the amount of $CaCO_3$ increases by 31%. The 7 days curing shows a great improvement towards carbonation as bound water and portlandite are reduced by 22% and 19% respectively, whereas $CaCO_3$ increases by 11%. The increase of $CaCO_3$ is linked to the dissolution of portlandite and ettringite; and the precipitation of calcite, vaterite,

and aragonite. In the powder samples, vaterite and aragonite are below the detection limit meaning that the presence is mainly at the surface of the sample.

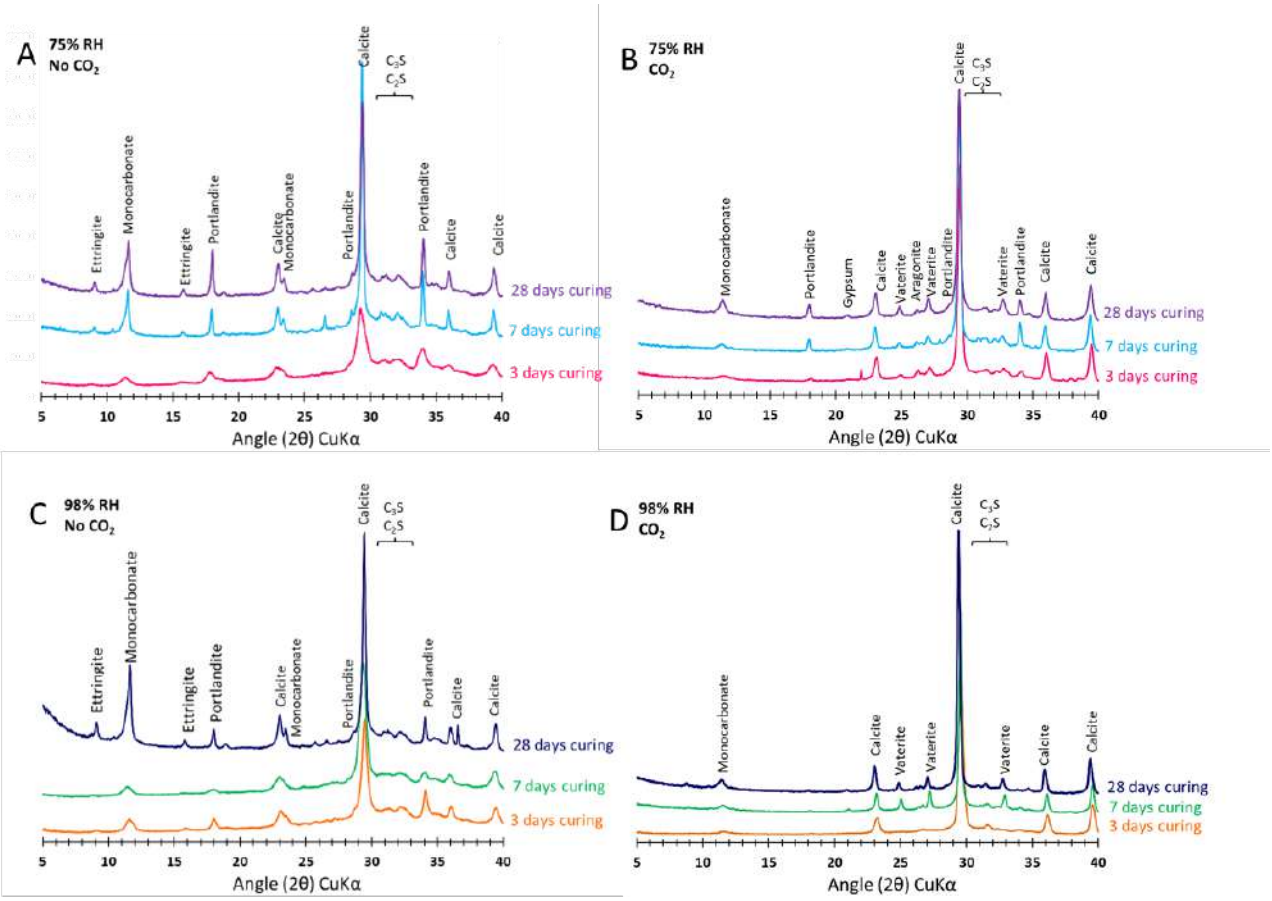


Figure 1: Diffractogram of the investigated samples on the surface cured for 3,7 and 28 days at 75%RH and no CO_2 (A), 75%RH and CO_2 (B), 98%RH and no CO_2 (C). 98%RH and CO_2 (D)

Table 1: Quantification in wt% of bound water (BW), portlandite (CH), and $CaCO_3$ realized by TGA.

RH (%)	Test age (Days)	Absence of CO_2			Presence of CO_2		
		BW	CH	$CaCO_3$	BW	CH	$CaCO_3$
75	3	16	7.8	19	9.4	3.1	31
	7	16	8.1	19	12	5.1	26
	28	17	7.8	18	15	6.4	23
98	3	17	7.5	18	15	5.8	23
	7	17	8.1	18	15	5.6	24
	28	18	9.0	17	16	5.6	22

4. Conclusions

At 98% RH, the sample surface is fully carbonated. However, a similar amount of bound water, portlandite, and $CaCO_3$ regardless of the curing time, meaning that the carbonation is rather low. At 75% RH, vaterite, aragonite, and a trace of gypsum are observed at the surface together with portlandite. It shows that carbonation of other hydrates such as C-S-H and ettringite can occur while portlandite is still present. Even if cement hydrates are observed at the surface, the amount of portlandite significantly drops whereas the amount of $CaCO_3$ increases in the powder sample with the reduction of the curing time meaning that the carbonation of the sample is higher than at 98%.

More investigation is needed on the short curing time of binders toward carbonation. This work is part of an ongoing study that investigates different binder systems containing slag, slag-limestone and fly ash-limestone mixes; and will be extended to slag-fly ash-limestone, calcinated clay-limestone, and bio ash binders. The carbonation will be studied for a longer time and also on mortar to determine the impact on compressive strength.

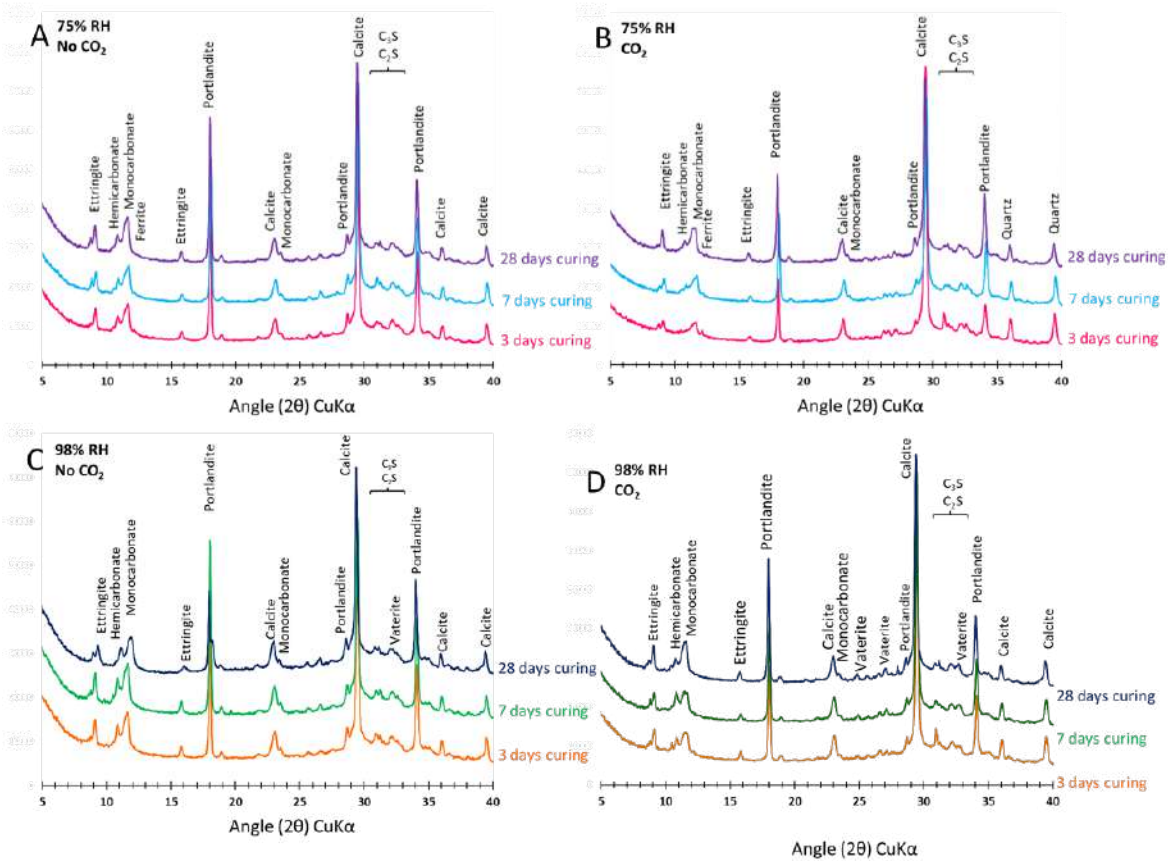


Figure 2: Diffractograms of powder samples cured for 3,7 and 28 days at 75%RH and no CO_2 (A), 75%RH and CO_2 (B), 98%RH and no CO_2 (C). 98%RH and CO_2 (D)

Acknowledgments

The project is co-funded by RISE and the Consortium for the Financing of Fundamental Concrete Research (consisting of Cementa, Thomas Betong, ABetong, Strängbetong, Betongindustri, and Swerock), which is warmly acknowledged here.

References

Herterich, J. (2017). Microstructure and phase assemblage of low-clinker cements during early stages of carbonation, *Doctoral dissertation*, University of Leeds.

Shah, V., Scrivener, K., Bhattacharjee, B., & Bishnoi, S. (2018). Changes in microstructure characteristics of cement paste on carbonation. *Cement and Concrete Research*, 109, 184-197.

Soja, W. (2019). Carbonation of low carbon binders, *Doctoral dissertation No.9400*. EPFL.

Steiner, S., Lothenbach, B., Proske, T., Borgschulte, A., & Winnefeld, F. (2020). Effect of relative humidity on the carbonation rate of portlandite, calcium silicate hydrates and ettringite. *Cement and Concrete Research*, 135, 106116.

Vogler N., Drabetzki P., Lindemann M., Kühne H.C. (2022). Description of the concrete carbonation process with adjusted depth-resolved thermogravimetric analysis. *Journal of Thermal Analysis and Calorimetry*, Vol. 147, pp. 6167-6180.

The 16th International Congress on the Chemistry of Cement 2023 (ICCC2023)
"Further Reduction of CO_2 -Emissions and Circularity in the Cement and Concrete Industry"
September 18–22, 2023, Bangkok, Thailand

Effect of Admixture for Slag on the Strength Development of Cement blend containing Cement, Slag, and Calcium Carbonate

R. Mohammad[1*], R. Yasuda[2], H. Nishi[3], T. Torichigai[4]

[1]*Flowric Co.,Ltd., Tsukuba, Japan*

Email: rosyad_hm@flowric.co.jp
[2]*Flowric Co.,Ltd., Tsukuba, Japan*

Email: r_yasuda@flowric.co.jp
[3]*Flowric Co.,Ltd., Tsukuba, Japan*

Email: h_nishi@flowric.co.jp
[4]*Kajima Construction Co.,Ltd., Tokyo, Japan*

Email: torichig@kajima.com

ABSTRACT

Utilization of Blast Furnace Slag (BFS) as supplementary cementitious material (SCM) can reduce CO_2 emission that mainly comes from the manufacturing process of Portland cement (PC). A BFS substitution ratio of 70% significantly reduces carbon emission but delays early age strength development. Introducing Carbon Capture and Utilization material (CCU) to the concrete mixture can further reduce CO_2 emission. A newly developed CCU material, termed light calcium carbonate (EC), is a calcium carbonate-rich material. In this study, we investigated the PC-BFS-EC ternary binder hydration products and strength development when using admixture for slag. Adding EC to the binder improves the strength development and it is more pronounced in a mixture with a high amount of BFS. This strength development might be linked to the increase of hemicarboaluminate and monocarboaluminate formation. Furthermore, adding EC and accelerator for the slag to the admixture helps mitigate the low 3 days strength of a high BFS ratio binder.

KEYWORDS: *carbon reduction, blast furnace slag, slag accelerator, light calcium carbonate, hydration phases*

1. Introduction

Using ground granulated Blast Furnace Slag (BFS) as Supplementary Cementitious Material (SCM) can significantly reduce the concrete carbon footprint from Portland cement production. The Japanese standard JIS R 5211 has stipulated a maximum BFS substitution of 70%. At this substitution ratio, the low reactivity of binary cement blends considerably delays the setting time and prolongs the framework application during the early curing stages.

Another means to reduce the carbon footprint is using Carbon Capture and Utilization (CCU) material in a concrete mixture. A newly developed CCU material termed light calcium carbonate (EC) is a $CaCO_3$-rich material in powder form. The manufacturing process combines the CO_2 from industrial waste gas with high-alkali concrete wastewater. The manufacturing process reduces the CO_2 emission to the atmosphere, and the utilization of concrete potentially reduces the concrete carbon footprint to zero. A study by Hoshino (2006) shows that adding limestone powder increases the strength development of a binder system containing BFS. Analogously, adding EC in a ternary binder of PC-BFS-EC could help the strength development. However, the study on the material is limited.

This study aims to evaluate the properties of mortar of the PC-BFS-EC ternary binder system. Accelerator for slag (ACS), which is a sulfur-based inorganic salt additive, were added in various dosage and the effects on mortar properties, especially the early strength of the BFS-containing binder were

studied. In addition, quantification of the hydration phases was performed by X-ray diffraction (XRD) analysis to evaluate the strength development.

2. Experiment material and procedures

We used water (W) from tap water and fine aggregate (S) from mountain sand with an absolute density of 2.59 g/cm3. For the binder, The Portland cement (PC) was from Taiheiyo Cement, ground granulated blast furnace slag (BFS) from Nippon Steel Esment Kanto, and light calcium carbonate (EC) from Nippon Concrete Industries. Table 1 presents the physical and chemical compositions of each material.

Table 1. Physical and chemical properties of cement blend material

Material	Density (g/cm^3)	Surface area		Loss of Ignition (%)	Chemical composition (%)							
		BET (m^2/g)	Blaine's (cm^2/g)		SiO_2	CaO	$CaCO_3$	Al_2O_3	Fe_2O_3	MgO	SO_3	Others
PC	3.16	0.584	3240	2.58	20.63	65.11	-	5.52	2.95	0.92	1.82	1.521
BFS	2.89	1.196	4390	0.93	32.19	46.62	-	11.48	0.37	4.66	4.66	-
EC	2.46	3.840	3000	43.9	0.85	-	96.22	0.01	0.19	0.12	2.62	-

We divided the experiment into two series. Series I evaluate the mortar properties and the required admixture dosage to obtain a mortar flow value of 175 ± 10 mm for various mortar mixture, as shown in Table 2. Series II evaluate the effect of varying addition of the ACS on the mortar properties of the mixture with high BFS content.

Table 2. Proportion of volume (ml/L) for various mortar mixture

W/P	Series I						Series I						Series I, II					
	Mix	W	PC	BFS	EC	S	Mix	W	PC	BFS	EC	S	Mix	W	PC	BFS	EC	S
50%	PC0	277	175	0	0	538	BB0	277	96	86	0	531	BC0	277	53	134	0	527
47%	PC3	269	170	0	13		BB3	269	94	84	13		BC3	269	51	130	13	
44%	PC6	261	165	0	25		BB6	261	91	81	27		BC6	261	49	126	27	
42%	PC9	253	160	0	38		BB9	253	88	79	39		BC9	253	48	122	39	

Binder (B) refers to the total mass of PC and BFS, and powder (P) refers to the total mass of PC, BFS, and EC. Regarding the notation, PC, BB, and BC refer to the BFS substitution ratio by mass in B of 0%, 45%, and 70%, respectively. The last number on the mix refers to the EC substitution ratio by replacing total volume of water and binder by 3%, 6%, and 9% and keep their ratio constant. EC addition is in powder form, increasing powder amount in the mixture, thus reducing the water-to-powder ratio by weight (W/P) as shown in Table 2. The air is 10 ml/L, and the water-to-binder ratio by weight (W/B) is 50% for all mixtures. The admixture Ad has no addition of ACS, while Ad+A, and Ad+AA, differ with varying addition of ACS of 0.75%/B, and 1.5%/B respectively, where %/B refers to percentage amount of binder mass.

The mixing was conducted at 20°C room temperature. After mixing powder and sand thoroughly, water and admixture are added, and mortar is mixed for 30 seconds on low speed (62 rpm), then 90 seconds on high speed (125 rpm) using an high-power mortar mixer by Maruto. The flow value (FL) is the spread measurement of mortar, obtained after lifting a mortar cone, which is a half-sized version of concrete slump measurement according to JIS A 1101. For compressive strength measurement, the mortar is poured into ⌀5x10 plastic mold and plastic seal cured for 3d, 7d, and 28d for Series I and 24H, 3d, and 7d for Series II.

XRD analysis was performed on the paste sample for the following mixture: PC0, PC6, BB0, BB6, BC0, and BC9. The sample was prepared by immersion in acetone and then dried in an N_2-flowing desiccator before being finely ground. Corundum (α-Al_2O_3) of 10 mass % was added as an internal standard in a laboratory ball mill. The condition of measurement was using a CuKα target, tube voltage of 45 kV, tube current of 40 mA, a scan range of 2θ = 5-65°, and step width of 0.03°. The measured phases were alite (C_3S), belite (C_2S), aluminate (C_3A) and ferrite (C_4AF), calcium hydroxide (CH), ettringite (Ett), calcite (CC), monosulphate (Ms), hemicarboaluminate (Hc), and monocarboaluminate (Mc).

3. Results and Discussion

3.1 Admixture dosage

Table 3 shows the results of the fresh mortar test. In series I, the required dosage for the same EC ratio to obtain the target flow value for BB and BC is similar and lower than for PC, which indicates that the substitution of BFS improves the flow behaviour of mortar. However, when the EC content is increased, the flow value decreases, thus requiring a substantial increase in the admixture dosage. We suspect that the reduction in flow value is due to the dry powder flocculation, thus reducing the available water and admixture content for dispersion in the system. In Series II, we observed that adding ACS reduces the flow value, especially with a high EC content.

Table 3. Required dosage and flow value of mortar for Series I and Series II experiment.

Series I									Series II			
Ad										Ad:	Ad	Ad+A	Ad+AA
Mix	dosage	FL	Mix	dosage	FL	Mix	dosage	FL	Mix	dosage	FL	FL	FL
	%/B	mm		%/B	mm		%/B	mm		%/B	mm	mm	mm
PC0	0.9	182	BB0	0.9	183	BC0	0.9	182	BC0	0.8	168	160	146
PC3	1.5	184	BB3	1.4	183	BC3	1.4	185	BC3	1.4	175	145	128
PC6	2.2	182	BB6	1.9	183	BC6	2.0	185	BC6	2.0	177	131	110
PC9	3.8	173	BB9	3.0	182	BC9	3.0	183	BC9	3.0	177	134	117

3.2 Compressive strength

Figure 1 shows the change in compressive strength with varying mixtures and admixtures. The continuous and dashed grey line indicates the 3d and 7d strength for PC0 mixture (Portland cement-only binder) as a reference.

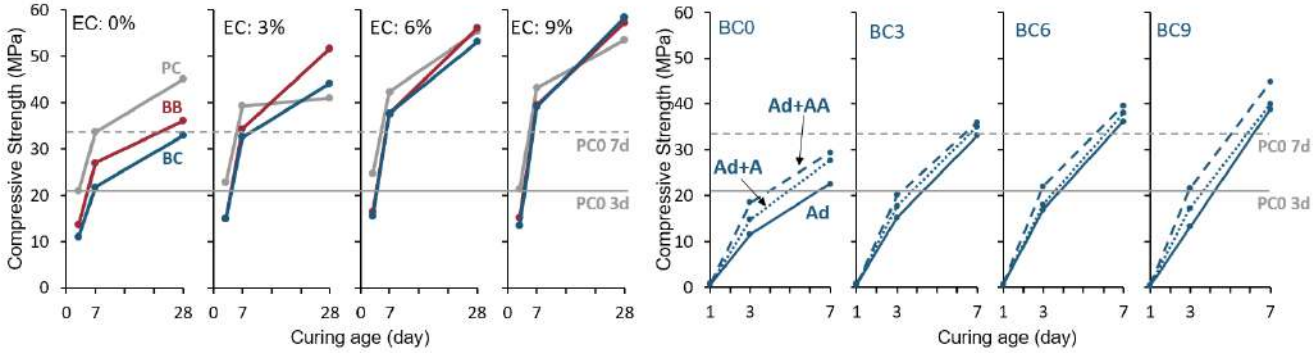


Figure 1. Compressive strength with varying mixture (left) and varying admixture on BC mixture (right)

Replacement of binder from PC0 to BB0 and BC0 shows a reduction of strength at all ages. Adding EC in PC, BB, and BC mixture increases the strength at all ages. For BB and BC, the strength gap to PC decreases with increasing EC content at a high EC ratio, indicating that the effect of EC on strength development is more pronounced in the PC-BFS binder system than PC-only system. The addition of EC in BB and BC mixture resulted in higher strength than PC0 starting from 7 days of age. From Figure 1 (left), the addition of ACS results in a strength increase starting from 3 days of age. From Figure 1 (right) the PC0 strength at 3 days can be achieved for the case of Ad + AA and when EC is added.

3.3 Hydration phases

Figure 2 shows the hydration products change with age for different mixtures, and Figure 3 shows the phase evolution for 2θ = 8-13°. The white region shows the total amount of Calcium Silicate Hydrate (CSH) gel or Calcium Aluminate Silicate Hydrate (CASH) gel, and amorphous phases of BFS. Hc and Mc are formed in all cases due to the small content of limestone powder in composite components of Portland cement. Since the amount of Portland cement in BB and BC is low, we observe a lower amount of Hc and Mc. Upon depletion of reactive CC, C_3A and C_4AF react with Ett to form Ms. When a large amount of CC is present from the addition of EC, we observe the higher formation of Hc and Mc as well as no formation of Ms. Weerdt (2010) and Zajac (2013), reported that in the presence of CC, the

consumption of Ett to Ms is prevented, thus keeping the Ett constant. The voluminous properties of Ett are thought to increase the mortar's compressive strength.

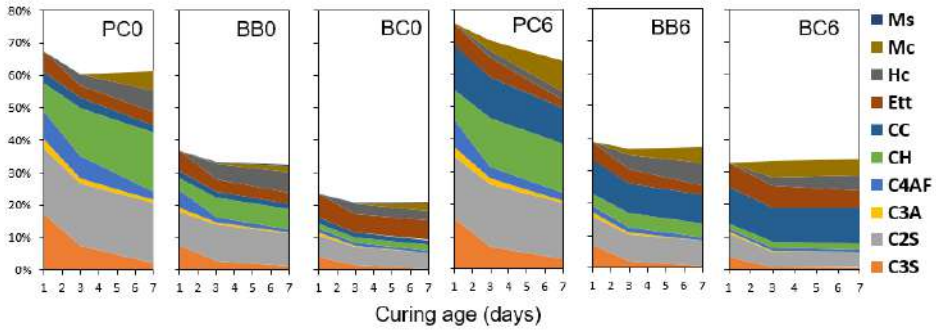


Figure 2. The change of hydration product composition with curing age.

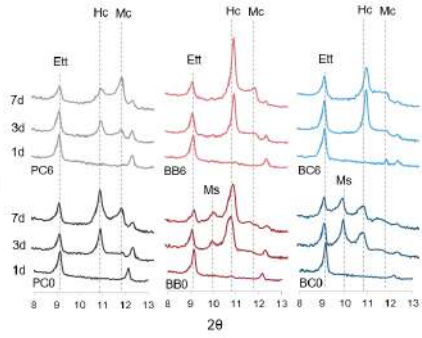


Figure 3. Phase evolution to 3 days

However, we observed a slight decrease in Ett in the case of the EC-added mixture. We suspect that the CC reacts with Ett to form Hc and Mc, thus releasing the sulfate ion free into the system. The free sulfate ion can be used again to form Ett with the remaining C_3A and C_4AF. Therefore, we assume that Hc and Mc will be formed as long as there is remaining CC, C_3A and C_4AF, and Ett in the system. However, further study is needed regarding this reaction.

From Figure 3, the EC-added mixture shows no peak of Ms and higher peaks of Hc and Mc, and Hc is formed earlier than Mc. With age, the Ett and Hc are decreasing, and Mc is increasing for the case of PC6 and BC6, while the Hc and Mc are increasing for the case of BB6. Since Ett is decreasing, the strength development in the EC-added mixture might be slightly related to the amount of Ett phase. An observation made by Zunino (2021) found that Hc and Mc phases increase the strength development by pore filling. This mechanism is likely linked to the strength increase in the PC-BFS-EC binder, which explains the similarity in BB and BC achieving the same strength as the PC-only binder at age 7 days.

4. Conclusions

In this study, we investigate the effect EC on the fresh mortar properties and compressive strength of PC-BFS-EC ternary binder when using admixture for slag. EC addition reduces the flow value of mortar, thus requiring additional admixture dosage to maintain the same flow. EC addition into PC-BFS binder lead to the increase of Mc and Hc formation, which might be linked to strength development on PC-BFS binder. The addition of ACS in admixture and EC addition combined can mitigate the problem of low early strength on the PC-BFS binder.

Acknowledgements

This paper is based on results of “Development of Materials, Manufacturing Methods and a Quality Control System on Innovative Carbon Negative Concrete”, JPNP21014, commissioned by the New Energy and Industrial Technology Development Organization (NEDO).

References

Hoshino, S. Yamada, K. Hirao, H. (2006) “XRD/Rietveld Analysis of the Hydration and Strength Development of Slag and Limestone Blended Cement”, *Journal of Advanced Concrete Technology*, Vol.4, No. 3: 357-367

Weerdt, K.D., Haha, M.B, Saout, G.L., Kjellsen, K.O., Justnes, H., Lothenbach, B. (2010) “Hydration mechanism of ternary Portland cements containing limestone powder and fly ash”, *Cement and Concrete Research*, 41: 279-291

Zajac, M., Rossberg, A., Saout, G.L., Lothenbach, B. (2013) “Influence of limestone and anhydrite on the hydration of Portland cements”, *Cement & Concrete Composites*, 46: 99-108

Zunino, F., Scrivener, K. (2021) “The reaction between metakaolin and limestone and its effect in porosity refinement and mechanical properties”, Cement and Concrete Research, 140: 106307

The 16th International Congress on the Chemistry of Cement 2023 (ICCC2023)
"Further Reduction of CO_2 -Emissions and Circularity in the Cement and Concrete Industry"
September 18–22, 2023, Bangkok, Thailand

Refinement of activation methods for increased reactivity of kaolinitic and illitic clays

G. Plusquellec[1*], O.A. Chaudhari[1], E. L'Hôpital[1] and K. Malaga[1]

[1] *RISE Research Institute of Sweden, Borås, Sweden*
Email: gilles.plusquellec@ri.se

ABSTRACT

Using kaolinitic clays is one of the best available options to reduce the environmental footprint linked to cement. Indeed, the production of an LC3-type binder (limestone calcined clay cement) leads to a CO_2 emission reduction of about 40% compared to plain Portland cement. The activation of kaolinitic clays is generally made by calcination between 600 and 800°C. This process gives, however, unsatisfactory results with illitic clays, another type of clay widely available in many places of the world, and only leads to a low reactive material that is not viable to use as SCM (supplementary cementitious material). This project aims to find alternative activation methods and refine them to increase the reactivity of clays (illitic and kaolinitic). Mechanochemical activation by ball milling (with and without triethanolamine (TEA) as a grinding aid) and calcination were applied on kaolinitic and illitic clays, and on their corresponding pure phases, kaolinite and illite. It was found that illitic clays reached a reactivity similar to calcined kaolinitic clays.

KEYWORDS: *Clay, activation, reactivity, sustainability, SCM*

1. Introduction

The use of activated clay as SCM is considered one of the best alternatives to reduce the CO_2 emissions linked to cement production. Clays are available in large amounts in many places of the world and are present in various forms, depending on which minerals compose them. The most common groups of clay minerals are kaolinite, smectite and illite. Clays need to be activated to be reactive in cementitious systems. Activation of clay refers to the process by which the structure of the clay minerals is partially destroyed (dehydroxylation) and become amorphous, thus able to participate in the hydration reaction of cement *via* a pozzolanic reaction. However, the most used activation method, i.e. calcination between 600 and 800°C, is only effective with kaolinitic and smectitic clays but has little or no effect on illitic clays (Plusquellec et al. (2021)). Consequently, illitic clays are, to this day, not considered a viable SCM. It is therefore important to develop and refine activation methods for different types of clays, not only to enhance their reactivity and reach the best properties of the cementitious system but also to allow the use of our natural resources to their full potential. A previous study from Tole et al. (2018) showed the potential of using mechanochemical activation on illitic clays, by which dehydroxylation of illite occurs due to the combined effect of various forces (impact, compression, friction, shear). The project focuses here on two types of clay, kaolinitic and illitic, and compares them to pure phases (i.e. kaolinite and illite). The impact of various activation methods on the reactivity is assessed.

2. Material and methods

Two clays were selected for the study. The kaolinitic clay (KC) (from Strobel Quarzsand, Germany) contained 40 to 45% of kaolinite. The illitic clay (IC) (from BaraMineraler, Sweden) contained 35% illite and 5% kaolinite. Both clays also had quartz (20% for IC, unknown amount for KC). The chemical composition is reported in Table 1. Two pure phases were also studied: kaolinite (provided by Merck) and

illite (provided by Alfa Chemistry). In addition, a series of experiments were done in the presence of Triethanolamine (TEA) (from Sigma-Aldrich), a grinding aid often used in cement plants. Grinding aids can increase the efficiency of grinding (reduction of the agglomeration of the particles, a decrease of the hardness by facilitating the movement of dislocations towards the surface, etc.) as shown by Prziwara et al. (2020). Furthermore, the potential influence of quartz (hard material present in the clays) during ball milling of clays was checked by investigating a mix made of 80% illite and 20% quartz.

Table 1: composition of clays.

Compound	Kaolinitic clay (wt.%)	Illitic clay (wt.%)
SiO_2	61	65
Al_2O_3	28	18
Fe_2O_3	4.6	8.1
K_2O	0.3	4.1
MgO		1.6
CaO		1.0

The samples were activated by calcination (furnace from Carbolite) during 1h at 600°C or 800°C, and/or by a mechanical treatment by ball milling (planetary ball mill PM 100 from Retsch). Different parameters were investigated, summarized in Table 2.

Table 2: parameter used for the different activation methods.

Calcination		Ball milling		Ball milling + calcination	
Duration (min)	60	Speed (rpm)	250	Ball milling	500 rpm
Temperature (°C)	600		300		20 min
	800		500		Balls Ø 20 mm
		Duration (min)	20		Ball/powder = 25
			40	Calcination	60 min - 600°C
			60		60 min - 800°C
		Balls Ø (mm)	20		
		Ball/powder (mass)	25		
		Grinding aid (TEA wt.%)	0.01 – 2		

After activation, the reactivity was assessed by the "R3 test" (Snellings et al. (2019)), during which the heat production of a model mix was measured by isothermal calorimetry (TAM Air) at 40°C for 7 days. The model mix consisted of the SCM to test, portlandite (portlandite/SCM = 3 by weight), calcite (calcite/SCM = 0.5 by weight), and a solution containing 4 g/l of KOH and 20 g/l of K_2SO_4 to reach a solid-to-liquid ratio of 1.2. The higher the total heat at 7 days of hydration (J/g SCM) is, the more reactive the corresponding SCM is.

3. Results

Figure 1 presents the reactivity of the pure phases and the clays after various treatments, and Figure 2 the impact of TEA on the reactivity of the IC during ball milling.

As expected, the highest reactivity of kaolinite was reached after calcination (948 J/g SCM). By using ball milling instead, the reactivity was significantly reduced for each tested parameter. The best result was obtained with 500 rpm and 20 min (634 J/g SCM, a decrease of about 33% compared to calcination). A decrease by half of the grinding speed (250 rpm) led to a significant decrease in reactivity, even by tripling the grinding time (60 min) (385 J/g SCM). However, milling with a speed of 300 rpm during 60 min gave similar results to the milling at high speed (500 rpm, 20 min), with 549 J/g SCM. The reactivity of illite after ball milling was not greatly influenced by the different studied parameters. The presence of 20% quartz when grinding illite resulted in a 15% increase in reactivity.

Concerning the activation of clays, the calcined KC reached the highest reactivity of all (481 J/g SCM). The various treatment made on the IC led to significant differences in reactivity. While calcination or ball

milling with a low speed (250 rpm) resulted in a rather low reactivity (between 145 and 190 J/g SCM), ball milling at 500 rpm/20 min and 300 rpm/60 min led to a significantly higher reactivity (330 and 310 J/g SCM respectively). Best, the combination of both calcination and ball milling resulted in a reactivity comparable to the one of the KC (up to 420 J/g SCM).
The addition of TEA during a ball milling of 60 min at 300 rpm did not results in a significant increase of the reactivity of the IC, but rather a decrease for all samples (except one at 0.2 wt.% TEA, which probably resulted from an experimental error, considering the shape of the curve).

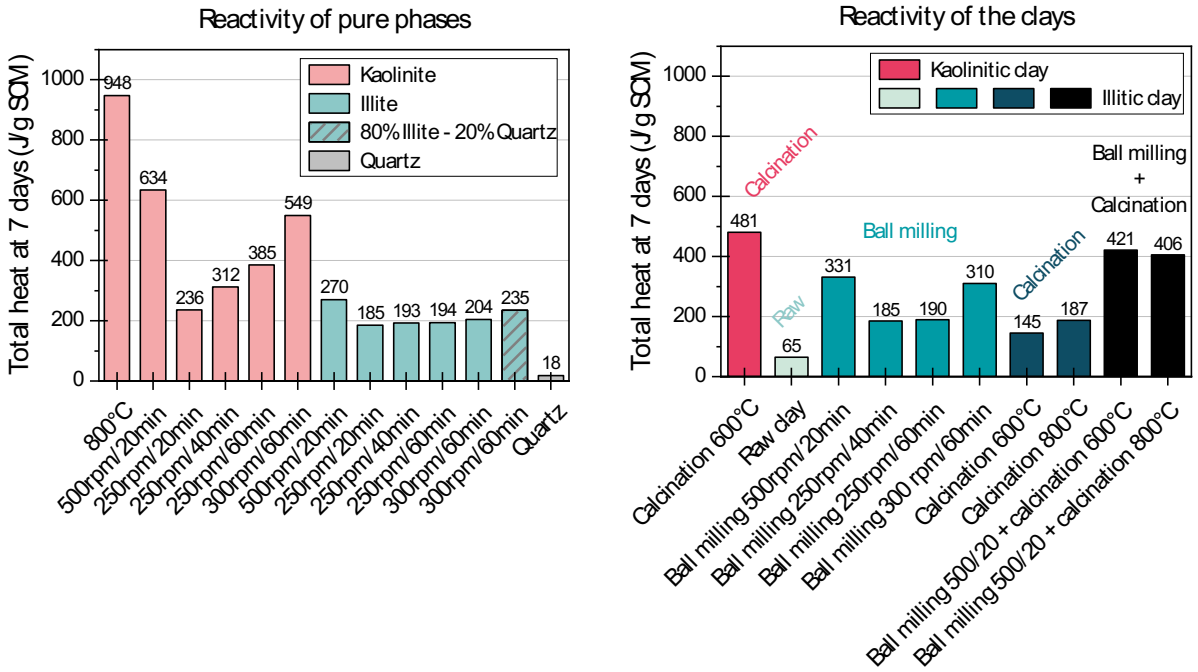


Figure 1: influence of the activation method on the reactivity of pure phases (left) and clays (right). R3 test.

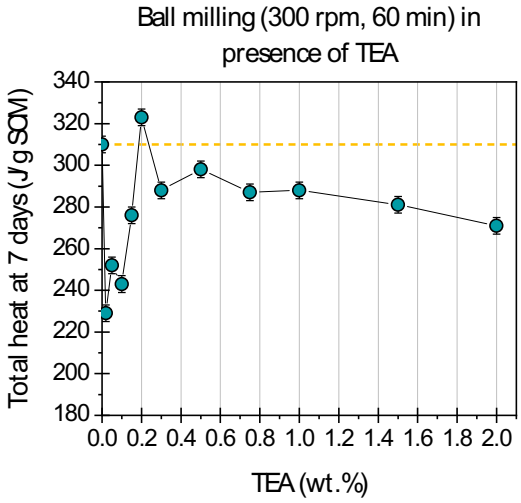


Figure 2: influence of the presence of the grinding aid TEA during ball milling (300 rpm, 60 min) on the reactivity of the illitic clay. R3 test. The dotted line represents the reactivity reached without TEA.

4. Discussion

The results presented here confirm that kaolinite and kaolinitic clays are well activated by calcination instead of a ball milling treatment. During ball milling, the variation of the speed and time parameters does not result in significant changes in the reactivity of illite (contrary to kaolinite). However, the presence of quartz does increase the illite reactivity, most likely due to the high hardness of quartz (7

Mohs) compared to that of illite (1-2 Mohs). Hence, the presence of quartz in natural clay is beneficial when using a mechanochemical activation method and is an important parameter to consider when choosing clay. This could also explain the significant differences in reactivity measured after using parameters for the ball milling of IC, while no significant impact was noted with illite. In particular, it was shown here that a ball milling at high speed and short milling time (500 rpm, 20 min) can be replaced by a much lower speed by increased timing (300 rpm, 60 min). This opens the door to potential industrial use of this method if further improvements are made. Unfortunately, the addition of TEA, a grinding agent, did not lead to any improvement. Garces-Vargas et al. (2022) used TEA during the grinding of an LC3-type cement (with a kaolinitic clay) and observed a positive effect of the presence of TEA in both early age calorimetry on cement paste (higher heat release) and strength of mortar. However, the present results suggest that TEA doesn't positively affect the reactivity of the IC. This could mean that TEA does not affect illite but only kaolinite. But this is unlikely since illite has solvated cation on its surface and space in the interlayer, unlike kaolinite (Tournassat et al. (2015)), making illite more prone to interact with TEA than kaolinite. Other explanations could be that a grinding agent such as TEA might help to decrease the water demand of clay, resulting in better rheology and hydration of the system and higher strength, or that TEA only affects cement particles during grinding.
Finally, it was demonstrated here that the activation of the IC by grinding and calcination led to a reactivity comparable to that of the KC. A previous study (Plusquellec et al. (2021)) showed that illite's structure was affected by calcination only at high temperatures (1000°C), but underwent vitrification which negatively impacted the reactivity. In the present study, the ball milling was performed before the calcination. The structure of the illite was thus already partially destroyed before calcination, which might allow further dehydroxylation during calcination at temperatures lower than 1000°C, avoiding the vitrification. This promising result shows that illitic clays can be considered a viable material for LC3-type binder. The refinement of the activation method is still ongoing, by testing e.g. flash calcination.

5. Conclusion

The reactivity of two clays, illitic and kaolinitic, and their corresponding pure phase, illite and kaolinite, was assessed after various activation treatments. As expected, calcination works best on kaolinite and kaolinitic clays. Illitic clays can reach a reactivity similar to kaolinitic clays after a ball milling treatment (300 rpm, 60 min, ball-to-powder ratio of 25 by mass, Ø 20 mm ball) followed by calcination (1h, 600°C). It is supposed that the dehydroxylation of illite starts during ball milling, allowing further dehydroxylation during calcination at a temperature lower than needed without grinding. Moreover, the presence of quartz in the clay was found to improve the efficiency of ball milling.

Acknowledgements

The project is co-funded by RISE and the Consortium for the Financing of Fundamental Concrete Research (consisting of Cementa, Thomas Betong, ABetong, Strängbetong, Betongindustri and Swerock), which is warmly acknowledged here.

References

Garces-Vargas, JF, Y Díaz-Cardenas, F Zunino, J Ribalta-Quesada, K Scrivener, and F Martirena. 2022. 'The Challenge of Grinding Ternary Blends Containing Calcined Clays and Limestone'. *Mdpi.Com*.

Plusquellec, G, A Babaahmadi, E L'Hopital, and U Mueller. 2021. 'Activated Clays as Supplementary Cementitious Material'. https://www.diva-portal.org/smash/record.jsf?pid=diva2:1534080.

Prziwara, P, and A Kwade. 2020. 'Grinding Aids for Dry Fine Grinding Processes – Part I: Mechanism of Action and Lab-Scale Grinding'. *Powder Technology* 375: 146–60.

Snellings, R, X Li, F Avet, and K Scrivener. 2019. 'Rapid, Robust, and Relevant (R3) Reactivity Test for Supplementary Cementitious Materials'. *ACI Materials Journal* 116 (4): 155–62.

Tole, I, K Habermehl-Cwirzen, M Rajczakowska, and A Cwirzen. 2018. 'Activation of a Raw Clay by Mechanochemical Process—Effects of Various Parameters on the Process Efficiency and Cementitious Properties'. *Materials* 11 (10): 1860.

Tournassat, C, IC Bourg, CI Steefel, and F Bergaya. 2015. 'Surface Properties of Clay Minerals'. *Developments in Clay Science* 6 (January): 5–31.

The 16th International Congress on the Chemistry of Cement 2023 (ICCC2023)
"Further Reduction of CO_2 -Emissions and Circularity in the Cement and Concrete Industry"
September 18–22, 2023, Bangkok, Thailand

Effect of temperature on the heat of hydration and compressive strength of ternary blends

N. Chitvoranund[1,a*], G. Plusquellec[1,b], E. L'Hôpital[1,c], N.L. Dedousi[1,d], U. Mueller[¤,e] and K. Malaga[1,f]

[1] *RISE Research Institute of Sweden, Borås, Sweden*

[a] *natechanok.chitvoranund@ri.se*
[b]*gilles.plusquellec@ri.se*
[c]*emilie.lhopital@ri.se*
[d]*natalia.ioanna.dedousi@ri.se*
[e]*urs.mueller@schwenk.se*
[f]*katarina.malaga@ri.se*

ABSTRACT

Supplementary cementitious materials (SCM) become a common practice in the cement and concrete industry. A high substitution level of SCM is an efficient and sometimes affordable solution that can lower CO_2 emissions. This study aims to investigate the relationship between the heat of hydration and the compressive strength of different binders under different temperatures. Ground granulated blast furnace slag, coal fly ash, calcined clay, and limestone were used in ternary mixes with 45 % total replacement of SCM. A fixed water to binder ratio of 0.45 without any admixtures was applied to this study. The effect of temperature on the heat of hydration was investigated by isothermal calorimetry at 8, 20, and 38 ˚C. Elevated temperature enhances the reaction of cement and SCM. The calcined clay-limestone system has higher reactivity than the other blended systems at early age, but the reaction slows down quite early at the high temperature. The heat of hydration of the slag-containing systems can reach a similar range as the calcined clay-limestone system within 7 days at 38 ˚C and tends to continue the heat development after 7 days. The compressive strength results show a similar trend as the heat of hydration results at early age, but the trend of the samples cured at 38 ˚C starts to deviate from the heat of hydration. The relationship between the heat of hydration and compressive strength under different temperatures of the ternary blends was investigated. Overall, a linear trend of the compressive strength as a function of cumulative heat of hydration was observed for all curing temperatures. It shows a good correlation at early age for different types of binders. This result indicates that the early strength of mortar can be estimated by cumulative heat of hydration.

KEYWORDS: *Temperature, Supplementary cementitious materials, Heat of hydration, Compressive strength,*

1. Introduction

The trend of high clinker substitution by using supplementary cementitious materials (SCMs) has been developed to reduce CO_2 emissions in the cement and concrete industries. SCMs have been used for many decades and often combine two types or more of SCMs leading to a synergy effect. The chemical composition of blended cement is shifted to high Al_2O_3, SiO_2, and low CaO content, leading to changes in chemical and mechanical properties. One of the common SCM that has been used in cement and concrete for many years is ground granulated blast furnace slag (GGBS). GGBS provides good late-age performance and good durability (Osborne, 1999). Coal fly ash is also widely used in concrete as SCM. Both GGBS and coal fly ash cement exhibit lower compressive strength at early ages compared to plain Portland cement (PC) (Oner et al., 2005; Oner & Akyuz, 2007). Alternative sources like calcined clay

containing metakaolin blended with limestone become of interest because it is more reactive than siliceous fly ash (Skibsted & Snellings, 2019). Frølich et al. (Frølich et al., 2016) showed that isothermal calorimetry measurements on cement paste can partially replace compressive strength measurements on cement mortar tested at 20 ˚C.
On a construction site in Europe, the ambient temperature can rise from low to high. The temperature variations can have a large impact on the hydration kinetics and performance of the blended cement with a high substitution of SCM (Deschner et al., 2013). Therefore, the research aims to study the effect of temperature on the heat of hydration and compressive strength development of ternary blends with a 45% of substitution level. The correlation between these two parameters was investigated under different temperatures (8, 20, and 38 ˚C) to implement it for screening other binder combinations in the future for high replacement cement.

2. Materials and methods

The raw materials used in this study are Portland cement (CEM I 52.5 R from Cementa), calcined clay, ground granulated blast furnace slag, coal fly ash, and limestone (Limus 25 from Nordkalk). The binder composition is shown in Table 1. The dry powder and deionized water were equilibrated overnight at the intended curing temperature (8, 20, and 38 ˚C) before mixing. The water to binder ratio (*w*/*b*) of 0.45 was used in this study.

Table 1 The binder composition (wt. %) of the investigated systems.

Binders	*Portland cement 52.5R*	*Calcined clay*	*Granulated blast furnace slag*	*Coal fly ash*	*Limestone*
Portland cement	100	0	0	0	0
Calcined clay - Limestone	55	30	0	0	15
Slag- Limestone	55	0	30	0	15
Fly ash - Limestone	55	0	0	30	15
Slag – Fly ash	55	0	30	15	0

The heat evolution was measured by isothermal calorimetry at 8, 20, and 38 ˚C. The dry powders of 10 g were gently mixed by hand for 1 min, then deionized water was added to the dry powder. The paste was mixed with a spatula for 2 min by hand at room temperature before introducing it into a glass ampule of approximately 5 g of paste. The mass of the sample in the glass ampule was measured before sealing, then the ampule was placed in the isothermal calorimetry directly after mixing. Water was used as a reference sample. For the experiment at 8 ˚C, the experiment was carried out in a controlled temperature chamber at 8 ˚C to avoid condensation. The cumulative heat release was calculated starting 45 min after casting to avoid the effect of thermal equilibration of the sample within the calorimetry. The cumulative heat values per gram of total powder at 2 and 7 days for all temperatures were taken.
The mortar samples were prepared according to the standard EN196-1 for cement testing, except for the water to binder ratio and curing temperature. The standardized sand (CEN Normsand DIN EN 196-1 from NORMENSAND) was used in a sand to binder ratio of 3 by mass. After casting, the mortar samples were stored for 24 hours in a controlled condition chamber at the intended temperature and high humidity. For 20 ˚C curing, the samples were stored in a moist cabinet at 20 ˚C with 95% RH, while the 8 and 38 ˚C samples were placed in a closed box with water at the bottom of the box and a controlled temperature room. After demolding, the mortar prisms were submerged vertically in the water with the addition of $Ca(OH)_2$ for the prevention of leaching. The containers were placed in climate-controlled rooms at 8, 20, and 38 ˚C (±2 ˚C). The compressive strength was tested according to the EN196-1 standard to 40x40x160 mm prisms at 2 and 7 days.

3. Results and discussions

3.1 Effect of temperature on the heat of hydration

The cumulative heat of the investigated systems up to 7 days at 8, 20, and 38 ˚C are shown in Figure 1. The PC system shows higher heat of hydration compared to the blended systems at all temperatures. The overall reaction is enhanced with increasing temperature. The calcined clay-limestone blended system shows slightly higher reactivity than the other SCM at all temperatures. At 8 ˚C, similar heat development when using slags or fly ash is observed. At 20 ˚C, the cumulative heat of the blended systems is developed similarly up to 2 days, then it shows slightly different values: calcined clay-limestone > slag-limestone ≈ slag-fly ash > fly ash-limestone. The slope indicates that the heat of hydration is significantly developed at 38 ˚C before 1 day. The heat of hydration of the PC system at 38 ˚C is slightly lower 20 ˚C at 7 days. The calcined clay-limestone system slows down significantly after 2 days. For the slag-containing systems, the heat of hydration develops and reach the same heat as the calcined clay-limestone blended system at 7 days of hydration. The data of the fly ash-limestone blended system at 38 ˚C is not reported in this paper due to ongoing work.

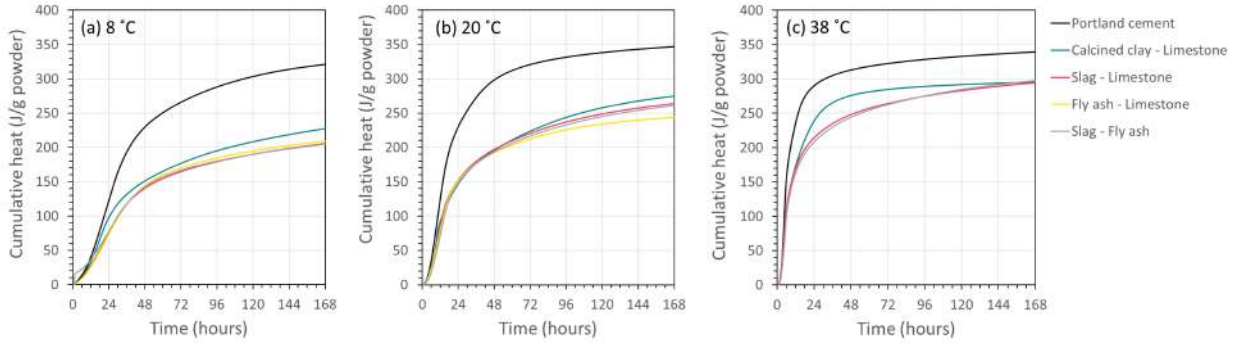


Figure 1 The cumulative heat of the investigated system measured up to 7 days at (a) 8, (b) 20, and (c) 38 ˚C.

3.2 Effect of temperature on compressive strength

The compressive strength of investigated systems cured at 8, 20, and 38 ˚C was tested at 2 and 7 days (Figure 2). Portland cement cured at 8 and 20 ˚C shows higher compressive strength than the blended systems at all ages. Considering the blended systems, calcined clay-limestone shows higher compressive strength development compared to the other blended systems at all temperatures. At 8 ˚C, the strength development is quite similar for the blended systems up to 7 days. At 20 ˚C, the calcined clay – limestone system shows a significant increase after 2 days compared to the other blended systems. At 38 ˚C, the development of hydration for Portland cement and calcined clay-limestone blends is slower after 2 days. The compressive strength cured at 38 ˚C is slightly lower than the compressive strength cured at 20 ˚C probably due to a lack of superplasticizer in the mix design. The mortar of the Portland cement system and the calcined clay-limestone system during mixing at 38 ˚C were quite dried. The slag – fly ash system starts to present a higher strength development than the slag – limestone system after 2 days, while the fly ash – limestone system has the slowest strength development.

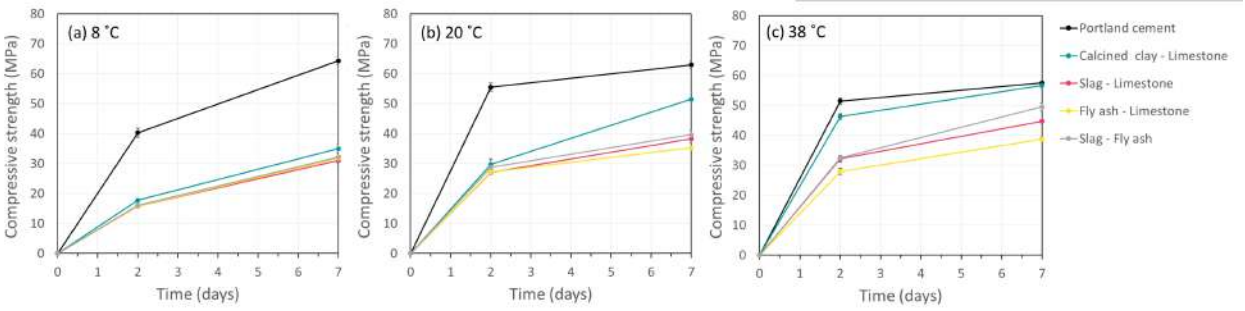


Figure 2 Compressive strength up to 7 days of investigated systems at different temperatures (a) 8, (b) 20, and (c) 38 ˚C.

3.3 Relationship between the heat of hydration and compressive strength

A strong correlation between the heat of hydration and mortar compressive strength of the studied systems cured at 8, 20, and 38 ˚C can be observed (Figure 3). The types of binder in this study does not affect the correlation.

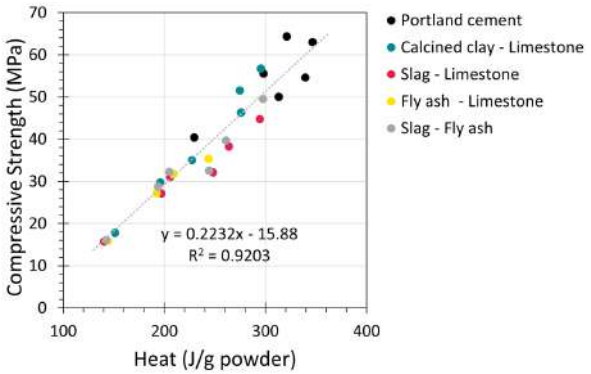


Figure 3 The correlation between the heat of hydration and compressive strength at 2 and 7 days of investigated systems cured at 8, 20, and 38 ˚C.

4. Conclusions

The effect of temperature on the heat of hydration and compressive strength of the ternary blends with 45% of replacement was investigated by isothermal calorimetry and compressive strength measurements. The results clearly show that temperature accelerates the hydration of cement and SCM at early age. The calcined clay-limestone system shows higher heat development and higher compressive strength at all temperatures than the other SCMs at early age. The compressive strength of the calcined clay - limestone system can reach a similar range as Portland cement at 38 ˚C for 7 days.

The obtained correlation between the heat of hydration and mortar compressive strength is good. From this study, the heat of hydration measured by isothermal calorimetry can predict compressive strength at early age (up to 7 days) for various systems which cured at the temperature range of 8 – 38 ˚C.

Further investigation on hydration is needed to compare the hydration development between early age and late age at different temperatures.

Acknowledgment

The author would like to thank for A-Consortium in Sweden for the financial support.

References

Deschner, F., Lothenbach, B., Winnefeld, F., and Neubauer, J. (2013) "Effect of temperature on the hydration of Portland cement blended with siliceous fly ash", *Cement and Concrete Research*, *52*: 169–181.

Frølich, L., Wadsö, L., and Sandberg, P. (2016) "Using isothermal calorimetry to predict one day mortar strengths", *Cement and Concrete Research*, *88*:108–113.

Oner, A., and Akyuz, S. (2007) "An experimental study on optimum usage of GGBS for the compressive strength of concrete", *Cement and Concrete Composites*, *29*(6): 505–514.

Oner, A., Akyuz, S., and Yildiz, R. (2005) "An experimental study on strength development of concrete containing fly ash and optimum usage of fly ash in concrete" *Cement and Concrete Research*, *35*(6): 1165–1171.

Osborne, G. J. (1999) "Durability of Portland blast-furnace slag cement concrete", *Cement and Concrete Composites*, *21*: 11–21

Skibsted, J., and Snellings, R. (2019) "Reactivity of supplementary cementitious materials (SCMs) in cement blends", *Cement and Concrete Research*, *124*(June), 105799.

The 16th International Congress on the Chemistry of Cement 2023 (ICCC2023)
"Further Reduction of CO_2 -Emissions and Circularity in the Cement and Concrete Industry"
September 18–22, 2023, Bangkok, Thailand

Alkali-carbonate activated waste glass-based cements

Simon Blotevogel[1,2*], Louise Lemesre[3,4], Falak Milki[3], Céline Bacquié[1,2], Thomas Wattez[1,2], Martin Cyr[3] and Rachida Idir[4]

[1] *Ecocem Materials, Dublin, Ireland*

[2] *Labcom Orison, LMDC - Ecocem, Toulouse, France*

[3] *LMDC, Université de Toulouse, INSA/UPS Génie Civil, Toulouse, France*

[4] *Cerema, Univ Gustave Eiffel, UMR MCD, Sourdun, France*

Email: sblotevogel@ecocem.ie

louise.lemesre@cerema.fr

falakmilky@gmail.com

cBacquie@ecocem.ie

twattez@ecocem.ie

martin.cyr@insa-toulouse.fr

rachida.idir@cerema.fr

ABSTRACT

Many supplementary cementitious materials (SCM) and precursors for alkali-activated materials (AAM) are amorphous silicates. In many locations, waste glass can be a significant source of amorphous silicate material. Glass wastes, either from flat glass or container bottle production, have been shown to be suitable SCMs in cement and precursors material for alkali-activated cements. In this paper it is shown that the activation of waste glass powders using Na_2CO_3 can produce AAMs of good long-term strength but low early strength. Furthermore, it is shown that early strength can be increased by optimizing activator dosage and to some extent by the use of accelerating salts. During the early cementitious reaction Na_2CO_3 is transformed into hydrated Na-carbonates, trona and thermonatrite. The ratio of trona increases over the first week of hydration, suggesting an ongoing transformation of thermonatrite to trona. At later ages a dense Na and Si bearing gel is observed as hydration product. Raman analysis suggest lesser Si polymerization in the gel than in the precursor glass likely due to the insertion of Na in the silicate matrix.

KEYWORDS: *waste glass, alkali activation, carbonates, microstructure, sustainable*

1. Introduction

Waste glass has received much attention as a precursor of alkali activated materials, because of its wide availability in some countries and for the high compressive strength at older ages (Liu et al., 2019). It is interesting to note that highest compressive strength at all ages are not obtained for the highest alkaline activator concentrations (Cyr et al., 2012; Vafaei and Allahverdi, 2017; Rivera et al., 2018). This opens the door to use less corrosive reagents such as Na-carbonate as activators, which are safer to handle at construction sites. In the present study data are reported on compressive strength and microstructure of Na-carbonate activated glass powder.

2. Materials and methods

Glass powders were obtained by cleaning glass bottles (especially removing glue and etiquettes) and grinding them to about 6000 cm²/g Blaine fineness in different laboratory mills. Compressive strength tests on cement pastes were carried out on a mixed color glass sample (Lemesre, 2021). Mortar strength tests were carried out on a different sample containing exclusively transparent glass. Both glasses were fully amorphous and had very similar chemical compositions (Table 1), that were determined through ICP-OES analysis after alkaline fusion. Anhydrous Na-carbonate powder with a purity >99% was obtained from Honeywell. Anhydrous form of Na_2SO_4 and Triisopropanolamine (Tipa) of high purity (>99%) were both obtained from SigmaAldrich.
Cement paste compressive strength tests were carried out on 2 x 2 x 2 cm^3 cube samples using a w/c ratio of 0.3. Different levels of Na-carbonate contents (5 wt%, 10 wt%, 15 wt% and 25wt%) were tested. Furthermore, mortar tests were carried out on 4 x 4 x 16 cm^3 samples, using a w/c ratio of 0.3. The binder content was increased to 560g so that the paste content remained constant compared to standard mortars preparation (450g binder and w/b=0.5). In mortar samples the impact of 1 wt% addition of accelerating salts Na_2SO_4 and Tipa was tested. All samples were demoulded after one day and cured under endogenous at 20°C conditions until testing.

Table 1. Chemical composition of the two glass samples, as determined by ICP-OES after alkaline fusion.

	K_2O wt%	Na_2O wt%	SiO_2 wt%	Al_2O_3 wt%	CaO wt%	Cr_2O_3 wt%	Fe_2O_3 wt%	MgO wt%
Glass for mortars (transparent)	0.48	12.14	73.06	1.19	10.89	0.00	0.77	1.09
Glass for pastes (mixed color)	0.58	12.76	71.32	1.47	10.61	0.10	0.95	1.25

The evolution of mineralogy in paste samples was analysed through quantitative XRD, on hydration stopped samples. Therefore, the samples were coarsely crushed and placed in an isopropanol suspension for at least 24h. The isopropanol was then filtered off and samples were oven dried at 40°C for up to 4h. Resulting powders were gently ground in an agate mortar to pass an 80µm sieve and then mixed with 5-10 wt% of CaF_2 as in internal standard. XRD scans were carried out on backloaded samples, in a Bruker D8 in Bragg-Bretano configuration using Cu radiation. Scan duration was 3h20 from 3-100° 2 theta.
Raman analyses were carried out on a polished thin section of a 90 wt% glass powder 10 wt% Na-carbonate sample that was cured at 40 °C to speed up hydration reaction. Raman spectra were measured on a Horiba Xplora Raman microscope, equipped with a 512 nm laser, accumulating 4 spectra acquisitions between 100 and 1800 cm^{-1} and an acquisition time of 30s.

3. Results and discussion

Results of compressive strength tests on paste samples are displayed in Figure 1a (Lemesre, 2021). Except for the sample with 25 wt% of Na_2CO_3 there is only little strength development during the first 28 days. After three month the strength development is between 40 MPa for the 10 wt% Na_2CO_3 sample and 10 MPa for the 5 wt% Na_2CO_3. Strength development keeps on increasing over time to reach just below 50 MPa in the 5wt% Na_2CO_3 sample and more than 70 MPa in the 10 wt% Na_2CO_3 sample after 365 days curing. These results show that Na_2CO_3 activation of glass powder results in good strength pastes at later age, but suffers from slow initial reaction rates. The case of the 25 wt% Na_2CO_3 sample is somewhat different, as it gives good early strength, 15 MPa already after one day, and only slightly increases over time to reach 40 MPa after one year.
For mortar strength tests, the Na-carbonate content was fixed at 10 wt% as the best compromise between the rather expensive activator content and physical performance (Figure 1b). The results show low strength of about 0.5 MPa for all mixes and combination of activators. After 7-days there are significant differences between the 10 wt% Na_2CO_3 activated sample presenting a strength of 3.0 MPa and the samples containing Tipa and Na_2SO_4 acceleration with 5.3 and 5.4 MPa, respectively. After 28 days all samples showed a compressive strength of about 25 MPa. These results show that the compressive strength of Na-carbonate – glass powder mortars appears to be higher than in pastes, but also that strength may be dependend on the type of glass used. Furthermore, there appears to be an acceleration potential using traditional cement accelerators, even though the mecanism is not clear.

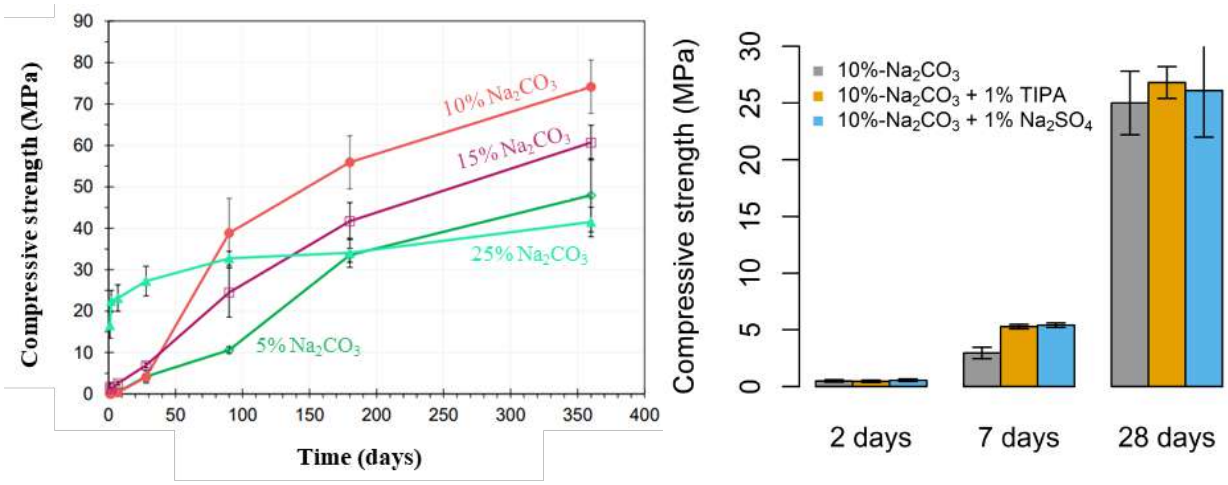


Figure 1. Compressive strength results of (a) glass powder Na-cabonate pastes at different carbonates contents and (b) mortar samples using different accelerator slats and Na-carbonate contents.

Table 2. Rietveld analysis of glass powder, Na-carbonate cement pastes after 7-days of hydration.

7-days	10 wt% Na_2CO_3	15wt% Na_2CO_3	20wt% Na_2CO_3	25wt% Na_2CO_3
Gaylussite	1.0	2.4	2.4	1.7
Trona	12.5	7.9	11.3	14.3
Thermonatrite	5.2	8.8	12.7	14.6
Amorphous	81.2	80.8	73.6	69.4
Initial Na_2CO_3 content (calculated including mixing water)	7.7	11.5	15.4	19.2
Initial Glass content (calculated including mixing water)	69.2	65.4	61.5	57.7

Quantitative XRD analyses (Table 2) show that the initial Na_2CO_3 is transformed into its hydrated forms such as trona and thermonatrite. After 7 days, the trona content is relatively constant whereas the thermonatrite content increases with increasing inital Na_2CO_3 addtion. Besides Na-carbonates, also gaylussite ($Na_2Ca(CO_3)_2 \cdot 5H_2O$) forms, indicating a dissolution of Ca from the soda-lime glass. The formation of gaylussite was reported in Na-carbonate alkali-activated slags to be a necessary precursor for the silicate reaction by consuming CO_3^{2-} ions and raising pH (Bernal et al., 2015).

Raman analyses of the hydrated samples are shown in Figure 2. Leftover glass particles in the sample show the characteristic peaks of Si-O-Si bending at around 560 cm^{-1} and Si-O streching at about 1050 cm^{-1} (McMillan, 1984). In the space-filling gel, the 560 cm^{-1} shifts towards higher wavenumbers, whereas the 1050 cm^{-1} band shifts towards lower wavenumbers. Both shifts are linked to a depolymerization of the silicate structure, likely due to the inclusion of network modifing ions such as Na or Ca, into the amorphous network. The above results are in line with a reaction mecanism similar to alkali-activated slags, with the formation of cabonates that consume CO_3^{2-} ions and delayed slicate raction and the formation, in the case of glass, of N-(C)-S-H gels as main hydrate phase (Bernal et al., 2015; Lemesre, 2021).

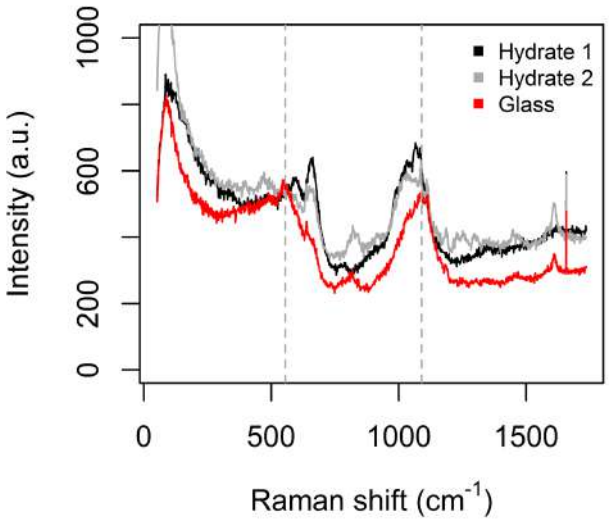


Figure 2. Raman spectra of remaining glass particles (red) and the pore filling gel (black and dark grey). Dashed vertical lines indicate. Expected peak positions for soda-lime glass.

3. Conclusion

The use of waste glass powders in Na-carbonate activated cements is a promising route to increase the volume of available alternative cements. In this study, it is shown that activating waste glass powder with 10%wt of Na_2CO_3 results in binders that have long-term strength of more than 40 MPa after 90 days. However, the low early strength, with only a few MPa after 7 days, currently limits the use. Yet traditional cement accelerators, as well as modification of the activation system, may increase the early hydration kinetics. Microstructural analysis in this study suggests that the hydration mechanism is similar to that reported for Na-carbonate activated slag cements, with a precipitation of mixed carbonates that raise pH and initiate a delayed silicate reaction. The main hydrate is likely N-S-H (Bernal et al., 2015; Lemesre, 2021).

Acknowledgements

Sebastien Moyano from the CEMES is acknowledge for help with the acquisition of Raman spectra.

References

Bernal S. A., Provis J. L., Myers R. J., San Nicolas R. and van Deventer J. S. J. (2015) Role of carbonates in the chemical evolution of sodium carbonate-activated slag binders. *Mater Struct* **48**, 517–529.

Cyr M., Idir R. and Poinot T. (2012) Properties of inorganic polymer (geopolymer) mortars made of glass cullet. *J Mater Sci* **47**, 2782–2797.

Lemesre L. (2021) Formulation et caractérisation de composites bas carbone à base de poudre de verre alcali-activée. PhD Thesis, Université Paul Sabatier - Toulouse III.

Liu Y., Shi C., Zhang Z. and Li N. (2019) An overview on the reuse of waste glasses in alkali-activated materials. *Resources, Conservation and Recycling* **144**, 297–309.

McMillan P. (1984) Structural Studies of Silicate Glasses and Melts-Applications and Limitations of Raman Spectroscopy. *American Mineralogist - AMER MINERAL* **69**, 622–644.

Rivera J. F., Cuarán-Cuarán Z. I., Vanegas-Bonilla N. and Mejía de Gutiérrez R. (2018) Novel use of waste glass powder: Production of geopolymeric tiles. *Advanced Powder Technology* **29**, 3448–3454.

Vafaei M. and Allahverdi A. (2017) High strength geopolymer binder based on waste-glass powder. *Advanced Powder Technology* **28**, 215–222.

The 16th International Congress on the Chemistry of Cement 2023 (ICCC2023)
"Further Reduction of CO_2 -Emissions and Circularity in the Cement and Concrete Industry"
September 18–22, 2023, Bangkok, Thailand

Alkali-activation and chemical stabilization of incineration fly ash using slag for dangerous waste storage

T. Jalloux[1,2*], S. Meille[1], E. Prud'homme[1] and J-Y. Richard[2]

[1] *Univ Lyon, INSA Lyon, UCBL, CNRS, MATEIS UMR5510, F-69621 Villeurbanne, France*
[2] *SARPI MINERAL SOLUTIONS (groupe VEOLIA), 3 Allée Toscane, 69800 Saint-Priest, France*

ABSTRACT

The process of solidification and stabilization of Municipal Solid Waste Incinerator Fly Ash (MSWIFA) in dangerous waste landfills usually involves mixing the solid waste with cementitious materials. However, due to environmental concerns, this study explores the possibility of using alkali-activation without any cement as a way of solidifying, chemically stabilizing and reducing the solubility of the stored wastes. In this work, the MSWIFA's microstructure and chemical composition have been analysed and mixed in high mass ratio (> 50% of waste in the total wet mix) with Ground Granulated Blast Furnace Slag (GGBFS), NaOH, sodium silicate and water. Samples were casted at room temperature and cured at 20°C and 80 % RH for periods of time ranging from 24 h to 91 days. The influence of the concentration in NaOH and sodium silicate on the mechanisms of alkali-activation has been investigated using XRD and measurement of the cold crushing strength. The leaching behaviour of the solid samples, as well as the mechanisms of stabilization of salts, have been studied using soluble fraction measurements of the leachate. This study demonstrates the possibility of using alkali-activation to mechanically and chemically stabilized MSWIFA, validating the normative criteria for dangerous waste storage in France, with cold crushing strength up to 5.8 MPa after 91 days and less than 10 % soluble fraction.

KEYWORDS: *Alkali-activation, waste, incineration, stabilization, leaching*

1. Introduction

The incineration of municipal solid waste has been the preferred way of reducing their volume for the past decades in France. Those incinerators generate dangerous materials in the form of Municipal Solid Waste Fly Ash (MSWIFA). Tong and Hu (2022) explain that those ashes are collected via electrochemical and bag filters and treated by addition of calcium oxide or sodium bicarbonate to reduce acidity and airborne emission. Due to the presence of heavy metals and soluble salts, this powdery mix needs to be solidified, stabilized and stored in hazardous waste landfills to prevent leaching in the environment. According to Ren et al (2022) the process of solidification and stabilisation is accomplished by mixing the solid waste with cement, Ground Granulated Blast Furnace Slag (GGBFS) and water. This process was developed in the 90s to reduce the potential hazards in waste landfills, but due to environmental concerns about the carbon emissions related to cement production and lower availabilities in raw materials, the development of a new process of stabilisation and solidification like alkali-activation is showing more and more interests. The solidification happening at low temperature is obtained by mixing an aluminosilicate rich material and an alkaline activator. This process is known to give mechanical properties close to those of cementitious materials with a smaller carbon footprint. Lancellotti et al. (2010), Liu et al (2016) and Krausova Rambure (2014) showed that alkali activation can have a positive impact on salt storage and on MSWIFA stabilization, keeping mechanical strength higher than required by the regulation on dangerous waste storage ("Annèxe I : Critère d'admission En Installation de Stockage de Déchets Dangereux,"). However, those studies are focused on waste recycling and thus neither of them can directly be used in the domain of waste storage due to way too small amounts of waste materials in the mix (< 40 wt%). That is why this study will be focused on raw material wet mixes with around 50 %wt. of MSWIFA.

2. Materials and methods

The MSWIFA selected for this study comes from Neovaly incinerator in Lyon's agglomeration and the GGBFS is produced and commercialised by ECOCEM, France. The activator solution is prepared with 97 % purity NaOH in the form of pellets and a 1.5 g.mL^{-1} solution of sodium silicate with a molar ratio Si/Na of 1.1, both from Fisher Scientific.

The samples' synthesis starts with the preparation of three activator solutions with three different concentrations in Na (4, 6 and 8 mol.L^{-1}): NaOH pellets, sodium silicate and deionized water are mixed in a Teflon beaker following the compositions reported in Table 1. This solution is sealed and left to cool for 24 h. After that period of time, dry materials are weighed and dry mixed in a stand mixer for a minute after which the solution is added all at once and mixed for 2 minutes. The paste is then quickly poured in lubricated cylindrical moulds with a diameter of 2 cm and height of 4 cm or a diameter of 4 cm and height of 8 cm depending of the planned tests. Those moulds are sealed with a plastic wrap and cured 24 h before demoulding. The curing continues in a controlled chamber at 20°C and 80 % RH for 7, 28 or 91 days.

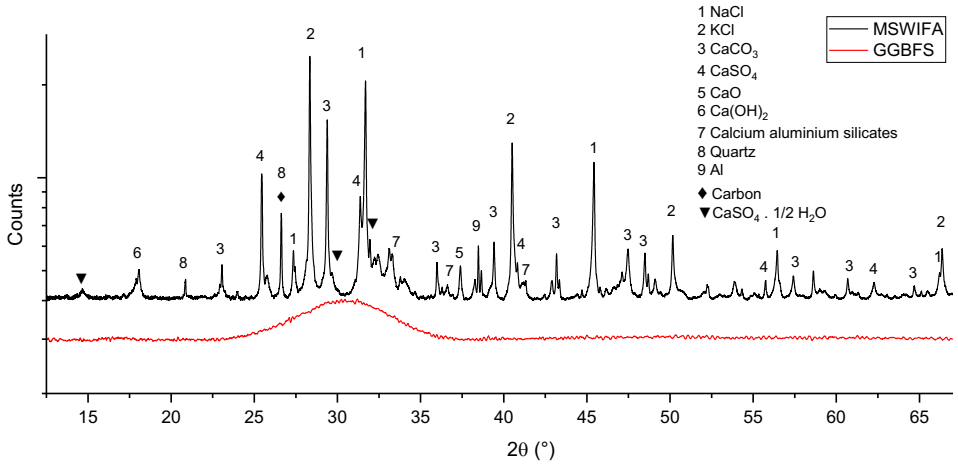


Figure 1: XRD diagrams of MSWIFA (black) and the GGBFS (red)

XRD characterisation

Materials were ground in an agate mortar and dried in a desiccator for 7 days before analysis. Analysis were performed with a Bruker-AXS D8 Advance with Cu Kα radiation (λKα = 1,54056 Å) from 12° to 70°.

Cold Crushing Strength

CCS is performed on cylindrical samples with a diameter of 2 cm and height of 4 cm after 7, 28 and 91 days of cure. The compression press is a ZwickRoell 1195 equipped with a 5 kN sensor. The crosshead speed is 0.5 mm/min. The lower limit to consider the waste solidified is fixed at 1 MPa ("Annèxe I : Critère d'admission En Installation de Stockage de Déchets Dangereux,").

Soluble fraction

Soluble fraction is determined following NF EN 12457-2 ("NF EN 12457-2 : Lixiviation - Essai de Conformité Pour Lixiviation Des Déchets Fragmentés et Des Boues,"). Cylindrical samples of diameter of 4 cm and height of 8 cm are suspended in deionized water with a mass ratio L/S of 10/1 for 24 h with continuous agitation. The water is then vacuum filtered through a 0.45 µm pore diameter membrane and dried in a 110°C oven as well as the sample. The upper limit to get stored in dangerous waste landfills is fixed at 10 % ("Annèxe I : Critère d'admission En Installation de Stockage de Déchets Dangereux,").

Apparent density

The apparent density refers to the ratio of the mass and the volume of the test specimen. The volume is that occupied by the sample, including hollow spaces. It is evaluated on cylindrical samples dried for 24h at 110°C after 91 days of curing. The mass is measured using a 0.001 g precision scale and volume is calculated by measuring height and diameter of the samples using a calliper. Densities in Table 1 are mean values obtained on 3 specimens for each mix reference.

Table 1: Mix compositions of the samples in weight percent and apparent density

Mix references	MSWIFA (%)	GGBFS (%)	NaOH (%)	Na_2SiO_3 (%)	H_2O (%)	Density (kg/m^3)
CAL4M	52,14	13,04	3,20	8,00	23,62	1113
CAL6M	49,77	12,44	4,73	11,82	21,23	1070
CAL8M	47,43	11,86	6,23	15,56	18,92	1010

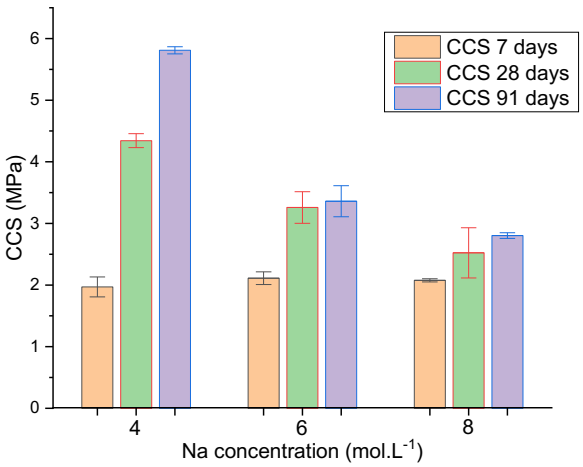


Figure 2: CCS values of samples after 7, 28 and 91 days of curing as a function of Na concentration

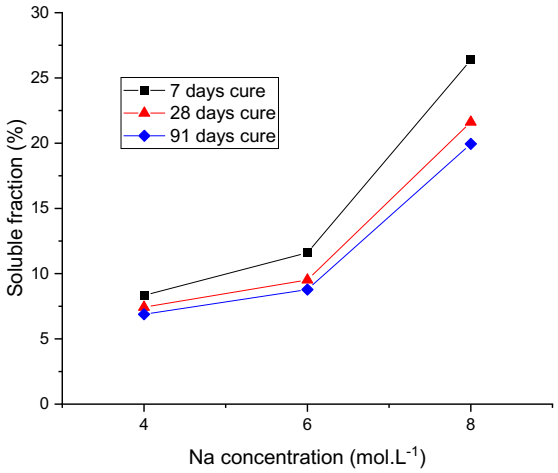


Figure 3: Soluble fraction of samples cured for 7, 28 and 91 days as a function of Na concentration

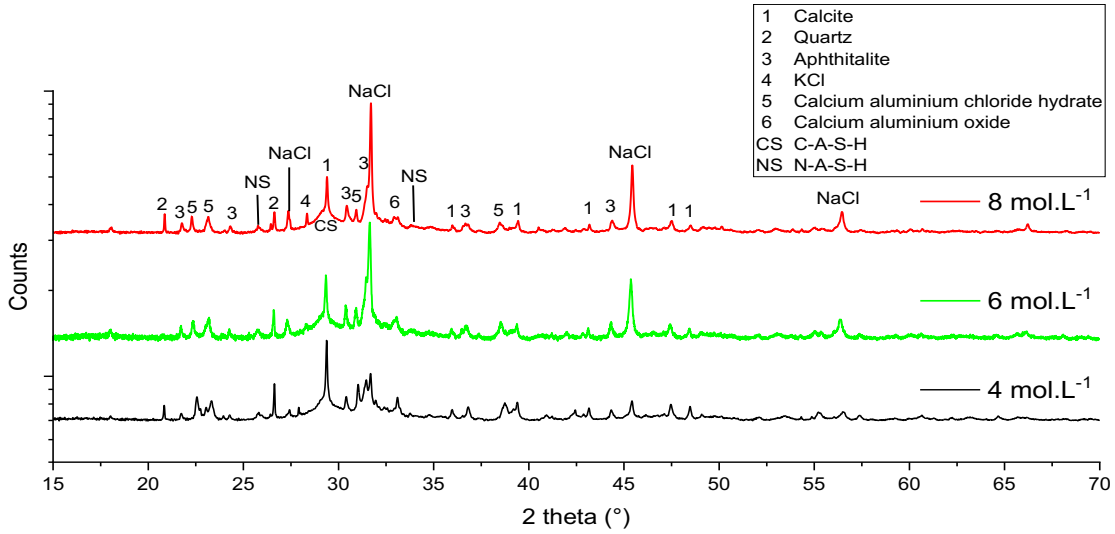


Figure 4: XRD patterns of CAL4M (black), CAL6M (green) and CAL8M (red) after 91 days of cure

3. Results

The MSWIFA studied has a soluble fraction of 29.8 %. XRD pattern of MSWIFA (see Figure 1) shows that it is mainly composed of NaCl and KCl salts which are responsible of the soluble fraction of this waste. The first observation that could be done on the samples studied in this research is the behaviour of the paste while casting in the moulds. In the first 5 minutes after the addition of the activator a dihydrogen release occurred in all pastes. This release made the paste bubbly and foamy. Increase of this gas release was observed with higher concentration of Na, as the paste was getting out of the moulds with the dihydrogen pressure. This increase in volume at early age lead to variations of density in the cured and dried samples as it can be noted with the decrease of density from 4 to 8 $mol.L^{-1}$ of Na. This release of dihydrogen seems linked to the aluminium content in the MSWIFA. This aluminium reacts with the water molecules in alkaline condition and generates dihydrogen.

Regarding mechanical properties, for each concentration of Na, an increase in CCS can be observed in relation to time of curing (Figure 2). This is obviously due to the solidification process of alkali activated slag which takes more time than cement to obtain their final mechanical properties. From 28 to 91 days of curing, CCS decreases with the increase in concentration of Na. This decrease can be partly explained by the lower densities observed at high concentration of Na. At 28 days CCS is rather constant no matter the Na concentration. As the 8M samples is more porous that the other samples, this implies that the matrix at high concentration of Na, is stronger than at lower concentration. This could mean that the reaction products are different or that the reaction is more advanced with higher concentration of Na. In regard to the regulation for dangerous waste storage in France, all mixes presented in this study have CCS values higher than 1 MPa after 7 days of cure and thus validate the mechanical criteria.

XRD patterns for the different mixes after 91 days of cure (Figure 4) does not show clear differences in the reaction products at different concentration in Na. However, it shows a clear increase in intensity of NaCl peaks with Na concentration. At 4 $mol.L^{-1}$ concentration NaCl and KCl are no longer the dominant species in the mix, this means the ions are probably included in the matrix.

In terms of chemical stabilisation, a clear increase in soluble fraction with the Na concentration can be observed on Figure 3, in good coherence with XRD measurements. Increasing curing time reduces soluble fraction. This improvement in stabilisation is directly linked to the development of the reaction products in the matrix. However, mechanical properties obtained with a Na concentration of 8 $mol.L^{-1}$ and 91 days of cure may be better than any 7 days of curing one, with a lower concentration, but the soluble fraction is lower at lower concentrations, when the porosity is the lowest. Higher porosity leads to a larger contact area with the extraction liquid and increases the diffusion speed. The limit of soluble fraction for admission in dangerous waste landfills is fixed at 10 % and should be obtained before 91 days. Only the mixes activated with a concentration in Na of 4 and 6 $mol.L^{-1}$ could validate this criterion.

Conclusion

Alkali-activation of MSWIFA with GGBFS can be a valid replacement method for storing dangerous wastes in landfills. Even though the mixes studied here have higher mass fraction of MSWIFA than those studied in the literature, they are able to validate criteria for dangerous waste storage. CCS values can go as high as 5.8 MPa and soluble fraction as low as 7 % after 91 days of cure. The GGBFS matrix enables the storage of NaCl and KCl at low concentration in Na. High concentration of Na in the activator has a negative impact on the mechanical and stabilisation properties of the mix as it increases the porosity of the material. In regard to the importance of the porosity in the chemical stabilisation. Improvements on the understanding of the triggering mechanisms of dihydrogen release has to be done.

References

"Annèxe I : Critère d'admission En Installation de Stockage de Déchets Dangereux." *Journal Officiel de La République Française*, 6758–60.

Krausova Rambure, Katerina. 2014. "Vers de Nouvelles Matrices Minérales Pour l'immobilisation et La Valorisation Des Déchets Ultimes de l'incinération Des Déchets Ménagers." thèse soutenue à l'Université Paris Est. https://tel.archives-ouvertes.fr/tel-00975213.

Lancellotti, Isabella, Elie Kamseu, Marco Michelazzi, Luisa Barbieri, Anna Corradi, and Cristina Leonelli. 2010. "Chemical Stability of Geopolymers Containing Municipal Solid Waste Incinerator Fly Ash." *Waste Management* 30 (4): 673–79. https://doi.org/10.1016/j.wasman.2009.09.032.

Liu, Yiquan, Weiping Zhu, and En Hua Yang. 2016. "Alkali-Activated Ground Granulated Blast-Furnace Slag Incorporating Incinerator Fly Ash as a Potential Binder." *Construction and Building Materials* 112 (June): 1005–12. https://doi.org/10.1016/J.CONBUILDMAT.2016.02.153.

Ren, Pengfei, Kim Hung Mo, and Tung-Chai Ling. 2022. *Stabilization/Solidification of Municipal Solid Waste Incineration Fly Ash*. *Low Carbon Stabilization and Solidification of Hazardous Wastes*. INC. https://doi.org/10.1016/b978-0-12-824004-5.00030-x.

Tong, Lizhi, and Qing Hu. 2022. *Physicochemical Properties of Municipal Solid Waste Incineration Fly Ash*. *Low Carbon Stabilization and Solidification of Hazardous Wastes*. INC. https://doi.org/10.1016/b978-0-12-824004-5.00011-6.

The 16th International Congress on the Chemistry of Cement 2023 (ICCC2023)
"Further Reduction of CO_2 -Emissions and Circularity in the Cement and Concrete Industry"
September 18–22, 2023, Bangkok, Thailand

Impact of calcination technology on the properties of a low kaolinite calcined clay

C.P. Rodriguez[1*], C.A. Orozco[2], and A.C. Gómez[3]

[1] *Cementos Argos, Medellín, Colombia*
Email: crodriguro@argos.com.co
[2] *Cementos Argos, Medellín, Colombia*
Email: corozco@argos.com.co
[3] *Cementos Argos, Medellín, Colombia*
Email: acgomezgo@argos.com.co

ABSTRACT

There are two most relevant processes for clay calcination: Rotary kiln and flash calciner. The two thermal processes differ significantly, affecting the mineralogy and morphology of the clay after calcination and, consequently, the properties of mortar and concrete. To better understand these effects, comparative calcination runs were carried out in a pilot scale (100-120 kg/h). A low kaolinitic content clay (40-50%) was used for comparison, and a cementitious system consisting of 20% calcined clay (CC) and 80% OPC cement was studied. The water demand was lower when the calcination temperature was increased. The lowest water demand of the calcined clay (CC) compared to OPC cement was found at 950°C (+6%) for the flash calciner and at 870°C (+3%) for the rotary kiln. The rheological results of the pastes magnified this difference; an increase in yield stress between 30 and 60% was measured. The strength activity indices were slightly higher for the clay calcined in a rotary kiln (+5%) than in a flash calciner. Conversely, energy release measured with the R3 – Protocol showed higher values for flash calcination. As for the physical properties, comparable specific surface areas - BET were obtained at similar temperature ranges, but very different morphologies were observed. Some spheres and rounded shapes were found in the flash-calcined clay, while the clay calcined in the rotary kiln exhibited regular platy shapes, which were not associated with any improvement in water demand.

KEYWORDS: *Calcined clays, rotary kiln, flash calciner, morphology*

1. Introduction

Many studies have shown that several factors including temperature, heating rate, time, and cooling rate, can affect the dehydroxylation process of clay minerals, which is necessary to produce calcined clays for the cement or ready-mix industry (RMX). There is some disagreement among scientists regarding the optimal calcination temperature and heating time with suggested ranges including 1-12 hours and 600-850 °C (Rashad, 2013). The most common clay calcination processes are rotary kiln and flash calciner. The rotary kiln provides flexibility in the feed size and moisture content of the clays, whereas flash calcination has quick responses to temperature changes and a lower chance of undesirable solid-solid reactions. Additionally, the differences in temperature between the gas and solids are between 100 to 200°C in the rotary kiln, while in a flash calciner, the differences are above 200°C (Hanein et al., 2022), which can make it challenging to determine the most appropriate calcination method to use. Regarding the properties of calcined clay, He et al. (1995) found that the pozzolanic activity of six standard clays (kaolinite, illite, Na and Ca-Montmorillonite, mixed-layer montmorillonite/illite, and sepiolite) was related to the burning temperature. Finally, the purpose of this paper is to compare the performance of low kaolinitic content clay after it has been calcined in a rotary kiln and flash calciner. The goal is to identify the pros and cons of each firing technology for calcined clays based on practical experiences.

2. Materials and Methods

2.1 Characterization of materials

A poor kaolinite content clay was chosen for the tests. The chemical composition was determined by using X-Ray Fluorescence (XRF) as shown in Table 1 for raw and calcined clays. Kaolinite content (39-42%) was determined by Thermogravimetric analysis (TGA-DTA). In table 1 calcined clays are labelled according to the calcination technology, rotary kiln (RK) or flash calciner (FC), followed by the temperature of calcination. Using X-Ray Diffraction (XRD) kaolinite, quartz, anatase, gibbsite, and minerals from the mica group were found in the raw clay, whereas quartz, rutile, magnetite/maghemite were found in the calcined clays. Mullite were observed in both calcined clays from the rotary kiln but only in the 950°C from the flash calciner.

Table 1. XRF composition of raw and calcined clays

	Raw clay	RK 775°C	RK 870°C	FC 800°C	FC 950°C
LoI	10.8	0.7	0.0	1.0	0.0
SiO_2	51.3	56.6	55.4	59.2	60.5
Al_2O_3	23.4	25.9	26.2	25.0	24.7
Fe_2O_3	11.2	12.9	13.6	11.0	10.9
MgO	0.4	0.4	0.5	0.5	0.5
Na_2O	0.3	0.3	0.4	0.3	0.3
K_2O	1.1	1.2	1.3	1.3	1.4

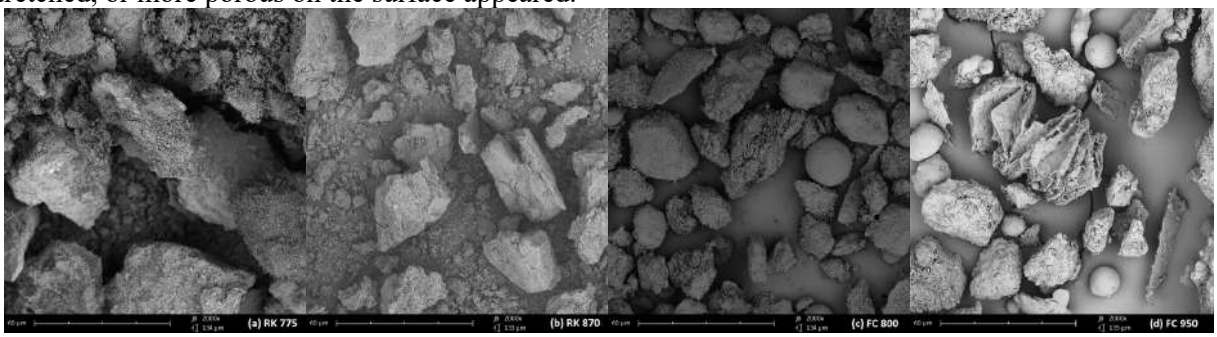
2.2 Clay calcination and grinding

For the rotary kiln (0.9 m diameter x 15.2 long), the clay was air-dried and it was screened at 0.6 mm to prevent any blockages. The kiln was set at 0.5 rpm and fed at 110 kg/hr, resulting in a kiln residence time of 4 hours. A small amount of water (3.78 lph) was sprayed into the discharge hood, and N_2 was injected into the cooler to promote color control. Temperatures of calcination were set and measured in the kiln hood. For the flash calciner, the raw clay was dried and crushed to obtain >95% passing 400 microns. Then, the material was fed at a rate of 100 kg/h with a retention time of 1-1.5 sec. The calciner suspension air was preheated to 800 °C by an electric hot gas generator. Thereafter, partially by stages, gas firing was used to reach the target temperature at the top of the cyclone. Then calcined clay went into a reduction zone for color conversion and cooled in two parallel gas suspension cyclones. For both trials, natural gas was used, and calcined clay samples were ground in a ball mill with classifier, aiming for a fineness of 25-30% retained on mesh 325, which meets the ASTM C618 standard for class N pozzolans.

3. Results and discussion

3.1 Clay calcination-physical qualities

Scanning Electron Microscopy (SEM) images were taken of the clays after calcination (Figure 1). Calcined clays (a,b) from the rotary kiln clay show disaggregated coarse particles covered by small ones, with no particular shape whereas on the flash calcined clays rounded-shape particles like spheres appeared. The particles calcined at the highest temperature, 870°C in the rotary kiln and 950°C in the flash calciner, suggest discreet fusion spots as the shape of some particles were seem inter-bounded or stretched, or more porous on the surface appeared.



(a) RK 775°C, (b) RK 870°C, (c) FC 800°C, (d) FC 950°C

Figure 1. SEM images of calcined clays

Physical features of the ground clays such as BET specific surface area (SSA), Blaine, and weight retained on mesh 325 or 45 microns are presented in table 2. Only the RK 775°C was finer than expected. SSA and Blaine results show a significant decrease compared to the raw clay as the temperature of calcination was increased in each thermal regime.

Table 2. Physical characteristics of the calcined clays

	Raw clay	RK 775°C	RK 870°C	FC 800°C	FC 950°C
BET-SSA (m^2/g)	34	11	9	19	5
R/325 (%)		21	30.3	30.9	32.9
Blaine (m^2/kg)		724	579	935	458

3.2 R3 and compressive strength

Calcined clays reactivity were evaluated using the R3 isothermal calorimetry procedure according to the ASTM C1897 (ASTM, 2021). Table 3 presents the cumulative heat released of the four calcined clays for 168 hours. Cumulative heat values ranged from 237 to 411 J/g of calcined clay which are comparable to others reports (Ramanathan et al., 2020). The highest heat releases were found at the lowest calcination temperatures (775°C and 800°C), with the FC 800°C showing the highest release. One interesting feature is that the heat values of the FC 950°C was similar to the FC 775°C, indicating that higher calcination temperatures were achieved in the latter, consistently with the presence of mullite.
Compressive strengths of 20% calcined clay and 80% Ordinary Portland Cement (Type I/II) were assessed in standard mortars and the strength activity index (SAI) is calculated following the ASTM C618 (Astm, 2019). Similarly, mortar cubes were evaluated by fixing the water-to-binder ratio (w/b) at 0.485 using a commercial high water reducer admixture (HWRA), and both results are presented in Table 3.
As for water demand, the clays calcined in the flash showed higher water demand than those calcined in the rotary kiln, indicating that no benefits could be obtained from the rounded particles seen after calcination. More correspondence is found with the BET-SSA as the FC 800°C has the highest specific surface area and water demand, 19 m2/g and 110% respectively.

Table 3. R3 and Compressive strength

						Fixed water (0.485)		
	R3 (J/g)	w/b	Water demand (%)	SAI 7d (%)	SAI 28d (%)	HWRA (%)	SAI 7d (%)	SAI 28d (%)
Cem I/II - 20% RK 775°C	287	0.500	103%	76%	94%	0.08	79%	92%
Cem I/II - 20% RK 870°C	237	0.498	103%	63%	87%	0.07	67%	86%
Cem I-II - 20% FC 800°C	411	0.533	110%	79%	87%	0.13	83%	79%
Cem I-II - 20% FC 950°C	292	0.515	106%	76%	88%	0.09	78%	87%

Compressive strength-wise, when water was adjusted according to each calcined clay, acceptable strength development was derived for both calcination conditions. The lowest temperature evaluated (775 and 800°C) showed the best compressive results in both calcination scenarios. Using the HRWA or fixing the water in the cementitious system caused only a modest (+2-5%) improvement in the compressive strength for both types of calcined clay at 7 days.

3.3 Rheology

Cement IL and 20% of each calcined clay were stirred with a w/b of 0.4 and the HRWR dosage that targeted a minislump flow of 75 +/- 5 mm, then samples were poured into a Kinexus rheometer using a plate-plate geometry. Bingham model was used to determine yield stress and viscosity. Table 4 presents the HRWR admixture dosage, flow and the yield stress. Lower calcination temperatures resulted in clays with higher HWRA (+38-254%) requirements, which is consistent with mortar evaluation. Even targeting

same flow, higher yield stress (+136-156%) were found with calcined clays. This finding requires further evaluation in concrete applications to determine wheather it offers benefits or challengues.

Table 4. R3 and Compressive strength

	HRWR (%)	Flow (mm)	Yield stress (Pa)	Rel. yield stress (%)	Rel. HRWR (%)
IL Cement	0.065%	78	29		
Cem IL - 20% RK 775°C	0.16%	73	45	156%	146%
Cem IL - 20% RK 870°C	0.13%	76	44	153%	92%
Cem IL - 20% FC 800°C	0.23%	77	39	136%	254%
Cem IL - 20% FC 950°C	0.09%	74	43	149%	38%

3. Conclusions

- A flash calciner and a rotary kiln can produce calcined clay with similar qualities, but the comparison involves technological challenges, such as confidence in the actual temperature of the material. Although the flash calciner promotes rounded particles, no improvement in rheology or water demand was observed.
- During calcination, the proper balance between compressive strength and water requirement should be sought. The best compressive strengths are found at lower calcination temperatures when water demand is high, but control of water is also needed to improve compressive strengths and to use the calcined clay technology in concrete applications.
- Water demand and rheology are complementary metrics for understanding the performance of calcined clay in the early-fresh state. Both responses are consistent with the specific surface area of the calcined clay, which can also be seen as a result of the calcination temperature. Measurements of compressive strength with fixed water and R3 show consistency in results.

References

Astm. (2019). Standard Specification for Coal Fly Ash and Raw or Calcined Natural Pozzolan for Use. *Annual Book of ASTM Standards*, *C*, 3–6. https://doi.org/10.1520/C0618-19.2

ASTM. (2021). *C 1897-20 Standard Test Methods for Measuring the Reactivity of Supplementary Cementitious Materials by Isothermal Calorimetry and Bound Water Measurements*. *04*, 3–7. https://doi.org/10.1520/C1897-20.2

Hanein, T., Thienel, K. C., Zunino, F., Marsh, A. T. M., Maier, M., Wang, B., Canut, M., Juenger, M. C. G., Ben Haha, M., Avet, F., Parashar, A., Al-Jaberi, L. A., Almenares-Reyes, R. S., Alujas-Diaz, A., Scrivener, K. L., Bernal, S. A., Provis, J. L., Sui, T., Bishnoi, S., & Martirena-Hernández, F. (2022). Clay calcination technology: state-of-the-art review by the RILEM TC 282-CCL. *Materials and Structures/Materiaux et Constructions*, *55*(1). https://doi.org/10.1617/s11527-021-01807-6

He, C., Osbaeck, B., & Makovicky, E. (1995). Pozzolanic reactions of six principal clay minerals: Activation, reactivity assessments and technological effects. *Cement and Concrete Research*, *25*(8), 1691–1702. https://doi.org/10.1016/0008-8846(95)00165-4

Ramanathan, S., Kasaniya, M., Tuen, M., Thomas, M. D. A., & Suraneni, P. (2020). Linking reactivity test outputs to properties of cementitious pastes made with supplementary cementitious materials. *Cement and Concrete Composites*, *114*(July). https://doi.org/10.1016/j.cemconcomp.2020.103742

Rashad, A. M. (2013). Metakaolin as cementitious material: History, scours, production and composition-A comprehensive overview. *Construction and Building Materials*, *41*, 303–318. https://doi.org/10.1016/j.conbuildmat.2012.12.001

The 16th International Congress on the Chemistry of Cement 2023 (ICCC2023)
"Further Reduction of CO_2 -Emissions and Circularity in the Cement and Concrete Industry"
September 18–22, 2023, Bangkok, Thailand

Fresh and hardened state properties of ternary slag cement concrete with high filler content

M. Cruickshank[1,2*], E. Myrtja[1,2], R. Alfani[1,2], L. Frouin[1] and M. Chaouche[2,3]

[1] *ECOCEM Materials, Paris, France*
[2] *MC²E, LMPS-ECOCEM Common Laboratory, Gif-sur-Yvette, France*
[3] *Université Paris-Saclay, CentraleSupélec, ENS Paris-Saclay, CNRS, Laboratoire de Mécanique Paris-Saclay, Gif-sur-Yvette, France*
mcruickshank@ecocem.ie, emyrtja@ecocem.ie, ralfani@ecocem.ie, lau.frouin@gmail.com, mohend.chaouche@ens-paris-saclay.fr*

ABSTRACT
The cement and concrete industries are facing an urgent need to reduce their CO_2 emissions. An emerging strategy is to use ternary binders combining Portland cement, limestone filler and supplementary cementitious materials. The recent European CEM VI allows for up to 20% limestone filler, which is insufficient for the industries to reach their sustainability targets. In this study, a ternary binder of Portland cement, ground granulated blast furnace slag, and limestone filler was investigated at a filler content significantly higher than what is currently permitted in EN 197.
The ternary blended cement was investigated at the paste and concrete level, at low water content. The rheological properties at the paste level were evaluated via rotational rheometry and the cement showed exceptional suitability for high filler – low water concrete applications. Further, at the concrete level, satisfactory workability was achieved without requiring a significant increase in cement content (300 kg/m^3). The concrete also showed satisfactory early strength and high strength development resulting in a binder intensity much lower than what is typically observed at industrial scale.

KEYWORDS: *Limestone filler, GGBS, rheology, low-carbon, ternary blended cements*

1. Introduction

In the coming years, the global demand for cement and concrete is expected to increase, especially in the developing world (Scrivener et al., 2018). This massive need for cement and concrete coincides with increasing attention being paid to the environmental impacts of human activities. Given the significant contribution of the production of cement and concrete to overall anthropogenic CO_2 emissions, it is tempting to suggest that cement and concrete production be phased out and replaced with more sustainable alternatives (Habert et al., 2020). However, when the situation is examined more closely, it becomes clear that this is not a feasible option. The world relies and will continue to rely on concrete for the foreseeable future. Thus, to drastically reduce CO_2 emissions, changes must be sought in the way that cement and concrete are formulated.
One of the proposed strategies to drastically reduce CO_2 emissions at the concrete level is the production of concrete with low binder intensity and low CO_2 intensity (John et al., 2018). Binder intensity is a measure of the amount of reactive binder per cubic metre of concrete, divided by its compressive strength at 28 days. CO_2 intensity is a measure of the CO_2 emitted per cubic metre of concrete, divided by its compressive strength at 28 days (Damineli et al., 2010). To achieve low binder intensity for conventional concrete, mix designs are formulated with high filler content (typically limestone) and low water content. Such concretes have been therefore given the name high filler low water (HFLW) concretes.
The production of HFLW concrete requires a meaningful reduction in the water-powder (reactive binder + filler) ratio which necessitates more attention being paid to the concrete mix design like the challenges associated with formulating high-performance concrete (HPC) or ultra-high-performance concrete (UHPC). However, whereas increased binder contents are tolerated for HPC or UHPC, the conventional

ready-mix concrete market is unlikely to tolerate an increase in cement content for economic reasons. It is therefore crucial that HFLW concrete present acceptable workability, and especially viscosity, without an increase in cement content.
A handful of studies have shown that it is possible to formulate concrete with binder and CO_2 intensities much lower than what is currently achieved at industrial scale (for example: (Damineli, 2013; de Grazia, 2018; Mueller et al., 2017; Neufert et al., 2016; Vogt, 2010)). However, so far, these concretes have largely remained in the lab. One reason for this is that the amount of filler used in the cement formulations exceeds what is permitted in most, if not all, cement standards. Further, questions remain regarding the fresh state properties (primarily viscosity), early strength development, and durability. This paper aims to address some of these concerns with a ternary blended cement prepared with CEM I (20%), GGBS (30%), and limestone filler (50%) employed at paste volumes significantly lower than in previous studies on HFLW concrete prepared using ternary slag blended cements. This blended cement is examined at the paste level via rotational rheometry and at the concrete level via typical fresh and hardened state properties.

2. Materials and Methods

2.1 Materials

Binary blended cements (B) were prepared using 40% CEM I 52.5 R and 60% GGBS. Ternary blended cements (T) were prepared using 20% CEM I 52.5 R, 30% GGBS, and 50% limestone filler.
For concrete, crushed dolomitic limestone aggregates were used. All pastes and concretes were prepared using the same high-range water reducing commercial superplasticizer.

2.2 Rotational Rheometry of Cement Pastes

Rheological characterization at the paste scale was carried out using an AR2000ex rheometer made by TA Instruments. The rheometer was equipped with a cylindrical cup and vane geometry. All measurements were taken at a constant temperature of 20°C.
The testing cycle was initiated with the geometry rotated at a shear rate of 30 s^{-1} for 30s, a stabilization phase during which no measurements were taken. Next, the pastes were subjected to two cycles of shear stress evaluation where the shear rate was increased from 0.1 to 150 s^{-1} and then decreased from 150 to 0.1 s^{-1}. The shear rate was varied logarithmically. The apparent viscosity at a shear rate of 150 s^{-1} was adopted as the viscosity criteria, similar to the procedure adopted in (Damineli et al., 2016).

2.3 Concrete – Fresh and Hardened State Properties

Concrete was prepared according to the mix design shown in Table 1. The ternary blended cement was used at 300 kg/m^3 and a water-to-powder ratio of 0.32. This represents a significant reduction in paste volume compared to previous high filler – low water concrete prepared with ternary slag cements prepared by Neufert et al (Neufert et al., 2016) (390 kg/m^3, water-powder ratio of 0.35).
In the fresh state, the concrete was tested both for slump (according to NF EN 12350-2:2019) and flow time (according to the French standard XP P18-469). Flow time is measured by filling the Abrams cone with the larger end facing upward. The cone is lifted and the time is recorded for the concrete to completely exit the cone. This is considered a proxy measurement for viscosity. 150mm concrete cubes were prepared to test compressive strength at 1, 2, 7, and 28 days. Further, five 110x220mm cylinders were prepared to test the elastic modulus at 28 days according to NF EN 12390-13. All specimens were demoulded after 24 hours and submerged in water at 20°C prior to testing.

Table 1 – High filler – low water concrete mix design

Mix Component	[kg/m^3]
CEM I 52.5 R	60
GGBS	90
Limestone Filler	150
Fine Aggregate	921
Coarse Aggregate	1106
Absorbed Water	22
Effective Water	96
Total Water	118
Superplasticizer	3.75

3. Results and Discussion

3.1 Rotational Rheometry of Cement Pastes

Cements used at low water content and requiring high flowability employ the use of superplasticizers. Superplasticizers are often able to significantly reduce yield stress, but the paste can remain sticky and viscous due to the high solids fraction. Further, shear thickening behaviour can be problematic at low water-powder ratios, especially at low paste volumes where the distance between aggregates is decreased, increasing the shear rate experienced by the paste. Apparent viscosity of a paste at high shear rate can therefore act as a suitability indicator for a HFLW cement paste for use in concrete.

Figure 1 presents the deflocculation curves for the binary blended cement and the ternary blended cement. The apparent viscosity values at the highest tested superplasticizer dosage are indicated for each curve, approximating the minimum apparent viscosity achieved for each condition. The binary blend was evaluated at water-powder ratios of 0.26, 0.30, and 0.34. The ternary blended cement was evaluated only at a water-powder ratio of 0.24. The results show that the ternary blend, at a water-powder ratio of 0.24, demonstrates a lower apparent viscosity at high shear rate compared to the binary blend at all tested water-powder ratios. Thus, within the context of the materials evaluated here, the ternary blend is much better suited for HFLW concrete compared to the binary blend, with respect to workability. This provides an example for how the use of limestone fillers can be rheologically favourable, allowing for concrete mix designs with lower water contents and pastes volumes than are typically employed for more conventional cements.

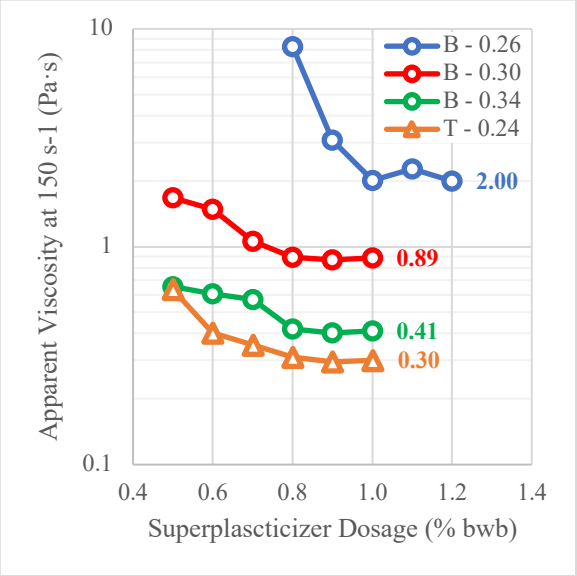


Figure 1 – Deflocculation curves for binary (B) and ternary blended (T) cements at different water-powder ratios

3.2 Concrete Prepared with a High Filler Ternary Blended Cement

Concrete was prepared using 300 kg/m^3 of the ternary blended cement, as outlined previously in Table 1. This value is lower than the average binder content used for ready-mix concrete in the European Union (ERMCO - European Ready Mixed Concrete Organization, 2019).

In the fresh state, the concrete had a slump of 210 mm, meeting the requirements for S4 according to NF EN 12350-2:2019 and a flow time of 8.5s according to XP P18-469. Thus, despite the low water content and low paste volume, the concrete was still highly workable as expected based on the rheological testing at the paste level. Importantly, the concrete did not demonstrate the sticky and honey-like consistency often observed for concrete prepared with superplasticizers at low water content.

Cubes were crushed for compressive strength testing at 1, 2, 7, and 28 days and the results are shown in Table 2. At 24 hours, the cubes reached 13.6 MPa, easily meeting the requirements for formwork removal for most worksites in France. At 28 days, the cube strength reached 66.8 MPa and the cylinder strength reached 60.8 MPa. These values result in a binder intensity of 2.5 (kg/m^3)/MPa when measured according to the cylinder strength. This binder intensity is half of the lower industrial limit estimated by Damineli (Damineli et al., 2010) for concrete reaching compressive strengths of 50 MPa or greater (5 (kg/m^3)/MPa). For modulus of elasticity, a value of 56.6 GPa was measured at 28 days, more than what is required considering the compressive strength.

Table 2 – Compressive strength development for HFLW concrete

Specimen Type	Age (Days)	Compressive Strength (MPa)
Cube	1	13.6
	2	19.5
	7	44.7
	28	66.8
Cylinder	28	60.8

4. Conclusion

High filler – low water concretes provide one pathway for the cement and concrete industries to significantly reduce CO_2 emissions. This paper presents an example of a high filler ternary blended slag-limestone cement which presents suitable rheological properties for use in concrete at a significantly lower water content than its filler-free binary counterpart. The rheological properties of the paste permit the formulation of a highly workable concrete suitable for ready-mix concrete applications without increasing the binder content, as is typically done for concretes with low water-powder ratios. The concrete reached a binder intensity of 2.5 kg/m^3 at 28 days, representing a significant improvement compared to concretes typically prepared in industrial settings.

5. References

Damineli, B. L. (2013). Conceitos para formulação de concretos com baixo consumo de ligantes: Controle reológico, empacotamento e dispersão de partículas. University of Sao Paulo.

Damineli, B. L., John, V. M., Lagerblad, B., & Pileggi, R. G. (2016). Viscosity prediction of cement-filler suspensions using interference model: A route for binder efficiency enhancement. Cement and Concrete Research, 84, 8–19. https://doi.org/10.1016/j.cemconres.2016.02.012

Damineli, B. L., Kemeid, F. M., Aguiar, P. S., & John, V. M. (2010). Measuring the eco-efficiency of cement use. Cement and Concrete Composites, 32(8), 555–562. https://doi.org/10.1016/j.cemconcomp.2010.07.009

de Grazia, M. T. (2018). Contribution to the understanding of fresh and hardened properties of low cement concrete. University of Ottawa, Canada.

ERMCO - European Ready Mixed Concrete Organization. (2019). Read-Mixed Concrete Industry Statistics—Year 2018. ERMCO - European Ready Mixed Concrete Organization.

Habert, G., Miller, S. A., John, V. M., Provis, J. L., Favier, A., Horvath, A., & Scrivener, K. L. (2020). Environmental impacts and decarbonization strategies in the cement and concrete industries. Nature Reviews Earth & Environment, 1(11), Article 11. https://doi.org/10.1038/s43017-020-0093-3

John, V. M., Damineli, B. L., Quattrone, M., & Pileggi, R. G. (2018). Fillers in cementitious materials—Experience, recent advances and future potential. Cement and Concrete Research, 114, 65–78. https://doi.org/10.1016/j.cemconres.2017.09.013

Mueller, H. S., Haist, M., Moffatt, J. S., & Vogel, M. (2017). Design, Material Properties and Structural Performance of Sustainable Concrete. Procedia Engineering, 171, 22–32. https://doi.org/10.1016/j.proeng.2017.01.306

Neufert, W., Reuken, I., Weber, G., Muller, C., Palm, S., Severins, K., Graubner, C.-A., Proske, T., & Rezvani, M. (2016). Erforschung des Dreistoffgemisches Klinker, Hüttensand und Kalksteinmehl mit dem Ziel der Absenkung des Klin-keranteils im Zement zur Verminderung der CO2-Emissionen in der Zementproduktion.

Scrivener, K. L., John, V. M., & Gartner, E. M. (2018). Eco-efficient cements: Potential economically viable solutions for a low-CO2 cement-based materials industry. Cement and Concrete Research, 114, 2–26. https://doi.org/10.1016/j.cemconres.2018.03.015

Vogt, C. (2010). Ultrafine particles in concrete—Influence of ultrafine particles on concrete properties and application to concrete mix design. Royal Institure of Technology, Stockholm, Sweden.

The 16th International Congress on the Chemistry of Cement 2023 (ICCC2023)
"Further Reduction of CO_2 -Emissions and Circularity in the Cement and Concrete Industry"
September 18–22, 2023, Bangkok, Thailand

LC^3 application in Non-structural Concrete

Narendra Kumar[1]*, Lupesh Dudi[2], Lav Singh[3], and Shashank Bishnoi[4]

[1]*Department of Civil Engineering, IIT Delhi, New Delhi, India*
Email: narendrkumar42@gmail.com
[2]*Department of Civil Engineering, IIT Delhi, New Delhi, India*
Email: lupeshdudi@gmail.com
[3]*Department of Civil Engineering, IIT Delhi, New Delhi, India*
Email: singh.lav1987@gmail.com
[4]*Department of Civil Engineering, IIT Delhi, New Delhi, India*
Email: bishnoi@iitd.ac.in

ABSTRACT

The conventional use of cement as a binder in construction activities contributes significantly to carbon dioxide emissions. To mitigate this environmental impact, reducing the clinker factor presents a viable solution. Non-structural applications offer an immediate opportunity for clinker factor reduction. This paper explores the suitability of using limestone calcined clay cement (LC^3) with clinker factors ranging from 0.5 to 0.3 in non-structural concrete applications. Specifically, the study investigates two applications: paver blocks (rectangular and I-shape) and low-strength concrete cast by semi-skilled workers for temporary structures. In the case of paver blocks, the compressive and tensile strength development of LC^3 concrete is compared with ordinary Portland cement (OPC) for clinker factors varying from 0.5 to 0.3. The results are analyzed based on strength requirements outlined in Indian standards for different categories. For the second application, the compressive strength development of LC^3 concrete is compared with portland pozzolanic cement (PPC). The study also includes a survey of semi-skilled masons who worked with LC^3, gathering their feedback to evaluate the ease of working with LC^3 compared to other cement types. This study provide insights for the practical implementation of LC^3 in non-structural applications.

KEYWORDS: ***Non-structural concrete, Mechanical strength, Limestone calcined clay cement (LC^3)***

1. Introduction

Concrete, being a cost-effective and versatile material, is widely used and forms the backbone of modern society's infrastructure. A key component of concrete is clinker, which is produced by heating raw materials like limestone and clay to extreme temperatures of around 1450℃. Unfortunately, this high-temperature process heavily relies on the burning of fossil fuels, leading to the emission of substantial amounts of carbon dioxide. In fact, approximately 8% of global carbon dioxide emissions are attributed to clinker production, making it a significant contributor to climate change. To address the environmental impact of clinker production, there is a growing need to reduce its carbon footprint. One promising solution is the adoption of limestone calcined clay cement (LC^3), which offers a low-clinker alternative bringing carbon emission down by 30% (Sharma et al. (2021)). LC^3 consists of clinker, calcined clay, limestone, and gypsum, and it has been demonstrated that LC^3 with a 50% clinker factor can perform equivalently to ordinary Portland cement in various applications (Parashar and Bishnoi (2021)).
While LC^3 has shown promise in structural applications, there is a significant portion of cement usage in non-structural applications, particularly in the unorganized sector where traditional manual concrete production methods are prevalent. These applications, such as paver blocks, sidewalks, and low-strength concrete for general purposes, often do not require the high mechanical strength typically associated with structural elements. This raises the possibility of further reducing the clinker factor for non-structural applications, thereby reducing the carbon footprint even more. Moreover, it is crucial to evaluate the performance of LC^3 in the unorganized sector, where manual concrete production methods without the aid of machinery are utilized. Understanding how LC^3 performs in these traditional practices and assessing its feasibility in such contexts will provide valuable insights for sustainable construction practices.

In this study, we aim to explore the non-structural applicability of LC^3 in two specific areas: paver blocks (including rectangular and I-shape designs) and low-strength concrete cast by semi-skilled laborers for general purposes. By investigating these applications, we can determine the potential for further reducing the clinker factor while maintaining satisfactory performance. Additionally, we will evaluate the usability and acceptance of LC^3 within the unorganized sector, considering the ease of use and practical aspects as reported by the laborers involved.

2. Materials and Methods

2.1 Materials

Two grades of ordinary Portland cement (OPC-1 and OPC-2) were obtained from the local market. Limestone calcined clay (LC^2) and fly ash (FA) were sourced from cement manufacturers and the National Thermal Power Corporation Limited near New Delhi, respectively. The chemical oxide composition of all raw materials is presented in Table 1. Natural coarse aggregates with sizes of 10mm and 20mm, and specific gravities of 2.68 and 2.81, respectively, were procured from around New Delhi. River sand, with a specific gravity of 2.62, was used as the fine aggregate. Blends of the raw powder materials were prepared in a laboratory ball mill through interblending.

Table 1. Oxides composition of raw materials.

	SiO_2 (%)	Fe_2O_3 (%)	Al_2O_3 (%)	CaO (%)	MgO (%)	SO_3 (%)	Na_2O (%)	K_2O (%)	TiO_2 (%)	LOI (%)	Sp. Gravity
OPC-1	19.44	6.17	4.78	62.33	1.27	2.02	0.15	0.50	0.92	1.76	3.20
OPC-2	19.98	5.04	4.66	61.87	1.42	3.41	0.10	0.45	0.63	1.92	3.21
LC^2	34.51	3.55	27.86	14.11	1.56	1.25	0.78	0.37	2.07	13.46	2.61
FA	52.99	8.38	27.50	1.56	1.26	0.54	0.00	1.20	2.93	1.06	2.33

2.2 Mix design

Paver blocks: For the casting of two type of paver blocks (rectangular and I-shape designs), the nominal mix design method was employed. The cement to sand to coarse aggregate ratio used was 1:3:4, with a water-to-binder ratio of 0.43. The maximum size of the coarse aggregate was limited to 10 mm. The clinker factor was varied from 50% to 30%. Two types of LC^3 were prepared, both using the same LC^2 but different OPC types. In the study, the nomenclature LC3-A-X was used, where A represents the OPC used (1 or 2), and X denotes the clinker factor in the blend. To mitigate the water demand resulting from the high clay content, a high-range water reducing superplasticizer was employed.

Concrete casting by semi-skilled masons: In this study, a comparison was made between LC^3 and Portland pozzolana cement (PPC), which is commonly used in the unorganized sector in India. LC^3 was prepared using a blend of 50% OPC-1 and 50% LC^2, while PPC was prepared using a blend of 70% OPC-1 and 30% FA. Two nominal mix designs were adopted, with cement to sand to coarse aggregate ratios of 1:1.5:3 and 1:2:2. Coarse aggregates of 10 mm and 20 mm were used in equal proportions. To understand the variation, 3 pair of masons were employed to perform casting. The water-to-binder ratio was not controlled, and masons were allowed to freely add water to achieve workable concrete using shovels and trowels. Subsequently, the prepared concrete was cast into 150 mm cubes for conducting compressive strength testing at both 7 and 28 days.

2.3 Methods

Paver blocks' compressive and splitting tensile strength: Mechanical properties for paver blocks were determined according to the IS 15658:2021 at 7 days and 28 days. For rectangular paver blocks only compressive strength was determined, while for T-shape both mechanical properties were determined.

Compressive Strength of cubes: Compressive strength of concrete cubes were determined at specified age as per IS 516:2021.

3. Results and Discussion

3.1 Compressive and Splitting tensile strength of Paver block

Analysis of the compressive strength development curves for rectangular and I-shape paver blocks revealed a decrease in strength as the clinker factor decreased. However, even at a clinker factor as low as 0.3, rectangular paver blocks were found to be suitable for use in non-traffic areas, while I-shape paver blocks could be used in light-traffic areas (refer to Figure 1). On the other hand, there was no clear trend observed in the splitting tensile strength with respect to the clinker factor. However, on average, the splitting tensile strength increased as the clinker factor increased from 0.3 to 0.5. The reduction in strength as the clinker factor decreases can be attributed to the limited production of portlandite due to the reduced amount of clinker, which subsequently limits the hydration reaction of the calcined clay. The results obtained with both types of OPC exhibited similar trends across the investigated range of clinker factors, indicating that LC^2 is compatible with the OPC available in the market and can be directly blended at the construction site.

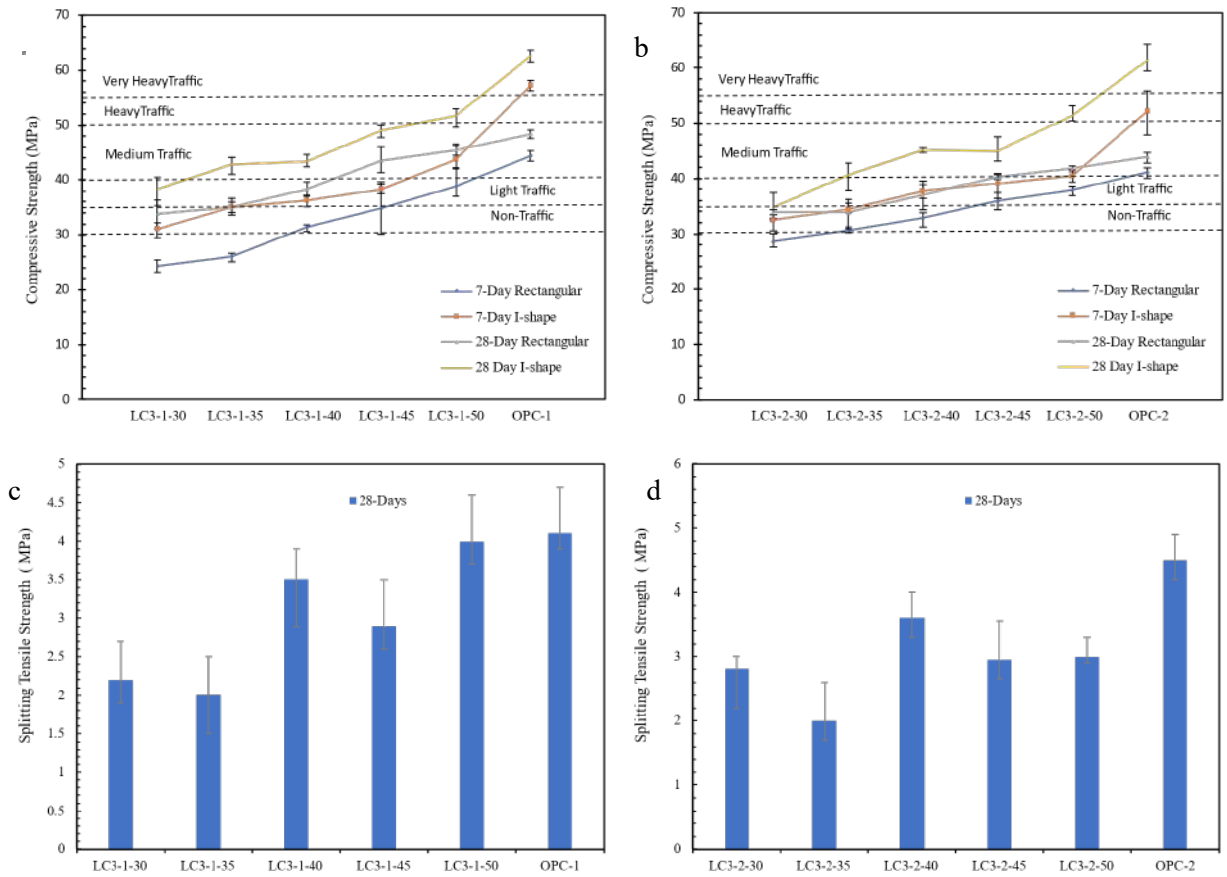


Figure 1. a) & b) compressive strength of paver blocks made with OPC-1 and OPC-2, respectivey, c) & d) splitting tensile strength of I-shape paver blocks made with OPC-1 and OPC-2 respectively.

3.2 Compressive strength of cube cast by semi-skilled masons

The results of the compressive strength tests on cubes cast by masons revealed significant variations in strength among different masons, as indicated in Table 2. Interestingly, this variation was observed to be similar for both LC^3 and PPC. Another noteworthy observation was the higher strength achieved at 7 days for LC^3, which can be attributed to the participation of calcined clay in the hydration reaction from an early age, in contrast to fly ash. However, by the age of 28 days, in some cases, PPC slightly outperformed LC^3, likely due to the higher water content added to achieve similar workability in LC^3 mixes. Nonetheless, for lower slump values of LC^3, the compressive strength obtained was comparable or slightly better than that of PPC.

A general survey related to working with these cements was taken from masons (see Figure 2.). Masons reported the following points:

- Clear difference between the cement colurs (LC^3 prepared was without colour control)
- No difference in the trovel and shovels movement during concrete poduction and application process

- Stiffer LC^3 mixes as compared to PPC mixes.

Table 2. Compressive strength of LC^3 and PPC, concrete prepared by masons.

Masons Group	Mix Design	Slmp (mm)		7 -Days Compressive Strength (MPa)		28 -Days Compressive Strength (MPa)	
		PPC	LC3	PPC	LC3	PPC	LC3
A	1:2:2	140	165	8.4	7.94	13.98	12.57
B	1:2:2	180	130	12.64	13.2	20.50	17.95
C	1:2:2	120	190	9.34	8.86	15.84	13.74
A	1:1.5:3	155	145	9.37	12.72	18.38	14.83
B	1:1.5:3	40	40	11.86	15.2	19.40	20.86
C	1:1.5:3	85	30	9.37	12.72	15.34	15.27



Figure 2. Process of concrete preparation, slump measurement and cubes cast by masons.

4. Conclusion

The findings from this research contribute to the broader understanding of LC^3's potential in non-structural applications and its viability in the unorganized sector. The findings demonstrate that a clinker factor as low as 0.3 can be immediately implemented for LC^3, particularly for applications such as paver blocks in low-traffic areas. Additionally, the results from the unorganized sector indicate that concrete production using LC^3 is comparable to Portland pozzolana cement (PPC) and can be easily adopted by masons without specialized training. Ultimately, reducing the clinker factor and promoting the adoption of LC^3 in these contexts can significantly contribute towards minimizing the carbon footprint of the construction industry and advancing sustainable practices.

Acknowledgements

The authors are grateful for the support of Swiss Agency for Development and Cooperation (SDC) in the low carbon cement project. Aalborg cement is acknowledged for making the Future-cem technology available to us.

References

Parashar, A., & Bishnoi, S. (2021). Hydration behaviour of limestone-calcined clay and limestone-slag blends in ternary cement. *RILEM Technical Letters*, *6*, 17–24. https://doi.org/10.21809/rilemtechlett.2021.134

Sharma, M., Bishnoi, S., Martirena, F., & Scrivener, K. (2021). Limestone calcined clay cement and concrete: A state-of-the-art review. *Cement and Concrete Research*, *149*, 106564. https://doi.org/10.1016/j.cemconres.2021.106564

Indian Standard 15658, (2021). Concrete paving blocks- Specification. *Bureau of Indian Standards*, New Delhi, India.

Indian Standard 516, (2021). Hardened concrete - Methods of test, Part 1: Testing of strength of hardened concrete. *Bureau of Indian Standards*, New Delhi, India.

The 16th International Congress on the Chemistry of Cement 2023 (ICCC2023)
"Further Reduction of CO_2 -Emissions and Circularity in the Cement and Concrete Industry"
September 18–22, 2023, Bangkok, Thailand

Functionalization of Metakaolin with Non-Ionic Surfactants: Swelling and Pozzolanic Reactivity

D. Luo, J. Wei*

University of Massachusetts Lowell, Lowell, MA, United States
Email: Dayou_Luo@uml.edu; Jianqiang_Wei@uml.edu

ABSTRACT

Metakaolin (MK) has been widely used in modifying cement and designing high-performance concrete, while the role of this alumino-silicate mineral has not been fully exploited due to its low reaction degree, especially at high-volume incorporations. To enhance the pozzolanic reactivity, functionalization of MK particles with two non-ionic surfactants, namely polyoxyethylene (9) nonylphenylether (PONPE9) and t-octyl phenoxy poly ethoxyethanol (TX100), are investigated in this study under a hypothesis that the intercalations of the surfactants into MK's interlayer space can trigger changes in structure and properties. The dry MK particles were mixed with aqueous solutions with two surfactant concentrations to reach two surfactant loadings in MK at its 1.0 and 6.0 cation exchange capacity (CEC). The surfactant uptake behavior of MK and its influence on the hygroscopic swelling, pozzolanic reactivity, and dissolution behavior in simulated cement pore solution were characterized. The results indicate that, compared with TX100, PONPE9 can be absorbed by MK more easily. After functionalization at 1.0 and 6.0 CEC, MK exhibited surfactant mass fractions of 1.85% and 3.81% for TX100, and 1.95% and 5.39% for PONPE9, respectively. The intercalation of surfactants resulted in an up to 28.6% increase in the swell index of MK when absorbing water. A more robust aluminum and silicon dissolution behavior in the simulated cement pore solution was observed from the functionalized MK. Increases in reaction heat and lime consumption capacity were obtained in the MK-lime blends indicating the enhanced pozzolanic reactivity of MK after functionalization and paving a path to enhance the role of MK in future sustainable concrete design.

KEYWORDS: *Metakaolin, functionalization, non-ionic surfactants, swelling, pozzolanic reactivity*

1. Introduction

Metakaolin (MK) has been widely used as a supplementary cementitious material (SCM) in concrete to improve mechanical and durability properties due to its highly pozzolanic reactivity. However, it was reported by Wild and Khatib (1997) that the pozzolanic reaction of MK in the cement matrix becomes low after 14 days, due to the formation of an inhibiting layer of reaction products on the MK particles, resulting in less strength gain. Moreover, the optimal cement substitution with MK was found to be between 10% to 15%. A higher dosage is desired to achieve robust reductions in cement consumption and CO_2 intensity of concrete, while it might lead to compromised mechanical strength, which might be caused by its extremely high-water absorption capacity (Brykov et al. (2015)), poor dispersion in the ion-rich cement matrix (Paiva et al. (2012)) and low degree of reaction. Although the use of MK in concrete becomes increasingly common, the aforementioned challenges still remain and impede the high-volume incorporation of MK in the development of sustainable and high-performance cementitious composites.
Organic functionalization has been validated as an effective approach to modify clay particles, e.g., montmorillonite (MT), as the surfactants can be intercalated into the interlayer space, thereby enhancing the pozzolanic reactivity, water uptake capacity, and dispersion of clay particles to improve the performance of concrete (Luo and Wei (2022a)). Different from the 2:1 layered structure of MT, MK possesses a unique 1:1 layer structure of tetrahedral silicate and octahedral aluminate. Our previous success in functionalizing MT paves a path for the modification of MK. In this study, the functionalization of MK with two non-ionic surfactants and its effect on the properties of MK in terms of dispersion, swelling, ion exchange, and pozzolanic reactivity are investigated.

2. Materials and methods

2.1 Materials and functionalization of MK

The MK used in this study has a mean particle size, specific surface area, and cationic exchange capacity (CEC) of 3.79 µm, 3.0 m^2/g, and 7.47 meq/100g respectively. Two non-ionic surfactants, polyoxyethylene (9) nonylphenylether (PONPE9) and t-octyl phenoxy poly ethoxyethanol (TX100) with an average molar mass of 660 and 647 g/mol, respectively, were used to functionalize MK by following the ionic exchange method (Taleb et al. (2018)). Firstly, the raw MK was oven-dried at 105°C for 24 h. Then, the MK particles were mixed with aqueous surfactant solutions with dosages of 1.0CEC and 6.0 CEC of MK at a clay concentration of 100g/L by stirring at 500 rpm for 30 min at room temperature. The organically functionalized MK (OMK) was collected by centrifuging the suspensions at 14000 rpm for 15 min followed by oven drying at 70°C for 24 h and grinding with a ball mill at 900 rpm for 2 h.

2.3 Characterization methods

The intercalation of the surfactants in MK and the pozzolanic activity of the Mk samples in terms of lime consumption capacity were determined via thermogravimetric analysis (TGA) using a TGA 4000 from PerkinElmer. Approximately 30 mg of MK and OMK particles were tested from 30 °C to 800 °C at a heating rate of 15 °C/min in an inert environment of N_2 gas. UV-Vis spectroscopy was performed on suspensions of MK and OMK in both deionized (DI) water and a simulated cement pore solution (pH = 13.5) using a Cary 8454 spectrophotometer to evaluate the dispersion behavior of MK and OMK. ASTM D5890 was followed for the swelling behavior analysis. The heat flow and accumulative heat release from the reactions between MK/OMK and calcium hydroxide (CH) up to 50 h at 25 °C were performed with an I-Cal 2000 HPC high-precision isothermal calorimeter. For the lime consumption test, 39 g of MK/OMK-CH blends with an MK/OMK to CH ratio of 0.3 and a water/solid ratio of 2.0 was cast in a sealed bottle. The blends were collected at 1, 7, and 28 days to determine the CH consumption with the TGA procedures mentioned above. The Al and Si release behavior of MK and OMKs were determined by mixing 5 g of MK/OMKs with 200 mL of simulated pore solution stirred at 500 rpm and 40 ºC. 2.5 mL of the solutions were withdrawn after 2, 5, 10, 20, and 30 min for inductively coupled plasma optical emission spectrometry (ICP-OES) after stabilizing with 2% nitric acid (a dilute factor of 250).

3. Results and discussion

3.1 Intercalation of surfactants into MK

As shown in Figs. 1a and 1b, TGA was used to determine the amounts of surfactants intercalated into MK based on the weight drop in the temperature range of 150°C to 375°C, which was observed from OMK only, but not appeared in raw MK. Another main mass loss between 375°C to 650°C was caused by the dehydroxylation of residual kaolinite in the MK. By quantifying the weight drop between the first peak, the amount of surfactant by mass of the clays can be extracted and shown in Fig. 1c. 1.9% and 2.0% of 1.0TX100-MK and 1.0PONPE9-MK were occupied by the surfactants, respectively, while they increased to 3.8% and 5.4% when 6.0 CEC surfactants were applied.

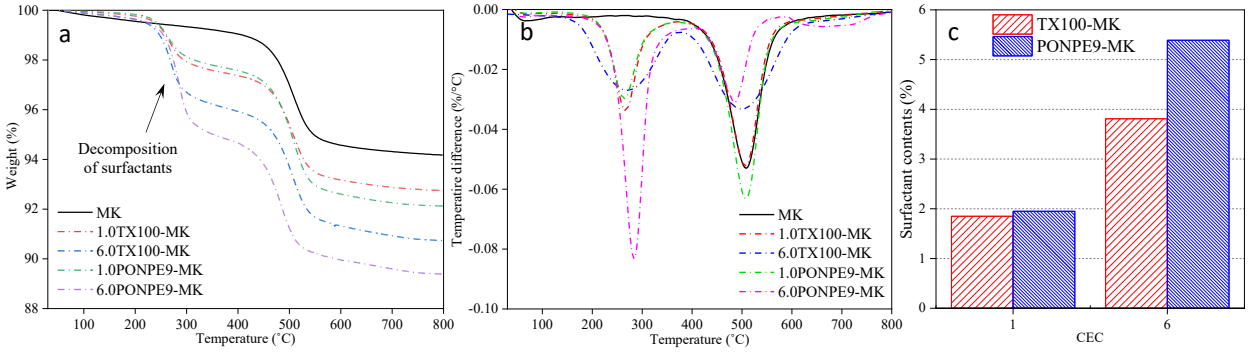


Fig. 1 (a) TGA, (b) DTG curves of MK/OMK, and (c) surfactant contents intercalated into MK.

3.2 Dispersion and swell behavior

As shown in Fig. 2a, no absorbance peak can be observed from the UV-Vis spectra of the raw MK-DI water suspension, while two peaks at 224 nm and 274 nm appeared from the suspensions with the functionalized MK, which increased with the dosage of surfactants. PONPE9 showed a higher efficiency than TX100 in improving the dispersion behavior of MK. Lower absorbances were yielded from the MK/OMK-simulated cement pore solution suspensions (see Fig. 2b), unveiling the lower dispersion of clay particles in the ion-rich cement matrix than that in DI water. A peak at 216 nm was observed from the suspension with the raw MK, while the higher dispersion of OMKs was indicated by two peaks at 224 nm and 274 nm. As shown in Fig. 2c, the raw MK exhibited a swell index of 3.5 mL/2g, which was increased to 4 mL/2g and 4.5 mL/2g, respectively, when 1.0CEC and 6.0CEC surfactants were applied for functionalization. The increased swelling behavior of MK might be favorable for using OMK as an internal curing agent to partially replace cement in concrete, as the improved swelling of MK can provide additional precipitation space for the gradual formation of cement hydration products, i.e., C-S-H and C-A-S-H. It is interesting to see the comparable role of PONPE9 and TX100 in this test.

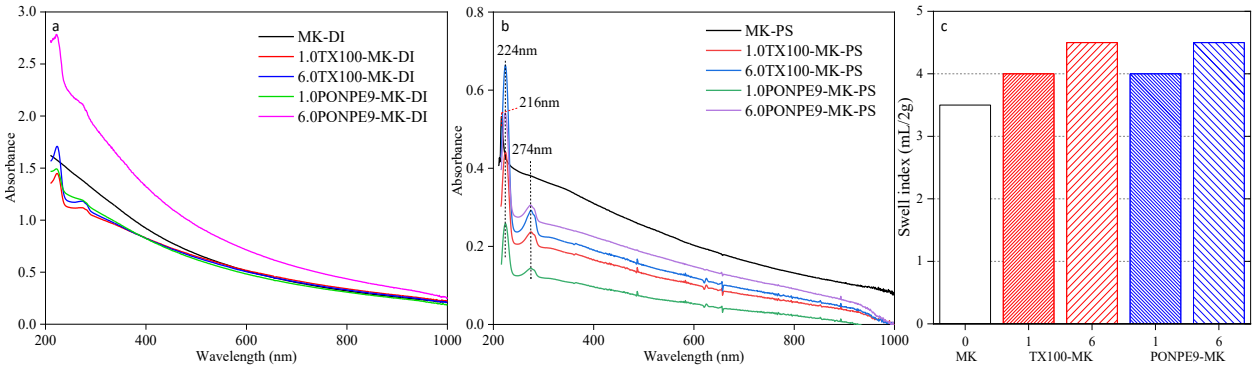


Fig. 2 UV-Vis spectrum of MK and OMKs in (a) DI water and (b) simulated pore solution, and (c) swell index

3.3 Pozzolanic reactivity

The heat flow and cumulative heat release generated from the reactions between MK/OMKs and CH are shown in Figs. 3a and 3b, respectively. A higher heat flow peak at 0.04 h and more cumulative heat release than that of MK were yielded by 6.0PONEPE9-MK indicating the improved pozzolanic reactivity after functionalization. However, the heat flow peaks observed from other OMKs are lower than MK, indicating the decreased pozzolanic reactivity, at least during the early-age reactions. Although 1.0PONPE9-MK yielded a lower heat flow peak, its cumulative heat release exceeded that of MK after 9 h, indicating the retarded reaction, but a higher overall pozzolanic reactivity.

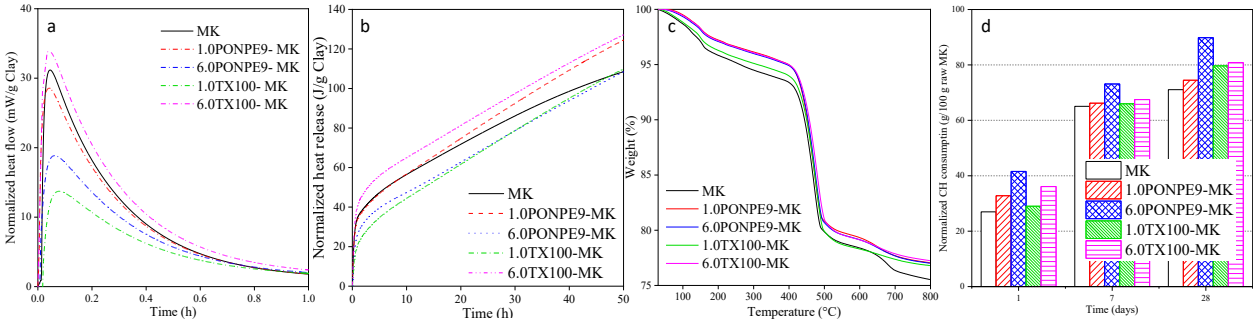


Fig. 3 (a, b) Calorimetry results, (c) representative TGA curves, and (d) normalized CH consumption.

From the TGA curves in Fig 3c, the remaining CH from the reactant system can be quantified, which enables the quantification of the consumed CH (Fig. 3d). The raw MK yielded a lime consumption capacity of 27.0, 65.1, and 71.1 g/100g MK after 1, 7, and 28 days, respectively. Enhanced pozzolanic reactivity was obtained from the functionalized MK. 6.0PONPE9-MK exhibited the most enhanced lime consumption, which are 54.1%, 12.3%, and 26.3% higher than that of MK for the three testing ages.

3.4 Ion release behavior

The dissolution of MK in terms of Al and Si releases in the cement system governs its pozzolanic reactivity and the formation of additional C-S-H or C-A-SH. As shown in Fig. 4, the raw MK released 6.6 mmol/100g Al and 2.7 mmol/100g Si after 30 min. Slight increases in Al dissolution were observed from 1.0PONPE9-MK and 1.0TX100-MK. However, significant enhancements of Al release were observed from 6.0PONPE9-MK and 6.0TX100-MK at an early age and they gradually increased to 10.9 mmol/100g MK and 9.5 mmol/100g MK, respectively, after 30 min. Different from the release of Al, the functionalization did not result in a remarkable increase in early-age Si dissolution, until 20 min. After 30 min, 4.5 mmol/100g MK and 4.3 mmol/100g MK of Si were released from 6.0PONPE9-MK and 6.0TX100-MK, respectively, which are 1.7 and 1.6 times that of MK.

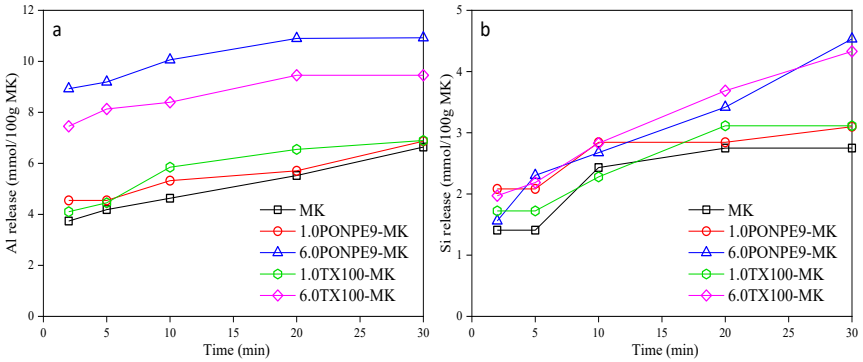


Fig. 4 (a) Al and (b) Si release behavior of MK and OMKs in a simulated cement pore solution.

4. Conclusions

The functionalization of MK by two non-ionic surfactants and its effects on modifying the properties of MK were investigated in this study. Through a simple functionalization procedure, intercalations of 5.4% PONPE9 and 2.0% TX100 (by weight of MK) into MK were reached at a dosage of 6.0 CEC. An increased hygroscopic swelling index of MK by up to 28.6% was obtained after the functionalization. The dispersion of MK in both DI water and simulated cement pore solution was also improved. Moreover, improvement in the pozzolanic reactivity of MK after functionalization was demonstrated by the increased reaction heat and the raised lime consumption capacity, which can be further explained by the enhanced dissolution of OMK in terms of Al and Si releases in the simulated pore solution.

Acknowledgements

This work was supported by the United States National Science Foundation (award No. 1935799).

References

Brykov, A., Krasnobaeva, S., and Mokeev, M. (2015) "Hydration of Portland cement in the presence of highly reactive metakaolin", *Materials Sciences and Applications*, 6: 391

Luo, D., and Wei, J. (2022a) "Hydration kinetics and phase evolution of Portland cement composites containing sodium-montmorillonite functionalized with a Non-Ionic surfactant", *Construction and Building Materials*, 333: 127386

Luo, D., and Wei, J. (2022b) "Upgrading sodium montmorillonite into a reactive internal curing agent for sustainable cement composites through non-ionic functionalization", *Composites Part B: Engineering*, 242: 110076

Paiva, H., Velosa, A., Cachim, P., and Ferreira, V. (2012) "Effect of metakaolin dispersion on the fresh and hardened state properties of concrete", *Cement and Concrete Research*, 42: 607-12.

Taleb, K., Pillin, I., Grohens, Y., and Saidi-Besbes, S. (2018) "Gemini surfactant modified clays: Effect of surfactant loading and spacer length", *Applied Clay Science*, 161: 48-56

Wild, S., and Khatib, J. (1997) "Portlandite consumption in metakaolin cement pastes and mortars", *Cement and Concrete Research*, 27: 137-46

The 16th International Congress on the Chemistry of Cement 2023 (ICCC2023)
"Further Reduction of CO_2 -Emissions and Circularity in the Cement and Concrete Industry"
September 18–22, 2023, Bangkok, Thailand

Reactivity (R^3) and hydration products of Fe(II)-rich slags: from $CaO\text{-}FeO_x\text{-}SiO_2$ to $CaO\text{-}Al_2O_3\text{-}Na_2O\text{-}FeO_x\text{-}SiO_2$

V. Hallet[1*], M. Giels[2], J. Van De Sande[3,4], R. Murillo Alarcón[5] and Y. Pontikes[6]

[1*] *KU Leuven, Department of Materials Engineering, Kasteelpark Arenberg 44, 3001 Leuven, Belgium*
Email: Vincent.hallet@kuleuven.be
[2] *KU Leuven, Department of Materials Engineering, Kasteelpark Arenberg 44, 3001 Leuven, Belgium*
Email: Michiel.Giels@kuleuven.be
[3] *Vrije Universiteit Brussel, Department of Materials and Chemistry, Pleinlaan 2, 1050, Brussels, Belgium*
[4] *KU Leuven, Department of Materials Engineering, Kasteelpark Arenberg 44, 3001 Leuven, Belgium*
Email: Jorn.Van.De.Sande@vub.be
[5] *KU Leuven, Department of Materials Engineering, Kasteelpark Arenberg 44, 3001 Leuven, Belgium*
Email: Robertoeduardo.Murilloalarcon@kuleuven.be
[6] *KU Leuven, Department of Materials Engineering, Kasteelpark Arenberg 44, 3001 Leuven, Belgium*
Email: Yiannis.pontikes@kuleuven.be

ABSTRACT

In order to reduce the CO_2 emissions of the construction industry, alternative supplementary cementitious materials remain one of the most promising routes. While many different materials have been investigated, most of them are found within the $CaO\text{-}Al_2O_3\text{-}SiO_2$ system. In contrast, Fe-rich and especially Fe(II)-rich materials have received far less attention in literature. Hence, in this work, 3 synthetic, water-granulated slags in the $CaO\text{-}FeO_x\text{-}SiO_2$, $CaO\text{-}Al_2O_3\text{-}FeO_x\text{-}SiO_2$ and $CaO\text{-}Al_2O_3\text{-}Na_2O\text{-}FeO_x\text{-}SiO_2$ systems were investigated using R^3 (rapid, robust, relevant) reactivity tests. The hydration products formed by the end of this test were characterized through the use of X-ray diffraction and thermogravimetric analysis. The presence of Al_2O_3 and to a lesser extent of Na_2O significantly enhanced the slag reactivity from one similar to siliceous fly ash to one closer but slightly lower than calcareous fly ash. Ettringite was stable only in the presence of Al_2O_3 and absence of Na_2O. Moreover, Al_2O_3 in the slag yielded the formation of a Fe(II)-Al-layered double hydroxide, which remained present when Na_2O was present as well. The results of this study can have important implications both for slag producers, who might consider slag modifications for higher reactivity, as well as for the cement and concrete industry, where these new insights can help in the potential adoption of these slags as alternative SCMs.

KEYWORDS: *Fe(II)-rich slag, reactivity, supplementary cementitious materials, hydration products, slag composition*

1. Introduction

The supply of classic supplementary cementitious materials (SCMs) is expected to reduce and their chemistry and mineralogy will likely change due to continued decarbonization of the steel and energy generation industries. Hence, other SCMs need to be sourced (locally) to ensure future reductions in the clinker factor and the accompanied CO_2 reductions. One type of alternative SCMs is Fe(II)-rich slags, such as those from the non-ferrous metallurgical industry. The composition of those Fe(II)-rich slags can vary significantly depending on their origin and any pre-processing steps, such as slag cleaning operations (Piatak et al. 2015). Nevertheless, limited knowledge exists on the impact of the chemical composition of these slags with respect to their reactivity and hydration products. Some authors have investigated the effect of increasing the CaO content as a route to enhanced reactivity, such as (Feng et al. 2020). Yet, the impact of other elements typically present in these slags such as Al_2O_3 and Na_2O remain unclear and will be even more relevant considering upcoming potential SCMs such as vitrified bauxite residue (Giels et al. 2022).

Therefore, this work aims to elucidate the effect of the presence of these oxides, mainly with respect to reactivity, through R^3 (rapid, robust, relevant) reactivity tests, and to the hydration products that can be expected from these slags, by investigating the hydrated pasts at the end of the R^3 procedure by X-ray diffraction (XRD) and thermogravimetric analysis (TGA).

2. Materials and methods

Three synthetic slags, S, S-A, and S-A-N, were produced using a method similar to that described in (Van De Sande et al. 2020) by heating up and melting together the appropriate amounts of Fe_2O_3, metallic Fe, SiO_2, Al_2O_3, $CaCO_3$ and Na_2CO_3 (all > 99% purity) to 100 °C above the expected liquidus temperature determined by FactSage V8.1, using the FactPS and FToxid databases (Bale et al. 2016) in a steel crucible. The chemical composition (powder XRF; Bruker, S8 TIGER) and phase assemblage (QXRD; Bruker D2 Phaser; using either 10 wt.% zincite as internal standard (S, S-A) or TiO_2 (Kronos) as external standard (S-A-N)) are presented in table 1. The slags were milled to a specific surface area, as determined by the Blaine permeability method (EN196-6) of 400 ± 20 m^2/kg, except for slag S, which had a specific surface area of 450 ± 20 m^2/kg as it originated from a previous study (Van De Sande et al. 2020).

Table 1: Chemical composition and phase assemblage of the synthetically produced slags used in this work.

Oxide content (wt.%)	FeO	SiO_2	CaO	Al_2O_3	Na_2O	Other	Am. Content (wt.%)	Other phases
S	50	28	20	0.5	0	< 2	93	Fe_2SiO_4
S-A	50	25	19	5	0	< 1	96	$Fe_{1-x}O$
S-A-N	45	25	19	6	5	< 1	87	$Fe_{1-x}O$

The reactivity of the slags was determined using the R^3 reactivity test, as described in ASTM C1897. Isothermal calorimetry (TA Instruments, TAM Air) was used to determine the released heat during the procedure. After 7 days, the hydration of the pastes was stopped by immersion in isopropanol for 15 min, followed by vacuum filtration and rinsing with isopropanol and diethylether. In the end, the hydration stopped paste was dried for 8 min at 40 °C. The content of bound water (BW) and $Ca(OH)_2$ (CH) was determined using TGA under N_2 flow rather than by the oven procedure described in ASTM C1897 in order to avoid oxidation. In the TGA procedure, the paste was covered by a N_2 flow (100 ml/min) at room temperature for 5 min to remove any remaining traces of diethylether. Afterwards, the temperature was increased to 1000 °C (10 °C/min) under the same N_2 flow. The R^3 bound water is determined as the difference in weight between 40 °C and 350 °C, while the remaining $Ca(OH)_2$ content is determined using the tangent method (Lothenbach et al. 2015). Finally, the crystalline phases resulting from the R^3 procedure were measured using XRD on the hydration stopped pastes.

3. Results and discussion

The isothermal calorimetry results of the R^3 reactivity test (Figure 1) show that the presence of even small amounts of Al_2O_3 (S-A) and Na_2O (S-A-N) significantly enhance the reactivity of the slag. Especially the presence of Al_2O_3 strongly increases the slag reactivity. In comparison, the impact of Na_2O seems rather limited. Since it is expected that the wüstite phase ($Fe_{1-x}O$) does not react in cementitious systems, the higher content of this phase in S-A-N, and corresponding lower reactive amorphous content, is expected to reduce the slag reactivity. Hence a comparison based on the amorphous content is made as well (Figure 1, right), where the impact of Na_2O is slightly increased. It should be noted that the formation of a higher amount of $Fe_{1-x}O$ will reduce the Fe content of the slag, which might affect the reactivity of the amorphous phase as well. At the present, it is unclear whether a lower Fe content will enhance or reduce the reactivity of the amorphous phase. A comparison of the R^3 indicators for the slags (Table 2) with values published in literature (Li et al., 2018) shows that in absence of Al_2O_3 and Na_2O, the slag (S) has a low reactivity, comparable to siliceous fly ash. However, by adding Al_2O_3 (and to a lesser extent Na_2O), the reactivity increases and becomes closer, but slightly lower, than that of calcareous fly ash. Compared to ground granulated blast furnace slag (GGBFS), the reactivity is lower as well. This increase in reactivity can be

explained by the fact that Na_2O and Al_2O_3 have been linked to increased glass depolymerization, disorder and (chemical) glass weakening, which thus leads to enhanced glass reactivity (Kucharczyk et al., 2019).

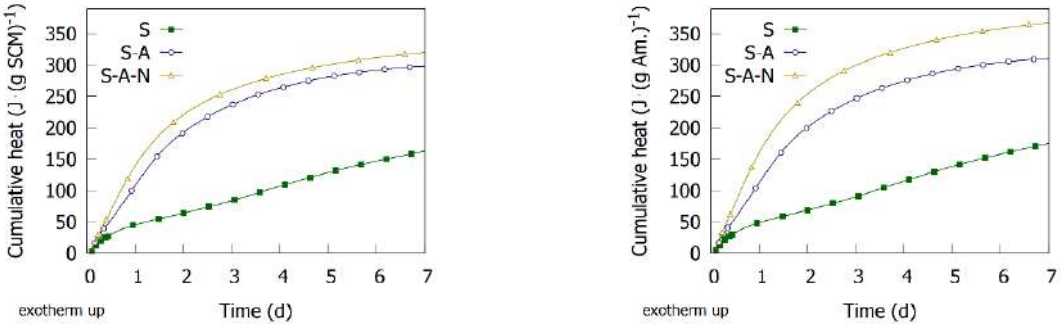


Figure 1: Heat released in isothermal calorimetry by the R³ pastes in J/g SCM (left) and J/g amorphous SCM (right).

Table 2: Results of the various R³ tests conducted on the different slags in this work.

	R³ heat 3 days (J/g SCM)	R³ heat 7 days (J/ g SCM)	R³ bound water (g/100 g dried basis)	R³ $Ca(OH)_2$ consumption (g/100 g SCM)
S	84	163	2.2	100.6
S-A	237	298	3.5	99.8
S-A-N	261	320	3.8	101.5

An examination of the hydration products after the 7 day R³ procedure (Figure 2) at 40 °C reveals considerable differences due to the presence of Al_2O_3 (S-A) or Na_2O (S-A-N). In the absence of both Al_2O_3 and Na_2O (S), the main hydration products are monosulfoaluminate (Ms) and C-S-H. Despite the presence of $CaCO_3$, no (mono)carbonate Fe-AFm (Fe-Mc) is formed, which can be explained by its slow formation kinetics (Dilnesa et al. 2011). As no Fe is taken up by carbonate Fe-AFm, more Fe is available to combine with the sulfates in the solution, which can explain the lack of AFt formation. Furthermore, (Dilnesa et al. 2012) indicated that Fe-AFt destabilizes around 40 °C in favor of Fe-AFm.

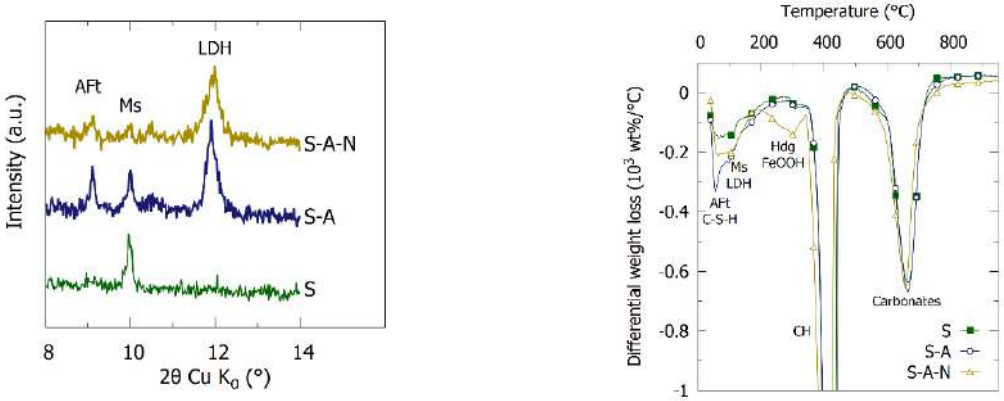


Figure 2: the XRD pattern in the low 2θ range (left) and differential weight loss curves (right) for the hydration stopped R³ pastes after 7 days of curing at 40 °C. AFt = ettringite, Ms = monosulfoaluminate, LDH = Fe-Al-layered double hydroxide, Hdg = (siliceous) hydrogarnet, CH = $Ca(OH)_2$.

When Al_2O_3 is present (S-A), also (Al-)AFt is formed as the Al-form tends to be stable both up to higher temperatures and with respect to Fe-AFt. In addition, another reflection at 2θ = 11.9 (d = 7.43 Å) is present, which has been recently attributed to a Fe(II)-Al-layered double hydroxide (LDH) phase (Hallet et al. 2022), and this becomes one of the main crystalline hydrates. Finally, the inclusion of Na_2O in the slag reduces the formation of AFt and Ms while the Fe-Al-LDH is still formed to a large extent. While no other crystalline hydration products could be observed, TGA reveals a significant loss of bound water around 250-300 °C, which could be attributed to (Fe-rich, semi-amorphous) siliceous hydrogarnet (Hdg) (Dilnesa et al. 2014) or amorphous FeOOH phases (Möschner et al. 2009).

4. Conclusions

In this work, the impact of Al_2O_3 and Na_2O on Fe(II)-rich slags was investigated, showing their importance in the enhancement of the reactivity and in the formation of different hydration products. The presence of at least some Al_2O_3 in the slag is observed to be essential for obtaining a good reactivity, almost similar to calcareous fly ashes. Hence, from the point of view of reactivity, such slags can be considered interesting alternative SCMs to reduce the CO_2 emissions of the construction industry. Furthermore, when both Fe(II) and Al are present, a Fe(II)-Al-layered double hydroxide appears to form, remaining stable even in the presence of significant alkalis (5 wt.% Na_2O) in the slag. Hence, to further understand the use of, and potentially valorize, Fe(II)-rich slags, the implications of this phase with respect to (blended) cement properties need to be clarified. Particularly in more alkaline systems where this phase might remain, in contrast to other typical cement phases such as ettringite.

Acknowledgements

The authors would like to thank the Center for Resource Recovery and Recycling (CR^3) for funding this work.

References

Bale, C. W., Bélisle, E., Chartrand, P., Decterov, S. A., Eriksson, G., Gheribi, A. E., … Van Ende, M.-A. (2016). FactSage thermochemical software and databases, 2010–2016. *Calphad*, *54*, 35–53. https://doi.org/10.1016/j.calphad.2016.05.002

Dilnesa, B. Z., Lothenbach, B., Le Saout, G., Renaudin, G., Mesbah, A., Filinchuk, Y., … Wieland, E. (2011). Iron in carbonate containing AFm phases. *Cement and Concrete Research*, *41*(3), 311–323. https://doi.org/10.1016/j.cemconres.2010.11.017

Dilnesa, B. Z., Wieland, E., Lothenbach, B., Dähn, R., & Scrivener, K. L. (2014). Fe-containing phases in hydrated cements. *Cement and Concrete Research*, *58*(April), 45–55. https://doi.org/10.1016/j.cemconres.2013.12.012

Dilnesa, Belay Zeleke, Lothenbach, B., Renaudin, G., Wichser, A., & Wieland, E. (2012). Stability of monosulfate in the presence of iron. *Journal of the American Ceramic Society*, *95*(10), 3305–3316. https://doi.org/10.1111/j.1551-2916.2012.05335.x

Feng, Y., Chen, Q., Zhou, Y., Yang, Q., Zhang, Q., Jiang, L., & Guo, H. (2020). Modification of glass structure via CaO addition in granulated copper slag to enhance its pozzolanic activity. *Construction and Building Materials*, *240*, 117970. https://doi.org/10.1016/j.conbuildmat.2019.117970

Giels, M., Hertel, T., Gijbels, K., Schroeyers, W., & Pontikes, Y. (2022). High performance mortars from vitrified bauxite residue; the quest for the optimal chemistry and processing conditions. *Cement and Concrete Research*, *155*(March), 106739. https://doi.org/10.1016/j.cemconres.2022.106739

Hallet, V., Pedersen, M. T., Lothenbach, B., Winnefeld, F., De Belie, N., & Pontikes, Y. (2022). Hydration of blended cement with high volume iron-rich slag from non-ferrous metallurgy. *Cement and Concrete Research*, *151*(September 2021), 106624. https://doi.org/10.1016/j.cemconres.2021.106624

Kucharczyk, S., Zajac, M., Stabler, C., Thomsen, R. M., Ben Haha, M., Skibsted, J., & Deja, J. (2019). Structure and reactivity of synthetic CaO-Al2O3-SiO2 glasses. *Cement and Concrete Research*, *120*(December 2018), 77–91. https://doi.org/10.1016/j.cemconres.2019.03.004

Li, X., Snellings, R., Antoni, M., Alderete, N. M., Ben Haha, M., Bishnoi, S., … Scrivener, K. L. (2018). Reactivity tests for supplementary cementitious materials: RILEM TC 267-TRM phase 1. *Materials and Structures*, *51*(6), 151. https://doi.org/10.1617/s11527-018-1269-x

Lothenbach, B., Durdziński, P. T., & Weerdt, K. De. (2015). Thermogravimetric analysis. In K. L. Scrivener, R. Snellings, & B. Lothenbach (Eds.), *A Practical Guide to Microstructural Analysis of Cementitious Materials* (pp. 177–211). Boca Raton: CRC Press, Taylor & Francis Group.

Möschner, G., Lothenbach, B., Winnefeld, F., Ulrich, A., Figi, R., & Kretzschmar, R. (2009). Solid solution between Al-ettringite and Fe-ettringite (Ca6[Al1 - xFex(OH)6]2(SO4)3·26H2O). *Cement and Concrete Research*, *39*(6), 482–489. https://doi.org/10.1016/j.cemconres.2009.03.001

Piatak, N. M., Parsons, M. B., & Seal, R. R. (2015). Characteristics and environmental aspects of slag: A review. *Applied Geochemistry*, *57*, 236–266. https://doi.org/10.1016/j.apgeochem.2014.04.009

Van De Sande, J., Peys, A., Hertel, T., Rahier, H., & Pontikes, Y. (2020). Upcycling of non-ferrous metallurgy slags: Identifying the most reactive slag for inorganic polymer construction materials. *Resources, Conservation and Recycling*, *154*(December 2019), 104627. https://doi.org/10.1016/j.resconrec.2019.104627

The 16th International Congress on the Chemistry of Cement 2023 (ICCC2023)
"Further Reduction of CO_2 -Emissions and Circularity in the Cement and Concrete Industry"
September 18–22, 2023, Bangkok, Thailand

Bauxite residue as a new source of SCM: its impact on cement hydration and interaction with fly ash

L. M. V. Silveira[1*], R. C. O. Romano[1], R. G. Pileggi[1] and M. A. Cincotto[1†]

[1] *University of Sao Paulo, Sao Paulo, Brazil*
*Email: luana.silveira@lme.pcc.usp.br**
Email: cesar.romano@lme.pcc.usp.br
Email: rafael.pileggi@usp.br

ABSTRACT

The use of Supplementary Cementitious Materials (SCM) is a strategy to produce sustainable and low-carbon emissions cement components. Bauxite residue from the Bayer process (BR) was studied in this work as a new type of SCM, due to its composition with aluminum, calcium, and silica. However, BR has a high pH and leachable alkalis, being the main barrier to the implementation of this residue worldwide. As established in the literature, some SCMs can be alternatives to fix alkali during the cement reaction, and this can be a route to find a safe use of BR in cementitious compositions. This work aimed to analyze the chemical reaction and microstructure of cement paste systems made with partial replacement of BR and BR + fly ash, using calorimetry, XRD, TGA, and SEM analysis. The results indicate that BR interacts with cement, forming new hydrated products with the presence of sodium and aluminum, and that fly ash could influence the reactions of minerals with these elements.

KEYWORDS: *Cement hydration, bauxite residue, Bayer process, new SCM, fly ash.*

1. Introduction

The use of Supplementary Cementitious Materials (SCMs) produces sustainable, low-carbon cement. However, their finite availability necessitates the search for new high-quality sources (Scrivener, John, and Gartner 2018). Bauxite residue from the Bayer process (BR) has been studied to add to the exploited potential of use in association with cement, and address the waste generated by the aluminum industry (IAI 2020).

During the alumina refining stage, after the bauxite ore processing, a concentrated caustic soda solution at high pressure and elevated temperature is mixed to process the alumina. Part of the powder in suspension is unable to dissolve, generating an insoluble residue, discarded by washing during the filtration step (Ruys 2019). Due to this process, BR has a high pH and leachable products, and if these alkalis are free and soluble, pathologies in cementitious components and soil pollution can occur, due to the leaching of contaminating elements, alkali-silica reaction, and efflorescence, for example (Evans 2016). Understanding the BR-cement interaction is crucial for safe large-scale application.

Certain SCMs can reduce alkali concentration in cementitious components (Tapas et al. 2021). Therefore, the inclusion of materials with this potential can be a route to the safe use of BR in cementitious compositions through chemical interaction.

This work aimed to analyze the chemical reaction and microstructure of cement paste made with partial replacement of BR and BR + fly ash. The additions come from the same alumina plant, to facilitate the implementation of the combined use, considering logistic issues as well. Isothermal conduction calorimetry, XRD, TGA, and SEM analysis were conducted.

2. Materials and methods of characterization

BR and fly ash (FA) from the same alumina plant in the north of Brazil were used. The cement (PC) is named according to Brazilian standards (NBR 16697/18) as CPV-RS, which is the purest cement commonly

used in the region, with the addition of up to 10% of pozzolan to resist sulfate attack. When the materials were received, BR and FA were dried at 105 °C, ground, and sieved through a 106 μm mesh opening.
The specific surface area (SSA), according to BET method, of PC is 1.38 m²/g, BR is 7.74 m²/g and FA is 12.4 m²/g. The chemical composition (Table 1) was determined by X-ray fluorescence in a PANalytical spectrometer, Zetium model, with sample preparation using a pressed tablet and tests following the general guidelines of ISO 29581-2/10. Loss on ignition (LOI) was performed at 1020 °C for 2 h.

Table 1. Chemical composition of raw materials (oxide).

Material	LOI	SiO_2	CaO	MgO	Fe_2O_3	Al_2O_3	MnO	TiO_2	SO_3	Na_2O	K_2O	P_2O_5	BaO	SrO	ZrO_2
PC	5.13	17.7	60.8	4.4	3.45	4.01	0.15	0.23	2.41	<0.10	0.42	0.1	-	<0.10	-
BR	8.4	16.3	1.15	<0.10	**36.2**	**22.1**	0.07	5.27	-	**9.72**	0.03	0.05	-	-	0.62
FA	17.7	**33.8**	16.4	1.39	7.93	13.8	0.08	0.69	**5.01**	1.04	1.25	0.28	0.18	0.16	0.06

Mineralogical composition was determined by X-ray diffraction (XRD), PANalytical diffractometer, Empyrean III model. Tests were carried out with copper radiation, an automatic gap of 0.5°, nickel filter, and spinning frequency of 2 seconds per spin, step of 0.013°, staying at each step for 60 s, in the range of $5° < 2\theta < 70°$. The minerals identified in the cement were: brownmillerite (B), alite, belite, calcium aluminate, gypsum (G), calcite, portlandite (CH), and bassanite; in BR: sodalite (S), gibbsite (Gb), goethite (Go), hematite, anatase, kaolinite, and rutile; and in FA: calcite, quartz, hematite, anidrite, enstatite, and muscovite.
Thermogravimetric analysis (TGA), shown in Figure 1, was obtained in a Netzsch equipment, T209 F1.

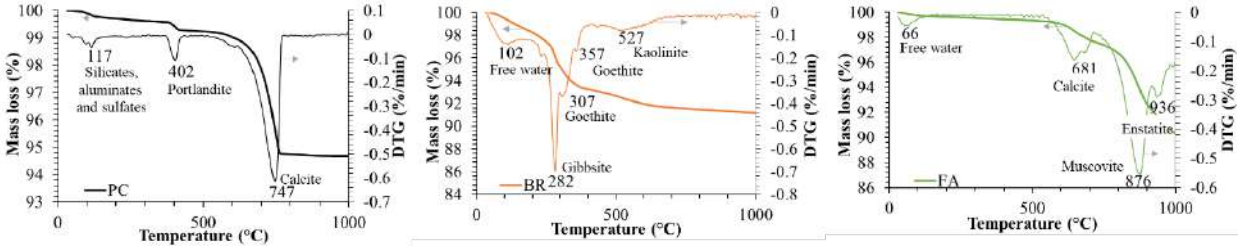


Figure 1. Thermogravimetric analysis of raw materials.

3. Experimental program

Four pastes were produced with a fixed water-to-solid ratio of 0.5-wt, being the reference paste (only cement) and the others with 70% of cement and 30% of additions (in volume): 100PC, 70PC-30BR, 70PC-30FA, 70PC-15BR-15FA.
The mixing procedure started by putting the water into a cup with the powders, manual premixing it for 1 minute using a spoon. Then, the container was placed in a Flacktek speed mixer equipment, where it was mixed for 2 minutes at a rotational speed of 1500 rpm.
To quantify the heat flow of each paste during the chemical reaction of cement, an isothermal conduction calorimeter was used, equipment Calmetrix I-CAL 8000 HPC, with a controlled temperature of 23 ºC for 72 hours (graphical results will be shown only until 48 h, due to no significant changes after this time). The formation of hydrated products was accompanied using the XRD and TGA methods, with the same equipment described previously. To perform the tests, the hydration was stopped moments after the events with higher heat released with the solvent exchange method.
At 28 days of hydration, the pastes were subjected to scanning electron microscopy (SEM) in an equipment Quanta FEG650, Thermo Fisher Scientific.

4. Results and Discussion

4.1 Hydration kinetics

Figure 2 shows the heat released during the chemical reaction of the four compositions, normalized by cement mass, to emphasize the effect of additions. The main hydrated products have been highlighted in the graphs (*: CH and C-S-H; #: AFt; and +: AFm).

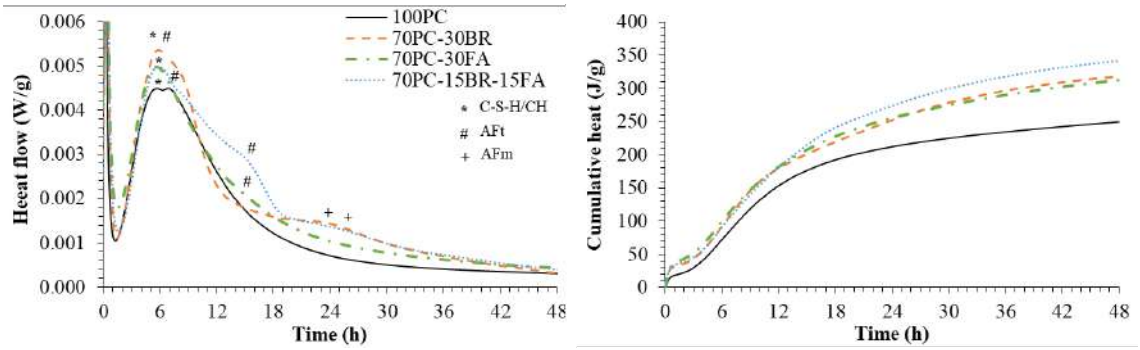


Figure 2. Heat flow (left) and cumulative heat released (right) of pastes.

The profile of the hydration curves is different in each composition, demonstrating that the additions have physical and chemical interactions with cement, changing the hydration process. It can be seen that in the ternary system there is an interaction between BR and FA, as the total cumulative heat of 70PC-15BR-15FA is greater than that of the other two blends, whose cement percentage is the same.

During the acceleration period, it is possible to notice the same profile of the curves, indicating that cement is the material that governs the reaction of silicate phases of clinker at this period. In this case, the additions have, above all, a physical role of nucleation of the hydrated products (Deschner et al. 2012; Scrivener, Juilland, and Monteiro 2015), perceived by the intensification of the C-S-H/CH peak, with more heat being released comparing with the reference composition. So, the greater SSA supplied by the particles from the additions, provides more space and surface area with greater shear for hydrates formation and growth.

The main chemical influence provided by BR is the acceleration of aluminates reactions, as the ettringite (AFt) peaks overlaps with C-S-H/CH peaks for 70PC-30BR, and it's possible to see the formation of monossulfoaluminate (AFm) for both pastes with BR, also observed by (Fujii et al. 2015), with a peak of heat released at ~24 h. Figure 3 shows two aluminates being formed at 30 h for pastes with BR. Due to the poor crystallinity of AFm, it was not possible to detect the mineral itself in the diffractograms, but other AFm phases (Lothenbach, Scrivener, and Hooton 2011) were seen at this time: hemicarboaluminate (Hc) and monocarboaluminate (Mc). The TGA shown in Figure 4, indicates that BR culminates the formation of new hydrated products with the presence of sodium (Na) e aluminum (Al).

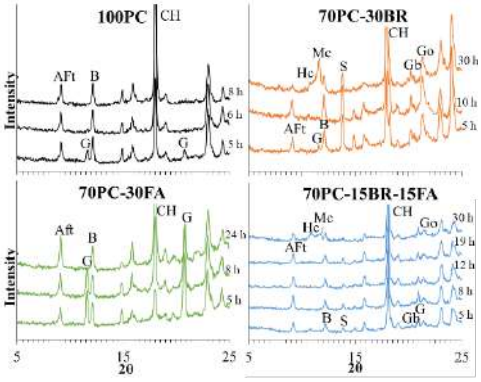


Figure 3. XRD of hydration evolution of pastes.

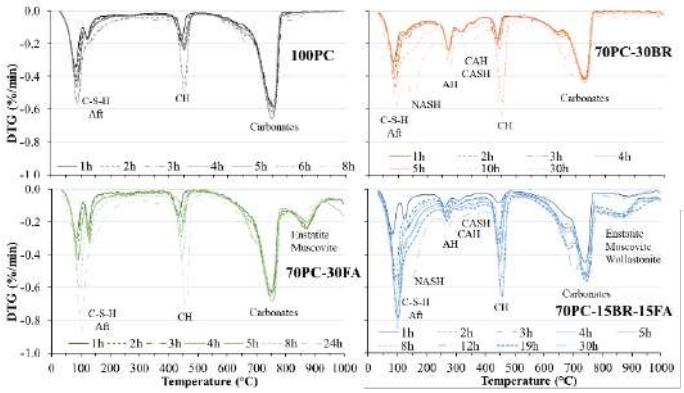


Figure 4. TGA of hydration evolution of pastes.

For FA, the formation of new hydrated products was not observed, as evidenced in Figure 4, but the AFt formation occurred later. This behavior can be attributed to large amount of sulfate in FA, increasing the time for its depletion (evident in Figure 3, that already happened for 100PC at 8 h, and for 70PC-30FA at 24 h), and thus the peak of AFt formation. The large amount of sulfate is not common for ordinary FA, but this may have occurred due to contamination of the waste in the generating plant.

The evolution of crystalline phases of 70PC-15BR-15FA (Figure 3) show that peaks of sodalite (S) and goethite (Go) lose intensity during the 30 hours analyzed, which doesn't occur for 70PC-30BR. Despite the fact that ternary paste has less BR, this could indicate that FA accelerates the reaction of minerals containing Na and Al.

4.3 SEM analysis

Figure 5 shows the SEM and energy dispersive X-ray spectroscopy (EDS) analysis of the pastes, revealing distinct microstructures. Colors represent the prominent elements present in the observed components.

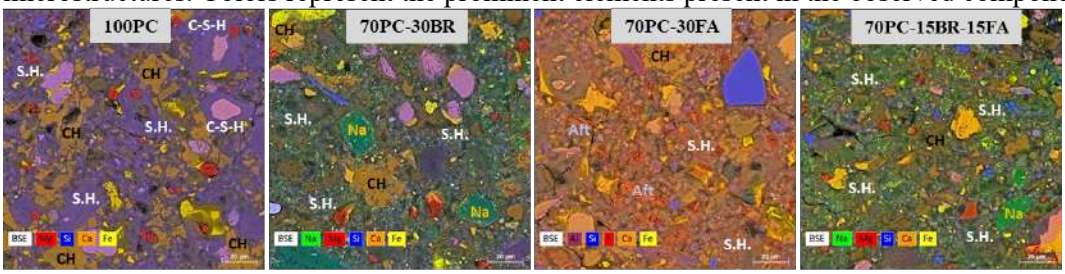


Figure 5. SEM-EDS analysis of pastes at 28 days.

Notably, the 100PC paste exhibits a higher content of CH, corresponding to its binder content. The areas containing silicate hydrates (S.H.) between the fillers and anhydrous grains in BR-containing compositions exhibit a significant presence of sodium (Na). AFt needles were observed in the 70PC-30FA paste, indicating the influence of FA on the formation of this product. In the ternary system, it is observed that the areas of silicate hydrates surpass the anhydrous grains in comparison to the binary systems, indicating synergism between BR and FA. These results align with previous findings that FA can accelerate the formation of minerals containing Na and Al.

5. Conclusions

The results indicate that both BR and FA have an impact on the cement hydration process. During the acceleration period, the observed differences in hydration were primarily due to physical mechanisms (filler effect). This can be attributed to the higher specific surface area of BR and FA compared to cement, which enhanced the C-S-H/CH peak. Moreover, BR exhibited a chemical interaction with cement, leading to the formation of new hydrated products containing sodium (Na) and aluminum (Al), while also accelerating the reaction of aluminate products. In ternary systems, FA played a role in accelerating the dissolution of phases containing these elements. These interactions were evident in the microstructure, as observed through the formation of constituents and the presence of diluted elements.

Acknowledgements

The authors wish to recognize and thank the incredible late PhD Maria Alba Cincotto for the initial supervision. We also thank CAPES (Research Grant – 88887.704012/2022-00) for the financial support.

References

Deschner, F. et al. (2012) “Hydration of Portland Cement with High Replacement by Siliceous Fly Ash”, *Cement and Concrete Research,* 42(10): 1389–1400

Evans, K. (2016) “The History, Challenges, and New Developments in the Management and Use of Bauxite Residue”, *Journal of Sustainable Metallurgy,* 2(4): 316–31

Fujii, A. L. et al. (2015) “Impact of Superplasticizer on the Hardening of Slag Portland Cement Blended with Red Mud”, *Construction and Building Materials,* 101: 432–39

IAI. (2020) "*Technology Roadmap: Maximising the Use of Bauxite Residue in Cement",* International Aluminium Institute

Lothenbach, B., Scrivener, K., and Hooton, R.D. (2011) “Supplementary Cementitious Materials”, *Cement and Concrete Research,* 41(12): 1244–56

Ruys, A. (2019) “Refining of Alumina: The Bayer Process”, *Alumina Ceramics*, Elsevier, 49–70

Scrivener, K.L., John, V.M. and Gartner, E.M. (2018) “Eco-Efficient Cements: Potential Economically Viable Solutions for a Low-CO2 Cement-Based Materials Industry”, *Cement and Concrete Research,* 114: 2–26

Scrivener, K.L., Juilland, P. and Monteiro, P.J.M. (2015) “Advances in Understanding Hydration of Portland Cement”, *Cement and Concrete Research,* 78: 38–56

Tapas, M.J. et al. (2021) “Efficacy of SCMs to Mitigate ASR in Systems with Higher Alkali Contents Assessed by Pore Solution Method”, *Cement and Concrete Research,* 142: 106353

The 16th International Congress on the Chemistry of Cement 2023 (ICCC2023)
"Further Reduction of CO_2 -Emissions and Circularity in the Cement and Concrete Industry"
September 18–22, 2023, Bangkok, Thailand

Development of supplementary cementitious materials using weathered volcanic eject

Y. Fukushima[1*], T. Ito[2*], M. Osaki[3*] and T. Saito[4*]

[1] *Mitsubishi UBE Cement Corporation, Ube, Japan*
Email: yuta.fukushima@mu-cc.com
[2] *Mitsubishi UBE Cement Corporation, Ube, Japan*
Email: Takayasu.ito@mu-cc.com
[3] *Mitsubishi UBE Cement Corporation, Ube, Japan*
Email: Masashi.osaki@mu-cc.com
[4] *Niigata university faculty of engineering, Japan*
Email: tsaito@niigata-u.ac.jp

ABSTRACT

Supplementary Cementitious Materials (SCMs), such as fly ash and blast-furnace slag are used to reduce CO_2 emissions from cement production. However, since these materials are by-products of coal-fired power generation and steel production, the use of renewable energy and the reduction of CO_2 emissions through increased recycling of energy-intensive materials such as metals will reduce the supply of conventional SCMs. Therefore, we need to investigate other available material resources.

Volcanic ejecta is rich in Japan. This material is composed volcanic glass, crystalline materials, pumice stone and weathering products. Volcanic glass is known as pozzolana. Japan Industrial Standard for volcanic glass for use in concrete (JIS A 6209:2020) recently has been established, and research has begun on its use in construction industry.

In this study, we focused on clay contained in weathered volcanic ejecta. The use of clay as a cementitious material has been reported using calcined clay such as metakaolin. Cement blended with calcined clay and limestone is known as LC^3. However, its use as cementitious material for industrial is difficult because the amount of kaolin produced is a little in Japan. Therefore, we are researching the feasibility of using the other clays which formed by weathering of volcanic ejecta and report the strength development of blended cements with calcined clay.

KEYWORDS: *SCMs, volcanic ejecta, weathering, strength, clay*

1. INTRODUCTION

Supplementary Cementitious Materials (SCMs) have been promoted as one of the ways to reduce CO_2 emissions from cement. Fly ash and blast furnace slag are commonly used as SCMs, but the supply of these materials will decrease due to the use of renewable energy and increased recycling of energy-intensive raw materials such as metals in the future.
The availability of calcined clay recently has been reported as a SCMs. Clay is an abundant resource worldwide, and especially kaolinite, a type of clay mineral, has been shown to increase pozzolanic reactivity by calcination (Fernandez et al (2011)). Scrivener et al（2018） reported Limestone calcined clay cement (LC3), using a mixture of calcined clay and limestone. However, the amount of kaolinite is a little in Japan, making a stable supply difficult, we must investigate new material resources.
Volcanic ejecta is a candidate material for use in the SCMs, this material is widely covered throughout Japan, especially in Hokkaido, Kanto, and Kyushu. Volcanic ejecta sediment is composed of volcanic glass, crystalline materials, pumice stone, and weathering products. Concrete with volcanic glass has been reported to have high compressive strength and good resistance to various chemical attacks (Labbact et al (2017)). In Japan, Japan Industrial Standard for volcanic glass for concrete (JIS A 6209:2020) has been established. Volcanic ejecta also begins to leach silicon, sodium, and potassium through weathering, eventually producing clays such as allophane and halloysite (Delmelle et al (2015)). These clays have a 1:1 overlapping crystal structure of Si-O tetrahedral and Al-O octahedral structures, like kaolinite, and are expected to be used as SCMs by calcination, but there are few reports using these materials.
In this study, we focused on the feasibility of using clay produced by weathering of volcanic ejecta and we evaluated the performance of calcined weathered volcanic ejecta containing allophane as SCMs.

2. EXPERIMENTAL

2.1 Materials

Ordinary Portland cement (OPC manufactured by Mitsubishi UBE Cement Co.) was used. OPC was composed of 58.8% alite, 14.5 % belite, 9.7% aluminate, and 9.0% ferrite. KANUMA soil (manufactured by Akagi Horticulture), contained allophane, 63% (KN) was used. The chemical compositions of the sample were determined by X-ray fluorescence (XRF). The chemical compositions of the materials are shown in Table1.

Table1 Chemical compositions of materials（mass%）

Materials	SiO_2	Al_2O_3	FeO_2	CaO	MgO	SO_3	Na_2O	K_2O	TiO_2	MnO	LOI
OPC	20.51	5.56	2.95	64.26	0.91	1.87	0.17	0.43	0.29	0.08	2.59
KN	42.52	33.75	2.32	1.25	0.23	0.03	0.89	0.56	0.33	0.06	17.6

2.2 Experiment

KN was calcined at 900°C for 1h (CKN). KN and CKN were used as SCMs. A fixed water-to-cement ratio of 0.50 was used for mixing mortar with a cement-to-sand ratio of 1:3 by mass. The prepared mortar was molded 40 mm×40 mm×160mm. After demolding, the mortar was cured at 7 and 28 days. The compressive strength test was measured under Japan Industrial Standard for Physical testing methods for cement (JIS R5201:2015). Pore volume in the binder was measured by the mercury intrusion porosimetry. Portlandite (CH) content in the binder was determined from the weight loss at 405-515 °C with the DTG curve.
X-ray diffractometer (XRD) patterns were collected with a Ni filter and Cu Kα radiation ($\lambda = 0.154$ nm) was generated at 30 kV and 10 mA. The specimens were investigated from 10° to 50° (2θ) with a step size of 0.02° and a measuring time of 0.8 s per step.
Al-NMR measurements were performed using the single-pulse method with a MAS frequency of 20 kHz, a pulse width of 90° (0.6 μS), a repetition wait time of 1 sec., and a total number of 256 integrations.

3. RESULT AND DISCUSSION

Fig. 1 shows the compressive strength of mortars with OPC-KN and CKN at 7 and 28 days. The mortar with CKN had improved compressive strength compared to KN, and the mortar with OPC:70% and CKN:30% seemed to have greater compressive strength than the mortar with OPC:100%.

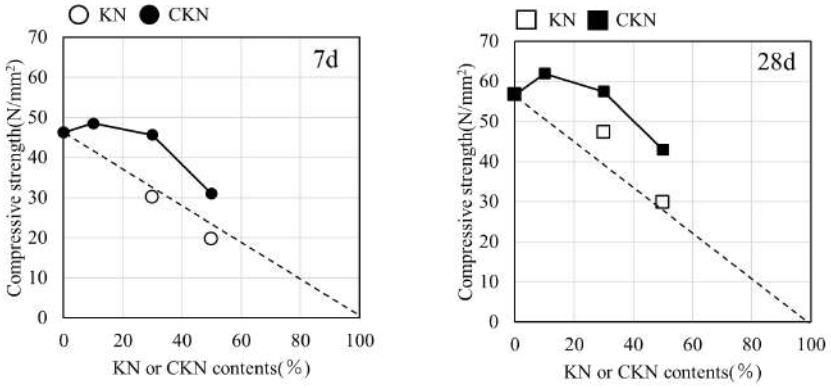


Fig. 1 Compressive strength of mortars used KN or CKN as SCMs at 7 and 28 days.

Fig. 2 shows the pore volume of the binder and compressive strength of the mortar. A negative correlation is obtained between the pore volume of the binder and compressive strength. The decrease in pore volume at 28 days indicates that the hydration reaction has progressed and the structure has become density.

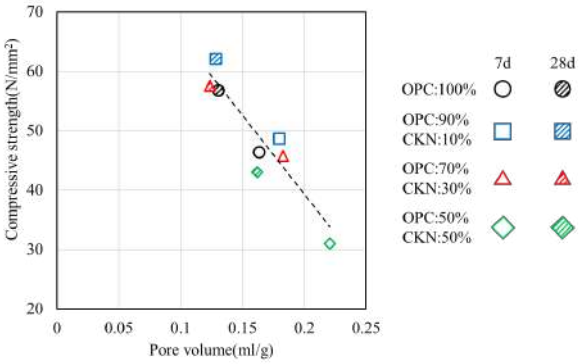


Fig. 2 Pore volume and compressive strength at 7 and 28 days.

Fig. 3 shows CH contents in the binder with different countents of CKN substitution. The dotted line in the figure represents the estimated amount of CH produced from OPC. The replacement of OPC with CKN shows that the amount of CH in the binder has decreased from the estimated value.This is likely due to the consumption of CH in the pozzolanic reaction.

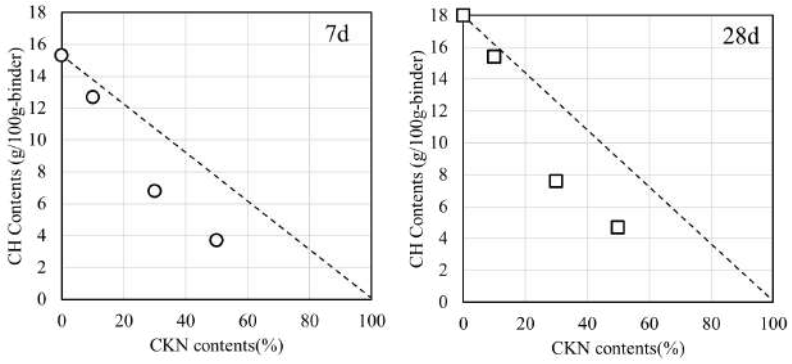


Fig. 3 CH contents in OPC-CKN binder at 7 and 28days.

Compressive strength of the mortar is enhanced by admixture of KN or CKN with OPC, and the effect is especially significant when CKN is mixed. Fig. 4 shows the XRD patterns and Al-NMR spectra for the influence of KN by calcination. KN and CKN have broad reflections at 17-35°(2θ). KN also has a broad reflection at 40°(2θ), which is an imogolite structure in allophane, which disappears in CKN, indicating that the crystal structure was destroyed partially by calcination. From the Al-NMR measurements, 4- and 6-coordinated peaks attributed to aluminum are observed in KN, and 4- and 6-coordinated and 5-coordinated peaks are observed CKN. 5-coordinated aluminum may be attributed to the breakdown of the allophane crystal structure due to calcination.

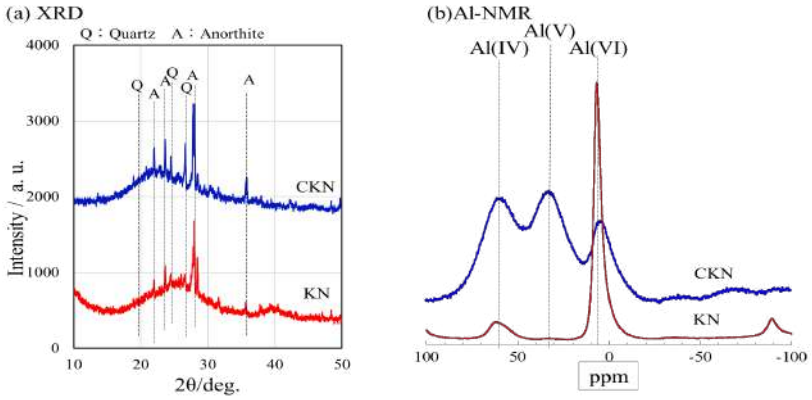


Fig. 4 (a) XRD patterns and (b) Al-NMR spectrums of KN and CKN.

4. Conclusion

In this study, we were researching the feasibility of using the other clays which formed by weathering of volcanic ejecta and report the strength development of blended cements with calcined clay. Compressive strength increased when CKN was used, and strength was retained up to 30% of the CKN of OPC substitution. The aluminum coordination number of KN is changed by calcination. This phenomenon was the same as kaolinite.

Acknowledgements

We received cooperation from Niigata University for solid-state NMR measurements in this research. Here we express our gratitude.

References

Brigatti M. F. et al (2006)" Structures and mineralogy of clay minerals", *Developments in Clay science*, Vol. 1：19-86

Castelein O. et al (2001) "The influence of heating rate on the thermal behaviour and mullite formation from a kaolin raw material", *Ceramics International*, 27：517-522

Delmelle P. et al (2015)" Volcanic Soils", *The Encyclopedia of Volcanoes*, Chapter72：1253-1264

Fernandez R. et al (2011) "The origin of the pozzolanic activity of calcined clay minerals A comparison between kaolinite, illite and montmorillonite", *Cem. Concr. Res.*, Vol. 41：113-122

Kitagawa Y. (1977) "Rapid Determination of Allophane and Amorphous Inorganic Materials in Soils"

Labbact Y. et al (2017) "The use of the volcanic powders as supplementary cementitious materials for environmental-friendly durable concrete" *Construction and Building Materials*, Vol. 133：468-481

Scrivner K. et al (2018) "Calcined clay limestone cements (LC^3)" *Cem. Concr. Res.*, Vol. 114：49-56

Tomoyose A. et al (2018) "Utilization of volcanic ejecta as a high performance supplementary cementitious materials by gravity classification and pulverization." *RILEM Technical Letters,(3)*：66-74

https://soil-inventory.rad.naro.go.jp/explain/D.html

The 16th International Congress on the Chemistry of Cement 2023 (ICCC2023)
"Further Reduction of CO_2 -Emissions and Circularity in the Cement and Concrete Industry"
September 18–22, 2023, Bangkok, Thailand

Beyond kaolinite content: untangling the influence of other clay properties on the reactivity of calcined clays

A.T.M. Marsh[1], Y. Dhandapani[2], S. Krishnan[3], S. Rahmon[4], M.C.G. Juenger[5] and S.A. Bernal[6*]

Email: A.Marsh@leeds.ac.uk
[1]*School of Civil Engineering, University of Leeds, Leeds, United Kingdom*

Email: Y.Dhandapani@leeds.ac.uk
[2]*School of Civil Engineering, University of Leeds, Leeds, United Kingdom*

Email: S.Krishnan1@leeds.ac.uk
[3]*School of Civil Engineering, University of Leeds, Leeds, United Kingdom*

Email: ushsar@leeds.ac.uk
[4]*School of Civil Engineering, University of Leeds, Leeds, United Kingdom*

Email: mjuenger@mail.utexas.edu
[5]*Architectural and Environmental Engineering, University of Texas at Austin, USA*

Email: S.A.BernalLopez@leeds.ac.uk
[6]*School of Civil Engineering, University of Leeds, Leeds, United Kingdom*

ABSTRACT

Vast quantities of clays are available worldwide for the production of supplementary cementitious materials. However, they have a drawback – their variation in mineralogy and purity. The correlation between kaolinite content and reactivity is well-established for kaolinitic clays. However, a detailed understanding remains incomplete for other mineralogical factors that could also influence reactivity. This study investigated over twenty different kaolinitic, montmorillonitic and mixed clays from various locations and geological origins. Mineralogical and chemical composition were measured via standard characterization techniques. Clays were calcined in a laboratory static furnace; some industrially-calcined clays were also sourced. Chemical reactivity was measured using 7-day cumulative heat via the R3 method (ASTM C1897-20). The influence on early age hydration of blended Portland cements (30 wt.% replacement) was investigated via isothermal calorimetry. A calcined high-purity montmorillonitic clay had equivalent reactivity to a 50% metakaolin calcined clay. In mixed mineralogy clays, Fe-based associated minerals contributed to higher specific surface area; this in turn accelerated hydration kinetics in blended cements containing those calcined clays, leading to under-sulphation. These findings highlight that mixed clays, found in many world regions, have potential beyond what their kaolinite content alone suggests – however, they do present additional challenges around characterization and blend formulation. Whilst kaolinite content can be a useful 'rule of thumb' in screening clays, it cannot be solely relied upon as an accurate predictor of reactivity and other key parameters to formulate a blend composition.

KEYWORDS: *associated minerals; blended cements; calcined clays; chemical reactivity; kaolinite*

1. Introduction

To exploit diverse clay resources from a variety of locations for the large scale adoption of calcined clay cement, several research challenges remain. These include understanding how different mineralogical factors affect the reactivity of calcined clays and how to effectively design formulations of calcined clay blended cements. Alongside kaolinite, many different types of clay minerals can be present in clays. 2:1 clay minerals have a layer structure consisting of an octahedral sheet sandwiched between two tetrahedral sheets. This layer structure gives 2:1 clay minerals lower intrinsic reactivity than kaolinite (Fernandez et

al., 2011), yet they can still make a modest contribution to reactivity. 'Associated minerals' refer to all other minerals in a clay which are not classified as clay minerals. Whilst associated minerals are largely (but not exclusively) unreactive, they can strongly influence the physico-chemical properties of clays (e.g. specific surface area, adsorption capacity), which could then influence workability and early age hydration kinetics of calcined clay cements. In the United Kingdom (U.K.) and in southern areas of the United States of America (U.S.A.), there are substantial resources of 2:1 clay deposits and mixed mineralogy clays. The mineralogical composition of these clays deviates significantly from the 'classic' kaolinitic clays on which the majority of research has been carried out. Kaolinite content has been a highly effective predictor of performance for some kaolinitic clays (Avet and Scrivener, 2018). But to facilitate the adoption of the low purity and/or mixed mineral clays of the U.K. and southern U.S.A., they need to be assessed on their reactivity potential, rather than solely on their kaolinite content. It is imperative to relook at the composition-processing-performance relationships for clays based on reactivity alone, as calcined clays with similar reactivity could present challenges during blend formulation (Zunino et al., 2022). This study uses data for a range of clays from the U.K. and U.S.A. to highlight how mineralogical factors beyond kaolinite can influence calcined clays' reactivity, as well as the reaction kinetics and blend formulation of calcined clay blended cements.

2. Materials and Methodology

Six clays were chosen from 22 sourced clays (11 from the U.K. and 11 from the U.S.A), and classified into three categories, based on their mineralogy. Kaolinitic clays contained kaolinite as the sole clay mineral ("Kn" prefix); mixed clays contained ≥2 clay minerals (e.g. MixedClay_B contained kaolinite and chlorite) or a high proportion of Fe-rich associated minerals (e.g. MixedClayA contained 29 wt.% goethite) ("MixedClay" prefix), and montmorillonitic clays contained montmorillonite as the sole clay mineral ("Mnt" prefix). Table 1 lists the kaolinite content obtained using TGA, and montmorillonite content using Quantitative XRD with a 10% ZnO internal standard. The clays were calcined for 1 hour in a static furnace at the calcination temperatures listed in Table 1, or industrially calcined. Specific surface area (SSA) of calcined clays were measured via the BET method for N_2 sorption isotherms, degassed at 135°C for ≥5 h.

Table 1: Summary of source clays and calcination temperatures. SSA values are for post-calcination.

Reactivity groups	Clay notation	Kaolinite (wt.%)	Montmorillonite (wt.%)	Calcination temperature (°C)	SSA (m^2g^{-1})	d_{50} (µm)
Group A	Kn_A	50%	-	Flash calcined industrially	13.9	24.2
	MixedClay_A	48%	-	Flash calcined industrially	60.9	8.1
	Mnt_A	-	78%	820 °C	47.9	14.1
Group B	Kn_B	26%	-	800 °C	4.8	82.9
	MixedClay_B	29%	-	800 °C	21.0	8.0
	Mnt_B	-	61%	820 °C	5.6	47.6

Reactivity of the calcined clays was measured via the R3 test cumulative heat method (ASTM, 2020), using a TAM Air isothermal calorimeter. Blended cement pastes were prepared with a 52.5R ordinary Portland cement from Heidelberg cement, using a 30 wt.% replacement ratio. Reaction kinetics of the blended cements were measured at 20°C for 9 g of paste, using a TAM Air isothermal calorimeter.

3. Results and Discussion

3.1 Influence of 2:1 clay minerals and associated minerals on reactivity

Data for the calcined clays are plotted in two groups, based on their similar range of R3 cumulative heat (Table 1): 400-550 J / g of SCM for Group A (Fig.1A,C) and 300-350 J / g of SCM for Group B (Fig.1B,D). All these calcined clays were classified as 'moderately reactive' (>190 J / g of SCM, 90% confidence limit) as per Londono-Zuluaga et al. (2022). Despite their lack of meta-kaolinite, Mnt_A and Mnt_B exhibit similar 7 day reactivity to the two calcined kaolinitic clays Kn_A and Kn_B, albeit these latter two have a

lower clay mineral content. A distinct difference between these calcined clays' cumulative heat curves is the kinetics of heat evolution, shown in the profile of the cumulative heat curves – Mnt_A and Mnt_B react more slowly, and exhibit non-negligible heat flow at 7 days. Fig.1B presents the cumulative heat curves from the R3 test for the Group B calcined clays. Despite the as-received clays containing similar proportions of montmorillonite, Mnt_A has a noticeably higher 7 day cumulative heat (502 J/g of SCM) than Mnt_B (358 J/g of SCM). This difference is partly attributed to the siliceous associated mineral opal-CT in Mnt_A, as previously observed in similar montmorillonitic clays (He et al., 1996). These examples show how 2:1 clay minerals and associated minerals can make non-negligible contributions to reactivity, which is especially relevant for moderately reactive calcined clays.

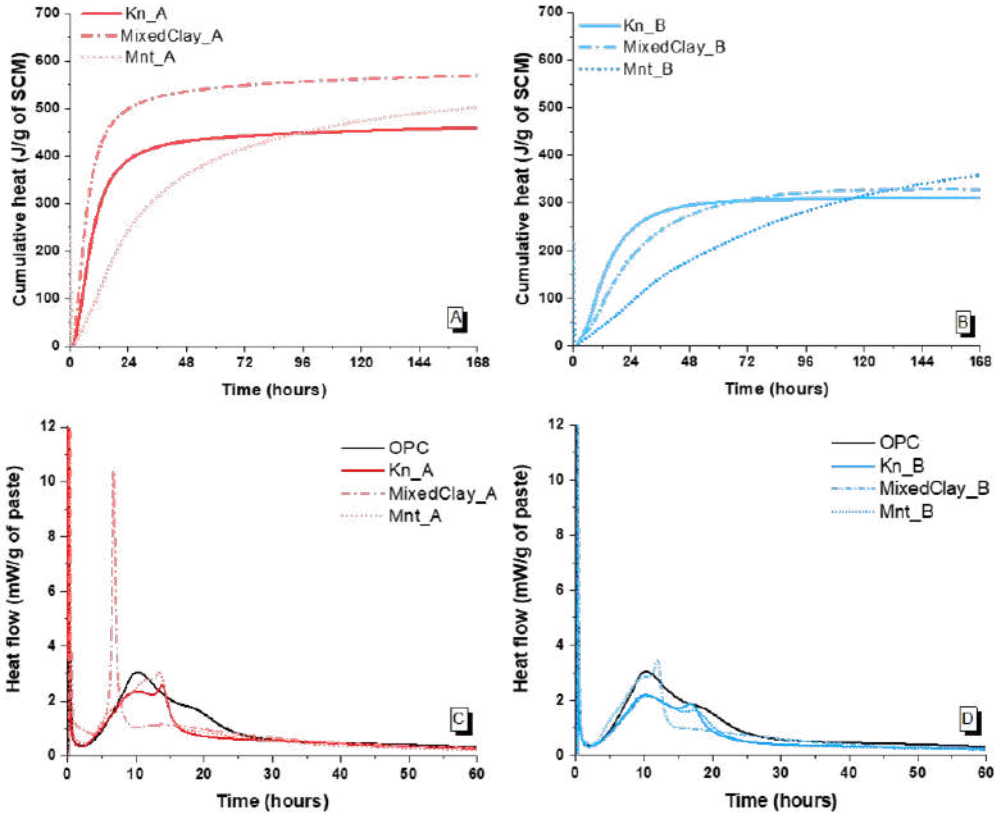


Figure 1: A, B) R3 cumulative heat for calcined clays; C, D) heat flow for calcined clay blended cements.

3.2 Influence of specific surface area on reaction kinetics

Kn_A and MixedClay_A had very different specific surface areas (13.9 and 60.9 m^2/g, respectively), but similar kaolinite content (50 and 48 wt.%, respectively) in their un-calcined clays. Despite having similar reactivity (Fig.1A), the reaction kinetics of their calcined clay blended cements are markedly different (Fig. 1C). The high intensity and early onset of the aluminate peak centred at ~8 hours in MixedClay_A was attributed to enhanced heterogenous nucleation of aluminate phases on extremely fine particles, consistent with its high specific surface area. This was likely to involve the meta-kaolinite themselves – given the MixedClay_A has a lateritic origin, the meta-kaolinite particles are very fine and likely to be highly disordered. A similar earlier onset and higher intensity of aluminate peak for a calcined clay with higher specific surface area was attributed by Tironi et al. (2014) to more extensive structural disorder of kaolinite in the un-calcined clay. Another possible contribution to enhanced nucleation came from extremely fine particles of hematite, which made up 24 wt.% of MixedClay_A. The comparison between Kn_A and MixedClay_A demonstrates the influence that the nature of the meta-kaolinite in a calcined clay (beyond meta-kaolinite content alone), and its associated minerals, can have on reaction kinetics in calcined clay blended cements. Beyond this direct comparison of Kln_A and MixedClay_A, for a range of calcined kaolinitic clays, mixed clays and 2:1 clays, Fig.2 shows that the aluminate peak tends to occur earlier in clays with higher specific surface area.

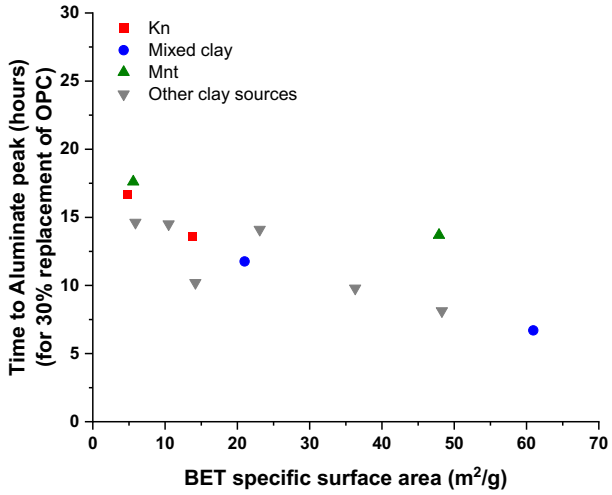


Figure 2: Time to aluminate peak in calcined clay cements as a function of calcined clays' BET surface area

4. Conclusions

Comparing calcined clays with similar reactivity, there was substantial variation in the reaction kinetics in the R3 test and also in the hydration kinetics of calcined clay cements, both of which influence the formulation of binders. Given that specific surface area can be strongly influenced both by the type of clay minerals and associated minerals present in a clay, it is important to understand the various possible mineralogical contributions to sulphate depletion before designing a blend formulation. On a practical basis, it is advisable to measure the specific surface area of a given calcined clay to optimise sulphate adjustments. Whilst kaolinite content may remain the single most important attribute in many kaolinitic clays, this study highlights that the content of 2:1 clay minerals and specific surface area are significant factors affecting reactivity and reaction kinetics for clay resources with non-kaolinitic or mixed clay mineralogy.

Acknowledgements

This study was sponsored by the UK Engineering and Physical Sciences Research Council (EPSRC) via the Early Career Fellowship EP/R001642/1 and EP/T008407/1, and the US National Science Foundation via award 1903457.

References

ASTM (2020) "C1897 − 20. Standard Test Methods for Measuring the Reactivity of Supplementary Cementitious Materials by Isothermal Calorimetry and Bound Water Measurements", West Conshohocken, PA: ASTM International.

Avet, F. and Scrivener, K. (2018) "Investigation of the calcined kaolinite content on the hydration of Limestone Calcined Clay Cement (LC3)", *Cement and Concrete Research,* 107**,** 124-135.

Fernandez, R., Martirena, F. and Scrivener, K.L. (2011) "The origin of the pozzolanic activity of calcined clay minerals: A comparison between kaolinite, illite and montmorillonite", *Cement and Concrete Research,* 41**,** 113-122.

He, C., Makovicky, E. and Osbaeck, B. 1996. "Thermal treatment and pozzolanic activity of Na- and Ca-montmorillonite", *Applied Clay Science,* 10**,** 351-368.

Londono-Zuluaga, D., Gholizadeh-Vayghan, A., Winnefeld, F., Avet, F., Ben Haha, M., Bernal, S.A., Cizer, Ö., Cyr, M., Dolenec, S., Durdzinski, P., Haufe, J., Hooton, D., Kamali-Bernard, S., Li, X., Marsh, A.T.M., Marroccoli, M., Mrak, M., Muy, Y., Patapy, C., Pedersen, M., Sabio, S., Schulze, S., Snellings, R., Telesca, A., Vollpracht, A., Ye, G., Zhang, S. & Scrivener, K.L. (2022) "Report of RILEM TC 267-TRM phase 3: Validation of the R3 reactivity test across a wide range of materials", *Materials and Structures,* 55 **(**142).

Tironi, A., Trezza, M.A., Scian, A.N. and Irassar, E.F. (2014) "Thermal analysis to assess pozzolanic activity of calcined kaolinitic clays", *Journal of Thermal Analysis and Calorimetry,* 117**:** 547-556

Zunino, F., Dhandapani, Y., Ben Haha, M., Skibsted, J., Joseph, S., Krishnan, S., Parashar, A., Juenger, M. C. G., Hanein, T., Bernal, S. A., Scrivener, K. L. and Avet, F. (2022) "Hydration and mixture design of calcined clay blended cements: review by the RILEM TC 282-CCL", *Materials and Structures*, 55 (234).

The 16th International Congress on the Chemistry of Cement 2023 (ICCC2023)
"Further Reduction of CO_2 -Emissions and Circularity in the Cement and Concrete Industry"
September 18–22, 2023, Bangkok, Thailand

Use Of Supplementary Cementitious Materials For Composite Cements: An Overview

Anwesa Satapathy[1]* and Shashank Bishnoi[1]

[1] *Department of Civil Engineering, IIT-Delhi, New Delhi, India*

Email: anwesasatapathy.as@gmail.com, bishnoi@iitd.ac.in*

ABSTRACT

The cement industry has witnessed a significant advancement in the recent times; however, it still contributes to 5-8% of global carbon dioxide emissions annually. One of the primary approaches to reduce the carbon footprint of the cement production process is by the partial substitution of clinker with several supplementary cementitious materials (SCMs) like slag, fly ash, calcined clay, etc. This paper aims to present a comprehensive overview of various SCMs used in composite cements (CC). The influence of incorporation of ultrafine materials has also been reviewed. This study considers an approach where a synergistic design of binders based on their chemical and physical characteristics, such as particle size and morphology, is carried out so as to achieve an acceptable performance in concrete, without the need for a high clinker content. The work presents data that will help push the limits of existing standards, further reducing clinker content using traditional SCMs.

KEYWORDS: *Low-clinker cement, Composite cement, Supplementary cementitious materials, Fly-ash, Slag*

1. Introduction

Cement has become one of the largest mass-produced materials on Earth. With rapid urbanization and infrastructure development, this demand will only increase over time. However, the cement industry is responsible for about 5-8 % of anthropogenic carbon emissions (Scrivener et.al.). Thus comes the need for more ecologically sustainable materials. There are various approaches to this out of which the most effective method is to reduce the clinker content. Cement has to be replaced with other cementitious materials to achieve a lower clinker content. Some commonly used supplementary cementitious materials are fly ash, slag, silica fume, etc. While reducing clinker content has become a new trend among researchers it is also important to produce an economically sustainable product that satisfies the current requirements. Extensive research has been conducted on various supplementary cementitious materials such as fly ash, slag, etc.

The use of slag dates back to the early 1960s in India while the utilization of fly ash in cement was around the late 1990s.(Kaur et. al.) While slag has been used up to 90% replacement, the use of fly ash generally limits between 50-60%. This lower use of fly ash is mainly due to its inhomogeneity. The present work analyses the use of various SCMs in producing low-clinker cement as well as studying the various factors affecting the strength and durability of these cements.

2. Overview of various SCMs used for cement replacement

2.1 Fly ash and Slag

Fly ash is a by-product of thermal power plants, produced from coal combustion and obtained by air classification. Fly ash exhibits cementitious properties only upon activation. Fly ash is classified as Class F and Class C fly ash. According to ASTM C 618, Class C fly ash possesses cementitious and pozzolanic properties whereas class F fly ash only has pozzolanic properties. Class F fly ash is common in India and

used for major construction practices. Due to its spherical shape and finer size, better packing and reduced water demand have been observed. Specimens with fly ash generally tend to have lower early strength. It is due to its dependency on CH, which is produced at later stages of cement hydration. (Giergiczny et. al. 2019) Reactivity of fly ash also depends on the glass content also known as basicity.(Sakai et. al. 2004)
Slag is a by-product of the steel industry, produced from melting of pig iron. Due to higher calcium content the replacement level is higher than that of fly ash. Slag has latent hydraulic property. It only needs activation. (Giergiczny et. al. 2019)

The amount of slag produced is much less than that of cement and fly ash and tends to decrease in the near future due to the shutting of steel industries in many countries. So even if we can replace clinker in large proportion with slag it won't be an ecologically viable solution.
So, it becomes necessary to find a suitable product that is abundantly available in the surroundings to produce an eco-efficient cement.

2.2 Ultra-fine materials

Considering the availability of various SCMs, it is essential to produce cement with readily available raw materials. Thus, the inclination to move towards finer cements is increasing daily. Use of finer materials in the system helps in increasing the packing density, providing a denser microstructure and hence helps in improving the durability. Various ultrafine materials used among the researchers are nano silica, ultrafine fly ash (UFFA), ultrafine blast furnace slag (UFBFS), metakaolin (MK), etc.
Ultrafine fly ash (UFFA) is generally obtained by mechanical grinding of the fly ash. They have similar composition as fly ash but vary in particle size and morphology which upgrades the activation of fly ash. UFFA contains more amorphous content than fly ash which helps accelerate the pozzolanic reaction. When combined with High volume fly ash (HVFA), UFFA tends to overcome the lower early strength due to increased pozzolanic activity and provide better-performing cement. (Shaikh et. al 2015, Han et. al. 2019) Typical usage of these finer materials ranges from 8-12%. An increase in finer materials in a system affects the transport properties too. The various benefits observed with having UFFA in the system are a denser microstructure, enhancement in compressive strength, minimized cracking, alkali-silica reaction, etc. Figure 1, shows that having only ultrafine material in the cement can result in a major increase in the strength of the concrete. Apart from strength, these materials also have a significant role in chloride resistance, water sorptivity, workability, etc. Figure 2 represents the amount of charge passed through particular sample. The amount of charge passed is inversely related to the resistivity of the structure to chloride ion penetration. (Dave et al. 2016) Metakaolin is another ultrafine material that has high pozzolanic activity. It helps improve concrete quality like workability, strength, etc. it also helps improve the chloride ingress resistance, reducing chloride-induced corrosion, helps in reducing autogenous shrinkage, alkali-aggregate reaction, etc. (Li et. al. 2002) Despite having all these advantages, one of the major issues with metakaolin is that of fluidity.
In order to overcome the disadvantages of the above materials, the use of ternary and quaternary binders came into the research. Combining various materials showed a synergistic effect, which helped overcome the disadvantage of one over the other and enhance the overall performance.

Table 1 Composite cements

No.	Cement Composition	w/b	Properties	Ref.
1	OPC with 30, 50, 70, 90% replacement with superfine blast furnace slag	0.4	Significant increase in mechanical properties of 70% sample. The addition of nanosilica further improved the performance.	Jiang et. al.
2	OPC with 30 and 50% FA replacement OPC with 30FA, 10SF and 10GGBS (1:3,1:4 binder:sand exhibited better results)	0.5	Delayed setting time, 30%FA showed better compressive strength at 90 days Better binder strength, better resistance to charge passed, delayed setting time.	Dave et. al.
3	OPC with 20, 40 and 50% slag by volume replacement	0.4	Lower early strength in binary blend, Accelerated slag hydration in presence of LS, increase in total porosity at later stages	Arora et. al.

4	OPC with 20, 40, 60% FA (2 basicity of FA considered: 0.24 and 0.40)	0.4	Glass content of FA → basicity of FA affects the reactivity and thereby the pore structure FA addition affected cement hydration	Sakai et. al.
5	OPC + BFS (Blast furnace slag) + LS (Limestone)	0.32	LS filler reduces heat flow, provide nucleation site and dilution effect, Slag and LS combinedly reduced chemical shrinkage, refined pore structure along with filling effect. Reduced early age mechanical performance and delay in cracking time with increasing 10-20% LS dosage	Bouasker et. al.
6	OPC with 30%FA and 15%LS (3 types of LS used based on dolomitic content and two types of FA based on fineness)	0.4	Finer FA showed better performance than coarser FA. Better strength observed for lower dolomitic limestones. Better strength development for ternary blend when compared with binary blends → due to synergistic effect Decrease in bound water content.	Aritra Pal
7	High volume fly ash with UFFA : UFFA8% and 12% with 40 and 60% FA.	0.4	Only UFFA – reduced workability, 8%UFFA exhibited better strength, decreased rate of water absorption, better chloride resistance HVFA showed better workability than OPC, better sorptivity, significant corrosion observed 32HVFA + 8UFFA – greater workability, improved compressive strength than HVFA, reduced capillary absorption, lowest chloride ion penetration at 28 days, denser microstructure due to increased reactivity, better corrosion resistance due to synergistic effect.	Shaikh et. al.

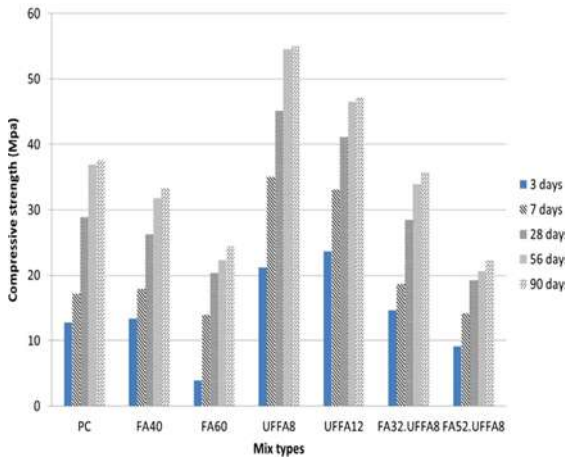


Figure 1 Compressive strength of FA, UFFA and ternary mix (Shaikh et. al. 2015)

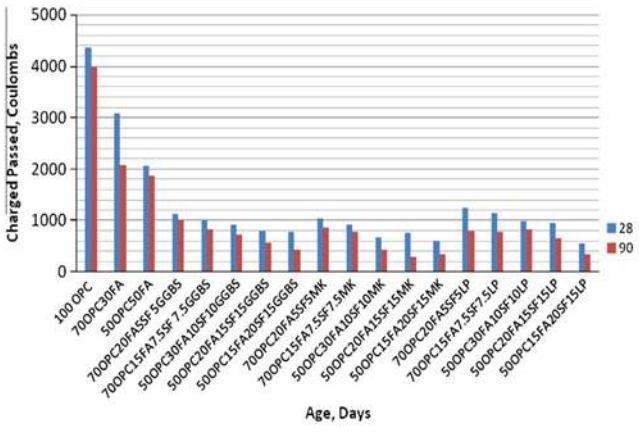


Figure 2 Amount of Charge passed through various blends (Dave et. al. 2016)

3. Conclusions

Need to find sustainable options is increasing with increasing demand of concrete. One of the effective ways of doing that is by lowering the clinker content and substituting it with other supplementary cementitious materials. The most common SCMs being FA, GGBFS, SF, etc. Blended cements with ternary and quaternary systems have often been found to be useful in enhancing the mechanical performance and durability of the concrete. The addition of ultrafine materials helps in further enhancement of the performance. Thus, this study presents an overview of how combining various SCMs can produce better blended cements as well as producing low cost and ecologically efficient cement.

Acknowledgment:

The authors are grateful for the financial support provided by Ecocem for conducting this research work.

References

Environment, U. N., Scrivener, K. L., John, V. M., & Gartner, E. M. (2018). Eco-efficient cements: Potential economically viable solutions for a low-CO2 cement-based materials industry. *Cement and concrete Research*, *114*, 2-26.

American Society for Testing and Materials. (2012). ASTM C 618-Standard specification for coal fly ash and raw or calcined natural pozzolan for use in concrete. West Conshohocken: ASTM.

Shaikh, Faiz UA, and Steve WM Supit. (2015) "Compressive strength and durability properties of high volume fly ash (HVFA) concretes containing ultrafine fly ash (UFFA)," *Construction and building materials* 82: 192-205.

Kaur, A., Bishnoi, S., & Bhattacharjee, B. (2017). Characteristics of fly ashes in India for use in cement and concrete. *Advances in Cement Research*, *29*(6), 258-268.

Shaikh, F. U., & Supit, S. W. (2015). Compressive strength and durability properties of high volume fly ash (HVFA) concretes containing ultrafine fly ash (UFFA). *Construction and building materials*, *82*, 192-205.

Li, Z., & Ding, Z. (2003). Property improvement of Portland cement by incorporating with metakaolin and slag. *Cement and concrete research*, *33*(4), 579-584.

Pal, A. (2018). Developing low-clinker ternary blends for indian cement industry. *Journal of The Institution of Engineers (India): Series A*, *99*, 433-447.

Dave, N., Misra, A. K., Srivastava, A., & Kaushik, S. K. (2016). Experimental analysis of strength and durability properties of quaternary cement binder and mortar. *Construction and Building Materials*, *107*, 117-124.

Giergiczny, Z. (2019). Fly ash and slag. *Cement and Concrete Research*, *124*, 105826.

Bouasker, M., Khalifa, N. E. H., Mounanga, P., & Kahla, N. B. (2014). Early-age deformation and autogenous cracking risk of slag–limestone filler-cement blended binders. *Construction and Building Materials*, *55*, 158-167.

Han, X., Yang, J., Feng, J., Zhou, C., & Wang, X. (2019). Research on hydration mechanism of ultrafine fly ash and cement composite. *Construction and Building Materials*, *227*, 116697.

Sakai, E., Miyahara, S., Ohsawa, S., Lee, S. H., & Daimon, M. (2005). Hydration of fly ash cement. *Cement and Concrete Research*, *35*(6), 1135-1140.

Arora, A., Sant, G., & Neithalath, N. (2016). Ternary blends containing slag and interground/blended limestone: Hydration, strength, and pore structure. *Construction and Building Materials*, *102*, 113-124.

The 16th International Congress on the Chemistry of Cement 2023 (ICCC2023)
"Further Reduction of CO_2 -Emissions and Circularity in the Cement and Concrete Industry"
September 18–22, 2023, Bangkok, Thailand

Application of Interparticle Spacing Model to Maximize Filler Content in Cementitious Pastes

D.A. Silva[1]*, R.G. Pileggi[2], M.S. Rebmann[2], A.J. Aldykiewicz Jr.[1], J.G. Hemrick[1], W.Y. Tsai[1]

[1] *Oak Ridge National Laboratory, Oak Ridge, United States*
Emails: silvada@ornl.gov, aldykiewajjr@ornl.gov, hemrickjg@ornl.gov, tsaiw@ornl.gov
[2] *University of São Paulo, São Paulo, Brazil*
Emails: rafael.pileggi@lme.pcc.usp.br, markus.rebmann@lme.pcc.usp.br

ABSTRACT

One of the most impactful ways to reduce concrete's embodied carbon in the near term is by partially replacing Portland cement with supplementary cementitious materials and/or fillers. This article describes an approach to reduce cement content in concrete through the development of high filler, low water (HFLW) cementitious pastes. Pastes with cement content as low as 50% (% weight of fines) were designed by applying models that maximize the particle packing density and that calculate interparticle spacing (IPS), thereby enabling pastes with higher solids concentration and lower water demand. Strong correlations were found between IPS, the consistency index of the Herschel-Bulkley rheological model, and cement hydration kinetic parameters of pastes containing Portland limestone cement and up to two different types of ground limestone. The approach showed to be feasible for the design of HFLW concrete paste fraction.

KEYWORDS: *limestone filler, interparticle spacing, particle packing model, HFLW concrete*

1. Introduction

The improvement of cement efficiency use in the design and production of cement-based materials is being pointed out as one of a few measures that have the potential to importantly decrease carbon emissions by the concrete industry in the near term (Habert et al, 2020). An approach to improve cement efficiency involves the minimization of the porosity of the granular skeleton of concrete mixtures combined with rheology adequacy, allowing cement use reduction by as much as 70% and water reduction by as much as 50% (John et al, 2018). In such an approach, fillers partially replace cement and fill the voids between cement particles, resulting in high filler, low water systems (HFLW). The simultaneous reduction of cement and water can provide concrete mixtures with similar or superior performance properties, and similar or reduced cost compared to conventional concrete. However, rheological adequacy must be ensured because the higher packing density can be detrimental to concrete flow. In this article, the initial technical steps taken to apply the HFLW concrete design approach to one precast producer in the United States are described. The precast concrete industry was selected for being less challenging in this initial introductory phase of the technology due to less demanding slump retention requirements.

2. Materials and Methods

One ASTM Type IL Portland cement (Portland Limestone Cement or PLC) and two grades of ground limestone (Fillers 1 and 2) were used. Their compositions determined by X-ray fluorescence and Rietveld-refined X-ray diffraction are shown in Table 1, along with their particle size distributions (laser diffraction of isopropanol-diluted samples in a Microtrac SYNC instrument), specific surface areas (BET SSA from N_2 adsorption isotherms using the Brunauer–Emmett–Teller method in a Micromeritics 3Flex; fillers dried for 16 hours under vacuum at 200ºC and PLC at 40ºC under constant N_2 flow). Filler 1 is >96% pure $CaCO_3$ that is expected to occupy the voids between PLC grains due to its higher fineness. Filler 2 is a >98% pure dolomitic limestone coarser than PLC and should fill the voids between cement and sand grains. A commercially available polycarboxylate ether (PCE)-based dispersant with 33% total solids was used.

Table 1 – Composition and physical properties of cement and fillers (all percentages are on weight basis)

Parameter	*PLC*	*Filler 1*	*Filler 2*
SiO_2 (%)	18.44	1.31	1.3
Al_2O_3 (%)	4.07	0.22	0.24
Fe_2O_3 (%)	3.05	0.09	0.15
CaO (%)	62.16	53.74	30.4
MgO (%)	2.15	0.63	20.13
SO_3 (%)	3.18	0.02	0.23
Na_2O (%)	0.09	0.01	<0.01
K_2O (%)	0.52	0.02	0.04
L.O.I. (%)	5.62	43.4	46.87
D(10) (μm)	1.225	1.097	4.9
D(50) (μm)	9.22	3.960	65.72
D(95) (μm)	37.68	8.510	395.5
Mean ϕ (μm)	13.93	4.130	111.5

Parameter	*PLC*	*Filler 1*	*Filler 2*
C_3S (alite) (%)	63.1	-	-
C_2S (belite) (%)	7.9	-	-
Cubic C_3A (%)	3.1	-	-
C_4AF (ferrite) (%)	9.3	-	-
Gypsum (%)	3.7	-	-
CaO (free lime) (%)	1.3	-	-
$Ca(OH)_2$ (portlandite) (%)	0.6	-	-
MgO (periclase) (%)	1.4	-	-
$CaCO_3$ (calcite) (%)	8.6	96.3	1.2
$MgCa(CO_3)$ (dolomite) (%)	0.5	0.5	98.4
SiO_2 (quartz) (%)	0.7	3.2	0.4
SSA (m^2/g)	1.37	2.00	0.71
Density (g/cm^3)	3.068	2.831	2.920

$$IPS = \frac{2}{VSA} x \left[\frac{1}{\phi s} - \left(\frac{1}{(1-Pof)}\right)\right] \quad (1)$$

The algorithm developed by Westman and Hugill (1930) for discrete spherical particle size distributions was used to identify the minimum porosity (P_{of}) of the pastes. Together with the volumetric specific area of the dry mixture of particles (*VSA*) and the volume fraction of each solid (ϕ_s), P_{of} was used to determine the interparticle spacing (IPS, Equation 1). The IPS concept, introduced by Funk and Dinger (1994), generically determines the viscosity of a dispersion, which decreases as IPS increases (Pileggi et al, 2000). Pastes containing PLC and one or two fillers were mixed in a high shear blender as described by ASTM C1738/C1738M-19 (*High-Shear Mixing of Hydraulic Cement Pastes*) to maximize particle dispersion and minimize the influence of mixing on the rheological history of the pastes. The dispersant was first dissolved in distilled water, and this solution was transferred to a jacketed blender kept at 23ºC. PLC was added to the blender within 10 seconds, and the blender turned on at 500 r.p.m. followed by filler addition within 10 and 30 seconds of mixing at 4.000 r.p.m., 30 seconds of mixing at 10.000 r.p.m, 10 seconds of scraping, 140 seconds of rest, and 30 seconds of mixing at 10.000 r.p.m., totalling 4 minutes mixing. The pastes were immediately submitted to rheometry and isothermal calorimetry.

Paste rheometry was measured using a sand-blasted concentric cylinder geometry with a 26.66 mm diameter cylinder and 1mm measuring gap in an Anton Paar MCR 302e rheometer equipped with a Peltier temperature control device kept at 23ºC using a tested paste volume of approximately 19.3 cm^3. The rheometry routine included a $10s^{-1}$ pre-shear step for 10 seconds followed by two identical cycles where the shear rate was ramped up and down between 0 and $300s^{-1}$ for 60 seconds for each ramp, in a total of 4 minutes testing after pre-shearing. Shear stress and apparent viscosity during the second upward ramp from 0 to $300s^{-1}$ (or 3rd testing interval) were analyzed with most tests replicated or triplicated.

Isothermal calorimetry was performed using an eight-cell Calmetrix Ultra-Cal isothermal calorimeter set at 23ºC. Paste samples weighing around 7 grams were introduced in the calorimeter around 5 minutes and 30 seconds after cement and water came into contact and heat flow data was acquired for up to 48 hours. The impact of dispersant and fillers on selected kinetic parameters of PLC hydration was assessed.

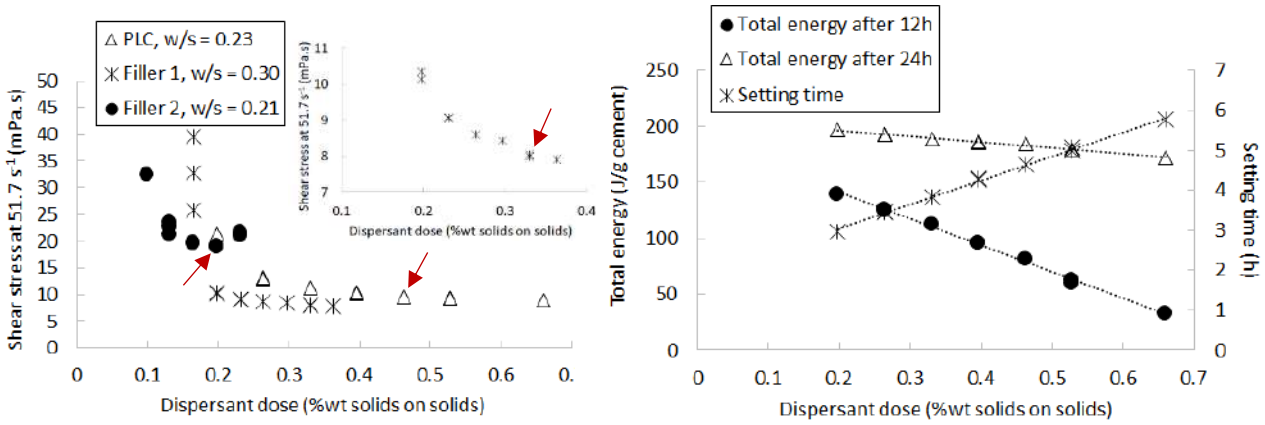
An effective application of particle packing models for the design of concrete's fine fraction requires all particles to be fully dispersed. Hence, an effective dispersant must be added to overcome interparticle attractive forces and agglomeration until concrete placement. The impact of dispersant dose on flow curves and hydration kinetics of unitary pastes was assessed to find the amount needed in binary and ternary pastes.

3. Results

3.1 Determination of dispersant content

Firstly, the water content for the maximum possible solid concentration was determined in unitary pastes following the procedure described by Fennis (2011). The dispersant dose required for the unitary pastes to achieve the lowest apparent viscosity, shear stress, and hysteresis was selected. Some of the rheometry

results are shown in Fig. 1(a) and Fig. 1(b) shows the impact of the dispersant on the hydration kinetics of unitary PLC pastes. The dispersant has a linear retardation effect on setting times and total heat evolved after 12 and 24 hours. Using weighed average approach, the calculated dispersant dose in binary and ternary pastes should range between 0.33% and 0.42% s/s (% weight of solids on solids), which is substantially higher than typically added to conventional concrete. The authors opted to use the lowest value (0.33%wt s/s) to minimize retardation of cement hydration. The results shown in Fig. 1 indicate that a balance between the desired dispersion effect and the required engineering properties of the concrete must be considered for a successful application of the HFLW concrete technology, especially for concrete elements that are subjected to early loading, such as precast/prestressed concrete.



(a) (b)

Figure 1 – (a) Shear stress at 51.7s^{-1} as a function of dispersant dose for unitary pastes, with dose for full dispersion indicated for each paste; (b) Impact of dispersant dose on hydration kinetic parameters of 0.23 w/s PLC pastes.

3.2 Determination of concrete paste fraction composition

The objective of the research is to develop binary and ternary pastes with up to 50%wf fillers (% weight of fines), which implies on a concrete paste with clinker factor as low as 40%wf. Table 2 shows the compositions of the pastes, their mean particle diameter, P_{of} and *VSA*. ϕs and IPS were calculated for HFLW pastes with a water to solids (w/s) ratio of 0.23 and for the reference paste (100% PLC, #10 in Table 2) with a w/s of 0.40 to simulate the conventional concrete mixture practiced by the precast plant. The table shows that IPS ranges between 0.19 and 0.38μm for the binary and ternary pastes, while the reference paste has an IPS of 0.53μm.

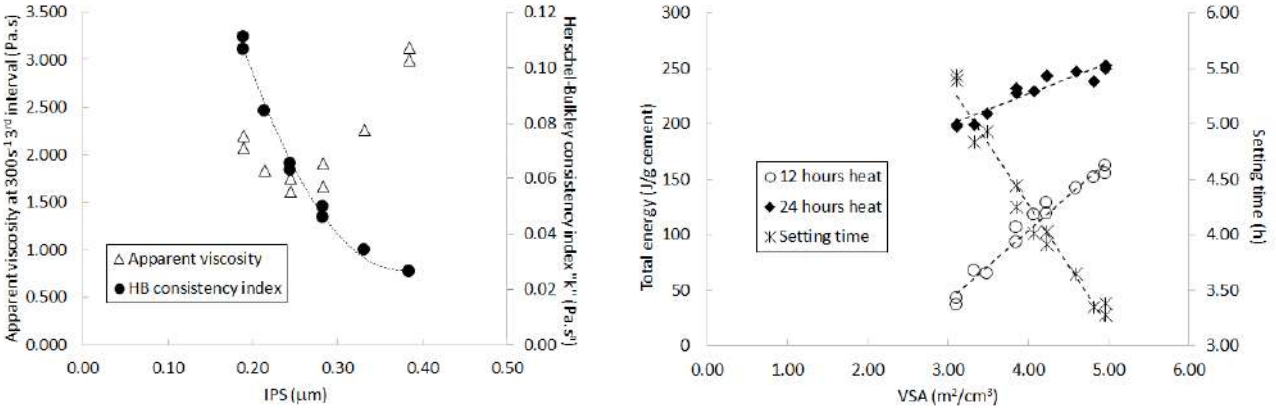
Table 2 –Compositional and calculated parameters of HFLW and reference pastes.

#	*Weight fraction, dry, %*			*Volume fraction, dry, %*			*Mean ϕ*	P_{of}	*VSA*	ϕs	*IPS*
	PLC	*Filler 1*	*Filler 2*	*PLC*	*Filler 1*	*Filler 2*	*μm*	*%*	m^2/cm^3	*%*	*μm*
1	50	50	-	48.0	52.0	-	8.7	17.2	4.963	59.6	0.19
2	50	-	50	48.8	-	51.2	66.2	8.2	3.112	59.2	0.38
3	50	10	40	48.6	10.5	40.9	54.5	9.8	3.487	59.3	0.33
4	50	20	30	48.5	21.0	30.5	42.9	12.1	3.860	59.4	0.28
5	50	30	20	48.3	31.4	20.3	31.4	14.1	4.230	59.5	0.25
6	50	40	10	48.2	41.7	10.1	20.0	15.8	4.597	59.5	0.21
7	60	40	-	58.1	41.9	-	9.6	16.1	4.816	59.4	0.20
8	60	20	20	58.4	21.1	20.5	32.5	12.5	4.076	59.3	0.27
9	60	-	40	58.8	-	41.2	55.8	8.8	3.326	59.1	0.36
10	100	-	-	100.0	-	-	13.4	10.9	4.204	44.9	0.53

The rheology data was fitted to the Herschel-Bulkley (HB) model ($R^2 > 0.9997$) shown in Equation (2), where τ is the shear stress, τ_y is the yield stress, k is the consistency index, γ is the shear rate, and n is the flow index. Fig. 2(a) plots apparent viscosity (measured at 300s^{-1} at the second shear rate cycle) and HB's consistency index k as a function of IPS. The fact that IPS did not lead to lower apparent viscosity indicates that the pastes were not in equilibrium under the testing conditions. The strong correlation between IPS and k confirms the soundness of the approach to design HFLW concrete's paste fraction.

$$\tau = \tau_y + k\dot{\gamma}^n \quad (2)$$

Heat of cement hydration parameters correlated well to *VSA* (Fig. 2(b)), hence to IPS and *k* (plots not shown). Higher *VSA* leads to shorter setting times and higher early age heat energy. With other parameters unchanged, a lower IPS should lead to faster buildup of the hydrated microstructure and faster hydration kinetics (Berodier, 2015). Fig. 2 indicates that a balance between rheology adequacy and hydration kinetics should be pursued in the formulation of HFLW systems.



(a) (b)

Figure 2 – Correlation between (a) IPS and consistency (apparent viscosity at $300s^{-1}$ and HB's consistency index *k*), and (b) cement hydration kinetics, for binary and ternary HFLW pastes.

3. Conclusions

HFLW cement-based pastes with up to two types of limestone fillers were designed using Westman and Hugill's particle packing density algorithm and Funk and Dinger's interparticle spacing (IPS) model. Strong correlations were found between IPS and the consistency index of the Herschel-Bulkley rheology model. Cement hydration kinetics parameters showed strong dependency on surface area and therefore on IPS. The results validate the method to design cementitious mixes of low carbon footprint.

Acknowledgements

This research is funded by the US Department of Energy's Office of Energy Efficiency and Renewable Energy, Building Technologies Office under Contract No. DE-AC05-00OR22725 with UT-Battelle, LLC. The authors acknowledge the support from the Precast Concrete Institute and Gate Precast (samples supply), Laurel Hilger (rheometry testing setup), Nidia Gallego (pycnometry testing), Kris Jones (particle size distribution testing) and Diana Hun (overall support).

References

Berodier, E.M.J. (2015). "Impact of the supplementary cementitious materials on the kinetics and microstructural development of cement hydration". Doctoral thesis, EPFL.

Fennis, S.A.A.M. (2008). "Measuring water demand or packing density of micro powders – comparison of methods." Delft University of Technology, Civil Engineering and Geosciences, Institutional Repository, 21p.

Funk, J.E. and Dinger, D.R. (1994). "Derivation of the Dinger-Funk particle size distribution equation". In *Predictive Process Control of Crowded Particulate Suspensions*. Springer, Boston, MA.

Habert, G., Miller, S.A., John, V.M., Provis, J.L., Favier, A., Horvath, A. and Scrivener, K.L. (2020). "Environmental impacts and decarbonization strategies in the cement and concrete industries". *Nature Reviews Earth & Environment*, 1(11): 559-573

John, V.M., Damineli, B.L., Quattrone, M. and Pileggi, R.G. (2018) "Fillers in cementitious materials – experience, recent advances and future potential". *Cement and Concrete Research*, 114: 65-78

Pileggi, R.G., Studart, A.R. and Pandolfelli, V.C. (2000). "A new model to predict the minimum viscosity of ceramic suspensions". *Cerâmica*, 46: 160-165

Westman, A.R. and Hugill, H.R. (1930). "The packing of particles". *Journal of the American Ceramic Society*, 13(10): 767-779

The 16th International Congress on the Chemistry of Cement 2023 (ICCC2023)
"Further Reduction of CO_2 -Emissions and Circularity in the Cement and Concrete Industry"
September 18–22, 2023, Bangkok, Thailand

Effects of Blast Furnace Slag Fineness on Cement Physical, Mechanical and Chemical Properties

U.E. Şenbil[1]

[1] *Akkim Kimya, Yalova, Turkey*
Email: ugur.senbil@akkim.com.tr

ABSTRACT

Clinker substitution with supplementary cementitious materials became much important and critical subject over recent years due to high amount of CO_2 emissions coming from the cement manufacturing process. Ground granulated blast furnace slag (GGBFS) is one of the most used cementitious materials. Fineness characteristics of the GGBFS plays a critical role in the hydration development and the compressive strength of the cement, also it effects the rheological behavior of concrete. In this study, a blast furnace slag was grinded at different times to change its' fineness. Three different slags which have different fineness level were obtained. Light scattering (particle size distribution), air jet sieving and air permeability (specific surface area) methods were applied to the slags grinded at different times to characterize the fineness. Each slag was substituted with cement at %25 and physical, mechanical, chemical effects of the substitution were measured. Light scattering, air permeability, air jet, flow test and pack-set index measurement methods were applied for the physical characterization; compressive strengths were measured for the mechanical characterization; scanning electron microscope and isothermal calorimeter hydration heat measurement methods were applied to monitor the hydration process and setting times were also measured to observe the setting process.

KEYWORDS: *Supplementary cementitious material, slag, fineness, cement, CO_2*

1. Introduction

One of the important main industrial CO_2 emission sources is cement sector, Zhang et al (2018). The share of global anthropogenic CO_2 emissions due to cement sector is between %5, Chen et al (2010), Mikulčić et al (2013) - %7, Benhelal et al (2013), Chen et al (2010). Carbon-footprint of the cement production is formed by calcination of calcium carbonate through directly and indirectly through the fossil fuel burning, processing of minerals and conveyance, Crossin (2015), Teh et al (2017). One of the methods to reduce CO_2 in cement industry is adding high volume of supplementary cementitious materials (SCMs) such as ground granulated blast furnace slag, fly ash, and/or silica fume, Gartner (2004). Blast furnace slag is a by-product of a pig iron production in the blast furnace and it involves of silicates and alumino-silicates of calcium and other bases, ACI 116R00 (2005). These kinds of slags show excellent cementitious properties either used with Portland cement or alkali activated cement when they are grounded finely, Hwang and Lin (1986). Particle size distribution and fineness characteristics are very critical properties in terms of the cement performance and it was seen that many cement performance properties can be changed when the particle size distribution is changed, Senbil (2022).

2. Materials and Method

2.1.1 Cement

CEM I 42,5 R type of cement was taken from one of the biggest cement company in Turkey.

2.1.2 Slag

The ground granulated blast furnace slag used in the experiments was taken from iron and steel plant in Turkey. Slag was grinded in laboratory type ball mill at different times respectively 90, 120, 150 minutes (min.) to change its' fineness characteristics. Each slag was mixed with the cement at the ratio of % 75 cement and % 25 slag.

3. Results and discussion

3.1 Test results of the grinded slags

Grinding times, specific surface area (blaine), particle size distribution, air jet sieving results are shown in the Table 1:

Table 1: Physical test results of the grinded slags

Grinding time (min.)	Specific surface area (cm^2/g)	Dx (10) (µm)	Dx (50) (µm)	Dx (90) (µm)	32 µm sieve residue (%)	45 µm sieve residue (%)	63 µm sieve residue (%)	90 µm sieve residue (%)
90	3560	2.9	17.8	55.7	2.1	0.9	0.2	0.1
120	3980	2.3	14.1	43.7	1.1	0.3	0.0	0.0
150	4420	1.6	8.7	35.8	0.9	0.2	0.0	0.0

Particle size distribution and air jet sieving results are in parallel. In both test as the grinding time was increased, the particles became finer. Specific surface area results also support the particle size distribution and air jet sieving results, as the grinding time was increased the specific surface area of the slags were increased. The fineness results of the slags were changed from coarser to the finer as it was planned. The names of the cement-slags mixes and their ratios are shown in the Table 2:

Table 2: The names of the cement-slag mixes and their mixing ratio

Name	CEM I 42.5 R (%)	90 min. grinded slag (%)	120 min. grinded slag (%)	150 min. grinded slag (%)
C-1	100	0	0	0
C-2	75	25	0	0
C-3	75	0	25	0
C-4	75	0	0	25

3.2 Physical test results of the mixes

The physical test results of the cement-slag mixes (slag cements) are shown in the Table 3:

Table 3: The physical test results of the cement-slag mixes

Name	Specific surface area (cm^2/g)	Dx (10) (µm)	Dx (50) (µm)	Dx (90) (µm)	32 µm sieve residue (%)	45 µm sieve residue (%)	63 µm sieve residue (%)	90 µm sieve residue (%)	Pack-set index	Paste flow (W/C=0,50 (cm)
C-1	3720	1.5	9.9	33.9	7.9	3.0	0.6	0.1	3	19.4
C-2	3320	1.8	11.2	38.6	10.2	4.1	0.9	0.2	5	20.6
C-3	3460	1.7	11.1	35.3	9.0	3.6	0.7	0.1	4	20.4
C-4	3610	1.6	9.9	34.6	8.4	3.3	0.6	0.1	4	20.8

CEM I 42.5 R type of cement has the finest particles. Slag addition made the cement much coarser. Between the slag cements C-4 is the finest and C-2 is the coarsest cement. C-1 has the lowest pack-set index value as the grinding aid was used in its' commercial production. Adding slag, increased the pack-set index values. As the C-1 is the finest cement it has the lowest flow value because of the higher water demand (Table 4); adding slag increased the flow value of the cement as coarser particles were increased in the mixes.

3.3 Water demand and compressive strength test results of the mixes

The water demand and the compressive strength test results of the cement-slag mixes are shown in the Table 4:

Table 4: Water demand and compressive strengths of the cement-slag mixes

Name	Water Demand (%)	W/C	1 day (Mpa)	2 day (Mpa)	7 day (Mpa)	28 day (Mpa)
C-1	32	0.50	19.8	27.1	47.4	58.4
C-2	31	0.48	14.6	22.3	34.6	49.9
C-3	31	0.48	15.0	22.6	35.6	52.5
C-4	31	0.48	15.4	23.1	36.5	54.9

W/C ratios were set according to the water demand results. C-1 has the highest compressive strengths in all ages. When slag cements are compared to each other C-4 has the highest compressive strengths in all ages as it has much finer particles than the C2 and C3. This shows the importance of the fineness effects on the compressive strengths.

3.5 SEM analysis of the mixes

SEM pictures of slag cements tested at 1 days and 28 days are shown in Figs. 1-4 and Figs. 5-8, respectively.

3.5.1 1-day SEM pictures



Figure 1: C-1 1-day

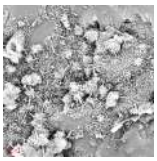


Figure 2: C-2 1-day

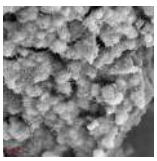


Figure 3: C-3 1-day



Figure 4: C-4 1-day

3.5.2 28-day SEM pictures

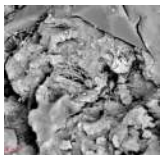


Figure 5: C-1 28-day

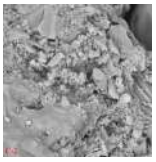


Figure 6: C-2 28-day

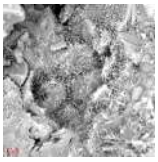


Figure 7: C-3 28-day

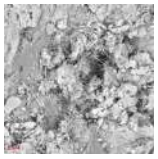


Figure 8: C-4 28-day

When 1-day SEM pictures are evaluated, calcium-silica-hydrates (C-S-H) gels are much more in the picture of C-1. This can be explained as C-1 has the highest hydration heat (Table 6) and this was resulted higher hydration products such as C-S-H phases. This situation may also be the explanation of the higher compressive strength results of C-1. When 28-day SEM pictures are evaluated, the hydration of the slag cements are still going on as there are still increasing the C-S-H phases in the environment. Slag addition can be caused this situation.

3.6 Hydration heat analysis and setting time results of the mixes

Hydration heat analysis which were carried out using by isothermal calorimeter and setting time results are shown in the Table 6:

Table 6: Hydration heat and setting time results of the cement-slag mixes

Name	1-day (J/g)	2-day (J/g)	7-day (J/g)	28-day (J/g)	Initial setting (min.)	Final setting (min)
C-1	230.4	293.1	364.0	392.4	150	249
C-2	178.6	235.4	304.5	334.0	168	257
C-3	170.8	229.3	303.7	336.5	172	268
C-4	173.7	234.4	312.4	347.0	170	271

C-1 cement has the highest hydration heat in all ages. This result contributes the compressive strength test results as C-1 has the highest compressive strength values in all ages. The finest slag cement C4, has the highest 28-day hydration heat among slag cements. This situation also resulted highest 28-day compressive strength among slag cements. Slag addition to the cement extend the initial and final setting times. C-4 has the longest setting time values among the cement-slag mixes. Results show that as the fineness increases the setting time increases between the slag cements.

4. Conclusions

It is seen that the change in the fineness level of the slag affects all the properties of the cement. This study revealed that how each parameter of the cement is changed when the slag fineness is changed. It is very critical to know these results while the usage of the slag is increased to reduce the CO_2. It is suggested to enlarge these kinds of studies to increase the knowledge and also to enlighten the relationship between the slag fineness effects to durability.

Acknowledgements

I would like to express my deepest thanks to Akkim Kimya for the valuable support to given this study.

References

ACI 116R00, (2005) *Cement and Concrete Terminology*, Detroit, Michigan

Benhelal, E., Zahedi, G., Shamsaei, E. and Bahadori, A. (2013) "Global strategies and potentials to curb CO2 emissions in cement industry", 51:142-161

Chen, C., Habert, G., Bouzidi, Y. and Jullien, A. (2010) "Environmental impact of cement production: Detail of the different processes and cement plant variability evaluation", *Journal of Cleaner Production*, 18(5): 478-485

Crossin, E. (2015) "The greenhouse gas implications of using ground granulated blast furnace slag as a cement substitute", *Journal of Cleaner Production*, 95:101-108

Gartner, E. (2004), "Industrially interesting approaches to "low-CO2" cements", *Cement and Concrete Research*, 34(9): 1489-1498

Hwang, C.L. and Lin, C.Y. (1986) "Strength development of blended blast furnace slag cement mortars, in: V.M. Malhotra (Ed.), Proceedings of the 2nd International Conference on Fly Ash, Silica Fume, Slag and Natural Pozzolans in Concrete", Madrid, Spain, SP 91-65, Detroit, MI:ACI, 1986, pp. 1323–1340

Mikulčić, H., Vujanović, M. and Duić, N. (2013) "Reducing the CO2 emissions in Croatian cement industry", *Applied Energy*, 101:41-48

Senbil, U.E. (2022) "Effect of Particle Size Distribution on the Properties of Cements", PhD thesis, Ege University, Turkey, 142 pp.

Teh, S.H., Wiedmann, T., Castel, A. and de Burgh, J. (2017) "Hybrid life cycle assessment of greenhouse gas emissions from cement, concrete and geopolymer concrete in Australia", *Journal of Cleaner Production*, 152: 312-320

Zhang, C., Han, R., Yu, B. and Wei, Y. (2018) "Accounting process-related CO2 emissions from global cement production under Shared Socioeconomic Pathways", *Journal of Cleaner Production*, 184: 451-465

The 16th International Congress on the Chemistry of Cement 2023 (ICCC2023)
"Further Reduction of CO_2 -Emissions and Circularity in the Cement and Concrete Industry"
September 18–22, 2023, Bangkok, Thailand

Improving early-age strength of limestone-calcined clay cement by using finer cement and cement kiln dust

Meenakshi Sharma[1*], Vootukuri Charitha[1] and Karen Scrivener[2]

[1] *Indian Institute of Technology Hyderabad, Hyderabad, India*
Email: Meenakshi1783@gmail.com

[2] *École Polytechnique Fédérale de Lausanne, Lausanne, Switzerland*
Email: karen.scrivener@epfl.ch

ABSTRACT

Limestone calcined clay cement (LC^3) has gained significant interest in the last decade due to its low clinker content and improved performance compared to ordinary Portland cement (OPC) and other blended cements. However, its lower early-age strength is one of the major hurdles to its introduction in the construction. This study explored the possibility of improving the early strength of LC^3 a) by using a fine cement to produce LC^3 and b) by using cement kiln dust as a partial substitute for limestone. Mini-slump test and isothermal calorimetry were performed to evaluate the workability and hydration of OPC and LC^3 pastes. Comparison of accelerated LC^3 mortars, containing finer cement and cement kiln dust, with conventional LC^3 and OPC mortars showed significant improvement in 1-day and 3-day compressive strength. It was found that the use of fine cement in LC^3 results in higher 1-day strength compared to OPC, while the use of cement kiln dust results in comparable 3-day strength to OPC.

KEYWORDS: *Early-age, calcined clay, cement kiln dust, fineness, compressive strength*

1. Introduction

Limestone calcined clay cements (LC^3) are a family of ternary blended cements that replace up to 50% of ordinary Portland cement with blends of limestone and calcined clays. They offer superior resistance to chloride diffusion and alkali-silica reaction compared to ordinary Portland cement (Scrivener et al., 2018). In addition, the distribution of clay worldwide makes the production of LC^3 feasible globally. Based on the literature available, it can be concluded that LC^3 has great advantages in durability, reduction in CO_2 emissions, and energy usage.

One of the greatest challenges for the usage of LC^3 practically is its low early-age strength. LC^3 mixes have lower early strength compared to OPC, especially at 1 day of hydration. However, there are studies on improving the early strength and workability of LC^3 by using nano-silica or by the addition of superplasticizers (Lin et al., 2022; Matos et al., 2022). In comparison to OPC, calcined clays tend to have a higher specific surface area, which tends to increase water consumption. Therefore, the amount of chemical admixture to be added to achieve the desired slump is higher. Reactivity can be improved by grinding cement finer (Zunino, 2020). Therefore, this article focuses on improving early-age performance by adding finer cement and cement dust kiln (CKD). The hydration of the LC^3 cement, workability, and compressive strength are studied.

2. Materials and methods

A commercially available ordinary Portland cement (OPC) conforming to EN 197-1 as CEM I 42.5 N is used. A medium grade kaolin clay procured from Bhuj, India was calcined at 800ºC for 45 minutes and used to replace 30% of OPC in the mixes. Mineral grade limestone and gypsum were used to produce LC^3.

Cement kiln dust (CKD) was produced in the laboratory by grinding 80% limestone, 15% K_2SO_4, 5% KCl for 30 seconds.
The raw materials were ground to increase hydration at early ages, thereby increase the early-age strength of LC^3. The fineness of OPC and CKD was increased by grinding. Calcined clay and limestone become much finer on grinding and can influence workability. Therefore, OPC used in this study was ground separately for 30, 60, and 120 seconds. The specific surface area (SSA) of raw materials before and after grinding was measured by nitrogen adsorption, using BET theory. The specific surface area increased to 1.6 m^2/g, 1.8 m^2/g and 2.3 m^2/g from 0.6 m^2/g upon grinding for 30, 60 and 120 seconds, respectively. The specific surface area of calcined clay, limestone and CKD was found to be 9.9 m^2/g, 2.4 m^2/g and 2.4 m^2/g, respectively.

The influence of fineness by grinding the OPC and incorporating CKD is compared to the unground OPC in LC^3 system. The reference LC^3 system consists of 54% OPC, 30% Bhuj CC, 15% limestone and 1% gypsum. The details of the mixtures are shown in Table 1.

Table 1: Mixture proportions of OPC, LC^3 and LC^3+CKD

Mix	OPC surface area (m^2/g)	OPC (%)	Calcined clay (%)	Limestone (%)	Gypsum (%)	Cement Kiln Dust (%)	BET SSA (m^2/g)
OPC-0.60 m^2/g	0.60	100					0.6
LC^3-0.60 m^2/g(OPC)	0.60	54	30	15	1		3.7
LC^3-1.61 m^2/g(OPC)	1.61	54	30	15	1		4.2
LC^3-1.77 m^2/g(OPC)	1.77	54	30	15	1		3.7
LC^3-2.34 m^2/g(OPC)	2.34	54	30	15	1		3.7
LC^3-0.5% CKD		54	30	14.5	1	0.5	3.7
LC^3-1% CKD		54	30	14	1	1	3.7
LC^3-2% CKD		54	30	13	1	2	
LC^3-4% CKD		54	30	11	1	4	
LC^3-8% CKD		54	30	7	1	8	

The influence of admixuitre on various LC^3 mixes was studied using mini-slump test. The influence of finer OPC and addition of CKD was studied using iso-thermal calorimtery. Paste samples at 0.4 w/c were mixed at 1600 rpm for two minutes using a high-shear mixer. The mini-slump cone test was used to evaluate the workability of different LC^3 paste formulations. The paste was filled in 2 layers in the mini-slump and the cone was lifted in less than 3 minutes from the initial contact with water. The diameter of the spread is measured by vernier calipers in 4 directions and approximated. The spread of LC^3 mixtures is adjusted through admixtures. Using a TAM air isothermal calorimeter set to 20°C, measurements of the heat evolution of various mixes are carried out for three days.

3. Results and discussion

3.1 Heat of hydration

The impact of grinding of OPC and the addition of CKD on the isothermal curves of LC^3 mixes are depicted in Figure 1. Fineness of the cement enhanced the reactivity of the LC^3 mix. The first and second exothermic peaks in the acceleration period is related to the reaction of C_3S and the overlap of renewed dissolution of the aluminium phase and C_3S reaction (Krishnan & Bishnoi, 2018; Lin et al., 2021). By incorporating CKD into the LC^3 mix, enhancement of the aluminate peak is observed. Furthermore, a reduction in the height alite peak as compared to the LC^3 system was noticed. Higher the replacement percentage of limestone with CKD, the higher the height of the second peak and the lower the first C_3S peak. In all the LC^3 mixes, 1% gypsum was found sufficient to delay the aluminate peak and achieve different alite and aluminate peaks, as observed in OPC. This suggest that using a finer OPC or replacing limestone with CKD doesn't influence the gypsum requirement of LC^3.

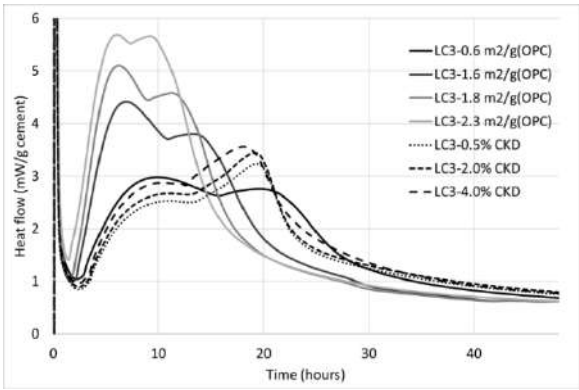


Figure 1: Effect of grinding and incorporation of CKD on heat flow in LC^3 system

3.2 Workability

From Figure 2, a correlation between workability and admixture dosage for different LC^3 mixes is shown. It can be noted that with increase in admixture dosage, spread is also increased. To maintain the same flow, the amount of admixture for LC^3 mix with cement ground for 2 min is higher than control LC^3 paste. With increase in fineness, the quantity of admixture required to maintain the same flow is high. Increase in admixture content from 0.6% to 1.6%, increased slump diameter by 72% (from 40 mm to 140mm) in LC^3 mix with 8% CKD.

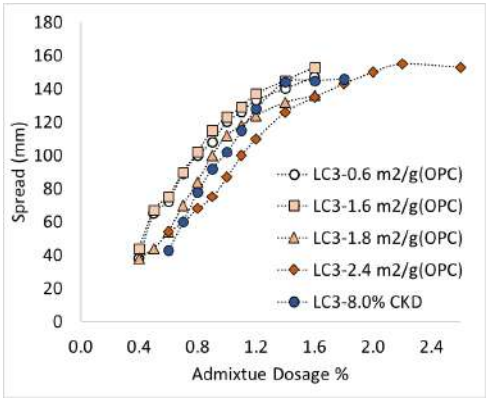


Figure 2: Spread versus admixture dosage percentage for LC^3 systems

3.3 Compressive strength

The compressive strength results at 1, 3, 7 and 28 days are shown in Figure 3. At 1 day, the strength of OPC paste specimens is higher than LC^3 and LC^3+CKD. However, as the hydration proceeds, LC^3 specimens with 8% CKD reported high strength after 3 days of hydration compared to LC^3 control. Similar trend in strength gain is noticed from 7 days to 28 days. Only a minor difference is observed in LC^3 specimens with CKD at all levels of replacement and the LC^3 with CKD reported higher strength than OPC and LC^3 specimens at 28 days of hydration. The effect of grinding OPC on compressive strength in LC^3 is shown in Figure 3(b). At one day, the compressive strength of LC^3 specimens with finest OPC is greater than OPC and LC^3 control specimens. The early age hydration and thereby strength of the LC^3 can be improved by increasing the fineness of the cement by grinding.

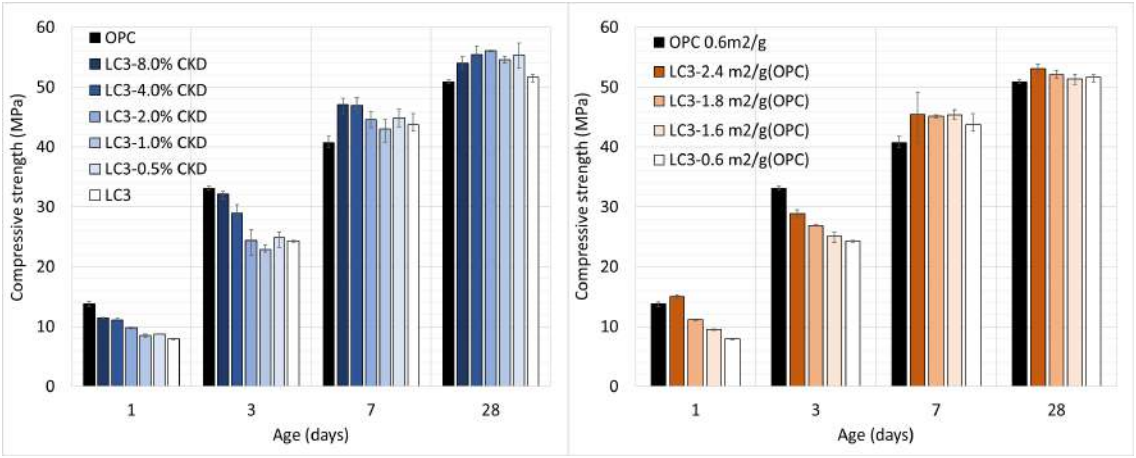


Figure 3: Compressive strength of LC^3 paste mixes a) by incorportaing CKD and b) grinding OPC

3. Conclusions

The key findings from this study are discussed below:

- Using finer OPC to produce LC^3, results in significant enhancement of alite peak and marginally decelerates (time shifts) the aluminate peak.
- The increase in hydration due to finer OPC increases the early-age strength of LC^3.
- With increase in the fineness of cement, the dosage of admixture to be added to maintain the same flow is also increased.
- Addition of cement kiln dust improves the early age and later age strength of LC^3.

Acknowledgements

Financial support from Swiss Agency for Development and Cooperation (SDC) is acknowledged by the authors.

References

Krishnan, S., & Bishnoi, S. (2018). Understanding the hydration of dolomite in cementitious systems with reactive aluminosilicates such as calcined clay. Cement and Concrete Research, 108(September 2017), 116–128. https://doi.org/10.1016/j.cemconres.2018.03.010

Lin, R. S., Lee, H. S., Han, Y., & Wang, X. Y. (2021). Experimental studies on hydration–strength–durability of limestone-cement-calcined Hwangtoh clay ternary composite. Construction and Building Materials, 269, 121290. https://doi.org/10.1016/j.conbuildmat.2020.121290

Lin, R. S., Oh, S., Du, W., & Wang, X. Y. (2022). Strengthening the performance of limestone-calcined clay cement (LC^3) using nano silica. Construction and Building Materials, 340(November 2021), 127723. https://doi.org/10.1016/j.conbuildmat.2022.127723

Matos, P. R., Andrade Neto, J. S., Sakata, R. D., Campos, C. E. M., Kirchheim, A. P., & Rodríguez, E. D. (2022). Effect of superplasticizer addition time and metakaolin source on the early-age hydration of limestone calcined clay cement (LC^3). Materials and Structures/Materiaux et Constructions, 55(8). https://doi.org/10.1617/s11527-022-02049-w

Scrivener, K., Martirena, F., Bishnoi, S., & Maity, S. (2018). Calcined clay limestone cements (LC^3). Cement and Concrete Research, 114(March 2017), 49–56. https://doi.org/10.1016/j.cemconres.2017.08.017

Zunino, F. (2020). Limestone calcined clay cements (LC^3): raw material processing, sulfate balance and hydration kinetics. 212. http://infoscience.epfl.ch/record/277799

The 16th International Congress on the Chemistry of Cement 2023 (ICCC2023)
"Further Reduction of CO_2 -Emissions and Circularity in the Cement and Concrete Industry"
September 18–22, 2023, Bangkok, Thailand

Alkali-activated fly ash synthetized with pre-polymerized suspension combined with ultrafine fly ash at ambient temperature

H.M. Zhu*, X.Z. Wu, Y.W. Zhang, H. Li*

College of Material Science and Engineering, Xi'an University of Architecture and Technology, Xi'an 710055, China

ABSTRACT

Alkali-activated fly ash (AAFA) can offer both significant performance benefits and environmental advantages in corrosive and high-temperature environments. However, the slow setting and limited early strength development of AAFA at ambient temperature strict its use to pre-cast elements that must be cured using elevated temperatures. In order to address this limitation, this experiment pursued a distinctive approach to produce a pre-polymerized suspension (PPS) using ultrafine fly ash (UFA) that was activated with NaOH, and then which was used alongside UFA in conjunction to prepare AAFA. Incorporating PPS into the AAFA mixture while reducing UFA use by 50% resulted in an initial setting time of only 30 mins and an ambient curing compressive strength of 15 MPa after 3 days, which was significantly improved compared to the nearly 3 days required by the control sample to initially set. By using PPS, the dependency on UFA and its accompanying high energy consumption was dramatically reduced. Additionally, the fast-setting and high early strength properties of the optimized AAFA paste make it ideal for in-situ construction, thereby extending the usage of fly ash resources.

KEYWORDS: *alkali-activated fly ash, ambient curing, preparation method, early properties*

1. Introduction

In this study, we aimed to synthesize AAFA at ambient temperature with a reduced usage of UFA. To improve the early properties of AAFA, we proposed to use the polymerization products (N-A-S-H gel and zeolite) seeds as nucleation templates. This approach built on the success of using calcium silicate hydrate (C-S-H gel) seeds to induce Portland cement hydration (Das et al., 2020). However, the current methods for synthesizing N-A-S-H gels (Wang et al., 2022) and zeolites (Liu et al., 2018) typically require meticulous raw materials and complicated preparation processes since the aim is to obtain high-purity phases for theoretical exploration. Consequently, these methods are not practical for large-scale applications. To overcome this limitation, we proposed an easy-to-use method for obtaining a pre-polymerized suspension (PPS) by NaOH-activating UFA sufficiently. This method yielded predominantly N-A-S-H gel and zeolite products, which can then be used as the activation solution to mix with the UFA and original fly ash. This approach reduced costs and energy consumption by avoiding thermal-curing and reducing UFA usage, thereby promoting the convenient application of AAFA in in-situ constructions.

2. Experimental methods

2.1 Materials

The chemical compositions of the original Class F-I fly ash (OFA) and ultrafine fly ash (UFA) were used. The OFA had a d_{50} of 15.93 μm, while the UFA was obtained by milling OFA with a tumbling ball and had a d_{50} of 2.26 μm. An 8 Mol. alkaline activator solution was prepared by mixing NaOH pellets with distilled water.

2.2 Methods

AAFA synthesized with OFA was set as the reference sample, with three substitutions of UFA to OFA at mass ratios of 30%, 50%, and 70%. Table 1 demonstrated that AAFA samples were prepared using two

methods: the conventional method and the mixed with PPS method. Under the conventional method, AAFA samples were prepared by mixing fly ash with NaOH solution and then being cured at 20°C and 95% RH. Under the mixed with PPS method, a pre-activation process was first conducted by activating a small amount of UFA (25:2 in mass ratio) with 8 Mol NaOH solution to obtain PPS. This pre-activation process was strengthened with a magnetic stirrer at 80°C for 20 minutes. Then, PPS was mixed with the remaining UFA and OFA to prepare AAFA samples, which were cured at 20°C and 95% RH.

Table 1 Mixture proportions of AAFA paste, mass/g

Mix designation		PPS		Mixed materials		
		UFA	NaOH solution	OFA	UFA	NaOH solution
Conventional	O	/	/	100	0	50
	OU3			70	30	50
	OU5			50	50	50
	OU7			30	70	50
Mixed with PPS	P-O	4	50	96	0	/
	P-OU3	4	50	70	26	/
	P-OU5	4	50	50	46	/
	P-OU7	4	50	30	66	/

3. Results

3.1 Setting time

The initial setting time of AAFA pastes is displayed in Fig. 1. The initial setting time of the reference AAFA paste was 4117 mins, resulting in a delay in the construction progress of nearly 3 days. However, the incorporation of UFA in the mix led to a significant reduction in the initial setting time of AAFA. For instance, the initial setting time of the mixture containing 30% UFA decreased to 72 mins. Moreover, AAFA pastes mixed with PPS exhibited much shorter setting time than those prepared using conventional methods. PPS decreased the initial setting time of the mixture with 30% UFA from 72 to 31 mins, which was even shorter than the sample prepared using conventional method that had 50% UFA. Therefore, using PPS can help achieve equivalent setting time with reduced UFA usage, thereby avoiding workability deterioration and minimizing energy consumption during UFA grinding.

3.2 Compressive strength

Fig. 2 shows the effect of UFA replacement and PPS mixing on the compressive strength of ambient-cured AAFA samples. The compressive strength of the control sample (O) cannot be determined before 7 days as it has not yet hardened to a testable strength. At 3 days, the compressive strength of AAFA with 30% UFA (OU3) reached 6.3 MPa, demonstrating an improvement in the early strength of AAFA due to UFA. An increase in UFA content resulted in further improvement of the compressive strength of AAFA at all curing ages. The 3-day compressive strength for mixtures with UFA at 50% and 70% replacement were 12.78 MPa and 18.89 MPa, respectively. At 28 days, the compressive strength of AAFA containing 30%, 50%, and 70% UFA reached 20 MPa, 28.2 MPa, and 38.5 MPa, respectively. Furthermore, the addition of PPS significantly increased the compressive strength of AAFA samples at early curing ages, with a gain of 2.1 MPa for Mix P-O at 7 days. However, this gain decreased progressively with the extension of curing age, and the use of PPS in the sample with 50% UFA (P-OU5) improved the compressive strength by 22%, 19%, and 9% more than OU5 at 3, 7, and 28 days, respectively.

3.3 XRD results

Fig. 3 depicts the XRD curves of all AAFA samples, indicating that mullite and quartz from fly ash were the primary crystals present. Notably, Mix OU5 and P-OU5 exhibited wide diffraction peaks near 11.5°(2θ) and 29.2°(2θ) (labelled as G), indicating the presence of poorly ordered N-A-S-H gel phase (Abdulrahman et al., 2022; Mucsi et al., 2015), while not found in Mix O and Mix P-O. This suggested that the addition of UFA accelerated the formation of geopolymerization products for AAFA and supported the compressive strength results. Furthermore, the XRD curve of P-OU5-7d indicated a new N-A-S-H gel diffraction peak near 11.55°(2θ), which was not seen in P-OU5-28d. This highlighted the positive effect of PPS on AAFA geopolymerization at the early curing age and was consistent with the compressive strength results.

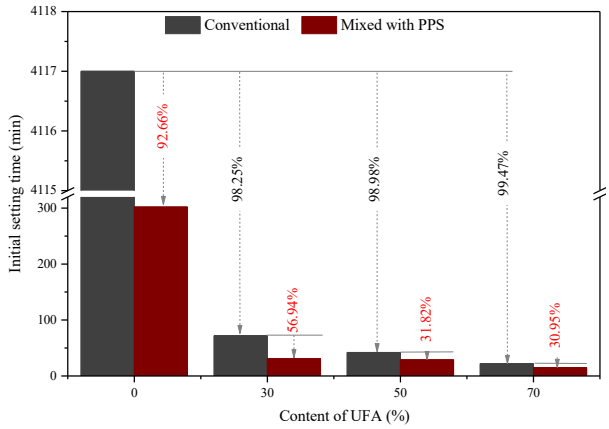


Fig. 1 Initial setting time of ambient-cured AAFA samples

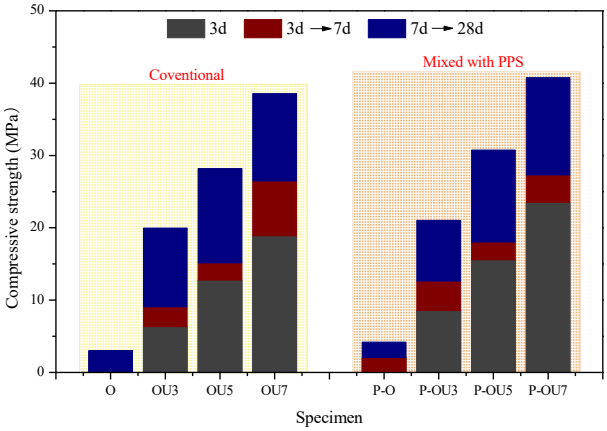


Fig. 2 Influence of UFA replacement and PPS mixing on compressive strength of ambient-cured AAFA samples

3.4 FTIR results

According to Fig. 4, comparing the Si-O-Si (Al) peaks around 1000 cm^{-1} in FTIR spectra (Band e) allowed us to distinguish the transformation of amorphous N-A-S-H gel in AAFA paste (Criado et al., 2007). The Si-O-Si (Al) peak centered at 1004 cm^{-1} for O-7d shifted to 1000 cm^{-1} in OU5-7d and P-O-7d, while that of O-28d shifted to 1000 cm^{-1} for OU5-28d and to 1001 cm^{-1} for P-O-28d, indicating that the Si-O-Si (Al) peak shifted to lower wavenumbers upon the usage of UFA and PPS. Notably, the combination of UFA and PPS resulted in the lowest peak wavenumber of 996 cm^{-1} for P-OU5-7d and 997 cm^{-1} for P-OU5-28d. Furthermore, the shift scope of Si-O-Si (Al) caused by PPS in the 7-day samples was wider than that of the 28-day samples, indicating again the more pronounced effect of PPS on AAFA geopolymerization at the early curing age. The shift of Si-O-T peak to lower wavenumber implied a different doping degree of Al in the reaction products, suggesting the formation of N-A-S-H gels. In-situ ATR-FTIR spectra of AAFA within 3 days after preparation showed that the main band centered at 1055 cm-1 in the FTIR spectrum of fly ash shifted to lower wavenumbers and decreased in intensity over time due to the formation of a new Al-enriched gel phase (Rees et al., 2007). The increase in Si-O-Si (Al) peak intensity was also observed in the FTIR spectrum of OU5 and P-O in comparison with Mix O, further supported the growing geopolymerization degree for AAFA samples incorporating UFA and PPS.

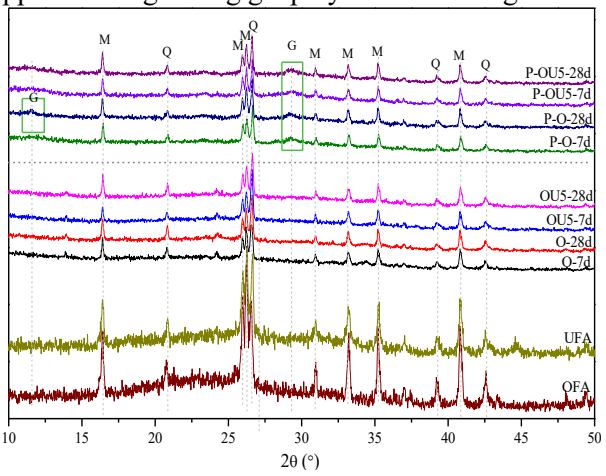


Fig. 3 XRD curves of ambient-cured AAFA samples at 7 and 28 days

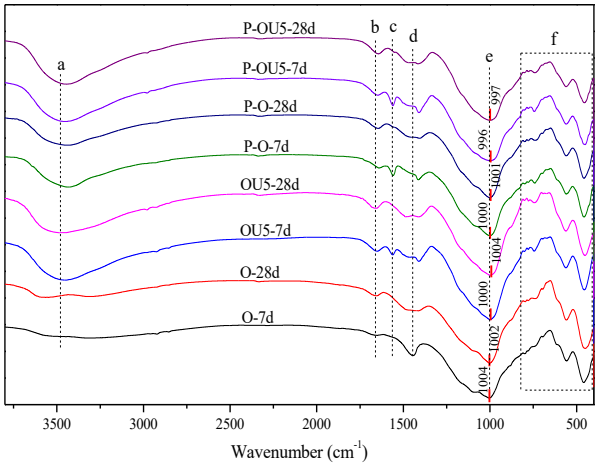


Fig. 4 FTIR spectrums of ambient-cured AAFA samples at 7 and 28 days

3.5 MIP results

It is widely accepted that the pore size of hardened cementitious paste can be classified into three categories, namely gel pores (<10 nm), capillaries (10-1000 nm), and macropores (>1000 nm). Table 2 represents the cumulative pore volume of AAFA samples according to this classification. Compared with the reference sample (O and OU5), the cumulative porosity of P-O and P-OU5 decreased significantly when dealing with PPS, resulting in decreased porosity of 31.02%, 22.08%, from 39.94%, 26.39%,

respectively. The reduction in pores in P-O was mainly due to the reduction in the proportion of macropores from 67.57% to 31.61%. On the other hand, the reduced pores in P-OU5 were mainly capillaries, decreasing from 60.22% to 22.55%. These changes resulted in a significant reduction in the average pore diameter of the samples with PPS. Additionally, the combined adoption of UFA and PPS in P-OU5 led to the smallest average pore size of 13.93 nm, the largest gel pore ratio of 44.96%, and the smallest capillary ratio of 22.55%, giving it the densest microstructure among the four mixtures. This improvement in pore structure can be attributed to the formation of N-A-S-H gels resulting from the adoption of UFA and PPS, as also evidenced by the XRD, FTIR, and SEM results of this experiment.

Table 2 Total porosity and pore size distribution analysis of ambient-cured AAFA samples at 7 days

AAFA	Porosity (%)	Average pore diameter (nm)	Pores distribution (%)		
			0-10 nm	10-1000 nm	> 1000 nm
O	39.94	176.49	1.62	30.81	67.57
OU5	26.39	20.83	18.31	60.22	21.47
P-O	31.02	138.74	0.59	67.8	31.61
P-OU5	22.08	13.93	44.96	22.55	32.49

3. Conclusions

This experiment aimed to prepare fast setting and high early strength AAFA at ambient temperature through pre-polymerized suspension (PPS) and partial adoption of UFA. The key findings are as follows:
AAFA synthetized by PPS mixing 50%OFA-50%UFA in mass ratio attained an initial setting time of 30 minutes and displayed a compressive strength of 15 MPa after 3 days of curing, while the compressive strength of the control group was not testable even after 7 days of curing. This method thus represented a viable mean of producing fast-setting and high-early strength AAFA products at room temperature.
The superior early properties of AAFA synthesized with PPS and UFA can be explained by the mutual coupling between the accelerated dissolution of active Si/Al ions found in the precursor and the promoted nucleation process of the reaction products in AAFA. As a result of this coupling, the formation of N-A-S-H gels accelerated rapidly, leading to the formation of a denser and rapidly developed hardened structure for AAFA. This process resulted in increased early strength properties for AAFA, making it an effective material for in-situ construction applications.

Acknowledgements

This work was supported by the Key R&D Project in Shaanxi Province (2023-YBGY-498).

References

Leung, C.K.Y. and Cao, Q. (2010) “Development of Pseudo-ductile Permanent Formwork for Durable Concrete Structures”, *RILEM Materials and Structures*, 43(7): 993-1007

Das, S., Ray, S., Sarkar, S.(2020) “Early strength development in concrete using preformed CSH nano crystals”, *Constr. Build. Mater.* 233, 117214

Wang, Y.R., Cao, Y.B., Zhang Z.H., Huang J.Z., Zhang P., Ma Y.W., Wang H. (2022) “Study of acidic degradation of alkali-activated materials using synthetic C-(N)-A-S-H and N-A-S-H gels”, *Compos. Part B-Eng.* 230, 109510

Liu, Y., Yan, Ch.J., Zhao, J.J., Zhang, Z.H., Wang, H.Q., Zhou, S., Wu, L.M. (2018) “Synthesis of zeolite P1 from fly ash under solvent-free conditions for ammonium removal from water”, *J. Clean, Prod.* 202, 11-22

Abdulrahman, H., Muhamad, R., Visintin, P., Shukri, A.A. (2022) “Mechanical properties and bond stress-slip behaviour of fly ash geopolymer concrete”, *Constr. Build. Mater.* 327, 126909

Mucsi, G., Kumar, S., Csoke, B., Kumar, R., Molnár, Z., RáczÁ., Mádai, F., Debreczeni Á. (2015) “Control of geopolymer properties by grinding of land filled fly ash”, *Int. J. Miner. Process*. 143, 50-58

Criado, M., Fernández-Jiménez, A., Palomo, A. (2007) “Alkali activation of fly ash: Effect of the SiO_2/Na_2O ratio: Part I: FTIR study”, *Microporous Mesoporous Mater.* 106, 180-191

Rees, C.A., Provis, J.L., Lukey, G.C., van Deventer J.S.J. (2007) “In situ ATR-FTIR study of the early stages of fly ash geopolymer gel formation”, *Langmuir.* 23, 9076-908

The 16th International Congress on the Chemistry of Cement 2023 (ICCC2023)
"Further Reduction of CO_2 -Emissions and Circularity in the Cement and Concrete Industry"
September 18–22, 2023, Bangkok, Thailand

A unified method for efficient and reliable determination of pozzolanic reaction degree of SCMs in blended cement pastes

T. Wang[1*], S. Medepalli[2], Y. Zheng[3] and T. Ishida[4]

[1] *Tongji University, Shanghai, China*
Email: wangtiao@tongji.edu.cn
[2] *The University of Tokyo, Tokyo, Japan*
Email: satya@g.ecc.u-tokyo.ac.jp
[3] *The University of Tokyo, Tokyo, Japan*
Email: zheng@concrete.t.u-tokyo.ac.jp
[3] *The University of Tokyo, Tokyo, Japan*
Email: tetsuya.ishida@civil.t.u-tokyo.ac.jp

ABSTRACT

Using supplementary cementitious materials (SCMs) to produce low-carbon concrete is an effective way to utilize solid waste and achieve carbon neutrality. The pozzolanic reaction processes of SCMs significantly affect the microstructure, mechanical properties, and durability of concrete blended with SCMs. Although several methods, such as X-ray diffraction analysis and thermodynamic modeling of pozzolanic reactions using Gibbs energy minimization software, have been developed to determine the pozzolanic reaction processes of SCMs, these methods require special analytical skills and may not be reliable. Ethylenediaminetetraacetic acid (EDTA) with NaOH is an efficient and reliable dissolving agent for dissolving calcium-rich phases (e.g., cement clinkers and hydration products) without dissolving low-calcium SCMs. The selective dissolution test based on EDTA with NaOH is widely used to determine the pozzolanic reaction processes of low-calcium fly ash, but it can be tedious, especially for fine SCMs like silica fume and metakaolin. A unified method that combines EDTA with NaOH dissolving agent and Inductively Coupled Plasma (ICP) analysis has been developed to determine the pozzolanic reaction processes of SCMs efficiently and reliably. Experimental results have shown that this method is useful for determining the pozzolanic reaction processes of low-calcium SCMs. Moreover, coupled with quantitative phase analysis with XRD and thermogravimetric analysis (TGA), the Ca/Si ratio of aluminum-incorporated calcium silicate hydrate (C-(A)-S-H) gel can be further determined based on conservation of mass. This method is thus helpful for investigating the effect of pozzolanic reactions of SCMs on the performance of blended concrete.

KEYWORDS: *Supplementary cementitious materials (SCMs), pozzolanic reaction, selective dissolution method, Inductively coupled plasma (ICP) analysis, Ca/Si ratio*

1. Introduction

Blended cements that incorporate supplementary cementitious materials (SCMs) are commonly used to enhance the performance of concrete and promote sustainability in construction. The extent of the pozzolanic reaction degree is a critical factor that influences the performance of SCMs in concrete. This reaction impacts the pore solution chemistry, microstructure, mechanical properties, and durability of the concrete, ultimately affecting its overall performance. (Megat Johari et al. 2011).

Several methods have been developed to determine the pozzolanic reaction degree of SCMs, including X-ray diffraction analysis, thermodynamic modeling (Scrivener et al. 2015). While most of these methods provide valuable insights, their reliability may be compromised due to the various assumptions. Apart from the advanced techniques such as NMR, selective dissolution method is one of the most commonly used direct methods to measure the extent of reaction of SCMs such as silica fume and metakaolin (Poon et al. 2001; Wei et al. 2012). However, the results vary widely and are not consistent for fine SCMs. It is

important to exercise caution when using this method for high-fineness SCMs, as their small particle size can affect the accuracy of the results.

To address the limitations of the selective dissolution method for high-fineness SCMs, a new method was proposed by combining the existing selective dissolution method with Inductively coupled plasma (ICP) analysis. This new method, which uses EDTA-NaOH dissolving agent and ICP analysis, efficiently and reliably determines pozzolanic reaction processes of SCMs, and when combined with XRD and TGA analysis, can further provide valuable information on the chemical compositions of C-(A)-S-H gel. The results are compared with the selective dissolution method, which uses the same dissolving agent to ensure comparability. However, the two methods differ in their measurement approaches, with selective dissolution method relying on the effectiveness of filter paper, the EDTA-ICP method uses the actual dissolved ions from the cement paste obtained from ICP for accurate determination.

2. Materials

One ordinary Portland cement (OPC) and two low-calcium SCMs (silica fume and metakaolin), were used in this study. The physical and chemical properties of the raw materials are summarized in Table 1. A fixed water to binder ratio of 40% and a SCM replacement of 20% was used to prepare blended cement pastes and sealed cured at 20 °C. The procedure for preparing cement pastes for hydration and reaction tests was based on a previous study (Wang et al. 2021).

Table. 1 Material properties of cement and SCMs

、	SiO_2 (wt.%)	Al_2O_3 (wt.%)	Fe_2O_3 (wt.%)	CaO (wt.%)	MgO (wt.%)	Density (g/cm^3)	Specific surface area (cm^2/g)	LOI (wt.%)
Cement	16.74	5.01	3.16	71.04	-	3.15	3,370	2.43
Silica fume	97.03	0.38	0.25	0.35	0.43	2.470	125,088	1.49
Metakaolin	49.66	47.22	0.60	0.14	0.05	2.340	16,194	1.55

3. Selective dissolution test with ICP analysis

3.1 Measurement procedures

The experimental procedures using EDTA-NaOH to dissolve blended cement paste were described in previous study (Wang et al. 2021). The tested material were added into solution (solution-solid ratio is 2,000) and strirred for one hour. The dissolved ion concentration of Ca, Si, and Al was measured using ICP analysis. The reaction degree of SCMs R_{SCMs} is determined based on the concentration of dissolved ion from cement paste (Eq. (1))

$$R_{SCMs} = \frac{\left(C_{Si}^{Total} - C_{Si}^{Cement}\right)\frac{M_{SiO_2}}{M_{Si}} + \left(C_{Al}^{Total} - C_{Al}^{Cement}\right)\frac{M_{Al_2O_3}}{M_{Al}}}{r_{SCMs} m_{raw}^{paste} (f_{SiO_2}^{SCMs} + f_{Al_2O_3}^{SCMs})} \quad (1)$$

where C_{Si}^{Total} is the dissovled Si ion concentration in EDTA-NaOH solution; C_{Si}^{Cement} is the the dissovled Si ion concentration from cement (Table 1); M_{SiO_2} is molar mass of SiO_2; M_{Si} is molar mass of Si; r_{SCMs} is the replacement ratio of SCMs; m_{raw}^{paste} is the raw cementious powder of tested material determined by thermogravimetric analysis (TGA); $f_{SiO_2}^{SCMs}$ is the mass fraction of SiO_2 in target SCMs (Table 1). Similar definitions were used for Al ion and Al_2O_3.

3.2 Dissolving properties and linear measurement range of dissolving solution of EDTA-NaOH

The dissolving properties and linear measurement range in EDTA-NaOH solution were studied in this section. Raw materials (cement, silica fume and metakaolin) and cement paste were used to study the dissolving properties of EDTA-NaOH solution. To verify whether EDTA-NaOH solution affects the measurement of Si and Al, standard solutions of Al and Si were introduced into EDTA-NaOH solution to

investigate the linear working range. Experiment results (Fig. 1a) showed that EDTA-NaOH efficiently dissolved the raw cement and cement paste but slightly dissolved low-calcium SCMs. The dissolving solution of EDTA-NaOH has a wide linear measurement range (Fig. 1b), which is sufficient to determine the reaction degree of SCMs. In conclusion, the dissolving solution of EDTA-NaOH is efficient and reliable.

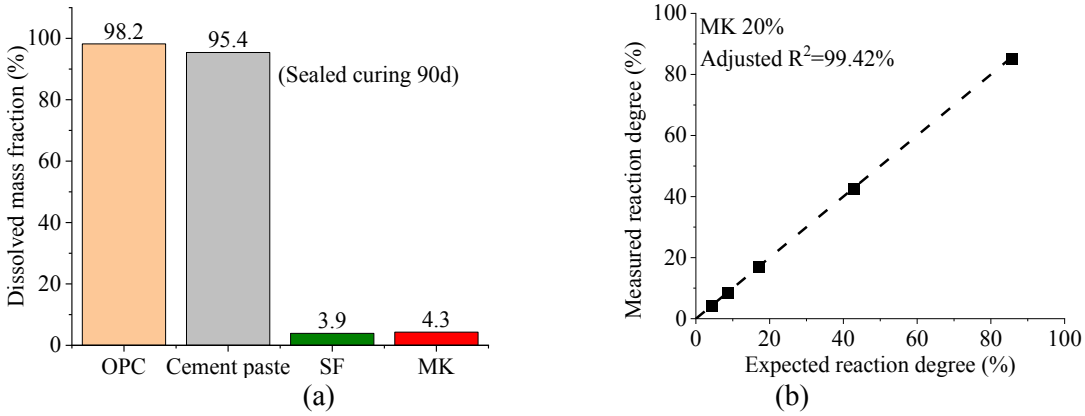


Fig. 1. (a) Dissolving properties of dissolving agent of EDTA-NaOH (b) Linear measurement range: Expected reaction degree is determined based on the actual concentration of standard solutions introduced, while measured reaction degree is obtained by analyzing the concentrations of ions measured from ICP.

3.3 Experimental results

Fig. 2(a) and Fig. 2(b) show the pozzolanic reaction degree results for silica fume and metakaolin respectively. The results were compared with the retained mass obtained by membrane filter paper. The retained size of filter paper is 0.1μm, which retained up to 99.4% of raw silica fume. Despite using a 0.1μm membrane filter, the method using filter paper shows higher values, possibly because some of the fine particles may become even smaller and escape through the filter papers after the reaction. The EDTA with ICP analysis provides more realistic result since it directly measured the ion concertation in solution. Moreover, the EDTA with ICP analysis is much efficient than the method using filter paper. The measurement using filter paper takes 8-9 hours but the method using ICP analysis only takes a few minutes.

Table. 2 Dissolution degree of raw silica fume using filter paper

Type of filter paper	Particle retention size (μm)	Retention (mass %)	Dissolution degree (mass %)	Filtration time
Membrane filter	0.1	99.4	0.6	8-9 hours

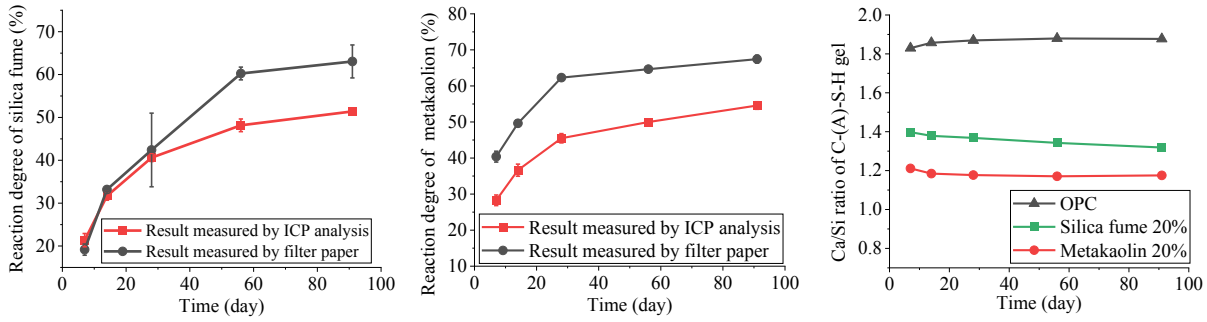


Fig. 2. Pozzolanic reaction degree of (a) silica fume and (b) metakaolin in SCM blended cement pastes with 20% replacement (c) Ca/Si ratio of C-(A)-S-H gel

The Ca/Si ratio of the C-(A)-S-H gel can be further determined when coupled with XRD and TGA tests. The XRD-Rietveld method was used to quantify crystalline phase in the blended cement paste, including unhydrated clinker phases, portlandite, calcium aluminum hydroxides, carbonates and others. The Ca/Si ratios of the C-(A)-S-H gel was determined through a mass balance approach. Specifically, the Ca, Si, and Al contents in the C-(A)-S-H gel are calculated by subtracting the ion concentrations obtained from XRD for each element from the total ion concentrations measured from ICP. The concentration of Ca ion in C-(A)-S-H is calculated according to Eq. (2) and can be similarly calculated for Si ion and Al ion. Mass ratio of Ca and Si ions in C-A-S-H are then used to calculate Ca/Si ratio.

$$C_{si}^{C-(A)-S-H} = C_{si}^{EDTA-ICP} - C_{si}^{XRD} \quad (2)$$

where $C_{si}^{C-(A)-S-H}$ is the silicon content in C-(A)-S-H gel, $C_{si}^{EDTA-ICP}$ is the dissolved Si ion of the SCM cement paste in EDTA-NaOH solution and C_{si}^{XRD} is the calculated Si ion concentration in the total crystalline fractions obtained from XRD-Rietveld. These values are normalized to 100% raw fraction using TGA weight fractions at 1000 ℃. Experimental results were summarized in Fig.2c. The Ca/Si ratio of the C-(A)-S-H gel decrease as the reaction progresses in SCM blended cement pastes.

4. Conclusions

This study highlights the limitations of existing methods for determining reaction degree, which can be tedious and prone to errors such as selective dissolution method. To address this, a new method based on selective dissolution in combination with ICP was proposed and validated. The new method was found to accurately determine the reaction degree of various low calcium SCMs, and can also be used to determine Ca/Si of C-(A)-S-H gel when combined with XRD and TGA. The test duration is significantly shorter and could be finished in less than an hour for multiple samples. In summary, the innovative approach proposed in this study offers a more efficient and accurate means of assessing the pozzolanic reaction degree of SCMs in cementitious systems, which has potential applications in the development of more sustainable and eco-friendly construction materials. Although this method has been developed for low calcium SCMs in this study, there is potential for its extension to high calcium SCMs, e.g., slags.

Acknowledgements

The authors are grateful for the financial support from Fundamental Research Funds for the Central Universities in China, Taisei Foundation (Grant project in 2020), Japan Cement Association (Grant projects in 2022) and Japan Concrete Institute (Grant project in 2022).

References

Megat Johari, M. A., J. J. Brooks, Shahid Kabir, and Patrice Rivard. (2011). "Influence of supplementary cementitious materials on engineering properties of high strength concrete", *Construction and building materials*, 25 (5): 2639-48.

Poon, C. S., L. Lam, S. C. Kou, Y. L. Wong, and Ron Wong. (2001). "Rate of pozzolanic reaction of metakaolin in high-performance cement pastes", *Cement and Concrete Research*, 31 (9): 1301-06.

Scrivener, Karen L., Barbara Lothenbach, Nele De Belie, Elke Gruyaert, Jørgen Skibsted, Ruben Snellings, and Anya Vollpracht. (2015). "TC 238-SCM: hydration and microstructure of concrete with SCMs", *Materials and Structures*, 48 (4): 835-62.

Wang, Tiao, Tetsuya Ishida, Rui Gu, and Yao Luan. (2021). "Experimental investigation of pozzolanic reaction and curing temperature-dependence of low-calcium fly ash in cement system and Ca-Si-Al element distribution of fly ash-blended cement paste", *Construction and building materials*, 267: 121012.

Wei, Yongqi, Wu Yao, Xiaoming Xing, and Manjian Wu. (2012). "Quantitative evaluation of hydrated cement modified by silica fume using QXRD, 27Al MAS NMR, TG–DSC and selective dissolution techniques", *Construction and building materials*, 36: 925-32.

The 16th International Congress on the Chemistry of Cement 2023 (ICCC2023)
"Further Reduction of CO_2 -Emissions and Circularity in the Cement and Concrete Industry"
September 18–22, 2023, Bangkok, Thailand

Power ultrasound assisted production of sustainable concrete

R. Remus[1*], C. Rößler[2], P. Hesse[1], S. Nune[1] and H.-M. Ludwig[3]

[1] *Sonocrete GmbH, Cottbus, Germany, Email: ricardo@sonocrete.com*
[2] *Bauhaus-University, Weimar, Germany, Email: christiane.roessler@uni-weimar.de*
[3] *Bauhaus-University, Weimar, Germany, Email: horst-michael.ludwig@uni-weimar.de*

ABSTRACT

Researchers, Institutions and Companies investigating, testing, and implementing ways to massively reduce the CO_2 emissions of the building industry. Depending on the country, carbon neutrality wants to be achieved within the next 20 – 25 years. However, a central approach to reduce the carbon footprint of concrete is decreasing the clinker content of cement. This will have significant effects on its early age performance and thus limits the applicability of low-CO_2 concretes, especially in the precast concrete production. Previous investigations have shown that the application of power ultrasound accelerates the hydration of Normal Portland cement [1].

Here we show how power ultrasound allows to incorporate high amounts of blended cements while maintaining high early compressive strengths for an ecologic and economic precast production. Thereby the application of power ultrasound does not increase mixing time of concrete. This procedure was developed and tested in the lab and finally applied on a federal construction site for prestressed girders in Germany. It is shown that ultrasound pre-mixing of cement suspension leads to formation of C-S-H phases and portlandite at very early ages, serving as an accelerator for the ongoing hydration. This significantly increases early compressive strength. Results show that this technology enables to reduce CO_2 emissions of concrete by 30 % while still maintain high early compressive strength.

KEYWORDS: *ultrasound, precast concrete, clinker reduction, performance*

1. Introduction

Regional and global cement and concrete associations (GCCA, PCA and VDZ) forcing the change to a greener concrete production. This comes along with strongly reduced clinker content in cement, since the CO_2-emissions of clinker production or the energy related to its storage/usage is huge [2].
Besides novel developments in cement and concrete composition, mixing of concrete was and is of increasing interest to improve concrete properties [3 bis 6]. Dollimore and Mangabhai for example [3] described that increasing mixing time decreases the induction time and increases the rate of heat evolution of cement paste. They concluded that prolonged mixing influences setting time and strength development. Later, Yang and Jennings [7] reported a strong influence of mixing methods on rheological behavior and appearance of agglomerates within the cement paste. They found that high energy mixing reduces shear stress of fresh cement paste by breaking down agglomerates. In the past decade, much research was done investigating physical and chemical aspects of different mixing methods [8 bis 11].
A relatively new approach in mixing cement paste is the application of power ultrasound. Power ultrasound application is not very common in the concrete industry but well known in other industrial applications. For example, for the segregation of particles, deagglomeration, homogenization, for cleaning, and many more. Toumbakari et al. [12] describe an improved injectability of sonicated grouts. The study compared high turbulence mixer with ultrasound application. It was found that a grout composition with very fine materials, like silica fume, high turbulence mixing was unable to produce an injectable grout. However drastically increased water and superplasticiser content produces injectable grouts. Ultrasound mixing produces injectable grouts with high penetrability and limited water content, even when silica fume is added. Previous studies of the authors revealed, that ultrasound is able to accelerate cement respectively alite hydration [13, 14]. This effect induces faster setting of cement and higher early strength of mortar and

concretes produced [1, 15]. In the present paper the technology of sonicating cement suspensions in industrial scale, the effects on cement hydration and an application where the technology was used to produce concrete elements for a federal construction site will be discussed.

2. Materials and Methods

2.1. Lab investigations

Sonication of cement suspensions was performed by taking a part of cement (e.g. 20%) and mixing it with water to create a cement suspension with a w/c-ratio of 1. For processing the cement suspension in the plant, it was found the more fluid suspensions tend to cause less problems, like clogging in pipes or sedimentation when stirred. For the lab investigations ultrasound-treated and non-treated samples were compared. Therefore, an ultrasound lab device was used (20 kHz, 2000 W max. power output, 50 – 75 Ws/ml energy input). The sonication took about 1 – 2 minutes directly after mixing of cement and water. After mixing and sonicating, the cement suspension was stored in a stirred vessel to follow further reaction. Hydration was stopped at several time steps via solvent exchange (isopropanol) and subsequent filtration with N_2-pressure gas to get the pore solution and the solids for further investigations. Analysis of calcium- and silicon-ion concentration of the pore solution was done with optical emission spectroscopy (ICP-OES, Horiba Jobin Yvon). Portlandite formation was calculated from thermogravimetric data according to [16]. Scanning electron microscopy (device) was performed to evaluate microstructural changes of the cement suspension.

2.2. Field trials

For the field trials, a sonocrete device for concrete plants was used. This device is designed to mix and sonicate up to 3000 l of cement suspension. The suspension was prepared (w/c = 1.0, 50 Ws/ml ultrasound energy input) and pumped into the concrete mixer via a hose pump.

3. Results

3.1. Lab investigations

In **Error! Reference source not found.** the development of the Si and Ca-ion concentrations over time for the stirred suspension with and without sonication is shown. As can be seen, the Ca-ion concentration is decreasing slowly for the reference suspension, indicating a consumption of Ca-ions caused by the formation of hydrate phases (C-S-H and portlandite). The ultrasound sample however, exhibits a

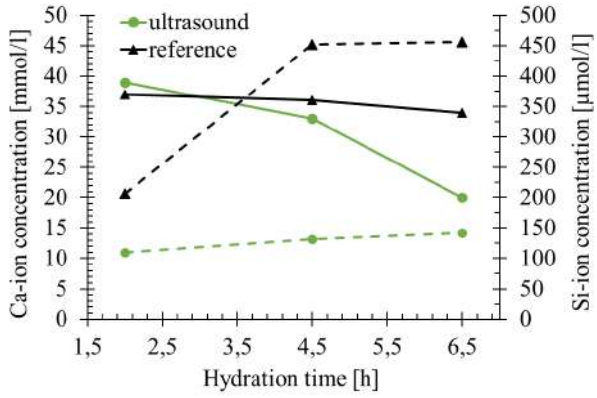


Figure 1: Ca-Ion (solid line) and Si-ion (dotted line) development of a stirred cement suspension (w/c = 1)

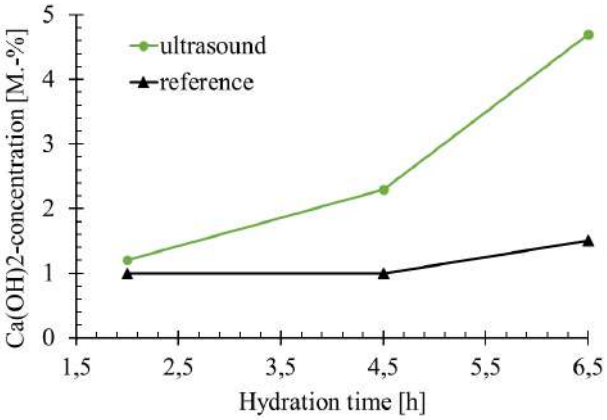


Figure 2: Portlandite concentration derived from thermogravimetric measurements.

significantly increased Ca-ion consumption during the same time. This indicates an accelerated formation of hydrate phases. Additionally, the development of Si-ion concentrations is shown. Here, in contrast to Ca the Si-ion concentration is increasing over time in the reference sample whereas the sonicated sample remains at a low level. This indicates that dissolution and precipitation is balanced. The reference sample therefore, exhibits a stronger dissolution than precipitation leading to increased Si-ion concentrations. In addition, the development of portlandite concentration is shown in *Figure 2*. As can be seen, portlandite concentration of the sonicated stirred suspension is increasing at a much higher rate that the non-treated

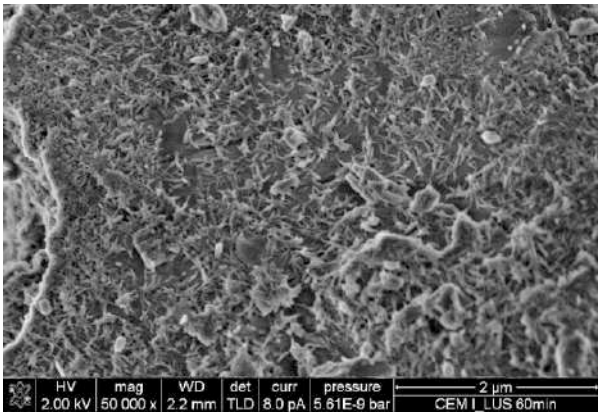


Figure 3: Mortar (CEM I, w/c = 0,50) with sonicated suspension after 60 Minutes. SEM-SE, TLD detector

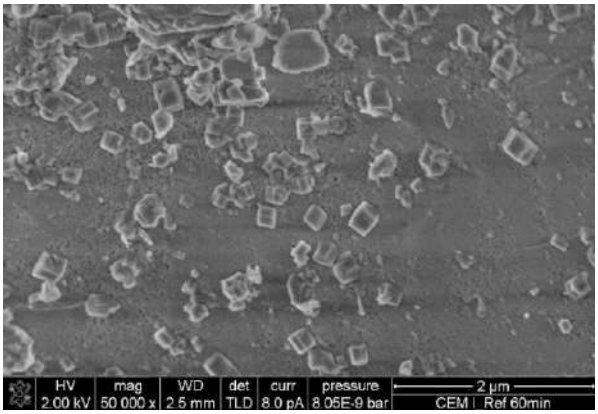


Figure 4: Mortar (CEM I, w/c = 0,50) with non-treated suspension after 60 Minutes. SEM-SE, TLD detector

reference suspension. Increased amounts of portlandite indicates that more C-S-H has already formed, since portlandite and C-S-H re both a product of C_3S-hydration.
From this graph it can be concluded that hydration is accelerated in the sonicated suspension, whereas the non-treated reference suspension exhibits almost no hydration, since portlandite amount did not vary much over time. This clearly demonstrates that sonication of cement suspension accelerates hydration.
In Figure 3 the surface of a mortar 60 min after mixing fresh cement and water with pre-mixed and sonicated cement suspension (ratio 80% fresh/ 20% pre-mixed cement) is shown. As can be seen, the surface of the cement particle is already partially covered with small fibrous C-S-H
phases. In Figure 4, the mortar without pre-mixed cement suspension is shown. Here after 60 min of hydration, no C-S-H phases but only ettringite are visible.

3.2 Field investigations

Additional to the preliminary investigations, concrete production was performed with an industrial ultrasound pre-mixing device in a concrete plant in Germany. To reduce the clinker content of the concrete



Figure 5: Sonocrete device for concrete plants

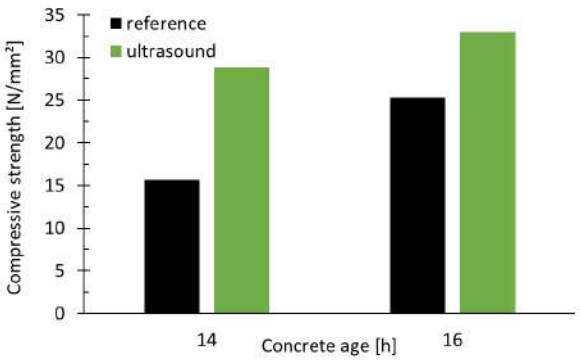


Figure 6: Early compressive strength of a precast concrete with 20% CEM I and 80% CEM II/B-S

the amount of Portland cement was reduced and substituted with 80% of a GGBFS-blended cement (CEM II/B-S 52,5 N). The overall amount of cement was reduced from 370 kg/m³ to 340 kg/m³, which decreases the embedded CO_2 of the cement fraction of about 30%. Since sonication solely relies on electrical energy, CO_2-footprint of the electrical energy used should be considered as well. In Figure 6, the early compressive strength of the concrete is shown. As can be seen, early compressive strength can be increased significantly with power ultrasound premixing. Even at an industrial scale. The energy consumption of the sonication process was for the before mentioned results between 1.5 to 2 kWh/m³, which is from the environmental as well as the economic perspective just minor.

3. Conclusions

Application of power ultrasound pre-mixing was investigated in the lab for a long time. Since the beginning of last year an industrial device for sonication of cement suspension is available and was tested in different

precast concrete plants for different products (pre-stressed girders, beams, walls, garages, and smaller products). It was demonstrated that the acceleration gained from the seeding effect with pre-hydrated cement suspension is capable of being used in an industrial setting. Microstructural investigations showed that sonication clearly accelerates and enhances the formation of hydrate phases like C-S-H and portlandite. This potential can be used to reduce clinker content of concretes without compromising early compressive strength. With this technology, a carbon reduction of up to 30% could be proofed in a precast plant using an industrial ultrasound mixing unit. Further optimization of process and the cement/concrete composition will allow to further reduce the carbon footprint of precast concrete.

Literature

[1] Remus, R., Rößler, C. u. Ludwig, H.-M.: Power ultrasound-assisted concrete production-workability, strength development, and durability. American Concrete Institute, ACI Special Publication 2018-October (2018) SP 330, S. 135–149

[2] IEA: Cement, Paris 2022. https://www.iea.org/reports/cement

[3] Dollimore, D. u. Mangabhai, R. J.: Effect of mixing time on heat evolution pattern of cement pastes. Thermochimica Acta 85 (1985), S. 223–226

[4] Klieger, P.: Effect of Mixing and Curing Temperature on Concrete Strength. ACI Journal Proceedings 54 (1958) 6, S. 1063–1081

[5] Ferraris, C. F.: Concrete Mixing Methods and Concrete Mixers: State of the Art. Journal of research of the National Institute of Standards and Technology 106 (2001) 2, S. 391–399

[6] Dils, J., Schutter, G. de u. Boel, V.: Influence of mixing procedure and mixer type on fresh and hardened properties of concrete: a review. Materials and Structures 45 (2012) 11, S. 1673–1683

[7] Yang, M. u. Jennings, H. M.: Influences of mixing methods on the microstructure and rheological behavior of cement paste. Advanced Cement Based Materials 2 (1995) 2, S. 70–78

[8] Collin, V. u. Jézéquel, P.-H.: Mixing of concrete or mortars: Distributive aspects. Cement and Concrete Research 39 (2009) 8, S. 678–686

[9] Han, D. u. Ferron, R. D.: Influence of high mixing intensity on rheology, hydration, and microstructure of fresh state cement paste. Cement and Concrete Research 84 (2016), S. 95–106

[10] Jézéquel, P.-H. u. Collin, V.: Mixing of concrete or mortars: Dispersive aspects. Cement and Concrete Research 37 (2007) 9, S. 1321–1333

[11] Juilland, P., Kumar, A., Gallucci, E., Flatt, R. J. u. Scrivener, K. L.: Effect of mixing on the early hydration of alite and OPC systems. Cement and Concrete Research 42 (2012) 9, S. 1175–1188

[12] Toumbakari, E.-E., van Gemert, D., Tassios, T. P. u. Tenoutasse, N.: Effect of mixing procedure on injectability of cementitious grouts. Cement and Concrete Research 29 (1999) 6, S. 867–872

[13] Peters, S.: The Influence of power ultrasound on setting and strength development of cement suspensions. Weimar: Bauhaus-Universität Weimar 2017

[14] Rößler, C., Stoeckigkt, M., Peters, S. u. Ludwig, H.-M.: Power ultrasound: An effective method to accelerate strength and early strength development of concrete. International Congress of Cement Chemistry (ICCC), Madrid (2011)

[15] Remus, R., Rößler, C., Ludwig, H.-M. u. Orben, J.: Power ultrasound-assisted concrete production - Scale up of laboratory experiments. Betonwerk und Fertigteil-Technik/Concrete Plant and Precast Technology 83 (2017) 5, S. 48–54

[16] Bellmann, F., Sowoidnich, T., Ludwig, H.-M. u. Damidot, D.: Dissolution rates during the early hydration of tricalcium silicate. Cement and Concrete Research 72 (2015), S. 108–116

The 16th International Congress on the Chemistry of Cement 2023 (ICCC2023)
"Further Reduction of CO_2 -Emissions and Circularity in the Cement and Concrete Industry"
September 18–22, 2023, Bangkok, Thailand

Feasibility of using volcanic debris from the island of La Palma as building materials

M.M. Alonso[1*], J.L. Costa-Krämer[2], M. Pankhurst[3], F. Puertas[1], A. Caño[1] and J.A. Suarez Navarro[4]

[1]*Eduardo Torroja Institute for Construction Sciences (IETcc-CSIC), Madrid, Spain*

Email: mmalonso@ietcc.csic.es, puertasf@ietcc.csic.es; andres.cano@csic.es

[2] *IMN-Instituto de Micro y Nanotecnología (CNM-CSIC), 28760 Tres Cantos, Madrid, Spain*

Email: jl.costa.kramer@csic.es

[3] *Institute of Technology and Renewable Energies (ITER), Tenerife, Spain*

Email: mpankhurst@iter.es

[4] *Centre of Energy, Environment and Technology Research (CIEMAT), Madrid, Spain*

Email: ja.suarez@ciemat.es

ABSTRACT

In 2021 a significant eruption of the Tajogaite volcano on the island of La Palma took place, leaving large quantities of volcanic material on roads, villages and crops. The possibility of using these materials in building materials is of great environmental interest. This work studies three samples (two solid volcanic flow samples and one volcanic ash) from different locations of the volcanic deposits. They have been characterized chemical, mineralogical and radiologically. The results have shown that all samples have a composition based mainly on clinopyroxenes, olivine and plagioclases. In addition, all three samples have been shown to be radiologically safe. Also, mortars were prepared using these volcanic samples. The replacement of aggregate in mortars is the most reasonable option for both volvanic lava wastes, due to their low pozzolanity. The volcanic ash, in contrast, displays pozzolanic behaviour and 34.5% of reactive SiO_2, so it may be used to substitute for cement.

KEYWORDS: *Volcanic debris, La Palma island, Mortars, Radioactiviy, Aggregates*

1. Introduction

On 19 September 2021, the Tajogaite volcano erupted in the area of "Cabeza de Vaca" (La Palma island). Its activity lasted eighty-five days, causing serious damage to crops, homes, buildings in general and all types of infrastructures. Removal and storage of these volcanic deposits is an economic and management problem, and so the possibility of reusing these debris as building materials is of great interest. However, this volcanic material may contain a large amount of natural radionuclides that could pose a risk to health and the environment (Sabarese et al 2021, Puertas et al 2021). In this sense, the work of Hernandez (Hernandez 2022), showed that the concentration of radionuclides from 238U and ^{232}Th series as well as ^{40}K in samples from the 2021 eruption of La Palma was comparable to previous samples from Cumbre Vieja soils and rocks (López-Pérez et al, 2021). On the other hand, there are several studies that have demonstrated the feasibility of using volcanic ash both as a cement replacement due to its pozzolanic characteristics (Alqarni 2022) or as a precursor for alkali-activated cements (Robayo-Salazar et al. 2018).However, there is no work to date that has used these volcanic deposits as a replacement for either binder or aggregate, so the study of this possibility would result in materials with a low CO_2 footprint.

2. Materials and methodology

Three volcanic debris samples named A1, A2 (solid flow samples) and VA (volcanic ash), were collected from different locations on the island of La Palma. Three equal portions of each sample were ground to a

grain size of less than 125 µm, and were characterised chemically by XRF and mineralogycaly by means of XRD. The pozzolanicity test was also carried out according to UNE-EN 196-5 (2011) standard. Finally their radiological content was determined by gamma spectrometry. With the radionuclide activity values of ^{226}Ra, ^{212}Pb (from thorium series) and ^{40}K for A1, A2 and VA, their ACI (Activity Concentration Index) was determined from the following equation:

$$ACI = \frac{C_{226_{Ra}}}{300} + \frac{C_{232_{Th}}}{200} + \frac{C_{40_K}}{3000}$$

Once A1, A2 and VA were characterised, A1 and A2 samples were mixed, ground and sieved to obtain the same particle size as a standard sand according to DIN EN 196. This sand resulting from the A1 + A2 mixture will be referred hereinafter as A3.Cement mortars were prepared with two different binders: 100%CEM I 42.5R and 70%CEM I 42.5R/30%VA and with two different aggregate proportions (100% siliceous sand and 50%/50%wt siliceous sand/volcanic sand). All mortars were prepared with an aggregate/cement ratio of 3/1 (Table 1). The mechanical performance was then tested.

Table 1. Mortars tested

	Binder (%)		Aggregate (%)	
	CEM	VA	Siliceous sand	A3 sand
Mortar 1	100	-	100	-
Mortar 2	100	-	50	50
Mortar 3	70	30	100	-
Mortar 4	70	30	50	50

3. Results and discussion

Table 2 shows the chemical composition of samples A1, A2 and VA, and Figure 1 their mineralogical characterization by XRD, as well as loss on ignition and SiO_2 reactive.

Table 2. Chemical composition (% oxides) for A1, A2 and VA

	SiO_2	Al_2O_3	Fe_2O_3	CaO	MgO	MnO	Na_2O	K_2O	TiO_2	Others	LoI	SiO_2 reactive %
A1	41.2	13.3	14.1	11.3	9.7	0.2	4.2	1.4	3.6	1,01	0	-
A2	42.0	13.5	13.7	11.6	8.7	0.2	4.3	1.5	3.5	1.0	0	-
VA	42.6	14.2	13.8	11.4	7.0	0.2	4.1	1.6	4.0	0.99	0	34.5

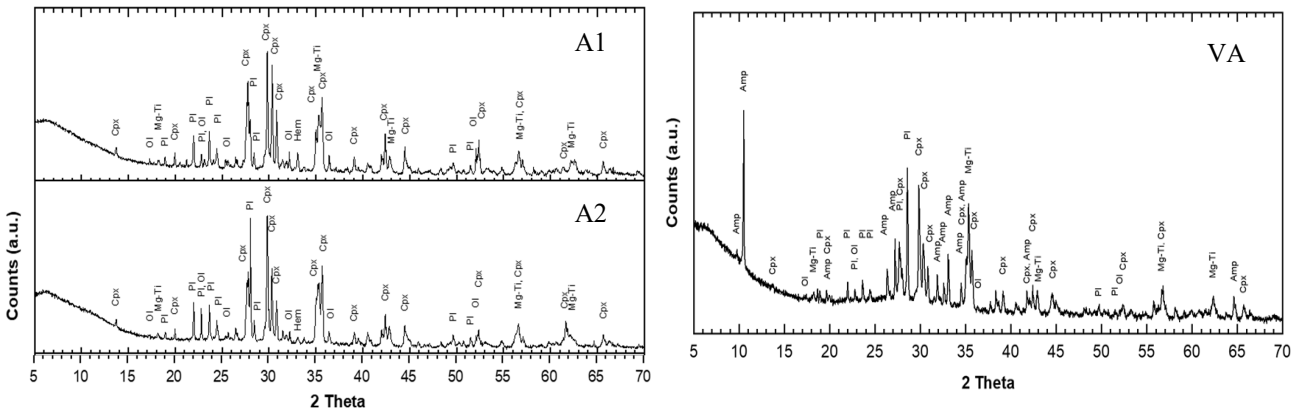


Figure 1. XRD of aggregates samples A1, A2 and VA. (Cpx=clinopiroxene; Ol=olivine; Pl= plagioclase; Mg-Ti= magnesium titanate; Hem=hematite; Amp=amphiboles)

The chemical and mineralogical characterisation illustrates that the three samples are highly similar in all major oxides (SiO_2, Al_2O_3, Fe_2O_3, CaO and MgO) and mineralogical phases (clinopyroxenes, plagioclase

and olivine), which is in agreement with previous works on volcanic material from this same area. (Arroyo, et al 2021, Pankhurst, et al 2022). Only the VA sample shows a halo, indicative of amorphous content, as well as the presence of amphibole. From the presence of olivine and absence of quartz, it can be determined that this material was formed from SiO_2-under-saturated magma (Bowen, N 1956).
The results obtained for the pozzolanicity test are shown in Table 3. Notice, that only sample VA shows pozzolanic behaviour, and its $\%SiO_2$ reactive is 34.5% and can therefore be used as a Supplementary Cementitious Material (SCM). On the contrary, samples A1 and A2 could only be used as aggregate replacement in mortars and concretes.

Table 3. Pozzolanity results for A1, A2 y VA.

Samples	[CaO] mol		[OH^-] mol	
	8d	**15d**	**8d**	**15d**
A1	13.2	11.1	56.0	66.0
A2	12.7	11.5	56.0	60.0
VA	6.3	6.8	54.2	56.7

Regarding the radiological characterisation, the activity concentration of ^{226}Ra, ^{212}Pb and ^{40}K as well as ACI of the three samples are shown in Table 4.

Table 4. ACI and activity concentration for the gamma emitters in the naturally occurring ^{226}Ra, ^{212}Pb and ^{40}K in A1, A2 and VA.

	^{226}Ra	**^{212}Pb**	**^{40}K**	**ACI**
A1	54.6 ± 7.2	33.0 ± 2.7	350 ± 16	0.46
A2	40.4 ± 8.5	31.7 ± 2.6	328 ± 15	0.41
VA	29.3 ± 3.9	32.6 ± 1.9	385 ± 12	0.47

The ACI for all three samples comply with Directive 2013/59/EURATOM (EU, 2013), being less than 1, thus indicating full radiological safety when using these volcanic materials as building materials. Previous works have proven (Bellia et al 1997, Alonso et al 2020) that these volcanic materials can contain variable amounts of radionuclides, so a radiological characterisation is necessary to guarantee a responsible use of these materials.
The nomenclatures used for mortars, the l/s ratio to obtain equal consistency, the compressive strength and total porosity (by means of Hg intrusion porosimetry) obtained at 2 and 28 days are shown in Table 5.

Table 5. Compressive strength of mortars with A1, A2 and VA.

	Compressive strength (MPa)		**Total porosity %**	
	2d	**28d**	**2d**	**28d (% decrease)**
Mortar 1	36.7 ± 1.8	63.8 ± 1.7	9.88	8.77 (11%)
Mortar 2	29.4 ± 1.3	65.7 ± 7.3	11.83	8.53 (27%)
Mortar 3	19.9 ± 1.3	44.8 ± 1.3	12.94	11.8 (9%)
Mortar 4	15.7 ± 1.2	40.3 ± 1.2	17.97	14.13 (21%)

To begin with, it can be observed that the compressive strengths at 28 days are higher than those at 2 days, as is to be expected. On the other hand, CEM I 42.5R mortars (numbers 1 and 2) have higher compressive strengths than those corresponding to 70% CEM I 42.5R/30%VA mortars (numbers 3 and 4) as expected, due to the slower hydration reactions in these types of pozzolanic blended cements.
The replacement of 50% of the siliceous aggregate by the A1+A2 volcanic sand mixture leads to a reduction in mechanical strengths of 20 % for all mortars at 2 days. However, after 28 days of testing, both mortars 1 and 2 and mortars 3 and 4 with 30% VA show differences in their compressive strengths of less than 10%, which indicates that the volcanic aggregate is suitable for use, although it reduces the strengths at early ages. This decrease in compressive strength is in accordance with porosity values, which at the age of 2d are higher for mixes with 50%siliceous sand/50%mixed sand. However, at 28 days the porosity values of all mortars are lower than at two days due to the progress of hydration, with a steeper decrease in mortars with a 50/50 aggregate mix (See Table 5) . In mortars 1 and 2, in fact, there is

hardly any difference in mechanical strength and porosity at the age of 28 days. In mortars 3 and 4, the pozzolanic reaction is slower and the porosity is reduced less than in mortars 1 and 2.

Conclusions

The possibility of using volcanic ashes from La Palma as SCMs in cement mortars is demonstrated, given their pozzolanic character. Furthermore, the solid deposits of lava flows are viable as replacements for aggregates in mortars, also complying with the radiological safety conditions.

Acknowledgements

Authors wish to thank the support of Project PID2020-116002RB-100/AEI/10.13039/501100011033 (HORRADIONEX). The authors would also like to thank the MICINN for the pre-doctoral contract (PRE2021-098535) of Andrés Caño Blanes. We also acknowledge project S2018/NMT-4291 TEC2SPACE

References

Alqarni. A.S. (2022) “A comprehensive review on properties of sustainable concrete using volcanic pumice powder ash as a supplementary cementitious material” Construction and Building Materials, 323, 126533

Alonso, M.M., Suárez-Navarro, J.A., Pérez-Sanz, R., Gascó, C., Moreno de los Reyes, A.M., Lanzón, M., Blanco-Varela, M.T., Puertas, F. (2020) “Data on natural radionuclide's activity concentration of cement-based materials” *Data in Brief*. 33,106488.

Arroyo, X., Andreu, L., López-Andrés, S., García-Lorenzo, M.L., Huertas, M.J. Ancochea, E. (2021) “Caracterización de materiales geológicos del volcán de Cumbre Vieja (La Palma, España) y su posible revalorización como materia rrima en aplicaciones ambientales”, *XXVII Reunión de la Sociedad Española de Arcillas,* 13-14.

Bellia, S., Brai, M., Hauser, S., Puccio, P., Rizzo, S. (1997) “Natural eeerialesRadioactivity in a Volcanic Ustica, Southern Italy Island". *Applied Radiation and lsotopes* 48, No. 2, pp. 287-293.

Bowen, N. L. Evolution of the Igneous Rocks H. S.Yoder Jr. Ed.1979 Princeton University Press (New York).

EU (2013) Council Directive 2013/59/Euratom of 5 Dec. Laying down basic safety standards for protection against the dangers arising from exposure to ionising radiation, and repealing Directives 89/618/Euratom, 90/641/Euratom, 96/29/Euratom, 97/43/Euratom and 2003/122/Euratom, vol 57. L13, vol ISSN 1977-0677. European Commission,

Hernández, J. (2022) “Natural radionuclides in volcanic materials from La Palma eruption 2021”. Degree proyect. Universidad de la Laguna

López-Pérez, M., Martín-Luis, C., Hernández, F., Liger, E., Fernández-Aldecoa, J. C., Lorenzo-Salazar, J. M., Hernández-Armas, J., y Salazar-Carballo, P. A. (2021). “Natural and artificial gamma-emitting radionuclides in volcanic soils of the Western Canary Islands”. Journal of Geochemical Exploration, 229, 106840.

Pankhursth, M.J., Scarrow, J.H., Barbee, O.A., Hickey, J., Coldwell, B.C., Rollinson, G.K., Rodríguez-Losada, J.A., Martín-Lorenzo, A., Rodríguez, F., Hernández, W., Calvo Fernández, D., Hernández, P.A., Pérez, N.M. (2022) “Rapid response petrology for the opening eruptive phase of the 2021 Cumbre Vieja eruption, La Palma, Canary Islands”. *Volcanica*, 5 (1), 1-10

Puertas, F., Suárez-Navarro, J.A., Alonso, M.M., Gascó, C. (2021) “NORM waste, cements, and concretes. A review”. Mater. Construcc. Vol. 71, 344, e259

Sabbarese, C., Ambrosino, F., D’Onofrio, A., Roca, V. (2021) Radiological characterization of natural building materials from the Campania region (Southern Italy). *Construction and Building Materials* 268, 121087.

UNE-EN 196-5 (2011) Methods of testing cement - Part 5: Pozzolanicity test for pozzolanic cements.

The 16th International Congress on the Chemistry of Cement 2023 (ICCC2023)
"Further Reduction of CO_2 -Emissions and Circularity in the Cement and Concrete Industry"
September 18–22, 2023, Bangkok, Thailand

Blended systems with OPC-Pozzolan-High limestone filler

P. Laniesse[1,2*], T. Gutsalenko[1,3], T. Wattez[1,2], R. Alfani[1], L. Frouin[1], M. Chaouche[3,4] and M. Cyr[2,5]

[1] *ECOCEM Materials, Paris, France*

Email: ralfani@ecocem.ie

Email: lau.frouin@gmail.com

[2] ORISON, LMDC-ECOCEM Common Laboratory, Toulouse, France

Email: planiesse@ecocem.ie

Email: twattez@ecocem.ie

[3] *MC²E, LMPS-ECOCEM Common Laboratory, Gif-sur-Yvette, France*

Email: tgutsalenko@ecocem.ie

[4] *Université Paris-Saclay, CentraleSupélec, ENS Paris-Saclay, CNRS, Laboratoire de Mécanique Paris-Saclay, Gif-sur-Yvette, France*

Email: mohend.chaouche@lmt.ens-paris-saclay.fr

[5] *LMDC-INSA/UPS-Université de Toulouse, Toulouse, France*

Email: martin.cyr@insa-toulouse.fr

ABSTRACT

Even if LC3 binders enables a significant improvement regarding carbon footprint, it still contains a large amount of OPC. Therefore, it is important to search for binders that provides an even more significant impact on carbon emissions, while maintaining sufficient mechanical properties and acceptable rheology. This work focuses on the design of a binder that presents a 1-to-1 OPC-to-Pozzolan ratio and with high limestone filler content (at least 50%). At such low cement content, it matters to reduce the water-to-binder ratio to ensure sufficient compressive strength development: thanks to the use of a high-range water reducing admixture the w/b was reduced up to 0.3 in mortars. A panel of natural pozzolans was tested to assess their properties and those of the subsequent binder. The hydration process was characterized, combining several technics, such as XRD, with Rietveld quantification and TGA. When comparing such ternary binders with their binary counterpart, where no limestone filler was introduced and the OPC-to-Pozzolan ratio kept constant, several observations were made. In both cases, it was observed that the chemical composition of the pozzolan, and more particularly of its amorphous phase, along with its granulometry are the main drivers for their reactivity at 28 days. On the other hand, the introduction of 50% limestone filler enhanced the pore size refinement with time through the precipitation of significant amounts of hemicarboaluminate phase, along with the common CSH, ettringite and portlandite.

KEYWORDS: *Low Carbon binders, Pozzolan, Hydration, sustainability*

1. Introduction

Ternary blends made of clinker, pozzolanic materials and ground limestone have been getting a lot of attention thanks to their ability to decarbonize the cement industry at scale and their performance. Those blends, containing either natural pozzolans or calcined clays, often recognized under the name of LC3 (Scrivener et al., 2018), now included in the cement European standards, still rely on significant amounts of clinker (≥50%). By adopting a reduction strategy in both the reactive binder content and the water-to-

binder ratio, as shown by John et al. (2018), we increased the limestone filler content above 50% of the total binder composition, therefore providing a scalable lower CO_2 footprint solution.
In the meantime, though natural pozzolans have been used and studied in OPC-rich systems for several decades (Hewlett and Liska, 2019), literature does not evaluate their properties and performance in the case of binders with reduced clinker contents. This study aims to evaluate, based on 10 different sources, how physical and chemical properties of natural pozzolans affect the performance of clinker-poor and limestone-rich ternary blends.

2.1. Materials & Methods

Ordinary Portland Cement (OPC) used in this work is a CEM I European standard EN 197-1 compliant cement which presented a density of 3.1 g/cm^3 and a Blaine fineness of 4300 cm^2/g; limestone filler presented a density of 2.7 g/cm^3 and a Blaine fineness of approximately 9000 cm^2/g.
Table 1 shows the chemical composition, obtained by means of ICP-OES, the particle size distribution (psd), measured by a laser granulometer in liquid phase (ethanol) and the amorphous phase content, calculated through Rietveld refinement of X-Ray Diffraction (XRD) pattern for each of the 10 different sources of natural pozzolan (NP).

Table 1 - Chemical composition, particle size distribution and amorphous content for all pozzolans.

	NP1	NP2	NP3	NP4	NP5	NP6	NP7	NP8	NP9	NP10
K_2O (%)	0.4	0.6	0.8	0.3	2.7	2.8	4.3	1.8	4.5	1.6
Na_2O (%)	1.9	2.2	2.9	1.8	2.3	3.5	3.4	2.2	4.0	3.8
SiO_2 (%)	44.1	43.3	46.8	44.5	73.4	71.0	74.1	44.0	50.1	46.3
Al_2O_3 (%)	14.8	12.4	12.8	13.3	11.9	12.1	11.8	15.9	17.6	15.7
CaO (%)	12.6	10.2	10.3	11.8	4.6	1.3	0.7	9.3	4.0	9.4
Fe_2O_3 (%)	12.6	15.0	16.2	13.7	1.4	2.8	1.0	8.2	5.3	12.0
MgO (%)	11.5	4.2	4.7	7.0	0.3	0.3	0.1	4.0	1.6	6.5
TiO_2 (%)	1.5	4.4	4.3	1.9	0.1	0.1	0.1	1.9	0.8	2.3
d_{10} (µm)	0.9	1.5	1.0	1.3	1.4	1.9	1.8	1.5	2.6	1.8
d_{50} (µm)	3.1	8.9	4.9	8.2	4.5	9.7	7.2	7.3	16.7	12.2
d_{90} (µm)	8.0	25.2	17.0	25.4	11.0	39.6	23.1	33.2	52.5	33.5
Amorphous content	89%	96%	95%	52%	85%	82%	99%	51%	56%	16%

Respectively NP2-NP3 and NP5-NP6 pairs are each time the same source of natural pozzolan ground to different finenesses. Table 1 covers a large variety of materials in terms of both chemical and physical properties in the set of natural pozzolans evaluated.
Pozzolans were individually evaluated in a ternary binder composed of 20% OPC, 20% Natural Pozzolan and 60% Limestone filler. All samples were prepared with a water-to-binder (w/b, binder here considers OPC, Pozzolan and Limestone filler) ratio of 0.3 and placed in sealed plastic bags at 20°C.
Phase assemblage of our ternary binder was assessed on pastes for NP1, NP4 and NP5 after 2 and 28 days curing by means Q-XRD and TGA. The TGA was first used to calculate the amount of calcite and portlandite contained in the samples. Internal standard (TiO_2 Rutile) was used to further refine the phase assemblage in Q-XRD, in terms of anhydrous clinker phases consumption (C_3S, C_2S, C_3A, C_4AF) and hydrates (CSH, Ettringite, Hemicarboaluminate) precipitation. For all the samples and at all time steps, the hydration reaction was stopped by solvent (isopropanol) exchange (Scrivener et al., 2016).
Mortars prisms were prepared by mixing 560 grams of the ternary binder with 1350 grams of silica sand and 168 grams of water. Sufficiently fluid mortars for their placement in the moulds were obtained by adding between 0.1% and 0.4% by binder weight of a high-range water reducing admixture. Strengths were evaluated on prisms (4x4x16 cm) cured in sealed bags after 1 and 28 days.
Reactivity of each pozzolan was assessed by means of the R3 tests (Avet et al., 2016) at 7 days.

2.2. Results

Table 2 below summarizes results of the R3 test for all 10 NPs considered. Variations of reactivity cover one order of magnitude of cumulated heat at the end of the 7 days test ensuring diversity of the NPs.

Table 2 - R3 test value for each natural pozzolan.

	NP1	NP2	NP3	NP4	NP5	NP6	NP7	NP8	NP9	NP10
R3 at 7 days (J/g)	447	230	327	213	229	221	173	117	202	51

Table 3 below shows the mechanical performance obtained on mortar prisms after 1 and 28 days curing.

Table 3 - Mortar compressive strengths at 1 and 28 days for each natural pozzolan tested.

	NP1	NP2	NP3	NP4	NP5	NP6	NP7	NP8	NP9	NP10
Compressive strength at 1 day (MPa)	7.1	5.8	5.4	4.8	6.6	4.8	5.5	4.1	5.1	5.1
Compressive strength at 28 days (MPa)	36.9	23.3	28.1	22.1	24.7	23.2	25.4	16.5	22.7	13.3

The mechanical performance at 1 day appears to be relatively independent of the pozzolan source and mostly related to the CEM I reactivity. Overall, the 28 days strength at mortar scale appeared to be quite strongly related to the R3 value (R^2=0.9232). The best performing pozzolan was NP1, which also displayed the highest R3 value, also displays the finest particle size distribution (Table 1). Change of fineness led to varied response, with an increase of strength and R3 value for the NP2-NP3 pair and no significant changes for the NP5-NP6 pair. Eventually, NP10 which displayed the lowest amorphous content (16%) also provided the lowest levels of performance for the 28 days compressive strength.

Table 4 below summarizes phase assemblage calculations obtained for NP1, NP4 and NP5.

Table 4 - Phase assemblage at 2 and 28 days for 3 different natural pozzolans.

	NP1			NP4			NP5		
	Initial	**2 days**	**28 days**	**Initial**	**2 days**	**28 days**	**Initial**	**2 days**	**28 days**
C_3S	9.8	0.6	0.2	9.8	0.6	0.1	9.8	0.6	0.2
C_2S	1.7	1.9	0.7	1.7	1.7	0.6	1.7	1.2	0.4
C_3A	0.5	-	-	0.5	-	-	0.5	-	-
C_4AF	1.8	0.5	0.1	1.8	0.3	0.0	1.8	0.5	0.1
Portlandite	-	4.3	2.7	-	3.7	2.4	-	4.3	2.7
Ettringite	-	2.1	1.3	-	1.5	1.4	-	1.7	1.5
Hemicarboaluminate	-	6.4	7.0	-	6.5	6.9	-	6.2	5.8
C-S-H	-	3.2	3.5	-	3.9	4.2	-	3.0	3.5
Calcite	47.4	46.2	45.7	47.4	46.2	45.7	47.4	46.2	45.9

From the table above, we observed that in these high limestone filler ternary systems:

- All C_3A and almost all C_3S was consumed after 2 days of hydration while the C_2S takes up to 28 days for most of it to be consumed as typically observed.
- Hydration products were mostly made of CSH, Ettringite, that formed with sulfate-OPC and Hemicarboaluminate that formed in the presence of calcite (and its subsequent consumption).
- Portlandite was formed as well and though its quantity decreased between the two measurements, due to the pozzolanic reaction taking place with the NP, remaining contents after 28 days were indicative of potential further performance developments of such ternary systems.

Despite the differences in the inner properties of the evaluated NPs, the obtained phase assemblages and associated kinetics did not seem to differ strongly from one natural pozzolan to another. Both lack of precision in Q-XRD induced by calcite preferential oriental and assumption of identical C-S-H structure for all evaluated NPs were deemed to be the limiting factors at this stage in further differentiating hydration kinetics and products' contents.

Table 5 below provides the chemical composition of the assumed amorphous phase. This amorphous phase chemical composition is calculated as the normalized difference between the overall chemistry (Table 1) and the chemical contribution of each mineralogical phase identified in the Rietveld refinement.

Table 5 - Normalized chemical composition of the amorphous phase of each natural pozzolan.

	NP1	NP2	NP3	NP4	NP5	NP6	NP7	NP8	NP9	NP10

K_2O (%)	0.5	0.7	0.9	0.7	3.3	3.7	4.6	3.3	6.5	2.9
Na_2O (%)	2.2	2.5	3.1	2.0	2.8	4.1	3.5	4.2	3.1	15.9
SiO_2 (%)	44.4	46.9	47.3	42.2	77.4	76.3	77.6	54.8	48.3	46.5
$Al2O_3$ (%)	16.1	13.1	12.4	13.6	10.7	12.1	12.3	18.0	23.5	0.0
CaO (%)	13.4	10.5	9.8	7.4	3.5	0.0	0.7	2.3	5.0	0.0
Fe_2O_3 (%)	14.3	17.0	17.2	30.0	1.7	3.7	1.1	11.7	11.0	22.9
MgO (%)	7.5	4.3	4.7	0.0	0.4	0.1	0.1	2.1	0.8	0.0
TiO_2 (%)	1.7	5.0	4.6	4.2	0.1	0.1	0.1	3.5	1.7	11.8

Among the 10 NPs presented in Table 5, we can visually separate them in three different groups based on their differences in chemical properties: 1 group presenting high CaO, MgO and Fe_2O_3 contents (NP1, NP2, NP3, NP4); 1 group presenting both high SiO_2 and Al_2O_3 contents (NP5, NP6, NP7); 1 group constituted of a blend of materials of varied properties (NP8, NP9 and NP10) with intermediate to low amorphous contents. Overall, 28 days strength of such CEM I – pozzolans – limestone blends was dictated by assumed synergies between the fineness, the amorphous content and the amorphous phase chemical composition. For the first identified group of NPs (Ca-rich, Si-poor), the fineness was the key factor in order to leverage the 28 days strength performance. For the second group made of Si-rich and Ca-poor NPs, the amorphous content was the predominant factor that affected the 28 days mechanical strength at mortar scale. The third group consisting of NPs of mixed nature and containing side minerals troublesome in the reactivity of our systems (zeolites or clays) did not provide a clear trend. The amorphous structure of our NPs could be described similarly to Si-based glasses. The first group being Ca-richer than the second one, was then assumed to present a more depolymerized network, therefore easier to dissolve in the alkaline environment provided by OPC, hence their expected higher reactivity at equivalent fineness. In the meantime, the same set of NPs presented high Fe_2O_3 contents. Siakati et al. (2020) indicated that Fe in Si-glass could both act as network former or modifier depending on the cooling conditions in which it was prepared. Little information is known on the cooling history of the studied NPs, therefore, though it remained a topic of importance, it was impossible at this stage to define Fe contribution to NPs reactivity.

3. Conclusions

The following conclusions were drawn out of this study:
- Ternary blends made of OPC, natural pozzolan and high volumes of limestone filler can provide a significant step forward in decarbonisation of the cement industry.
- In doing so, careful control of the NPs properties must be realized as well as adjustement of the ternary blend design in terms of OPC:NP ratio and sulfate balance to improve early age and long term performance.
- The R3 test result after 7 days of isothermal calorimetry at 40°C proved to be a rapid satisfactory differentiation tool to assess NP reactivity in those systems.
- Further work is required to overcome current limiting hypothesis and fully evaluate both hydration mechanisms and microstructure of such systems, and the subsequent durability properties.

References

Avet, F., Snellings, R., Diaz, A. A., Haha, M. B., & Scrivener, K. (2016). Development of a new rapid, relevant and reliable (R3) test method to evaluate the pozzolanic reactivity of calcined kaolinitic clays. *Cement and Concrete Research*, *85*, 1-11.

Hewlett, P., & Liska, M. (Eds.). (2019). *Lea's chemistry of cement and concrete*. Butterworth-Heinemann.

John, V. M., Damineli, B. L., Quattrone, M., & Pileggi, R. G. (2018). Fillers in cementitious materials—Experience, recent advances and future potential. *Cement and Concrete Research*, *114*, 65-78.

Scrivener, K., Martirena, F., Bishnoi, S., & Maity, S. (2018). Calcined clay limestone cements (LC3). *Cement and Concrete Research*, *114*, 49-56.

Scrivener, K., Snellings, R., & Lothenbach, B. (Eds.). (2016). *A practical guide to microstructural analysis of cementitious materials* (Vol. 540). Boca Raton, FL, USA:: Crc Press.

Siakati, C., Douvalis, A. P., Ziogas, P., Peys, A., & Pontikes, Y. (2020). Impact of the solidification path of FeOx–SiO2 slags on the resultant inorganic polymers. *Journal of the American Ceramic Society*, *103*(3), 2173-2184.

The 16th International Congress on the Chemistry of Cement 2023 (ICCC2023)
"Further Reduction of CO_2 -Emissions and Circularity in the Cement and Concrete Industry"
September 18–22, 2023, Bangkok, Thailand

Relationship between reactive alumina content of Calcined Clays and fresh cement pastes behaviour.

C. Pedrajas[1]*, V. Rahhal[2] C. Aramburo[3], and R. Talero[4]

[1] Aramburo&Pedrajas Consultant, Madrid, Spain
Email: cpedrajas@aramburopedrajas.com.com
[2] UNPCBA, Olavarría, Argentina
Email: vrahhal@fio.unicen.edu.ar
[3] Aramburo&Pedrajas Consultant, Cali, Colombia
Email: caramburov@aramburopedrajas.com
[4] SACAH S.L., Madrid, Spain
Email: rtalero@sacach.com

ABSTRACT

Calcined clays have quickly become one of the most interesting supplementary cementitious materials in the cement industry to achieve the clinker substitution levels set for the future. The incorrect use of this pozzolanic addition in cement and concrete can cause serious problems in the fresh state of these construction materials. In this research, the influence of the reactive alumina content of the calcined clays on the performance of their fresh cement pastes was analyzed. For this purpose, several calcined clay samples with different reactive alumina content and very close physical properties were selected. The main analytical techniques used to study these effects were: conduction calorimetry, rotational rheometry, and early age Frattini pozzolanicity test.

The results obtained showed that these calcined clays caused different effects depending on their reactive chemical composition, in particular their reactive alumina content. So, the quantity of reactive alumina generated during the thermal activation process has a completely influence in every fresh cement paste properties like heat of hydration and rheological performance. These results are a consequence of the different chemical effect from the pozzolanic activity of the calcined clay which is a function of the reactive alumina content.

KEYWORDS: *Low Carbon Cement, Supplementary Cementitious Material, Calcined Clays, Heat of Hydration, Rheology*

1. Introduction

In recent years, cement industry has been working to search and use new supplementary cementitious materials (SCMs) that allow the reduction of the clinker/cement factor significantly. Nowadays, there are several industrial developments that demonstrate the industrial feasibility of the clay thermal activation process to produce a SCM which the cement producer has control of its production capacity and quality (Arango et al. (2022)). Through the industrial development of this technology, the cement sector can achieve greater sustainability since this production process can have a reduction in CO_2 emission levels close to 70% compared to clinker and also a significant reduction in energy consumption depending on the activation process.

The greater or lesser pozzolanic activity of each calcined clay (CC), depends primarily on their amorphism, state and reactive nature of their structure, (Metha (1983), Trusilewicz et al. (2012)), Skibted and Snellings (2019)). The activation phenomenon of clays occurs at the temperature range from 600 to 850 °C that forms in the clay dihydroxylation process an amorphous phase (Garg and Skibsted (2019)).

According to Talero (1986), calcined clays are aluminic pozzolans in chemical character, so their influence in fresh state properties of cement and concrete materials will be very important (Rahhal and Talero (2008), Aramburo et al. (2018)). This influence chemically depends on the early, high and quick pozzolanicity activity generated by the $Al_2O_3^{r-}$ of the CC, which from the beginning of hydration affects the heat released and the rheological behaviour of the cement and its final products. For this reason, in the present research the influence of the $Al_2O_3^{r-}$ content generated in the thermal activation process on the fresh state properties of different cement pastes has been evaluated.

2. Materials and Methodology

The materials selected (Table 1) for this study were:

- A Portland cement (PC) with a high C_3A content, around 14%. Its physical parameters are a density of 3,08 g/cm^3 and a Blaine specific surface (BSS) of 319 m^2/kg.
- Three calcined clays, activated at 800ºC in every case, with different content of reactive silica (SiO_2^{r-}) and reactive alumina ($Al_2O_3^{r-}$). Their grinding fineness were obtained with a maximum retention of 20% of the wet material on the nº. 325 (45 µm) sieve.
- Distilled water as mixing water to prepare the pure and blended cement pastes.

Firstly, three blended cements with PC/CC ratios of 60%/40% (=60/40) (by mass) were prepared with the Portland cement the three CC.

Table 1. Chemical Parameters of every material used in this research.

Chemical Parameters (%)	PC	CC1	CC2	CC3
L.O.I.	1,6	0,4	0,6	0,6
I.R.	0,7	-	0,2	-
SiO_2	19,2	57,4	73,6	64,6
Al_2O_3	6,4	41,6	23,1	19,7
Fe_2O_3	1,7	0,5	1,2	10,6
CaO	63,9	0,0	0,3	0,5
MgO	1,5	-	0,0	0,8
Na_2O	0,9	-	0,1	0,0
K_2O	0,5	-	0,7	2,5
TiO_2	0,2	0,2	0,3	1,3
SO_3	3,3	-	-	-
TOTAL	100,0	100,1	100,1	99,9
Free CaO	1,9	-	-	-

Bogue Potential Composition (%)	PC
C_3S	51,0
C_2S	16,5
C_3A	14,1
C_4AF	5,3

Hydraulic Factors (%)	CC1	CC2	CC3
SiO_2^{r-}	48,5	38,5	31,3
$Al_2O_3^{r-}$	29,0	14,6	8,1

The Frattini test procedure was used to analyse the blended cements liquid phases (EN 196-5 (2011)). Data were taken at several ages: 20 min, 60 min, the first nadir calorimetric conduction curve time, Initial Setting Time (I.S.T.), Final Setting Time (F.S.T.), 1 day and 2 days.

The variation in the heat released by the cement pastes was then measured with conduction calorimetry technique (AJFK calorimeter at 25°C registering a data value every 2 min). The baseline temperature for the measurements was 25°C and the water/binder (w/b) ratio for all the cement pastes was 0.5 by mass. Data were recorded for the first 48 h of hydration.

Rheological trials were also run on a rotational rheometer fitted with a profiled rotor blade with serrated surface [Internal Diameter (Ri) = 19.010 mm; height (h) = 55 mm], a profiled cylinder, a temperature control unit for coaxial cylinders and a circulation thermostat. A scheme was made to show the evolution of the cement pastes as they achieve the biggest hysteresis loop (thixotropic behaviour). A control shear rate test (or CR test) was chosen for every case. The scheme designed was as follows: 10” from 0 to 45 rad/s; 30” at 45 rad/s; 10” from 45 to 27 rad/s; 10” at 9 rad/s; 10” from 9 to 0 rad/s. Trials were conducted during latent hydration at 25 ºC.

3. Results and Discussion

Figure 1 shows the [CaO] and [OH^-] determined for the four cements used in this research. The evolution of the portlandite content of each cement at early ages was different depending on the CC. The PC/CC1 60/40 blended cement was the one that experienced the most pozzolanic behaviour because at all test ages their points were below the solubility isotherm. CC1 was the one that developed the highest, fastest and earliest pozzolanic activity.

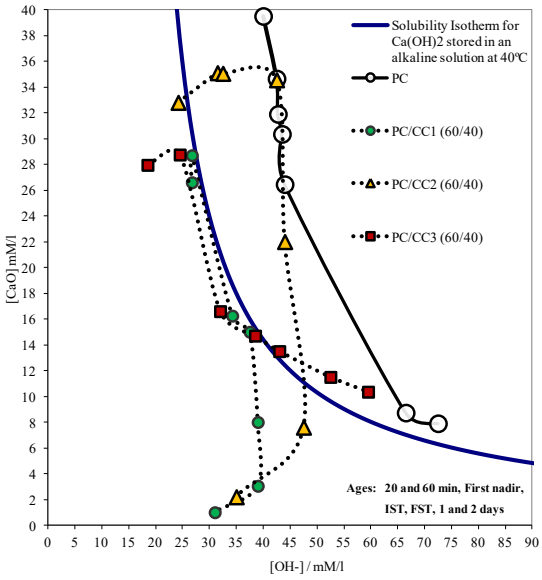


Figure 1. Frattini test at early ages for PC cement and its blended cements.

On the other hand, the calcined clays CC2 and CC3 showed lower pozzolanic activity than CC1 due to their lower reactive alumina content. In addition, their pozzolanic characteristics and, as a consequence, the $Ca(OH)_2$ content in the liquid phase of the cement pastes were proportional to that $Al_2O_3^{r-}$ content. As an example of this, it could be cited the case of CC3, with the lowest content of $Al_2O_3^{r-}$, caused the least stimulation of hydration by indirect way of the PC, (Aramburo et al. (2018)), therefore, the liquid phase was maintained for a longer time in the low-saturation zone at the beginning of hydration process. On the other hand, at the final ages of the Frattini test, 1 and 2 days, the cement paste remained in the upper-saturation zone due to the lower pozzolanic activity developed by CC3.

Figures 2(a) shows the calorimetric curves plotted during the first 48 h for PC alone and with CC1, CC2 and CC3. The three peaks on all cements correspond to initial hydrolysis, C_3S hydration and transformation of the AFt to the AFm phase, respectively. The first nadir is shifted to the left and attenuated, while the second and third peaks are likewise shifted to the left and larger for all the blended cements containing CC. These findings denote dilution of the silicate phase due to replacement of the PC by the CC, and simultaneously, the Synergistic Calorific Effect, SCE, produced between the C_3A from the PC and the $Al_2O_3^{r-}$ from the CC. The PC hydration was indirectly stimulated by the strong pozzolanic activity of CC, so heat values were greater than the values for the Portland cement. The effect grew with the reactive alumina, $Al_2O_3^{r-}$ content as shown in Table 1.

In addition, the transformation peak of AFt into AFm of the aluminic phase of the CC was faster and much higher with the more $Al_2O_3^{r-}$ content of the CC, which in turn also showed that at very early ages, the pozzolanic activity of $Al_2O_3^{r-}$ caused a more intense hydration of C_3A than of C_3S. This peak was more intense due to the decrease in the SO_3/Al_2O_3 molar ratio caused by the reactive alumina content of each CC. Therefore, the AFt became AFm generating intense heat.

In summary, the indirect stimulation of PC hydration by the three CC increases with their respective $Al_2O_3^{r-}$ contents. This behaviour is due to the SCE, between the C_3A on PC and $Al_2O_3^{r-}$ from CC for those pastes prepared with Portland cements with a high C_3A content and low C_3S content.

According to rheological measurement results, when PC was replaced by CC1 and CC2, the shear stress was much higher in all the singular points. In turn, for the CC3 was very close to PC shear stress values. This behaviour can be attributed primarily to the early, rapid and very high pozzolanicity developed by the $Al_2O_3^{r-}$ of CC1 and CC2. This stimulation phenomenon was more specific than generic, prompting more intense C_3A than C_3S hydration and very related with the $Al_2O_3^{r-}$ content of each CC. These findings denote dilution of the silicate phase due to replacement of the PC by the respective CC, and simultaneously, the Synergistic Effect, SE, produced between the C_3A from the PC and the $Al_2O_3^{r-}$ from the CC1 and CC2 because this content was so high.

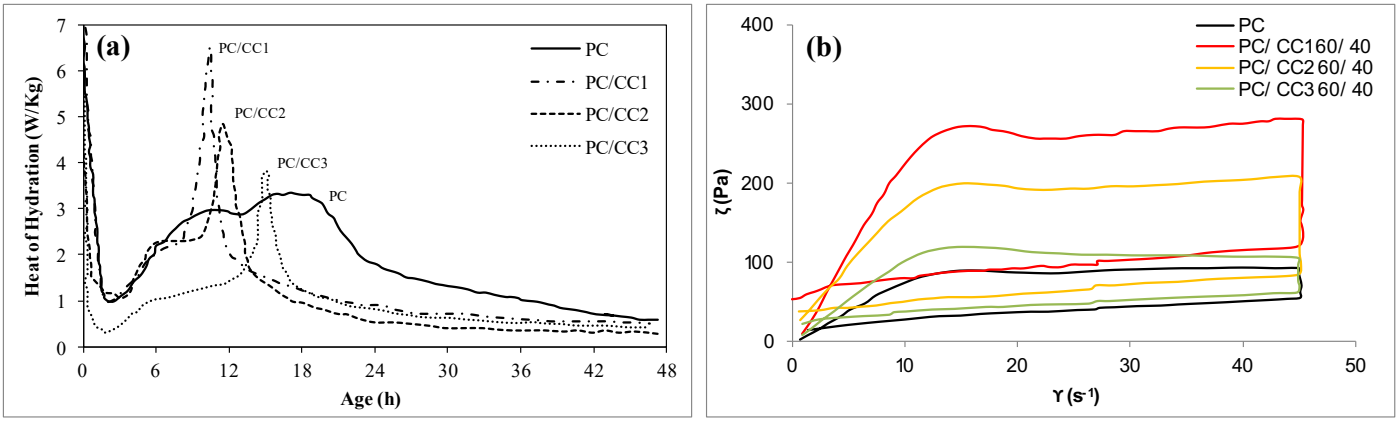


Figure 2. (a) Calorimetric curves for PC and its blended cements. (b) Rheological measurements for PC and its blended cements.

4. Conclusions

- The amount of $Al_2O_3^{r-}$ generated during the clay activation process is a key parameter to predict the behaviour of a cement that contains calcined clays such as SCM.
- Any calcined clay that contains enough content of $Al_2O_3^{r-}$ will develop a high, rapid and early pozzolanic activity from the beginning of the hydration of the cement and will stimulate the clinker to be able to cause a synergic effect between its C3A and the $Al_2O_3^{r-}$ of the CC.
- The stimulation of cement hydration and the great decrease in portlandite levels from very early ages, caused by the $Al_2O_3^{r-}$ of the CC, will have a very important influence on the properties of the cements in the fresh state. Specifically, in the heat released and its rheological behaviour.

References

Aramburo, C., Pedrajas, C., Rahhal, V., González, M., Talero, R. (2018). "Calcined clays for low carbon cement: Rheological behaviour in fresh Portland cement pastes". *Materials Letters*, 239: 24-28.

Arango, S.E., Pedrajas, C., Rodriguez, C.P., Vásquez O. (2022). "Pozzolanic mixture and cementing composition". Patent for Colombia. C04B 14/00. Cementos Argos.

EN 196-5:2011 Standard, Methods for Testing Cement. Part 5: Pozzolanicity Test for Pozzolanic Cements, AENOR, 2011

Garg, N., Skibsted, J. (2019). „Dissolution kinetics of calcined kaolinite and montmorillonite in alkaline conditions: Evidence for reactive Al(V) sites". *Journal of the American Ceramic Society,* 102(12): 7720-7734.

Mehta, P.K. (1983) "Pozzolanic and Cementitious By-products as Mineral Admixtures for Concrete—A Critical Review". *Fly Ash, Silica Fume Slag & Other Mineral By-Products in Concrete*; American Concrete Institute, (1): 1–46.

Rahhal, V., Talero, R. (2008). "Calorimetry of Portland cement with metakaolins, quartz and gypsum additions". *Journal of Thermal Analysis and Calorimetry*, 91(3): 825-834.

Skibsted, J. and Snellings, R. (2019) "Reactivity of supplementary cementitious materials (SCMs) in cement blends". *Cement and Concrete Research*, 124: 105799.

Talero, R. (1986). “Contribution to the Analytical and Physical-Chemical Study of the System: Pozzolanic Cements—Gypsum—Water (at 20±2ºC) ”. Ph.D. Thesis, Complutense University of Madrid, Madrid, Spain.
Trusilewicz, L., Fernandez Martinez, F. and Talero, R. (2012) “TEM and SAED characterization of metakaolin. Pozzolanic activity”. *Journal of America Ceramic Society*, 95: 2989–2996.

The 16th International Congress on the Chemistry of Cement 2023 (ICCC2023)
"Further Reduction of CO_2 -Emissions and Circularity in the Cement and Concrete Industry"
September 18–22, 2023, Bangkok, Thailand

Quantitative microstructure analysis of SCM-blended cementitious materials through deep learning-based computer vision methods

YAN Yu[1], GENG Guoqing[1*]

[1] *Department of Civil and Environmental Engineering, National University of Singapore, Singapore*
Email: yan_yu@nus.edu.sg, ceegg@nus.edu.sg

ABSTRACT

Supplementary cementitious materials (SCM) are increasingly used in concrete owing to the carbon footprint and economic reasons. The characterization of SCMs, for example the reaction degree and the distribution of hydration products, are essential to estimate the systems' properties. However, a reliable morphological study at microscale requires the analysis of large quantities of SEM-BSE images, which is impractical to be investigated by human eyes. Moreover, the chemical and mineralogical complexity of SCM phases makes the analysis rather qualitative. In this study, the microstructure of white cement paste with/without SCM (limestone, slag, quartz and metakaolin), has been investigated. We explore the application of multiple advanced deep learning-based image processing algorithms on the SCM-blended BSE images. Pixel-level semantic segmentation models based on U-Net architecture and ResNet backbone can robustly segment limestone, quartz and slag particles from complicated BSE images. Image enhancement methods including image denoising, super-resolution further help to optimize the image quality and improve the accuracy of phase assemblage. By automating the segmentation process and enhancing image quality, valuable insights into SCM phase microstructure and distribution within cement paste can be obtained, contributing to a better understanding of the properties and performance of SCM-based concrete systems.

KEYWORDS: *Supplementary cementitious materials, image processing, deep learning, segmentation*

1. Introduction

The scanning electron microscope (SEM) plays a crucial role in investigating the microstructure of modern concrete. The quantification of phase composition within the cement matrix is commonly achieved through the segmentation of BSE images using threshold methods based on grayscale values derived from the average atomic number of local areas (Scrivener 2004). However, determining fixed threshold values for image analysis proves impractical due to the substantial impact of sample preparation techniques and image acquisition parameters. Furthermore, conducting a thorough morphological analysis necessitates the examination of a considerable number of images, thereby increasing the time required for analysis. Nowadays, in the pursuit of greener, more cost-effective, and durable concrete, the utilization of supplementary cementitious materials (SCMs) has gained prominence. SCMs, in comparison to clinker minerals, exhibit relatively lower average atomic numbers (Snellings, Mertens, and Elsen 2012), resulting in the grey value distribution of SCM phases being closer to that of hydration products. Consequently, the segmentation of SCM particles and the corresponding hydration products present significant challenges in image analysis.

Recently, the advancement of deep learning, particularly computer vision technology, has revolutionized pixel-level microscopic image segmentation in materials science (Ge et al. 2020; Midtvedt et al. 2021). In this study, we investigate the potential of advanced deep learning-based image processing algorithms for segmenting complex BSE images of SCM-blended cement. Additionally, we explore the effectiveness of other deep learning-based image enhancement techniques, including denoising and super-resolution, to improve the accuracy of SCM particle segmentation in BSE images. By leveraging these cutting-edge

approaches, we aim to enhance the analysis and understanding of SCM-blended cement microstructures, paving the way for more accurate and efficient characterization of these materials.

2. Materials and methods

White Portland cement (manufactured by MAPEI) was used as the binding phase. The mineralogical composition measured by XRD are as follows: 54.6% C_3S, 28.9% C_2S, 1.2% C_3A, 0.7% C_4AF, 9.2% calcite, 4.6% gypsum. Four types of supplementary cementitious materials, namely limestone, metakaolin, quartz and slag, were used to prepare SCM-blended cement paste. A water-to-solid ratio of 0.45 was used to prepare all cement pastes. All experiments were carried out at 25 ± 2 °C.

Hitachi Regulus 8230 FE SEM was used to capture backscattered electron microscopic images of SCM-blended cement pastes. All the samples were studied at a voltage of 15 kV with a YAG detector. the magnification was set at 200 times. The image resolution was fixed at 5120 × 3840, with a 0.125 μm pixel resolution. In this study, we employed APEER by Zeiss (https://www.apeer.com) for manual annotation of the BSE images. Subsequently, the raw images and annotated masks were cropped and organized into 280 image pairs, each with a resolution of 256 × 256 pixels. To augment the dataset, various techniques such as image rotation, flipping, blurring, and noise addition were applied. The resulting dataset consisted of 7560 image pairs, which were used for training the networks. The training and validation images were split in a ratio of 9:1, ensuring robust model training and evaluation.

We used U-Net (Ronneberger, Fischer, and Brox 2015) as the architecture of semantic segmentation CNN model and replaced the encoder part with ResNet (He et al. 2016) using Segmentation Models (Iakubovskii 2019) (version 0.2.1). To compare the results, trainable Weka segmentation (TWS) (Arganda-Carreras et al. 2017) with a random forest classifier, a plugin from ImageJ, was also used to segment SCM particles from BSE images. ImageJ was also used for noise addition (standard deviation=15) and image resolution adjustment (bilinear interpolation) during denoise and super-resolution model training. A DnCNN model (Zhang et al. 2017) and a ESRGAN mode (Wang et al. 2018) were used to remove noise and enhance image resolution of BSE images. All the experiments in the present study were developed under Python 3.9.7, TensorFlow 2.9.1, CUDA 11.8 and performed on a workstation with a single graphics processing unit (Quadro RTX 4000).

3. Results and discussion

Figure 1 (a) to (c) provides an overview of the microstructure of SCM particles and illustrates the impact of SCM addition on the greyscale value of white cement paste. Cement particles exhibit distinctive characteristics that facilitate image segmentation, including a narrow distribution of greyscale values, a noticeable difference in greyscale values compared to adjacent phases, and being surrounded exclusively by inner C-S-H with a uniform greyscale distribution. Notably, characteristic peaks of anhydrous cement are discernible from the histogram. However, with the addition of SCMs, the transition between adjacent characteristic peaks becomes less prominent. From the perspective of single particle morphology, the transition from SCM particles to hydrated cement paste is less abrupt compared to cement particles, presenting as a weak-feature area spanning several pixels in width. Consequently, thresholding segmentation becomes disabled for SCM-blended systems. Metakaolin particles, due to their smaller size and orientation, exhibit minimal differences in greyscale values from the surrounding phases, posing difficulties even for experienced researchers to identify them visually. Therefore, relying solely on graphic information renders metakaolin segmentation unreliable.

Figure 1 (d) demonstrates the segmented outputs from the trained U-Net model with ResNet 101 backbone. Remarkably, an intersection over union (IOU) exceeding 0.9 can be easily achieved after 50 epochs of training. In most cases, limestone, quartz, and slag particles can be successfully segmented, even when they possess indistinct boundaries and exhibit similar greyscale distributions as the surrounding phases. Notably, all the BSE images of SCM-blended samples were raw images without adjustments to greyscale values and contrast. Deep learning models can reasonably segment SCM particles from a high-resolution 4k × 4k pixel BSE image within seconds. In comparison, traditional watershed segmentation (TWS) assists in approximating the location of larger particles, but it fails to provide satisfactory labeling for small particles and accurate boundaries for larger particles. As depicted in Figure 1 (e), TWS exhibits a relatively significant error of approximately 35%, whereas the utilization of deep learning models significantly

enhances accuracy to over 80%. Overall, the segmentation accuracy follows the order of limestone > quartz > slag. Notably, the segmentation error of deep learning models is highly sensitive to the edges of SCM particles and increases exponentially with every one percent increment in edge error.

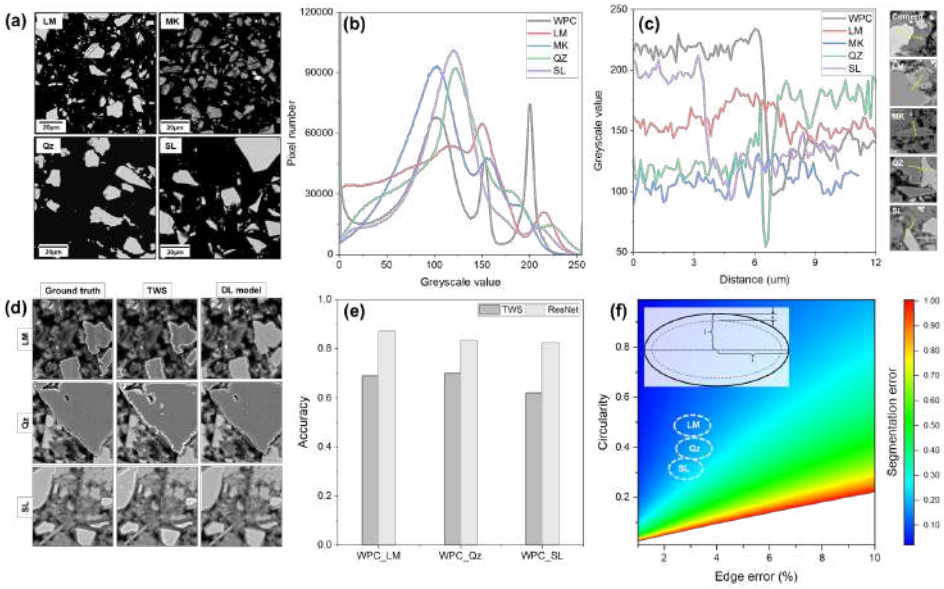


Figure 1 (a) BSE images of raw SCM particles. (b) Greyscale value distribution of WPC-blended paste with different SCMs. (c) Grey value change over the boundary of abovementioned particles in the cement paste. (d) Segmentation of limestone, quartz, and slag particles with TWS and deep learning model. (e) Segmentation accuracy compared to QXRD (limestone and quartz) and EDS mapping result (slag). (f) The effect of circularity and edge error on the accuracy of segmentation results.

In order to enhance the accuracy of segmentation, we implemented two additional models, namely the denoise model and the resolution enhancement model, to optimize the quality of the input image. Figure 2 illustrates the results obtained after denoising, where a more uniform greyscale value is observed within the SCM particles. The grayscale distribution diagram reveals distinct characteristic peaks atop the broader peaks of hydration products, predominantly portlandite and C-S-H. While the presence of these characteristic peaks does not simplify the problem to a mere threshold segmentation, the denoising process aids in enhancing the grayscale features of SCM particles and sharpening their edges.

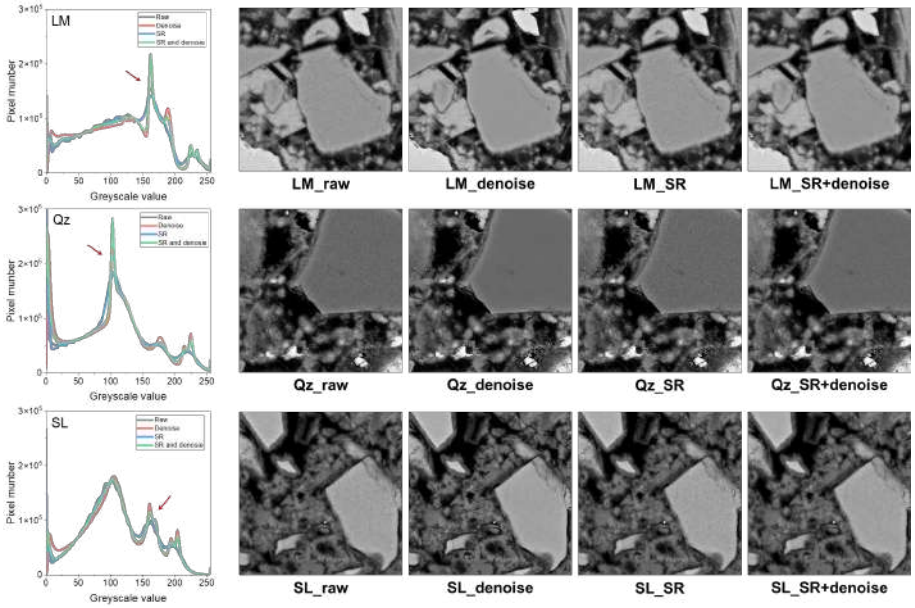


Figure 2 Example application of denoise and resolution enhancement models on BSE images of SCM particle.

On the other hand, the resolution enhancement has a limited impact on the greyscale value distribution of the BSE image. However, the output image consistently exhibits superior visual quality, displaying more realistic and natural textures on the edges of SCM particles when compared to the original image. Consequently, the transition between SCM particles and the background becomes more discontinuous, which proves advantageous for the semantic segmentation task. By combining image enhancement as a pre-processing step with deep learning-based semantic segmentation, we present a promising approach for effectively segmenting SCM particles from BSE images.

4. Conclusions

This study explored the potential application of deep leaning techniques in processing BSE image of complex SCM-blended cement paste, a task that cannot be effectively achieved through traditional thresholding methods. Four types of SCMs, including limestone, slag, quartz, metakaolin were analyzed. While metakaolin proved challenging to accurately segment based solely on graphical information, the remaining three SCMs exhibited robust segmentation with an accuracy of over 80% compared to QXRD. By employing denoise and resolution enhancement models, the grayscale features of SCM particles were enhanced, and the impact of edge errors on overall segmentation accuracy was reduced. These findings underscore the efficacy of deep learning techniques in improving the segmentation process of SCMs in complex cementitious materials, thereby highlighting their potential for advancing the field of cement research.

Acknowledgements

This research is funded by Singapore Minister of Education Tier 1 project under WBS A-0009288-01-00.

References

Arganda-Carreras, Ignacio, Verena Kaynig, Curtis Rueden, Kevin W Eliceiri, Johannes Schindelin, Albert Cardona, and H Sebastian Seung. 2017. “Trainable Weka Segmentation: A Machine Learning Tool for Microscopy Pixel Classification.” *Bioinformatics* 33 (15): 2424–26.

Ge, M., F. Su, Z. Zhao, and D. Su. 2020. “Deep Learning Analysis on Microscopic Imaging in Materials Science.” *Materials Today Nano* 11. https://doi.org/10.1016/j.mtnano.2020.100087.

He, Kaiming, Xiangyu Zhang, Shaoqing Ren, and Jian Sun. 2016. “Deep Residual Learning for Image Recognition.” In *Proceedings of the IEEE Conference on Computer Vision and Pattern Recognition*, 770–78. https://doi.org/10.1002/chin.200650130.

Iakubovskii, Pavel. 2019. “Segmentation Models Pytorch.” GitHub. 2019. https://github.com/qubvel/segmentation_models.pytorch.

Midtvedt, Benjamin, Saga Helgadottir, Aykut Argun, Jesús Pineda, Daniel Midtvedt, and Giovanni Volpe. 2021. “Quantitative Digital Microscopy with Deep Learning.” *Applied Physics Reviews* 8 (1). https://doi.org/10.1063/5.0034891.

Ronneberger, Olaf, Philipp Fischer, and Thomas Brox. 2015. “U-Net: Convolutional Networks for Biomedical Image Segmentation.” In *International Conference on Medical Image Computing and Computer-Assisted Intervention*, 234–41. Springer.

Scrivener, Karen L. 2004. “Backscattered Electron Imaging of Cementitious Microstructures: Understanding and Quantification.” *Cement and Concrete Composites* 26 (8): 935–45. https://doi.org/10.1016/j.cemconcomp.2004.02.029.

Snellings, Ruben, Gilles Mertens, and Jan Elsen. 2012. “Supplementary Cementitious Materials.” *Reviews in Mineralogy and Geochemistry* 74 (Blezard 2001): 211–78. https://doi.org/10.2138/rmg.2012.74.6.

Wang, Xintao, Ke Yu, Shixiang Wu, Jinjin Gu, and Yihao Liu. 2018. “ESRGAN: Enhanced Super-Resolution Generative Adversarial Networks.” *Proceedings of the European Conference on Computer Vision (ECCV) Workshops*, 1–16.

Zhang, Kai, Wangmeng Zuo, Yunjin Chen, Deyu Meng, and Lei Zhang. 2017. “Beyond a Gaussian Denoiser: Residual Learning of Deep CNN for Image Denoising.” *IEEE Transactions on Image Processing* 26 (7): 3142–55. https://doi.org/10.1109/TIP.2017.2662206.

The 16th International Congress on the Chemistry of Cement 2023 (ICCC2023)
"Further Reduction of CO_2 -Emissions and Circularity in the Cement and Concrete Industry"
September 18–22, 2023, Bangkok, Thailand

Effect of steam curing on the hydration of limestone calcined clay cements (LC^3) with low kaolinite content

Y. Hu[1] and G. Geng[1*]

[1] *Department of Civil and Environmental Engineering, National University of Singapore, 117576, Singapore*
Email: yc_hu@nus.edu.sg
**Email: ceegg@nus.edu.sg*

ABSTRACT

Limestone calcined clay cement (LC^3) is one of the promising blended cements with good performance (strength and durability) at a significantly low clinker content. However, early strength of LC^3 is usually lower than OPC concrete because of the reduced early stage cementing reaction. This study presents the influence of steam curing of 80 °C for 6h on the strength development and hydration of LC^3 containing low kaolinite content (less than 40%). Blends of different ratios of replacement level of clinker (30% and 50%) were employed at fixed w/c ratio. XRD were employed to detect the formation of hydration products to evaluate the degree of hydration. Results indicated that the early strength of steam curing samples of LC^3 would be higher than normal curing ones because of the acceleration of OPC hydration and pozzolanic reaction due to higher temperature. However further strength development of steam curing ones is not so significant from three days onwards. Detailed investigation on the hydration reveals that this issue is related to the slowing down of clinker hydration and conversion of ettringite and carboaluminate, which influence the pore structure and strength development significantly at later stage.

KEYWORDS: *LC^3, Steam curing, SCM, Hydration, Compressive Strength*

1. Introduction

Supplementary cementitious materials (SCM), like slag and fly ash, have been extensively studied and used to partially replace ordinary Portland cement (OPC). However, these materials are not always available in countries with limited industry scale, such as Singapore. Clay, abundant globally and generated as waste from excavation works before, has pozzolanic reactivity when its metakaolin (MK) component is activated at 700 °C (Fernandez, 2016). Moreover, limestone powder (LS) is commonly used as a filler to improve the performance of cementitious materials and (Scrivener et al.,2018) suggests that the calcite in limestone can interact with C_3A in clinker and metakaolin, forming stronger phases with better stability. This has led to the production of a new type of promising blended cement called limestone calcined clay cement (LC^3), which has significantly reduced clinker content and demonstrates good performance of strength and durability.

However, according to (Avet and Scrivener, 2018), the early strength of LC^3 is not satisfactory due to limited clinker hydration, which can be improved through steam curing. Steam curing (A.C. 517) is a method of heat curing with high moisture content that accelerates cement hydration. It leads to the rapid development of strength by increasing the rate of cement hydration through higher temperature and longer curing periods. Until now, the performance of cementitious materials blended with a combination of low-grade clays and LS under steam curing conditions is not well understood. Therefore, this study aims to leverage the high reactivity of LC^3 and its synergistic effect with limestone powder to achieve desirable early age mechanical properties.

2. Materials and methods

Marine clay samples from Singapore were excavated and treated as follows: oven-dried at 80°C for 48h, pre-milled in a ball miller at 300 rpm/min for 20 min. The kaolinite content of marine clays was found to be less than 20% after characterization. To address this, the marine clays were mixed with Kaolin clay (purchased from Kaolin SDN BHD, with a kaolinite content of 58%) using ball milling for 10 min, resulting in a mixture with a kaolinite content of 38% (determined by XRD/Rietveld). The mixture was then calcined at 700°C for two hours and cooled to room temperature. In addition, this study also used OPC (CEM I 52.5N), limestone, gypsum, and natural sands.

A mixture of calcined clay and limestone, in a weight ratio of 2:1 (Scrivener et al.,2018), substituted 50% and 30% of OPC (named LC^3_50 and LC^3_70 in this study). In accordance with Scrivener et al. (2018), a combination of calcined clay and limestone was used as a substitute for Ordinary Portland Cement (OPC) in the ratios of 2:1 by weight. This substitution resulted in two variants: LC^3_50, where 50% of OPC was replaced, and LC^3_70, where 30% of OPC was replaced. Gypsum was added at a 2% content to control flash setting, determined through preliminary calorimetry trials. Compressive strength of mortar was evaluated using 40 mm cube samples with a water:binder:sand weight ratio of 0.4:1:2.75, following ASTM C109 guidelines. Workability was enhanced by adjusting the superplasticizer (SP) content. After casting, half of the cubes were steam cured as depicted in Fig 1, after which all specimens were then placed in a fog room (30 °C, 100% RH) until testing ages of 1, 3, 7, and 28 days. Cement pastes with a w/c ratio of 0.4 were prepared for XRD tests. They were ground into powders to analyze the quantities of portlandite, ettringite, and AFm formed. To compensate for the presence of amorphous phases, the internal standard method employed 20 wt.% pure fluorites. Rietveld refinement was performed using the HighScore Plus v5.1 software.

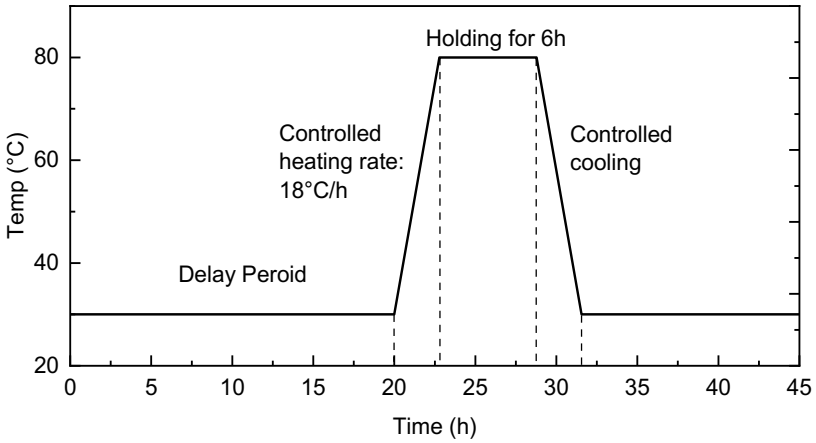


Fig. 1. Steam curing process in this study.

3. Results

3.1 Compressive Strength

The compressive strength variation of different mixes, both normal and steam curing, up to 28 days is depicted in Figure 2. The inclusion of clay and limestone as cement replacements led to a decrease in strength at early and late ages compared to the reference mix, regardless of the curing conditions. Notably, the effect of steam curing was significantly pronounced at 1 day for all three mixes, exhibiting a substantial strength improvement of over 30%. Particularly, LC^3_50 mix showed a remarkable doubling of strength in steam curing samples compared to those curing under normal conditions. However, this enhanced effect became relatively stable at day 3, in which only LC^3_50 showing a 27% improvement compared to the normal curing samples. Concurrently, the strength of steam curing specimens declined compared to the day 1 strength. There are two main factors contributing to this phenomenon. Firstly, the rapid evaporation of internal moisture due to high temperature hinders the ongoing hydration process. Secondly, elevated temperature stress induces the enlargement of pores in the outer layer and leads to the formation of cracks in the interfacial transition zone (Shi et al.,2021). As the curing period progressed beyond 3 days, the

strength of steam curing samples consistently remained lower than their counterparts subjected to normal curing. This effect persisted until the 28 days, where the strength began to rise again. At this stage, the compressive strengths of LC^3 samples approached those of the normal curing samples, while the strength of OPC was 23% lower than that of the normal curing samples. Meanwhile, in both curing conditions, the strength of LC^3 blends at 28 days are similar regardless of the replacement level.

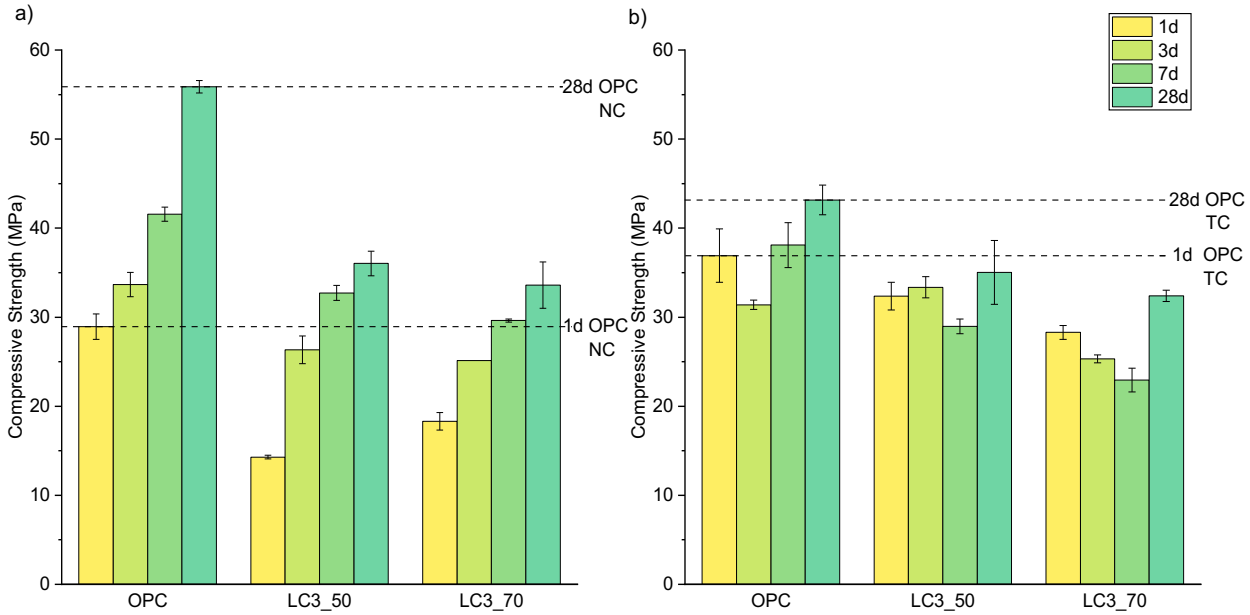


Fig. 2. Compressive Strength development of a) Normal Curing and b) Steam Curing samples.

3.2 Hydration Products

In Figure 3, the portlandite content in the pastes is shown from 3 days to 28 days, which reflecting clinker hydration and pozzolanic reaction to some extent. The reference mix consistently exhibits the highest portlandite content until 28 days, with a slower rate of increase between 3-7 days, similar to the trend in strength development. In LC^3 blends, the portlandite content initially increases from 3-7 days, indicating dormant clinker hydration, but decreases after 7 days as more metakaolin starts to form C-A-S-H in presence of more of generated portlandite until 28 days.

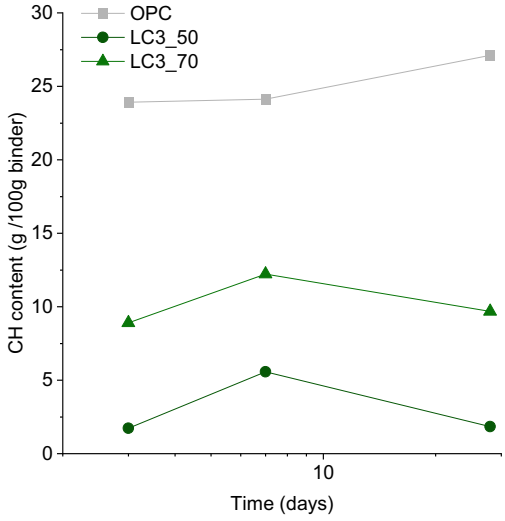


Fig. 3. Portlandite quantification by XRD as a function of time of steam-curing samples.

Figure 4(a), (b), and (c) present XRD plots of the paste samples at 3, 7, and 28 days, respectively. The presence of peaks corresponding to ettringite (AFt), monosulphate (Ms), hemicarboaluminate (Hc), and

monocarboaluminate (Mc) in the blended mixes indicates synergistic reactions between OPC, limestone, and metakaolin.

By comparing the intensity of four peaks, significant transformations of ettringite and CO_3-Afm to monosulphate can be observed over time. In OPC samples, the amount of ettringite and monosulphate increases gradually. In contrast, for LC^3 blends, ettringite and monosulphate coexist at low levels at 3 days. At 7 days, there is a higher content of ettringite and CO_3-AFm, while monosulphate disappears. Finally, at 28 days, the monosulphate content significantly increases while ettringite decreases and CO_3-AFm disappears. This indicates that steam treatment significantly destabilizes ettringite and CO_3-AFm, causing them to degrade rapidly into sulphate-AFm. This degradation process can result in delayed ettringite formation and subsequent volumetric expansion, which ultimately affects the development of strength.

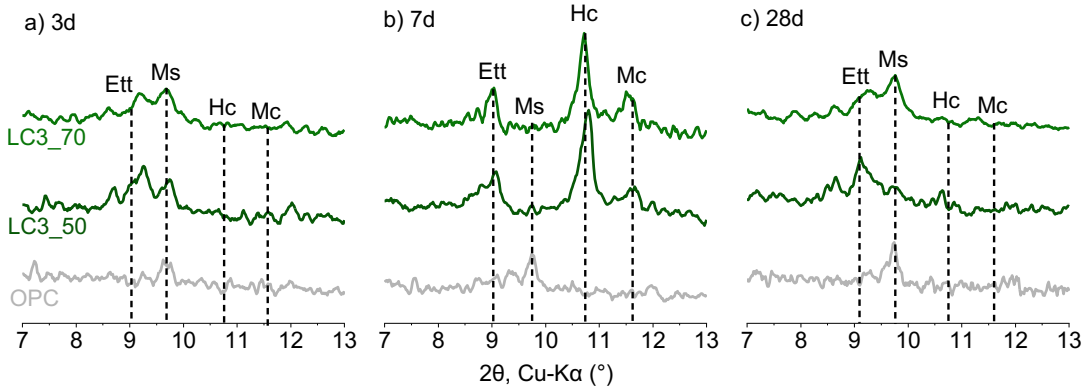


Fig. 4. XRD patterns at a)3 days, b) 7 days, and c) 28 days of hydration for steam-curing samples.

4. Conclusions

This study holds great significance as it provides evidence that steam curing at high temperatures effectively enhances the early stages strength (> 2 times of strength at 1 day for LC^3_50 samples using low-grade clays). However, it is important to note that as the curing period progressed, the positive impact of steam curing diminished, and in some cases, it even had a negative influence on the strength development.

Analyzing the hydration products provides valuable insights into the intricate relationship between hydration and strength development in OPC and LC^3 blends. Following the acceleration due to steam curing, the degree of hydration inhibits, impacting the overall hydration process. Additionally, there is a gradual transformation of ettringite and CO_3-Afm into monosulphate over long-term, resulting in less stable components in the bulk that affect the strength.

References

ACI Committee 517. (1992) "Accelerated Curing of Concrete at Atmospheric Pressure: State of the Art." American Concrete Institute.

Avet, F., and Scrivener, K., (2018) "Investigation of the calcined kaolinite content on the hydration of limestone calcined clay cement (LC^3)", *Cement and Concrete Research*, 107,124-135

Fernandez, R., Martirena, F., Scrivener, K.L., (2011) "The origin of the pozzolanic activity of calcined clay minerals: a comparison between kaolinite, illite and montmorillonite", *Cement and Concrete Research*, 41, 113-122

Scrivener, K., Martirena, F., Bishnoi, S., Maity, S., (2018) "Calcined clay limestone cements (LC^3)", *Cement and Concrete Research* ,114, 49-56

Shi, J.Y., Liu, B.J., Zhou, F., Shen, S., Guo, A., Xie, Y., (2021) "Effect of steam curing regimes on temperature and humidity gradient, permeability and microstructure of concrete", *Construction and Building Materials,* 281,122562

The 16th International Congress on the Chemistry of Cement 2023 (ICCC2023)
"Further Reduction of CO_2 -Emissions and Circularity in the Cement and Concrete Industry"
September 18–22, 2023, Bangkok, Thailand

Relationship between rate of hydration and physical and chemical characteristics of Portland cement

Aydin Saglik, MSCE
General Directorate of State Hydraulic Works, Technical Research & Quality Control Dept.
Cankaya/Ankara/TURKIYE
aydinsaglik@dsi.gov.tr

Abstract
A mathematical model for the rate of reaction between Portland cement and water has been applied to determine activation energies and preexponential terms for each stage of hydration of three different cements: ordinary Portland cement (OPC), white Portland cement (WPC), and C_3S. The influence of particle size distribution (PSD) is also considered. This combined mathematical model fits experimental results very well, and provides a basis for detailed analysis of the kinetics of different types of cement. The rate constants during Stage I are correlated with fineness of cement, and during Stage II, with the content of C_3S. No physical or chemical quantities could be correlated to the rate constants of the third stage reaction. These trends help define a model that depends only on knowledge of starting materials and reaction conditions instead of a model for which adjustable parameters must be found using a fitting procedure.

Keywords : hydration of cement, activation energy, particle size distribution, nucleation and growth, phase boundary, diffusion, heat of hydration, degree of hydration.

1. Introduction

The ability to quantitatively predict the rate of heat generation during the hydration of Portland cement is important for at least two reasons: 1) heat provides information about kinetics and this serves as a basis for understanding the mechanisms of the chemical reactions, and 2) heat can serve as a basis for modeling engineering characteristics, such as, the rise in temperature and volume stability of a large structure during hardening. The hydration of Portland cement and its constituents has been studied extensively (Kondo and Ueda, 1968; Knudsen, 1984; Brown et al. 1985). The complex kinetics of the hydration of Portland cement and its principal component, tricalcium silicate (C_3S), exhibits several stages as shown in Fig. 1a and 1b. The initial peak is attributable to a combination of exothermic wetting and early dissolution. During the induction period, very little product forms. After the induction period, when the reaction rate increases and almost all kinetic models have essentially ignored the induction period, two basic mechanisms have been debated for years: a through-solution mechanism (Chatelier, 1905), and a topochemical mechanism (Kondo and Ueda, 1968). The following main peak corresponds to the main reaction, and the late reaction is slow. According to Van Breugel, 1991, models can be divided into four general classes:

1) Models of overall kinetics; rate of reaction typically controlled by nucleation and growth, phase boundary or diffusion processes.
2) Models of particle kinetics or models that explicitly incorporate the influence of particle size distribution, but ignore the influence of particles interaction.
3) Hybrid kinetic models that account for all of the effects in 1 and 2.
4) Holistic models that are in the early stages of development.

Within the first category, models have been developed that are based on a simple rate-controlling step (Taplin, 1968; Fujii and Kondo, 1974; Bezjak, 1980; Cohen and Cohen, 1987). The nucleation and growth model (Avrami, 1939, 1940, 1940; Erofeev, 1946) has been used to predict the degree of hydration for the overall reaction. Models based on the phase-boundary and diffusion processes developed by some authors (Kondo and Ueda, 1968; Knudsen, 1984; Pommersheim et al., 1982) present another approach.

The latter approach essentially overlooks other parameters related to multiple reactions that proceed simultaneously in Portland cement. In other words, it assumes that a single rate-controlling mechanism is sufficient to describe the sum of all the reactions. Frequently these models are difficult to reconstruct based only on published information, mainly because values for constants are not the same for different cements, and some mathematical procedures are not described fully. Other models (Brown et al., 1985; Knudsen, 1984; Pommersheim et al., 1982) are conceptually and physically more detailed, however, their usefulness is limited because they contain many parameters that need to be determined before obtaining a result. Finally, the influence of particle size distribution has been considered (Taplin, 1968; Knudsen, 1980; Cohen and Cohen, 1987) but, again in this case, the chemistry is largely ignored and only the influence of this one variable is considered. Van Breugel has reviewed presently available mathematical models of cement hydration and has proposed a detailed model that accounts for both chemistry as well as the influence of particle size distribution. No attempt is made, however, to determine activation energies of cement hydration, and he notes that values of activation energy reported in the literature are scattered. These activation energies are shown in Table 1. Van Breugel also did not use a three-stage reaction, in particular, he did not include a separate expression for the nucleation and growth stage, (Taplin, 1962, 1968; Copeland, 1968; Fierence, 1982; Brown et al., 1985).

Table 1. Comparison of activation energies in the literature for C_3S

Authors	E_a [kJ/mol]	Remarks
Taplin (1968)	31	-
Taplin (1962)	~42	Temperature = 4-40 °C
Copeland (1968)	41-26	α = 0.6 - 0.7
Fierencs et al. (1982)	50-49	w/s = 0.6, Temp = 5 - 45°C
Brown (1985)	54-155 21	(Kondo and Ueda, 1969) for acceleration period. (Fujii and Kondo, 1974) for post-acceleration period.
Present Model	61.8 22.0 35.2	Nucleation and Growth-Controlled Reaction Phase-Boundary-Controlled Reaction Diffusion-Controlled Reaction

The model developed in this research combines several models that have been published in the literature. The major new aspect of the model is simply to include an Arrhenius term for the rate constant and evaluate activation energies and preexponential terms for different cements. The goal is to develop a model that is easy to apply to different cements. In particular, all constants ideally should be defined in terms of physical characteristics of the cement. Rate then can be predicted by applying the model without having to fit constants to data which has already been attained. The rate of reaction is divided into three stages, each controlled by a specific process:

I. A nucleation and growth of products during the acceleration stage of hydration,
II. A phase-boundary reaction for the transition period between acceleration and deceleration stages. This period is a special case of diffusion-controlled reaction where the layer through which components diffuse is thin,
III. A diffusion-controlled hydration process for later stages.

Additionally, following the lead of others (Brown et al., 1979; Pommersheim et al., 1980; Bezjak, 1986; Pommersheim, 1987) the role of particle size distribution (PSD) is included. The model is formulated in such a way that the rate constants k's include an activation energy. The activation energies are estimated by applying the mathematical model to a range of hydration data obtained at different temperatures. The general Arrhenius equation is:

$$k = k_o \exp(E_a / RT) \tag{1}$$

where, E_a is the activation energy, R is the gas constant, and k_o is the preexponential constant or frequency term. Another term of the reported research is to evaluate E_a and k_o for various cements. This requires that rate of reaction be measured at several temperatures and then the results must be analyzed with the complete mathematical model.

2. Development of the Model

Since there are significant differences in the mathematics between the model described here and other models in the literature, the formulation is outlined first. As an extension to Van Breugel's formulation, the effects of particle size distribution (PSD) are incorporated into the nucleation and growth stage for early reaction, which is treated separately, in addition to the diffusion stage for the later reaction. Because the phase-boundary stage is short, PSD is not included in the phase boundary stage of the reaction. Each stage is controlled by a separate equation. As stated above, this model has been developed as a first step towards a future model that has as inputs: 1) composition of cement, 2) temperature, 3) particle size distribution, and possibly 4) water/cement ratio.

Stage I is controlled by nucleation and growth where each particle reacts independently. Growth of product is controlled by a chemical reaction at the product surface. The product then coalesces and the reaction slows. Stage II is a phase-boundary reaction. Here the product continues to grow without further coalescence. In this case, the layer thickens in a relatively short time within 3 to 5 hours. During stage III, the reaction of solid particles continues. The reaction is controlled by the diffusion of species through the reaction product. For this, an equation has been chosen, which has already been developed to include the effects of PSD.

The times at which one stage ends and the next begins are determined by an iterative best-fit procedure. The sensitivity of these times in relation to the accuracy of fit will be discussed below. If only the equation for stage I is used, i.e. when nucleation and growth is taken as the rate-determining reaction for the entire hydration process, the degree of reaction values predicted by the equation starts to deviate from actual data at an early stage. This occurs at a degree of reaction of approximately 0,1. Generally, this deviation has been found to correspond to approximately the highest point of the heat evolution curve. Similarly, if only equations for stage I and II are used, the results from the model start to deviate from experimental data at a degree of hydration of approximately 0,2 . This value therefore corresponds to the start of the diffusion-controlled stage, for which the third-stage equation is used.

2.1 Stage I : Nucleation and Growth-Controlled Reaction

The Avrami-Erofeev model, (Avrami, 1939, 1940, 1940; Erofeev, 1946), is modified here and applied to the early stages of the hydration process - the principle modification being that PSD taken into account from the beginning of the hydration process. The general form of the Avrami-Erofeev model can be written as:

$$-\ln\left[1-(\alpha-\alpha_N)\right] = k_G(t-t_N)^n \tag{2}$$

where, α_N is the degree of hydration at the beginning of the nucleation process at time t_N, and k_G is the rate constant for growth of products during the acceleration period, and does not cover the induction period. The value of n in the above equation is called "the determinator for product type" and may take values between 0.5 and 4.0 (Erofeev, 1946; Brown et al., 1979). If the percentage, or degree of reaction for an individual particle that originally had a radius R is $\alpha(t,R)$, then the total degree of reaction of a dispersion is given by:

$$\alpha(t) = \int_{R_{\min}}^{R_{\max}} \alpha(t,R)\, W(R)\, dR \tag{3}$$

where, W(R) is the weight fraction of material with particle size R, and R_{min} and R_{max} are the radii of the smallest and largest particles in the system. After a certain point in time, smaller particles stop contributing to the overall hydration process because they have already been fully hydrated (Pommersheim, 1987). Therefore, the total degree of hydration of all particles can be expressed as:

$$\alpha(t) = \int_{R_{\min}}^{R^*(t)} W(R)\, dR + \int_{R^*(t)}^{R_{\max}} \alpha(t,R)\, W(R)\, dR \tag{4}$$

where, $R^*(t)$ is the original radius of the particle that at time t has just become fully hydrated. These particles are called "dead particles."

In order to solve Eq. (4), a particle size distribution function must be introduced. Perhaps the most commonly used PSD for Portland cement is the Rosin-Rammler distribution function:

$$W(R) = \frac{n_R}{R_o}\left(\frac{R}{R_o}\right)^{n_R-1} \exp\left[-\left(\frac{R}{R_o}\right)^{n_R}\right] \tag{5}$$

where W(R) is the fractional weight distribution function of particle sizes, n_R is a measure of the shape of the distribution function, and R_o is the average size of the particles. Using Eq. (2) and (5) in Eq. (4) yields:

$$\alpha(t) = \left[1 + \alpha_N - \exp(-k_{NG}(t - t_N)^n)\right] f_1(t_R) + f_2(t_R) \tag{6}$$

where,

$$f_1(t_R) = \exp\left[-\left(\frac{R^*(t)}{R_o}\right)\right]^{n_R} - \exp\left[-\left(\frac{R_{\max}}{R_o}\right)\right]^{n_R}, \text{ and } \quad f_2(t_R) = \exp\left[-\left(\frac{R_{\min}}{R_o}\right)\right]^{n_R} - \exp\left[-\left(\frac{R^*(t)}{R_o}\right)\right]^{n_R}$$

It should be noted that in above Eq. (6) the rate constant, k_{NG}, does include the induction period. First, $R^*(t)$, the dead particle size as a function of time, needs to be inferred from PSD data, then values for the constant k_{NG} and n in Eq. (6) can be determined. $R^*(t)$ may be chosen to satisfy two boundary conditions during the nucleation and growth stage:

$$R^*(t) = R_{min} \quad \text{at} \quad t = t_{min} = t_N \quad \text{and} \quad R^*(t) = R_P \quad \text{at} \quad t = t_P$$

where t_{min} is the time that nucleation and growth start and R_{min} is the size of the smallest particle and equal to $R^*(t_N)$. In this work, t_{min} has been chosen as t_N, the beginning of nucleation and growth process. Although it may be an approximation to equate t_N with the time the smallest particles reacted completely, it is a necessary condition in order to conveniently make R^* a function of t. Since the smallest particles are very small and relatively few in number, this approximation is acceptable. If the particle size distribution narrows so that the smallest particles become large by this standard, then it is noted that the influence of PSD on the rate is diminished. From PSD data, R_{min} has been determined to be about 0.1 μm. R_p is the size of particles that are completely hydrated at time t_p , which is the end of the nucleation and growth period. From (Taylor, 1990), one may approximate the sizes of unreacted particles at different times of hydration and R_p is thus determined to be 0.5 μm. The equation that satisfies these conditions well has been found by best-fit techniques to be:

$$R^*(t) = R_{t=0} \exp(t / \tau) \tag{7}$$

where $R_{t=0}$ and τ are the empirical constants related to PSD and it can be determined by using the boundary conditions described by R_{min} and R_p.

2.2 Stage II : Phase-Boundary-Controlled Reaction

When the nucleation and growth process come to an end, at approximately the highest point of the rate of heat evolution curve in Fig. 1a, an intermediate process occurs before the diffusion process takes over. In this process, the product is no longer coalescing as in nucleation and growth, but is undergoing a uniform thickening process, i.e. one dimensional growth. The layer, however, is not yet thick enough to control the rate of reaction by diffusion, the rate is still controlled by chemical reaction with product growing in one direction. The model for this intermediate process is termed a "phase boundary model," or "contracting-volume kinetic model." The phase boundary model has been derived by supposing that the reaction proceeds at a rate which is proportional to the surface area of the unreacted cement particles. The general form of a phase boundary equation is

$$\left[1 - (1 - \alpha)^{1/3}\right] = kt / R \tag{8}$$

where k is the rate constant, which is known as the mass-transfer coefficient. Eq.(8) applies to the reaction of a single particle with radius R. Theoretically, the PSD should be considered. however, because this period is short, the associated mathematical complexities can be avoided without much loss of accuracy. With experimental data at different temperatures, k_p's and the activation energy for this stage can be determined by a simplified form of Eq. (8)

$$\left[1 - (1 - \alpha)^{1/3}\right]^N = k_p t \tag{9}$$

where k_p is equal to k/R and N is an empirical constant such that when N=1, the process is phase-boundary controlled reaction, and when N=2, the process is diffusion-controlled and Eq.(9) reduces to the

Jander equation (Jander, 1927). Values of N less than 1 have been associated with an autocatalytic reaction (Kondo and Ueda, 1968; Pommersheim et al. 1979). Eq. (9) may also be written in a form that applies only after the nucleation and growth process stops. Thus:

$$\alpha(t) = 1 + \alpha_p - \left[1 - (k_p(t - t_p))^{1/N}\right]^3 \tag{10}$$

2.3 Stage III : Diffusion-Controlled Reaction

Phase-boundary reaction proceeds for several hours, at which point the diffusion process starts to control the rate of reaction. A diffusion model developed by (Brown et al., 1985) is called "dispersion model" or "shrinking core model." This model pertains only to monodispersed particles. (Knudsen, 1984) derived a model that includes the influence of PSD. He proposed the following equation for a single particle reacting independently:

$$-\ln \alpha = R/(kt)^m \tag{11}$$

where m describes the type of kinetic model; m=1 for a linear type of reaction like the phase boundary controlled reaction; and m=0.5 for a parabolic type of kinetics like the diffusion-controlled reaction. Knudsen simplified the Rosin-Rammler distribution function Eq.(5) as follows:

$$W(R) = R_o^{-1} \exp(-R/R_o) \tag{12}$$

Eq.(11) and (12) are both substituted into Eq.(4), which now has the lower and upper bounds of 0 and infinity. Eq.(4) is solved separately for the values of m yielding the solutions:

$$t = t_o + t_1 A \quad \text{for m = 1, and} \quad t = t_o + t_2 A^2 \quad \text{for m = 0.5} \tag{13a-b}$$

The final combined form of the equation for Knudsen's dispersion model is:

$$t = t_o + t_1 A + t_2 A^2 \tag{14}$$

where t time t_o is the integration constants describing the beginning time of the diffusion process, t_1 and t_2 are time constants depending on temperature, and A, the hydration ratio, is defined as $\alpha/(1-\alpha)$. Eq. (13a) and (13b) define the limiting cases of Eq.(14) when either t_1 or t_2 takes on the value 0. This model does not contain the n_R value from the distribution function. Bezjak (1986) extended Knudsen's model and also improved the PSD functions by including n_R from the Rosin-Rammler distribution function. This form of the equation is an extended version of Eq. (11) and the function $\Phi(t)$ is defined as

$$\alpha(t, R) = \exp\left[\frac{-R^{n_R}}{\Phi^{n_R}(t)}\right], \qquad \Phi(t) = \left[\left(\frac{k_2}{2k_1}\right)^2 + k_2(t - t_D)\right]^{1/2} - \frac{k_2}{2k_1} \tag{15a-b}$$

where k_1 is actually a mass-transfer coefficient of the diffusion process, and has the unit of μm/hr, and k_2 is the diffusion coefficient of the entire diffusion process with a unit of μm^2/hr. Therefore, the activation energy for each rate constant is calculated independently. The total degree of hydration for this stage is now written as

$$\alpha(t) = \int_{R_{\min}(t_D)}^{R_{\max}(t_D)} \alpha(t, R)\, W(R)\, dR \tag{16}$$

where $R_{min}(t_D)$ and $R_{max}(t_D)$ are the sizes of the smallest and largest particles which are not fully hydrated at time t_D, the end of the phase-boundary stage. Substitution of Eq. (5) and (15) into Eq. (17) yields:

$$\alpha(t) = \alpha_D + \left[\frac{\left(\Phi(t)/R_o\right)^{n_R}}{\left(\Phi(t)/R_o\right)^{n_R} + 1}\right] \exp\left[-\left(\frac{1}{R_o^{n_R}} + \frac{1}{\Phi^{n_R}(t)}\right) R_{\min}^{n_R}\right] \tag{17}$$

This equation is applied over the diffusion stage of hydration and the rate constants are computed by non-linear regression analysis.

D. Total Reaction

The total degree of hydration is computed by combining Eq. (6), (10), and (18) as follows:

$$\alpha(t) = \int_{R_{min}(t_N)}^{R^*(t)} W(R)\,dR + \int_{R_{min}(t_N)}^{R_{max}(t_N)} \alpha(R,t)\,W(R)\;dR + \int_{R_{min}(t_P)}^{R_{max}(t_P)} \alpha(R,t)\,W(R)\;dR + \int_{R_{min}(t_D)}^{R_{max}(t_D)} \alpha(R,t)\,W(R)\;dR \qquad (18)$$

Integration yields Eq. (6), (10), and (18), which are solved in sequence. Thus, three sequential models that include the influence of PSD have been derived and combined for the kinetics of hydration of Portland cement.

3. Experimental Study

In order to compute the activation energy for each stage, experiments to determine the degree of hydration as a function of time were carried out at 10°C, 20°C, 30°C, and 40°C. The particle size distribution was measured using a light diffraction method which measures particles diameters in the range of 0.1 to 80 μm (Table 2).

Table 2. PSD characteristics for the cements used in this study.

Cement	R_{min} (μm)	R_{max} (μm)	R_o (μm)	n_R
OPC - I	0.1	70	15.25	0.94
OPC - II	0.1	75	19.89	0.94
WPC	0.1	40	12.90	0.94
C_3S	0.1	55	15.31	0.94
C_3S (sieved to 30 μm)	0.1	30	14.80	0.94
C_3S (sieved to 60 μm)	0.1	60	17.00	0.94

The data for the early and later age of hydration were obtained using an isothermal scanning calorimeter at the appropriate constant temperature and loss of Ignition (LOI), respectively. The degree of hydration at early ages is then the ratio of the total heat liberated at the given time to the total heat liberated for complete hydration.

The measurement of LOI of prepared samples was done according to ASTM C114 standard. The factor for full hydration is 0.24 grams of non-evaporable water per gram of ignited cement. Plotting the logarithm of the rate constant vs. the reciprocal of the absolute temperature yields a slope of E_a/R, where R is the gas constant. For the calculation of hydration of C_3S in stage III, the experimental data obtained by Fujii and Kondo, 1974 was used.

4. Results of the Study

Fig.6 shows the observed and fitted data points for one of the cements at four different temperatures. Four curves at 10, 20, 30, 40 ºC are given. The model fits data well with a confidence of almost 100% for each temperature and this accuracy is achieved with all cements examined to date. Table 3 lists the rate constants and empirical model constants for each stage of hydration. Table 4 shows the activation energies and preexponential terms, composition, and Blaine fineness of four types of cement used in this study.

Table 3. The rate constants and empirical model constants

Ordinary Portland Cement (OPC - I)					
Process	**T ºC**	**k_{NG} (hr^{-1})**	**n**	**t_N (hr)**	**$\alpha(t_N)$**
Nucleation and Growth	10	0.004358	0.98	8.10	0.02
	20	0.008875	0.97	4.00	0.02
	30	0.020012	1.12	2.70	0.02
		k_p (hr^{-1})	**N**	**t_p (hr)**	**$\alpha(t_p)$**
Phase Boundary	10	0.003129	1.00	19.20	0.1
	20	0.005744	1.05	9.40	0.1
	30	0.012992	0.98	6.22	0.1
		k_1 (μm/hr)	**k_2 (μm^2/hr)**	**t_D (hr)**	**$\alpha(t_D)$**
Diffusion	10	0.01981	0.08055	30.2	0.2
	20	0.04701	0.20977	14.5	0.2
	30	0.09400	0.48056	9.00	0.2

White Portland Cement (WPC)					
Process	**T ºC**	**k_{NG} (hr^{-1})**	**n**	**t_N (hr)**	**$\alpha(t_N)$**
Nucleation and Growth	10	0.004506	0.90	10.4	0.02
	20	0.005546	0.80	6.04	0.02
	30	0.016588	0.87	2.86	0.02
	40	0.026819	0.89	1.81	0.02
		k_p (hr^{-1})	**N**	**t_p (hr)**	**$\alpha(t_p)$**
Phase Boundary	10	0.003585	1.06	18.39	0.1
	20	0.006822	1.05	10.15	0.1
	30	0.011149	1.09	4.73	0.1
	40	0.019066	1.02	3.08	0.1
		k_1 (μm/hr)	**k_2 (μm^2/hr)**	**t_D (hr)**	**$\alpha(t_D)$**
Diffusion	10	0.025220	0.122244	26.53	0.2
	20	0.051277	0.326679	14.47	0.2
	30	0.102915	0.716580	7.03	0.2
	40	0.136366	1.066468	4.65	0.2
C_3S					
Process	**T ºC**	**k_{NG} (hr^{-1})**	**n**	**t_N (hr)**	**$\alpha(t_N)$**
Nucleation and Growth	10	0.005860	0.96	11.80	0.02
	20	0.014341	1.20	3.21	0.02
		k_p (hr^{-1})	**N**	**t_p (hr)**	**$\alpha(t_p)$**
Phase Boundary	10	0.001667	1.18	19.22	0.1
	20	0.002294	1.23	9.22	0.1
		k_1 (μm/hr)	**k_2 (μm^2/hr)**	**t_D (hr)**	**$\alpha(t_D)$**
Diffusion	10	0.0511	0.2902	14.0	0.2
	20	0.1022	0.5804	7.0	0.2
	30	0.1406	0.8053	5.0	0.2
	40	0.2141	1.2769	3.0	0.2

Table 4. Preexponential Terms, Activation Energies, Compositions, and Blaine Finenesses

Cement	**OPC - I**	**OPC - II**	**WPC**	**C_3S**	**C_3S (30μm)**	**C_3S (60μm)**
k_o (Stage I)	4.48E7	2.33E10	2.54E6	1.45E9	1.32E7	8.20E8
Ea (Stage I), kJ/mol	54.3	69.1	47.4	61.8	51.1	61.4
k_o (Stage II)	5.07E6	5.46E6	1.10E5	1.93E1	8.59E5	1.80E8
Ea (Stage II), kJ/mol	50.0	50.2	40.6	22.0	45.7	59.2
k_o (Stage III)	3.67E8	9.00E6	1.98E6	1.10E5	5.35E5	3.50E5
Ea (Stage III), kJ/mol	63.6	40.7	54.0	35.2	35.6	34.8
%C_3S	54	52.4	73	100	100	100
% C_2S	19	20.1	15	0	0	0
% C_3A	6	8.6	5	0	0	0
% C_4AF	10	8	1	0	0	0
Blaine Fineness (cm^2/g)	3850	3118	4460	3500	-	-

Table 5. Comparison of values for E_a and k_o from the present model and those from the Eq. (20)

Controlling Mechanism	**Pastes**	**E_a (kJ/mol)**	**E_a^ (kJ/mol)**	**$\ln k_o$**	**$\ln k_o$^**
Nucleation and Growth	C_3S (30μm)	51.1	96.8^{*1}, 100.8^{*2}	16.4	33.8^{*1}, 35.3^{*2}
	C_3S (60μm)	61.4	84.9^{*1}, 87.1^{*2}	20.5	29.2^{*1}, 30.0^{*2}
	OPC-I	54.3	83.4	17.6	28.3
	WPC	47.4	$-22.8^{\#1}$	14.8	$1.7E\text{-}6^{\#2}$
Diffusion	C_3S (30μm)	35.6	34.0^{*1}, 32.0^{*2}	13.2	9.55^{*1}, 8.86^{*2}
	C_3S (60μm)	34.8	25.4^{*1}, 21.3^{*2}	12.8	5.98^{*1}, 4.26^{*2}
	OPC-I	63.6	25.1	19.7	5.67
	WPC	54.0	8.36	14.5	0.34

(E_a^ and k_o^ were calculated by the integration of Eq.(19) and the values with * varied according to the points picked for calculation where t_N < (*1) < (*2) < t_D. t_N and t_D are shown in Table 3. The negative activation energy #1 and very small preexponential term #2 , which are unreasonable, are also shown.

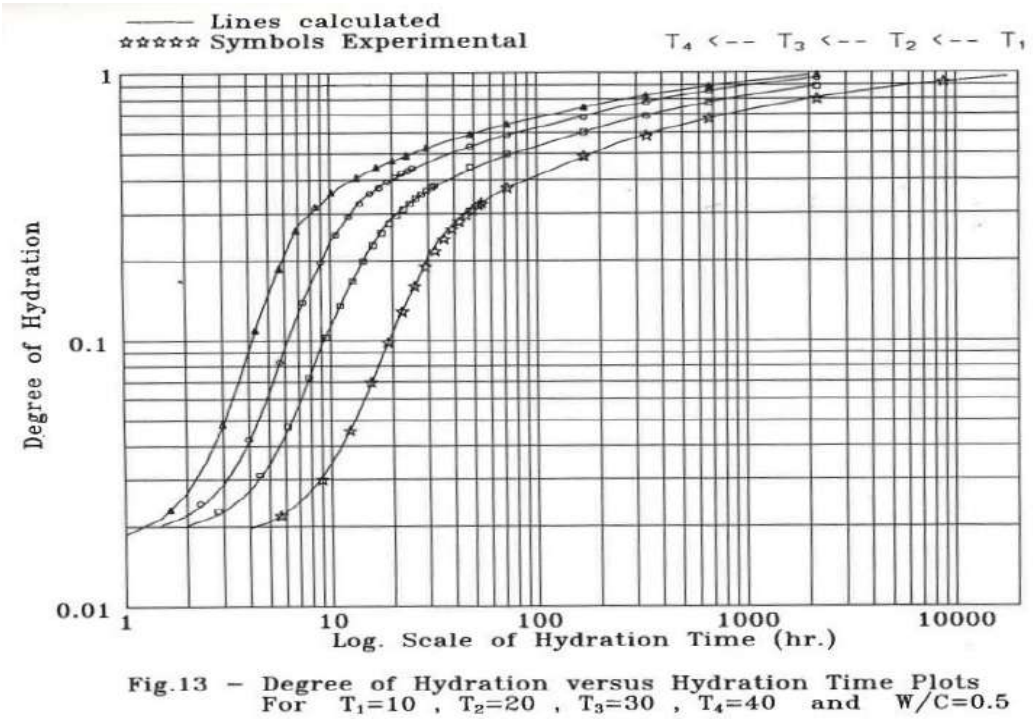


Figure 6. Comparison of the degree of hydration vs. time curves derived from Eq.(6) for stage I, from Eqs.(6,10) for Stages I,II, and from Eqs.(6,10,18) for Stages I,II,III.

Stage I : Nucleation and Growth-Controlled Reaction

Included in Table 3 are the values for t_N , n, $\alpha(t_N)$, and k_{NG} for stage I. As stated above, a value for $\alpha(t_N)$ of 0.02 was found to be consistent with best-fit results. The remaining values were calculated using linear regression techniques. The value of R^2 , the coefficient of determination, was found to be close to 1 for the calculation of t_N, n, and k_{NG}. The k_{NG} values were used to calculate an activation energy, E_a , for each cement using Eq. (1). The Arrhenius plots are shown in Fig.3.

Stage II : Phase-Boundary-Controlled Reaction

The rate constant for the phase-boundary reaction is k_p . A value of N, close to 1 has been determined, for stage II as expected. Values for terms in Eq. (10), calculated by linear regression, and are shown in Table 3. The Arrhenius plots for stage II are shown in Fig.4.

Stage III : Diffusion-Controlled Reaction

As stated in section II, B, the value for N, is 2 for a diffusion-controlled reaction. The change to stage III is assumed, therefore, to occur when N gets close to a value of 2. This change from a phase-boundary to a diffusion-controlled reaction occurs consistently at a degree of hydration of approximately 0.2. Fig.2 shows that when only equations from stage I and II are used, the results start deviating from actual data as α=0.2. The values for k_1, k_2, and t_d were calculated using non-linear regression and are shown in Table 3. The Arrhenius plots are shown in Fig. 5a and 5b.

4.1 Sensitivity of Rate to Reaction Constants

Since all of the reaction constants have been determined by best-fit processes, it is important to understand how sensitive the predicted rate is to the values of the constants. This is especially important if any physical interpretation is to be associated with values such as E_a and k. The percent reacted at the start of the nucleation and growth stage is of interest, in part because we have found it to be a constant value of 0.02, which may have some chemical significance. To illustrate sensitivity, other values of α have been assumed and best-fit values of k_{NG} and its R^2 have been computed. These results are listed in Table 5. As shown in Table 5, k_{NG} is sensitive to values of $\alpha(t_N)$, and $\alpha(t_N)$=0.02, the most suitable value to calculate k_{NG} . This then results in R^2 being close to 1.

5. Discussion of Test Results

The model proposed in this paper fits experimental data very well with a confidence close to 100%. This accuracy has been seen in all cements. The activation energies and pre-exponential terms for each cement are shown in Table 4. Various literature values are included in Table 1. Since the model fits the observed data for a variety of cements with a high level of confidence, and since these are actually a number of different reactions occurring simultaneously, there may be an apparent conflict. In other words, all of these reactions, principally the hydration of the silicates and the aluminates, can be described by a single apparent activation energy. Either the chemical reactions are similar, or the rate-controlling step of nucleation, surface diffusion, and/or a volume diffusion are similar. The ability to predict an activation energy for a cement from some known physical or chemical properties of that cement would be valuable, but no such correlations have previously been reported. A few relationships have been found.

An increase in the fineness of a cement increases the maximum value of dQ/dt and the rate of hydration in the initial stages. In general, the more accelerated the hydration reaction, whether because of admixtures or fineness, the taller the second peak. Therefore, in stage I, an accelerator has the same effect on the activation energy as does increasing the Blaine fineness, and the peak is higher. Similarly, retarders have the same effect as decreasing the fineness and the peak is lower. In stage II, the wider the peak, the greater the activation energy. Reducing the C_3S content narrows the peak.

While no trends were established for stage III, some important observations can be made. Widely quoted results of (Copeland and Kantro, 1968) show that when the hydration of C_3S becomes diffusion-controlled, the rate is no longer sensitive to temperature. In other words, the degree of hydration vs. time curve becomes less dependent of the temperature after about 24 hours than it is before 24 hours. Our data does not show any trend in activation energy in stage III. It is also important to note that the activation energies calculated in this work for stage II are significantly higher than those published elsewhere. Using the reported lower activation energy, 12.5 kJ/mol, our model temperature predictions agree with Copeland and Kantro. This observation made by Copeland and Kantro may only be valid for cements which have low activation energy in the third stage. To explain the dependence of E_a and k_o on the model, E_a and k_o were calculated from an equation relating the degree of hydration to rate constant as shown below:

$$\partial\alpha / \partial t = k_o \exp(-E_a / RT) \tag{19}$$

where α is the degree of hydration at time t, and k_o and E_a are the preexponential term and activation energy, respectively. E_a and k_o can be calculated by integration of α and plot of $\ln(\alpha/Dt)$ vs. 1/RT. When the above equation was used, the values for E_a and k_o varied according to the points we selected for calculation (* in Table 6). Also they showed unreasonable values (# in Table 6).

6. Conclusions

A mathematical model for the hydration of cement paste which includes an activation energy term has been applied to several cements. The reaction process is divided into into three stages : 1) nucleation and growth controlled reaction for the acceleration stage, 2) phase-boundary controlled reaction as transition from acceleration to deceleration stage, and 3) diffusion controlled reaction for the deceleration and the final stages of the hydration process. The influence of particle size distribution (PSD) of the cement on the rate of reaction is included. Excellent correlations between model predictions and experimental results were obtained for all cements studied. Experiments have been carried out that measure the rate of reaction of several cements at three or four different temperatures. By applying the model to experimental data, both the activation energy and the preexponential terms are calculated. The activation energies for the early stage of hydration (nucleation and growth) are dependent on the Blaine fineness, and consequently, on the PSD. The activation energies for the middle stage of hydration (phase-boundary reaction) are controlled by the chemical composition of the cement, in particular the C_3S content. The activation energies for the later stage of reaction (diffusion) have not been correlated to any physical and chemical characteristic of the cement. Similar trends were found for the preexponential terms.

The model is a first step towards predicting the rate of reaction from the physical and chemical characteristics of the starting material. It is not simply curve fitting. The model is not yet completely predictive in that a few parameters, such as the constants k_1, k_2, and E_a for stage III, can not be predicted from the starting materials. The beginning degrees of hydration for the three stages have only been approximated as 0.02, 0.1, and 0.2. These numbers appear to be constant from one cement to another.

References

[1] Avrami, M., "Kinetics of Phase Change-I,II,III," *J. Chem. Phys*., 7, 8, 8, 1103-1112, 212-224, 177-184, (1939), (1940), (1940).

[2] Bezjak, A., "An Extension of the Dispersion Model for the Hydration of Portland Cement," *Cem. Concr. Res*., 16, 260-264, (1986).

[3] Bezjak, A., "On the Determination of Rate Constants for Hydration Prosesses in Cement Pastes," *Cem. Concr. Res*., 10, 553-563 (1980).

[4] Braunauer, S., Greenberg, S.A., "The Hydration of C_3S and β-C_2S at Room Temperature," *Proc. 4th Int. Symp. Chem. Cem*., Washington (1960).

[5] Brown, P.W., Pommersheim, J.M., Frohnsdorff, G.J., "A Kinetic Model for the Hydration of C_3S," *Cem. Concr. Res*., 15, 35-41, (1985).

[6] Brown, P.W. et. al., *Cem. Concr. Res*., Vol.15, 35-41, (1985).

[7]Brown, P.W., Pommersheim, J.M., Frohnsdorff, G., "Kinetic Modeling of Hydration Prosesses," *Cem. Res. Prog*. (1979), Amer. Cer. Soc., Ohio, Chp.13, 246-260.

[8] Chatelier, L.H., "Experimental Researches on the Constitution of Hydraulic Mortars," translated by Mack, J.L.) *McGraw-Hill Pub. Co*., N.Y. (1905).

[9] Cohen, M.D., Cohen, R.D., "Kinetics of Depletion of a Population of Hydrating Cement Particles," *Journal of Materials Science*, 22, 2032-2036, (1987).

[10] Copeland, L.E., Kantro, D.L., "Hydration of Portland Cement," *Proc. 5th Int. Symp. Chem. Cem*., Tokyo (1968), II-5, 387-421.

[11] Erofeev, B.V., "A Generalized Equation of Chemical Kinetics and Its Application in Reactions Involving Solids," (Doklady) *Acad. Sci*. USSR, L11 (6), 511-514, (1946).

[12] Fierence, P., et al., *Cem. Concr. Res*., Vol.12, 191-198, (1982).

[13] Fujii, K., Kondo, W., "Kinetics of the Hydration of C_3S," *J. the Amer. Cer. Soc*., Vol. 57, No.11, 492-497, (1974).

[14] Jander, W., "Reaction in the Solid State at High Temperature," *Z. Anorg. Allgem. Chem*., 163, 1-30, (1927).

[15] Knudsen, T., "On the Particle Size Distribution in Cement Hydration," *Proc. 7th Int. Symp. Chem. Cem*., Paris (1980), Vol. II, 170-175.

[16] Knudsen, T., "The Dispersion Model for Hydration of Portland Cement, I. General Concepts," *Cem. Concr. Res*., 14, 622-630, (1984).

[17] Kondo, R., Diamon, M., "Early Hydration of C_3S: A Solid Reaction with Induction and Acceleration Periods," *J. of the Am. Cer. Soc*., Vol.52, No.9, 503-508, (1969).

[18] Kondo, R., Ueda, S., "Kinetics and Mechanisms of the Hydration of Cements," *Proc.5th. Int. Symp. Chem. Cem*., Tokyo (1968), Vol.II, 203-255.

[19] Pommersheim, J.M., Clifton, S.R., "Special Review; Mathematical Models of Cement Hydration," *Cem. Res. Prog*., (1979), Chp.13, 281-307, (1980).

[20] Pommersheim, J.M., Clifton, J.R., Frohnsdorff, G.J., "Mathematical Modeling of C_3S," *Cem. Concr. Res*., 12, 765-772, (1982).

[21] Pommersheim, J.M., "Effect of Particle Size Distribution on Hydration Kinetics," *Materials Research Soc*., Vol.85, 301-306, (1987).

[22] Taplin, J. H., *Proc. 4th Int. Symp. Chem. Cem*. Washington, Vol I, 263-266, (1962).

[23] Taplin, J. H., "On the Hydration Kinetics of Hydraulic Cements," *Proc. 5th. Int. Symp. Chem. Cem*., Tokyo, (1968), II-70, 337-348.

[24] Taylor, H.F.W., "Cement Chemistry," *Academic Press Inc*., San Diego, CA, (1990).

[25] Van Breugel, K., "Simulation of Hydration and Formation of Structure in Hardening Cement-Based Systems," PhD Thesis, *Tech. Uni. of Delft*, November (1991).

The 16th International Congress on the Chemistry of Cement 2023 (ICCC2023)
"Further Reduction of CO_2 -Emissions and Circularity in the Cement and Concrete Industry"
September 18–22, 2023, Bangkok, Thailand

Combined use of laboratory X-ray diffraction and microtomography in early age cement hydration

A. Cuesta, S. Shirani, A.G. De la Torre, I. Santacruz, A. Morales-Cantero, I. Koufany, C. Redondo-Soto, I.R. Salcedo, L. León-Reina and M.A.G. Aranda*

Universidad de Málaga, Málaga, Spain
Email: g_aranda@uma.es, a_cuesta@uma.es, shiva_shirani@uma.es, mgd@uma.es, isantacruz@uma.es, alejandrom@uma.es, imane.k@uma.es, cinthyars@uma.es, inesrs@uma.es, lauralr@uma.es

ABSTRACT

In situ laboratory X-ray powder diffraction (LXRPD) is widely used for studying cement hydration at early ages. However, this approach has limitations due to the intrinsic characteristics of the main methodologies (flat sample and capillary) and their blindness to the amorphous phases and microstructures. In addition, laboratory X-ray microtomography (μ-CT) is being used for several applications but the accuracy of the obtained results is not established. Here, we present an innovative approach where LXRPD and μ-CT data are taken in the same volume of the same hydrating paste within a thick capillary with time. The results from both techniques should agree, resulting in more reliable information. The methodology developed here is based on capillaries of 2 mm of diameter to minimize self-drying and to have very good powder averaging. In this proof-of-principle investigation, μ-CT data have been collected for a PC-42.5R paste, w/c=0.50, at 12 hours and 1, 3 and 7 days, and for LXRPD at 1, 3 and 7 days. Powder diffraction data have been analysed by the Rietveld method and the results have been verified by mass balance calculations. μ-CT data have been segmented. The results indicate that the developed methodology is accurate. The long-term aim of this research is to be able to monitor the reaction of the amorphous components of widely-used supplementary cementitious materials (SCMs) like the amorphous silica in fly/volcanic ashes or the metakaolin in calcined clays.

1. Introduction

The quantitative phase analysis of crystalline phases in hydrating cements by LXRPD is well established (Aranda et al., 2012). Furthermore, the overall amorphous content can be determined by using internal (De la Torre et al., 2001) or external (Jansen et al., 2011) standard approaches. Conversely, the quantitative analysis of the hydrating components and microstructures by μ-CT (Withers et al., 2021) is still challenging (Brisard et al., 2020; Kong et al., 2020). Interested readers are addressed to these two reviews to have better insights about the features that can be studied and eventually quantified by μ-CT.
One of the applications of μ-CT is to follow *in situ* 4D (3D + time) the hydration of cements (Gallucci et al., 2007; Gastaldi et al., 2012). These early works reported the component evolution qualitatively but quantitative data, for instance segmentations, were not reported. Synchrotron μ-CT is being used for *in situ* characterization of cement hydration (Parisatto et al., 2015; Moradian et al., 2019; Poirier et al., 2022; Vigor et al., 2022), but their limited availability often prevents investigations lasting more than 1-2 days. Moreover, the accuracy of the obtained results was not investigated. Here, we report an investigation for a standard PC-42.5R cement where the evolution of the crystalline phases has been quantitatively determined by the Rietveld method. Moreover, the μ-CT data have been quantitatively analysed and the results agree relatively well with those obtained from the diffraction study.

2. Materials and Methods

2.1 Materials

The employed commercial PC conforms to CEM I 42.5R according to EN 197-1. Pastes were prepared with a water-to-cement (w/c) mass ratio of 0.50, at 25±2 ºC and without admixture(s). The paste was loaded in a glass capillary, ϕ=2 mm, for the X-ray powder diffraction and microtomographic studies.

2.2 Methods

LXRPD measurements for the paste within a capillary of 2 mm of diameter were collected on a D8 ADVANCE (Bruker AXS) diffractometer using strictly monochromatic MoKα_1 radiation (λ=0.7093 Å). The acquisition time per full pattern was 3 h 08 min. Data collection and analysis details are the same than those previously reported (Salcedo et al., 2021) unless the overall acquisition time that it was 1 h longer. Laboratory μ-CT data, for the same paste loaded within the same capillary, were acquired on a SKYSCAN 2214 (Bruker) scanner. Each scan time took 3 h 45 min. Data acquisition and reconstruction protocols are similar to those already reported (Salcedo et al., 2021). The voxel size here is 1.1 μm. For early age *in situ* studies, the timing is important. Data from both techniques are not taken simultaneously but sequentially. For instance, the 1 d μ-CT dataset started ~22 h after water mixing and finished ~26 h. The powder patterns were collected just after the μ-CT data. Hence, the degree of reactions from LXRPD should be slightly larger than those obtained from μ-CT.

3. Results and discussion

The three powder patterns collected at 1, 3 and 7 days of hydration have been analysed by the Rietveld method. The plots for the patterns taken at 1 and 7 days are shown in Figure 1, as examples. The quantitative results are given in Table 1 together with the Rietveld quantitative phase analysis (RQPA) of the initial cement. The results are obtained in weight percentages and referred to 100 g of paste for a direct comparison. This is done by calculating the mass amount of C-S-H gel, assumed stoichiometry $(CaO)_{1.8}(SiO_2)\cdot 4H_2O$, knowing the mass ratio between portlandite and the gel, 2.62 (Cuesta et al, 2018). Moreover, the free water, i.e. H_2O in Table 1, is reduced by the amount incorporated in the hydrated phases. These values can also be expressed in vol% considering the mass densities. This will allow us to make a comparison with the results from the μ-CT analyses, see next.

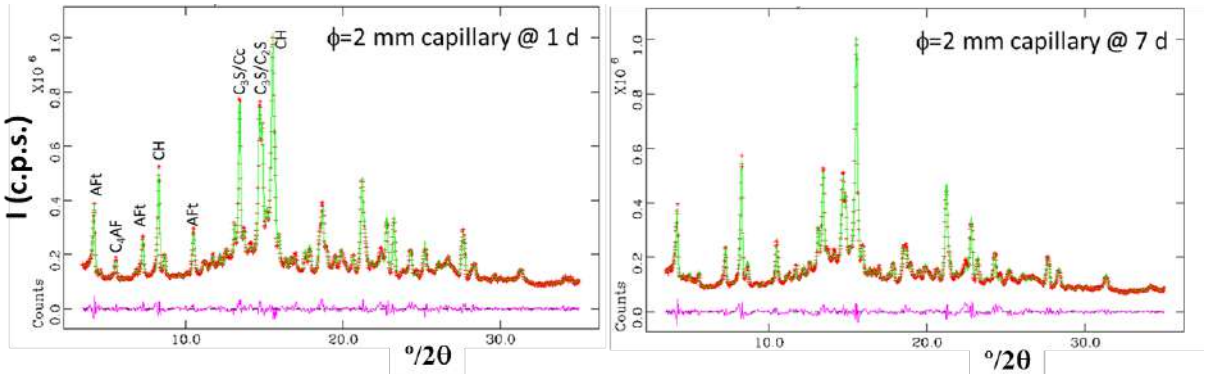


Figure 1. Rietveld plots (λ=0.7093 Å) of the hydrating pastes at 1 day (left) and 7 days (right). Key diffraction peaks are labelled. The decrease in the intensities for C_3S and the increase for CH peaks is evident.

Table 1. *In situ* RQPA results for a PC 42.5 R paste, w/c=0.50, expressed in wt%.

time	C_3S	C_2S	C_3A	C_4AF	Cc[#]	minors[$]	H_2O[&]	AFt	CH	C-S-H[&]	Hc[#]
t_0	38.9	8.6	4.5	6.9	3.5	4.3	33.3	-	-	-	-
1 d	15.5	8.3	2.2	6.3	4.8	0.5	19.0	9.1	9.1	25.2	-
3 d	7.9	8.9	1.0	4.8	5.3	0.3	14.5	10.7	12.3	34.1	0.2
7 d	6.6	8.6	0.5	4.6	5.0	0.4	13.4	11.3	13.2	36.2	0.3

[#] Cc stands for calcite. Hc stands for hemicarbonate. [$] Minors are the summary of the remaining crystalline phases including gypsum, bassanite and quartz (from the addition in the cement). [&] The amounts of H_2O and C-S-H gel are obtained from the known hydration reactions.

We consider that the renormalization to 100 g of paste is correct because three independent verifications. Firstly, belite content should remain constant, within the variability of the analyses, as this phase does not hydrate during the first week. This is indeed the case, see Table 1. Secondly, the theoretical portlandite content can be determined from the degree of reaction of C_3S, (Cuesta et al, 2018). The expected values are 8.9, 11.9 and 12.4 wt% at 1, 3 and 7 days. The values reported in Table 1 are 9.1, 12.3 and 13.2 wt%, respectively; the agreement is remarkable. Moreover, this cement had 3.9 wt% of SO_3 and hence, the maximum amount of ettringite that can be formed would be 13.6 wt%. This value agrees relatively well with the measured AFt content at 7 days, 11.3 wt%, which is still slightly growing. Therefore, the LXRPD study is accurate, and now we focus on the μ-CT study for the same hydrating specimen.

Mounting the capillary for μ-CT study must ensure that the same volume is being scanned in the different measurements. This is indeed the case as it is evident from Figure 2, which shows selected orthoslices displaying the evolution of cement hydration. Clearly and as expected, small whitish particles (anhydrous cement particles) react much faster than the bigger ones. This is highlighted in the enlarged views also shown in the bottom row of Figure 2.

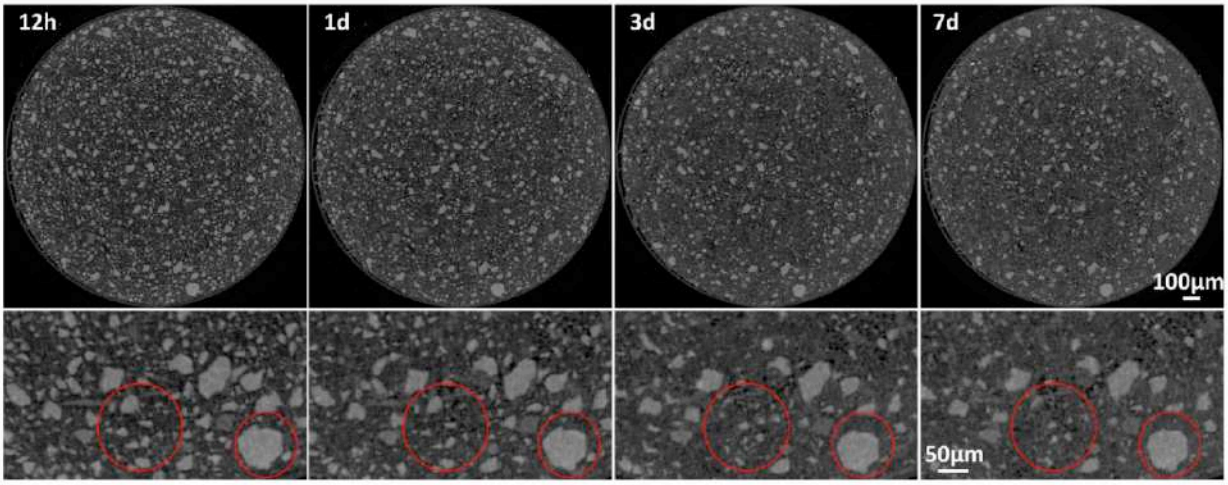


Figure 2. Top row: Selected orthoslices of the studied capillary, ϕ=2.0 mm, showing the cement hydration evolution with time. The whitish particles are the anhydrous Cement Particles (CP) and the grey regions are the Hydrated Products (HP). Porosity develops as blackish regions. Bottom row: enlarged views to highlight the observed densification and the preferential hydration of the smallest CP, see red circles.

A first qualitative study can be carried out by inspecting the evolution of the resulting grey-value histograms for the same hydrating volume, see Figure 3. Three main features can be observed in Figure 3.

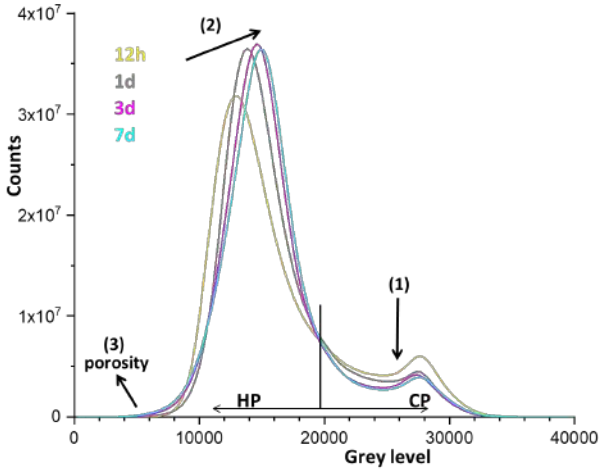


Figure 3. Grey level histograms showing the overall evolution of the different components with time. For the description of the labels, see the text.

(1) The number of voxels corresponding to the CP decreases with time as expected. (2) The area of the peak corresponding to the HP increases with time and it densifies (it moves to higher grey level values). This densification is due to the reaction of free water and CP to give further HP, including portlandite. It is worth noting that due to the spatial resolution of the measurements, the water capillary porosities at 12 h cannot be disentangled from the HP main peak. HP mainly contains C-S-H gel, portlandite and ettringite. (3) After 1 day, shrinkage and air porosity development is evident as the tiny increase of the amount of low grey level voxels. However, the spatial resolution of these measurements, 3-4 μm, is not sufficient to accurately quantify this developing microporosity.

The quantitative μ-CT study was carried out by global thresholding segmentation. The threshold for the HP/CP boundary was found constant, i.e. 19850 grey level, see Figure 3. The thresholds for porosity/HP boundary were variable, close to 9000 grey level. The segmentations were carried out with the Dragonfly software and the results are given in Table 2. This table also displays the values obtained from LXRPD, but expressed as vol% taken into account the mass densities of the different components. The agreement between both sets of data is noteworthy, keeping in mind that there is a time delay of about three hours.

Segmentations by Machine Learning methodology is being carried out and the results will be reported elsewhere. This second approach could lead to adequate segmentations of amorphous SCMs in low-carbon blends. This is not possible with the global thresholding approach used here, because of the similarities in the attenuation coefficients. The redundancy in the *in situ* data will also help. The SCMs particles can only decrease in volume, meanwhile the volume of the hydration products should increase.

Table 2. Segmentation results for the in situ μ-CT study for the hydrating PC 42.5 paste with w/c=0.50 at RT. These values are compared to the ones obtained in the LXRPD study.[$]

Components[#]	12h/vol%	1d/vol%	*1d/vol% LXRPD*	3d/vol%	*3d/vol% LXRPD*	7d/vol%	*7d/vol% LXRPD*
Porosity	0.5	1.4	-	2.5	-	2.6	-
HP	78.2	81.0-*82.2*	*81.3*	82.0-*84.1*	*87.1*	82.1-*84.3*	*88.3*
CP	21.3	17.6-*19.8*	*18.7*	15.5-*15.9*	*12.9*	15.3-*15.7*	*11.7*

[$]The amounts of the components from the μ-CT study are renormalized to exclude porosity (italics) for direct comparison to LXRPD. [#]Calcite in LXRPD data is computed within HP because of its attenuation coefficient.

4. Conclusions

An accurate experimental protocol for *in situ* cement hydration studies has been established for pastes sealed in thick capillaries, i.e. 2 mm of diameter to have excellent powder averaging. Rietveld quantitative phases analyses have been obtained by using MoKα_1 strictly monochromatic radiation. The results agree very well with the expected values from mass balance calculations. Moreover, microtomographic data have also been collected for the same volume of the studied specimen. The quantitative results from segmentations have been compared to those calculated from the diffraction study. This is a first step in our long-term research intended to quantitatively analyse the pozzolanic reactions of SCMs by combing diffraction and tomographic techniques which are highly complementary.

Acknowledgements

Financial support from PID2020-114650RB-I00 research grant, co-funded by FEDER, is acknowledged.

References

Aranda, M.A.G., De la Torre, A.G., Leon-Reina, L. (2012) "Rietveld Quantitative Phase Analysis of OPC Clinkers, Cements and Hydration Products", *Rev. Mineral. Geochemistry,* 74: 169–209.

Brisard, S., Serdar, M., Monteiro, P.J.M. (2020) "Multiscale X-ray tomography of cementitious materials: A review", *Cem. Concr. Res.* 128: 105824.

Cuesta, A., Zea-Garcia, J.D., Londono-Zuluaga, D., De la Torre, A.G., Santacruz, I., Vallcorba, O., Dapiaggi, M., Sanfélix, S.G., Aranda, M.A.G. (2018) "Multiscale understanding of tricalcium silicate hydration reactions", *Sci. Rep.* 8: 8544.

De la Torre, A.G., Bruque, S., Aranda, M.A.G. (2001) "Rietveld quantitative amorphous content analysis", *J. Appl. Crystallogr.* 34: 196–202.

Gallucci, E., Scrivener, K.L., Groso, A., Stampanoni, M., Margaritondo, G. (2007) "3D experimental investigation of the microstructure of cement pastes using synchrotron X-ray microtomography (μCT)", *Cem. Concr. Res.,* 37: 360–368.

Gastaldi, D., Canonico, F., Capelli, L., Boccaleri, E., Milanesio, M., Palin, L., Croce, G., Marone, F., Mader, K., Stampanoni, M. (2012) "In situ tomographic investigation on the early hydration behaviors of cementing systems", *Constr. Build. Mater.,* 29: 284–290.

Jansen, D., Goetz-Neunhoeffer, F., Stabler, C., Neubauer, J. (2011) "A remastered external standard method applied to the quantification of early OPC hydration", *Cem. Concr. Res.*, 41: 602–608.

Kong, W., Wei, Y., Wang, S., Chen, J., Wang, Y. (2020) "Research progress on cement-based materials by X-ray computed tomography", *Int. J. Pavement Res. Technol.*, 13: 366–375.

Moradian, M., Hu, Q., Aboustait, M., Ley, M.T., Hanan, J.C., Xiao, X., Rose, V., Winarski, R., Scherer, G.W. (2019) "Multi-scale observations of structure and chemical composition changes of portland cement systems during hydration", *Constr. Build. Mater.,* 212: 486–499.

Parisatto, M., Dalconi, M.C., Valentini, L., Artioli, G., Rack, A., Tucoulou, R., Cruciani, G., Ferrari, G. (2015) "Examining microstructural evolution of Portland cements by in-situ synchrotron micro-tomography", *J. Mater. Sci.,* 50: 1805–1817.

Poirier, M., Blotevogel, S., Noiriel, C., Bonnin, A., Kaknics, J., Olbinado, M., Steger, L., Patapy, C., Cyr, M. (2022) "Synchrotron X-ray micro-tomography investigation of the early hydration of blended cements: A case study on CaCl2-accelerated slag-based blended cements", *Constr. Build. Mater.*, 321: 126412.

Salcedo, I.R., Cuesta, A., Shirani, S., León-Reina, L., Aranda, M.A.G. (2021) "Accuracy in Cement Hydration Investigations: Combined X-ray Microtomography and Powder Diffraction Analyses", *Materials,* 14, 6953.

Vigor, J.E., Bernal, S.A., Xiao, X., Provis, J.L. (2022) "Time-resolved 3D characterisation of early-age microstructural development of Portland cement", *J. Mater. Sci.*, 57: 4952–4969.

Withers, P.J., Bouman, C., Carmignato, S., Cnudde, V., Grimaldi, D., Hagen, C.K., Maire, E., Manley, M., Plessis, A. Du, Stock, S.R. (2021) "X-ray computed tomography", *Nat. Rev. Methods Prim.*, 1: 18.

The 16th International Congress on the Chemistry of Cement 2023 (ICCC2023)
"Further Reduction of CO_2 -Emissions and Circularity in the Cement and Concrete Industry"
September 18–22, 2023, Bangkok, Thailand

Characterization of siliceous hydrogarnet ($Ca_3Al_2(SiO_4)_x(OH)_{12-4x}$) by solid-state NMR spectroscopy

S. Nie*, J. Skibsted

Department of Chemistry and Interdisciplinary Nanoscience Center (iNANO), Aarhus University, Langelandsgade 140, DK-8000C Aarhus, Denmark

Email: shuainie@chem.au.dk, jskib@chem.au.dk

ABSTRACT

Katoite ($Ca_3Al_2(OH)_{12}$, C_3AH_6) is a thermodynamically stable phase which may form in hydrated high-alumina cements and in under-sulphated Portland cement cured at room temperature. Katoite can be considered as the end-member of the hydrogarnet family ($C_3AS_xH_{6-2x}$), where four hydroxyl groups are replaced by a SiO_4 unit. Siliceous hydrogarnets may form in autoclaved cements and in matured Portland cement systems, and they have only sparsely been characterized and identified in solid-state NMR studies of cementitious materials. In this work, nine siliceous hydrogarnets ($C_3AS_xH_{6-2x}$), targeting x = 0.2 – 3.0, have been synthesized at 110 °C in autoclaves for 5 days. The structures of the individual samples are investigated by ^{1}H, ^{27}Al, and ^{29}Si NMR spectroscopy as well as powder X-ray diffraction. Only one resonance at approx. -79.4 ppm is observed in the ^{29}Si NMR spectra for the samples with $x < 0.84$, whereas additional resonances from 11Å tobermorite and C-(A)-S-H phases are identified as impurity phases for x = 0.84 – 3. The resonance at -79.4 ppm is significantly enhanced in ^{29}Si{^{1}H} cross-polarization experiments. Moreover, ^{29}Si{^{1}H} REDOR NMR experiments for this resonance in the $C_3AS_{0.2}H_{5.6}$ and $C_3AS_{0.84}H_{4.32}$ samples allow estimation of the internuclear Si – H distances, which are found to be approx. 3.0, 3.5 and 4.0 Å. Multiple octahedrally coordinated Al sites are apparent in the siliceous hydrogarnets, as observed by ^{27}Al MAS and MQMAS NMR, and their quadrupolar interaction parameters have been determined. For $C_3AS_{0.2}H_{5.6}$ three distinct AlO_6 sites are observed, whereas four sites are apparent for $C_3AS_{0.84}H_{4.32}$. A broad ^{1}H resonance in the range of 0 – 3 ppm is observed in the ^{1}H MAS NMR spectra and assigned to hydroxyl groups associated with siliceous hydrogarnet. The NMR data reported in this study are discussed using earlier reported structural data and provide more insight into the structural variation with Si substitution for siliceous hydrogarnets.

KEYWORDS: *siliceous hydrogarnet, ^{1}H NMR, ^{27}Al NMR, ^{29}Si NMR, REDOR*

1. Introduction

Siliceous hydrogarnet ($C_3AS_xH_{6-2x}$) is a calcium aluminum garnet series, which may be present in autoclaved cements and in matured Portland cement systems. Katoite can be considered as the end-member of the hydrogarnet family, which structure has been well studied by X-ray diffraction (XRD) (Dilnesa et al. (2014)) and solid-state NMR spectroscopy (Skibsted et al. (1993)). When Si is present in the hydrogarnet structure, four hydroxy groups are replaced by a SiO_4 unit, forming siliceous hydrogarnet. Siliceous hydrogarnets with various Si contents have been synthesized at different conditions (Jappy and Glasser (1991), Kyritsis et al. (2009)) and characterized by conventional techniques, e.g., XRD, IR and Raman spectroscopy. However, siliceous hydrogarnet formed in cementitious environments have only sparsely been characterized and identified in solid-state NMR studies. In this work, nine siliceous hydrogarnets ($C_3AS_xH_{6-2x}$), targeting x = 0.2 – 3.0, have been synthesized at 110 °C in autoclaves for 5 days. The structures of the individual samples are investigated by ^{1}H, ^{27}Al, and ^{29}Si NMR spectroscopy as well as powder X-ray diffraction.

2. Material and Methods

The syntheses of siliceous hydrogarnets ($C_3AS_xH_{6-2x}$, targeting x = 0.2 – 3.0) were made from $AlCl_3{\cdot}6H_2O$, $Na_2SiO_3{\cdot}5H_2O$ and $Ca(NO_3)_2{\cdot}4H_2O$ in stoichiometric proportions. The solids were mixed with 2M KOH at a liquid/solid ratio of ~ 25 and cured at 110 °C in autoclaves for 5 days. After reaction, the solids were filtered in a glovebox with an N_2 atmosphere and the residues were dried in a desiccator over silica gel for 3 days. The dried samples were stored in sealed glass containers prior to the analysis.
Solid-state ^1H and ^{27}Al MAS NMR spectra were acquired on Bruker Avance 950 MHz (22.3 T) spectrometer using Bruker triple-resonance MAS probes (1.9 mm for ^1H with a spinning speed of ν_R = 40 kHz and 2.5 mm for ^{27}Al with ν_R = 25 kHz). The ^{29}Si MAS NMR experiments (9.4 T) were conducted on a Bruker 4 mm CP/MAS probe at a MAS frequency of ν_R = 10 kHz. ^1H, ^{27}Al and ^{29}Si NMR chemical shifts are relative to neat TMS ($Si(CH_3)_4$), using external samples of adamantane ($\delta_{iso}(^1H)$ = 1.87 and 1.76 ppm), 1.0 M aqueous $AlCl_3{\cdot}6H_2O$ (δ_{iso} (^{27}Al) = 0 ppm) and larnite (C_2S, δ_{iso} (^{29}Si) = -71.33 ppm), respectively.

3. Results and Discussion

The XRD patterns of the nine synthesized siliceous hydrogarnet ($C_3AS_xH_{6-2x}$) samples are illustrated in Figure 1. Only siliceous hydrogarnet and minor impurities of portlandite are observed when $x \leq 0.84$, and the widths of peaks from siliceous hydrogarnet increase with the Si content in the samples. In addition to siliceous hydrogarnet, 11-Å tobermorite and C-(A)-S-H phase are seen when $x > 0.84$.

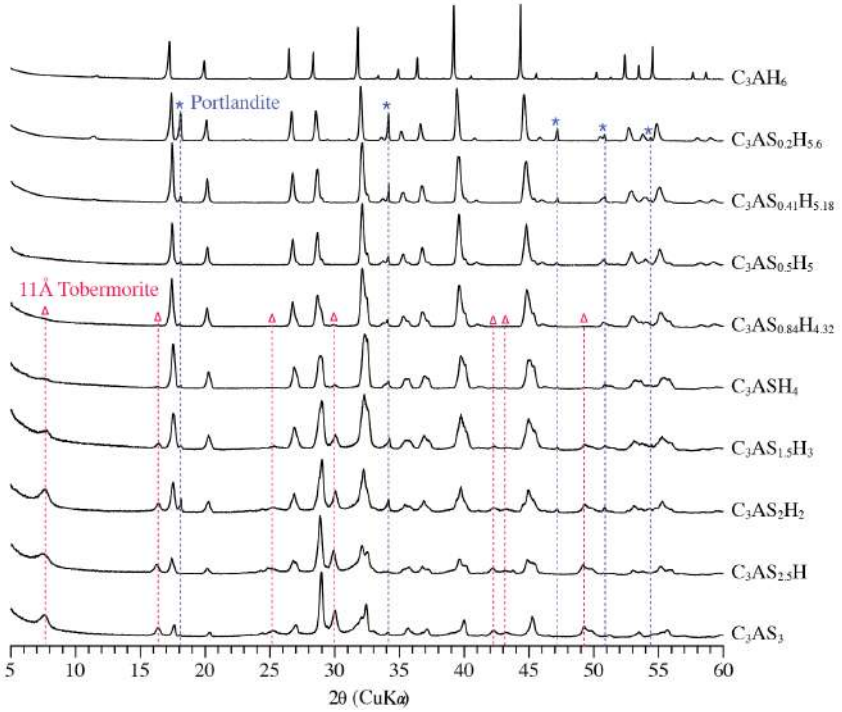


Figure 1. Powder XRD patterns of nine siliceous hydrogarnet ($C_3AS_xH_{6-2x}$, x = 0.2 – 3.0) synthesized at 110 °C.

3.1 ^{27}Al MAS NMR

The ^{27}Al MAS NMR spectra of the synthesized katoite and siliceous hydrogarnet recorded at 22.3 T are shown in Figure 2 and illustrate the spectral region for the ^{27}Al central transitions of tetrahedrally (AlO_4 species) and octahedrally (AlO_6 species) coordinated aluminum. For katoite, only a sharp resonance at 12.4 ppm is observed, in agreement with earlier studies (Skibsted et al. (1993)). In addition to the resonance assigned to katoite, more resonances at lower frequencies are present in the siliceous hydrogarnet samples ($x \leq 0.84$) and dominate the spectra with increasing Si content of the samples. Moreover, three distinct resonances from tetrahedrally coordinated are observed with significant intensities when the Si/Al ratios of the samples are higher than 0.42. Combined with the results from the XRD analysis, the tetrahedrally coordinated resonances are assigned to C-(A)-S-H phases and 11-Å tobermorite whereas the octahedral AlO_6 species originate from siliceous hydrogarnet.

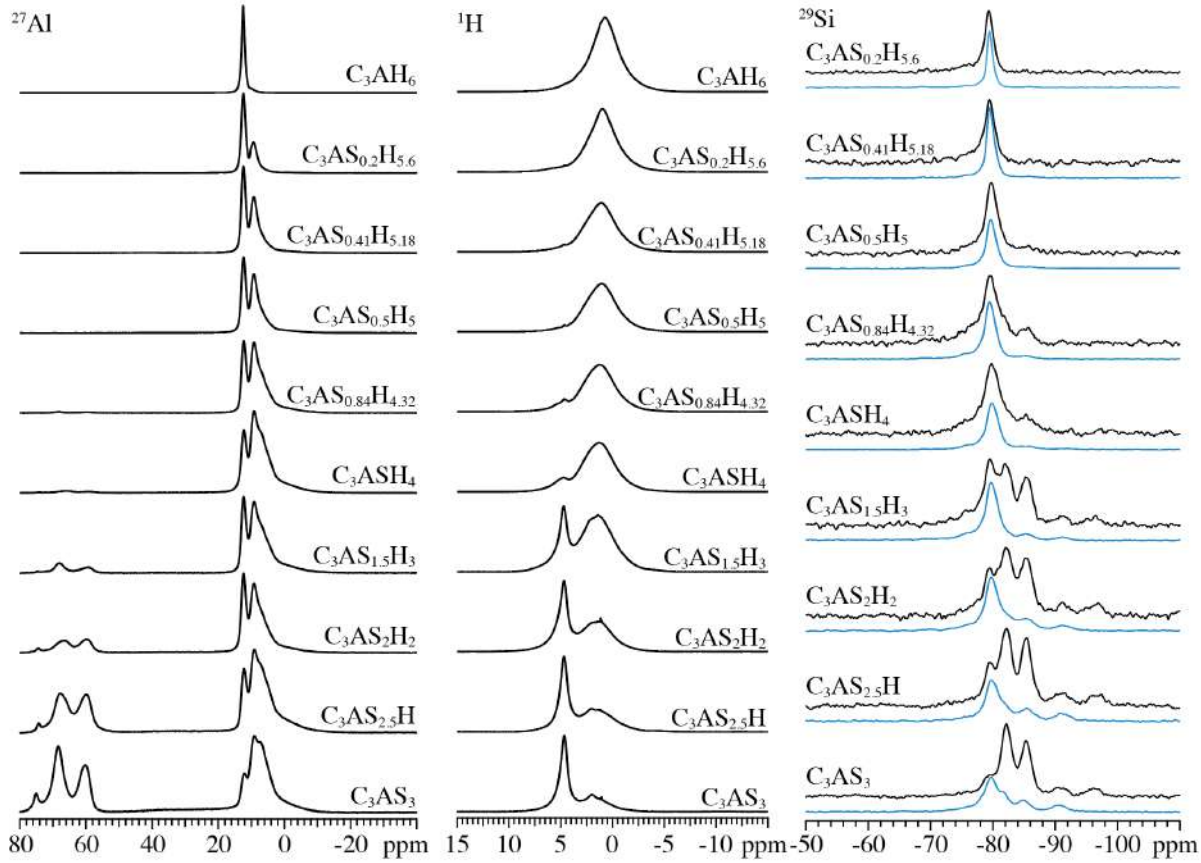


Figure 2. ^{27}Al (22.3 T, ν_R = 25 kHz, left), ^{1}H (22.3 T, ν_R = 40 kHz, middle), and ^{29}Si (black)/^{29}Si{^{1}H} CP (blue) (9.4 T, ν_R = 10 kHz, right) MAS NMR spectra for the synthesized katoite and siliceous hydrogarnet samples.

Multiple quantum magic-angle spinning (MQMAS) NMR experiments (spectra not shown) have been obtained to confirm the multiple Al sites in the octahedral region for the synthesized siliceous hydrogarnets. These spectra show that three distinct Al sites are present in $C_3AS_{0.2}H_{5.6}$, $C_3AS_{0.41}H_{5.12}$, and $C_3AS_{0.5}H_5$, whereas four different Al sites are observed in $C_3AS_{0.84}H_{4.32}$ and the samples with even higher Si content. The isotropic chemical shifts (δ_{iso}), quadrupolar coupling constants (C_Q) and asymmetry parameters (η_Q) of the four distinct Al sites for $C_3AS_{0.84}H_{4.32}$ are determined from simulations of the full ^{27}Al MAS NMR spectrum for central and satellite transitions (not shown), the data being summarized in Table 1.

Table 1. ^{27}Al isotropic chemical shifts (δ_{iso}) and quadrupolar coupling parameters (C_Q, η_Q) for the four distinct Al sites in the synthesized sample of $C_3AS_{0.84}H_{4.32}$

		δ_{iso}	C_Q	η_Q
$C_3AS_{0.84}H_{4.32}$	Al(1)	12.3	0.73	1.00
	Al(2)	10.5	3.33	0.55
	Al(3)	8.3	3.19	0.84
	Al(4)	5.5	2.67	1.00

3.2 ^{1}H MAS NMR

High-resolution solid-state ^{1}H MAS NMR spectra have been acquired for the synthesized siliceous hydrogarnets (Figure 2), by utilizing very fast magic-angle spinning and in combination with a very high magnetic field. One dominant broad peak at ~ 1.0 ppm is observed in the synthesized samples with low Si content ($x \leq 0.84$), whereas another resonance at ~ 4.5 ppm is clearly resolved with increasing Si content ($x > 0.84$). These two peaks are assigned to the resonances from siliceous hydrogarnet (~ 1.0 ppm) and 11-Å tobermorite/C-(A)-S-H phases (~ 4.5 ppm), respectively, considering the results from ^{27}Al NMR and powder XRD.

3.3 ^{29}Si MAS NMR

^{29}Si MAS and ^{29}Si{^{1}H} CP/MAS NMR experiments have been conducted for the nine synthesized siliceous hydrogarnets and the spectra are illustrated in Figure 2. For the ^{29}Si MAS NMR spectra, only one peak at approx. -79.4 ppm is observed in the samples of $C_3AS_{0.2}H_{5.6}$, $C_3AS_{0.41}H_{5.12}$, and $C_3AS_{0.5}H_5$. Moreover, a Q^2 resonance at ~ -85 ppm appears in $C_3AS_{0.84}H_{4.32}$ and C_3ASH_4, and additional Q^2 (~ - 82 ppm) and Q^3 (~ -91 ppm and ~ 96 ppm) resonances are observed in the samples with higher Si content (x > 1). ^{29}Si{^{1}H} CP/MAS NMR experiments show that the resonance at -79.4 ppm is significantly enhanced, indicating that the Si site is surrounded by protons (^{1}H). ^{29}Si{^{1}H} REDOR experiments have been implemented to estimate internuclear Si – H distances, utilizing the dephasing of the signal by ^{1}H – ^{29}Si dipolar couplings. The result is shown in Figure 3 and the distances are found to be approx. 3.0, 3.5 and 4.0 Å in the siliceous hydrogarnet samples independent of the Si contents.

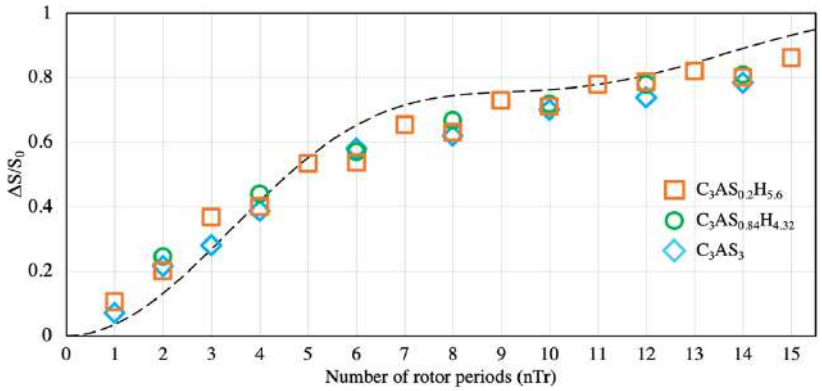


Figure 3. Experimental (dots) ^{29}Si{^{1}H} REDOR NMR fractions ($\Delta S/S_0$) and simulated result (dash line). The simulation is implemented in the SIMPSON package for a system with three H spins and one Si spin with the internuclear Si – H distances of r_{Si-H} = 3.0, 3.5, and 4.0 Å.

4. Conclusions

Siliceous Hydrogarnets with different Si contents have been successfully synthesized at 110 °C in autoclaves with 2.0 M KOH solution for 5 days. Only siliceous hydrogarnet ($C_3AS_xH_{6-2x}$) can be detected by either XRD or ^{1}H, ^{27}Al and ^{29}Si NMR spectroscopy with x in the range of 0.2 – 0.84, whereas C-(A)-S-H and 11-Å tobermorite phases are identified as impurity phases for x = 0.84 – 3, reflected by the tetrahedrally coordinated Al sites present in ^{27}Al MAS NMR spectra. In addition to the resonance from katoite, three and four octahedrally coordinated Al sites are observed by ^{27}Al MAS and MQMAS experiments for $x < 0.84$ and $x \geq 0.84$, respectively. Two types of ^{1}H resonances are detected in the ^{1}H MAS NMR spectra, which can be assigned to hydroxyl groups associated with siliceous hydrogarnet (~ 1 ppm) and 11 Å tobermorite/C-(A)-S-H phases (~ 4.5 ppm), respectively. The ^{29}Si MAS NMR spectra suggest that only one Si site is present in the siliceous hydrogarnets with different Si contents, whereas the ^{29}Si{^{1}H} REDOR NMR experiments have allowed estimation of the internuclear Si – H distances. The present results from solid-state NMR spectroscopy have provided detailed local structural information of the siliceous hydrogarnets with different levels of Si substitution.

References

Dilnesa, B. Z.; Lothenbach, B.; Renaudin, G.; Wichser, A.; Kulik, D. (2014) "Synthesis and Characterization of Hydrogarnet $Ca_3(Al_xFe_{1-x})_2(SiO_4)_y(OH)_{4(3-y)}$", *Cement and concrete research*, 59: 96–111.

Jappy, T. G.; Glasser, F. P. (1991) "Synthesis and Stability of Silica-Substituted Hydrogarnet $Ca_3Al_2Si_{3-x}O_{12-4x}(OH)_{4x}$", *Advances in Cement Research*, 4(13): 1–8.

Kyritsis, K.; Meller, N.; Hall, C. (2009) "Chemistry and Morphology of Hydrogarnets Formed in Cement-Based CASH Hydroceramics Cured at 200°C to 350°C", *Journal of the American Ceramic Society*, 92(5): 1105–1111.

Skibsted, J.; Henderson, E.; Jakobsen, H. J. (1993) "Characterization of Calcium Aluminate Phases in Cements by ^{27}Al MAS NMR Spectroscopy", *Inorganic chemistry*, 32(6): 1013–1027.

The 16th International Congress on the Chemistry of Cement 2023 (ICCC2023)
"Further Reduction of CO_2 -Emissions and Circularity in the Cement and Concrete Industry"
September 18–22, 2023, Bangkok, Thailand

Influence of MgO on formation of clinker with different alumina modulus based on big data

J.Y. Ye[1*], Z.B. Luan[2], W.S. Zhang[3], X.H. Ren[4], H.T. Zhang[5]

State Key Laboratory of Green Building Materials, China Building Materials Academy, Beijing, China)

Email: [1] *yejiayuan2017@163.com*

[2] *zbluan604@163.com*

[3] *wensheng_zhang01@163.com*

[4] renxue968@163.com

[5] *zhtcbma@163.com*

ABSTRACT

This work investigates the influence of MgO on formation of clinker with different alumina modulus (AM) by combining laboratory data with industrial big data. Laboratory clinker prepared with analytical reagents. High–temperature microscopy (HTM), X–ray diffraction (XRD), optical microscopy, and backscattered electrons–energy–dispersive spectrometry (BSE–EDS) examine the clinkering mechanism. The analysis method of industrial big data is mainly unsupervised learning. The results show that a reduced AM improves the burnability of the raw meal and the formation of more regular and larger alite particles. An increased alumina modulus contributes to reducing the size of the periclase and causes the shape of its particles to be round. An alumina modulus of 1.1 leads to the lowest liquidus temperature and increased tricalcium silicate (C_3S) content. In this case, a maximal solid solubility and a minimal crystallinity of MgO can be obtained. The highest content of C3S and tetra-calcium aluminoferrite (C_4AF) can be achieved at an MgO content of 3%–6%.

KEYWORDS: *Alumina modulus, High–magnesium clinker, Unsupervised learning, Morphological evolution*

1. Introduction

During the calcination process of clinker, the appropriate content of MgO can reduce the liquidus temperature, increase the liquid content, and slightly decline the liquid viscosity (Li et al (2012) and Li et al (2014)). However, only approximately 2% of MgO can dissolve in clinker, and the excess MgO crystallizes into periclase (Hewlett (2004)) when the MgO content exceeds the maximum solid solubility. When coarse and complete periclase is hydrated to generate $Mg(OH)_2$, the volume of cement expands by 118% (Mo et al (2014)), leading to cement cracking and the problem of soundness.

The ferrite phase is one of the primary components of liquid clinker, and the ratio of the alumina phase to its content, i.e., alumina modulus (AM), determines the liquid properties of clinker and directly affects the formation of clinker and the solid solution and crystallization of MgO (Altun (1999) and Liu et al (2005)). More ferrite phases can enhance the solid solubility of MgO (Taylor (1997) and Kurdowski (2014)).

The density functional theory (DFT) shows that the solid solubility of MgO is higher in C4AF than in other phases (Zhao et al (2021)). Accordingly, the variation of the AM has a direct and remarkable influence on the morphological evolution of MgO, and the coupling of the AM and MgO affects the clinker formation. Thus, this paper models typical clinker compositions using chemical reagents and discusses the clinker calcination, mineral composition, the morphology of alite and periclase, and the solid solubility of MgO.

2. Experimental procedures

Clinkers of Magnesium-free, low-magnesium with 3% of MgO, and high-magnesium with 6% and 12% of MgO were prepared with analytical reagents. With the same MgO content, the AM of the clinkers was designed as 0.64, 0.8, 1.1, 1.4, 1.7, 3, 7 and ∞ respectively. In addition, the lime saturation ratio (KH) and the silica modulus (SM) were set at 0.898 and 2.55 respectively. MgO content and AM are included in the sample number. For example, M6_1.1 indicates clinker with 6% MgO content and 1.1 AM.
The raw meals were pressed into pellets with a diameter of φ 33 mm × 5 mm. They were burned for 0.5 h in a muffle furnace at 900 °C and were quickly transferred to an elevator furnace at 1450 °C for 0.5 h.
The free calcium oxide (f-CaO) content was determined using the ethylene glycol–ethanol method. High–temperature microscopy (HTM), X–ray diffraction (XRD), optical microscopy, and backscattered electrons–energy–dispersive spectrometry (BSE–EDS) examine the clinkering mechanism. The analysis method of industrial big data is mainly unsupervised learning.

3. Results and discussion

3.1. Burnability of raw meal

As shown in Fig. 1, when the AM is 0.64, the f-CaO content of samples is less than 0.5%, and increasing the AM enlarges the f-CaO content of the clinkers. The viscosity of the liquid rises with the increasing AM (Wu et al (1992)), which hinders the reaction between the f-CaO and dicalcium silicate (C_2S), thereby raising the content of f-CaO.

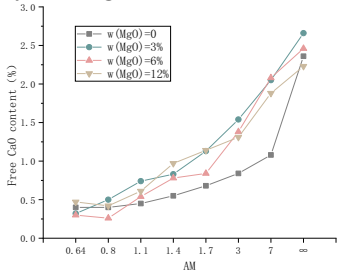


Fig. 1. The f-CaO content of the clinker samples.

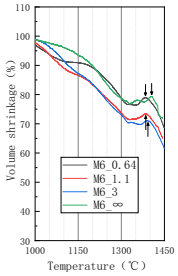


Fig. 2. The volume shrinkage of the clinker samples.

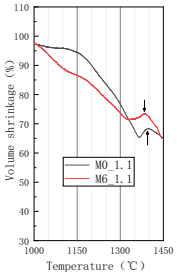


Fig. 3. The volume shrinkage of the clinker samples.

3.2. Liquidus temperature

Figs. 2 and 3 delineate the volume shrinkage–temperature curves of samples during the calcination process. Fig. 2 demonstrates that the liquidus temperatures of specimens M6_0.64 and M6_1.1 are almost similar and lower than those of samples M6_3 and M6_∞. The liquidus temperature of specimens M6_3 and M6_∞ increases, and specimen M6_∞ has the highest liquidus temperature. According to Fig. 3, the liquidus temperature of sample M0_1.1 is higher than that of specimen M6_1.1. In fact, the liquidus temperature of the clinker declines after adding 6% of MgO, which with the related literature (Li et al (2012) and Li et al (2014)), implying that MgO can lower the liquidus temperature of the clinker.

3.3. Mineral composition of clinker

Fig. 4 depicts the contents of mineral phases such as C_3S, C_2S, C_3A, C_4AF, and periclase in the clinker. In general, the C_3S content of the clinker enlarges with the increasing AM from 0.64 to 1.4, but it declines as the AM exceeds 1.4 (see Fig. 4(a)). However, the variation of the C_2S content of the clinker is opposite to that of the C_3S content(Fig. 4(b)). This is caused by a combination of liquid content and viscosity.
As shown in Fig. 4(e), adding MgO increases the periclase content of the clinker: the periclase content of the clinker is the lowest at an AM of 1.1. Significantly, the periclase content of the clinker with 12% of MgO is remarkably lower than that of the other clinkers. It should be mentioned that, according to Fig. 4(a) and 4(b), when the AM equals 1.1, the C3S content of the clinker is higher; it is only lower than that of the clinker with an AM of 1.4.

Compared with the clinker without MgO, adding 3% or 6% of MgO increases the C_3S and C_4AF contents of the clinker but reduces its C_2S and C_3A contents since magnesium preferentially dissolves in C4AF (Zhao et al (2021)), giving rise to the replacements of calcium and ferrum. In addition, MgO can reduce the liquidus temperature (as verified in Section 3.2), increase the liquid volume, and slightly decline the liquid viscosity (Li et al (2012) and Li et al (2014)), which may give rise to the above results. The above figures and results demonstrate that the highest C_3S and C_4AF contents of the clinker form at an MgO content of 3%–6%.

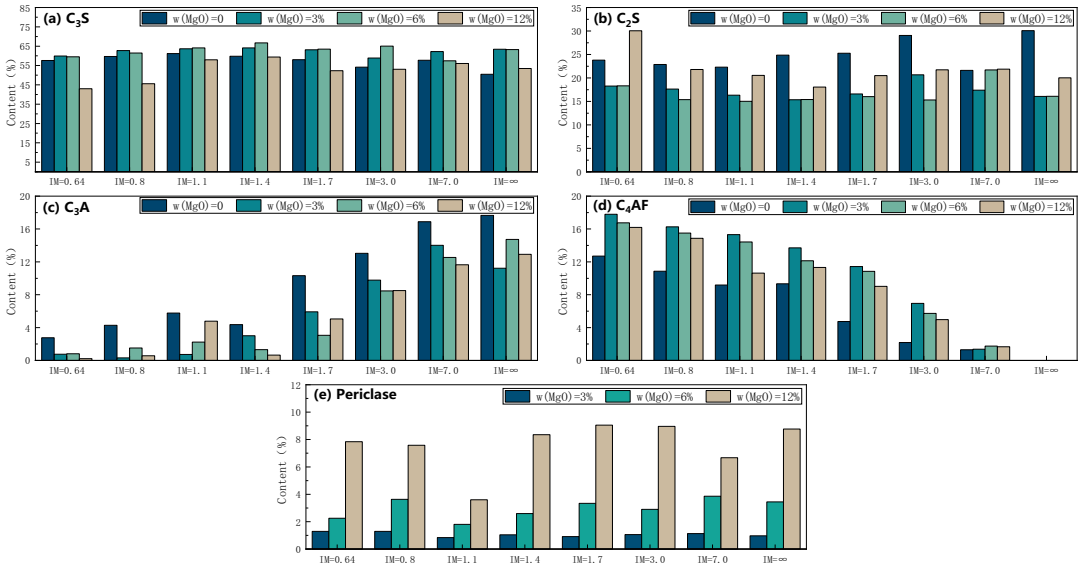


Fig. 4. The quantitative analysis of each phases (a) C_3S, (b) C_2S, (c) C_3A ,(d) C_4AF, and (e) periclase.

3.4. Morphological characteristics of alite

Figs. 5 illustrate the lithofacies photos of the high-magnesium clinker (w(MgO) = 6%). At a lower AM, alite is mainly hexagonal and prismatic. Due to the low viscosity of the liquid, the boundary between the crystals is blurred. The size of the alite of specimens M6_0.64 is mostly about 50 μm (see Figs. 5(a)). Increasing the AM raises the viscosity and makes the alite formation more difficult. The alite gradually presents a complex polygon and elongated strip, and the boundary between the crystals clarifies. The length of the alite drops to about 15 μm or even less than 5 μm (Figs. 5(d)).

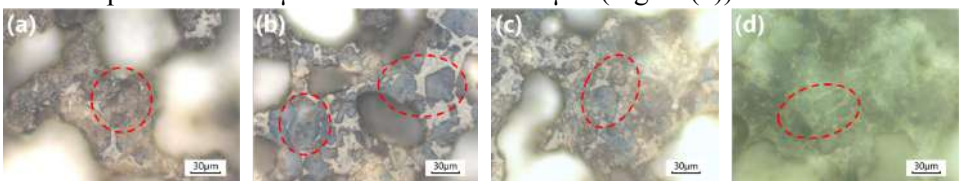


Fig. 5. The optical microscopy images of the clinker samples with different alumina moduli and an MgO content of 6%: (a) specimen M6_0.64, (b) specimen M6_1.1, (c) specimen M6_3, and (d) specimen M6_∞.

3.5. Morphological characteristics of MgO

As shown in Table 1, the solid solubility of MgO in the clinker is the highest at an AM of 1.1, while the periclase content is the lowest, agreeing with Section 3.3.

Table 1 The everage Mg content of the clinker mesophases with various alumina moduli.

	M6_0.64	M6_1.1	M6_3.0	M6_∞
Mg content (%)	1.61	1.75	1.09	1.04

The size of the periclase changes with the AM: when the AM is low, the size of the periclase ranges from 4 to 12 μm (Fig. 6(a)), and there are a few circles. Moreover, the viscosity of the liquid increases at higher alumina moduli. At an AM of infinity, the size of the periclase decreases to 2–6 μm (see Fig. 6(d)), and the number of rounded periclases rises; however, but quadrilaterals still dominate. Therefore, increasing the AM benefits the formation of smaller round periclases.

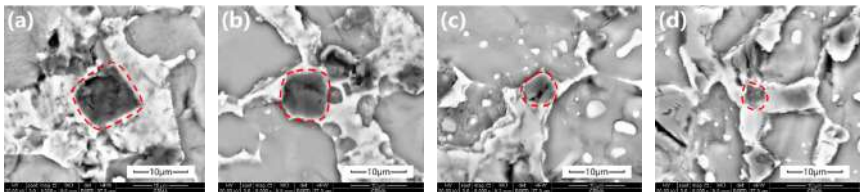


Fig. 6. The BSE images of the clinker samples with various alumina moduli and an MgO content of 6%: (a) specimen M6_0.64, (b) specimen M6_1.1, (c) specimen M6_3, and (d) specimen M6_∞.

3.6. Big data analysis

Unsupervised learning cluster analysis K value method was used to analyze the chemical composition, AM and f-CaO content of more than 500 clinkers distribution relationship and characteristics. The result shows that clinker with high KH and low SM has higher f-CaO content. The lower AM, the lower f-CaO content. This indicates that the appropriate reduction of AM and increase of MgO content can promote the clinker formation. This is consistent with the above experimental results.

4. Conclusions

- Reducing the AM could improve the burnability of the raw meal. When the AM was 1.1, the solid solubility of MgO was the highest, and the content of periclase was the lowest. Further, under the same conditions, the liquidus temperature of the raw meal was lower, and the C_3S content of the clinker was higher. The clinker with a lower or higher AM, had a high periclase and low C_3S content.
- Increasing the AM of the high-magnesium clinker hindered the development of alite and periclase. Alit becomes more complex in shape and smaller in size. The shape of the periclase changes from quadrilateral to circular, and the size decreases.
- An appropriate MgO content could increase the C_3S and C_4AF but decrease the C_2S and C_3A contents of the clinker. The highest C_3S and C_4AF contents of the clinkers were achieved at an MgO content of about 3%–6%. In this sense, MgO was beneficial to the formation of clinker.

Acknowledgements

The authors gratefully acknowledge the financial support of the National Natural Science Foundation of China (No. 51872272) and the Key Technologies R&D Program of CNBM (No. 2021YCJS01).

References

Li, X.R., Huang, H., Xu, J., et al. (2012) "Statistical research on phase formation and modification of alite polymorphs in cement clinker with SO_3 and MgO", *Construction and Building Materials*, 37: 548–555.

Li, X.R., Xu, W.L., Wang, S.P., et al. (2014) "Effect of SO_3 and MgO on Portland cement clinker: Formation of clinker phases and alite polymorphism", *Construction and Building Materials*, 58: 182–192.

Hewlett, P.C. (2004) "Lea's chemistry of cement and concrete", *Fourth Edition, Butterworth-Heinemann*, Oxford.

Mo, L.W., Deng, M., Tang, M.S., et al. (2014) "MgO expansive cement and concrete in China: Past, present and future", *Cement and Concrete Research,* 57: 1–12.

Altun, I.A. (1999) "Effect of CaF2 and MgO on sintering of cement clinker", *Cement and Concrete Research*, 29: 1847–1850.

Liu, X.C., Li, Y.J. (2005) "Effect of MgO on the composition and properties of alite-sulphoaluminate cement", *Cement and Concrete Research,* 35: 1685–1687.

Taylor, H.F.W. (1997) "Cement Chemistry", *Thomas Telford*, London.

Kurdowski, W. (2014) "Cement and Concrete Chemistry", *Springer-Verlag*, Berlin.

Zhao, R.Q., Zhang, L., Fan, G.G., et al. (2021) "Probing the exact form and doping preference of magnesium in ordinary Portland cement clinker phases: A study from experiments and DFT simulations", *Cement and Concrete Research*, 144(106420).

Wu, Y.R., Wu, Z.F., Long, S.Z. (1992) "MgO distribution in clinker containing fluorine sulfur and high ferrite and its influence on expansion in cement autoclave test (in Chinse)", *Cement*, 12: 15-18+14.

The 16th International Congress on the Chemistry of Cement 2023 (ICCC2023)
"Further Reduction of CO_2 -Emissions and Circularity in the Cement and Concrete Industry"
September 18–22, 2023, Bangkok, Thailand

Multiscale investigation on the thermal stability of synthetic C-S-H pastes according to Ca/Si ratios

S.M. Im[1], S.C. Bae[2*]

[1] *Hanyang University, Seoul, Republic of Korea*

Email: isumin@hanyang.ac.kr

[2] *Hanyang University, Seoul, Republic of Korea*

Email: sbae@hanyang.ac.kr

ABSTRACT

As one of the most voluminous binding phases of cementitious materials, calcium-silicate-hydrate (C-S-H) dominantly affects the thermal decomposition behavior of concrete at elevated temperatures. Further, the hierarchical porous structure of C-S-H over a wide length scale from angstrom to micrometer depends on its calcium-to-silicon (Ca/Si) ratios. Hence, this study intends to clarify the correlation between thermal stability and fractal-like nano-structural changes of synthetic C-S-H pastes with a Ca/Si ratio ranging from 0.6 to 1.0 via synchrotron small- and wide-angle X-ray scattering experiments with in-situ loading systems. The experimental results revealed that thermal phase transformations of the C-S-H phase into crystalline β-wollastonite over three distinct stages regardless of Ca/Si ratios: dehydration, decomposition, and recrystallization. Until heating up to 500 ℃, the thermal shrinkage of the intralayer of C-S-H pastes increased and decomposed at lower temperatures due to an increase in water molecules at a high Ca/Si ratio of 1.0. As shown in the X-ray scattering curves at low Q regions (Q = 0.005–0.2 $Å^{-1}$), the surface fractal correlation length (ξs) derived from surface fractal components decreased with increasing temperatures owing to the thermal shrinkage of C-S-H pastes at the decomposition stage. In addition, the shrinkage of C-S-H paste with a Ca/Si ratio of 1.0 was observed more apparent than that with a Ca/Si ratio of 0.6.

KEYWORDS: *Calcium silicate hydrate (C-S-H), thermal stability, small-angle X-ray scattering (SAXS), wide-angle X-ray scattering (WAXS), pair distribution function (PDF)*

1. Introduction

Portland cement (PC)-based concrete has been used as the primary building material for civil infrastructure from the 19th century to the present, with a worldwide annual cement production of 4.1 billion metric tons (Shakouri et al. 2020). In addition, the mechanical, durability properties, and thermal stability of concrete are dependent on the main reactive binder component, cement clinker, which is composed of four main phases: alite (C_3S), belite (C_2S), tricalcium aluminate (C_3A), and ferrite (C_4AF). Among them, the main hydration product of C_3S and C_2S, calcium-silicate-hydrate (C-S-H), accounts for more than 50 vol.% of the total composition of hydration products including portlandite, ettringite, and others (Im et al. 2021). Because of the cement clinkerization process, the cement industry currently consumes approximately 7% of industrial energy and accounts for 8% of total global anthropogenic CO_2 emissions (Kusuma et al. 2022). Therefore, significant attempts have been made to reduce CO_2 emissions by utilizing supplementary cementitious materials (SCMs) as partial replacements for PC, such as blast-furnace slag, fly ash, and silica fume. Despite the partial substitution of cement by SCMs, the hardening, strength development, and thermal decomposition of PC-based concrete are still primarily governed by the physicochemical characteristics of C-S-H with various Ca/Si ratios ranging from 0.6 to 1.7 (Richardson 2014).

The C-S-H in PC-based concrete possesses a structural similarity with the imperfect fractal-like form of natural calcium silicate hydrate minerals, such as tobermorite and jennite, which consist of CaO_7 double layers bonded with infinite silicate chains (Richardson 2014). Furthermore, C-S-H is well known as a hierarchically structured material with multiscale pores spanning a wide length scale from angstrom-to-micrometer such as interlayer pores, gel pores, and capillary pores (Im et al. 2023). To date, numerous studies have indicated that an increase in Ca^{2+} intercalation with an increase in Ca/Si ratio results in a change from foil-like to fibrillar morphology in accordance with a reduction in silicate chain length and interlayer spacing from 14 to 9 Å (Richardson 2014). The morphological change according to Ca/Si ratios significantly affects the thermal decomposition behaviors of C-S-H that occurred in three distinct phases: dehydration, decomposition, and recrystallization to β-wollastonite (Tajuelo Rodriguez et al. 2017). However, the deterioration of physicochemical properties caused by fractal-like structural deformation behavior of C-S-H phases after exposure to high temperatures is still ambiguous due to its heterogeneous and hierarchically porous structure.
To elucidate the thermal decomposition behavior of the C-S-H phase in PC excluding the influence of other hydration products, most conventional analyses have been conducted on pure C-S-H systems synthesized in powder form rather than paste form that contains lots of air voids (Tajuelo Rodriguez et al. 2017). The main purpose of this study is to investigate the fractal-like structural deformation behavior and interatomic structural changes in synthesized C-S-H pastes with Ca/Si ratios of 0.6, 0.8, and 1.0, respectively, after heating from room temperature (20±2 ℃) up to 800 ℃ via synchrotron small- and wide-angle X-ray scattering experiments (SAXS and WAXS). Based on the experimental data, the correlation between the thermal shrinkage behavior of C-S-H pastes including mesopores obtained by the fractal model (Allen, Thomas, and Jennings 2007) and nanocrystalline structure deformation behavior is discussed in this study.

2. Experimental procedure

2.1 Materials and synthesis process

Pure C-S-H pastes (5 × 5 × 10 mm^3) were synthesized using the pozzolanic method with distilled water, $Ca(OH)_2$ (2.21 g/cm^3, Sigma-Aldrich, USA), and silica gel (1.43 g/cm^3, Fluka silica gel 60, particle size 40–63 μm, Sigma-Aldrich, USA). The final Ca/Si molar ratio of C-S-H was controlled by the dosage of $Ca(OH)_2$ and silica gel to be 0.6, 0.8, and 1.0, respectively. In addition, polycarboxylate superplasticizers (SP) were added to achieve similar workability of composites with different Ca/Si ratios. Detailed synthesis procedures were reported in our previous work (Im et al. 2023). After a curing period of 90 days, the C-S-H pastes were heated at a rate of 10 ℃/min from room temperature to the target temperature (starting at 105 ℃ and increasing every 100 ℃ increment from 200 to 800 ℃) and then maintained at the target temperature for 2 h in the furnace.

2.2 Synchrotron small- and wide-angle X-ray scattering experiments

After heating up to 105, 200, 400, and 500 ℃, slice C-S-H samples with 1 mm thickness were taken from the middle part of C-S-H prisms to collect SAXS data using synchrotron X-rays with a wavelength of 0.73 Å at 4C beamline in Pohang Accelerator Laboratory (PAL, Pohang, Korea) (Kim et al. 2017, 2020). The 2D SAXS images to cover low Q regions ranging from 0.005 to 2.7 $Å^{-1}$ were obtained with an imaging plate with a sample-to-detector distance of 5, 1, and 0.2 m, respectively. The collected SAXS configurations, with Q ranging from 0.005 to 0.2 $Å^{-1}$, were analyzed using the *Irena* and *Nika* software packages, along with the surface and volume fractal model suggested by Allen et al (2007) (Ilavsky and Jemian 2009). The scattering invariant is calculated using equation (1):

$$Q_{INV} = 2\pi^2\varphi_T(1-\varphi_T)|\Delta\rho|^2 = \int_0^\infty Q^2 \frac{d\Sigma}{d\Omega}(Q)dQ \quad (1)$$

where φ_T is the solid volume fraction, $\Delta\rho^2$ is the scattering contrast between voids and solids.
In addition, WAXS configurations with Q regions ranging from 1 to 18 $Å^{-1}$ were obtained using synchrotron X-rays with a wavelength of 0.18 Å at BL22XU beamline in SPring-8 (Hyogo, Japan). The 2D WAXS images were collected using a flat panel (FP) detector (PerkinElmer XRD1621, Germany) with a sample-

to-detector distance of 0.654 and 0.304 m to achieve high Bragg peak resolution and long Q-range order for the pair distribution function (PDF) (Im et al. 2023). The PDFs (*G(r)*) was directly calculated from a Fourier transformation of the total scattering structure function, *S(Q)*, using PDFgetX3, as presented in equation (2):

$$G(r) = 4\pi r[\rho(r) - \rho_0] = \frac{2}{\pi}\int_{Q_{min}}^{Q_{max}} Q[S(Q) - 1]\sin(Qr)\,dQ \quad (2)$$

3. Results and discussion

3.1 Synchrotron small-angle X-ray scattering

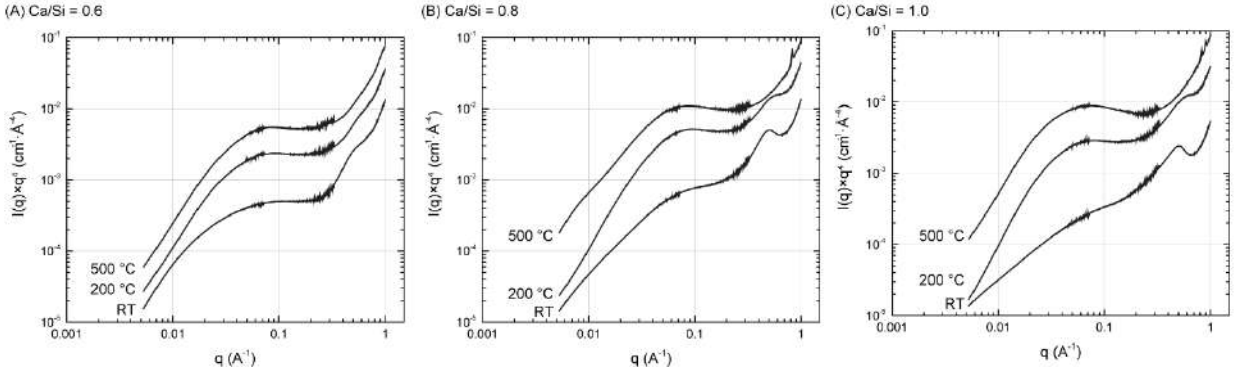


Figure 1. Synchrotron SAXS data for C-S-H pastes before heating and after heating up to 200 and 500 °C: (A) Ca/Si = 0.6, (B) Ca/Si = 0.8, and (C) Ca/Si = 1.0. Data for different heating temperatures are offset.

SAXS data plotted as $I(Q) \times Q^4$ versus Q are shown in Figure 1. With a decrease in Ca/Si ratios from 1.0 to 0.6, a plateau with a wide Q range was observed due to the changes from fibrillar to foil-like morphology (Richardson 2014). Furthermore, at overall Ca/Si ratios, the peaks that are typically associated with the interlayer spacing of C-S-H pastes were observed at approximately 0.5 $Å^{-1}$ shifted to a higher Q range with increasing temperatures owing to the dehydration behaviors (Im et al. 2021). At a Ca/Si ratio of 1.0, a plateau was found after heating up to 200 °C and the thermal shrinkage rate of the interlayer was higher than other C-S-H pastes with Ca/Si ratios of 0.6 and 0.8.

3.2 Synchrotron wide-angle X-ray scattering

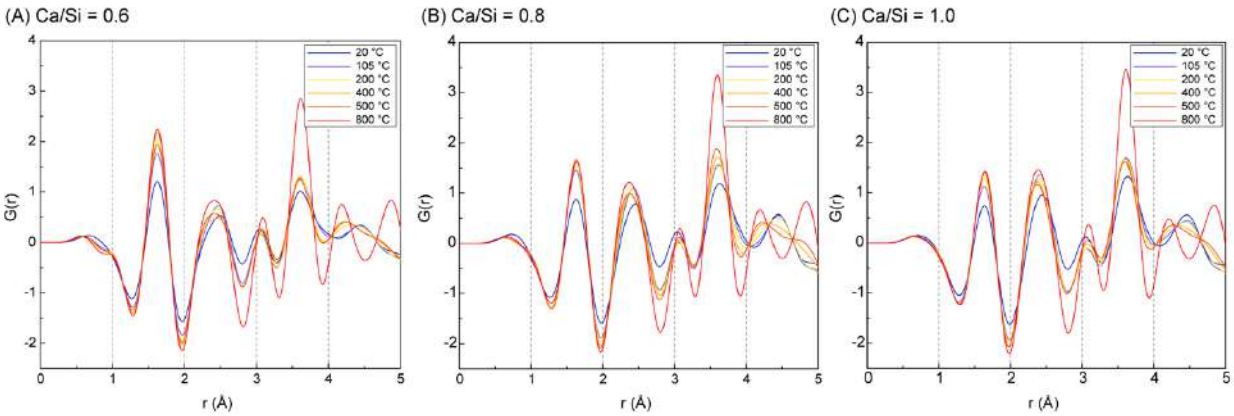


Figure 2. PDFs of C-S-H pastes after exposure to high temperatures of 105, 200, 400, 500, and 800 °C: (A) Ca/Si = 0.6, (B) Ca/Si = 0.8, and (C) Ca/Si =1.0

Figure 2 depicts the converted wide-angle X-ray scattering data to PDFs of C-S-H pastes after heating up to 105, 200, 400, 500, and 800 °C, respectively. The intensity ratio between the correlation of Si_1-O_1 (~1.6 Å) and Ca_1-O_1 (~2.4 Å) decreased with an increase in temperatures due to the decalcification behavior. In addition, Ca_1-O_1 and Ca_1-O_2 (~4.2 Å) related to the presence of CaO_7 polyhedral structures decreased proportionally with increasing temperatures while Si_1-O_1 increased.

4. Conclusions

In this study, the thermal transformation of C-S-H pastes with Ca/Si ratios of 0.6, 0.8, and 1.0 was elucidated using synchrotron small- and wide-angle X-ray scattering experiments. The obtained results are summarized as follows:

- As the Ca/Si ratio increased from 0.6 to 1.0, a plateau disappeared at the SAXS data plotted as $I(Q) \times Q^4$ versus Q due to the changes from foil-like to fibrillar morphology. After heating up to 200 ℃, the plateau was observed due to thermal shrinkage related to the dehydration behavior of C-S-H pastes. Furthermore, the thermal shrinkage rate was higher than that of C-S-H paste with other Ca/Si ratios of 0.6 and 0.8.
- The overall Ca/Si ratios decreased due to the decalcification effect of C-S-H phases after exposure to high temperatures. In particular, the difference in Ca/Si ratios before heating and after heating up to 800 ℃ was more pronounced, as the Ca/Si ratio increased from 0.6 to 1.0.
- Regardless of Ca/Si ratios, the correlations related to Ca_1-O_1 and Ca_1-O_2 decreased proportionally with increasing target temperatures owing to the thermal shrinkage of CaO_7 polyhedral structures.

Acknowledgements

This study was supported by the National Research Foundation of Korea (NRF) grant funded by the Korea government (MSIT) (grant number NRF- 2022R1A2C2010350). The synchrotron-radiation X-ray diffraction experiments were performed using BL22XU, SPring-8, with the approval of the Japan Synchrotron Radiation Research Institute (Proposal Nos. 2019A3784) and BL4C of Pohang Accelerator Laboratory (Proposal Nos. 2022-2nd-4C-053).

References

Allen, Andrew J., Jeffrey J. Thomas, and Hamlin M. Jennings. 2007. “Composition and Density of Nanoscale Calcium-Silicate-Hydrate in Cement.” Nature Materials 6(4):311–16. doi: 10.1038/nmat1871.

Ilavsky, Jan, and Peter R. Jemian. 2009. “Irena: Tool Suite for Modeling and Analysis of Small-Angle Scattering.” Urn:Issn:0021-8898 42(2):347–53. doi: 10.1107/S0021889809002222.

Im, S., H. Jee, H. Suh, M. Kanematsu, S. Morooka, K. Taku, N. Yuhei, A. Machida, J. Kim, and S. Bae. 2021. “Temperature Effects on Local Structure, Phase Transformation, and Mechanical Properties of Calcium Silicate Hydrates.” Journal of the American Ceramic Society 104(9). doi: 10.1111/jace.17881.

Im, Sumin, Hyeonseok Jee, Heongwon Suh, Manabu Kanematsu, Satoshi Morooka, Hongbok Choe, Nishio Yuhei, Akihiko Machida, Jihoon Kim, Seungmin Lim, and Sungchul Bae. 2023. “Insight on the Mechanical Properties of Hierarchical Porous Calcium-Silicate-Hydrate Pastes According to the Ca/Si Molar Ratio Using in-Situ Synchrotron X-Ray Scattering and Nanoindentation Test.” Construction and Building Materials 365. doi: 10.1016/J.CONBUILDMAT.2022.130034.

Kim, Jun Ha, Byoungseok Min, Young Duck Yun, Hyeong Joo Choi, and Kyeong Sik Jin. 2020. “Size-Exclusion Chromatography Coupled with Small-Angle X-Ray Scattering on the 4C Small-Angle X-Ray Scattering Beamline at Pohang Light Source II.” Bulletin of the Korean Chemical Society 41(11):1052–55. doi: 10.1002/BKCS.12119.

Kim, Kwang-Woo, Jehan Kim, Young Duck Yun, Hyungju Ahn, Byoungseok Min, Na Hyung Kim, Seungyu Rah, Hyo-Yun Kim, Chae-Soon Lee, In Deuk Seo, Woul-Woo Lee, and Hyeong Joo Choi and Kyeong Sik Jin*. 2017. “Small-Angle X-Ray Scattering Beamline BL4C SAXS at Pohang Light Source II.” BIODESIGN 5(1):24–29.

Kusuma, Ravi Teja, Rahul B. Hiremath, Pachimatla Rajesh, Bimlesh Kumar, and Suresh Renukappa. 2022. “Sustainable Transition towards Biomass-Based Cement Industry: A Review.” Renewable and Sustainable Energy Reviews 163:112503. doi: 10.1016/J.RSER.2022.112503.

Richardson, Ian G. 2014. “Model Structures for C-(A)-S-H(I).” Acta Crystallographica Section B: Structural Science, Crystal Engineering and Materials 70(6):903–23. doi: 10.1107/S2052520614021982.

Shakouri, Mahmoud, Christopher L. Exstrom, Sivakumar Ramanathan, Prannoy Suraneni, and James S. Vaux. 2020. “Pretreatment of Corn Stover Ash to Improve Its Effectiveness as a Supplementary Cementitious Material in Concrete.” Cement and Concrete Composites 112:103658. doi: 10.1016/J.CEMCONCOMP.2020.103658.

Tajuelo Rodriguez, Elena, Krassimir Garbev, Daniela Merz, Leon Black, and Ian G. Richardson. 2017. “Thermal Stability of C-S-H Phases and Applicability of Richardson and Groves’ and Richardson C-(A)-S-H(I) Models to Synthetic C-S-H.” Cement and Concrete Research 93:45–56. doi: 10.1016/J.CEMCONRES.2016.12.005.

The 16th International Congress on the Chemistry of Cement 2023 (ICCC2023)
"Further Reduction of CO_2 -Emissions and Circularity in the Cement and Concrete Industry"
September 18–22, 2023, Bangkok, Thailand

MOLECULAR DYNAMICS ON THE PRESSURE EXERTED BY WATER MOLECULES CONFINED IN MICROPOROUS C-S-H

Shota Takinami 1*, Ryo Yoshida2, and Ryo Kobayashi3

[1] *Nagoya Institute of Technology, Aichi, Japan*
Email: clz16025@ict.nitech.ac.jp
[2] *Nagoya Institute of Technology, Aichi, Japan*
Email: yoshida.ryo@nitech.ac.jp
[3] *Nagoya Institute of Technology, Aichi, Japan*
Email: kobayashi.ryo@nitech.ac.jp

ABSTRACT

Many experiments have shown that water in the pores of concrete plays an important role in the capabilities and deterioration process of cement paste, but there are many unclear issues about the calcium silicate hydrate (C-S-H) of its microstructure.

One of these concerns is the change in volume of C-S-H with water content. Ca/Si ratio of the crystal structure has a significant effect on the volume change of C-S-H, which varies with the type of concrete. Ordinary Portland Cement (OPC) has a large Ca/Si ratio and a small volume change. There are many experiments and analysis that ignore the volume change due to drying and wetting. Recently, however, environmentally friendly Blast Furnace Slag (BFS) has increasingly been in use. It has a smaller Ca/Si ratio than OPC, and its volume change is larger. It is therefore necessary to reconsider the assumptions of many experiments.

In this study, Molecular Dynamics method (MD method) was used to understand the physical properties of C-S-H. Water molecules were arranged between two C-S-H layers to verify water transfer. After investigating the pressure of C-S-H layer by changing the number density of water molecules, the interlayer distance, and the temperature, it was confirmed that a water column was formed by the intermolecular force of water molecules at a certain number of water molecules. This water column exerts pressure on layers of C-S-H in the direction of contraction. It was confirmed that pressure is transmitted to the wall in the expansion direction above a certain number of water molecule densities dependent on the temperature. Suggestively, this pressure-induced volume change process could be an event to be considered in many studies and experiments.

KEYWORDS: *Molecular dynamics, calcium silicate hydrate (C-S-H),simulation*

1. Introduction

According to some estimates, global cement production is estimated to be more than 4 billion tons as of 2019, and the cement industry accounts for about 8% of global CO2 emissions, which is higher than that of airplanes and ships. If we compare the cement industry to a country, CO2 emissions are the third largest after China and the United States. Considering that there are no practical construction materials to replace concrete in modern times, The scientific understanding of cement, which is the base of concrete, is of great importance for sustainable development.
The microstructure of cement is calcium silicate hydrate, which goes without saying that it is the most important substance that determines the physical properties and durability of cement, but many of the structure, composition, and physical properties of C-S-H have not been clarified.

In this study, the molecular dynamics (MD) method was used to understand the physical properties of C-S-H. In particular, the pressure exerted on C-S-H was examined from the amount of C-S-H and water content.

2.Method

2.1 C-S-H model

Existing studies suggest that C-S-H is similar to the crystal structure of Tobemorite, an inorganic mineral. C-S-H is a structure consisting of calcium layers and silicate chains, and other calcium and water molecules can penetrate between the layers, which changes the interlayer distance. It is known that there are interlayers of 14, 11, and 9 Å from XRD patterns.

In this study, we used the Tinf_14sc model proposed by Richardson with an interlayer distance of 14Å and a space group "P21/c", which is an orthorhombic model. However, orthogonalization was performed to simplify numerical calculations. A simple point charge SPC model was used for water molecules. The unit cell shown in the figure was constructed by sandwiching the water molecules between C-S-H from above and below.

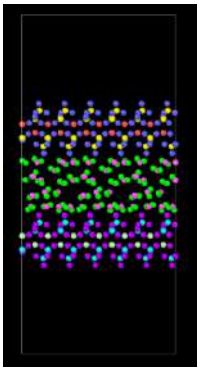


Figure 1 C-S-H unit cell

Table 1 Physical quantity of SPC model

O(g/mol)	H(g/mol)	q_O(C)	q_H(C)	r(Å)	θ(°)
15.994	1.008	-0.82	0.41	1	109.5

Table 2 σ and ε of the Lennard-Jones potential for the SPC

i	j	σ_{ij}(Å)	ε_{ij}(Kcal/mol)
O_w	O_w	3.16412	0.161776
H_w	O_w	-	-
H_w	H_w	-	-

The molecular dynamics method describes the behavior of molecules using Newton's second law and is a numerical analysis suitable for observing the evolution of molecules.

In this study, equation (1) was used as the intermolecular force.

$$U=\sum_i\sum_{j>i} 4\varepsilon_{ij}\left[\left(\frac{\sigma_{ij}}{r_{ij}}\right)^{12}-\left(\frac{\sigma_{ij}}{r_{ij}}\right)^{6}\right]+\sum_i\sum_{j>i} k\frac{q_i q_j}{r_{ij}} \quad (1)$$

where r_{ij} is the distance between two atoms, k is the proportionality constant that defines Coulomb's potential, and q_i is the atomic charge. The first term is Leonard Jones' potential, which describes the repulsive force due to the overlapping of atoms and the attraction due to the Van der Waals interaction. The second term is the Coulomb potential representing the electrostatic interaction.

The following adams et al. equation was used to determine the charge

$$q_{Ai}=\frac{V_{id}(A_i)}{\sqrt{n_{Ai}}}\sqrt{\frac{\sum_j \frac{V_{id}(X_j)N_{Xj}}{\sqrt{n_{Xj}}}}{\sum_i \frac{V_{id}(A_i)N_{Ai}}{\sqrt{n_{Ai}}}}},\quad q_{Xi}=\frac{V_{id}(X_j)}{\sqrt{n_{Xj}}}\sqrt{\frac{\sum_i \frac{V_{id}(A_i)N_{Ai}}{\sqrt{n_{Ai}}}}{\sum_j \frac{V_{id}(X_j)N_{Xj}}{\sqrt{n_{Xj}}}}} \quad (2)$$

where A_i is the i-th cation, $X_j$the j-th anion, V_{id} the ideal charge of the element, N the number of atoms in the system, and n the principal quantum number. The result was q_{Ca}=1.1939 C, q_{Si}=2.7573 C, and q_O=-1.18425 C.

Since the Lennard-Jones potential in the first term of equation (1) is an empirical law, it is necessary to determine σ and ε based on physical principles. Therefore, equations (3) and (4) used by P.A. Bonnaud et al.

$$U_{ij}(r_{ij})=A_{ij}\exp(-b_{ij}r_{ij})-\sum_{n=3}^{5} f_{2n}(r_{ij})\frac{C_{2n}^{ij}}{r_{ij}^{2}} \tag{3}$$

$$f_{2n}(r_{ij})=1-\sum_{m=0}^{2n}\frac{(b_{ij}r_{ij})^{m}}{m!}\exp(-b_{ij}r_{ij}) \tag{4}$$

This is a quantum chemical calculation model, and when applied to the Tobermorite structure, the parameters are as shown in the table.3

Table 3 Parameters of the Tobermrite model according to the PN-TrAZ model

i	j	C_6[Ha. a_0^6]	C_8[Ha. a_0^8]	C_{10}[Ha. a_0^{10}]	A[Ha]	b[a_0^{-1}]
Ca	O_w	17.9006	343.0666	11191.4996	495.3671	2.2146
Si	O_w	10.0686	145.3636	4673.8324	1235.5866	2.2235
O	O_w	35.5305	603.071	20553.6465	618.3243	2.1309
Ca	H_w	3.906	75.5199	2210.7227	36.4076	2.2344
Si	H_w	2.4156	31.445	964.788	90.8109	2.2435
O	H_w	8.4253	133.4797	4167.9202	45.4445	2.1493

By setting σ and ε in table.4 as shown in the table, the first terms in Eqs. (3), (4) and (1) draw very similar potential functions as shown in the graph, so we use these σ and ε.

Table 4 PN-TrAZ parameters approximated to the Lennard-Jones potential, σ and ε

i	j	σ_{ij} (Å)	ε_{ij} (Kcal/mole)
Ca	O_w	3.211577733	0.0993886
Si	O_w	3.844182653	0.01794068
O	O_w	2.66	0.1272912
Ca	H_w	2.65	0.0675658
Si	H_w	3.3979572	0.00959296
O	H_w	3.27333	0.163726

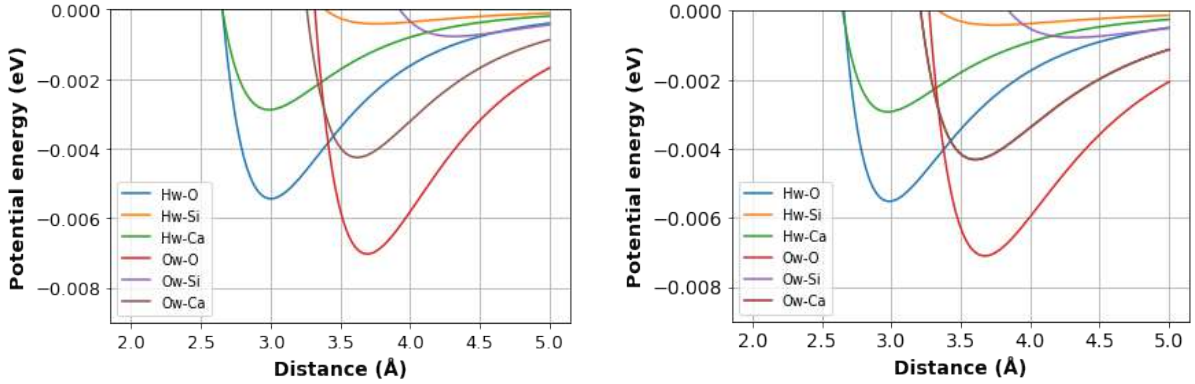
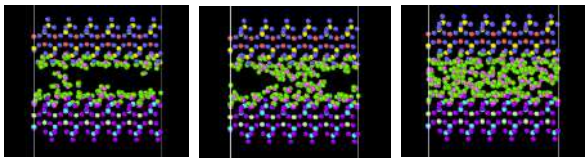


Figure 2 Potential functions of the PN-TrAZ model (a) and the Lennard-Jones potential (b)

3.Result

When the interlayer distance H was set to 10 Å and the temperature of water molecules T was set to 300 K, the number density of water molecules was increased and the movement of water inside the interlayer was examined. At a certain water molecule number density, water columns were formed that were connected to the top and bottom walls. This is caused by the strong intermolecular force between water molecules, which generates pressure in the direction of cohesion.



(a) (b) (c)

Figure 3 Formation of water column

(Number density (a)0.0181, (b)0.0217, (c)0.0301/m^3)

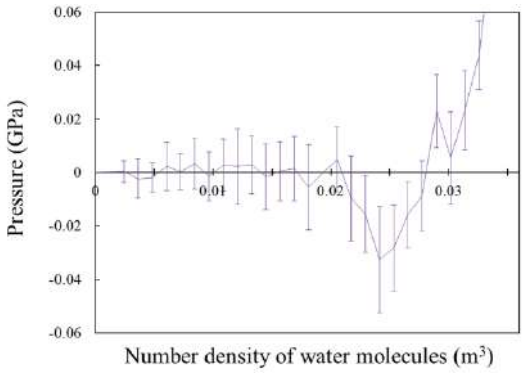
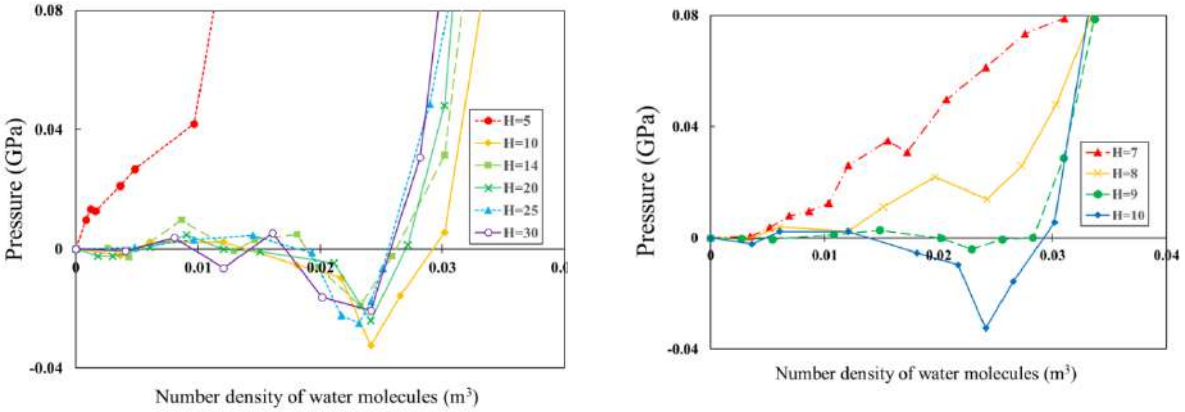


Figure 4 Pressure in the direction of expansion

When the interlayer distance H is varied from 5~30Å, a graph like the one shown in the figure is drawn For interlayer distances greater than H=9Å, pressure in the direction of cohesion is generated, but for interlayer distances less than 9Å, pressure in the direction of cohesion is not generated. This is because a small interlayer distance leaves no space for a water column to form.



(a) **(b)**

Figure 5 Interlayer distance and pressure (a) 5~30Å (b) around 9Å

4.Result

The following was clarified

1)Water molecules are adsorbed on the C-S-H wall, and as the number density of water molecules are increased, a column of water is generated to link the upper and lower C-S-H, which generates pressure in the direction of cohesion. As the number density of water molecules is further increased and the interlayer space is filled, the pressure is transferred to the direction of expansion.

2) In the Tinf_14sc model, water columns in the C-S-H interlayer are formed at interlayer distances of 9 Å or greater, generating pressure in the direction of cohesion.

Acknowledgements

We are grateful to Mr. Hiroaki Hara for his programming advice in conducting this study.

References

P.A Bonnaud, Q.Ji, B Coasne ,R.J-M.Pellenq, and K.J.Van Vliet : Thermodynamics of Water Confined in Porous Calcium-Silicate-Hydrates, Langmuir 2012, volume 28, issue 31, pages 11422–11432, June.2012

Stefan Adams, R.Prasada Rao:High power lithium ion battery materials by computational design, physica status solidi applications and materials science, volume 208, issue 8,pages 1746-1753, August.2011

Ian G. Richardson: Model structures for C(A)-S-H(I), Acta Crystallographica Section B, B70, pp903-923, Dec.2014

The 16th International Congress on the Chemistry of Cement 2023 (ICCC2023)
"Further Reduction of CO_2 -Emissions and Circularity in the Cement and Concrete Industry"
September 18–22, 2023, Bangkok, Thailand

Investigation of Selective Dissolution Method for Separation of Ferrite Phase in Cement and Characterization

T. Mizuno[1*], T. Hayakawa[2]

[1] *Japan Cement Association, Toshima, Kita-ku, Tokyo, Japan*
Email: tetsunari-mizuno@jcassoc.or.jp
[2] *Japan Cement Association, Toshima, Kita-ku, Tokyo, Japan*
Email: tomoyuki-hayakawa@jcassoc.or.jp

ABSTRACT

Cement industry is known as energy-intensive industry. The energy efficiency of cement industry of Japan is one of the highest levels in the world. However, it is expected that further energy conservation will be required to reduce the amount of CO_2 emissions in the future. In cement manufacturing process, reduction of the clinker burning temperature is one of the ways to reduce energy consumption. As the way related to the sintering reaction of clinker, even though it is known to increase the amounts of liquid phases, especially ferrite phase, it has not been considered about a role of the ferrite phase for the strength of hardened cement. We focused on ferrite phase in this study because from now on when the liquid phases are increased, ferrite phase will need to play an important role, too.
The selective dissolution method, which utilizes the difference in solubility of substances in acids or alkalis, is known in order to separate or extract each clinker phases from cement. Various methods have been proposed for each target substances. Even though there is the method with combination of salicylic acid-methanol solution and acetic acid aqueous solution as one of methods for separation of ferrite phase, the method is not enough to get a lot of samples of ferrite phase fast. Therefore, we investigated the selective dissolution methods with acetic acid or formic acid to separate ferrite phase.
Also, it is known that lattice parameter of unit cell of ferrite phase is changed by molar ratio of aluminum and iron. We performed powder X-ray diffraction measurement and calculated lattice parameter using samples of ferrite phase separated by the investigated selective dissolution method from several cements. In addition, we analyzed chemical composition of the samples and investigated the relationship of Al/Fe ratio and lattice parameter.

KEYWORDS: *ferrite phase, selective dissolution, lattice parameter*

1. Introduction

The selective dissolution method, which utilizes the difference in solubility of substances in acids or alkalis, is known in order to separate or extract each clinker phases from cement. There is the method with combination of salicylic acid-methanol solution and acetic acid aqueous solution as one of methods for separation of ferrite phase (Yamaguchi and Takagi (1968)). However, it is not well-known selective dissolution method for separating ferrite phase in one-step. We investigated the selective dissolution methods with acetic acid or formic acid to directly separate ferrite phase from cement. Also, it is known that lattice parameter of unit cell of ferrite phase is changed by molar ratio of aluminum and iron. We analyzed chemical composition of the separated ferrite phase and investigated the relationship of Al/Fe ratio and lattice parameter.

2. Experiment

2.1 Samples

Eight kinds of cement were used. All cements do not contain any blending materials. The chemical

composition of cements is shown in Table 1. The symbols in the table are as follows; N is ordinary Portland cement, H is high early strength Portland cement, M is moderate heat Portland cement, L is low heat Portland cement.

Table 1 Chemical composition of cements

	Ig.loss	Insol.	SiO_2	Al_2O_3	Fe_2O_3	CaO	MgO	SO_3	Na_2O	K_2O	TiO_2	P_2O_5	MnO
N1	0.71	0.08	20.89	5.44	2.94	65.11	1.54	2.08	0.27	0.53	0.26	0.14	0.05
N2	0.97	0.08	21.41	4.84	3.20	65.01	1.08	2.02	0.33	0.43	0.24	0.18	0.10
H1	1.63	0.06	20.32	4.72	3.02	65.33	0.78	2.97	0.24	0.34	0.26	0.10	0.06
H2	1.12	0.07	20.32	5.04	2.79	65.29	0.87	2.88	0.27	0.34	0.33	0.24	0.13
M1	0.55	0.06	23.26	3.73	4.42	63.29	1.25	2.06	0.30	0.38	0.20	0.16	0.16
M2	0.50	0.05	23.95	3.70	3.64	63.72	1.27	2.21	0.18	0.34	0.18	0.07	0.08
L1	0.86	0.05	25.71	3.07	3.50	62.01	0.85	2.70	0.34	0.33	0.20	0.22	0.16
L2	0.60	0.06	26.44	2.65	3.14	63.43	0.70	2.35	0.16	0.32	0.14	0.09	0.14

2.2 Examination of conditions for selective dissolution

A method for separation of ferrite phase from cement by using acetic acid aqueous solution or formic acid aqueous solution was investigated. Cement samples were added to acetic acid aqueous solution or formic acid aqueous solution, and stirred with a magnetic stirrer for predetermined time. After that, residue and solvent were separated by suction filtration. The residue was washed with ethanol and then dried in oven at 105°C. The crystalline phase of dried residue was identified by powder X-ray diffraction measurement. In this examination, ordinary Portland cement (N1) was used, and concentration of acid, amount of solvent and dissolution time were varied.

2.3 Calculation of lattice parameter

Equation (1) was used to calculate the lattice parameter. Since ferrite phase is orthorhombic system, three Miller index of (2 0 0), (2 0 2) and (0 8 0) were used for the calculation. The values of interplanar spacing were calculated from Bragg's equation.

$$\frac{1}{d^2} = \frac{h^2}{a^2} + \frac{k^2}{b^2} + \frac{l^2}{c^2} \quad (1)$$

2.4 Chemical analysis of cement

The residue obtained by dissolved cements with formic acid aqueous solution was dissolved using (1+1) hydrochloric acid. The solution was transferred to 250 mL volumetric flask and made up to the mark with water to prepare sample solution. Aluminum and Iron in the sample solution were measured by the standard addition method with inductively coupled plasma optical emission spectrophotometry.

3. Results and discussion

3.1 Examination of conditions for selective dissolution

Table 2 shows the amounts of residue of the cement (N1) dissolved in acetic acid aqueous solution with varying concentrations and dissolution times. The amount of solvent was 100 mL per 1 g of sample. Figure 1 shows the powder X-ray diffraction pattern of the residue dissolved for 15 minutes. The peak of aluminate phase was observed in the residue dissolved in 0.5mol/L acetic acid. In the residue dissolved in 1 mol/L acetic acid for 15 minutes, no peaks other than the ferrite phase were observed. However, a halo pattern was observed around 20 to 30 degrees. This was thought to be caused by precipitation of silicate in cement. Table 3 shows the amounts of residue of the cement (N1) dissolved in formic acid aqueous solution with varying concentrations and dissolution times. The amount of solvent was varied 100 to 200 mL per 0.5 g of sample. Figure 2 shows the powder X-ray diffraction pattern of the residue dissolved for 10 minutes. When dissolved with 0.25 v/v% formic acid aqueous solution, peaks of clinker phases other than ferrite phase were also observed. When dissolved with 0.5 v/v%, the peak of the aluminate phase was observed at 100 mL of solvent for 0.5 g of sample. When the amount of solvent for 0.5 g of sample was 150 mL or 200 mL, no peaks other than the ferrite phase were observed after dissolving for 10 minutes or more. In addition, the halo pattern, which was seen in the residue dissolved with acetic acid aqueous solution, could not be

confirmed, and it is considered that the precipitation of silicate is small. On the other hand, there is a tendency that the higher concentration of the formic acid and the longer dissolution time, the less residue. Therefore, it is thought that part of the ferrite phase is also dissolved.

Table 2 Amounts of residue dissolved cements with acetic acid aqueous solution (%)

Concentration of acid	Dissolution time		
	5min.	10min.	15min.
0.5mol/L	21.3	17.9	16.5
1mol/L	13.3	11.9	11.1

Table 3 Amounts of residue dissolved cements with formic acid aqueous solution (%)

Concentration of acid	Solvent for 0.5g of sample	Dissolution time		
		5min.	10min.	15min.
0.25%	100mL	—	50.5	—
0.5%	100mL	14.8	11.4	12.2
0.5%	150mL	7.5	5.2	—
0.5%	200mL	7.6	4.8	2.8
1%	200mL	5.9	3.6	—

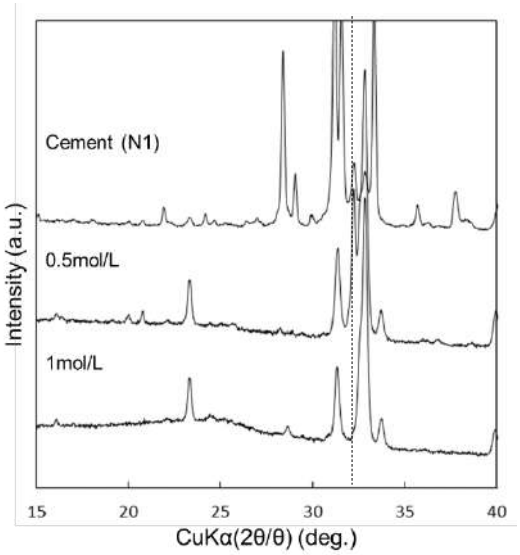


Figure 1 X-ray diffraction pattern of samples dissolved 15min. in acetic acid aqueous solution

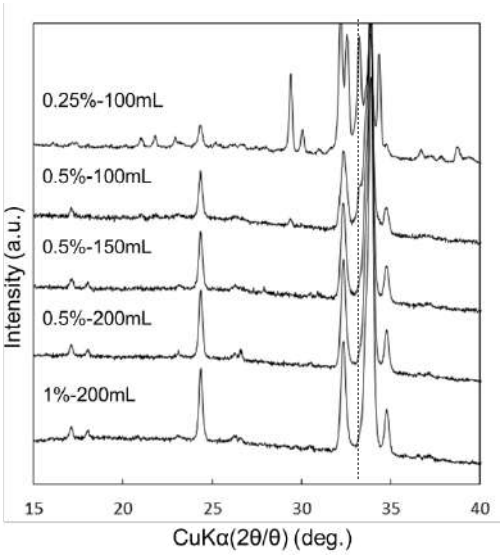


Figure 2 X-ray diffraction pattern of samples dissolved 10min. in formic acid aqueous solution

3.2 Separation of ferrite phase dissolved by formic acid solution

Table 4 shows the results of cements dissolved with formic acid aqueous solution. This treatment was carried out twice in order to confirm the repeatability. Considering the results in 3.1, the dissolution conditions with formic acid aqueous solution were determined as follows. Concentration of formic acid is 0.5 v/v%, amount of solvent is 300 mL, sample weight is 1 g, and dissolution time is 10 minutes.

Table 4 Residue dissolved by formic acid aqueous solution

Sample	N1	N2	H1	H2	M1	M2	L1	L2
1	5.1	5.8	6.6	8.2	6.6	9.7	5.6	4.7
2	5.3	6.7	6.8	8.2	6.8	9.5	5.7	5.5
Ave.	5.2	6.3	6.7	8.2	6.7	9.6	5.7	5.1

3.3 Lattice parameter and Al/Fe molar ratio of extracted ferrite phase

Table 5 shows the calculated lattice parameter of the extracted ferrite phases. In addition, Table 6 shows the lattice parameter of ferrite phases with different ratios of Al and Fe in previous reports (Taylor (1997)). Table 7 shows the result of chemical analysis of extracted ferrite phase (Al_2O_3 and Fe_2O_3) and calculated Al/Fe molar ratio. Figure 3 shows the relationship between lattice parameter of the extracted ferrite phase and the Al/Fe molar ratio. Lattice parameter tends to decrease as the Al/Fe molar ratio of ferrite phase

increases. This is same tendency with previous reports. However, there is a difference in the rate of change, especially on the b-axis. As one of the reasons, it is thought to be that ferrite phase is solid solution containing other elements (Yamaguchi and Takagi (1968)) rather than pure C_4AF synthesized using reagents.

Table 5 Lattice parameter of extracted ferrite phases

Sample	Lattice parameter (Å)		
	a	b	c
N1	5.531	14.559	5.323
N2	5.545	14.563	5.336
H1	5.544	14.582	5.340
H2	5.537	14.563	5.342
M1	5.555	14.573	5.341
M2	5.555	14.548	5.335
L1	5.555	14.570	5.345
L2	5.556	14.588	5.351

Table 6 Lattice parameter of ferrite phases in $Ca_2(Al_xFe_{1-x})_2O_5$ series

x	Lattice parameter (Å)		
	a	b	c
0	5.5980	14.7687	5.4253
0.285	5.588	14.61	5.380
0.36	5.583	14.58	5.374
0.50	5.5672	14.521	5.349

Table 7 Content of Al_2O_3 and Fe_2O_3 in extracted ferrite phase and Al/Fe molar ratio

Sample	N1	N2	H1	H2	M1	M2	L1	L2
Al_2O_3 (%)	16.1	15.0	14.0	13.1	13.7	17.9	11.2	12.0
Fe_2O_3 (%)	17.0	19.8	17.7	16.2	23.7	23.3	23.6	22.0
Al/Fe (molar ratio)	1.49	1.19	1.24	1.27	0.91	1.20	0.75	0.85

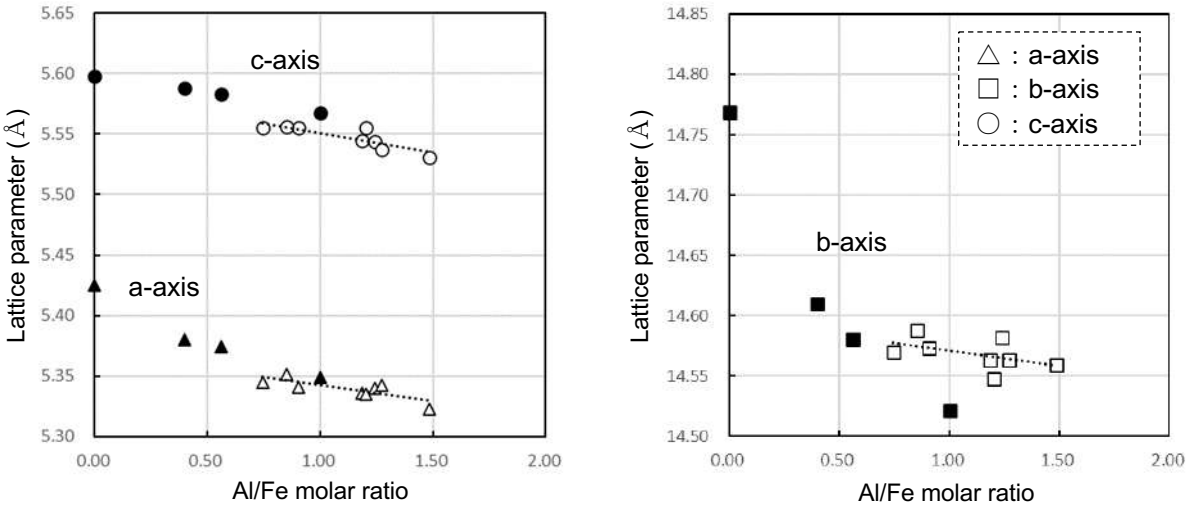


Figure 3 Relationship between Al/Fe molar ratio and lattice parameter of extracted ferrite phase (Black symbols are previously reported value shown in Table 6)

4. Conclusion

(1) When the cement samples are dissolved with formic acid aqueous solution, almost only the ferrite phase can be extracted more quickly and easily than the other methods.

(2) As the result from the investigation of the relationship between the lattice parameter and the Al/Fe molar ratio of extracted ferrite phase, the change of a-axis and c-axis of the lattice parameters for the Al/Fe ratio were the same tendency as the previous report of synthesized ferrite phase but the change of the b-axis was different tendency in the case of the ferrite phases extracted from actual cements.

References

Yamaguchi. G. and Takagi. S. (1968) "The Analysis of Portland Cement Clinker", Proceedings of the Fifth International Symposium of the Chemistry of Cement, Vol.1.: 181-225

Taylor, H.F.W (1997) *CEMENT CHEMISTRY 2nd edition*, Thomas Telford Ltd.: 24-28

The 16th International Congress on the Chemistry of Cement 2023 (ICCC2023)
"Further Reduction of CO_2 -Emissions and Circularity in the Cement and Concrete Industry"
September 18–22, 2023, Bangkok, Thailand

A comparative study of tribometer rotor configurations and analytical methods for concrete pumping pressure prediction

Fumin Li[1, 2, 3, a], Qiang Yuan[4, b], Caijun Shi[1, 2, 3, c*]

[1]*College of Civil Engineering, Hunan University, Changsha 410082, China*

[2]*Key Laboratory for Green & Advanced Civil Engineering Materials and Application Technologies of Hunan Province, Changsha 410082, China*

[3]*International Innovation Center for Green & Advanced Civil Engineering Materials of Hunan Province, Changsha 410082, China*

[4]*School of Civil Engineering, National Engineering Research Center of High-Speed Railway Construction, Central South University, Changsha 410075, China*

[a]*lifumin@hnu.edu.cn*

[b]*yuanqiang@csu.edu.cn*

[c]*cshi@hnu.edu.cn*

ABSTRACT

Pumping of highly flowable concrete (HFC) is a vital construction technique. Tribometers have been designed to provide rheological data for pumpability assessments. Meanwhile, various analytical methods are claimed to have sound accuracy in predicting the pumping pressure loss for concrete. Naturally, curiosities are aroused in which combination of analytical method and measuring apparatus predicts pumpability result that better agrees with the actual flow behavior for highly flowable concrete. To examine this issue, a total of 60 HFC mixtures are pumped at constant flow rates in a 280-meter-long pipeline. Test results reveal that tribometer and rheometer with cone-shape rotor produce pressure prediction results that are almost 6 times more accurate than those with cylindrical-shape rotor. Both assuming constant rheological properties, Kaplan method is more accurate than Kwon method when using results by the cone-shape rotor, but less accurate when using results by the cylindrical-shape rotor.

KEYWORDS: *Highly flowable concrete (HFC); pumping pressure prediction; tribometer; pumpability*

1. Introduction

Sound pumping pressure loss prediction has been a crucial parameter to ensure the successful pumping of concrete. Among many prediction methods, Kaplan method and Kwon method are two commonly cited ones and both of them requires lubrication layer properties as inputs (Kaplan et al., 2005; Kwon et al., 2013b). On the one hand, the applicability and accuracy of both methods need to be studied and compared against a long-distance pumping setup, which has become increasingly popular in the construction industry. On the other hand, the answer to what kind of tribometer rotor configuration can provide reliable lubrication layer inputs for each method is also pending. Cone-shape rotor (Feys et al., 2014) and cylindrical-shape rotor (Ngo et al., 2010) are two common tribometer rotors. The latter was initially designed for traditional concrete. Therefore, it is important to compare the accuracy of each type of rotor against the nowadays widely used highly flowable concrete, which has different mixture composition and rheological characteristics comparing to the traditional concrete. Besides, it is also important to study the compatibility of each tribometer with different prediction method.

To answer questions above, this study conducted a horizontal pumping test with a 280-meter-long pipeline with 60 HFC mixtures. The pumping flow rate ranged from 4 to 16 L/s. Rheological testing results and comparisons between the measured pressure loss and calculated pressure losses by Kaplan and Kwon methods are presented and discussed.

2. Experimental program

2.1 Materials and mixture proportions

60 highly flowable concrete mixtures were used. Portland cement (P.O. 42.5) that meet the Chinese Standard GB 175-2007 were used. Class C fly ash (CFA), ground granulated blast furnace slag (GGBS), and silica fume were used as the supplementary materials. Well-graded siliceous river sand (0-4.75 mm with a fineness modulus of 2.8) and crushed limestone (5-20 mm) were employed as fine and coarse aggregates, respectively, to produce the concrete. The chemical and physical properties of the cementitious materials used in this study are listed in Table 1. A polycarboxylate high-range water-reducing agent (HRWRA), with a solid content of 19.3%, was used in the concrete mixtures with different strength grades. Mixture proportions are shown in Table 2.

Table 1 Chemical and physical properties of the binders

	P.O. 425	CFA	GGBS	Silica fume		P.O. 425	CFA	GGBS	Silica fume
Density, kg/m^3	3020	2170	2910	2210	Blaine fineness, m^2/kg	333	363	394	-
SiO_2, %	20.94	49.93	32.34	98.48					
Al_2O_3, %	5.09	21.53	14.05	-	SO_3, %	2.66	0.93	2.85	-
Fe_3O_4, %	3.48	3.97	0.4	-	LOI, %	4.08	5.18	0	-
CaO, %	60.53	15.46	40.16	-	C_3S, %	55.1	-	-	-
MgO, %	2.54	1.14	8.44	-	C_2S, %	11.94	-	-	-
K_2O, %	0.64	1.07	0.4	-	C_3A, %	2.08	-	-	-
Na_2O, %	0.06	0.2	0.39	-	C_4AF, %	10.81	-	-	-

Table 2 Concrete mixture design (kg/m^3)

Sample	Cement	CFA	GGBS	Silica fume	Water	w/cm Ratio	Sand	Aggregate	HRWRA
1	399.33	90.17	80.08	30.00	124.42	0.21	829.08	897.08	11.50
2	399.33	90.08	80.00	30.00	144.33	0.24	808.50	894.58	12.25
3	403.08	89.92	79.75	30.00	140.50	0.23	807.83	894.33	12.25
4	238.00	70.08	60.00	-	147.25	0.40	908.50	958.50	5.30
5	237.17	69.42	59.58	-	160.25	0.44	888.25	959.67	4.06
6	388.42	76.67	107.50	-	146.92	0.26	780.08	1142.33	6.97
7	237.17	110.42	69.58	-	183.00	0.44	928.42	878.58	6.49
8	422.67	95.33	82.92	30.00	141.25	0.22	767.00	998.83	13.87
9	400.67	89.50	79.42	30.00	138.92	0.23	780.17	928.67	12.60
10	408.33	93.33	79.75	30.00	160.25	0.26	736.25	971.67	12.09
11	400.17	90.42	79.83	30.00	138.50	0.23	706.75	998.75	12.14
12	400.67	90.50	79.58	30.00	129.67	0.22	780.83	928.08	12.00
13	353.92	67.58	96.58	-	133.00	0.26	700.50	1015.42	7.33

2.2 Experiment setups

A pipeline with length of 280 meters was used for the horizontal pumping campaign. The pipelines consist of straight pipes with radii of 125 mm and 150 mm and 90° bends with curvature radii of 0.5 meters and 1 meter. Pressure sensors with a capacity of 0-60 MPa and a measurement accuracy of 0.05% were used in each of the three pipelines. Pressure sensors were fixed on the pipe by placing them in the steel cylindrical supports welded on the pump pipe. After approximately 1.5 times the volume of the pipeline of concrete was discharged, pumped concrete was sampled at the tail of the pipeline (see Table 3).

Table 3 Flow rate of each mixture

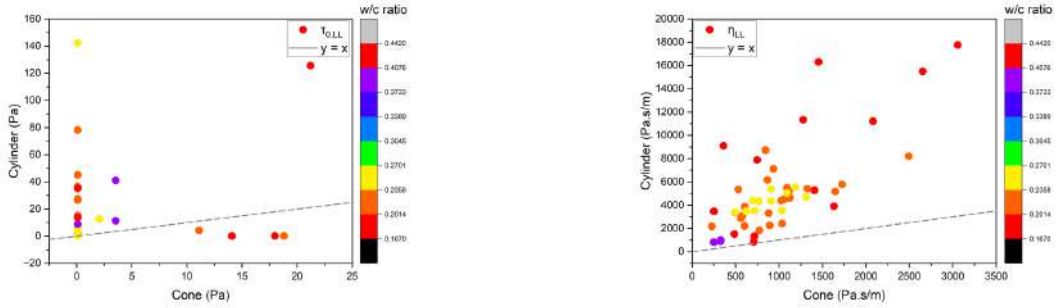
Sample	**Q (L/s)**	**Sample**	**Q (L/s)**	**Sample**	**Q (L/s)**	**Sample**	**Q (L/s)**	**Sample**	**Q (L/s)**	**Sample**	**Q (L/s)**
1-1	4.46	**3-3**	9.37	**5-2**	8.74	**7-4**	13.51	**9-5**	12.26	**11-5**	12.94
1-2	8.35	**3-4**	12.12	**5-3**	9.63	**7-5**	15.74	**10-1**	3.22	**12-1**	2.73
1-3	13.19	**4-1**	5.80	**5-4**	14.04	**8-1**	3.40	**10-2**	5.16	**12-2**	4.97
2-1	4.69	**4-2**	7.01	**6-1**	4.39	**8-2**	5.89	**10-3**	7.08	**12-3**	8.88
2-2	5.82	**4-3**	9.12	**6-2**	6.93	**8-3**	8.51	**10-4**	8.82	**12-4**	11.07
2-3	8.27	**4-4**	11.83	**6-3**	8.31	**8-4**	12.45	**10-5**	10.82	**13-1**	3.80
2-4	8.50	**4-5**	13.28	**6-4**	9.01	**9-1**	3.80	**11-1**	3.14	**13-2**	5.17
2-5	10.98	**4-6**	17.00	**7-1**	4.31	**9-2**	5.31	**11-2**	6.17	**13-3**	7.62
3-1	3.29	**4-7**	18.20	**7-2**	6.71	**9-3**	7.64	**11-3**	8.91	**13-4**	8.87

3-2	7.72	**5-1**	5.50	**7-3**	10.57	**9-4**	10.41	**11-4**	11.25	**13-5**	11.05

Concrete bulk properties were tested by an ICAR concrete rheometer and lubrication layer properties were tested by two tribometers with different rotors. The testing sequence included a 30-s pre-shearing period at 0.5 rev/s, followed by the decrease of the rotational speed from 0.5 to 0.03 rev/s in six steps. The Bingham model (Tattersall & Banfill, 1983) parameters of mixtures were determined by Reiner-Riwlin equations to estimate the applied maximum shear rate during pumping. The cone-shape tribometer rotor has the same configuration as described by Feys et al. (2014), and the cylindrical-shape tribometer has the same configuration as described by Kwon et al. (2013). Lubrication layer properties were determined according to Feys et al. (2014) and Kwon et al. (2013).

3. Results and discussion

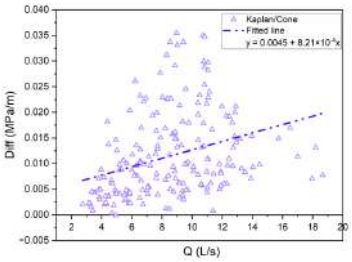
Two pumping pressure loss prediction methods were used. The first equation adopted is Kaplan method (Kaplan et al., 2005) and the second equation adopted is Kwon method (Kwon et al., 2013b).
Test results by two triometers are shown in Figure 1. For the yield stress of the lubrication layer (Figure 1-a), generally, tribometer with the cylindrical-shape rotor offered higher results, especially when the w/c ratio of the material is high. For the viscous constant of the lubrication layer (Figure 1-b), all results by the cylindrical-shape rotor are higher than those by the cone-shape rotor. The difference tend to be more pronounced when the material has low w/c ratio. Averagely, the yield stress and the viscous constant by the cylindrical-shape rotor is 4.63 and 4.30 times larger than that by the cone-shape rotor, respectively. The shape of rotor is indeed influential to rheological properties.



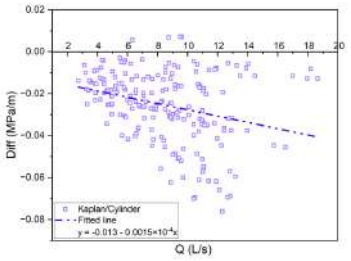
(a) yield stress (b) viscous constant

Figure 1 Comparison between the tested lubrication layer properties by the cone-shape tribometer (x-axis) and the cylindrical-shape tribometer (y-axis). Color of each point represents its corresponding w/c ratio.

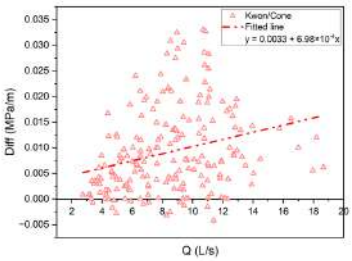
Differences in the tested rhological property introduced large distinctions when predicting concrete pumping pressure loss (Figure 2). Using lubrication layer properties by cone-shape rotor tribometer, Kaplan method and Kwon method missed the actual pressure loss by 0.0092 MPa/m and 0.0278 MPa/m, respectively. Figure 2-a and 2-c show that although Kwon method has smaller error range, Kaplan method has higher accuracy rate. Similarly, using lubrication layer properties by cylindrical-shape rotor tribometer, Kaplan method and Kwon method missed the actual pressure loss by 0.0874 MPa/m and 0.0624 MPa/m, respectively. Therefore, the cylindrical rotor tribometer is more compatible with Kwon method, and the the cone-shape rotor tribometer is more compatible with Kaplan method. Overall, the combination of Kaplan method and cone-shaped tribometer has the highest accuracy among all four combinations. It is also worthnoting that in all four cases, higher pumping flow rate caused lower accuracy in pressure prediction. This could be a result due to the pumping-induced concrete property change (Li et al., 2022).



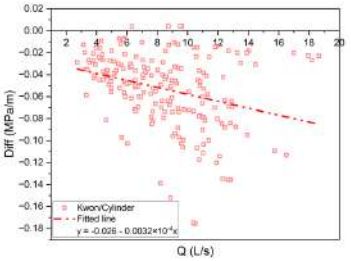
(a) Kaplan method and cone-shape rotor



(b) Kaplan method and cylinder-shape rotor



(c) Kwon method and cone-shape rotor



(d) Kwon method and cylinder-shape rotor

Figure 2 Difference between actual and calculated concrete pressure vs. the pumping flow rate

4. Conclusions

Concrete tribometer can assess properties of lubrication layer and the yield stress and viscous constant are two main parameters produced by tribometer. The shape of tribometer rotor has a profound influence on the measurement of parameters. The yield stress and the viscous constant by the cylindrical-shape rotor is averagely 4.63 and 4.30 times larger than that by the cone-shape rotor, respectively.

Two popular prediction methods are evaluated against the experimental result. Generally, Kaplan method is more accurate than Kwon method. The combination of Kaplan method and inputs by cone-shape tribometer rotor predicts the most accurate pressure loss, among all four combinations studied. Comparing to the cone-shape rotor, Kwon method is more compatible with cylinder-shape rotor, but Kaplan method is more compatible with cone-shape rotor comparing to the cylindrical-shape rotor.

Acknowledgements

The presented work was financially supported by the National Key R&D Program of China (2017YFB0310100) and the National Natural Science Foundation of China (51778629 and 51922109).

References

Feys, D., Khayat, K. H., Perez-Schell, A., & Khatib, R. (2014). Development of a tribometer to characterize lubrication layer properties of self-consolidating concrete. *Cement and Concrete Composites*, 54, 40–52.

Kaplan, D., de Larrard, F., & Sedran, T. (2005). Design of concrete pumping circuit. *ACI Materials Journal*, 102(2), 110–117.

Kwon, S. H., Park, C. K., Jeong, J. H., Jo, S. D., & Lee, S. H. (2013a). Prediction of concrete pumping: Part i-development of new tribometer for analysis of lubricating layer. *ACI Materials Journal*, 110(6), 647–655.

Kwon, S. H., Park, C. K., Jeong, J. H., Jo, S. D., & Lee, S. H. (2013b). Prediction of concrete pumping: Part II-analytical prediction and experimental verification. *ACI Materials Journal*, 110(6), 657–667.

Li, F., Shen, W., Yuan, Q., Hu, X., Li, Z., & Shi, C. (2022). An overview on the effect of pumping on concrete properties. *Cement and Concrete Composites*, 129(May), 104501.

Ngo, T. T., Kadri, E. H., Bennacer, R., & Cussigh, F. (2010). Use of tribometer to estimate interface friction and concrete boundary layer composition during the fluid concrete pumping. *Construction and Building Materials*, 24(7), 1253–1261.

Tattersall, H., & Banfill, G. (1983). *The rheology of fresh concrete*, Research report.

The 16th International Congress on the Chemistry of Cement 2023 (ICCC2023)
"Further Reduction of CO_2 -Emissions and Circularity in the Cement and Concrete Industry"
September 18–22, 2023, Bangkok, Thailand

Microstructural analysis of the effect of clinker phase distribution on cement hydration using computer-based approaches

S.-Y. Chung[1*], S.-E. Oh[2] and S.-S. Jo[3]

[1] *Department of Civil and Environmental Engineering, Yonsei University, Seoul, South Korea*

Email: sychung@yonsei.ac.kr

[2] *Department of Civil and Environmental Engineering, Sejong University, Seoul, South Korea*
Email: ohseoeun21418@sju.ac.kr

[3] *Department of Civil and Environmental Engineering, Sejong University, Seoul, South Korea*
Email: susung1996@sju.ac.kr

ABSTRACT

This study aims to investigate the effect of clinker phase distribution on cement hydration. In particular, the different spatial distributions of clinker phases were modeled and compared to examine their impact on cement hydration. For this purpose, a model for generating virtual cement specimens was proposed using only very limited information, such as sample images and chemical composition. To control the spatial distribution of clinker phases, e.g., clustering degree of cement particles, the cement particles with different sizes were firstly modeled based on the experimental data, and phase clustering of the main components, such as C_3S, C_2S, C_3A, and $C4_AF$, was controlled according to the chemical composition and quantitative information obtained from the sample SEM image. The obtained results confirmed that the spatial distributions of the clinker phases significantly affect the cement hydration, even in the conditions that the materials have the same phase volume fraction.

KEYWORDS: *Cement hydration, Microstructure, Reconstruction, Phase distribution, Simulation*

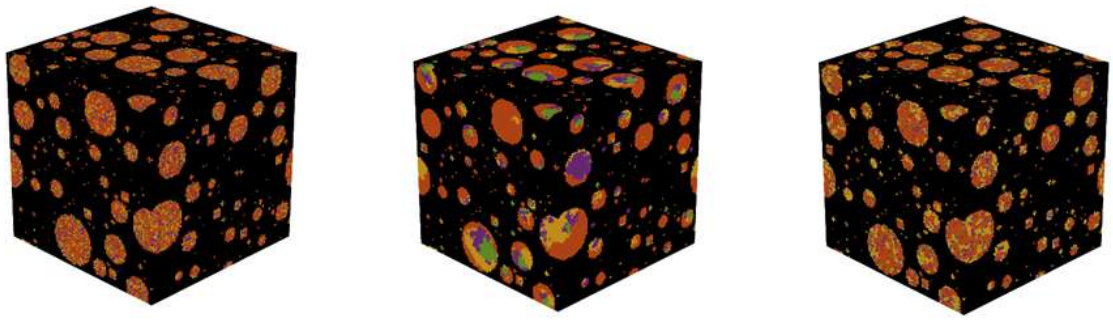
Introduction

Microstructural characteristics of cement-based composites are crucial in determining the mechanical properties of the materials. For a better understanding of the behavior of cementitious materials, microstructural characterization, and reconstruction methods, coupled with modeling and simulation, have been issued in the field of computational modeling of cement paste. For instance, microstructural imaging techniques such as a scanning electron microscope (SEM) image and its probabilistic description have been widely used to generate multi-phase microstructure. However, because of the complexity and limitations of the current approaches, it is highly desirable to develop a new method to model cement particles effectively.

This study aims to propose a model for generating a virtual pre-hydrated specimen of cement paste using only limited information, such as chemical composition and particle size distribution. In particular, the influences of the particle distribution and clustering degree of cement particles on the hydration process were investigated using computational simulation. For this purpose, the cement particles with different sizes were modeled based on the experimental data, and phase clustering of the main components, such as C_3S, C_2S, C_3A, and C_4AF, was controlled according to the chemical composition and quantitative information of several types of cement. Using the probabilistic description methods, the degree of phase clustering can be adjusted, and the virtual pre-hydrated cement microstructures with different phase distributions can be generated. The results of hydration for 28 days of each microstructure were obtained from a numerical approach using CEMHYD3D and then compared with the experimental data of a target cement.

Modeling Approach

To generate efficient cement particle virtual specimens using only limited information such as particle size distribution and chemical composition information measured from real cement, cement particles were arranged according to their particle size distribution within a microscale three-dimensional virtual microstructure. The phases were distributed by adjusting the degree of clustering of major cement components such as C_3S, C_2S, C_3A, and C_4AF in each particle, and the virtual cement particles were reconstructed to reflect the phase distribution state of real cement obtained from SEM images using CCFs (Co-occurrence Correlation Functions), one of the probability distribution functions that can express the phase distribution state in the form of a probability distribution. To compare the hydration reaction results according to the degree of clustering, three-dimensional virtual cement particles were modeled to have different degrees of clustering, considering the case of randomly distributed phases, the case of random clustering without reconstruction, and the case of clustering through reconstruction, as shown in Figure 1.



(a) Random (b) Clustered model (c) Reconstructed model

Figure 1. 3D virtual specimens with different degrees of clustering of clinker phases

Hydration results

To analyze the effect of phase distribution and particle aggregation on the cement hydration response, CEMHYD3D, a computational hydration model, was used to compare qualitative and quantitative information such as heat of hydration and hydration degree during 28 days of hydration of virtual specimens of unhydrated cement with different aggregation degrees as shown in Figure 2, and the effect of phase distribution and particle aggregation on hydration was closely analyzed through comparison with actual experimental data of the cement used for modeling the virtual specimens.

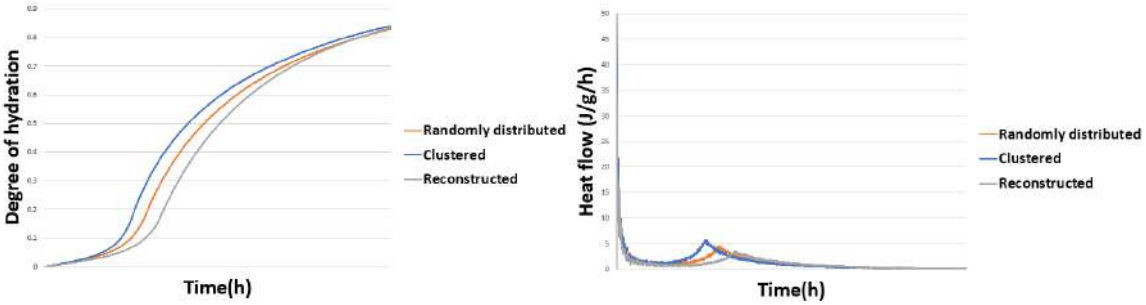


Figure 2. Degree of hydration and heat flow of the specimens at 28 days

Conclusions

The obtained results confirmed that the spatial distributions of the clinker phases significantly affect the cement hydration, even in the conditions that the materials have the same phase volume fraction. Particularly, a virtual cement specimen with relatively large clusters shows a faster hydration profile than

a material with a random distribution. In addition, it was confirmed that the surface area where the clinker phases come into contact with water is the critical factor that affects the hydration process. The results indicate that the spatial distribution of clinker phases can affect the initial cement hydration, which can affect the mechanical properties of cement paste and relevant characteristics. Therefore, it can be concluded that the investigation of microstructural characteristics during the hydration process according to the degree of clustering can provide insights for a better understanding of multi-phase cement-based materials.

Acknowledgements

This work was supported by the National Research Foundation of Korea (NRF) grant funded by the Korea government (MSIT) (No.2022R1C1C1004684).

References

Torquato, S. (2002) Random Heterogeneous Materials: Microstructure and Macroscopic Properties, Springer-Verlag.

Bostanabad, R., Zhang, Y., Li, X., Kearney, T., Brinson, L.C, Apley, W., Liu, W.K., Chen, W. (2018) "Computational microstructure characterization and reconstruction: Review of the state-of-the-art techniques", *Progress in Materials Science,* 95: 1-41

Bentz, D.P. CEMHYD3D: A Three-Dimensional Cement Hydration and Microstructure Program. I. Hydration Rate, Heat of Hydration, and Chemical Shrinkage, NISTIR 5756, U.S. Department of Commerce.

The 16th International Congress on the Chemistry of Cement 2023 (ICCC2023)
"Further Reduction of CO_2 -Emissions and Circularity in the Cement and Concrete Industry"
September 18–22, 2023, Bangkok, Thailand

Application of artificial intelligence on the reconstruction of multi-phase cement paste microstructures

Sung-Wook Hong[1*], Donghwi Eum[2], and Tong-Seok Han[3]

[1] *Yonsei University, Seoul, Republic of Korea*
Email: sw_hong@yonsei.ac.kr
[2] *Yonsei University, Seoul, Republic of Korea*
Email: dh_eum@yonsei.ac.kr
[3] *Yonsei University, Seoul, Republic of Korea*
Email: tshan@yonsei.ac.kr

ABSTRACT

In cement-based materials, phases with different properties are randomly distributed. Reconstructing virtual specimens is often challenging when evaluating material properties in simulations and supplementing experimental results. In previous studies, the two-phase (pore-solid) microstructures of cementitious materials were successfully reconstructed using stochastic optimization methods. However, due to the expensive computational cost of reconstructing microstructures using stochastic optimization methods, it is not practical to prepare virtual microstructures of cementitious materials composed of more than two phases. To accelerate the virtual specimen reconstruction of multi-phase materials, we investigated a deep neural network approach in this study. The purpose of this study is to propose a framework for reconstructing four-phase (pores, outer and inner products, and clinkers) cement paste virtual specimens. Those virtual specimens have similar phase distribution characteristics to the real microstructures. Using the generative adversarial network (GAN), four-phase virtual microstructures are reconstructed. Microstructures are segmented into four-phase based on the grayscale data of micro-CT images and are used for training the GAN model. This study demonstrates that the 3D four-phase microstructures are successfully reconstructed.

KEYWORDS: *Cement paste, Microstructure reconstruction, Deep learning, Generative adversarial networks*

1. Introduction

The cement paste can be subdivided into multiple phases according to hydration reactants and degree. In general, real experiments determining the correlation between microstructure distribution and material properties are often considered labor-intensive and time-consuming. Virtual experiments using simulation tools can save time and effort needed to develop new materials and to evaluate performance of existing materials. The purpose of this study is to reconstruct 3D cement paste microstructures composed of several phases that can be used for virtual experiments. The microstructures of cement paste composed of four-phase were reconstructed using the generative adversarial network (GAN, Zhu et al., 2017), one of the most widely accepted approach in generating images in practice. In this study, 2D cement paste microstructures were first reconstructed to increase the learning efficiency of deep learning algorithms at limited hardware performance. Then the 3D microstructure was reconstructed by filling the areas between the reconstructed 2D microstructures. The results of this study demonstrated that the microstructures that were reconstructed by the proposed approach showed similar characteristics of distribution for each phase with those of actual cement paste microstructures.

2. Microstructure datasets

In this study, the phases constituting the cement paste are classified into pore, outer product, inner product, and unhydrated cement phases as shown in Figure 1. The microstructures of cement paste were obtained from high-resolution synchrotron (Pohang accelerator laboratory, PAL) micro-CT images with the voxel size of 0.65 μm. The pore phase was separated from the solid phases using a phase separation threshold of the pore and the solid phase (Kim et al., 2020). The threshold was determined using a gray-scale distribution of the cement paste micro-CT image. A nanoindentation experiment was performed to further segment the solid phase (Hu and Li., 2015). Based on the histogram distribution of the mechanical properties of each phase obtained through nanoindentation, the solid phase was subdivided into outer product, inner product, and unhydrated cement phases. The four-phase virtual cement paste specimen was found to appropriately simulate the mechanical responses and the crack patterns (Kim et al., 2022).

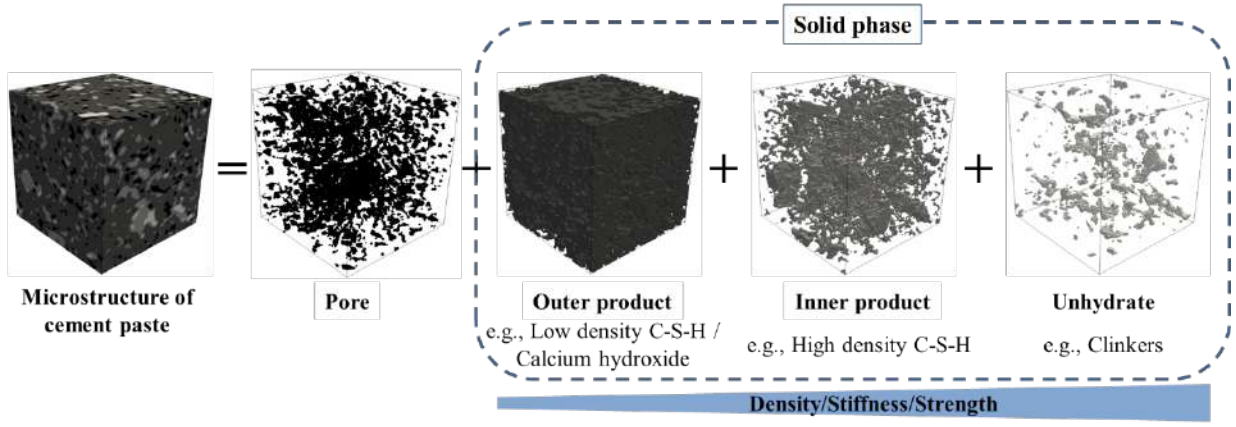


Figure 1. A cement paste microstructure divided into four phases

3. Microstructure reconstruction framework

GAN has achieved impressive results in image generation and editing. The key to the success of GAN is the concept of adversarial loss, which aims to make the generated data indistinguishable from the real data. The generator in GAN creates fake data that follows a probability distribution similar to the real data, while the discriminator learns to distinguish whether a given data is real or fake. TensorFlow-based GAN was adopted to reconstruct the 3D cement paste microstructure consisting of four phases. While GAN is highly precise in reconstructing images, the algorithm requires high computational burden, because the algorithm is comprised of the two models (i.e., a generator model and a discriminator model) and has quite a few parameters. In this study, to reduce the computational cost required for learning and reconstructing the 3D cement paste microstructure, GAN was divided into three stages as shown in Figure 2. In the first step, three 2D images (128×128) are extracted from a 3D cement paste microstructure (128×128×128) obtained from the micro-CT. As for the 2D image, the bottom, middle, and top images were selected in the height direction of the 3D microstructure. In the second step, 2D microstructural images were reconstructed using the 2D GAN for each extracted 2D microstructure image. Finally, a 3D cement paste microstructure (128x128x128) was reconstructed by filling the space between the reconstructed 2D cross-sectional images using the 2D-3D GAN. For the conversion of a 2D image to a 3D image, the 2D deconvolution layers of the generator were modified to 3D deconvolution layers. In the proposed method (Ying et al., 2019), the 2D convolution layer was first applied to a 2D image to produce a flattened 1D vector, which was then passed through a fully connected layer. Subsequently, the resulting output was reshaped into a 3D image form to connect the 2D convolution layer and 3D deconvolution layer. For the 2D GAN, 491,500 different 2D microstructural images were used for training, and 3,200 different 3D microstructural images were used for training the 2D-3D GAN.

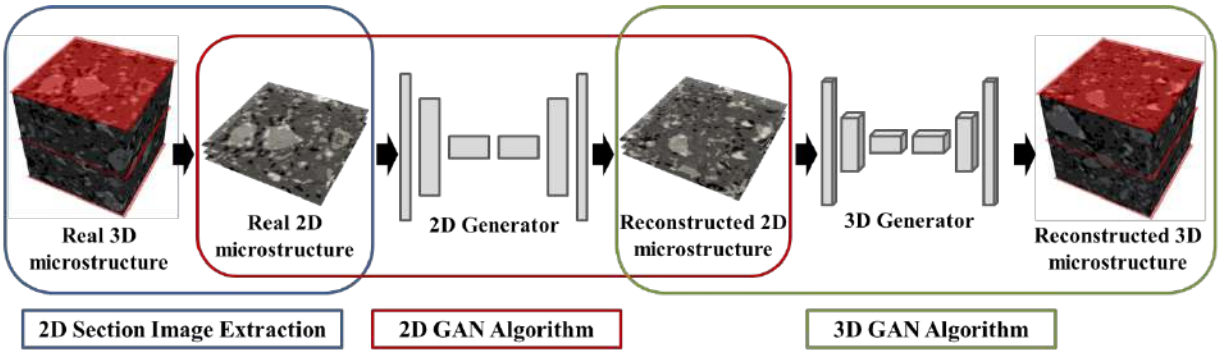
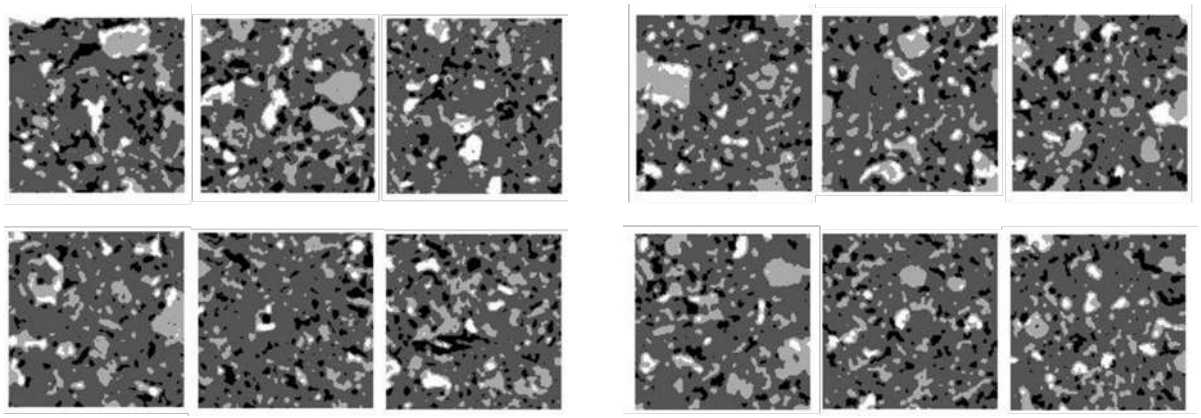


Figure 2. Schematic of microstructure reconstruction process

3. Reconstructed microstructures

The 2D cement paste microstructural images reconstructed using the 2D generator are shown in Figure 3. The similarity between the reconstructed microstructure and the actual microstructure was verified by comparing phase ratio and continuity factor (l_l). l_l is a scalar value for characterizing the degree of phase clustering that cannot be identified by the phase volume fractions (Han et al., 2018). The comparison analysis between the reconstructed microstructures against the real microstructures showed that the actual microstructures were properly reconstructed with high similarities in the phase distributions for pore and unhydrated cement phases. The errors of the phase ratio and l_l between the real and reconstructed 2D microstructures were within 2% and 5%, respectively.



(a) Real microstructure of cement paste (b) Reconstructed microstructure of cement paste

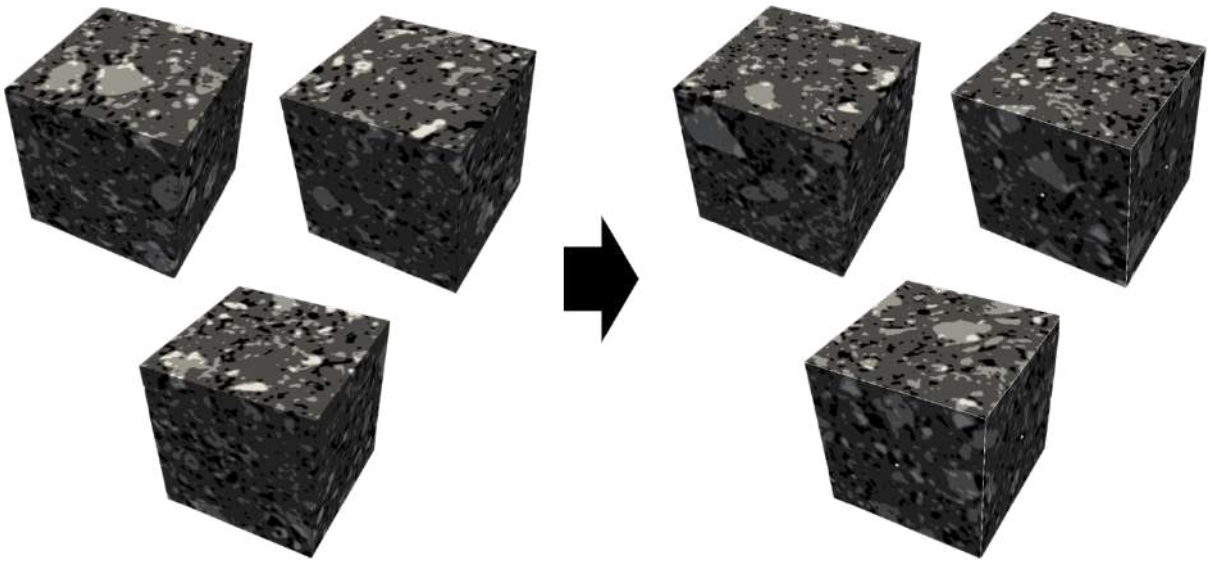
Figure 3. Reconstruction of 2D four-phase cement paste microstructures

Figure 4 shows the 3D microstructures constructed based on the reconstructed 2D microstructural images. As shown in Figure 4(b), it should be emphasized that the microstructural features of reconstructed 3D cement paste were continuous in the height direction where only three 2D samples (bottom, middle, and top) were provided for the 3D microstructure reconstruction. The results demonstrated that the 3D microstructures were properly generated from 2D microstructural images using the 2D-3D GAN. When comparing the volume ratio and l_l of the pore phase and unhydrated cement phase of the real and reconstructed 3D microstructures, the errors for volume ratio and l_l were less than 7% and 15%, respectively.

4. Conclusions

This study developed a framework to reconstruct complex microstructures of cement paste composed of four phases using a deep learning technique. The significance of the proposed approach is that the complex microstructures of cement paste can be generated without excessive efforts and computational resources. To reduce the computational cost, the proposed framework divided the training algorithm into three steps

so that the three-dimensional microstructures of the cement pastes could be efficiently reconstructed. It is expected that the proposed framework can be used as an effective tool for generating virtual specimens for simulations, which can supplement time and effort intensive real experiments for evaluating properties of multi-phase cement pastes.



(a) Real microstructure of cement paste (b) Reconstructed microstructure of cement paste

Figure 4. Reconstruction of 3D four-phase cement paste microstructures

Acknowledgements

This study was supported by the National Research Foundation of Korea (NRF_2022R1A4A1033925).

References

J. Y. Zhu, T. Park, P. Isola and A.A. Efros (2017) "Unpaired image-to-image translation using cycle-consistent adversarial networks", *In Proceedings of the IEEE international conference on computer vision,* 2223-2232

J.-S. Kim, S.-Y. Chung, T.-S. Han, D. Stephan and M. Abd Elrahman (2020) "Correlation between microstructural characteristics from micro-CT of foamed concrete and mechanical behaviors evaluated by experiments and simulations", *Cement and Concrete Composites*, 112: 103657

C. Hu and Z. Li (2015) "A review on the mechanical properties of cement-based materials measured by nanoindentation", *Construction and Building Materials*, 90: 80-90

J.-S. Kim, J.-H. Lim, D. Stephan, K. Park and T.-S. Han (2022) "Mechanical behavior comparison of single and multiple phase models for cement paste using micro-CT images and nanoindentation", *Construction and Building Materials*, 342: 127938

X. Ying, H. Guo, K. Ma, J. Wu, Z. Weng, and Y. Zheng (2019) "X2CT-GAN: reconstructing CT from biplanar X-rays with generative adversarial networks", *Proceedings of the IEEE/CVF conference on computer vision and pattern recognition,* 10619-10628

T.-S. Han, X. Zhang, J.-S. Kim, S.-Y. Chung, J.-H. Lim and C. Linder (2018) "Area of linal-path function for describing the pore microstructures of cement paste and their relations to the mechanical properties simulated from μ-ct microstructures", *Cement and Concrete Composites*, 89: 1-17

S.-Y. Kim, J. S. Kim, J.-W. Kang, and T.-S. Han (2019) "Construction of virtual interfacial transition zone (ITZ) samples of hydrated cement paste using extended stochastic optimization", *Cement and Concrete Composites*, 102: 84-93

The 16th International Congress on the Chemistry of Cement 2023 (ICCC2023)
"Further Reduction of CO_2 -Emissions and Circularity in the Cement and Concrete Industry"
September 18–22, 2023, Bangkok, Thailand

Numerical Model for Growth and Porosity of C-S-H Structures in Cement Hydration

L. Nguyen-Tuan[1*], C. Rößler[1], M. Etzold[2] and H.M. Ludwig[1]

[1] *F.A. Institute of Building Material Science, Bauhaus-University Weimar, Germany*
Email: [long.nguyen.tuan, christiane.roessler, horst-michael.ludwig]@uni-weimar.de
[2] *Former member of Department of Applied Mathematics and Theoretical Physics, University of Cambridge, UK*
Email: mae38@cam.ac.uk

ABSTRACT

In this paper, we propose a model based on surface reactions and ion transport to capture the development of C-S-H not only at early age but also at later age of hydration. With the assumption of the mass balance between dissolution and precipitation processes, we derive an equation for the C-S-H precipitation rate. The model takes both the coverage of C-S-H on C_3S surfaces and the ion diffusion through a semi-permeable layer of C-S-H into account. The C-S-H growth model is implemented and investigated in 'sheet growth' geometrical platform (Etzold, et al., 2015) with kinetic Monte Carlo method. Furthermore, we introduce a random sampling method to quantify pore volumes and phase fractions in the simulation, which are shown to be consistent with those obtained from experimental data (X-ray diffraction-XRD and 1H NMR).

KEYWORDS: *C-S-H calcium-silicate-hydrate, micro-structure, numerical simulation, kinetic Monto Carlo*

1. Introduction

Calcium silicate hydrate (C-S-H) determine the performance of cementitious materials. Understanding the microstructure and the formation process of this phase is a key for improving material properties and minimizing the impact on the CO_2 footprint. Most studies concerning nucleation and growth of C-S-H phases in experiments as well as in modelling focus on the development of C-S-H at early ages (Thomas, et al., 2011; Bullard, et al., 2015; Ouzia & Scrivener, 2019; Nguyen-Tuan, et al., 2020). This early reaction rate is observed indirectly via heat flow measured by means of calorimetry. However, 80 % of the strength of cement paste develops at later ages i.e. from 24 hours to 28 days (Marchese, 1983), when C-S-H fibres mostly fill the capillary pore and interlock with each other. Many authors (Nguyen-Tuan, et al., 2020; Scherer & Bellmann, 2018; Bellmann, et al., 2019) have proposed growth models assuming that the coverage of C-S-H on C_3S surface determines the decelerating rate of C-S-H formation. The simulation results showed a qualitative agreement with the reaction rate measured by calorimetry within 48 hours. However, for long-term hydration, when the C_3S surface is fully covered, these models no longer fit experimental data, where it is observed that the growth of C-S-H still continues (Muller, et al., 2013).

Here we introduce a model, which associates ion transport with the sheet growth geometrical model (Etzold, et al., 2015; Nguyen-Tuan, et al., 2020) to capture the growth as well as the transient structures of C-S-H during hydration process. The growth model is based on the physical and chemical laws on surface reaction and transport. The mass balance between dissolution and precipitation processes is used with the assumption that the ion transport is at steady state. The model takes thereby both the coverage of C-S-H on C_3S surfaces (Bellmann, et al., 2019) and the ion diffusion through a semi-permeable layer of C-S-H (Hou, et al., 2015; Gartner, et al., 2002) into account, which allows simulating a slow growth of C-S-H at the later age. The model is implemented in the 'sheet growth' geometrical platform (Etzold, et al., 2015), where the solid element is represent of Calcium-Silicate (C-S) sheet, the space between the sheets is interlayer water. Several aspects of the model will be presented in this short paper.

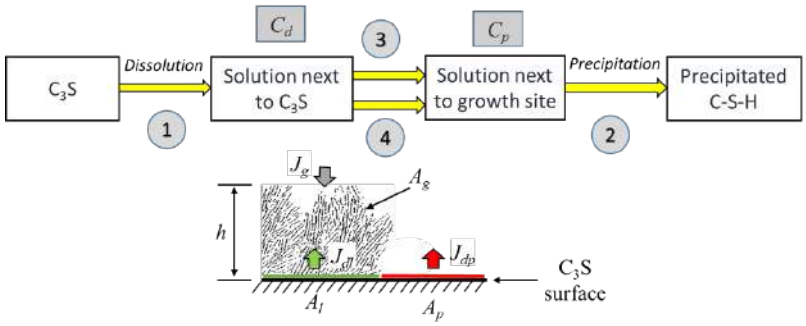


Figure 1: Scheme describing dissolution-precipitation processes: ① Reaction at C_3S surface, ② Reaction at C-S-H surface, ③ Diffusive transport through C-S-H layer, ④ Diffusive transport through pore fluid. The lower figure visualizes the parameters contributing to the process; J_{dl} and J_{dp} are the diffusion though C-S-H layer and pore, respectively; $J_g$is the precipitation rate.

2. Modelling

2.1 Growth model

It is denoted that D_{CSH} and D_d are the diffusions coefficients of the C-S-H layer and the pore water; h is the thickness of the C-S-H layer; A is the total surface of C_3S grain; A_p and A_l are the free and covered surfaces of C_3S grain respectively (Fig.1); A_g is the available C-S-H surface where other C-S-H elements can grow; c_d and c_p are the ion concentrations for dissolution and precipitation at the respective surfaces; C_{deq} and C_{peq} are the equilibrium concentrations at dissolution and precipitation surfaces; k_d and k_g are the reaction rates at surfaces of C_3S and C-S-H, respectively.
The model is based on the mass balance concept, assuming that ion transports takes place in steady state (Nicoleau, et al., 2013), i.e. the mass transport of dissolution is equal to the mass transport in precipitation. The flowchart presenting the mass transport processes is shown in Fig.1, the lower figure describes the quantities and parameters. A series of processes is presented here. In the first step, the ions dissolve from the unhydrated surface to the pore fluid next to the surface. This process is controlled by the reaction rate, according to the first-order reaction. The next process is the ion transport from the surface to the fluid next to the growth site, assuming that the transport length is the C-S-H layer thickness as Fig.1. This transport occurs in two parallel processes: The transport through pore fluid and the transport through C-S-H layer, both are described by Fick's law (Fick, 1855). The transport through the pore fluid dominates at initial state, whereas, the transport through the C-S-H layer dominates at the final state, when C-S-H covers all the unhydrated surface. Finally, the reaction process describes the precipitation of ions to C-S-H at its surface. The processes from 1 to 4 are described in Eq. 1 to 4, respectively.

- Reaction at the C_3S surface as the dissolution is calculated via net rate of dissolution of C_3S

$$J_d = -A\,k_d\left(C_d - C_{deq}\right) \tag{1}$$

- Reaction at the C-S-H surface as precipitation is calculated via net rate of product of C-S-H

$$J_g = A_g k_g\left(C_p - C_{peq}\right) \tag{2}$$

- Diffusive transport through the pore fluid defined by Fick's law:

$$J_{dp} = -A_p D_p \frac{C_p - C_d}{h} \tag{3}$$

- Diffusive transport through C-S-H layer defined by Fick's law:

$$J_{dl} = -A_l D_{CSH} \frac{\left(C_p - C_d\right)}{h} \tag{4}$$

where the total C_3S surface is the sum of two surfaces

$$A = A_p + A_l \tag{5}$$

The total area A is normalized as area fractions and is equal to 1, $A_l = \phi$ the fraction of the surface covered by C-S-H phases. Finally, the mass balance conditions at steady state lead to

$$J_d = J_g, \qquad J_{dl} + J_{dp} = J_d, \tag{6}$$

substituting Eq. 6 to Eqs. 1 to 4.

$$J_g = \frac{A_g k_g k_d \left(C_{deq} - C_{peq}\right)\left[D_{\{CSH\}(1-\phi)} + D_p \phi\right]}{D_{CSH}(k_d + A_g k_g)(1-\phi) + D_p k_d \phi + A_g k_g (h k_d + D_p \phi)} \text{(mol/h)} \tag{7}$$

Assuming that the density of a C-S element does not change during the hydration. At steady state, the precipitation rate is proportional to the volumetric growth or $\kappa = \lambda J_g$, where κ (h^{-1}) is volumetric growth rate, λ (mol^{-1}) ratio converting from molar mass to number of a C-S backbone element. The rate R using in kinetic Monte Carlo approach can be computed as

$$R = \kappa S, \tag{8}$$

Where S is the number of available surface for the element growth.

2.2 Parameters

The geometrical parameters (i.e. A_l, ϕ, A_g and h) are determined directly from model geometry. The thickness of C-S-H layers h is the difference between highest C-S solid elements and the substrate. The C-S-H interface (A_g) is calculated by the number of available surfaces S (Nguyen-Tuan, et al., 2020). The covered surface A_l is computed each time step via geometry of C-S-H phases, A_l is the projected area of all C-S-H elements, which place at the height smaller than 10 nm from the bottom side of the domain. The pre-determined parameters (i.e. $D_{CSH}, D_p, C_{deq}, C_{peq}$) are from literature, the growth parameters (k_g and k_d) are assumed.

3. Model evaluation

The growth model allows to simulate the acceleration and deceleration of C-S-H growth at early age (up to 24 h). Furthermore, the model can capture the slow growth at later age (i.e. 10 days), which has been determined by means of ^{1}H NMR spectroscopy (Muller, et al., 2013). Results in Fig. 2 show how the variation of model parameters affects the hydration kinetics. It is obvious, that the variation in ion diffusion coefficient of C-S-H insignificantly affects the growth rate at the early age, however, it affects the cumulative C-S-H growth at the later ages (Fig. 2, a and c). The change in ion diffusion coefficient of the pore water affects significantly the growth rate and cumulative C-S-H at both early and later ages (Fig. 2, b and d).

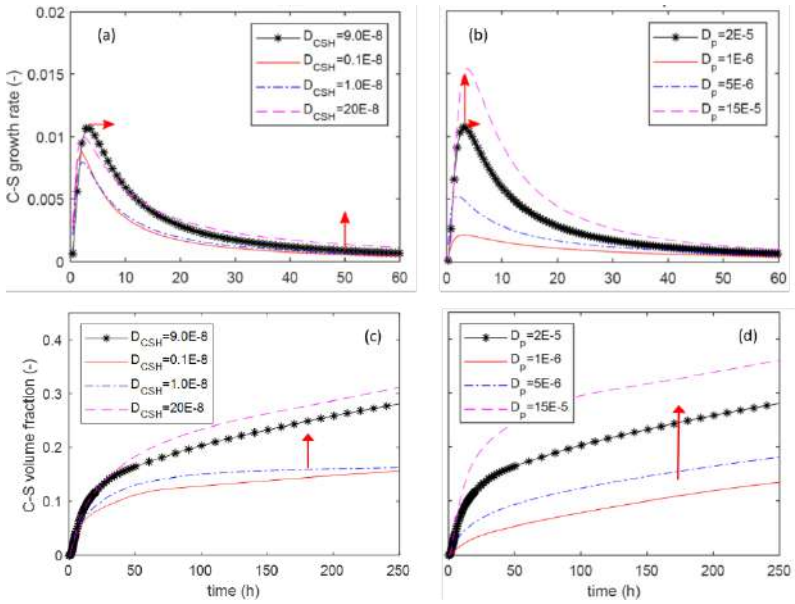


Figure 2: Model evaluation using one-at-a-time sensitivity analysis for diffusion parameters (D_{CSH} and D_p): (a,b) Growth rate; (c,d) Cumulative growth.

With combination with the 'sheet growth' geometrical model, the model can capture the rate of C_3S surface coverage, the development of C-S-H, and the development of pores in C-S-H. The long-term development of the C-S-H phases up to 28 days is validated with the in-situ measured data from XRD experiments. We propose a random sampling method to quantify pore and phase fractions, which are proved to be consistent with those measured in experimental data like NMR, SEM analyses. The developments of the pore size distribution are compared with those obtained from H^1-NMR experiment and Scanning Electron Microscopy (SEM) image analysis. However, due to limitation of the paper length, these aspects of the model will be only shown in our presentation.

4. Conclusion

It is generally believed that C-S-H phases surrounding C_3S grains are semi-permeable and the diffusion through this layer attributes to a slow C-S-H formation at the later ages. Based on this idea, we propose a physico-chemical model for the C-S-H growth, which considers surface reactions and ion transports as factors controlling the growth rate. Therefore, the new model allows simulating not only the acceleration and deceleration of C-S-H growth at the early age but also the slowing growth of C-S-H at the later hydration age. The model results are validated with experimental data such as XRD, H^1-NMR, and SEM image analysis and will be shown in our presentation.

Acknowledgements

The research was supported by the Deutsche Forschungsgemeinschaft (DFG) under grant number 344069666.

References

Bellmann, F., Neubauer, J., Ludwig, H.-M. & Naber, C., 2019. *A simple model to predict C3S hydration kinetics.* 15th International Congress on the Chemistry of Cement (ICCC2019), 2019, 1-11

Bullard, J. W., Scherer, G. W. & Thomas, J. J., 2015. Time dependent driving forces and the kinetics of tricalcium silicate hydration. *Cement and Concrete Research,* Volume 74, pp. 26-34.

Etzold, M. A., McDonald, P. J., Faux, D. A. & Routh, A. F., 2015. Filling of three-dimensional space by two-dimensional sheet growth. *Phys. Rev. E,* October, 92(4), p. 042106.

Gartner, E., F. Young, J., Damidot, D. & Jawed, I., 2002. *Hydration of Portland Cement.* Structure and Performance of Cements, 2nd Edition, 2002, 2, 57-113.

Hou, D., Li, Z., Zhao, T. & Zhang, P., 2015. Water transport in the nano-pore of the calcium silicate phase: reactivity, structure and dynamics. *Phys. Chem. Chem. Phys.,* 17(2), pp. 1411-1423.

Marchese, B., 1983. Microstructure and Strength Development in Cement Paste. In: S. N. GHOSH, ed. *Advances in Cement Technology.* Pergamon, 1983, pp. 441-466

Muller, C. A., Scrivener, K., Gajewicz-Jaromin, A. & J. McDonald, P., 2013. Densification of C-S-H measured by ^{1}H NMR relaxometry. *The Journal of Physical Chemistry C,* December, Volume 117, p. 403–412.

Nguyen-Tuan, L., Etzold, M. A., Roessler, C. & Ludwig, H.-M., 2020. Growth and porosity of C-S-H phases using the sheet growth model. *Cement and Concrete Research,* Volume 129, p. 105960.

Nicoleau, L., Nonat, A. & Perrey, D., 2013. The di- and tricalcium silicate dissolutions. *Cement and Concrete Research,* Volume 47, pp. 14-30.

Ouzia, A. & Scrivener, K., 2019. The needle model: A new model for the main hydration peak of alite. *Cement and Concrete Research,* Volume 115, pp. 339-360.

Scherer, G. W. & Bellmann, F., 2018. Kinetic analysis of C-S-H growth on calcite. *Cement and Concrete Research,* Volume 103, p. 226–235.

Thomas, J. J. et al., 2011. Modeling and simulation of cement hydration kinetics and microstructure development. *Cement and Concrete Research,* Volume 41, pp. 1257-1278.

The 16th International Congress on the Chemistry of Cement 2023 (ICCC2023)
"Further Reduction of CO_2 -Emissions and Circularity in the Cement and Concrete Industry"
September 18–22, 2023, Bangkok, Thailand

Micromechanical properties of C-A-S-H and C-A-S-H/CH mixtures based on nanoindentation

J.W. Wang[1*], Z.L. Hu[2*], and J.P. Liu[3]

[1] *Southeast university, Nanjing, China*
Email: wjw@seu.edu.cn
[2] *Southeast university, Nanjing, China*
Email: zhanglihu@seu.edu.cn
[3] *Southeast university, Nanjing, China*
Email: liujiaping@cnjsjk.cn

ABSTRACT

Calcium-alumina-silicate-hydrate (C-A-S-H) is the main hydration product in cement-based materials, which plays important roles on the mechanical properties and volume deformation of cement-based materials. The aim of this paper is to elucidate the effects of porosity and chemical composition of C-A-S-H on their micromechanical properties using nanoindentation. The intrinsic micromechanical properties of C-A-S-H are enhanced as Ca/Si decreases. In addition to the influence of Al on the mean chain length and basal spacing, it is also mainly affected by the existence of Q^3 (Al).Furthermore, the influence of impurities inevitably generated during the synthesis process, CH, on the micromechanical properties of C-A-S-H has been investigated. As the CH content increases, the overall indentation modulus, indentation hardness and creep modulus of the mixture increase, while the characteristic time shortens.

KEYWORDS: *C-A-S-H, nanoindentation, micromechanical properties*

1. Introduction

C-A-S-H is one of the important hydration products of cementitious materials, which accounts for approximately 70% of the total hydrated products. It has an essential influence on the mechanics, durability and deformation of cementitious materials. The Ca/Si and Al/Si are considered to be the "genes" of C-A-S-H, which determines the performance of C-A-S-H (Wang, Gao et al. 2023). However, the effects of Ca/Si and Al/Si on the micromechanical properties of C-A-S-H are still controversial. The increase in Ca/Si leads to a decrease in the layer spacing, which in turn enhances the micromechanical properties of C-A-S-H (Nguyen, Alizadeh et al. 2012, Geng, Myers et al. 2017). In contrast, the decrease in Ca/Si leads to a decrease in defects, which enhances the C-A-S-H micromechanical properties (Pelisser, Gleize et al. 2012, Pourbeik, Beaudoin et al. 2013). The effect of aluminium incorporation on the micromechanical properties of C-A-S-H has been poorly studied. Only some of the studies reveal the effect from the atomic scale using High pressure XRD(Geng, Vasin et al. 2018).Nanoindentation is a promising method to probe micromechanical properties, which has now been widely used in cement-based materials. However, due to the complexity of the cement hydration products, the nanoindentation technique cannot precisely distinguish the micromechanical properties of the different phases. Further, in order to realistically probe the micromechanical properties of C-A-S-H, the strategy of synthesizing C-A-S-H by chemistry is proposed(Kumar, Walder et al. 2017). Herein, the chemical composition-phase composition-microstructure-micromechanical properties relationship of C-A-S-H is revealed by chemical synthesis of C-A-S-H with different Ca/Si and Al/Si, combined with nanoindentation technique. This provides a solid foundation for further research on the role of C-A-S-H in cementitious materials.

2. Materials and methods

2.1 Synthetic C(-A)-S-H

C-A-S-H was synthesized by co-precipitation method. Calcium nitrate, sodium silicate, and aluminium nitrate were used as sources of calcium, silicon, and aluminium, respectively. To study the effect of Ca/Si and Al/Si, Ca/Si of 0.8 and 1.2 and Al/Si of 0.1, 0.2 and 0.3 were adopted. Target Ca/Si and Al/Si were controlled by initial reactant dosing. The results of the filtrate analysis and thermal analysis indicated that the obtained Ca/Si and Al/Si were consistent with the initial reactant dosing. The specific synthesis and drying details can refer to our previous studies (Wang, Hu et al. 2022). The porosity of the powder was controlled by varying the applied stress.

2.2 Designed C-A-S-H mixture systems

In order to study the effects of the common hydration product, CH, on the micromechanical properties of C-A-S-H, different amounts of CH were physically incorporated into the dried C-A-S-H. The Ca/Si and Al/Si of C-A-S-H were 0.8 and 0.1, respectively. According to the proportion of CH in cement hydration products, the incorporation of CH was 0%, 5%, 10%, 20%, 40%, 60%, 80%. Pure C-A-S-H powders and mixed C-A-S-H powders were pressed into blocks with porosities of about 10%, 20%, 40% and 60% by using a pressure device. For the C-A-S-H mixture system, controlling the porosity to around 30% was necessary.

2.3 Nanoindentation

The above-mentioned block samples were first fixed by epoxy resin, and then polished according to a certain protocol to meet the roughness requirements of the nanoindentation test (Rq < 50 nm). Nanoindentation was performed on a nano performance test system with a Berkovich indeter. For pure C-A-S-H and mixture C-A-S-H, the maximum load were set to 1.3 mN and 40 mN, respectively, the loading and unloading rates were 0.05 mN/s and 2 mN/s, respectively, and the holding time was 60s. The indent array with 4 x 4 was employed in each sample. Indentation hardness (H), indentation modulus (M), elastic modulus (E) and creep modulus (C) can be calculated by analyzing the load-depth curve.

3. Results and discussion

3.1 Effect of Ca/Si and Al/Si

In order to exclude the effect of porosity on micromechanical properties, intrinsic micromechanical properties were obtained by using power law model, combined with the inverse derivation of properties at different porosities, as shown in Table 1. It is obvious that the micromechanical properties of C-A-S-H decreased significantly with the increase of Ca/Si. This can be attributed to the fact that the higher Ca/Si leads to more defects, which can be demonstrated in the pore structure(Guan, Ji et al. 2013) and morphology(Abdolhosseini Qomi, Krakowiak et al. 2014). Further, the following two mechanisms were often employed to reveal their intrinsic causes: 1. As the Ca/Si decreases, the polymerization degree of the silicon chain increases, and the length of the silicon chain increases, which strengthens the skeleton Ca-O layer of C-S-H. 2. As the Ca/Si decreases, the packing of C-S-H is more compacted.
The incorporation of Al is also considered to modify the micromechanical properties of C-A-S-H. The incorporation of Al can also increase the mean chain length of C-S-H, which in turn enhances the micromechanical properties. This is similar to the effect of Si. Apart from that, whether Al can form Q^3(Al) between C-S-H layers also has a significant effect on the C-S-H micromechanical properties, which was confirmed in High pressure-XRD.

Table 1 Intrinsic micromechanical properties of C(-A)-S-H

Samples	M (GPa)	H (GPa)	E (GPa)	C (GPa)
CSH08	44.35	1.49	25.62	95.65
CASH0801	37.03	0.97	21.39	102.80

CASH0802	43.75	1.42	25.27	83.74
CASH0803	34.66	1.24	20.02	84.78
CSH12	37.06	1.03	21.40	77.21
CASH1201	34.60	1.06	19.98	73.44
CASH1202	36.31	1.21	20.98	71.58
CASH1203	39.16	1.71	22.62	65.44

3.2 Effect of CH

The effect of inevitable cement hydration products (CH and $Al(OH)_3$) on the micromechanical properties of C-A-S-H was also investigated. The results of the micromechanical properties of the C-A-S-H and CH mixture system were shown in Fig. 1. With the increase of CH content, indentation hardness, indentation modulus and creep modulus gradually increased, while characteristic time gradually shortened. This indicated that the incorporation of CH enhanced the strength and elastic modulus of C-A-S-H and reduced the creep. This may be due to the following two reasons: CH itself has high mechanical properties(Shahsavari, Buehler et al. 2009) (E_{ch}=51.9 GPa), which enhances the overall micromechanical properties. 2. The spatial accumulation of CH and C-A-S-H inhibits the slip deformation of C-A-S-H.

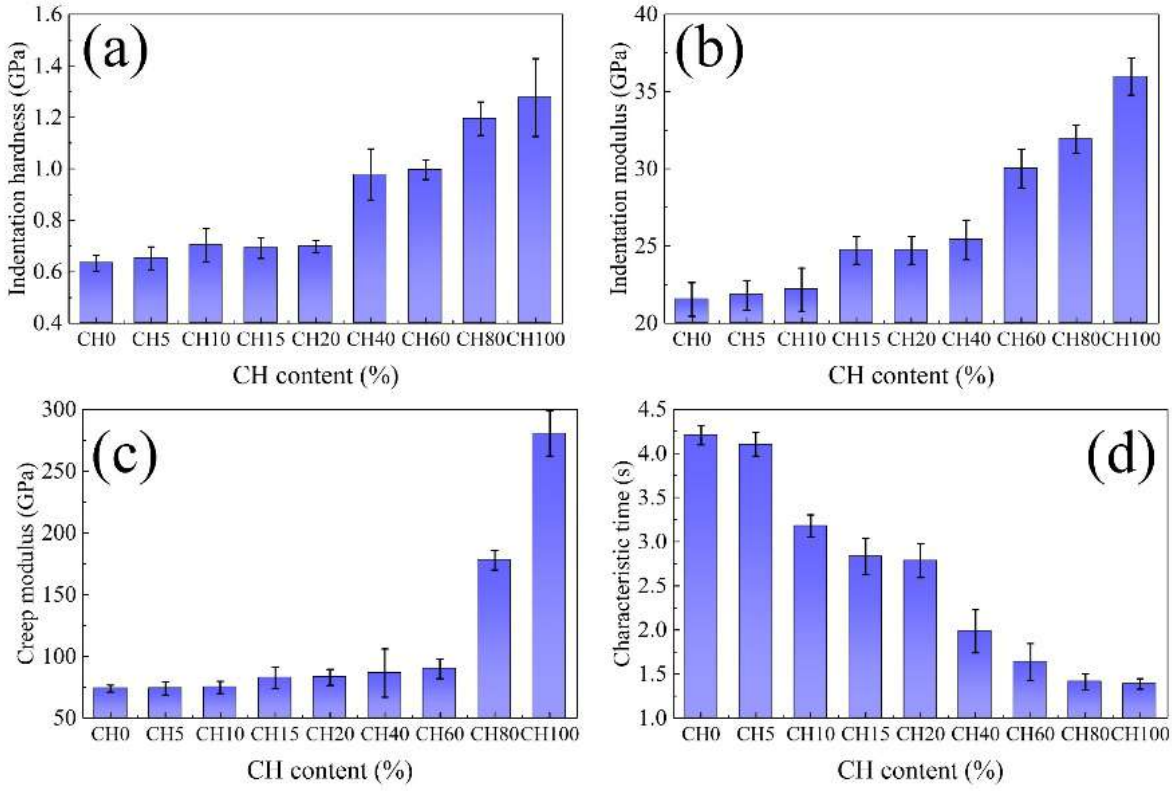


Figure 1 Effect of CH content on micromechanical properties of C-A-S-H

3. Conclusions

The micromechanical properties of C-A-S-H are enhanced with the increase of Ca/Si. The addition of Al may change the structure of C-A-S-H in addition to changing the mean chain length of C-A-S-H to affect the mechanical properties. The influence of other phases on the mechanical properties of C-A-S-H is related to the micromechanical properties of the phases themselves and morphology. The addition of CH enhances the micromechanical properties of C-A-S-H.

Acknowledgements

This work was supported by the National Key R&D Program of China (Grant No. 2021YFF0500802) and the National Natural Science Foundation of China (Grant No. 52008096).

References

Abdolhosseini Qomi, M. J., K. J. Krakowiak, M. Bauchy, K. L. Stewart, R. Shahsavari, D. Jagannathan, D. B. Brommer, A. Baronnet, M. J. Buehler, S. Yip, F. J. Ulm, K. J. Van Vliet and R. J. Pellenq (2014). "Combinatorial molecular optimization of cement hydrates." Nature communications **5**: 4960.

Geng, G., R. J. Myers, M. J. A. Qomi and P. J. M. Monteiro (2017). "Densification of the interlayer spacing governs the nanomechanical properties of calcium-silicate-hydrate." Scientific reports **7**(1): 10986.

Geng, G., R. N. Vasin, J. Li, M. J. A. Qomi, J. Yan, H.-R. Wenk and P. J. M. Monteiro (2018). "Preferred orientation of calcium aluminosilicate hydrate induced by confined compression." Cement and Concrete Research **113**: 186-196.

Guan, W., F. Ji, Q. Chen, P. Yan and Q. Zhang (2013). "Preparation and phosphorus recovery performance of porous calcium–silicate–hydrate." Ceramics International **39**(2): 1385-1391.

Kumar, A., B. J. Walder, A. Kunhi Mohamed, A. Hofstetter, B. Srinivasan, A. J. Rossini, K. Scrivener, L. Emsley and P. Bowen (2017). "The atomic-level structure of cementitious calcium silicate hydrate." The Journal of Physical Chemistry C **121**(32): 17188-17196.

Nguyen, D.-T., R. Alizadeh, J. J. Beaudoin and L. Raki (2012). "Microindentation creep of secondary hydrated cement phases and C–S–H." Materials and Structures **46**(9): 1519-1525.

Pelisser, F., P. J. P. Gleize and A. Mikowski (2012). "Effect of the Ca/Si Molar Ratio on the Micro/nanomechanical Properties of Synthetic C-S-H Measured by Nanoindentation." The Journal of Physical Chemistry C **116**(32): 17219-17227.

Pourbeik, P., J. J. Beaudoin, R. Alizadeh and L. Raki (2013). "Mechanical property–porosity relationships of layered calcium silicate hydrate phases." Materials and Structures **46**(9): 1489-1495.

Shahsavari, R., M. J. Buehler, R. J. M. Pellenq and F. J. Ulm (2009). "First‐principles study of elastic constants and interlayer interactions of complex hydrated oxides: Case study of tobermorite and jennite." Journal of the American Ceramic Society **92**(10): 2323-2330.

Wang, J., C. Gao, J. Tang, Z. Hu and J. Liu (2023). "The multi-scale mechanical properties of calcium-silicate-hydrate." Cement and Concrete Composites **140**: 105097.

Wang, J., Z. Hu, Y. Chen, J. Huang, Y. Ma, W. Zhu and J. Liu (2022). "Effect of Ca/Si and Al/Si on micromechanical properties of C(-A)-S-H." Cement and Concrete Research **157**: 106811.

The 16th International Congress on the Chemistry of Cement 2023 (ICCC2023)
"Further Reduction of CO_2 -Emissions and Circularity in the Cement and Concrete Industry"
September 18–22, 2023, Bangkok, Thailand

Methods for measuring internal stress and expansion deformation of fresh concrete during steam curing

Y. Xiang[1*], K. Yang[2], Y.J. Li[3], and W.R. Xu[4], and Y.J. Xie[5]

[1] *Central South University, Changsha, P.R. China*
Email: Neish2013@126.com
[2] *Central South University, Changsha, P.R. China*
Email: 646833037@qq.com
[3] *Central South University, Changsha, P.R. China*
Email: 510018454@qq.com
[4] *Central South University, Changsha, P.R. China*
Email: xuwenrui0103@csu.edu.cn
[5] *Central South University, Changsha, P.R. China*
Email: xieyj@csu.edu.cn

ABSTRACT

Residual expansion deformation is one of the main forms of thermal damage of steam-cured concrete, which causes damage to the volume stability and durability of steam-cured concrete prefabricated components. Due to the rapid development of elastic modulus of fresh concrete in the process of steam curing, it is difficult to calculate the residual expansion deformation as well as the relevant internal stress. In view of the inadequacy of the above research, this research has developed two sets of monitoring equipments to realize the development of dynamically monitoring fresh concrete expansion deformation and its internal stress during steam curing. This method has a good evaluation on measures to reduce the residual expansion deformation and its internal stress of steam-cured concrete, such as improvement of cementitious components and optimization of curing system. Results showed that replacing 30%wt of the cement with fly ash and slag, as well as adding super absorbent plastic, or extending the pre-curing time to 6hrs and adopting a maximum curing temperature of 45℃, could reduce the maximum residual expansion deformation and internal stress of concrete at the end of temperature rising period, as well as the final residual expansion deformation and internal stress at the end of the cooling period. This research can provide technical support for the development and application of steam-cured concrete.

KEYWORDS: *Fresh concrete, Steam curing, Internal stress, Residual expansion, Measurement*

1. Introduction

Steam-cured prefabricated concrete is widely used in the construction of high-speed railway infrastructure in China. Usually, 45~60℃ steam curing system under atmospheric pressure is used, which mainly includes four stages: setting period, 2hrs of temperature rising period, 8hrs of constant temperature curing period, and 2hrs of cooling period. During the steam curing process, the fresh concrete will produce a certain degree of shrinkage and temperature expansion deformation. The concrete volume deformation process is driven by the combined effect of different expansion stress, shrinkage stress, moisture stress, and temperature stress. Residual expansion deformation is the unrecoverable volume expansion deformation of concrete after going through the complete steam curing process. The more intense the expansion deformation, the more severely the pore structure coarsening will be, which will have a detrimental effect on the mechanical and durability performance of the steam-cured concrete prefabricated elements. Therefore, it is necessary to grasp the internal stress development law of concrete, and at the same time propose methods to inhibit or reduce the residual expansion deformation of steam-cured concrete. In this paper, the expansion deformation under unrestricted conditions and the internal

stress under restricted shrinkage conditions test methods for steam-cured concrete are described in detail. The internal stress and expansion deformation development law of steam-cured concrete is revealed, and its suppression method based on the optimization of steam curing system and composition materials is also proposed.

2. Experimental methodology

2.1. Raw materials

Portland cement (PC) labelled as P.I 42.5 produced by the China Building Materials Academy without blending any mixing materials is used. Clinker composition of PC is displayed in Table 1. Class I fly ash (FA) produced by Xiangtan Power Plant and class S95 granulated ground blast furnace slag (GGBS) produced by Pingxiang Iron and Steel Plant New Materials Co., Ltd are adopted. Main oxide compositions of PC, FA, and GGBS are shown in Table 2.

Table 1 Relative content of PC clinker (%)

Type	C_3S	C_2S	C_3A	C_4AF	Other
Ratio	59.38	15.59	7.28	11.64	6.11

Table 2 Main oxide composition of PC, FA, and GGBS

Type	Oxide composition (%)									
	SiO_2	Al_2O_3	Fe_2O_3	CaO	MgO	SO_3	Na_2O_{eq}	f-CaO	Loss	Cl^-
PC	20.08	5.09	3.81	63.41	2.06	2.33	0.55	0.88	1.72	0.016
FA	48.84	28.8	6.16	8.42	1.24	1.72	1.22	/	/	0.021
GGBS	31.02	13.75	1.0	36.27	5.53	2.17	0.38	/	/	0.024

The fine aggregate (S) is Xiangjiang River sand with fineness modulus of 3.1. The coarse aggregate (G) is crushed limestone gravel with particle size between 5~20mm, and 40% is 5~10mm aggregate and 60% is 10~20mm aggregate. Super absorbent plastic (SAP) is adopted as internal curing material with the particle size of 120~180 mesh. Water reducing agent is PCA-I polycarboxylic acid (SP) and the mixing water (W) is ordinary tap water at room temperature (20~23℃).

2.2. Sample mix proportion, preparation, and curing system

The mixing proportions of steam-cured concrete are presented in Table 3.

Table 3 Mixing proportions of steam-cured concrete (kg/m^3)

Group	PC	FA	GGBS	S	G	W	SAP	SP
C0	450	0	0	660	1210	135	0	3.6
FG	315	90	45	660	1210	135	0.9	4.0

The preparation process of fresh concrete could be divided into two steps: (i) blending all aggregates into the mixer and mixing for 30s, and then adding all cementitious materials into the mixer and mixing for another 30s; (ii) gradually pouring the mixing water and SP into the mixer. The total feeding time needs to be controlled within 2min; while, the total mixing time is 4min. When casting process is accomplished, the surface of concrete specimen needs to be covered with a layer of plastic film; then, placing the specimens in the testing environment (temperature holds at 20±2℃ and relative humidity (RH) nears 60%) for setting. The setting times for group C0 and FG are 3hrs, and 6hrs respectively, and the highest curing temperatures for them are 60℃, and 45℃, respectively.

2.3. Test method

(i) Internal stress test

The internal stress of fresh concrete in the steam curing process can be calculated by the radial stress of the inner and outer steel ring according to formula (1). Details can be seen in Xie et al (2021).

$$\begin{cases} P_I = -\varepsilon_I \cdot E_S \cdot \left(\dfrac{R_{IO}^2 - R_{II}^2}{2R_{IO}^2} \right) \\ P_O = \varepsilon_O \cdot E_S \cdot \left(\dfrac{R_{OO}^2 - R_{OI}^2}{2R_{OI}^2} \right) \\ \sigma_\theta = \dfrac{P_I \cdot R_{IO}^2 - P_O \cdot R_{OI}^2}{R_{IO}^2 - R_{IO}^2} + \dfrac{(P_I - P_O) \cdot R_{IO}^2 \cdot R_{OI}^2}{R_{OI}^2 - R_{IO}^2} \cdot \dfrac{1}{r^2} \end{cases} \quad (1)$$

where: P_I and P_O are the radial stress of the concrete ring acting on the inner and outer steel rings, respectively, MPa; E_s is the elastic modulus of both steel rings, and it is taken as 210GPa because it changes very little under 100℃; σ_θ is the annular stress of the concrete ring inside at different radii, MPa; r is the radius of the concrete ring, which ranges from 75~185mm; and ε_I and ε_o are the strains generated by the inner and outer steel rings, respectively. In this paper, all calculations involving the internal stress are carried out with r of 75mm, that is, the stress of the concrete ring at the minimum radius is discussed. Internal stress test device and its schematic diagram can be seen in Figure 1.

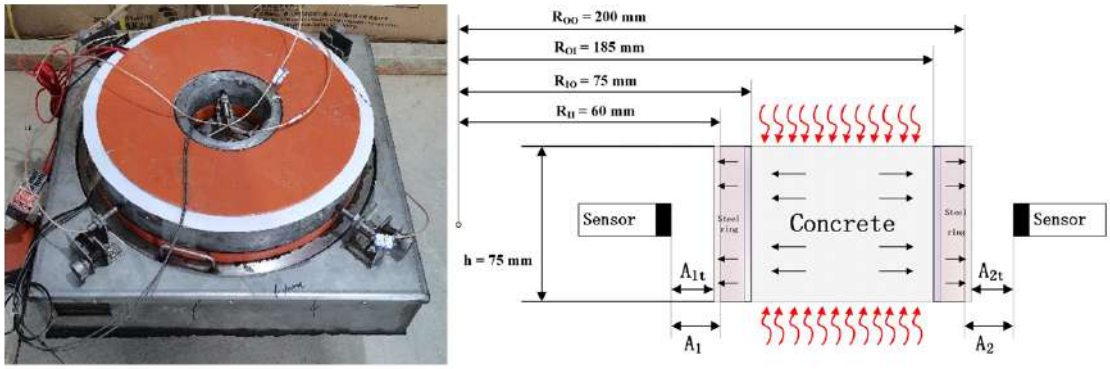


Figure 1. Internal stress test device and its schematic diagram

(ii) Expansion deformation test

The residual expansion deformation (strain) of fresh concrete in the steam curing process can be calculated by formula (2). Details can be seen in Xiang et al (2021) and Long et al (2020).

$$\varepsilon_{re} = \varepsilon_t + 0.9 \cdot \varepsilon_m - \varepsilon_T. \tag{2}$$

where: ε_{re} is the residual expansion strain; ε_t is the tested value of expansion deformation strain; ε_m is the temperature strain of the steel mould; and ε_T is the temperature strain of concrete specimen. Test device, schematic diagram, and temperature strains of steel mould and concrete can be seen in Figure 2.

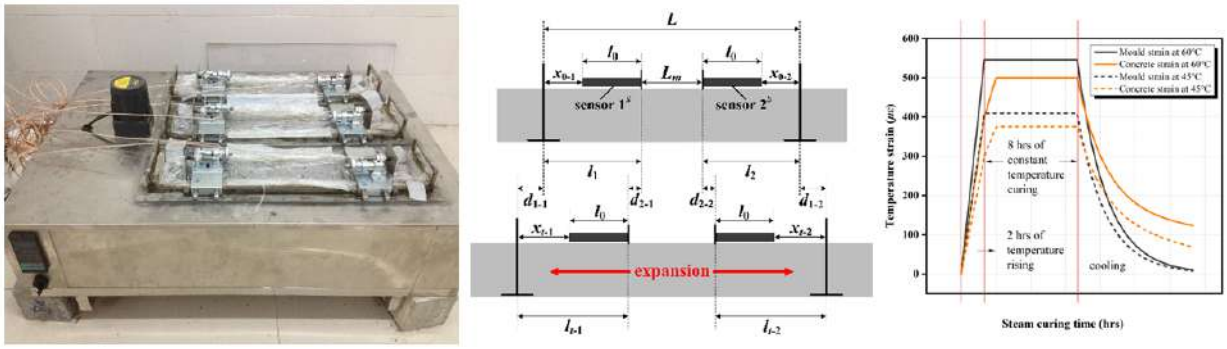


Figure 2. Expansion deformation test device and its schematic diagram

3. Experimental results and discussion

Test results of internal stress and expansion deformation of steam-cured concrete are shown in Figure 3.

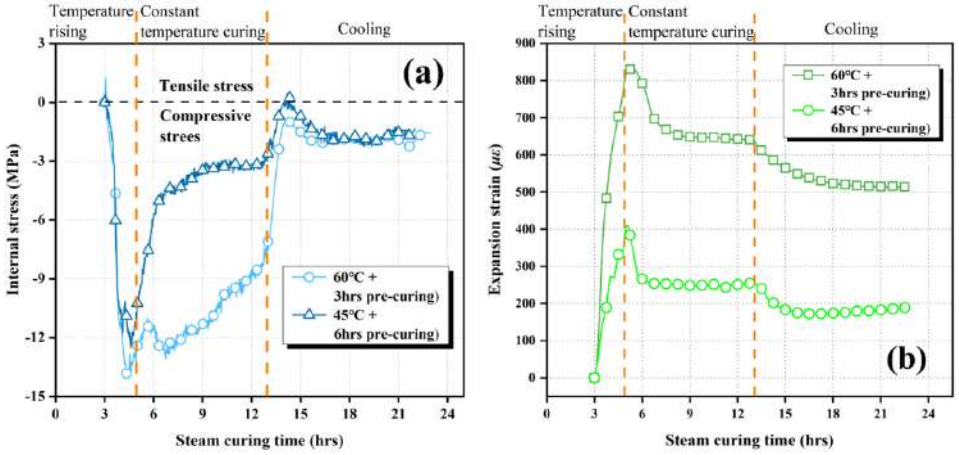


Figure 3. Test results: (a) internal stress, and (b) expansion deformation

It can be seen in Figure 3(a) that the internal stress of concrete increases sharply and then decreases gradually under the restraint of double steel rings. When the heating period is finished, the peak internal stress of both group C0 and FG are 14MPa and 11Mpa, respectively. The residual expansion pressure generated by the concrete ring acted on the outside of the inner steel ring, raised with the increase of expansion of different components in the system. However, due to the mineral admixtures reduced the hydration heat released during the steam curing process, and SAP further reduced the free water content in the system, the internal expansion pressure of concrete is controlled well. Besides, delaying the pre-curing time could also help the structure grow which makes the concrete own a better resistance of deformation. During the constant temperature curing period, the internal stress of concrete decreases significantly. The internal stress of group C0 decreases by near 49% while that of group FG is reduced by near 74%. Since the curing temperature has reached a constant state, the steel ring and the concrete gradually reach the same temperature, the thermal expansion of the concrete decreases. Yet, the self-drying shrinkage and chemical shrinkage gradually appear. At the same time, the compressive stress could be partially offset by the increasing shrinkage stress in the concrete, which results in the overall decrease of the internal stress of the concrete. The difference between group C0 and FG is mainly because the influence of concrete composition materials and curing system on its early structure. Finally, the internal residual compressive stresses of both group C0 and FG are about 1MPa.

As seen in Figure 3(b), concrete presents expansion deformation to a certain extent in the process of steam curing without restraint. At the same time, concrete gradually changes from plasticity to a certain rigidity state in the process of steam curing, which also has an inhibition effect on expansion deformation. The evolution characteristics of concrete expansion deformation are: expansion deformation increases rapidly in the heating stage, decreases gradually in the constant temperature stage; then, after entering the cooling stage, that deformation continues to decrease. The peak residual expansion strain of both group C0 and FG are near 530$\mu\varepsilon$ and 390$\mu\varepsilon$, respectively. While, the final residual expansion strain of group FG is only near 200$\mu\varepsilon$ which is 40% of that of group C0. In addition, during the constant temperature stage, there is a corresponding relationship between the reduction of concrete expansion deformation and the reduction of internal stress. The causes for the differences of reduction of expansion deformation are similar with the internal stress'.

4. Conclusions

(i) In the process of steam curing, the internal stress of concrete under the restraint is mainly compressive stress. It rapidly increases in the heating stage, then gradually declines in the constant temperature curing stage and continuous declines in the cooling stage, but the downward trend would be slowed down.

(ii) The expansion deformation characteristics of steam-cured concrete are mainly manifested as the rapid expansion in the heating stage, rapid shrinkage in the constant temperature curing stage, and the gradual change in the cooling stage. There is unrecoverable expansion deformation after cooling.

(iii) Reducing the initial free water content, improving the initial compactness and the initial structural strength, and reducing the maximum curing temperature are important technical ways to reduce the internal stress of concrete under restricted shrinkage conditions and expansion deformation under unrestricted conditions during steam curing.

(iv) Methods for measuring the internal stress and expansion deformation of steam-cured concrete proposed by this article can provide technical suggestion for proportion and curing system optimization of steam-cured concrete.

Acknowledgements

This work was supported by the National Natural Science Foundation of China (No. U1534207 and 51801560).

References

Xie, Y.J., Xiang, Y. and Long, G.C. et al. (2021) "Integrated testing device and method for measuring stress-strain of concrete during hydrothermal curing", *Chinese paten*, No. CN 111912686 B. (in Chinese)

Xiang, Y., Xie, Y.J. and Long, G.C. et al. (2021) "Residual expansion deformation of high-speed railway steam-cured concrete: mechanism, modeling, and measurement", *Archives of Civil and Mechanical Engineering*, 21:138.

Long, G.C., Xiang, Y. and Xie, Y.J. et al (2020) "Dynamic test method for deformation of cement-based materials during thermal curing", *Chinese paten*, No. CN 109458925 B. (in Chinese)

The 16th International Congress on the Chemistry of Cement 2023 (ICCC2023)
"Further Reduction of CO_2 -Emissions and Circularity in the Cement and Concrete Industry"
September 18–22, 2023, Bangkok, Thailand

Mineralogical Investigation of Coal Fly Ash using Combined SEM-EDS and Raman Spectroscopy

A.C. Witte* and N. Garg

Department of Civil and Environmental Engineering, University of Illinois Urbana Champaign, Champaign, United States
Email: dreww2@illinois.edu

ABSTRACT

The mineralogical composition of a supplementary cementitious material (SCM) dictates its performance when used as a cement replacement binder; characterizing mineralogy is thus critical. X-ray Fluorescence (XRF) and X-ray Diffraction (XRD) are well-established materials characterization techniques that provide comprehensive insight on bulk properties. Scanning Electron Microscopy with Energy Dispersive X-ray Spectroscopy (SEM-EDS), also an established technique, is unique because it provides elemental data mapped at sub-micron level resolutions. However, sub-micron mapping of mineral phases currently relies on adapting purely elemental data from SEM-EDS scans. This study develops the potential for Raman spectroscopy as a mineralogical characterization tool used jointly with SEM-EDS for sub-micron mapping of both elemental and mineralogical data. In particular, we explore the dual system's capabilities in characterizing amorphous aluminosilicate glasses critical to pozzolanic performance. We find that the Raman spectra observed on the amorphous phases are broad bands in the range of 600 – 1200 cm^{-1}. Furthermore, the band location is confirmed to correlate with the polymerization of the glassy phase as expressed by the ratio of Non-Bridging Oxygens to Tetrahedrals (NBO/T), such that lower wavenumber locations (600 – 850 cm^{-1}) correlate with high calcium contents (> 50% Ca/(Ca+Si+Al)), calcium being a network modifier that increases the NBO count of the glassy matrix.

KEYWORDS: *Raman spectroscopy, fly ash, aluminosilicate glass, SEM-EDS.*

1. Introduction

Coal fly ash is the most widely used supplementary cementitious material (SCM) in the global concrete industry. The primary mechanism by which fly ash improves concrete is through the pozzolanic reaction between calcium hydroxide ($Ca(OH)_2$ or CH) and amorphous alumino-silicates. Normally, CH is abundant in pore solutions and vulnerable to calcium leaching, but, when a pozzolan is introduced, it reacts to form calcium silicate hydrate (C-S-H) gel. The rate at which the reaction occurs depends on the pozzolan's dissolution rate. Thus, characterizing glassy alumino-silicate phases in fly ash is directly relevant to evaluating its pozzolanic performance.

Established techniques for the characterization of coal fly ashes include X-ray Fluorescence (XRF) and X-ray Diffraction (XRD), which can be used jointly to determine bulk elemental and mineralogical properties even of glassy phases (Glosser et al. (2021)). Meanwhile, Scanning Electron Microscopy with Energy Dispersive X-ray Spectroscopy (SEM-EDS) can map the elemental compositions of individual particles (Durdzinski et al. (2015)). Raman spectroscopy is also capable of analyzing systems with a sub-micron resolution, but instead of providing elemental data, it directly interrogates the mineralogical structure of the sample using the Raman effect/Raman scattering. Thus, mineral phases can be mapped at a high resolution (Polavaram and Garg (2021a)). Furthermore, Raman spectroscopy has been used to

study other cementitious materials including anhydrous OPC (Polavaram and Garg (2021b)) portlandite (Srivastava and Garg (2022)), and C-S-H (Kirkpatrick et al. (1997)). Because both have sub-micron resolution mapping capabilities, this study explored Raman spectroscopy as a complementary technique to SEM-EDS, supplementing elemental data with mineralogical data (Raman spectra) on individual particles of four class C ashes and five class F ashes.

2. Methods

2.1 X-ray Fluorescence

The bulk elemental properties of each ash were determined using a Shimadzu EDS-7000 X-ray fluorescence spectrometer. The ash powder samples were placed in a sample holder wrapped in a thin film of ultralene and directly exposed to X-rays. Spectra were acquired between 0-40 keV with a Helium atmosphere, a Rhodium anode as the X-ray source, and a 10 mm collimator.

2.2 Epoxy Disc Sample Preparation

Epoxy discs were prepared for use in both SEM-EDS and Raman analyses. Fly ashes were mixed with low-viscosity epoxy (L.R. white resin, medium grade) at a ratio of 3:1. After mixing, the paste was put into a cylindrical mold and left in a vacuum for 12 hours to remove air bubbles. The mold was cured in a furnace at 60 °C for 24 hours. After removing the epoxy disc, cutting was performed using a Buehler isomet low-speed saw. Polishing was performed in eight stages using 400, 800, 600, and 1200 grit silicon-carbide sandpaper and four stages of diamond polishing paste (sizes 5, 3, 1, and 0.25 μm).

2.3 SEM-EDS

SEM-EDS data was collected using a ThermoFisher Axia ChemiSEM with a ThermoFisher SDD detector for EDS (resolution 129 eV, detector size 25 mm2). SEM Images were collected in low vacuum mode with a chamber pressure of 50 Pa, a spot size of 5.0 nm, a working distance of 10 mm, and an accelerating voltage of 5 kV. The accelerating voltage was increased to 20 kV when collecting EDS elemental quantification maps. Typical scan areas were 550 x 350 μm using 400X magnification.

2.4 Raman Spectroscopy

A WITec alpha3000 Raman confocal microscope was used to collect Raman phase maps and point spectra. The laser excitation wavelength was 532 nm for all scans and spectra obtained. The laser power was set between 15-18 mW for area scans, while the grating was set at 600 g/mm BLZ = 500nm, allowing for a spectral resolution of ~4.9 cm^{-1} and a spectral range of 130-3600 cm^{-1}. A 20x objective was used with a working distance of 2.2 mm and a numerical aperture of 0.5. When collecting point spectra, the laser power was adjusted in a few cases to see if fluorescence could be reduced, or the signal could be increased.

Project FIVE software, developed by WITec, was used to perform cosmic ray removal and background subtraction. Raman spectra were collected at 240 alumino-silicate particles containing various levels of calcium. Center-of-mass calculations were performed manually in MATLAB by performing a weighted Riemann sum computation.

3. Results and Discussion

3.1 Raman and SEM-EDS analyses

SEM-EDS has been used previously on fly ashes to locally map elemental distributions of individual particles (Durdzinski et al. (2015)). The elemental distribution maps (Figure 1b) allow for the determination of the elemental composition at any point on the map, which can be used to identify the type(s) of alumino-silicate glass present in an individual particle. While most small particles were

observed to be homogenous/contain uniform elemental compositions, homogeneity is not universal. Indeed, large particles (> 50 μm) are rarely homogenous and can contain distinct glass/mineral phases melded together.

Using elemental wt% data, the number of non-bridging oxygens per tetragonal oxygens (NBO/T) of the characteristic glass of a particle can be approximated by evaluating the relationship between silicon (the primary network former in silicate glass), calcium (the primary cation/network modifier in fly ash), and aluminum (which may act as a network former or modifier depending on the charge balance conditions). The NBO/T is approximated for each particle using Eqn. (1):

$$NBO/T = 2(X_{CaO} - X_{Al2O3})/(X_{SiO2} + X_{Al2O3}) \quad (1)$$

Here, X is the molar fraction of a given oxide. Thus, the numerator expresses the available network modifying oxides, while the denominator expresses the network forming oxides, meaning the NBO/T is approximated as the ratio between them (Mills et al., (2014)).

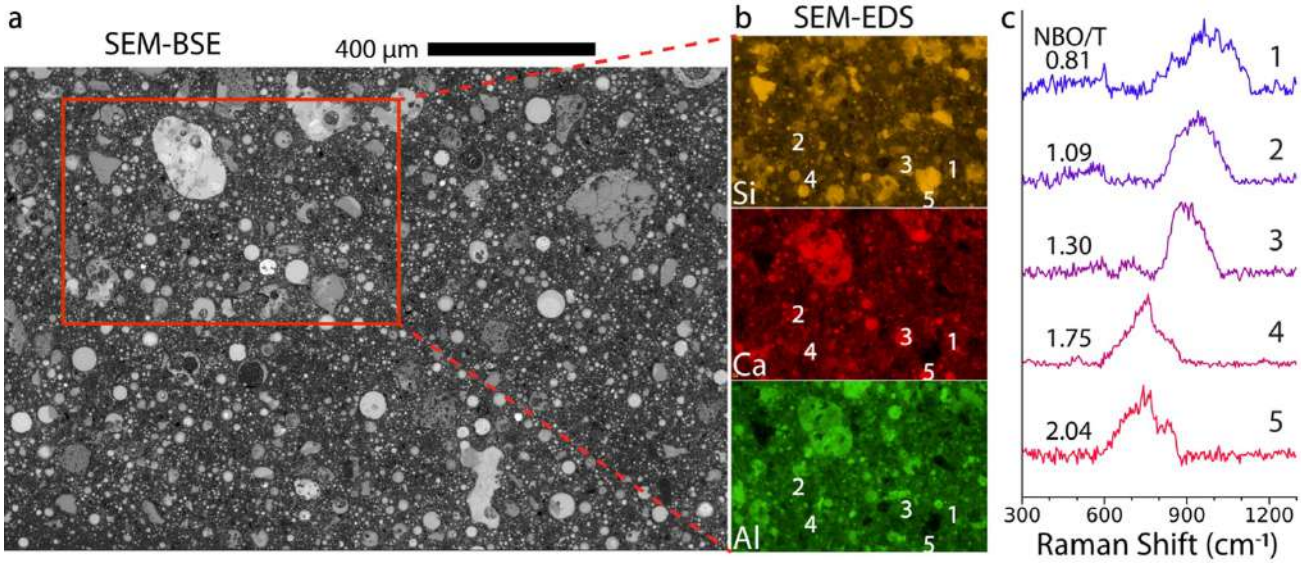


Figure 1. Individual particle analyses of a class C fly ash using a) SEM, b) SEM-EDS, and c) Raman spectroscopy (resolution is < 1 μm). The NBO/T of each particle is calculated based on the elemental composition maps (b), which can then be compared to the Raman shift of that same particle.

3.2 Interpretation of Raman spectra and comparison with elemental composition

The NBO/T has been previously observed to be related to broad Raman bands associated with symmetric stretching (SS) of silica tetrahedrals (McMillan et al. (1984)). More specifically, SS of silicon tetrahedra are associated with strong bands located at 1100 – 1050 cm^{-1}, 1000 – 950 cm^{-1}, 900 cm^{-1}, and 850 cm^{-1}, corresponding with one, two, three, and four non-bridging oxygens per tetrahedra, respectively (expressed using Q_x notation, the bands correspond to Q_3, Q_2, Q_1, and Q_0 respectively). Furthermore, Q_4 vibrational bands associated with a fully polymerized silicate network (NBO = 0) are found at 1200 and 1060 cm^{-1}. High levels of calcium (a network modifier) were thus found to be associated with lower Raman shifts (600 – 850 cm^{-1}), as shown in Figure 2. However, several particles with a low calcium content were observed to have low Raman shift center of mass (CoM) wavenumbers, though this could be explained by the high aluminum content in these particles, suggesting aluminum acted as a network modifier in these low-calcium particles.

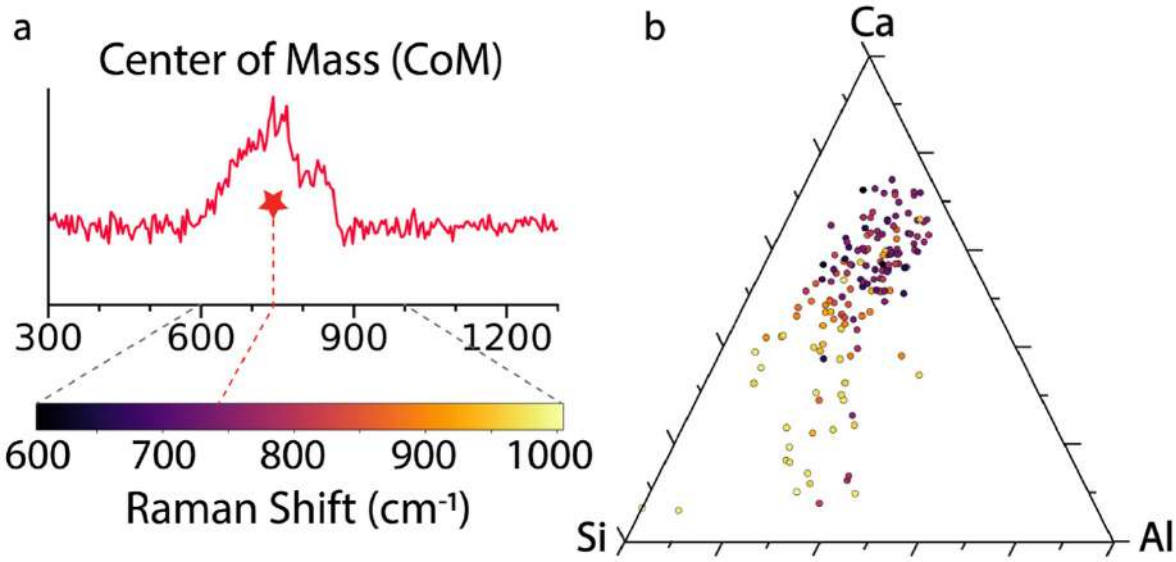


Figure 2. Distribution of Raman spectra Center of Mass (CoM) with respect to Ca, Si, and Al elemental composition. a) The CoM of each Raman spectra is calculated using a Riemann sum type weighted average in the wavenumber range 500 – 1300 cm^{-1}. b) The elemental distribution of particles, as determined by SEM-EDS. Each point has a color that corresponds to the CoM value of the Raman spectra of that respective particle.

4. Conclusions

Using Raman spectroscopy and SEM-EDS as complementary techniques allows for the comprehensive elemental and mineralogical analysis of individual fly ash particles. Particles that were rich in calcium (greater than 50% calcium out of the ternary Al-Ca-Si system) were observed to have lower Raman band CoM wavenumbers in the range of 600 – 850 cm^{-1} compared to particles with less than 50% calcium and 18% aluminum. Notably, three low calcium-particles with greater than 18% aluminum were observed to have low CoM wavenumbers, likely due to the aluminum acting as a network modifier in the absence of a cation charge balance. Thus, the Raman band associated with symmetric stretching of silicon tetrahedral is validated as an indicator of the degree of polymerization in glassy alumino-silicate phases.

Acknowledgements

This research was carried out in part in the Materials Research Laboratory Central Research Facilities, and the Core Facilities at the Carl R. Woese Institute of Genomic Biology, both at the University of Illinois. The authors thank Ecomaterials and IDOT for providing the fly ashes used in this study.

References

Durdzinski, P.T. et al. (2015) "A new quantification method based on SEM-EDS to assess fly ash composition and study the reaction of its individual components in hydrating cement paste", *Cement and Concrete Research*, 73

Glosser, D. et al. (2021) "Using glass content to determine the reactivity of fly ash for thermodynamic calculations", *Cement and Concrete Composites*, 115

Kirkpatrick, R.J. et al. (1997) "Raman spectroscopy of C-S-H, Tobermorite, and Jennite", *Advn Cem Bas Mat*, 5

McMillan, P. (1984) "Structural studies of silicate glasses and melts – applications and limitations of Raman spectroscopy", *American Mineralogist*, 69: 662-644

Mills, K.C. et al. (2014) "The Structure and Properties of Silicate Slags", in S. Seetharaman, *Treatise of Process Metallurgy: Process Fundamentals*. (149-289). Elsevier.

Polovaram, K.C. and Garg, N. (2021a). "High-fidelity and high-resolution phase mapping of granites via confocal Raman imaging", *Scientific Reports*, 11

Polovaram, K.C. and Garg, N. (2021b). "Enabling phase quantification of anhydrous cements via Raman imaging", *Cement and Concrete Research*, 150

Srivastava, S. and Garg, N. (2022) "Tracking spatiotemporal evolution of cementitious carbonation via Raman imaging", *Journal of Raman Spectroscopy*

The 16th International Congress on the Chemistry of Cement 2023 (ICCC2023)
"Further Reduction of CO_2 -Emissions and Circularity in the Cement and Concrete Industry"
September 18–22, 2023, Bangkok, Thailand

Study of alite and belite dissolution by kinetic Monte Carlo simulations and its effect in cement hydration.

P. Martin[1,2,*], H. Manzano[1] and M.J. Abdolhosseini Qomi[2]

[1] *University of Basque Country UPV/EHU, Condensed Matter Physics department, Bilbao, Spain*

[2] *University of California Irvine, Civil Engineering department, Irvine, USA*

Email: pablo.martin@ehu.eus
Email: hegoi.manzano@ehu.eus
Email: mjaq@uci.edu

ABSTRACT

Understanding the dissolution of alite and belite in cement is of great importance from a technological point of view. Atomistic Kinetic Monte Carlo (KMC) simulations have already been employed in different geochemistry fields to investigate the dissolution of materials at the nano-microscales. Unfortunately, current models usually assume far equilibrium conditions and fail to capture the dissolution mechanisms that take place close to chemical equilibrium between the dissolved ions and the material. Herein, we use a newly developed C++ program named KIMERA that considers the subtle interplay between dissolution and precipitation processes, and it is capable for the first time to reproduce the different mechanisms described in the literature as a function of the free energy (ΔG) and their dissolution rate. Moreover, we have proved wrong the assumption taken in the bibliography that the dislocation coalescence reduces the mineral dissolution rate, and we have proposed dislocation exhaustion as a plausible explanation for the deceleration phase in the cement hydration process. Overall, we highlight the importance of the mechanisms taking place at the nanoscale to describe macroscopic properties and show the potential of KIMERA to perform studies in other minerals and/or dissolution conditions.

KEYWORDS: *Mineral Dissolution, Kinetic Monte Carlo, Alite Dissolution, Belite Dissolution, Cement Hydration.*

1. Introduction

The impact on the cement of the dissolution of reactive minerals (alite, belite, aluminate) is directly observable in the cement calorimetry curve which shows the heat released during the hydration as a function of time (Scrivener et al (2019)). The evolution of the heat release is proportional to the dissolution rate of cement minerals and the precipitation of hydration products (portlandite, C-S-H), and indicates that there are several well-differentiated stages in cement hydration (see Figure 1).

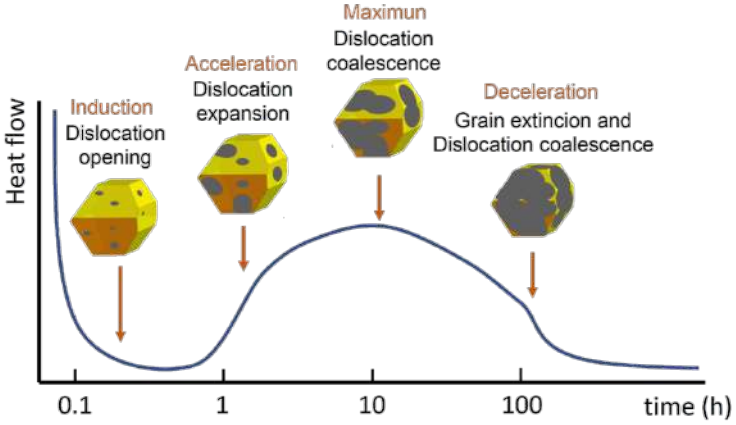


Figure 1. Calorimetry curve for the cement hydration. According to the dissolution theory, alite dissolution is responsible for the different stages. Adapted from (Juilland et al (2017)).

After very fast hydration in the first few minutes, there is an induction period of about an hour in which the hydration rate is very low. Then, there is an acceleration stage until a maximum rate is reached at around 10 hours. After the maximum, there is a deceleration of the dissolution rate until it becomes almost negligible after some days. Herein, we study here the dissolution of the main dissolving minerals in cement matrix, alite, and belite, and obtain their activation energy, dissolution rate dependence with ΔG, and dissolution rate dependence with dislocation coalescence. Results help to shed light on the cement hydration understanding and question suggested theories in the bibliography.

2. Methods

We use the newly developed KMC code, KIMERA (Martin et al 2020), which is efficient and versatile to perform dissolution simulations in the specific structure of any mineral with any initial topography (planes or grains), and Gibbs free energy (ΔG) with the solution by taking ab initio or MD simulation results as necessary input parameters. We use the specific atomic structure in belite, but for alite, we use the known Kossel crystal or terrace-ledge-kink (TLK) model (Oura et al (2003)) since MD simulations (Manzano et al (2015)) and experimental observations (Pustovgar et al (2016)) indicate that alite fast forms a fuzzy surface structure in contact with water, which is more homogeneous than the bulk alite.

3 Results

3.1 Dissolution rate with Delta G

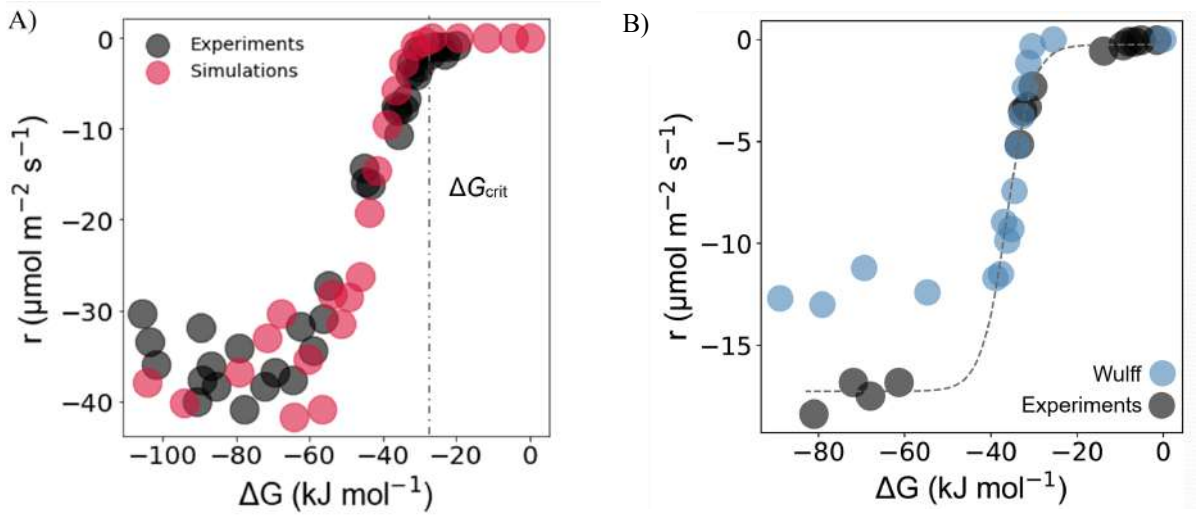


Figure 2. Dissolution rate dependence with ΔG in A) alite and B) belite. Experimental data is extracted from Juilland et al (2017) and Juilland and Gallucci (2015) respectively.

Sigmoid dissolution rate dependence with ΔG is shown in Figure 2 for both alite and belite. The sigmoidal is perfectly reproduced, as well as the critical free energy value ΔG_{crit} when the transition between the low and high rates takes place due to etch pit formation. The three well-known dissolution mechanisms are produced sequentially along the ΔG curve (Martin et al (2019). Starting at low to equilibrium, only low coordinated atoms can dissolve ΔG > -31 kJ mol^{-1} (mechanism I). Moving away from equilibrium ΔG < 31 kJ mol^{-1}, dislocations start to open (mechanism II). Finally, at far from equilibrium conditions, ΔG < 85 (60 in belite) kJ mol^{-1}, Spontaneous pit opening (mechanism III) is produced where etch pits are formed without dislocation assistance. Mechanism III produces a small increment in the dissolution rate which is expected to be hard to detect in experiments because of the overshadowing experimental dispersion.

3.2 Dissolution rate with temperature and activation energy

Figure 3 shows the logarithm of the dissolution rate versus the inverse of temperature to extract the activation energy in alite (A) and belite (B). The activation energy does not change substantially with the change of mechanism (I, II, and III) in different scenarios of ΔG in Alite. Comparison of our simulations

with experiment data (Juilland and Gallucci (2015)) where activation energy decrease to 13-26 kJ mol^{-1} (downward pointing triangles) supports the idea that there is a change of mechanism in the dissolution from surface controlled to transport controlled when moving away from equilibrium since ions cannot evacuate fast enough. Figure 3B shows the results for belite in the planes {001} {010} and {100}, and the Wulff-shaped grain of 40x40x40 belite unit cells. {010} plane presents a dissolution rate around one order of magnitude faster. Such difference is produced by the initial higher density of low coordinated sites. Results of activation energy are close to the known experimental value, in alite Ea = 54.1 ± 1.0 kJ mol^{-1} (49 and 51.1 kJ mol^{-1} in experiments (Juilland and Gallucci (2015) and Thomas (2012))) and in belite Ea = 58 ± 3 kJ mol^{-1} (55 kJ mol^{-1} in experiments (Thomas et al (2017))).

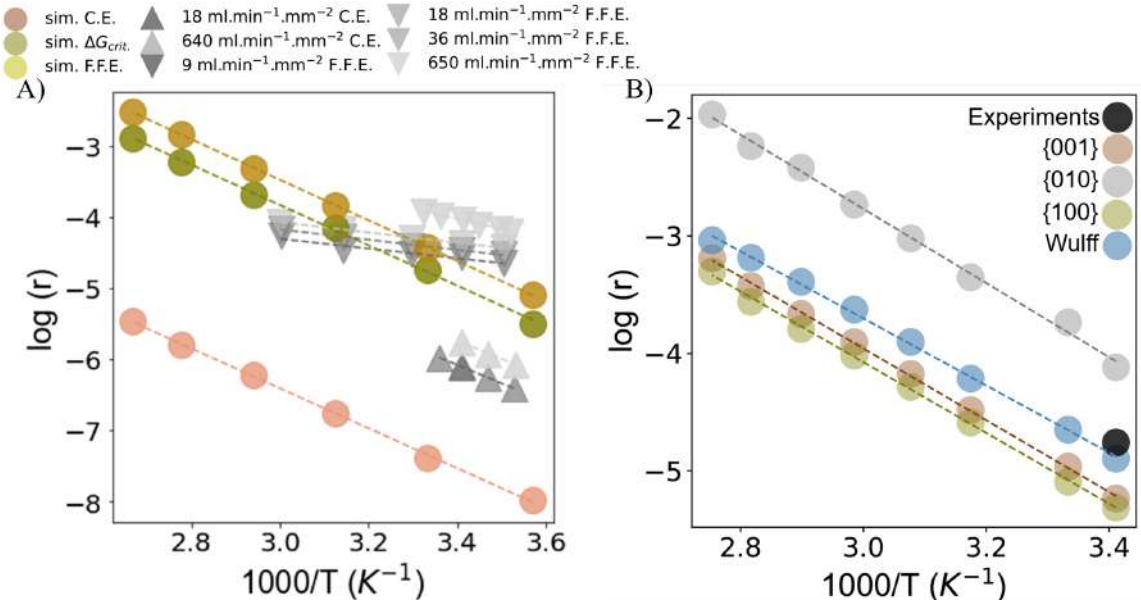


Figure 3. Dissolution rate dependence with temperature in A) alite and B) belite. Experimental data is extracted from Juilland et al (2017) and Juilland and Gallucci (2015) respectively. Triangles in grey in alite represent different water flows. C.E. stands for close to equilibrium and F.F.E. for far from equilibrium. Sim stands for simulations.

3.3 Dissolution rate and dislocation coalescence and exhaustion

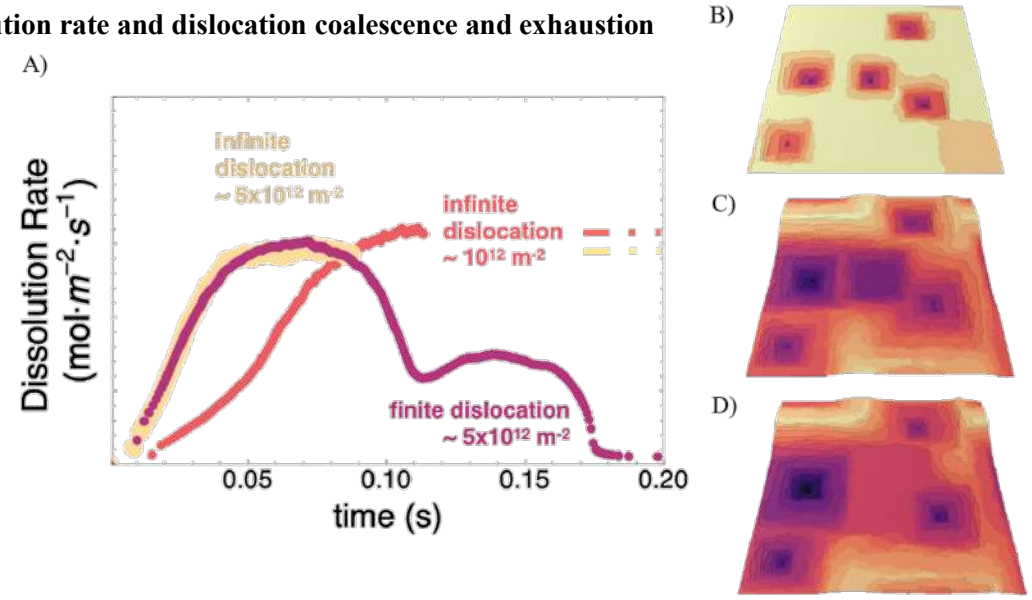


Figure 4. A) Time evolution of the dissolution rate in alite at ΔG = -48 kJ mol^{-1}. B) Snapshot at the biggening of the dissolution in a system with 5 dislocations. C) and D) Exhaustion of the dislocation in the centre.

We have done simulations in alite in 1-dislocation and 5-dislocation systems which correspond to a dislocation density of 10^8 cm^{-2} and 5 10^8 cm^{-2} respectively. Figure 4A represents the time evolution of the dissolution rate for both systems in orange and yellow. Both lines show an acceleration of the dissolution rate with time and reach a similar steady-state indicated by the dotted lines. The steady-state rate is the

same for any dislocation density and its only effect is how fast it is reached, as proposed by Lasaga and Luttge (2001,2003).
The recent dissolution theory proposed by Juilland and Gallucci (2015) attributes the acceleration period to dislocation opening and the deceleration phase to dislocation coalescence. Although the former is supported by our simulations, coalescence does not decrease the dissolution rate. Dislocation coalescence marks the beginning of the dissolution steady state. We propose a possible explanation for the deceleration period, the so-called dislocation exhaustion. In a crystal, the number of dislocations may decrease with the depth, like in $SrTiO_3$ oxide (Szot et al (2018)). Therefore, we perform a simulation in the same 5 dislocation system as before, but with finite dislocations of variable depths. The time evolution of the dissolution rate is represented in the purple line of figure 4A. Figures 4B-D show the etch pitch evolution with time for three different stages. We can observe that the initial acceleration of the rate is analogous to the infinite dislocation systems. When the bottom dislocation is reached, the dissolution rate decreases gradually. When no dislocations are left in the system, the spontaneous pit opening's pace determines the low remnant dissolution rate (mechanism III).

4. Conclusions

We conclude that the coalescence of dislocations will not reduce the dissolution rate of the crystal under ideal conditions. One possible mechanism to reduce the dissolution rate is the exhaustion of dislocations. The preferable dissolution of dislocation spots makes eventually reaches the origin of the crystallographic defect that originates it. Alite and belite activation energy are close in value, 54.1 ± 1.0 kJ mol^{-1} and 58 ± 3 kJ mol^{-1} respectively. This activation energy suffers no change in the different dissolution mechanisms with ΔG. and it suffers a small reduction when considering irregular systems, like grains. Finally, sigmoid function dependence of the dissolution rate with ΔG is reproduced for both minerals. Agreement with experimental observations supports the validity of both our model and the tool KIMERA to perform studies in other minerals.

References

Juilland, P. and Gallucci, E. (2015). "Morpho-topological investigation of the mechanisms and kinetic regimes of alite dissolution". *Cement and Concrete Research*, *76*, 180-191.

Juilland, P., Nicoleau, L., Arvidson, R. S. and Gallucci, E. (2017). "Advances in dissolution understanding and their implications for cement hydration". *RILEM Technical Letters*, *2*, 90-98.

Lasaga, A. C. and Luttge, A. (2001). "Variation of crystal dissolution rate based on a dissolution stepwave model". *Science*, *291*(5512), 2400-2404.

Lasaga, A. C. and Luttge, A. (2003). "A model for crystal dissolution". *European Journal of Mineralogy*, *15*(4), 603-615.

Manzano, H., Durgun, E., López-Arbeloa, I. and Grossman, J. C. (2015). "Insight on tricalcium silicate hydration and dissolution mechanism from molecular simulations". *ACS applied materials & interfaces*, *7*(27), 14726-14733.

Martin, P., Gaitero, J. J., Dolado, J. S., and Manzano, H. (2020). "KIMERA: a kinetic Montecarlo code for mineral dissolution". *Minerals*, *10*(9), 825.

Martin, P., Manzano, H., and Dolado, J. S. (2019). "Mechanisms and dynamics of mineral dissolution: A new kinetic Monte Carlo model". *Advanced Theory and Simulations*, *2*(10), 1900114.

Oura, K., Lifshits, V. G., Saranin, A. A., Zotov, A. V, and Katayama, M. (2013). *Surface science: an introduction*. Springer Science & Business Media.

Pustovgar, E., Sangodkar, R. P., Andreev, A. S., Palacios, M., Chmelka, B. F., Flatt, R. J. and d'Espinose de Lacaillerie, J. B. (2016). "Understanding silicate hydration from quantitative analyses of hydrating tricalcium silicates". *Nature communications*, *7*(1), 10952.

Scrivener, K., Ouzia, A., Juilland, P. and Mohamed, A. K. (2019). "Advances in understanding cement hydration mechanisms". *Cement and Concrete Research*, *124*, 105823.

Szot, K., Rodenbücher, C., Bihlmayer, G., Speier, W., Ishikawa, R., Shibata, N. and Ikuhara, Y. (2018). Influence of dislocations in transition metal oxides on selected physical and chemical properties. *Crystals*, *8*(6), 241.

Thomas, J. J. (2012). "The instantaneous apparent activation energy of cement hydration measured using a novel calorimetry-based method". *Journal of the American Ceramic Society*, *95*(10), 3291-3296.

Thomas, J. J., Ghazizadeh, S. and Masoero, E. (2017). "Kinetic mechanisms and activation energies for hydration of standard and highly reactive forms of β-dicalcium silicate (C2S)". *Cement and Concrete Research*, *100*, 322-328.

The 16th International Congress on the Chemistry of Cement 2023 (ICCC2023)
"Further Reduction of CO_2 -Emissions and Circularity in the Cement and Concrete Industry"
September 18–22, 2023, Bangkok, Thailand

Machine learning atomic potential for C-S-H

J. López-Zorrilla[1*], X. M. Aretxabaleta[2], I. Etxebarria[3] and H. Manzano[4]

[1] *Physics department, University of the Basque Country (UPV/EHU), Leioa, Spain*
Email: jon.lopezz@ehu.eus
[2] *Physics department, University of the Basque Country (UP V/EHU), Leioa, Spain*
Email: xabier.mendez@ehu.eus
[3] *Physics department, University of the Basque Country (UPV/EHU), Leioa, Spain*
Email: inigo.etxebarria@ehu.eus
[4] *Physics department, University of the Basque Country (UPV/EHU), Leioa, Spain*
Email: hegoi.manzano@ehu.eus

ABSTRACT

This paper presents a machine learning atomic potential (MLP) based on artificial neural networks (ANNs) to simulate cement-based materials. The dataset developed for this study consists of nearly 25.000 density functional theory calculations for bulk systems containing combinations of the four main elements present in cement: Ca/Si/O/H, including liquid water, silicon dioxide polymorphs, calcium oxide and hydroxide, tobermorites, alite, belite, and small C-S-H models. Taking that database as an starting point, we train and test a MLP for our systems. Its performance is compared to the reference DFT calculations, and it is found to have high accuracy and efficiency. We show the predictive power of the resulting MLP by computing elastic properties, performing molecular dynamics simulations and computing radial distribution functions for some of the phases included in the data set. Ultimately, this MLP provides a tool to enable atomistic simulations with quantum chemical accuracy but computational impact close to that of classical interatomic potential.

KEYWORDS: *Atomic simulation, Machine learning atomic potential, C-S-H*

1. Introduction

Computational materials science has undergone a transformation in recent years due to the availability of powerful computational tools and the increasing need for materials with specific properties. However, simulating large systems with quantum physical accuracy is often computationally prohibitive, and most computational works on materials rely on less accurate classical force fields. This is particularly true for cement-based materials, which are of great industrial and scientific interest due to their ubiquitous use in construction and their complex microstructures. Several classical force fields have been developed over the years [Mishra et al (2017)], yet it is usually preferable to be able to work at the quantum level.
One approach to overcome the limitations of classical force fields is the use of artificial neural networks (ANNs). In recent years, machine learning potentials (MLPs) [Behler (2011)] have emerged as a promising tool to enable simulations with high accuracy and several orders of magnitude lower computational impact, allowing the simulation of large complex systems with quantum physical accuracy. The ANN potential is trained on a dataset of density functional theory (DFT) calculations for the desired system, and later it can be used to predict the energy and forces of new structures not present in that data set. In fact, this method allows the training of the potential in small systems and then using it to predict the properties of larger ones. Moreover, the time needed for those predictions scales linearly with the system size, while in DFT calculations the scaling is cubic. Another benefit of these models is that chemical bonds are not explicitly included in the potential, thus allowing the study of chemical reactions.
In this work, we present a dataset of DFT calculations for bulk systems containing combinations of the four main elements present in cement: Ca/Si/O/H. This dataset includes liquid and solid water, several

polymorphs of silicon dioxides and calcium oxides and hydroxides, 9-, 11- and 14-tobermorite, alite, belite, and several small C-S-H models. Taking this set of calculations as a starting point, we construct and test an ANN-based MLP for these systems, which is expected to be a powerful tool to simulate cement-based materials.
The potential developed here provides a highly accurate and efficient tool to simulate large-scale cement phases, which is crucial for the design of new materials and the understanding and optimization of existing ones. This approach has the potential to significantly accelerate the pace of materials discovery, paving the way for the development of materials with desired properties for various applications.

2. Related work

There have been several studies published in recent years on the topic of simulating atomic systems using machine learning. Water is a common subject of study in this field due to its complexity, and as a result, many force fields have been developed for it [Cheng et al (2019)]. Silicon oxides have also been studied using this method [Bartók et al (2018)], and there are several potentials available that can replicate various properties of different polymorphs, such as elastic properties and phonon band structures. Similar studies have been developed for calcium oxides [Wu et al (2022)].
In the case of C-S-H-specific phases, there are fewer published works. Kobayashi et al. (2021) developed a machine learning potential for tobermorite minerals that was able to replicate its elastic properties and its interaction with water. They also provided a dataset of nearly 80,000 DFT calculations for tobermorite and liquid and solid water. Zhou et al. (2022) developed another potential for tobermorite minerals and attempted to further improve its performance by testing its ability to simulate disordered C-S-H models. However, this resulted in less accurate predictions.
To the best of our knowledge, these are the only two published works in this area. Our focus is on creating a more general potential that can simulate many of the phases that can appear in cement chemistry, rather than just the tobermorite crystal phases. This includes the above-mentioned water, silicon, and calcium oxides, but also some C_2S and C_3S phases and some C-S-H models.

3. Computational details

The dataset used in this study was constructed through DFT calculations performed using the Quantum Espresso [Giannozzi et al (2009)] package with ONCVPSP norm-conserving pseudopotentials under the generalized gradient approximation. The PBE exchange-correlation functional was utilized, incorporating the Grimme D3 correction to account for the van der Waals interactions. A k-point mesh was chosen to ensure the spacing between k-points in reciprocal space was $0.3Å^{-1}$, allowing for the application of the same principle to systems with different cell sizes. Finally, a plane wave energy cut-off of 100 Ry was used in all cases.
The development of the MLPs was carried out using the ænet-PyTorch package [López-Zorrilla et al (2023)], using the Chebyshev polynomials [Artrith et al (2017)] as atomic descriptors. The selected MLP architecture consists of two hidden layers with 10 neurons each, resulting in a 44-10-10-1 architecture for each atomic element.

4. Results

4.1 Dataset

The systems selected for the database are α-quartz, α-cristobalite, coesite and stishovite SiO_2 polymorphs, cubic and hexagonal CaO, $Ca(OH)_2$ phases from I to V [Aretxabaleta et al (2022)] and portlandite, β-belite, M1-alite, wollastonite, and 9-, 11- and 14-tobermorite. Several small CSH models were also generated based on the brick model proposed by Mohamed et al (2018).
The scheme to construct the database is the following:

- A set of initial structures for the selected system with different unit cell sizes and angles were created. These structures were then relaxed to their corresponding minimum energy configurations using a DFT-based optimization scheme.

- Molecular dynamics (MD) simulations were performed using the LAMMPS software with the reaxFF classical force field at a range of temperatures (300K to 900K) and unit cell sizes (including compressed and expanded cells) to sample the potential energy surface of the systems more thoroughly. Thus the database can provide information about the system's behavior under different thermodynamic conditions. For each simulation, snapshots were taken and their energy and forces were computed using DFT.
- To account for the behavior of the system under non-crystalline conditions, amorphous structures were added to the database, in the same manner as the previous step.

This resulted in a total of 23.478 DFT calculations: 4.038 for water, 5.513 for SiO_2, 1.001 for CaO, 3.700 for $Ca(OH)_2$, 4.980 for systems with Ca/Si/O, and 4.246 for tobermorite crystals and CSH models.

4.2 MLP for Ca/Si/O/H

The MLP for our systems was trained using a combination of reference energy and a 10% fraction of atomic forces in the training process. The resulting potential was evaluated on an independent set of reference calculations that were not part of the training. The evaluation showed high accuracy, with root mean squared errors of 7 meV/atom and 0.4 eV/Å for energy and forces, respectively. The mean relative accuracy of energy and forces was 0.5% and 4%. To test the suitability of our MLP for larger-scale simulations, we conducted three experiments, the results of which are shown in figure 1. It must be noted that each of these simulations was carried out for specific systems, but all of them can be extended to any of the systems included in the dataset with equal accuracy.

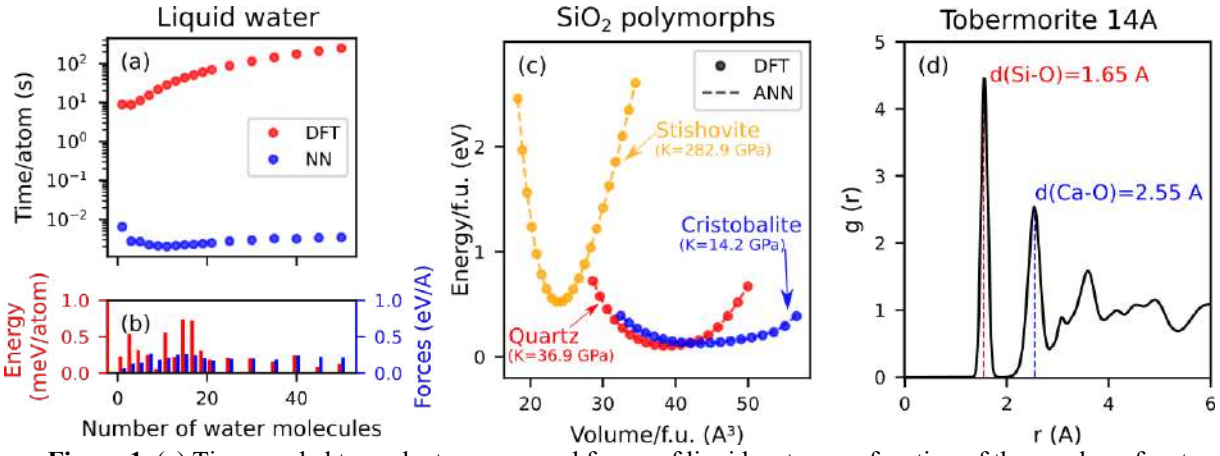


Figure 1. (a) Time needed to evaluate energy and forces of liquid water as a function of the number of water molecules and (b) error of the ANN prediction with respect to DFT for energies and forces. (c) Energy as a function of the unit cell volume for three SiO_2 polymorphs using DFT (circles) and the ANN potential (dashed line). The bulk modulus calculated using the ANN is shown in brackets. (d) Total radial distribution function for tobermorite 14A computed from a MD simulation using the ANN potential. Hydrogen atoms have been excluded from the calculation. The Si-O and Ca-O bond lengths are highlighted in the figure.

Firstly, we measured the speedup of MLPs compared to DFT in evaluating the energy and forces of liquid water. Fig. 1(a) illustrates the time required to evaluate these quantities as a function of the number of water molecules in the unit cell (note that the scale for the time per atom is logarithmic), while Fig. 1(b) shows the corresponding accuracy for each case. The results demonstrated that a well-trained MLP could reproduce the energy and forces of systems not included in the training set with high accuracy and significantly lower computational cost. This is especially relevant for large systems, speeding up the calculations by more than 5 orders of magnitude.

Secondly, we evaluated the energy-volume relationship for some of the silicon oxide polymorphs included in the training set, as shown in Fig. 1(c). The MLP accurately reproduced the DFT equations of state, leading to accurate predictions of elastic properties such as the bulk modulus, in excellent agreement with experimental values and previous works [Bartók et al (2018)].

Finally, we demonstrated the effectiveness of MLPs in combination with molecular dynamics simulations by conducting a simulation of tobermorite 14 Å and computing its radial distribution function from the

resulting trajectory, shown in Fig. 1(d). The simulation was run for 100 ps with a step of 0.5 fs in the NPT ensemble using a 2x2x2 supercell, showing that our potential is able to produce long, stable MD simulations for systems with many atomic species. It also shows that structural properties such as the Si-O and Ca-O bond lengths are in great agreement with the experimental values [Kobayashi et al (2021)].

5. Conclusions

In this work, we present a data set of DFT calculations for bulk systems containing combinations of the four main elements present in cement: Ca/Si/O/H, focusing on creating a general potential that can simulate many of the phases that can appear in cement chemistry, rather than specific crystal phases. Based on this dataset, we develop a machine learning potential and show that it is sufficient to enable simulations on many of those phases, by accurately predicting both system energies and atomic forces of configurations not included in the training data set. Besides the examples shown in this paper, similar results can be achieved for every phase included in the training set. Moreover, the addition of surfaces and clusters is straightforward following the indications proposed in this paper for the construction of the database. We believe that the potential developed in this work provides a highly accurate and efficient tool to simulate large-scale cement phases, and will be a powerful tool for future computational works in the field.

Acknowledgements

This work has been supported by the ‘‘Departamento de Educación, Política Lingüística y Cultura del Gobierno Vasco’’ (IT1458-22), the ‘‘Ministerio de Ciencia e Innovación" (PID2019-106644GB-I00). The authors thank the technical and human support provided by SGIker (UPV/EHU/ ERDF, EU). J.L.-Z. acknowledges financial support from the Basque Country Government (PRE_2019_1_0025).

References

Aretxabaleta, X. M., et al. "A potential CSH nucleation mechanism: atomistic simulations of the portlandite to CSH transformation." Cement and Concrete Research 162 (2022): 106965

Artrith, N. , Urban, A., and Ceder G.. "Efficient and accurate machine-learning interpolation of atomic energies in compositions with many species." Physical Review B 96.1 (2017): 01411

Bartók, A. P., Kermode, J., Bernstein, N., and Csányi, G. (2018). “Machine learning a general-purpose interatomic potential for silicon” *Physical Review X*, 8(4): 041048

Behler, J (2011) "Neural network potential-energy surfaces in chemistry: a tool for large-scale simulations" *Physical Chemistry Chemical Physics,* 13.40: 17930-17955

Cheng, B., Engel, E. A., Behler, J., Dellago, C. and Ceriotti, M. (2019) “Ab initio thermodynamics of liquid and solid water” *Proceedings of the National Academy of Sciences,* 116: 1110–1115

Giannozzi, P., et al. "QUANTUM ESPRESSO: a modular and open-source software project for quantum simulations of materials." Journal of physics: Condensed matter 21.39 (2009): 395502

Kobayashi, K., Nakamura, H., Yamaguchi, A., Itakura, M., Machida, M., & Okumura, M. (2021). “Machine learning potentials for tobermorite minerals” *Computational Materials Science*, 188: 110173

López-Zorrilla, J., Aretxabaleta, M. X., Yue, I., Etxebarria, I., Manzano, H. and Artrith, N. (2023) “ænet-PyTorch: a GPU-supported implementation for machine learning atomic potentials training” *The Journal of Chemical Physics, 158(16).*

Mohamed, A. K., Parker, S. C., Bowen, P., & Galmarini, S. (2018). “An atomistic building block description of CSH-Towards a realistic CSH model” *Cement and Concrete Research*, 107: 221-235

Wu, F., Zheng, F., He, W., Cao, X., Lü, T. Y., Zhu, Z. Z., and Wu, S. (2022). “Deep learning interatomic potential for Ca-O system at high pressure” *Physical Review Materials*, 6(10): 103802

Zhou, Y., Zheng, H., Li, W., Ma, T., & Miao, C. (2022). “A deep learning potential applied in tobermorite phases and extended to calcium silicate hydrates” *Cement and Concrete Research*, 152: 106685

The 16th International Congress on the Chemistry of Cement 2023 (ICCC2023)
"Further Reduction of CO_2 -Emissions and Circularity in the Cement and Concrete Industry"
September 18–22, 2023, Bangkok, Thailand

Assessment of Radiation-Induced Degradation in a Siliceous Rock via Correlative Characterization

K.C. Polavaram and N. Garg*

Department of Civil and Environmental Engineering, University of Illinois Urbana-Champaign, Urbana, United States

Email: kcp3@illinois.edu, nishantg@illinois.edu

ABSTRACT

Deteriorating nuclear infrastructure escalates the need for accurate characterization of radiation damage in various structural components of a nuclear power plant, including the concrete biological shield (CBS). Prolonged exposure of concrete in CBS to neutron radiation induces damage from cracking and residual stresses caused by radiation-induced volumetric expansion (RIVE) of the different mineral components in aggregates. Most studies have investigated irradiation damage in pure and single-phased minerals. However, a comprehensive assessment of irradiated multi-phase polycrystalline materials such as siliceous rocks via spatial characterization has not been performed. Here, we adopt a multi-modal imaging protocol using chemical (Raman imaging, laser microscopy, scanning electron microscopy) and mechanical (nano-indentation) methods to create information-rich hypermaps of pristine and irradiated surfaces of minerals in a siliceous rock. Specifically, we utilize Si^{2+} ions to mimic neutron radiation and irradiate multi-phase siliceous species (anorthite and augite) that are relevant to concrete. Using this multi-imaging dataset, we elucidate the RIVE of minerals such as anorthite (293.4 nm) using 10 MeV Si^{2+} ions. Likewise, the nanoindentation modulus of anorthite subject to irradiation deteriorates from 103.4 to 91.1 GPa. This multi-modal imaging protocol aids in determining the relative susceptibilities of different minerals to amorphization and advancing the understanding of irradiated silicates.

KEYWORDS: *Raman Imaging, silicates, radiation-induced volumetric expansion, scanning confocal microscopy, multi-modal imaging*

1. Introduction

Extension in the lifetime of nuclear power plants has developed an interest in the long-term aging behavior of concrete. Cracking and radiation-induced volumetric expansion (RIVE) (Le Pape et al. (2020)) of the mineral components in aggregates occur as a result of neutron radiation, and depends on several factors such as the mineralogical characteristics and chemical nature of the aggregates e.g., composition, crystallinity, grain size, and phase distribution. Previous studies on radiation damage quantified the change in bulk properties and the dosages at which certain siliceous minerals get amorphized. However, a thorough assessment of the damaged and irradiated surfaces has not been done.

Several methods have been developed to characterize and understand the chemical and phase composition of composite aggregates. For rock mineralogy, the methods typically used are optical petrography (Williams et al. (1982)), scanning electron microscopy using Energy Dispersive X-ray Spectroscopy (SEM-EDS) (Münch et al. (2015)), Electron Probe Micro Analysis (Genkin et al. (1998); Torpy et al. (2020)) (EPMA), X-ray diffraction (XRD) on bulk specimens (Artioli et al. (2010)), near (Rossel & Chen (2011)) and mid-range (Christensen et al. (2004)) infrared spectroscopy (IR), and Raman imaging (Polavaram & Garg (2021b, 2021a); Srivastava & Garg (2022)). Here, we use Raman imaging and SEM imaging combined with laser microscopy and nano-indentation to comprehensively assess the irradiated

surfaces before and after conducting irradiations. Specifically, we developed a multi-modal imaging protocol to assess the extent of radiation damage on different mineral surfaces.

2. Methods

2.1 Sample Preparation

A natural siliceous rock was cored to a diameter of 0.5", and the cores were sliced into thin discs of 2 mm thickness. These discs were polished using Si-C paper (1200, 800, 600, and 400 grit) and diamond pastes (5, 3, 2, and 1 μm).

2.2 Raman Imaging

Raman spectra were collected using a Raman confocal microscope (WITec Alpha 300 series SNOM microscope) on a siliceous rock. Polarized Raman spectra were obtained using a 532 nm excitation laser with an excitation power of 10 mW and a 600 gr/mm grating coupled with a charged coupled device (CCD).

2.3 Scanning Electron Microscopy

Electron imaging and EDS mapping were done using an environmental scanning electron microscope coupled with an Energy Dispersive X-ray Spectrometer (EDS). Secondary electron and backscattered images were captured in low vacuum mode with an accelerating voltage of 10.00 kV, a spot size of 5 nm, and a chamber pressure of 1 Torr.

2.4 Confocal Laser Scanning Microscopy

Optical and height images of the surfaces were measured using a confocal laser scanning microscope (CLSM Keyence VK-X1000). Regions of interest (ROI, 2.5 x 5 mm) were scanned using a 20x objective. The resolutions of the measurements were 0.05 μm in the x and y dimensions and 0.02 μm in the z dimensions.

2.5 Nanoindentation

Modulus mapping was done using a nanoindenter (Hysitron TI-950 Triboindenter) equipped with a Berkovich tip. Scans with a grid spacing of 3 μm were performed using the scanning capability of the indenter transducer. The maximum force and spacing were carefully selected so that the individual indents did not affect each other.

3. Results and Discussion

3.1 Chemical Imaging

Silicon ion radiation (10 MeV energy and 10^{16} Si/cm^2 fluence) was used to irradiate an area rich in anorthite and augite on a siliceous rock. Raman imaging was performed on this sample (on irradiated area), and the corresponding phase maps of the different minerals are shown in Fig. 1a. Augite-1, and augite-2 are two forms of augite (grains with different crystalline orientations) that are present in this sample, along with anorthite. The corresponding Raman spectra of these phases are shown in Fig. 1b. The back-scattered image in Fig. 1c shows a contrast between the augite and anorthite phases. Augite has heavy elements like Fe in it and hence, appears brighter when compared to anorthite in the back-scattered image. Finally, the difference profile in Fig. 1d obtained from the height (pre and post) images shows the radiation-induced volumetric expansion in these minerals. The blue and red regions denote expansion and contraction, respectively. We can also observe that the augite region expands more (step height of 698.4) than the anorthite region (step height of 293.4 nm) from its brighter shade of blue.

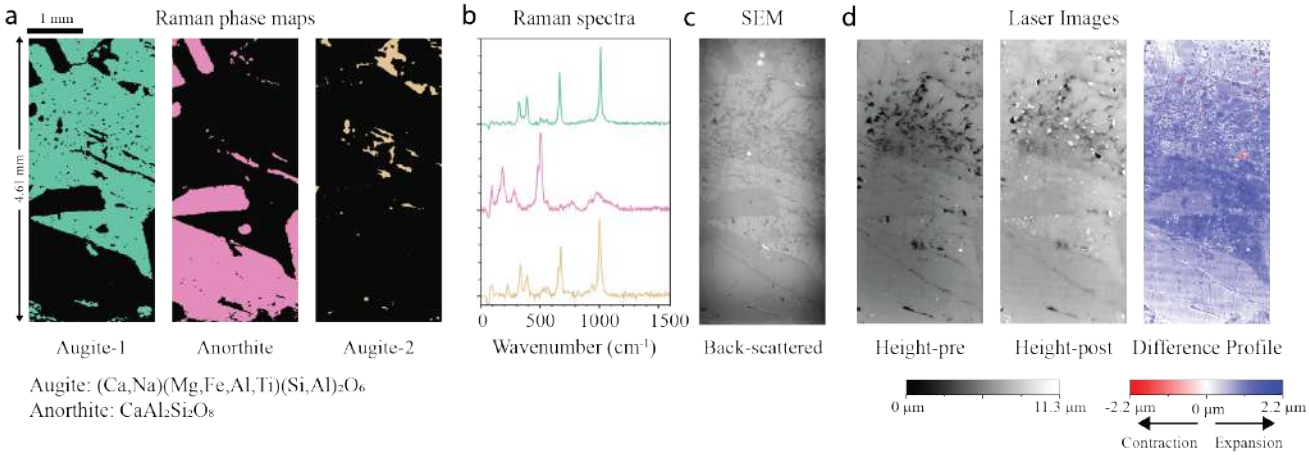


Figure 1. Multi-imaging on a siliceous rock. a) Raman imaging, b) Raman spectra of phases, c) Back-scattered image, and d) Height profiles obtained before and after radiation exposure along with difference image.

The volumetric expansions quantified from the difference profiles shown in Fig. 1 for different minerals can be used to calculate the apparent deformation (ratio of volumetric expansion to the projected range of ions into the mineral). Using the expansion measured using laser microscopy (293.4 nm) and known value of ion penetration calculated from SRIM (Ziegler et al., 2010) (4090 nm), the apparent deformation is 0.071 for anorthite in the current context. This is greater than the theoretical amorphization limit (0.068) of anorthite irradiated with 10 MeV Si^{2+} ions, indicating that the mineral is amorphized.

3.2 Mechanical Imaging

Nanoindentation was performed on pristine and irradiated surfaces of an irradiated window in a siliceous rock. The nanoindentation modulus of a mineral obtained after irradiation depends largely on the change in elastic modulus of each crystal present and the cumulative characteristics of grain boundaries in a rock. Hence, we measured the modulus at the center of the grains and assumed a direct dependence of the elastic modulus with the reduced modulus obtained from nanoindentation. Moreover, the Raman phase maps indicate that at a particular location (where mineral phase maps do not overlap), the observed mineral is present all the way from the surface and within the axial resolution limit (1450 nm) of the Raman microscope. Hence, we can make an unfailing assumption that the indents are made at locations where multiple phases are not present along the indentation depth. The corresponding modulus maps are reported in Fig. 2a. The drop in nanoindentation modulus from the pristine (103.4 GPa) to irradiated (91.1 GPa) regions of anorthite can be seen from these maps. Fig. 2b shows the shift in the probability density peak to the left (softening). By assimilating all the maps, we can elucidate RIVE and the associated mechanical properties of siliceous minerals subject to irradiation.

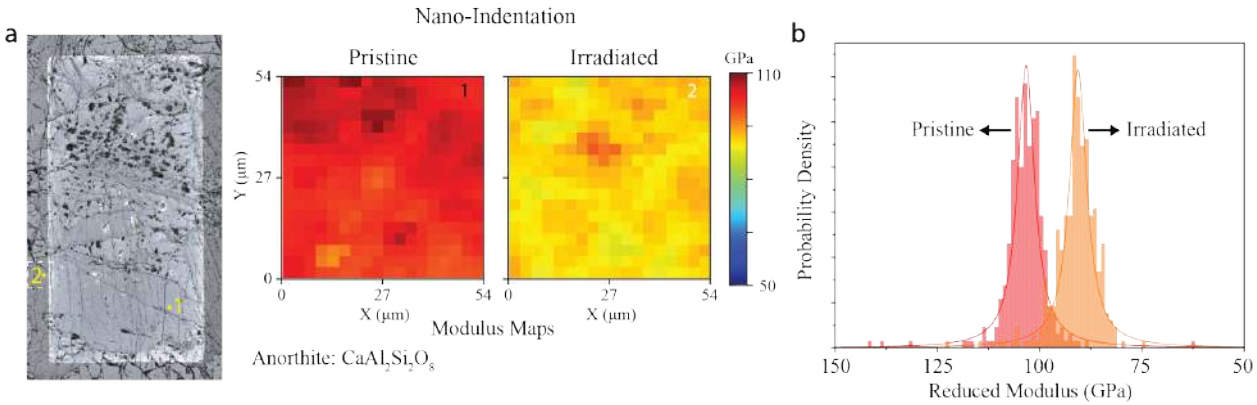


Figure 2. a) Nanoindentation performed on pristine and irradiated surfaces on a siliceous rock. The modulus maps of region 1 (pristine) and region 2 (irradiated) are shown. b) Probability density distribution of reduced modulus of anorthite on pristine and radiated surfaces. The shift of peak towards the left (reduction in modulus from 103.4 to 91.1 GPa) upon irradiation can be seen.

4. Conclusions

The apparent deformations obtained from merging Raman imaging and laser microscopy can be compared with the theoretical amorphization limits to determine the dosage parameters resulting in the amorphization of a particular mineral. The drop in the nanoindentation modulus of various grains (103.4 to 91.1 GPa for the chosen grain) enables an understanding of the effect of grain orientation relative to the direction of incoming irradiation on radiation damage. Moreover, the different minerals in the chosen rock are present in a composite environment, similar to the heterogeneous distribution of minerals in concrete. Hence, analyzing the drop in modulus and measuring the volumetric expansion in a composite, multi-phase environment results in a realistic understanding of radiation damage.

Acknowledgments

This research was carried out in part in the Materials Research Laboratory Central Research Facilities, Microscopy Suite at the Beckman Institute of Advanced Science and Technology, and Core Facilities at the Carl R. Woese Institute of Genomic Biology at the University of Illinois. In addition, the authors acknowledge support from the Center for Integrated Nanotechnologies (CINT), Los Alamos National Laboratory (LANL). The authors also acknowledge support from the U.S. Department of Energy's Nuclear Energy University Program (DOE-NEUP: DE- NE0008886).

References

Artioli, G., Cerulli, T., Cruciani, G., Dalconi, M. C., Ferrari, G., Parisatto, M., Rack, A., & Tucoulou, R. (2010). X-ray diffraction microtomography (XRD-CT), a novel tool for non-invasive mapping of phase development in cement materials. *Analytical and Bioanalytical Chemistry*, *397*(6), 2131–2136.

Christensen, P. R., Jakosky, B. M., Kieffer, H. H., Malin, M. C., McSween, H. Y., Nealson, K., Mehall, G. L., Silverman, S. H., Ferry, S., Caplinger, M., & Ravine, M. (2004). The Thermal Emission Imaging System (THEMIS) for the Mars 2001 Odyssey Mission. *Space Science Reviews*, *110*(1), 85–130.

Genkin, A. D., Bortnikov, N. S., Cabri, L. J., Wagner, F. E., Stanley, C. J., Safonov, Y. G., Mcmahon, G., Friedl, J., Kerzin, A. L., & Gamyanin, G. N. (1998). A multidisciplinary study of invisible gold in arsenopyrite from four mesothermal gold deposits in Siberia, Russian Federation. *Economic Geology*, *93*(4), 463–487.

Le Pape, Y., Sanahuja, J., & Alsaid, M. H. F. (2020). Irradiation-induced damage in concrete-forming aggregates: revisiting literature data through micromechanics. *Materials and Structures*, *53*, 1–35.

Münch, B., Martin, L. H. J., & Leemann, A. (2015). Segmentation of elemental EDS maps by means of multiple clustering combined with phase identification. *Journal of Microscopy*, *260*(3), 411–426.

Polavaram, K. C., & Garg, N. (2021a). Enabling phase quantification of anhydrous cements via Raman imaging. *Cement and Concrete Research*, *150*, 106592.

Polavaram, K. C., & Garg, N. (2021b). High-fidelity and high-resolution phase mapping of granites via confocal Raman imaging. *Scientific Reports*, *11*(1), 8022.

Rossel, R. A. V., & Chen, C. (2011). Digitally mapping the information content of visible–near infrared spectra of surficial Australian soils. *Remote Sensing of Environment*, *115*(6), 1443–1455.

Srivastava, S., & Garg, N. (2022). Tracking spatiotemporal evolution of cementitious carbonation via Raman imaging. *Journal of Raman Spectroscopy*, *n/a*(n/a).

Torpy, A., Wilson, N. C., MacRae, C. M., Pownceby, M. I., Biswas, P. K., Rahman, M. A., & Zaman, M. N. (2020). Deciphering the Complex Mineralogy of River Sand Deposits through Clustering and Quantification of Hyperspectral X-Ray Maps. *Microscopy and Microanalysis*, 768–792.

Williams, H., Turner, F. J., & Gilbert, C. M. (1982). *Petrography: an introduction to the study of rocks in thin sections.* W.H.Freeman.

Ziegler, J. F., Ziegler, M. D., & Biersack, J. P. (2010). SRIM – The stopping and range of ions in matter (2010). *Nuclear Instruments and Methods in Physics Research Section B: Beam Interactions with Materials and Atoms*, *268*(11), 1818–1823.

The 16th International Congress on the Chemistry of Cement 2023 (ICCC2023)
"Further Reduction of CO_2 -Emissions and Circularity in the Cement and Concrete Industry"
September 18–22, 2023, Bangkok, Thailand

Solid state NMR study of the hydration of a fast-setting ternary binder added with lithium carbonate or trisodium-citrate

R. Sassi, F. Fayon, E. Chesneau and V. Montouillout *

CEMHTI, CNRS-UPR3079, Univ. Orléans, F-45071 Orléans, France

franck.fayon@cnrs-orleans.fr

erwanchesneau@gmail.com

valerie.montouillout@cnrs-orleans.fr

ABSTRACT

In this study, high resolution solid-state NMR was used to investigate the hydration kinetic and the structural modifications within a ternary binder composed of white Portland cement, calcium aluminate cement and calcium sulfate, with or without addition of two set modifiers separately (the lithium carbonate Li_2CO_3 and the tri-sodium citrate $Na_3C_6H_5O_7$). ^{27}Al MQ-MAS and {^{1}H}-^{27}Al Cross-Polarization MAS NMR experiments were combined to distinguish all the aluminum species present in the system before and during the hydration process. Similarly, {^{1}H}-^{29}Si CP-MAS NMR and ^{29}Si MAS NMR were employed to characterize the different silicate phases on the mixture during the cement setting. The NMR experiments were performed ex-situ on samples hydrated between two hours and 28 days. Simultaneous fits of complete set of spectra with stoichiometric constraints were performed to quantify the aluminum and silicon present in each phase. The precipitation kinetic and proportions of hydrate phases and their microstructural organization were correlated to the early age mechanical strength. The plain ternary binder was considered as a reference to observe the acceleration and delay as well as the structural impact of the set accelerator and the set retarder.

KEYWORDS: *NMR, cement, hydration, microstructure, additives*

1. Introduction

The fast-setting tile adhesive formulations generally include a mix of multiple mineral binders with additives such as set retarders, accelerators, rheology modifiers, water reducers, etc. These additives are commonly used to modify and tailor cement properties like mechanical strength development over short and long periods. However, their effects on the structure and microstructure of the phases resulting from the hydration remain rather unclear. Indeed, cement hydration is already a complex process involving precipitation of multiple stable and metastable phases and the addition of set modifiers can make its hydration process even harder to tackle. In addition to DRX, high-resolution solid-state Nuclear Magnetic Resonance appears as a powerful tool to identify and quantify the aluminate and silicate, crystalline, disordered and amorphous phases in the systems, which represent the main phases involved in the strengthening, Walkley (2019), Skibsted (1993), Skibsted (1995).

In our study, the fast-setting binder is composed of ordinary white Portland cement, OPC, supplemented with the calcium aluminate cement, CAC and addition of anhydrite as sulfates source. By now, it is well established that the phases formed during hydration were Ettringite, AFm, Stratlingite and C-A-S-H. However, their kinetic of formation as well as the amount formed can be modified according to the starting proportions, the w/c ratio and the possible addition of additives. These modifications would have a significant impact on the mechanical properties of the system. The aim of this work is to study the

effect of two additives, lithium carbonate or trisodium citrate, on the hydration kinetics of the binder described above. The impact of the latter have been widely described from a mechanical point of view, Cau Dit Coumes (2017), Castro-Cabado (2016), but only few researches were focused on the microstructural changes that occur in the systems. Then, we propose to follow the consumption and the formation of phases, ex-situ, on samples hydrated between two hours and 28 days using DRX and a panel of high-resolution solid-state NMR techniques. ^{27}Al and ^{29}Si MAS NMR experiments allow the highlighting and quantification of silicates and aluminates species even at the early stages of hydration.

2. Materials and methods

The studied system is composed of 53 wt.% white Portland cement (CEMII52.5 N white Le Tail) and 32 wt.% calcium aluminate cement CAC (Ternal White) obtained from Lafarge-Holcim cement Co. and IMERYS cement Co. respectively. The main source of calcium sulfate was 15 wt.% anhydrite originated from SMA Faulquemont. To this mixture is added either 0.33% lithium carbonate or 0.5% tri-sodium citrate. The dry mixing powders were stirred for 10 minutes, and left to rest for 24 hours. Then, they were hydrated with water to binder ratio equals to 0.72 in endogenous conditions to avoid their carbonation. The solvent exchange method, using acetone, was applied to stop the reaction at different stages [4]. The pastes were mashed then dipped in acetone for 15 minutes before being filtered on a Büchner filter. In the last step, the powders were dried in a vacuum (10^{-3} bars) for 15 minutes. The obtained samples were then characterized shortly after the hydration stoppage to prevent any possible continuation of the hydration or contamination with atmospheric CO_2.

In order to follow the structural changes of the materials during hydration, all samples have been characterized by high-resolution solid-state NMR. Quantitative single pulse ^{27}Al NMR experiments as well as ^{27}Al shifted echo MQ-MAS Massiot (1996) providing very high-resolution 2D spectra and ^{1}H-^{27}Al CP-MAS experiments allowing the selective observation of nuclei in the hydrated phases were performed on a Bruker 850 AVANCE III (20.0 T) spectrometer operating at a Larmor frequency of 221.6 MHz for ^{27}Al and 850 MHz for ^{1}H. 2.5 mm Bruker MAS probe was used allowing the rotors to reach a spinning frequency of 30 kHz. For all these experiments, the chemical shifts were referenced towards $Al(NO_3)_3$, 1 mol L^{-1} In parallel, ^{29}Si single pulse MAS and ^{1}H-^{29}Si CP-MAS NMR experiments were performed on a Bruker 400 AVANCE II spectrometer using 4 mm Bruker MAS probe, a spinning rate of ν_{rot}=10kHz and the chemical shifts were referenced relatively to TMS (tetramethylsilane). All the ^{27}Al spectra were fitted using the DMFit software available free on the web, Massiot (2002).

3. Results and discussion

The obtained MAS NMR spectra are complex because they contain both the anhydrous starting products and the hydrated phases; most of the signals overlap. However, the joint use of MQMAS and CP-MAS experiments allow us to simulate the ^{27}Al MAS spectrum and to estimate the proportion of aluminum present in each phase. The procedure is the same for silicon spectra. Figure 1 shows an example of deconvolution for a sample that has been hydrated for 3 days. The assignment of the different components was based on pure phase spectra when possible and on literature data.

Thus, thanks to an important and rigorous work of simulation, we were able to estimate the composition of the cementitious matrix at each deadline and then to trace the kinetics of hydration of the mixture (cf Figure 2).

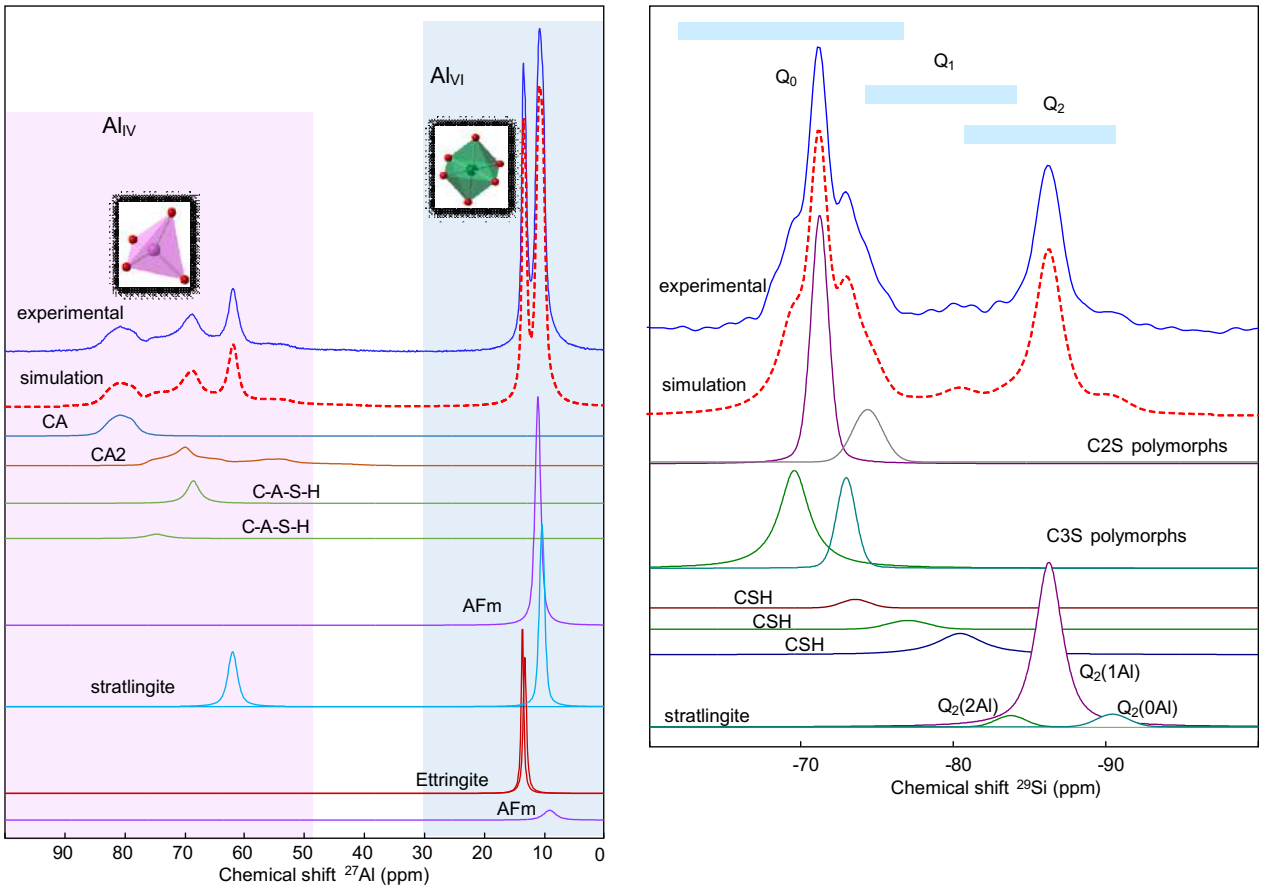


Fig. 1: Deconvolution and attribution of the different components of the ^{27}Al and ^{29}Si spectra of a sample hydrated for 3 days.

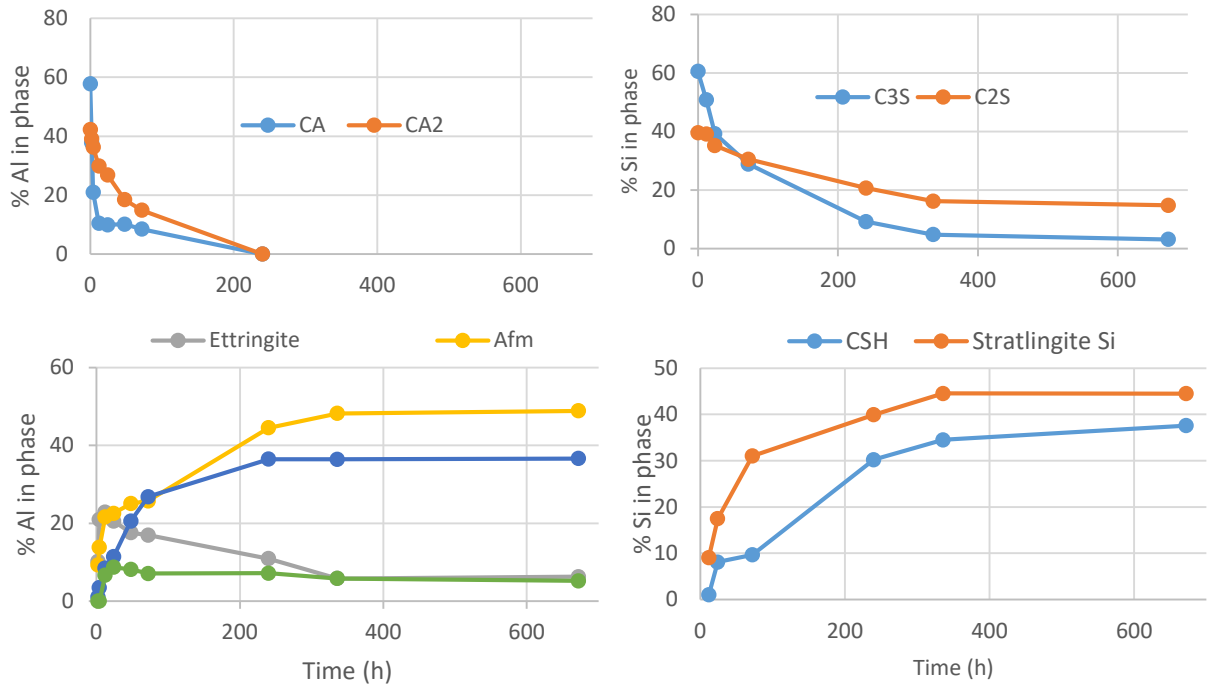


Fig. 2: Kinetics of hydration of a ternary binder

It appears clearly that the aluminate phases of the CAC dissolve almost instantaneously, allowing by reaction with the sulfates of the anhydrite, the very fast precipitation of Ettringite and AFm. The dissolution of silicates occurs only in a second time, after 12 hours of hydration. It is then that the hydrated alumino-silicate phases Stratlingite and C-A-S-H, begin to precipitate which will give the final mechanical properties. The same analyses were conducted on fast-setting binder with additive. The DRX analyses indicate that the same phases are formed as in the case of ternary system. However, the NMR study shows different dissolution and precipitation kinetics.The lithium carbonate has the effect of promoting the precipitation of aluminosilicate phases that appear from the first 4 hours of hydration. These phases intensify the rigidification of the material and take part in the early development of mechanical resistances. However, in the long term, they seem to hinder the dissolution of the CA and CA2 phases which are still present even after 28 days of hydration. On the other hand, trisodium citrate plays well the role of retarder. It binds to the CA and CA2 grains and prevents the precipitation of AFm. This effect ceases after about 10 hours of hydration, the time it takes for the solution to become saturated with ions. The reactions then follow as in the ternary systems.

4. Conclusion

We have shown that in high aluminum content cementitious systems, aluminate phases created in the first hours generate early mechanical properties, but that very quickly aluminosilicate phases precipitate playing a crucial role in the medium and long term properties. If stratlingite has a well defined structure, C-(A)-S-H are much more complex, with variable chain lengths and the substitution of silicon by aluminum in various proportions. The addition of molecules in the system modifies the kinetics of dissolution-precipitation reactions. However, the terms "retarder" or "accelerator" are very simplistic. Indeed, these compounds do not only have the effect of shifting all the kinetics, they play specifically on the formation of certain phases and lead to modifications of the whole chemistry of the systems. Their influence is visible in the properties at 28 days

References

Castro-Cabado M., Casado A., San Rom´ an J. (2016), “Effect of CaO in the thermal crosslinking of maltodextrin and citric acid: a cooperative action of condensation and ionic interactions“, *J. Appl. Polym. Sci*. 133, 44203.

Cau Dit Coumes, C.; Dhoury, M.; Champenois, J.-B.; Mercier, C.; Damidot, D. (2017) “Physico-chemical mechanisms involved in the acceleration of the hydration of calcium sulfoaluminate cement by lithium ions“ *Cem. Concr. Res.* 96(4) 42-51

Massiot D., Touzo B., Trumeau D., Coutures J.P., Virlet J., Florian P., Grandinetti P.J. (1996) 'Two-dimensiontal Magic-Angle Spinning Isotropic Reconstruction Sequences for Quadrupolar Nuclei.', *Solid State NMR* 6 73-83

Massiot D., Fayon F., Capron M., King I., Le Calvé S., Alonso B., Durand J.O., Bujoli B., Gan Z., Hoatson G., (2002) “Modelling one and two-dimensional solid-state NMR spectra. “, *Magn. Reson. Chem*. 40 70-76

Skibsted J., Henderson E., Jakobsen H.J., (1993) “Characterization of calcium aluminate phases in cements by ^{27}Al MAS NMR spectroscopy“, *Inorg. Chem.* 32 1013 – 1027.

Skibsted J., Jakobsen H.J., Hall C. (1995), “Quantification of calcium phases in Portland cements by ^{29}Si MAS NMR spectroscopy“, *J. Chem. Soc. Faraday Trans.* 91 4423 – 4430.

Walkley, B.; Provis, J. L. (2019) “Solid-State Nuclear Magnetic Resonance Spectroscopy of Cements“. *Materials Today Advances*, 1, 100007.

The 16th International Congress on the Chemistry of Cement 2023 (ICCC2023)
"Further Reduction of CO_2 -Emissions and Circularity in the Cement and Concrete Industry"
September 18–22, 2023, Bangkok, Thailand

Exploring C-S-H clusters with evolutionary algorithms

X. M. Aretxabaleta[1*], J. López-Zorrilla[1], I. Etxebarria[1,2] and H. Manzano[1]

[1] *Fisika Saila, Euskal Herriko Unibertsitatea, UPV/EHU, Sarriena Auzoa z/g 48940 Leioa, Basque Country, Spain*
[2] *EHU Quantum Center, Euskal Herriko Unibertsitatea, UPV/EHU, Spain*

** Email: xabier.mendez@ehu.eus*

ABSTRACT

The C-S-H gel is one of the most important phases in cement hydration. Its nucleation is governed by a non-classical nucleation which contains several steps. In this work it is suggested that pre nucleation clusters (PNCs) play a key role in C-S-H nucleation. Therefore, evolutionary algorithms are used to find the best C-S-H cluster for different stoichiometries. Among other clusters, one very similar to tobermorite, the crystaline structure of C-S-H, is found.

KEYWORDS: *Nucleation, PNC, C-S-H, Evolutionary, Algorithms*

1. Introduction

Cement is the most manufactures material in the world with an annual production of 4 million tons. Once hydrated, C-S-H is one of the main phases of hydrated cement, and thus, it's formation and and atomic structure is of great interest for the cement industry. The atomistic mechanism of the nucleation of C-S-H is still unknown although some theories have already been proposed [Aretxabaleta et al. (2022)]. Time resolved potentiometry and turbidimetry showed that the nucleation of C-S-H is a two-step process, thus probably belonging to the non-classical nucleation framework [Krautwurst et al. (2018)]. There are several nucleation paths within the non-classical nucleation methods. However, most of them have in common the formation of pre-nucleation clusters (PNCs) [Gebauer et al. (2011)]. Therefore, in this paper we propose a nucleation mechanism for C-S-H in which PNCs are an intermediate step in the whole nucleation.

Predicting the structure of low energy clusters can be done using a variety of methods. Simulated annealing (SA) has been used frequently to explore the minimum energy configuration for different materials [Ballone (1990)]. Another very popular method is genetic algorithms (GA) which has been very prosperous in finding the lowest energy clusters in various types of systems such as Lennard Jones clusters [Lyakhov et al. (2013)], TiO2 clusters [Hamad et al. (2005)] or MgO clusters [Johnston et al. (2003)]. Although SA has been successful in exploring the potential energy surface, it has been found to be slower than GA in finding the lowest energy cluster for the ArnH2 system and even unable to find the lowest energy cluster for some Lennard-Jones clusters. It has also been stated that, in general, GA obtain better results than SA especially for larger systems [Judson (1992)].

Therefore, GA have been used in this work to find the best C-S-H PNCs. For that purpose, three different stoichiometries have been chosen and the best clusters were found for those stoichiometries. We have studied clusters with one Ca and Si atom, clusters with two Ca and Si atoms and finally clusters with four Ca and Si atoms. That is to say, the studied clusters are $CSH_{10,}$ $C_2S_2H_{12}$ and $C_4S_4H_8$ where C stands for CaO, S for SiO_2 and H for H_2O. The number of water molecules was chosen so that the first hydration layer is completed.

2. Methods

The prediction of the best clusters for each stoiquiometry was done using the USPEX code, based on an evolutionary algorithm featuring local optimization, real-space representation, and flexible physically motivated variation operators (Lyakhov, 2013 & Oganov, 2006). For each stoiciometry a first generation of 500 clusters were created and relaxed using the ReaxFF force-field [Van Duin et al. (2003), Manzano et al. (2012)]. From this first generation the best clusters were selected to start the evolutionary algorithm with 25 structures per generation. Each generation, the clusters were relaxed using ReaxFF first and then DFT. The DFT minimizations were done using the SIESTA code [Soler et al. (2002)].

To calculate the structural distance between the cluster, the smooth overlap of atomic positions (SOAP) was used [Bartók et al. (2013)]. The calcium, silicon and oxygen atoms were used as center from which the SOAP descriptor was computed using a cut-off of 3.5. 16 radial functions and 12 angular functions were used to expand the descriptor and the best-match structural kernel was used to compute the final structural distance between structures. Then, a dimensionality reduction method called Sketch-map was used to obtain a 2d representation of the explored phase space [Ceriotti (2011)].

3. Results

First, lets analize the results obteined for the CSH_{10} clusters. The structural distance between the clusters have been calculated with SOAP and then a dimensionality reduction method called Sketch-map has been used to plot the estructural distances in a 2d plot. This is shown in Fig. 1 where each point represents a cluster and distance between points represent the structural similarity between those two clusters. The closer they are the more alike they are and viceversa. The sketch-map shows that the low energy complexes [labeled as group I in Fig. 1(a)] all contain a silicate tetrahedrom bonded to a 6 or 7-fold coordinated calcium atom [fig. 1(c)]. There are also some structures with silicate pentahedra. However, the appearance of pentacoordinated silica is expected since silicate pentahedra is a common transition state structure during condensation reactions, especially in high ph environments. The silicon and calcium atom is mostly bonded by one oxygen when silicate tetrahedrom is present. When the silicon atom is pentacoordinated, then the silicon and calcium atoms can also be bonded by two oxygen atoms [Fig. 1(d)].

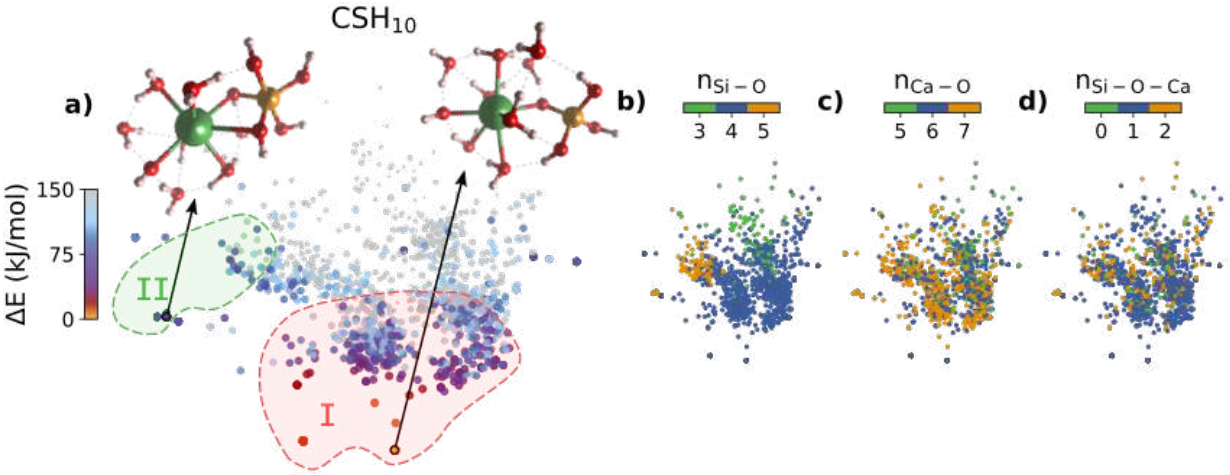


Figure 1: Sketch-map representation of the complex structures found by evolutionary algorithms. Each point represents a different complex, and the distances between points represent the structural similarity between the complexes. The closer the points are, the more similar their structures is and vice versa. In each figure the color represents different properties of the structures. The atomic structure of the best complexes is also shown in (a) where Ca atoms are represented in green, Si atoms in orange, O atoms in red and H atoms in white.

Second, let's analyze the clusters with stoichiometry $C_2S_2H_{12}$. In this case two groups were also found. In group I (where the most stable candidates are found), we found clusters with two silicon monomers, separated from each other. In group II, the founded clusters have a slightly higher energy and contains a silicon dimer. Although the most stable clusters do not contain dimers, we know that in the formation of C-S-H dimers appear from the early stages of hydration and are more common than monomers. For that

reason, clusters with monomers could be an intermediate step in the formation of clusters containing dimers. The transformation from a cluster with monomers to a cluster containing a dimer should have similar energy to that of the condensation reaction, ΔG = 42.28 kJ/mol [Aretxabaleta et al. (2022)].

Finally, looking at the results of the clusters with stoichiometry C_4S_4H, two major groups of low-energy clusters with stoichiometry C4S4H8 have been found. As shown in Fig. 2(a), the main difference between the two main groups is the arrangement of the four silicate monomers. In group I, which contains the more stable clusters, the clusters present a n_{Chain}=4 arrangement, thus containing a trimer. It is known that trimers do not appear at the early stages of C-S-H formation. However, in our simulations they appear as the most stable clusters, probably due to the vacuum conditions in the simulations. On the other hand, group II contains clusters with the arrangement n_{Chain}=2, thus containing a dimer. These clusters agree much more with the experimental results since dimers appear from the early stages of cement hydration.
The dehydration of this kind of clusters has been also studied looking for the best clusters with $C_4Si_4H_4$ and $C_4S_4H_2$ stoiquiometries [Fig. 2(h)]. It can be seen that the dehydration of the clusters can lead to stabilization of the dimers. Moreover, following the trend of the two most hydrated clusters, we clearly see how this dehydrated cluster looks even more like tobermorite. In fact, it is very similar to the cluster presented by Manzano et al. (2007) which was obtained directly from tobermorite. In fact, the cluster found by Manzano et al. was also found by the evolutionary algorithm used in this work, but presented a higher energy of 24 kJ / mol. This result is very important because it shows that the dehydration of the clusters may lead to the formation of tobermorite-like clusters, which could later lead to C-S-H nucleation.

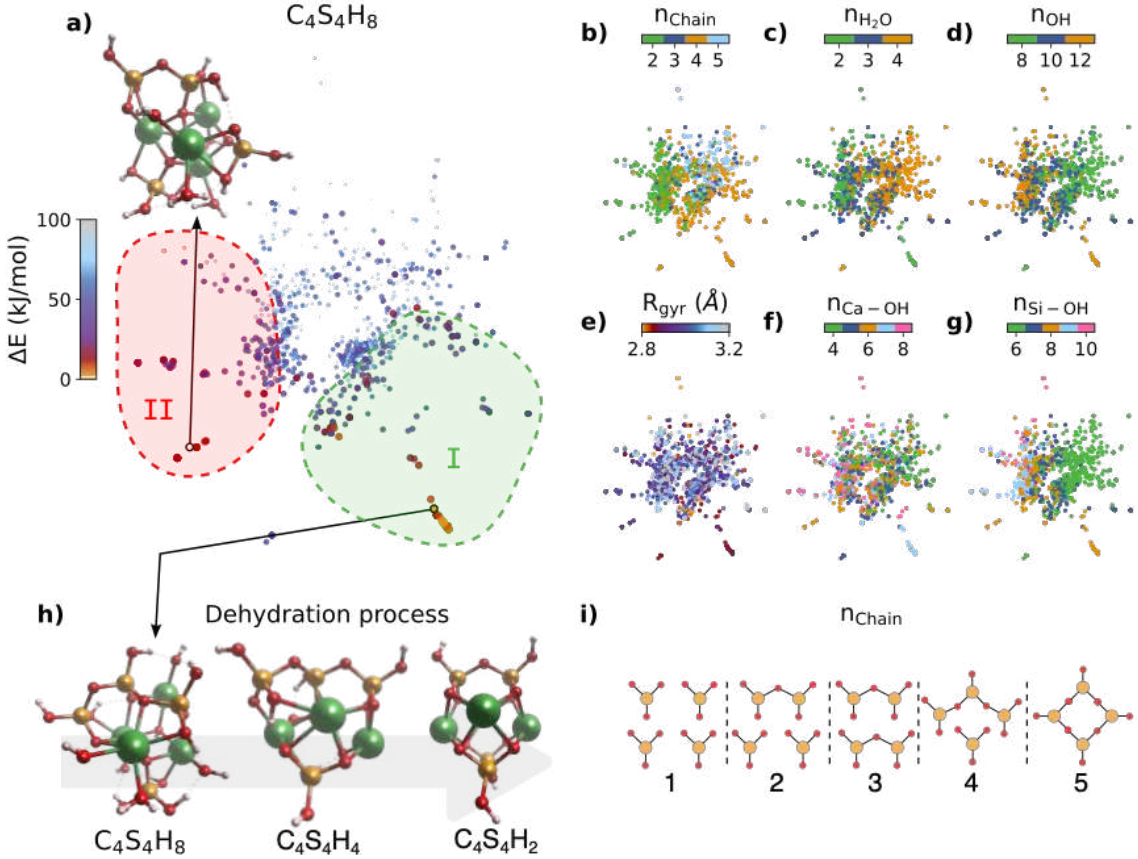


*Figure 2: Sketch-map representation of the PNCs found by evolutionary algorithms. Each point represents a different complex, and the distances between points represent the structural similarity between the complexes. The closer the points are, the more similar their structures is and vice versa. In each figure the color represents different properties of the structures. In figures **(a-g)** the points color represents different properties of the structures. The atomic structure of the best PNC are also shown in **(a)** where Ca atoms are represented in green, Si atoms in orange, O atoms in red and H atoms in white. **(h)** shows the dehydration process of the PNC and **(i)** the different arrangements of the silicates in the clusters.*

4. Conclusions

Evolutionary algorithms have been found to be very useful for exploring the best clusters for different stoichiometries of C-S-H. Exploring the first complexes that would appear in cement hydration, it has been shown that those complexes are formed by a silicate tetrahedrom bonded to a 6 or 7 folded Ca atom.
With the exploration of larger PNCs, there are two main conclusions. The first one is that although knowing that trimers do not appear in cement hydration, in this work it is shown that some of the best clusters contain silicate trimers within their structures. This difference may be attributed to the fact that the cluster search calculations have been made in vacuum or to the fixed stoichiometry of the calculations. Probably, bigger clusters with more Si atoms would present more dimers or pentamers, which are very common in cement hydration. The second conclusion is that the dehydration of the clusters stabilizes the dimers, and therefore, monomers and trimers are less likely to form in less hydrated clusters.
Finally, a very dehydrated cluster has been found that looks very similar to a tobermorite layer. This result is very remarkable since a proposal of a tobermorite-like cluster was presented before taking a small section of a tobermorite layer and minimizing it. The fact that we have now found a similar result with evolutionary algorithms reaffirms the possibility that these clusters form at the early stages of cement hydration. Whether these clusters could form larger tobermorite-like clusters is unknown, but undoubtedly, it would be a study of great interest, as it could broaden the knowledge of the C-S-H nucleation mechanisms.

References

Aretxabaleta, X. M., López-Zorrilla, J., Labbez, C., Etxebarria, I., & Manzano, H. (2022). A potential CSH nucleation mechanism: atomistic simulations of the portlandite to CSH transformation. Cement and Concrete Research, 162, 106965.

Ballone, P., & Milani, P. (1990). Simulated annealing of carbon clusters. Physical Review B, 42(5), 3201.

Bartók, A. P., Kondor, R., & Csányi, G. (2013). On representing chemical environments. Physical Review B, 87(18), 184115.

Ceriotti, M., Tribello, G. A., & Parrinello, M. (2011). Simplifying the representation of complex free-energy landscapes using sketch-map. Proceedings of the National Academy of Sciences, 108(32), 13023-13028.

Gebauer, D., & Cölfen, H. (2011). Prenucleation clusters and non-classical nucleation. Nano Today, 6(6), 564-584.

Hamad, S., Catlow, C. R. A., Woodley, S. M., Lago, S., & Mejias, J. A. (2005). Structure and stability of small TiO2 nanoparticles. The Journal of Physical Chemistry B, 109(33), 15741-15748.

Johnston, R. L. (2003). Evolving better nanoparticles: Genetic algorithms for optimising cluster geometries. Dalton Transactions, (22), 4193-4207.

Judson, R. S., Colvin, M., Meza, J. C., Huffer, A., & Gutierrez, D. (1992). Do intelligent configuration search techniques outperform random search for large molecules?. International Journal of Quantum Chemistry, 44(2), 277-290.

Krautwurst, N., Nicoleau, L., Dietzsch, M., Lieberwirth, I., Labbez, C., Fernandez-Martinez, A., ... & Tremel, W. (2018). Two-step nucleation process of calcium silicate hydrate, the nanobrick of cement. Chemistry of Materials, 30(9), 2895-2904.

Lyakhov, A. O., Oganov, A. R., Stokes, H. T., & Zhu, Q. (2013). New developments in evolutionary structure prediction algorithm USPEX. Computer Physics Communications, 184(4), 1172-1182.

Manzano, H., Ayuela, A., & Dolado, J. S. (2007). On the formation of cementitious C–S–H nanoparticles. Journal of computer-aided materials design, 14, 45-51.

Manzano, H., Pellenq, R. J., Ulm, F. J., Buehler, M. J., & Van Duin, A. C. (2012). Hydration of calcium oxide surface predicted by reactive force field molecular dynamics. Langmuir, 28(9), 4187-4197.

Oganov, A. R., & Glass, C. W. (2006). Crystal structure prediction using ab initio evolutionary techniques: Principles and applications. The Journal of chemical physics, 124(24), 244704.

Soler, J. M., Artacho, E., Gale, J. D., García, A., Junquera, J., Ordejón, P., & Sánchez-Portal, D. (2002). The SIESTA method for ab initio order-N materials simulation. Journal of Physics: Condensed Matter, 14(11), 2745.,

Van Duin, A. C., Strachan, A., Stewman, S., Zhang, Q., Xu, X., & Goddard, W. A. (2003). ReaxFFSiO reactive force field for silicon and silicon oxide systems. The Journal of Physical Chemistry A, 107(19), 3803-3811.

The 16th International Congress on the Chemistry of Cement 2023 (ICCC2023)
"Further Reduction of CO_2 -Emissions and Circularity in the Cement and Concrete Industry"
September 18–22, 2023, Bangkok, Thailand

Structure and mechanical properties of calcium silicate hydrate and calcium carbonate nano composites resolved by reactive molecular dynamics simulations

R.J. Wen[1], Q. Zeng[1*], and B.Q. Gao[1]

[1] *College of Civil Engineering and Architecture, Zhejiang University, Hangzhou, 310058, PR China*
Email: rongjia.wen@zju.edu.cn; Email: cengq14@zju.edu.cn; Email: bqgao@zju.edu.cn

ABSTRACT

Carbonation of concrete generally leads to decalcification of calcium silicate hydrates (CSH) and generation of calcium carbonate (CC), however, the structure and engineering properties of CSH-CC nano composites are far from being fully addressed. Herein, structures of CSH-CC composites in atomic scales are established, and the Ca/Si ratio in CSH is decreased progressively from 1.7 to 0.5 with step width of 0.4 to represent different carbonation degrees. The mechanical properties of the CSH-CC hybrids are explored by reactive molecular dynamics simulations. It shows that the structural patterns of the CSH-CC hybrids greatly depend on the Ca/Si ratio, resulting in different adhesion energy and volume. The decalcification of CSH leads to a significant decrease in the mechanical properties of CSH-CC. Moreover, the dissociation of intralayer calcium can cause the polymerization of silicon chains, the shortening of Ca-O ionic bonds, and the transformation of structural water morphology. The findings would deepen the mechanistic understandings of structural alterations of CSH caused by decalcitification.

KEYWORDS: *Cement nanocomposite; Carbonate; Interfacial strength; Reactive molecular dynamics simulation*

1. Introduction

Over 40 billion tons of concrete produced each year contribute 5-10 % of global anthropogenic carbon dioxide emissions, and one strategy to reduce this environmental footprint is to improve the stiffness or strength of concrete by optimizing the molecular level performance of calcium silicate hydrates (CSH) (Abdolhosseini Qomi *et al.*, 2014). In order to fully understand the properties of cement and develop advanced structural materials with optimal strength and efficiency, it is crucial to decipher the complexity of the atomic structure and mechanical properties of CSH.

Carbonation of concrete generally leads to decalcification of CSH and generation of calcium carbonate (CC). During the decalcification process, the molecular structure of CSH changes from layered crystal to cross-linked glass-like structure, the bound water changes into hydroxyl group with diffusion kinetics (Zhang *et al.*, 2022). The dissociation of intralayer calcium (Ca_s) can significantly aggravate these structural alterations, so Ca/Si ratio may be a key parameter to govern the mechanical response of CSH gels and their actions with other phases e.g., geopolymer binder (GB) (Sadat, Muralidharan and Zhang, 2018) and calcium hydroxide (CH) (Liang, 2020). For the carbonated cement-based materials, the interfacial bonding between CSH and CC may be enhanced due to the strong bridging effect of calcium (Sekkal and Zaoui, 2017). However, it is unclear how does decalcification affect the bonds between CSH and CC.

To this end, a CSH-CC composites model in atomic scales was established, and the Ca/Si ratio in CSH was decreased progressively from 1.7 to 0.5 with step width of 0.4 to represent different carbonation degrees. Based on the reactive force field (ReaxFF), the mechanical properties and interface interaction of the CSH-CC composite were studied by reactive molecular dynamics (MD) simulation.

2. Methodology

2.1. Modeling process

Firstly, based on the tobermorite cell with a layer spacing of 14 Å, the silicon chain was broken by removing the partially neutral SiO_2 (located in the bridged silicon oxygen tetrahedron) to meet the measured Q_n distribution (Q_0 = 0, Q_1 = 0.6, Q_2 = 0.4). Subsequently, the Monte Carlo method was performed to absorb water molecules and calcium ions into above-mentioned model (between Ca-Si layers) to satisfy the measured Ca/Si ratio and H_2O/Si ratio (both 1.7). At the same time, some hydroxyl groups were also absorbed to balance the charge. These parameters are derived from previous reports (Kunhi Mohamed *et al.*, 2018).

To create different initial CSH models with varying Ca/Si ratios, Ca ions were selectively removed from the CSH structure following a specific order of interlayer and then intralayer (Zhang *et al.*, 2022). As for the initial CC model, its cell was expanded to match the lattice parameters of CSH as closely as possible. According to previous reports (Sekkal and Zaoui, 2017), the connection between the surface of (001) CSH and the (104) CC is the most stable, and the initial energy is the lowest when the initial interval between the two is set to 1 Å, so the same setting was adopted in this paper.

2.2 Force field

Compared with the classical ClayFF, ReaxFF consumes more computing resources, but it can describe the breaking and formation of chemical bonds. Therefore, the ReaxFF was used to investigate the structure and mechanical properties of CSH-CC with different Ca/Si ratio in this paper. The ReaxFF is a potential function based on bond order, and its expression is shown in formula 1. The parameters related to C are derived from the metal carbonate force field (Dasgupta, Chen and Van Duin, 2022), and the parameters related to Ca are derived from the Zhang force field (Zhang *et al.*, 2022). The remaining parameters are based on the clay-zeolite force field (Pitman and Van Duin, 2012).

$$E_{sys} = E_{bo} + E_{over} + E_{under} + E_{va} + E_{to} + E_{lp} + E_{vd} + E_{co} \quad (1)$$

Where, E_{sys} is the total energy of system; E_{over} and E_{under} are the energy penalty for over- and under-coordination of atoms, respectively; E_{bo}, E_{va}, E_{to}, E_{lp}, E_{vd} and E_{co} are the bond energy, valence angle energy, torsion angle energy, lone pair energy, Van der Waals energy and Coulomb energy, respectively.

2.3 Simulation detail

MD simulation was carried out in lammps software.

Equilibrium process: the ReaxFF was used in the whole process, and the time step was set to 0.25 fs. First, the temperature was gradually increased from 300 K to 600 K to break through the energy barrier that inhibits structural relaxation. After that, at a constant pressure and temperature (NPT ensemble, 300 K, 1 atm), the final equilibrium state was then reached by further relaxation of 100 ps.

Tensile process: uniaxial tension tests also used NPT ensemble and ReaxFF. The whole system was gradually stretched along the Z direction at a rate of 0.01/ps to study the mechanical response of the systems with different Ca/Si ratios. During the tensile process, the pressure in the X and Y directions was set to 0 to consider the Poisson effect.

3. Results and discussion

Figure 1 illustrates the structural evolution of the CSH-CC composite under tension in the Z direction. The CSH-CC composite is more prone crack at the interlayer position than at the interface, implying that the interfacial bonding strength between CSH and CC is greater than that between Ca-Si layers in CSH,

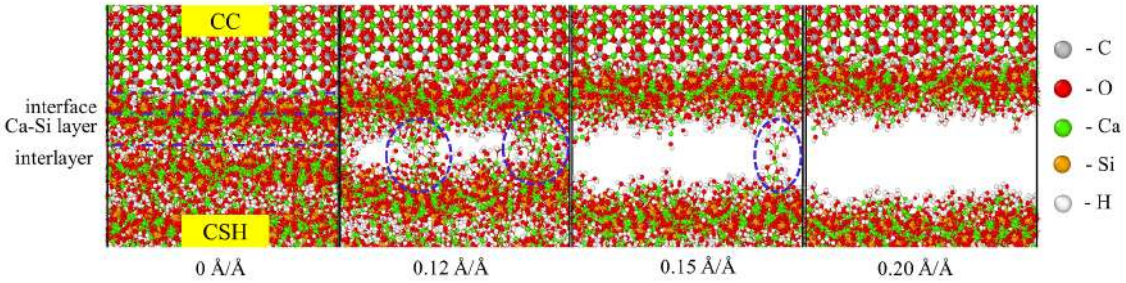


Figure 1. Structural evolutions of CSH-CC composite with Ca/Si ratio of 1.7 at different strain

which is similar to the results of CSH-CH (Liang, 2020) and CSH-GB (Sadat, Muralidharan and Zhang, 2018) composite. During the loading process, the Ca-O ionic bond between the Ca-Si layers is gradually broken, and finally the Ca-Si layer is completely separated.

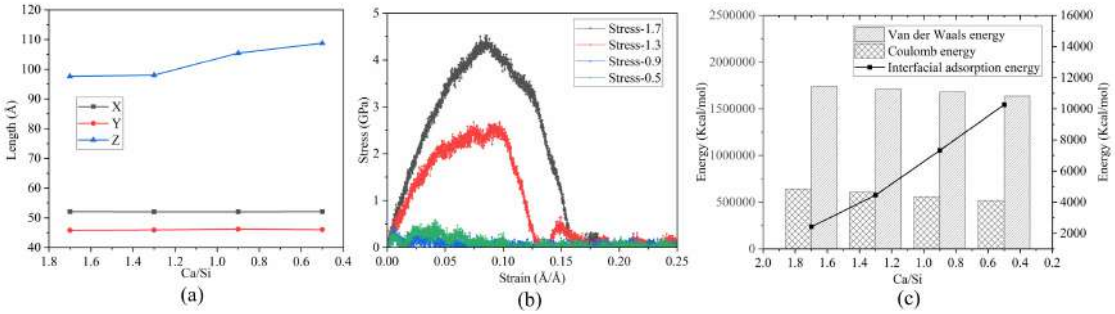


Figure 2. (a) Size, (b) mechanical response and (c) energy of CSH-CC composites with different Ca/Si ratios

Figure 2a shows that the size of CSH-CC composite in X and Y directions remain constant as the Ca/Si ratio decreases. However, when the Ca/Si ratio drops below 0.9 (the interlayer calcium (Ca_w) ions are completely dissociated), the Z direction begins to expand. This expansion is due to the massive loss of calcium as a connecting medium for silicate chains, resulting in electrostatic repulsion between silicate chains. Volume expansion is the prelude of system disintegration. Figure 2b demonstrates that the tensile strength of CSH-CC composite decreases significantly during the decalcification process, as the number of Ca-O ionic bonds is drastically reduced. When Ca_w is completely lost, the bonding between Ca-Si layers is maintained only by hydrogen bond (H-bond). Because the strength of the H-bond is much weaker than the Ca-O ion bond, the tensile strength of the system is almost completely lost. Figure 2c shows the variation of system energy with Ca/Si ratio. With the decrease of Ca/Si ratio, the total energy of the system decreases gradually, signifying the CSH-CC composite becomes more stable after decalcification. Meanwhile, the interfacial adsorption energy of the system increases gradually, suggesting that the connection between CSH and CC also becomes more stable.

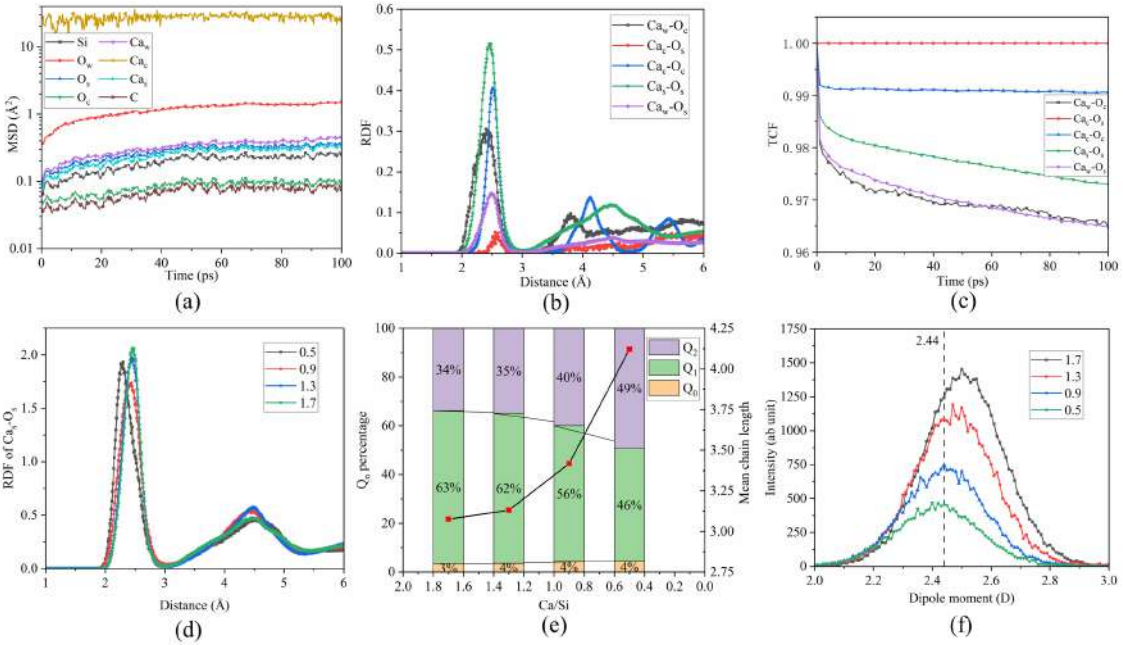


Figure 3. The (a) MSD, (b) RDF, and (c) TCF in CSH-CC with Ca/Si ratio of 1.7; The (d) RDF of Ca_s-O_s, (e) Qn distribution, (f) dipole moment of water in CSH-CC with different Ca/Si ratio

For mean square displacement (MSD), the larger the value, the stronger the motion ability of the corresponding atom. Figure 3a shows the calcium in CC (Ca_c) has the strongest motion capacity among all atoms, even stronger than the oxygen atoms in structural water (O_w). By contrast, the carbon and oxygen atoms in CC (O_c) are less athletic. Therefore, Ca_c may dissociate into the interface area. For radial distribution function (RDF) and time correlation function (TCF), the former can be used to measure whether the ion pair is bonded (the first peak of RDF represents the equilibrium bond length of corresponding ion pair), and the latter can be used to judge the stability of the chemical bond (the larger

the area enclosed by TCF and X axis, the more stable the corresponding chemical bond). From Figure 3b and c, Ca_c can form ionic bonds with the oxygen atoms in silicon chain (O_s), and its stability is the strongest among various Ca-O ionic bonds. This can explain why the cracking position of the CSH-CC composite is not in the interface region during tension. Moreover, on the one hand, Ca-O ionic bonds shorten significantly when the Ca/Si ratio is lower than 0.9 (Figure 3d). Meanwhile, the distribution of Q_n changes (Figure 3e, Q_2 increases and Q_1 decreases). This means that the polymerization of silicon chains occurs. On the other hand, the mean dipole moment of water molecules decreases gradually (Figure 3f), indicating that the structural water changes into free water (2.44 D). These phenomena imply that CSH tends to disintegrate at low Ca/Si ratio.

4. Conclusions

In this paper, reactive molecular dynamics simulations were used to investigate the interfacial interaction mechanism of CSH-CC composites and the influence of Ca/Si ratio. The major conclusions can be summarized as follows:

1. In the CSH-CC composite, due to the bridging interaction of Ca_c-O_s ionic bond, the weakest position is located between the Ca-Si layers in CSH during tension, not at the interface between CSH and CC.
2. The tensile strength of CSH-CC decreases significantly with decalcification. When the interlayer calcium is completely dissociated, the strength drops almost to zero and the volume expands.
3. When the intralayer calcium begins to dissociate, the silicon chain will polymerize, resulting in the change of Q_n distribution in CSH. Meanwhile, the bond length of Ca-O is shortened, and the structural water changes into free water. These indicate that CSH tends to disintegrate at low Ca/Si ratio.

Acknowledgements

This project is financially supported by the National Natural Science Foundation of China (grant no. 52038004).

References

Abdolhosseini Qomi, M.J., Krakowiak, K.J., Bauchy, M., Stewart, K.L., Shahsavari, R., Jagannathan, D., Brommer, D.B., Baronnet, A., Buehler, M.J., Yip, S., Ulm, F.J., Van Vliet, K.J. and Pellenq, R.J.M. (2014) 'Combinatorial molecular optimization of cement hydrates', *Nature Communications*, 5: 1–10.

Dasgupta, N., Chen, C. and Van Duin, A.C.T. (2022) 'Development and application of ReaxFF methodology for understanding the chemical dynamics of metal carbonates in aqueous solutions', *Physical Chemistry Chemical Physics*, 24(5): 3322–3337.

Kunhi Mohamed, A., Parker, S.C., Bowen, P. and Galmarini, S. (2018) 'An atomistic building block description of C-S-H - Towards a realistic C-S-H model', *Cement and Concrete Research*, 107(January): 221–235.

Liang, Y. (2020) 'Mechanical and fracture properties of calcium silicate hydrate and calcium hydroxide composite from reactive molecular dynamics simulations', *Chemical Physics Letters*, 761(October): 138117.

Pitman, M.C. and Van Duin, A.C.T. (2012) 'Dynamics of confined reactive water in smectite clay-zeolite composites', *Journal of the American Chemical Society*, 134(6): 3042–3053.

Sadat, M.R., Muralidharan, K. and Zhang, L. (2018) 'Reactive molecular dynamics simulation of the mechanical behavior of sodium aluminosilicate geopolymer and calcium silicate hydrate composites', *Computational Materials Science*, 150(January): 500–509.

Sekkal, W. and Zaoui, A. (2017) 'Enhancing the interfacial bond strength of cement nanocomposite with carbonate nanostructure', *Composites Part B: Engineering*, 124: 111–119.

Zhang, Y., Guo, L., Shi, J., Luo, Q., Jiang, J. and Hou, D. (2022) 'Full process of calcium silicate hydrate decalcification: Molecular structure, dynamics, and mechanical properties', *Cement and Concrete Research*, 161(April): 106964.

The 16th International Congress on the Chemistry of Cement 2023 (ICCC2023)
"Further Reduction of CO_2 -Emissions and Circularity in the Cement and Concrete Industry"
September 18–22, 2023, Bangkok, Thailand

MD study of radiocesium immobilization in the geopolymer matrix

E. Duque-Redondo[1*], K. Yamada[2], E. Masoero[3], J. Bañuelos Prieto[4], and H. Manzano[5]

[1] Department of Physical Chemistry, University of the Basque Country UPV/EHU, 48080, Bilbao, Spain.

School of Engineering, Newcastle University, Newcastle upon Tyne NE17RU, UK.

Email: eduardo.duque@ehu.eus

[2] Fukushima Branch, National Institute for Environmental Studies, Miharu, Tamura, Fukushima 963-7700, Japan

Email: yamada.kazuo@nies.go.jp

[3] School of Engineering, Newcastle University, Newcastle upon Tyne NE17RU, UK.

School of Engineering, Cardiff University, Cardiff CF24 3AA, UK.

Email: Enrico.Masoero@newcastle.ac.uk

[4] Department of Physical Chemistry, University of the Basque Country UPV/EHU, 48080, Bilbao, Spain.

Email: jorge.banuelos@ehu.eus

[5] Department of Physics, University of the Basque Country UPV/EHU, 48080, Bilbao, Spain.

Email: hegoi.manzano@ehu.eus

ABSTRACT

The high adsorption capacity and low leachability of geopolymers make them potential substitutes for Portland cement in the immobilization of pollutants. Their practical application of geopolymers in this field is limited by a lack of knowledge about how adsorption occurs and how their release can be avoided. Molecular Dynamics simulations were employed in this study to investigate the immobilization of Cs ions in geopolymers, focusing on the role of composition and structural order. Results showed that the most stable configurations for adsorption are found in more crystalline systems and with higher Al contents since they present more favorable adsorption enthalpies and lower diffusion coefficients. In particular, these stable configurations are located near the center of regular 6-membered aluminosilicate rings, where the coordination of Cs with the geopolymer was maximized. The structure of the geopolymers, with closed cavities, also contributes to reduce the migration and enhance the confinement of Cs ions.

KEYWORDS: *Molecular dynamics, Geopolymer, Adsorption, Immobilization, Cesium*

1. Introduction

The geopolymer is an aluminosilicate formed by the reaction of Si- and Al-rich materials with an alkaline activator. This reaction results in a gel structure with mechanical strength similar to that of Portland cement (PC) (Singh and Middendorf, 2020). Geopolymers also exhibit high thermal and chemical resistance, low leachability, and high adsorption capacity (Singh and Middendorf, 2020), making them a promising candidate to replace PC in multiple applications, such as the immobilization of contaminants (Perera *et al.*, 2006). Geopolymers have zeolite-like close cavities at the nanometer level, in which the contaminants can be effectively confined, but their retention capacity depends on several factors, such as the composition, structure, and charge distribution of the geopolymer, or the size and charge of the pollutants.

In this work, we employed molecular dynamics (MD) simulations to study the potential of geopolymers to immobilize radiocesium, one of the most hazardous radioisotopes in spent nuclear fuel due to a long half-life and high specific radioactivity. We analyzed the role of composition and structural order in Cs uptake

by considering geopolymers with Si/Al ratios between 1.4 and 2.0 and three different levels order: crystalline, amorphous, and defective, based on the models from ref (Lolli *et al.*, 2018).

2. Methodology

Twelve different geopolymer systems were simulated, corresponding to the crystalline, defective, and amorphous models, whose development is detailed in ref. (Lolli *et al.*, 2018), with four Si/Al ratios (1.4, 1.6, 1.8, and 2.0) each. A (Na+Cs)/Al ratio of 1, and a Cs/Na ratio of 0.5 was maintained in all systems. The reactive force field ReaxFF (van Duin *et al.*, 2001; Russo and van Duin, 2011) was used to equilibrate the geopolymer models, including a set of parameters for Cs (Fedkin *et al.*, 2019). An equilibration process analogous to that described in ref (Lolli *et al.*, 2018) was followed, involving energy minimization, MD simulations in the isobaric-isothermal (NPT) ensemble at 300K and 1 atm for 1 ns, and further relaxation in the canonical (NVT) ensemble for an additional 1 ns at 300K. Finally, to capture the properties of the system a 5 ns trajectory was recorded in the NVT ensemble at 300K.

3. Results and discussion

To quantitatively study the immobilization of Cs ions in geopolymers as a function of the structural order and matrix composition, the coordination sphere of the Cs ions, the adsorption enthalpies, and the lifetime of the interactions between these ions and the geopolymer have been analyzed for the models with different degree of crystallinity and Si/Al ratios between 1. 4 y 2.0. Likewise, the ability of the ions to move along the pores has been also investigated by calculating the diffusion coefficients.

3.1 Coordination shell of Cs ions

The radial distribution functions (RDFs) and coordination numbers (CNs) of Cs ions to oxygens form the geopolymer (O_{geo}) and water molecules (O_w) were computed to analyze the coordination shells of these ions (see Figure 1). The Si/Al ratio does not significantly affect either the RDFs or the CNs of the Cs-O pairs, but the order of the structure does have a noticeable impact on the intensity and shape of the peaks. In all cases, the Cs-O distances are around 3.1-3.3 Å, in agreement with distances reported from previous studies of 3.0-3.3 Å (Mile *et al.*, 2009; Mähler and Persson, 2011).

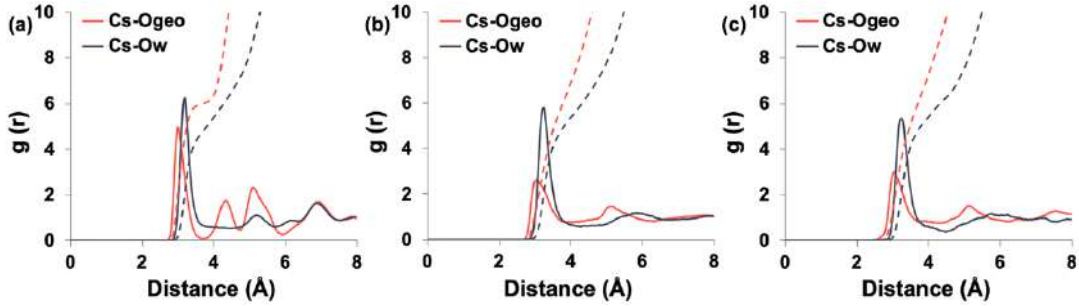


Figure 1. Average RDFs (continuous lines) and CNs (dashed lines) for Cs-O_{geo} (in red) and Cs-O_w (in black) pairs in the (a) crystalline, (b) defective, and (c) amorphous geopolymers.

Table 1. Average CNs for Cs to oxygen atoms from the geopolymer and water at the different levels of disorder.

CN	Crystalline	Defective	Amorphous
Cs-O_{geo}	6.0	5.7	5.8
Cs-O_w	4.7	4.7	4.6
Sum	10.7	10.4	10.4

The crystalline structure of the geopolymer is formed by the bonding of 4- and 6-membered rings, whereas in the non-crystalline systems, larger rings can be found (Lolli *et al.*, 2018). It is known that Cs ions tend to be located in the center of 8-membered rings (Lee *et al.*, 2017), but due to the absence of those rings in the crystalline system, Cs ions are accommodated near the center of 6-membered rings slightly displaced towards the cavity since they do not fit in those rings**.** In this way, Cs ions in the crystalline model coordinate with the 6 oxygen atoms that form the ring (Cs-O_{geo} CN = 6) and complete its coordination sphere with

nearly 5 water molecules from the cavity, as seen in Table 1. The defective model exhibits structural similarity to the crystalline model, with many 6-membered rings where Cs ions can still be adsorbed. However, unlike the crystalline model, these rings are not regular, which makes it difficult to effectively coordinate the Cs ions to all the oxygens in the ring, resulting in CN < 6. To a lesser extent, Cs can be found in larger rings, including 8-membered ones, but these also exhibit a high degree of distortion which, again, results in low CN. On the other hand, the complex structure of the amorphous geopolymer exhibits highly distorted 6- and 8-membered rings that coexist with larger rings where Cs can be accommodated resulting in an average coordination of Cs to O_{geo} of approximately 6. In all systems, Cs ions complete their coordination shells with ~4.6 water molecules leading to total CNs between 10.2 and 10.7, in line with the values found by other authors between 6.5 and 12.0 (Mile *et al.*, 2009; Mähler and Persson, 2011).

3.2 Lifetime of Cs-O interactions

The average autocorrelation functions for Cs-O_{geo} pairs for the three degrees of disorder are shown in Figure 2 (a). The lifetime of Cs-O_{geo} pairs in the crystalline model is approximately 0.22 ns, twice that of defective and amorphous structures, with lifetimes of 0.12 and 0.09 ns, respectively. This indicates stronger Cs-O_{geo} interactions in the former model than in the latter ones. The faster decay for the defective model, in comparison to the crystalline one, is consistent with the lower coordination of Cs with the geopolymer (see Table 1). However, the amorphous structure, with a comparable coordination number to the crystalline one, displays an even faster decay than the defective one, suggesting that structural distortions can significantly impact interaction energies and therefore ion diffusion in these structures.

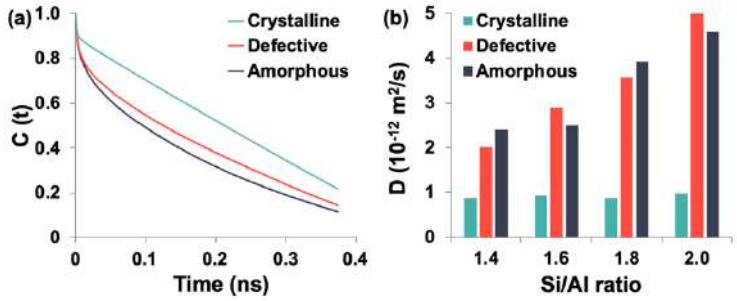


Figure 2. (a) Average autocorrelation functions of Cs–O_{geo} and (b) diffusion coefficients for Cs ions in the crystalline (blue), defective (red), and amorphous (yellow) geopolymer models.

3.3 Adsorption enthalpies of Cs ions

The adsorption enthalpies have been calculated to assess the energy state of Cs ions in the geopolymers at the analyzed Si/Al ratios and level of disorder. These values are shown in Table 2, in which the more negative the value, the more stable the sorption of these cations. Thus, the Cs adsorption is more favorable at lower Si/Al ratios due to the larger presence of negatively charged tetracoordinated Al and in more crystalline systems, where the Cs-O_{geo} interactions are stronger, as seen in Figure 2 (a).

Table 2. Adsorption enthalpies (in kcal/mol) of Cs confined in the analyzed systems.

Si/Al ratio	Crystalline	Defective	Amorphous
1.4	-50.6	-46.7	-44.8
1.6	-48.9	-43.5	-44.2
1.8	-47.8	-42.0	-41.3
2.0	-46.8	-39.7	-40.4

3.4 Diffusion coefficients of Cs ions

To analyze the potential migration of Cs through the porous matrix of the geopolymers, the diffusion coefficients were computed, showing strong dependence not only on the structural order but also on the Si/Al ratio, as can be seen in Figure 2 (b). On the one hand, the increase in the diffusion coefficients observed with increasing Si/Al ratio is due to the decrease of the negative charge of the geopolymers and the consequent reduction of the electrostatic confinement of the Cs cations. On the other hand, the higher

diffusivities in non-crystalline systems can be attributed to the fact that the structural distortions in these systems lead to less energetically stable configurations than in the crystalline system, which facilitates their release and mobility. This is in the line with the adsorption enthalpies shown in Table 2. In any case, the reported values for geopolymer are up to three orders of magnitude lower than in C-(A-)S-H gel (Duque-Redondo *et al.*, 2018, 2021) and bulk water (Yuan-Hui and Gregory, 1974).

4. Conclusions

MD simulations have shown that geopolymers are able to immobilize Cs ions efficiently, even better than other materials like C-(A-)S-H gel, due to structural and electrostatic confinement provided by its structure. The simulations revealed that the local structure in which the ions can be adsorbed is key. In crystalline geopolymers, Cs ions maximize their coordination with the geopolymer when they are located near the center of the 6-membered rings, albeit slightly displaced towards the cavity due to its size. Similar Cs-O_{geo} CNs are found in the non-crystalline structures, as although there are larger rings, they are generally distorted. These distortions reduce the effectiveness of these interactions, lowering the stability of adsorption configurations, especially in the amorphous geopolymer, as revealed by the computed Cs-O_{geo} lifetime and the adsorption enthalpies. Thus, the retention is worse in the amorphous model than in the defective, while Cs immobilization is higher in the crystalline system. Besides, the lower retention capacity translates into higher mobility of Cs ions and higher diffusion coefficients for the Cs confined in the non-crystalline systems. Moreover, as the Si/Al ratio decreases, the electrostatic interactions between Cs and the negatively charged geopolymer increase, improving their adsorption and reducing their diffusivities.

Acknowledgements

The Basque Government funded this research through the IT1639-22 project. E.D.-R. acknowledges the postdoctoral fellowship provided by the "Programa Posdoctoral de Perfeccionamiento de Personal Investigador Doctor" of the Basque Government. We also acknowledge computational resources provided by the Scientific Computing Service from SGIker (UPV/EHU/ERDF, EU).

References

van Duin, A C T *et al.* (2001) 'ReaxFF: A reactive force field for hydrocarbons', *Journal of Physical Chemistry A*, 105(41), pp. 9396–9409. doi: 10.1021/jp004368u.

Duque-Redondo, E. *et al.* (2018) 'Cs-137 immobilization in C-S-H gel nanopores', *Physical Chemistry Chemical Physics*. Royal Society of Chemistry, 20(14), pp. 9289–9297. doi: 10.1039/C8CP00654G.

Duque-Redondo, E. *et al.* (2021) 'Microscopic mechanism of radionuclide Cs retention in Al containing CSH nanopores', *Computational Materials Science*. Elsevier, 190, p. 110312.

Fedkin, M. V *et al.* (2019) 'Development of the ReaxFF Methodology for Electrolyte–Water Systems', *The Journal of Physical Chemistry A*. ACS Publications, 123(10), pp. 2125–2141.

Lee, H. Y. *et al.* (2017) 'Selective removal of radioactive cesium from nuclear waste by zeolites: on the origin of cesium selectivity revealed by systematic crystallographic studies', *The Journal of Physical Chemistry C*. ACS Publications, 121(19), pp. 10594–10608.

Lolli, F. *et al.* (2018) 'Atomistic simulations of geopolymer models: the impact of disorder on structure and mechanics', *ACS applied materials & interfaces*. ACS Publications, 10(26), pp. 22809–22820.

Mähler, J. and Persson, I. (2011) 'A study of the hydration of the alkali metal ions in aqueous solution', *Inorganic chemistry*. ACS Publications, 51(1), pp. 425–438.

Mile, V. *et al.* (2009) 'Understanding the structure of aqueous cesium chloride solutions by combining diffraction experiments, molecular dynamics simulations, and reverse monte carlo modeling', *The Journal of Physical Chemistry B*. ACS Publications, 113(31), pp. 10760–10769.

Perera, D. S. *et al.* (2006) 'Immobilization of Cs and Sr in geopolymers with Si/Al molar ratio of~ 2', *Ceramic Transactions*. Wiley Online Library, 176, p. 91.

Russo, M. and van Duin, A. C. T. (2011) 'Atomistic-scale Simulations of Chemical Reactions: Bridging from Quantum Chemistry to Engineering', *Nuclear Inst. and Methods in Physics Research B*, 269, pp. 1549–1554.

Singh, N. B. and Middendorf, B. (2020) 'Geopolymers as an alternative to Portland cement: An overview', *Construction and Building Materials*. Elsevier, 237, p. 117455.

Yuan-Hui, L. and Gregory, S. (1974) 'Diffusion of ions in sea water and in deep-sea sediments', *Geochimica et Cosmochimica Acta*, 38(5), pp. 703–714. doi: 10.1016/0016-7037(74)90145-8.

The 16th International Congress on the Chemistry of Cement 2023 (ICCC2023)
"Further Reduction of CO_2 -Emissions and Circularity in the Cement and Concrete Industry"
September 18–22, 2023, Bangkok, Thailand

Modelling of the Flocculated Polydisperse Microstructure of Fresh Cement Paste

Y.Q, Zhao[1*], M. Hlobil[2], and D.S. Kammer[3]

[1] *ETH Zürich, Zürich, Switzerland*
Email: zhaoya@student.ethz.ch
[2] *ETH Zürich, Zürich, Switzerland*
Email: michal.hlobil@ifb.baug.ethz.ch
[3] *ETH Zürich, Zürich, Switzerland*
Email: dkammer@ethz.ch

ABSTRACT

Granular materials present in nature are commonly polydisperse, featuring an inconsistent grain size distribution. This characteristic directly affects particle packing, and consequently influences attributes such as maximal packing fraction, bulk density, rheology, and derived properties. For cement, this has direct consequences as polydispersity, among other factors, influences considerably the rheology and concurrent microstructural build-up in the fresh paste. Previous studies on polydispersity in granular systems considered only mechanical contact forces among particles, but omitted non-contact colloidal interactions, which dominate the microstructure in cement paste. Therein, the flocculation of particles, caused by these interactions, creates a percolated network, which is strongly affected by the polydispersity, but is not fully understood yet. In this paper, we show how flocculation affects the microstructural build-up and the resulting rheological and mechanical properties of fresh cement paste. By accounting for flocculation in our numerical modelling, we can produce statistically representative microstructures, which maintain physically consistent rheological properties. We observed that the mechanical properties of percolated particle networks due to flocculation depend on their packing fraction and size distribution. A higher packing ratio offers a higher shear resistance of the fresh paste. Accounting for polydispersity in flocculated build-up does influence the shear resistance, as opposed to a granular system with only contact forces, where the shear strength is independent of grain size span. Our model provides insight into the micro-mechanical origin of the rheology of fresh cement paste, contributing to a better balance between workability and buildability in early stage, and to a better understanding reignited for the design of new concrete mixtures for digital fabrication.

KEYWORDS: *Polydispersity, flocculation, fresh cement paste, colloidal interaction, granular system.*

1. Introduction

Printable concrete shows its strong potential in construction with two main advantages: free-form architecture and precision material placement, see Wangler et al (2019). As cement is the governing material of concrete in the hardening process, optimization between workability and early shear strength of cement paste is of great interest. It was observed in experiments that the particle size distribution of cement grains and water-to-cement ratio are the two major factors influencing the rheological properties of cement paste, but the underlying mechanisms have not been fully understood yet.

In industry, raw cement has a very broad particle size span, usually from sub-micron to 100 microns, with different particle size distributions depending on their producers. As the size of cement particle is on a scale of microns, there are not only contact forces but also non-contact

colloidal interactions between cement particles to be considered. In close vicinity, cement particles interact via van der Waals forces, see Flatt (2004), and electrostatic forces that result from the presence of adsorbed ions at the surface of the particles, see Flatt and Bowen (2003). Due to these colloidal interactions, a phenomenon called flocculation will happen. It is a physical process of agglomerating fine particles to form large flocs. For dense highly-polydispersed colloidal suspensions such as cement slurry, the flocculation process will finally build up a percolated microstructure that can resist external forces.

2. Numerical Model

We consider an equilibrium state of a particle-based microstructure. The system of interest is built by means of the molecular statics methods. We use a particle size distribution (PSD) obtained from the measurement of a real ordinary Portland cement (OPC) powder. The PSD is re-discretized into 8 size bins, trimming off the particle sizes that are smaller than 1 microns, which occupies a small volume fraction but a giant number of particles, and those larger than 50 microns, which can lead to high inhomogeneity in force transmissions in a small simulation box, see Cantor et al (2018). Particles are assumed to be spherical. Simulations are conducted with solid volume fractions (p) 0.45, 0.55, and 0.65. For the given solid volume fraction and PSD, the number of particles for each size is calculated.

For OPC, like other colloidal particles, the main interaction forces between particles consists of van-der-Waal force and electrostatic force, see Flatt and Bowen (2006):

$$\mathrm{F_{vdw}} \approx \frac{1}{12}\mathrm{A_h}\frac{\overline{r}}{h^2}, \tag{1}$$

$$\mathrm{F_{es}} \approx -2\pi\epsilon\epsilon_0\psi^2\frac{\kappa e^{-\kappa(h-2L_e)}}{(1+e^{-\kappa(h-2L_e)})}\overline{r}, \tag{2}$$

where h is the separation distance between particles, $\overline{r}$ is the harmonic average of the radii $\overline{r} = 2r_1r_2/(r_1+r_2)$ of the two particles of size $\mathrm{r_1}$ and $\mathrm{r_2}$. According to DLVO theory, the equilibrium position of each particle pair varies with particle sizes and their electrostatic properties. To simplify the interaction potential function in our simulations, we use the shifted Lennard-Jones (LJ) potential for the OPC interaction. The well of the LJ potential is set at a center-to-center distance equal to the sum of the radii of the two particles and a constant tiny separation distance. The depth of the potential well is also scaled proportional to the harmonic mean of the radii of the pair of particles $\overline{r}$. The potential function has the following form:

$$\mathrm{U} = 4\epsilon\left[\left(\frac{\sigma}{r-\Delta}\right)^{12} - \left(\frac{\sigma}{r-\Delta}\right)^{6}\right] \tag{3}$$

where Δ is the shift distance, namely the sum of the radii of the particle pair and the separation distance at equilibrium.

We randomly distribute particles into a cubic simulation box with length 200 microns. The potential energy of samples is minimized to eliminate the overlapping of particles. This process is further repeated under a given tiny random displacement, until the potential energy of the system remains constant. This approach leads to an initial configuration with a stable particle network.

Based on this energy-minimized microstructure, simple shear tests are applied on the samples. The simulation box has periodic boundary conditions in *x,y,z* directions. The cubic simulation box is tilted in *xz* plane with a constant increment of 0.005% of the length of the simulation box. Each time the box shape is changed, particle positions are remapped to the new box via an affine

transformation to match the box deformation. The remapped particle positions are generally out of balance. Thus, each box deformation and its resulting remapping require an energy minimization. With the energy-minimized stable configuration, we can measure the shear force that is needed to remain this deformation.

To study the effect of solid volume fraction on the mechanical behavior of the flocculated particle network, we conduct a parameter. To investigate the effect of solid volume fraction, we study the development of the initial-stage shear modulus with respect to the increasing solid volume fraction. The analysis is further extended to the relationship between the shear modulus and the connectivity of particle network.

3. Results and discussion

In all our simulations, the flocculation process eliminates the floating particles, and turns the random packed configuration into a percolated microstructure, as shown in Fig 1.

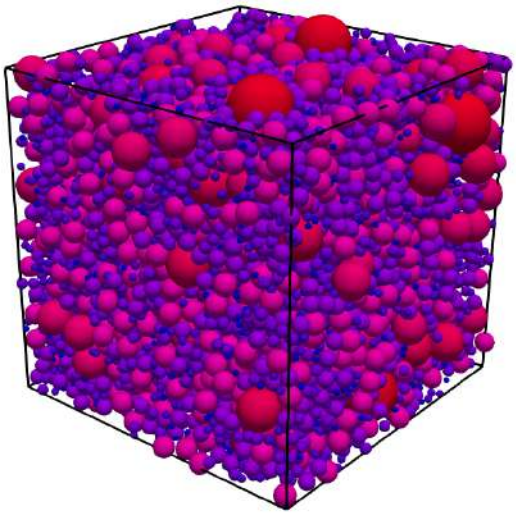


Figure 1 Flocculated microstructure of cement suspension with p = 0.55. The color indicates the size of particles: smaller particles tend to blue colors while larger particles tend to red colors.

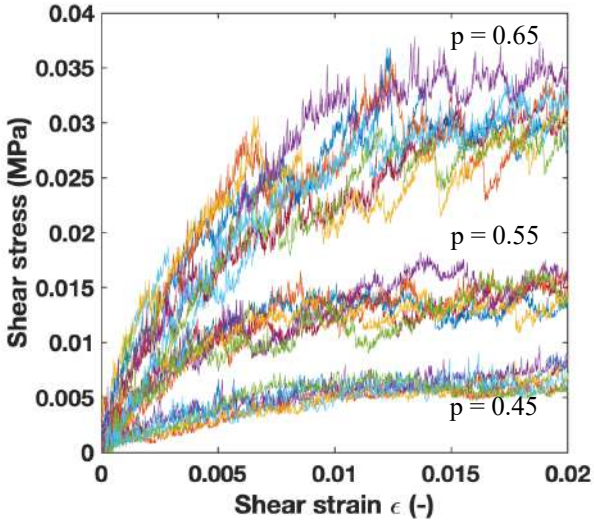


Figure 2 Shear stress- strain curves for 3 simulation groups of 6 runs, each with p = 0.45, 0.55, 0.65.

The static stress-strain curves are directly affected by their solid volume fractions (see Fig 2). We directly observe the stress/strain slope, the shear modulus, increases with the solid volume fraction. In other words, a denser particle microstructure has a better resistance against external forces, which is a behaviour we expected.

The curves in Fig 3(a) are simulation results with p = 0.55 taken from Fig 2. We observe that, in the very first stages of the shearing test, the shear stress increases very rapidly with the shear strain. Then, at a critical shear strain, the curve slope drops abruptly, keeping an increasing tendency with the shear strain. This curve qualitatively corresponds to the reference experimental results of a Vane test on a cement paste with a water to cement ratio of 0.4 (see Fig 3(b)), that the shear stress-strain curve also consists of two regimes: the first is with a steep slope while the second is flatter, see Roussel et al (2012).

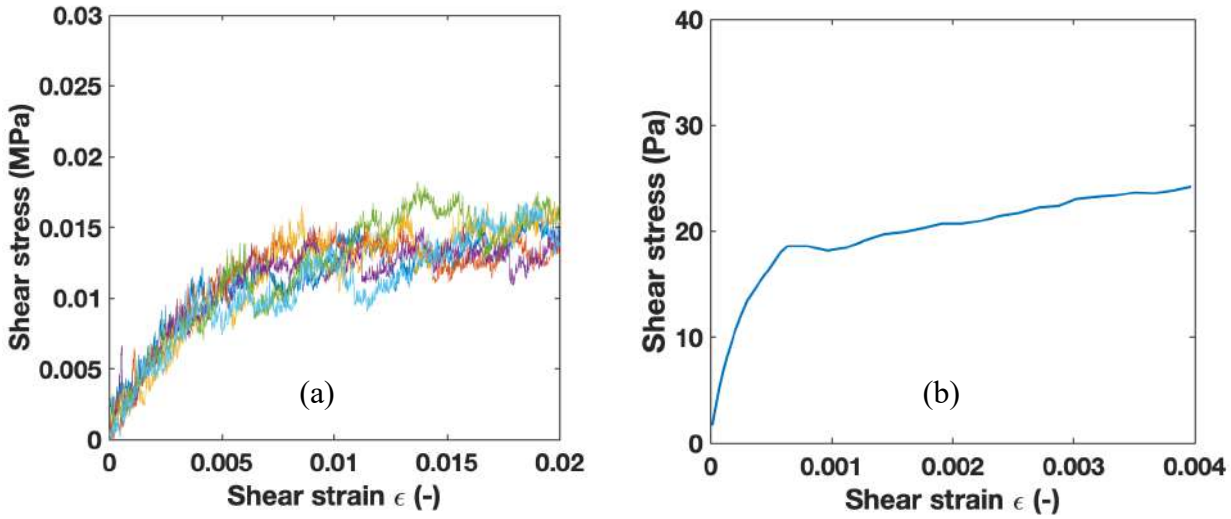


Figure 2 Evolution of shear stress σ as a function of the shear strain γ. (a) Shear stress-strain curves from simulations with 6 runs of p = 0.55. (b) Shear stress-strain curves from experiment during a Vane test on a cement paste with a water to cement ratio of 0.4, extracted from (Roussel, N., Ovarlez, G., Garrault, S., & Brumaud, C. (2012)) Fig. 2(b).

4. Conclusions

In this paper, we simulated the shear loading process on the flocculated microstructural build-up of fresh cement paste, to investigate its rheological and mechanical properties. We presented a systematic analysis of the influence of solid volume fraction on the shear modulus of the fresh cement paste that is composed of spherical particles. It is shown that the shear modulus increases with increasing solid volume fraction, which agrees with our common sense. Our analysis also remarks that in the very first stages of the shearing test, the stress/strain curves clearly have two regimes: initially, it increases steeply, then it flattens. This behavior qualitatively agrees with a reference experimental result of fresh cement paste.

Acknowledgements

The authors acknowledge the support by the Swiss National Science Foundation under grant 200021_200343.

References

Wangler, T., Roussel, N., Bos, F. P., Salet, T. A., & Flatt, R. J. (2019). Digital concrete: a review. Cement and Concrete Research, 123, 105780.

Flatt, R. J. (2004). Dispersion forces in cement suspensions. Cement and Concrete Research, 34(3), 399-408.

Flatt, R. J., & Bowen, P. (2003). Electrostatic repulsion between particles in cement suspensions: Domain of validity of linearized Poisson–Boltzmann equation for nonideal electrolytes. Cement and concrete Research, 33(6), 781-791.

Flatt, R. J., & Bowen, P. (2006). Yodel: a yield stress model for suspensions. Journal of the American Ceramic Society, 89(4), 1244-1256.

Cantor, D., Azéma, E., Sornay, P., & Radjai, F. (2018). Rheology and structure of polydisperse three-dimensional packings of spheres. *Physical Review E*, *98*(5), 052910.

Roussel, N., Ovarlez, G., Garrault, S., & Brumaud, C. (2012). The origins of thixotropy of fresh cement pastes. Cement and Concrete Research, 42(1), 148-157.

The 16th International Congress on the Chemistry of Cement 2023 (ICCC2023)
"Further Reduction of CO_2 -Emissions and Circularity in the Cement and Concrete Industry"
September 18–22, 2023, Bangkok, Thailand

Simulation of heat transport in extruded concrete structure

M. Hlobil[1*] and D. S. Kammer[1]

[1] *Institute for Building Materials, ETH Zurich, Switzerland*
Email: michal.hlobil@ifb.baug.ethz.ch
[2] *Institute for Building Materials, ETH Zurich, Switzerland*
Email: dkammer@ethz.ch

ABSTRACT

The extrusion-based additive manufacturing process is rapidly establishing itself as a plausible construction alternative to the traditional design paradigm employed for building concrete structures. The structure can be newly produced by successively stacking extruded filaments of fluid concrete, which rapidly harden without the need for traditional formwork. This feature frees the constraints from traditional concrete design and is capable of delivering shape-optimized structures into common practice. However, the material requirements for successful production often pose a significant challenge from a technological perspective. The interconnection between neighboring extruded filaments depends on their mutual adhesion. Any interruption in the production process, resulting in a prolonged deposition of the successive layer, results in the formation of a "cold joint". This planar inter-layer region with increased porosity effectively compromises the long-term durability of the extruded structure. The present paper sets the framework for an initial assessment of cold joint formation. The cementitious binder used in concrete generates notable heat during hardening, which accelerates humidity transport throughout the extruded structure. Herein, we address the temperature fluctuation within the concrete structure at two scales. By reflecting the microstructural development during cement hydration at the microscale, the accompanying heat release serves as an internal heat source and fuels the temperature fluctuation at the mesoscale of the extruded concrete structure. A fully-developed multiscale model should provide indicators for optimal material design for this technological process.

KEYWORDS: *Additive manufacturing, Heat transport, Hydration modeling, Portland cement*

1. Introduction

Traditional concrete construction technology relies on the use of temporary barriers, i.e. formwork, that shape the future structure. The formwork holds the initially-fluid concrete after its deposition until it hardens and maintains the desired contour. However, with the advent and rise of digitization across every industrial field over the last decades, new possibilities emerged for concrete construction technology, in particular with the onset of digital fabrication.

Digital fabrication exploits the synergies that arise from computer-aided design and robotics to deliver a potentially promising innovation in the form of an extrusion-based additive manufacturing process. With this technology, the freshly mixed concrete is first pumped into a robotically-controlled printing head, which then ejects and deposits a thin concrete filament onto its defined location, see De Schutter et al. (2018). Subsequent stacking of extruded filaments then produces the final structure without the use of a traditional formwork, as the concrete mix is designed to rapidly harden and develop a sufficient capacity for sustaining the weight of the successively added layers. This production process opens the door for designing shape-optimized structures, as the material is deposited only where needed, thus potentially providing lighter structures with an improved cost-to-performance ratio.

As any rapidly developing technological process in its infancy, even the extrusion-based additive manufacturing of concrete brings technological challenges that require a fundamental understanding before a widespread adoption of this technology occurs, see Buswell et al. (2018). The absence of traditional formwork during extrusion renders the outer structural surface unprotected, which accelerates concrete

drying. Should the top filament surface remain uncovered longer than necessary, e.g., due to an unexpected interruption in the extrusion process, a solid crust will form atop, limiting the adhesion to the sequentially deposited layer. Consequentially, this leads to the formation of a structural defect denoted as a “cold joint”, see Keita et al. (2019).
Our aim in this paper is to coin the basis for the understanding of cold joint formation from a material perspective, focusing herein on the temperature distribution within the extruded concrete filament. The microstructural formation within cement paste at the microscale is accompanied by the release of thermal energy, which fuels the temperature fluctuation within the concrete structure. This effect consequently accelerates the moisture transport, leading to a nonuniform drying and to the formation of a solid crust at the exposed surface of the filament.

2. Model formulation

We here formulate a model to link the microstructural evolution accompanied by a heat release with the macroscopic temperature fluctuation within the cross-section of an extruded concrete filament. The proposed model resolves the different physical and chemical phenomena at two hierarchically separated length scales. At the microscale, the exothermic chemical reactions accompanying cement hydration create an internal heat source, which fuels the temperature fluctuation at the concrete mesoscale, see Fig. 1.

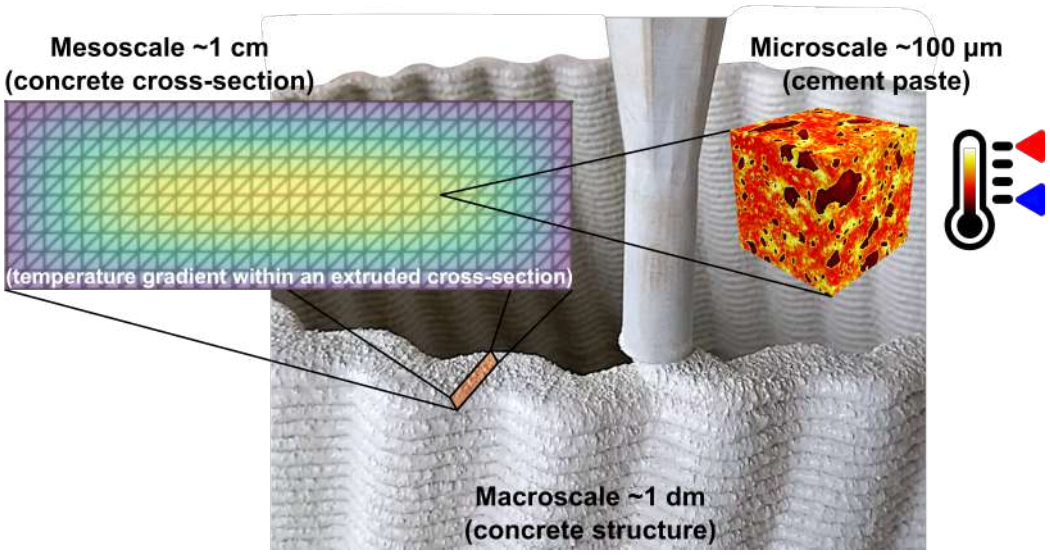


Fig. 1: Hierarchical organization of the model for extrusion-based manufacturing of concrete.

As the starting step in model development, we aim at linking the microstructural evolution in cement paste during hydration to its heat release. To this end, we introduce the term chemical affinity, $\tilde{A}$, as coined by Ulm and Coussy (1995), accounting for the rate of microstructural development in hydrating paste over time. This can be mathematically expressed as

$$\tilde{A}(\alpha, T) = \frac{d\alpha}{dt}, \tag{1}$$

where α represents the degree of cement hydration and t the elapsed hydration time. From a thermodynamic perspective, $\tilde{A}$ is proportional to the difference in chemical potentials between the reactants (cement grains and water) and the reaction products (i.e. hydrates).
As cement hydration is a thermally activated process, the rate of reaction kinetics is affected by the material composition and any variation in the curing temperature. However, it is possible to decouple the effects of microstructural formation and the role of temperature via

$$\tilde{A}(\alpha, T) = \tilde{A}_{ref}(\alpha)\beta_T(T) \tag{2}$$

where $\tilde{A}_{ref}$ is the chemical affinity accounting for microstructural development determined for a reference temperature, and β_T a scaling factor described later.

For a computational implementation, we first employ an analytical form of $\tilde{A}_{ref}$ introduced by Jendele et al. (2014) in the form of

$$\tilde{A}_{ref}(\alpha) = B_1 \left(\frac{B_2}{\alpha_{inf}} + \alpha \right) (\alpha_{inf} - \alpha) exp \left(-\eta \frac{\alpha}{\alpha_{inf}} \right), \tag{4}$$

where B_1 = 0.5095 [h^{-1}], B_2 = 0.0041 [-], η = 6.1044 [-] represent best-fit parameters for the given cement tested, and α_{inf} = 0.85 [-] the maximum reachable degree of cement hydration based on composition and curing conditions. Then, to account for a possible temperature fluctuation from the mesoscale, we introduce an Arrhenius-type scaling factor β_T as

$$\beta_T(T) = exp \left[\frac{E_a}{R} \left(\frac{1}{T_{ref}} - \frac{1}{T} \right) \right], \tag{2}$$

where T_{ref} [K] represents the reference temperature (for which $\tilde{A}_{ref}$ is initially determined), T [K] the temperature at a given material point in the structure, R = 8.3144 J/(mol K) the universal gas constant, and E_a=38300 J/mol the apparent activation energy accompanying cement reaction.
Given the temporal evolution of $\tilde{A}$, one can determine the heat release rate $\bar{Q}$ accompanying cement hydration at the microscale via

$$\bar{Q}(\alpha, T) = \tilde{A}(\alpha, T)\, Q_{tot}, \tag{5}$$

where Q_{tot} represents the weighted average of enthalpies at complete hydration of all clinker compounds. Evaluation of Eq. (5) then provides a value of the internal heat source that is projected to the mesoscale.
At the mesoscale, we resolve the temperature distribution over the concrete filament cross-section by formulating a transient heat diffusion problem with an internal heat source, conveniently defined as a thermal equilibrium over a differential element as

$$\lambda \nabla^2 T(x) + \bar{Q}(x, \alpha, T) = \rho c \frac{\partial T(x,t)}{\partial t}, \tag{6}$$

where λ, c, and ρ represent the material properties of concrete at the mesoscale, namely the heat conductivity, specific capacity, and mass density, respectively, while the T denotes the sought temperature field at the mesoscale. While we acknowledge the dependence of the material properties on the state of microstructural evolution, however, we consider, as a first-order simplification, λ = 1.98 W/(m K), c = 1052 J/(kg K), and ρ = 2637 kg/m^3 as immutable during the numerical evaluation.
The transient conduction problem was numerically solved using the Finite Element Method with implicit Euler time discretization, implemented in the open-source FEniCS package. To solve Eq. (6), it is necessary to consider realistic initial and boundary conditions. We initially prescribe a constant temperature field T_{ini} = 20°C throughout the concrete cross-section. As a first-order approximation, we then consider a Dirichlet boundary condition on the edges of the cross-section, amounting to T_{edge}= 20°C. During the evaluation, the degree of hydration α in Eq. (1) needs to be numerically integrated as no closed-form equation is available for its determination.

3. Results and discussion

The heat release accompanying cement dissolution serves as an indicator for microstructural development within the hydrating paste. This can be experimentally quantified outside the numerical model using isothermal calorimetry for a given cement paste composition and constant temperature. Throughout this experiment, the cumulative heat development Q (obtained by a performing a time integration of the recorded $\bar{Q}$ evolution) can be translated into the evolution of the degree of cement hydration via $\alpha = Q/Q_{tot}$. This experimental α can then be directly compared with its simulated counterpart from the implemented numerical framework, see Eq. (1), evaluated for a constant temperature of 20°C. A mutual comparison of both α evolutions shown in Fig. 2 validates the implementation of the numerical framework.

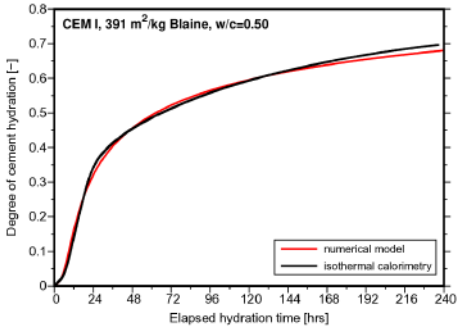


Fig. 2: Comparison of microstructural development from simulation to experimental measurement.

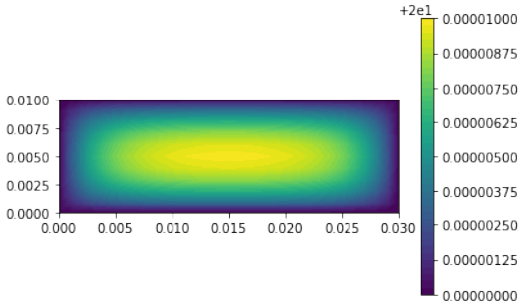


Figure 3: Temperature profile in concrete filament cross-section after 24 hours of hydration.

The computed temperature field throughout the extruded concrete filament cross-section at the mesoscale captures a temperature gradient, which manifest from the core toward the filament edges, as shown in Fig. 3 for t=1 day of elapsed hydration.

It should be noted that the described isothermal calorimetry measurement and the simulated heat development at the mesoscale were calibrated with data from a regular ordinary Portland cement paste. This particular mix contained no chemical additives affecting the hydration kinetics, workability, and/or setting time of cement. As such, the results provided herein serve for model validation purposes in controlled laboratory conditions and do not reflect any actual mix design used in field conditions for extrusion-based additive manufacturing process.

4. Conclusions

This paper serves as a stepping stone for modeling cold joint formation via a multiphysics framework. Herein, we formulate the basis for a reciprocal relation between the microstructural development stemming from cement hydration at the microscale and the fluctuating temperature field within an extruded concrete filament cross-section at the macroscale. To simulate the microstructural development, we consider an analytical hydration model based on chemical affinity, which is calibrated from isothermal calorimetry measurements of ordinary Portland cement paste. This analytical hydration model is then implemented within a FEM-based numerical framework of a transient heat diffusion problem at the macroscale and yields a basis for the understanding of the role of internal temperature increase originating from cement hydration.

Acknowledgements

The authors acknowledge support by the Swiss National Science Foundation grant 200021_200343.

References

De Schutter, G., Lesage, K., Mechtcherine, V., Nerella, V., Habert, G., Agusti-Juan I., "Vision of 3D printing with concrete - technical, economic and environmental potentials", *Cement and Concrete Research,* 112: 25-36

Buswell, R., Leal de Silva, R., Jones, S., Dirrenberger, J. (2018) "3D printing using concrete extrusion: A roadmap for research", *Cement and Concrete Research*, 112: 37-49

Keita, E., Bessaies-Bey, H., Zuo, W., Belin, P., Roussel, N. (2019) "Weak bond strength between successive layers in extrusion-based additive manufacturing: measurement and physical origin", *Cement and Concrete Research*, 123: 105787

Ulm, F.-J. and Coussy, O. (1995) "Modeling of thermochemomechanical couplings of concrete at early ages", *Journal of Engineering Mechanics,* 121 (7): 785-794

Jendele, L., Šmilauer, V., Červenka, J. (2014) "Multiscale hydro-thermo-mechanical model for early-age and mature concrete structures", *Advances in Engineering Software.* 72: 134-146

The 16th International Congress on the Chemistry of Cement 2023 (ICCC2023)
"Further Reduction of CO_2 -Emissions and Circularity in the Cement and Concrete Industry"
September 18–22, 2023, Bangkok, Thailand

In situ monitoring of microstructure evolution of C_3A –gypsum system by low field NMR

A.M. She[1*], G. Li[1], K. Ma[1], G. Liao[1], and J.Q. Zuo[2]

[1] *Key Laboratory of Advanced Civil Engineering Materials of Ministry of Education, School of Materials Science and Engineering, Tongji University, Shanghai, PR China*
**Email: sheanming@tongji.edu.cn*
[2] *Shanghai Construction Group Co., Ltd., Shanghai, PR China*

ABSTRACT

Tricalcium aluminate (C_3A) is one of the major minerals of Portland cement, which is vital to the early property and durability of concrete. However, the consensus on the hydration mechanism of C_3A has not been reached, especially the interaction between C_3A and gypsum, which is usually introduced in Portland cement. Low-field nuclear magnetic resonance (NMR) is advantaged in monitoring the hydration of cement, due to its fast, continuous and nondestructive operation. The goal of this work is to study the hydration process of C_3A-gypsum system by using ^1H as the probe. The ^1H signal intensity and transverse relaxation time (T_2) were used to characterize the hydration kinetics and reveal the microstructure, respectively. The results showed that gypsum can remarkably decelerate the hydration rate of C_3A and the hydration products were depended on the dosage of gypsum. When gypsum was sufficient, the main hydration product was ettringite (AFt), otherwise, AFt started to transform to monosulfoaluminate (AFm) after about 12 h of hydration. The transformation of AFt to AFm was detected by low-field NMR. In addition, according to the decline rate of ^1H signal intensity, the hydration process of C_3A can be divided into three stages.

KEYWORDS: *low field NMR, hydration, microstructure, tricalcium aluminate, gypsum*

1. Introduction

Tricalcium aluminate (C_3A), one of the major components of Portland cement, plays a crucial role in the hydration Portland cement. In recent years, the hydration process of C_3A has been extensively studied, and some recognized knowledge have been gained (Quennoz et al 2012; Joseph et al 2019). For pure C_3A, its hydration process is relatively simple. Once contacting with water, C_3A immediately reacts with water to generate calcium aluminate hydrates. After adding gypsum, the hydration of C_3A becomes complex. The final products of C_3A-gypsum system are dependent on the dosage of gypsum. In the first case, when gypsum is abundant, the main product is ettringite (AFt). In another case, after complete depletion of gypsum, the remaining C_3A will renew hydration and the newly-formed C_4AH_{13} will react with the previously-formed AFt, generating monosulfoaluminate (AFm) as shown.

The process during which AFt converts to AFm is sophisticated, which is difficult to monitor and not fully understood yet, and there are two prevailing hydration kinetics mechanisms to describe this process. One is the dissolution-controlled mechanism first reported by Minard (Minard et al 2007) and the other mechanism is about the nucleation and growth of AFm proposed by Quennoz (Quennoz et al 2012). Although the retardation effect of gypsum on C_3A is remarkable, there is still little consensus on its mechanism. Hence, researchers did much work and proposed different hypothesis to interpret this effect. One hypothesis claimed that AFt acts as the barrier layer that blocks the reaction between C_3A and water, thus slowing down the hydration of C_3A and reducing the released heat. However, Myers (Myers et al 2017) found that AFm is not suitable to be a barrier layer due to its needle-like crystalline morphology

and highly porous structure. Afterwards, scholars proposed a surface passivation mechanism, which was related to ion exchange and adsorption of solute species or solids (Scrivener et al 2019). At present, one widely-accepted hypothesis is that the complexation of Ca^{2+}-SO2- 4ion pair adsorbed on the Al-rich leached layer of C_3A impedes the dissolution of C_3A, thus providing the key inhibiting effect (Myers et al 2017).

For hydration of C_3A, it has been usually neglected that water is also the major reactant, which affects hydration reaction in the whole process. At present, no research on the hydration of C_3A-gypsum using water as the probe have been reported. Our previous work proved that low-field nuclear magnetic resonance (NMR) with ^1H as the probe displayed some superiorities in investigating the hydration process of Portland cement due to its continuity and nondestructive feature (She et al 2021). Furthermore, researches show that the hydration products of C_3A are sensitive to the inner relative humidity (RH), and the stability of AFm is strongly affected by RH. As RH declines from 100% to lower values, the moles of water per mole of AFm change drastically (ie, 16, 14, 12, 10.5, or 9 in easing RH), thus resulting in huge change in its crystalline structure (Baquerizo et al 2015). Therefore, it's promising to provide some new insights into the hydration of C_3A-gypsum system by using low-field NMR.

Herein, the main purpose of this work is to characterize the impact of gypsum on the hydration of C_3A and reveal its microstructure by using low-field NMR. The signal intensity of ^1H and transverse relaxation time T_2 were measured to characterize the content of water and its state, thus providing the information about the hydration of C_3A.

2. Experimental

2.1 Sample preparation

The C_3A used in the experiment was lab-prepared by mineral sintering. To evaluate the impact of the content of gypsum on C_3A hydration, three gypsum dosages were selected, namely, molar ratios of C_3A to gypsum were 1:0, 1:1 and 1:3 corresponding to the sample label of CG-10, CG-11 and CG-13, respectively. This is chosen based on the molar ratio of C_3A to gypsum in the chemical equation that generates AFt. The water-material (w/m) ratio was fixed at 0.5. All hydration processes in the experiment were carried out at 30 °C.

2.2 Low-field NMR analysis

The low field NMR instrument with a constant magnetic field strength of 0.28 T and a 25 mm magnet coil was used in this research. The resonant frequency was 11.9 MHz for the proton. T_2 and ^1H relaxation signal intensity of hydrating pastes were measured using a CPMG pulse sequence. After debugging, the suitable sequence parameters were set for samples: Sampling frequency (SW)=200 KHz, Repetition delay (TW)=1000 ms, Sampling points (TD) =800, Pulse gap (TE)=0.09 ms, Scanning Number (NS)=32. The signal-to-noise ratio of the data varied with the hydration process, ranging from 23 to 34. After setting up parameters, the prepared paste was filled into a sealed glass bottle and placed in a magnetic cavity, and ^1H signal intensity was measured at an interval of 10 min for 48 h.

3. Results and discussion

3.1 Evolution of ^1H signal intensity

Low field NMR can continuously monitor the hydration process of C_3A by detecting the ^1H signal intensity. As the hydration progressed, the total signals intensity detected were proportional to the amount of physically bound water in the samples, and the hydration rate is related to the decline rate of ^1H signal intensity to some extent. As Fig. 1 illustrated, the ^1H signal intensity of the three samples decreases with hydration time because of the continuous consumption of water in the hydration reaction. And the decline rate of ^1H signal intensity changed with time, indicating that the rate of C_3A hydration varies in a nonlinear and non-monotonic manner with respect to time. Specifically, the ^1H signal intensity of CG-10 decreases monotonically after hydration for 48 h (Fig.1(a)), suggesting that the hydration of C_3A continues despite of flash setting. For CG-11, the ^1H signal intensity decreases by about 65% at 10 h (Fig.

1(b)), and after 48 h of hydration, the ^{1}H signal intensity curve becomes flat. While for CG-13, ^{1}H signal intensity only decreases by 35% after hydration for 10 h due to higher addition of gypsum (Fig. 1(c)), and still declines at a higher rate after hydration for 48 h. This proves that gypsum has a significant retardation effect on the early hydration of C_3A.

It should be noted that there is a small peak in the curve of CG-11at around 12 h of hydration (Fig. 1(b)). However, no similar peaks appeared in CG-10 and CG-13. When the gypsum in C_3A-gypsum system is insufficient, the transformation of AFt to AFm will occur in hydration products. It is deduced that a certain amount of physically bound water will be re-generated during the transformation, this leads to an upward 'shoulder' in ^{1}H signal intensity.

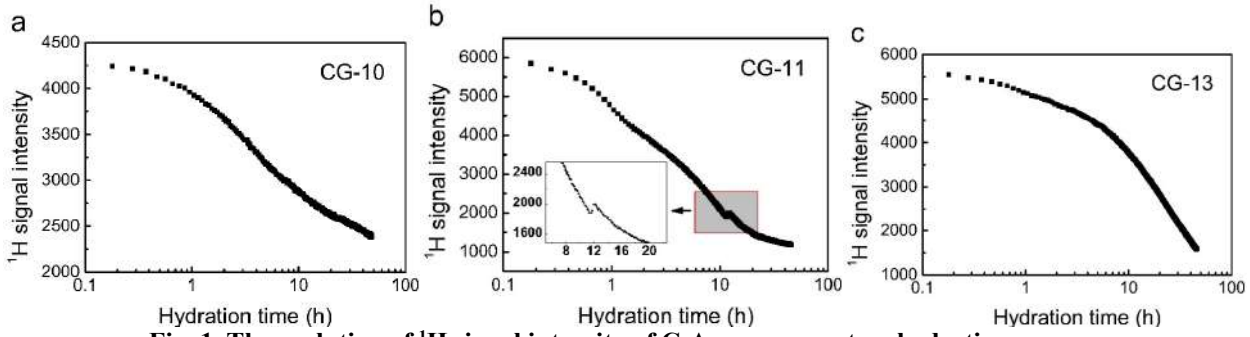


Fig. 1 The evolution of ^{1}H signal intensity of C_3A-gypsum system hydration process

3.2 T_2 relaxation time analysis

Figure 2 shows the plots of T_2 weighted average value (W-T_2) of samples during hydration. As hydration progresses, the microstructure of these paste samples becomes denser, so W-T_2 present a downward trend for all samples during the whole hydration process. Due to the different dosage of gypsum, W-T_2 of CG-10, CG-11 and CG-13 are distinct. In Fig.2(a), the curve can be divided into three stages according to the decline rate of W-T_2, namely, first stage (0-0.5 h), second stage (0.5-10 h), and third stage (10-48 h). In the first stage, owing to the flash setting, unhydrated C_3A is wrapped by calcium aluminum hydrate and ion migration is inhibited, and consequently W-T_2 remain stable; in the second stage, as the product film covered on C_3A particles breaks, the remaining C_3A can renew hydration, thus generating more hydration products and forming porous structure. These pore structures are filled with left free water, which significantly reduces T_2; in the third stage, the hydration of C_3A was relatively complete, the sample is the most compacted, and T_2 drops to around 11 ms and keeps at this level. As shown in Fig.2(b), a small peak also appeared in the CG-11 at around 12 h of hydration. Because the density of AFm (1.99g/cm^3) is higher than that of AFt (1.75g/cm^3), and AFm has better crystallinity, the transformation of AFt to AFm will cause chemical shrinkage inside the paste in theory. Consequently, this transformation process will lead the original micropores to become larger pores and reduce the specific surface area of solid phase. But as the gypsum is sufficient, this transformation does not occur, and the value of T_2 is a continuous curve as shown in Fig.2 (c).

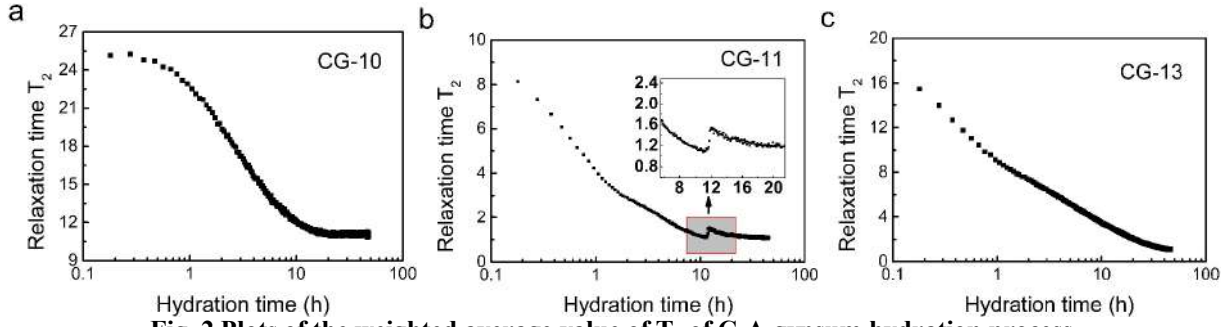


Fig. 2 Plots of the weighted average value of T_2 of C_3A-gypsum hydration process

Based on T_2 value, the specific surface area can be calculated. As depicted in Fig.3(a), there are also three stages in the specific surface area curve of CG-10. In the first stage, the change of specific surface area is slight, indicating a slow hydration process, and the specific surface area even decreases slightly due to the formation of C_3AH_6 with higher density from C_4AH_{13} and C_2AH_8. In the second stage, massive hydration products are generated and continuously fill the pores, thus reducing the pore diameter and the

specific surface area. In the third stage, the specific surface area decreases sharply, because the internal self-drying induced by the fast hydration of C_3A causes a significant decrease in specific surface area. On the other hand, some newly-generated pores are not filled with water, which can't be detected by low-field NMR using ^1H as the probe, so the specific surface area will decline. The same downward trend also appeared in CG-11 (Fig.3(b)) and CG-13 (Fig.3(c)) after 10 h of hydration. However, for CG-11, the decline rate of specific surface area suddenly slows down after 12 h. This can be attributed to the transformation of AFt to AFm as mentioned before. Because the density of AFt is lower than that of AFm, and this transformation will result in smaller pores and thus reduce the decline rate of specific surface area. As shown in Fig.3(b) and Fig.3(c), the decline process of specific surface area caused by self-contraction is obviously prolonged by increasing gypsum addition.

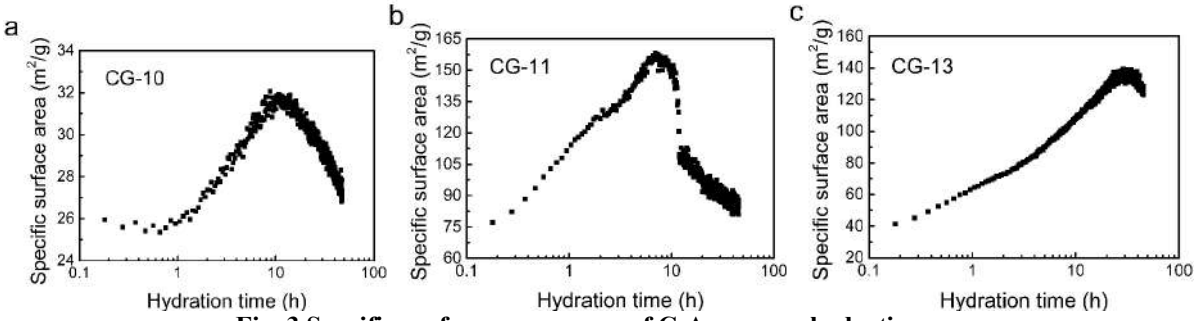


Fig. 3 Specific surface area curves of C_3A-gypsum hydration process

4. Conclusions

(1) Low field NMR can sensitively monitor the hydration process of C_3A-gypsum and reveal the microstructure information of hydration products to some extent. According to the results of ^1H signal intensity and T_2, the transformation of AFt to AFm can be detected at about 12 h of hydration as the molar ratio of C_3A to gypsum is 1:1, accompanying with some free water released.

(2) The decline rate of ^1H signal intensity is related to the hydration rate of C_3A, based on which, the early hydration process of plain C_3A can be approximately divided into three stages.

(3) The specific surface area of hydration products can be derived from T_2. The results show that the shrinkage induced by the self-drying of C_3A will resulte in the decrease of specific surface area.

Acknowledgements

This work was supported by the National Key R&D Program of China [grant No. 2021YFB3802001], the National Natural Science Foundation of China [grant No. 51108341].

References

Baquerizo, L.G., Matschei, T., Scrivener, K.L., Saeidpour, M. and Wadsö, L. (2015) "Hydration States of AFm Cement Phases", *Cement and Concrete Research*, 73(7): 143-157

Joseph, S., Skibsted, J. and Cizer, Ö. (2019) "A Quantitative Study of the C_3A Hydration", *Cement and Concrete Research*, 115(1):145-159

Minard, H., Garrault, S., Regnaud, L., and Nonat, A. (2007) "Mechanisms and Parameters Controlling the Tricalcium Aluminate Reactivity in the Presence of Gypsum", *Cement and Concrete Research*, 37(10):1418-1426

Myers, R.J., Geng, G., Rodriguez, E.D., da Rosa, P., Kirchheim, A.P. and Monteiro, P.J.M. (2017) "Solution Chemistry of Cubic and Orthorhombic Tricalcium Aluminate Hydration", *Cement and Concrete Research*, 100(10): 176-185

Quennoz, A., and Scrivener K.L. (2012) "Hydration of C_3A–gypsum Systems", *Cement and Concrete Research*, 42(7):1032-1041

She, A., Ma, K., Liao, G., Yao, W. and Zuo, J. (2021) "Investigation of Hydration and Setting Process in Nanosilica-cement Blended Pastes: In Situ Characterization Using Low Field Nuclear Magnetic Resonance", *Construction and Building Materials*, 304(10): 124631

Scrivener, K., Ouzia, A. and Kunhi Mohamed, A. (2019) "Advances in Understanding Cement Hydration Mechanisms", *Cement and Concrete Research*, 124(10): 105823

The 16th International Congress on the Chemistry of Cement 2023 (ICCC2023)
"Further Reduction of CO_2 -Emissions and Circularity in the Cement and Concrete Industry"
September 18–22, 2023, Bangkok, Thailand

Thermodynamic modelling of Portland cement clinkers.

W. Abdul [1,2*], C. Rößler[3], C. Mawalala[2,4], A. Pisch[4], T. Hanein[2] and M. Bannerman[1]
[1] *University of Aberdeen, Aberdeen, United Kingdom*
[2] *University of Sheffield, Sheffield, United Kingdom*
[3] *Bauhaus-Universität Weimar, Weimar, Germany*
[4] *Grenoble INP, Grenoble, France*
**Email: w.abdul@sheffield .ac.uk*

ABSTRACT
Research into thermodynamic modelling allows for product and process optimisation of Portland cement clinkers. Due to the magnitude and chemistry of clinker production, there is a great challenge in modelling such a complex system. The CALPHAD (CALculation of PHAse Diagrams) approach provides a method in overcoming this challenge, by constructing a model, step-by-step with increasing complexity, i.e., starting with the pure solids and liquid to modelling binary and ternary melts, and moving on to higher-order systems, and with the possibility to eventually embed mobility. This approach has had great success in the metals industry and has allowed for production optimisation for a variety of alloys. In this project, we have developed a thermodynamic database for the CaO-Al_2O_3-SiO_2-Fe-O-MgO system. This provides a much-needed update to the underlying thermodynamic data. In addition, prediction calculations made with our thermodynamic database are compared against technical clinkers analysed by XRD, XRF, and SEM-EDX. Future work will include developing further extensions to the thermodynamic database to include other elements such as sulfur to further model clinker diversity.

KEYWORDS: *Thermodynamic modelling, Clinker, Clinker prediction, CALPHAD, Characterisation*

1. Introduction

There is an immediate need to make Portland cement (PC) more environmentally friendly by optimising the clinker production process. There are huge potentials in the research of the high temperature chemistry within the cement kiln (Ludwig and Zhang (2015)), plenty of which related to efficiency has already been realised. Research into new clinker chemistries are mostly "trial and error" and would be aided by a thermodynamic model of the clinker production process, and with the growing pool of raw materials targeted for use in clinker manufacture. Thermodynamic models and databases have greatly aided the metals industry in material development, which have been rapidly developed using the CALPHAD that provides a step-by-step approach to rapidly develop thermodynamic databases through the calculation of phase diagrams. The effectiveness of the CALPHAD approach has been studied by De Noirfontaine et al. (2012), who reviewed the models of the CaO-$Al_2O_{3\backslash}$-SiO_2 system and carried out calculations in the clinkering zone. Barry and Glasser (2000), and Tazuddin et al. (2018) used commercial thermodynamic databases to carry out clinker predictions for synthetic clinkers and Tazuddin et al. (2020) was also able to study the effect of minor elements on clinker phase formation. Furthermore, Hanein et al. (2020) developed a stoichiometric thermodynamic database for PC and C$A clinkers and Meyer et al. (2016) developed a kiln simulator (KilnSimu) from a thermodynamic model with great success. As a part of this work, a thermodynamic database for the CaO-Al_2O_3-SiO_2-Fe-O-MgO system was developed. This includes the modelling of the main clinker phases: alite, belite, aluminate and ferrite. This database serves as a single source of thermodynamic data for the solid, liquid, solid solutions and the melt phases specifically created for PC clinkers. In this paper, we present the results of the clinker predictions resulting from the Scheil cooling calculations (Scheil (1942)) using the developed thermodynamic database. These values are compared with the analysis of 27 technical clinkers that were also analysed as part of this project. Finally, the power of the modelling work is presented through the comparisons of the calculated MgO content in the belite phase against the energy dispersive X-Ray (EDX) analysis of the clinkers.

2. Thermodynamic Modelling and Clinker analysis

The thermodynamic database for the CaO-Al_2O_3-SiO_2-Fe-O-MgO system that was developed in this work, made use of the latest 3rd generation CALPHAD function for the solid and liquid phases and the associate's

model for the melt phase. Novel fitting methodologies were used to fit the relevant parameters in the binary, ternary, and higher order systems; details on this approach are discussed in the $CaO\text{-}SiO_2$ assessment carried out by Abdul et al. (2022). Modelling of the full thermodynamic system was found not to be necessary and instead only the PC relevant ternary systems were modelled and combined to give the final database, this includes: $CaO\text{-}Al_2O_3\text{-}SiO_2$ (which contains C_3A, C_2S and C_3S), $CaO\text{-}Al_2O_3\text{-}Fe\text{-}O$ (which contains ferrite) and $CaO\text{-}MgO\text{-}SiO_2$ (which contains the substitution of MgO into C_2S). The thermodynamic database was used to carry out Scheil cooling calculations from 1500°C for a given clinker oxide composition. Scheil cooling is a set of equilibrium calculations that describes the rapid cooling of a melt like that which occurs in the cement kiln. This results in the calculated values of the precipitated clinker phases, which can be compared against experimental XRD data. Figure 1 presents a graph of a Scheil cooling precipitation that was conducted using the present thermodynamic work. The calculated values match closely with the values from Barry and Glasser (2000).

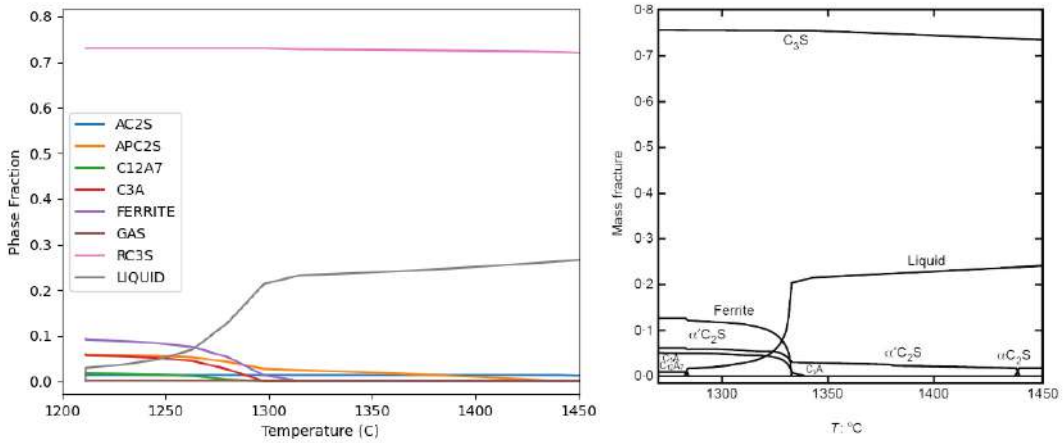


Figure 1 Accumulated phase fraction from the Scheil cooling calculation from 1450°C for the Barry and Glasser (2000) clinker composition (wt %): CaO 69, Fe_2O_3 3.6, SiO_2 22, Al_2O_3 5.4. (left) Results of the presently developed database. (right) Results of Barry and Glasser using MTDATA. Abbreviations are as follows, "AC2S": α-C_2S, "APC2S": α'-C_2S, "RC3S":C_3S (rhombohedral).

A total of 27 clinkers were received from industrial partners and analysed using X-ray diffraction (XRD) Rietveld analysis, X-ray fluorescence (XRF) analysis on molten beads XRF, and SEM-EDX mapping analysis, the methodology and full dataset is presented in a future paper. The EDX mapping analysis was carried out at various resolutions. High resolution (approx. 0.1µm step size) was used for characterisation of the ferrite phases and lower resolution (approx. 0.2µm step size) but large area analyses were used for belite characterisation respectively. In addition, Shim et al. (2021) collated the XRD and XRF analysis of 50 clinkers from literature, this provides a comparison of "historical" clinkers against the modern clinker dataset.

3. Results and Discussion

3.1. Clinker prediction

The difference (in weight %) of the calculated values of the clinker phases using the presently developed thermodynamic database, compared against the XRD analysis within the current clinker dataset and the dataset of Shim et al. is presented in Fig. 2. The figure shows that the calculated values of the belite, aluminate and ferrite phases are in good agreement with XRD values, especially for the clinkers in the dataset of Shim et al. There is a slight over-prediction in the alite phase, which is expected as the alite phase in the thermodynamic modelling was not modelled as a solid solution like the belite phase, this means the effects of MgO are not considered for alite formation. This requires further experimental work to accurately model this behaviour. A summary of the average error for the prediction of the 4 main clinker phases calculated using different calculation methods is presented in Table 1. The results confirm earlier conclusions by Taylor (1997), that the Bogue over-predicts the alite phase and under-predicts the belite phase. The modified Bogue is better at predicting the alite and belite phases but has poor prediction of the aluminate and ferrite phases. The calculations of Hanein et al. (2020) are generally in agreement with the experimental values for all clinker phases. Finally, the results of the thermodynamic database are favourable when compared against the previous calculation methods, with equal or better agreement for the prediction

of all clinker phases except alite, where values of alite match the predictions of the Bogue equation.

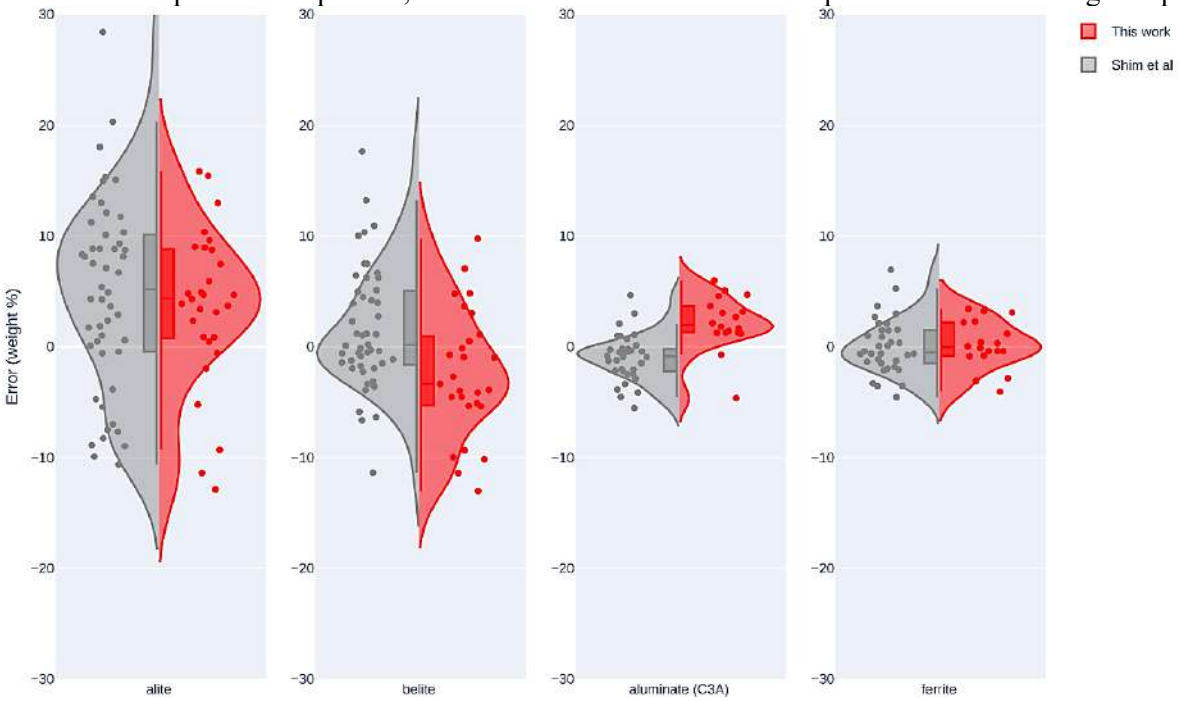


Figure 2 Violin plots of the error (in weight %) of the calculated values and the experimental XRD values of the present clinker dataset (this work) and the dataset of Shim et al (2021).

Table 1 Summary of the error in weight % between the calculated values of the clinker phases compared against the experimental XRD values of the present clinker dataset and the collated dataset of Shim et al. (2020).

Calculation	Bogue	Modified Bogue	Hanein et al. (2020)	This work
Alite (Present)	3.11 ± 6.95	-1.64 ± 7.38	-3.32 ± 6.32	3.62 ± 7.03
Alite (Shim et al.)	5.84 ± 7.50	-1.80 ± 8.04	0.911 ± 7.46	4.68 ± 8.63
Belite (Present)	-1.93 ± 6.75	2.18 ± 7.28	2.92 ± 6.26	-2.40 ± 5.69
Belite (Shim et al.)	-3.14 ± 8.10	-0.12 ± 8.75	0.569 ± 7.79	1.63 ± 5.49
Aluminate (Present)	0.981 ± 2.47	7.45 ± 6.21	3.70 ± 2.15	2.20 ± 2.40
Aluminate (Shim et al.)	-2.10 ± 2.67	3.73 ± 6.04	0.614 ± 4.20	-0.982 ± 2.11
Ferrite (Present)	0.130 ±1.83	-6.88 ± 9.40	0.130 ± 1.83	0.179 ± 2.15
Ferrite (Shim et al.)	0.15 ± 2.43	-5.64 ± 8.84	0.152 ± 2.43	0.038 ± 2.49

3.2. Belite and Ferrite substitution

Whilst the results of the clinker prediction are favourable, further calculations can be done with the thermodynamic database, where the previous calculations cannot predict. A cross-plot of the MgO/CaO ratios for selected belite clinker phases is presented in Fig. 3 and shows an almost linear relationship between the calculated and experimental values, showing good agreement in the prediction of MgO in the belite phase using the thermodynamic database. Furthermore, a similar cross-plot for the Al_2O_3/CaO ratio in ferrite, shows excellent prediction in clinkers with an alumina-poor ferrite phase (near C_4AF) and disagreements in the clinkers with alumina-rich ferrites (near C_6A_2F). This is due to the use of a simple sublattice model for the ferrite phase, which does not account for the substitution of Fe_2O_3 in other clinker phases.

4. Conclusion

A thermodynamic database was developed in this work, with a specific application of PC clinkers. The effectiveness of the developed models was shown through the prediction of real clinkers that were also analysed in this work. This resulted in a good prediction for the main clinker phases compared against the experimental values and the results are favourable against the more “traditional” calculation methods. Furthermore, the modelling of MgO in the thermodynamic database, allowed for the prediction of the MgO/CaO ratio in the belite phase, with these in good agreement with the EDX analysis. Similar predictions

were also made for the composition of the ferrite phase, which showed excellent predictions for alumina-poor ferrites. Further improvements in the ferrite model as well as the modelling of Fe_2O_3 substitution in the other clinker phase, would solve the issues with alumina-rich ferrites. The developed thermodynamic database shows promising results with regards to clinker phase and clinker substitution predictions. This database will be useful to the wider cement research community as it serves as a single open-source database for models and thermodynamic data for cement clinker. The thermodynamic database also has potential uses for modelling carbonation-hardening cements as it includes a full CaO-Al_2O_3-SiO_2 model. Furthermore, the oxygen dependence of iron is modelled in this system; this inclusion will make the addition of SO_3/SO_2 easier. Finally, minor elements like fluorine can be easily added to the current thermodynamic model, but the addition of molten salts and resolution of the volatilisation cycle will require more work. Future work will include extending the thermodynamic database to include other elements and species like SO_3, for further modelling of PC and other cement formulations such as calcium sulfo-aluminate based cements. The thermodynamic model/dataset developed here can also be combined with heat transfer and kinetic models to develop advanced thermal kiln models for cement production.

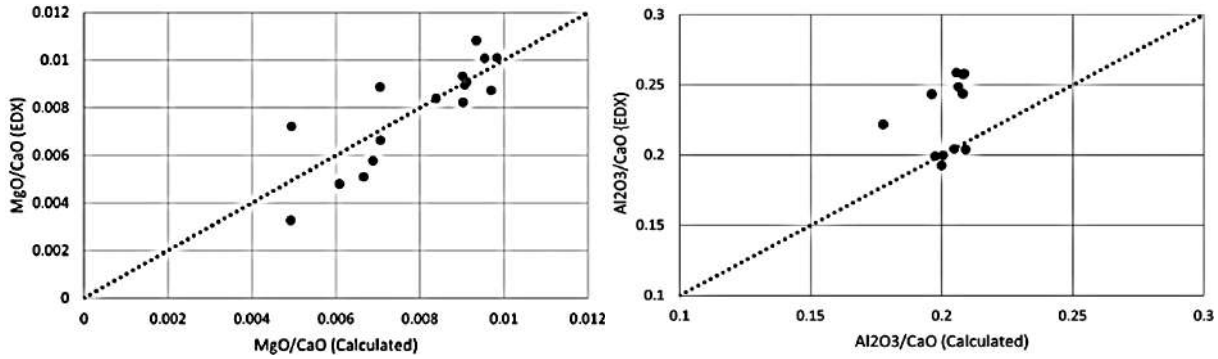


Figure 3 Cross-plot of the experimental and calculated values of the (left) MgO/CaO ratio in the belite phase and the (right)Al_2O_3/CaO ratio in the ferrite phase for selected clinkers in the clinker dataset. The dashed line represents the y=x relationship, indicating exact agreement.

Acknowledgements

The authors would like to acknowledge the financial support of Nanocem/Innovandi for the funding of Core Project 17, of which this work was a part of. T. Hanein and W. Abdul were also supported by UKRI Future Leaders Fellowship (MR/V023829/1).

References

Abdul, W., Malawala, Ch., Pisch, A. and Bannerman, M. (2022) 'CaO-SiO_2 assessment: 3rd generation modelling of thermodynamic properties', *Cement and Concrete Research* (submitted).

Barry, T. I and Glasser, F. (2000) 'Calculation of Portland cement clinkering reactions', *Advances in Cement Research*, 12: 19–28.

De Noirfontaine, M. N., Tusseau-Nenez, S., Girod-Labianca, C. and Pontikis, V. (2012) 'CALPHAD formalism for Portland clinker: Thermodynamic models and databases', *Journal of Materials Science* 47(3): 1471–1479.

Hanein, T., Glasser, F. and Bannerman M. N. (2020) 'Thermodynamic data for cement clinkering', *Cement and Concrete Research* 132(106043).

Meyer, V., Pisch, A., Penttila, K. and Koukkari, P. (2016), 'Computation of steady state thermochemistry in rotary kilns: Application to the cement clinker manufacturing process', *Chemical Engineering Research and Design*, 115(B):335-347.

Ludwig, HM. and Zhang, W. (2015) 'Research review of cement clinker chemistry', *Cement and Concrete Research*, 78(A): 24-37.

Scheil, E. (1942) 'Bemerkungen zur schichtkristallbildung', *International Journal of Materials Research*, 34(3):70-72

Shim, SH., Lee, TH., Yang, SJ., Noor, N. B. Md. and Kim, JHJ. (2021) 'Calculation of Cement Composition Using a New Model Compared to the Bogue Model', *Materials,* 14(16).

Taylor, H.F.W. (1997) *Cement chemistry,* 2nd edition, Thomas Telford Publishing.

Tazuddin, A., Hemantkumar N. A. and Chatterjee, A. (2018) 'Phase equilibria studies of CaO-SiO_2-Al_2O_3-Fe_2O_3-MgO system using CALPHAD', *Calphad* 60: 116–125.

Tazuddin, A., Hemantkumar N. A. and Chatterjee, A. (2020) 'Thermodynamic simulation in evaluating the role of minor oxides and mineralizers in Portland cement clinker phase formation', *SN Applied Sciences* 2(10): 17–37.

Calcium Silicate Hydrate Surface

Ziga Casar[1a], Paul Bowen[2a], Aslam Kunhi Mohamed[3bc], Karen Scrivener[4a]

[a] *Laboratory of Construction Materials, Institut des Matériaux, Ecole Polytechnique Fédérale de Lausanne (EPFL), CH-1015 Lausanne, Switzerland*
[b] *Institute for Building Materials, Department of Civil, Environmental and Geomatic Engineering, ETH Zürich, CH-8093 Zürich, Switzerland*
[c] *current address: Dept. of Civil Engineering, Indian Institute of Technology Madras, Chennai, TN 600036, India*

[1] *ziga.casar@epfl.ch*
[2] *paul.bowen@epfl.ch*
[3] *akm@civil.iitm.ac.in*
[4] *karen.scrivener@epfl.ch*

Abstract

Key to lowering the unsustainable footprint of cement lies in understanding the surface chemistry of the hydrated and anhydrated phases. While the bulk structure of the main hydration phase calcium silicate hydrate (C-S-H) is today well understood, the C-S-H surface is still not explored, and somewhat of a mystery. It is known that C-S-H has a high specific surface area (200 - 300m^2/g), which makes it de facto of great importance for concrete properties. There are many unknown interactions at the interface of C-S-H, including sulfate adsorption, additives and chloride binding and transport which cause major durability issues in service life of reinforced concrete structures. To study and understand these phenomena a description of the surface is needed, which should come in the form of a realistic-pragmatic model surface, since C-S-H is poorly nanocrystalline, meaning there will be no long-range order as we observe in crystalline systems. Here we present a new multiparameter approach in defining the atomistic structure of the C-S-H nanofoil with its basal (001) surface. We show that the typically measured properties of C-S-H (Ca/Si ratio, mean chain length, relative concentration of silanol and hydroxide groups) are sufficient for describing the atomistic structure. Further we argue that contrary to common believes, the surface is mainly calcium terminated instead of silicate terminated, at applied system Ca/Si ratios. Finally, an atomistic model of the C-S-H nanofoil is proposed, which agrees with measured C-S-H properties.

Keywords: calcium silicate hydrate, atomistic model, molecular dynamics

1. Introduction

Calcium silicate hydrate (C-S-H) is the main hydration product of Portland and blended cements and the primary binder. This porous network controls the transport of ions, including chloride ingress, which causes durability issues in steel reinforced concrete structures (Wilson 2022). TEM images of C-S-H (Kumar 2017) show a nanofoil morphology. The reported length of C-S-H nanofoils in literature lies between 100 and 200 nm (Kumar 2017, Andalibi 2018) with a thickness of below 5 nm (Andalibi 2018). Zeta potential values of C-S-H in high pH and calcium rich solutions are consistently positive (Yoshida 2021), suggesting an overcompensation of the negative surface charge by strongly sorbed and immobile cations (Predota 2016).

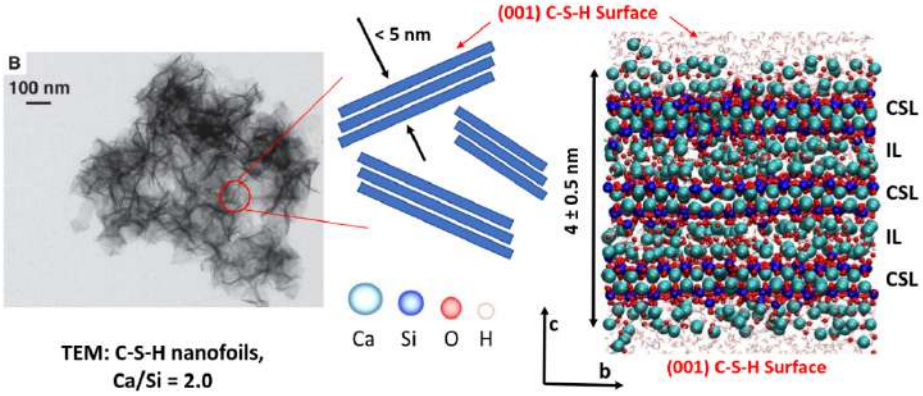


Figure 1. C-S-H nanofoils. Left TEM image of synthetic C-S-H with Ca/Si = 1.7. Right: computational model of 3 layers, 2 interlayers thick C-S-H nanofoil with the dominant (001) basal surfaces at Ca/Si = 1.7. I – interlayer, CSL – calcium-silicate layer

Contrary to the atomic structure of bulk C-S-H, which is today well understood (Kumar 2017, Mohamed 2018), the C-S-H surface is poorly explored. Previous studies (Duque-Redondo 2022) assumed a Q^{2b} silicate termination of the (001) surface. The overall Ca/Si ratios of the model systems were kept below 1.4 and were used to study adsorption phenomena. However, it is well known that the Ca/Si ratio has a significant effect on the adsorption properties of C-S-H (Heinz 2021).

The present paper shows a new multiparameter approach in describing the C-S-H nanofoil with the basal (001) surface. Same as for the C-S-H bulk, there is no single solution to describing the C-S-H surface. The surface configuration strongly depends on the Ca/Si ratio. Finally, we propose a full atomistic model of the C-S-H nanofoil structure with a Ca/Si = 1.7.

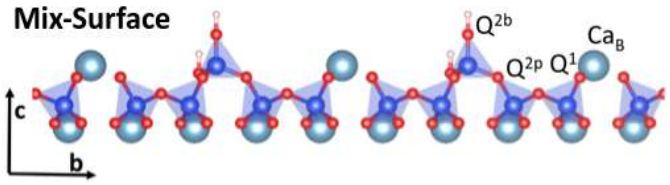


Figure 2. Investigated surface termination. Color legend same as in figure 1.

2. Methods

The C-S-H atomistic models were generated with the brick model of Mohamed et al. (2018). In short, first a C-S-H bulk structure was constructed with Ca/Si = 1.7. The bulk was generated by introducing defects into the tobermorite 14 Å structure. To generate a model of the C-S-H nanofoil with the (001) basal surface, calcium-silicate chains were added at the top and the bottom of the structure. The chains represent the

surface termination of C-S-H (see figure 2). Q^{2b} silicates were randomly removed and replaced by Ca_B, with which the targeted MCL for each silicate chain was achieved.

Classical molecular dynamics was used to relax the structures. All simulations were carried out with LAMMPS. The used force field was a modified version of the CemFF2 force field (Mohamed 2020). The simulations were 20 ns long with a timestep of 0.28 fs.

3. Results

3.1 Thickness and surface area

As seen from table 1, the C-S-H nanofoil model with 3 layers, 2 interlayers thickness is in best accordance with the experimental data (SSA and thickness). The exact model is seen in figure 1. While the 4 layers, 3 interlayers model is indeed below 5 nm thick, it is evident from the underestimated SSA that it does not fully replicate the experimental observed quantities.

With this we conclude that the C-S-H nanofoils are indeed 100 to 200 nm long, and only 3 layers, 2 interlayers thick, which results in a thickness of 3.5 nm, when ion adsorption is not considered.

Table 1. Calculated specific surface area and thickness as a function of the number of interlayers. The thickness is measured between surface Q^{2b} silicates, and it does not include adsorb ions. The experimental data is taken from Yoshida et al. (2021) and Andalibi et al. (2018).

Number of layers (Number of interlayers)	Approximated specific (001) surface area [m^2/g]	Approximated thickness of the C-S-H foil [nm]
2 (1)	360	2.2 nm
3 (2)	220	3.5 nm
4 (3)	160	4.9 nm
Experimental	200-300	3.5-4.0 nm

3.2 Surface termination

The surface termination was generated with the idea that there is no evidence of why the bulk, or the surface would favor Q^{2b} connectivity of dimers. Therefore, each silicate chain (bulk and surface) has the same MCL of 3.0. We decided to fix the bulk Ca/Si at 1.7, which results in an overall Ca/Si of 1.48. The Ca/Si ratio can be increased with calcium adsorption onto the surface, which is suggested by zeta potential measurements (Yoshida 2021). To achieve an overall Ca/Si of 1.7 for the Mix-Surface with 3 layers, 2 interlayers thick bulk with Ca/Si = 1.7, four Ca^{2+} need to be adsorbed per surface Q^{2b} silicate.

3.3 Calcium adsorption

The large hydration radius of calcium and the repulsive electrostatic forces likely hinder the adsorption of Ca^{2+} (Döpke 2019). However, at high pH the dominant species in solution is the $Ca(OH)^+$ complex and not Ca^{2+}. It is expected that hydroxide ions will act as an adsorption bridge for Ca^{2+}, as observed on gibbsite (Siretanu 2014). This is further supported by positive zeta potentials for low Ca/Si C-S-H when titrated with $Ca(OH)_2$ (Yoshida 2021). Indeed, the Mix-Surface with additional calcium on the surface, requires hydroxide ions to accumulate all the needed calcium in proximity of the surface. Around 30% of Ca^{2+} are inner sphere adsorbed preferentially on top of a dimer (Q^1-Q^1 or Q^{2p}-Q^{2p}) where it coordinates to 2-3 oxygens of the dimer pair and an additional OH^-, which acts as a bridge to the main layer in-surface calcium. Further the MD results suggest a formation of a calcium-hydroxide network on top of the (001) surface, which starts from Ca_B and inner sphere adsorbed calcium on top of the dimers.

4. Conclusions

Due to the nanocrystalline nature of C-S-H a solution and bulk depended surface complexation is expected. In the present article we show a new multiparameter approach for a pragmatic and realistic description of the C-S-H nanofoil with the (001) surface. The parameters used are the typical parameters in C-S-H characterization: Ca/Si, MCL, Si-OH/Si and Ca-OH/Ca. With the brick model we constructed a model of the C-S-H nanofoil (figure 1) which to the best possible extend mimics the experimental data for C-S-H with Ca/Si = 1.7, as seen in table 2 and figure 1.

Table 2. Comparison of structural properties of C-S-H bulk, surface and overall (C-S-H nanofoil) with the experimental data. **90% deprotonation of surface silanol groups assumed. Experimental data taken from Duque-Redonto et al. (2022).

Property	C-S-H bulk	C-S-H Surface	C-S-H nanofoil	Experimental
Ca/Si	1.72	1.66	1.7	1.7
MCL	3.0	3.0	3.0	3.0
Si-OH/Si	11%	2.1%**	9%	9%
Ca-OH/Ca	37%	44%	39%	45%

Acknowledgments

The authors would like to thank the Swiss National Foundation for financing the contribution of Ziga Casar (grant no. 179076).

References

Wilson, W.; Gonthier, J. N.; Georget, F.; Scrivener, K. L. Insights on Chemical and Physical Chloride Binding in Blended Cement Pastes. Cem Concr Res 2022, 156.

Kumar, A.; Walder, B. J.; Kunhi Mohamed, A.; Hofstetter, A.; Srinivasan, B.; Rossini, A. J.; Scrivener, K.; Emsley, L.; Bowen, P. The Atomic-Level Structure of Cementitious Calcium Silicate Hydrate. The Journal of Physical Chemistry C 2017, 121 (32), 17188–17196.

Andalibi, M. R.; Kumar, A.; Srinivasan, B.; Bowen, P.; Scrivener, K.; Ludwig, C.; Testino, A. On the Mesoscale Mechanism of Synthetic Calcium-Silicate-Hydrate Precipitation: A Population Balance Modeling Approach. J Mater Chem A Mater 2018, 6 (2), 363–373.

Yoshida, S.; Elakneswaran, Y.; Nawa, T. Electrostatic Properties of C–S–H and C-A-S-H for Predicting Calcium and Chloride Adsorption. Cem Concr Compos 2021, 121, 104109.

Předota, M.; Machesky, M. L.; Wesolowski, D. J. Molecular Origins of the Zeta Potential. *Langmuir* **2016**, *32* (40), 10189–10198.

Duque-Redondo, E.; Bonnaud, P. A.; Manzano, H. A Comprehensive Review of C-S-H Empirical and Computational Models, Their Applications, and Practical Aspects. Cem Concr Res 2022, 156, 106784.

Heinz, O.; Heinz, H. Cement Interfaces: Current Understanding, Challenges, and Opportunities. Langmuir 2021, 37 (21), 6347–6356.

Kunhi Mohamed, A.; Parker, S. C.; Bowen, P.; Galmarini, S. An Atomistic Building Block Description of C-S-H - Towards a Realistic C-S-H Model. Cem Concr Res 2018, 107 (March), 221–235.

Kunhi Mohamed, A.; Moutzouri, P.; Berruyer, P.; Walder, B. J.; Siramanont, J.; Harris, M.; Negroni, M.; Galmarini, S. C.; Parker, S. C.; Scrivener, K. L.; Emsley, L.; Bowen, P. The Atomic-Level Structure of Cementitious Calcium Aluminate Silicate Hydrate. J Am Chem Soc 2020, 142 (25), 11060–11071.

F. Döpke, M.; Lützenkirchen, J.; A. Moultos, O.; Siboulet, B.; Dufrêche, J.-F.; T. Padding, J.; Hartkamp, R. Preferential Adsorption in Mixed Electrolytes Confined by Charged Amorphous Silica. The Journal of Physical Chemistry C 2019, 123 (27), 16711–16720.

Siretanu, I.; Ebeling, D.; Andersson, M. P.; Stipp, S. L. S.; Philipse, A.; Stuart, M. C.; van den Ende, D.; Mugele, F. Direct Observation of Ionic Structure at Solid-Liquid Interfaces: A Deep Look into the Stern Layer. Sci Rep 2014, 4.

The 16th International Congress on the Chemistry of Cement 2023 (ICCC2023)
"Further Reduction of CO_2 -Emissions and Circularity in the Cement and Concrete Industry"
September 18–22, 2023, Bangkok, Thailand

Experimental thermodynamic study of selected cement clinker phases

C.M. Moundounga[1,2*], Theodore Hanein[2], A. Pisch[1]

[1] *Université Grenoble Alpres CNRS-SiMaP, Grenoble, France*
Email: alexander.pisch@simap.grenoble-inp.fr

[2*] *University of Sheffield, MSE, Sheffield, England*
Email: c.mawalalamoundounga@sheffield.ac.uk and t.hanein@sheffield.ac.uk

ABSTRACT

High quality data for the thermodynamic properties of clinker phases is important to optimize the synthesis conditions at high temperature and to characterize their reactivity behaviour during hydration or carbonation. However, there is still some uncertainty for these properties even for some key mineralogical phases of an Portland cement (PC) clinker. For example, the heat capacity and the enthalpy of formation of the ferrite phase $Ca_2Fe_{2-x}Al_xO_5$ as a function of composition was never determined.
The aim of the present study is the experimental determination of the heat contents H(T)-H(298K) as well as the enthalpies of formation of the compounds Ca_2SiO_4 (γ, α', α), the solid solution $Ca_2Fe_{2-x}Al_xO_5$ and the stoichiometric compounds $Ca_5Al_6O_{14}$, $CaAl_{12}O_{19}$, and $Ca_3Si_2O_7$ using isothermal drop calorimetry (SETARAM MHTC96 calorimeter). These new data will help to generate an updated thermodynamic database allowing the calculation of a series of phase diagrams reproducing the characteristic chemical features of a clinker.
The standard heat of formation of these compounds and solutions is determined by high temperature drop solution calorimetry. A novel oxide solvent, rich in CaO and Al_2O_3 at 1450°C, was used for the dissolution experiments and the obtained results are reported. Dissolution times of the dropped solid compounds do not exceed 30 min, which makes it particularly suited for the determination of the standard heat of formations. The obtained values will also be compared to theoretical values using DFT calculations.

KEYWORDS: *Thermodynamic, heat content, heat of formation, drop calorimetry*

1. Introduction

Knowledge of the thermodynamic behaviour of the major mineralogical phases of an PC (Portland Cement) clinker is necessary to understand the factors that govern their formation and stability. The main aim of this research is to review and to study experimentally the thermodynamic properties of some selected compounds and solid solutions of the main mineralogical phases of an PC clinker. The various polymorphs of belite (Ca_2SiO_4) and rankinite ($Ca_3Si_2O_7$) are important constituents of Portland type and carbonatable clinkers, the solid solution $Ca_2Al_xFe_{2-x}O_5$ (brownmillerite), also known as C_4AF in cement chemistry nomenclature, is one of the four constituents commonly found in PC clinker. An interesting feature of brownmillerite is its ability to resist sulfates, which is an important property for heavy construction in water contact areas. Regarding $Ca_5Al_6O_{14}$, DFT calculations suggest that this compound is the most stable in the CaO-Al_2O_3 system. In addition, $Ca_5Al_6O_{14}$ and $CaAl_{12}O_{19}$ are important for CaO-Al_2O_3 phase diagram calculation, but lack of extensive data on these phases does not lead to a full understanding of the binary system. The standard heats of formation were determined with a newly developed solution calorimetric method using a CaO-Al_2O_3 rich based solvent. All measurements were performed on carefully synthesized and characterized samples. This work will provide new data to supplement all those existing in literature.

2. Experimental study

The syntheses of all compounds were done by solid-state reaction. The powder precursors $CaCO_3$ (Alpha Aesar, 99.5%), SiO_2 (Sibelco, 99%) Al_2O_3 (Alpha Aesar, 99.95%), Fe_2O_3 (Alpha Aesar 99.5%) are dried in muffle furnace at 500°C for 24hrs, mixed respecting the stoichiometry, calcined at 1000°C for 1hr then annealed according to the following parameters: $Ca_2Fe_{2-x}Al_xO_5$ 1250°C/2hrs; Ca_2SiO_4 1550°C/8hrs; $Ca_5Al_6O_{14}$ 1250°C/380hrs; $CaAl_{12}O_{19}$ 1300°C/12hrs and $Ca_3Si_2O_7$ 1420°C/12hrs.

The mineralogical composition of the samples was determined using X-ray diffraction (X'Pert Pro MPD, PANalytical), with CuKα radiation of λ= 1.5419 Å. The DSC Labsys^{TM} Evo was used to measure the transition temperatures. A MHTC96 (Setaram) high temperature isoperibolic calorimeter with a drop measuring head (S, 1300°C max & B 1500°C max) was used for the heat contents as a function of temperature. The standard heat of formation was measured by drop solution calorimetry using a pure oxide-based solvent type as proposed by C-S-A-M described by Koryttseva & Navrotsky (2017). The main difference is the type of solvent. While Koryttseva & Navrotsky used a $CaO-SiO_2$ based acid solvent, we decided to use a $CaO-Al_2O_3$ based amphoteric solvent with a nominal composition: CaO 48 mol%, Al_2O_3 45 mol%, SiO_2 3 mol% and MgO 4 mol%. The calibration of the calorimeter was carried out from 600°C to 1480°C by dropping Al_2O_3 pellets using the tabulated data from the Factsage pure substance database (www.factsage.com) as reference values. For the DSC measurements, the melting point of NaCl and the transition and melting point of K_2SO_4 served as references for temperature calibration.

3. Results and discussion

3.1. Heat contents as a function of temperature

3.1.1 Ca_2SiO_4

The experimental heat contents as a function of temperature of Ca_2SiO_4 are plotted in Fig. 1. There are no heat content measurements of the γ→α' Ca_2SiO_4 transition published in the literature. Coughlin & O'Brien (1957) measured the β, α'-Ca_2SiO_4 relative enthalpy by an inversed drop calorimetric technique. The temperature of transition γ→α' is situated near 847°C (Coughlin & O'Brien, 1957). Therefore, in this present work the measured values include the γ-Ca_2SiO_4 to α'- Ca_2SiO_4 in the range 700-1480°C.

Coughlin & O'Brien (1957) carried out thermodynamic measurements by using two distinct polymorphs as reference, namely γ- Ca_2SiO_4, the more stable form, and β- Ca_2SiO_4 containing 0.32% aluminium and iron oxide and 0.14% magnesium oxide. To be able to compare our data with the one from Coughlin & O'Brien, their experimental values for α',α -Ca_2SiO_4, Coughlin & O'Brien (1957) were adjusted using the γ-Ca_2SiO_4→ β- Ca_2SiO_4 enthalpy of transition from Forest (1971), in order to have the same reference state. For γ- Ca_2SiO_4→ α'- Ca_2SiO_4, there is good agreement with Coughlin & O'Brien (1957). Similarly, for γ- Ca_2SiO_4→ α- Ca_2SiO_4 we agree with the adjusted values.

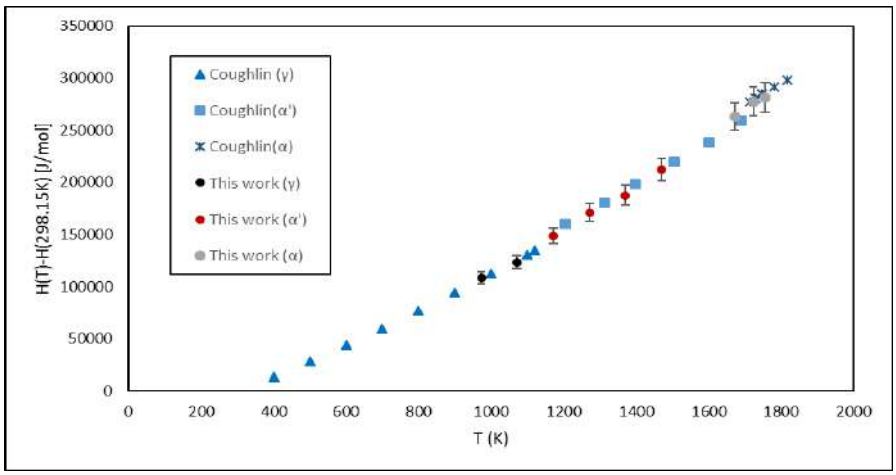


Fig. 1. Experimental heat content values for Ca2SiO4 as compared to Coughlin & O'Brien's experimental data. Coughlin & O'Brien's data for α', α -Ca_2SiO_4 was adjusted with the enthalpy of transition γ-Ca_2SiO_4→ β- Ca_2SiO_4 from Forest (1971) to have the same reference state.

3.1.2 $CaFeAlO_5$

The heat content of brownmillerite Ca_2FeAlO_5 with equimolar Fe and Al content was measured from 590 to 1096°C. The experimental data is presented in Fig. 2 and is compared to calculated values using the Factsage FTOxid database. The is a reasonable quantitative agreement for temperatures below 900°C.The main discrepancy between both data sets is observed at high temperature at which the calculated data points at 1096°C and 985°C are respectively 13.6KJ.mole^{-1} and 14.5KJ.mole^{-1} higher than our experiment results.

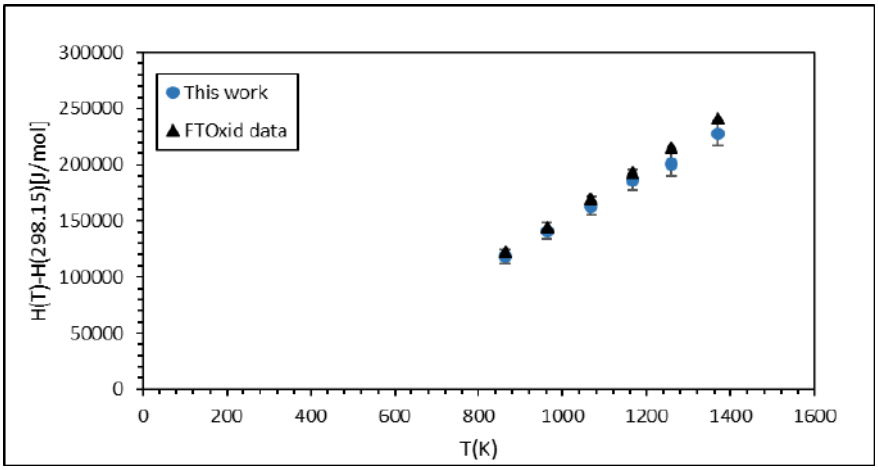


Fig. 2. Experimental heat content as a function of temperature for Ca_2FeAlO_5 plotted together with calculated data using the FTOxid database from FactSage.

3.2 Standard heat of formation of Ca_2FeAlO_5

The standard heat of formation of equimolar brownmillerite Ca_2FeAlO_5 was measured using dissolution calorimetry. Two series of Ca_2AlFeO_5 samples were dissolved in the oxide solvent. The experimentally observed values for the heat of dissolution are presented in Fig. 3.

In the case of brownmillerite, the heat of dissolution varies linearly with composition. To calculate the standard heat of formation, the value at infinite dilution in the solvent was calculated using a linear regression of all datapoints. The obtained value is given by:

$$Q_{diss}\ (25°C) = 453.6 \pm 44.0\ \text{kJ.mole}^{-1}.$$

The reported uncertainty corresponds to a 95% confidence interval of the mean slope of the curve. Using the heat of dissolutions for pure CaO, Al_2O_3 and Fe_2O_3, (77.6±2.7 kJ.mole^{-1}, 148.6±2.7 kJ.mole^{-1} and 352.5±7.4 kJ.mole^{-1}) the standard heat of formation can be calculated and the value is:

$$\Delta_f H(25°C) = -62.4 \pm 59.2\ \text{J.mole}^{-1}$$

Our new value is in reasonable agreement with the one reported by $\Delta_f H(25°C)$ = -47±2 kJ.mole-1 by Ayed et al (1993). However, it is important to mention, that the large uncertainty for the heat of dissolution of brownmillerite is due to an insufficient number of dissolutions and a high confidence interval of 95%. Further experiments are needed (at least two other dissolution series for Ca_2FeAlO_5 and Fe_2O_3) to improve this value. But, the lowest uncertainty which can be achieved with the MHTC 96 equipment is in the 10 to 15 kJ.mole^{-1} range.

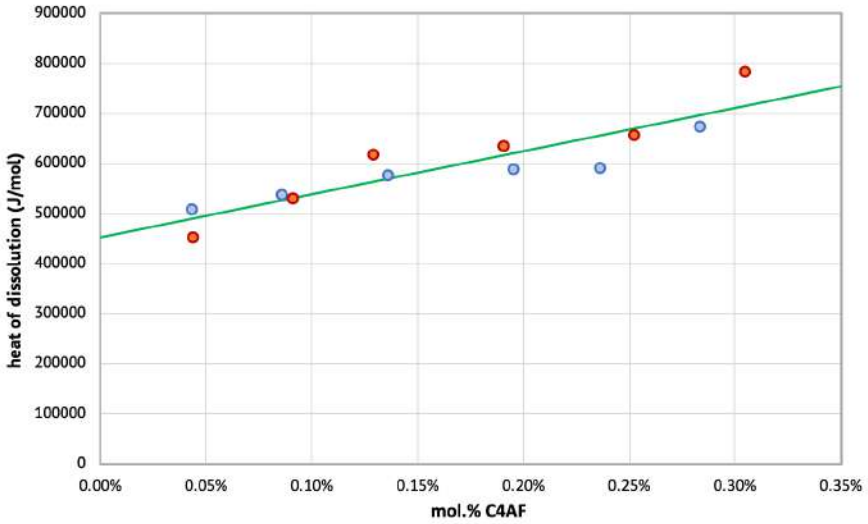


Fig. 3. Experimental heat of dissolution of Ca_2AlFeO_5 in a novel oxide solvent.

4. Conclusion

A thorough knowledge of the thermodynamic properties as a function of temperature for the main mineralogical phases of a PC clinker is of fundamental importance to be able to predict their synthesis conditions and stability. In this work, presented new data on the relative enthalpies of γ- Ca_2SiO_4→α'-Ca_2SiO_4, γ- Ca_2SiO_4→α- Ca_2SiO_4 and for Ca_2AlFeO_5 using drop calorimetry. In addition, we determined the standard heat of formation of equimolar brownmillerite and the observed value is in reasonable agreement with the only experimental datapoint available in the literature.

Acknowledgement

The authors would like to acknowledge the financial support of Nanocem/Innovandi for the funding of Core Project 17, of which this work was a part of. T. Hanein and C. Mawalala Moundounda were also supported by UKRI Future Leaders Fellowship (MR/V023829/1) which allowed them to perform low temperature Cp measurements for C_4AF.

References

Koryttseva, A., & Navrotsky, A. (2017) "High-temperature calorimetric study of oxide component dissolution in a CaO–MgO–Al_2O_3–SiO_2 slag at 1450° C". *Journal of the American Ceramic Society*, 100(3): 1172-1177

Ayed, F., Sorrentino, F., & Castanet, R. (1993). Determination par calorimetrie de dissolution des enthalpies de formation de quelques silicates, aluminates et alumino-silicates de calcium. *Journal of Thermal Analysis, 41*, 755-766.

Coughlin, J. P., & O'Brien, C. (1957). High temperature heat contents of calcium orthosilicate. *Journal of Physical Chemestry, 61*, 767-769.

Forest, J. (1971). Connaissance de l'orthosilicate de calcium. *Bulletin de la Société française de Minéralogie et de Cristallographie, 94*, 118-137.

The 16th International Congress on the Chemistry of Cement 2023 (ICCC2023)
"Further Reduction of CO_2 -Emissions and Circularity in the Cement and Concrete Industry"
September 18–22, 2023, Bangkok, Thailand

Atomic Scale Insight of Hydration Temperature Rise Inhibitors (TRI) Affecting Calcium Activity via AIMD

Jiale Huang[1,2,3*], Hegoi Manzano[2], Zhangli Hu[1,3], and Jiaping Liu[1,3]

1 School of Materials Science and Engineering, Southeast University, Nanjing, China
Email: jialehuang07@foxmail.com
2 Fisika saila, Euskal Herriko Unibertsitatea UPV/EHU, Sarriena Auzoa z/g, 48940 Leioa, Basque Country, Spain
3 State Key Laboratory of High Performance Civil Engineering Materials, Jiangsu Research Institute of Building Science Co., Nanjing, China

ABSTRACT

Thermal shrinkage and cracking are one of the main concerns for mass concrete. Small molecule sugar, known as hydration temperature rise inhibitors (TRI), can effectively control the hydration temperature of concrete. However, the atomic scale mechanism of TRI has not been clarified and the structural functioning relationship has not been established, which brings difficulties to the efficient application and targeted design of TRI. This study employs ab initio molecular dynamics simulations to investigate the complexation behavior of various small sugar molecules with calcium ions and to elucidate the underlying factors responsible for their differences. The aim is to explore the impact of such additives on the chemical reactivity of calcium ions. Our findings indicate that the charged characteristics of small sugar molecules play a crucial role in determining the complexation ability of calcium ions. Additionally, our analysis of Bader charges reveals that calcium ions interact with organic molecules through electron exchange, thereby disturbing their own reactivity. This may affect the 'dissolution-precipitation' equilibrium in the hydration process, leading to macroscopic perturbations such as delayed gelation or reduced heat of hydration. The present study sheds light on the atomic-level mechanism by which small sugar molecules affect the hydration environment and provides a basis for further research on molecular simulation and design theory for regulating early hydration.

KEYWORDS: *Hydration temperature rise inhibitors; atomic scale; ab initio molecular dynamics; chemical reactivity*

1. Introduction

In the construction of large infrastructure projects, the heat release problem caused by the hydration of large volume concrete can be difficult to mitigate. Unbalanced heat release can lead to the concentration of thermal stress, resulting in local thermal cracks in the concrete structure (Bullard et al., (2011); Scrivener et al., (2015)). In recent years, regulating cement hydration heat release has become an urgent problem for concrete engineers. Organic additives, such as hydration temperature rise inhibitors, are used as raw materials to assist in adjusting the reaction, known as the organic-inorganic composite reaction, to modify the hydration heat release (Yan et al., (2021), (2020)). The hydration of cement plays a crucial role in determining the microstructure of concrete. The reaction process is dependent on the balance between the dissolution and precipitation of cement minerals and the reaction environment (Mehta and Monteiro, (2017)). Understanding the impact of organic matter on the balance and reaction environment is crucial for controlling the cement hydration process. By doing so, it can be ensured that the process proceeds as required and achieves the desired outcome (Flatt and Houst, (2001); Marchon and Flatt, (2016)). The calcium ion is a pivotal factor in the equilibrium and reaction environment of cement hydration, as its reactivity can greatly influence the robustness of the hydration process. Therefore, understanding the behaviour of calcium ions during hydration is crucial for optimizing the performance and properties of cement-based materials (Lina et al., (2021)). Furthermore, the nano mechanisms by

which admixtures control the hydration process largely depend on phenomenological characterization. However, due to the limitations of current testing equipment resolution, it is a significant obstacle to gain a deeper understanding of the physical and chemical nature of control mechanisms and to develop admixture structures in reverse. In recent years, molecular dynamics simulation has played a fundamental role in providing necessary data for analytical models such as ion dissolution complexation, organic-inorganic interface interaction and structural design of chemical additives, but this accuracy depends on the choice of empirical force field (Manzano et al., (2015), (2011)). Ab initio Molecular Dynamics (AIMD) is a computational technique that employs quantum mechanics to investigate the characteristics of molecules and condensates. Through the analysis of electronic structure, Ab initio Molecular Dynamics (AIMD) offered valuable insights into the impact of external factors on the reactivity of chemical reactions, specifically regarding the ability to gain or lose electrons. In this work, AIMD was employed to explore the complexation differences and origins between calcium ions and various small molecule sugars, such as adsorption energy and electron transfer. Our particular emphasis was on elucidating the impact of electron transfer on the activity of calcium ions, thereby providing atomic-level insights into the modulation of hydration processes by chemical additives.

2. Methods

All calculations were performed within the framework of density functional theory (DFT) using the CP2K/QUICKSTEP package(Hutter et al., (2014); Kühne et al., (2020)). A mixed basis set consisting of Gaussian basis and plane waves (GPW) (Lippert et al., (1997)) was employed, with the Gaussian basis set using double-zeta valence plus polarization functions (DZVP) (VandeVondele and Hutter, (2007)) and the plane wave cutoff set to 350 Ry. Matrix diagonalization was employed to optimize the wave functions, with Fermi tail smearing aiding self-consistent field (SCF) convergence and the remaining core electrons represented by Goedecker-Teter-Hutter (GTH) pseudopotentials(Goedecker and Teter, (1996)). Initially, four small molecule sugars were placed in a cubic lattice with dimensions a=20 Å, b=20 Å, c=20 Å, and their geometries were optimized using the Broyden-Fletcher-Goldfarb-Shanno (BFGS) (Vandevondele et al., (2005)) minimizer to locate the positions of highest activity. Calcium ions were subsequently placed in the vicinity of the optimized positions, and the resulting complexes were subjected to geometry optimization. The ENERGY_FORCE function in the CP2K package was then utilized to analyze the electronic structure evolution of the small molecule sugars before and after complexation.

3. Results and discussion

Calcium atoms were placed at the positions of highest activity for four types of small molecule sugars, and AIMD was employed to investigate the complexation effects between the small molecule sugars and calcium ions. The adsorption energy results are presented in Table 1. As can be seen from the table 1, the adsorption energy of D-galactarate with calcium ions is much higher than that of the other three small molecule sugars, due to the higher activity of the ester functional group compared to the hydroxyl functional group. Additionally, D-galactarate is overall negatively charged, and in solution, calcium ions tend to complex with D-galactarate, possibly due to charge-driven effects. D-galactitol and α-D-glucopyranose are both hydroxyl-containing compounds with similar complexation abilities toward calcium ions. To investigate the possible role of charge in ion complexation, α-D-glucopyranose was selected and protonated, resulting in a decrease in adsorption energy from -0.2455 eV to -3.5384 eV. This suggests that charge plays a critical role in ion complexation, and therefore, it is particularly important to investigate the charge transfer between small molecule sugars and calcium ions.

Table 1 Adsorption energy of small molecule sugar and calcium ion

Type	D-galactarate	D-galactitol	α-D-Glucopyranose	Deprotonated α-D-Glucopyranose
E_{ads} (ev)	-6.4755	-0.2395	-0.2455	-3.5384

D-galactarate and D-galactitol were selected as the objects of study for charge transfer, since these two types of small molecule sugars exhibit the most significant difference in binding energy with calcium

ions. As shown in Table 2 and Fig 1, the Bader charge of calcium increased by 1.5639 |e| upon binding with D-galactarate, indicating the loss of 1.5639 |e| from calcium. In contrast, the result for D-galactitol showed a much smaller increase in the Bader charge of calcium, only 0.1754 |e|. Compared to D-galactarate, the binding of D-galactitol does not cause a significant change in the charge state of calcium, which may explain the poor condensation effect of D-galactitol due to its relatively weak influence on the hydration environment of calcium ions, such as the chemical state of calcium ions.

Table 2 Bader charge evolution of adsorption sites of small sugar and calcium ions

Sugar type	Atom	Bader Charge before composite	Bader Charge after composite
D-galactarate	Ca	0	1.5639
	O1	-1.5309	-1.817
	O2	-1.5677	-1.7748
	O3	-1.4336	-1.7096
D-galactitol	Ca	0	0.1754
	O1	-1.0029	-0.9984
	O2	-0.9706	-1.1057
	O3	-1.0596	-1.0548

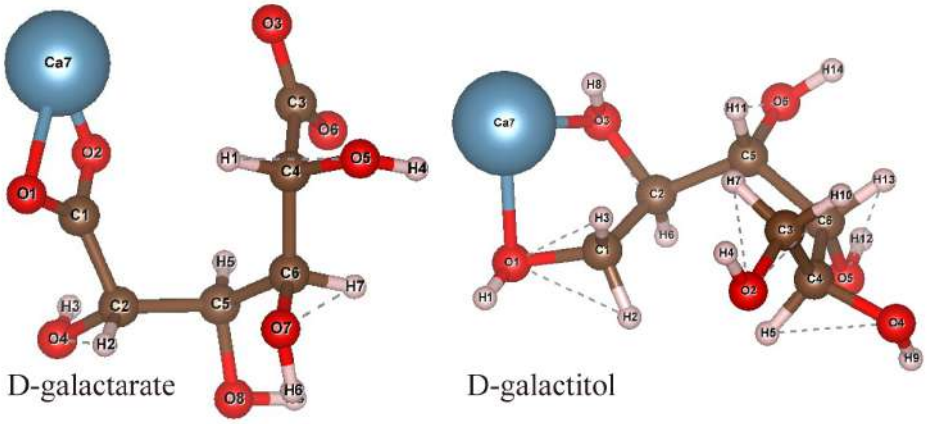


Fig 1 Structure diagram of small molecule sugar and calcium ion adsorption sites

4. Conclusion

In this study, we employed first-principles calculations to investigate the complexation behaviour of calcium ions with three small sugar molecules and the underlying factors for their differences. Our results indicate that the charged properties of α-D- Glucopyranose and its protonated form significantly affect the complexation ability of calcium ions. Furthermore, the Bader charge analysis results reveal that calcium ions interact with organic molecules through electron exchange, which disturbs the reactivity of the calcium ions themselves. This could potentially affect the "dissolution-precipitation" equilibrium in the hydration process, leading to disturbances in the macroscopic hydration processes such as slowing down of the hydration or decreasing the heat of hydration. Experimentally detecting the electron exchange phenomenon accompanying chemical reactions would be a formidable challenge. The first-principles provides an electron-scale perspective, laying a solid foundation for the design of future admixture.

Acknowledgements

The authors gratefully acknowledge the research supports provided by the National Natural Science Foundation of China (Grant No.:51738004), the scientific and techno-logical research and development plan of China railway corporation (Contract No.: 2017g006-b), the “Departamento de Educación, Política

Lingüística y Cultura del Gobierno Vasco" (Grant No. IT1458-22), the "Ministerio de Ciencia e Innovación" (TED2021-130860B-I00), and the Transnational Common Laboratory "LTC-Green Concrete". Jiale Huang gratefully acknowledges financial support from China Scholarship Council (CSC number: 202106090091). And the authors also greatly appreciate the State Key Laboratory of High-Performance Civil Engineering Materials for funding the research project and Beijng PARATERA Tech CO.,Ltd. For providing HPC resources that have contributed to the research results reported within this paper.

References

Bullard, J.W., Jennings, H.M., Livingston, R.A., Nonat, A., Scherer, G.W., Schweitzer, J.S., Scrivener, K.L., and Thomas, J.J., (2011). "Mechanisms of cement hydration." *Cement and Concrete Research*, 41, 1208–1223

Scrivener, K.L., Juilland, P., and Monteiro, P.J.M., (2015). "Advances in understanding hydration of Portland cement." *Cement and Concrete Research*, 78, 38–56

Yan, Y., Scrivener, K.L., Yu, C., Ouzia, A., and Liu, J., (2021). "Effect of a novel starch-based temperature rise inhibitor on cement hydration and microstructure development: The second peak study." *Cement and Concrete Research*, 141, 106325

Yan, Y., Ouzia, A., Yu, C., Liu, J., and Scrivener, K.L., (2020). "Effect of a novel starch-based temperature rise inhibitor on cement hydration and microstructure development." *Cement and Concrete Research*, 129, 105961

Mehta, P.K., and Monteiro, P.J.M., (2017). Concrete microstructure, properties and materials

Marchon, D., and Flatt, R.J., (2016). "Impact of chemical admixtures on cement hydration." *Science and Technology of Concrete Admixtures*, 279–304

Flatt, R.J., and Houst, Y.F., (2001). "A simplified view on chemical effects perturbing the action of superplasticizers." *Cement and Concrete Research*, 31, 1169–1176

Lina, B., Barbara, L., Alejandro, F.M., and Christophe, L., (2021). "Portlandite solubility and Ca2+ activity in presence of gluconate and hexitols." *Cement and Concrete Research*, 149, 106563

Manzano, H., Durgun, E., López-Arbeloa, I., and Grossman, J.C., (2015). "Insight on tricalcium silicate hydration and dissolution mechanism from molecular simulations." *ACS Applied Materials and Interfaces*, 7, 14726–14733

Manzano, H., Durgun, E., Abdolhosseine Qomi, M.J., Ulm, F.J., Pellenq, R.J.M., and Grossman, J.C., (2011). "Impact of chemical impurities on the crystalline cement clinker phases determined by atomistic simulations." *Crystal Growth and Design*, 11, 2964–2972

Kühne, T.D., Iannuzzi, M., Del Ben, M., Rybkin, V. V., Seewald, P., Stein, F., Laino, T., Khaliullin, R.Z., Schütt, O., Schiffmann, F., Golze, D., Wilhelm, J., Chulkov, S., Bani-Hashemian, M.H., Weber, V., Borštnik, U., Taillefumier, M., Jakobovits, A.S., Lazzaro, A., Pabst, H., Müller, T., Schade, R., Guidon, M., Andermatt, S., Holmberg, N., Schenter, G.K., Hehn, A., Bussy, A., Belleflamme, F., Tabacchi, G., Glöß, A., Lass, M., Bethune, I., Mundy, C.J., Plessl, C., Watkins, M., VandeVondele, J., Krack, M., and Hutter, J., (2020). "CP2K: An electronic structure and molecular dynamics software package -Quickstep: Efficient and accurate electronic structure calculations." *Journal of Chemical Physics*, 152

Hutter, J., Iannuzzi, M., Schiffmann, F., and Vandevondele, J., (2014). "Cp2k: Atomistic simulations of condensed matter systems." *Wiley Interdisciplinary Reviews: Computational Molecular Science*, 4, 15–25

Lippert, G., Hutter, J., and Parrinello, M., (1997). "A hybrid Gaussian and plane wave density functional scheme." *Molecular Physics*, 92, 477–488

VandeVondele, J., and Hutter, J., (2007). "Gaussian basis sets for accurate calculations on molecular systems in gas and condensed phases." *Journal of Chemical Physics*, 127

Goedecker, S., and Teter, M., (1996). "Separable dual-space Gaussian pseudopotentials." *Physical Review B - Condensed Matter and Materials Physics*, 54, 1703–1710

Vandevondele, J., Krack, M., Mohamed, F., Parrinello, M., Chassaing, T., and Hutter, J., (2005). "Quickstep: Fast and accurate density functional calculations using a mixed Gaussian and plane waves approach." *Computer Physics Communications*, 167, 103–128

The 16th International Congress on the Chemistry of Cement 2023 (ICCC2023)
"Further Reduction of CO_2 -Emissions and Circularity in the Cement and Concrete Industry"
September 18–22, 2023, Bangkok, Thailand

Impact of autoclaving on the phase assemblage of Portland cement: Experiment and thermodynamic modelling

T. Hirsch[1,*], M. Voigt[2], C. Lehmann[1], B. Meng[2], and B. Lothenbach[3,4]

[1] *Technische Universität Berlin, Faculty VI Planning Building Environment, Building Materials and Construction Chemistry, Berlin, Germany*
Email: t.hirsch@tu-berlin.de, c.lehmann@tu-berlin.de

[2] *Bundesanstalt für Materialforschung und -prüfung, Fachbereich 7.1 Baustoffe, Berlin, Germany*
Email: marieke.voigt@bam.de, birgit.meng@bam.de

[3] *Empa, Concrete & Asphalt Laboratory, Dübendorf, Switzerland*
[4] *NTNU, Department of Structural Engineering, Trondheim, Norway*
Email: barbara.lothenbach@empa.ch

ABSTRACT

Even after autoclaving for 2 weeks in the temperature range of 120 to 200 °C, CEM I paste with a water-to-cement ratio of 0.5 still contains some low-crystalline C-S-H. The conversion of low-crystalline C-S-H to crystalline is faster with increasing temperature. The observed low-crystalline and crystalline C-S-H phases (reinhardbraunsite, jaffeite) indicate that the samples have not reached equilibrium yet under these experimental conditions. However, there is a good agreement between experiment and thermodynamic modelling for the other solids indicating that the used datasets are suitable for this application.

KEYWORDS: *Autoclaving, Crystalline C-S-H, Scawtite, Hydroxylellestadite*

1. Introduction

When concrete is exposed to hydrothermal conditions beyond 100 °C, the phase assemblage changes substantially (Werder et al. 2021; Tian et al. 2022). Such conditions are typically applied in the production of autoclaved (aerated) concrete, calcium silicate bricks and other autoclaved calcium silicate building products (Society of Chemical Industry 1967; Kikuma et al. 2009). The low-crystalline C-S-H gel observed at room temperature is replaced by crystalline C-S-H phases. Sulfate is bound in calcium sulfates or hydroxylellestadite. Depending upon the system chemistry, portlandite and hydrogarnet may occur.
Thermodynamic modelling is frequently performed for temperatures below 100 °C and has strongly enhanced the understanding of cement hydration and deterioration (Lothenbach and Zajac 2019). Beyond 100 °C, however, thermodynamic data for hydrated cements is lacking. The current publication compares experimental observations for a CEM I paste with predictions made by the combination of thermodynamic datasets commonly used in cement science with the recent dataset of Hirsch et al..

2. Materials and methods

The oxide composition of the CEM I 52.5 R (Dyckerhoff) used was determined by X-ray fluorescence (XRF) using a WD-RFA PW 2400 (Philips) based on powder tablets as well as fused discs. Water and carbon dioxide were quantified by thermogravimetric analysis (TG) using a TG2 09 F3 Tarsus (Netzsch) heating at 10 °C/min from room temperature to 850 °C in a nitrogen atmosphere with a flow rate of 40 mL/min. The results are presented in Table 1.

Table 1: Oxide composition of used CEM I as determined by XRF and TG.

Al_2O_3	CaO	Fe_2O_3	K_2O	MgO	MnO	Na_2O	P_2O_5	SiO_2	SO_3	TiO_2	CO_2	H_2O	Sum
3.64	66.24	1.44	0.6	0.91	0.04	0.3	0.16	21.78	2.72	0.21	1.57	0.86	100.47

Cement paste was prepared at a water-to-cement ratio of 0.5 using a planetary centrifugal mixer. The paste was filled in cylindrical molds of 22.6 by 22.6 mm, covered with foil, and stored at 23 °C and 50% relative humidity for 24 h. After demolding, the samples were autoclaved at the target temperatures (120 to 200 °C in 20 K increments) for 14 days under saturated water vapor pressure and, after this, cooled in the autoclave to room temperature. Subsequently, the samples were crushed, ground with isopropanol in a McCrone mill and dried under vacuum at 40 °C for 2 days. The powder samples were mixed with an internal standard (10 wt% of ZnO). X-ray diffraction was performed with a Bragg-Brentano diffractometer (Empyrean, PANalytical). The Cu Kα radiation was generated with 40 kV and 40 mA, filtered by Ni and measured by a PiXcel^{1D}. For phase quantification, Rietveld refinements were performed using HighScore Plus 4.8. The structure data used for the refinements was taken from ICSD and is listed in Table 2.

Table 2: Phases with ICSD structure numbers used for Rietveld refinements.

Alite	22501	Portlandite	73467
Tricalcium aluminate	1880	Hydroxylellestadite	39775
Hydrogarnet (larger unit cell)	49772	Jaffeite	39725
Hydrogarnet (smaller unit cell)	172076	Reinhardbraunsite	200924
Calcite	166364	ZnO	155780

The thermodynamic modelling was conducted using the thermodynamic software GEMS (Kulik et al. 2012; Wagner et al. 2012) version 3.7. The databases PSI/Nagra 12/07 (Thoenen and Kulik 2003; Thoenen et al. 2014), Cemdata18 (Lothenbach et al. 2019) and datasets for zeolites (Ma and Lothenbach 2020a, 2020b) provided basic thermodynamic properties. Furthermore, the database cCSH for crystalline C-S-H and some additional phases forming at elevated temperatures and pressures (Hirsch et al.) was included. As the datasets of Ma and Lothenbach contain data for zeolites, the zeolites of Cemdata18 were deactivated for internal consistency. The species $Si_4O_8(OH)_4^{4-}$ of PSI/Nagra was deactivated as its data are only reliable for ambient conditions.

3. Results

The experimental results are presented in Figure 1. Despite a dwell time of 2 weeks, the samples autoclaved at 120 to 160 °C still contain small quantities of clinker phases, which diminish with rising temperature.

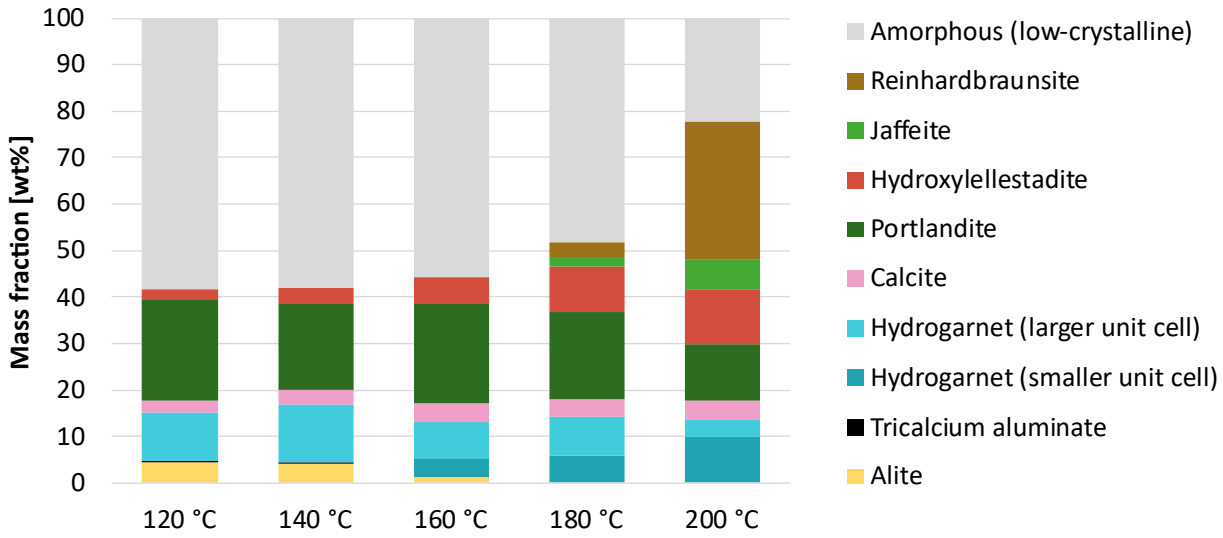


Figure 1: Solid phase assemblage in autoclaved pastes as determined by Rietveld refinement.

In general, the samples are quite similar in their phase assemblage. Nevertheless, a splitting of the hydrogarnet reflexes in XRD occurs in the temperature range between 140 and 160 °C, which persists at higher temperature. The summed share of the two hydrogarnets varies however only slightly between all samples. The share of calcite is nearly constant and increases only very slighty between 120 and 160 °C.

Further phases present in all samples are a low-crystalline phase (very likely C-S-H), portlandite and hydroxylellestadite. At lower temperatures, the low-crystalline C-S-H accounts for more than half of the sample. In the samples autoclaved at 180 and 200 °C, the two crystalline C-S-H phases reinhardbraunsite and jaffeite appear. While their share is still small at 180 °C, both, in particular reinhardbraunsite, gain at 200 °C while the portion of low-crystalline C-S-H diminishes. Simultaneously, a strong increase in the quantities of hydroxylellestadite and decrease of portlandite can be observed. Both of these effects are likely due to the reaction of low-crystalline C-S-H, which liberates the sulfate adsorbed on its large surface (Barbarulo et al. 2007). The destabilization of low-crystalline C-S-H leads consequently to release of sulfate, which is bound in hydroxylellestadite. Portlandite is likely consumed as the formation of reinhardbraunsite and jaffeite from low-crystalline C-S-H requires additional Ca.
Thermodynamic modelling predicts the formation of hillebrandite in the whole temperature range and meta-ettringite around 200 °C. Ettringites are known to be low temperature phases (Zhou and Glasser 2001), indicating an overestimation of the metaettringite stability at 200°C. Hillebrandite was not observed in the current experiments, and is known to form very slow or not at all depending on the experimental conditions (Garbev 2004). Consequently, both phases were deactivated in the modelling. The resulting thermodynamic models are qualitatively quite close to the experiment (Figure 2). The existence of portlandite, hydrogarnet, hydroxylellestadite and a small quantity of calcite agrees well with the experimental observations. The modelling even predicts the formation of two individual hydrogarnets indicating that the persistence of one sole hydrogarnet in the low-temperature samples may be due to kinetic reasons. Hydrotalcite and pyrolusite are predicted as well but not observed experimentally, which might be due to their small quantities and potentially low crystallinity (pyrolusite is not visible in Figure 2 due to low quantity). In experiment and simulation, the phase assemblage is dominated by C-S-H phases. The low-crystalline C-S-H in the experiment is likely metastable as:

- Experiments in the literature show that increase in dwell time and water content yield in more crystalline C-S-H phases
- Thermodynamic modelling predicts crystalline C-S-H (Figure 2)
- At higher temperature, the low-crystalline C-S-H decreases in quantity and crystalline C-S-H phases form, which occur in the thermodynamic predictions (Figure 1)

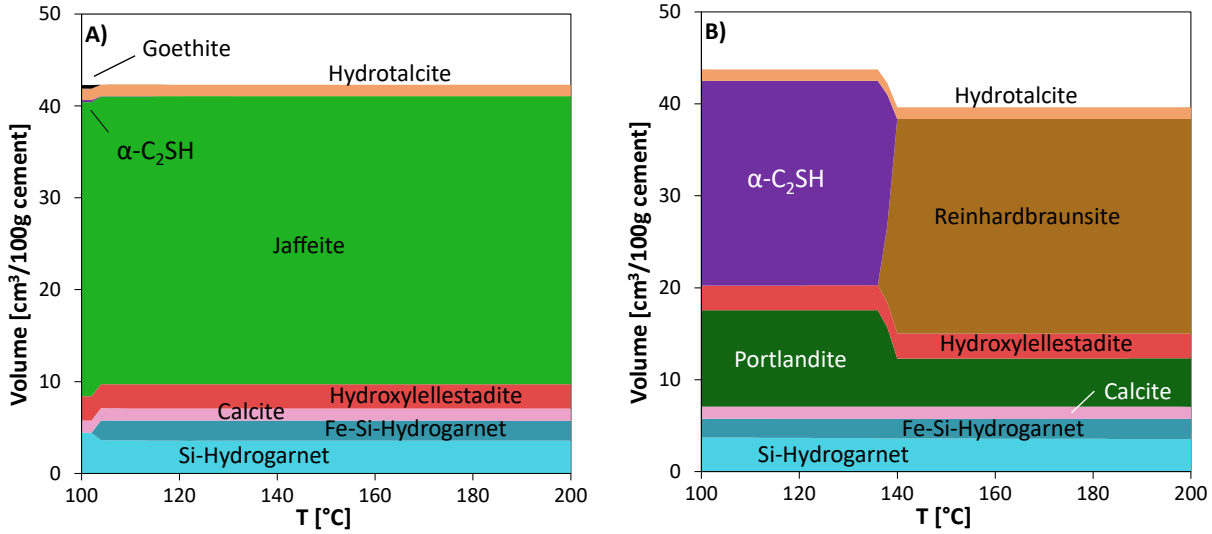


Figure 2: Thermodynamic modelling of the phase assemblage in autoclaved CEM I paste. A) with suppressed formation of metaettrinigte and hillebrandite, B) with suppressed formation of metaettrinigte, hillebrandite and jaffeite.

Hillebrandite formation seems to be kinetically hindered in the experiments. If hillebrandite is suppressed in the modelling, the formation of jaffeite is predicted but not of reinhardbraunsite. Reinhardbraunsite is only predicted if also jaffeite is prohibited to form. The samples at higher temperature possess higher shares of reinhardbraunsite than jaffeite. This could be interpreted in the way that reinhardbraunsite forms faster

than jaffeite (and hillebrandite) under the experimental conditions, potentially because less portlandite is required for the reaction of low-crystalline C-S-H to reinhardbraunsite than is needed for the reaction to jaffeite.

4. Conclusions

Combining several thermodynamic databases, the experimentally observed phase assemblage of a CEM I paste exposed to autoclaving was modelled successfully. Experimental results and modelling indicate that the C-S-H phases are still far from equilibrium after 2 weeks. Crystalline C-S-H phases were not observed in samples autoclaved between 120 and 160 °C. The other phases are found in the experiment as predicted by thermodynamic modelling disregarding minor phases. Further comparison studies between experimental work and thermodynamically predicted phase assemblages should be untertaken to test and refine the datasets.

Acknowledgements

The authors are grateful for founding of this work by German Federal Ministry of Economic Affairs and Energy in scope of the project “BeHeWaDS” (03ET1537A).

References

Barbarulo, R.; Peycelon, H.; Leclercq, S. (2007): Chemical equilibria between C–S–H and ettringite, at 20 and 85 °C. In *Cem. Concr. Res.* 37 (8), pp. 1176–1181. DOI: 10.1016/j.cemconres.2007.04.013.

Garbev, K. (2004): Struktur, Eigenschaften und quantitative Rietveldanalyse von hydrothermal kristallisierten Calciumsilikathydraten (C-S-H-Phasen). Forschungszentrum Karlsruhe in der Helmholtz-Gemeinschaft, Wissenschaftliche Berichte FZKA 6877. Doctoral thesis. Ruprecht-Karls-Universität Heidelberg, Heidelberg. Institut für Technische Chemie.

Hirsch, T.; Lothenbach, B.: Phase stabilities and thermodynamic properties of crystalline $CaO–SiO_2–H_2O$ phases above 100 °C (to be submitted).

Kulik, D.A.; Wagner, T.; Dmytrieva, S.V.; Kosakowski, G.; Hingerl, F.F.; Chudnenko, K.V.; Berner, U.R. (2012): GEM-Selektor geochemical modeling package: revised algorithm and GEMS3K numerical kernel for coupled simulation codes. In *Comput. Geosci.* 26 (012025), p. 189. DOI: 10.1007/s10596-012-9310-6.

Lothenbach, B.; Kulik, D.A.; Matschei, T.; Balonis, M.; Baquerizo, L.; Dilnesa, B. et al. (2019): Cemdata18: A chemical thermodynamic database for hydrated Portland cements and alkali-activated materials. In *Cem. Concr. Res.* 115, pp. 472–506. DOI: 10.1016/j.cemconres.2018.04.018.

Lothenbach, B.; Zajac, M. (2019): Application of thermodynamic modelling to hydrated cements. In *Cem. Concr. Res.* 123, p. 105779. DOI: 10.1016/j.cemconres.2019.105779.

Ma, B.; Lothenbach, B. (2020a): Synthesis, characterization, and thermodynamic study of selected Na-based zeolites. In *Cem. Concr. Res.* 135, p. 106111. DOI: 10.1016/j.cemconres.2020.106111.

Ma, B.; Lothenbach, B. (2020b): Thermodynamic study of cement/rock interactions using experimentally generated solubility data of zeolites. In *Cem. Concr. Res.* 135, p. 106149. DOI: 10.1016/j.cemconres.2020.106149.

Thoenen, T.; Hummel, W.; Berner, U.; Curti, E. (2014): The PSI/Nagra Chemical Thermodynamic Database 12/07. PSI report 14-04. Edited by Nuclear Energy and Safety Research Department Laboratory for Waste Management (LES). Paul Scherrer Institut (PSI). Villigen, Switzerland.

Thoenen, T.; Kulik, D. (2003): Nagra/PSI Chemical Thermodynamic Data Base 01/01 for the GEM-Selektor (V.2-PSI) Geochemical Modeling Code: Release 28-02-03. Internal Report TM-44-03-04. Edited by Paul Scherrer Institut (PSI). Available online at http://gems.web.psi.ch/TDB/doc/pdf/TM-44-03-04-web.pdf.

Tian, H.; Hirsch, T.; Stephan, D.; Lehmann, C. (2022): The Influence of Long-Term Autoclaving on the Properties of Ultra-High Performance Concrete. In *Front. Mater.* 9, Article 844268, p. 38. DOI: 10.3389/fmats.2022.844268.

Wagner, T.; Kulik, D.A.; Hingerl, F.F.; Dmytrieva, S.V. (2012): GEM-Selektor geochemical modeling package: TSolMod library and data interface for multicomponent phase models. In *Can. Mineral.* 50 (5), pp. 1173–1195. DOI: 10.3749/canmin.50.5.1173.

Werder, J. von; Simon, S.; Gardei, A.; Fontana, P.; Meng, B. (2021): Thermal and hydrothermal treatment of UHPC: influence of the process parameters on the phase composition of ultra-high performance concrete. In *Mater Struct* 54 (1), p. 250. DOI: 10.1617/s11527-021-01633-w.

Zhou, Q.; Glasser, F.P. (2001): Thermal stability and decomposition mechanisms of ettringite at <120°C. In *Cem. Concr. Res.* 31 (9), pp. 1333–1339. DOI: 10.1016/S0008-8846(01)00558-0.

A Multi-scale Model of Reinforcement Bars Corrosion Based on the Concentrated Electrolyte Theory and Three Dimensional Hierarchical Structure of Concrete

K. Szyszkiewicz-Warzecha[1], J. Deja[1], A. Lewenstam[1], A. Łagosz[1], J. Migdalski[1], J. Stec[1], A. Górska[1], R. Filipek[1]*

[1] *AGH University of Science and Technology, Faculty of Materials Science and Ceramics, Kraków, Poland*
Email: rof@agh.edu.pl

ABSTRACT

A 3D corrosion model of reinforced concrete structures based on the theory of conjugate transport in multicomponent concentrated electrolytes is formulated. A three-dimensional hierarchical structure of concrete containing aggregates together with their interfacial transition zones (ITZ), air pores, cracks and capillary pores was determined from XCT measurements and is an essential and novel element of the proposed model of rebars corrosion in concrete. The model is solved numerically using the finite element method and software COMSOL Multiphysics by the implementation of user defined governing equations together with proper initial and boundary conditions based on Butler–Volmer kinetics. Sensitivity analysis, including the influence of model parameters on the rate of reinforcement corrosion is performed. Verification of the reinforcement corrosion model in concrete of a real 3D hierarchical structure is performed. Corrosion tests on reinforced concrete specimens prepared from CEM I 42.5R and/or CEM III/A 42.5N cements with various w/c, aggregates sizes, capillary porosity and concrete cover thicknesses in various corrosive environments: chloride and/or carbonation are performed. The samples were examined by non-destructive methods: electric potential mapping on the concrete surface, electrochemical impedance spectroscopy and galvanostatic pulse, and compared with data obtained from the corrosion model simulations. That interpretation of measured impedance spectra is carried out on the basis of the proposed model.

KEYWORDS: *concrete, 3D model of rebars corrosion, hierarchical three dimensional structure, multi-scale model, X-ray computed tomography*

1. Introduction

Corrosion of the reinforcing steel in concrete structures is a serious problem from the perspective of both safety and economy and affects directly the sustainability and life-time of the infrastructure. Reinforced concrete has been used on a great scale in a variety of civil engineering constructions for a long time now hence the problems related to its durability and maintenance are of considerable importance because of the enormous scale of its usage and expected long service-time. Corrosion of reinforcing steel is one of the most common degradative processes which can affect reinforced concrete structures causing their loss of serviceability, needs for repairs, premature pulling down, and in extreme cases can lead to structural collapse (as in the case of the Genoa bridge collapse in 2019).

Despite ubiquity of its applications and long history during which engineers and scientists have been gathering practical knowledge on the corrosion behavior of reinforcing bars (rebars) in concrete, there are still important questions that are not satisfactorily answered. Especially significant are the interpretation of data obtained from short-term electrochemical tests and identification of the most vulnerable areas of corrosion attack. In order to achieve these goals it is important to improve a fundamental understanding of the electrochemistry of this complex and variable system.

A survey of published papers relevant to the outlined field shows that they usually tend to concentrate on one of the aspects that constitute the complex phenomena of transport in porous media coupled with the

corrosion heterogeneous reactions. Broadly speaking the focus is either on the electrochemical corrosion reactions and depassivation mechanisms (Hu, Q. *et al*. (2011), Poursaee, A. *et al*. (2010) and Liu, M. *et al*. (2017)) or on the transport of components in concrete matrix (Samson, E. *et al*. (2007) and Isgor, O.B. *et al*. (2019)). There are, of course, works which combine these two processes but they suffer from severe simplifications, such as the consideration of a limited number of species (usually – one) (Ožbolt, J. *et al.* (2011)), modeling the potential distribution in the framework of primary or secondary current distribution only (Isgor, O.B. (2016) and Warkus, J. *et al.* (2006)), and, in rare cases of simulating the multi-ion transport, using the dilute electrolyte theory of transport (Nernst–Planck flux) (Liu, C. *et al.* (2014) and Liu, Q.F. *et al.* (2015)). Most of models assume 1D and 2D geometries, rarely 3D geometry (Clément, A. *et al.* (2012) and Tian, Ye *et al.* (2019)). Moreover, durability of concrete has been a subject of internationally recognized protocols and methods such as DuraCrete (2020) and fib Model Code for Service-Life Design (International Federation for Structural Concrete (2006)).

2. Mathematical model

Thermodynamics of irreversible processes postulates that movement of mass in a system depends on the negative gradient of the (electro)chemical potential, $\tilde{\mu}_i$. More specifically, the electro-diffusion flux of *i*-th species in a multicomponent mixture is given by

$$\mathbf{J}_i = -L_i \nabla\left(\frac{\tilde{\mu}_i}{T}\right), \tag{1}$$

where L_i is the linear phenomenological coefficient for diffusional flow of *i*-th species which is related to the diffusion coefficient by the relation $L_i = c_i D_i / R$ where c_i is concentration of *i*-th species (mol m^{-3}) and R is the universal gas constant. The electrochemical potential is usually split into "chemical" part and "electrical" part $\mu_i = \mu_i^{\ominus} + RT\ln(\gamma_i c_i) + z_i F\varphi$, where γ_i is the activity coefficient, z_i is the charge number of *i*-th species ($z_i = 0$ for a neutral species), φ is the electric potential, F is the Faraday constant. Putting all these relations together we obtain the following flux for an isothermal process in concentrated electrolyte:

$$\mathbf{J}_i = -D_i \nabla c_i - D_i c_i \nabla(\ln \gamma_i) - D_i z_i \frac{F}{RT} c_i \nabla \varphi. \tag{2}$$

This flux is useful for computing concentration distribution provided that we can insert into (2) a correct expression for activity coefficients as functions of concentrations, $\gamma_i = \gamma_i(c_1,\ldots,c_N)$. The Pitzer theory, described below, will be utilized for this purpose here.

The flux (2) is used in a mass balance equation for each species

$$\frac{\partial c_i}{\partial t} + \nabla \cdot \mathbf{J}_i = R_i, \quad i = 1,\ldots,N, \tag{3}$$

where R_i is the reaction term for *i*-th species. In the presented model we consider five species: Na^+, Cl^-, OH^-, Fe^{2+}, O_2.

Two of them are involved in a bulk reactions:

$$Fe^{2+} + 2OH^- \rightarrow Fe(OH)_2 \tag{4}$$

$$4Fe(OH)_2 + O_2 + 2H_2O \rightarrow 4Fe(OH)_3 \tag{5}$$

Assuming that the intermediate form $Fe(OH)_2$ in reactions (4) and (5) is very short-lived we can consider a summary reaction:

$$4Fe^{2+} + 8OH^- + O_2 + 2H_2O \rightarrow 4Fe(OH)_3 \tag{6}$$

Hence reaction terms will be

$$R_{Na^+} = R_{Cl^-} = 0,\ R_{OH^-} = -2k c_{O_2} c_{Fe^{2+}} c_{OH^-},\ R_{Fe^{2+}} = -k c_{O_2} c_{Fe^{2+}} c_{OH^-},\ R_{O_2} = -\tfrac{1}{4} k c_{O_2} c_{Fe^{2+}} c_{OH^-}, \tag{7}$$

where k is a rate constant for the precipitation reaction (mol^{-2} dm^6 s^{-1}).

Boundary conditions result from the assumed corrosion reactions

$$\begin{aligned} &\textit{iron oxidation}: && \mathrm{Fe} \rightarrow \mathrm{Fe}^{2+} + 2e^{-} \\ &\textit{oxygen reduction}: && \mathrm{O_2} + 2\mathrm{H_2O} + 4e^{-} \rightarrow 4\mathrm{OH}^{-} \end{aligned} \tag{8}$$

The Butler–Volmer equation which connects the electrode potential with the rate of reaction serves as a boundary condition for species Fe^{2+}, O_2 and OH^-. Hence, we have the following equalities on the boundary:

$$\begin{aligned} &\textit{anode}: \quad -\boldsymbol{n}\cdot\mathbf{J}_{\mathrm{Fe}^{2+}} = \frac{1}{2F} i_{\mathrm{Fe}}, \quad \textit{cathode}: \quad -\boldsymbol{n}\cdot\mathbf{J}_{\mathrm{O_2}} = \frac{1}{4F} i_{\mathrm{O_2}}, \quad -\boldsymbol{n}\cdot\mathbf{J}_{\mathrm{OH}^-} = \frac{1}{F} i_{\mathrm{O_2}}, \\ &i_{\mathrm{Fe}} = i_{\mathrm{Fe}}^{0} \cdot \exp\left(\alpha_{\mathrm{Fe}} \frac{F}{RT} (U_{app} - \varphi - E_{\mathrm{Fe}}^{eq}) \right), \quad i_{\mathrm{O_2}} = -i_{\mathrm{O_2}}^{0} \cdot (c_{\mathrm{O_2}} / c_{ref}) \cdot \exp\left(-\alpha_{\mathrm{O_2}} \frac{F}{RT} (0 - \varphi - E_{\mathrm{O_2}}^{eq}) \right). \end{aligned} \tag{9}$$

where $i_{\mathrm{Fe}}^{0}, i_{\mathrm{O_2}}^{0}$ are exchange current densities (A cm^{-2}), $\alpha_{\mathrm{Fe}}, \alpha_{\mathrm{O_2}}$ transfer coefficients, and $E_{\mathrm{Fe}}^{eq}, E_{\mathrm{O_2}}^{eq}$ equilibrium potential for oxidation and reduction reactions (8), respectively. The remaining boundary conditions assume blocking barrier (zero-flux) conditions

$$-\boldsymbol{n}\cdot\mathbf{J}_i = 0, \quad i = \mathrm{Na}^{+}, \mathrm{OH}^{-}, \mathrm{Fe}^{2+}, \mathrm{Cl}^{-}, \mathrm{O_2}. \tag{10}$$

3. Three dimensional concrete structure

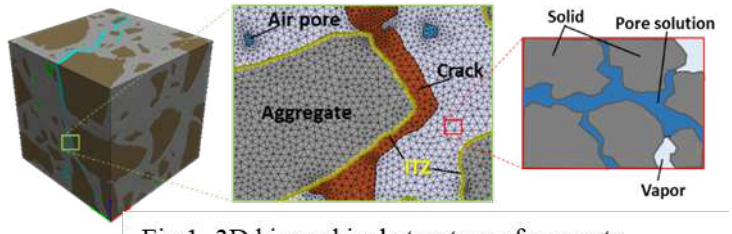


Fig.1. 3D hierarchical structure of concrete.

A three-dimensional hierarchical structure of concrete containing aggregates together with their interfacial transition zones (ITZ), air pores, cracks and capillary pores were determined (Fig. 1). A 3D structure of real concrete samples, which is an essential and novel element of the proposed model of corrosion, was reconstructed based on X-ray computed tomography (XCT) measurements and developed algorithms (Stec, J. *et al*. (2019)). Capillary pore structure (pore size distribution, porosity, tortuosity and constrictivity) was explored using XCT and mercury intrusion porosimetry.

4. Ions activities in liquid in pores

We implemented the Pitzer model of ionic activity coefficients in electrolytes and obtained expressions for activity coefficient of cations (Na^+, K^+, Ca^{2+}) and anions (OH^-, Cl^-) in an aqueous solution of electrolyte (liquid in concrete pores). The Pitzer model can be used for concentrated electrolytes (up to 6 mol dm^{-3}) and contrary to other models, is the most accurate in representation of the mean ionic activities.

5. Results

A multi-scale 3D corrosion model of reinforcement in concrete encompassing a real hierarchical structure and using the concentrated electrolyte fluxes was formulated and solved numerically using the finite element method and COMSOL Multiphysics platform by implementing user defined governing equations together with proper initial and boundary conditions. Tests of the model and its sensitivity analysis, including the influence of model parameters on the rate of reinforcement corrosion were performed.
The simulations were performed for a cylindrical sample of 25 mm diameter and 50 mm height with the steel rod embedded inside (Fig. 2a). The sample was submerged in an external electrolyte (5 % NaCl) that filled a cubic container. The concrete cover is a porous medium (a network of connected micropores), thus the electrolyte can penetrate the pore system from the external electrolyte. The 3D microstructure of the concrete sample was obtained by X-ray computed tomography. The detailed positions of mortar, aggregates, and the steel rebar were identified by segmentation procedure performed by the SimpleWare ScanIP software (Simpleware, 2023) – Fig. 2 b and c.

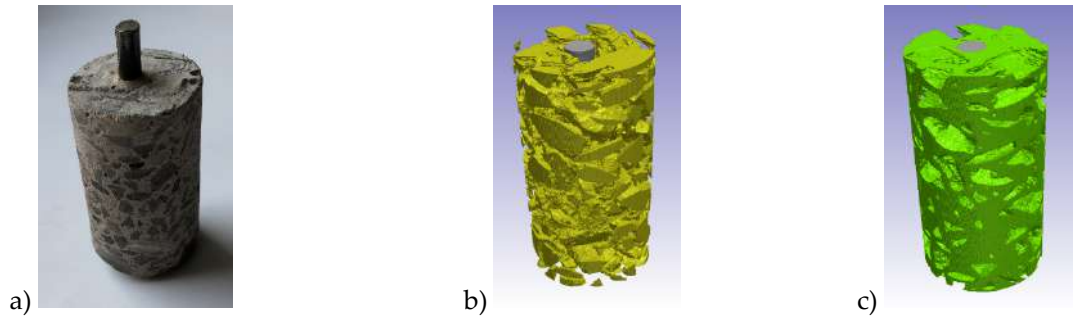


Fig. 2. A photograph of the concrete sample for which simulations in were performed (a). Computed tomography reconstruction of: (b) aggregates in the sample – yellow, and (c) mortar – green. The steel rod is displayed as dark-grey color.

Diffusion coefficients of ions in external solution were assumed to be equal to their diffusion coefficients in aqueous solution (Jasielec J.J. *et al*. 2020). Effective diffusion coefficients $D_i^{eff} = \phi D_i / \tau^2$ are modified molecular diffusion coefficients by two empirical parameters which characterize a porous medium: porosity (ϕ) and tortuosity (τ). The effective diffusion coefficient of chloride ions were calculated using the inverse method and experimentally measured chlorides penetration depth (Jasielec J.J. *et al*. 2020). Based on chloride diffusion coefficient in electrolyte and effective chloride diffusion coefficient, the geometry coefficient of porous structure of cementitious material: $\phi / \tau^2 = D_{\mathrm{Cl}}^{eff} / D_{\mathrm{Cl}} = 2.9 \cdot 10^{-3}$ was calculated. Using the geometry coefficient ϕ / τ^2, the effective diffusion coefficients of sodium, potassium and hydroxide ions were calculated.

A quantitative description of ions transport in cementitious materials was studied. Important differences in the ions transport rates for mortar sample and concrete sample (including its microstructure, aggregates, and porosity) are observed. Fig. 3 shows chloride concentration in concrete sample immersed in NaCl solution (a) and the differences between chloride ions concentration with or without activities, i.e., when activity coefficient is equal to 1 (b).

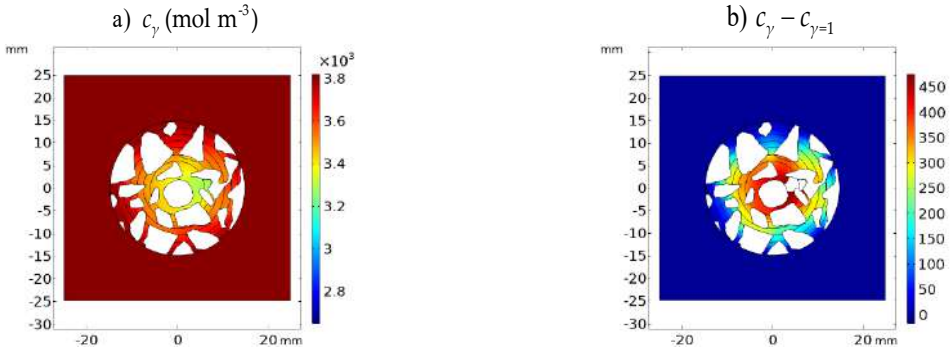


Fig. 3. Calculated concentration distribution c_γ of Cl^- in the concret sample after 1200 h of immersion in 20% NaCl water solution assuming Pitzer activity model a). Deviation of Pitzer activity model solution with ideal solution approximation (γ=1) $c_\gamma - c_{\gamma=1}$ for Cl^- b).

It can be observed that the potential is higher when activities are used. This is particularly pronounced close to the sample rebar. The effect of activity on the ion distribution shows that a concentration due to the ionic activity is observed for Na^+ and Cl^- ions. The 3D concrete structure and ions activities have a particularly pronounced impact on electric potential in the sample and consequently on the speed of reinforcement corrosion (see Fig. 4).

Verification of the model was carried out using a real 3D hierarchical structure extracted from XCT measurements of reinforced concrete samples prepared from CEM I 42.5R and CEM III/A 42.5N cements with various w/c, aggregates sizes, capillary porosity and concrete cover thicknesses in corrosive environments containing chlorides.

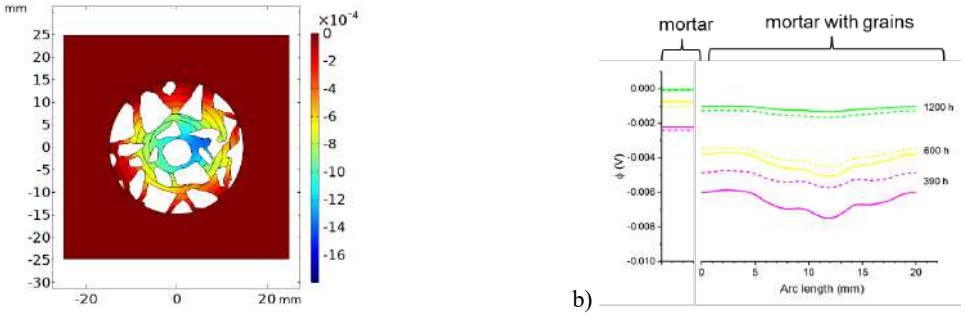


Fig. 4. a) Non-uniform potential distribution (V) in a concrete sample. b) Calculated potential distribution in the mortar and concrete samples at the surface of the steel rod – comparison.

6. Conclusions

The proposed model includes a real concrete structure and sample geometry (obtained from X-ray computed tomography) and takes into account ionic chemical activity using an advanced Pitzer model. Non-destructive methods: electric potential mapping on the concrete surface, electrochemical impedance spectroscopy and galvanostatic pulse can be interpreted on the basis of the proposed corrosion model. The results of the galvanostatic pulse method is compared with the simplified analysis based on the Randles and extended Randles (capacitance replaced by a constant phase element, CPE) circuits. They illustrate the capabilities of the proposed model and its possible applications.

Acknowledgements

This research was funded by the National Science Center, Poland, grant No. 2020/37/B/ST8/02805.

References

Hu, Q. *et al*. (2011) "The crevice corrosion behavior of stainless steel in sodium chloride solution", *Corr. Sci.* 53: 4065-4072

Poursaee, A. *et al*. (2010) "Corrosion of steel bars in OPC mortar exposed to NaCl, $MgCl_2$ and $CaCl_2$: Macro- and micro-cell corrosion perspective", *Cem. Concr. Res.* 40: 426-430

Liu, M. et al. (2017) "Corrosion behavior of low-Cr steel rebars in alkaline solutions with different pH in the presence of chlorides", *J. Electroanal. Chem.* 803: 40-50

Samson, E. et al. (2007) "Modeling the transport of ions in unsaturated cement-based materials", *Computers and Structures* 85: 1740–1756

Isgor, O.B. *et al*. (2019) "A nearly self-sufficient framework for modelling reactive transport processes in concrete", *Materials and Structures* 52:3: 1–17

Ožbolt, J. *et al.* (2011) "3D Numerical modelling of steel corrosion in concrete structures", *Corr. Sci.* 53: 4166-4177

Isgor, O.B. (2016) "Modeling corrosion of steel in concrete" *in "Corrosion of Steel in Concrete Structures"*, edit. A. Poursaee, Elsevier Ltd.

Warkus, J. *et al.* (2006) "Numerical modelling of corrosion – Theoretical backgrounds", *Mater. Corr.* 57: 614–617

Liu, C. *et al.* (2014) "The Use of Finite Element Methods in the Modeling of Localized Corrosion", ECS Interface winter: 47–51

Liu, Q.F. *et al.* (2015) "A numerical study on chloride migration in cracked concrete using multi-component ionic transport models", *Comput. Mater. Sci.* 99: 396-416

Clément, A. *et al.* (2012) "Numerical study of the linear polarisation resistance technique applied to reinforced concrete for corrosion assessment", *Eur. J. Environ. Civ. Eng.* 16: 491–504

Tian, Ye *et al.* (2019) "An investigation on the three-dimensional transport of chloride ions in concrete based on X-ray computed tomography technology", *Constr. Build. Mat.* 221: 443–455

DuraCrete (2020) Final Technical Report EU – Brite EuRam III, DuraCrete – Probabilistic performance based durability design of concrete structures, Document BE95-1347/R17, CUR, Gouda, The Netherlands

International Federation for Structural Concrete (2006) "Model code for service life design", *fib* Bulletin 34, Lausanne.

Stec, J., Tarasiuk, J., Nagy, S., Smulski, R., Gluch, J., Filipek, R. (2019), "Non-destructive investigations of pore morphology of micropore carbon materials", *Ceramics International*, 45:3483-3491

Jasielec, J. J.; Stec, J.; Szyszkiewicz-Warzecha, K.; Łagosz, A.; Deja, J.; Lewenstam, A.; Filipek, R. (2020) "Effective and Apparent Diffusion Coecients of Chloride Ions and Chloride Binding Kinetics Parameters in Mortars: Non-Stationary Diffusion–Reaction Model and the Inverse Problem", *Materials*, *13*: 5522–5545

Simpleware ScanIP (2023) Available online: https://www.synopsys.com/simpleware/software/scanip.html/

The 16th International Congress on the Chemistry of Cement 2023 (ICCC2023)
"Further Reduction of CO_2 -Emissions and Circularity in the Cement and Concrete Industry"
September 18–22, 2023, Bangkok, Thailand

Multi-scale model for characterizing thermal conductivity of cement-based materials with nano inclusions

Jiahan Liu[1*]

[1] *Department of Civil Engineering, Shanghai Normal University, Shanghai, China*
Email: liujh@shnu.edu.cn

ABSTRACT

High carbon emissions generated by energy consumption has restricted the further coordinated development of construction industry seriously. Thermal conductivity is the most basic factor of researching energy consumption and developing energy-saving buildings. Hence, predicting the thermal properties of cement-based materials accurately is very important to quantify the thermal stresses in structures. This study aims to establish a multiscale model for the thermal conductivity of cement-based materials with considering the influence of interfacial thermal resistance and inclusion size. Nano-scale materials, such as carbon nanotube(CNT) with high thermal conductivity, has been widely used in developing heat storage concrete material. Hence, we focus on the effects of the thermal properties and microstructure of inclusions in nanoscale. The results showed that thermal properties of inclusions in nanoscale plays an important role on predicting the effective thermal conductivity of cement-based materials. The findings of this study help predict the thermal properties of old cement-based materials accurately and design new heat storage cement-based composites rationally.

KEYWORDS: *Energy consumption, Thermal conductivity, Cement-based materials, Multi-scale, Nano materials*

1. Introduction

Thermal properties of cement-based materials, the most extensively used materials in construction, are essentially important for energy consumption and developing energy-saving buildings. Predicting the thermal properties of cement-based materials accurately is essentially important to quantify the thermal stresses in structures and deepen the scientific understanding of thermally insulating effects of the materials for construction (Xiong et al.(2016)).

According to the recent research, there are some factors influencing the thermal conductivity, including type and volume fraction of aggregate, mineralogical character, water-to-cement ratio and saturation degree as well. Previous studies have proposed some experimental methods and calculation models of thermal conductivity. However, these methods are purely empirical and independent. Multi scale method is one of the most important theories in the study of heterogeneous materials. In microscale, cement-based composites can be treated as a porous inorganic material with microstructure, including C-S-H matrix, CH crystals, cement clinker and micro-meter porosity. Multi scale method is widely used in analysis of thermal and mechanical property of composite materials (Ji et al.(2014), Wei et al.(2013)).

Based on Eshelby equivalent inclusion principle and multi-scale nature of the microstructure of cement-based composites, this study attempted to employ micromechanical approach to evaluate the thermal properties of the composites using Mori-Tanaka homogenization method. A generalized multi-scale micromechanical model is developed to capture the thermal conductivity of the cement-based composites. Nano-scale materials, as carbon nanotube(CNT) which has high thermal conductivity, has been widely used in developing heat storage concrete material. The modelled results are comparable to the data from experimental measurement of cement-based materials with CNTs to verify the accuracy.

2. Micromechanical model of thermal conductivity

2.1 Multi-scale nature of cement-based materials

It is generally accepted that cement-based materials are typically multi-scale composite materials with extreme complexities in chemical components, and heterogeneities in physical properties and spatial distributions. By connecting the physical and chemical properties of each scale, a systematic understanding of the nature of materials will be established. Here the multi-scale microstructure of cement-based materials in four elementary levels is revisited; see Figure 1 (Constantinides et al. (2004), Jennings(2000), Sadat et al. (2018), Krakowiak et al. (2015)).

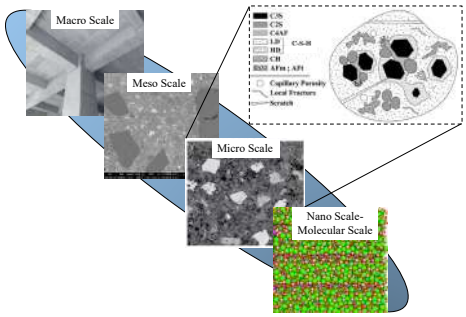


Figure 1 Four-level microstructure of cement-based composites

Level Ⅰ (10^{-8}-10^{-6}m): The presence of C-S-H is estimated at this scale, which is the hydration products of C_2S and C_3S. It is now established that C-S-H exists in two different forms, a low density (LD) and a high density (HD). The distinction of the two types is the difference of microstructure.
Level Ⅱ (10^{-6}-10^{-4}m): The C-S-H matrix with large CH crystals, cement clinker and micrometer porosity forms the cement paste. The cement clinker is including C_2S, C_3S, C_3A and C_4AF as well. The property of micrometer porosity is related to w/c.
Level Ⅲ (10^{-4}-10^{-2}m): This scale refers to mortar, which is a three phase composite material composed of cement pastes, sand particle inclusions, and an ITZ.
Level Ⅳ (10^{-2}-10^{-1}m): Concrete is considered as a three phase material composed of aggregates embedded in a mortar matrix and an ITZ in this scale.
Once the type, volume fraction and physical properties of the phases in a level are known, by using an appropriate homogenization method, the mechanical and thermal properties of the composite at a higher level can be calculated. In this way, a multi-scale model can be established to predict the physical properties of cement-based materials.

2.2 Thermal conductivity multi-scale model of composite materials

Mean-field theories present a consistent physical-mechanical framework to describe the behavior of composite materials with inhomogeneous structures. Based on the theories, the thermal properties of a material in a scale can be obtained by averaging the local phases in the subscale. The homogenized thermal conductivity at level i+1 is supposed to be $\boldsymbol{K}_{\text{hom}}(\boldsymbol{X})$, which is $\boldsymbol{K}_i(\boldsymbol{x})$ at level i. And $\boldsymbol{X}$, $\boldsymbol{x}$ are position vectors at level i+1 and level i, respectively. By spatially averaging the former identity, the homogenized thermal conductivity is expressed like:

$$\boldsymbol{K}_{\text{hom}}(\boldsymbol{X}) = \left\langle \boldsymbol{K}_i(\boldsymbol{x}) \cdot \boldsymbol{A}(\boldsymbol{x}) \right\rangle_V \tag{1}$$

V is the volume of representative volume element (RVE).

Based on mean-field theory, temperature gradients at levels i and i+1 can be assumed to be linearly related via a second order localization tensor at point x, $\boldsymbol{A}(\boldsymbol{x})$. Here the Mori-Tanaka method was used, so the localization tensor is expressed as:

$$\boldsymbol{A}_s = [\boldsymbol{I} + \boldsymbol{S}_s : (\boldsymbol{K}_{\text{M}}^{-1}\boldsymbol{R}\boldsymbol{K}_s\boldsymbol{R}^T - \boldsymbol{I})]^{-1} \left\langle [\boldsymbol{I} + \boldsymbol{S}_s : (\boldsymbol{K}_{\text{M}}^{-1}\boldsymbol{R}\boldsymbol{K}_s\boldsymbol{R}^T - \boldsymbol{I})]^{-1} \right\rangle_V^{-1} \tag{2}$$

Where $\boldsymbol{S}$ is an Eshelby tensor for the thermal conducting problem(Eshelby(1957)), $\boldsymbol{I}$ is the unit tensor, and $\boldsymbol{K}_M$, $\boldsymbol{K}_T$ are the thermal conductivity of the matrix and inclusion, respectively. The rotation matrix $\boldsymbol{R}$ is used to transform the local to global coordinate systems.
With the absence of preferential orientation for inclusions, the rotation matrix is reduced to $\boldsymbol{R} = \boldsymbol{I}$. Use the above equation in (2) (Qomi et al.(2015)):

$$\boldsymbol{A}_s = \boldsymbol{A}_s \boldsymbol{I} = \frac{3K_{\mathrm{M}}}{2K_{\mathrm{M}} + K_s} \tag{3}$$

We can obtain the generalized multi-scale micromechanical model:

$$K_{\mathrm{MT}} = \frac{f_{\mathrm{M}} K_{\mathrm{M}} + \sum_{s=1}^{n} f_s K_s A_s}{f_{\mathrm{M}} + \sum_{s=1}^{n} f_s A_s} \tag{4}$$

Where f_{M}, f_s are the volume fraction of the matrix and inclusion, respectively, n is the number of the inclusion phases, K_{M}, K_s are the thermal conductivity of the matrix and inclusion, respectively.

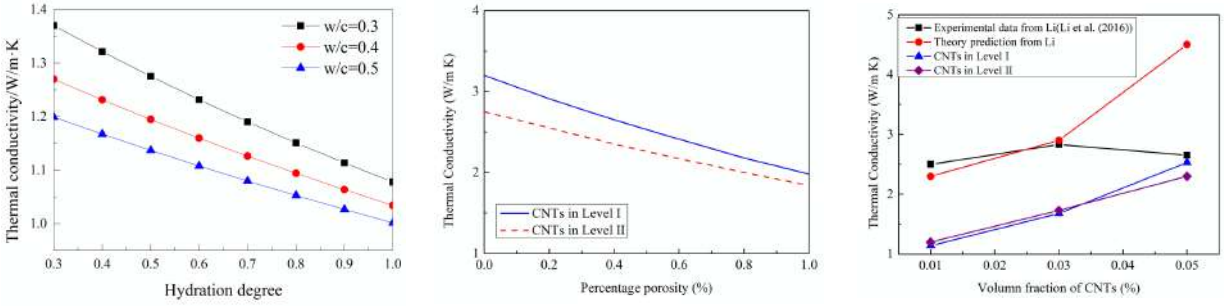
3. Application to cement-based materials with nano inclusions

In this paper, we choose carbon nanotube as nano inclusions of cement-based materials.The experimental data including the properties of nanotube and thermal conductivitis of composies are from Du et al. (2020), Li et al (2013).Based on the scale of nano inclusions, the nano materials can be assumed in level I or level II. Hence, we considered two situation to calculate the thermal conductivity of cement-based materials with nano inclusions.

The multi-scale model of cement paste is simplified to be a two-scale model from level I to level II. It need two times homogenization in the calculation of the thermal conductivity. The components and thermal conductivity of each solid phases need to be known. In the current work, the aluminate-related phases, such as C_3A and C_4AF, and their hydration products were regarded as C_3S and C-S-H to estimate the thermal conductivity of a cement paste due to the lack of data. The densities and thermal conductivities of C_2S, C_3S, CH, C-S-H, air and water are listed in Table 1 (Qomi et al.(2015), Farouki (1986)).

Table 1. Density and thermal conductivity of main phases in cement paste.

	Density (g/cm^3)	Thermal conductivity (W/m·K)	Sources
C_2S	3.55	3.45	Qomi et al. (Qomi et al.(2015))
C_3S	3.57	3.35	Qomi et al. (Qomi et al.(2015))
CH	2.25	1.32	Qomi et al. (Qomi et al.(2015))
C-S-H	2.40	0.98	Qomi et al. (Qomi et al.(2015))
Air		0.026	Farouki (Farouki.(1986))
Water	1	0.06	Farouki (Farouki.(1986))



(a) (b) (c)

Figure 2 (a)Plots of predicted thermal conductivity of cement pastes against hydration degree;(b) Predicted thermal conductivity with different volume fraction of porosity percentage; (c) Comparation of predicted and experimental data of cement paste with CNTs

Figure 2(a) presents the predicted thermal conductivity of cement pastes with different w/c ratios against hydration degree. We focus that the thermal conductivity of cement paste decreases with increasing hydration degree. This is because the thermal conductivity values of CSH and CH are lower than those of clinker phases. Figure 2(b) and (c) presents the comparison of predicted and measured thermal conductivity in of a cement paste with carbon nanotube with w/c ratio of 0.4. Figure 2(b)shows the predicted thermal conductivity with different volume fraction of porosity percentage. We focus the

thermal conductivity decrease with increasing volume fraction of CNTs. This is because the thermal conductivity values of CNTs are much higher than other phases. Actually, CNT can decrease the porosity of cement-based materials significantly. Hence, the prediction of cement-based materials with nano inclusions in this paper consider the range of porosity percentage. Figure 2(c) shows the comparation of predicted and experimental data of cement paste with CNTs. It is found that the predicted values are in a good agreement with the experimental results with high CNT volume fraction.

4. Conclusions

Based on Eshelby equivalent inclusion principle and multi-scale nature of microstructure of cement-based composites, this study attempted to employ micromechanical approach to evaluate the thermal conductivity. Using Mori-Tanaka homogenization method, a generalized multi-scale micromechanical model is developed to capture the thermal conductivity of the cement-based composites. The modelled results are comparable to the experimental measurement of cement-based materials with CNTs. The following is research findings from the study.

1) The main factors influencing the thermal conductivity of cement-based materials are w/c, volume fraction of the phases and hydration degree. For composites with nano materials, the thermal properties and volume fraction of nano materials are also important for predicting the thermal conductivity.

2) It is verified that The CNT can decrease the porosity of cement-based materials, which will affect the thermal properties of the composites.

3) There are errors between the predicted and experimental values of thermal conductivity of cement-based materials. This is because the simplification of the spatial distribution and thermal property of pore water by utilizing the Eshelby equivalent inclusion principle and Mori-Tanaka homogenization method.

Acknowledgements

The authors acknowledge the National Natural Science Foundation of China (No. 5220080300 for JHL).

References

Xiong, M.X. and Liew, J.Y.R. (2016) “Mechanical behavior of ultra-high strength concrete at elevated temperatures and fire resistance of ultra-high strength concrete filled steel tubes”, *Materials and Design*, 104:414-427.

Ji, R., Zhang, Z., Liu, L. and Wang, X. (2014) “Development of the random simulation model for estimating the effective thermal conductivity of insulation materials”, *Building and Environment*, 80: 221-227.

Wei, S., Chen, Y., Zhang, Y. and Jones, MR. (2013) “Characterization and simulation of microstructure and thermal properties of foamed concrete”, *Construction and building materials*, 47: 1278-1291.

Constantinides, G. and Ulm, F.J. (2004) “The effect of two types of CSH on the elasticity of cement-based materials: Results from nanoindentation and micromechanical modeling”, *Cement & Concrete Research*, 34 (1): 67-80.

Jennings, H.M. (2000) “A model for the microstructure of calcium silicate hydrate in cement paste”, *Cement & Concrete Research*, 30 (1): 101-116.

Krakowiak, K.J., Thomas, J.J., Musso, S., James, S., Akono, A.T. and Ulm, F.J. (2015) “Nano-chemo-mechanical signature of conventional oil-well cement systems: Effects of elevated temperature and curing time”, *Cement & Concrete Research*, 67: 103-121.

Sadat, M.R., Muralidharan, K. and Zhang, L.Y. (2018) “Reactive molecular dynamics simulation of the mechanical behavior of sodium aluminosilicate geopolymer and calcium silicate hydrate composites”, *Computational Materials Science*, 150: 500-509.

Eshelby, J.D. (1957) “The determination of the elastic field of an ellipsoidal inclusion, and related problems”, *Proceedings of the Royal Society of London A: Mathematical, Physical and Engineering Sciences. The Royal Society*. 241(1226): 376-396.

Qomi, M.J.A., Ulm, F.J. and Pellenq, R.J.M. (2015) “Physical origins thermal properties of cement paste”, *Physical Review Applied*, 3(6): 064010.

Farouki, O.T. (1986) “Thermal properties of soils”.

Du, M., Jing, H., Gao, Y., Su, H. and Fang, H. (2020)“Carbon nanomaterials enhanced cement-based composites: advances and challenges”, *Nanotechnology Reviews*, 9(1):115-135.

Li, H., Zhang, Q. and Xiao, H. (2013) “Self-deicing road system with a CNFP high-efficiency thermal source and MWCNT/cement-based high-thermal conductive composites”, *Cold Regions Science & Technology*, 86(FEB.):22-35.